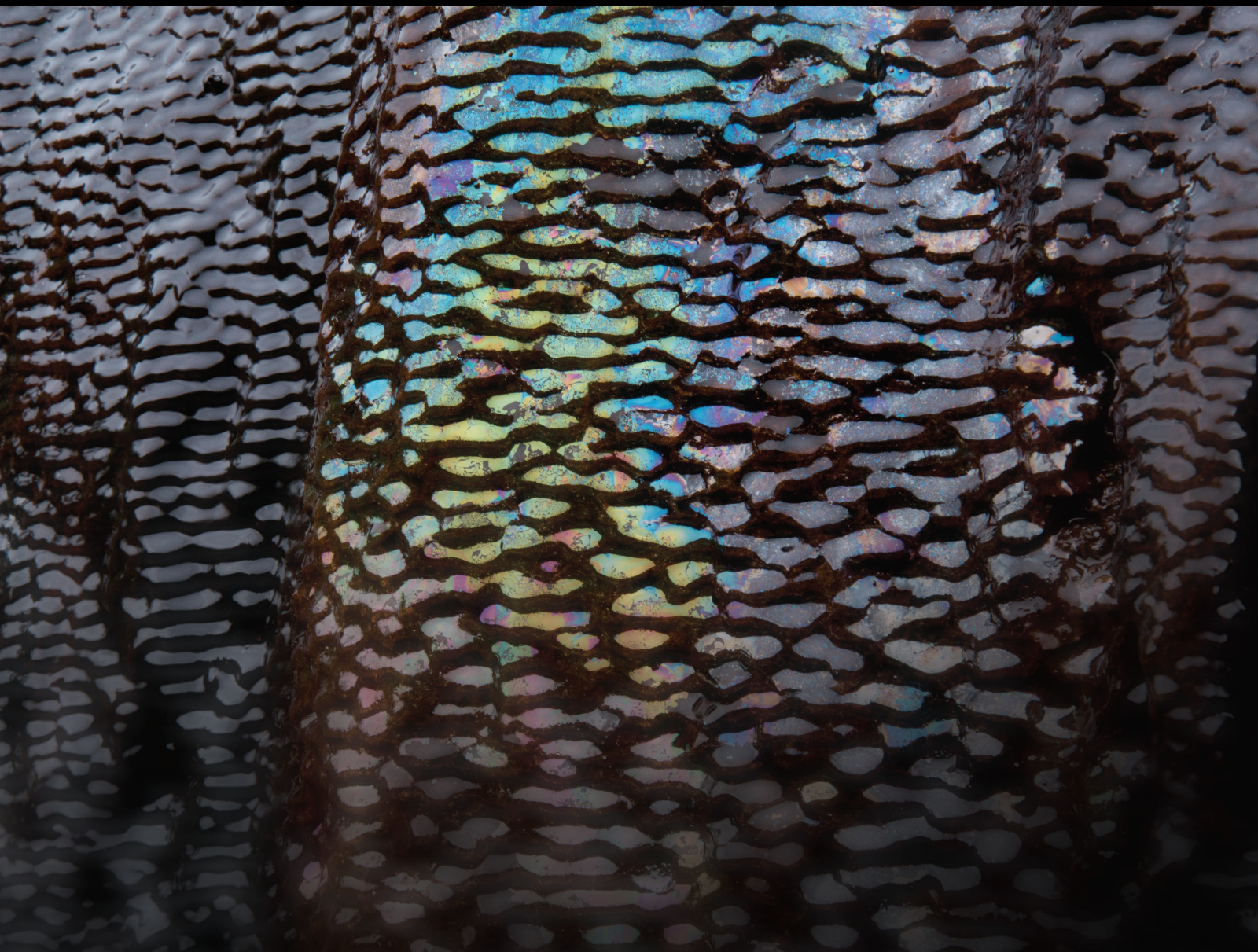


Multiscale and Multiphysical Approaches to Fluids Flow in Unconventional Reservoirs

Lead Guest Editor: Jianchao Cai

Guest Editors: Muhammad Sahimi, Wen-Dong Wang, Stefan Iglauer, and Wei Wei





Multiscale and Multiphysical Approaches to Fluids Flow in Unconventional Reservoirs

Geofluids

**Multiscale and Multiphysical
Approaches to Fluids Flow in
Unconventional Reservoirs**

Lead Guest Editor: Jianchao Cai

Guest Editors: Muhammad Sahimi, Wen-Dong
Wang, Stefan Iglauer, and Wei Wei







Copyright © 2021 Hindawi Limited. All rights reserved.

This is a special issue published in "Geofluids." All articles are open access articles distributed under the Creative Commons Attribution License, which permits unrestricted use, distribution, and reproduction in any medium, provided the original work is properly cited.



























Chief Editor

































Umberta Tinivella, Italy

Associate Editors

Paolo Fulignati , Italy
Huazhou Li , Canada
Stefano Lo Russo , Italy
Julie K. Pearce , Australia

Academic Editors


Basim Abu-Jdayil , United Arab Emirates
Hasan Alsaedi , USA
Carmine Apollaro , Italy
Baojun Bai, USA
Marino Domenico Barberio , Italy
Andrea Brogi , Italy
Shengnan Nancy Chen , Canada
Tao Chen , Germany
Jianwei Cheng , China
Paola Cianfarra , Italy
Daniele Cinti , Italy
Timothy S. Collett , USA
Nicoló Colombani , Italy
Mercè Corbella , Spain
David Cruset, Spain
Jun Dong , China
Henrik Drake , Sweden
Farhad Ehya , Iran
Lionel Esteban , Australia
Zhiqiang Fan , China
Francesco Frondini, Italy
Ilaria Fuoco, Italy
Paola Gattinoni , Italy
Amin Gholami , Iran
Michela Giustiniani, Italy
Naser Golsanami, China
Fausto Grassa , Italy
Jianyong Han , China
Chris Harris , South Africa
Liang He , China
Sampath Hewage , Sri Lanka
Jian Hou, China
Guozhong Hu , China
Lanxiao Hu , China
Francesco Italiano , Italy
Azizollah Khormali , Iran
Hailing Kong, China

Karsten Kroeger, New Zealand
Cornelius Langenbruch, USA
Peter Leary , USA
Guangquan Li , China
Qingchao Li , China
Qibin Lin , China
Marcello Liotta , Italy
Shuyang Liu , China
Yong Liu, China
Yueliang Liu , China
Constantinos Loupasakis , Greece
Shouqing Lu, China
Tian-Shou Ma, China
Judit Mádl-Szonyi, Hungary
Paolo Madonia , Italy
Fabien Magri , Germany
Micòl Mastroicco , Italy
Agnes Mazot , New Zealand
Yuan Mei , Australia
Evgeniy M. Myshakin , USA
Muhammad Tayyab Naseer, Pakistan
Michele Paternoster , Italy
Mandadige S. A. Perera, Australia
Marco Petitta , Italy
Chao-Zhong Qin, China
Qingdong Qu, Australia
Reza Rezaee , Australia
Eliahu Rosenthal , Israel
Gernot Rother, USA
Edgar Santoyo , Mexico
Mohammad Sarmadivaleh, Australia
Venkatramanan Senapathi , India
Amin Shokrollahi, Australia
Rosa Sinisi , Italy
Zhao-Jie Song , China
Ondra Sracek , Czech Republic
Andri Stefansson , Iceland
Bailu Teng , China
Tivadar M. Tóth , Hungary
Orlando Vaselli , Italy
Benfeng Wang , China
Hetang Wang , China
Wensong Wang , China
Zhiyuan Wang , China
Ruud Weijermars , Saudi Arabia







Bisheng Wu , China
Da-yang Xuan , China
Yi Xue , China
HE YONGLIANG, China
Fan Yang , China
Zhenyuan Yin , China
Sohrab Zendeboudi, Canada
Zhixiong Zeng , Hong Kong
Yuanyuan Zha , China
Keni Zhang, China
Mingjie Zhang , China
Rongqing Zhang, China
Xianwei Zhang , China
Ye Zhang , USA
Zetian Zhang , China
Ling-Li Zhou , Ireland
Yingfang Zhou , United Kingdom
Daoyi Zhu , China
Quanle Zou, China
Martina Zucchi, Italy

Contents


Experimental Investigation on Organic Matter Orientation Characteristics of Terrestrial and Marine Shale in China

Dunqing Liu, Hongkui Ge , Yinhao Shen, and Kui Zhang
Research Article (21 pages), Article ID 8895350, Volume 2021 (2021)


Laboratory Study on Hydrate Production Using a Slow, Multistage Depressurization Strategy

Yanlong Li , Chuqiao He, Nengyou Wu , Qiang Chen , Changling Liu , Zhixue Sun , Yurong Jin , and Qingguo Meng
Research Article (13 pages), Article ID 4352910, Volume 2021 (2021)


Estimation of the Resistivity Index via Nuclear Magnetic Resonance Log Data Based on Fractal Theory

Cheng Feng , Chuang Han, Wenxing Duan, Wei Wang, Yuntao Zhong, Ziyang Feng, and Ning Zhang
Research Article (10 pages), Article ID 8871096, Volume 2020 (2020)



A Model for a Multistage Fractured Horizontal Well with Rectangular SRV in a Shale Gas Reservoir

Jianfa Wu, Jian Zhang, Cheng Chang, Weiyang Xie , and Tianpeng Wu
Research Article (18 pages), Article ID 8845250, Volume 2020 (2020)


A Review of Gas Flow and Its Mathematical Models in Shale Gas Reservoirs

Bo-ning Zhang, Xiao-gang Li, Yu-long Zhao , Cheng Chang, and Jian Zheng
Review Article (19 pages), Article ID 8877777, Volume 2020 (2020)


A Simplified Capillary Bundle Model for CO₂-Alternating-Water Injection Using an Equivalent Resistance Method

Wendong Wang , Fankun Meng , Yuliang Su, Lei Hou, Xueyu Geng, Yongmao Hao, and Lei Li
Research Article (14 pages), Article ID 8836287, Volume 2020 (2020)




Experimental Study on the Effective Utilization of Reserves in Tight Sandstone Gas Reservoirs and Their Applications

Jie Zhang, Feifei Fang , Weijun Shen , Huaxun Liu, Shusheng Gao, and Liyou Ye
Research Article (13 pages), Article ID 8854299, Volume 2020 (2020)


A New Methodology for the Multilayer Tight Oil Reservoir Water Injection Efficiency Evaluation and Real-Time Optimization

Lin Cao, Jianlong Xiu , Hongjie Cheng, Hui Wang, Shujian Xie, Hui Zhao, and Guanglong Sheng
Research Article (17 pages), Article ID 8854545, Volume 2020 (2020)


A Digital Twin for Unconventional Reservoirs: A Multiscale Modeling and Algorithm to Investigate Complex Mechanisms

Tao Zhang , Yiteng Li, Jianchao Cai, Qingbang Meng , Shuyu Sun , and Chenguang Li
Research Article (12 pages), Article ID 8876153, Volume 2020 (2020)

Investigation on the Secondary Generation of Natural Gas Hydrates in Horizontal Wellbore Caused by Pressure Jump during the Depressurization Development of Hydrate Bearing Layers


Qingjun Du, Yongge Liu, Jian Hou, Lina Shi , Wenbin Wang, and Kang Zhou
Research Article (14 pages), Article ID 8815455, Volume 2020 (2020)

Study on a New Rock Fracability Evaluation Model of Shale Gas Reservoir

Fei Wang , Yonghao Zhang, Xin Li, and Xue Han

Research Article (11 pages), Article ID 8882899, Volume 2020 (2020)

The Determination of a Damage Model for Mudstone under Uniaxial Loading in Acidic Conditions

K. Cao, L. Ma , Y. Wu, A. J. S. (Sam) Spearing, Naseer Muhammad Khan, and Y. Xie


Research Article (12 pages), Article ID 8888750, Volume 2020 (2020)

Gas Transport in Shale Nanopores with Miscible Zone

Xiang Li , Sai Xu , Youzhi Hao , Daolun Li , and Detang Lu 

Research Article (14 pages), Article ID 6410614, Volume 2020 (2020)

Verification of Fracture Reorientation and Analysis of Influence Factors in Multiple Fracturing Treatment

Mingjing Lu , Yuliang Su, Marte Gutierrez, Yaohua Zhan, Kai Chen, and Bintao Zheng

Research Article (13 pages), Article ID 2457814, Volume 2020 (2020)

A New Model to Calculate Oil-Water Relative Permeability of Shaly Sandstone

Huiyuan Bian , Kewen Li, Binchi Hou, and Xiaorong Luo


Research Article (11 pages), Article ID 8842276, Volume 2020 (2020)

Multifractal Analysis of Pore Structure and Evaluation of Deep-Buried Cambrian Dolomite Reservoir with Image Processing: A Case from Tarim Basin, NW China

Xiaojun Zhang, Haodong Han , Jun Peng , and Yingchun Gou

Research Article (18 pages), Article ID 7131573, Volume 2020 (2020)

Investigation of Multistage Hydraulic Fracture Optimization Design Methods in Horizontal Shale Oil Wells in the Ordos Basin

Suotang Fu, Jian Yu, Kuangsheng Zhang, Hanbin Liu, Bing Ma , and Yuliang Su

Research Article (17 pages), Article ID 8818903, Volume 2020 (2020)

Analysis of Dynamic Damage-Induced Porosity Changes of Granites in Leaching Mining Technique Based on SHPB Test

Yichen Miao , Changwu Liu , Zhiliang He, Yuanjun Ma, Haikuan Wu, and Ding Wang


Research Article (12 pages), Article ID 8844168, Volume 2020 (2020)

Permeability Characteristics of Coal after Supercritical CO₂ Adsorption at Different Temperatures

Xueying Liu , Jin Yu , Di Wu , and Xiaochun Xiao 

Research Article (8 pages), Article ID 8836349, Volume 2020 (2020)


Permeability of the Hydrated Shale under Cyclic Loading and Unloading Conditions

Liu Xianshan , Li Man, Xu Ming, and Kang Zhiyong

Research Article (16 pages), Article ID 8863249, Volume 2020 (2020)

Contents

Apparent Permeability Prediction of Coal Matrix with Generalized Lattice Boltzmann Model considering Non-Darcy Effect

Zhigao Peng , Shenggui Liu, Yingjun Li, and Qi Yao


Research Article (14 pages), Article ID 8830831, Volume 2020 (2020)

Representative Elementary Volume of Rock Using X-Ray Microcomputed Tomography: A New Statistical Approach

Taufiq Rahman, Hamed Lamei Ramandi , Hamid Roshan, and Stefan Iglauer

Research Article (13 pages), Article ID 8866486, Volume 2020 (2020)

Experiments and Modeling on the Influence of Interfacial Tension on Imbibition Height of Low-Permeability Reservoir

Xiaoxia Ren , Aifen Li, Piyang Liu, and Bingqing He


Research Article (10 pages), Article ID 8837897, Volume 2020 (2020)

Multiple Approaches to Quantifying the Effective Porosity of Lacustrine Shale Oil Reservoirs in Bohai Bay Basin, East China

Binyu Ma, Qinhong Hu , Shengyu Yang , Na Yin, Hongguo Qiao, Tao Zhang, and Mianmo Meng

Research Article (13 pages), Article ID 8856620, Volume 2020 (2020)

A New Upscaling Method for Fluid Flow Simulation in Highly Heterogeneous Unconventional Reservoirs

Qi Zhang, Huibin Yu , Xiaofeng Li, Tiesheng Liu, and Junfeng Hu


Research Article (11 pages), Article ID 6213183, Volume 2020 (2020)

Multifractal Analysis of Acoustic Emissions during Hydraulic Fracturing Experiments under Uniaxial Loading Conditions: A Niutitang Shale Example

Jingqiang Tan , Jun Xie , Lei Li , Qiao Lyu , Jianqiang Han , and Zhengguang Zhao 






Research Article (19 pages), Article ID 8845292, Volume 2020 (2020)

Transient Flow Theory of Multiple-Fractured Horizontal Wells with Complex Mechanisms in Shale Gas Reservoirs

Dianfa Du , Genkai Zhang, Yanwu Zhao, Xiaofei Sun, and Bin Zhang



Research Article (17 pages), Article ID 7364734, Volume 2020 (2020)

Investigating the Influences of Pore-Scale Characteristics on Tight Oil Migration by a Two-Phase Pore Network Model

Jianhui Zeng , Yongchao Zhang , Jingsheng Ma , Changling Liu , and Zhe Cao 

Research Article (13 pages), Article ID 4890758, Volume 2020 (2020)

Pore Structure Fractal Characterization and Permeability Simulation of Natural Gas Hydrate Reservoir Based on CT Images



Hang Bian, Yuxuan Xia, Cheng Lu , Xuwen Qin , Qingbang Meng, and Hongfeng Lu

Research Article (9 pages), Article ID 6934691, Volume 2020 (2020)


Maximum Sizes of Fluid-Occupied Pores within Hydrate-Bearing Porous Media Composed of Different Host Particles

Lele Liu , Nengyou Wu , Changling Liu , Qingguo Meng, Haitao Tian, Yizhao Wan, and Jianye Sun
Research Article (14 pages), Article ID 8880286, Volume 2020 (2020)


A Numerical Study on Gas Flow through Anisotropic Sierpinski Carpet with Slippage Effect

Shuxia Qiu, Lipai Zhang, Zhenhua Tian, Zhouting Jiang, Mo Yang , and Peng Xu 
Research Article (12 pages), Article ID 2396704, Volume 2020 (2020)

A Discrete Fracture Modeling Approach for Analysis of Coalbed Methane and Water Flow in a Fractured Coal Reservoir


Tianran Ma, Hao Xu, Chaobin Guo, Xuehai Fu , Weiqun Liu, and Rui Yang
Research Article (15 pages), Article ID 8845348, Volume 2020 (2020)

Effect of Perforation Interval Design on Gas Production from the Validated Hydrate-Bearing Deposits with Layered Heterogeneity by Depressurization

Yingli Xia, Tianfu Xu, Yilong Yuan, and Xin Xin 
Research Article (20 pages), Article ID 8833884, Volume 2020 (2020)

Research Article

Experimental Investigation on Organic Matter Orientation Characteristics of Terrestrial and Marine Shale in China

Dunqing Liu,^{1,2} Hongkui Ge ,^{1,2} Yin hao Shen,^{1,2} and Kui Zhang³

¹State Key Laboratory of Petroleum Resources and Prospecting, China University of Petroleum, Beijing 102249, China

²Unconventional Natural Gas Institute, China University of Petroleum, Beijing 102249, China

³CNPC Engineering Technology R&D Company Limited, Beijing 100007, China

Correspondence should be addressed to Hongkui Ge; gehongkui@163.com

Received 10 April 2020; Revised 24 August 2020; Accepted 6 March 2021; Published 7 April 2021

Academic Editor: Constantinos Loupasakis

Copyright © 2021 Dunqing Liu et al. This is an open access article distributed under the Creative Commons Attribution License, which permits unrestricted use, distribution, and reproduction in any medium, provided the original work is properly cited.

As an essential component in shale, OM (organic matter) grains and their arrangements may play essential roles in affecting the anisotropy of the reservoir. However, OM grains are commonly treated as an evenly distributed isotropic medium in current studies, and few works have been done to investigate their detailed arrangement characteristics. In this study, terrestrial and marine shale samples were collected from three different shale plays in China, and the arrangement characteristics of OM grains in each sample were investigated by SEM (scanning electron microscope) image analysis. The results indicate that OM grains in shale are not evenly distributed in isotropic medium, and their directional alignment is pervasive in both marine and terrestrial shale. OM grains in shale tend to subparallel to the bedding section, and their orientation degree and controlling factors differ among different shales. OM grains in samples from terrestrial C-7 (Chang-7 Formation) exhibit the strongest directionality in their arrangement, and OM grains in samples from marine LMX (Longmaxi Formation) shale in the Fuling area also exhibit strong directional alignment. While in samples from marine LMX shale in the Baojing area, their directional alignment is much weaker. Shales with high clay content, high TOC (total organic carbon), low thermal maturity, and flat reservoir structure get more OM grains parallel to the bedding section. The biogenetic texture of graptolite in marine LMX shale is the dominating factor leading to the strong directional alignment of the OM grains. However, syncline structure may disorganize the preformed directional alignment and weaken the directionality of the OM grains, which results in the OM arrangement difference between LMX samples from Fuling and Baojing. While the compaction of the layered clay particles is the dominating mechanism leading to the strong directional alignment of the OM grains in terrestrial shale samples from C-7.

1. Introduction

Shales are multiphase, multiscale, and compositionally diverse sedimentary rock, and with the development of horizontal drilling and hydraulic fracturing technology in recent years, shale has become a research hotspot across the world [1, 2]. Besides their low porosity and ultralow permeability, shales also get more complex mineral composition than conventional reservoirs. Besides quartz, feldspar, and calcite, they also contain considerable amounts of clay minerals, and a few but nonnegligible OM is another essential component of shale [3]. The complexity in mineral constituent results in the complex pore structure and fickle mineral

arrangement, and both factors endowed shale with much stronger anisotropy than conventional reservoirs [4, 5].

The manifestation of anisotropy in shale is diverse, among which elastic wave velocity, permeability, and mechanical properties are the most focused points from the field to the lab. These anisotropic characteristics play critical roles in the exploration and development of the shales, and scholars focus on this topic believe the anisotropy exhibited in shale is mainly attributed to the alignment of clay minerals, nonspherical pores, or microcracks [6, 7]. Their effects on gas transport, methane adsorption, fracture development, and other aspects have been widely investigated [8–11]. Among these studies, the alignment of clay minerals and

natural fractures is the most emphasized factors, and they were regarded as the major factors controlling the heterogeneity of shale [12–14]. Besides, several compositional and arrangement models have been presented to predict the petrophysical parameters of the shales [15, 16]. However, the arrangement of OM was not considered in these models.

Besides clay and fractures, many researchers have pointed out that certain OM particles are not evenly distributed in the shale matrix, and some OM particles may get an elongated shape and show specific directionality in their alignment [17, 18]. Nevertheless, detailed studies on OM grains orientation have seldom been carried out, and OM is still regarded as an evenly distributed isotropic medium in most of the models. The orientation of the OM grain was neglected in these models, and the corresponding excuse is their low content. However, the TOC in some shales with rich OM sources can reach 20% [19], and OM grains may take a very considerable volume due to their much lower density. Additionally, new nanocomputed tomography and SEM studies have revealed that OM grains with highly developed pores may form into continuous organic frameworks, and these OM grains with good connectivity may form a dominant pathway in shale. Thus, their arrangement may intensify the permeability anisotropy of shale [20]. Furthermore, studies also indicated that some types of OM grains without organic pores might still exhibit anisotropy in their inner structure due to their biogenetic texture [21], which may also affect the anisotropy of shale if they were directionally arranged.

Besides organic pores, studies have also shown that microfractures in shale are closely related to the elongated OM particles [22]. Recent nanoindentation and AFM (atomic force microscope) studies have proved that Young's modulus of the OM grains in shale is much lower than clay or other inorganic minerals and OM is the softest part in shale [23–25], and the development of organic pores may further lower their Young's modulus [26]. Besides, OM grains also get a much larger thermal expansivity than the ambient inorganic mineral particles [27]. These features make OM grains in shale more sensitive to the stress and thermal change during deposition, compaction, and thermal maturation. Thus, fractures are more likely to be formed at the boundary between OM and inorganic mineral particles, which may further affect the anisotropy on permeability, elastic wave velocity, and other vital features in return. Thus, the orientation of OM grains in shale deserves more attention and investigation.

In this study, marine and terrestrial shale samples were collected from 4 wells in China, and their mineral constituent, TOC, and R_o were investigated. The morphological and arrangement characteristics of OM grains in each sample were compared and investigated by SEM image processing. Moreover, the effects of mineral contents, TOC, and thermal maturity on OM grain orientation and the corresponding forming mechanism were also discussed.

2. Samples and Methods

The detailed parameters of the shale samples used herein are listed in Table 1. The mineralogical composition was

obtained by XRD (X-ray diffractometer) (model Bruker D8, 45kv, 35 mA) at State Key Laboratory of Petroleum Resources and Prospecting at China University of petroleum, Beijing. The analysis was performed in accordance with Chinese Oil and Gas Industry Standard SY/T 5163-2010. The TOC of samples JY11 and JY45 was obtained by a carbon and sulfur analyzer (model LECO CS844) in the test center of Exploration and Development Institute in Jiangnan Oil Field, Wuhan, and the analysis was performed in accordance with Chinese National Standard GB/T 19145-2003. The TOC of the rest two samples and R_o data were acquired from relevant literature.

Sample JY11 and JY45 were collected from Fuling shale gas play in Chongqing, which is the largest shale gas play in China. Sample BY was collected from an exploratory well in the Baojing area, Hunan. These three samples were all collected from LMX, which is characterized by high OM abundance and favorable organic types to generate large amounts of gas. Sampled JY11 and JY45 were collected from the same submember of LMX, and their TOC, R_o , and mineral constituent are very similar. Their TOC is around 3%, and their R_o ranges from 1.8% to 2.9%, suggesting a stage of high maturity and more complicated diagenesis. While the R_o of sample BY is 3.28%, which is the highest among the four samples. Sample YY was collected from C-7, Shanxi, which is a typical terrestrial shale. The TOC of the samples from C-7 ranges from 1.7% to 9.8%, with a mean value of 5.73%. The R_o of samples from C-7 is much lower than LMX, which ranges from 0.7% to 1.3%, indicating sample YY is within the oil window stage.

According to the XRD results, siliceous and clay minerals are the dominating minerals in the four samples. Sample YY has the highest clay content, which is over 50%, and quartz occupied another 25.1%. While in sample JY11, JY45, and sample BY, the clay content is around 30% and quartz occupied about 40%. The specific types of clay minerals in these samples were not further analyzed. According to the researches of Yang et al. [28] and Ji et al. [31], the predominant clay mineral in LMX shale is illite, which accounts for more than 65%, and the primary clay mineral in terrestrial C-7 shales is illite-smectite mixed layers (with an average value of 43%) and then followed by illite ranging from 25% to 48%.

During the sample preparation, abundant graptolites were found on samples collected from LMX, and their amount is much larger in samples from Fuling than that in samples from Baojing. Researches have indicated that graptolites in shale can contribute to TOC [32, 33], and as Figure 1(a) shown, these graptolites are usually subparallel to the bedding section. Thus, it may be an important part of contributing to the directionality of the OM grains in shale. As shown in Figure 1(b), small shale pieces were collected to investigate the mineral constituent and detailed microstructure of the graptolites. A field emission SEM (model FEI quanta200) was adopted to capture SEM images of the graptolites. These small samples were not polished to keep their microstructure, and they were all coated with a thin gold film to enhance the image quality.

Besides these small samples, slice samples were also prepared to investigate the OM orientation. As shown in

TABLE 1: Parameters of the shale samples.

Sample	Formation	Sedimentary Environment	Source	TOC (wt%)	R_o (%)	Clay	Mineralogical composition (wt%)			
							Quartz	Feldspar	Calcite	Pyrite
JY11	LMX	Marine	Jaoshiba	3.3	1.8-2.9 ^a	28.9	47.1	8.8	10.8	4.4
JY45	LMX	Marine	Jaoshiba	3.03	1.8-2.9 ^a	32.2	39.5	8.3	15.7	4.3
BY	LMX	Marine	Baojing	2.33 ^b	3.28 ^b	27.5	44.9	12.2	11.3	4.1
YY	C-7	Terrestrial	Yanchang	1.7-9.8 ^c	0.7-1.3 ^{a,c}	50.3	25.1	2.2	17.2	5.2

Note: ^aThe data was from [28]. ^bThe data was from [29]. ^cThe data was from [30].

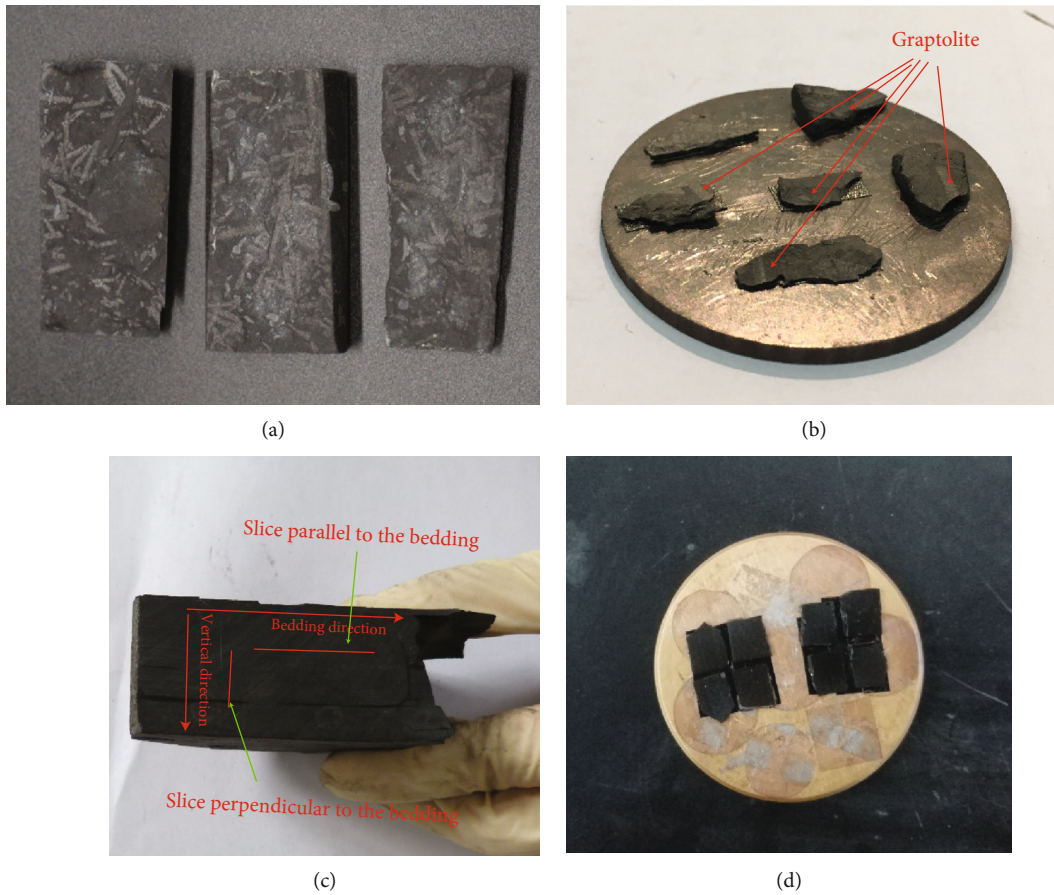


FIGURE 1: Shale samples used in this study. (a) Samples with abundant graptolites. (b) Samples for graptolite observation. (c) Schematic plot of the cutting direction. (d) Slice samples after polishing and coating.

Figure 1(c), two slices were orthogonally cut out from each sample, among which one sample is parallel to the bedding section and the other is vertical to the bedding section. For the convenience of the expression in the rest of this paper, we call the profile parallel to bedding direction as TS (transverse section), and the profile vertical to bedding direction as LS (longitudinal section). The slice samples were firstly mechanically polished and then polished by argon-ion to enhance surface flatness. Moreover, all these slice samples were coated with a thin gold film to enhance the image quality. Slice samples complete coating and polishing are shown in Figure 1(d), and a cold field emission SEM (model Hitachi SU8010) was adopted to capture images from these slice samples.

According to our tests, SEM images captured at $\times 500$ or $\times 1000$ magnification can reach the right balance between ideal OM grain quantity and acceptable sharpness, and both factors are critical to the accuracy of the subsequent image processing and analysis. The SEM image capturing was conducted in the State Key Laboratory of Petroleum Resources and Prospecting at China University of Petroleum, Beijing. As SEM images herein were saved as 8 bits grayscale figures, the brightness of the particles is in direct proportion to the atomic number of the elements inside. Thus, OM grains in SEM images usually are much darker than the ambient inorganic minerals, and pyrite grains usually are the brightest [34]. Based on that brightness contrast, the Weka Trainable Segmentation plugin in Image J segmented the OM grains

and pyrite grains in all SEM figures. This plugin is a machine learning-based semiautomatic tool to produce pixel-based segmentations, and it has been widely used as a powerful and efficient tool in SEM image processing [35].

Figure 2 demonstrates the image processing steps. After the OM and pyrite segmentation, they were identified and numbered by Analyze Particles Function in Image J. This function can find the major axis and minor axis of the identified particle, and the AR (aspect ratio) as well as the angle between the major axis and horizontal axis was then calculated. The AR can reflect the shape of the grains, and the angle represents their orientation. Particles with an area smaller than 20 pixel^2 (the resolution of the SEM image is 1280×960) were excluded to reduce the influence of pixel noises. The segmented OM and pyrite grains were then merged into one figure to investigate their coexistence relationship. 7 to 9 images were captured from each slice sample, and the statistical data of MA (mean angle) and SDA (standard deviation of the angles) of each image were then calculated. The MA indicates the central tendency of the grain orientation, and the SDA indicates the dispersion degree of the grain orientation. Sample with smaller SDA means OM grains inside get more definite directionality in their orientation, and there are more OM grains parallel to the MA direction.

3. Results

3.1. Characteristics of the Graptolite under SEM. Graptolites are widely distributed in organic-rich LMX shale in South China, and it has been reported to be closely related to the OM enrichment in LMX shale [36, 37]. According to the core observation, most graptolites are preserved as black or gray lamellate films, and their distribution can be clump together or randomly dispersed. Due to the overlap effect, the size of the graptolite in core scale can reach several centimeters, and their abundance varies a lot from one core to another.

The chemical composition of graptolite is controversial, and the chitinous substance was initially believed to be the main composition. Subsequent studies demonstrated that aromatic structure with aliphatic groups consisted of the main body of graptolite. Thus, it will dealkylate during the maturation and can act as good hydrocarbon-generating material in shale [38]. The EDS results shown in Figure 3 indicate that carbon is the dominant element of the graptolite in our samples, and several related studies have also drawn similar conclusions [39, 40]. Due to its unique biogenetic texture, the geometrical characteristic of graptolite may differ significantly from other OM grains.

As shown in Figure 4(a), the graptolite (indicated by the yellow dash line) is in a lamellar structure with a width of several millimeters, while the length can reach several centimeters. The main body of graptolite is made up of cortex and central canal (Figure 4(b)), and the size of these lamellar cortexes is around dozens of microns, which is much larger than the ambient inorganic grains. Moreover, a sharp boundary can be observed between the lamellar cortex and the outside matrix (Figures 4(b) and 4(c)).

Unlike most OM grains in shale that developed with massive spongy pores, only a few shallow pores can be observed on these lamellar cortexes (Figure 4(c)). Some lamellar cortex has broken into several fragments, suggesting lamellar cortex may be more brittle than those amorphous OM grains (Figure 4(d)), and the surface of these lamellar cortexes is much smoother than other grains in the matrix, which may reduce its adhesive strength with the ambient mineral particles. Besides the shallow holes, a few moldic pores were found on the graptolite surface (Figure 4(e)), and the diameter of which can reach $2.5 \mu\text{m}$. Organic pores in amorphous OM grains are usually under micron scale, while nanoscale organic pores were not observed in graptolites collected from Fuling samples. The absence of the nanoscale organic pores may cause by the shielding of the gold film, or it may be the result of low thermal maturity. In other studies, abundant nanometer-sized spongy pores were observed on the graptolites from LMX (Figures 4(g)–4(i)), and these spongy pores exhibited anisotropy inner the lamellar cortex. Moreover, most elongated organic pores were subparallel to the bedding section [36, 37]. The difference of the organic pore development in the graptolites indicates that the maturity of the graptolites may vary significantly among different shale plays.

The maturity of graptolite is not easy to be identified from SEM images, but the color of graptolites with lower thermal maturity is usually much darker [33]. Moreover, spongy pores are more developed in OM particles with higher thermal maturities. These features can help estimate the maturity of the OM grains. The color of the graptolites in our sample is dark black, and pores inner graptolites are less developed, both of which suggest the thermal maturity of the graptolite in LMX samples herein may be much lower than those amorphous OM grains. According to the SEM images, due to the biogenetic texture, these graptolites derived OM grains with lower thermal maturity may exhibit much stronger anisotropy in its structure and orientation.

3.2. Distribution Characteristics of the OM Particles

3.2.1. OM Orientation in Sample BY. As shown in Figures 5(a) and 5(b), most OM particles in sample BY are amorphous and they are dispersed randomly in both LS and TS, and the occurrence relationship between OM and pyrite particles is also irregular in both LS and TS. Pyrite grains in shale are usually coexisted with the OM particles [28], but the later OM maturation and diagenesis may alter their coexistence relationship. The OM particles in sample BY are not closely adjoined to those pyrite grains, suggesting sample BY may undergo intricate diagenetic processes, and these pyrite or OM grains may have migrated away from its original position.

Unlike graptolite-derived OM shown in Figure 3, the shape of most OM grains in sample BY is flocculent. According to the research of Curtis et al. [41] and Nie et al. [42], these flocculent or amorphous OM grains usually get higher maturity as the maturation may increase the inner pressure and induce more spongy pores. Those organic pores may destroy the structural integrity of the OM grains, and the

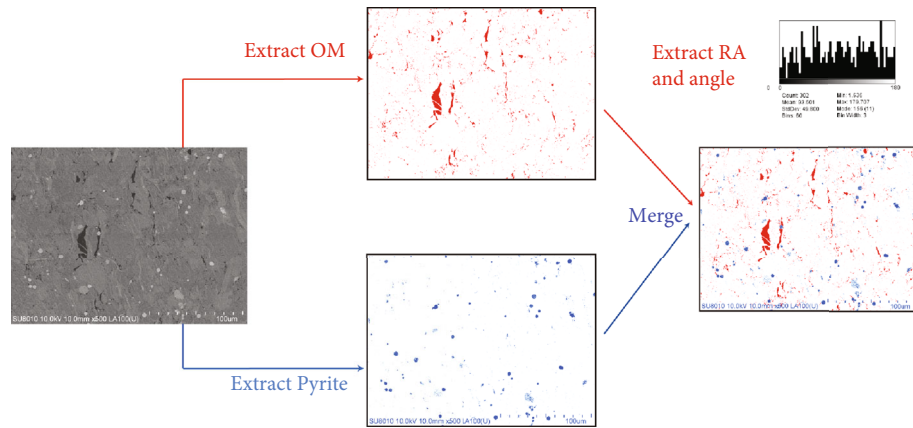
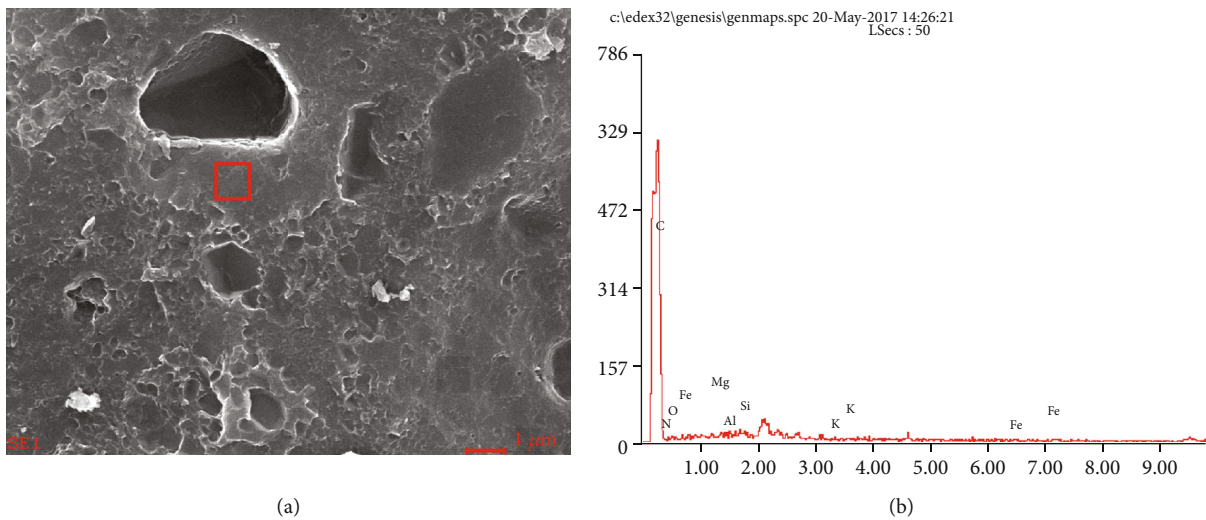


FIGURE 2: Typical image processing procedures.



CK	89.09	91.17
NK	06.38	05.60
OK	03.80	02.92
MgK	00.16	00.08
AlK	00.22	00.10
SiK	00.24	00.10
KK	00.00	00.00
FeK	00.11	00.02
Matrix	Correction	ZAF

(c)

FIGURE 3: EDS (energy dispersive spectrometer) spectrums and elements content of graptolite. (a) The red box indicates the area where the element was analyzed. (b) The spectrum of the EDS. (c) Elements content results.

increasing inner pressure may push OM into other intergranular pores or fractures. Moreover, subsequent sedimentation and compaction may intensify the distortion of the OM grains.

Besides these flocculent OM particles, a few banded OM grains were also observed in LS (indicated by dash boxes in Figure 5(a) (vi, vii, viii)), which get sharp edges and elongate structure. It is quite easy to identify graptolites in cores or

outcrop due to their biological structures, but it is challenging to identify them under $\times 500$ or $\times 1000$ magnification because their biological structure was weakened by the cutting and polishing processes. In contrast to those flocculent OM particles, graptolite remains get much larger AR and most of them are subparallel to TS. Considering the geometrical feature of those OM grains and the morphology study of Luo et al. [33], we believe those banded OM grains in sample BY are highly

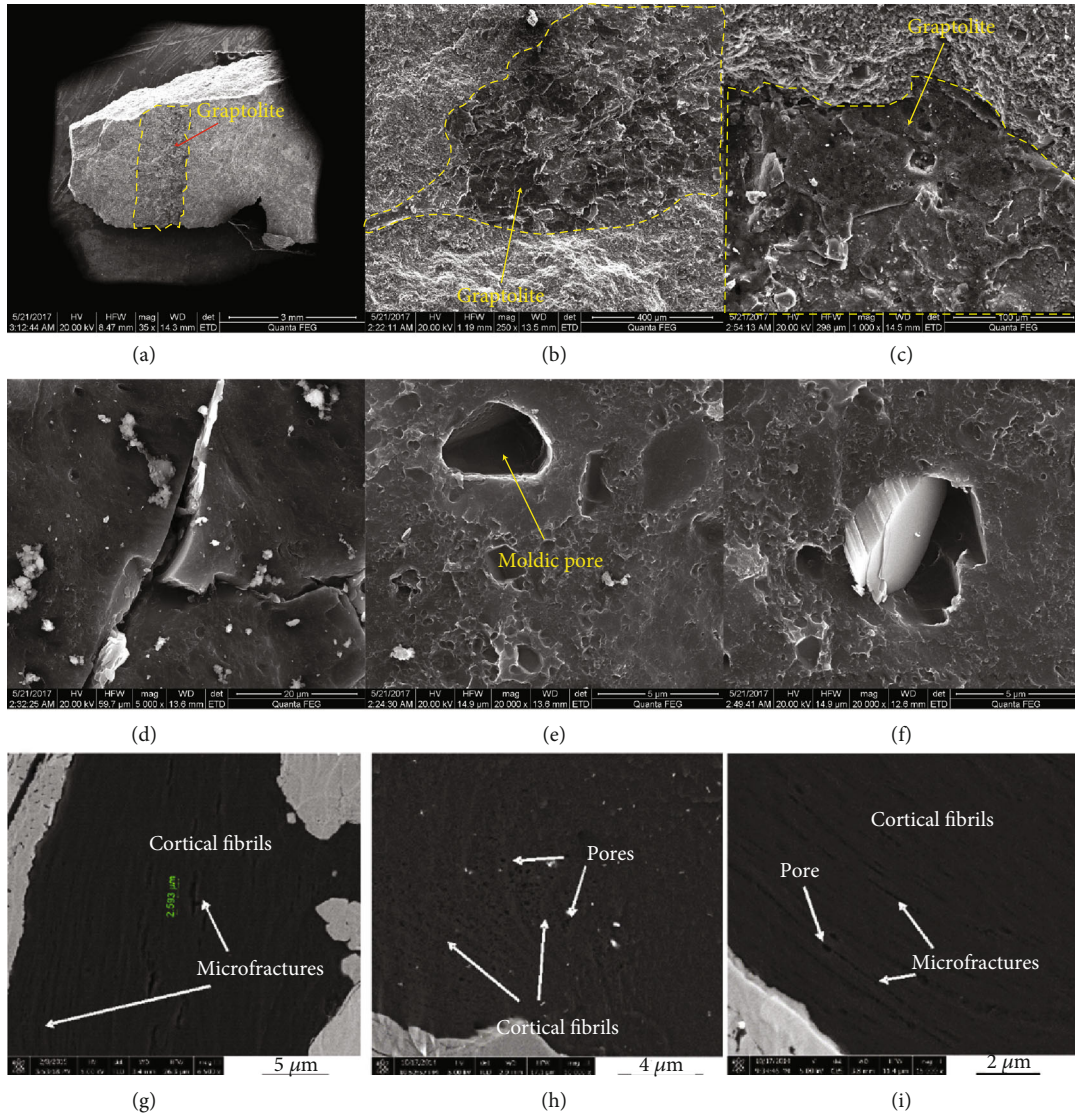


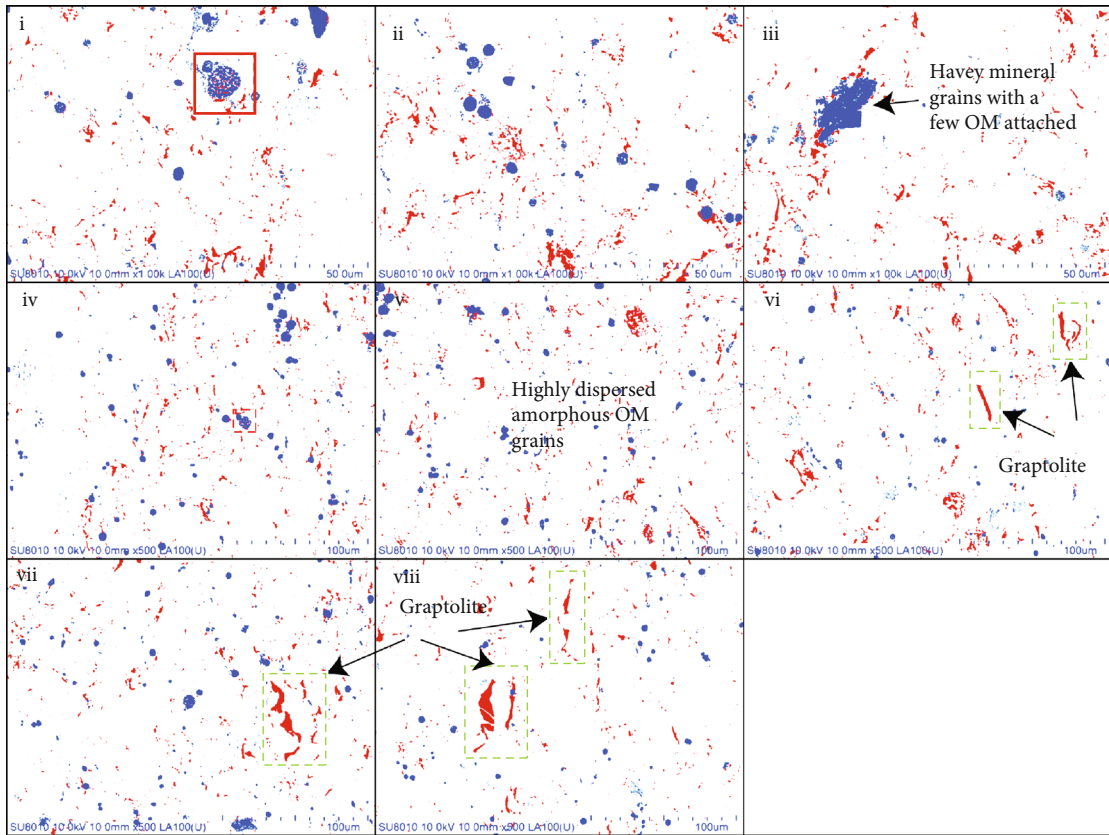
FIGURE 4: Microstructure of the graptolite under SEM. (g)–(i) are modified from [36].

likely to be graptolite remains, and they may contribute more to the anisotropy than these amorphous OM grains due to their more directed orientation and much larger AR. However, their overall contribution to the anisotropy may be limited by their quantity shortage.

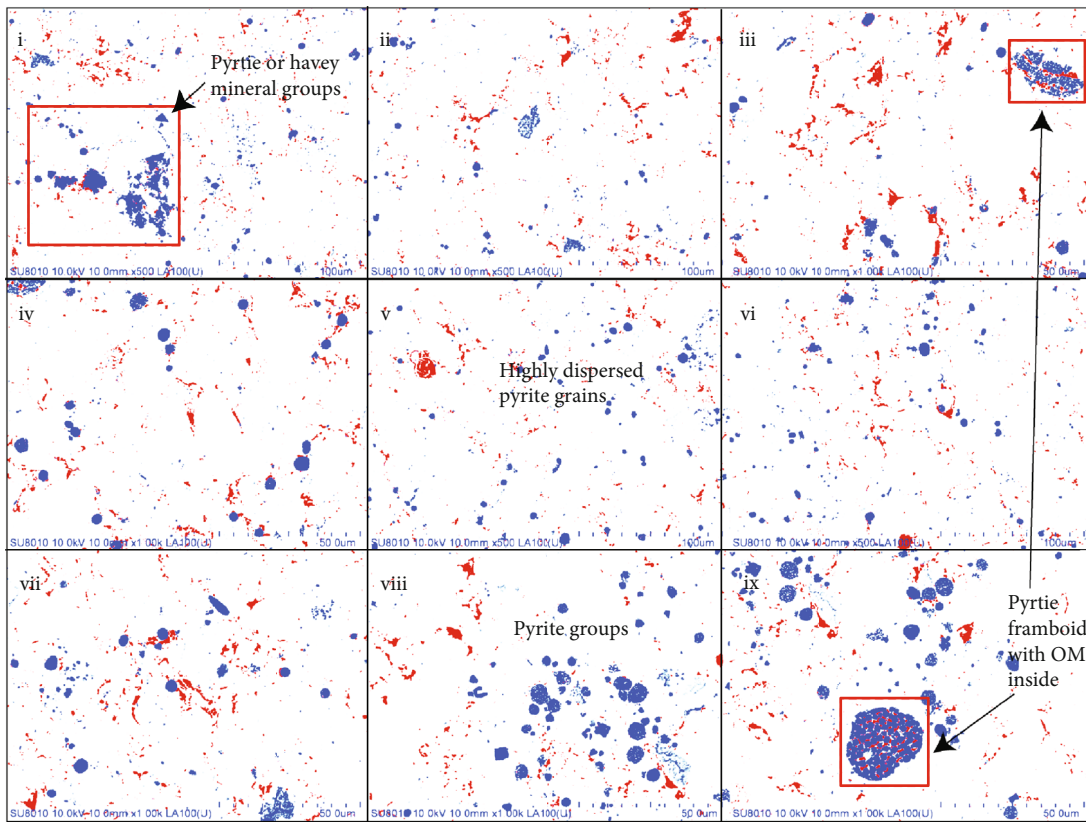
As Figure 5(b) shows, OM gains are filled inner the intergranular pores of the pyrite grains (indicated by red dash line boxes) in LS, and the size of these pyrite grains is much larger than those without OM. The distribution of the OM grains in TS is more agminated than LS, and very few banded OM grains are observed in TS. Moreover, the orientation of these banded OM grains is more random in TS, while the distribution of pyrite grains is more inhomogeneous in both LS and TS, and their size in TS is slightly larger than the ones in LS. Due to the FOV (field of view) limitation, these inhomogeneous exhibited in grain size and distribution in sample BY are limited under the submillimeter scale. Besides those bonded OM grains in LS, most OM grains in sample BY exhibit weak directionality in their orientation in both LS and TS.

As shown in Figures 5(c) and 5(d), though it is unobvious in SEM images, the image processing results indicate that OM grains in LS of sample BY still show specific directionality, while the trend is much weaker in TS. The statistical results indicate that the average MA of the OM grains in LS is 95.07° , and the average SDA is 45.39° , while in TS, the average MA is 89.25° , and the average SDA is 53.02° . The average SDA indicates that the directionality of OM grains in LS is much stronger than TS in sample BY.

3.2.2. OM Orientation in Sample YY. Sample YY is a typical terrestrial shale, as shown in Figure 6(a), the structure of OM grains in sample YY differs quite a lot from sample BY. Due to its much higher TOC, the area and size of the OM grains in sample YY are much larger than that in sample BY, and most OM particles in sample YY are banded grains with lengths larger than several hundred of microns. The position of the pyrite grains in sample YY is much closer to OM grains than that in sample BY, and some pyrite grains (indicated by the black dash line boxes in Figure 5(a)) also

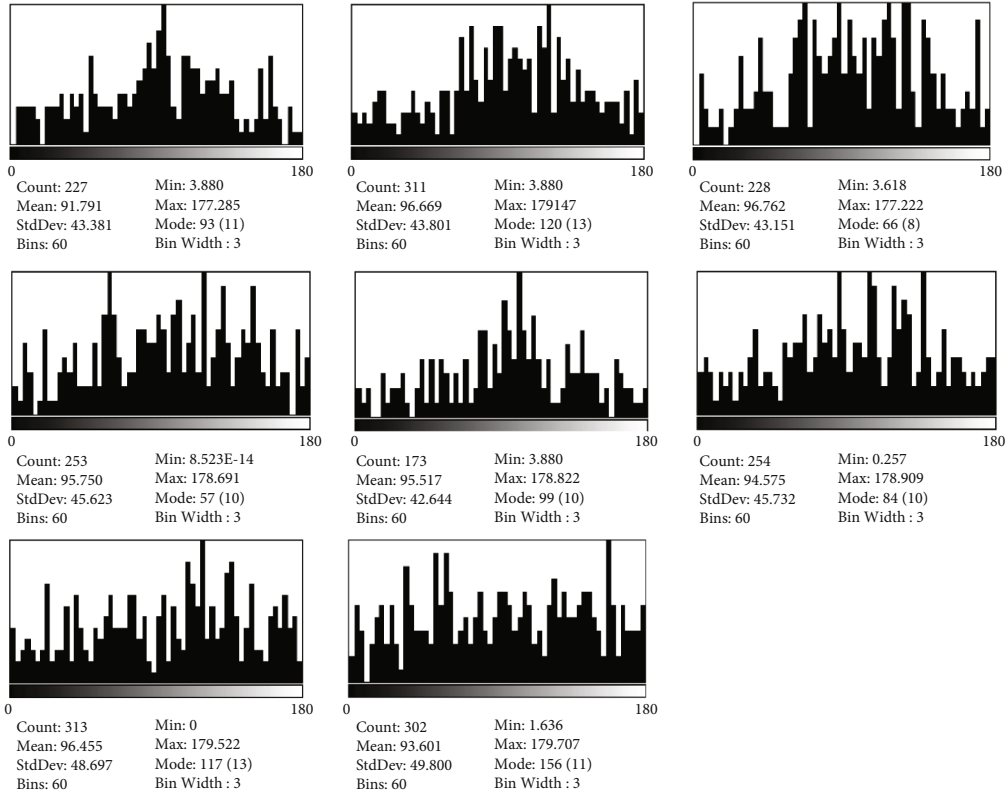


(a)

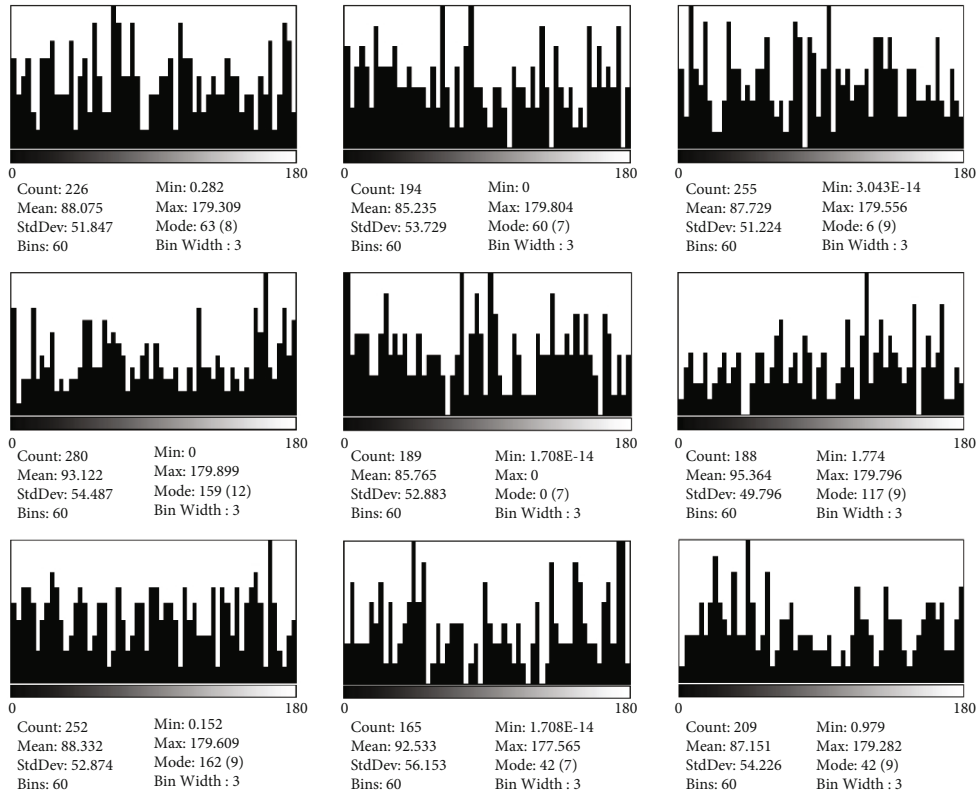


(b)

FIGURE 5: Continued.

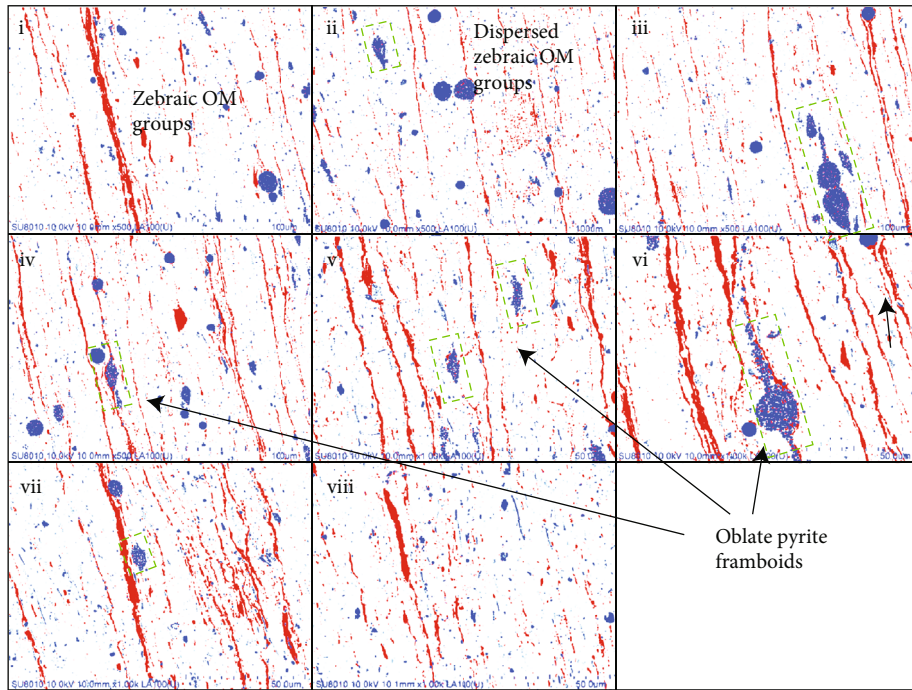


(c)

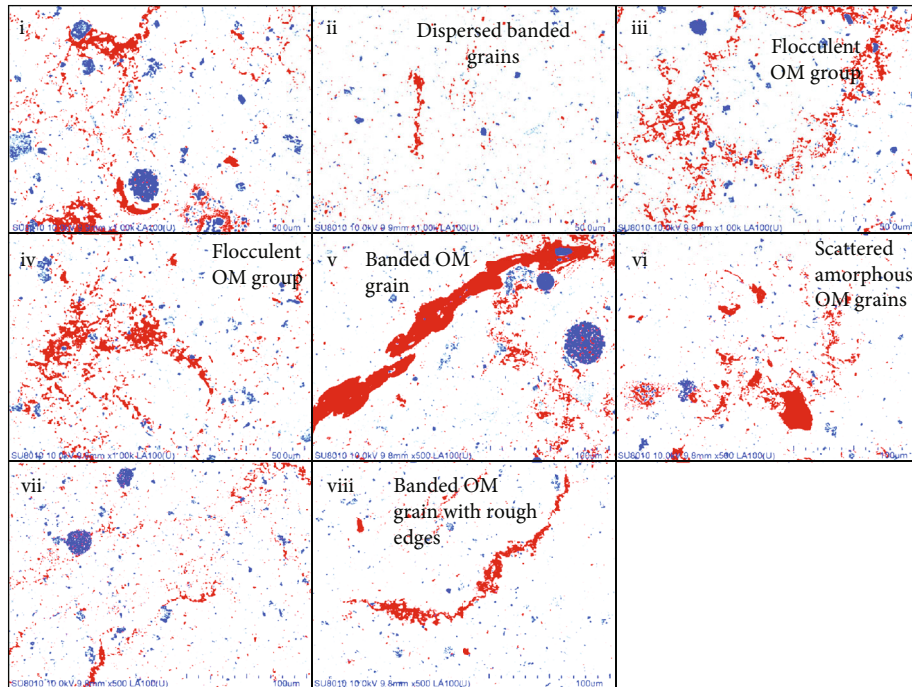


(d)

FIGURE 5: Images of sample BY after segmentation. The red part is OM, and the blue part is pyrite. (a) and (b) Merged images of sample BY in LS and TS. (c) and (d) The long axis angle distribution of the OM grains in LS and TS.



(a)



(b)

FIGURE 6: Continued.

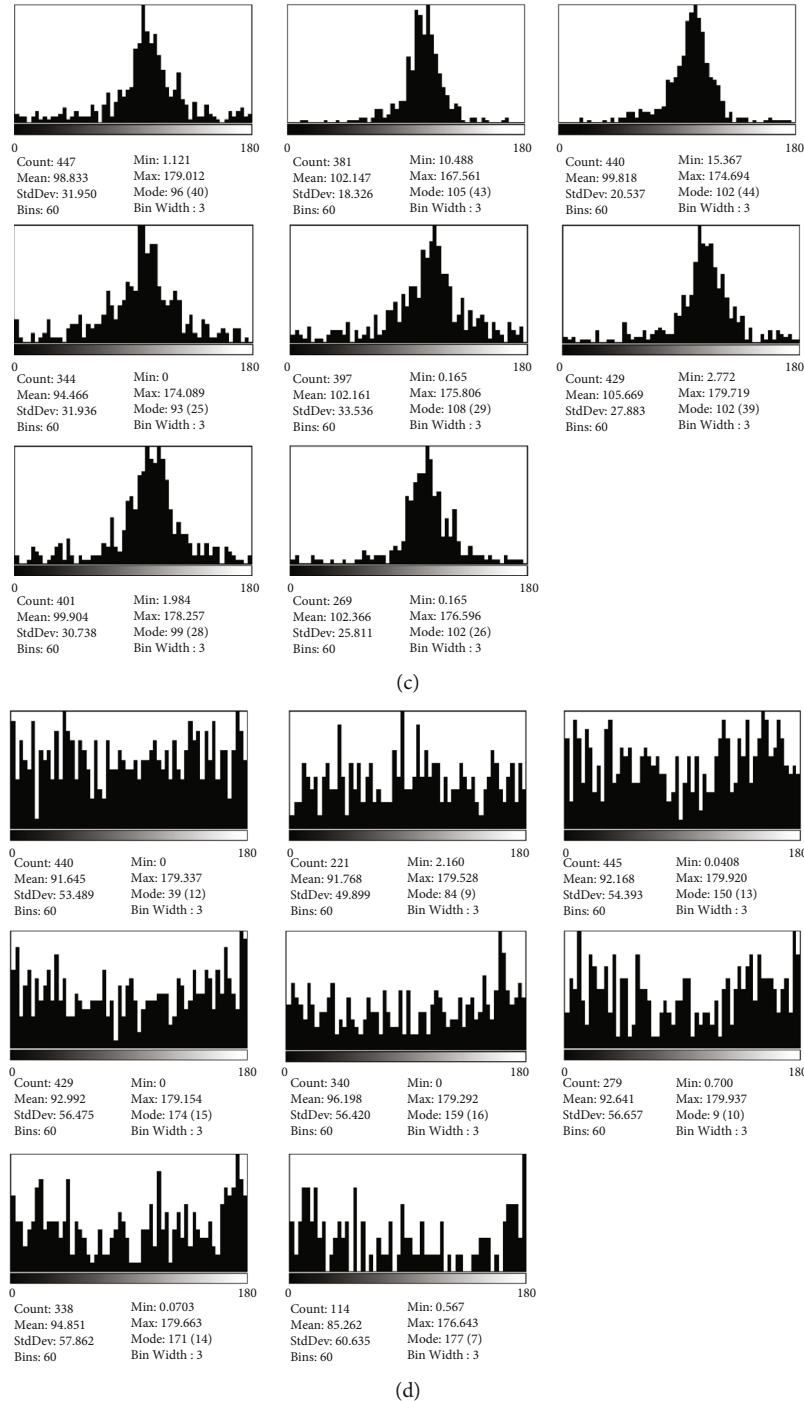


FIGURE 6: Images of sample YY after segmentation. The red part is OM, and the blue part is pyrite. (a) and (b) Merged images of sample BY in LS and TS. (c) and (d) The long axis angle distribution of the OM grains in LS and TS.

get banded shape. The directionality of the OM and pyrite particles in LS is much stronger and more evident than that in sample BY, and most OM and pyrite particles are subparallel to the bedding section. The boundaries of the banded OM grains in sample YY are not as smooth and clear as the ones in sample BY, but these OM particles contain very few inorganic mineral grains and get a more intact structure. As shown in Figures 6(c) and 6(d), the long axis angle distribution of the OM grains in sample YY is far more concentrated

in LS, and the peak positions are almost the same. According to the statistical analysis, the average MA of the OM grains is 100.67° , and the average SDA is 27.59° in LS, which is much smaller than that in sample BY, indicating that OM grains in the LS of sample YY are strictly directionally orientated.

Though OM grains quantity is smaller in LS of sample YY, their size is much larger than that of sample BY. Banded OM grains were also observed in TS of sample YY, but they are much thicker than the ones in the LS. There are very

few amorphous OM grains in LS, but it can be widely observed in TS of sample YY, and its morphology shows certain differences with the ones in sample BY. The amorphous OM grains in sample BY get irregular edges and relatively intact inner structure, while in sample YY they get similar snatchy edges but contain more inner pores. Besides, the size of the amorphous OM grains in sample YY is much larger than the ones in sample BY. These differences indicate that mechanisms forming the amorphous OM grains in two samples may be different. Nevertheless, as Figure 6(d) shows, these OM grains in the TS of sample YY also exhibit no directionality as the ones in sample BY. The average MA is 92.19° and the average SDA is 55.73° , which is similar to that of sample BY.

3.2.3. OM Orientation in Sample JY45. Sample JY45 was collected from the largest gas shale play in China, and beddings are highly developed in the main production layer. As Figure 7(a)(i), (ii), (vii) shown, the banded OM grains are of the largest size among the four samples, but many inorganic grains are firmly attached or embedded in these the banded OM. As Figure 7(a) (iv), (v), (vi) shown, amorphous OM grains are also widely distributed in the TS of sample JY45, and their morphological characteristics are similar with ones in sample BY.

These banded OM grains in sample JY45 are highly likely to be graptolite remains cause their thickness is over dozens of microns, and the embedded inorganic grains may from the overlap of graptolite layers. These graptolites, as we observed from the core samples, are tabular organic films with centimeter-scale. They are well parallel to the bedding direction on the core scale, and their directionality is still distinct in these micron-scale SEM images. The quantity of the banded OM grains in LS of sample JY45 is much smaller than sample YY, but they also exhibit specific directionality in their orientation. However, due to their less intact structure, these banded OM grains may be identified as several smaller independent particles by the software, and, thus, the holistic orientation of the banded grains may be weakened in the image analysis results. According to which, the average MA and average SDA of the amorphous OM grains are 90.66° and 49.2° in LS, respectively. While SDA of the bonded OM grains ranges from 45° to 46° , both of which are much larger than sample YY.

While in TS, the distribution of OM grains in sample JY45 is as dispersed as sample BY. The size of the OM grains is much smaller than LS, and only a few annular OM grains can be observed (Figure 7(b) (i, ii, iii)). The number of pyrite grains in TS of sample JY45 is much smaller than sample BY, and the distribution of amorphous OM in sample JY45 is relatively wider than sample BY, and their structure is also more complicated. According to the image analyses shown in Figures 7(c) and 7(d), the average MA of the OM grains in TS is 87.89° , and the average SDA is 54.67° . Which is much larger than the LS, but it is almost the same with that in sample BY.

3.2.4. OM Orientation in Sample JY11. Sample JY11 was collected from the same shale play with sample JY45, and they

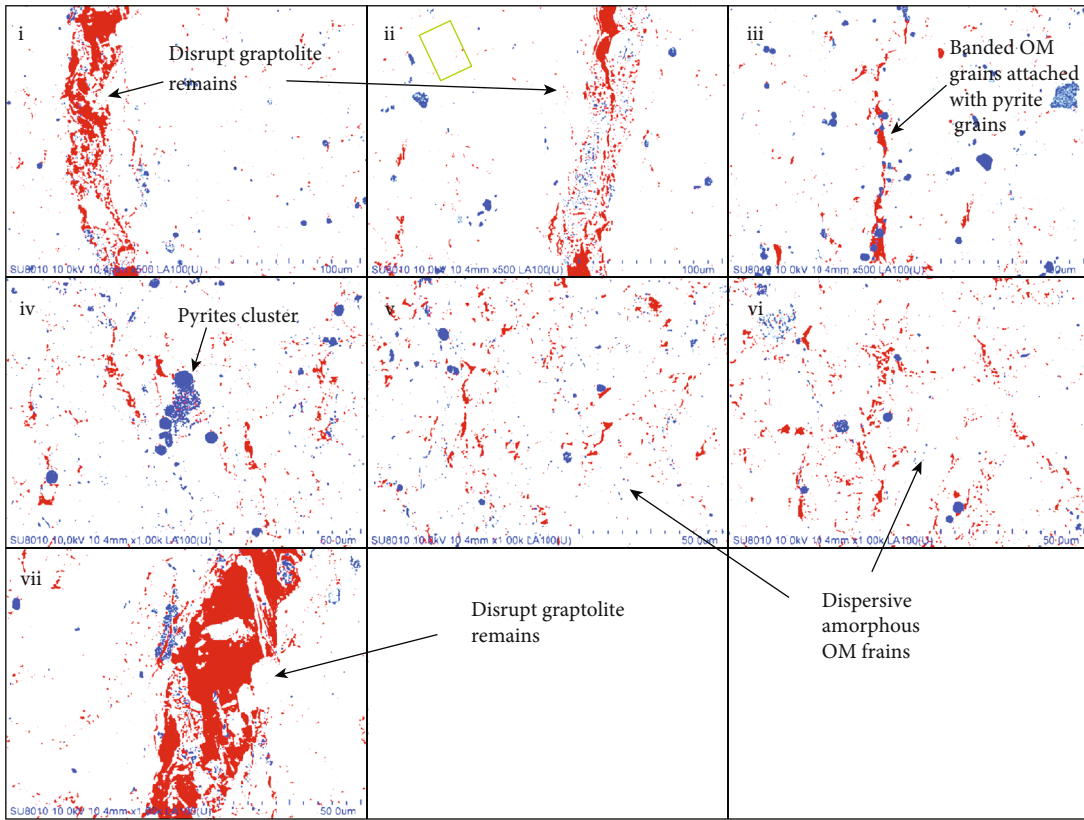
are from the same sub-member of the major pay zone. However, the morphology of the OM grains in sample JY11 exhibits noticeable differences from sample JY45. As Figure 8(a) shows, the banded OM grains in sample JY11 are much thinner, and some are of rich branches (Figure 8(a) (i, ii, viii)). These ramifications may derive from the compressed graptolite multilayers, and some OM grains also involved many inorganic particles, but their overall structural integrity is much better than the banded ones in sample JY45. The distribution of pyrite grains in sample JY11 is also dispersive.

As Figure 8(c) shows, the angle distribution of the OM grains in sample JY11 is more centralized than sample JY45, and most peaks are located around 90° , suggesting the OM grains in the LS of sample JY11 tend to subparallel to the bedding direction. According to the image analysis, the average MA of the OM grains in sample JY11 is 94.5° in LS, and the average SDA is 41.93° , which is smaller than that of sample JY45 and sample BY, but much larger than sample YY, and the result agree well with the intuitive observation of the SEM images.

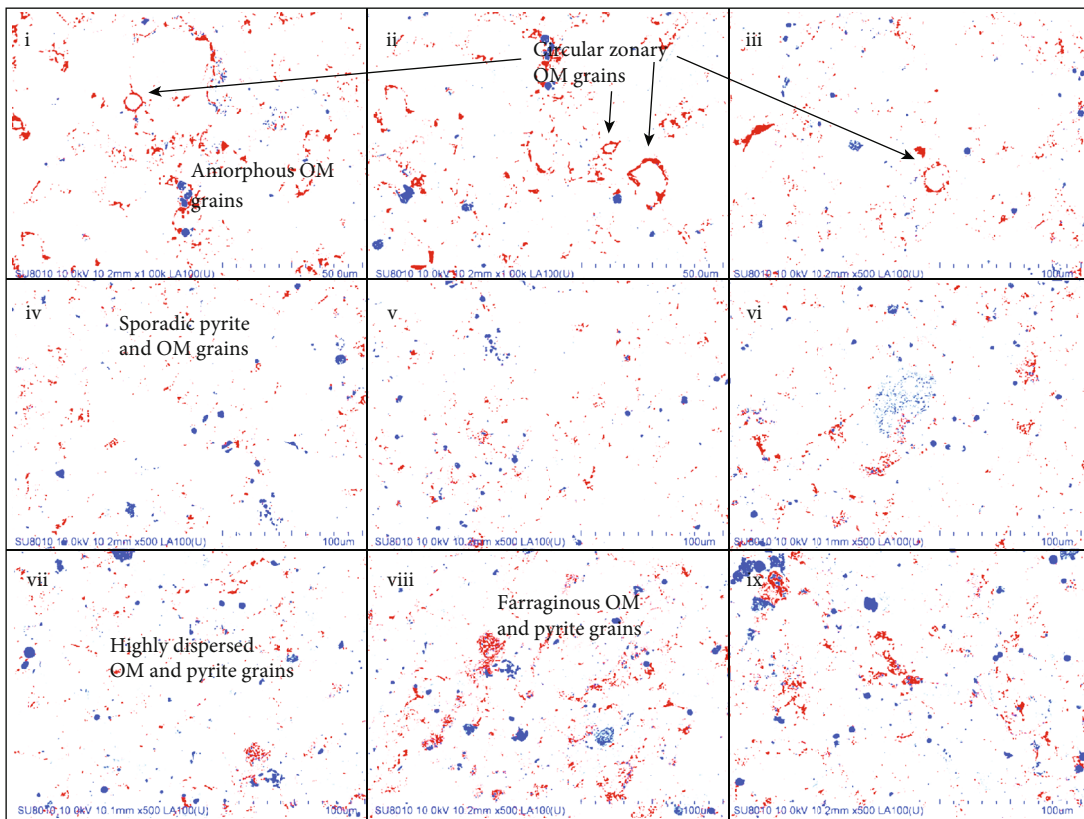
While in TS, the amount of the OM grain is the smallest and their distribution is also highly dispersed, and almost no banded OM grains were observed. The MA and SDA of the OM grains in sample JY11 are 94.5° and 54.29° in TS, indicating that the directionality of the OM grains in sample JY11 is much weaker in TS. The position of the pyrite grains in sample JY11 shows no significant correlation with the OM particles, especially in TS. While in sample JY45, more pyrite grains are involved with the OM grains.

4. Discussion

4.1. The Representativeness of SEM Images. The magnification used in this study was fixed to $\times 500$ and $\times 1000$ to ensure SEM images contain enough target particles and with acceptable sharpness as well. However, if the magnification is too large, the FOV will be too small to represent the characteristics of the sample. To estimate the representativeness of the SEM images, we calculated the area ratio of OM and pyrite grains in each image. As shown in Figure 9(a), the area ratio of OM grains in both LS and TS of the four samples exhibits a well positive correlation with the TOC data. While the consistency between pyrite area ratio and pyrite content calculated from XRD is weaker (Figure 9(b)), which may cause by the misidentification of Ca or Ba, as particles contain Ca or Ba in shale get similar brightness with pyrite, thus, they may be misidentified as pyrites. Nevertheless, the identification of OM is more precise cause OM grains get more evident differences in their density and composition. The TOC and XRD data of the four samples are derived from experiments according to relevant industry standards, and these results can accurately indicate the amount of the OM and pyrite in each sample. Thus, the positive correlation between XRD, TOC, and area percentage can prove the SEM images used herein can represent the difference of the OM grains in the four samples.



(a)



(b)

FIGURE 7: Continued.

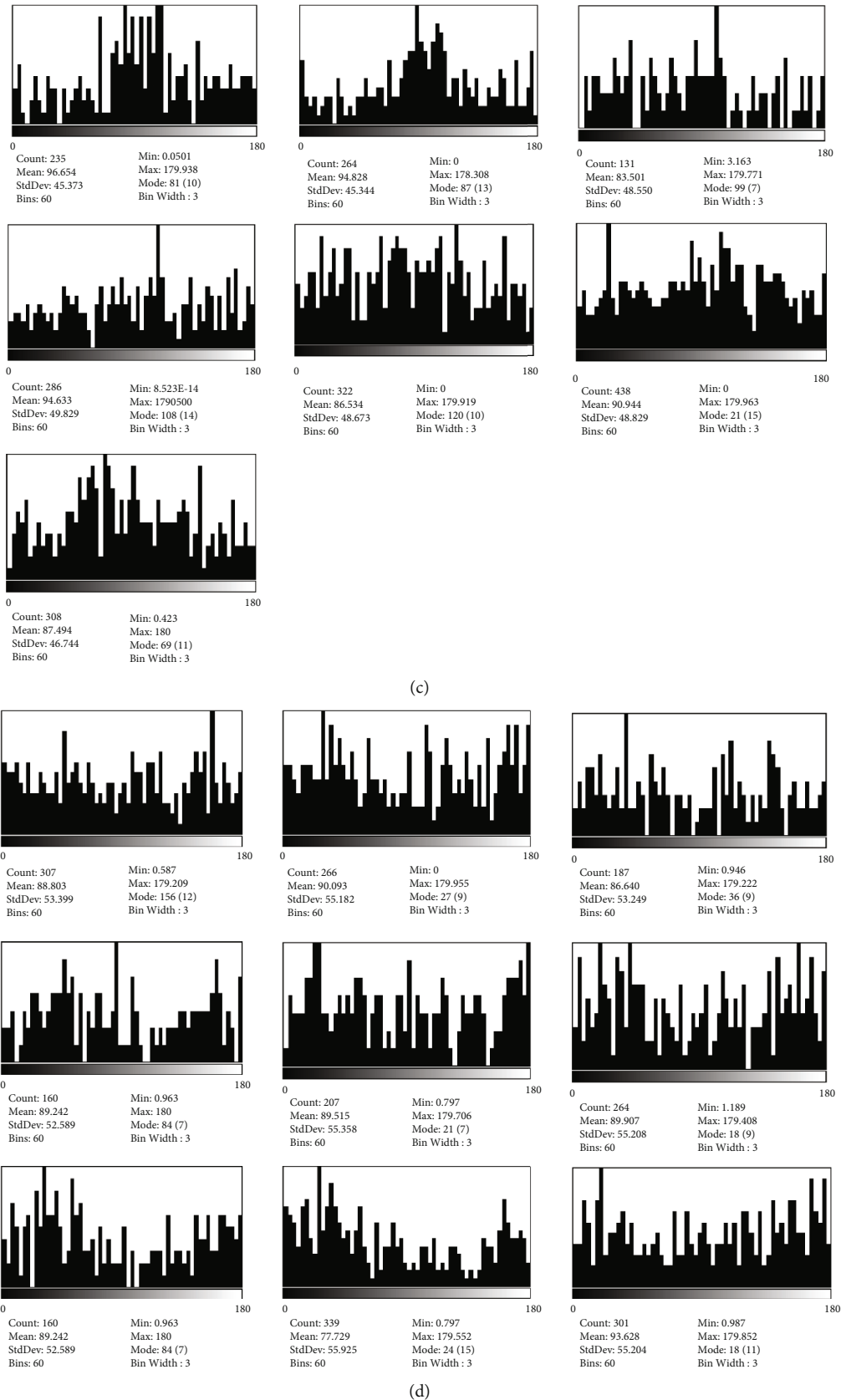
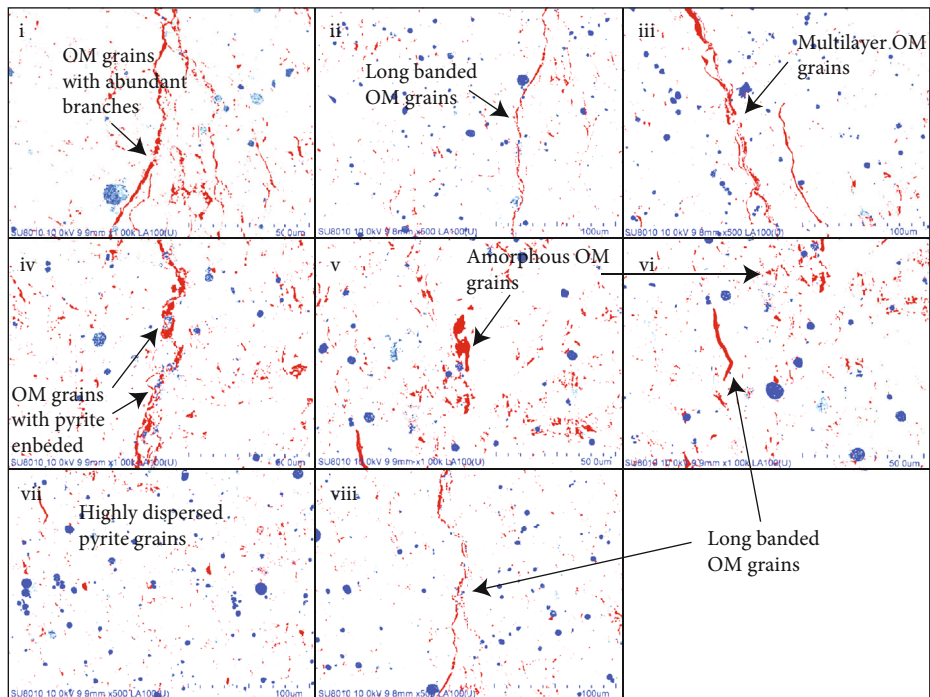
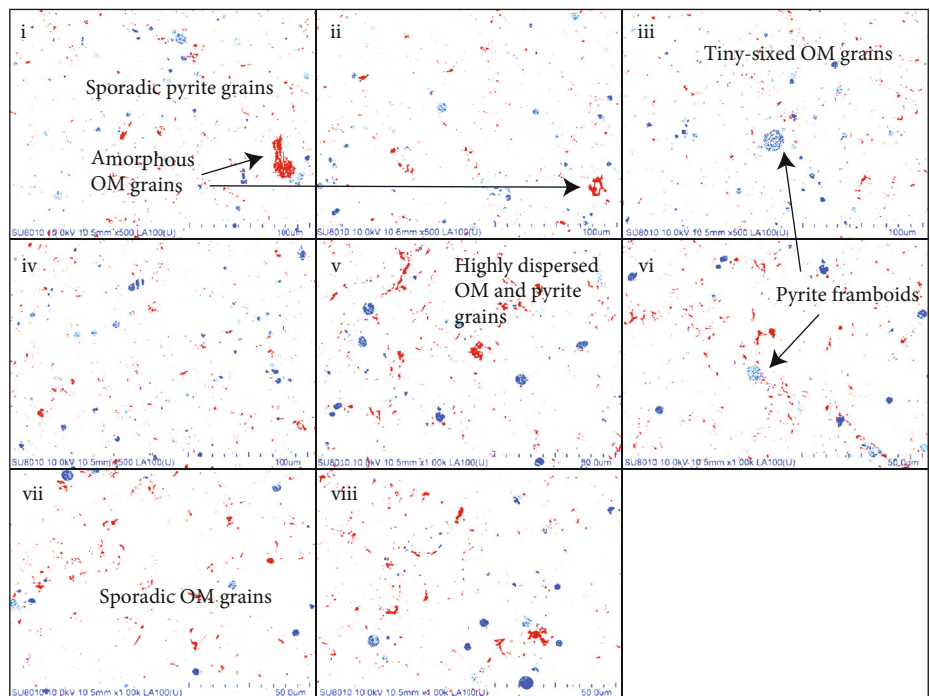


FIGURE 7: Images of sample JY45 after segmentation. The red part is OM, and the blue part is pyrite. (a) and (b) Merged images of sample BY in LS and TS. (c) and (d) The long axis angle distribution of the OM grains in LS and TS.



(a)



(b)

FIGURE 8: Continued.

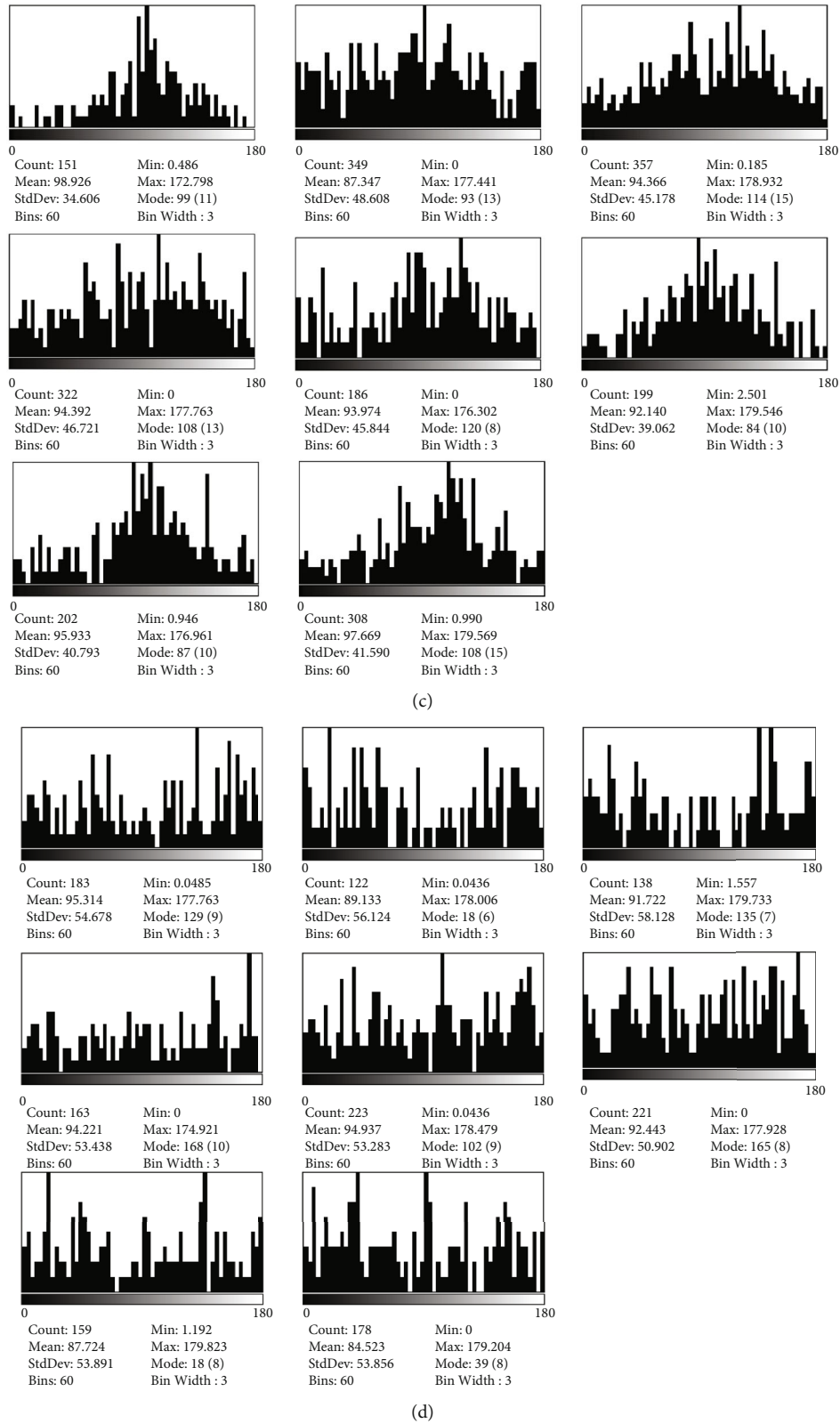


FIGURE 8: Images of sample JY11 after segmentation. The red part is OM, and the blue part is pyrite. (a) and (b) Merged images of sample BY in LS and TS. (c) and (d) The long axis angle distribution of the OM grains in LS and TS.

4.2. *The Directional Characteristics of the OM Grains.* As shown in Figure 10(a), the MA of the OM grains in both LS and TS of the four samples ranges between 85° to 95°, indicat-

ing the general tendency of the OM orientation in four samples is similar, all of which are subparallel to the bedding section and it may be a universal phenomenon in shale.

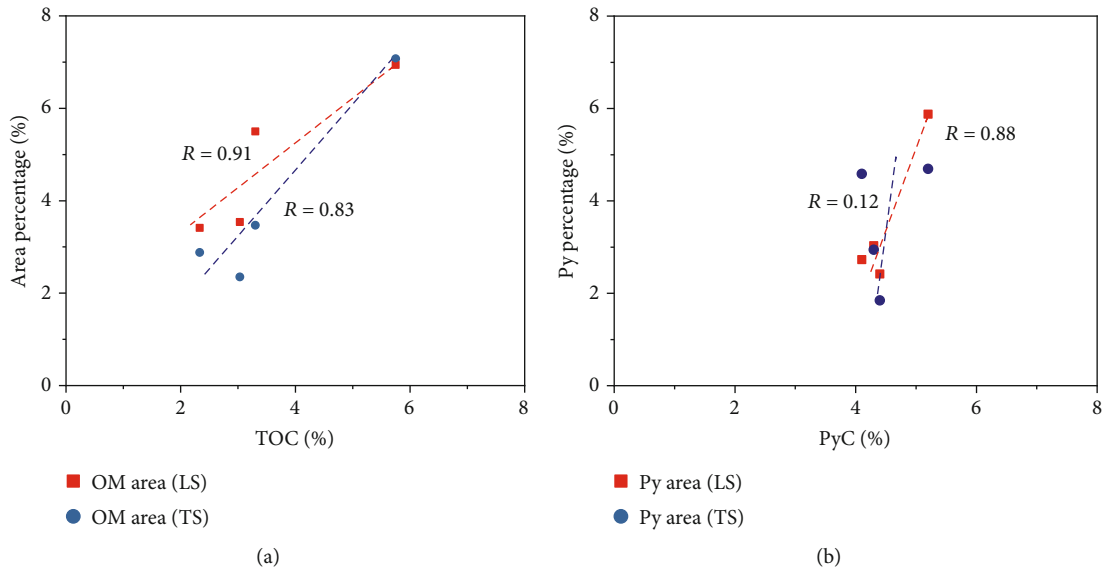


FIGURE 9: Area percentage of the grains in each image. (a) OM grains. (b) Py stands for pyrite grains. PyC stands for pyrite content.

The tendency of the OM grains orientation among the four samples seems counterintuitive cause it shows obvious differences in SEM images, especially for OM grains with large AR in sample BY and JY. However, due to the inner fractures or embedded inorganic mineral particles, many banded OM grains with obvious directionality may be identified as several individual particles during the binarization and segmentation, and this effect may be prominent in sample JY11 and JY45 due to the embedded inorganic particles in OM grains. As Figure 10(c) shows, OM grains in sample JY11 and JY45 get similar AR with sample BY, while the banded OM grains get much larger AR in the SEM images, suggesting the calculated AR of the OM grains after segmentation is much smaller than that in SEM images. OM grains in LS of sample YY still get much larger AR after segmentation, because OM grains in sample YY are much lathy and very few inorganic particles are embedded.

As many banded OM grains are identified as several individual particles, the quantity of the segmented OM grains is much larger than we perceptually observed from SEM images. The number of OM grains identified by software ranges from 100 to 500 (Figure 10(d)), and the average number in sample JY11 is even larger than that of sample BY, which is counterintuitive to the SEM image observation. As Figure 10(b) shows, the SDA of sample JY45 is similar to sample BY, but OM grains in sample JY45 exhibit more definite directionality than sample BY in SEM images. The discrepancy may be the result of the disintegration of the banded grains, as the increment in grain quantity may heighten the dispersibility of the OM orientation and weaken the difference induced by banded OM grains. Moreover, the disintegration of the banded grains also decreases the AR of the grains, which may further weaken their directionality.

However, the holistic directional differences of the OM grains exhibited in LS and TS can still be fully embodied by the SDA. As shown in Figure 10(b), there are more OM grains arranged parallelly to bedding direction in LS of the

samples, especially for sample YY. While in TS, the OM grains in four samples exhibit similar dispersions in their orientation and thus get very familiar SDA, which means the directivity of the OM grains in shale mainly exhibits in the LS of the formation, and this may be one of the reasons why some researchers regard shale as a transversely isotropic medium.

The image analyses indicate that many OM grains in shale are directionally arranged and are subparallel to the bedding section. However, the orientation degree of the OM grains varies significantly among different samples. In the four samples studied herein, OM grains in samples collected from C-7 formation exhibit the strongest directional alignment, and most OM grains are parallel to the bedding section. The alignment of OM grains in LMX shale samples collected from the Fuling area also exhibits strong directionality, while the directionality of the OM grains in LMX samples collected from Baojing is the weakest. Additionally, most OM grains in LMX shale that exhibited directional alignment are derived from graptolite.

4.3. Factors Affecting the Directionality of the OM Grains.

According to the cross plots shown in Figure 11, OM grains in shale samples with higher clay content, TOC, and lower thermal maturity may exhibit more definite directionality in their orientation. As previously discussed, the major clay minerals of the shale samples herein are illite and illite/smectite mixed-layers, and both minerals get layered structure and of rich intergranular fractures. Additionally, they are usually subparallel to bedding sections, and, thus, they are commonly regarded as one of the vital factors affecting the anisotropy of shale.

Though clay minerals are usually treated as “soft” minerals in shale, recent AFM and nanoindentation studies have proved that OM grains are the softest component in shale [22, 23], and thus OM grains may be the first components to be squeezed and out of shape during the sedimentation.

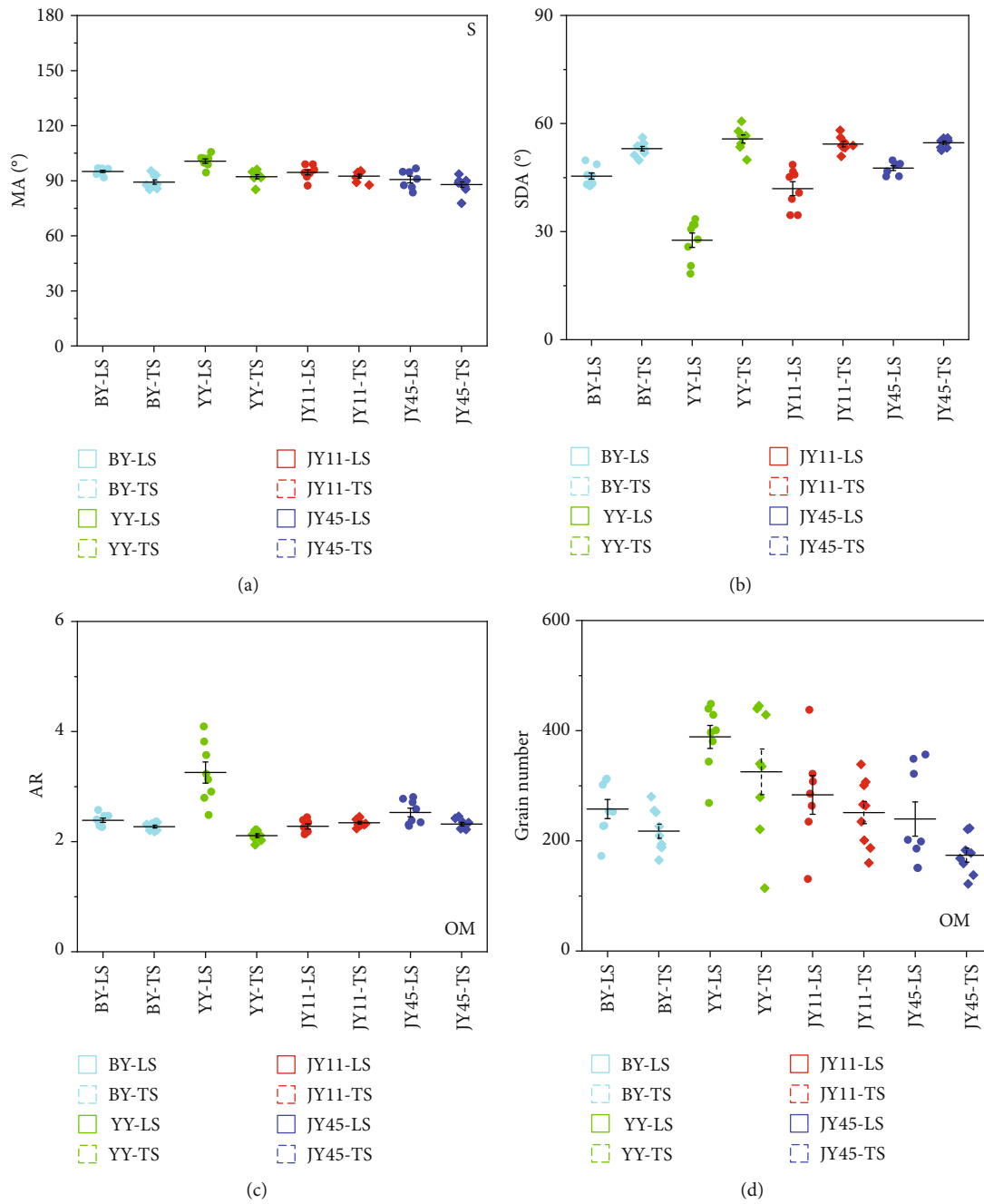


FIGURE 10: Statistical information of the OM grains in the four samples. (a) MA of OM grains in each image. (b) SDA of the OM grains angle in each image. (c) Average AR of the OM grains in each image. (d) OM grain numbers in each image.

They may be directly squeezed into strips by those layered clay minerals or be pushed into the fractures inner these layered clay minerals by other hard minerals, and both will increase the directionality of the OM grains. As samples from the C-7 Formation get the highest clay content and their OM grains are mainly derived from planktonic algae and lower hydrobiont [43], both types of OM get much weaker inherent structural anisotropy than graptolite. With the compaction of layered structure clay minerals, these OM grains are more likely to be deposited as banded grains. Therefore, the squeezing of the laminar clay minerals may be the dominant

mechanism leading to the strong directionality of the OM grains in samples from C-7, and samples that contain more clay minerals tend to exhibit stronger directionality in the OM orientation. In comparison, banded OM grains in samples collected from LMX are mainly derived from graptolite remains. Due to its biogenetic texture, its directional orientation may be controlled by other mechanisms.

As Figure 12 shows, the inorganic mineral particles in shale samples from LMX (Figures 12(a) and 12(b)) are much larger than the sample from C-7(Figure 12(c)), and their average size is around 20~30 μm . While the average

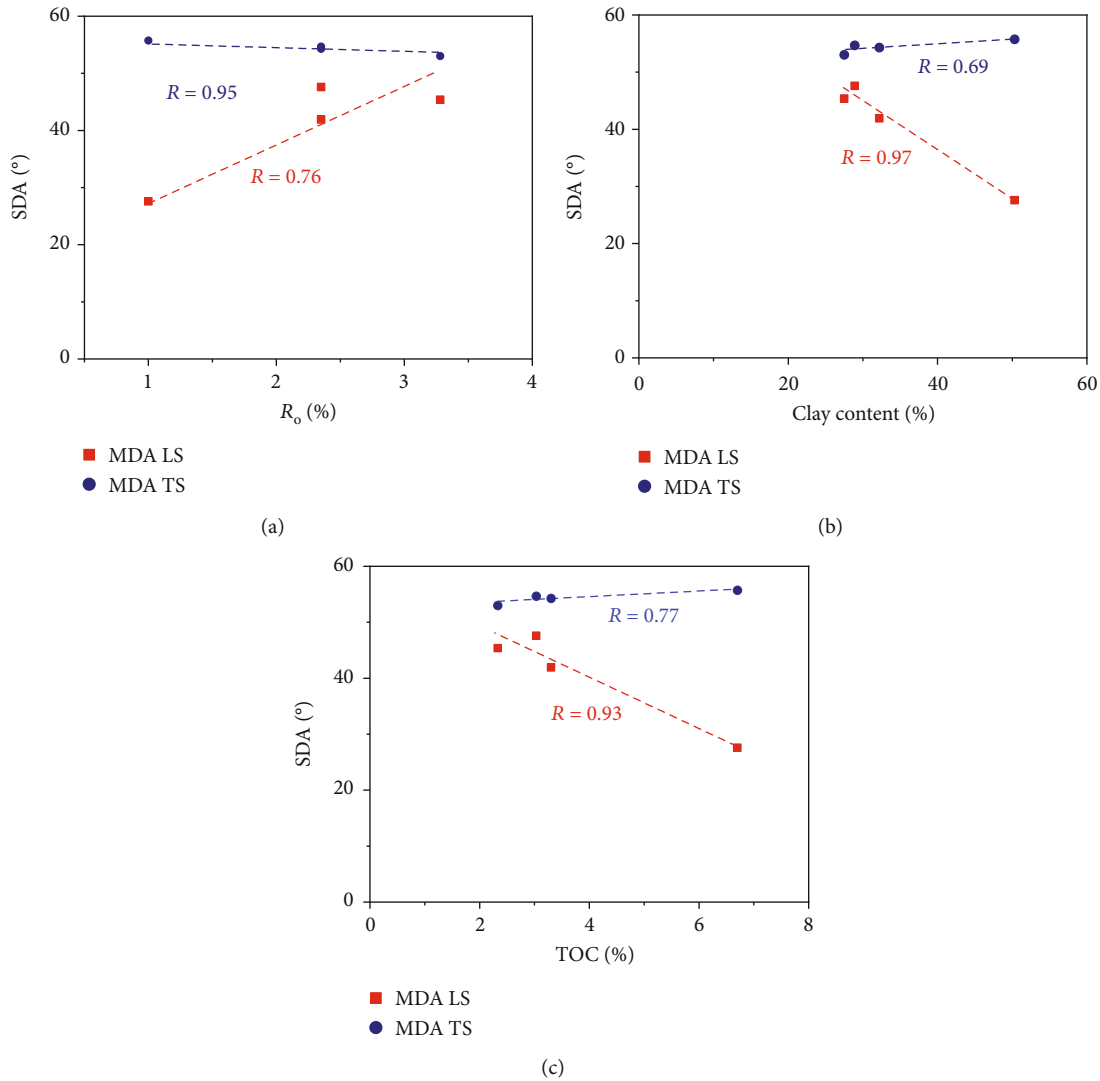


FIGURE 11: (a) Relationships between R_o and SDA. (b) Relationships between clay content and SDA. (c) Relationships between TOC and SDA.

grain size in sample YY is smaller than $10\ \mu\text{m}$ and the largest grain is OM particles. The sedimental source mainly controls the grain size, and it may be the factor affecting the morphology of the OM edges. The sizes of the clay and mica particles in samples from LMX are similar to the adjacent OM grains, and these clay and mica grains usually get smooth edges. Thus, the adjoining OM grains may get similar smooth edges as the clay and mica particles after the squeezing.

While OM grains in sample YY border a mass of rugged small-sized clay or other inorganic mineral particles, the shape of the rugged inorganic particles may stamp on the OM grains after compaction, and, thus, jagged edges are formed in these OM grains. With part of the jagged edges being polished, these banded OM grains may exhibit as flocculent OM grains in TS of the samples, while the flocculent OM grains in samples from LMX may derive from the real amorphous OM grains.

The stress conditions may also affect the arrangement of the grains. Most clay or mica particles in LMX samples are subparallel to the banded OM grains in LS (Figures 12(a)

and 12(b)), and some clay sheets are thicker than the adjacent OM grains in samples from LMX (Figure 12(c)). If the main extrusion force is orthometric to grains depositional plane, the adjacent OM grains will be squeezed into strips by these clay minerals, and this phenomenon is widely observed in samples JY45 and JY11. While in sample BY, the structure of clay minerals is more jumbly due to their much smaller size (Figure 12(e)). Though their inner sheet structures can still be observed, their orientation is more changeable, and, thus, the adjoining OM grains are of various shapes, suggesting these OM and clay grains may be squeezed from multiple directions. While most clay grains in sample YY are well parallel and OM grains are embedded in these directionally arrayed clay sheet clusters (Figure 12(f)), which implies the main extrusion force in sample YY is also perpendicular to the depositional plane. The difference in clay and OM arrangement in sample BY may mainly be caused by the tectonism, because sample BY is collected from the bottom of a syncline, where the horizontal stress is much higher. The high horizontal stress may disorganize the preformed laminated structure and deform the shape of the laminar OM

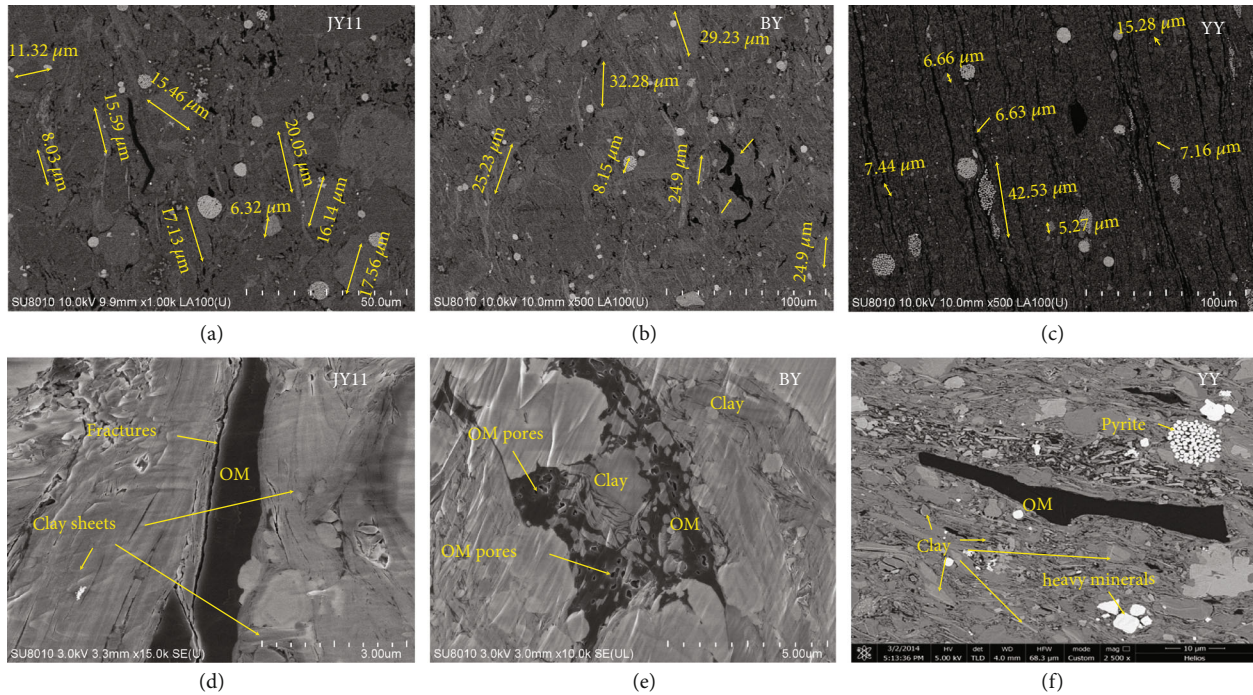


FIGURE 12: Size and morphology of the mineral grains in LS and TS of the four samples.

and clay grains. While sample YY, JY11, and JY45 are all collected from formations with the flatter structure and weaker horizontal stress. Thus, the laminated structure of the clay and OM grains is better preserved.

As shown in Figure 11(a), thermal maturity is closely related to the directional arrangement of OM in shale. Due to the sedimental environment differences, OM in sample YY is mainly derived from planktonic algae and lower hydrobiont. While in LMX samples, OM is mainly originated from planktons (graptolite, radiolarian, etc.), microbes, and algae [44]. Among these OM grains, algae are relatively harder to be preserved during the thermal maturation, and their structural features are almost indistinguishable when R_o is larger than 1.0 [45]. These OM may entirely or partially decompose as the thermal maturity goes higher. Consequently, their inner pressure will increase and organic pores may appear, and both will alter the geometry and arrangement of the OM grains. Thus, OM grains in samples with higher thermal maturity usually exhibit weaker directionality in their orientation.

However, the development of organic pores varies among different OM types. Bitumen usually gets well-developed pores, and algal fragments may have angular pores, while graptolites are relatively tight and usually have few or no pores [22]. Sample YY gets the lowest thermal maturity, and organic pores are less developed among most OM grains. Thus, the structure and shape of the OM grains in sample YY are well preserved. OM grains that exhibited directionality in samples from LMX mostly are derived from graptolite, though the thermal maturity of sample JY is much higher than sample YY, graptolite in LMX can be well preserved due to the componential difference [36], and the structure of graptolite is lamellate. Thus, graptolite may contribute

more to the OM directionality than other types of OM in LMX. However, the maturation may still decompose or reshape other types of OM, which may decrease the total amount of the directionally distributed OM grains and thus weaken the holistic directionality. Considering graptolites account for 20 to 93% of the dispersed OM in LMX [33], the intrinsic biological structural characteristics of graptolites may be the dominating factor leading to the directional array of OM grains in samples from LMX. Nevertheless, complex tectonic movement may disorganize all the previously formed directional arrangement of OM or other grains in both marine and terrestrial shale. Thus, the influence factors of OM grains orientation in shale are diversified and complicated, and the orientation of OM grains in shales should be specifically analyzed, and OM grains should not be treated as an equally distributed medium in shale.

5. Conclusions

- (1) OM grains in shale are not evenly distributed in isotropic medium, and their directional orientation is pervasive in both marine and terrestrial shale. Most OM grains in LS of the formation tend to array sub-parallel to the bedding section, while their orientation in TS is nearly random
- (2) The orientation degree of the OM grains and their controlling factor differ a lot among different shales. OM grains in shale samples from C-7 and LMX in the Fuling area exhibit strong directional orientation, while OM grains in samples from LMX in the Baojing area exhibit much weaker directionality. The orientation of the OM grains in shale is closely related to the

clay content, thermal maturity, content and type of the OM, and tectonism of the formation

- (3) The directional orientation of OM grains in samples from C-7 is mainly dominated by their high TOC and clay content, and the compaction of the directional arrayed platy clay minerals in the primary mechanism. The biogenetic texture of graptolite is the dominating mechanism leading to the directional alignment of the OM grains in LMX shale in the Fuling area. The weak directional arrangement of the OM grains in LMX shale in Baojing area may be mainly caused by the horizontal squeezing induced by the syncline structure

Data Availability

The data used to support the findings of this study are available from the corresponding author upon request.

Conflicts of Interest

The authors declare that they have no conflicts of interest.

Acknowledgments

The authors are thankful to two anonymous reviewers for their insightful comments and suggestions that have significantly improved the manuscript. This work was supported by the Chinese National Science and Technology Major Project (2017ZX05039-004) and Strategic Cooperation Technology Projects of CNPC and CUPB (ZLZX2020-01). The authors would like to thank Jiangnan Oilfield Company for providing part of the core samples.

References

- [1] C. Bobko and F. J. Ulm, "The nano-mechanical morphology of shale," *Mechanics of Materials*, vol. 40, no. 4-5, pp. 318-337, 2008.
- [2] S. Zamiran, S. Rafieepour, and M. Ostadhassan, "A geomechanical study of Bakken formation considering the anisotropic behavior of shale layers," *Journal of Petroleum Science and Engineering*, vol. 165, pp. 567-574, 2018.
- [3] D. B. Shaw and C. E. Weaver, "The mineralogical composition of shales," *Journal of Sedimentary Research*, vol. 35, no. 1, pp. 213-222, 1965.
- [4] S. Zhou, N. Yang, and H. Wang, "Investigation of methane adsorption mechanism on Longmaxi shale by combining the micropore filling and monolayer coverage theories," *Advances in Geo-Energy Research*, vol. 2, no. 3, pp. 269-281, 2018.
- [5] T. Zhang, G. S. Ellis, S. C. Ruppel, K. Milliken, and R. Yang, "Effect of organic-matter type and thermal maturity on methane adsorption in shale-gas systems," *Organic Geochemistry*, vol. 47, pp. 120-131, 2012.
- [6] Z. Guo, X.-Y. Li, and C. Liu, "Anisotropy parameters estimate and rock physics analysis for the Barnett Shale," *Journal of Geophysics and Engineering*, vol. 11, no. 6, Article ID 065006, 2014.
- [7] X. Li, X. Lei, and Q. Li, "Response of velocity anisotropy of shale under isotropic and anisotropic stress fields," *Rock Mechanics and Rock Engineering*, vol. 51, no. 3, pp. 695-711, 2018.
- [8] W. Zhang and Q. Wang, "Permeability anisotropy and gas slippage of shales from the Sichuan Basin in South China," *International Journal of Coal Geology*, vol. 194, pp. 22-32, 2018.
- [9] Y. Wan, Z. Pan, S. Tang, L. D. Connell, D. D. Down, and M. Camilleri, "An experimental investigation of diffusivity and porosity anisotropy of a Chinese gas shale," *Journal of Natural Gas Science and Engineering*, vol. 23, pp. 70-79, 2015.
- [10] M. Mokhtari and A. N. Tutuncu, "Characterization of anisotropy in the permeability of organic-rich shales," *Journal of Petroleum Science and Engineering*, vol. 133, pp. 496-506, 2015.
- [11] H. Zhu, Y. Ju, C. Huang, F. Chen, B. Chen, and K. Yu, "Microcosmic gas adsorption mechanism on clay-organic nanocomposites in a marine shale," *Energy*, vol. 197, article 117256, 2020.
- [12] C. M. Sayers and L. D. den Boer, "Shale anisotropy and the elastic anisotropy of clay minerals," in *2014 SEG Annual Meeting*, Society of Exploration Geophysicists, 2014.
- [13] D. N. Dewhurst and A. F. Siggins, "Impact of fabric, microcracks and stress field on shale anisotropy," *Geophysical Journal International*, vol. 165, no. 1, pp. 135-148, 2006.
- [14] O. Kwon, A. K. Kronenberg, A. F. Gangi, B. Johnson, and B. E. Herbert, "Permeability of illite-bearing shale: 1. Anisotropy and effects of clay content and loading," *Journal of Geophysical Research: Solid Earth*, vol. 109, no. B10, 2004.
- [15] B. E. Hornby, L. M. Schwartz, and J. A. Hudson, "Anisotropic effective-medium modeling of the elastic properties of shales," *Geophysics*, vol. 59, no. 10, pp. 1570-1583, 1994.
- [16] G. Panizza and C. L. Ravazzoli, "An efficient rock-physics workflow for modeling and inversion in anisotropic organic-shales," *Journal of Petroleum Science and Engineering*, vol. 180, pp. 1101-1111, 2019.
- [17] K. Liu, M. Ostadhassan, T. Gentzis, H. Carvajal-Ortiz, and B. Bubach, "Characterization of geochemical properties and microstructures of the Bakken shale in North Dakota," *International Journal of Coal Geology*, vol. 190, pp. 84-98, 2018.
- [18] P. Cosenza, D. Prêt, A. L. Fauchille, and S. Hedan, "Representative elementary area of shale at the mesoscopic scale," *International Journal of Coal Geology*, vol. 216, p. 103316, 2019.
- [19] S. Lohr, E. T. Baruch, P. A. Hall, and M. J. Kennedy, "Is organic pore development in gas shales influenced by the primary porosity and structure of thermally immature organic matter?," *Organic Geochemistry*, vol. 87, pp. 119-132, 2015.
- [20] F. P. Wang and R. M. Reed, "Pore networks and fluid flow in gas shales," in *Paper presented at the SPE Annual Technical Conference and Exhibition*, New Orleans, Louisiana, October 2009.
- [21] Q. Luo, G. Fariborz, N. Zhong et al., "Graptolites as fossil geothermometers and source material of hydrocarbons: an overview of four decades of progress," *Earth-Science Reviews*, vol. 200, p. 103000, 2020.
- [22] W. Zhang, W. Hu, T. Borjigin, and F. Zhu, "Pore characteristics of different organic matter in black shale: a case study of the Wufeng-Longmaxi formation in the Southeast Sichuan Basin, China," *Marine and Petroleum Geology*, vol. 111, pp. 33-43, 2020.

- [23] Y. Liu, Y. Xiong, and Y. Li, "Effect of thermal maturation on chemical structure and nanomechanical properties of solid bitumen," *Marine and Petroleum Geology*, vol. 92, pp. 780–793, 2018.
- [24] S. Emmanuel, M. Elyahu, R. J. Day-Stirrat, R. Hofmann, and C. I. Macaulay, "Impact of thermal maturation on nano-scale elastic properties of organic matter in shales," *Marine and Petroleum Geology*, vol. 70, pp. 175–184, 2016.
- [25] K. Liu, M. Ostadhassan, and B. Bubach, "Applications of nano-indentation methods to estimate nanoscale mechanical properties of shale reservoir rocks," *Journal of Natural Gas Science and Engineering*, vol. 35, pp. 1310–1319, 2016.
- [26] W. Li and A. Sakhaee-Pour, "Macroscale Young's moduli of shale based on nanoindentations," *Petrophysics*, vol. 57, no. 6, pp. 597–603, 2016.
- [27] A. Gabova, E. Chekhonin, Y. Popov et al., "Experimental investigation of thermal expansion of organic-rich shales," *International Journal of Rock Mechanics and Mining Sciences*, vol. 132, p. 104398, 2020.
- [28] C. Yang, J. Zhang, X. Tang et al., "Comparative study on micro-pore structure of marine, terrestrial, and transitional shales in key areas, China," *International Journal of Coal Geology*, vol. 171, pp. 76–92, 2017.
- [29] C. Cui, Z. Dong, and D. Wu, "Rock mechanics study and fracability evaluation for Longmaxi formation of Baojing block in Hunan Province," *Natural Gas Geoscience*, vol. 30, no. 5, pp. 626–634, 2019.
- [30] J. Cui, R. Zhu, S. Li, Y. Qi, X. Shi, and Z. Mao, "Development patterns of source rocks in the depression lake basin and its influence on oil accumulation: case study of the Chang 7 member of the Triassic Yanchang formation, Ordos Basin, China," *Natural Gas Geoscience*, vol. 4, no. 4, pp. 191–204, 2019.
- [31] W. Ji, F. Hao, Y. Song, J. Tian, M. Meng, and H. Huang, "Organic geochemical and mineralogical characterization of the lower Silurian Longmaxi shale in the southeastern Chongqing area of China: implications for organic matter accumulation," *International Journal of Coal Geology*, vol. 220, p. 103412, 2020.
- [32] Z. Qiu, C. Zou, X. Li et al., "Discussion on the contribution of graptolite to organic enrichment and gas shale reservoir: a case study of the Wufeng-Longmaxi shales in South China," *Journal of Natural Gas Geoscience*, vol. 3, no. 3, pp. 147–156, 2018.
- [33] Q. Luo, N. Zhong, N. Dai, and W. Zhang, "Graptolite-derived organic matter in the Wufeng-Longmaxi Formations (Upper Ordovician-Lower Silurian) of southeastern Chongqing, China: implications for gas shale evaluation," *International Journal of Coal Geology*, vol. 153, pp. 87–98, 2016.
- [34] T. Saif, Q. Lin, A. R. Butcher, B. Bijeljic, and M. J. Blunt, "Multi-scale multi-dimensional microstructure imaging of oil shale pyrolysis using X-ray micro-tomography, automated ultra-high resolution SEM, MAPS mineralogy and FIB-SEM," *Applied Energy*, vol. 202, pp. 628–647, 2017.
- [35] I. Arganda Carreras, V. Kaynig, C. Rueden et al., "Trainable Weka segmentation: a machine learning tool for microscopy pixel classification," *Bioinformatics*, vol. 33, no. 15, pp. 2424–2426, 2017.
- [36] Y. Ma, N. Zhong, L. Cheng et al., "Pore structure of the graptolite-derived OM in the Longmaxi shale, southeastern upper Yangtze region, China," *Marine and Petroleum Geology*, vol. 72, pp. 1–11, 2016.
- [37] C. Yan, Z. Jin, J. Zhao, W. Du, and Q. Liu, "Influence of sedimentary environment on organic matter enrichment in shale: a case study of the Wufeng and Longmaxi formations of the Sichuan Basin, China," *Marine and Petroleum Geology*, vol. 92, pp. 880–894, 2018.
- [38] R. Morga and M. Kamińska, "The chemical composition of graptolite periderm in the gas shales from the Baltic basin of Poland," *International Journal of Coal Geology*, vol. 199, pp. 10–18, 2018.
- [39] R. Morga and M. Pawlyta, "Microstructure of graptolite periderm in Silurian gas shales of northern Poland," *International Journal of Coal Geology*, vol. 189, pp. 1–7, 2018.
- [40] C. M. Link, R. M. Bustin, and F. Goodarzi, "Petrology of graptolites and their utility as indices of thermal maturity in lower Paleozoic strata in northern Yukon, Canada," *International Journal of Coal Geology*, vol. 15, no. 2, pp. 113–135, 1990.
- [41] M. E. Curtis, B. J. Cardott, C. H. Sondergeld, and C. S. Rai, "Development of organic porosity in the Woodford shale with increasing thermal maturity," *International Journal of Coal Geology*, vol. 103, pp. 26–31, 2012.
- [42] H. Nie, Z. Jin, and J. Zhang, "Characteristics of three organic matter pore types in the Wufeng-Longmaxi shale of the Sichuan Basin, Southwest China," *Scientific Reports*, vol. 8, no. 1, pp. 1–11, 2018.
- [43] X. Z. Wang, J. C. Zhang, J. Z. Cao et al., "A preliminary discussion on evaluation of continental shale gas resources: a case study of Chang 7 of Mesozoic Yanchang formation in Zhiluo-Xiasiwan area of Yanchang," *Earth Science Frontiers*, vol. 19, no. 2, pp. 192–197, 2012.
- [44] C. Liang, Z. Jiang, C. Zhang, L. Guo, Y. Yang, and J. Li, "The shale characteristics and shale gas exploration prospects of the lower Silurian Longmaxi shale, Sichuan Basin, South China," *Journal of Natural Gas Science and Engineering*, vol. 21, pp. 636–648, 2014.
- [45] J. Cai, X. Zhu, J. Zhang, M. Song, and Y. Wang, "Heterogeneities of organic matter and its occurrence forms in mudrocks: evidence from comparisons of palynofacies," *Marine and Petroleum Geology*, vol. 111, pp. 21–32, 2020.

Research Article

Laboratory Study on Hydrate Production Using a Slow, Multistage Depressurization Strategy

Yanlong Li ^{1,2}, Chuqiao He,^{1,3} Nengyou Wu ^{1,2}, Qiang Chen ^{1,2}, Changling Liu ^{1,2}, Zhixue Sun ³, Yurong Jin ^{1,4} and Qingguo Meng^{1,2}

¹Key Laboratory of Gas Hydrate, Ministry of Natural Resources, Qingdao Institute of Marine Geology, Qingdao 266071, China

²Laboratory for Marine Mineral Resources, Qingdao National Laboratory for Marine Science and Technology, Qingdao 266237, China

³College of Petroleum Engineering, China University of Petroleum, Qingdao 266555, China

⁴Petroleum Systems Engineering, Faculty of Engineering and Applied Science, University of Regina, Regina, Canada

Correspondence should be addressed to Nengyou Wu; wuny@ms.giec.ac.cn and Zhixue Sun; szx1979@126.com

Received 31 January 2020; Revised 4 April 2020; Accepted 3 February 2021; Published 24 February 2021

Academic Editor: Keni Zhang

Copyright © 2021 Yanlong Li et al. This is an open access article distributed under the Creative Commons Attribution License, which permits unrestricted use, distribution, and reproduction in any medium, provided the original work is properly cited.

Optimization of the depressurization pathways plays a crucial role in avoiding potential geohazards while increasing hydrate production efficiency. In this study, methane hydrate was formed in a flexible plastic vessel and then gas production processes were conducted at constant confining pressure and constant confining temperature. The CMG-STARs simulator was applied to match the experimental gas production behavior and to derive the hydrate intrinsic dissociation constant. Secondly, fluid production behavior, pressure-temperature (P - T) responses, and hydrate saturation evolution behaviors under different depressurization pathways were analyzed. The results show that integrated gas-water ratio (IGWR) decreases linearly with the increase in depressurizing magnitude in each step, while it rises logarithmically with the increase in the number of steps. Under the same initial average hydrate saturation and the same total pressure-drop magnitude, a slow and multistage depressurization strategy would help to increase the IGWR and avoid severe temperature drop. The pore pressure rebounds logarithmically once the gas production is suspended, and would decrease to the regular level instantaneously once the shut-in operation is ended. We speculate that the shut-in operation could barely affect the IGWR and formation P - T response in the long-term level.

1. Introduction

Natural gas hydrate (NGH) is an ice-like compound formed from water and gas molecules under relatively low-temperature and high-pressure conditions [1]. NGH is considered as the most promising alternative fossil fuel due to its great energy potential [2]. Hydrate-related field exploration and exploitation attract attentions from both the international ocean discovery program (IODP) and national plans such as the United States, Japan, China, South Korea, and India [3, 4].

To extract natural gas from hydrate-bearing sediments (HBS), four methods have been proposed based on thermodynamic conditions of NGH, i.e., depressurization [5, 6], thermal stimulation [7], CO_2 - CH_4 exchange [8], and chemi-

cal injection. These methods aim to promote hydrate in-situ decomposition and then produce gas and water by using the methods that are widely applied in conventional oil-gas industry. Depressurization is considered to be the most efficient and technically feasible method [9, 10]. However, field production test in Mallik 2L-38 project (2007-2008) [11], AT1-P project (2013) [10], AT1-P2~AT1-P3 projects (2017) [12], and SHSC-4 project (2017) [13] showed relatively low gas productivity, which is far to reach the commercial requirements.

Depressurization is also restricted by potential geohazards such as severe sand production [14-16], wellbore instability [17], and deformation of the sediment [18, 19]. These potential geohazards are mainly controlled by the mechanical properties of HBS [20, 21]. Both numerical simulation

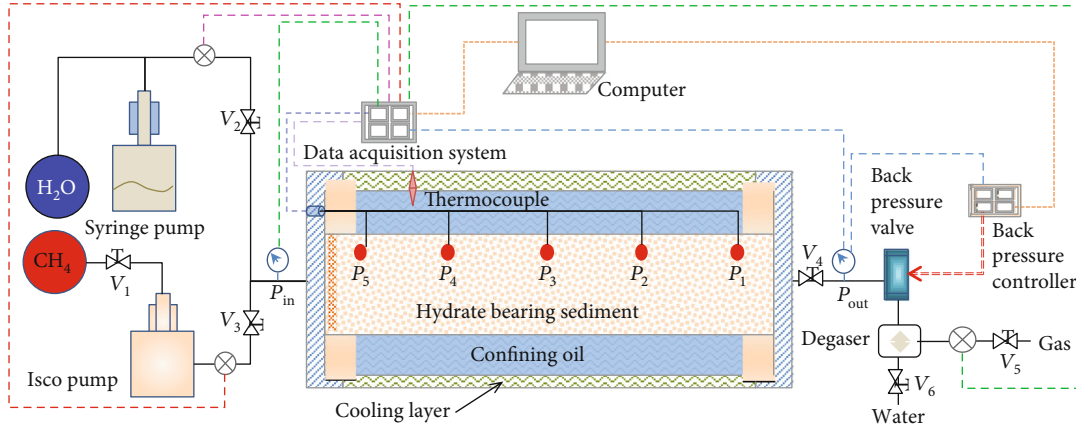


FIGURE 1: Schematic diagram of the hydrate production simulation device.

[22] and experiments [23] reveal that sand production rate tends to become severe with the increase in the magnitude of total pressure-drop and depressurizing rate. Hydrate production test can be forced to terminate once the sand production rate exceeds the tolerance of wellbore or platform [10]. Besides, the influence of geological parameters, such as compressibility [24, 25], absolute permeability [26, 27], relative permeability [25, 28], and clayey content [29], on the gas production behavior has been covered both in lab-scale [7, 9] and field-scale [10] studies.

The depressurization parameters, which mainly include pressure-drop magnitude and depressurizing rate, would also affect gas production behaviors [9, 30–32]. Aggressive depressurization would increase gas production rate in a certain extent [5, 33], but causes unpredictable occurrence of hydrate reformation [34]. There are many pathways to reach the same pressure-drop magnitude such as one-step quick depressurization and slow-stepwise depressurization [30]. The number of steps, the pressure-drop magnitude in each step, and the average depressurizing rate could be used to characterize the depressurization pathways under the same total pressure-drop magnitude.

Therefore, balancing the gas productivity and potential geohazards is crucial during depressurization [35, 36]. The influences of depressurization pathways on gas-water production behaviors and formation response need to be clarified. In this paper, we form methane hydrate in a flexible rubber sleeve. Two depressurizing gas production experiments were conducted at constant confining pressure and temperature. A numerical simulation model based on CMG-STARS module was developed to match the measured gas production, as well as pressure evolutionary behaviors. Then, the verified numerical model was employed to investigate the influence of depressurization pathways on gas-water production behaviors, as well as formation pressure-temperature (P - T) and hydrate saturation responses.

2. Experiments

The hydrate production simulation device is shown in Figure 1. The device consists of (a) a self-developed cylindrical

pressure vessel system, (b) a reactant supply system for injecting gas and water into the pressure vessel, (c) a thermostatic chamber to monitor the temperature, and (d) a system controlling and data acquisition system.

The main body of the pressure vessel is made from titanium alloy with maximum experimental pressure of 15 MPa. A flexible rubber sleeve ($\Phi 60 \text{ mm} \times 1000 \text{ mm}$) is installed inside the titanium alloy vessel. The annulus between the rubber sleeve and inner of the titanium alloy vessel is filled with confining oil. Sediment for HBS formation is packed inside the rubber sleeve. Five pressure sensors ($P_1 \sim P_5$), with measurement accuracy of 0.01 MPa and measuring ranges of $\sim 10 \text{ MPa}$, are installed linearly on the rubber sleeve to test the real-time pore pressure. The distance from P_1 to the outlet of the vessel is 50 mm, and the distance between each of the two sensors is 200 mm.

The maximum effective confining pressure (difference between confining pressure and pore pressure) for the rubber sleeve is 8 MPa when it was packed with sediment. During hydrate formation and dissociation, the temperature and pressure of the confining oil remain constant, indicating that a constant temperature and constant pressure boundary condition could be reached during the experiments. Depressurization process is achieved by adjusting the back pressure valves at the outlet.

Quartz sand with diameter of 0.12 mm–0.18 mm was used in the experiments. The average porosity of the sediment is 39.9%. Methane gas with purity of 99.99% and distilled water were used to form hydrate. Detailed sand packing and fluid injection procedures could be found in Jin et al. [37].

We tested the intrinsic permeability of the sediment before hydrate formation. The confining pressure was adjusted to 2 MPa after the sediment was packed into the rubber sleeve. Then, distilled water was injected into the sediment at a rate of 35 ml/min. During the process of water injection, the pressure in the sediment was recorded by a pressure sensor. When the pressure values remained constant, we considered that the water flow in the sediment is a steady-state flow. The pressure difference between P_1 and P_5 was about 0.11 MPa, providing that the viscosity of water at 300 K is 0.855 mPa·s. The intrinsic permeability of the

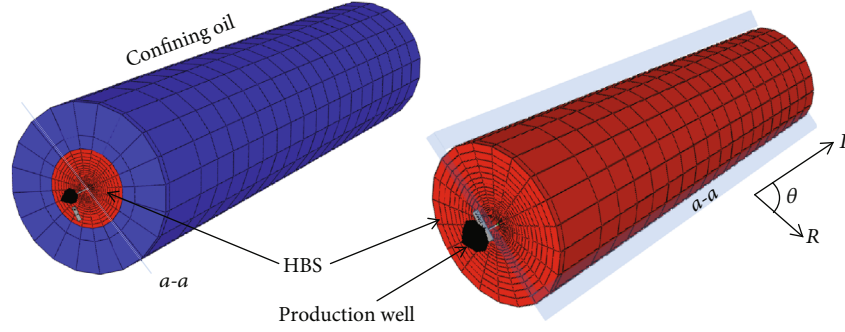


FIGURE 2: Numerical model and grid block distribution. The model boundary condition of the model is the same with experimental condition, with constant confining pressure and temperature. No mass exchange occurs between the confining oil and the HBS.

sediment could be obtained according to Darcy's law, which is about 606 mD in this manuscript.

The average hydrate saturation in the HBS, which is determined by the volume of gas consumption, was controlled around 30%. The confining pressure was set as 8 MPa, and the temperature was set as 3.5°C while forming HBS. Once the HBS formation process was completed, the confining pressure was adjusted to 6 MPa, while the effective confining pressure was about 2 MPa.

The one-step quick depressurization and two-step multi-step depressurization schedules were applied to simulate hydrate production process. In the one-step quick depressurization experiment, the pressure at the outlet was controlled to decrease to the atmospheric pressure within 5 minutes. The pressure-drop magnitude was 4 MPa during gas production. In the two-step depressurization experiment, the pressure at the outlet was firstly controlled at 2 MPa for 4 hours. Then, it was decreased to the atmospheric pressure within 5 minutes.

3. Numerical Modeling and Verification

The TOUGH+HYDRATE (Lawrence Berkeley National Laboratory, USA) [38], MH21-Hydrates (AIST Group, Japan) [39], STOMP-HYD (Pacific Northwest National Laboratory, USA) [39], and CMG-STARs (Computer Modeling Group Ltd., Canada) [39] are widely adopted to simulate hydrate production processes. In these simulators, the hydrate intrinsic dissociation constant is normally taken from bulk hydrate dissociation. However, recent study documented that the hydrate intrinsic dissociation constant varies with the characteristics of porous media [40]. Therefore, numerical simulation should firstly verify the hydrate intrinsic dissociation constant based on experimental results.

The CMG-STARs is primarily developed for thermal recovery. The simulator considers the coupling effect of fluid flow, heat transfer, and fines transport in porous media and wellbore. In simulating hydrate production process, the hydrate is considered as "unmovable heavy oil" phase filled in the porous media [40, 41], while the other part of the pore space is saturated by either water or gas phase. Based on Kim-Bishnoi model, Uddin et al. [42] modified

the hydrate dissociation kinetic equation into the following equation:

$$\frac{dc_h}{dt} = k_d^0 A_h S_w S_h \phi^2 P_{eq} \left(1 - \frac{1}{K(P, T)}\right) \exp\left(\frac{-\Delta E}{RT}\right), \quad (1)$$

where dc_h/dt is the hydrate dissociation rate in $\text{gmol}/[\text{m}^3 \cdot \text{d}]$. k_d^0 represents the intrinsic hydrate decay rate in $\text{gmol}/[\text{m}^2 \cdot \text{kPa} \cdot \text{d}]$. A_h is the specific area of hydrate particles, $3 \times 10^5 \text{ m}^2/\text{m}^3$. S_w and S_h are water saturation and hydrate saturation, respectively. ϕ is the porosity of the sediment, $\phi = 39.9\%$. ΔE is the activation energy, $76.516 \text{ kJ}/[\text{mol} \cdot \text{K}]$. R is the universal gas constant, $8.3144 \text{ J}/[\text{mol} \cdot \text{K}]$. T is the temperature in K . P_{eq} is the water-hydrate-vapour equilibrium pressure in kPa . $K(P, T) = P_e/P_g$.

In Equation (1), the mass concentration of water and hydrate during dissociation can be written as $D_w = \phi S_w \rho_w$, $D_h = \phi S_h \rho_h$. Equation (1) can be written as follows:

$$\frac{dc_h}{dt} = K_D (\phi S_w \rho_w) (\phi S_h \rho_h) P_{eq} \left(1 - \frac{1}{K(P, T)}\right) \exp\left(\frac{-\Delta E}{RT}\right), \quad (2)$$

where K_D is the modified hydrate intrinsic dissociation constant for CMG-STARs.

To simulate the constant temperature and constant pressure boundary experimental conditions, a numerical model is built with three-dimensional cylindrical shape (Figure 2). The cross-sectional area and length of the model are the same with the rubber sleeve ($\Phi 60 \text{ mm} \times 1000 \text{ mm}$). The model is divided into 20 grid blocks in the I -direction and 25 grid blocks in the R -direction. The cross section of the model is divided into 20 grid blocks in the θ -direction. Each grid block has the same lengths in the I -direction (50 mm) and R -direction (3 mm), and the same coverage angle of 18 degree in the θ -direction. In order to investigate physical response inside the formation, a longitudinal section ($a-a$ in Figure 3) was taken along the I -direction. The longitudinal section crosscuts the model in the R -direction. There is no mass exchange between the confining oil and the HBS.

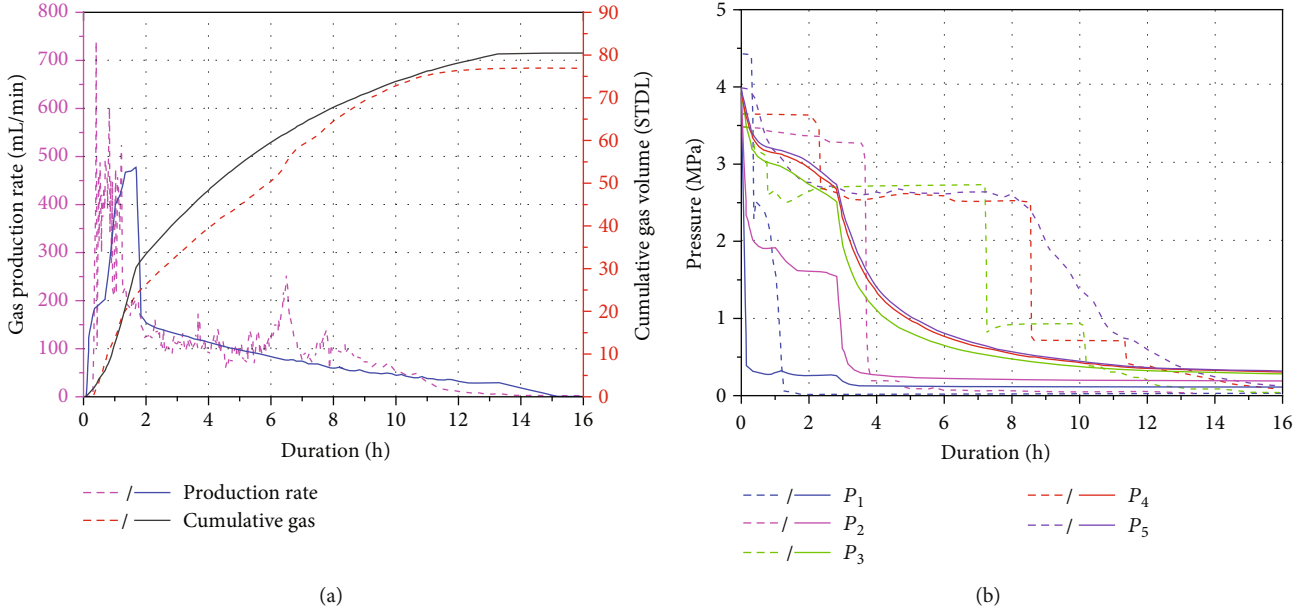


FIGURE 3: Comparison between the numerical results and experimental results for one-step quick depressurization. (a) The gas production rate and cumulative gas production evolution behaviors with time. (b) The pressure evolutionary behaviors at different locations in the HBS. The dash lines represent experimental results, while the solid lines represent numerical results.

TABLE 1: Basic parameters for numerical model.

Parameter	Value	Parameter	Value
Thermal conductivity of hydrate	0.392 J/(m·s·K)	Initial average water saturation	70% ($\pm 1\%$)
Thermal conductivity of pore water	0.58 J/(m·s·K)	Initial average hydrate saturation	30% ($\pm 1\%$)
Thermal conductivity of sediment	5 J/(m·s·K)	Initial pore pressure	4 MPa
Dry density of sediment	2650 kg/m ³	Initial confining pressure	6 MPa
Density of hydrate	919.7 kg/m ³	Initial formation temperature	3.5°C
Hydration number	5.75	Confining temperature	7°C

The initial average hydrate saturation is 30% according to the experiments. The input parameters for numerical simulation are listed in Table 1. Detailed parameters of adjusting and regressing methods can be found in Ajayi et al. [41]. The one-step depressurization experiment is used for matching the modified hydrate intrinsic dissociation constant. The two-step depressurization experiment is used for verifying the adaptability of the numerical model.

Relative permeability of the HBS was calculated from Stone's equation [43].

$$\begin{aligned}
 k_{rA} &= \max \left\{ 0, \min \left\{ \left[\frac{S_A - S_{irA}}{1 - S_{irA}} \right]^n, 1 \right\} \right\}, \\
 k_{rG} &= \max \left\{ 0, \min \left\{ \left[\frac{S_G - S_{irG}}{1 - S_{irG}} \right]^{nG}, 1 \right\} \right\}, \\
 k_{rH} &= 0,
 \end{aligned} \quad (3)$$

where k_{rA} and k_{rG} are the relative permeabilities of water and gas, respectively. S_{irA} is the immobile water saturation,

whereas S_{irG} is the immobile gas saturation. $S_{irA} = 0.25$, $S_{irG} = 0.01$, $n = 3.5$, and $nG = 2.5$ [44].

Comparisons between the experimental and numerical results for one-step quick depressurization and two-step multistage depressurization are shown in Figures 3 and 4, respectively. Solid lines in Figures 3 and 4 represent the numerical results, while the dash lines represent the experimental results.

Figures 3 and 4 indicate that the gas production behaviors between numerical and experimental results match favorable with each other. The one-step quick depressurization witnessed only one local peak in transient gas production rate during the whole production process. However, the two-step multistage depressurization procedure saw another local peak in transient gas production rate immediately after the second depressurization step.

Under the same initial average hydrate saturation, the same boundary temperature, the same pore pressure, and the same host sediment, the cumulative gas volume from two-step multistage depressurization would be a little more than that from one-step quick depressurization. However,

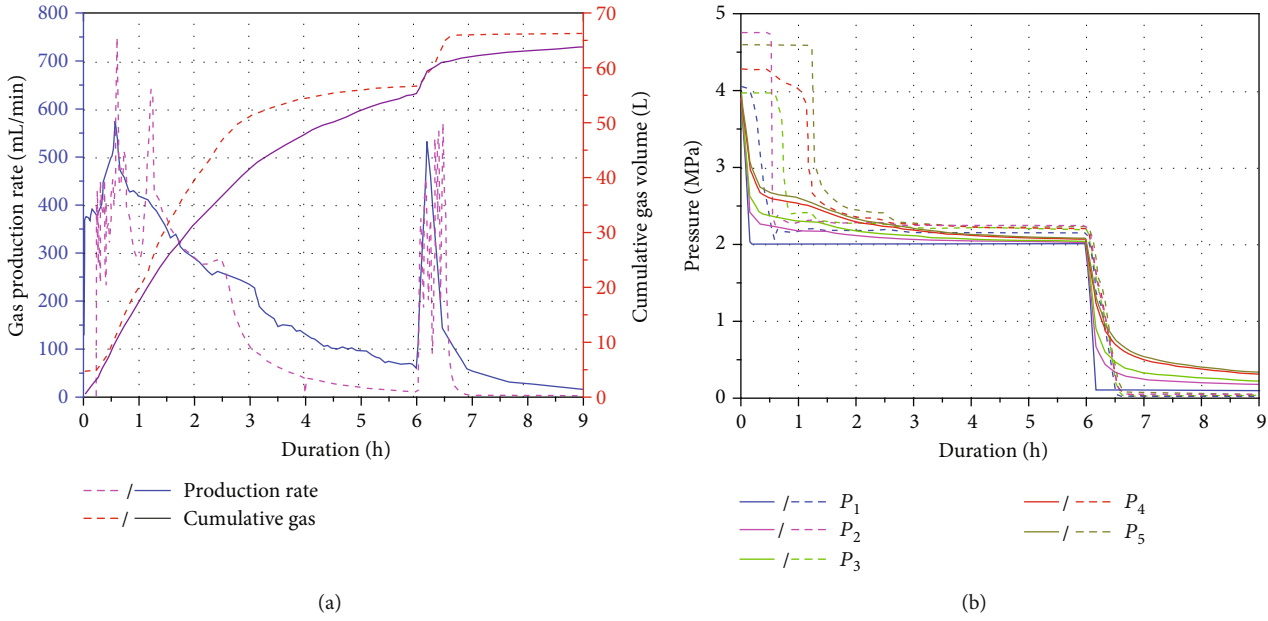


FIGURE 4: Comparison between the numerical results and experimental results for two-step multistage depressurization. (a) The gas production rate and cumulative gas production evolution behaviors with time. (b) The pressure evolutionary behaviors at different locations in the simulated formation. The dash lines represent experimental results, while the solid lines represent numerical results.

the duration for gas production process from two-stepwise depressurization is shorter than that from one-step quick depressurization.

The pressure evolutionary behaviors from the experiments showed obvious hysteresis, though the trend is similar with that from numerical simulation. This could be attributed to the reformation of hydrate or icing at the inlet of pressure sensor in the experiment [45]. Once the hydrate particles accumulate at the inlet of the pressure sensor, the pressure sensor would not be able to record the real-time pore pressure. Further depressurization would dissociate hydrate accumulated at the inlet of pressure sensor; hence, a plummet in pressure would follow. The modified hydrate intrinsic dissociation constant K_D is $2.43 \times 10^4 \text{ mol/m}^2 \cdot \text{Pa}$ according to the regression.

4. Numerical Simulation and Result Discussion

4.1. Depressurization Pathways. Based on the verified numerical model, field hydrate reservoir temperature and pressure conditions in 2017 offshore methane hydrate production test in the Nankai Trough of Japan are taken as the initial conditions. The average pore pressure and temperature at the middle of the hydrate reservoir are 13 MPa and 13.5°C, respectively [33]. The confining pressure of the hydrate reservoir is set as 15 MPa according to hydrostatic pressure, and the confining temperature is 17°C. Three hydrate saturation conditions (~75%, ~50%, and ~10%) would be considered. The size and boundary conditions of the model are the same with the experiments (Table 1).

During depressurization, the driving force for hydrate dissociation comes from the difference between water-hydrate-vapour equilibrium pressure and real-time bottom-

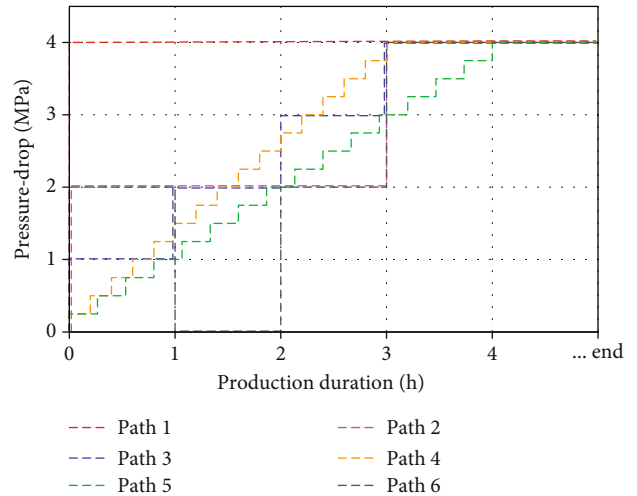


FIGURE 5: Pressure-drop controlling schedules for numerical simulation.

hole flow pressure. Therefore, the water-hydrate-vapour equilibrium pressure at the reservoir temperature (10.0 MPa at 13.5°C) is taken as the reference to choose the depressurization pathways. The total pressure drop is fixed to 4 MPa, which is the same with the experiments. Hence, the final pore pressure for all simulation cases is 6 MPa. We defined six depressurization pathways to reach the total pressure-drop magnitude of 4 MPa (Figure 5).

In Figure 5, the 1st pathway represents one-step quick depressurization, while paths 2~6 are multistage depressurization pathways. In the paths 2nd~4th, the bottom-hole pressure is decreased to 6 MPa within 3 hours, indicating the same average depressurizing rate of 4 MPa/3h. The

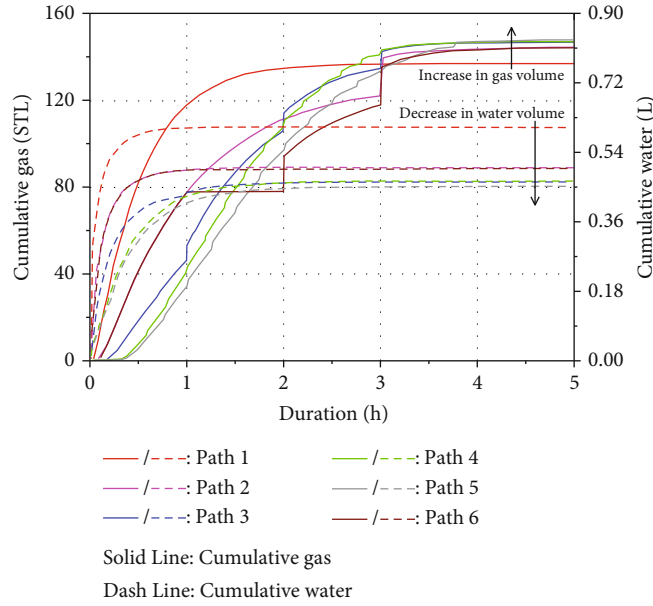


FIGURE 6: Evolutionary behaviors of cumulative gas and cumulative water under different depressurization modes. The initial hydrate saturation is 10% for all simulation cases in this figure.

depressurization processes are divided into 2 steps, 4 steps, and 16 steps equidistantly in the paths 2nd~4th, respectively. In the 5th path, the bottom-hole pressure is decreased to 6 MPa within 4 hours, indicating an average depressurizing rate of 4 MPa/4 h. The 6th path is taken as an example to investigate the influence of shut-in operation during production. The depressurization procedure for the 6th path is the same with the 2nd pathway except the shut-in operation (from 1 h to 2 h).

4.2. Cumulative Gas-Water Production. Figure 6 shows the evolutionary behaviors of cumulative gas and water when the initial hydrate saturation is 10% (the initial water saturation is 90%). It could be concluded from Figure 6 that depressurization pathways could dramatically affect the final cumulative gas and water volume, even though the total pressure-drop magnitude is fixed. Compared with the one-step quick depressurization (the 1st path), stepwise depressurization could increase the final cumulative gas volume and decrease the final cumulative water volume to some extent. This implies that depressurization mode would have some significant influences on formation multiphase seepage field, as well as the residual fluid saturation.

Therefore, we define the ratio of final cumulative gas volume and water volume as the integrated gas-to-water ratio (IGWR, Equation (4)). The IGWR could be used to evaluate the influence of depressurization pathways on fluid production behaviors.

$$\text{IGWR} = \frac{V_g}{V_w}. \quad (4)$$

When the total pressure-drop magnitude is fixed, we use the depressurizing magnitude in each step and the number of steps to identify and characterize different depressurization

pathways. Under the same total pressure drop, the influence of depressurizing magnitude in each step and the number of steps on IGWR are shown in Figure 7. Generally, the IGWR increases greatly with the increase in initial hydrate saturation. Under the same initial hydrate saturation, the IGWR decreases linearly with the increase in depressurizing magnitude in each step, while increases logarithmically with the increase in the number of steps.

In Figure 7(a), if the linear fitting curves for the IGWR and depressurizing magnitude in each step are extended leftwards to the y -axis, we obtain the theoretical maximum IGWRs for stepwise depressurization. The maximum IGWR is mainly affected by the initial hydrate saturation (Figure 8). The theoretical maximum IGWR could be reached only if the depressurizing magnitude in each step becomes minimum, indicating that the depressurization procedure is conducted linearly at a constant depressurizing rate. However, this is almost impossible to be realized in a field operation.

On the other hand, when the number of steps is low, the IGWR increases rapidly with the increase in the number of steps. However, the IGWR keeps almost constant once the number of steps exceeds a certain value. The logarithmic relationships between IGWR and the number of steps indicate that it is unnecessary to maximize the number of steps in fieldwork. In short, stepwise depressurization is important for increasing the IGWR at the same total magnitude of pressure drop. However, it is unnecessary to maximize the number of steps, which would affect the difficulties of field operation.

A comparison between the 5th path and the 4th path indicates that a slower average depressurizing rate would improve the IGWR within a certain scope, although the depressurizing magnitude in each step and the number of steps are the same. However, the IGWR for the 2nd path almost equals to that for the 6th path, indicating that the

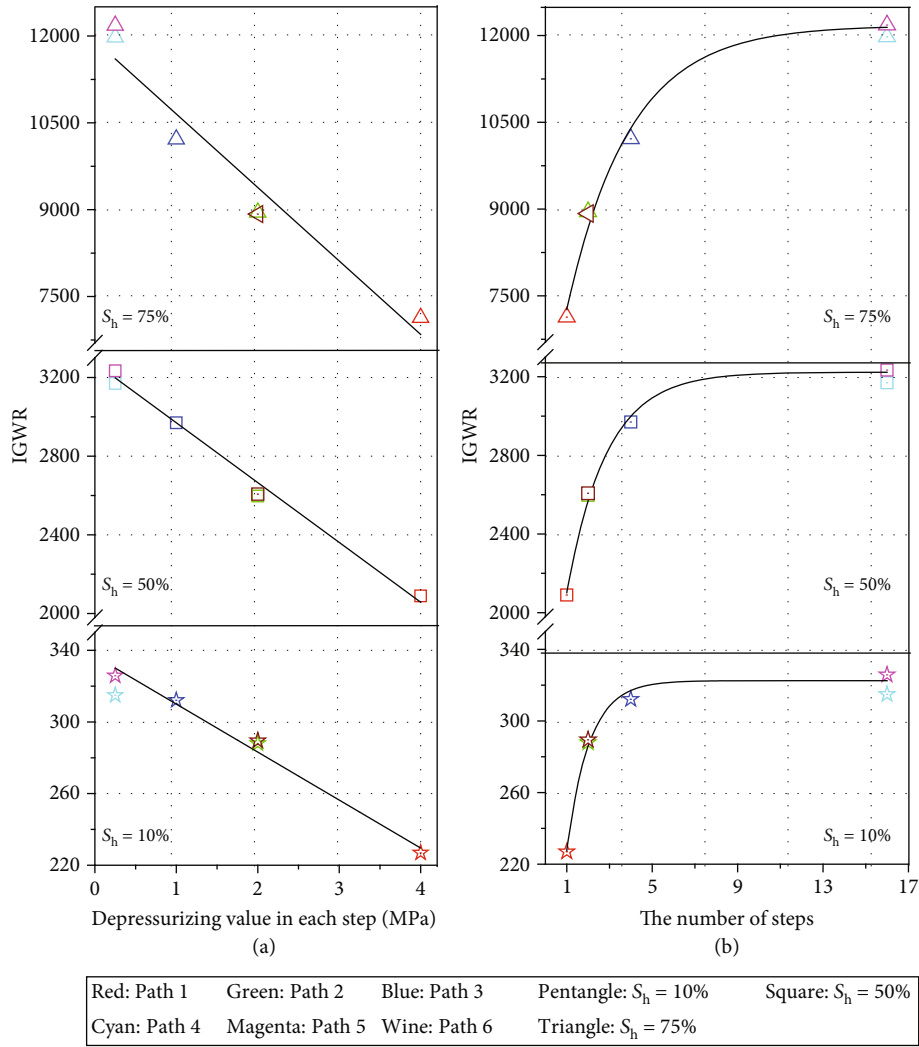


FIGURE 7: The influence of depressurizing magnitude in each step and the number of steps on the IGWR when the total pressure drop is 4 MPa.

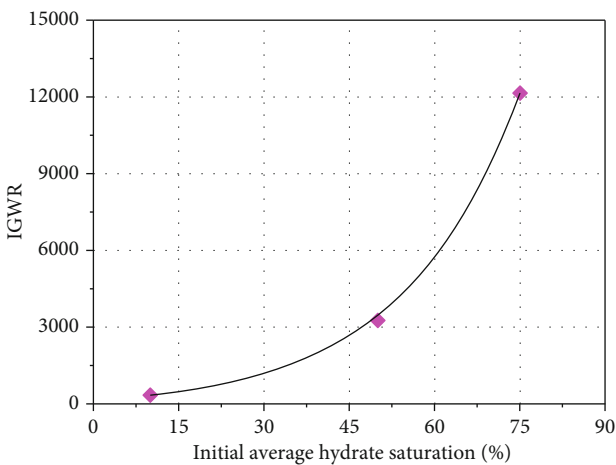


FIGURE 8: The IGWR increase with the increase in initial hydrate saturation.

shut-in operation could barely affect the IGWR. When the average depressurizing rate is low, the transient hydrate dissociation rate would be relatively low. Hence, gas phase would be separated from the water phase. Under the condition of relatively low seepage rate, the water phase cannot be carried by gas phase. As a result, the IGWR increases with the decrease in the average depressurizing rate.

4.3. *Temperature Evolutionary Behavior.* The temperature of the HBS during hydrate production is mainly determined by the combination of endothermic hydrate dissociation process, Joule-Thomson effect, and heat supply from the confining formation. The 3rd path, with an initial hydrate saturation of 75%, is taken as an example to explore temperature field changing behaviors. Figure 9 shows the temperature distribution on the section *a-a* (Figure 3). Point A in Figure 9 represents the geometric core of the section *a-a*. The right side of the model (marked by rightwards arrow) represents the outlet of the model.

The low-temperature area initiates at the outlet (production well) and propagates in a nonpiston style towards the far

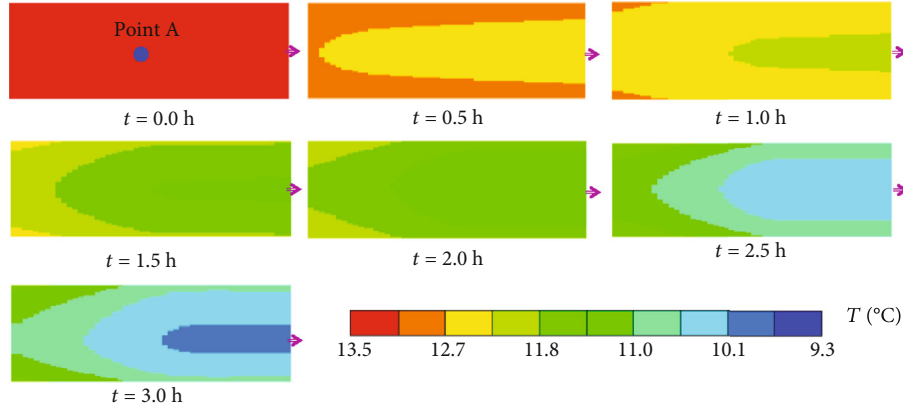


FIGURE 9: Temperature field on the section *a-a* (Figure 2) during the 3rd depressurization when initial hydrate saturation is 75%. Point A represents the geometric core of the section *a-a*.

side of the model in the *I*-direction. However, the temperature field shows obvious axisymmetrical evolutionary behaviors in the *R*-direction once the hydrate dissociation process is initiated. We attribute the axisymmetrical characteristics to the cylindrical heat supply from the confining oil. These evolutionary phenomena in temperature field were also observed in other simulation cases.

To further investigate the influence of depressurization mode on temperature, the depressurization pathways in Figure 5 are divided into two categories. The average depressurizing rate for the 2nd~4th paths is 4 MPa/3 h, while the numbers of steps and pressure drop in each step are different. Therefore, the 2nd~4th paths can be used to determine the influence of depressurization mode on temperature under the condition of the same total pressure-drop magnitude and the same average depressurizing rate. On the other hand, the average depressurizing rates for the 1st, 4th, and 5th paths are 4 MPa/5 min, 4 MPa/3 h, and 4 MPa/4 h, respectively. Hence, they could be set into the same category to explore the influence of overall depressurizing rate.

Temperature of the confining oil is constant and equivalent for all simulation cases. Therefore, temperature differences among different simulation cases are probably caused by the combination of hydrate dissociation and Joule-Thomson effect, which are both endothermic processes. Figure 10 shows that the minimal temperature value decreases with the increase in hydrate saturation. It is easy to understand because higher hydrate saturation implies more heat would be consumed by hydrate dissociation.

Most interestingly, it can be seen from Figures 10(a), 10(c), and 10(e) that a decrease in the overall depressurizing rate could significantly alleviate the temperature drop. This is in consistency with that obtained by Zhao et al. [46]. Furthermore, a slower depressurization mode would postpone the appearance of minimal temperature value to a certain extent.

Under the same total pressure-drop value (4 MPa) and average depressurizing rate (4 MPa/3 h), increase in the number of steps (or decrease in the pressure-drop magnitude in each step) would benefit for the smoothness of the temperature behaviors. The minimal temperature value decreases in a

very narrow range with the increase in the number of steps. However, the depressurization modes have little influences on temperature rebounding process once the production duration exceeds the minimal temperature.

In field operation, temperature drop is an unwanted factor during hydrate production because of potential hydrate reformation risk [34]. However, we infer from the results that we could hardly avoid temperature drop by only increasing the number of steps or decreasing the magnitude of pressure drop in each step. The best choice for avoiding temperature drop would be decreasing the average depressurizing rate. A slow, multistage depressurization strategy would be the best choice.

4.4. Hydrate Saturation Evolutionary Behavior. The hydrate saturation field evolutionary behaviors for the 3rd depressurization pathway when initial hydrate saturation is 75% are shown in Figure 11. Figure 11 suggests that the hydrate dissociation initiates at the edge of the model near the outlet ($t = 0.0$ h) and then propagates uniformly and randomly ($t = 0.5$ h). This would be probably caused by the abundant heat supply from the confining oil.

Hereafter, the hydrate dissociation front extends towards the far side of the model in the *I*-direction. The hydrate dissociation front showed obvious nonpiston characteristics, which corresponds to the temperature field changing behaviors in Figure 9. In the *R*-direction, the hydrate saturation field shows obvious axisymmetric evolution behaviors, indicating that the hydrate dissociation process is mainly controlled by the temperature field.

To determine the influence of depressurization modes on hydrate dissociation processes, we define the hydrate dissociation duration as the time when the hydrate saturation at the core of the far side of model (point B in Figure 11) is decreased to less than 0.1%. We collected the hydrate dissociation duration for all simulation cases under different hydrate saturations. The results are shown in Figure 12.

It could be concluded from Figure 12 that hydrate dissociation duration varies greatly with depressurization mode. The hydrate dissociation duration would increase remarkably with the decrease of average depressurizing rate (paths

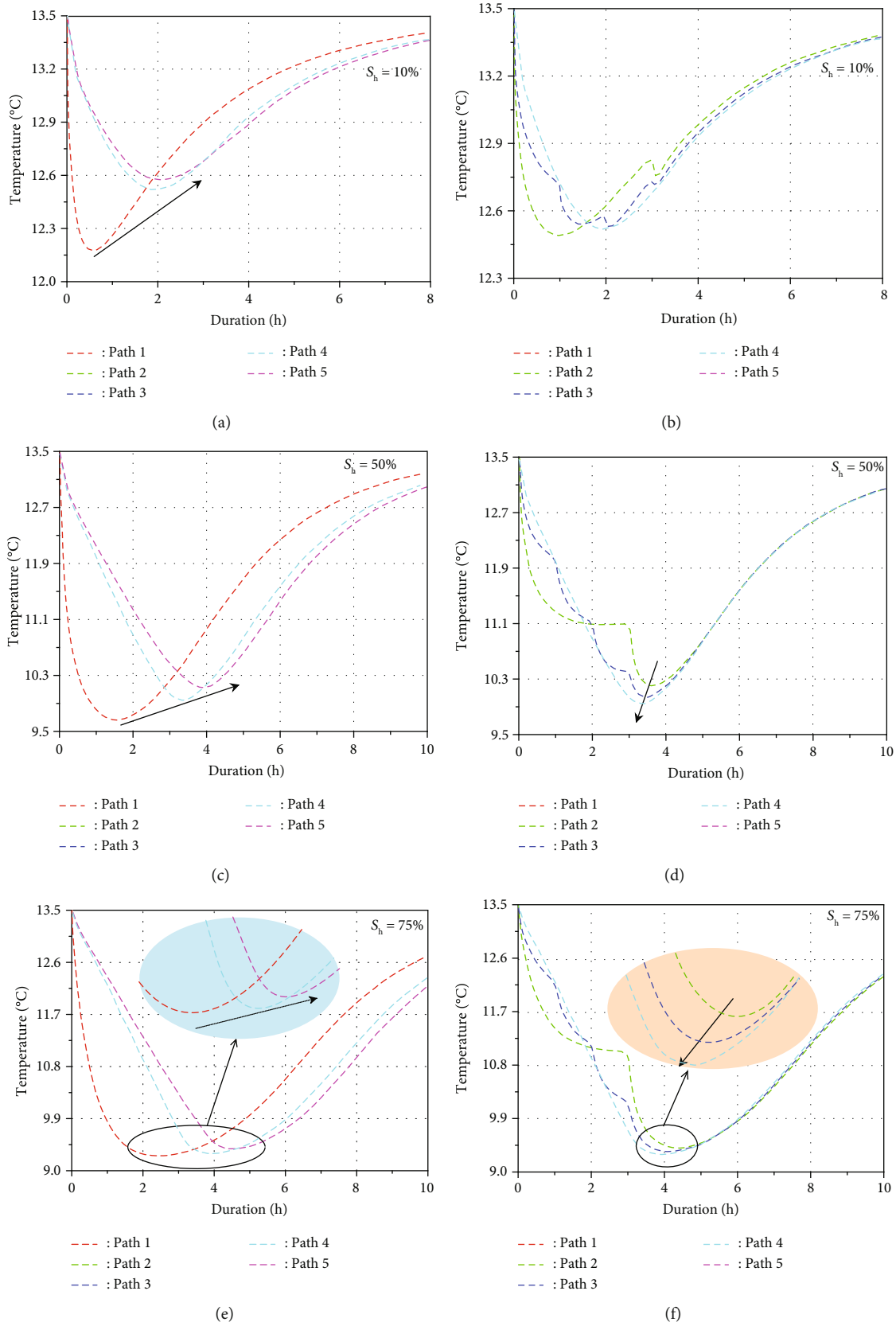


FIGURE 10: Temperature changing behaviors at the core of the model (point A). Panels (a), (c), and (e) compare the differences among pressurization pathways 1, 4, and 5; panels (b), (d), and (f) compare the differences among pressurization pathways 2, 3, and 4.

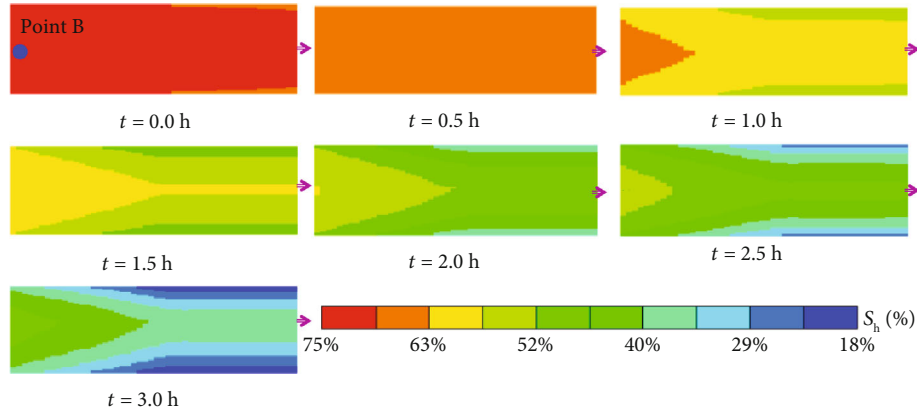


FIGURE 11: The hydrate evolutionary behaviors during the 3rd depressurization path when initial hydrate saturation is 75%. Point B represents the center of the far side of mode on the section *a-a*.

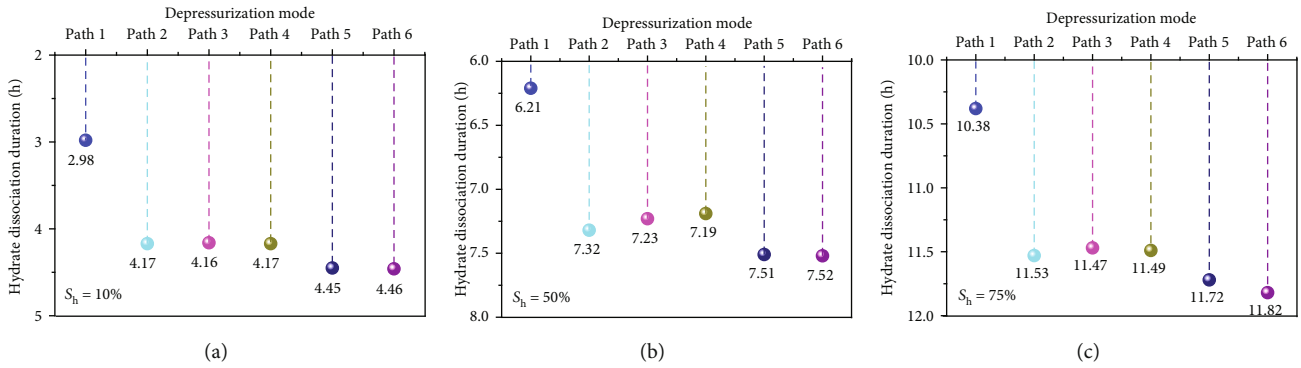


FIGURE 12: Hydrate dissociation varies with the depressurization mode under different hydrate saturations.

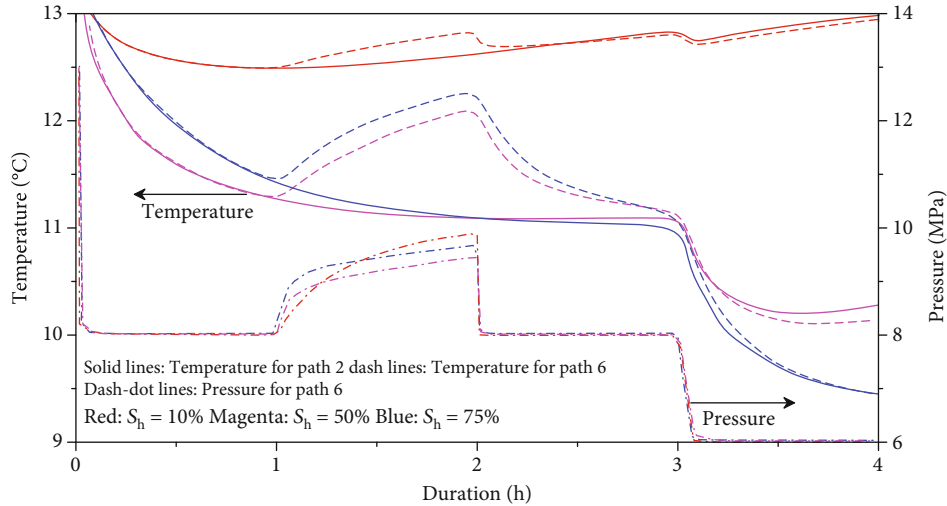


FIGURE 13: Formation pore pressure-temperature response to the shut-in operation.

1, 4, and 5). However, when the average depressurizing rate is fixed, the depressurization mode could hardly affect the hydrate dissociation duration (paths 2, 3, and 4). However, the shut-in operation (path 6) would postpone the hydrate dissociation duration greatly (compared with path 2).

4.5. *Influence of Well Shut-In Operation.* During marine hydrate production process, the gas production process might have to be suspended due to failure in down-hole equipment or irresistible factors such as typhoon [13]. Therefore, shut-in operation is unavoidable in fieldwork, especially for a long-term production. The temperature and pressure

recovery behaviors at point A (Figure 9) are taken to explore the influence of shut-in operation (Figure 13).

It could be concluded from Figure 13 that the pore pressure would rebound logarithmically once the gas production is suspended. The higher the hydrate saturation, the faster the pressure recovery rate would be. However, at the late stage of shut-in period, the pressure for the lower hydrate saturation (10%) case exceeds the higher hydrate saturation (50% or 75%) cases. This is because the temperature of the sediment for lower hydrate saturation (10%) case is much higher than that when hydrate saturation is 50% and 75%.

When the shut-in operation is ended, the pore pressure would decrease to the regular level (path 2) instantaneously, whereas the temperature decreases logarithmically. This is quite important for field operation because it can be inferred from Figure 13 that the shut-in operation could only affect the pressure-temperature (P - T) changing behaviors in a short range. Therefore, we infer from the combination results from Figures 7 and 13 that the shut-in operation could hardly affect the fluid production behaviors (represented by IGWR) and formation P - T response in the long run.

All the simulation cases in this paper were conducted under the constant confining pressure and constant confining temperature conditions at lab scale. The hydrate production processes are compared qualitatively between lab scale and field scale, although the lab-scale results might be influenced by the boundary effect. The conclusions obtained in this paper would have significant importance for field hydrate production operation.

5. Summary and Conclusions

Both experimental and numerical simulations were conducted in the lab-scale to determine the gas-water production behaviors and formation physical responses to depressurization modes. Two experiments were used to verify the numerical model and to get the accurate value of hydrate intrinsic dissociation constant under constant confining temperature and pressure conditions. Based on the verified lab-scale numerical model, we carried out a series of numerical simulations to determine the influences of depressurization modes on cumulative gas-water production behaviors, formation temperature, and hydrate saturation. All simulation cases were conducted under the same total pressure drop (4 MPa). The influences of shut-in operation were also discussed in this paper. This study yields the following results and conclusions.

- (1) The gas production behaviors match well with those of numerical simulation. However, the pressure evolutionary behaviors from experiments showed obvious hysteresis, although the trend is similar with that from numerical results. We inferred that the inlet of pressure sensor in the experiments could be blocked by secondary hydrate. The modified hydrate intrinsic dissociation constant K_D is 2.43×10^4 (mol/m²·Pa) according to the matching

- (2) The influences of depressurization mode on multi-phase seepage field and the residual fluid (gas or water) saturation field could be characterized by the integrated gas-water ration (IGWR). The IGWR increases greatly with the increase in initial hydrate saturation. Under the same initial hydrate saturation and the same total pressure-drop magnitude, the IGWR decreases linearly with the increase in depressurizing magnitude in each step, while increase in a logarithmic style with the increase in the number of steps. Therefore, a multistep depressurization is vital for increasing the IGWR
- (3) Both the temperature decrease and hydrate dissociation initiate at the outlet and propagate towards the far side of the model in a nonpiston style in the I -direction. In the R -direction, the hydrate saturation and temperature evolve axisymmetrically under the combination of endothermic hydrate dissociation process, Joule-Thomson effect, and heat supply from the confining oil. Slow and multistage depressurization strategy would help to alleviate temperature drop; hence, it probably benefits for avoiding potential hydrate reformation
- (4) The pore pressure rebounds logarithmically if the gas production is suspended. Once the shut-in operation is ended, the pore pressure would decrease to the regular level instantaneously. Furthermore, the shut-in operation could only affect the IGWR and formation P - T response in a short response, rather than in the long-term level. However, the shut-in operation would prolong the hydrate dissociation duration greatly

Data Availability

Data are available on request.

Conflicts of Interest

The authors declare that they have no conflicts of interest.

Acknowledgments

This research was supported by the Taishan Scholar Special Experts Project (No. ts201712079), the National Natural Science Foundation of China (No. 41976074), and the National Key Research and Development Plan (No. 2017YFC0307600). These supports are gratefully acknowledged.

References

- [1] E. D. Sloan, "Fundamental principles and applications of natural gas hydrates," *Nature*, vol. 426, no. 6964, pp. 353–359, 2003.
- [2] Z. R. Chong, S. H. B. Yang, P. Babu, P. Linga, and X.-S. Li, "Review of natural gas hydrates as an energy resource: prospects and challenges," *Applied Energy*, vol. 162, pp. 1633–1652, 2016.

- [3] W. Zhang, J. Liang, J. Wei, P. Su, L. Lin, and W. Huang, "Origin of natural gases and associated gas hydrates in the Shenhu area, northern South China Sea: results from the China gas hydrate drilling expeditions," *Journal of Asian Earth Sciences*, vol. 183, p. 103953, 2019.
- [4] W. Zhang, M. Shao, C. Jiang, and Q. Tian, "World progress of drilling and production test of natural gas hydrate," *Marine Geology & Quaternary Geology*, vol. 35, no. 8, pp. 1–13, 2018.
- [5] M. Terzariol, G. Goldsztein, and J. C. Santamarina, "Maximum recoverable gas from hydrate bearing sediments by depressurization," *Energy*, vol. 141, pp. 1622–1628, 2017.
- [6] Z. R. Chong, J. W. R. Moh, Z. Yin, J. Zhao, and P. Linga, "Effect of vertical wellbore incorporation on energy recovery from aqueous rich hydrate sediments," *Applied Energy*, vol. 229, pp. 637–647, 2018.
- [7] B. Wang, H. Dong, Z. Fan et al., "Numerical analysis of microwave stimulation for enhancing energy recovery from depressurized methane hydrate sediments," *Applied Energy*, vol. 262, p. 114559, 2020.
- [8] D. Lim and H. Ro, "Electrical resistivity measurements of methane hydrate during N₂/CO₂ gas exchange," *Energy & Fuels*, vol. 31, no. 1, pp. 708–713, 2016.
- [9] C. Liu, Y. Li, L. Liu, G. Hu, Q. Chen, and N. Wu, "An integrated experimental system for gas hydrate drilling and production and a preliminary experiment of the depressurization method," *Natural Gas Industry B*, vol. 7, no. 1, pp. 56–63, 2020.
- [10] K. Yamamoto, Y. Terao, and T. Fujii, "Operational overview of the first offshore production test of methane hydrates in the Eastern Nankai Trough," in *2014 Offshore Technology Conference*, Houston, Texas, USA, 2014.
- [11] K. Heeschen, E. Spangenberg, J. M. Schicks, M. Priegnitz, R. Giese, and M. LH, Eds., "Simulating the gas hydrate production test at Mallik using the pilot scale pressure reservoir LARS," in *EGU General Assembly Conference Abstracts*, Vienna, Austria, 2014.
- [12] K. Yamamoto, X. Wang, M. Tamaki, and K. Suzuki, "Hydrate reformation characteristics in natural gas hydrate dissociation process: a review," *RSC Advances*, vol. 256, pp. 113878–116013, 2019.
- [13] J. F. Li, J. L. Ye, X. W. Qin et al., "The first offshore natural gas hydrate production test in South China Sea," *China Geology*, vol. 1, no. 1, pp. 5–16, 2018.
- [14] L. I. Yanlong, H. U. Gaowei, L. I. Changling et al., "Gravel sizing method for sand control packing in hydrate production test wells," *Petroleum Exploration and Development*, vol. 44, no. 6, pp. 1016–1021, 2017.
- [15] Y. L. Li, N. Y. Wu, F. L. Ning et al., "A sand-production control system for gas production from clayey silt hydrate reservoirs," *China Geology*, vol. 2, no. 2, pp. 1–13, 2019.
- [16] Y. Li, F. Ning, N. Wu et al., "Protocol for sand control screen design of production wells for clayey silt hydrate reservoirs: a case study," *Energy Science & Engineering*, vol. 8, no. 5, pp. 1438–1449, 2020.
- [17] Ş. Merey, "Evaluation of drilling parameters in gas hydrate exploration wells," *Journal of Petroleum Science and Engineering*, vol. 172, pp. 855–877, 2019.
- [18] J. Sun, F. Ning, H. Lei et al., "Wellbore stability analysis during drilling through marine gas hydrate-bearing sediments in Shenhu area: a case study," *Journal of Petroleum Science and Engineering*, vol. 170, pp. 345–367, 2018.
- [19] L. Liu, X. Lu, X. Zhang, C. Liu, and B. Du, "Numerical simulations for analyzing deformation characteristics of hydrate-bearing sediments during depressurization," *Advances in Geo-Energy Research*, vol. 1, no. 3, pp. 135–147, 2017.
- [20] X. Sun, L. Wang, H. Luo, Y. Song, and Y. Li, "Numerical modeling for the mechanical behavior of marine gas hydrate-bearing sediments during hydrate production by depressurization," *Journal of Petroleum Science and Engineering*, vol. 177, pp. 971–982, 2019.
- [21] L. Dong, Y. Li, H. Liao et al., "Strength estimation for hydrate-bearing sediments based on triaxial shearing tests," *Journal of Petroleum Science and Engineering*, vol. 184, p. 106478, 2020.
- [22] S. Uchida, A. Klar, and K. Yamamoto, "Sand production model in gas hydrate-bearing sediments," *International Journal of Rock Mechanics and Mining Sciences*, vol. 86, pp. 303–316, 2016.
- [23] L. Haojia, L. Yanlong, L. Changling, D. Changyin, W. Nengyou, and S. Jianye, "Calculation model for critical velocity of sand movement in decomposed hydrate cemented sediment," *Marine Geology & Quaternary Geology*, vol. 37, no. 5, pp. 166–173, 2017.
- [24] X. Sun, Y. Li, Y. Liu, and Y. Song, "The effects of compressibility of natural gas hydrate-bearing sediments on gas production using depressurization," *Energy*, vol. 185, pp. 837–846, 2019.
- [25] J. Cai, Y. Xia, S. Xu, and H. Tian, "Advances in multiphase seepage characteristics of natural gas hydrate sediments," *Chinese Journal of Theoretical and Applied Mechanics*, vol. 52, no. 1, pp. 208–223, 2019.
- [26] X. Sun, T. Luo, L. Wang, H. Wang, Y. Song, and Y. Li, "Numerical simulation of gas recovery from a low-permeability hydrate reservoir by depressurization," *Applied Energy*, vol. 250, pp. 7–18, 2019.
- [27] J. Cai, Y. Xia, C. Lu, H. Bian, and S. Zou, "Creeping microstructure and fractal permeability model of natural gas hydrate reservoir," *Marine and Petroleum Geology*, vol. 115, p. 104282, 2020.
- [28] L. Dong, Y. Li, C. Liu et al., "Mechanical properties of methane hydrate-bearing interlayered sediments," *Journal of Ocean University of China*, vol. 18, no. 6, pp. 1344–1350, 2019.
- [29] Y. Sun, X. Ma, W. Guo, R. Jia, and B. Li, "Numerical simulation of the short- and long-term production behavior of the first offshore gas hydrate production test in the South China Sea," *Journal of Petroleum Science and Engineering*, vol. 181, p. 106196, 2019.
- [30] S. C. Phillips, P. B. Flemings, K. You, D. W. Meyer, and T. Dong, "Investigation of in situ salinity and methane hydrate dissociation in coarse-grained sediments by slow, stepwise depressurization," *Marine and Petroleum Geology*, vol. 109, pp. 128–144, 2019.
- [31] Z.-F. Sun, S. Jia, Q. Yuan, C.-Y. Sun, and G.-J. Chen, "One-dimensional study on gas production characteristics of methane hydrate in clayey sediments using depressurization method," *Fuel*, vol. 262, p. 116561, 2020.
- [32] Y. Li, H. Sun, Q. Meng, C. Liu, Q. Chen, and L. Xing, "2-D electrical resistivity tomography assessment of hydrate formation in sandy sediments," *Natural Gas Industry*, vol. 39, no. 10, pp. 133–139, 2017.
- [33] T. Yu, G. Guan, A. Abudula, A. Yoshida, D. Wang, and Y. Song, "Gas recovery enhancement from methane hydrate reservoir in the Nankai Trough using vertical wells," *Energy*, vol. 166, pp. 834–844, 2019.

- [34] M. Yang, J. Zhao, J. Zheng, and Y. Song, "Hydrate reformation characteristics in natural gas hydrate dissociation process: a review," *Applied Energy*, vol. 256, article 113878, 2019.
- [35] Y. Li, C. Liu, L. Liu, J. Sun, H. Liu, and Q. Meng, "Experimental study on evolution behaviors of triaxial-shearing parameters for hydrate-bearing intermediate fine sediment," *Advances in Geo-Energy Research*, vol. 2, no. 1, pp. 43–52, 2018.
- [36] M. T. Reagan, A. F. Queiruga, and G. J. Moridis, "Simulation of gas production from multilayered hydrate-bearing media with fully coupled flow, thermal, chemical and geomechanical processes using TOUGH+Millstone. Part 3: production simulation results," *Transport in Porous Media*, vol. 129, no. 1, pp. 179–202, 2019.
- [37] Y. Jin, D. Yang, and S. X. Li, "Hydrate dissociation conditioned to depressurization below the quadruple point and salinity addition," *Fuel*, vol. 255, p. 115758, 2019.
- [38] G. J. Moridis, M. B. Kowalsky, and K. Pruess, *TOUGH+HYDRATE v1.0 User's Manual: A Code for the Simulation of System Behavior in Hydrate-Bearing Geologic Media. Report LBNL-00149E*, Lawrence Berkeley National Laboratory, Berkeley, CA, 2008.
- [39] Computer Modeling Group (CMG) Ltd, *STARS User Guide—Advanced Processes and Thermal Reservoir Simulator*, Computer Modeling Group (CMG) Ltd, Calgary, Alberta, Canada, 2016.
- [40] J. Sun, F. Ning, L. Zhang et al., "Numerical simulation on gas production from hydrate reservoir at the 1st offshore test site in the eastern Nankai Trough," *Journal of Natural Gas Science and Engineering*, vol. 30, pp. 64–76, 2016.
- [41] T. Ajayi, B. J. Anderson, Y. Seol, R. Boswell, and E. M. Myshakin, "Key aspects of numerical analysis of gas hydrate reservoir performance: Alaska North Slope Prudhoe Bay Unit "L-Pad" hydrate accumulation," *Journal of Natural Gas Science and Engineering*, vol. 51, pp. 37–43, 2018.
- [42] M. Uddin, D. Coombe, D. Law, and B. Gunter, "Numerical studies of gas hydrate formation and decomposition in a geological reservoir," *Journal of Energy Resources Technology*, vol. 130, no. 3, pp. 0195–0738, 2008.
- [43] H. L. Stone, "Probability model for estimating three-phase relative permeability," *Journal of Petroleum Technology*, vol. 22, no. 2, pp. 214–228, 1970.
- [44] T. Yu, G. Guan, A. Abudula, A. Yoshida, D. Wang, and Y. Song, "Heat-assisted production strategy for oceanic methane hydrate development in the Nankai Trough, Japan," *Journal of Petroleum Science and Engineering*, vol. 174, pp. 649–662, 2019.
- [45] K. A. Birkedal, C. M. Freeman, G. J. Moridis, and A. Graue, "Numerical predictions of experimentally observed methane hydrate dissociation and reformation in sandstone," *Energy & Fuels*, vol. 28, no. 9, pp. 5573–5586, 2014.
- [46] J. Zhao, Y. Liu, X. Guo et al., "Gas production behavior from hydrate-bearing fine natural sediments through optimized step-wise depressurization," *Applied Energy*, vol. 260, p. 114275, 2020.

Research Article

Estimation of the Resistivity Index via Nuclear Magnetic Resonance Log Data Based on Fractal Theory

Cheng Feng ¹, Chuang Han,² Wenxing Duan,² Wei Wang,³ Yuntao Zhong,¹ Ziyang Feng,¹ and Ning Zhang¹

¹Faculty of Petroleum, China University of Petroleum-Beijing at Karamay, Karamay, China

²Research Institute of Exploration and Development, Tarim Oilfield Company, PetroChina, Korla, China

³Research Institute of Exploration and Development, Xinjiang Oilfield Company, PetroChina, Karamay, China

Correspondence should be addressed to Cheng Feng; fcvip0808@126.com

Received 9 April 2020; Revised 1 October 2020; Accepted 1 December 2020; Published 22 December 2020

Academic Editor: Wei Wei

Copyright © 2020 Cheng Feng et al. This is an open access article distributed under the Creative Commons Attribution License, which permits unrestricted use, distribution, and reproduction in any medium, provided the original work is properly cited.

The resistivity index is an important parameter for determining the rock saturation index. However, the saturation index changes greatly in unconventional reservoirs, which leads to oil saturation estimation with great difficulty. Hence, we try to establish the relationship between the resistivity index and log data. Firstly, a novel model of estimating the resistivity index with T_2 time was derived based on fractal theory, the relationship between nuclear magnetic resonance (NMR) T_2 spectrum and capillary pressure curve (T_2 - P_c), and Archie formula. It regards the logarithm of the resistivity index as the dependent variable, with T_2 time and T_2 time when water saturation is 100% as the independent variables. Second, 17 cores were drilled, and T_2 spectrum and the relationship between the resistivity index and water saturation (I_r - S_w) were jointly measured. Next, the experimental results were substituted into the established model to get the model parameters via the multivariate statistics regression method. Then, the experimental data engaged and not engaged in modeling were used to test the established model. The average relative errors of estimated resistivity indices and experimental results are smaller than 8%, and those of the regressed saturation index are smaller than 5%. Finally, the established model was applied in log data processing and interpretation with good effects. It thus proves that the method of the estimating resistivity index with T_2 time is reliable, which provides a novel solution for determining rock electrical parameter of unconventional reservoirs.

1. Introduction

The saturation model has always been a puzzle troubling petrophysicists. In the classical rock saturation model, the saturation index has always been an indispensable parameter [1–3]. It is obtained by regression of the I_r - S_w relationship. Therefore, the accurate resistivity index is very important.

In previous researches, the saturation index is usually obtained through the measured I_r - S_w relationship by regression [4–6]. One saturation index is used in the same studied interval. This way of acquiring results features high accuracy and witnesses good application effect in conventional reservoirs. However, as the main research object turns to unconventional reservoirs, the complicated lithology and pore structure lead to wider variation range of the saturation index. Moreover, the rock electrical experiment becomes

more difficult, and the unified saturation index by experiment will bring great error to the evaluation of oil saturation [7]. Hence, in recent years, petrophysicists try to establish the relationship between the resistivity index and well log data, for the purpose of continuously calculating the saturation index.

The basis of the method is that there is certain relationship between the pore structure and conductive property of the rock [8–10]. According to the Archie formula, the resistivity index can be expressed as the quantitative function of water saturation. Meanwhile, previous researches indicate that capillary pressure can also be expressed as the function of wetting-phase saturation. It can either be the linear relationship based on the capillary model [11], or the power function relationship by fractal theory [12, 13]. Besides, Longeron et al. also carried out experimental analysis on this [14]. According to fractal theory, Ge et al. acquired the

relationship between the resistivity index and capillary pressure (I_r - P_c) through experimental data fitting [15]. However, it was not applied in log data processing and interpretation. As a result, it is feasible to try to establish the I_r - P_c relationship [12, 13]. Although capillary pressure is only an experimental data, the reconstruction of pseudocapillary pressure curve with NMR data has been a very mature technology [16, 17]. Therefore, petrophysicists are also trying to establish the relationship between the resistivity index and T_2 time for realizing the estimation of the resistivity index via log data [18–20].

In order to obtain the relationship mentioned above, the model of the estimating resistivity index using T_2 time and T_2 time when water saturation is 100% was first derived based on fractal theory, T_2 - P_c relationship, and Archie formula. Then, the cores acquired from the study area were analyzed, and the above model is calibrated by the experimental data. Finally, the modeling data, the data not engaged in modeling, and the actual log data were used to test the application effect of the model, respectively, from three aspects.

2. Methodology

2.1. Geological Background. Ordos basin, located in North China (Figure 1(a)), is a sedimentation basin and rich in oil and gas resources [22]. According to basement property, tectonic evolution, and current tectonic pattern of the basin, it can be divided into 6 first-order tectonic units (Figure 1(b)). The internal structure is relatively simple with a stable formation and the inclination angle less than 1° generally, while the disrupted fold is relatively developed along the margin of the basin [23–25]. The study area is at the lower-middle parts of the border between Tianhuan depression and North Shaanxi slope, which extends from Dingbian county in the north to Zhenyuan county in the south and stretches from Mahuang mountain in the west to Youfangzhuang village in the east across the Tianhuan depression tectonic belt (Figure 1(b)). The study area is the Chang 8 stratum, being the main pay zone of Triassic Yan-chang formation (Figure 1(c)). In the sedimentation stage of Chang 8 stratum, it is located at a relatively stable structural environment—a typical shallow water delta sedimentation. The distribution of the sand body has a characteristic that partial thick sand body along the direction of the river channel is distributed in a cusped shape. The fine sandstone, siltstone, and mudstone are the main lithology. The porosity and permeability are within the range of 6%–14% and $0.05 \times 10^{-3} \mu\text{m}^2 - 1 \times 10^{-3} \mu\text{m}^2$, respectively, which belongs to a typical tight sandstone reservoir.

2.2. Estimation of the I_r - S_w relationship based on NMR T_2 spectrum. Based on fractal theory, Toledo et al. and Li and Williams considered that rock resistivity bears the following relationship with the corresponding wetting-phase saturation [12, 13]:

$$\frac{1}{R_t} \propto (S_w)^{\frac{1}{\beta(3-D_f)}}, \quad (1)$$

where R_t refers to rock resistivity, $\Omega \cdot \text{m}$; S_w refers to water (wetting-phase) saturation, %; β refers to a model coefficient, irrelevant to water film thickness and dimensionless; D_f refers to fractal dimension, dimensionless.

Besides, Toledo et al. and Li and Williams together considered that the wetting-phase saturation of the rock and the corresponding capillary pressure satisfy the fractal theory [12, 13], as shown in the following relationship:

$$S_w \propto (P_c)^{-(3-D_f)}, \quad (2)$$

where P_c indicates the capillary pressure, MPa.

There have been a lot of publications to discuss how to reconstruct capillary pressure curve by using T_2 spectrum based on the former research results, and the technique seems to run smoothly [26–28]. Scholars believe that on the premise of fixed wetting-phase saturation [17], there is an obvious power function relationship between the P_c and T_2 time, as shown in Eq. (3):

$$P_c = m \times \left(\frac{1}{T_2} \right)^{n^*}, \quad (3)$$

where T_2 indicates the transversal relaxation time, ms; m and n^* mean the model coefficient, which are dimensionless.

Equation (1), Eq. (2), and Eq. (3) have been verified by petrophysical experimental results in different study areas. Equation (4) can be obtained in combination of Eq. (1), Eq. (2), and Eq. (3) under the fixed wetting-phase saturation.

$$R_t \propto \left(\frac{C}{T_2} \right)^{\frac{n^*}{\beta}}, \quad (4)$$

where C is a constant, dimensionless.

Equation (4) reflects that the rock resistivity and T_2 time conform to the relationship mentioned above with the fixed wetting-phase saturation. Therefore, when the wetting-phase saturation is 100%, Eq. (4) can be expressed as Eq. (5).

$$R_0 \propto \left(\frac{C}{T_{2,S_w=100\%}} \right)^{\frac{n^*}{\beta}}, \quad (5)$$

where $T_{2,S_w=100\%}$ indicates the corresponding T_2 time under water-saturated condition, ms; R_0 refers to the rock resistivity under water-saturated condition, $\Omega \cdot \text{m}$.

Equation (6) can be obtained by combining Eq. (4) and Eq. (5) under the fixed wetting-phase saturation.

$$\frac{R_t}{R_0} = A \times \left(\frac{T_2^*}{T_{2,S_w=100\%}} \right)^{-\frac{n^*}{\beta}}, \quad (6)$$

where A indicates the model coefficient, which is dimensionless; T_2^* indicates the corresponding T_2 time under the fixed wetting-phase saturation, ms.

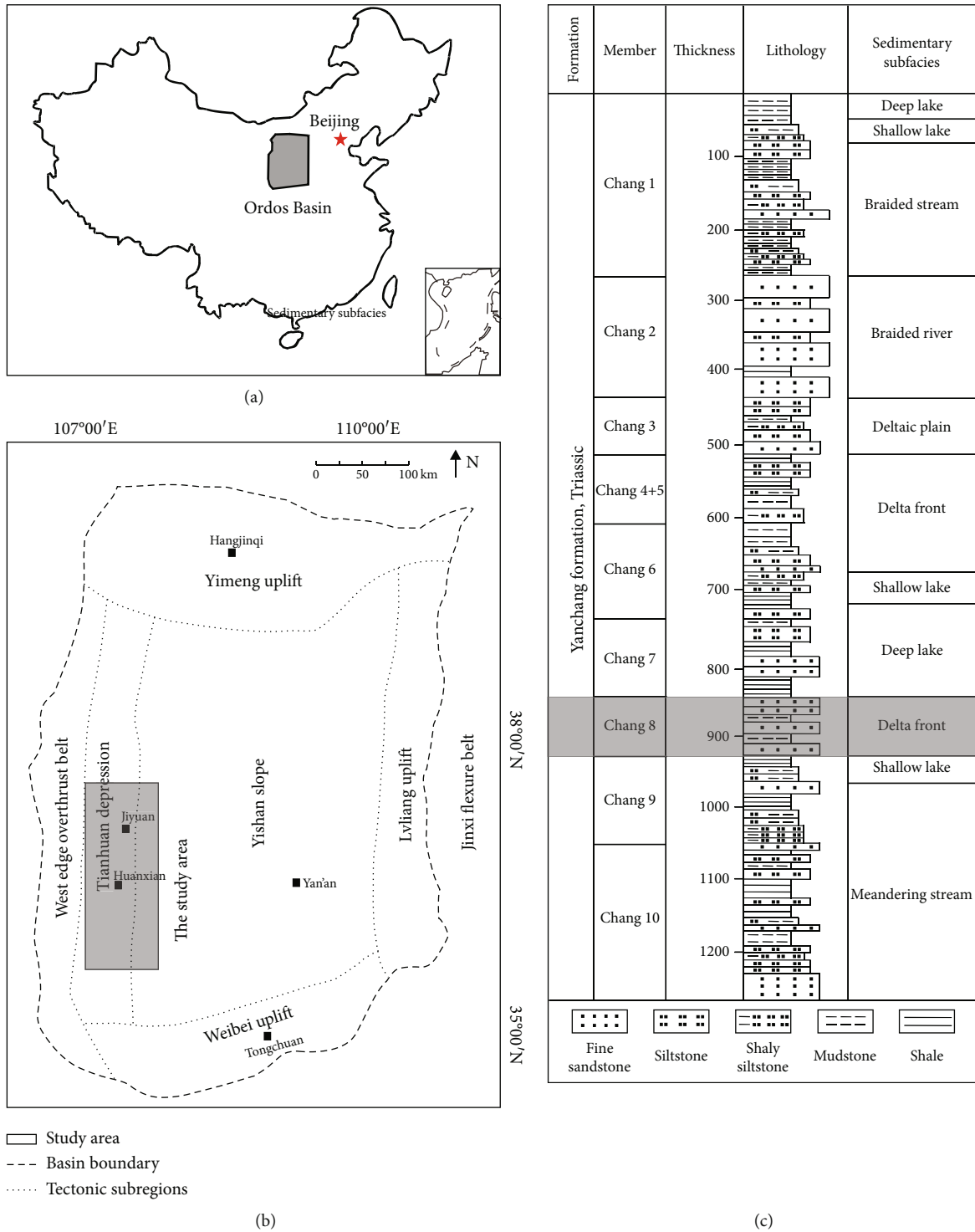


FIGURE 1: Location of the study area [21].

According to the Archie formula [(1)], the resistivity index can be expressed by Eq. (7).

$$I = \frac{R_t}{R_0}, \quad (7)$$

where I indicates the resistivity index, which is dimensionless.

In fact, in the water-saturated state, R_t equals to R_0 ($I = 1$), which have similar physical significance. Hence, at this time, I is an independent variable. However, in other states, the value of I is related to petrophysical properties of rock, and it becomes dependent.

Under the fixed saturation, substitute Eq. (6) into Eq. (7) and take the same logarithm based on 10 on both ends of the new equation to obtain Eq. (8).

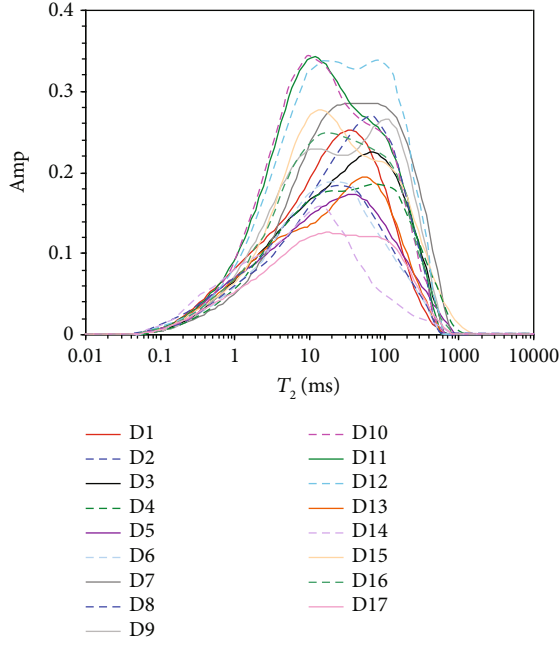


FIGURE 2: The experimental data of T_2 spectrum under water-saturated condition.

$$\lg(I) = \frac{n^*}{\beta} \times (\lg(T_{2,S_w=100\%}) - \lg(T_2^*)) + \lg(A). \quad (8)$$

For the convenience of parameter regression, we define

$$\gamma = \frac{n^*}{\beta}, \quad (9)$$

$$E = \lg(A), \quad (10)$$

where γ and E indicate the model coefficient, which is dimensionless.

Equation (11) can be obtained by combining Eq. (8), Eq. (9), and Eq. (10). There is a linear relationship between $\lg(I)$ and $\lg(T_{2,S_w=100\%}/T_2^*)$ with γ as slope and E as intercept obviously.

$$\lg(I) = \gamma \times \lg\left(\frac{T_{2,S_w=100\%}}{T_2^*}\right) + E, \quad (11)$$

where γ and E are obtained directly by model fitting between the raw data of the T_2 spectrum and the values of I .

3. Results and Discussions

3.1. Experimental Data. To establish the quantitative relationship between the resistivity index and T_2 spectrum, 17 sandstone cores (D1, D2...D17) were drilled in the study area. After processing, core plungers with length of about 4 cm and diameter of 1 inch were formed, respectively. They are complete and strong bonding with no fragmentation. The distribution scopes of porosity and permeability are 6.03%-14.13% and $0.02 \times 10^{-3} \mu\text{m}^2 - 1.34 \times 10^{-3} \mu\text{m}^2$, respectively. NaCl solution was prepared based on the average salinity of

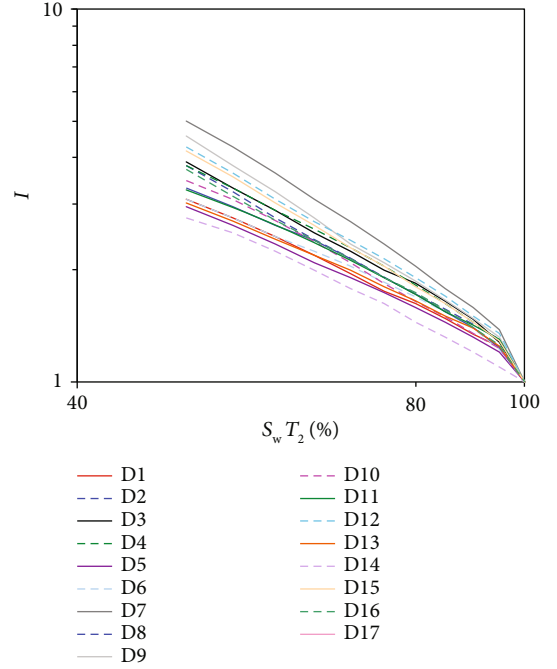


FIGURE 3: The experimental data of the I_r - S_w curve.

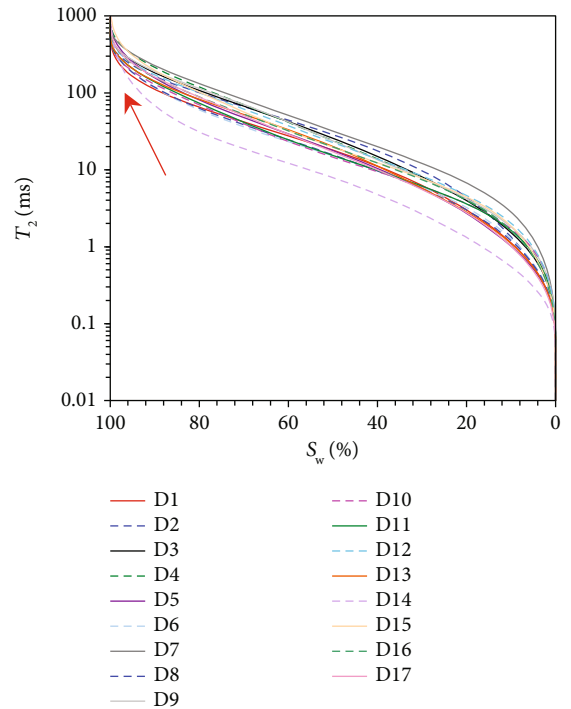


FIGURE 4: The cumulative curves converted by the measured T_2 spectra.

formation water as the experimental water. After the preparation of experimental materials, the cores were saturated with experimental water. The T_2 spectra under water-saturated condition were measured by the MARAN DRX2 experiment device manufactured by Oxford Instruments. The experimental data are shown in Figure 2. Then, the resistivity indices under different water saturations by gas

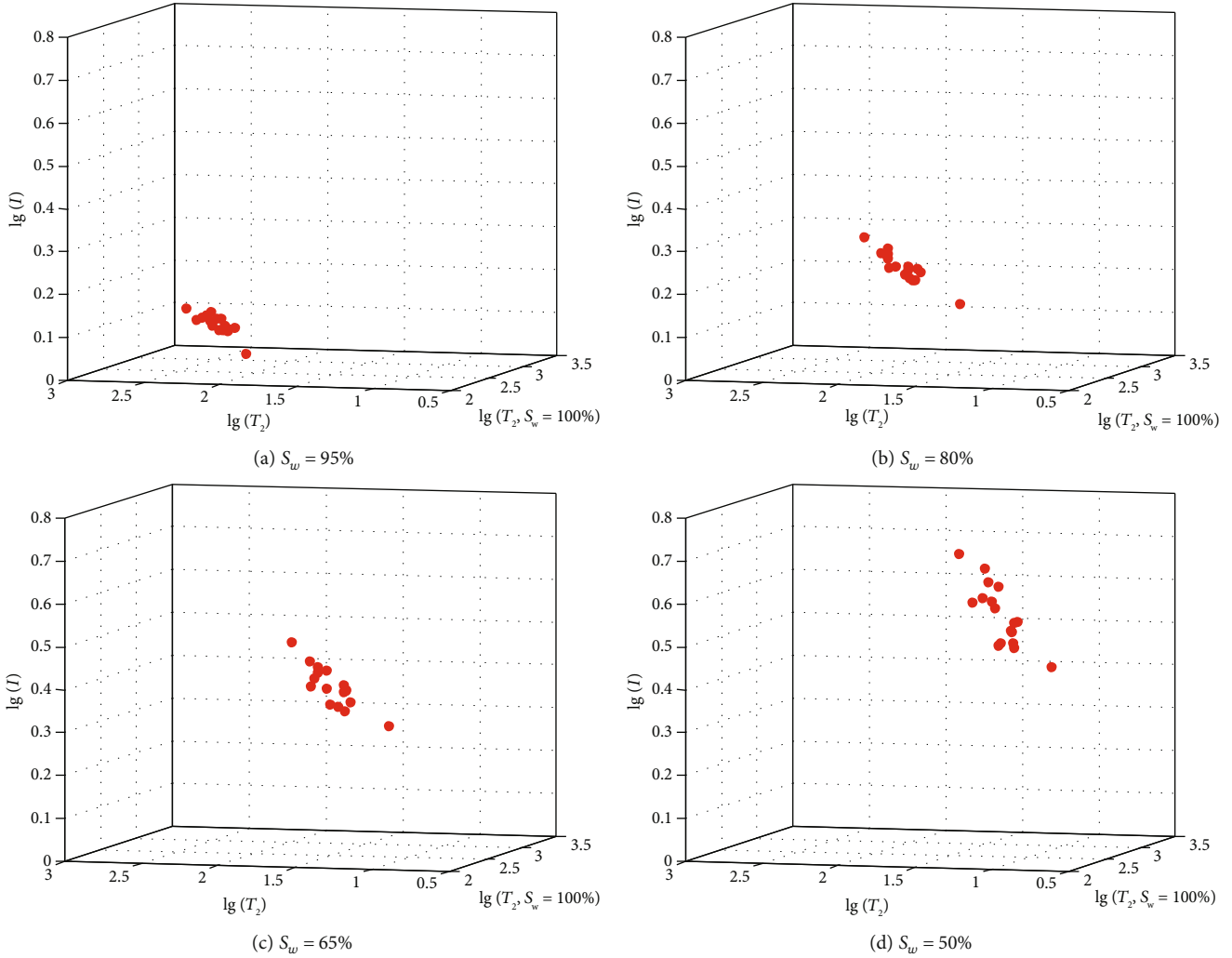


FIGURE 5: The correlation between the resistivity index, T_2 time, and T_2 time when the water saturation is 100% of different cores. (a)–(d) represent that water saturation equals to 95%, 80%, 65%, and 50%, respectively.

TABLE 1: The models for predicting the resistivity index from T_2 time and T_2 time when the water saturation is 100%.

Water saturation	Models	Correlation coefficient
95%	$\log_{10}(I(i)) = 0.192 \times \log_{10}(T_2(i)) - 0.192 \times \log_{10}(T_{2,S_w=100\%}) + 0.166$	0.81
80%	$\log_{10}(I(i)) = 0.229 \times \log_{10}(T_2(i)) - 0.229 \times \log_{10}(T_{2,S_w=100\%}) + 0.417$	0.92
65%	$\log_{10}(I(i)) = 0.276 \times \log_{10}(T_2(i)) - 0.276 \times \log_{10}(T_{2,S_w=100\%}) + 0.689$	0.85
50%	$\log_{10}(I(i)) = 0.411 \times \log_{10}(T_2(i)) - 0.411 \times \log_{10}(T_{2,S_w=100\%}) + 1.138$	0.81

displacing water were measured. As shown in Figure 3, the saturation indices obtained by regression based on the power function are distributed in 1.47-2.16. It reflects that the measured saturation index is of large change scope, and great errors can be caused if the average value is taken in the study area.

3.2. Determination of the T_2 Time when the Water Saturation Is 100%. According to Eq. (11), it will have a great influence on the model accuracy to acquire the accurate T_2 time when the water saturation is 100%. In Figure 2, each NMR curve

represents a core under the condition of saturated water. The integrals of these NMR curves were computed from small T_2 time to big T_2 time that correspond with the x -axis, which reflected the amount of pore water is more and more. Convert the measured T_2 spectrum into a cumulative curve (Figure 4) on the basis of the experimental results in Figure 2. As shown in the position indicated by the arrow, read the corresponding value on the y -axis when the value of the x -axis is 100%. This value is namely the corresponding T_2 time when the water saturation is 100%.

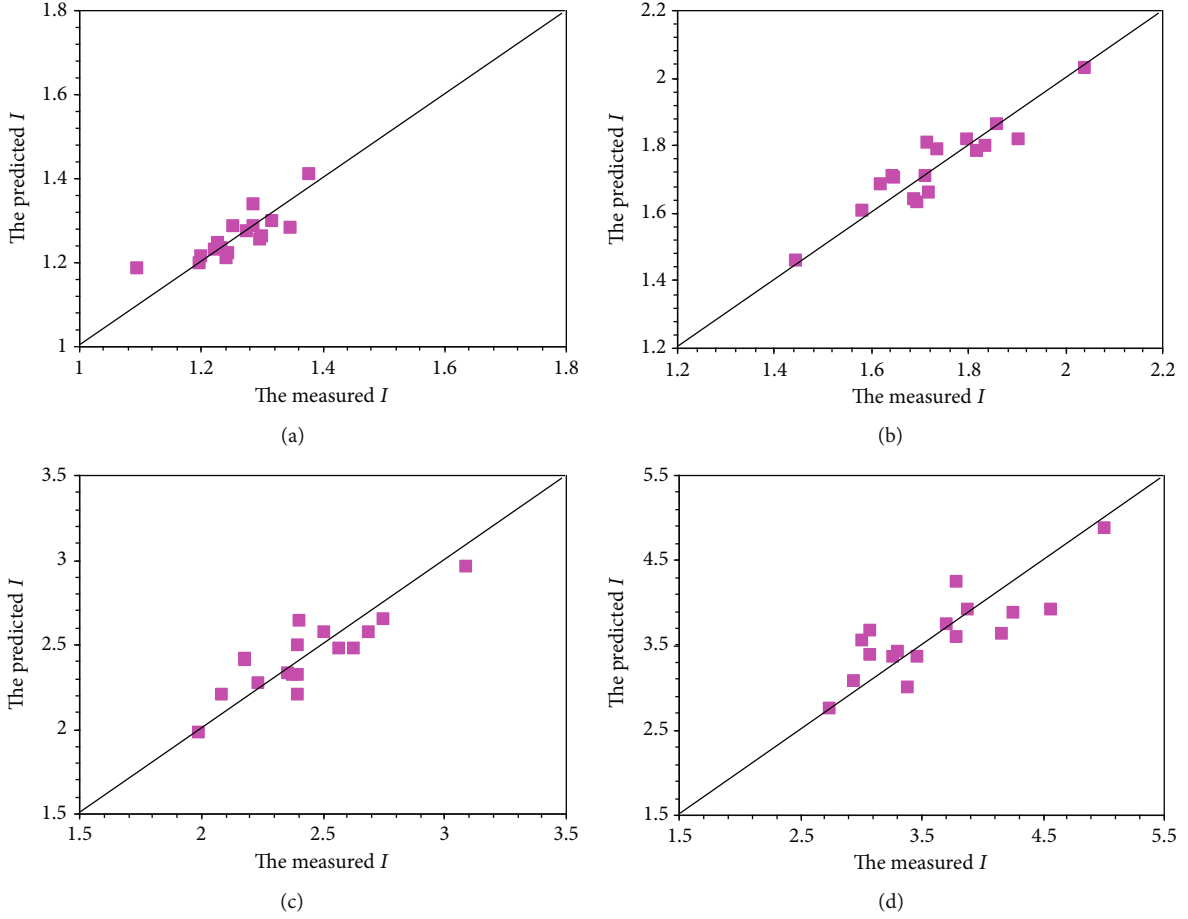


FIGURE 6: The comparison results of the measured and predicted resistivity indices. (a)–(d) represent that water saturation equals to 95%, 80%, 65%, and 50%, respectively.

3.3. Model Establishment. During experimental measurement, the I_r - S_w in Figure 3 is different from the sampling point on the cumulative curve of T_2 spectrum in Figure 4. Hence, unify the sampling points of the two figures prior to the model establishment. Set a fixed water saturation value. Then make statistics, respectively, for the resistivity index in correspondence to different water saturation in Figure 3 and the T_2 time in correspondence to different water saturation in Figure 4. Take logarithm based on 10, respectively, to form a data set for calibrating the model established in Eq. (11).

After the establishment of data set, draw the 3D scatter diagram to present visually. As shown in Figure 5, x -axis, y -axis and z -axis represent, respectively, the value of three parameters after taking the logarithm. It is obvious that in a three-dimensional space, data points form in a similar but not exactly the same tendency under different water saturations. When the water saturation is reduced, the data point is more scattered relatively. Therefore, substitute the data point under different water saturations in Figure 5 into Eq. (11), respectively. Obtain the model parameters γ and E under different water saturations by multivariate statistics regression [22]. As shown in Table 1, the related coefficients of the model are greater

TABLE 2: The average values and relative errors of the predicted and measured resistivity indices.

Water saturation	Average predicted resistivity indices	Average measured resistivity indices	Average relative errors
95%	1.2590	1.2610	2.29%
80%	1.7339	1.7347	2.49%
65%	2.4248	2.4291	4.81%
50%	3.6050	3.6220	7.56%

than 0.8, indicating a better fitting effect and higher model accuracy.

According to the above theoretical model analysis, experimental data presentation (Figure 5), and models established (Table 1), there is a quantitative relationship as shown in Eq. (11) and Table 1 among the resistivity index, the T_2 time of corresponding saturation, and the T_2 time when the water saturation is 100%. The proposed models are supported by the modeling data.

3.4. Model Test. To test the reliability of models established in Table 1, this paper sets forth from two aspects. First, judge

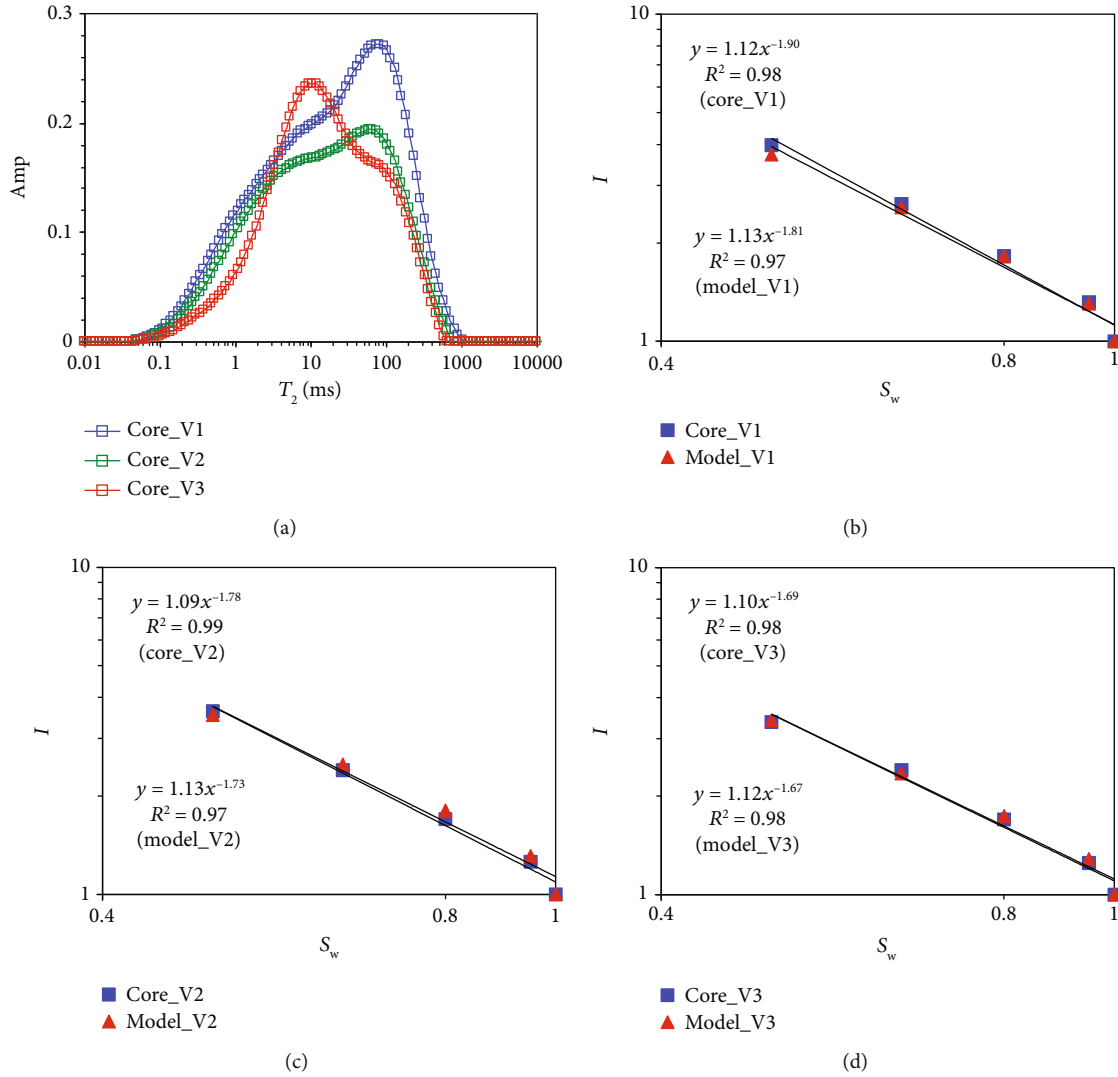


FIGURE 7: The comparison results of the measured and predicted I - S_w (a) represents the T_2 spectra of three cores under water-saturated condition. (b)–(d) represent the comparison results of cores V1, V2, and V3, respectively.

the resistivity indices of cores involved in the model establishment with the established models. Then, estimate the resistivity index and saturation index of cores not involved in the model establishment with the established models.

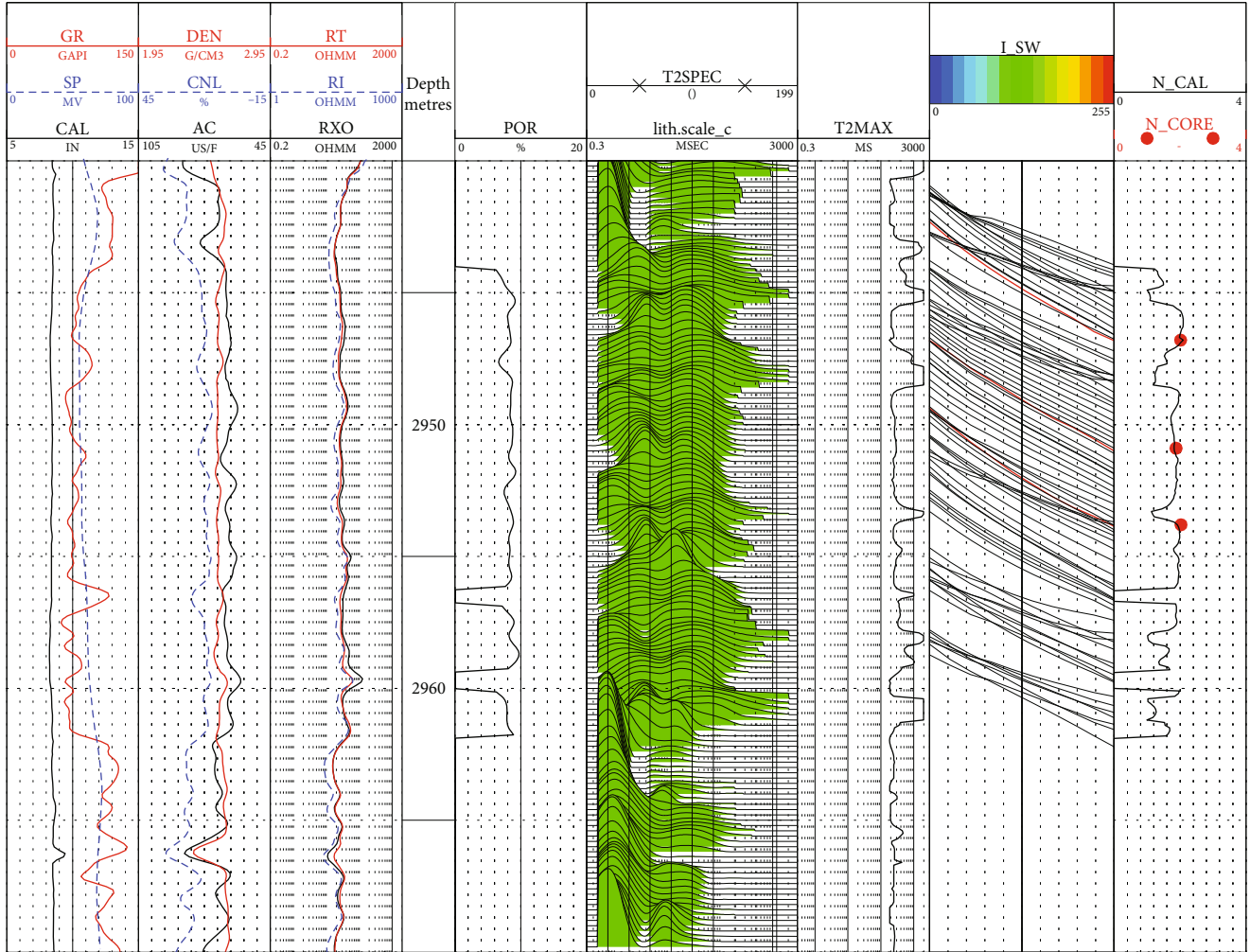
As can be seen from Figures 2 and 3, the experimental results of 17 cores were used for modeling based on Table 1. Under the condition of fixed water saturation, T_2 time and T_2 time when the water saturation is 100% in the modeling data set were, respectively, substituted into the models established in Table 1 to estimate the resistivity indices of 17 cores under different water saturation states. Then, the estimated resistivity indices and the measured results were analyzed by cross plot, as shown in Figure 6. The ordinate refers to the estimated resistivity index, and the abscissa refers to the measured one. When water saturation is less than 80%, most of the data points are distributed near the diagonal, which indicates that the estimated resistivity indices are close to the experimental results. When the water saturation is 95%, a small amount of estimated results is

significantly different from the measured results, which may be the interference caused by measurement error. Table 2 lists the average values and average relative errors between the estimated and measured resistivity indices under the condition of fixed water saturation. As seen from the table, the average values are very consistent, and the average relative errors are less than 8%, indicating that the estimated results are consistent with the measured ones.

Figure 7(a) shows the T_2 spectrum experimental results of 3 cores not used for modeling. First, the T_2 spectra in Figure 7(a) were converted into the cumulative distribution curves by the order of water saturation from low to high. T_2 time corresponding to the set water saturation (95%, 80%, 65%, 50%) and T_2 time when the water saturation is 100% on the cumulative distribution curve were read, respectively. Then, they were, respectively, substituted into Table 1 to calculate the resistivity indices under different water saturation states. As shown in Figures 7(b)–(d), the estimated and measured I_r - S_w relationships were analyzed by cross

TABLE 3: The comparison results of the measured and predicted rock electrical parameters.

No.	b_{core}	b_{model}	Relative errors of b	n_{core}	n_{model}	Relative errors of n
V1	1.12	1.13	0.89%	1.90	1.81	4.74%
V2	1.09	1.13	3.67%	1.78	1.73	2.81%
V3	1.10	1.12	1.82%	1.69	1.67	1.18%

FIGURE 8: A field study of the proposed model for resistivity prediction via T_2 spectrum.

plot; wherein, the three figures represent cores V1, V2, and V3, respectively. As can be seen from them, the estimated data points (red) almost coincide with the measured data points (blue), indicating both results are in high consistency. In addition, the regressed and measured rock electrical parameter b and saturation index n are shown in Table 3. The estimated results of the no matter rock electrical parameter b or saturation index n are in high consistency with the measured results, showing that the relative error is basically below 5%.

Whether through the experimental results involved in modeling or the ones not involved in modeling, the test results of the model are good, indicating that the estimation model established is reliable.

3.5. Analysis of the Application Effect. The above results show that the established estimation model of the resistivity index is reliable from the point of view of the core. Now it is analyzed with actual log data from a water layer. Figure 8 is a log interpretation result of well B in the study area. In the figure, the first track is the lithologic logs (natural gamma ray curve, spontaneous potential curve, and caliper curve); the second one is the porosity logs (density curve, neutron porosity curve, and acoustic curve); the third one is the resistivity logs (deep, medium, and shallow resistivity curves); the fifth one is the porosity curve calculated by density log data; the sixth one is the NMR log curve; the seventh one is T_2 time calculated when the water saturation is 100%; the eighth one is the I_r-S_w relationship curve; and the ninth one is the

saturation index curve. Among them, the black curves in the eighth and ninth tracks are the results estimated by the established model, and the red curves and scatter points in both tracks are the analysis results of the core experiment. As seen from Figure 8, the I_r - S_w relationship curves estimated in the eighth track have the same trend as the analysis results of the core experiment, with similar curve shape and good coincidence. The errors between the predicted and measured saturation indices in the ninth track are very small.

To sum up, it is feasible to estimate the resistivity index by T_2 spectrum. Furthermore, the established estimation model is reliable.

4. Conclusions

Based on fractal theory, T_2 - P_c relationship, and Archie formula, a corresponding model is derived, which regards the logarithm of the resistivity index as the dependent variable and regards T_2 time and T_2 time when the water saturation is 100% as the independent variable. The model parameters under different water saturation states were obtained by the multivariate statistical regression method, in combination with the NMR T_2 spectra and I_r - S_w relationships of 17 cores in the study area. Then, the reliability of the models was verified by experimental results of modeling data and nonmodeling data, with errors of less than 8% and 5%. Finally, the processing and interpretation results of the actual log data further verify the good application effect of the models. It thus proves that the method of the estimating resistivity index with T_2 time is reliable, which provides a novel solution for determining the rock electrical parameter of unconventional reservoirs.

Nomenclature

R_l :	Deep lateral resistivity, can measure the undisturbed formation, Ω -m
R_0 :	Rock resistivity under water-saturated condition, Ω -m
S_w :	Water saturation, %
D_f :	Fractal dimension, dimensionless
P_c :	Capillary pressure, Mpa
m :	The index of pore structure related to formation factors by Archie formula, dimensionless
n^* :	The saturation index associated with the resistance increase index in The Archie formula, dimensionless
T_2 :	Transverse relaxation time used to characterize the decay of the NMR spin-echo signal, s
$T_{2,S_w=100\%}$:	Corresponding T2 time under water-saturated condition, s
I :	Resistivity index in Archie formula, dimensionless
A, β, γ, E :	The parameters of models, dimensionless.

Data Availability

The data used but not presented in the manuscript will be provided on request.

Conflicts of Interest

The authors declare that they have no conflicts of interest.

Acknowledgments

Research for this paper was supported by the National Natural Science Foundation of China (No. 42004089), the Major National Oil & Gas Specific Project of China (No. 2016ZX05050008), the Natural Science Foundation of Xinjiang Uygur Autonomous Region (No. 2017D01B57), the Natural Science Project of Xinjiang Uygur Autonomous Region Education Department (No. XJEDU2017S063, XJEDU2019Y070), the Young Elitist Scientific Research Project of China University of Petroleum, Beijing at Karamay (No. BJRC20170001), and the Scientific Research Starting Foundation of China University of Petroleum, Beijing at Karamay (No. RCYJ2016B-01-008).

References

- [1] G. E. Archie, "The electrical resistivity log as an aid in determining some reservoir characteristics," *Transactions of the AIME*, vol. 146, no. 3, pp. 54–61, 2013.
- [2] M. H. Waxman and L. J. M. Smits, "Electrical conductivities in oil-bearing shaly sands," *SPE Journal*, vol. 8, no. 8, pp. 107–122, 1968.
- [3] C. Clavier, G. Coates, and J. Dumanoir, "Theory and experimental basis for the dual-water model for interpretation of shaly sands," *SPE Journal*, vol. 24, no. 2, pp. 153–168, 1984.
- [4] W. G. Anderson, "Wettability literature survey-part 2: wettability measurement," *Journal of Petroleum Technology*, vol. 38, no. 11, pp. 1246–1262, 1986.
- [5] Z. Q. Mao, C. G. Zhang, and C. Z. Lin, "The effect of wettability of reservoir on the log derived water saturation," *Well Logging Technology*, vol. 21, no. 1, pp. 50–54, 1997.
- [6] C. Feng, Z. Mao, W. Yin et al., "An experimental study on resistivity and conductive mechanism in low-permeability reservoirs with complex wettability," *Chinese Journal of Geophysics*, vol. 60, no. 2, pp. 164–173, 2017.
- [7] L. Zhu, C. Zhang, C. Zhang et al., "Challenges and prospects of digital core-reconstruction research," *Geofluids*, vol. 2019, 29 pages, 2019.
- [8] L. Z. Xiao, *NMR Image Logging and NMR in Rock Experiments*, Science Press, Beijing, 1998.
- [9] L. M. Zhang and Y. J. Shi, "On Archie's electrical parameters of sandstone reservoir with complicated pore structures," *Well Logging Technology*, vol. 29, no. 5, pp. 446–448, 2005.
- [10] X. Ge, Y. Fan, D. Yang, H. Hu, and S. Deng, "Study on the influential factors of saturation exponent based on the equivalent rock element theory," *Oil Geophysical Prospecting*, vol. 46, no. 3, pp. 477–481, 2011.
- [11] M. Szabo, "New methods for measuring imbibition capillary pressure and electrical resistivity curves by centrifuge," *SPE Journal*, vol. 14, no. 14, pp. 243–252, 1974.
- [12] G. T. Toledo, R. A. Novy, H. T. Davis, and L. E. Scriven, "Capillary pressure, water relative permeability, electrical conductivity and capillary dispersion coefficient of fractal porous media at low wetting phase saturation," *SPE Advanced Technology Series*, vol. 2, no. 1, pp. 136–141, 2013.

- [13] K. Li and W. Williams, "Determination of capillary pressure function from resistivity data," *Transport in Porous Media*, vol. 67, no. 1, pp. 1–15, 2007.
- [14] D. G. Longeron, M. J. Argaud, and L. Bouvier, "Resistivity index and capillary pressure measurements under reservoir conditions using crude oil," in *SPE Annual Technical Conference and Exhibition*, San Antonio, Texas, October 1989.
- [15] X. Ge, Y. Fan, S. Deng, and Q. Du, "Research on correlation between capillary pressure and resistivity index based on fractal theory," *Journal of China University of Petroleum*, vol. 36, no. 4, pp. 72–76, 2012.
- [16] J. Hofman, W. Slijkerman, W. Looyestijn, and Y. Volokitin, "Constructing capillary pressure curves from NMR log data in the presence of hydrocarbons," in *SPWLA Annual Logging Symposium*, Oslo, Norway, 1999.
- [17] Y. He, Z. Mao, L. Xiao, and Y. Zhang, "A new method to obtain capillary pressure curve using NMR T2 distribution," *Journal of Jiling University*, vol. 35, pp. 177–181, 2005.
- [18] X. Ge, Y. Fan, F. Wu, and P. Huang, "Correspondence of core nuclear magnetic resonance T2 spectrum and resistivity index," *Journal of China University of Petroleum*, vol. 36, no. 6, pp. 53–61, 2012.
- [19] Y. H. Guo, B. Z. Pan, L. H. Zhang, and C. H. Fang, "Research and application of the relationship between transverse relaxation time and resistivity index in tight sandstone reservoir," *Journal of Petroleum Science and Engineering*, vol. 160, pp. 597–604, 2018.
- [20] C. Feng, Z. Yang, Z. Feng, Y. Zhong, and K. Ling, "A novel method to estimate resistivity index of tight sandstone reservoirs using nuclear magnetic resonance logs," *Journal of Natural Gas Science and Engineering*, vol. 79, p. 103358, 2020.
- [21] F. Liu, X. Zhu, L. Yang, L. Xu, X. Niu, and S. Zhu, "Sedimentary characteristics and facies model of gravity flow deposits of late Triassic Yanchang formation in southwestern Ordos basin, NW China," *Petroleum Exploration and Development*, vol. 42, no. 5, pp. 633–645, 2015.
- [22] K. X. Xiao, *The researching of the characteristic and main controlling factors of Chang-8's oil reservoir in Jiyuan area, Ordos basin*, Chengdu University of Technology, 2011.
- [23] H. Yang and W. Z. Zhang, "Leading effect of the seventh member high-quality source rock of Yanchang formation in Ordos basin during the enrichment of low-penetrating oil-gas accumulation: geology and geochemistry," *Geochimica*, vol. 34, no. 2, pp. 147–154, 2005.
- [24] C. Feng, Y. Shi, J. Li, L. Chang, G. Li, and Z. Mao, "A new empirical method for constructing capillary pressure curves from conventional logs in low-permeability sandstones," *Journal of Earth Science*, vol. 28, no. 3, pp. 516–522, 2017.
- [25] C. Feng, Z. Wang, X. Deng et al., "A new empirical method based on piecewise linear model to predict static Poisson's ratio via well logs," *Journal of Petroleum Science and Engineering*, vol. 175, pp. 1–8, 2019.
- [26] P. Zhao, Z. Sun, X. Luo et al., "Study on the response mechanisms of nuclear magnetic resonance (NMR) log in tight oil reservoirs," *Chinese Journal of Geophysics*, vol. 59, pp. 1927–1937, 2016.
- [27] L. Zhu, C. Zhang, Y. Wei, and C. M. Zhang, "Permeability prediction of the tight sandstone reservoirs using hybrid intelligent algorithm and nuclear magnetic resonance logging data," *Arabian Journal for Science and Engineering*, vol. 42, no. 4, pp. 1643–1654, 2017.
- [28] P. Zhao, Z. Wang, Z. Sun, J. Cai, and L. Wang, "Investigation on the pore structure and multifractal characteristics of tight oil reservoirs using NMR measurements: Permian Lucaogou Formation in Jimusaer sag, Junggar Basin," *Marine and Petroleum Geology*, vol. 86, pp. 1067–1081, 2017.

Research Article

A Model for a Multistage Fractured Horizontal Well with Rectangular SRV in a Shale Gas Reservoir

Jianfa Wu, Jian Zhang, Cheng Chang, Weiyang Xie , and Tianpeng Wu

PetroChina Southwest Oil & Gas Field Co., Chengdu, Sichuan, China

Correspondence should be addressed to Weiyang Xie; johnhatteras@163.com

Received 27 March 2020; Revised 12 October 2020; Accepted 20 October 2020; Published 7 December 2020

Academic Editor: Wen-Dong Wang

Copyright © 2020 Jianfa Wu et al. This is an open access article distributed under the Creative Commons Attribution License, which permits unrestricted use, distribution, and reproduction in any medium, provided the original work is properly cited.

Although great success has been achieved in the shale gas industry, accurate production dynamic analyses is still a challenging task. Long horizontal wells coupling with mass hydraulic fracturing has become a necessary technique to extract shale gas efficiently. In this paper, a comprehensive mathematical model of a multiple fractured horizontal well (MFHW) in a rectangular drainage area with a rectangular stimulated reservoir volume (SRV) has been established, based on the conceptual model of “tri-pores” in shale gas reservoirs. Dimensionless treatment and Laplace transformation were employed in the modeling process, while the boundary element method was used to solve the mathematical model. The Stehfest numerical inversion method and computer programming techniques were employed to obtain dimensionless type curves, production rate, and cumulative production. Results suggest that 9 flow stages can be observed from the pseudopressure derivative type curve when the reservoir and the SRV are large enough. The number of fractures, SRV permeability, and reservoir permeability have no effect on the total production when the well is abandoned. As SRV and reservoir permeability increases, the production rate is much higher in the middle production stage. Although the SRV scale and its permeability are very important for early and intermediate production rates, the key factors restricting the shale gas production rate are the properties of the shale itself, such as adsorbed gas content, natural fractures, and organic content. The proposed model is useful for analyzing production dynamics with stimulated horizontal wells in shale gas reservoirs.

1. Introduction

Shale gas, together with coalbed methane, which was once the source rock of oil and gas. Shale gas is a typical unconventional gas stored with adsorbed, free gas ([1]; Li Yong et al., 2019). Shale gas consists mainly of methane, and there are many kinds of interlayers in shale strata, such as siltstone, silty mudstone, and polytite siltstone. Currently, shale gas extraction is developing rapidly and has played an important role in the US energy industry since 2000. It has spread quickly to China and Australia as a potential energy source [2]. For example, the annual production of shale gas in 2007 in the US was 56.4 billion cubic meters, while it reached 447.0 billion cubic meters in 2016; its proportion to the world annual production is 12% [3]. With the success of shale gas development, shale gas has the potential to become the primary energy source in the future.

Due to the special formation characteristics and pore types of a shale gas reservoir, exploiting shale gas requires hydraulic fracturing. Specifically, i.e., horizontal wells with massive hydraulic fracturing [4–6]. Massive hydraulic fracturing of horizontal wells in shale gas reservoirs creates a fracture network around the well called stimulated reservoir volume (SRV). The SRV, which is the main method of increasing shale gas production, consists of hydraulic fractures and a fracture network. Therefore, it is important to devise an effective and accurate model to describe the SRV and to help understand the flow characteristics of shale gas underground.

Kucuk and Sawyer [7] proposed a model to analyze the adsorption and desorption characteristics in fractured reservoirs and derived a numerical solution to the model considering the effects of desorption and slippage. Lancaster and Gatens III [8] analyzed postfractured well testing data of

eastern Devonian shale, which was described as a dual-porosity reservoir, and those data were used to estimate fracture length and fracture conductivity. Devonian shale wells showed that fracture half-lengths calculated from conventional postfracture pressure-buildup tests were shorter than designed, based on which Johnston and Lee [9] proposed a new method to determine net pay thickness and presented results suggesting that conventional tests of those wells are inadequate.

Brown et al. [10] and Ozkan et al. [11] assumed that the main flow type in fractured horizontal wells is linear, and established a trilinear flow model for a multistage fractured horizontal well in a shale gas reservoir using the model presented by Lee and Brockenbrough (Lee and Brockenbrough 1986). Based on the linear-flow theory, a plate dual-porosity model, and the Warren-Root block dual-porosity model, Bello and Watenbargen [12] and Al-Ahmadi et al. [13] proposed a model to analyze the production dynamics and pressures of MFHWs in shale gas reservoirs. Nobakht et al. (Nobakht et al., 2012) first proposed the conceptual model of different combinations of horizontal wells, porous media types, and hydraulic fractures in shale gas reservoirs, and then analyzed the different flow stages during the development process. Assuming SRV exists only in a limited region around the fractures and fracture half-lengths equal to the width of the reservoir, Stalgorova and Mattar [14] derived a modified trilinear flow model and obtained the solution of this model in Laplace space. Xu et al. [15] proposed an unsteady seepage model of a MFHW at constant rate production in a shale gas reservoir. The model assumed that the flow types in a fractured horizontal well are alternately linear and transitional, and the fracture network exists in a limited region around the hydraulic fractures.

To summarize, there are two types of models to analyze well production performance of MFHWs with SRVs in shale gas reservoirs. One is the linear flow model, which is based on the assumption that all fractures have the same length and conductivity and are spaced uniformly along the horizontal well ([11–21]; Zhao et al., 2016b; [22–25]), and the main related schematics of linear models are listed in Table 1. Although it is common field practice to design equally spaced hydraulic fractures, the requirements of equal properties and fracture lengths of shale gas reservoirs are hard to satisfy because of the development of natural fractures and their anisotropy and heterogeneity. The other type of flow model is the numerical simulation model based on finite-element, finite-difference, or other numerical methods [26–36].

Normal shale gas reservoirs have a dual-porosity nature, with macropores and micropores in matrix, and microfractures made by hydraulic fracturing (Ge & Zhang, 2012; [38–40]). The output process of shale gas from the reservoir can be subdivided into 4 stages: (1) the gas desorbed from the matrix particle surfaces, (2) diffusion from the matrix to the macropores, (3) flows from the macropores to the microfractures, and (4) Darcy flows through the fracture network to the bottom hole.

Well testing analysis is an important dynamic monitoring tool for petroleum engineers to accurately determine the parameters of oil and gas reservoir engineering, to evalu-

ate the stimulation in the shale gas reservoir, and to provide more effective plans for the oil field. In addition, a suitable mathematical model for horizontal wells with SRVs in shale gas reservoirs is vital to well testing.

As we can see from the above discussion, both analytical methods and linear flow models have their own deficiencies in obtaining production dynamics in shale gas reservoirs. On one side, analytical methods, such as point source and Green's function method, can only deal with seepage problems of shale gas in regular-shaped reservoirs, such as reservoirs with circular or infinite outer boundaries. However, the practical boundary of shale gas reservoirs is quite complex considering the effects of SRV, which in consequence cannot be handled by this traditional analytical method. On the other, linear flow models usually put the whole reservoir as a rectangular area, and subdivide the reservoir region into some small rectangular areas, as shown in Table 1. The subdivision principle of the small rectangular sections is the gas flow capacities in formations, i.e., a bigger flow capacity in the SRV region and a weaker flow capacity as the region. In linear flow models, a quarter of the area around a hydraulic fracture is usually studied for simplicity, which brings into another assumption that all hydraulic fractures are uniformly spaced and with the same length. These assumptions are also not in accordance with practical conditions of shale gas reservoirs. Besides, other flow patterns, such as radial flow and elliptical flow, and interferences among fractures cannot be reflected from the linear flow models. Thus, a more comprehensive and accurate model considering both the rectangular composite nature of a shale gas reservoir and the fracture heterogeneities need to be established in an effort to analyze production dynamics better in shale gas reservoirs. In this paper, we present a percolation model for a multistage horizontal well in a rectangular shale gas reservoir with an SRV considering unsteady transport theory, which cannot be tackled by analytical methods or linear flow conceptions. The boundary element method is employed to solve the proposed mathematical model, with parameter sensitivity analysis conducted for production dynamics. Results show that the model we propose should be useful for analyzing stimulated horizontal wells in shale gas reservoirs.

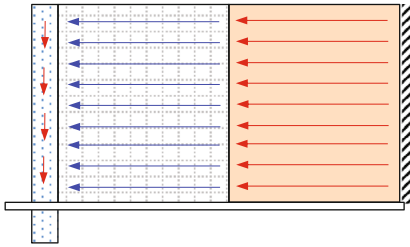
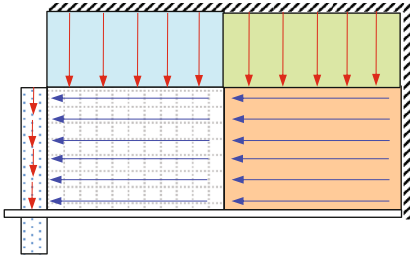
2. Transport Mechanism of Shale Gas

2.1. Characteristics of Shale Gas Reservoir. The characteristics of a shale gas reservoir are very different from those of a conventional gas well, in both the structure and the flow mechanism. The typical classification method is that of Loucks et al. [41]. They classified the pore types of the shale matrix and the natural microfractures; their classification is comprised of the following 4 types: intergranular pores, intragranular pores, organic pores, and natural microfractures (Figure 1 shows the main pore types of a shale gas reservoir). The first 2 pore types are related to the mineral grains. The difference between them is that intergranular pores develop between grains and intragranular pores develop within grains. Organic pores are intrapores of organic matter. In shale, the main pores are micropores, nanopores, and microfractures, so approximately 20% to 80% of the gas is absorbed by the

TABLE 1: Schematics of the linear models.

No.	Schematics of physical models	References
1		Xu et al. 2013 [15]
2		Nobakht and Clarkson 2013 [18]
3		Brown et al. 2009 [10] Ozkan et al. 2013 [11]
4		Bello and Wattenbarger (2010)
5		Al-Ahmadi et al. 2010 [13]
6		Nobakht et al. 2013 [19] Yao et al. 2013 [37]

TABLE 1: Continued.

No.	Schematics of physical models	References
7		Stalgorova and Mattar 2012 [14]
8		Stalgorova and Mattar 2013 [21]

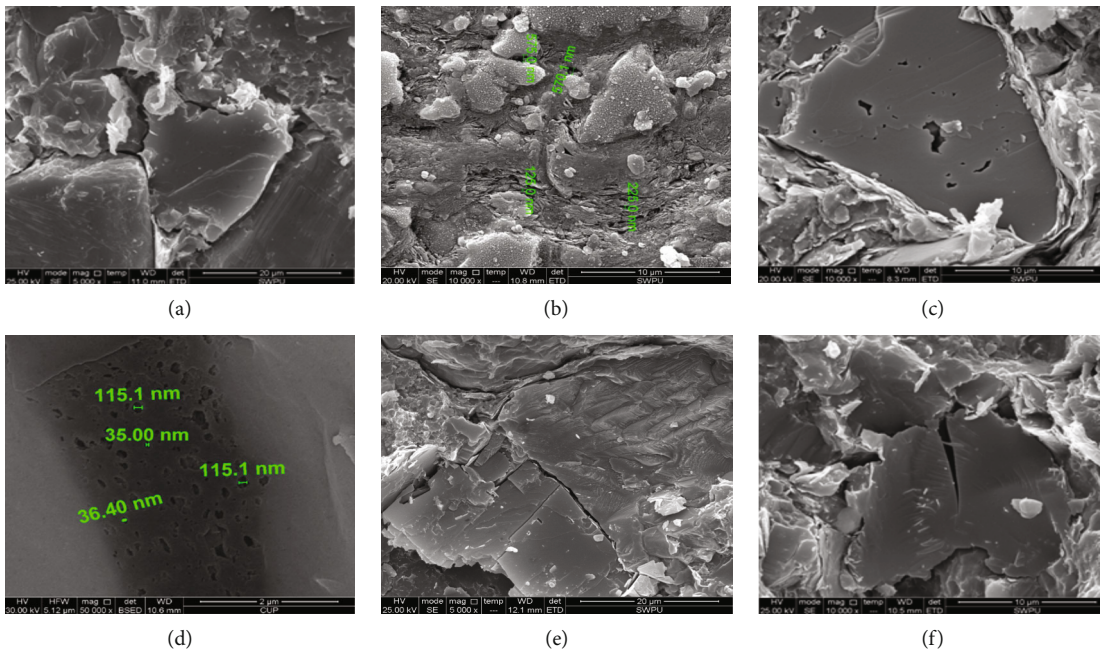


FIGURE 1: Main pore and fracture types in a shale gas reservoir. (a) Inorganic pores (intergranular pores). (b) Inorganic pores (intercrystalline pores). (c) Inorganic pores (intragranular dissolved pores). (d) Organic pores. (e) Cleavage fractures. (f) Intergranular fractures.

particles in the matrix, and the rest is free in the microfractures. Gas flow behaviors in shale nanopores are quite different from that of gas flow in conventional reservoirs [42–45]. The percolation mechanism includes diffusion, adsorption/desorption, and slip flow [46–48].

2.2. Adsorption Models of Shale Gas. The physical adsorption defined by Brunauer et al. [49] occurs when gas contacts a solid surface: some gas molecules are captured by the solid because of the intermolecular force. This means that if the volume of gas is constant, gas pressure drops; if the pressure is constant, the volume of gas decreases. The gas molecules

captured by the solid are said to be adsorbed, and the solid is called an adsorbent.

Because shale gas adsorption models are numerous, it is necessary to choose the best one before using it. Here, we use a nonlinear fitting method to analyze the degree of fit between adsorption models and some adsorption data from subcritical and supercritical states.

In the original state of a shale gas reservoir, adsorbed and desorbed gases are in dynamic pressure equilibrium. When the equilibrium is disturbed after production, the gas adsorbed in the organic matter surfaces begins to desorb, and then the desorbed gas becomes free and is stored in the

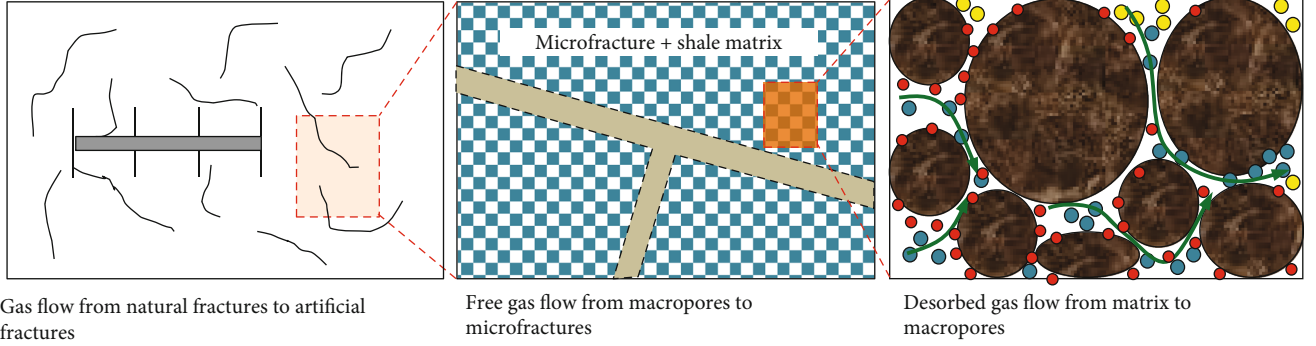


FIGURE 2: Physical model of pseudosteady flow when gas desorbs from the matrix and diffuses to a fracture [39, 50].

reservoir until the adsorbed and free gasses are in equilibrium again.

Congruent with the previous analysis, the Langmuir isotherm is one of the most popular models used to describe the gas adsorption/desorption process. The amount of gas adsorbed by a solid surface is given by the Langmuir equation below, characterizing the desorption processes as a function of pressure at constant temperature [33]:

$$V = V_L \frac{p_m}{p_L + p_m}, \quad (1)$$

where V is the volume of the adsorbed gas (cm^3/g), p_m is the gas pressure (MPa), V_L is the Langmuir volume (cm^3/g), p_L is the Langmuir pressure (1/MPa).

In addition, the expression of desorbed gas mass flux that desorbs from a reservoir whose volume is V_b during a unit of time is

$$q_{\text{des}} = \rho_{\text{gsc}} V_b \frac{\partial V}{\partial t}, \quad (2)$$

where q_{des} is the mass flow rate of gas desorption from the reservoir of volume V_b (kg/s), ρ_{gsc} is the density of shale gas under standard conditions (kg/m^3).

Incorporating equation (1) into equation (2) results in

$$q_{\text{des}} = \rho_{\text{gsc}} V_b V_L \frac{p_L}{(p_m + p_L)^2} \frac{\partial p_m}{\partial t}. \quad (3)$$

Introducing pseudopressure into equation (3), it can be rewritten as [50]

$$q_{\text{des}} = \rho_{\text{gsc}} V_b V_L \frac{m(p_L)}{(m(p_m) + m(p_L))^2} \frac{\partial m(p_m)}{\partial t}. \quad (4)$$

It is assumed that the desorbed process of shale gas is instantaneous and all the desorbed gas will become free gas, so equation (4) can be used as a continuity equation of a fracture network or matrix.

3. Model for Gas Flow in a Fractured Shale Gas Reservoir

3.1. Physical Model. Macropores exist in a practical shale matrix, which may lead to an error if gas storage and flow are ignored in these macropores. Therefore, researchers have devised a “tri-pore” conceptual model, where the shale gas reservoir consists of matrix pores, macropores, and microfractures. When the adsorbed gas desorbs from the surface of the matrix particles, it enters the macropores first and then flows into the microfractures [39, 50–52]. Figure 2 shows the physical model.

Song [39] first proposed a physical model concerning transfusion in the macropores of the matrix. But it was only a physical seepage-mechanism model, which was not modeled mathematically. In this paper, a mathematical model for this physical conception is proposed and solved. The interporosity flow of free gas between macropores and microfractures can be divided into 2 types: (1) a pseudosteady interporosity flow model and (2) a transient interporosity flow model.

3.2. Comprehensive Mathematical Model

3.2.1. Transient Interporosity Flow Model. When the gas flow from macropores to a fracture network is transient interporosity, the continuity equation in the fracture network is [53, 54]

$$\frac{1}{r^2} \frac{\partial}{\partial r} \left(\frac{k_f}{\mu_g} \rho_g r^2 \frac{\partial p_f}{\partial r} \right) = \frac{\partial (\phi_f \rho_g)}{\partial t} - q_m. \quad (5)$$

For unsteady interporosity and spherical matrix particles, the continuity equation in the matrix can be expressed as follows:

$$\frac{1}{r_m^2} \frac{\partial}{\partial r_m} \left(\frac{k_m}{\mu_g} \rho_g r_m^2 \frac{\partial p_m}{\partial r_m} \right) = \frac{\partial (\phi_m \rho_g)}{\partial t} + q_{\text{des}}. \quad (6)$$

Because the initial pressure is equal throughout the reservoir, the initial condition in the matrix equals to the initial reservoir pressure p_i :

$$p_m(t=0, r_m) = p_i. \quad (7)$$

Because seepage of the gas in the macropores is symmetrical, the inner boundary condition is

$$\frac{\partial p_m}{\partial r_m}(t, r_m=0) = 0. \quad (8)$$

Because the outer boundary of the spherical matrix particles is connected to the fracture system, the outer boundary pressure of the matrix is equal to the pressure of the fracture system:

$$p_m(t, r_m = R_m) = p_f. \quad (9)$$

When the flow between the macropores and the microfractures is unsteady, the interporosity flow rate is

$$q_m = - \left. \frac{3\rho_{gm} k_m \partial p_m}{R_m \mu_g \partial r_m} \right|_{r_m=R_m}. \quad (10)$$

By the Langmuir isotherm equation, the desorption rate of shale gas q_{des} can be written as

$$q_{des} = \rho_g (1 - \phi_f - \phi_m) \frac{V_L m(p_L)}{[m(p_L) + m(p_m)]^2} \frac{\partial m(p_m)}{\partial t}. \quad (11)$$

By introducing dimensionless variables into the above mathematical models and then reformatting them by several simple transformations (a detailed derivation process is described in Appendix A, while the dimensionless variables are shown in Appendix B), the dimensionless seepage equation of the fracture system can be obtained as

$$\frac{1}{r_D^2} \frac{\partial}{\partial r_D} \left(r_D^2 \frac{\partial \Delta \bar{m}_f}{\partial r_D} \right) = f(s) \Delta \bar{m}_f, \quad (12)$$

where the expression of $f(s)$ is

$$f(s) = \omega_f s + \frac{\lambda}{5} \left[\sqrt{\frac{15(1 - \omega_f + \omega_d)s}{\lambda}} \coth \sqrt{\frac{15(1 - \omega_f + \omega_d)s}{\lambda}} - 1 \right]. \quad (13)$$

3.2.2. Pseudosteady Interporosity Flow Model. For pseudosteady gas flow from the macropores to the fractures, incorporating pseudosteady interporosity flow rate and pseudopressure into the seepage equation of the fracture system, the seepage equation of fracture system can be written as

$$\frac{1}{r} \frac{\partial}{\partial r} \left(r^2 \frac{\partial m_f}{\partial r} \right) = \frac{\phi_f \mu_f c_{fgi}}{k_f} \frac{\partial m_f}{\partial t} - \frac{\alpha k_m}{k_t} [m_m - m_f]. \quad (14)$$

For pseudosteady gas flow from the matrix to the fractures, the seepage equation of the macropores is

$$-\alpha \frac{k_m}{k_f} [m_m - m_f] = \frac{\phi_m \mu_{gi} c_{mgi}}{k_f} \frac{\partial m_m}{\partial t} + \frac{\phi_m \mu_{gi} c_d}{k_f} \frac{\partial m_m}{\partial t}, \quad (15)$$

where c_d is an additional compressibility that considers the effect of desorption. The expression of c_d is

$$c_d = \frac{2T p_{sc}}{\phi_m \mu_{gi} T_{sc}} \frac{(1 - \phi_f - \phi_m) V_L m(p_L)}{[m(p_L) + m(p_m)]^2}. \quad (16)$$

Incorporating the above dimensionless variables into the seepage equation of the matrix and the fracture system, the dimensionless seepage equations of the matrix and the fracture system are

$$\frac{1}{r_D} \frac{\partial}{\partial r_D} \left(r_D^2 \frac{\partial \Delta m_f}{\partial r_D} \right) = \omega_f \frac{\partial \Delta m_f}{\partial t_D} - \lambda [\Delta m_m - \Delta m_f], \quad (17)$$

$$-\lambda [\Delta m_m - \Delta m_f] = (1 - \omega_f) \frac{\partial \Delta m_m}{\partial t_D} + \omega_d \frac{\partial \Delta m_m}{\partial t_D}. \quad (18)$$

Using the Laplace transform method, equations (17) and (18) can be rewritten as

$$\frac{1}{r_D} \frac{\partial}{\partial r_D} \left(r_D^2 \frac{\partial \Delta \bar{m}_f}{\partial r_D} \right) = \omega_f s \Delta \bar{m}_f - \lambda [\Delta \bar{m}_m - \Delta \bar{m}_f] s, \quad (19)$$

$$-\lambda [\Delta \bar{m}_m - \Delta \bar{m}_f] = (1 - \omega_f + \omega_d) s \Delta \bar{m}_m. \quad (20)$$

According to equations (19) and (20), the seepage equation of the fracture system is

$$\frac{1}{r_D^2} \frac{\partial}{\partial r_D} \left(r_D^2 \frac{\partial \Delta \bar{m}_f}{\partial r_D} \right) = f(s) \Delta \bar{m}_f, \quad (21)$$

where

$$f(s) = \frac{\lambda(1 + \omega_d) + \omega_f(1 - \omega_f + \omega_d)s}{\lambda + (1 - \omega_f + \omega_d)s} s. \quad (22)$$

4. MFHWs in a Rectangular Composite Shale Gas Reservoir with an SRV

4.1. Physical Model. In a shale gas or tight-gas reservoir, hydraulic fracturing is widely used to improve the productivity of the reservoir. A MFHW can make the cracks contact the matrix completely, form flow channels, and ensure efficient extraction from an unconventional reservoir [52, 55–58].

In 2008, Mayerhofer et al. [57] studied the change of cracks in Barnett shale by microseismic technology and proposed the SRV concept. The SRV refers to an effective reservoir that is made by hydraulic fracturing, with a composite

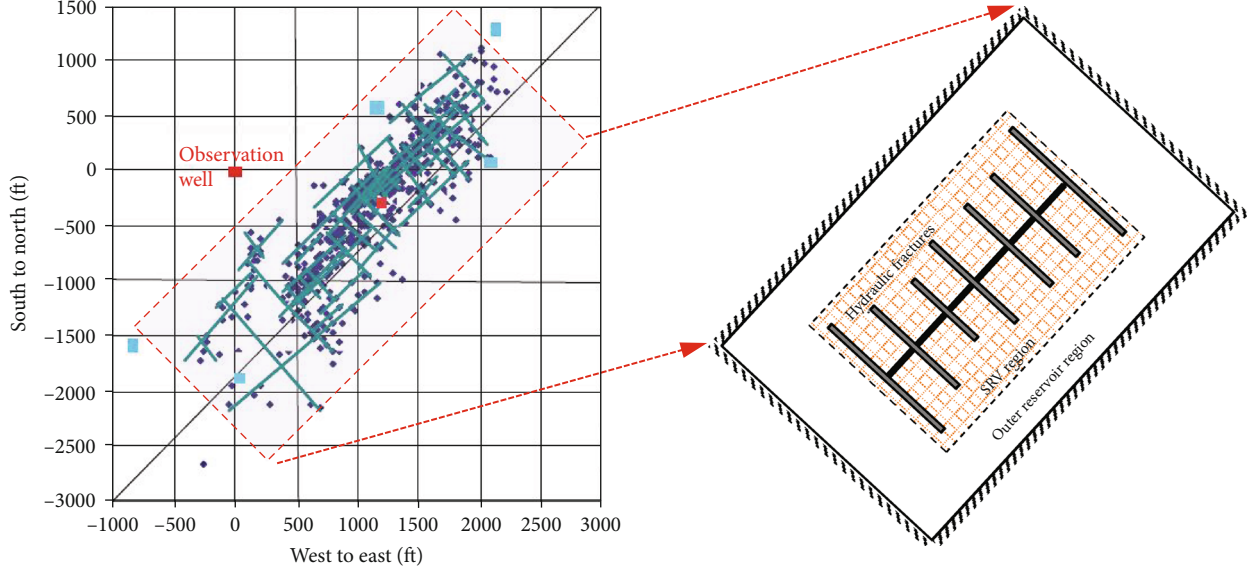


FIGURE 3: Physical model schematic of fractured wells considering SRV [56].

fracture network formed as a consequence. SRV can maximize the contact surface between matrix and fractures so that the seepage distance of oil and gas in any direction from matrix to cracks will be shortened, which improves the effective permeability of the entire reservoir. According to the microseismic monitoring map for an MFHW in Barnett shale reported by Fisher et al. [56], the physical model (Figure 3: left) can be approximated by the rectangular composite shale gas reservoir conceptual model (Figure 3: right) with enough accuracy, which is better than the circular composite conceptual model for long horizontal well cases.

To simplify the analysis, we use the following basic assumptions for this model: the MFHW is located at the center of a closed rectangular reservoir; the reservoir length, width, and height are x_e , y_e , and h , respectively; the fractures are perpendicular to the horizontal well and randomly distributed along it; the effective well length is L (from the leftmost to the rightmost fractures); each fracture is symmetrical or asymmetrical, and the fracture half-lengths are L_{fui} and L_{fji} ; the length and width of the SRV region are x_m and y_m , respectively; the number of fractures is M , and every fracture has infinite conductivity; no flow from the matrix to the wellbore and the pressure drop caused by the gas flow through the wellbore are ignored.

4.2. Boundary Element Model of a Composite Rectangular Gas Reservoir considering the SRV. According to the physical model described above, the governing equation for gas flow in an inner fracture network system is ([59–62], 2019)

$$\frac{\partial \Delta \bar{m}_{f1}}{\partial x_D^2} + \frac{\partial \Delta \bar{m}_{f1}}{\partial y_D^2} + \frac{\partial \Delta \bar{m}_{f1}}{\partial z_D^2} + \frac{2Tp_{sc} q_{v1}}{k_{f1} T_{sc} h s} \delta \cdot (x_D - x'_{s1D}, y_D - y'_{s1D}, z_D - z'_{s1D}) = f_1(s) \Delta \bar{m}_{f1}. \quad (23)$$

For the outer region

$$\frac{\partial \Delta \bar{m}_{f2}}{\partial x_D^2} + \frac{\partial \Delta \bar{m}_{f2}}{\partial y_D^2} + \frac{\partial \Delta \bar{m}_{f2}}{\partial z_D^2} + \frac{2Tp_{sc} q_{v2}}{k_{f2} T_{sc} h s} \delta \cdot (x_D - x'_{s1D}, y_D - y'_{s1D}, z_D - z'_{s1D}) = f_2(s) \Delta \bar{m}_{f2}. \quad (24)$$

The cohesive conditions on the surface between the inner and outer regions are

$$\Delta \bar{m}_{f1} = \Delta \bar{m}_{f2}, \quad (x_D, y_D, z_D) \in S_{\text{interface}}, \quad (25)$$

$$\frac{\partial \Delta \bar{m}_{f1}}{\partial n_D} = -\frac{1}{M_{12}} \frac{\partial \Delta \bar{m}_{f2}}{\partial n_D}, \quad (x_D, y_D, z_D) \in S_{\text{interface}}.$$

Because the outer boundary of our model is closed, the outer boundary condition is

$$\frac{\partial \Delta \bar{m}_{f2}}{\partial n} = 0, \quad (x_D, y_D, z_D) \in S_{\text{interface}}. \quad (26)$$

Incorporating the dimensionless variables defined in Appendix B into equations (23) and (24), the mathematical model in the Laplace space becomes

$$\frac{\partial \Delta m_{f1D}}{\partial x_D^2} + \frac{\partial \Delta m_{f1D}}{\partial y_D^2} + \frac{\partial \Delta m_{f1D}}{\partial z_D^2} = f_1(s) \Delta \bar{m}_{f1D} - \frac{2\pi q_{v1D}}{sM_{12}} \delta (x_D - x'_{s1D}, y_D - y'_{s1D}, z_D - z'_{s1D}), \quad (27)$$

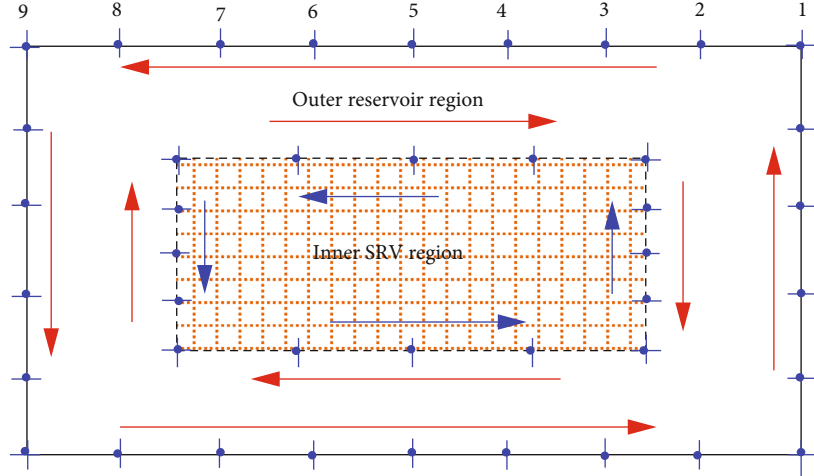


FIGURE 4: Grid of the inner and outer boundaries and the sequence of the discrete elements in a rectangular composite gas reservoir.

$$\begin{aligned} & \frac{\partial \Delta m_{f2D}}{\partial x_D^2} + \frac{\partial \Delta m_{f2D}}{\partial y_D^2} + \frac{\partial \Delta m_{f2D}}{\partial z_D^2} \\ &= f_2(s) \Delta \bar{m}_{f2D} - \frac{2\pi q_{v2D}}{s} \delta(x_D - x'_{s1D}, y_D - y'_{s1D}, z_D - z'_{s1D}), \end{aligned} \quad (28)$$

$$m_{f1D} = m_{f2D}, \quad (x_D, y_D, z_D) \in S_{\text{interface}}, \quad (29)$$

$$\frac{\partial m_{f1D}}{\partial n_D} = -\frac{1}{M_{12}} \frac{\partial m_{f2D}}{\partial n_D}, \quad (x_D, y_D, z_D) \in S_{\text{interface}}. \quad (30)$$

When using the boundary element method to solve the model above, the fundamental solutions of differential equations are needed. It is assumed that the fundamental solutions of the inner and outer regions in the shale gas reservoir are $E_1(R_D, R'_D, s)$ and $E_2(R_D, R'_D, s)$, respectively, which satisfy

$$\nabla^2 E_1(R_D, R'_D, s) - f_1(s) E_1(R_D, R'_D, s) + 2\pi \delta(R_D, R'_D) = 0, \quad (31)$$

$$\nabla^2 E_2(R_D, R'_D, s) - f_2(s) E_2(R_D, R'_D, s) + 2\pi \delta(R_D, R'_D) = 0. \quad (32)$$

Since the fractures are assumed completely open in this paper, the expressions of fundamental solutions E_1 and E_2 are

$$\begin{aligned} E_1 &= K_0 \left[\sqrt{f_1(s)} (R_D - R'_D) \right], \\ E_2 &= K_0 \left[\sqrt{f_2(s)} (R_D - R'_D) \right]. \end{aligned} \quad (33)$$

Both sides of equations (31) and (32) are multiplied by m_{f1D} and m_{f2D} , respectively, and the equations can be obtained by

$$m_{f1D} \nabla^2 E_1 - f_1(s) m_{f1D} E_1 + 2\pi m_{f1D} \delta(R_D, R'_D) = 0, \quad (34)$$

$$m_{f2D} \nabla^2 E_2 - f_2(s) m_{f2D} E_2 + 2\pi m_{f2D} \delta(R_D, R'_D) = 0. \quad (35)$$

Both sides of equations (23) and (28) are multiplied by E_1 and E_2 , respectively, and we have

$$E_1 \nabla^2 m_{f1D} = f_1(s) E_1 \Delta \bar{m}_{f1D} - E_1 \frac{2\pi q_{v1D}}{s M_{12}} \delta(R_D - R'_{wD}), \quad (36)$$

$$E_2 \nabla^2 m_{f1D} = f_1(s) E_2 \Delta \bar{m}_{f1D} - E_2 \frac{2\pi q_{v2D}}{s} \delta(R_D - R'_{wD}). \quad (37)$$

Using equations (34) and (35) minus equations (36) and (37), respectively, the equations can be transformed as

$$\begin{aligned} & m_{f1D} \nabla^2 E_1 - E_1 \nabla^2 m_{f1D} + 2\pi m_{f1D} \delta(R_D, R'_D) \\ &= E_1 \frac{2\pi q_{v1D}}{s M_{12}} \delta(R_D - R'_{wD}), \end{aligned} \quad (38)$$

$$\begin{aligned} & m_{f2D} \nabla^2 E_2 - E_2 \nabla^2 m_{f2D} + 2\pi m_{f2D} \delta(R_D, R'_D) \\ &= E_2 \frac{2\pi q_{v2D}}{s} \delta(R_D - R'_{wD}). \end{aligned} \quad (39)$$

Integrating equations (38) and (39) on the inner region Ω_1 and outer region Ω_2 , respectively, we have

$$\begin{aligned} & \int_{\Omega_1} \left[m_{f1D} \nabla^2 E_1 - E_1 \nabla^2 m_{f1D} + 2\pi m_{f1D} \delta(R_D, R'_D) - E_1 \frac{2\pi q_{v1D}}{s M_{12}} \right. \\ & \quad \left. \cdot \delta(R_D - R'_{wD}) \right] d\Omega_1 = 0, \end{aligned} \quad (40)$$

TABLE 2: Reservoir properties.

Reservoir property	Value	Reservoir property	Value
Permeability of SRV, k_{f1} (mD)	0.05	Porosity of SRV, ϕ_{f1} (fraction)	0.05
Permeability of outer reservoir, k_{f2} (mD)	0.01	Porosity of SRV, ϕ_{f2} (fraction)	0.002
Length of SRV, x_m (m)	1600	Width of SRV, y_m (m)	400
Inner matrix permeability, k_{m1} (mD)	0.0001	Inner matrix porosity, ϕ_{m1}	0.01
Outer matrix permeability, k_{m2} (mD)	0.0001	Outer matrix porosity, ϕ_{m2}	0.01
Wellbore storage coefficient, C_D (dimensionless)	1×10^{-4}	Gas relative density, γ_g (fraction)	0.65

$$\int_{\Omega_2} \left[m_{f2D} \nabla^2 E_2 - E_2 \nabla^2 m_{f2D} + 2\pi m_{f2D} \delta(R_D, R'_D) - E_2 \frac{2\pi q_{v2D}}{s} \cdot \delta(R_D - R'_{wD}) \right] d\Omega_2 = 0. \quad (41)$$

We use Green's second identity as follows [61, 62]:

$$\int_{\Omega} (\mu \nabla^2 v - v \nabla^2 \mu) d\Omega' = \int_S (\mu \nabla v - v \nabla \mu) dS', \quad (42)$$

where $S(S = \sum_i S_i)$ is the entire boundary of region Ω .

Based on the characteristics of equation (42) and the delta function, the differential equation of the inner and outer regions can be changed into an integral equation on the boundary, and the boundary integral equations of equations (40) and (41) are

$$m_{f1D}(R_D) = \frac{1}{2\pi} \int_{S_1} [E_1 \nabla m_{f1D} - m_{f1D} \nabla E_1] dS'_1 + \frac{1}{M_{12}s} \int_{\Omega_1} q_{v1D}(R'_{s1D}) E_1 d\Omega'_1, \quad (43)$$

$$m_{f2D}(R_D) = \frac{1}{2\pi} \int_{S_2} [E_2 \nabla m_{f2D} - m_{f2D} \nabla E_2] dS'_2 + \frac{1}{s} \int_{\Omega_2} q_{v2D}(R'_{s2D}) E_2 d\Omega'_2. \quad (44)$$

There are two kind of boundaries (the outer and the inner) in the gas reservoir. It is assumed that the outer boundary can be discretized into NO elements and the inner boundary can be discretized into NI elements, so the total number of the elements for the boundaries is NO + NI. The serial number of inner boundary elements is clockwise, while it is counterclockwise for outer boundary elements, as shown in Figure 4.

For the integral equation on the boundary, R_D is an arbitrary point on the boundary, while R'_D is an arbitrary point in the reservoir region. R'_{s1D} and R'_{s2D} are the dimensionless coordinates of source points in the inner and outer regions, respectively. If R'_D is not only in the reservoir region but also

on the boundaries, equations (43) and equations (44) can be rewritten as

$$\theta m_{f1D}(R_D) = \frac{1}{2\pi} \int_{S_1} [E_1 \nabla m_{f1D} - m_{f1D} \nabla E_1] dS'_1 + \frac{1}{M_{12}s} \int_{\Omega_1} q_{v1D}(R'_{s1D}) E_1 d\Omega'_1, \quad (45)$$

$$\theta m_{f2D}(R_D) = \frac{1}{2\pi} \int_{S_2} [E_2 \nabla m_{f2D} - m_{f2D} \nabla E_2] dS'_2 + \frac{1}{s} \int_{\Omega_2} q_{v2D}(R'_{s2D}) E_2 d\Omega'_2, \quad (46)$$

where θ is a constant related to the geometric shape of R'_D , and the expression of θ is [62]

$$\theta = \frac{\alpha}{2\pi}, \quad (47)$$

where α is the angle of the boundary tangent line at R'_D .

Incorporating the fundamental solutions E_1 and E_2 into equations (45) and (46), a series of linear equation sets can be obtained by solving the reservoir points R'_D along the boundary points and fracture points, after which the dimensionless pseudopressure response curves of the fractured well can be obtained by solving the equation sets above. Due to the complexity of the process, its details are not shown in this article; interested readers may consult these papers for details: [52, 59, 60, 63–71].

4.3. Pressure and Production Type Curve Analysis. The boundary element method is employed to acquire type curves of dimensionless bottomhole pressures at constant rate, and the production rate and cumulative production at a constant pressure are based on the parameters in Table 2.

Figure 5 shows the well-test type curves of reservoirs with different sizes and SRVs. The following flow stages can be observed when the reservoir and SRV sizes are large enough:

- (a) Stage 1: early wellbore storage
- (b) Stage 2: transition flow between wellbore storage and early linear flow of a fracture system. A hump is in the pseudopressure derivative curve for this stage,

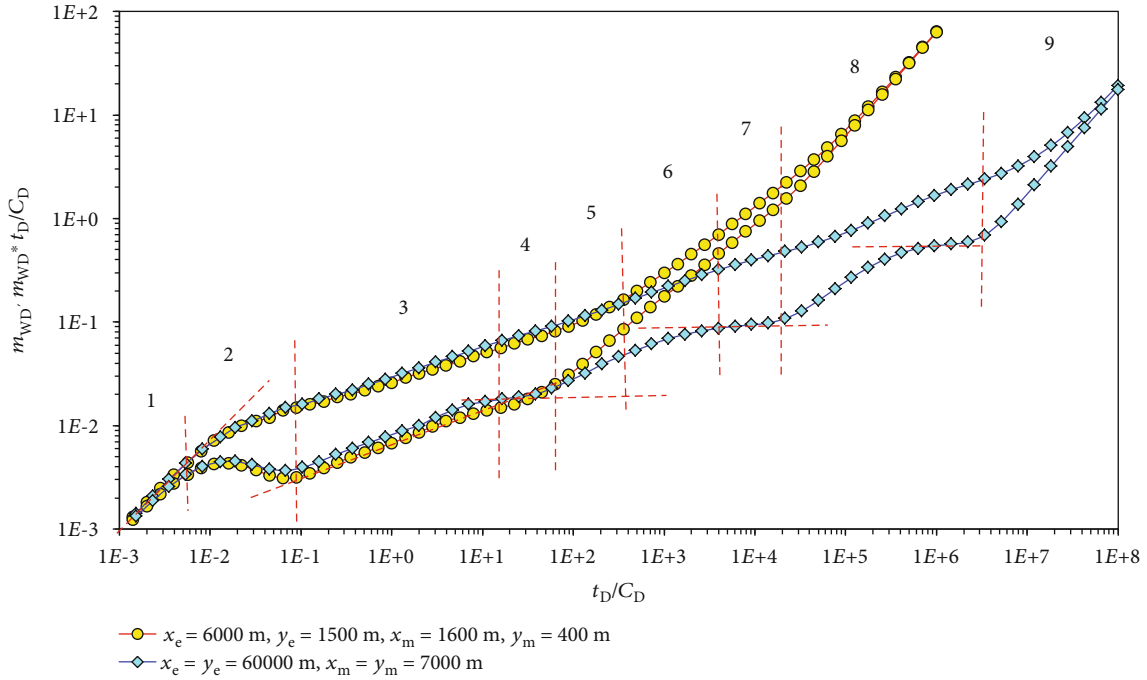


FIGURE 5: Effect of reservoir size on type curves.

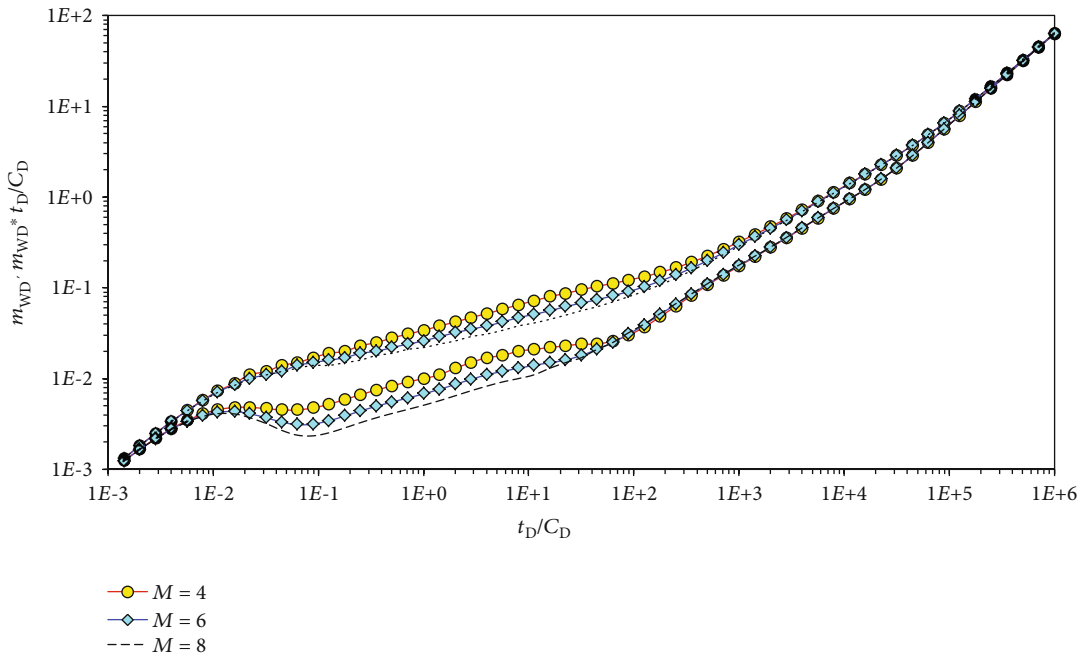


FIGURE 6: Effect of fractures number on well-test type curves.

and the height and width of the hump depend on the wellbore storage and skin factor

- (c) Stage 3: early linear flow of the fracture system. In this flow stage, the pseudopressure derivative curve is a straight line, and the slope is 0.5. The position of the straight line is controlled by the permeability of the SRV, and the length of this

straight line is related to the permeability of the SRV, the fracture length, and the distance between the fractures

- (d) Stage 4: early radial flow of fracture system. For this stage, the pseudopressure derivative curve is a portion of a horizontal straight line. In addition, when the height of the SRV is close to the length

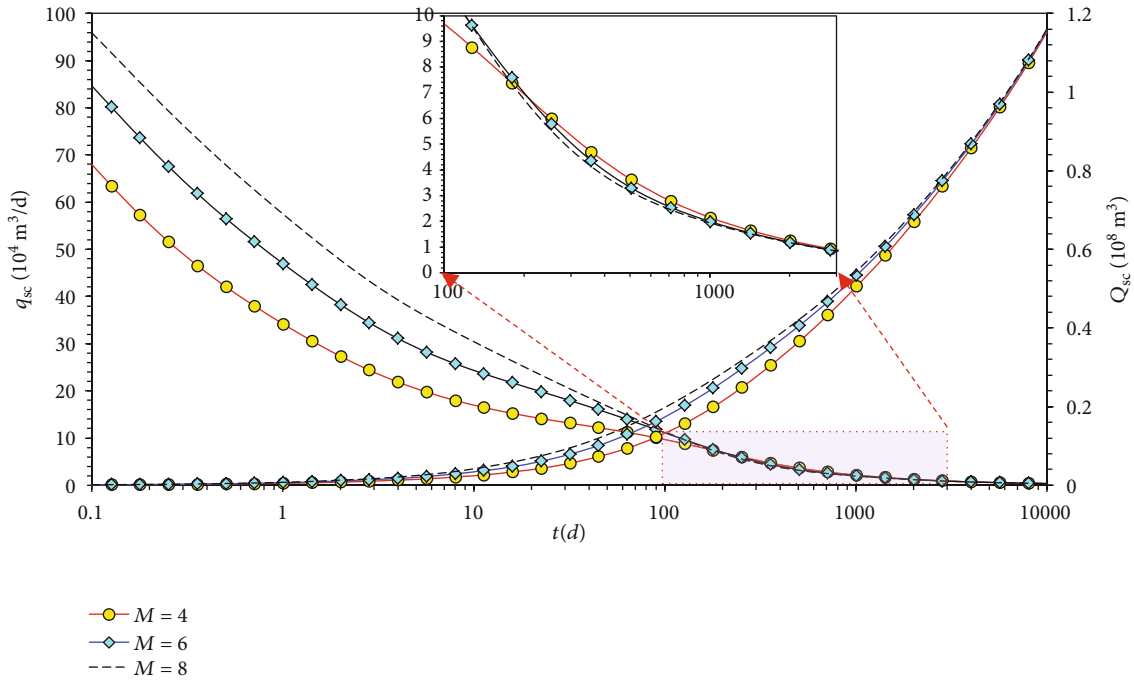


FIGURE 7: Effects of number of fractures on production rate and cumulative production curves.

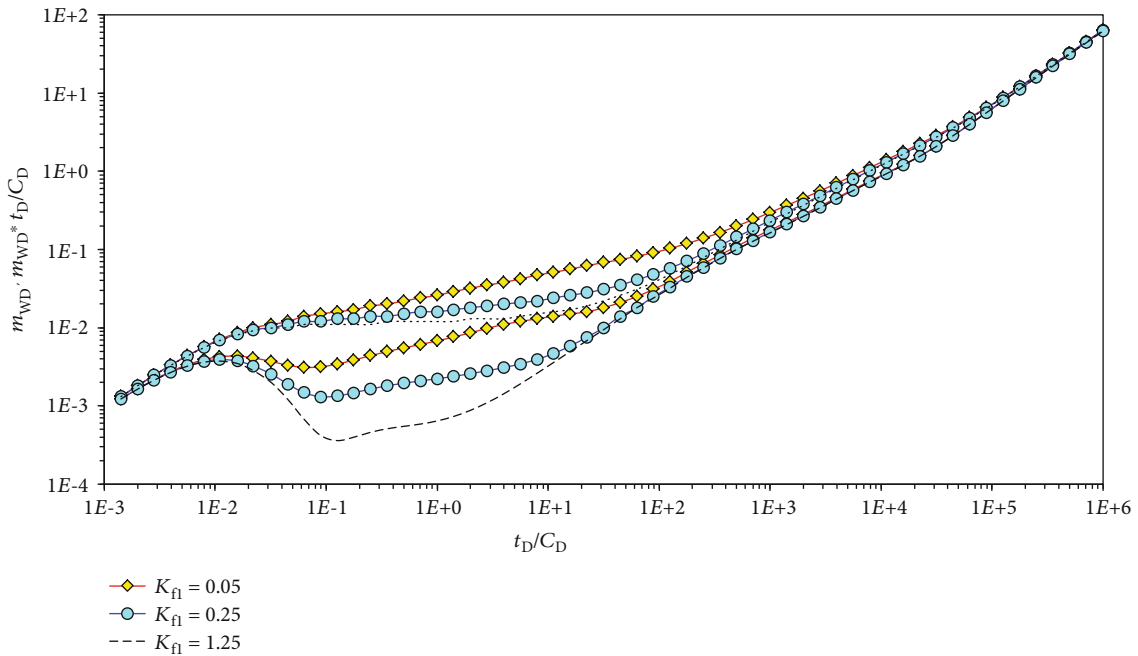


FIGURE 8: Effect of SRV permeability on well-test type curves.

of the fracture, this line may be covered or offset under the effect of outer reservoir properties

- (e) Stage 5: transition flow between early radial flow of the fracture system and radial flow of the SRV
- (f) Stage 6: radial flow of the SRV. For this stage, the pseudopressure derivative curve is a section of a horizontal straight line. It is found that the higher the

permeability of the SRV, the lower the position of this horizontal line

- (g) Stage 7: transition flow between radial flow of the SRV and radial flow of the outer region
- (h) Stage 8: radial flow of the outer region. In this stage, the pseudopressure derivative curve is a straight line whose slope is 0.5

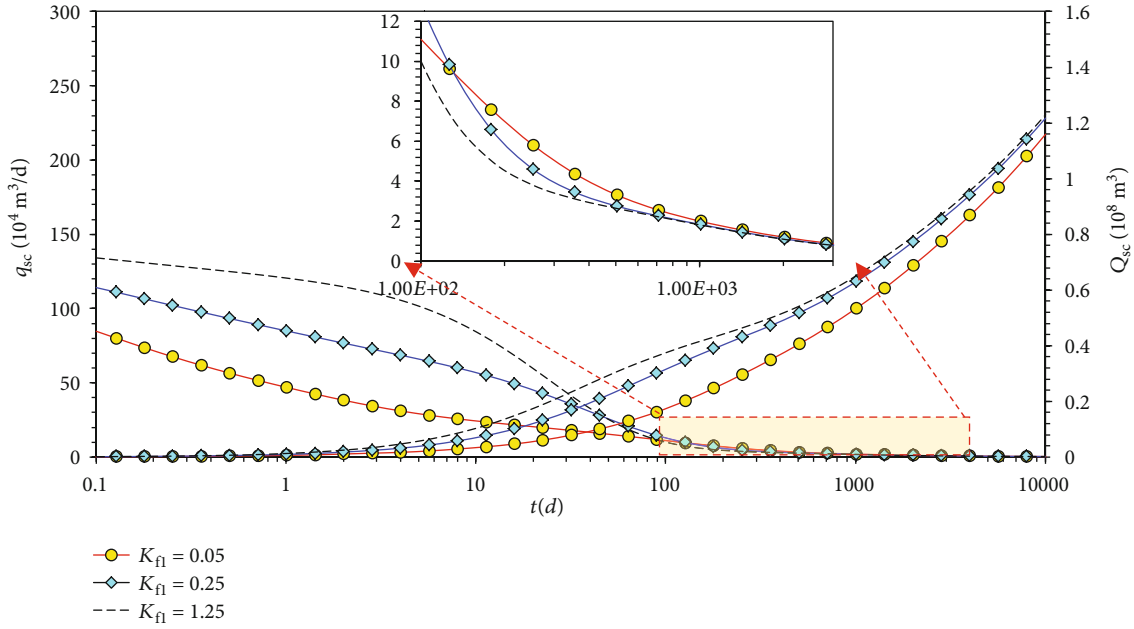


FIGURE 9: Effects of SRV permeability on production rate and cumulative production curves.

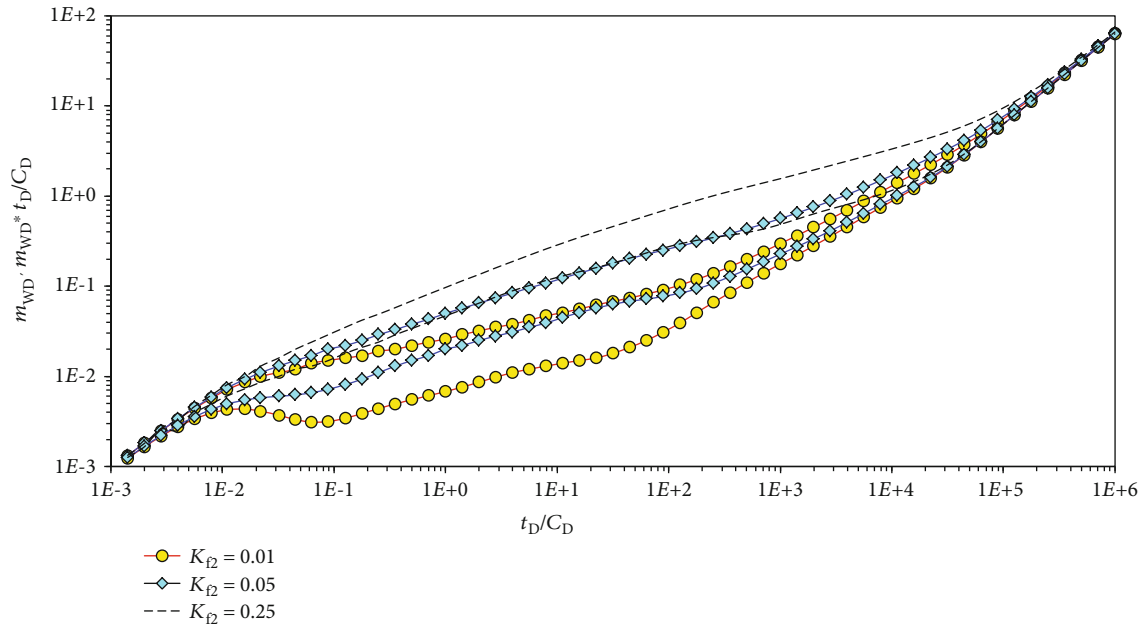


FIGURE 10: Effect of reservoir permeability on well-test type curves.

(i) Stage 9: boundary-dominated flow. For this stage, the pseudopressure and pseudopressure derivative curves overlap, and this section is a straight line with a slope of 1. Because $x_e = y_e = 60000$ m, there is no linear flow of the reservoir

so the curves turn upward, and then the pseudopressure and pseudopressure derivative curves are almost parallel to each other as a straight line, but the slope is not 0.5. When the pressure reaches the reservoir boundary, the 2 curves overlap.

When the sizes of the reservoir and the SRV are reasonable, the pseudopressure and pseudopressure derivative curves are shown in Figures 5–11 as the plots with yellow pellets. After the early linear flow of the fracture system, the pressure reaches the region close to the reservoir boundary,

Figures 6 and 7 show the effects of the fracture number on well-test type curves (dimensionless pseudopressure and its derivative) and production curves (production rate and cumulative production), respectively. As shown in Figure 6, for a constant reservoir size and SRV, the number of hydraulic fractures affects mainly the early flow periods following

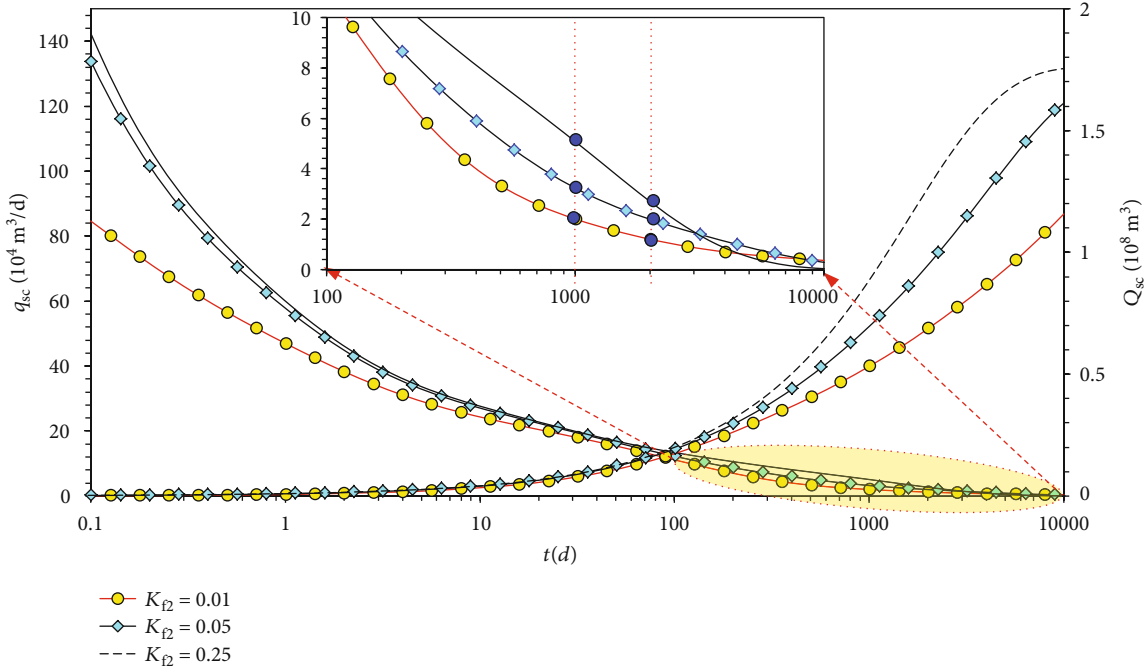


FIGURE 11: Effects of reservoir permeability on production rate and cumulative production curves.

TABLE 3: Well production rates for different reservoir permeabilities at different times.

Reservoir permeability (mD)	Production rate ($10^4 \text{ m}^3/\text{d}$)	
	1000 (d)	2000 (d)
0.25	5.42	2.78
0.05	3.41	2.01
0.01	1.99	1.19

the wellbore storage flow period. When the pressure wave transports to the outer region, the effects will vanish and all pressure and pressure derivative curves will coincide. When a well produces at a constant rate, the higher the fracture number, the higher the early production; this effect lasts for just a few years.

Figures 8 and 9 show the effects of different flow region permeabilities on well-test type curves and production curves, respectively. The effects occur in the middle flow stage. The position of the well-test type curves is lower when the SRV permeability is higher, but the difference between the well-test type curves becomes smaller and smaller as the pressure reaches the reservoir boundary. Figure 9 shows that when SRV permeability increases, the early production rate is higher than the previous one, the production rate is much higher in the middle stage, and the SRV permeability has no effect on the final cumulative production.

Figures 10 and 11 show the effects of reservoir permeability on type curves and production curves, respectively. Because the reference permeability in our model is the reservoir permeability, the reservoir permeability has the opposite effect on type curves compared to that of SRV. The higher the reservoir permeability, the higher the loca-

tion of the type curves (as shown in Figure 10), which does not mean that the drawdown pressure is higher. When the well is producing at constant pressure, the gas supply is timely due to the high permeability of the reservoir, and gas production rate increases with reservoir permeability increasing (as shown in Figure 11). Even in the later production period when the well has been producing for 1000 d and 2000 d, the well production rate for a reservoir with a higher permeability is still much higher, as shown in Table 3. Therefore, a desert area is very important for the exploitation and development of unconventional shale gas reservoirs.

5. Conclusions

We established a comprehensive mathematical model to describe a multistage fractured horizontal well in a rectangular composite shale gas reservoir with an SRV, and the solution was also obtained by a boundary element method. The main conclusions we derived are as follows:

- (1) A composite rectangular model of a fractured horizontal well using the “tri-pores” conceptual model is proposed in this paper, and the complex model was solved by BEM, which has not been comprehensively reported before
- (2) The number of fractures affects the well production rate at primarily the early flow period; the effect on the later flow period is weak
- (3) The permeability in the SRV region has a substantial effect on the early well production rate; the higher the permeability, the greater the rate will be

- (4) During the intermediate flow period, the effect will be the opposite, which can be explained by mass conservation for a closed constant-volume gas reservoir

Appendix

A. Transformations

Let $m_f = m(p_f)$ and $m_m = m(p_m)$; then the pseudopressure and gas density expression are introduced into equation (5), so the continuity equation in the fracture network is

$$\frac{1}{r^2} \frac{\partial}{\partial r} \left(r^2 \frac{\partial m_f}{\partial r} \right) = \frac{\mu_{gi} \phi_f c_{fgi}}{k_f} \frac{\partial m_f}{\partial t} + \frac{3}{R_m} \frac{k_m}{k_f} \frac{\partial m_m}{\partial r_m} \Big|_{r_m=R_m}. \quad (\text{A.1})$$

The shape factor of the spherical matrix particles is

$$\alpha = \frac{15}{R_m^2}. \quad (\text{A.2})$$

Inserting the shape factor into equation (A.1) yields

$$\frac{1}{r^2} \frac{\partial}{\partial r} \left(r^2 \frac{\partial m_f}{\partial r} \right) = \frac{\mu_{gi} \phi_f c_{fgi}}{k_f} \frac{\partial m_f}{\partial t} + \frac{\alpha R_m k_m}{5 k_f} \frac{\partial m_m}{\partial r_m} \Big|_{r_m=R_m}. \quad (\text{A.3})$$

Inserting equation (11) into equation (6) yields

$$\frac{1}{r_m^2} \frac{\partial}{\partial r_m} \left(\frac{k_m}{\mu_g} \rho_g r_m^2 \frac{\partial p_m}{\partial r_m} \right) = \frac{\phi_m \mu_{gi} c_{mgi}}{k_m} \frac{\partial m_m}{\partial t} + \frac{\phi_m \mu_{gi} c_d}{k_m} \frac{\partial m_m}{\partial t}, \quad (\text{A.4})$$

where c_d is an additional compressibility taking into account the effect of desorption; the expression is given in the following formula:

$$c_d = \frac{2T p_{sc}}{\phi_m \mu_{gi} T_{sc}} \frac{(1 - \phi_f - \phi_m) V_L m(p_L)}{[m(p_L) + m(p_m)]^2}. \quad (\text{A.5})$$

The initial condition of the spherical matrix is

$$m_m|_{(t=0, r_m)} = m(p_i). \quad (\text{A.6})$$

The inner boundary condition of the spherical matrix is

$$\frac{\partial m_m}{\partial r_m} \Big|_{(t, r_m=0)} = 0. \quad (\text{A.7})$$

The outer boundary condition of the matrix is

$$m_m|_{(t, r_m=R_m)} = m_f. \quad (\text{A.8})$$

All the dimensionless variables are defined as

$$\begin{aligned} r_{mD} &= \frac{r_m}{R_m}, \\ r_D &= \frac{r}{L_{ref}}, \\ t_D &= \frac{k_f t}{(\phi_m c_{mgi} + \phi_f c_{fgi}) \mu_{gi} L_{ref}^2}, \\ \omega_f &= \frac{\phi_f c_{fgi}}{\phi_m c_{mgi} + \phi_f c_{fgi}}, \\ \omega_d &= \frac{\phi_m c_d}{\phi_m c_{mgi} + \phi_f c_{fgi}}, \\ \lambda &= \alpha \frac{k_m}{k_f} L_{ref}^2, \\ \Delta m_f &= m(p_i) - m(p_f), \\ \Delta m_m &= m(p_i) - m(p_m). \end{aligned} \quad (\text{A.9})$$

Inserting the dimensionless variables above into the seepage model of the matrix and fracture network, we can rewrite the model as

$$\begin{aligned} \frac{1}{r_D^2} \frac{\partial}{\partial r_D} \left(r_D^2 \frac{\partial \Delta m_f}{\partial r_D} \right) &= \omega_f \frac{\partial \Delta m_f}{\partial t_D} + \frac{\lambda}{5} \frac{\partial \Delta m_m}{\partial r_{mD}} \Big|_{r_{mD}=1}, \\ \frac{1}{r_{mD}^2} \frac{\partial}{\partial r_{mD}} \left(r_{mD}^2 \frac{\partial \Delta m_m}{\partial r_{mD}} \right) &= \frac{15(1 - \omega_f)}{\lambda} \frac{\partial \Delta m_m}{\partial t_D} + \frac{15\omega_d}{\lambda} \frac{\partial \Delta m_m}{\partial t_D}, \\ \Delta m_m|_{(t_D=0, r_{mD})} &= 0, \\ \frac{\partial \Delta m_m}{\partial r_{mD}} \Big|_{(t_D, r_{mD}=0)} &= 0, \\ \Delta m_m|_{(t_D, r_{mD}=1)} &= \Delta m_f. \end{aligned} \quad (\text{A.10})$$

Using the Laplace transform method, we can get

$$\Delta \bar{m} = \int_0^\infty \Delta m e^{-st_D} dt_D. \quad (\text{A.11})$$

And the model above can be written as

$$\frac{1}{r_D^2} \frac{\partial}{\partial r_D} \left(r_D^2 \frac{\partial \Delta \bar{m}_f}{\partial r_D} \right) = \omega_f s \Delta \bar{m}_f + \frac{\lambda}{5} \frac{\partial \Delta \bar{m}_m}{\partial r_{mD}} \Big|_{r_{mD}=1}, \quad (\text{A.12})$$

$$\frac{1}{r_{mD}^2} \frac{\partial}{\partial r_{mD}} \left(r_{mD}^2 \frac{\partial \Delta \bar{m}_m}{\partial r_{mD}} \right) = \frac{15s(1 - \omega_f + \omega_d)}{\lambda} \Delta \bar{m}_m, \quad (\text{A.13})$$

$$\Delta \bar{m}_m|_{(t_D=0, r_{mD})} = 0, \quad (\text{A.14})$$

$$\frac{\partial \Delta \bar{m}_m}{\partial r_{mD}} \Big|_{(t_D, r_{mD}=0)} = 0, \quad (\text{A.15})$$

$$\Delta \bar{m}_m|_{(t_D, r_{mD}=1)} = \Delta \bar{m}_f. \quad (\text{A.16})$$

Do the following variable substitution

$$W = r_{mD} \Delta \bar{m}_m. \quad (\text{A.17})$$

Inserting equation (A.17) into equation (A.13), we have

$$\frac{\partial^2 W}{\partial r_{mD}^2} = \frac{15s(1 - \omega_f + \omega_d)}{\lambda} W. \quad (\text{A.18})$$

According to the characteristics of the above equation, the general solution of equation (A.18) can be obtained easily by

$$W = A \sinh(\sqrt{g} r_{mD}) + B \cosh(\sqrt{g} r_{mD}), \quad (\text{A.19})$$

where

$$g = \frac{15(1 - \omega_f + \omega_d)s}{\lambda}. \quad (\text{A.20})$$

Inserting equation (A.19) into equation (A.17),

$$\Delta \bar{m}_m = \frac{A \sinh(\sqrt{g} r_{mD}) + B \cosh(\sqrt{g} r_{mD})}{r_{mD}}. \quad (\text{A.21})$$

B can be determined by the inner boundary condition, and A can be determined by the outer boundary condition. A and B have the following values:

$$B = 0, \quad (\text{A.22})$$

$$A = \Delta \bar{m}_f / \sinh(\sqrt{g}).$$

Incorporating the value of A and B into equation (A.21) yields

$$\Delta \bar{m}_m = \frac{\Delta \bar{m}_f}{\sinh(\sqrt{g})} \frac{\sinh(\sqrt{g} r_{mD})}{r_{mD}}. \quad (\text{A.23})$$

The derivative of equation (A.23) is

$$\left. \frac{\partial \Delta \bar{m}_m}{\partial r_{mD}} \right|_{r_{mD}=1} = [\sqrt{g} \coth(\sqrt{g}) - 1] \Delta \bar{m}_f. \quad (\text{A.24})$$

Incorporating equation (A.24) into equation (A.12) and then simplifying it, we can then obtain the following:

$$\frac{1}{r_D^2} \frac{\partial}{\partial r_D} \left(r_D^2 \frac{\partial \Delta \bar{m}_f}{\partial r_D} \right) = f(s) \Delta \bar{m}_f, \quad (\text{A.25})$$

where the expression of $f(s)$ is

$$f(s) = \omega_f s + \frac{\lambda}{5} \left[\sqrt{\frac{15(1 - \omega_f + \omega_d)s}{\lambda}} \coth \sqrt{\frac{15(1 - \omega_f + \omega_d)s}{\lambda}} - 1 \right]. \quad (\text{A.26})$$

B. Dimensionless variables

All the dimensionless variables are defined as

$$\begin{aligned} r_D &= \frac{r}{L_{\text{ref}}}, \\ t_D &= \frac{k_f t}{(\phi_m c_{\text{mgi}} + \phi_f c_{\text{cgi}}) \mu_{\text{gi}} L_{\text{ref}}^2}, \\ \omega_f &= \frac{\phi_f c_{\text{fgi}}}{\phi_m c_{\text{mgi}} + \phi_f c_{\text{fgi}}}, \\ \omega_d &= \frac{\phi_m c_d}{\phi_m c_{\text{mgi}} + \phi_f c_{\text{fgi}}}, \\ \lambda &= \alpha \frac{k_m}{k_f} L_{\text{ref}}^2, \\ \Delta m_f &= m(p_i) - m(p_f), \\ \Delta m_m &= m(p_i) - m(p_m). \end{aligned} \quad (\text{B.1})$$

Data Availability

The production data used to support the findings of this study are included within the article.

Conflicts of Interest

The authors declare that they have not conflicts of interests.

Acknowledgments

This work was supported by the Demonstration Project of the National Science and Technology of China (Grant No. 2016ZX05062), the Science and Technology Major Project of PetroChina (Grant No. 2016E-0611), and the National Science and Technology Major Project of the Ministry of Science and Technology of China (Grant No. 2017ZX05037-001)

References

- [1] A. G. Adesida, I. Akkutlu, D. E. Resasco, and C. S. Rai, "Characterization of Barnett shale kerogen pore size distribution using DFT analysis and grand canonical Monte Carlo simulations," in *Paper SPE 147397-MS Presented at SPE Annual Technical Conference and Exhibition*, Denver, Colorado, USA, 2011.
- [2] C. McGlade, J. Speirs, and S. Sorrell, "Unconventional gas—a review of regional and global resource estimates," *Energy*, vol. 55, pp. 571–584, 2013.
- [3] A. Hadkin and R. Bloom, *Energy Information Administration*, 2016, //http://www.eia.gov/dnav/ng/ng_prod_sum_a_EPG0_FGW_mmcf_m.html.
- [4] M. E. Curtis and R. J. Ambrose, "Structural characterization of gas shale on the micro- and nano-scales," in *Paper SPE 137693-MS Presented at Canadian Unconventional Resources and International Petroleum Conference*, Calgary, Alberta, Canada, 2010.

- [5] C. J. Houghton and R. V. Westermark, "North Sea downhole corrosion: identifying the problem implementing solutions," *Journal of Petroleum Technology*, vol. 35, no. 1, pp. 239–246, 2013.
- [6] J. P. Vermylen and M. D. Zoback, "Hydraulic fracturing, micro seismic magnitudes and stress evolution in the Barnett shale," in *Paper SPE 140507-MS Presented at SPE Hydraulic Fracturing Technology Conference*, The Woodlands, Texas, USA, 2011.
- [7] F. Kucuk and W. K. Sawyer, "Transient flow in naturally fractured reservoirs and its application to Devonian gas shale," in *Paper SPE 9397-MS Presented at SPE Annual Technical Conference and Exhibition, 21-24 September*, Dallas, Texas, USA, 1980.
- [8] D. E. Lancaster and J. M. Gatens III, "Practical well test analysis methods for hydraulically fractured wells in dual-porosity reservoirs," in *Paper SPE 15924-MS Presented at SPE Eastern Regional Meeting, 12-14 November*, Columbus, USA, Ohio, USA, 1986.
- [9] J. L. Johnston and W. J. Lee, "Identification of productive layers in low-permeability gas wells," *SPE Journal of Petroleum Technology*, vol. 44, no. 11, pp. 1240–1248, 2013.
- [10] M. Brown, E. Ozkan, R. Raghavan, and H. Kazemi, "Practical solutions for pressure transient responses of fractured horizontal wells in unconventional reservoirs," in *Paper SPE 125043-MS Presented at SPE Annual Technical Conference and Exhibition, 4-7 October*, New Orleans, Louisiana, USA, 2009.
- [11] E. Ozkan, M. L. Brown, R. Raghavan, and H. Kazemi, "Comparison of fractured-horizontal-well performance in tight sand and shale reservoirs," *SPE Reservoir Evaluation & Engineering*, vol. 14, no. 2, pp. 248–259, 2013.
- [12] R. O. Bello and R. A. Watenbargen, "Multi-stage hydraulically fractured horizontal shale gas well rate transient analysis," in *Paper SPE 126754-MS Presented at the North Arica Technical Conference and Exhibition*, Cairo, Egypt, 2010.
- [13] H. A. Al-Ahmadi, A. M. Almarzooq, and R. A. Watenbargen, "Application of linear flow analysis to shale gas wells—field cases," in *Paper SPE 130370-MS Presented at the SPE Unconventional Gas Conference*, Pittsburgh, Pennsylvania, USA, 2010.
- [14] E. Stalgorova and L. Mattar, "Practical analytical model to simulate production of horizontal wells with branch fractures," in *Paper SPE 162515-MS Presented at the SPE Canadian Unconventional Resources Conference*, Calgary, Alberta, Canada, 2012.
- [15] B. Xu, M. Haghghi, X. Li, and D. Cooke, "Development of new type curves for production analysis in naturally fractured shale gas/tight gas reservoirs," *Journal of Petroleum Science and Engineering*, vol. 105, pp. 107–115, 2013.
- [16] J. A. Afsar, S. Shahab, and D. Hassan, "Analyzing the production data of fractured horizontal wells by a linear triple porosity model: development of analysis equations," *Journal of Petroleum Science and Engineering*, vol. 112, pp. 117–128, 2013.
- [17] F. J. Medeiros, E. Ozkan, and H. A. Kazemi, "Semianalytical approach to model pressure transients in heterogeneous reservoirs," *SPE Reservoir Evaluation & Engineering*, vol. 13, no. 2, pp. 341–358, 2010.
- [18] M. Nobakht and C. R. Clarkson, "A new analytical method for analyzing linear flow in tight/shale gas reservoirs: constant-flowing-pressure boundary condition," *SPE Reservoir Evaluation & Engineering*, vol. 15, no. 3, pp. 370–384, 2013.
- [19] M. Nobakht, C. R. Clarkson, and D. Kaviani, "New type curves for analyzing horizontal well with multiple fractures in shale gas reservoirs," *Journal of Natural Gas Science and Engineering*, vol. 10, pp. 99–112, 2013.
- [20] M. Nobakht, L. Mattar, S. Moghadam, and D. M. Anderson, "Simplified forecasting of tight/shale gas production in linear flow," *Journal of Canadian Petroleum Technology*, vol. 51, no. 6, pp. 476–486, 2013.
- [21] E. Stalgorova and L. Mattar, "Analytical model for unconventional multifractured composite systems," *SPE Reservoir Evaluation & Engineering*, vol. 16, no. 3, pp. 246–256, 2013.
- [22] W. Luo, C. Tang, Y. Zhou, B. Ning, and J. Cai, "A new semi-analytical method for calculating well productivity near discrete fractures," *Journal of Natural Gas Science and Engineering*, vol. 57, pp. 216–223, 2018.
- [23] M. Wei, J. Liu, D. Elsworth, and E. Wang, "Triple-porosity modelling for the simulation of multiscale flow mechanisms in shale reservoirs," *Geofluids*, vol. 2018, Article ID 6948726, 11 pages, 2018.
- [24] B. Yuan, G. R. Moghanloo, and D. Zheng, "A novel integrated workflow for evaluation, optimization, and production prediction in shale plays," *International Journal of Coal Geology*, vol. 180, pp. 18–28, 2017.
- [25] D. Zheng, B. Yuan, and R. G. Moghanloo, "Analytical modeling dynamic drainage volume for transient flow towards multi-stage fractured wells in composite shale reservoirs," *Journal of Petroleum Science and Engineering*, vol. 149, pp. 756–764, 2017.
- [26] Y. M. Cheng, "Pressure transient characteristics of hydraulically fractured horizontal shale gas wells," in *Paper SPE 149311 Presented at the SPE Eastern Regional Meeting*, Columbus, Ohio, 2011.
- [27] F. Dongyan, Y. Jun, S. Hai, Z. Hui, and W. Wei, "A composite model of hydraulic fractured horizontal well with stimulated reservoir volume in tight oil & gas reservoir," *Journal of Natural Gas Science and Engineering*, vol. 24, pp. 115–123, 2015.
- [28] C. M. Freeman, G. J. Moridis, D. Ilk, and T. A. Blasingame, "A numerical study of performance for tight gas and shale gas reservoir systems," in *SPE Paper 124961 Presented at the SPE Annual Technical Conference and Exhibition*, USA, New Orleans, Louisiana, 2009.
- [29] D. Li, C. Xu, J. Y. Wang, and D. Lu, "Effect of Knudsen diffusion and Langmuir adsorption on pressure transient response in tight- and shale-gas reservoirs," *Journal of Petroleum Science and Engineering*, vol. 124, pp. 146–154, 2014.
- [30] D. Li, L. Zhang, J. Y. Wang, and D. Lu, "Composition-transient analysis in shale-gas reservoirs with consideration of multi-component adsorption," *SPE Journal*, vol. 21, no. 2, pp. 648–664, 2016.
- [31] W. Luo, X. Wang, C. Tang, Y. Feng, and E. Shi, "Productivity of multiple fractures in a closed rectangular reservoir," *Journal of Petroleum Science and Engineering*, vol. 157, pp. 232–247, 2017.
- [32] V. Mongalvy, E. Chaput, S. Agarwal, and L. Lu, "A new numerical methodology for shale reservoir performance evaluation," in *Paper SPE 144154 Presented at the North American Unconventional Gas Conference and Exhibition*, The Woodlands, Texas, USA, 2011.

- [33] W. Yu and K. Sepehrnoori, "Simulation of gas desorption and geomechanics effects for unconventional gas reservoirs," *Fuel*, vol. 116, pp. 455–464, 2014.
- [34] R. H. Zhang, L. H. Zhang, R. H. Wang, Y. L. Zhao, and D. L. Zhang, "Research on transient flow theory of a multiple fractured horizontal well in a composite shale gas reservoir based on the finite-element method," *Journal of Natural Gas Science and Engineering*, vol. 33, pp. 587–598, 2016.
- [35] R. H. Zhang, L. H. Zhang, R. H. Wang, Y. L. Zhao, and R. Huang, "Simulation of a multistage fractured horizontal well with finite conductivity in composite shale gas reservoir through finite-element method," *Energy & Fuels*, vol. 30, no. 11, pp. 9036–9049, 2016.
- [36] Y. L. Zhao, L. H. Zhang, and B. C. Shan, "Mathematical model of fractured horizontal well in shale gas reservoir with rectangular stimulated reservoir volume," *Journal of Natural Gas Science and Engineering*, vol. 59, pp. 67–79, 2018.
- [37] S. Yao, F. Zeng, H. Liu, and G. Zhao, "A semi-analytical model for multi-stage fractured horizontal wells," *Journal of Hydrology*, vol. 507, pp. 201–212, 2013.
- [38] H. K. Nie and J. C. Zhang, "Types and characteristics of shale gas reservoir: a case study of Lower Paleozoic in and around Sichuan Basin," *Petroleum Geology & Experiment*, vol. 33, no. 3, pp. 219–232, 2011.
- [39] B. Song, *Pressure transient analysis and production analysis for New Albany shale gas wells*, Master Thesis, Texas A & M University, Texas, USA, 2010.
- [40] Y. Zhao, L. Zhang, Y. Xiong, Y. Zhou, Q. Liu, and D. Chen, "Pressure response and production performance for multi-fractured horizontal wells with complex seepage mechanism in box-shaped shale gas reservoir," *Journal of Natural Gas Science and Engineering*, vol. 32, pp. 66–80, 2016.
- [41] R. G. Loucks, R. M. Reed, S. C. Ruppel, and U. Hammes, "Spectrum of pore types and networks in mudrocks and a descriptive classification for matrix-related mudrock pores," *AAPG Bulletin*, vol. 96, no. 6, pp. 1071–1098, 2012.
- [42] F. Sun, Y. Yao, G. Li et al., "A slip-flow model for oil transport in organic nanopores," *Journal of Petroleum Science and Engineering*, vol. 172, pp. 139–148, 2018.
- [43] F. Sun, Y. Yao, G. Li, and X. Li, "Transport zones of oil confined in lipophilic nanopores: a technical note," *Arabian Journal of Geosciences*, vol. 12, no. 4, p. 136, 2019.
- [44] H. Singh, F. Javadpour, A. Etehadavakkol, and H. Darabi, "Nonempirical apparent permeability of shale," *SPE Reservoir Evaluation Engineering*, vol. 17, no. 3, pp. 414–424, 2014.
- [45] H. Singh and F. Javadpour, "Langmuir slip-Langmuir sorption permeability model of shale," *Fuel*, vol. 164, pp. 28–37, 2016.
- [46] T. Huang, L. Cao, C. Yuan, and P. Chen, "A novel numerical model of gas transport in multiscale shale gas reservoirs with considering surface diffusion and Langmuir slip conditions," *Energy Science Engineering*, vol. 7, no. 4, pp. 1315–1332, 2019.
- [47] M. Naraghi, F. Javadpour, and L. T. Ko, "An object-based shale permeability model: non-Darcy gas flow, sorption, and surface diffusion effects," *Transport in Porous Media*, vol. 125, no. 1, pp. 23–39, 2018.
- [48] F. Sun, Y. Yao, G. Li, and X. Li, "A slip-flow model for multi-component shale gas transport in organic nanopores," *Arabian Journal of Geosciences*, vol. 12, no. 5, p. 143, 2019.
- [49] S. Brunauer, L. S. Deming, W. E. Deming, and E. Teller, "On a theory of the van der Waals adsorption of gases," *Journal of the American Chemical Society*, vol. 62, no. 7, pp. 1723–1732, 1940.
- [50] Y. L. Zhao, L. H. Zhang, J. Z. Zhao, J. X. Luo, and B. N. Zhang, "Triple porosity" modeling of transient well test and rate decline analysis for multi-fractured horizontal well in shale gas reservoirs," *Journal of Petroleum Science and Engineering*, vol. 110, pp. 253–262, 2013.
- [51] T. Wu and S. Wang, "A fractal permeability model for real gas in shale reservoirs coupled with Knudsen diffusion and surface diffusion effects," *Fractals*, vol. 28, no. 1, p. 2050017, 2020.
- [52] L. H. Zhang, Z. X. Chen, and Y. L. Zhao, *Well Production Performance Analysis for Shale Gas Reservoirs*, Elsevier, Cambridge, United States, 2019.
- [53] X. H. Tan, J. Y. Liu, X. P. Li, L. H. Zhang, and J. Cai, "A simulation method for permeability of porous media based on multiple fractal model," *International Journal of Engineering Science*, vol. 95, pp. 76–84, 2015.
- [54] Y. Wang and X. Y. Yi, "Transient pressure behavior of a fractured vertical well with a finite-conductivity fracture in triple media carbonate reservoir," *Journal of Porous Media*, vol. 20, no. 8, pp. 707–722, 2017.
- [55] A.-R. Salam, "Performance-based comparison for hydraulically fractured tight and shale-gas reservoirs with and without non-Darcy-flow effect," *SPE Reservoir Evaluation & Engineering*, vol. 4, pp. 981–1006, 2018.
- [56] M. K. Fisher, C. A. Wright, B. M. Davidson et al., "Integrating fracture mapping technologies to optimize stimulations in the Barnett shale," in *Paper SPE 77441-MS Presented at Annual Technical Conference and Exhibition*, San Antonio, Texas, USA, 2002.
- [57] M. Mayerhofer, E. P. Lolon, and N. Warpinski, "What is stimulated rock volume?," in *Paper SPE 119890-MS Presented at SPE Shale Gas Production Conference, 16-18 November*, Fort Worth, Texas, USA, 2008.
- [58] Y. L. Zhao, L. H. Zhang, J. X. Luo, and B. N. Zhang, "Performance of fractured horizontal well with stimulated reservoir volume in unconventional gas reservoir," *Journal of Hydrology*, vol. 512, pp. 447–456, 2014.
- [59] K. Sato and R. N. Horne, "Perturbation boundary element method for heterogeneous reservoirs: part 1: steady-state flow problems," *SPE Formation Evaluation*, vol. 8, no. 4, pp. 306–314, 2013.
- [60] K. Sato and R. N. Horne, "Perturbation boundary element method for heterogeneous reservoirs: part 2—transient-flow problems," *SPE Formation Evaluation*, vol. 8, no. 4, pp. 315–322, 1993.
- [61] Y. Zhao, H. Li, L. Zhang, and B. Kang, "Pressure transient analysis for off-centered fractured vertical wells in arbitrarily shaped gas reservoirs with the BEM," *Journal of Petroleum Science and Engineering*, vol. 156, pp. 167–180, 2017.
- [62] Y. L. Zhao, B. C. Shan, L. H. Zhang, and Q. G. Liu, "Seepage flow behaviors of multi-stage fractured horizontal wells in arbitrary shaped shale gas reservoirs," *Journal of Geophysics and Engineering*, vol. 13, no. 5, pp. 674–689, 2016.
- [63] A. R. Salam and E. A. Fazil, "How much stimulated reservoir volume and induced matrix permeability could enhance unconventional reservoir performance," *Journal of Natural Gas Science and Engineering*, vol. 46, pp. 764–781, 2017.
- [64] A.-R. Salam, "Productivity-index behavior for hydraulically fractured reservoirs depleted by constant production rate

- considering transient-state and semisteady-state conditions,” *SPE Production & Operations*, vol. 33, no. 4, 2018.
- [65] J. Guo, Y. Li, J. Zhao, and Y. Ren, “The application of boundary element method to pressure behavior analysis in a composite reservoir with lateral drilling,” *Journal of Canadian Petroleum Technology*, vol. 43, no. 7, pp. 38–44, 2004.
- [66] K. Jongkittinarukorn, D. Tiab, and F. H. Escobar, “Interpretation of horizontal well performance in complicated systems by the boundary element method,” in *Paper SPE50437-MS Presented at the SPE International Conference on Horizontal Well Technology*, Calgary, Alberta, Canada, 1998.
- [67] J. Kikani and R. N. Horne, “Modeling pressure-transient behavior of sectionally homogeneous reservoirs by the boundary-element method,” *SPE Formation Evaluation*, vol. 8, no. 2, pp. 145–152, 2013.
- [68] L. S. Koh and D. Tiab, “3D. Boundary-element model for predicting performance of horizontal wells,” in *Paper SPE 26101-MS Presented at the SPE Western Regional Meeting, 26-28 May*, Anchorage, Alaska, USA, 1993.
- [69] W. Sung, W. Lee, and I. Kim, “Development and validation of interference testing analysis model using boundary element method for geometrically complex reservoirs,” in *Paper SPE 54272-MS Presented at the SPE Asia Pacific Oil and Gas Conference and Exhibition*, Jakarta, Indonesia, 1999.
- [70] H. T. Wang and L. H. Zhang, “A boundary element method applied to pressure transient analysis of geometrically complex gas reservoirs,” in *Paper SPE 122055-MS Presented at the Latin American and Caribbean Petroleum Engineering Conference*, Cartagena de Indias, Colombia, 2009.
- [71] L. H. Zhang, C. Y. Li, and Q. G. Liu, “The application of boundary element theory about seepage in complex boundary reservoir in horizontal wells,” *Computational Mechanics*, vol. 26, no. 2, pp. 287–290, 2009.

Review Article

A Review of Gas Flow and Its Mathematical Models in Shale Gas Reservoirs

Bo-ning Zhang,^{1,2} Xiao-gang Li,¹ Yu-long Zhao ,¹ Cheng Chang,³ and Jian Zheng⁴

¹State Key Laboratory of Oil and Gas Reservoir Geology and Exploitation, Southwest Petroleum University, Chengdu, Sichuan, China

²Chengdu North Petroleum Exploration and Development Technology Company Limited, Chengdu, Sichuan, China

³PetroChina Southwest Oil & Gasfield Company, Chengdu, Sichuan, China

⁴Sichuan Changning Natural Gas Development Co. Ltd., Chengdu, Sichuan, China

Correspondence should be addressed to Yu-long Zhao; swpuzhao@swpu.edu.cn

Received 13 July 2020; Revised 4 October 2020; Accepted 4 November 2020; Published 1 December 2020

Academic Editor: Wei Wei

Copyright © 2020 Bo-ning Zhang et al. This is an open access article distributed under the Creative Commons Attribution License, which permits unrestricted use, distribution, and reproduction in any medium, provided the original work is properly cited.

The application of horizontal wells with multistage hydraulic fracturing technologies has made the development of shale gas reservoirs become a worldwide economical hotspot in recent years. The gas transport mechanisms in shale gas reservoirs are complicated, due to the multiple types of pores with complex pore structure and special process of gas accumulation and transport. Although there have been many attempts to come up with a suitable and practical mathematical model to characterize the shale gas flow process, no unified model has yet been accepted by academia. In this paper, a comprehensive literature review on the mathematical models developed in recent years for describing gas flow in shale gas reservoirs is summarized. Five models incorporating different transport mechanisms are reviewed, including gas viscous flow in natural fractures or macropores, gas ad-desorption on shale organic, gas slippage, diffusion (Knudsen diffusion, Fick diffusion, and surface diffusion), stress dependence, real gas effect, and adsorption layer effect in the nanoshale matrix system, which is quite different from conventional gas reservoir. This review is very helpful to understand the complex gas flow behaviors in shale gas reservoirs and guide the efficient development of shale gas. In addition to the model description, we depicted the type curves of fractured horizontal well with different seepage models. From the review, it can be found that there is some misunderstanding about the essence of Knudsen/Fick diffusion and slippage, which makes different scholars adopt different weighting methods to consider them. Besides, the contribution of each mechanism on the transport mechanisms is still controversial, which needs further in-depth study in the future.

1. Introduction

The reserves of unconventional gas reservoirs, such as shale gas, coalbed methane, tight gas reservoirs, and natural gas hydrate, are rich around the world. The annual production of them has become increasingly important to the global energy supply. As a kind of unconventional natural gas, shale gas is trapped in the source rock with self-accumulation, which is very tight with the permeability range from nD to mD [1–7]. The shale gas storage in shale reservoirs are mainly with the status of free gas, adsorbed gas, and dissolved gas. The adsorbed gas can account for up to 85% of the total. Shale gas has become an increasingly important source of natural gas since the success of exploitation in the United

States, and interest has spread to potential shale gas reservoirs around the world [1–3]. The horizontal wells and the multistage hydraulic fracturing technique have proven to be the key for the cost-effective development of such tight reservoirs [1, 8–11].

While shale gas reservoirs have the characteristic of multiscaled space from ultramicropores (pore diameter < 0.7 nm), micropores (0.7 nm~2 nm), and mesopores (2 nm~50 nm) to macropores (>50 nm), the small-scale nanopores of less than 10 nm dominate in shale [1, 2, 5, 6]. Due to the complex pore size distribution and different gas storage mechanisms in shale gas reservoirs, which dominated by the viscous flow, slippage flow, Fick diffusion, Knudsen diffusion, surface diffusion, etc., gas transport mechanisms

in shale gas reservoirs are very complicated and vastly different from those in conventional reservoirs. Although many models have been proposed and used to analyze the gas flow behaviors in nanoscale, some of which are extended to the application of numerical simulation and well testing, there is no unified model that can be acceptable in the industry so far. The related studies on such topics are being widely reported. The objective of this paper is to review the progress of gas transport mechanisms and some mathematical models developed for shale reservoirs [1], which is of great significance to establish a shale gas reservoir development strategy that is completely different from the conventional gas reservoir. Only by revealing the complex transmission mechanism of shale gas in the micro-nanopore system can an accurate mechanism model be provided for the numerical simulation and production dynamic evaluation of shale gas.

2. Gas Flow and Transport Mechanisms

2.1. Pore Types in Shale Gas Reservoirs. Shale gas reservoirs are typical unconventional oil and gas reservoirs, which consist of fine-grained and organic-rich sedimentary rock. Shale is both the reservoir and the source of oil and gas [1, 9–12]. According to the International Union of Pure and Applied Chemistry (IUPAC), classification of pores in shale can be divided into organic intragranular pores, inorganic pores, and natural fractures [1].

In general, organic intragranular pores are formed only when thermal maturity (R_o) reaches 0.6% or above. When R_o is smaller than this value, few or no organic intragranular pores are developed. Organic pores in shale reservoirs are mainly developed during the thermal cracking of the hydrocarbon generation phase, and the sizes of organic pores range from 5 nm to 700 nm (as shown in Figure 1). Such organic nanometer pores are well developed in shale reservoirs, providing tremendous surface areas for shale gas adsorption as well as flow paths for gas flow [1, 6, 7].

The inorganic pores in shale matrix can be categorized as residual primary intergranular pores (as shown in Figure 2(a)), intercrystalline pores (as shown in Figure 2(b)), and secondary dissolved pores formed by dissolution of unstable minerals (e.g., calcite and feldspar, as shown in Figure 2(c)).

There are lots of natural fractures that are developed in shale gas reservoirs (as shown in Figure 3). Most natural fractures in shale reservoir developed during the organic evolution of hydrocarbon source rocks, and they are intermittently open or closed with the changes of reservoir pressure. Therefore, for those shale gas reservoirs with mass microfractures, the permeability of the fracture system is sensitive to stress caused by closing of the microfractures during reservoir development. Similar to conventional dual-porosity reservoirs, natural fractures are considered to the main flow channel for shale gas [1].

2.2. Gas Adsorption and Desorption. The physical properties, pore types, and accumulation mechanisms of shale gas reservoirs are different from those of conventional gas reservoirs, resulting in natural gas to exist in diverse states in shale.

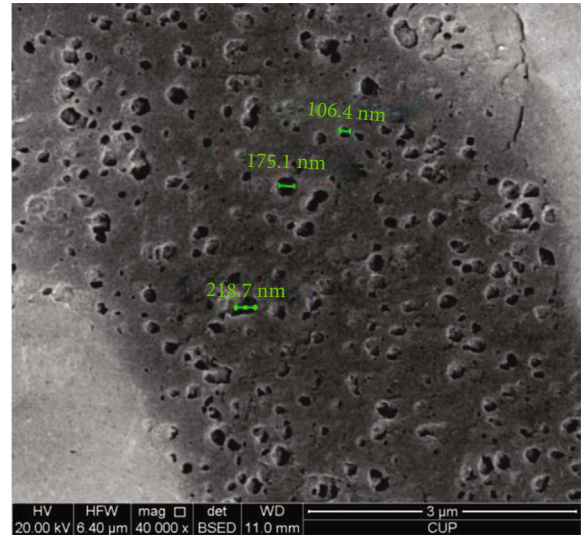


FIGURE 1: SEM images of shale organic pores [1].

Although a small amount of gas is dissolved in kerogen, asphaltene, liquid hydrocarbons, and formation water, the majority of natural gas exists in a free or an adsorbed state. Adsorbed shale gas is mainly adsorbed on the surface of organic matter with a single multimolecular layer, accounting for 20% to 85% of total reserves (as shown in Figure 4). Free gas is mainly stored in the pores of microfractures, inorganic and organic pores [14–16]. When the quantity of gas present in the reservoir is greater than the saturated adsorption capacity, free gas can exist [17, 18]. The relative proportion of adsorbed and free gas varies with temperature, pressure, organic matter content and quality, degree of microfracture development, and formation water content (the gas storage status of shale gas reservoirs is shown in Figure 4) [1, 13, 19].

As mentioned above, the amount of adsorbed gas can account for up to 85% of the gas reserve, which will be desorbed from the organic particle surface into free gas when the pressure is lower than the desorption pressure [1]. Therefore, the adsorption model is very important to describe the amount of gas in a given formation under certain conditions. According to the previous studies, there are two types of gas adsorption and desorption models—monomolecular layer model including the single layer adsorption model, such as Langmuir isothermal adsorption (L model); multimolecular layer model including the Freundlich adsorption model (F model), BET model, bi-parameter BET model (B-BET model), Toth adsorption model (T model), Langmuir-Freundlich adsorption model (L-F model), extended Langmuir model (E-L model), three-parameter BET model (T-BET model), and Dubinin-Radushkevich volume filling model (D-R model). These models can be used to calculate gas adsorption rate, pore size distribution, and desorption pressure. The formulas for these models are shown in Table 1 [17, 20, 21].

Figure 5 shows the fitting curves of the methane isotherm adsorption data from Barnett formation by different adsorption models, and Figure 6 shows the fitting curves of the test data by samples from the target layer of Longmaxi shale in

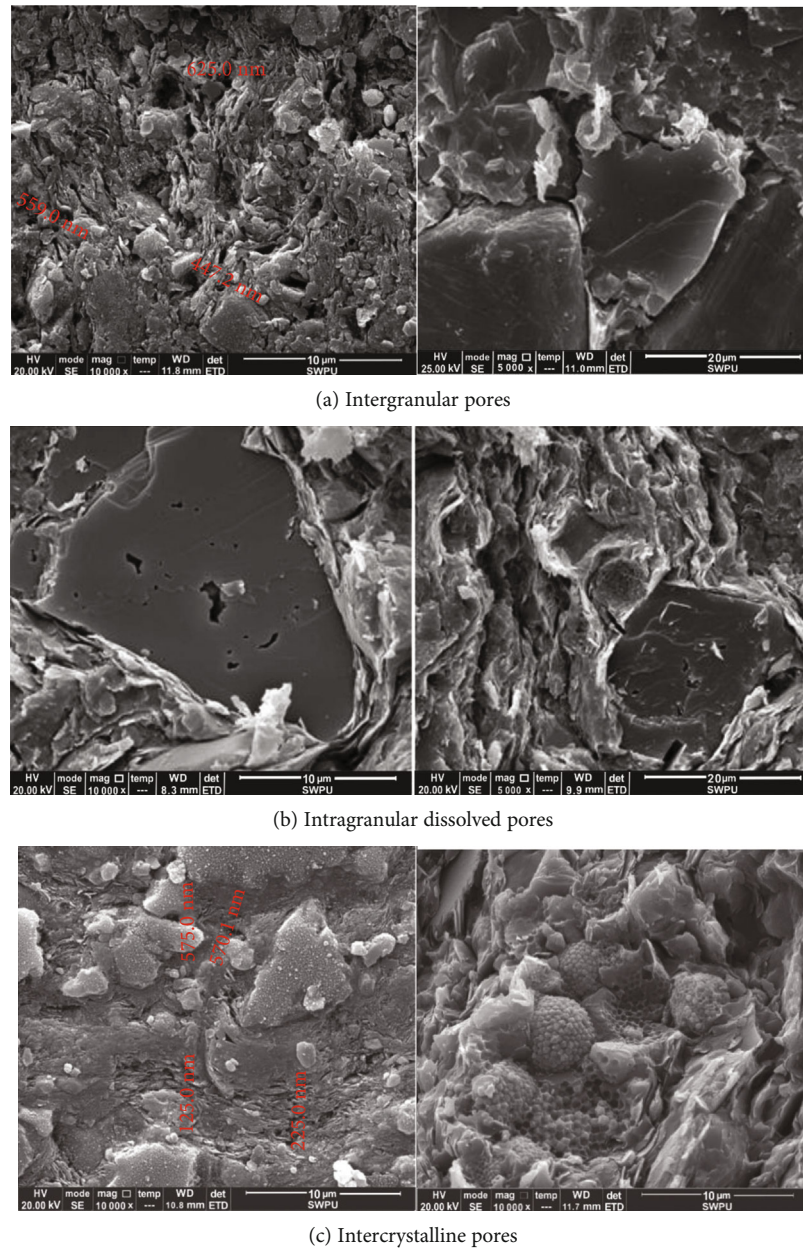


FIGURE 2: SEM images of shale inorganic pores [1] (the sample from Changning area of Weiyuan, Sichuan, China).

southern Sichuan Basin. From the fitting results, the following results can be obtained: in general, the single molecular adsorption model is much better for the North American Barnett shale gas reservoirs, and the multimolecular layer adsorption model of T-BET is much better for the Changning shale gas reservoirs of China.

3. Seepage Mechanism Models for Shale Gas Reservoirs

Due to the complex pore space and gas accumulation dynamics in shale gas reservoirs, the movement of shale gas occurs via complex mechanisms, including adsorption-desorption, diffusion, and seepage [23]. The specific flow processes are as follows. With decreasing reservoir pressure, the gas

adsorbed on the organic matter is desorbed. The desorbed gas then enters macropores, nanopores, and natural microfractures and becomes free gas. Due to the difference in gas concentration between kerogen/clay and organic nanopores, the gas flows to the low-pressure zone through diffusion (through matrix macropores or microfractures). Finally, free gas stored in matrix macropores and natural microfractures flows into wellbores and artificial hydraulic fractures under the pressure gradient [23, 24]. Gas flow in macropores, fractures, and wellbores follows Darcy's law [25].

Generally, continuity hypothesis or molecular hypothesis can be used to model fluid flow in nanopores. The continuity hypothesis model can be used to describe the relationship between macroscopic fluid properties and spatial coordinates, which is widely used in fluid flow. Knudsen number

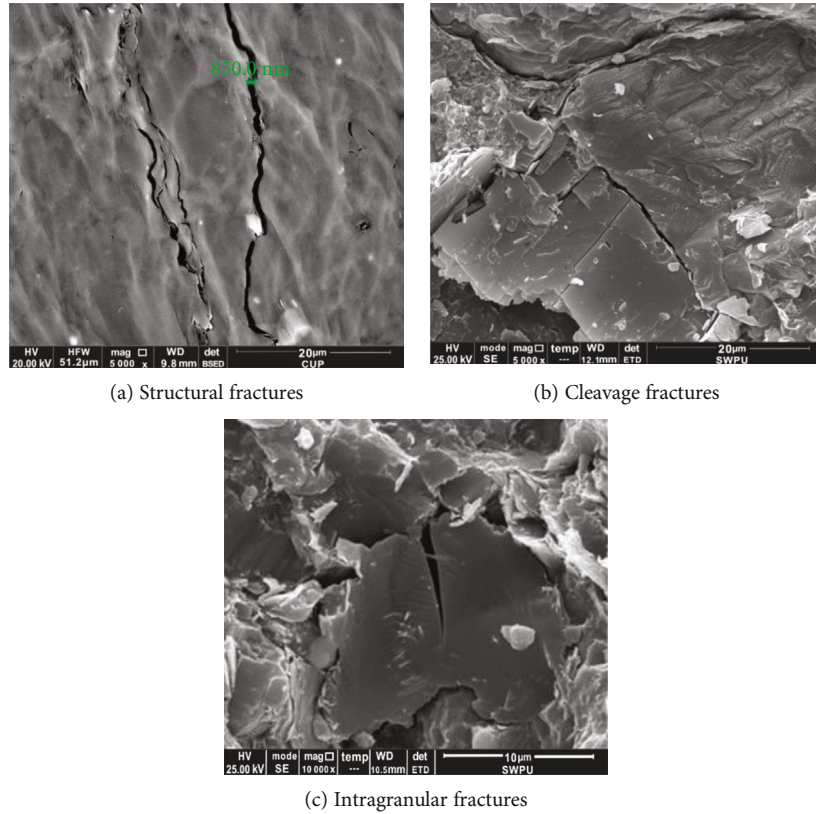


FIGURE 3: SEM images of natural fractures in shale [1].

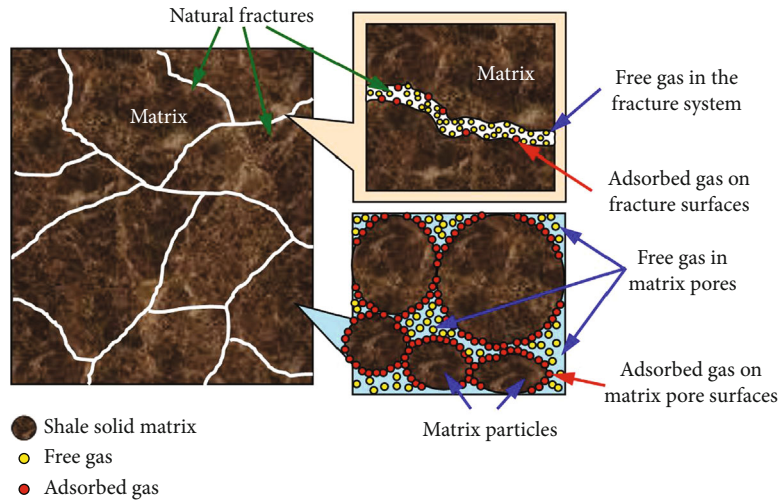


FIGURE 4: Schematic of gas storage in shale gas reservoirs [1, 13].

usually is used to justify if fluid flow satisfies the continuity hypothesis and then determine the fluid flow regime. Knudsen number K_n is defined as the ratio of gas molecular mean free path to the characteristic length of porous media, representing the relative degree of gas molecule collision with the gas molecules and pore walls. Its expression is

$$K_n = \frac{\lambda}{R_h}, \quad (1)$$

where λ is the gas molecular mean free path of gas (nm) and R_h is the average hydraulic radius of pore media (nm).

As shown in Figure 7, when $K_n < 0.001$, the gas molecule velocity of a pore wall is zero, and Darcy's law is valid. This transport mechanism is also known as continuum flow. When $0.001 < K_n < 10$, the gas molecule velocity of a pore wall is no longer zero, and, consequently, the gas flux is increased. Darcy's law is no longer valid, and this transport mechanism is referred to as rarefied gas transport. The rarefied gas transport is further subdivided into slip flow

TABLE 1: Adsorption models and formulas [17, 20, 21].

Model	Formula
Langmuir model (L model)	$V = V_L \frac{P}{p_L + P}$
Freundlich empirical formula (F model)	$V = K_b p^n$
Bi-parameter BET model (B-BET model)	$V = \frac{V_m C p}{(p^0 - p)[1 + (C - 1)(p/p^0)]}$
Toth adsorption model (T model)	$V = \frac{V_L K_b p}{[1 + (K_b p)^n]^{1/n}}$
Langmuir-Freundlich adsorption model (L-F model)	$V = \frac{V_L K_b p^n}{1 + K_b p^n}$
Extended Langmuir model (E-L model)	$V = \frac{V_L K_b p}{1 + K_b p + n \sqrt{K_b p}}$
Three-parameter BET model (T-BET model)	$V = \frac{V_m C p [1 - (n + 1)(p/p^0)^n + n(p/p^0)^{n+1}]}{(p^0 - p)[1 + (C - 1)(p/p^0) - C(p/p^0)^{n+1}]}$
Dubinin-Radushkevich volume filling model (D-R model)	$V = V_0 [-D \ln^2(p^0/p)]$

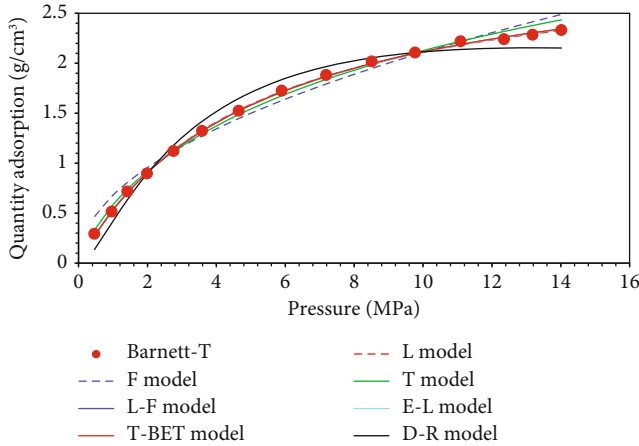


FIGURE 5: Fitting curves of different adsorption models for the Barnett shale reservoir sample [22].

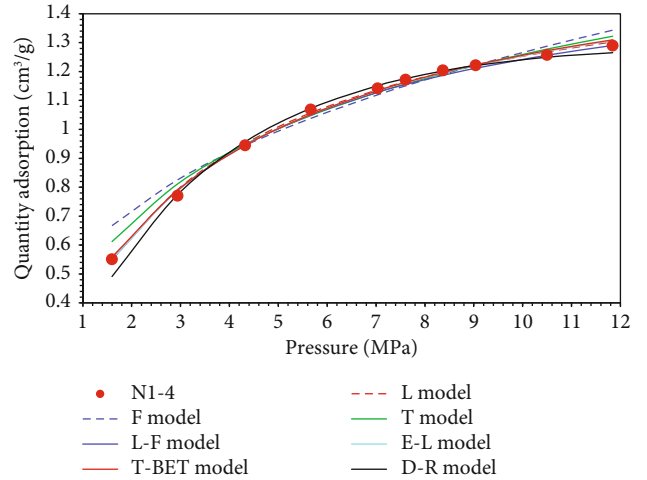


FIGURE 6: Fitting curves of different adsorption models for Changing shale reservoir.

($0.001 < K_n < 0.1$), transition flow ($0.1 < K_n < 10$), and free-molecular flow ($10 < K_n$). Under normal reservoir conditions of shale gas reservoirs, Knudsen number ranges from 0.0002 to 6 [1, 26].

By using Equation (1), the Knudsen number of pure methane under different pressure and different radius of pores with a temperature of 350 K can be calculated. And the results can be plotted as shown in Figure 8. We can clearly see that the gas flow in larger-scale pores, such as natural fractures, can be treated as a continuous flow. However, for small-scaled pores, the gas flow covers from slippage flow to transitional flow regimes, which is much more complicated than the continuous flow. The small scale pores always exist in the shale matrix.

To describe the mechanism of nanopore gas transport in continuous flow, slip flow, transition flow, and diffusion flow, scholars have proposed many coupling models considering dif-

ferent mechanisms. Ertekin et al. first established the coupling mechanism model considering continuous flow and Fick diffusion, and these two mechanisms directly adopted linear superposition. In this paper, the transport mechanism of gas in porous media was divided into bulk flow (intermolecular interaction), Knudsen diffusion (gas-solid interface interaction), and surface diffusion of the adsorption layer, among which the gas slip flow was essentially equivalent to Knudsen diffusion [28].

In 2007, Javadpour et al. proposed an apparent permeability model of shale matrix considering the dual mechanism of Knudsen diffusion and slip flow. The model had a similar form to the Darcy equation and was easy to apply [29]. Then, based on the Javadpour model, Darabi et al. introduced the influence of the pore-throat structure characteristics of the shale matrix on the gas flow law (the tortuosity and roughness, etc.) by introducing the fractal theory [30].

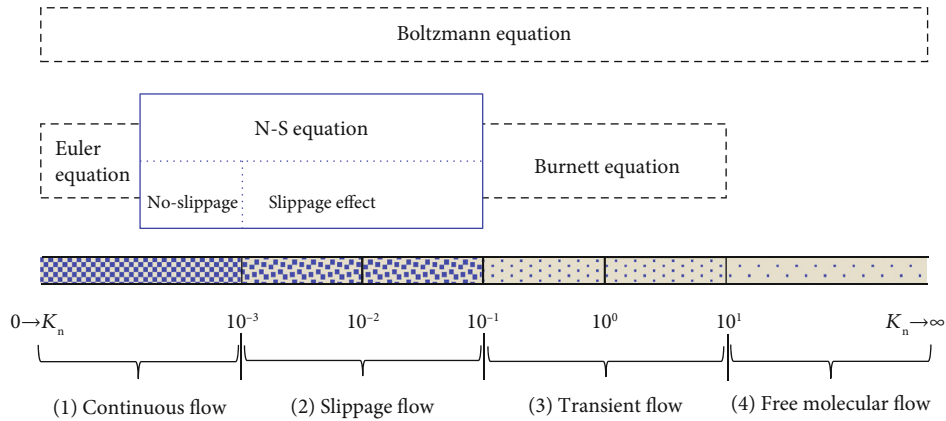


FIGURE 7: Knudsen number regimes [27].

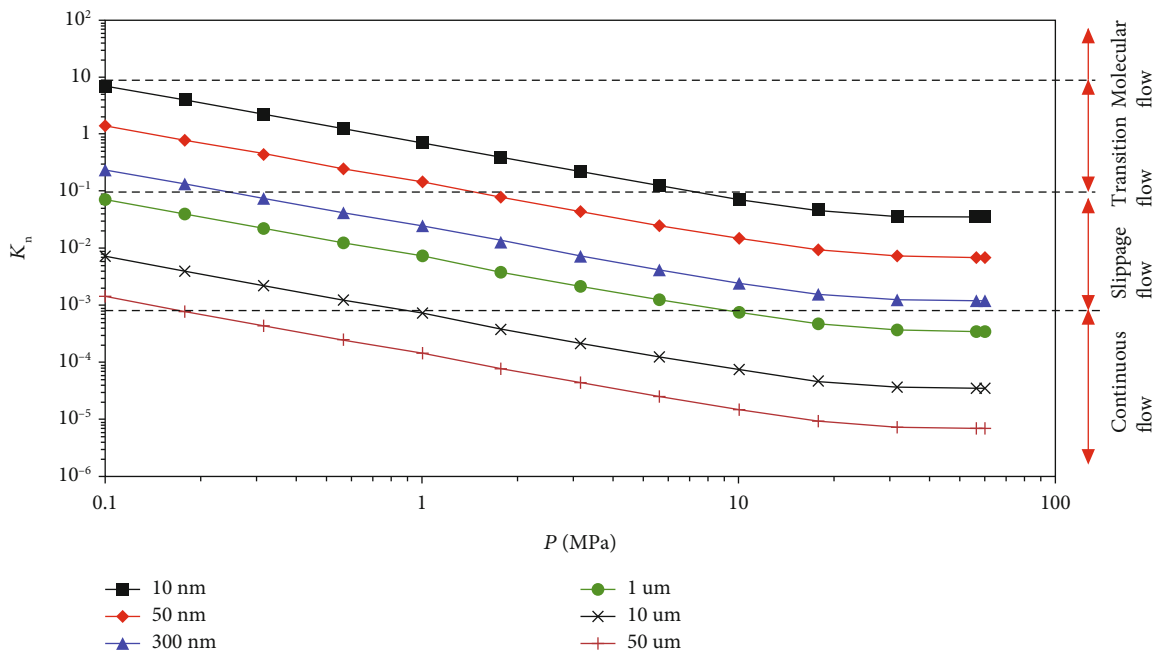


FIGURE 8: Flow regimes of methane under different pressure and pore radius.

In 2012, Shabro et al. established a shale gas flow mechanism model that considers dissolved gas diffusion, slip flow, Knudsen diffusion, and Langmuir desorption in kerogen [31]. In 2014, Mi et al. studied the apparent permeability model of the fracture system and matrix system, respectively, by linear superposition. The methods of establishing these models were based on Javadpour's model, which was to superimpose the slip flow and the diffusion. The difference was that Mi et al. divided the flow types into Knudsen diffusion, transitional diffusion, and Fick diffusion according to the K_n number [32].

In 2015, based on the transport mechanisms of slip flow and Knudsen diffusion, Wu et al. established a nanopore shale gas transmission model according to the ratio of the collision frequency between molecules and the collision frequency of molecules to the wall of the pores as the weighting factors of the slip flow and the Knudsen diffusion [26]. In the

same year, Sheng et al. proposed a comprehensive model for coupling gas viscous flow, slip flow, Knudsen diffusion, and surface diffusion based on the weighted superposition of Wu et al.'s [33]. Subsequently, according to different transport mechanisms and pore structure characteristics of the gas, various multiple apparent permeability models were successively proposed by using different superposition methods [34, 35].

In 2017, Li et al. published their research results in the Journal of Physics that both Nusen diffusion and surface diffusion are related to the gas-solid interaction at the interface [36]. Knudsen diffusion is a diffusion phenomenon that occurs after gas molecules collide with the wall surface. Surface diffusion is a process in which gas molecules continuously jump between adsorption sites on the pore surface. In both cases, the velocity of the gas molecules on the wall surface is not zero, which is consistent with the slip

phenomenon. Li et al. believed that it is debatable to superimpose the Knudsen diffusion and slip flow, or to superimpose the slip flow and surface diffusion, or to superimpose these three transport mechanisms in flow models. Since the shale gas mass transport mechanism was introduced from the theory of rarefied gas dynamics, the aerodynamic researcher also thought that, from the point of view of rarefied gas, slip flow was essentially the same as Knudsen diffusion, which was determined by the Boltzmann equation and gas-solid interaction, but the coefficients were different under different K_n [37, 38]. After that, Cai et al. proposed a very interesting apparent permeability model by accounting for three major fluid flow mechanisms in shale stratum, which is modeled as a 3D fractal media. This model can present the gas flow in shale pore media more accurately [39, 40].

Table 2 lists the apparent permeability models proposed by different scholars in recent years for different transport mechanisms of shale gas under different coupling methods. In general, scholars believe that the fluid flow mechanism in the micro-nanopore system of shale gas mainly includes viscous flow, slip flow, Knudsen diffusion, surface diffusion, adsorption layer effect, reservoir pore structure characteristics, and stress sensitivity. However, there are still differences in the essential relations between various mechanisms, which need to be further studied. Meanwhile, the existing mechanism models are not combined with the actual characteristics of pore-throat scale distribution. Whether the same mechanism model is applicable to reservoirs of various types of scales is still debatable and remains to be further studied. In order to better guide the efficient development of shale gas, only by revealing the complex transmission mechanism of shale gas in the micro-nanopore system can we provide an accurate mechanism model for shale gas numerical simulation and production dynamic evaluation.

R is the molar gas constant; M is the molar mass; k_{app} is the apparent permeability; k_0 is the absolute permeability; $\bar{\lambda}$ is the mean free path at mean pressure; r is the pore radius; a is the dimensionless rarefaction coefficient (when multiply by K), or tangential momentum accommodation coefficient (when in the denominator); a_0 is the rarefaction dimensionless coefficient at $K_n \rightarrow 0$; a_1 and a_2 are the fitting dimensionless constants that are obtained through molecular-simulation and experimental data, respectively; D_f is the fractal dimension of the pore surface; δ' is the ratio of normalized molecular size to local average pore diameter; D_k is the Knudsen diffusion coefficient; c_g is the gas compressibility; c_ϕ is the dimensionless material-specific constant; σ_m is the mean in situ effective stress; ζ_{mb} is the dimensionless correction factor of apparent permeability in nanopores of SGRs; T is the temperature; ω_m is the poromechanical-response dimensionless coefficient of shale matrix; ω_s is the sorption-induced-swelling-response dimensionless coefficient of shale matrix; η is the gas viscosity; C_{ads} is the adsorbed-phase concentration; ρ_{ads} is the adsorbed-phase density; R_e is the effective radius of the nanocapillary tube for free gas transport; R_0 is radius of the nanocapillary tube; D_s is the diffusion coefficient; α_p is the density ratio of adsorbed gas to free gas; n is the number of adsorbed layer; p_0 is the saturated adsorption

pressure of gas; Z is the gas deviation factor; D_{S0} is the corrected diffusivity; τ is the tortuosity; ρ_l is the sorbent density; θ is the surface coverage; δ is the molecular diameter; p_L is the Langmuir pressure; C_L is the maximum gas capacity; ψ is the TOC; w_v and w_k are the weight of the viscous molar flux and the Knudsen diffusion molar flux, respectively; ψ_{or} is the ratio of pores with adsorption capacity to total pores; ω_{or} and ω_{in} are coefficients of variation in pores with and without adsorption.

Taking the model proposed by Zhang et al. as an example, considering the properties of porous media and adsorptive gas occupation, the apparent permeability of shale matrix can be expressed as the sum of bulk transport and adsorbed gas transport in the following form [1, 5, 54]:

$$k_{app} = k_{slip} + k_{Knudsen} + k_{surface}. \quad (2)$$

For slippage flow, considering the effect of stress-dependence and adsorbed layer, its equivalent permeability could be expressed as

$$k_{slip} = \gamma_b F(K_n, p) \frac{r_{eff}^2}{8}. \quad (3)$$

For Knudsen diffusion, its equivalent permeability has the following form [5]:

$$k_{Knudsen} = \gamma_b (\delta')^{D_f-2} D_k c_g \mu. \quad (4)$$

Considering the influences of gas coverage ratio, porous media properties, and real gas effect, the equivalent permeability of surface diffusion could be expressed as

$$k_{surface} = \gamma_s D_s V_L \theta_{real} \frac{\mu Z T p_{sc}}{p^2 T_{sc}}, \quad (5)$$

$$F(K_n, p) = 1 + \frac{8\omega p_r}{p} K_n,$$

where V_L is the Langmuir volume, m^3/m^3 ; D_k is the Knudsen diffusion coefficient, m^2/s ; D_s is the surface diffusion coefficient, m^2/s ; c_g is gas concentration, mol/m^3 ; μ is gas viscosity, $Pa \cdot s$; p_r is the reference pressure, Pa ; K_n is the Knudsen number, dimensionless; D_f is the fractal dimension of pore surface, dimensionless; p is reservoir pressure, Pa ; Z is the gas deviation factor, dimensionless; T_{sc} and P_{sc} are the temperature and pressure at standard condition; b is the Langmuir equilibrium adsorption constant, Pa^{-1} ; ω is a parameter related to gas-solid interaction; γ_b is the correction factor from single capillary model to upscaled porous media model for bulk phase; γ_s is the correction factor from single capillary model to upscaled porous media model for surface diffusion.

θ_{real} is the gas coverage ratio on solid surfaces considering the real gas effect and thermodynamic phase changes, which

TABLE 2: Various apparent permeability models proposed for gas flow in the shale matrix.

No.	Apparent permeability formula	Authors
1	$k_{\text{app}} = k_0 \left(1 + \frac{4\lambda}{r} \right)$	Ertekin et al. [28]
2	$k_{\text{app}} = k_0 \left(1 + \left(\frac{8\pi RT}{M} \right)^{0.5} \right) \frac{\mu}{P_{\text{avg}}} r \left(\frac{2}{\alpha} - 1 \right)$	Ertekin et al. [28]
3	$k_{\text{app}} = k_0 + \frac{2\mu r}{3p} \left(\frac{8RT}{\pi M} \right)^{0.5}$	Ertekin et al. [28]
4	$k_{\text{app}} = k_0 \left((1 + \alpha K_n) \left(1 + \frac{4K_n}{1 - bK_n} \right) \right)$ $\alpha(K_n) = \alpha_0 \frac{2}{r} \tan^{-1}(\alpha_1 K_n^{\alpha_2})$	Beskok-Karniadakis [41]
5	$k_{\text{app}} = \frac{2r\mu M}{3RT P_{\text{avg}}} \left(\frac{8RT}{\pi M} \right)^{0.5} + F \frac{r^2}{8}$ $F = 1 + \left(\frac{8\pi RT}{M} \right)^{0.5} \frac{\mu}{\rho_{\text{avg}}} \left(\frac{2}{\alpha} - 1 \right)$	Javadpour et al. [29]
6	$k_{\text{app}} = k_0 \left((1 + \alpha K_n) \left(1 + \frac{4K_n}{1 + K_n} \right) \right)$ $\frac{\alpha_0}{\alpha(K_n)} - 1 = \frac{A}{K_n^B} \quad (A > 0, B > 0)$	Wu et al. [42, 43]
7	$k_{\text{app}} = \frac{\mu M}{RT \rho_{\text{avg}}} \frac{\phi}{\tau} (\delta')^{D_r - 2} D_k + k_0 \left(1 + \frac{b}{p} \right)$ $k_0 = r^2/8, D_k = (2r/3) (8RT/\pi M)^{0.5}, b = (8\pi RT/M)^{0.5} (\mu/r) (2/\alpha - 1)$	Darabi et al. [30]
8	$k_{\text{app}} = k_a + D\mu \frac{MC_{\text{max}} P_L}{(p + P_L)^2} (1 - \phi_{\text{eff}})$ $k_a = k_0 f(K_n), f(K_n) = (1 + \alpha K_n)(1 + (4K_n/1 + K_n))$	Xiong et al. [44]
9	$k_{\text{app}} = c_g D_k \mu + F k_0$ $F = 1 + \left(\frac{8\pi RT}{M} \right)^{0.5} \frac{\mu}{\rho_{\text{avg}}} \left(\frac{2}{\alpha} - 1 \right)$	Swami and Settari [45] Zhao et al. [46]
10	$k_{\text{app}} = k_0 + k_{\text{slip}} + k_{\Gamma} + k_{\text{D}}$ $k_0 = r^2/8, k_{\text{slip}} = F k_0, k_{\Gamma} = k_{\text{slip}} f + k_{\text{D}} (1 - f)$ $k_{\text{D}} = \left(2r\mu M / 3RT \rho_{\text{avg}} \right) (8RT/\pi M)^{0.5}, f = 1/[1 + (K_n/4.5)^4]$	Li et al. [25]
11	$k_{\text{app}} = c_g D\mu + F k_0$ $D_K = \frac{\phi}{\tau} \frac{k_{\text{BT}}}{3\pi\mu d_{\text{gas}}}, \quad 10 < K_n$ $D_F = \frac{\phi}{\tau} \frac{2r}{5} \left(\frac{8RT}{\pi M} \right)^{0.5}, \quad 0.1 < K_n$ $D = \begin{cases} (D_F^{-1} + D_K^{-1})^{-1}, & 0.1 < K_n < 10 \end{cases}$	Mi et al. [32]
12	$k_{\text{app}} = k_0 \left(1 + \frac{3\pi}{16k_0} \frac{\mu D_k}{p} + \frac{b}{4} \left(\frac{3\pi}{16k_0} \frac{\mu D_k}{p} \right)^2 \right)$ $D_k = \frac{2r}{5} \left(\frac{8RT}{\pi M} \right)^{0.5}$	Deng et al. [47]

TABLE 2: Continued.

No.	Apparent permeability formula	Authors
13	$k_{\text{app}} = k_0 \left(\frac{\sigma_m}{p_0} \right)^{-c_\phi} f(K_n)$ $k_{\text{app}} = \omega k_{\text{vs}} + (1-\omega)k_K + k_s$ $k_{\text{vs}} = \zeta_{\text{mb}} \omega_m \omega_s \frac{r^2(1+\alpha K_n)}{8} \left(1 + \frac{4K_n}{1-bK_n} \right)$ $k_K = \zeta_{\text{mb}} \omega_m \omega_s \frac{2r}{3} \left(\delta' \right)^{D-2} \left(\frac{8RT}{\pi M} \right)^{0.5} \frac{\eta}{p}$ $k_s = \zeta_{\text{ns}} D_s (C_s RT \mu / p^2 M), \omega = 1/1 + K_n$	Wang and Marongiu-Porcu [48]
14	$k_{\text{app}} = \omega k_v + (1-\omega)k_p + k_s$ $k_s = D_s(1-\phi)\mu C_{\text{ads}}/p\rho_{\text{ads}}, k_v = (r^2/8) + (D_s(1-\phi)\mu C_{\text{ads}}/p\rho_{\text{ads}}), k_p = (2\mu r/3\rho_g Z) (8M/\pi RT)^{0.5}, \omega = 1/1 + K_n$	Wu et al. [26, 42, 43]
15	$k_{\text{app}} = \begin{cases} k_0, & k_0 \gg k_{K_n} \text{ Continuum region} \\ k_a, & \text{Transient region} \\ k_{K_n}, & k_{K_n} \gg k_0 \text{ Knudsen region} \end{cases}$ $k_{\text{Kn}} = \mu D_K / p, k_a = k_0(1 + (k_{K_n}/k_0))$ $k_{\text{app}} = k_a + k_s$ $k_a = k_0 f(K_n)$ $k_s = \frac{\mu D_{\text{gs}}}{p_0 Z} \left\{ \frac{C[1-(n+1)\chi^n + n\chi^{n+1}]}{1+(C-1)\chi - C\chi^{n+1}} - \frac{Cn(n+1)\chi^n}{1+(C-1)\chi - C\chi^{n+1}} - \frac{C\chi(C-1-C(n+1)\chi^n)[1-(n+1)\chi^n + n\chi^{n+1}]}{(1-\chi)[1+(C-1)\chi - C\chi^{n+1}]} \right\} \left(1 - \frac{R^2}{R_0^2} \right) \left(1 - \frac{R^2}{R_0^2} \right)$ $\chi = \frac{p}{p_0 Z}$ $k_{\text{app}} = \left[1 + \frac{b}{p} \right] \frac{\phi^2}{8r} + \frac{\mu}{p_g T} \left[\frac{\phi}{RT} \left(\delta' \right)^{D-2} D_K + \frac{g\phi(1-\phi)D_{\text{so}}}{p} \right]$ $b = \left(\frac{8\pi RT}{M} \right)^{0.5} \frac{\mu}{\rho_{\text{avg}} r} \left(\frac{2}{\alpha} - 1 \right)$	Sheng et al. [33]
16		Ye et al. [49]
17		Wang et al. [50]
18		Zhang et al. [35]
19	$k_{\text{app}} = \frac{\phi_{\text{eff}}^2}{8\tau} \left(1 + \frac{128}{15\pi^2} \tan^{-1}(4K_n^{0.4})K_n \right) \left(1 + \frac{4K_n}{1+K_n} \right) + \mu M D_S C_{\text{max}} \frac{d\theta}{dp} \left[1 - \left(\frac{r_{\text{eff}}}{r_{\text{eff, stress}}} \right)^2 \right]$	Song et al. [51]
20	$f_c = 1 + \frac{\phi D_{\text{gs}} \mu}{\tau p k_{\text{so}}} = 1 + \frac{16}{3} \frac{\mu}{\alpha^3 r p} \sqrt{\frac{8ZRT}{\pi M}}$	Ren et al. [52]
21	$k_{\text{app}} = \frac{\mu M}{\rho_g} \left[\frac{1}{RT} \left(D_K + \frac{k_0}{\mu} p \right) + (1-\epsilon) A_{\text{sat}} \frac{bD_s}{1+bp} \right]$	Wang et al. [34]
22	$k_{\text{app}} = \frac{r^2}{8} + \frac{\mu D_{\text{I}}}{p} + \frac{\mu D_{\text{S, max}} RT C_s}{p^2}$ $D_{\text{I}} = (D_{\text{I}}^{-1} + D_{\text{K}}^{-1})^{-1}, D_{\text{F}} = k_{\text{B}} T / 3\pi \mu d_{\text{gs}}, D_{\text{K}} = (2r/3)(8RT/\pi M)^{0.5}$	He et al. [53]
23		Li et al. [36]

TABLE 2: Continued.

No.	Apparent permeability formula	Authors
24	$D_K = (2r_e/3)(8RT/\pi M)^{0.5} F = 1 + (8\pi RT/M)^{0.5} \left(\mu/\rho_{\text{avg}} r_c \right) (2/\alpha - 1), k_{0e} = r_e^2 \phi / 8\tau, r_e = r - (p/p + p_L) d_g$ $k_{\text{app}} = \gamma_b F(K_n, p) \frac{r_{\text{eff}}^2}{8} + \gamma_b (\delta^t)^{D_t-2} D_K c_g \mu + \gamma_s D_s V_L \theta_{\text{real}} \frac{\mu Z T p_{sc}}{P^2 T_{sc}}$ $F(K_n, p) = 1 + \frac{8\phi p_L}{P} K_n$	Zhang et al. [54]
25	$k_{\text{app}}^{\text{inorganic}} = (\phi/8\tau) (1 - \beta) \left[r_{e-\text{in}}^2 (1 + \alpha K_n/1 + K_n) (1 + (4K_n/1 - bK_n)) + (16C_g \mu r_{e-\text{in}}/3 (1 + 1/K_n)) (D_m/2r_{e-\text{in}})^{D_t-2} (8RT/\pi M)^{0.5} \right] \text{ (for inorganic pores)}$ $k_{\text{app}}^{\text{organic}} = (\phi\beta/8\tau) (r_{e-\text{or}}^2/r_{e-\text{or}}^2) \left[r_{e-\text{or}}^2 (1 + \alpha K_n/1 + K_n) (1 + (4K_n/1 - bK_n)) + (16C_g \mu r_{e-\text{or}}/3 (1 + 1/K_n)) (D_m/2r_{e-\text{or}})^{D_t-2} (8RT/\pi M)^{0.5} \right] + (\beta\phi\mu Z RT \rho_r V_L D_s / \tau p V_m) (d\theta/dp) (1 - r_{e-\text{or}}^2/r_{e-\text{or}}^2) \text{ (for organic pores)}$ $K_{\text{app}} = \psi \xi_{\text{or}} \frac{\int_{r_{\text{min}}}^{\text{max}} r_{\text{or}}^2 f(r) dr}{\int_{r_{\text{min}}}^{\text{max}} (f(Kn)(r_{\text{or}}^2/\delta) \cdot \delta_{\text{a}} + \delta_{\text{so}} Z^{0.5} D_{\text{so}} \mu c_g) r_{\text{or}}^2 f(r) dr} + (1 - \psi) \xi_{\text{in}} \frac{\int_{r_{\text{min}}}^{\text{max}} r_{\text{in}}^2 f(r) dr}{\int_{r_{\text{min}}}^{\text{max}} (f(Kn)(r_{\text{in}}^2/\delta) \cdot \delta_{\text{a}} + \delta_{\text{so}} Z^{0.5} D_{\text{so}} \mu c_g) r_{\text{in}}^2 f(r) dr}$	Wang et al. [38]
26	$\delta_{\text{sl}} = 1/1 + K_n, \delta_{\text{Kn}} = 1/1 + 1/K_n$ $k = k_v + k_t + k_s$ $k_v = \frac{\pi \lambda_{\text{max}}^{3+D_t}}{128 L_{\text{or}}^3} \frac{D_t}{3 - D_t + D_t}$ $k_t = \frac{\pi \mu}{12p} \sqrt{\frac{8RT D_t \lambda_{\text{max}}^{D_t}}{\pi M}} \frac{\lambda_{\text{max}}^{D_t}}{r_{\text{or}}^{D_t+1}} \int_{\lambda_{\text{min}}}^{\lambda_{\text{max}}} \frac{Kn}{Kn+1} \lambda^{1-D_t+D_t} d\lambda$ $k_s = \pi D_s \frac{C_1 D_m}{(p_1 + p)^2} \frac{D_1 \delta \theta \mu M}{\rho r_{\text{or}}^{D_t+1}} \left[\frac{\lambda_{\text{max}}^{D_t}}{D_t - D_t} \left(1 - \left(\frac{\lambda_{\text{min}}}{\lambda_{\text{max}}} \right)^{D_t - D_t} \right) + \frac{\delta \theta \lambda_{\text{max}}^{D_t-1}}{D_t - D_t - 1} \left(1 - \left(\frac{\lambda_{\text{min}}}{\lambda_{\text{max}}} \right)^{D_t - D_t - 1} \right) \right]$	Cai et al. [55]
27	$K_{\text{app}} = w_v \frac{\phi_o}{\tau_t} (1 + \alpha Kn) \frac{r^A}{8r_o^2} + w_k \frac{\phi_o}{3\pi r_o^2} \frac{r^A}{\tau_t} \delta^{D_t-2} P + \frac{\phi_o}{\tau_t} D_s C_{\text{smax}} \frac{P_L Z^2 c_r RT \mu}{M(P + ZP_L)^2}$	Zhang et al. [56]
29	$K_m = \left[\psi_{\text{or}} \omega_{\text{or}}^2 (1 - \zeta)^2 + (1 - \psi_{\text{or}}) \omega_{\text{in}}^2 \right] K_o + \left[\psi_{\text{or}} (1 - \theta) \omega_{\text{or}}^{3.5} (1 - \zeta)^3 \delta_{\text{or}}^{D_t-2} D_{\text{Kn}}^{\text{or}} + (1 - \psi_{\text{or}}) \omega_{\text{in}}^{3.5} \delta_{\text{in}}^{D_t-2} D_{\text{Kn}}^{\text{in}} \right] \frac{\mu \phi_o^3}{\tau_t P} + \psi_{\text{or}} \zeta \frac{\mu C_{\text{smax}} \theta D_o^3 [1 - \omega_{\text{or}} \phi_o (1 - \zeta)]}{P(1 - \theta)} \left[\frac{1}{\rho_g} + \frac{\theta \omega_{\text{or}} \phi_o (1 - \zeta)}{\rho_a} \right]$	Zhang et al. [57]

can be expressed as

$$\theta_{\text{real}} = \frac{bp/Z}{1 + bp/Z}. \quad (6)$$

r_{eff} is the effective hydraulic radius considering the effect of stress dependence and gas adsorption on a solid surface, m.

$$r_{\text{eff}} = r_0 \left[\frac{1 - (\sigma/p_1)^m}{1 - (\sigma_0/p_1)^m} \right]^{1.5} - d_m \theta_{\text{real}}, \quad (7)$$

where d_m is the gas molecular diameter, m; σ is the effective stress, Pa; σ_0 is the effective stress under initial state, Pa; p_1 and m are the parameters related to the pore stiffness and roughness, respectively; r_0 is the radius of the capillary tube, m.

4. Comprehensive Mathematical Models

The development of natural fracture in shale gas reservoir is very rich, which makes the development of shale gas reservoirs of economic value. Therefore, there are at least two types of pores in shale reservoirs including natural fractures and nanopores in the matrix system, which are properly presented by multiple medium models. Through the review of theories and models of transient well flow, the following three types of continuum models, as shown in Figure 9, are the most widely used [1, 58].

To sum up, the storage spaces in shale gas reservoirs span multiple scales, from matrix nanopores to artificial fractures; free, adsorbed, and dissolved gas coexist, with most in the adsorbed state; and gas migration mechanisms include adsorption-desorption, diffusion, and seepage. Models of gas flow must account for the physical properties of the reservoir. Current shale gas seepage models consist of adsorption-desorption models (equilibrium and nonequilibrium diffusion-percolation models) and models based on the reservoir medium (dual-, triple-, and quadruple-porosity models) [13, 23, 24, 58–63]. The models based on reservoir media considers the distribution of pore types and natural microfractures at different scales in the reservoir matrix, and they couple adsorption and desorption together.

The equilibrium ad/desorption-diffusion model is theoretically based and reflects physical phenomena. In this model, when reservoir pressure decreases, adsorbed gas instantly desorbs and enters macropores; the time required for gas to migrate into matrix nanopores (the desorption-diffusion time) is not considered, i.e., the pressure of gas adsorbed on micropore walls and the pressure of free gas in macroscopic pores are in a state of continuous equilibrium. The equilibrium adsorption model is a single-porosity partial differential equation that incorporates a pressure-dependent point source term in a conventional single- or multiporosity-medium model for the adsorption and desorption characteristics of shale/coal reservoirs, or it is obtained by adding ad/desorption compressibility to the total compressibility. The partial differential equation can be solved with analytic or numerical methods [13, 65–68]. A represen-

tative model of percolation was proposed by Bumb and McKee for gas seepage in coalbed methane, and this model has been widely used by other scholars [66]. Bumb and McKee used actual data to verify that desorption of coalbed methane and shale gas followed the Langmuir isotherm, and they proposed the concept of “modified ad/desorption compressibility” to consider the effect of desorption of coalbed methane during reservoir development. This concept refers to the compressibility of shale gas and shale reservoirs (the isothermal compression coefficient) and the isothermal adsorption characteristics of shale gas, which represents gas desorption. Using this method, Bumb and McKee examined the pressure response of a vertical well in a homogeneous reservoir. They concluded that although the shape of the test curve remained constant, the presence of adsorbed gas would shift the curve to the right in proportion to the quantity of adsorbed gas. Although Bumb and McKee did not consider natural fractures and only discussed the effects of adsorbed gas in homogeneous reservoir models, their method was widely used to examine seepage in coalbed and shale gas reservoirs. The model is simple to use, and the compressibility of the system can be adjusted to take into account the influence of adsorbed gas and different types of porous media on well production [65–69].

The nonequilibrium ad/desorption-diffusion model assumes that the adsorption, desorption, diffusion, and seepage of shale gas are interdependent and diffusion cannot be neglected [17, 70, 71]. Different from the equilibrium model, desorbed gas and fracture systems in the nonequilibrium adsorption-diffusion model do not reach equilibrium instantaneously but exist in dynamic equilibrium, which is described by diffusion equations. The nonequilibrium model can more accurately reflect the theoretical occurrence and migration of shale gas [27] and has been widely used for coalbed and shale gas reservoirs [17, 27, 31, 47, 70–72]. This model consists of Fick, Knudsen, and surface diffusion models. We summarize the conceptual models proposed to describe the gas flow in shale gas reservoirs by coupling different diffusion models and combinations of reservoir media, which can be divided into five types, as shown in Figure 10 [1].

4.1. Conceptual Model 1: Microfracture + Equilibrium Ad/Desorption Diffusion (“Quasi-Dual-Porosity”). The following assumptions are used for this model: the shale gas reservoirs are composed of only microfractures and matrix; adsorption and interporosity flow within the matrix are negligible; adsorbed gas only exists on the surface of matrix; and the microfractures are not only the storage space for free gas but also the main channels for desorbed gas flowing into hydraulic fractures or wellbores. The physical model is shown in Figure 10, 1 [64, 66, 69, 73, 74].

In spherical coordinates, the continuity equation of shale gas flow in fractures is

$$\frac{1}{r^2} \frac{\partial}{\partial r} \left(\frac{k_f}{\mu_g} \rho_g r^2 \frac{\partial p_f}{\partial r} \right) = \frac{\partial (\phi_f \rho_g)}{\partial t} + q_{\text{des}}, \quad (8)$$

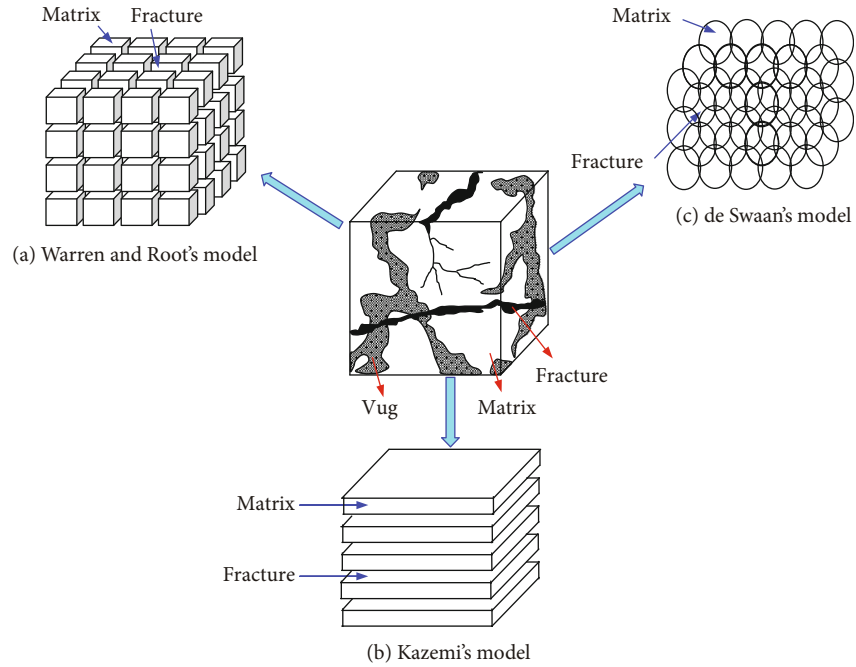


FIGURE 9: Conceptual model for dual-porosity formation [58–60, 64].

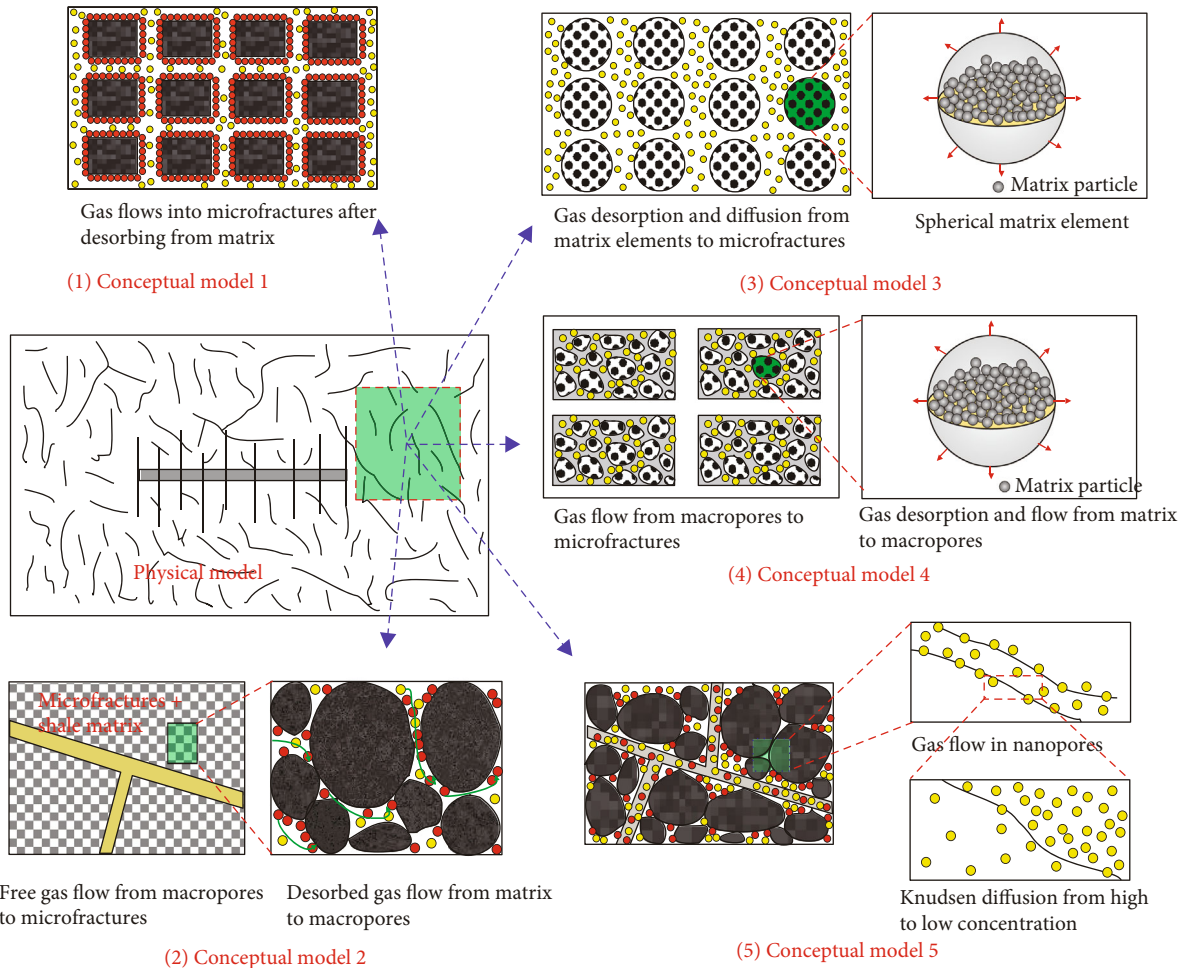


FIGURE 10: Conceptual models for gas transport mechanisms in shale gas reservoirs [1].

where p_f is the pressure of the microfracture system (Pa); ρ_g is the gas density at the given conditions (kg/m^3); ϕ_f is the porosity of the microfracture system (dimensionless); k_f is the permeability of the microfracture system (m^2); q_{des} is the gas mass by steady-state desorption from unit reservoir volume ($\text{kg/m}^3 \cdot \text{s}$); r is the radial coordinate (m); t is the production time (s).

For steady-state desorption and diffusion, according to Langmuir isothermal adsorption equation, we have

$$q_{\text{des}} = \rho_{\text{gsc}}(1 - \phi_f)V_L \frac{p_L}{(p_L + p_f)^2} \frac{\partial p_f}{\partial t}, \quad (9)$$

where ρ_{gsc} is the gas density at standard condition (kg/m^3); p_L is the Langmuir pressure (Pa).

4.2. Conceptual Model 2: Microfracture + Matrix Pores + Equilibrium Ad/Desorption Diffusion ("Triporosity"). When there are a large number of macropores developing in the shale reservoir matrix, it will result in a certain error to ignore gas containing and flowing in such pores. Therefore, some scholars proposed the conceptual model of triple porosity. In the triple porosity model, the adsorbed gas on the matrix surface goes into macropores instead of microfractures after desorption and then flows into microfractures from macropores (as shown in Figure 10, 2) [1, 13, 75].

In spherical coordinates, the continuity equation of shale gas flow in fractures is

$$\frac{1}{r^2} \frac{\partial}{\partial r} \left(\frac{k_f}{\mu_g} \rho_g r^2 \frac{\partial p_f}{\partial r} \right) + q_m = \frac{\partial (\phi_f \rho_g)}{\partial t}, \quad (10)$$

where q_m is the gas mass flow from the matrix macropores to microfractures in unit reservoir volume ($\text{kg/m}^3 \cdot \text{s}$).

4.2.1. Transient Interporosity Flow Model. When gas flow from matrix to fractures is transient interporosity flow, the continuity equation of gas flow in the matrix can be expressed as

$$\frac{1}{r_m^2} \frac{\partial}{\partial r_m} \left(\frac{k_m}{\mu_g} \rho_g r_m^2 \frac{\partial p_m}{\partial r_m} \right) = \frac{\partial (\phi_m \rho_g)}{\partial t} + q_{\text{des}}, \quad (11)$$

where k_m is the permeability of shale matrix (m^2); p_m is the pressure in the matrix system (Pa); r_m is the radius in the matrix (m).

Initialization condition and corresponding boundary conditions for the spherical matrix model have been reported by de Swaan [60].

The interporosity flow rate q_m can be expressed as

$$q_m = - \left. \frac{3\rho_g k_m}{R_m \mu_g} \frac{\partial p_m}{\partial r_m} \right|_{r_m=R_m}, \quad (12)$$

where R_m is the radius of the spherical matrix element (m).

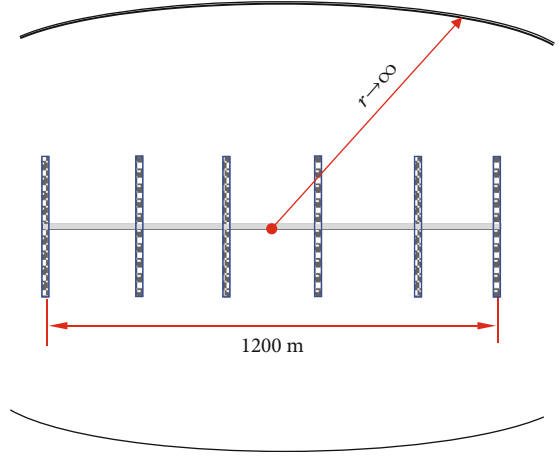


FIGURE 11: Schematic of a fractured horizontal well with infinite outer boundary.

For gas desorption rate q_{des} , according to Langmuir isothermal equation, there is

$$q_{\text{des}} = \rho_g(1 - \phi_f - \phi_m)G_L \frac{p_L}{(p_L + p_m)^2} \frac{\partial p_m}{\partial t}. \quad (13)$$

4.2.2. Pseudo-Steady-State Flow. When gas flow from macropores to microfractures is pseudo-steady-state flow, the interporosity flow in macropores can be represented as [59]

$$-q_m = \frac{\partial (\phi_m \rho_g)}{\partial t} + q_{\text{des}}. \quad (14)$$

Assuming the flow from the matrix to the fracture system is pseudo-steady-state flow, there is

$$q_m = \frac{\alpha k_m}{\mu_g} (\rho_{\text{gm}} p_m - \rho_{\text{gf}} p_f), \quad (15)$$

where α is the matrix shape factor ($1/\text{m}^2$); ρ_{gm} is the gas density at matrix pressure condition (kg/m^3); ρ_{gf} is the gas density at fracture pressure condition (kg/m^3).

4.3. Conceptual Model 3: Microfracture + Adsorbed Gas Desorption + Fick Diffusion in Matrix Pores. Gas diffusion is assumed as a steady state for the two models introduced above. Later on, the Fick diffusion theory was introduced to describe the desorption and diffusion of shale gas. Compared to model 1, Fick diffusion rather than steady-state diffusion is used in this model. The physical desorption and diffusion process is illustrated in Figure 10, 3 [1, 30, 76–78].

In spherical coordinates, the continuity equation of shale gas flow in fractures is

$$\frac{1}{r^2} \frac{\partial}{\partial r} \left(\frac{k_f}{\mu_g} \rho_g r^2 \frac{\partial p_f}{\partial r} \right) = \frac{\partial (\phi_f \rho_g)}{\partial t} + q_{\text{f}}. \quad (16)$$

TABLE 3: Parameters used for the models.

Variables	Value	Variables	Value
Reservoir pressure, p_i (MPa)	25	Reservoir temperature, T (K)	320
Formation thickness, h (m)	60	Fracture half length, x_f (m)	30
Gas-specific gravity, γ_g (fraction)	0.65	Well production rate, q_{sc} (m ³ /d)	1×10^4
Langmuir pressure, P_L (MPa)	4	Langmuir volume, G_L (m ³ /m ³)	10
Skin factor, S_{kin} (dimensionless)	0.1	Dimensionless wellbore storage, C_D	10^{-6}
Number of fracture, M	6	Horizontal well length, L (m)	1200
Conceptual model 1			
Permeability of natural fractures, k_f (mD)	0.01	Porosity of natural fractures, ϕ_f (fraction)	0.02
Conceptual model 2			
Permeability of natural fractures, k_f (mD)	0.01	Porosity of natural fractures, ϕ_f (fraction)	0.02
Permeability of macropores, k_m (mD)	0.0001	Porosity of macropores, ϕ_m	0.12
Shape factor, α (1/m ²)	10^{-5}		
Conceptual model 3			
Permeability of natural fractures, k_f (mD)	0.01	Porosity of natural fractures, ϕ_f (fraction)	0.02
Well production rate, q_{sc} (m ³ /d)	1×10^4	$(R_m)^2/D_F$	2×10^6
Conceptual model 4			
Permeability of natural fractures, k_f (mD)	0.01	Porosity of natural fractures, ϕ_f (fraction)	0.02
Permeability of macropores, k_m (mD)	0.0001	Porosity of macropores, ϕ_m	0.12
Well production rate, q_{sc} (m ³ /d)	1×10^4	$(R_m)^2/D_F$	2×10^6
Shape factor, α (1/m ²)	10^{-5}		
Conceptual model 5			
Permeability of natural fractures, k_f (mD)	0.01	Porosity of natural fractures, ϕ_f (fraction)	0.02
Permeability of matrix, k_m (mD)	0.0001	Porosity of matrix, ϕ_m	0.12
Shape factor, α (1/m ²)	10^{-5}	Knudsen diffusion coefficient, D_k (1/m ²)	10^{-6}

In unit reservoir volume, the diffusion of gas from matrix to fractures is

$$q_F = M_g(1 - \phi_f) \frac{dC_m}{dt}. \quad (17)$$

For pseudo-steady-state and unsteady-state gas diffusion from matrix to fractures, there is

$$\frac{dC_m}{dt} = \begin{cases} \left. \frac{3D_F}{R_m} \frac{\partial C_m}{\partial r_m} \right|_{r_m=R_m} & \text{unsteady-state diffusion,} \\ \frac{6D_F \pi^2}{R_m^2} [C_E(p_f) - C_m] & \text{pseudo-steady-state diffusion,} \end{cases} \quad (18)$$

where D_F is the Fick diffusion coefficient (m²/s); R_m is the radius of spherical matrix element (m); C_E is the gas molar concentration when the gas adsorption at the matrix surface is in equilibrium with free gas in microfractures (mol/m³).

For Fick diffusion, the following mathematical expression can be used to describe gas concentration change in matrix.

$$\frac{\partial C_m}{\partial t} = \frac{1}{r_m^2} \frac{\partial}{\partial r_m} \left(D r_m^2 \frac{\partial C_m}{\partial r_m} \right), \quad (19)$$

where C_m is the shale gas volume concentration in matrix under unsteady state (mol/m³); r_m is the inner diameter of sphere matrix element (m).

4.4. Conceptual Model 4: Microfracture + Matrix Macropores + Adsorbed Gas Desorption + Fick Diffusion in Nanopores. Similar to the steady-state diffusion model, if the macropores are well developed in shale matrix, desorption gas is assumed to flow into macropores and then into microfractures. This model is first proposed by us, and the physical process is shown in Figure 10, 4.

In spherical coordinates, the continuity equation of shale gas flow in the fractures is

$$\frac{1}{r^2} \frac{\partial}{\partial r} \left(\frac{k_f}{\mu_g} \rho_g r^2 \frac{\partial p_f}{\partial r} \right) + q_m = \frac{\partial (\phi_f \rho_g)}{\partial t}. \quad (20)$$

- (1) For transient interporosity flow from matrix to fractures, the continuity equation for flow in matrix is

$$\frac{1}{r_m^2} \frac{\partial}{\partial r_m} \left(\frac{k_m}{\mu_g} \rho_g r_m^2 \frac{\partial p_m}{\partial r_m} \right) = \frac{\partial (\phi_m \rho_g)}{\partial t} + q_F. \quad (21)$$

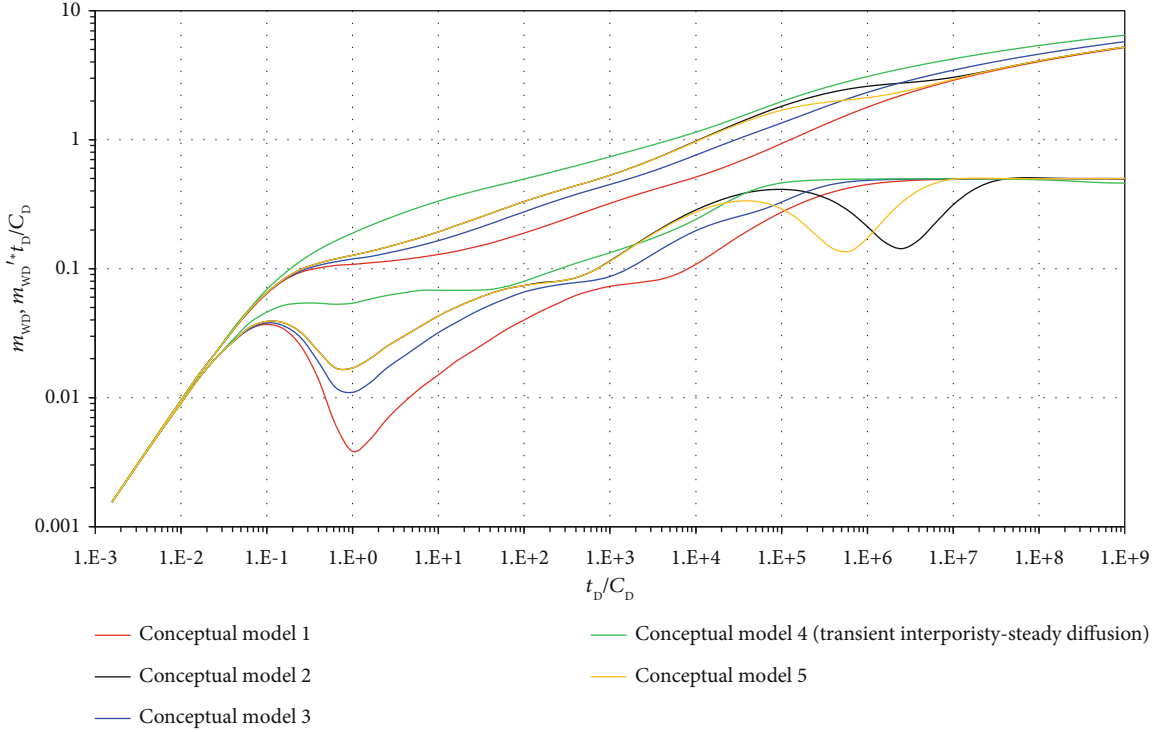


FIGURE 12: Type curves of fractured horizontal well with different conceptual models.

For unsteady-state flow from macropores to fractures, the flow rate q_m has a similar expression as Equation (12), and the diffusion rate caused by Fick diffusion q_F can be expressed as

$$q_F = M_g(1 - \phi_f)(1 - \phi_m) \frac{dC_m}{dt} \quad (22)$$

(2) For pseudo-steady-state flow from macropores to microfractures, the continuity equation for flow in macropores is

$$-q_m = \frac{\partial(\phi_m \rho_g)}{\partial t} + q_F, \quad (23)$$

where q_m has a similar expression as Equation (15)

4.5. Conceptual Model 5: Microfracture + Adsorbed Gas Desorption + Knudsen Diffusion in Nanopore Models. In recent years, the Knudsen diffusion model has been widely used to describe the gas flow process in nanopores. Most of the researchers thought that gas flow in shale nanopores is a kind of complex flow under the combined influence of multiple mechanisms, e.g., slippage effect, Darcy flow, Knudsen diffusion, and adsorption-desorption [1, 3, 17, 31, 59, 79–81]. The physical model of microscopic gas flow in shale reservoirs is shown in Figure 10, 5.

Since gas flow in the microfracture system follows Darcy's Law, the continuity equation is similar to those of previous models and can be expressed in spherical coordinates as [31]

$$\frac{1}{r^2} \frac{\partial}{\partial r} \left(\frac{k_f}{\mu_g} \rho_g r^2 \frac{\partial p_f}{\partial r} \right) + q_m = \frac{\partial(\phi_f \rho_g)}{\partial t}. \quad (24)$$

(1) For transient interporosity flow from matrix to fractures, the continuity equation of flow in matrix is

$$\frac{1}{r_m^2} \frac{\partial}{\partial r_m} \left(\frac{k_{app}}{\mu_g} \rho_g r_m^2 \frac{\partial p_m}{\partial r_m} \right) = \frac{\partial(\phi_m \rho_g)}{\partial t} + q_{des} \quad (25)$$

(2) For the pseudo-steady-state flow from macropores to microfractures, the continuity equation of flow in macropores is

$$-q_m = \frac{\partial(\phi_m \rho_g)}{\partial t} + q_{des} \quad (26)$$

In order to compare the effects of different conceptual models on type curves of fractured horizontal well in shale

gas reservoirs, there is a horizontal well with a length of 1200 m located at the center of a shale gas reservoir with infinite outer boundary (as shown in Figure 11). Six hydraulic fractures are uniformly distributed along the horizontal well. The essential parameters and some unique parameters for each model are listed in Table 3. For such models, the semi-analytical solutions can be easily derived by the source function idea and superposition theory, which has been reported and used to analyze the well production performance of complex structure wells, such as horizontal well, slanted well, fractured vertical well, and fractured horizontal well. Figure 12 compares the type curves of fractured horizontal well in shale gas reservoirs with different conceptual models. It can clearly see that the models mainly affect the early flow periods and the interporosity flow period during the gas flow from matrix pores into natural fractures. Here, we just list a set of type curves in Figure 12 for the physical models in Figure 11. Due to the consideration of different flow mechanisms or different pore types, the type curves have different characteristics. For model 1, adsorption and interporosity flow within the matrix are negligible, and the only flow channels are microfractures with high seepage capacity, so it is relatively easy to maintain the gas supply to the well, resulting in the most concave type curves among 5 curves of dimensionless pseudopressure derivative. Compared with model 2, model 5 considers the Knudsen diffusion effect in nanopores, which is equivalent to increasing the gas supply, so the concave of dimensionless pseudopressure derivative appears earlier before the boundary control flow stage. And there are many models that have been proposed, such as the liner flow model, discrete fracture models, and fractured horizontal well in different outer boundaries, so the readers can utilize the models presented in this paper to analyze the well production performance of different models. Besides, the conceptual model can also be considered in the numerical simulation [82–85].

5. Conclusions

This paper presents a comprehensive review for gas flow and the mathematical models of gas transport in multiscaled shale gas reservoir, which can be easily used to the well testing and flow performance analysis of wells in shale gas reservoirs by combing them with the well models.

The reported apparent permeability models are summarized firstly. Until now, there is no unified model that can be reliable and acceptable in the petroleum industry. Most expressions of apparent permeability are constructed by coupling slippage flow formula with the Knudsen diffusion formula with different weighting coefficient. For this method, the choice of weighting coefficient is always controversial.

Five comprehensive models are established under the assumption of a continuum medium model and single gas flow. Model 1 and model 2 are established under the equilibrium adsorption-diffusion model, model 1 does not consider the gas flow in the matrix system, and model 2 divides the formation into a natural fracture system and matrix macro-pore system. Model 3 is the classical transport model used in coalbed, which also divides the pores into two types. Different from model 2, model 3 considers the gas transport in

matrix pores by Fick diffusion. We proposed model 4, which divides the matrix pores into macro pores and nanopores, and the gas flow in nanopores follows Fick diffusion and in macropores follows conventional viscous flow. Model 5 is most widely used recently, which introduces an apparent permeability to take into account the complex transport mechanisms in shale matrix, including viscous flow, slippage flow, Knudsen flow, and surface flow.

Although many achievements have been made in the mechanism of shale gas seepage, most researches are carried out in the microscale. The application of shale gas complex transport mechanisms in numerical simulation and other fields is rare and needs to be studied urgently.

Conflicts of Interest

The authors declare that they have no conflicts of interest.

Acknowledgments

This work was supported by the National Natural Science Foundation of China (Key Program) (Grant No. 51534006), the National Natural Science Foundation of China (Grant Nos. 51874251 and 51704247), and the PetroChina Innovation Foundation (No. 2018D-5007-0218).

References

- [1] L. Zhang, Z. Chen, and Y. Zhao, *Well Production Performance Analysis for Shale Gas Reservoirs*, Elsevier, Cambridge, United States, 2019.
- [2] J. B. Curtis, "Fractured shale-gas systems," *AAPG Bulletin*, vol. 86, 2002.
- [3] Y. Zhao, L. Zhang, and B. Shan, "Mathematical model of fractured horizontal well in shale gas reservoir with rectangular stimulated reservoir volume," *Journal of Natural Gas Science and Engineering*, vol. 59, pp. 67–79, 2018.
- [4] Y. Zhao, X. Tang, L. Zhang, H. Tang, and Z. Tao, "Numerical solution of fractured horizontal wells in shale gas reservoirs considering multiple transport mechanisms," *Journal of Geophysics and Engineering*, vol. 15, no. 3, pp. 739–750, 2018.
- [5] Y. Mei-Juan, Y. Bo-Ming, X. Peng, and C. Jian-Chao, "Fractal analysis of power-law fluid in a single capillary," *Chinese Physics Letters*, vol. 25, no. 2, pp. 616–619, 2008.
- [6] J. He, J. Wang, Q. Yu et al., "Pore structure of shale and its effects on gas storage and transmission capacity in well HD-1 eastern Sichuan Basin, China," *Fuel*, vol. 226, pp. 709–720, 2018.
- [7] K. Liu, M. Ostadhassan, J. Zou et al., "Nanopore structures of isolated kerogen and bulk shale in Bakken Formation," *Fuel*, vol. 226, pp. 441–453, 2018.
- [8] C. Cipolla, E. Lolon, J. Erdle, and B. Rubin, "Reservoir modeling in shale-gas reservoirs," *SPE Reservoir Evaluation & Engineering*, vol. 13, no. 4, pp. 638–653, 2013.
- [9] J. Yao, H. Sun, D. Fan, C. Wang, and Z. Sun, "Numerical simulation of gas transport mechanisms in tight shale gas reservoirs," *Petroleum Science*, vol. 10, no. 4, pp. 528–537, 2013.
- [10] S. Kang, E. Fathi, R. Ambrose, I. Akkutlu, and R. Sigal, "Carbon dioxide storage capacity of organic-rich shales," *SPE Journal*, vol. 16, no. 4, pp. 842–855, 2013.

- [11] J. Hudson, F. Civan, G. Michel, D. Devegowda, and R. Sigal, "Modeling multiple-porosity transport in gas-bearing shale formations," in *SPE Latin America and Caribbean Petroleum Engineering Conference*, Mexico City, Mexico, April, 2012.
- [12] M. Curtis, R. Ambrose, C. Sondergeld, and C. Rai, "Transmission and scanning electron microscopy investigation of pore connectivity of gas shales on the nanoscale," in *Proceedings of the North American Unconventional Gas Conference and Exhibition*, The Woodlands, Texas, USA, June, 2011.
- [13] Y. Zhao, L. Zhang, J. Zhao, J. Luo, and B. Zhang, "'Triple porosity' modeling of transient well test and rate decline analysis for multi-fractured horizontal well in shale gas reservoirs," *Journal of Petroleum Science & Engineering*, vol. 110, pp. 253–262, 2013.
- [14] K. Bowker, "Barnett shale gas production, Fort Worth Basin: issues and discussion," *AAPG Bulletin*, vol. 91, no. 4, pp. 523–533, 2007.
- [15] M. Brittenham, "Unconventional discovery thinking in resource plays: Haynesville/Bossier trend, north Louisiana," *Houston Geological Society Bulletin*, vol. 53, no. 2, pp. 27–29, 2010.
- [16] D. Ross and R. Bustin, "Shale gas potential of the Lower Jurassic Gordondale Member, northeastern British Columbia, Canada," *Bulletin of Canadian Petroleum Geology*, vol. 55, no. 1, pp. 51–75, 2007.
- [17] F. Javadpour, "Nanopores and apparent permeability of gas flow in mudrocks (shales and siltstone)," *Journal of Canadian Petroleum Technology*, vol. 48, no. 8, pp. 16–21, 2013.
- [18] E. Umeozor and I. Gates, "Predictive modeling of energy and emissions from shale gas development," *Environmental Science & Technology*, vol. 52, no. 24, pp. 14547–14555, 2018.
- [19] G. Chen, D. Dong, and S. Wang, "A preliminary study on accumulation mechanism and enrichment pattern of shale gas," *Natural Gas Industry*, vol. 29, pp. 17–21, 2009.
- [20] G. King, "Material-balance techniques for coal-seam and Devonian shale gas reservoirs with limited water influx," *SPE Reservoir Engineering*, vol. 8, no. 1, pp. 67–72, 2013.
- [21] E. Ozkan, R. Raghavan, and O. Apaydin, "Modeling of fluid transfer from shale matrix to fracture network," in *In Proceedings of the SPE Annual Technical Conference and Exhibition*, Florence, Italy, September 2010.
- [22] T. Zhang, G. S. Ellis, S. C. Ruppel, K. Milliken, and R. Yang, "Effect of organic-matter type and thermal maturity on methane adsorption in shale-gas systems," *Organic Geochemistry*, vol. 47, pp. 120–131, 2012.
- [23] G. Moridis and C. Freeman, "The RealGas and RealGasH2O options of the TOUGH+ code for the simulation of coupled fluid and heat flow in tight/shale gas systems," *Computers & Geosciences*, vol. 65, pp. 56–71, 2014.
- [24] E. Ozkan, M. Brown, R. Raghavan, and H. Kazemi, "Comparison of fractured horizontal-well performance in conventional and unconventional reservoirs," *Dermatologic Surgery*, vol. 27, pp. 703–708, 2009.
- [25] Y. Li, X. Li, J. Shi, H. Wang, and L. Wu, "A nano-pore scale gas flow model for shale gas reservoir," in *Proceedings of the SPE Biennial Energy Resources Conference*, Port of Spain, Trinidad and Tobago, June 2014.
- [26] K. Wu, X. Li, C. Wang, Z. Chen, and W. Yu, "A model for gas transport in microfractures of shale and tight gas reservoirs," *AIChE Journal*, vol. 61, no. 6, pp. 2079–2088, 2015.
- [27] S. Roy, R. Raju, H. Chuang, B. Cruden, and M. Meyyappan, "Modeling gas flow through microchannels and nanopores," *Journal of Applied Physics*, vol. 93, no. 8, pp. 4870–4879, 2003.
- [28] T. Ertekin, G. King, and F. Schwerer, "Dynamic gas slippage: a unique dual-mechanism approach to the flow of gas in tight formations," *SPE Formation Evaluation*, vol. 1, no. 1, pp. 43–52, 2013.
- [29] F. Javadpour, D. Fisher, and M. Unsworth, "Nanoscale gas flow in shale gas sediments," *Journal of Canadian Petroleum Technology*, vol. 46, no. 10, pp. 55–61, 2007.
- [30] H. Darabi, A. Ettehad, F. Javadpour, and K. Sepehrnoori, "Gas flow in ultra-tight shale strata," *Journal of Fluid Mechanics*, vol. 710, pp. 641–658, 2012.
- [31] V. Shabro, C. Torres-Verdin, and F. Javadpour, "Pore-scale quantification of apparent permeability and electrical resistivity of hydrocarbon-bearing shale in the presence of gas desorption," in *Proceedings of the SPWLA 52nd Annual Logging Symposium*, Colorado Springs, Co. USA, May 2011.
- [32] L. Mi, H. Jiang, J. Li, and Y. Tian, "Mathematical characterization of permeability in shale reservoirs," *Journal of Petroleum*, vol. 35, pp. 928–934, 2014.
- [33] M. Sheng, G. Li, Z. Huang, S. Tian, S. Shah, and L. Geng, "Pore-scale modeling and analysis of surface diffusion effects on shale-gas flow in kerogen pores," *Journal of Natural Gas Science and Engineering*, vol. 27, pp. 979–985, 2015.
- [34] J. Wang, L. Chen, Q. Kang, and S. S. Rahman, "Apparent permeability prediction of organic shale with generalized lattice Boltzmann model considering surface diffusion effect," *Fuel*, vol. 181, pp. 478–490, 2016.
- [35] L. Zhang, D. Li, D. Lu, and T. Zhang, "A new formulation of apparent permeability for gas transport in shale," *Journal of Natural Gas Science and Engineering*, vol. 23, pp. 221–226, 2015.
- [36] Y. Li, X. Liu, Z. Hu, S. Gao, X. Rui, and J. Chang, "A new coupling method for shale gas slippage and diffusion transport mechanism," *Acta Physica Sinica*, vol. 66, p. 114702, 2017.
- [37] Y. Wang, S. Liu, and Y. Zhao, "Modeling of permeability for ultra-tight coal and shale matrix: a multi-mechanistic flow approach," *Fuel*, vol. 232, pp. 60–70, 2018.
- [38] S. Wang, J. Shi, K. Wang, Z. Sun, Y. Miao, and C. Hou, "Apparent permeability model for gas transport in shale reservoirs with nano-scale porous media," *Journal of Natural Gas Science and Engineering*, vol. 55, pp. 508–519, 2018.
- [39] J. Cai, D. Lin, H. Singh, S. Zhou, Q. Meng, and Q. Zhang, "A simple permeability model for shale gas and key insights on relative importance of various transport mechanisms," *Fuel*, vol. 252, pp. 210–219, 2019.
- [40] D. Chai, Z. Fan, and X. Li, "A new unified gas-transport model for gas flow in nanoscale porous media," *SPE Journal*, vol. 24, no. 2, pp. 698–719, 2019.
- [41] A. Beskok and G. Karniadakis, "A model for flows in channels, pipes, and ducts at micro and nano scales," *Microscale Thermophysical Engineering*, vol. 3, no. 1, pp. 43–77, 1999.
- [42] K. Wu, X. Li, C. Guo, C. Wang, and Z. Chen, "A unified model for gas transfer in nanopores of shale-gas reservoirs: coupling pore diffusion and surface diffusion," *SPE Journal*, vol. 21, no. 5, pp. 1583–1611, 2016.
- [43] K. Wu, Z. Chen, X. Li, C. Guo, and M. Wei, "A model for multiple transport mechanisms through nanopores of shale gas reservoirs with real gas effect-adsorption-mechanic coupling,"

- International Journal of Heat and Mass Transfer*, vol. 93, pp. 408–426, 2016.
- [44] X. Xiong, D. Devegowda, G. G. Michel, R. F. Sigal, and F. Civan, “A fully-coupled free and adsorptive phase transport model for shale gas reservoirs including non-Darcy flow effects,” in *Proceedings of the SPE Annual Technical Conference and Exhibition*, San Antonio, Texas, USA, October 2012.
- [45] V. Swami and A. Settari, “A pore scale gas flow model for shale gas reservoir,” in *Proceedings of the Americas Unconventional Resources Conference*, Pittsburgh, Pennsylvania, USA, June, 2012.
- [46] Y. Zhao, L. Zhang, Y. Xiong, Y. Zhou, Q. Liu, and D. Chen, “Pressure response and production performance for multi-fractured horizontal wells with complex seepage mechanism in box-shaped shale gas reservoir,” *Journal of Natural Gas Science and Engineering*, vol. 32, pp. 66–80, 2016.
- [47] J. Deng, W. Zhu, and Q. Ma, “A new seepage model for shale gas reservoir and productivity analysis of fractured well,” *Fuel*, vol. 124, pp. 232–240, 2014.
- [48] H. Wang and M. Marongiu-Porcu, “Impact of shale-gas apparent permeability on production: combined effects of non-Darcy flow/gas-slippage, desorption, and geomechanics,” *SPE Reservoir Evaluation & Engineering*, vol. 18, no. 4, pp. 495–507, 2016.
- [49] Z. Ye, D. Chen, and Z. Pan, “A unified method to evaluate shale gas flow behaviours in different flow regions,” *Journal of Natural Gas Science and Engineering*, vol. 26, pp. 205–215, 2015.
- [50] J. Wang, H. Liu, L. Wang, H. Zhang, H. Luo, and Y. Gao, “Apparent permeability for gas transport in nanopores of organic shale reservoirs including multiple effects,” *International Journal of Coal Geology*, vol. 152, pp. 50–62, 2015.
- [51] W. Song, J. Yao, Y. Li et al., “Apparent gas permeability in an organic-rich shale reservoir,” *Fuel*, vol. 181, pp. 973–984, 2016.
- [52] W. Ren, G. Li, S. Tian, M. Sheng, and X. Fan, “An analytical model for real gas flow in shale nanopores with non-circular cross-section,” *AIChE Journal*, vol. 62, no. 8, pp. 2893–2901, 2016.
- [53] Y. He, J. Cheng, X. Dou, and X. Wang, “Research on shale gas transportation and apparent permeability in nanopores,” *Journal of Natural Gas Science and Engineering*, vol. 38, pp. 450–457, 2017.
- [54] L. Zhang, B. Shan, Y. Zhao, J. Du, J. Chen, and X. Tao, “Gas transport model in organic shale nanopores considering Langmuir slip conditions and diffusion: pore confinement, real gas, and geomechanical effects,” *Energies*, vol. 11, no. 1, p. 223, 2018.
- [55] J. Cai, D. Lin, H. Singh, W. Wei, and S. Zhou, “Shale gas transport model in 3D fractal porous media with variable pore sizes,” *Marine and Petroleum Geology*, vol. 98, pp. 437–447, 2018.
- [56] L. Zhang, H. Liang, Y. Zhao, J. Xie, X. Peng, and Q. Li, “Gas transport characteristics in shale matrix based on multiple mechanisms,” *Chemical Engineering Journal*, vol. 386, p. 124002, 2020.
- [57] Q. Zhang, Y. Su, W. Wang, M. Lu, and G. Sheng, “Gas transport behaviors in shale nanopores based on multiple mechanisms and macroscale modeling,” *International Journal of Heat and Mass Transfer*, vol. 125, pp. 845–857, 2018.
- [58] J. Warren and P. Root, “The behavior of naturally fractured reservoirs,” *Society of Petroleum Engineers Journal*, vol. 3, no. 3, pp. 245–255, 2013.
- [59] H. Kazemi, “Pressure transient analysis of naturally fractured reservoirs with uniform fracture distribution,” *Society of Petroleum Engineers Journal*, vol. 9, no. 4, pp. 451–462, 2013.
- [60] A. de Swaan, “Influence of shape and skin of matrix-rock blocks on pressure transients in fractured reservoirs,” *SPE Formation Evaluation*, vol. 5, no. 4, pp. 344–352, 2013.
- [61] R. O. Bello and R. A. Wattenbarger, “Multistage hydraulically fractured horizontal shale gas well rate transient analysis,” in *Proceedings of the North Africa Technical Conference and Exhibition*, Cairo, Egypt, February, 2010.
- [62] H. A. Al-Ahmadi and R. A. Wattenbarger, “Triple-porosity models: one further step towards capturing fractured reservoirs heterogeneity,” in *Proceedings of the SPE/DGS Saudi Arabia Section Technical Symposium and Exhibition*, Al-Khobar, Saudi Arabia, May, 2011.
- [63] V. Tivayanonda, *Comparison of single, double, and triple linear flow models for shale gas/oil reservoirs*, Diss. Texas A&M University, 2012.
- [64] B. Xu, M. Haghghi, X. Li, and D. Cooke, “Development of new type curves for production analysis in naturally fractured shale gas/tight gas reservoirs,” *Journal of Petroleum Science & Engineering*, vol. 105, pp. 107–115, 2013.
- [65] Z. Xu and S. Guo, “Application of NMR and X-CT technology in the pore structure study of shale gas reservoirs,” *Advances in Earth Science*, vol. 29, pp. 624–631, 2014.
- [66] A. C. Bumb and C. R. McKee, “Gas-well testing in the presence of desorption for coalbed methane and Devonian shale,” *SPE Formation Evaluation*, vol. 3, no. 1, pp. 179–185, 2013.
- [67] H. S. Lane, A. T. Watson, and D. E. Lancaster, “Identifying and estimating desorption from Devonian shale gas production data,” in *Proceedings of the SPE Annual Technical Conference and Exhibition*, San Antonio, Texas, October, 1989.
- [68] J. P. Spivey and M. E. Semmelbeck, “Forecasting long-term gas production of dewatered coal seams and fractured gas shales,” in *Proceedings of the Low Permeability Reservoirs Symposium*, Denver, Colorado, March, 1995.
- [69] R. M. Bustin, C. R. Clarkson, and J. P. Seidle, “Production-data analysis of single-phase (gas) coalbed-methane wells,” *SPE Reservoir Evaluation & Engineering*, vol. 10, no. 3, pp. 312–331, 2007.
- [70] V. Shabro, C. Torres-Verdin, and K. Sepehrnoori, “Forecasting gas production in organic shale with the combined numerical simulation of gas diffusion in kerogen, Langmuir desorption from surfaces, and advection in nanopores,” in *Proceedings of the SPE Annual Technical Conference and Exhibition*, San Antonio, Texas, USA, October, 2012.
- [71] V. Swami, A. T. Settari, and F. Javadpour, “A numerical model for multi-mechanism flow in shale gas reservoirs with application to laboratory scale testing,” in *Proceedings of the EAGE Annual Conference & Exhibition incorporating SPE Europec*, London, UK, June 2013.
- [72] S. Harpreet, F. Javadpour, A. Etehadavakkol, and H. Darabi, “Nonempirical apparent permeability of shale,” *SPE Reservoir Evaluation & Engineering*, vol. 17, no. 3, pp. 414–424, 2014.
- [73] F. Civan, “Effective correlation of apparent gas permeability in tight porous media,” *Transport in Porous Media*, vol. 82, no. 2, pp. 375–384, 2009.
- [74] D. Ding, C. Wang, D. Didier, and Y. Wu, “Characterizing hydraulic fractures in shale gas reservoirs using transient pressure tests,” in *Proceedings of the SPE Hydraulic Fracturing Technology Conference*, The Woodlands, Texas, USA, February, 2013.

- [75] B. Song, *Pressure transient analysis and production analysis for New Albany shale gas wells*, Diss. Texas A&M University, 2010.
- [76] Z. Yu-long, Z. Lie-Hui, F. Guo-Qing, Z. Bo-Ning, and K. Bo, "Performance analysis of fractured wells with stimulated reservoir volume in coal seam reservoirs," *Oil & Gas Science and Technology*, vol. 71, no. 1, pp. 8–8, 2016.
- [77] L. Zhang, Z. Kou, H. Wang et al., "Performance analysis for a model of a multi-wing hydraulically fractured vertical well in a coalbed methane gas reservoir," *Journal of Petroleum Science & Engineering*, vol. 166, pp. 104–120, 2018.
- [78] G. J. I. Igwe, "Gas transport mechanism and slippage phenomenon in porous media," in *Proceedings of the SPE Conference*, Richardson, Texas, USA, 1985.
- [79] R. Zhang, L. Zhang, R. Wang, Y. Zhao, and D. Zhang, "Research on transient flow theory of a multiple fractured horizontal well in a composite shale gas reservoir based on the finite-element method," *Journal of Natural Gas Science and Engineering*, vol. 33, pp. 587–598, 2016.
- [80] Y. Li, Y. Wang, J. Wang, and Z. Pan, "Variation in permeability during CO₂-CH₄ displacement in coal seams: part 1 – experimental insights," *Fuel*, vol. 263, p. 116666, 2020.
- [81] Y. Li, D. Tang, H. Xu, Y. Meng, and J. Li, "Experimental research on coal permeability: the roles of effective stress and gas slippage," *Journal of Natural Gas Science and Engineering*, vol. 21, pp. 481–488, 2014.
- [82] Y. Zhao, L. Liu, L. Zhang, X. Zhang, and B. Li, "Simulation of a multistage fractured horizontal well in a tight oil reservoir using an embedded discrete fracture model," *Energy Science & Engineering*, vol. 7, no. 5, pp. 1485–1503, 2019.
- [83] S. Zhou, Y. Ning, H. Wang, H. Liu, and H. Xue, "Investigation of methane adsorption mechanism on Longmaxi shale by combining the micropore filling and monolayer coverage theories," *Advances in Geo-Energy Research*, vol. 2, no. 3, pp. 269–281, 2018.
- [84] H. Singh and J. Cai, "A mechanistic model for multi-scale sorption dynamics in shale," *Fuel*, vol. 234, pp. 996–1014, 2018.
- [85] H. Wang, "Performance of multiple fractured horizontal wells in shale gas reservoirs with consideration of multiple mechanisms," *Journal of Hydrology*, vol. 510, pp. 299–312, 2014.

Research Article

A Simplified Capillary Bundle Model for CO₂-Alternating-Water Injection Using an Equivalent Resistance Method

Wendong Wang^{1,2}, Fankun Meng³, Yuliang Su^{1,2}, Lei Hou⁴, Xueyu Geng⁴,
Yongmao Hao^{1,2} and Lei Li^{1,2}

¹Key Laboratory of Unconventional Oil & Gas Development, China University of Petroleum (East China), Ministry of Education, Qingdao 266580, China

²School of Petroleum Engineering, China University of Petroleum (East China), Qingdao 266580, China

³School of Petroleum Engineering, Yangtze University, Wuhan 430100, China

⁴School of Engineering, The University of Warwick, Coventry CV4 7AL, UK

Correspondence should be addressed to Fankun Meng; mengfk09021021@163.com

Received 26 June 2020; Revised 26 September 2020; Accepted 29 October 2020; Published 29 November 2020

Academic Editor: Micòl Mastrocicco

Copyright © 2020 Wendong Wang et al. This is an open access article distributed under the Creative Commons Attribution License, which permits unrestricted use, distribution, and reproduction in any medium, provided the original work is properly cited.

CO₂-alternating-water injection is an effective way of enhancing recovery for low-permeability oil reservoirs. The injection process is one of the essential issues that are facing severe challenges because of the low permeability and poor pore space connectivity. Previous researchers mentioned that water injection ability could be decreased by around 20% after the CO₂-flooding; hence, it is necessary to quantify the water injectivity variation during an alternated injection process. In this paper, a CO₂ convection-diffusion model is established based on the seepage law of CO₂ and dissipation effect. The relationship between the width of miscible flooding and injection time is defined. Besides, an equivalent resistance method is introduced for developing a capillary bundle model for featuring an unequal diameter for CO₂ water vapor alternate flooding. CO₂-oil and CO₂-water interactions are analyzed using the new model. The effects of oil viscosity, pore throat ratio, CO₂ slug size, and equivalent permeability of the capillary bundle on water injection are analyzed. The result indicates that water injection ability increases with the rise of CO₂ slug size and equivalent permeability of the capillary bundle and decreases with the increase of viscosity and pore throat ratio.

1. Introduction

The CO₂-alternating-water injection method, used in the low-permeability reservoirs, has the advantages of both CO₂ flooding and water flooding. It represents a promising method for improving the recovery of oil in the future. In 1957, Mobil Company has performed a pilot CO₂-alternating-water injection test in North Pembina of Alberta, and then, several tests were conducted in Canada and the United States. In the United States, many tests have been performed because of the sufficient CO₂ sources [1, 2], whereas in China, the first pilot field application was started by CNOOC in Qikou oil-field. The test showed that during the middle-late stage of the nonhomogeneous reservoir, the CO₂-alternating-water injection could not only block the advantage flow channel

but also contribute to the optimization of water injection [2]. Although its significant benefits, this method still has several problems. One serious problem is the decreasing of injection ability after CO₂-alternating-water has been injected into the formation [3, 4]. Therefore, it is significantly important to study the variation of injection ability with capillary bundle model during CO₂-alternating-water flooding process.

The CO₂-alternating-water injection in the low-permeability reservoirs is a multiphase flow process. Early researchers have studied the seepage and flooding mechanism of multiphase fluid in the porous medium. Dong et al. presented the results of immiscible WAG injection in a water-wet micromodel and found that in a gas/oil/water system, stable oil layers were formed between the gas and water phases [5]. Due to gas bubbles were always surrounded by oil layers, direct

gas/water displacements were not observed. Meanwhile, he found that the oil recovery declined greatly with WAG cycles. Wang and Dong developed an interacting triangular tube bundle model based on capillaries of equilateral triangle cross sections [6]. The relationship between the residual oil saturation and the complete capillary number (CA) was investigated, and the effects of the tube size, tube size distribution, and viscosity ratio on the magnitude of entrapment were also studied using this tube bundle model. Jovanović et al. presented both the stagnant film model and the moving film model to study the energy loss problem when the fluid flows in the capillary [7]. They considered the interfacial pressure drop and the frictional pressure drop with the tube wall, and the influence of the static and fluid boundary layer on the fluid seepage. As microscopic flow mechanics gradually became the focus of investigation, some researchers began to pay attention to the complex seepage mechanism of pore space in porous media. Some of those researchers have been focusing on the alternate injection of water and gas by pore structure by establishing a pore network model as a simulation platform. Piri developed a quasi-static pore network model by fully considering the seepage characteristics of oil, gas, and water three-phase flow in the pore throat [8]. The variation of saturation and relative permeability of each phase in the process of water seepage are compared with the existing experiment, and the data is well fitted. Yang et al. simulated the WAG displacement process in different wettability porous media from a microscopic point of view and analyzed the oil, gas, and water saturation and distribution during WAG displacement [9]. The changed law of position and displacement characteristics explains the microscopic mechanism of three-phase seepage in porous media. Helland pointed out that a bundle-of-triangular-tube model can reproduce the main characteristics of mixed-wet capillary pressure curves with hysteretic scanning loops [10].

The displacement core test could be used to study the effect on the injection of CO₂-alternating-water process. Jinan et al. designed an experimental unit for long core displacement by considering the necessity of similarities upon core length, the complex mechanism, and periodic physical-chemical reaction during multicontact miscible phases [11]. Zhao et al. analyzed the affecting factors of CO₂ flooding, which include permeability, the relative density of crude oil, layer heterogeneity, inter-layer heterogeneity, and layer fluid channeling by establishing the component numerical simulation model with Eclipse software [12, 13]. They concluded that it is appropriate to carry out CO₂ flooding for homogeneous and lightweight reservoirs in low-permeability oil fields. Zahoor et al. mentioned that proper water-alternating-gas process design and implementation requires better knowledge of wettability and wettability variations in particular [14]. Wettability, in addition to influencing flow parameters, strongly affects other design parameters such as the volumes of water and gas required for injection, well spacing, etc. Some other researchers also used experimental methods to study the increasing difficulty in injection. Prieditis et al. and Kamath et al. conducted displacement tests on carbonate and limestone cores and analyzed the factors that cause a decrease of injectivity [15, 16]. Prieditis et al. also performed a field test based on laboratory work and used a simple model to predict the injectivity, but good results

were not achieved [15]. Roper et al. used a compositional model to simulate and interpret an injectivity test conducted in the Mabee Field in the San Andres Formation, Martin County, Texas [17, 18]. They mentioned that the validation of compositional simulation as a means for interpreting field tests and developing improved predictions of reservoir injectivity performance and geostatistical techniques could be used successfully to characterize high heterogeneity in carbonate reservoirs for injectivity calculations. Yang et al. used core samples collected from tight formations to conduct a series of water-alternating-CO₂ flooding experiments with different water-alternating-CO₂ ratios and slug sizes [19]. They found that fluid injectivity is strongly dependent on slug size, water-alternating-CO₂ ratio, and cycle time.

Besides the experimental work, early researchers have done some theoretical modeling work. Li et al. derived the injectivity equation for water-alternating-gas injection based on similarity theory [20]. Zhou et al. analyzed the effects of injection pressure, injection speed, slug size, and gas-water slug ratio on oil displacement efficiency [21]. Yan et al. used a numerical simulation method to study the best injection parameters for CO₂ gas water alternative drive [22]. Hu substituted the permeability of the capillary model into low-permeability equation and used superposition method to get total flow rate and threshold pressure gradient of the rock [23]. This model gives a theoretical description of low-permeability seepage characteristics. Several researchers have studied the injection capacity of different reservoirs and found that the injection volume, injection velocity, formation temperature, formation pressure segment size, and proportion have an impact on the final oil displacement efficiency and recovery factor [24–29]. Pizarro and Lake considered the influence of heterogeneity and autocorrelation of reservoir permeability distribution on the injectivity [30]. This model gives insight into why injectivity calculated from a core permeability average is frequently different from the injectivity manifested by the well in question. Yang et al. performed numerical simulations to history-match the experimental measurements and conduct sensitivity analysis on operational parameters and achieved good matching [19].

Overall, researchers have done relatively thorough research on the decreasing injectivity happens in low-permeability reservoir during CO₂ injection. However, due to the complexity of flow behavior of water-oil-gas, just a few researchers have explained the abnormal variance of injectivity during water-alternating-CO₂ injection. In this paper, a new seepage diffusion equation is established by considering the CO₂ diffusion and seepage in the reservoir. It could effectively reflect the variance of CO₂ injectivity in water-alternating-CO₂ injection process. The distribution of oil, CO₂, and water in the capillary model with different diameters has been analyzed, and the influence of geology and fluid properties on injectivity has been provided.

2. CO₂ Flooding Dynamics considering Mass Transfer

2.1. Mathematical Modeling. Assuming that the CO₂ flooding process in the capillary model is a piston, the molecular

diffusion, convective diffusion, and viscosity difference diffusion due to the difference of viscosity between CO₂ and crude oil will occur at the interface between CO₂ and crude oil. From a thermodynamic point of view, diffusion coefficients are functions of pressure, temperature, and composition, and driven by chemical potential difference; however, the proposed model is complex and hard to use [31]. Therefore, in this paper, the classical Fick's law is utilized. According to the classical Fick's law, molecular diffusion is mainly caused by the change of CO₂ concentration in crude oil, and the diffusion coefficients are assumed to be constant. Convective diffusion is mainly affected by the complexity of the internal channels of the pores. The diffusion under the viscosity gradient is related to the difference of viscosity between CO₂ and crude oil, and it is also affected by molecular diffusion and convection-diffusion [32]. The diffusion equation is derived from mass transfer equations by considering the balance of matter into and out of the capillary unit. To derive the diffusion equation of CO₂ in the capillary, here, a $\pi R^2 dx$ flowing unit of the capillary tube is studied (Figure 1).

According to the principle of material balance, the influent mass = effluent mass + amount of substance accumulated in the unit, which is as follows:

$$\frac{\partial C}{\partial t} = -\frac{\partial v_D}{\partial x} - \omega \frac{\partial C}{\partial x}. \quad (1)$$

According to the diffusion law,

$$v_D = -D \frac{\partial C}{\partial x}. \quad (2)$$

Substituting Equation (2) into Equation (1), the material diffusion equation of the flow unit in the capillary is obtained.

$$\frac{\partial C}{\partial t} + \omega \frac{\partial C}{\partial x} = \frac{\partial}{\partial x} \left(D \frac{\partial C}{\partial x} \right), \quad (3)$$

where C is a unit concentration of CO₂ after a mixed phase of crude oil and CO₂, %; D is a comprehensive diffusion coefficient, cm²/s; ω is the flow velocity of the fluid in the capillary, cm/s. Here, the comprehensive diffusion coefficient D can be understood as a composite coefficient which not only considers the molecular diffusion and convection-diffusion of the single-phase fluid in the capillary but also considers the viscosity difference between the displacement and the displaced solution.

For the method of determining the diffusion coefficient, based on the Stokes-Einstein relation, Kooijman developed a correlation and used UNIFAC parameters to correct for particle roundness and size. Hayduk and Minhas developed a set of correlations, specific to certain types of mixtures. Sigmund developed a correlation for high-pressure gas and liquid binary mixtures with the expression that related the reduced density-diffusion coefficient product to a third-degree polynomial function of reduced density. For nonideal binary mixtures, Riazi and Whitson developed a correlation to predict gas and liquid diffusion coefficient. Currently, the most widely used correlation to calculate diffusion coefficient

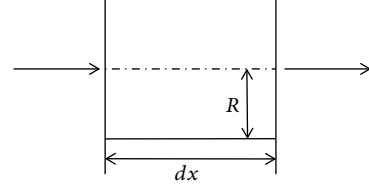


FIGURE 1: Flow unit of the capillary tube.

is presented by Wilke and Chang and is the function of viscosity, which is used in this paper [33].

The results of a displacement experiment in which a liquid is miscible with another liquid in the presence of differential pressure indicate that the best approximation of the overall diffusion coefficient is as follows:

$$\begin{aligned} D &= D_E (1 + K_\mu \nabla \mu_m), \\ D_E &= D_m + D_\mu, \\ D_\mu &= K_\omega \omega, \end{aligned} \quad (4)$$

where D_m is the molecular diffusion coefficient, cm²/s; D_u is the convection-diffusion coefficient of single-phase fluid, cm²/s; μ_m is the viscosity of two liquid mixtures, mPa·s; K_ω and K_μ are the experimental coefficients which consider the experimental coefficients of single-phase fluid convection and different viscosity diffusion, with the unit of cm and cm/(MPa·s).

From Equation (4),

$$D = D_m + D_u + (D_m + D_u) K_\mu \nabla \mu_m. \quad (5)$$

Meanwhile,

$$D_\mu = (D_m + D_u) K_\mu \nabla \mu_m. \quad (6)$$

D_μ is the diffusion coefficient of viscosity difference between displacement fluid and displaced fluid. Equation (6) shows that the comprehensive diffusion coefficient is the sum of the molecular diffusion coefficient, the convection-diffusion coefficient, and the diffusion coefficient of the viscosity difference between the displacement fluid and the displaced fluid, which is a mixing coefficient.

2.2. Solution Strategy. In miscible region, we assume that there is only a single phase, which is the mixture of oil and gas phase. We introduced a new variable, $\tau = t$, $\xi = x - u/\phi$, into Equation (3). Then, Equation (3) become the standard diffusion equation.

$$\frac{\partial C}{\partial \tau} = \frac{\partial}{\partial \xi} \left(D \frac{\partial C}{\partial \xi} \right), \quad (7)$$

where ξ is called the self-modulation variable which changes with time and space.

The boundary conditions are as follows:

$$C(-\lambda, t) = 1, \quad (8)$$

$$C(\lambda, t) = 0, \quad (9)$$

$$C(0, t) = 0.5, \quad (10)$$

where $\pm\lambda$ is the miscible half-width, cm.

Also, it is assumed that there is no CO_2 inflow or outflow at the boundary of the miscible zone.

$$\left. \frac{\partial C}{\partial \xi} \right|_{\xi=\pm\lambda} = 0. \quad (11)$$

The viscosity of the miscible zone μ_m is also given in Figure 2 and is considered to be linear, so the viscosity of the miscible zone is as follows:

$$\nabla \mu_m = \frac{\mu_2 - \mu_1}{2\lambda}. \quad (12)$$

Assuming $\beta = K_\mu(\mu_2 - \mu_1/2)$, then $K_\mu \nabla \mu_m = \beta/\lambda$. Equation (7) becomes the following:

$$\frac{\partial C}{\partial \tau} = \frac{\partial}{\partial \xi} \left[D_E \left(1 + \frac{\beta}{\lambda} \right) \frac{\partial C}{\partial \xi} \right]. \quad (13)$$

After solving Equation (13), the differential form solution can be obtained as follows:

$$\frac{d\lambda}{d\tau} = 4D_E \frac{1}{\lambda} \left(1 + \frac{\beta}{\lambda} \right). \quad (14)$$

Thus, the corresponding ‘‘integral form solution’’ is given as follows:

$$\frac{\lambda^2}{2} - \beta\lambda + \beta^2 \ln \left(\frac{\lambda + \beta}{\beta} \right) = 4D_E \tau. \quad (15)$$

If the full length of the mixed-phase zone is $\Lambda = 2\lambda$, Equation (15) can be transformed as follows:

$$\frac{\Lambda^2}{4} - \beta\Lambda + 2\beta^2 \ln \left(\frac{\Lambda + 2\beta}{2\beta} \right) = 8D_E \tau. \quad (16)$$

Equations (15) and (16) can be used to calculate the half-width λ or width Λ of the miscible region at any given time t , and $\lambda = \lambda(t)$ and $\Lambda = \Lambda(t)$ can be obtained by the iterative method that can be used to solve.

3. Unequal Diameter Capillary Beam Model for CO_2 -Alternating-Gas Flooding

3.1. Physical Model. It is assumed that the capillary beam model consists of n capillaries with different capillary radii.

Since in real oil reservoir, for any one flowing path, there are pores and throats; therefore, to reflect this pattern, for each capillary, the radius is not equal everywhere along the axis, and there is a throat. For the i th capillary, the pore throat structure is as follows in Figure 3.

The capillary length is L , the throat position is L_c from the injection end of the capillary section, throat length is L_t , the capillary radius is R_p , and the radius at the throat is as follows:

$$R(x) = \left(\frac{R_p + R_t}{2} \right) + \left(\frac{R_p - R_t}{2} \right) \cos \left(\frac{2\pi x}{L_t} \right), \quad (17)$$

where R_t is the throat radius, μm ; $R(x)$ is the radius of the junction of the pore and the throat, μm ; x is between $0 \sim L_t$, cm; the total volume of the throat is as follows:

$$V = \pi \int_0^{L_t} R^2(x) dx. \quad (18)$$

According to the definition of alternate driving of water and gas, the injection process can be divided into two stages, namely, CO_2 injection and water injection. Because the throat is arbitrarily distributed for the same capillary, the throat position is various for different capillaries, and the fluid distribution in the capillary is complicated because of the difference in CO_2 injection time.

In the process of CO_2 injection, six distribution patterns exist in the crude oil, mixed-phase zone, and CO_2 in the capillary tube, and in the process of water flooding process, there are three fluid distribution patterns. Schematics and descriptions for those fluid distribution patterns are shown in Table 1.

3.2. CO_2 Flooding Seepage Mode and Mathematical Description. To facilitate the solution and analysis of the mathematical model, CO_2/water is injected by constant pressure. The injection pressure of each capillary is equal, and the pressure difference between the injection end and the production end is ΔP . Introducing the seepage resistance coefficient to describe the magnitude of the seepage resistance and using the equivalent resistance model to solve the capillary beam injection flow rate are as follows [34]:

3.2.1. Fluid Distribution Pattern I. For the i th capillary, at the beginning of time j ($j = 1, 2, 3, \dots, N_{tg}$), when $x_{gi}^{j-1} + x_{\lambda i}^{j-1} < L_c$, the seepage resistance in the CO_2 zone is as follows:

$$W_{gi}^j = \frac{8\mu_g x_{gi}^{j-1}}{\pi R_{pi}^4}, \quad (19)$$

where $x_{gi}^{j-1} = 0$ is the length of CO_2 region at the $j-1$ moment for the i th capillary, cm; for the beginning, $x_{gi}^0 = 0$. μ_g is the CO_2 viscosity, $\text{mPa}\cdot\text{s}$; R_{pi} is the capillary radius, μm .

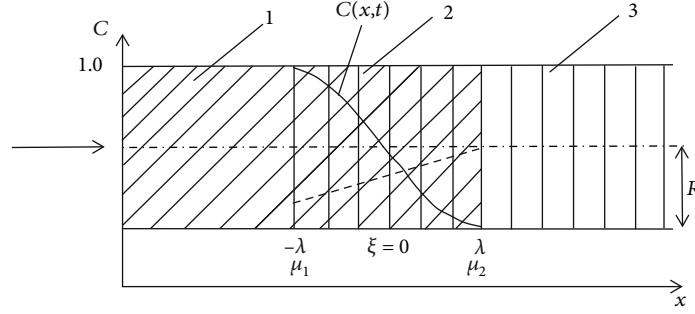


FIGURE 2: Schematic of CO₂ flooding (1: CO₂ region, 2: miscible region, and 3: oil region).

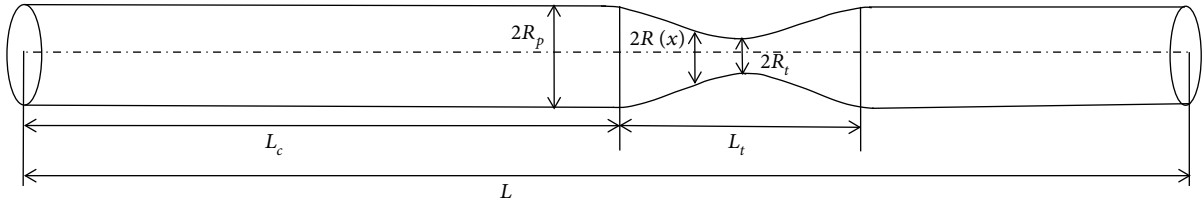


FIGURE 3: Structural schematic of pore and throat in the capillary tube.

The seepage resistance of the miscible zone is as follows:

$$W_{gi}^j = \frac{8\bar{\mu}_{og}x_{\lambda i}^{j-1}}{\pi R_{pi}^4}, \quad (20)$$

where $x_{\lambda i}^{j-1}$ is the miscible length at the moment of $j - 1$, cm; for the beginning, $x_{gi}^0 = 0$; $\bar{\mu}_{og}$ is the miscible fluid viscosity, mPa·s.

The seepage resistance in the crude oil zone is as follows:

$$W_{o,i}^j = \frac{8\mu_0(L - x_{gi}^{j-1} - x_{\lambda i}^{j-1} - L_{ti})}{\pi R_{pi}^4} + \mu_0 \int_0^{L_{ti}} \frac{dx}{G(x)}, \quad (21)$$

where G is the conductivity of a fluid per unit length, μm^4 .

$$G(x) = \frac{\pi}{128} \left(\sqrt{\frac{A_t}{\pi}} + R(x) \right)^4 = \frac{\pi}{8} R^4(x). \quad (22)$$

In the case of a constant pressure difference, the injection flow rate is as follows:

$$q_{gi}^j = \frac{\Delta P + P_{c,o-g}}{W_{eg}^j}, \quad (23)$$

where $W_{eq,i}^j = W_{g,i}^j + W_{\lambda,l}^j + W_{o,i}^j$, because there is no interfacial tension between CO₂ and crude oil, $P_{c,o-g} = 0$.

During the Δt time, it is assumed that the fluid seepage velocity in the capillary remains constant.

$$W_i^j = \frac{q_i^j}{\pi R_{pi}^2}. \quad (24)$$

The convection-diffusion coefficient between CO₂ and crude oil is as follows:

$$D_{Ei}^j = D_m + K_w W_{gi}^j. \quad (25)$$

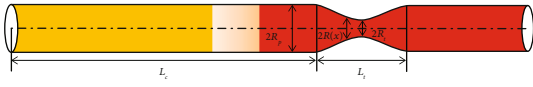
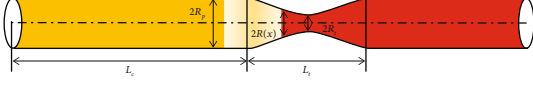
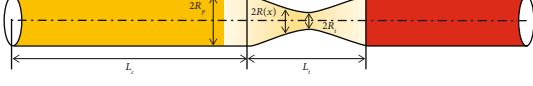
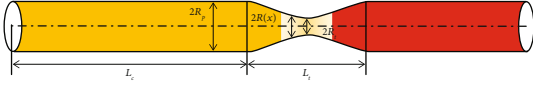
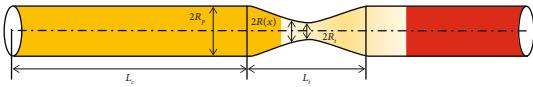
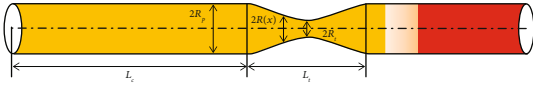
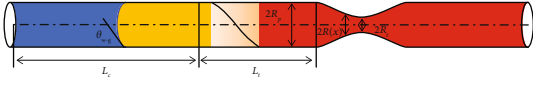
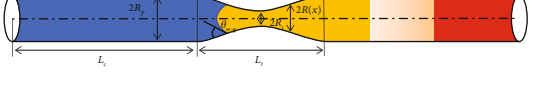
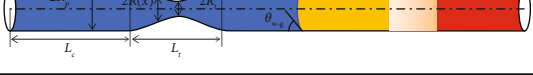
According to the derivation in Section 2.2, the relationship for the length of miscible band at time j is obtained, and the relevant parameters are substituted. Using the Newton iteration method, the length of miscible band at the end of time j can be obtained. Since in Equation (1), C is defined as the unit concentration of CO₂ in the mixture phase; it also can be seen as the volume ratio of CO₂ in the unit bulk volume approximately, as shown in Figure 2. Therefore, assuming the volume of dissolved CO₂ in the miscible zone occupies 1/2 of its total volume, the amount of CO₂ dissolved in the mixed phase is as follows:

$$V_{misi}^j = \left(\frac{1}{2}\right) \pi R_{pi}^2 x_{\lambda i}^j. \quad (26)$$

The length of the CO₂ zone formed at the beginning of the time $j + 1$ is as follows:

$$x_{gi}^j = \frac{V_{gi}^j}{\pi R_{pi}^2} = x_{gi}^{j-1} + \frac{q_{g,i}^j \Delta t - V_{misi}^j}{\pi R_{pi}^2}. \quad (27)$$

TABLE 1: Schematics for fluid distribution pattern during CO₂ and water flooding.

Process	Number	Fluid distribution pattern	Description
CO ₂ flooding	I		The front edge of the mixed-phase zone does not enter into the throat; the fluid in the throat is crude oil.
	II		The front of the CO ₂ flooding is not entering the throat, but the right end of the miscible belt has entered the throat and occupied a part of the throat.
	III		The front of the CO ₂ flooding is not entering the throat, but the right end of the miscible belt has entered the throat and occupied a part of the throat.
	IV		The leading edge of the CO ₂ displacement has not entered the throat, the volume of the mixed phase is larger than the volume of the throat, and the right end has passed through the throat.
	V		The leading edge of the CO ₂ displacement enters into the throat, and the right end of the miscible zone passes through the throat.
	VI		The leading edge of CO ₂ displacement passes through the throat and the throat is filled with CO ₂ .
Water flooding	VII		Water leading edge does not enter the throat.
	VIII		Water leading edge enters the throat.
	IX		Water leading edge passes through the throat.

The total amount of CO₂ injected into the bundle of tubes is as follows:

$$Q_g^j = \sum_{i=1}^n q_{g,i}^j. \quad (28)$$

If the calculated sum of the CO₂ zone x_{gi}^j and the miscible zone $x_{\lambda i}^j$ is less than L_{ci} , iterative calculation of $j + 1$ time can be performed according to the above steps.

3.2.2. Fluid Distribution Pattern II. At the beginning of j_n moment, when the sum of the obtained CO₂ zone and the miscible zone length is greater than L_{ci} , but the volume of the miscible belt is smaller than the volume of the throat, that is $x_{gi}^{j_n-1} + x_{\lambda i}^{j_n-1} \geq L_{ci}$, $x_{gi}^{j_n-1} \leq L_{ci}$, $2V_{misi}^{j_n-1} < V_{ti}$. At the end of the $j_n - 1$ moment, the length of the miscible belt in the throat $L_{\lambda i}^k$ ($k = 1, k = k + 1$) is as follows:

$$\left(x_{gi}^{j_n-1} + x_{\lambda i}^{j_n-1} - L_{ci}\right) R_{pi}^2 = \int_0^{L_{\lambda i}^k} R^2(x) dx. \quad (29)$$

The Lobatto numerical integral formula can be used to solve $L_{\lambda i}^k$; $x_{\lambda i}^{j_n-1}$ is the equivalent length of the miscible band, cm; the actual width of the miscible band is $x_{\lambda i}^{j_n-1} = L_{ci} - x_{gi}^{j_n-1} + L_{\lambda i}^k$. Meanwhile, the actual length of the crude oil zone is $x_{oi}^{j_n-1} = L - L_{ci} - L_{\lambda i}^k$.

The seepage resistance of the miscible zone includes two parts, one is the seepage resistance in the capillary at the left end of the throat and the other is the percolation resistance in the throat. The expression is as follows:

$$W_{\lambda,i}^{j_n-1} = \frac{8\bar{\mu}_{og} \left(L_{ci} - x_{gi}^{j_n-1}\right)}{\pi R_{pi}^4} + \bar{\mu}_{og} \int_0^{L_{\lambda i}^k} \frac{dx}{G(x)}. \quad (30)$$

The percolation resistance of crude oil and CO₂ in the capillary is as follows:

$$W_{oi}^{j_n} = \mu_0 \int_{L_{\lambda i}^k}^{L_{ti}} \frac{dx}{G(x)} + \frac{8\mu_0(L - L_{ci} - L_{ti})}{\pi R_{pi}^4}, \quad (31)$$

$$W_{g,i}^{j_n} = \frac{8\mu_o x_{gi}^{j_n-1}}{\pi R_{pi}^4}. \quad (32)$$

At the end of j_n moment, the injection amount of the i th capillary and the total injection amount of the capillary beam CO_2 can be calculated by Equations (23) and (28). At this time, the leading edge of CO_2 displacement is still outside the throat. Using Equations (27) and (26), the length of the CO_2 zone, $x_{gi}^{j_n}$, and the length of the equivalent miscible zone CO_2 , $x_{\lambda i}^{j_n}$, at the end of j_n can be obtained (regardless of the length of the throat).

3.2.3. Fluid Distribution Pattern III. At the beginning of j_n moment, when the sum of the lengths of the CO_2 region and the miscible region is greater than L_{ci} , that is, $x_{gi}^{j_n-1} + x_{\lambda i}^{j_n-1} \geq L_{ci}$, $2V_{mist}^{j_n-1} > V_n$, it indicates that at the beginning of j_n , the right end of the miscible band has begun to pass through the throat. The length of each zone and the seepage resistance are shown in Equations (30)–(32). The same iterative calculation procedure as in mode (2) is used to obtain the capillary tube injection flow rate.

The length of the miscible zone formed at the right end of the throat is $x_{r\lambda i}^m$ ($m = 1, m = m + 1$), and the expression is as follows:

$$x_{r\lambda i}^m = \left(x_{gi}^{j_d} + x_{\lambda i}^{j_d} - L_{ci} \right) - \frac{\left[\int_0^{L_{ti}} R^2(x) dx \right]}{R^2}. \quad (33)$$

The actual miscible band width is $x_{\lambda i}^{j_d} = L_{ci} - x_{gi}^{j_d} + L_{ti} + x_{r\lambda i}^m$. $x_{\lambda i}^{j_d}$ is the length of the equivalent miscible region at the end of j_d moment. The expression of seepage resistance in the miscible zone is as follows:

$$W_{\lambda,i}^{j_d+1} = \frac{8\bar{\mu}_{og} \left(L_{ci} - x_{gi}^{j_d} + x_{r\lambda i}^m \right)}{\pi R_{pi}^4} + \bar{\mu}_{og} \int_0^{L_{ti}} \frac{dx}{G(x)}. \quad (34)$$

The seepage resistance of the CO_2 zone and the crude oil zone in the capillary is as follows:

$$W_{gi}^{j_d+1} = \frac{8\mu_g x_{gi}^{j_d}}{\pi R_{pi}^4}, \quad (35)$$

$$W_{o,i}^{j_d+1} = \frac{8\mu_o (L - L_c - L_t - x_{r\lambda i}^m)}{\pi R_{pi}^4}. \quad (36)$$

At this time, CO_2 flooding interface is still outside the throat. Using Equations (27) and (26), the length of the CO_2 zone at the end of $j_d + 1$ is $x_{gi}^{j_d+1}$, and the length of the equivalent miscible zone is $x_{\lambda i}^{j_d+1}$. At this time, it is necessary to judge the relative size of $x_{gi}^{j_d+1}$ and L_{ci} . If $x_{gi}^{j_d+1} \leq L_{ci}$, the iterative calculation can be continued according to the steps in the distribution pattern II.

3.2.4. Fluid Distribution Pattern IV. Let CO_2 entering length is L_{gi}^a ($a = 1, a = a + 1$), and the expression is as follows:

$$\left(x_{gi}^{j_m} - L_{ci} \right) R_{pi}^2 = \int_0^{L_{gi}^a} R^2(x) dx, \quad (37)$$

where $x_{gi}^{j_m}$ is the equivalent length of the CO_2 zone, cm; actual length is $x_{gi}^{j_m} = L_{ci} + L_{gi}^a$.

It is assumed that after the CO_2 flooding leading edge enters the throat, CO_2 is no longer dissolved in the crude oil, and the equivalent length of the CO_2 zone remains constant. At the end of j_m , the seepage resistance in the CO_2 zone is as follows:

$$W_{gi}^{j_m+1} = \frac{8\mu_g L_{ci}}{\pi R_{pi}^4} + \mu_g \int_0^{L_{gi}^a} \frac{dx}{G(x)}. \quad (38)$$

Since the volume of the miscible zone is smaller than the throat volume, the actual length of the miscible zone in the throat at the end of j_m is $x_{\lambda i}^{j_m} = L_{\lambda i}^k - L_{gi}^a$ (k has been accumulated), where $L_{\lambda i}^k$ can be defined by the following:

$$R_{pi}^2 x_{\lambda i}^{j_m} = \int_{L_{gi}^a}^{L_{\lambda i}^k} R^2(x) dx, \quad (39)$$

where $x_{\lambda i}^{j_m}$ is the end of j_m , the equivalent length of the miscible band, cm.

Since CO_2 does not dissolve into the crude oil when the CO_2 flooding leading edge is in the throat, the equivalent length of the miscible zone remains constant until the CO_2 flooding leading edge passes through the throat. The seepage resistance of the miscible zone is as follows:

$$W_{\lambda,i}^{j_m+1} = \bar{\mu}_{og} \int_{L_{gi}^a}^{L_{\lambda i}^k} \frac{dx}{G(x)}. \quad (40)$$

The actual length of oil zone is $x_{oi}^{j_m} = L - L_{ci} - L_{ti} + (L_{ti} - L_{\lambda i}^k)$. The seepage resistance in the crude oil zone is as follows:

$$W_{o,i}^{j_m+1} = \frac{8\mu_o (L - L_{ci} - L_{ti})}{\pi R_{pi}^4} + \mu_o \int_{L_{\lambda i}^k}^{L_{ti}} \frac{dx}{G(x)}. \quad (41)$$

At the end of j_m , the length of the formed CO_2 zone is as follows:

$$x_{gi}^{j_m+1} = x_{gi}^{j_m} + \frac{q_{g,i}^{j_m+1} \Delta t}{\pi R_{pi}^2}. \quad (42)$$

The amount of CO_2 injected in the i th capillary and the total injection amount of the capillary bundle can be calculated by Equations (23) and (28).

3.2.5. *Fluid Distribution Pattern V.* At this time, the length of the miscible band formed in the capillary at the right end of the throat is $x_{r\lambda i}^b$ ($b = 1, b = b + 1$).

$$x_{r\lambda i}^b = x_{\lambda i}^j - \frac{\left[\int_{L_{gi}^a}^{L_{ti}} R^2(x) dx \right]}{R_{pi}^2}. \quad (43)$$

The actual width of the miscible band is $x_{\lambda i}^j = L_{ti} - L_{gi}^a + x_{r\lambda i}^b$. At the beginning of $j_m + 1$, the seepage resistance of the miscible zone is as follows:

$$W_{\lambda, i}^{j_m+1} = \frac{8\bar{\mu}_{og} x_{r\lambda i}^b}{\pi R_{pi}^4} + \bar{\mu}_{og} \int_{L_{gi}^a}^{L_{ti}} \frac{dx}{G(x)}. \quad (44)$$

The actual length of oil zone is $x_{oi}^j = L - L_{ci} - L_{ti} - x_{r\lambda i}^b$, and the seepage resistance in the crude oil zone is as follows:

$$W_{o, i}^{j_m+1} = \frac{8\mu_o (L - L_{ci} - L_{ti} - x_{r\lambda i}^b)}{\pi R_{pi}^4}. \quad (45)$$

The seepage resistance in the CO₂ zone is shown in Equation (38). The CO₂ injection amount in the i th capillary and the total injection amount in the capillary bundle can be obtained by Equations (23) and (28). The equivalent length of the miscible zone is constant, and the length of the formed CO₂ zone can be obtained by Equation (42).

3.2.6. *Fluid Distribution Pattern VI.* In the capillary, at the right end of the throat, the length of CO₂ region formed by x_{rgi}^c ($c = 1, c = c + 1$) is as follows:

$$\frac{q_{g, i}^c \Delta t - \int_{L_{gi}^a}^{L_{ti}} \pi R^2(x) dx}{\pi R_{pi}^2} = x_{rgi}^c. \quad (46)$$

At this moment, the CO₂ displacement front is outside the throat and CO₂ will continue to diffuse into the crude oil. At the beginning of $j_c + 1$, the actual length of the CO₂ zone is $x_{gi}^j = L_{ci} + L_{ti} + x_{rgi}^c$. The equivalent length of the miscible band is $x_{\lambda i}^j$, cm. Thereafter, the equivalent length of the miscible zone is equal to the actual length, and the actual length of the crude oil zone is $x_{oi}^j = L - x_{gi}^j - x_{\lambda i}^j$.

At the beginning of $j_c + 1$, the seepage resistance in the CO₂ zone is as follows:

$$W_{g, i}^{j_c+1} = \frac{8\mu_g (L_{ci} + x_{rgi}^c)}{\pi R_{pi}^4} + \mu_g \int_0^{L_{ti}} \frac{dx}{G(x)}. \quad (47)$$

The seepage resistances of the miscible zone and the crude oil zone are as follows:

$$W_{\lambda, i}^{j_c+1} = \frac{8\bar{\mu}_{og} x_{\lambda i}^j}{\pi R_{pi}^4}, \quad (48)$$

$$W_{o, i}^{j_c+1} = \frac{8\mu_o (L - x_{gi}^j - x_{\lambda i}^j)}{\pi R_{pi}^4}. \quad (49)$$

Knowing the magnitude of seepage resistance in each zone, the amount of CO₂ injection in the i th capillary and capillary bundle can be calculated by using Equations (23) and (28). According to Equations (47)–(49), combined with the formula of the mixed-phase band in Section 2, the length of CO₂ zone and the miscible zone can be obtained. Here, it should be noted that since the length of the miscible slug is constant when the leading edge of the CO₂ displacement is assumed to be in the throat, the calculation of the miscible zone is performed after deducting the period of the CO₂ displacement leading edge through the throat. In this way, according to the distribution pattern VI, the next iterative calculation is performed.

3.3. *Water Flooding Seepage Mode and Mathematical Description.* Suppose that the CO₂ injection time is T_g , the time step has N_{tg} ($N_{tg} = T_g/\Delta t$). At the beginning of $N_{tg} + 1$, the water is injected with a constant pressure difference, ΔP . Assuming that CO₂ is not dissolved in water, there is a gas-water interface. There is a capillary force, the CO₂-water interfacial tension is σ_{wg} , and the contact angle is θ_{w-g} . At the beginning of water injection, when the leading edge of CO₂ flooding is at the left end of the throat, during the subsequent water injection process, there may be six distribution patterns in the CO₂ flooding process, but on the other hand, due to water injection, the following three fluid distribution patterns appear.

3.3.1. *Fluid Distribution Pattern VII.* At this time, the seepage resistance of the water zone is as follows:

$$W_{w, i}^j = \frac{8\mu_w x_{wi}^{j-1}}{\pi R_{pi}^4}, \quad (50)$$

where x_{wi}^{j-1} is the length of the water zone in the capillary at the beginning of $N_{tg} + j$, cm, $x_{wi}^0 = 0$.

The pressure difference between the ends of the capillary bundle is $\Delta P + P_{ci}$, which is kept constant, and the flow rate of injected water is as follows:

$$q_{w, i}^j = \frac{\Delta P + P_{ci}}{W_{eq, i}^{N_{tg}+j}}, \quad (51)$$

$$P_{ci} = \frac{2\sigma_{w-g} \cos \theta_{w-g}}{R_{pi}},$$

where $W_{eq, i}^{N_{tg}+j} = W_{wi}^j + W_{g, i}^{N_{tg}+j} + W_{\lambda, i}^{N_{tg}+j} + W_{o, i}^{N_{tg}+j}$, $W_{g, i}^{N_{tg}+j}$, $W_{\lambda, i}^{N_{tg}+j}$, $W_{o, i}^{N_{tg}+j}$ is the magnitude of seepage resistance in the CO₂ zone, the miscible zone, and the crude oil zone at the beginning of $N_{tg} + j$.

The total amount of water injected is as follows:

$$Q_w^{N_{tg}+j} = \sum_{i=1}^n q_{w, i}^{N_{tg}+j}. \quad (52)$$

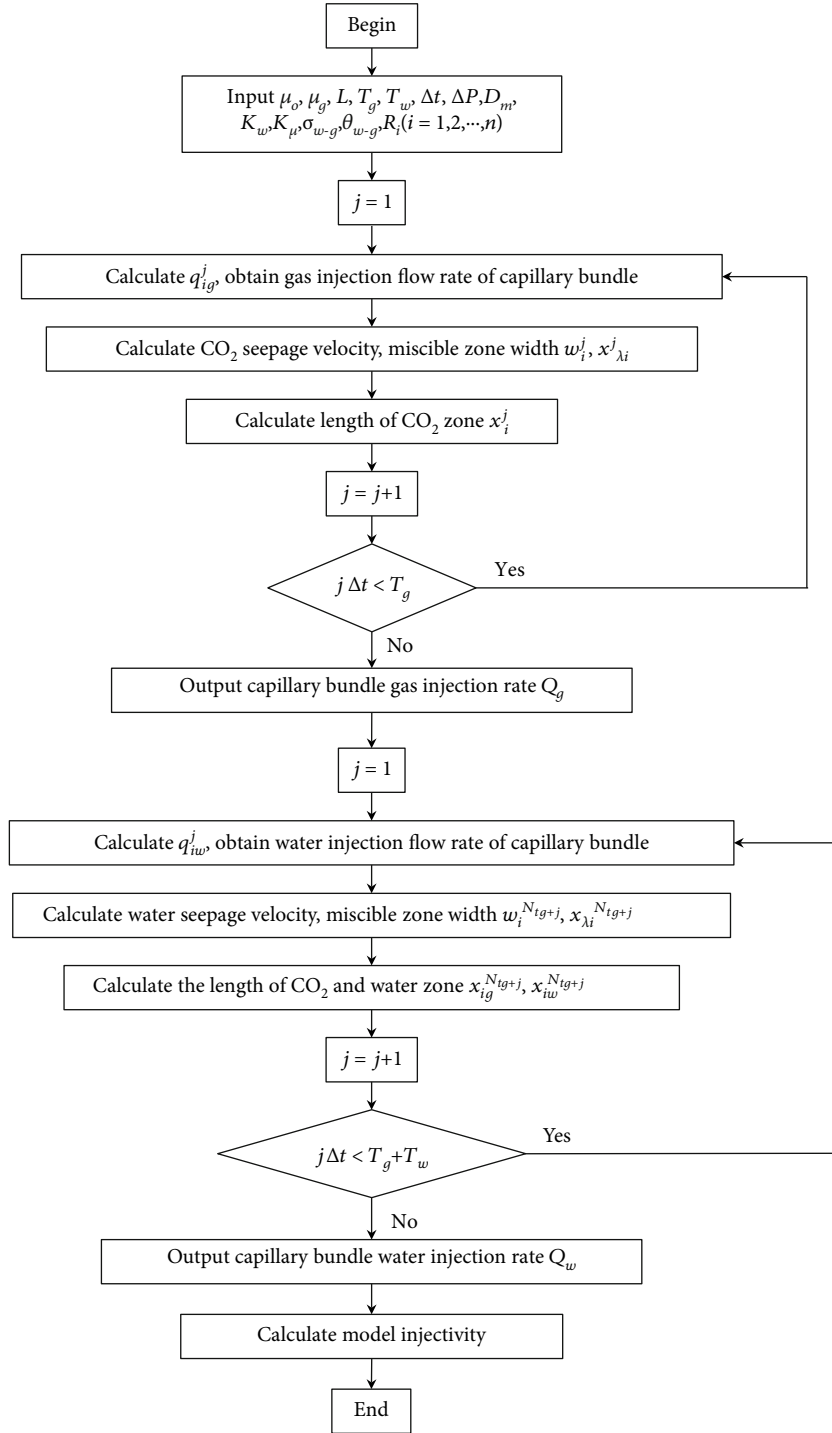


FIGURE 4: Flow diagram of solution.

During this process, the water seepage velocity is the same as CO₂.

$$W_{wi}^j = \frac{q_{w,i}^j}{\pi R_{pi}^2} = W_{gi}^{N_{tg}+j}. \quad (53)$$

According to the principle of material balance, due to the constant total injection volume, CO₂ will continue to diffuse

into the crude oil during the water injection process, the length of the CO₂ zone and the crude oil zone will decrease, the width of the miscible zone will increase, and the calculation formula of the miscible zone will be for the distribution mode. For the first, second, third, and sixth fluid distribution pattern, the formula for calculating the length of the CO₂ zone should be corrected to the following:

$$x_{gi}^{N_{tg}+j} = x_{gi}^{N_{tg}+j-1} - \frac{\Delta V_{misi}^j}{\pi R_{pi}^2}, \quad (54)$$

where ΔV_{misi}^j is the amount of increase in the amount of CO₂ dissolved in the miscible zone, cm³; $x_{gi}^{N_{tg}+j}$ and $x_{gi}^{N_{tg}+j-1}$ are the equivalent lengths of the CO₂ zone at the time of $N_{tg} + j$ and $N_{tg} + j - 1$, cm.

$$\Delta V_{misi}^j = V_{misi}^{N_{tg}+j} - V_{misi}^{N_{tg}+j-1} = \frac{1}{2} \pi R_{pi}^2 (x_{\lambda i}^{N_{tg}+j} - x_{\lambda i}^{N_{tg}+j-1}), \quad (55)$$

where $x_{\lambda i}^{N_{tg}+j}$ and $x_{\lambda i}^{N_{tg}+j-1}$ are the equivalent lengths of the miscible band at the time of $N_{tg} + j$ and $N_{tg} + j - 1$. Since the diffusion of CO₂ in water is not considered, the length of water zone in the capillary is as follows:

$$x_{wi}^j = x_{wi}^{j-1} + \frac{q_{wi}^j \Delta t}{\pi R_{pi}^2}. \quad (56)$$

3.3.2. Fluid Distribution Pattern VIII. Assuming at the beginning of $N_{tg} + j_w + 1$ moment (which is also at the end of $N_{tg} + j_w$ moment), the length of water zone is calculated as $x_{wi}^j > L_{ci}$. It means that at the end of $N_{tg} + j_w$, the injected water has entered the throat. The length needs to be corrected, and the actual water zone length is $x_{wi}^{j_w-1}$.

$$x_{wi}^{j_w} = L_{ci} + L_{wi}^d, \quad (57)$$

$$R_{pi}^2 (x_{wi}^{j_w} - L_{ci}) = \int_0^{L_{wi}^d} R^2(x) dx, \quad (58)$$

where $x_{wi}^{j_w}$ is the equivalent length of the initial water zone at the time of $N_{tg} + j_w + 1$, cm. L_{wi}^d ($d = 1, d = d + 1$) is the extended length of the injected water in the throat.

In the throat, the radius of the water-CO₂ interface changes, so it will affect the capillary force. The capillary radius and capillary force at L_{wi}^d are as follows:

$$R_i(L_{wi}^d) = \left(\frac{R_p + R_t}{2} \right) + \left(\frac{R_p - R_t}{2} \right) \cos \left(\frac{2\pi L_{wi}^d}{L_t} \right), \quad (59)$$

$$P_{ci}^d = 2\sigma_{w-g} \cos \frac{\theta + \gamma}{R_i(x)}, \quad (60)$$

$$\gamma = \tan^{-1} \left(\frac{dR(x)}{dx} \right), \quad (61)$$

$$\tan \gamma = \frac{dR(x)}{dx} = \frac{R_i(L_{wi}^d) - R_i(L_{wi}^{d-1})}{L_{wi}^d - L_{wi}^{d-1}}, \quad (62)$$

where $R_i(L_{wi}^0) = R_{pi}$, $L_{wi}^0 = 0$; γ is the correction value of the contact angle.

At the beginning of $N_{tg} + j_w + 1$, the actual CO₂ equivalent length is $x_{gi}^{N_{tg}+j_w}$, where the extension length at the right end of the throat is x_{rgi}^e ($e = 1, e = e + 1$).

$$x_{rgi}^e = x_{gi}^{N_{tg}+j_w} - \frac{\int_{L_{wi}^d}^{L_{ti}} R(x)^2 dx}{R_{pi}^2}. \quad (63)$$

The seepage resistances in the water area and CO₂ area are given in Equations (64) and (65).

$$W_{w,i}^{N_{tg}+j_w+1} = \frac{8\mu_w L_{ci}}{\pi R_{pi}^4} + \mu_w \int_0^{L_{wi}^d} \frac{dx}{G(x)}, \quad (64)$$

$$W_{g,i}^{N_{tg}+j_w+1} = \frac{8\mu_g x_{rgi}^e}{\pi R_{pi}^4} + \mu_g \int_{L_{wi}^d}^{L_{ti}} \frac{dx}{G(x)}. \quad (65)$$

At this time, the length of the crude oil zone is $L - L_{ci} - L_{ti} - x_{rgi}^e - x_{\lambda i}^{N_{tg}+j_w}$, and the resistance of the crude oil zone can be obtained by substituting Equation (49), and the seepage resistance of the mixed phase can be obtained by using Equation (48). By substituting the formula for seepage resistance in each zone into Equations (51) and (52), the water injection amount of the i th capillary and capillary bundle can be obtained. According to Equations (51)-(55), the length of the water zone and the CO₂ zone can be obtained, and the method of obtaining the miscible zone is the same as in previous cases.

3.3.3. Fluid Distribution Pattern IX. At the beginning of $N_{tg} + j_g + 1$, if the calculated L_{wi}^d is greater than L_{ti} , the water-CO₂ interface has passed through the throat, and the length formed at the right end of throat is x_{wri}^e ($e = 1, e = e + 1$), $x_{wri}^e = x_{wi}^{j_g} - L_{ci} - [\int_0^{L_{ti}} R_i^2(x) dx] / R_{pi}^2$.

At the end of $N_{tg} + j_g$, the actual length of the water area is $x_{wi}^{j_g} = L_{ci} + L_{ti} + x_{wri}^e$. $x_{wi}^{j_g}$ is the equivalent length of water zone, the length of CO₂ zone is $x_{gi}^{N_{tg}+j_g}$, the length of miscible zone is $x_{\lambda i}^{N_{tg}+j_g}$, and the length of the crude oil zone is $L - L_{ci} - L_{ti} - x_{\lambda i}^{N_{tg}+j_g} - x_{gi}^{N_{tg}+j_g} - x_{wri}^e$. Water-CO₂ interfacial tension remains constant.

At the beginning of $N_{tg} + j_g + 1$, the seepage resistance for each zone is as follows:

$$W_{w,i}^{N_{tg}+j_g+1} = \frac{8\mu_w (L_{ci} + x_{wri}^e)}{\pi R_i^4} + \mu_w \int_0^{L_{ti}} \frac{dx}{G(x)}, \quad (66)$$

$$W_{g,i}^{N_{tg}+j_g+1} = \frac{8\mu_g x_{gi}^{N_{tg}+j_g}}{\pi R_i^4}, \quad (67)$$

$$W_{\lambda,i}^{N_{tg}+j_g+1} = \frac{8\mu_{og} x_{\lambda i}^{N_{tg}+j_g}}{\pi R_i^4}, \quad (68)$$

$$W_{o,i}^{N_{tg}+j_g+1} = \frac{8\mu_o (L - x_{wi}^{j_g} - x_{gi}^{N_{tg}+j_g} - x_{\lambda i}^{N_{tg}+j_g})}{\pi R_i^4}. \quad (69)$$

TABLE 2: Parameters for CO₂ water-alternating-gas model.

Parameters	Value	Parameters	Value
Capillary radius (μm)	5~15	Capillary length (cm)	30
Water/CO ₂ interfacial tension (mN/m)	20	Water/CO ₂ contact angle (degree)	60
Crude oil viscosity (mPa·s)	5	CO ₂ viscosity (mPa·s)	0.05
Water viscosity (mPa·s)	2	K_w (cm)	0.001
K_μ (cm/(Pa·s))	0.001	CO ₂ injection time (s)	5
D_m (cm ² /s)	1×10^{-5}	Time interval (s)	0.1
Injection time (s)	5	Pore throat ratio	3
Pressure difference at both ends of the capillary bundle (MPa)	1	Distance between throat and inlet end (cm)	2~3
Throat length (cm)	1	Number of capillaries	11

Substituting Equations (66)-(69) into Equations (51)-(55), the length of the water zone and the CO₂ zone can be obtained, and the parameters such as β and D_E are substituted into Equation (40) to obtain the width of the miscible zone.

4. Sensitivity Analysis

4.1. Model Solving Process and Basic Parameter Settings. According to the above descriptions, the solution process can be divided into two steps, CO₂ injection and water injection, and the flow chart of solution is shown in Figure 4.

During water-alternating-gas flooding process, the injection capacity is defined as the ratio of injected CO₂/water rate to the pressure difference across the capillary bundle:

$$I = \frac{Q_{w,g}}{\Delta P_{w,g}}, \quad (70)$$

where I is the injection capacity, cm³/(MPa·s); $Q_{w,g}$ is the CO₂/water injection flow rate, cm³/s; $\Delta P_{w,g}$ is the pressure difference across the capillary beam, MPa.

For the convenience of analysis, it is stipulated that during the injection of CO₂ and water injection, the pressure difference across the capillary bundle is equal. To quantitatively characterize the ability of the capillary tube to flow, the equivalent permeability is introduced, and the expression is as follows:

$$k = \frac{L}{8 \sum_{i=1}^n R_{pi}^2 \left(\left(1/R_{pi}^4 \right) + \left(\int_0^{L_{ii}} (1/R_i^4(x)) dx \right) \right)}. \quad (71)$$

According to the variables used in the model derivation process, the pore throat size of the reservoir in low-permeability reservoirs and the characteristics of fluid properties of water-alternating-CO₂ injection are investigated [35], and the basic parameters of the model are set, as shown in Table 2.

4.2. Injection Capacity Analysis. To better reflect the change law of injectivity of CO₂, mixed-phase slug, and injection capacity, the throat is set closer to the injection end. Then, the influences of viscosity, pore throat ratio, CO₂ slug size,

and equivalent permeability on the variance of CO₂-alternating-water capacity have been studied.

4.2.1. Crude Oil Viscosity. Assuming the crude oil viscosities are 5 mPa·s, 6 mPa·s, and 7 mPa·s, and simultaneously keep all other parameters constant, the changing law of injectivity with time is plotted in Figure 5.

As it can be seen from Figure 5, the crude oil viscosity increases, and the viscous resistance that the fluid flow needs to overcome increases, thus causing the injectivity to decrease as the crude oil viscosity increases. After the capillary beam is transferred to water, the high-viscosity crude oil is driven out. Then, the total seepage resistance of the fluid in the capillary bundle is reduced, causing the increase of injectivity. However, when the water-flooding front enters the throat, the low-viscosity CO₂ is replaced. Then, the seepage resistance is increased, causing a decrease of injectivity. As the fluid percolation velocity decreases with the increase of the crude oil viscosity, the time that the front of the water flooding enters the throat continuously is delayed with the increase of the crude oil viscosity. When the water-gas interface, that is, the front edge of the water drive passes through the throat, the throat is occupied by water, the displacement will tend to be stable, and the water injection capacity will continue to increase.

4.2.2. Pore Throat Ratio. Since the capillary radius has been set to characterize the pore size, the pore throat ratio is defined as the ratio of the capillary radius to the radius at the narrowest point of the throat. Set them to 2.5, 3, and 3.5, respectively, and the injection capacity changes with time are shown in Figure 6.

When the capillary radius is constant (the pore radius is constant), the throat radius decreases with the increase of the pore throat ratio. Because the throat size has a great influence on the seepage resistance, the CO₂ water-gas alternate injection capacity decreases with the increase of throat ratio. The throat is closer to the injection end, and after the water is injected, the injectivity is increased because the crude oil in the capillary bundle is replaced by the injected water. Similar to Figure 5, the front edge of the water drive enters the throat, and the injectivity is rapidly reduced; after the front edge passes through the throat, the injection capacity will increase slowly. Because the seepage resistance generated by the fluid

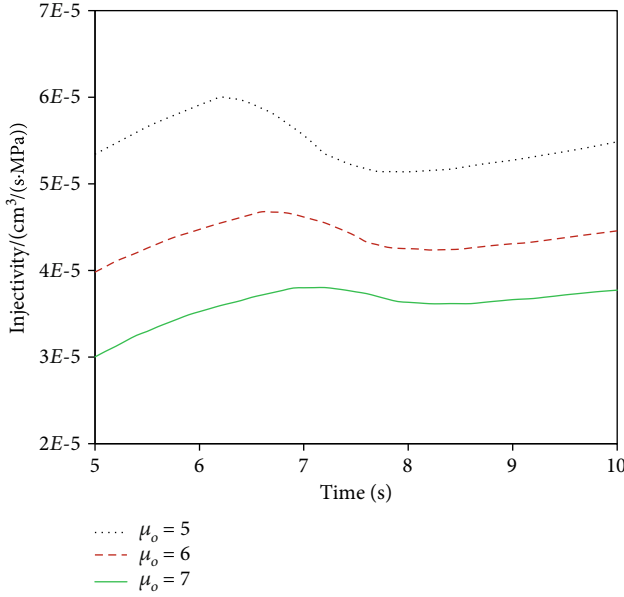


FIGURE 5: Injectivity change with time for different oil viscosity.

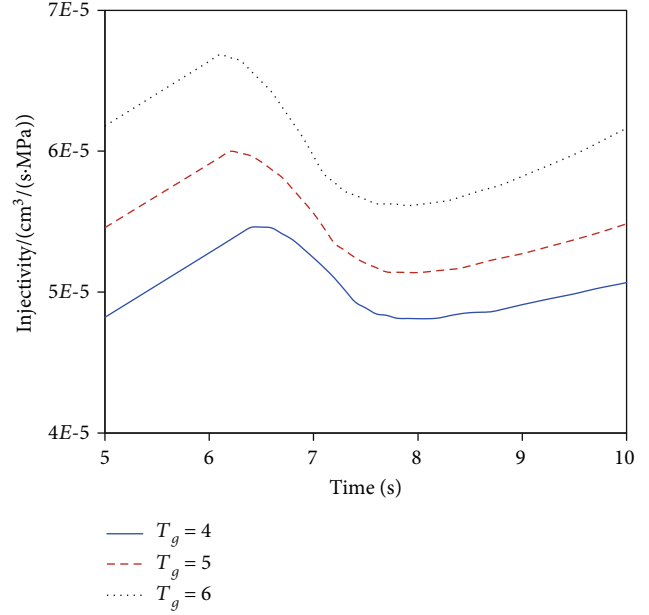


FIGURE 7: Injectivity change with time for different CO₂ slug size.

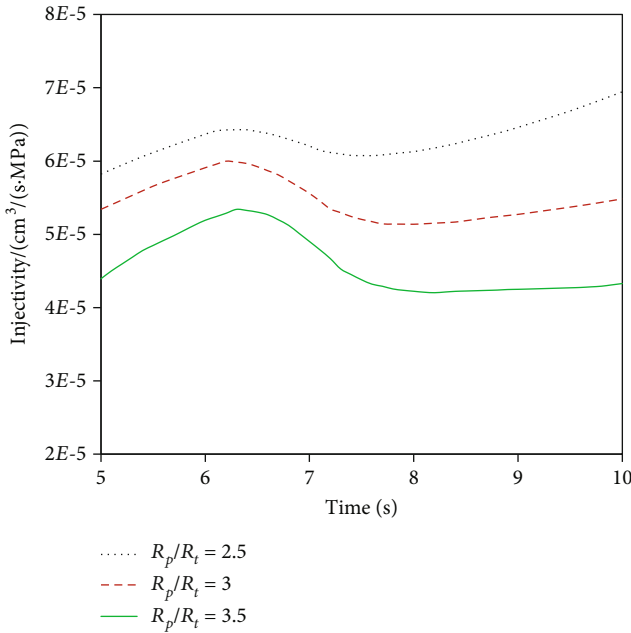


FIGURE 6: Injectivity change with time for different pore-throat ratio.

in the throat is large, after the water flooding front passes through throat, the rising rate of water injectivity will decrease with the increase of pore throat ratio.

4.2.3. CO₂ Slug Size. Because CO₂ is injected with constant pressure, the size of CO₂ slug cannot be changed by changing the CO₂ injection rate. However, CO₂ slugs with different sizes can be equivalently injected by setting different injection times. According to this treatment method, CO₂ injection time is set to be 4 s, 5 s, and 6 s, and then, different CO₂ slug size is obtained. After CO₂ injection, the changes of injectivity with time are shown in Figure 7.

The larger the CO₂ injection time is, the longer the CO₂ slug is formed, and the smaller the total seepage resistance of the fluid in the capillary bundle is, so the injection capacity increases with the injection time. The throat is closer to the injection end, and the injection capacity increases linearly before the front of the water drive enters the throat. When the front edge of the water drive enters the throat, the injectivity decreases sharply. When the water drive front passes through the throat, the injectivity will increase slowly.

4.2.4. Equivalent Permeability. Since the pore throat ratio between the capillary and the throat is constant, the capillary radius distribution range in the capillary bundle is changed, and the equivalent permeability under different capillary bundles can be obtained by Equation (71), which is $10.6 \times 10^{-3} \mu\text{m}^2$, $18.5 \times 10^{-3} \mu\text{m}^2$, and $28.5 \times 10^{-3} \mu\text{m}^2$. The injectivity is calculated at different permeability, and the resulting injection capacity changes with time are shown in Figure 8.

As can be seen from Figure 8, the smaller the equivalent permeability (the smaller the range of the capillary bundle radius) is given, the smaller the injectivity will be. The reason is that for crude oil with the same viscosity, the smaller the equivalent permeability, the greater the resistance to be overcome by the fluid flow. Under the same injection pressure difference, the smaller the injection flow rate, the lower the injection capacity. This change law indicates that for low-permeability reservoirs, the injection capacity is lower due to the smaller pore throat, and the required injection pressure difference is greater at the same injection amount compared with the high-permeability reservoir. Under the same injection amount, the required water injection pressure difference is larger. If the fluid is injected with constant pressure, it is hard to inject water, which has an impact on the oil recovery for low-permeability reservoirs. Comparing Figure 5 to Figure 8, it can be found that the change of equivalent permeability has the greatest influence on the injection capacity,

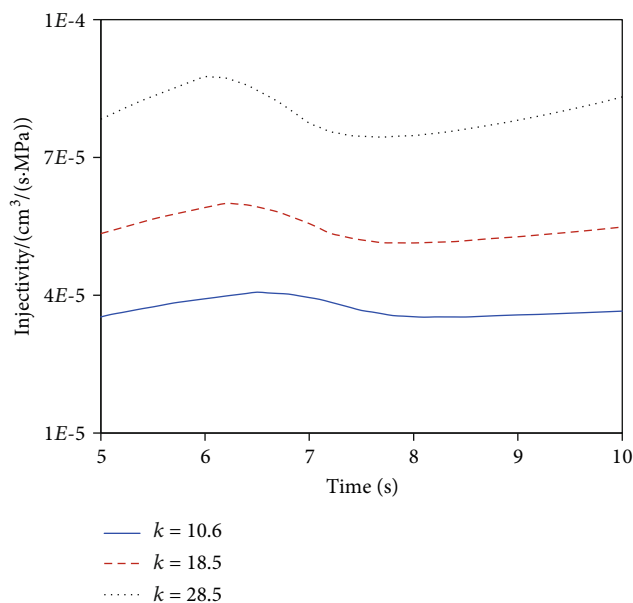


FIGURE 8: Injectivity change with time for different capillary tube radius.

which also indicates that in a practical pilot test for CO₂-alternating-water injection, the influence of permeability on injectivity should be fully considered.

5. Conclusions

- (1) Considering the seepage, mass transfer, and CO₂ diffusion during CO₂ flooding, a mathematical model of convection-diffusion is established and solved. The relationship between the width of the mixed-phase zone and the injection time is obtained
- (2) According to the difference of distribution forms for the unswept oil region, mixed-phase zone, CO₂ region, and water region in a capillary tube, six possible patterns are defined during CO₂ displacement, and three distribution patterns are described during water flooding. Through the introduction of the equivalent resistance model, the injectivity for each possible distribution pattern is evaluated during water-alternating-gas displacement
- (3) Through parameter analysis, the injectivity decreases with the increase of crude oil viscosity and pore throat ratio. Oppositely, the injectivity increases with the equivalent permeability and CO₂ slug size. The equivalent permeability has the greatest influence on injection capacity compared with other factors; therefore, in practice, the influence of permeability on injectivity should be carefully considered

Data Availability

The data used to support the findings of this study are available from the first author upon request.

Conflicts of Interest

The authors declare that they have no conflicts of interest.

Acknowledgments

This study was supported by the National Science Foundation (51804328 and 51974348), the Fundamental Research Funds for the Central Universities (18CX02168A), and the European Union's Horizon 2020 Research and Innovation Program (846775).

References

- [1] J. R. Christensen, E. H. Stenby, and A. Skauge, "Review of WAG field experience," *SPE Reservoir Evaluation & Engineering*, vol. 4, pp. 97–106, 2013.
- [2] R. L. Henry, G. L. Feather, L. R. Smith, and D. D. Fussel, *Utilization of composition observation wells in a West Texas CO₂ pilot flood*, 1981.
- [3] J. Zhao, J. Zheng, X. Hu, Z. Song, and P. Chen, "The WAG-surfactant flooding applied in the high-water-cut oil field: taking QK17-2 oilfield as an example," *Applied Science and Technology*, vol. 44, no. 4, pp. 75–77, 2017.
- [4] M. Meng and Z. Qiu, "Experiment study of mechanical properties and microstructures of bituminous coals influenced by supercritical carbon dioxide," *Fuel*, vol. 219, pp. 223–238, 2018.
- [5] M. Dong, J. Forai, S. Huang, and I. Chatzis, "Analysis of immiscible water-alternating-gas (WAG) injection using micromodel tests," *Journal of Canadian Petroleum Technology*, vol. 44, no. 2, pp. 17–25, 2005.
- [6] J. Wang and M. Dong, "Trapping of the non-wetting phase in an interacting triangular tube bundle model," *Chemical Engineering Science*, vol. 66, no. 3, pp. 250–259, 2011.
- [7] J. Jovanović, W. Zhou, E. V. Rebrov, T. A. Nijhuis, V. Hessel, and J. C. Schouten, "Liquid-liquid slug flow: hydrodynamics and pressure drop," *Chemical Engineering Science*, vol. 66, no. 1, pp. 42–54, 2011.
- [8] M. Piri, *Pore-Scale Modelling of Three-Phase Flow*, Imperial College London, London, 2003.
- [9] Y. Yang, Z. Yen, J. Yao, Y. Li, and C. Wang, "Porescale simulation of microcosmic flow during water-alternating-gas(-WAG) in porous media," *Earth Science Journal of China University of Geosciences*, vol. 38, no. 4, pp. 853–858, 2013.
- [10] J. O. Helland and S. M. Skjæveland, "Three-phase mixed-wet capillary pressure curves from a bundle of triangular tubes model," *Journal of Petroleum Science and Engineering*, vol. 52, no. 1-4, pp. 100–130, 2006.
- [11] W. Jinan, Y. Guangjun, Z. Jun, and X. Fengting, "Experimental study on physical modelling of crude displacement with carbon dioxide drive for long core," *Special Oil & Gas Reservoirs*, vol. 2, 2001.
- [12] M. Zhao and C. Liu, "The effect of CO₂ injection process on production response of Fang-48 Reservoir in Daqing Oil-field," *Xinjiang Petroleum Geology*, vol. 27, no. 4, pp. 449–451, 2006.
- [13] M. Zhao, X. Ding, and J. Li, "Injection parameter's optimization of water-CO₂ displacement in low permeable oilfield," *Science Technology and Engineering*, vol. 27, p. 046, 2012.

- [14] M. K. Zahoor, M. N. Derahman, and M. H. Yunan, "WAG process design—an updated review," *Brazilian Journal of Petroleum and Gas*, vol. 5, no. 2, pp. 109–121, 2011.
- [15] J. Prieditis, C. R. Wolle, and P. K. Notz, "A laboratory and field injectivity study: CO₂ WAG in the San Andres formation of West Texas," in *SPE Annual Technical Conference and Exhibition*, Society of Petroleum Engineers, 1991.
- [16] J. Kamath, F. M. Nakagawa, R. E. Boyer, and K. A. Edwards, "Laboratory investigation of injectivity losses during WAG in West Texas dolomrites," in *SPE Permian Basin Oil and Gas Recovery Conference*, Society of Petroleum Engineers, 1998.
- [17] M. K. Roper Jr., C. T. Cheng, J. E. Varnon, G. A. Pope, and S. Kamy, "Interpretation of a CO₂ WAG injectivity test in the San Andres Formation using a compositional simulator," in *SPE/DOE Enhanced Oil Recovery Symposium*, Society of Petroleum Engineers, 1992.
- [18] M. K. Roper Jr., G. A. Pope, and K. Sepehrnoori, "Analysis of tertiary injectivity of carbon dioxide," in *Permian Basin Oil and Gas Recovery Conference*, Society of Petroleum Engineers, 1992.
- [19] D. Yang, C. Song, J. Zhang, G. Zhang, Y. Ji, and J. Gao, "Performance evaluation of injectivity for water-alternating-CO₂ processes in tight oil formations," *Fuel*, vol. 139, pp. 292–300, 2015.
- [20] J. Li, T. Jang, W. Gao, and B. Liu, "Analysis and optimization of injection capacity of gas-water alternate flooding reservoirs," *Journal of Southwest Petroleum University*, vol. 30, no. 6, pp. 121–125, 2008.
- [21] X. Zhou, X. Liao, X. Zhao, J. Gao, and B. Luo, "Laboratory investigation of miscible CO₂ WAG process in permeability reservoir," *Journal of Shaanxi University of Science & Technology (Science Edition)*, vol. 34, no. 6, pp. 120–124, 2016.
- [22] X. Yan, C. Wang, and G. Zhang, "Optimization of injection parameters for CO₂ gas water alternative drive," *China's Manganese Industry*, vol. 35, no. 5, pp. 97–99, 2017.
- [23] H. Hu, M. Ma, and G. Li, "Establishment of single phase seepage model of low-permeability capillary bundle," *Journal of Chongqing University of Science and Technology (Natural Sciences Edition)*, vol. 13, no. 3, pp. 93–95, 2011.
- [24] Y. Xu, *Experimental Study on CO₂ Gas-Water Displacement in Low Permeability Reservoir*, Southwest Petroleum University, Chengdu, China, 2016.
- [25] M. Du and G. Liu, "Analysis on factors of enhancing oil recovery by CO₂ and water alternating flooding in low permeability reservoirs," *Liaoning Chemical Industry*, vol. 46, no. 4, pp. 354–356, 2017.
- [26] P. Guo, L. Huo, B. Jiang, and Y. Lei, "Parameter optimization of water alternating gas of Fang 48 CO₂ flooding pilot area," *Journal of China University of Petroleum (Edition of Natural Science)*, vol. 36, no. 6, pp. 89–93, 2012.
- [27] H. Liao, "Numerical simulation of oil displacement with carbon dioxide in DB34 well block, Yaoyingtai Oilfield," *Journal of Xi'an Shiyou University, Natural Science Edition*, vol. 25, no. 5, pp. 50–53, 2010.
- [28] M. Meng, Z. Zamanipour, S. Miska, M. Yu, and E. M. Ozbayoglu, "Dynamic stress distribution around the wellbore influenced by surge/swab pressure," *Journal of Petroleum Science and Engineering*, vol. 172, pp. 1077–1091, 2019.
- [29] B. Dong, M. Meng, Z. Qiu, Z. Lu, Z. Ye, and H. Zhong, "Formation damage prevention using microemulsion in tight sandstone gas reservoir," *Journal of Petroleum Science and Engineering*, vol. 173, pp. 101–111, 2019.
- [30] J. O. S. Pizarro and L. W. Lake, "Understanding injectivity in heterogeneous reservoirs," in *SPE/DOE Improved Oil Recovery Symposium*, Society of Petroleum Engineers, 1998.
- [31] H. Hoteit, "Modeling diffusion and gas–oil mass transfer in fractured reservoirs," *Journal of Petroleum Science & Engineering*, vol. 105, pp. 1–17, 2013.
- [32] Y. Su, *Reservoir displacement mechanism*, Petroleum Industry Press, Beijing, 2009.
- [33] A. Leahy-Dios and A. Firoozabadi, "Unified model for non-ideal multicomponent molecular diffusion coefficients," *AIChE Journal*, vol. 53, no. 11, pp. 2932–2939, 2010.
- [34] C. Zhang, W. Sun, J. Yang et al., "Pore and pore-throat size distributions of low permeability sandstone reservoir and their differential origin," *Acta Geologica Sinica*, vol. 86, no. 2, pp. 335–348, 2012.
- [35] M. Hu, "Study and application of microporous structure characteristics of low permeability reservoir," *24/5000 Langfang: Graduate School of Chinese Academy of Sciences (Institute of Seepage Fluid Mechanics)*, 2006.

Research Article

Experimental Study on the Effective Utilization of Reserves in Tight Sandstone Gas Reservoirs and Their Applications

Jie Zhang,^{1,2} Feifei Fang³, Weijun Shen^{1,4}, Huaxun Liu,^{2,5} Shusheng Gao,^{2,5} and Liyou Ye^{2,5}

¹School of Engineering Science, University of Chinese Academy of Sciences, Beijing 100049, China

²Department of Porous Flow & Fluid Mechanics, PetroChina Research Institute of Petroleum Exploration & Development, Langfang 065007, China

³School of Petroleum Engineering, Chongqing University of Science and Technology, Chongqing 401331, China

⁴Key Laboratory for Mechanics in Fluid Solid Coupling Systems, Institute of Mechanics, Chinese Academy of Sciences, Beijing 100190, China

⁵Research Institute of Petroleum Exploration & Development, PetroChina, Beijing 100083, China

Correspondence should be addressed to Feifei Fang; fangfeifei@cqust.edu.cn and Weijun Shen; wjshen763@imech.ac.cn

Received 25 May 2020; Revised 14 September 2020; Accepted 19 October 2020; Published 23 November 2020

Academic Editor: Wen-Dong Wang

Copyright © 2020 Jie Zhang et al. This is an open access article distributed under the Creative Commons Attribution License, which permits unrestricted use, distribution, and reproduction in any medium, provided the original work is properly cited.

The effective utilization of reserves in tight sandstone reservoirs is one of the major concerns in terms of the development of tight sandstone gas reservoirs. However, the characteristics of reserve utilization are not fully understood, and many uncertainties still exist in the process. For this purpose, long cores on the Su 6 block of Sulige tight sandstone gas field in China were selected, and a multipoint embedded measurement system was established to study the characteristics of effective reserve utilization. Then, the effects of the related reservoir properties and production parameters were investigated. Based on the similarity theory, the effective conversion relationship between the physical experiment and the actual field production was established. The results showed that the pressure distribution in the exploitation of tight gas reservoir is nonlinear, and water cut in the reservoir will hinder the effective utilization of reserves. The lower the reservoir permeability, the larger the negative effect of water on reservoir utilization. Lower gas production rate and higher original pressure are associated with a smoother drawdown curve, which results in larger reserve utilization. The moving boundary expands with time, and its initial propagation velocity increase and then decrease. Additionally, the water cut in the reservoir can delay the spread of moving boundary propagation. The experimental results are consistent with the actual results of the field production by the similarity criterion, which can reflect and predict the production performance in tight gas reservoirs effectively. These results can provide a better understanding of reservoir pressure distribution and effective utilization of reserves to optimize the gas recovery and development benefit in tight sandstone gas reservoirs.

1. Introduction

Tight sandstone gas reservoirs are widely distributed throughout the world with huge resource potential, which is playing an increasingly important role among energy sources [1, 2]. Up till 2019, the discovered tight sandstone gas field is more than 70 and the total amount of estimated recoverable is more than $45 \times 10^{13} \text{ m}^3$ [3]. According to the statistics, the recoverable reserves of tight sandstone gas in

China are about $13.4 \times 10^8 \text{ m}^3$, which accounts for more than 50% of the total natural gas reserves in the country. Therefore, the efficient development of tight sandstone gas is of great significance to the implementation of China's natural gas strategy [4]. At present, most of the tight sandstone gas reservoirs belong to lithologic gas reservoirs which are formed under the microstructure background, and they are characterized by small-scale, low reserve abundance, large amplitude change in production, and more development

difficulties [5, 6]. Due to the geological characteristics with low porosity, low permeability, and high water saturation, as well as the development characteristics of threshold pressure gradient, Klinkenberg effect, and stress sensitivity, the propagation law of the pressure disturbance in tight sandstone reservoirs significantly differs from conventional gas reservoirs [7, 8]. Moreover, the seepage laws in tight sandstone reservoirs also differ from Darcy's law. The characteristics of pressure propagation and pressure distribution in tight sandstone reservoirs are the direct reflection on the effective utilization range and utilization degree of the reservoir, which is also the theoretical basis for cognizing geofluid flow characteristics, gas production calculation, and well testing in gas reservoirs [9]. Therefore, there is great significance to understand the effective utilization of reserves for gas productivity and optimize the effective development in tight gas reservoirs.

In the last few decades, there has been a surge of interest in the characteristics of fluid flow and reservoir pressure distribution in the low permeability reservoirs [10]. Based on comprehensive consideration of threshold pressure gradient, nonlinear flow, and dynamic boundary effects, some scholars have established a large number of the percolation models of low-permeability reservoirs. Pascal analyzed the transient flow in a one-dimensional model with the threshold pressure gradient and derived the approximate analytical solution [11]. Feng and Ge [12] established the mathematical model of unsteady non-Darcy flow in the dual-medium reservoir and analyzed the change of bottom hole pressure in the different exploitation process. Wattenbarger et al. [13] analyzed the production decline curve analysis of linear flow into fractured tight gas wells. Considering the threshold pressure gradient and moving boundary factors, Deng and Liu [14] proposed a mathematical model of nonlinear steady flow and unsteady percolation in low permeability reservoirs and derived the reservoir pressure distribution of two percolation models. Hsieh et al. [15] used both analytical and numerical methods to estimate the pressure disturbance area from a producing well in an infinite reservoir. Feng et al. [16] established a mathematical model of nonlinear percolation in low-permeability gas reservoirs which considered the threshold pressure gradient. Wang et al. [17] derived a new analytical expression of pressure distribution and moving boundary propagation by approximate solving the mathematical model of nonlinear radial unstable fluid flow, which involved threshold pressure gradient and moving boundary using the integration method. Ji and He [18] established a non-Darcy radial percolation model for ultralow permeability reservoirs under constant flow and constant flow conditions, which considers the threshold pressure gradient. Nobakht and Clarkson [19, 20] studied the linear flow of fractured wells in tight gas reservoirs under constant-flowing-pressure boundary conditions and obtained the corresponding expressions of detection boundary propagation. Based on the trilinear flow model, Huang et al. [21] established a new analytical model of a multifractured horizontal well to recognize formation properties and forecast the dynamics of pressure and the production in tight gas reservoirs. Besides, there are some studies conducted in the physical experiments, and Hu et al. [22] conducted gas perco-

lation experiments to understand the changes in reservoir pressures during tight gas reservoir exploitation under the conditions of homogeneous cores. Based on the similarity theory of heterogeneous reservoir, Yu et al. [23] used low-permeability physical simulation by artificial core plate model to study on the seepage flow patterns in heterogeneous low permeability reservoir. However, although there have been a lot of numerical simulations studies, most of these studies have generally been restricted to the idealized conditional, which cannot truly represent the pressure disturbance propagation and the reserve utilization in the actual formation. Concerning physical simulation studies, the length of core commonly used is generally only 5-8 cm; thus, accordingly, the effect of end surface is obvious [24]. The existing long core experiments usually arrange the growing cores or multicores in series through the permeability harmonic average method, and there is a great error compared with actual formation [25, 26].

In this study, the multipoint embedded measurement system was established, and the 30 cm long core of the Sulige tight sandstone gas fields was selected by outcrop coring to simulate the variation law of reservoirs pressure in the different exploitation processes. The propagation characteristics of pressure disturbance and reserve utilization of tight sandstone gas reservoirs during the exploitation process were studied, and the effects of the related reservoir properties and production parameters such as permeability, pressure, water saturation, and gas production were investigated. Based on the above study, the effective conversion relationship between the physical experiment and the actual field production was established by the dimensional analysis, and the experimental results were transformed into the actual field production. These results can provide a better understanding of reservoir pressure distribution and effective utilization of reserves for improving the gas recovery and development benefit in tight gas reservoirs.

2. Experimental Samples and Methods

2.1. Experimental Samples. Sulige gas field, the biggest tight sand gas reservoir in China, is a gentle west-leaning monocline located in the Yishan slope of the Ordos Basin, which is a monoclinic structure inclined from northeast to southwest with an exploration area of about $4.0 \times 10^4 \text{ km}^2$ [25]. The Su 6 block is located in the middle of the Sulige gas field in the Ordos Basin, and it is one of the most favorable natural gas enrichment and key development blocks in the Sulige gas field.

In the previous studies, physical simulation experiments often use conventional cores with a length of 5-8 cm which can result in the effect of end surface. Although long core formed by splicing can weaken the effect of end surface, it differs significantly from the actual formation. Constrained by coring technology and coring equipment, conventional coring of long cores is very difficult. In this study, 30 cm lone core samples are collected by outcrop coring from the Su 6 block of the Sulige tight sandstone gas field. Then, three cores with permeability values of $1.49 \times 10^{-3} \mu\text{m}^2$, $0.32 \times 10^{-3} \mu\text{m}^2$, and $0.028 \times 10^{-3} \mu\text{m}^2$ are selected to understand the propagation characteristics of pressure disturbance and reserve utilization of tight sandstone gas reservoirs during the

TABLE 1: Basic properties of tight sandstone cores.

Core no.	Core type	Core size (cm) (length × diameter)	Permeability ($10^{-3} \mu\text{m}^2$)	Porosity (%)
Su1	Low permeability	30 × 3.76	1.49	14.6
Su2	Ultra-low permeability	30 × 3.72	0.32	11.7
Su3	Tight	30 × 3.77	0.028	8.8

exploitation. The basic properties of the tight sandstone cores used in this study are shown in Table 1.

Tight sandstone gas reservoirs are characterized by low permeability, high heterogeneity, and high water saturation [22, 27]. During the depletion-drive development, the reservoir pressure gradually decreases, and the pressure within the gas well drainage radius will exhibit a decreasing drawdown curve from the distal reservoir to the proximal. The physical properties and gas production rate of the reservoir are diverse; thus, the pressure drop profiles in the different development phases are also different, which reflects the imbalance in the utilization of reserves. According to the propagation characteristics of pressure disturbance and reserve utilization of tight sandstone gas reservoirs, the effects of the related reservoir properties and production parameters such as reservoir permeability, original pressure, water saturation, and gas production rate were considered, and the experiments of the effective utilization of reserves conducted on different conditions are summarized in Table 2.

2.2. Experimental Methods. In the study, the experimental system of multipoint embedded measurement in the gas reservoir development is illustrated in Figure 1, which was composed of a gas boosting section, core simulation section, and data acquisition section. The unique feature of this experimental system is that in addition to the two pressure points at the inlet and outlet ends, there are also three pressure points evenly distributed in the sidewall of the core holder. The pressure sensor corresponding to each pressure measuring point has an independent rigid collecting channel in which the apex has installed a filter. The fore-end of the pressure sensor is placed inside the core through the sealing isolating device of the pressure-receiving device, which can accurately measure the pressure changes at different positions on the core section during the gas reservoir development. The pressure point recording interval is 2 s. Through the data processing device, the pressure profiles of different development phases can be established according to the measured pressure, and determine reservoir pressure propagation and pressure distribution characteristics finally.

The following experimental processes are set up to simulate the effective utilization of reserves in tight sandstone gas reservoirs under different conditions: (1) According to the experimental scheme, the core samples were chosen (for the aqueous experiment, the irreducible water saturation was established on the core by the gas-drive method). Drill a radial hole in the core and put the core in the core holder, and then place the rigid collecting channel of the pressure sensor in the corresponding radial hole. (2) The nitrogen was previously pressurized to 20 MPa by gas booster pump

TABLE 2: Different experiments for the reservoir utilization conducted.

Experimental scheme	Core No.	Original pressure (MPa)	Gas production rate (mL/min)
1	Su1	20	2000, 6000, 10000
2	Su2	20	500, 1000, 1500
3	Su3	20	100, 300, 500
4	Su3	25	100, 300, 500

and stored in the high-pressure vessel. After the confining pressure was increased to 30 MPa, open the safety valve and the control valve 2, and the core samples was filled with high-pressure nitrogen. Then, the core samples were saturated with a set saturation pressure secondarily by a gas booster pump. When the pressure distribution inside the core was uniform, remove the high-pressure gas source and prepare to start the experiment. (3) Open the control valve 3 and release the gas at a constant gas production rate by regulating valve 3 at the outlet end during the initial stage. The regulator valve 3 was opened to release gas from the outlet end of the core holder, and the outlet end flow rate was controlled by the regulating valve 3. After the outlet pressure was reduced to the abandonment pressure 5 MPa, the experiment terminated, and the abandonment pressure P_a is calculated using the empirical formula of the constant volume reservoir, $P_a = (0.7 \sim 0.5)P_i Z_a / Z_i$. (4) At the end of the experiment, the drawdown curves were made with the experimental data. Then, the characteristics of drawdown curves and the effect of the different factors on the utilization of tight sandstone reservoirs were analyzed comprehensively. During the experiment, the core system of saturated high-pressure nitrogen was closed completely, and there was no other external energy supply. There is a great difference in the compressibility between the gas phase and the water phase, and thus, it could be ideally considered that the energy source of the product gas was the gas expansion caused by the reservoir pressure drop.

2.3. Basic Theory. The material balance equation has long been recognized as one of the basic tools for interpreting and predicting reservoir performance, which was presented by Schilthuis [29, 30]. The equation of the closed dry gas reservoir can be written as follows:

$$GB_{gi} = (G - G_p)B_g, \quad (1)$$

where G is the initial gas-cap gas; G_p is the cumulative gas produced; B_{gi} is the initial gas formation volume factor; B_g

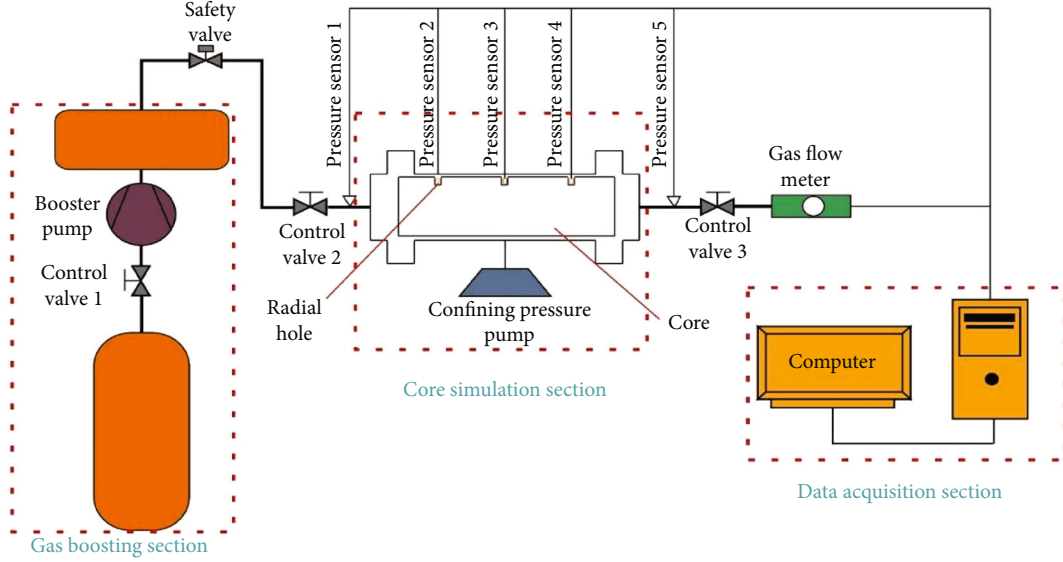


FIGURE 1: Measurement of multipoint embedded measurement in gas reservoir development.

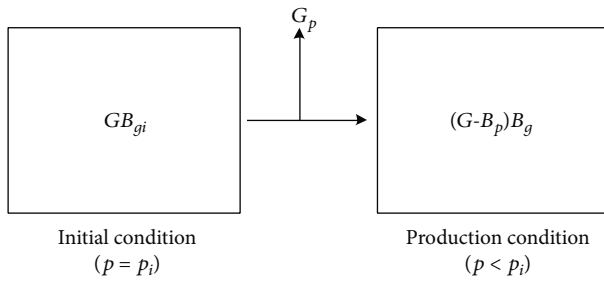


FIGURE 2: Tank model concept of the material balance equation [28].

is the gas formation volume factor; GB_{gi} is the reservoir volume filled with gas under the initial reservoir pressure, and it is the core pore volume for the dry core, while the water-bearing core is that the core pore volume minus the irreducible water volume; $(G - G_p)B_g$ is the reservoir volume filled with gas at the pressure P_i after gas production, which is illustrated in Figure 2.

By substituting the ratio of the gas formation volume factor under initial condition and production ($B_{gij}B_g = ZP_i$) into the Equation (1), thus, Equation (1) can be rewritten and expressed as

$$\frac{P}{Z} = \frac{P_i}{Z_i} - \frac{P_i}{Z_i G} G_p. \quad (2)$$

From Equation (2), it can be seen that the graph of P/Z versus G_p is a straight line if the reservoir is a closed boundary. Based on the curve of P/Z versus G_p in the depletion-drive development of tight sandstone gas reservoir, the dynamic reserve G can be obtained by the intercept.

In this study, the gas production rate (q) and the cumulative gas (G_p) can be measured, and the degree of reserve

TABLE 3: Changes of related parameters between dry core and aqueous cores.

Core No.	Permeability ($10^{-3} \mu\text{m}^2$)	Aqueous cores		Permeability loss
		Water saturation	Permeability ($10^{-3} \mu\text{m}^2$)	
Su1	1.49	38%	0.86	46%
Su2	0.32	43%	0.15	61%
Su3	0.028	48%	0.022	21%

recovery can be calculated from the cumulative gas and the dynamic reserve,

$$R = \frac{G_p}{G}. \quad (3)$$

Define the recovery at a point in the core segment as $(1 - Z_i P / Z P_i)$, where P is selected as the pressure at that point,

$$R' = \left(1 - \frac{Z_i P}{Z P_i}\right). \quad (4)$$

3. Results and Discussion

3.1. Effect of Reservoir Permeability and Water Saturation. The gas driving method was often used to establish the water saturation of the core. However, it is more difficult to establish water saturation for the 30 cm long core in the experiment. Here, the dry and irreducible water conditions were compared to study the effect of water saturation on reserve utilization in tight gas reservoirs. Based on the gas driving method, the irreducible water saturation was established for the cores, and the changes of related parameters between dry core and aqueous cores were shown in Table 3. According to the experimental scheme, the physical experiments of

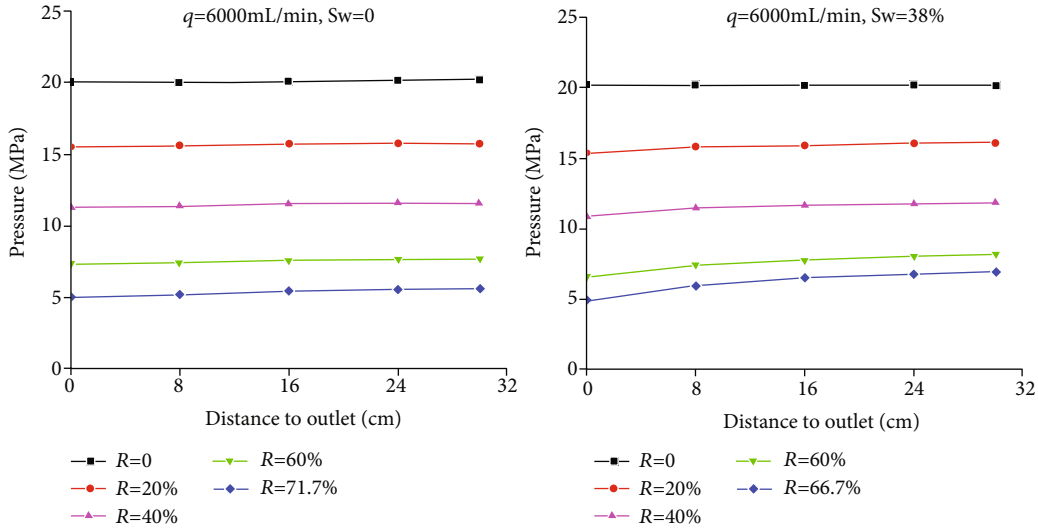


FIGURE 3: Comparisons of reserve utilization in the Su1 core under the dry and irreducible water conditions.

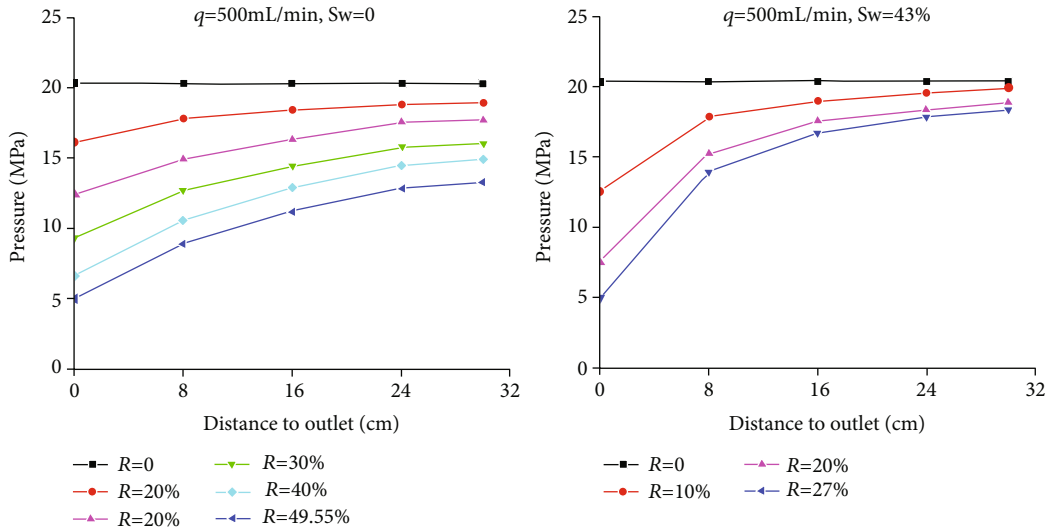


FIGURE 4: Comparisons of reserve utilization in the Su2 core under the dry and irreducible water conditions.

different permeability sandstone cores in the exploitation were conducted, and the propagation characteristics of pressure disturbance and reserve utilization were studied by the system of multipoint embedded measurement.

For the formation of a sandstone reservoir with permeability greater than $1 \times 10^{-3} \mu\text{m}^2$ represented by Su1 core, the reserve utilization under the dry and irreducible water conditions is illustrated in Figure 3. The fluid percolation channel is mainly capillary pore throat ($0.1 \mu\text{m} < r < 1 \mu\text{m}$) and supercapillary pore throat ($r > 1 \mu\text{m}$), and the resistance of single-phase gas to flow in the core is very small. From the results of the experiment, the internal pressure of the core is basically the same, with evenly decreasing, and the drawdown pressure is extremely small. The drawdown curve is approximately a straight line, and there is almost no pressure cone of depression. The average pressure in the dynamic control area is low when the core outlet reaches the abandonment pressure, and the reservoir is very well utilized. When

the gas production rate is 6000 mL/min, the experiment is carried out for 8.23 min, and then, the pressure at the outlet reaches the abandonment pressure. The pressure at the inlet and outlet of the dry core is 5.66 MPa and 5.03 MPa, respectively. The drawdown pressure is 0.63 MPa, and the ultimate recovery is 71.7%. When the reservoir contains irreducible water, the irreducible water is present in the form of a water film on the surface of the reservoir pore throat. The thickness of the water film is very small relative to the radius of the pore throat, so the influence on the gas seepage is negligible. In the study, the experiment was finished in 4.13 min, and the drawdown pressure and the ultimate recovery are 0.99 MPa and 66.7%, respectively.

For the formation of a sandstone reservoir with the permeability of $0.1 \sim 1 \times 10^{-3} \mu\text{m}^2$ represented by Su2 core, the reserve utilization under the dry and irreducible water conditions is illustrated in Figure 4. The fluid percolation channel is mainly microcapillary pore throat ($0.01 \mu\text{m} < r < 0.1 \mu\text{m}$)

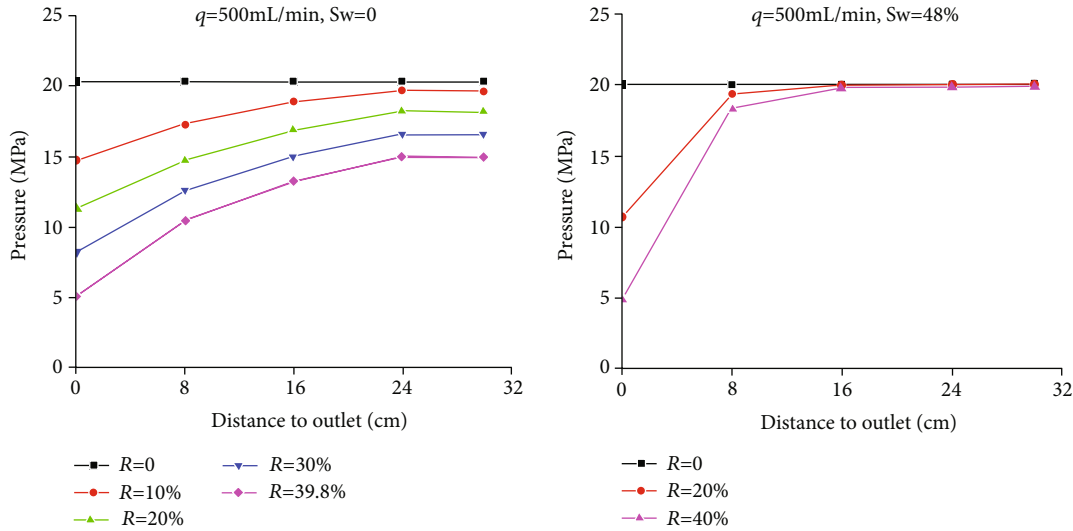


FIGURE 5: Comparisons of reserve utilization in the Su3 core under the dry and irreducible water conditions.

and capillary pore throat. From the result, it can be seen that there exists the obvious percolation resistance when the gas flows through in the core. The drawdown curve is nonlinear, which shows the pressure cone of depression. When the pressure drop reaches the end of the core, the pressure drop at each point decreases uniformly with the increase of time and reaches the pseudosteady state. When the gas production rate is 500 mL/min, the experiment is carried out for 5.38 min, and the outlet reaches the abandonment pressure. At the end of the experiment, the drawdown pressure is 8.29 MPa, and the ultimate recovery of the dry core is 49.55%. The reservoir contains the irreducible water, and the thickness of the irreducible water film is not negligible compared with the radius of the main control throat. The existence of the water film occupies the effective pore throat of the reservoir, and it reduces the effective pore throat radius and increases the percolation resistance to affect the effective gas flow, which results in a larger drawdown pressure than in the nonaqueous state to maintain the same gas production rate. When the core contains irreducible water, the experiment was finished in 1.67 min; the drawdown pressure and the ultimate recovery are 13.32 MPa and 27%, respectively.

For the formation of a sandstone reservoir with permeability less than $1 \times 10^{-3} \mu\text{m}^2$ represented by Su3 core, the reserve utilization under the dry and irreducible water conditions is illustrated in Figure 5. The microcapillary pore throat and nanopore throat ($r < 0.1 \mu\text{m}$) play the main control role in the permeability of the formation. Compared with Su2, Su3 has a smaller radius of the main control hole throat, and the gas is more resistant to percolation in such reservoirs. The drawdown curve is more nonlinear, and the pressure cone of depression is more obvious. The reserves can be utilized near the outlet while the reserves are utilized very poorly at a distance from the outlet. When the gas production rate is 500 mL/min, the experiment is carried out for 8 min, and the outlet reaches the abandonment pressure. At the end of the experiment, the drawdown pressure is 9.91 MPa, and the degrees of reserve recovery degrees in the pressure measurement points 1, 2, 3, 4, and 5 are 24.2%, 24%, 32.4%, 46.1%,

and 73.9%, respectively, and the degree of reserve recovery in the dry core is 49.55%. When the reservoir contains irreducible water, the main pore throat radius is smaller than that of the ultralow permeability sandstone reservoir, and the rock pore surface has a stronger ability to bind water molecules. Both the irreducible water saturation and the water film thickness are larger, and the thickness of the irreducible water film is even in the same order of magnitude as the radius of the pore throat because the influence of water-bearing gas percolation is greater. At the end of the experiment, the pressure near the inlet hardly decreased, and the reserves were basically not utilized. The pressures corresponding to the pressure measuring points 1, 2, 3, 4, and 5 were 19.90 MPa, 19.88 MPa, 19.83 MPa, 18.36 MPa, and 4.92 MPa, respectively, and reserve utilization in the pressure measurement points was 1.88%, 2%, 2.40%, 8.56%, and 74.31%, respectively. The drawdown pressure reaches 14.98 MPa, while the reservoir ultimate recovery is only 8.40%, and the ultimate recovery is reduced by 31.4% compared with the dry core.

3.2. Effect of Initial Pressure. The original pressure of tight sandstone gas reservoir is varied in different areas, which affects the ultimate recovery [31, 32]. In this study, the Su3 core with irreducible water was chosen to study the effects of different initial reservoir pressures in the reservoir utilization. The gas production rate and original pressure were 100 mL/min, 20 MPa, and 25 MPa, respectively, which was shown in Figure 6. When the original pressure of the core was 20 MPa, the gas production rate was 100 mL/min, and the experiment was completed in 20.07 min. The pressures corresponding to the pressure measurement point 1, 2, 3, 4, and 5 were 11.81 MPa, 11.59 MPa, 11.36 MPa, 8.54 MPa, and 5 MPa, respectively. The drawdown pressure was 6.81 MPa at the end of the experiment, and the ultimate recovery was 48.3%. While the initial saturation pressure was 25 MPa, the gas production rate was 100 mL/min, and the experiment was carried out for 34.12 min. The pressures corresponding to the pressure measurement points 1, 2, 3,

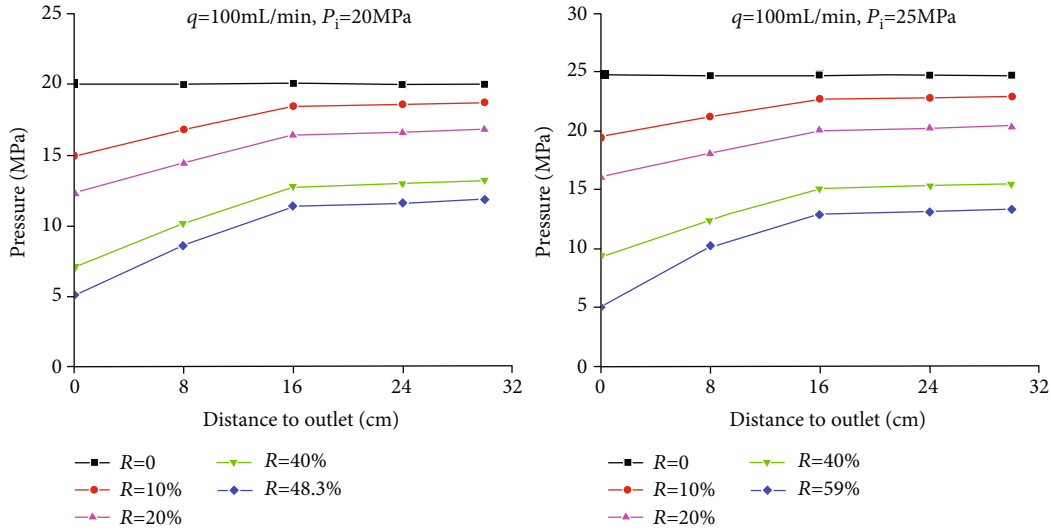


FIGURE 6: Comparisons of reservoir utilization in the Su3 core under different initial reservoir pressures.

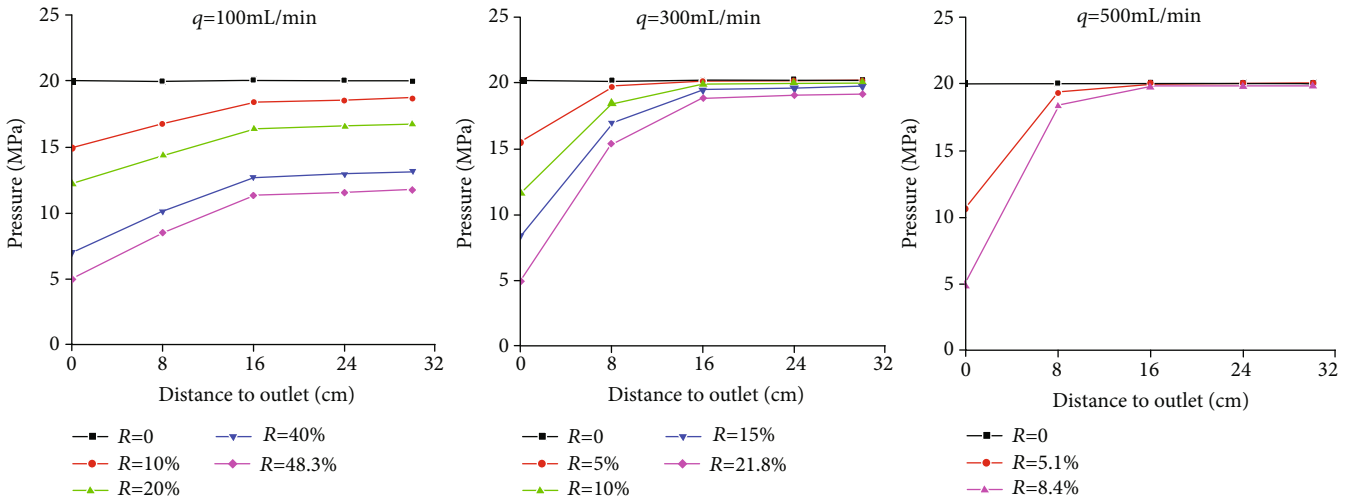


FIGURE 7: Comparisons of reservoir utilization in the Su3 core under different gas production rates.

4, and 5 were 13.27 MPa, 13.03 MPa, 12.87 MPa, 10.17 MPa, and 5 MPa, respectively, and the drawdown pressure and the ultimate recovery were 8.27 MPa and 59%, respectively. Compared with the initial saturation pressure of 20 MPa, the ultimate recovery was increased by 10.7%. This demonstrates that the greater the original pressure in tight sandstone reservoirs, the greater the elastic expansion energy that promotes the gas percolation. Therefore, the more gas that could be effectively utilized in the reservoir, and the greater the ultimate recovery.

3.3. Effect of Gas Production Rate. The gas production rate is an important parameter in the gas reservoir exploitation which can impact the productive life and the effective use of reservoir [28, 33]. When the gas production rate was too high, the drawdown pressure would increase rapidly. Besides, the pressure at the core outlet would drop to the abandonment pressure when the experiment was conducted for a short time. When the experiment was in the abandoned con-

ditions, the corresponding core inlet pressure was varied with different gas production rates. The higher gas production rate was significantly associated with larger drawdown and higher inlet pressure in abandonment conditions. As a result, the degree of reservoir utilization was very low, and the nonlinear pressure drop curve was stronger. The amount of produced gas was reduced, and the lower the ultimate recovery. As shown in Figure 7, the original pressure of the core was 20 MPa, and the gas production rate was 100 mL/min. When the experiment was carried out until 20.07 min, the outlet pressure was reduced to the abandonment pressure, and the corresponding pressures of the pressure measuring points 1, 2, 3, 4, and 5 were 11.81 MPa, 11.59 MPa, 11.36 MPa, 8.54 MPa, and 5 MPa, respectively. According to Equation (6), the corresponding recovery of each pressure point is 38.3%, 39.4%, 40.55%, 54.95%, and 73.51%, respectively, and the corresponding ultimate recovery at the gas production rate was 48.3%. When the gas production rate was 500 mL/min, the experiment was carried out

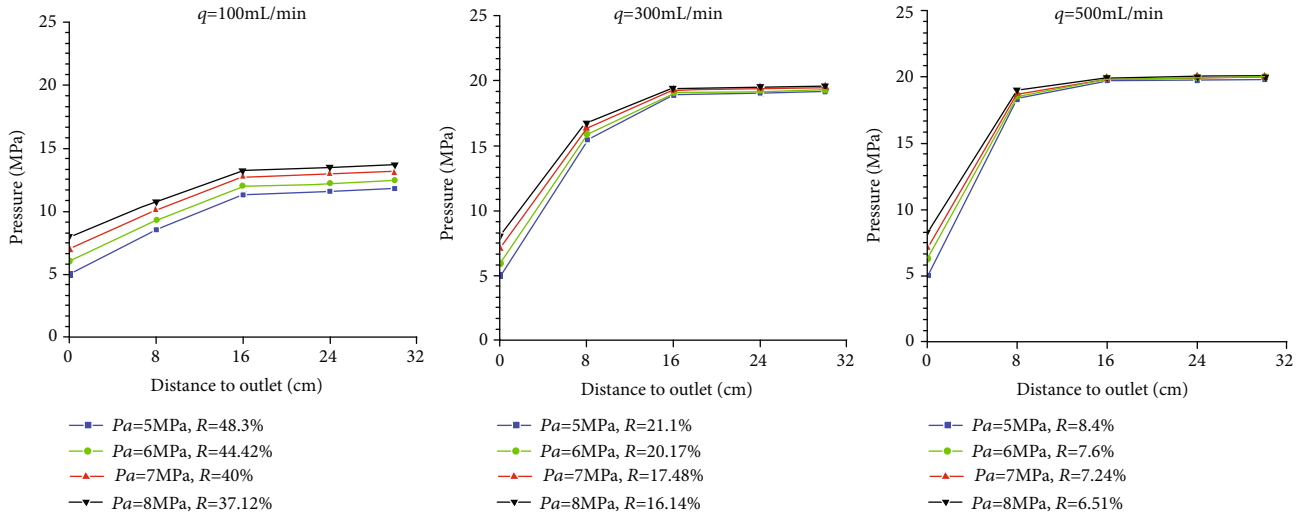


FIGURE 8: Drawdown curves of Su 3 under different abandonment pressure.

to 8 min, and the outlet pressure was reduced to the abandonment pressure. The corresponding pressures of the pressure measuring points 1, 2, 3, 4, and 5 were 19.9 MPa, 19.88 MPa, 19.83 MPa, 8.54 MPa, and 5 MPa, respectively. The reserves in the core end were basically not utilized, and the reservoir ultimate recovery was only 8.4%.

3.4. Effect of Abandonment Pressure. The abandonment pressure plays a significant role in determining recovery efficiency, and the reservoirs with low permeability will have higher abandonment pressures than reservoirs with high permeability [28, 34]. The characteristics of the drawdown curve under abandonment pressure reflected the distribution of remaining reserves. In this study, the abandonment pressure was uniformly set to 5 MPa; three abandonment pressures (6, 7, and 8 MPa) were set to study the effect on the utilization of tight sandstone gas reservoir. Then, the recovery factor and the drawdown curves of Su 3 under different abandonment pressure were analyzed and compared.

Figure 8 shows the drawdown curves of the Su3 core with irreducible water at different gas production rates when the outlet pressure drops to the abandonment pressure. It can be seen from the pressure distribution curve that the drawdown curve was sharp near the outlet and was gentler away from the outlet when the experiment was carried out to the abandoned pressure condition. The trend of drawdown curves is similar at the same production rate but different abandonment pressure. However, the increased gas production rate would make this trend more apparent. The results of this phenomenon indicate that reserves near the core outlet can be better utilized, but the reserves near the core end are less utilized. The reason for the above phenomenon was that the pore pressure was gradually reduced during the tight sandstone depletion-drive development, and the pore pressure was different at different locations in the core. Therefore, the effective stresses at different points inside the core were different. However, there was a strong stress sensitivity in the tight sandstone, so the permeability of the core at different locations was different in the mining process. The effec-

tive stress increased, and the permeability decreased along the seepage direction. In the case of constant flow condition, the drawdown pressure would gradually increase to ensure the gas supply, which was reflected in the drawdown curve.

3.5. Propagation Characteristic of the Moving Boundary. Pascal [11] and Liu [35] pointed out that there existed threshold pressure gradient in the low-permeability reservoirs. The propagation of pressure disturbances in the flow was not transmitted to infinity instantaneously like the high-permeability formation, but there existed a dynamic boundary which was the outer edge of the propagation of pressure disturbance. Tight sandstone gas reservoirs had similar dynamic boundary pressure propagation characteristics as low-permeability reservoirs. Analysis of gas reservoir pressure disturbance propagation could reflect the effective utilization range around gas wells, which was the theoretical basis for analyzing gas production performance.

Since there was the threshold pressure gradient in the tight sandstone gas reservoir, the pressure disturbance did not propagate to the end of the core instantaneously, while it would gradually move from the outlet end to the end of the core with the advance of time. As shown in Figure 9, the pressure wave propagated to pressure detecting points 4, 3, and 2, respectively, when the experiment was carried out for 6 s, 18 s, and 34 s, respectively, in the dry core, and it reached the core inlet when the time was 54 s. The corresponding times of the dynamic boundary propagation to each pressure measurement point in the condition of irreducible water were 8 s, 24 s, 52 s, and 92 s, respectively. Within the influence range of the moving boundary, the reservoir was utilized and formed a pressure profile. However, the reservoir was not utilized outside the influence range of the moving boundary. The moving boundary gradually expanded with the advance of time, and the propagation speed increase first and then decrease. The higher the gas production rate was, the faster the dynamic boundary propagation speed was. The irreducible water in the core would increase the threshold pressure gradient of the reservoir,

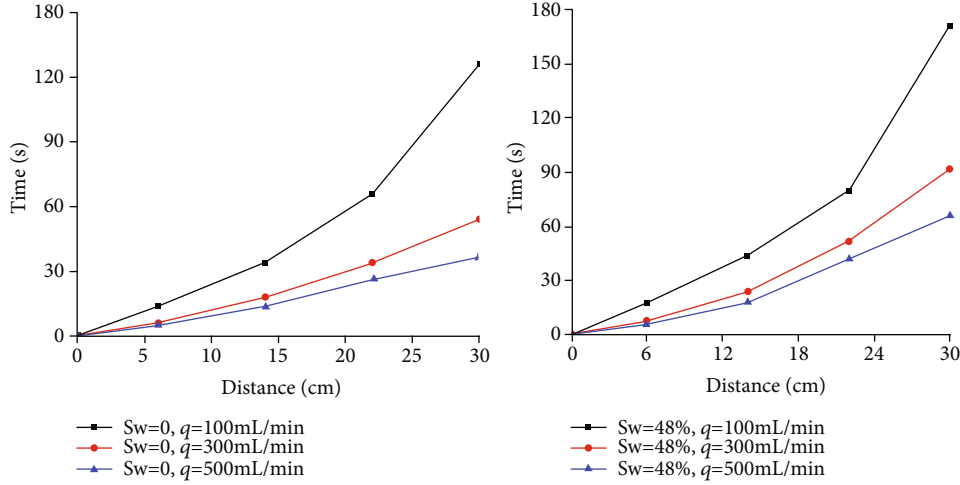


FIGURE 9: Time corresponding to the pressure drop propagated to each pressure measuring point in the Su3 core under the dry and bound water conditions.

which reduced the propagation velocity of the moving boundary and decreased the propagation velocity of the pressure disturbance. Therefore, the control area of a single well was limited in the tight reservoirs even if the formation was an infinite formation and there were no external boundary conditions.

4. Similarity Conversion between Physical Experiment and Gas Well Production

4.1. Similarity Criteria. Tight sandstone gas reservoirs are characterized by low permeability, and there is basically no natural productivity, and only after large-scale fracturing transformation can they obtain gas productivity [36, 37]. However, the gas can only flow effectively within the fracturing-affected area, and thus fracturing technology is widely used during the development to increase the discharge area of the gas well and increase productivity [38]. When there was a fractured horizontal well in the center of the tight sandstone gas reservoir, the gas flowed from the reservoir to cracks and then flowed from the crack to the wellbore. And the cracks were the main discharge surface and vertical cracks were the main flow lines in the reservoir. The vertical cracks were formed after fracturing in the gas well, which was with equal spacing distribution and symmetrical distribution on both sides of the gas well, and the cracks had infinite flow conductivity, illustrated in Figure 10. Therefore, the percolation problem of the segmented fracturing of horizontal wells in tight sandstone reservoir could be simplified into several one-dimensional percolation models. Considering that cracks were distributed along the wellbore with equal spacing, the production dynamics between the cracks did not interfere, and then, the contribution of each crack to the gas well production was consistent.

Similarity criterion refers to the effective conversion relationship between physical model experiment parameters and mineral parameters established through similarity theory. The similarity criterion can realize the effective application of the physical simulation experiment results in the actual

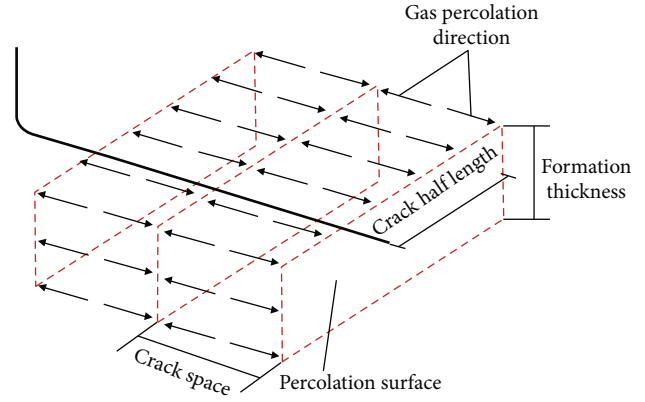


FIGURE 10: The fracturing flow field in the horizontal well.

mine field [39]. According to the percolation mechanics theory and gas reservoir engineering method, there are 13 independent variables and 1 dependent variable in the experiment, which contains 4 basic dimensions, as shown in Table 4. They are length dimension (L), mass dimension (M), time dimension (T), and temperature dimension (K), respectively. According to the similarity theory, there are 10 similarity numbers, and they can be expressed by the following form [40],

$$\pi = K^{x_1} \phi^{x_2} S_w^{x_3} L^{x_4} R_1^{x_5} R_2^{x_6} P_i^{x_7} q^{x_8} t^{x_9} z^{x_{10}} T^{x_{11}} T_{sc}^{x_{12}} P_{sc}^{x_{13}} P_5^{x_{14}}. \quad (5)$$

According to the homogeneous principle, the corresponding linear equations are as follows:

$$2x_1 + x_4 + x_5 + x_6 - x_7 + 3x_8 - x_{13} - x_{14} = 0, \quad (6)$$

$$x_7 + x_{13} + x_{14} = 0, \quad (7)$$

$$-2x_7 - x_8 + x_9 - 2x_{13} - 2x_{14} = 0, \quad (8)$$

$$x_{11} + x_{12} = 0. \quad (9)$$

TABLE 4: Physical simulation similarity of the tight sandstone gas reservoir development.

No.	Similarity	Similar attribute	Model value	Mine value
1	$\pi_1 = \phi$	Porosity	0.11	0.02~0.15
2	$\pi_2 = S_w$	Flow medium	0.42	0.4~0.8
3	$\pi_3 = z$	Gas compressibility	1.055	0.9~1.2
4	$\pi_4 = T/T_{sc}$	Temperature	1	1.1~1.3
5	$\pi_5 = R_2/R_1$	Geometric	1	10~50
6	$\pi_6 = R_2/L$	Geometric	0.126	0.3~1
7	$\pi_7 = P_{sc}/P_i$	Dynamic	0.005	0.002~0.005
8	$\pi_8 = P_a/P_i$	Dynamic	0.250	0.1~1.0
9	$\pi_9 = q/(\pi R_1 R_2 K K_{rg} T_{sc} P_i^2 / L \mu Z T P_{sc})$	Dynamic	0.097	0.1~0.3
10	$\pi_{10} = qt/(\pi R_1 R_2 L \phi S_g T_{sc} P_i / z T P_{sc})$	Recovery	0.479	0~0.95

Equations (6), (7), (8), and (9) are homogeneous equations of length dimension, mass dimension, time dimension, and temperature dimension, respectively. The corresponding equations are homogeneous linear equations. According to the matrix theory, there are 10 basic solutions for homogeneous linear equations and 10 independent similarity criteria. By solving the equation, then conducting derivation and transformation, the similarity criterion of the similarity physical simulation experiment of tight sandstone gas reservoir development is obtained (as shown in Table 4).

π_1 and π_2 are the porosity and water saturation (or gas saturation), respectively; π_3 is the gas compressibility similarity, and the deviation factor of nitrogen and formation natural gas used in the experiment changes around 1, which is basically consistent; π_4 is the ratio of temperature to the standard temperature. The physical experiment temperature is 298.13 K and the formation temperature is 373.15 K. The difference between the two and the standard temperature is small, and the similar criteria π_4 can be guaranteed to be basically consistent; π_5 and π_6 are the geometric similarity. In the physical experiment, π_5 is the ratio of the core long axis to the short half axis, which is generally 1. In the field, π_5 is the ratio between the width of the fracture percolation surface and the thickness of reservoir. It can be seen from Table 4 that it is difficult to achieve consistency between physical experiment and the field according to the similarity criterion π_5 , but it mainly represents the similarity of the vertical flow direction, which has little influence on the one-dimensional flow in the experiment, and the similarity requirement can be appropriately reduced; π_7 and π_8 are the dynamic similarities, and they are similar initial pressure and similar abandonment pressure. The denominator of the similarity criteria π_9 is the expression of open flow capacity, which means that the ratio of the experimental production rate to the core open flow capacity should be consistent with the ratio of the field production and the gas well open flow capacity, which is consistent with the production of 1/3 and 1/6 based on the open flow capacity, and the significance of the similarity criteria π_9 is to establish relative production. The similarity criteria π_{10} are the ratio of cumulative gas production to dynamic reserves, which reflects the degree of gas

recovery. According to calculations and statistics, the compact gas reservoir prototype similarity criteria π_{10} are between 0 and 0.6, and the physical experiment π_{10} is between 0 and 0.95, and thus, the similarity criteria are basically the same. It can be seen from the comparison between the similarity criteria of the physical experiment and the actual value of the field in Table 4 that they are the same basically, and so, the dynamic physical experiment of tight gas reservoir development can basically realize the effective simulation of the field.

4.2. Similarity Conversion. According to the similarity criterion π_9 , the velocity at the core outlet corresponds to the contribution of a single fracture to the gas well, which can be described as follows.

$$q_{sc} = \frac{bhKK_{rg}T_{sc}P_i^2}{a\mu zTP_{sc}} \left(\frac{qL\mu zTP_{sc}}{\pi R_1 R_2 K K_{rg} T_{sc} P_i^2} \right)_m, \quad (10)$$

where the subscript m is the experimental parameter.

Then, the horizontal well production is written as

$$q = n_f q_{sc}. \quad (11)$$

Based on the similar criteria π_{10} and the experimental time t_m , the actual production time in the field can be calculated as follows.

$$t = \frac{bha\phi S_w T_{sc} P_i}{qzTP_{sc}} \left(\frac{zTP_{sc} t_m}{\pi R_1 R_2 L \phi S_w T_{sc} P_i} \right) q_m. \quad (12)$$

According to the similarity criteria π_8 and material model core pressure P_j , the pressure P at different positions during the development process is calculated. Thus, the bottom hole pressure of gas well can be calculated based on the pressure at the outlet end of the physical model core.

$$P = P_i \left(\frac{P_j}{P_i} \right)_m. \quad (13)$$

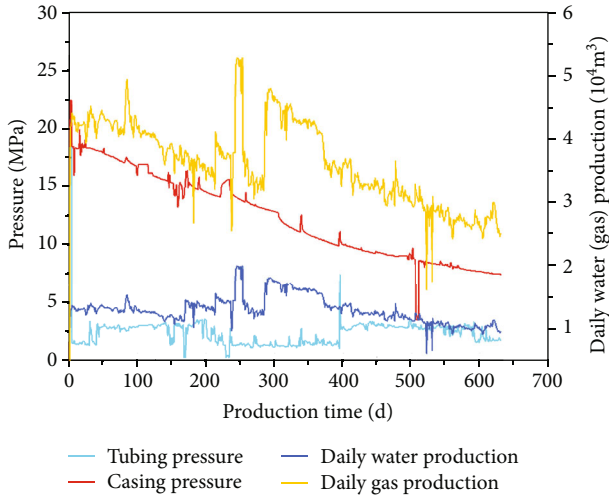


FIGURE 11: The production performance curve of Su-1 well.

4.3. Application of Similarity Criteria. To verify the accuracy of similarity criteria in the field, the Su-1 well of Sulige gas field was selected in this study, and they are similar in the reservoir characteristics. The original formation pressure of the reservoir is 29.23 MPa, and the reservoir thickness is 13.6 m, and the porosity, the water saturation, and the reservoir temperature are 8.7%, 42%, and 373.15 K, respectively. The length of the horizontal well is 1045 m, and the number of reconstruction sections is 8, and the length of the fracture is 90 m. Since April 2011, the production has started at $4.2 \times 10^4 \text{ m}^3/\text{d}$ in the initial stage and gradually decreased to about $2.5 \times 10^4 \text{ m}^3/\text{d}$ in the later stage. The average daily gas production is about $3.48 \times 10^4 \text{ m}^3/\text{d}$, and there is a small amount of water in the process, and the related production performance is shown in Figure 11.

According to the similarity π_g , the average daily gas production of the Su-1 well is $3.48 \times 10^4 \text{ m}^3/\text{d}$, which corresponds to the experimental flow rate of 100 mL/min. Based on the experimental result and the similarity criteria, the production performance curve can be calculated as shown in Figure 12. From the result of Figure 12, it can be seen that the production performance curve calculated by the experimental result and the similarity criterion is basically consistent with the actual gas production performance curve in the field. There exists a slight deviation, and the reason is that the influence of the fracture conductivity, the wellbore flow, and other production factors are not considered. Thus, the production prediction of gas reservoir development can be carried out based on similar criteria and the physical experiments.

5. Conclusions

The variation law of reserve utilization in tight sandstone gas reservoirs development was studied using the multipoint embedded measurement system, and the effects of the utilization of reservoir were analyzed. Besides, the effective conversion relationship between the physical experiment and the actual field production was established by the dimensional analysis. The conclusions are as follows:

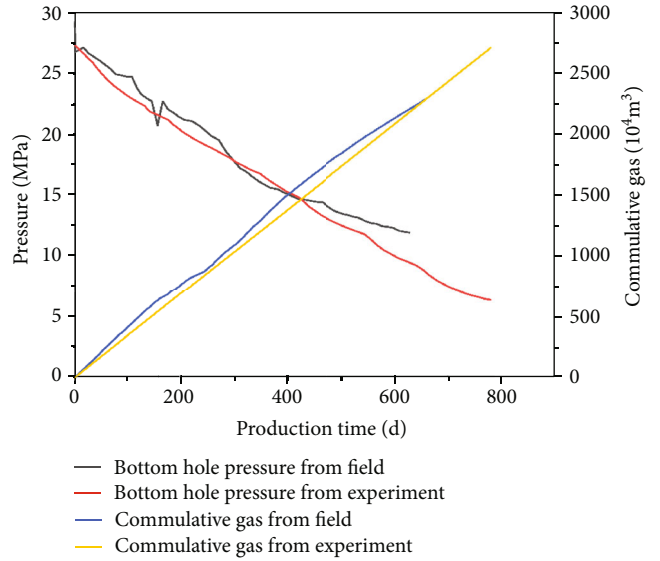


FIGURE 12: Model experiment and similarity transformation results of Su-1 well.

- (1) The multipoint embedded measurement system can accurately measure the pressure changes at different positions on the core section during the gas reservoir development. Selected 30 cm long core can weaken the effect of end surface and overcome the unreality of splicing long cores, and the experimental results are more representative of real reservoirs.
- (2) The water cut of tight sandstone gas reservoir has an impact on the gas flow characteristics and thus reduces the ultimate recovery. The lower the permeability is, the higher the effect of water on the reservoir utilization is, which is reflected in the drawdown curve as the drawdown curve is nonlinearly enhanced. The higher the reservoir pressure is, the lower the gas production rate is, and the smoother the drawdown curve is and the higher the ultimate utilization of the reservoir is.
- (3) There exists a moving boundary effect in the development of tight gas reservoirs. The velocity of the moving boundary becomes large and then reduces smaller, and the moving boundary will gradually expand with time. The water cut in the reservoir will reduce the velocity of the moving boundary.
- (4) Based on the similarity theory, the production performance curve calculated by the experimental result is basically consistent with that in the field. However, there exists a slight deviation between them as a result of the effects of the fracture conductivity, the wellbore flow, and other production factors.

Data Availability

The data used to support the findings of this study are available from the first author upon request.

Conflicts of Interest

The authors declare that there are no conflicts of interest regarding the publication of this paper.

Acknowledgments

This work is financially supported by the project of the National Natural Science Foundation of China (Nos. U1762216 and 11802312), National Science and Technology Major Project of the Ministry of Science and Technology of China (No. 2017ZX05030003), and Scientific Research and Technology Development Project of China National Petroleum Corporation (No. 2019B-1507). We thank the support from the Youth Foundation of Key Laboratory for Mechanics in Fluid Solid Coupling Systems, Chinese Academy of Sciences.

References

- [1] W. Wang, Y. Jiang, R. Swennen, J. Yuan, J. Liu, and S. Zhang, "Utility of inclusions for interpreting reservoir thresholds for tight sandstone gas accumulation in the Longfengshan and Dongling sags, Southeast China," *Journal of Natural Gas Science and Engineering*, vol. 61, pp. 270–283, 2019.
- [2] A. G. Oluwadebi, K. G. Taylor, and L. Ma, "A case study on 3D characterisation of pore structure in a tight sandstone gas reservoir: the Collyhurst Sandstone, East Irish Sea Basin, northern England," *Journal of Natural Gas Science and Engineering*, vol. 68, p. 102917, 2019.
- [3] B. Dong, M. Meng, Z. Qiu, Z. Lu, Y. Zhang, and H. Zhong, "Formation damage prevention using microemulsion in tight sandstone gas reservoir," *Journal of Petroleum Science and Engineering*, vol. 173, pp. 101–111, 2019.
- [4] X. Z. Li, Z. GUO, Y. WAN et al., "Geological characteristics and development strategies for Cambrian Longwangmiao formation gas reservoir in Anyue Gas Field, Sichuan Basin, SW China," *Petroleum Exploration and Development*, vol. 44, no. 3, pp. 428–436, 2017.
- [5] J. Zhang, X. Li, W. Shen et al., "Study of the effect of movable water saturation on gas production in tight sandstone gas reservoirs," *Energies*, vol. 13, no. 18, p. 4645, 2020.
- [6] K. Xie, X. Lu, H. Pan et al., "Analysis of dynamic imbibition effect of surfactant in microcracks of reservoir at high temperature and low permeability," *SPE Production & Operations*, vol. 33, no. 3, pp. 596–606, 2018.
- [7] W. J. Shen, F. Q. Song, X. Hu, G. M. Zhu, and W. Y. Zhu, "Experimental study on flow characteristics of gas transport in micro- and nanoscale pores," *Scientific Reports*, vol. 9, article 10196, no. 1, 2019.
- [8] Z. Sun, X. Li, W. Liu, T. Zhang, M. He, and H. Nasrabadi, "Molecular dynamics of methane flow behavior through realistic organic nanopores under geologic shale condition: pore size and kerogen types," *Chemical Engineering Journal*, vol. 398, p. 124341, 2020.
- [9] M. Q. Wei, Y. G. Duan, M. Z. Dong, Q. T. Fang, and M. Dejam, "Transient production decline behavior analysis for a multi-fractured horizontal well with discrete fracture networks in shale gas reservoirs," *Journal of Porous Media*, vol. 22, no. 3, pp. 343–361, 2019.
- [10] H. Zhang, Y. Zhong, E. Kuru, J. Kuang, and J. She, "Impacts of permeability stress sensitivity and aqueous phase trapping on the tight sandstone gas well productivity - a case study of the Daniudi gas field," *Journal of Petroleum Science and Engineering*, vol. 177, pp. 261–269, 2019.
- [11] H. Pascal, "Nonsteady flow through porous media in the presence of a threshold gradient," *Acta Mechanica*, vol. 39, no. 3–4, pp. 207–224, 1981.
- [12] W. G. Feng and J. L. Ge, "Single medium, the double medium unsteady seepage Darcy velocity," *Petroleum Exploration and Development*, vol. 12, no. 1, pp. 56–62, 1985.
- [13] R. A. Wattenbarger, A. H. El-Banbi, M. E. Villegas, and J. B. Maggard, "Production analysis of linear flow into fractured tight gas wells," in *Proceedings of SPE Rocky Mountain Regional/Low-Permeability Reservoirs Symposium*, pp. 1–12, Denver, Colorado, 1998.
- [14] Y. E. Deng and C. Q. Liu, "Mathematical model of nonlinear flow law in low permeability porous media and its application," *Acta Mechanica Sinica*, vol. 30, no. 4, pp. 72–77, 2001.
- [15] B. Z. Hsieh, G. V. Chilingar, and Z. S. Lin, "Propagation of radius of investigation from producing well," *Energy Sources, Part A: Recovery, Utilization, and Environmental Effects*, vol. 29, no. 5, pp. 403–417, 2007.
- [16] G. Q. Feng, Q. G. Liu, G. Z. Shi, and Z. H. Lin, "An unsteady seepage flow model considering kickoff pressure gradient for low-permeability gas reservoirs," *Petroleum Exploration and Development*, vol. 35, no. 4, pp. 457–461, 2008.
- [17] X. D. Wang, X. C. Hou, M. Q. Hao, and T. Yang, "Pressure transient analysis in low-permeable media with threshold gradients," *Acta Mechanica Sinica*, vol. 32, no. 5, pp. 847–851, 2011.
- [18] B. Y. Ji and Y. F. He, "Formation pressure distribution of a single well based on low-velocity non-Darcy flow," *Acta Mechanica Sinica*, vol. 32, no. 3, pp. 466–469, 2011.
- [19] M. Nobakht and C. R. Clarkson, "A new analytical method for analyzing linear flow in tight/shale gas reservoirs: constant-flowing-pressure boundary condition," *SPE Reservoir Evaluation & Engineering*, vol. 15, no. 3, pp. 370–384, 2013.
- [20] M. Nobakht and C. R. Clarkson, "A new analytical method for analyzing linear flow in tight/shale gas reservoirs: constant-rate boundary condition," *SPE Reservoir Evaluation & Engineering*, vol. 15, no. 1, pp. 51–59, 2013.
- [21] S. Huang, Y. D. Yao, R. Y. Ma, and J. W. Wang, "Analytical model for pressure and rate analysis of multi-fractured horizontal wells in tight gas reservoirs," *Journal of Petroleum Exploration and Production Technology*, vol. 9, pp. 383–396, 2018.
- [22] H. U. Yong, L. I. Xizhe, Y. WAN et al., "Physical simulation on gas percolation in tight sandstones," *Petroleum Exploration and Development*, vol. 40, no. 5, pp. 621–626, 2013.
- [23] Q. N. Yu, Y. K. Liu, S. Liang, X. Liu, D. Yao, and Y. Yu, "Experimental study on seepage flow patterns in heterogeneous low-permeability reservoirs," *Journal of Petroleum Exploration and Production Technology*, vol. 8, no. 2, pp. 589–596, 2018.
- [24] M. G. Lewis, M. M. Sharma, H. H. Dunlap, and M. H. Dorfman, "Techniques for measuring the electrical properties of sandstone cores," in *Proceedings of SPE Annual Technical Conference and Exhibition*, pp. 1–7, Houston, Texas, 1988.
- [25] H. S. Han, S. Li, D. S. Ma, Z. M. Ji, H. W. Yu, and X. L. Chen, "Investigation of flue gas displacement and storage after the water flooding in a full diameter conglomerate long-core,"

- Petroleum Exploration and Development*, vol. 45, no. 5, pp. 847–852, 2018.
- [26] X. L. Li, Z. Q. Li, P. Guo, H. C. Li, and X. S. Li, “Long core physical simulation for CO₂ miscible displacement,” *Petroleum Exploration and Development*, vol. 31, no. 5, pp. 102–104, 2004.
- [27] D. W. Meng, A. L. Jia, G. Ji, and D. B. He, “Water and gas distribution and its controlling factors of large scale tight sand gas fields: a case study of western Sulige gas field, Ordos Basin, NW China,” *Petroleum Exploration and Development*, vol. 43, no. 4, pp. 663–671, 2016.
- [28] T. Ahmed, “Reservoir Engineering Handbook,” in *Gulf Professional Publishing*, Imprint Elsevier, Oxford, UK, 4th edition, 2010.
- [29] R. J. Schilthuis, “Active oil and reservoir energy,” *Transactions of the AIME*, vol. 118, no. 1, pp. 33–52, 2013.
- [30] C. S. Kabir, B. Parekh, and M. A. Mustafa, “Material-balance analysis of gas and gas-condensate reservoirs with diverse drive mechanisms,” *Journal of Natural Gas Science and Engineering*, vol. 32, pp. 158–173, 2016.
- [31] X. H. Ma, A. Jia, J. Tan, and D. B. He, “Tight sand gas development technologies and practices in China,” *Petroleum Exploration and Development*, vol. 39, no. 5, pp. 572–579, 2012.
- [32] X. M. Xiao, B. Q. Zhao, Z. L. Thu, Z. G. Song, and R. W. T. Wilkins, “Upper Paleozoic petroleum system, Ordos Basin, China,” *Marine and Petroleum Geology*, vol. 22, no. 8, pp. 945–963, 2005.
- [33] L. A. Høy, P. Papatzacos, and S. M. Skjævel, “Critical rate for water coning: correlation and analytical solution,” *SPE Reservoir Evaluation & Engineering*, vol. 4, pp. 495–502, 1989.
- [34] J. J. Arps, “Estimation of primary oil reserves,” *Petroleum Transactions, AIME*, vol. 207, pp. 182–191, 1956.
- [35] C. Q. Liu, “Approximate solution of a starting gradient ratio consolidation problem,” *Chinese Journal of Geotechnical Engineering*, vol. 4, no. 3, pp. 107–109, 1982.
- [36] J. DAI, N. I. Yunyan, and W. U. Xiaoqi, “Tight gas in China and its significance in exploration and exploitation,” *Petroleum Exploration and Development*, vol. 39, no. 3, pp. 277–284, 2012.
- [37] X. Z. Li, X. H. Liu, Y. H. Sun et al., “Correlation between perwell average dynamic reserves and initial absolute open flow potential (AOFPP) for large gas fields in China and its application,” *Petroleum Exploration and Development*, vol. 45, no. 6, pp. 1088–1093, 2018.
- [38] M. Vishkai and I. Gates, “On multistage hydraulic fracturing in tight gas reservoirs: Montney Formation, Alberta, Canada,” *Journal of Petroleum Science and Engineering*, vol. 174, pp. 1127–1141, 2019.
- [39] Sedov, *Similar methods and dimension theory in mechanics*, Science Press, Beijing, China, 1982.
- [40] J. Worstell, “Mechanical/physical examples of dimensional analysis,” in *Dimensional Analysis*, Elsevier Inc, Oxford, UK, 2014.

Research Article

A New Methodology for the Multilayer Tight Oil Reservoir Water Injection Efficiency Evaluation and Real-Time Optimization

Lin Cao,^{1,2} Jianlong Xiu ,³ Hongjie Cheng,⁴ Hui Wang,⁵ Shujian Xie,⁶ Hui Zhao,⁶ and Guanglong Sheng⁶

¹School of Engineering Science, University of Chinese Academy of Sciences, Beijing 100049, China

²Institute of Porous Flow & Fluid Mechanics, Chinese Academy of Sciences, Langfang 065007, China

³PetroChina Research Institute of Petroleum Exploration & Development, Beijing 100083, China

⁴Exploitation and Development Research Institute, PetroChina Xinjiang Oilfield Company, Karamay, Xinjiang 834000, China

⁵The No. 2 Oil Production Plant, PetroChina Xinjiang Oilfield Company, Karamay, Xinjiang 834000, China

⁶College of Petroleum Engineering, Yangtze University, Wuhan, Hubei 430100, China

Correspondence should be addressed to Jianlong Xiu; xiujianlong69@petrochina.com.cn

Received 10 June 2020; Revised 20 August 2020; Accepted 21 August 2020; Published 10 November 2020

Academic Editor: Wei Wei

Copyright © 2020 Lin Cao et al. This is an open access article distributed under the Creative Commons Attribution License, which permits unrestricted use, distribution, and reproduction in any medium, provided the original work is properly cited.

It is important to determine the reasonable injection and production rates in the development of multilayer tight oil reservoir with water flooding treatment. Based on the INSIM (interconnection-based numeric simulation model), a connected network model, a new method is designed to evaluate the water injection efficiency of different layers in water flooding reservoirs and to optimize the injection-production system to produce more oil. Based on the types of sedimentary facies and corresponding injection-production data, the interwell connections are divided into four major categories (middle channel, channel edge, middle channel bar, and channel bar edge) and twelve subclasses. This classification standard of interwell connections could help to significantly improve the accuracy of judging the dominant flow path without constructing a complicated geological model. The interaction of interwells such as injection-production correlation and water injection efficiency could be revealed by simulating the production performance and computing the layer dividing coefficient and well dividing coefficient. A numerical example is used to validate this method by comparing results from FrontSim and this method, and the computational efficiency of this method is several dozen times faster than that of the traditional numerical simulation. This method is applied to quickly optimize the production schedule of a tight oil reservoir with the water flooding treatment, that is, the water injection rate of multilayer reservoirs could be optimized subtly by the injection efficiency of different layers, and the target of producing more oil with lower water cut could be achieved.

1. Introduction

Waterflooding operations are performed to improve the oil recovery of reservoirs worldwide [1]. In some oil fields with many wells and a long production history, the wide expansion of the injection water and the continuous changes in the flow field in the layer results in water channeling and dead oil areas [2, 3]. These problems are mainly due to two factors. First, the physical properties of the reservoir are affected by the sedimentary environment, tectonic movement, and diagenesis; there are intralayer and interlayer heterogeneities in the reservoir.

Second, unreasonable injection and production systems have exacerbated the phenomenon of injection water fingering and bottom water coning. Therefore, based on the existing reservoir development knowledge, it is important to identify the injection-production correspondence, to accurately determine the dominant flow path, and to evaluate the injection efficiency of the injectors [4, 5]. This forms both the key issue and the basic work to increase the high economic value oil production and to determine a reasonable injection-production system [6, 7].

Due to the relatively poor physical properties of tight oil reservoirs, the following measures were used to optimize

the development effect currently, including fracturing [8], asynchronous injection alternating production [9], water flooding huff-puff of horizontal wells [10], and CO₂ huff and puff of horizontal wells [11]. Flow paths can reflect the flow behavior of fluid in a period of time, so it is often used to evaluate the development effect of reservoir under a certain working system. Commonly used methods for distinguishing flow paths include the tracer method, reservoir numerical simulations [12–14], and data-driven models. The tracer test incurs significant time to acquire results, and some operations during the test have a certain impact on the normal reservoir production. In multilayer waterflooding reservoir, the capillary forces may have a significant effect to change the flow pathways [15]. Therefore, although this method has high accuracy, it is difficult to popularize and to apply on a large scale in a reservoir. Reservoir numerical simulation methods are restricted by model accuracy, and it is difficult to achieve accurate real-time analysis of the entire reservoir. Data-driven models, as part of a new class of dominant flow path identification methods, do not require complex geological modeling and can determine information such as fluid flow dynamics and water injection efficiency through the analysis of the production data. There are currently two kinds of data-driven models, namely, the CRM (capacitance-resistive model) and the INSIM (interconnection-based numeric simulation model). The CRM was first used by Yousef et al. [16] to determine the connectivity between wells in 2005. Following that, the model was used in waterflooding reservoirs [17], large-scale reservoirs [18], and analysis of the formation damage from injected water [19]. Zhao et al. [20] proposed the INSIM in 2015. By simplifying the characterization of the reservoir as a network of interconnected nodes that consider a series of complex geological features such as wells, water bodies, and faults, an interwell connection network is established. It is characterized by two parameters, connected volume and transmissibility, to fit the actual production dynamics, to correct the interwell connection parameters, and to make the model conform to the actual connectivity of the reservoir. Because a complex geological modeling process is not considered, the INSIM and its derived INSIM-FT (interconnection-based numeric simulation model with front-tracking algorithm) [21–22] and INSIM-FPT (interconnection-based numeric simulation model with the flow-path tracking strategy) [23] reduce the modeling time significantly, while considering reservoir properties and maintaining the calculation accuracy. Based on the distribution of sedimentary facies in each layer, this study identifies the influence of different sedimentary environments on the interwell connection relationship of INSIM. The pressure, saturation, and water cut of each node are solved by the connection parameters corrected by production data combined with the principle of material balance. Then, the vertical/plane dividing coefficient and water injection efficiency of the injector are obtained. Based on this, the water injection efficiency of each layer is calculated and combined by the optimization principle to optimize the injection and production systems [24, 25].

Since the main factors affecting the accuracy of the water injection efficiency evaluation method are INSIM's

modeling data and the model's historical fitting results, the method has good general applicability to the reservoirs applicable to INSIM. At present, the INSIM model has been widely used in sand reservoirs, carbonate reservoirs, fracture-cavity reservoirs, etc. This method has certain practical significance for evaluating the water injection efficiency of these types of reservoirs. Compared with the traditional reservoir numerical simulation method [26, 27], the calculation speed of the water injection efficiency is significantly improved. It is of great significance to accurately identify the injection-production correspondence relationship and increase oil production at a lower cost.

2. Water Injection Efficiency Evaluation Method and Optimization Theory

2.1. The Calculation of Water Injection Dividing Coefficient Based on INSIM. The interwell connection unit constructed by the INSIM model contains two characterization parameters: transmissibility and connection volume. Transmissibility represents the flow capacity of formation fluids in units under unit pressure difference, which is mainly affected by permeability and fluid properties. Connection volume reflects the material basis of units, mainly related to well spacing, effective thickness, and porosity of the reservoir. After establishing the INSIM (Figure 1), the material balance equation of the fluid in the connected unit can be obtained by

$$\sum_{k=1}^{N_i} \sum_{j=1}^{N_w} T_{ijk}(t) (p_j(t) - p_i(t)) + q_i(t) = \frac{1}{2} \frac{dp_i(t)}{dt} \sum_{k=1}^{N_i} C_{tk} \sum_{j=1}^{N_w} V_{ijk}(t). \quad (1)$$

The implicit difference discretization of Equation (1) can solve the bottom hole pressure of each well, then saturation and water cut of each node in the connected network can be calculated with the saturation-tracking method. Fitting the actual production data to correct the connection parameters is conducted to align the production result of the model with the actual production. Let the feature parameter matrix b denote the reservoir connectivity parameter, applying the stochastic perturbation approximate gradient algorithm (SPSA) to optimize the objective function $O(b)$ causes it to have a minimum value.

$$O(b) = \frac{1}{2} (b - b_r)^T G_B^{-1} (b - b_r) + \frac{1}{2} [k_{\text{obs}} - h(b)]^T G_D^{-1} [k_{\text{obs}} - h(b)] \quad (b \geq 0). \quad (2)$$

Using percolation theory and interwell connection parameters, the production index in the cross-well connectivity unit can be expressed as

$$J_{ijk}^n = \frac{4T_{ijk}^n \lambda_{ik}^{n-1}}{\lambda_{ijk}^{n-1} [\ln(0.5L_{ijk}/r_{ik}) + s_{ik} - 0.75]}. \quad (3)$$

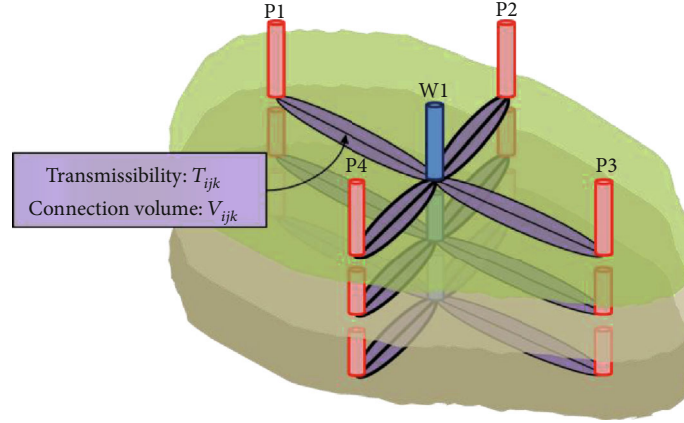


FIGURE 1: A sketch map of the INSIM in a multilayer reservoir.

Combining the bottom hole pressure and the production index, the phase mobility in the connected unit is determined by the upstream weight method:

$$\lambda_{ijk}^n = \begin{cases} \lambda_{ik}^{n-1} = K_{ijk} \left[\frac{K_{ro}(S_{wik}^{n-1})}{\mu_{ok}} + \frac{K_{rw}(S_{wik}^{n-1})}{\mu_{wk}} \right] & p_i^{n-1} \geq p_j^{n-1}, \\ \lambda_{jk}^{n-1} = K_{ijk} \left[\frac{K_{ro}(S_{wik}^{n-1})}{\mu_{ok}} + \frac{K_{rw}(S_{wik}^{n-1})}{\mu_{wk}} \right] & p_i^{n-1} < p_j^{n-1}. \end{cases} \quad (4)$$

Based on the above method, the total production index of well i can be determined:

$$J_i^n = \sum_{k=1}^{N_l} \sum_{j=1}^{N_w} J_{ijk}^n. \quad (5)$$

Therefore, the vertical dividing coefficient of well i in layer k is determined by the ratio of the sum of the production index of well i in layer k to the total production index of well i :

$$A_{ik}^n = \frac{J_{ik}^n}{J_i^n} = \frac{\sum_{j=1}^{N_w} J_{ijk}^n}{\sum_{k=1}^{N_l} \sum_{j=1}^{N_w} J_{ijk}^n}. \quad (6)$$

Meanwhile, the plane dividing the coefficient between wells i and j is determined by the transmissibility between the nodes and the pressure difference:

$$A_{ijk}^n = \frac{q_{ijk}^n}{q_{ik}^n} = \frac{T_{ijk}^n (p_j^n - p_i^n)}{\sum_{j=1}^{N_w} T_{ijk}^n (p_j^n - p_i^n)}. \quad (7)$$

Compared to the dividing coefficient calculation method proposed in this study, the reservoir engineering

method does not consider changes in pressure and uses only the percolation theory to calculate the dividing coefficient from the well properties.

$$A_{ik}^n = \frac{\sum_{j=1}^{N_w} (\overline{K}_{ij} \cdot \overline{h}_{ij} / L_{ij})}{\sum_{k=1}^{N_l} \sum_{j=1}^{N_w} (\overline{K}_{ij} \cdot \overline{h}_{ij} / L_{ij})}, \quad (8)$$

$$A_{ijk}^n = \frac{\overline{K}_{ij} \cdot \overline{h}_{ij} / L_{ij}}{\sum_{j=1}^{N_w} (\overline{K}_{ij} \cdot \overline{h}_{ij} / L_{ij})}. \quad (9)$$

2.2. Water Injection Efficiency Calculation and Optimization. After clarifying the dividing coefficient in each layer, the layered water injection efficiency of the injectors can be solved further, that is, the ratio of the amount of oil displaced by the injector to the surrounding producers in this layer and the water injection amount of this layer. The ratio of the total oil production of layer k to the total water injection of layer k is the average water injection efficiency of layer k and is expressed as

$$e_{ik}^n = \frac{\sum_{j=1}^{N_w} q_{ik}^n A_{ijk}^n (1 - f_{wjk}^n)}{q_{ik}^n}, \quad (10)$$

$$e_{xk}^n = \frac{\sum_{i=1}^{N_l} \sum_{j=1}^{N_w} q_{ik}^n A_{ijk}^n (1 - f_{wjk}^n)}{\sum_{i=1}^{N_l} q_{ik}^n}. \quad (11)$$

After obtaining the water injection efficiency of each well in this layer, it should be compared with the average water injection efficiency of this layer to determine the liquid volume adjustment measures. When the water injection efficiency is higher than the average, the injection is increased; otherwise, the injection is reduced, and the liquid volume of each well in this layer is determined by Equations (12) and (13).

$$q_{ik}^{n+1} = q_{ik}^n (1 + \eta_i), \quad (12)$$

$$\eta_i = \begin{cases} \eta_{\max} \left(\frac{e_{ik}^n - e_{xk}^n}{e_{\max}^n - e_{xk}^n} \right)^\alpha, & e_{ik}^n < e_{xk}^n \\ \eta_{\min} \left(\frac{e_{xk}^n - e_{ik}^n}{e_{xk}^n - e_{\min}^n} \right)^\alpha, & e_{ik}^n > e_{xk}^n \end{cases} \quad (13)$$

In Equation (13), η_{\max} and η_{\min} are assigned to the values of -0.5 and 0.5, respectively. Because the fractional part value is less than or equal to 1, it means that the liquid volume adjustment range for the next time step will not be greater than 50% of the liquid volume in the previous time step. As the injection volume of the reservoir will not change significantly in a short time, to keep the injection volume of the entire reservoir constant, it is necessary to adjust the injection volume of each layer according to Equation (14). The well water injection volume is equal to the sum of the injection volume of each layer, as shown in Equation (15).

$$q_{ik}^{(n+1)} = \frac{\sum_{i=1}^{N_i} \sum_{k=1}^{N_i} q_{ik}^n}{\sum_{i=1}^{N_i} \sum_{k=1}^{N_i} q_{ik}^{n+1}} q_{ik}^{n+1}, \quad (14)$$

$$q_i^{n+1} = \sum_{k=1}^{N_i} q_{ik}^{n+1}. \quad (15)$$

After determining the liquid volume adjustment of the injectors, assuming that the reservoir injection-production ratio in the optimization stage is constant, the liquid volume adjustment of the production well is calculated from the injection volume and the dividing coefficient, as shown in Equation (16).

$$q_j^{n+1} = q_j^n + \sum_{i=1}^{N_{ic}} \sum_{k=1}^{N_i} q_{ik}^{(n+1)} A_{ijk}^n. \quad (16)$$

3. The Conceptual Model

A two-layer model including five injectors and four producers is established to introduce the basic parameters of the INSIM and the workflow for calculating injection efficiency (IE). The producer-injector spacing is 200 m, and the thickness of each layer is 10 m. The range of permeability is 165.0 mD in the 1st layer and 171.6 mD in the 2nd layer, while the permeability field is shown in Figure 2. The initial oil saturation is 0.8. The viscosity of the formation water is 1.0 mPa s and the viscosity ratio of oil to water is 20. The daily water injection rate of each injector is 40 m³/d. Before 3000 days, the daily fluid production rate of each producers is 50 m³/d. From 3000–6000 days, the working system from P1 to P4 changes to 80 m³/d, 60 m³/d, 40 m³/d, and 20 m³/d, respectively, and the FrontSim streamline field is shown in Figure 3.

The initial value of the interwell connection parameters could be calculated from the well property data. Then, using the reservoir production data combined with the optimization theory, the initial value of the interwell connection parameters is corrected after the fitting indicators meet accu-

racy requirements. The final value of the interwell connection parameters is shown in Figure 4. The line between the wells shows the transmissibility of the reservoir; the red line indicates strong connectivity, the blue line indicates the second strongest connectivity, and the black line indicates weak connectivity. Upon comparing the distribution of strong connectivity with high permeability zones, these were found to be consistent. It shows that after correction, an INSIM could accurately characterize the reservoir properties and provide a reliable basis for calculating the dividing coefficient of injection water and evaluating the water injection efficiency.

In this study (Equation (6)), the reservoir engineering method (Equation (8)) and the streamline numerical simulation method are used to calculate the vertical dividing coefficient of each layer. Figures 5 and 6 show the difference between the calculation results of the INSIM method and other methods. From the result shown in Figure 6, the vertical dividing coefficient of the reservoir engineering method does not change because it does not consider the flow field change caused by the adjustment of the production system. However, the dominant seepage channel in the reservoir forms gradually and stabilizes with the development. Due to a superior physical property of the first layer in the model, the vertical dividing coefficient of the first layer gradually increases during the formation of the dominant seepage channel. Following the stabilization of the seepage channel, the vertical dividing coefficient also stabilizes. The method in this study and the streamline numerical method can reflect this law accurately.

Meanwhile, Equations (7) and (9) were used to calculate the plane dividing coefficient of the injection well at 6000 days. As shown in Figure 7, the plane dividing coefficient obtained based on this method is basically consistent with the results based on the streamline simulation, which verifies the reliability of this method. The reservoir engineering method cannot accurately reflect the plane dividing coefficient currently because it does not consider the changes in the reservoir production system. The streamline simulation method takes 25.54 seconds for one complete calculation. Compared to this method, the method in this study takes only 0.74 seconds for one complete calculation, which is faster by a factor of 35.

The single-well water injection efficiencies and average water injection efficiencies of the reservoir engineering method, streamline method, and method of this study are calculated using Equations (10) and (11), as shown in Figure 8. According to the reservoir engineering method, the water injection efficiency of each well is lower than the other two methods. Due to changes in the flow field, the division of injected water in each direction is different periodically. Some remaining oil is produced by adjusting the working system, and this volume of oil cannot be calculated using the reservoir engineering method. The method in this study solves this problem better by considering the change in the bottom hole pressure of each well, and the calculation results are basically consistent with the streamline method. By using the dividing coefficient and the water injection efficiency of the conceptual model in Equations (12), (13), (14), (15) and (16), the production system of each well in the optimization stage is calculated.

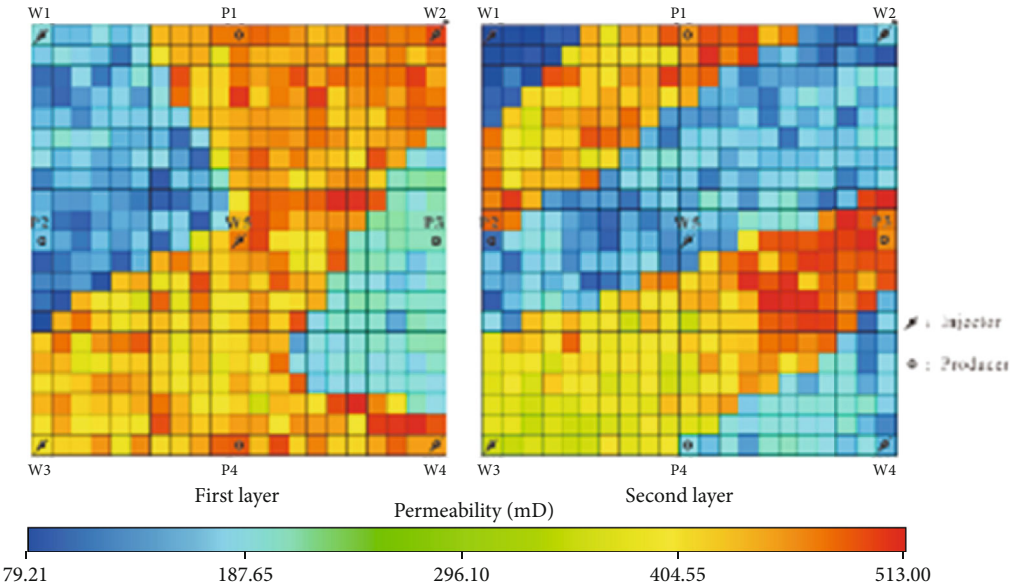


FIGURE 2: Model permeability field.

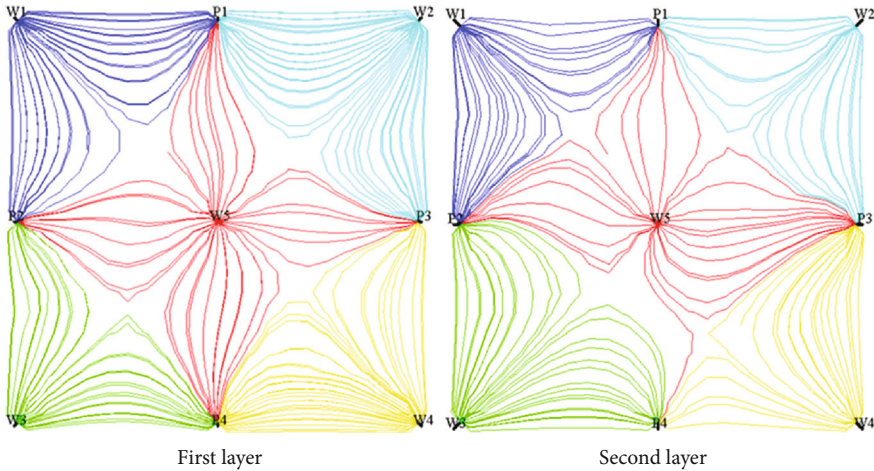


FIGURE 3: Streamline field in FrontSim.

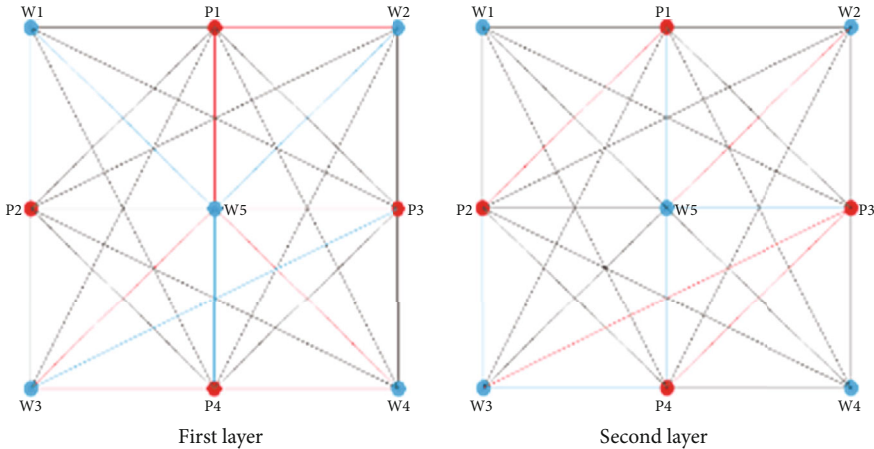


FIGURE 4: Model interwell connectivity field.

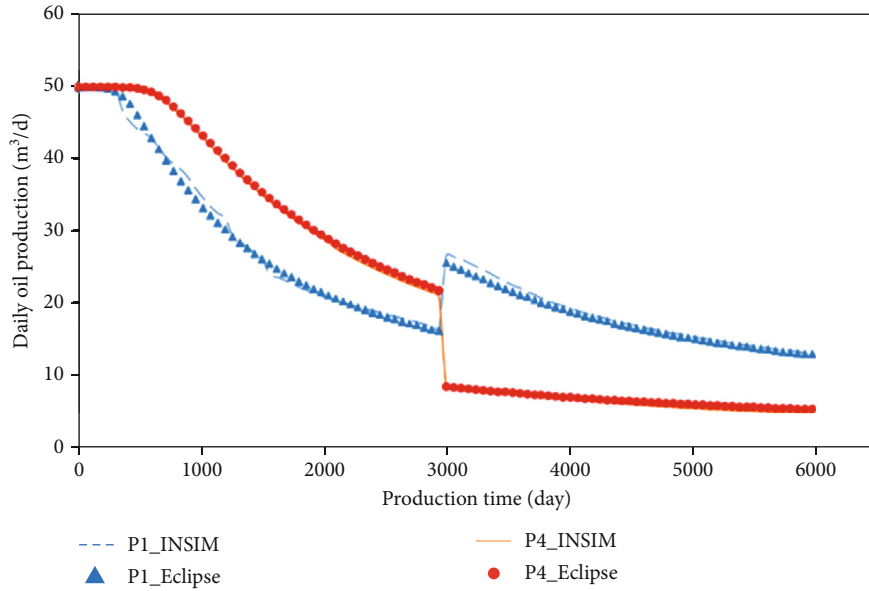


FIGURE 5: The fitting effect of daily oil production.

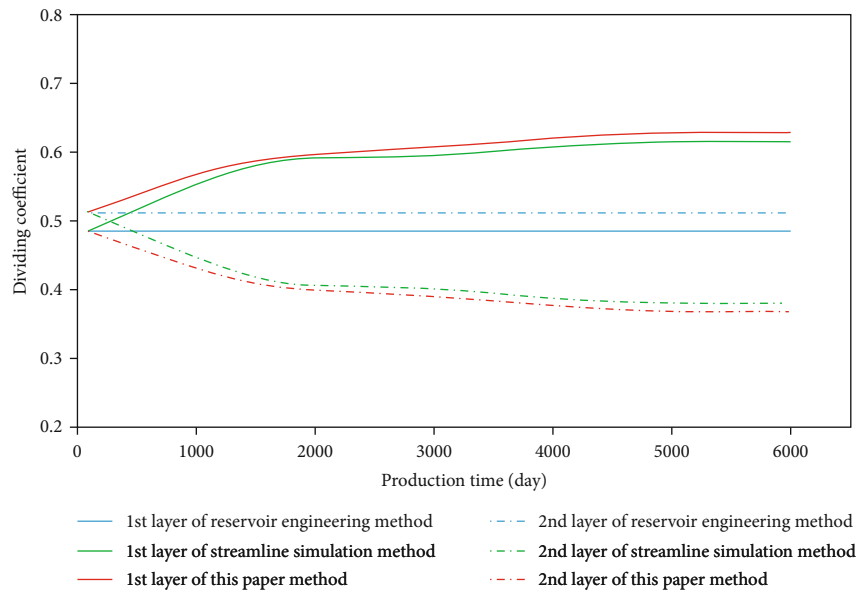


FIGURE 6: Vertical dividing coefficient of W5.

The production system of the original plan and the adjusted plan were brought into the Eclipse model to predict the oil production and the water cut of the reservoir after the implementation of the plan. As shown in Figure 9, five months after the implementation of the adjusted plan, the daily oil production of reservoir is increased, the comprehensive water cut of reservoir is decreased, and the adjusted plan had an optimized effect on the overall reservoir development.

4. Practical Applications

4.1. *The Characterization of the Interwell Connection and the Evaluation of the Water Injection Efficiency.* For the charac-

terization, the layered water injection efficiency evaluation method based on the INSIM was applied to a tight oil reservoir. The adjustments to the production system proposed in this method were implemented in the field, which achieved good development results. This tight oil reservoir is an edge water reservoir controlled by structural lithology. It has an oil-bearing area of 9.3 km^2 and an effective thickness of 26.3 m . The reservoir is divided into upper sandstone sections and lower conglomerate sections; a separated waterflooding and comingled producing technology is used between different rock sections. The average porosity of the reservoir was 16.9% , the average permeability was $182.27 \times 10^{-3} \mu\text{m}^2$, the central reservoir depth was 1650 m , and the geological reserves were $1530.70 \times 10^4 \text{ t}$. Since entering the

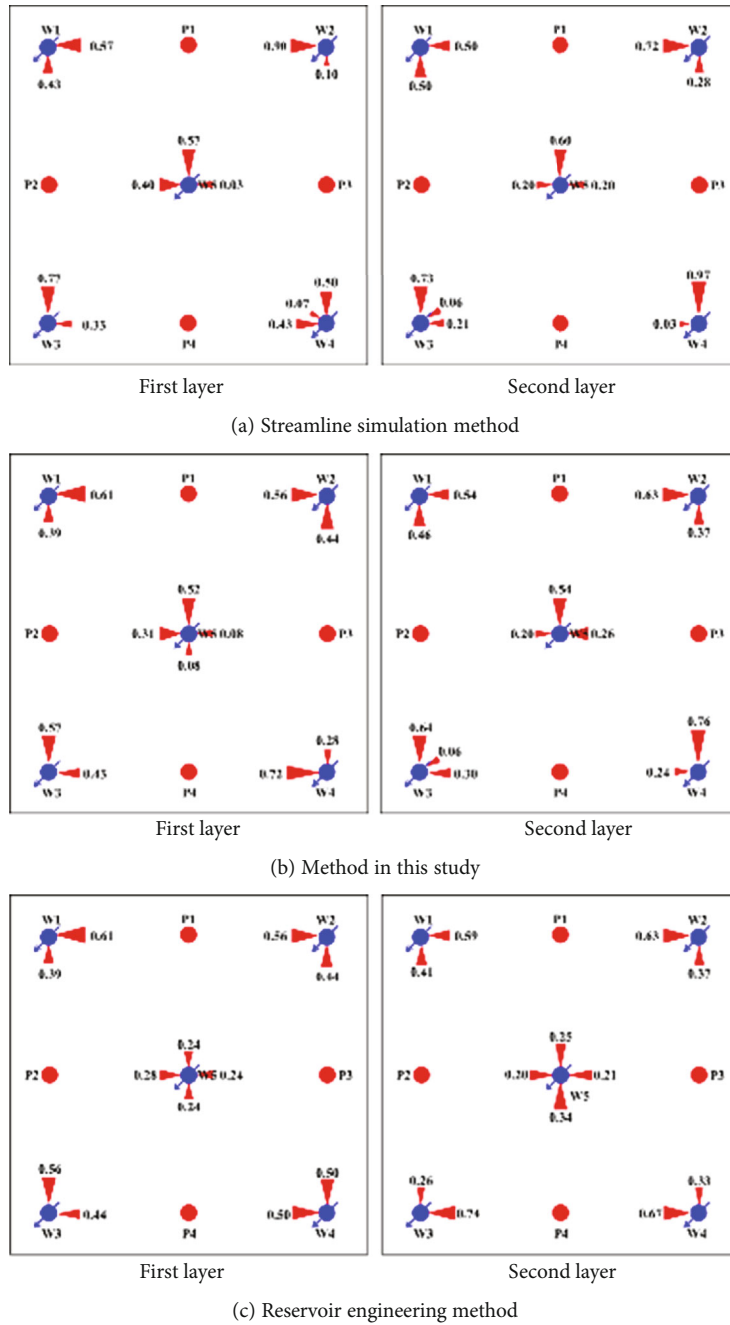


FIGURE 7: The plane dividing coefficient of injectors in 6000 d.

second development stage in 2016, a total of 213 new wells were deployed, accessing geological reserves of 1105.43×10^4 t, and the average well spacing was reduced to 150 m. At the end of June 2018, 96 water injection wells and 133 oil wells were opened. The daily liquid production was 2837 t, the daily oil production was 370 t, and the comprehensive water cut was 86.9%. The recycle of injection water is inefficient in such a high water cut reservoir.

After history matching the INSIM (Figure 10), the field interwell connection obtained by fitting the production dynamics is shown in Figure 11, in which the red line repre-

sents a strong connectivity, the green line represents the second strongest connectivity, and the black line represents weak connectivity.

Based on the sedimentary facies' types of reservoirs and the INSIM, an interwell connectivity classification standard is established, which reflects the similarities and differences in the various sedimentary facies. The orange area represents the channel bar, and the light yellow and bright yellow areas represent the river channels, as shown in Figure 12. Overall, the connectivity from sandstone to conglomerate in the vertical direction deteriorates, and the permeability decreases. In

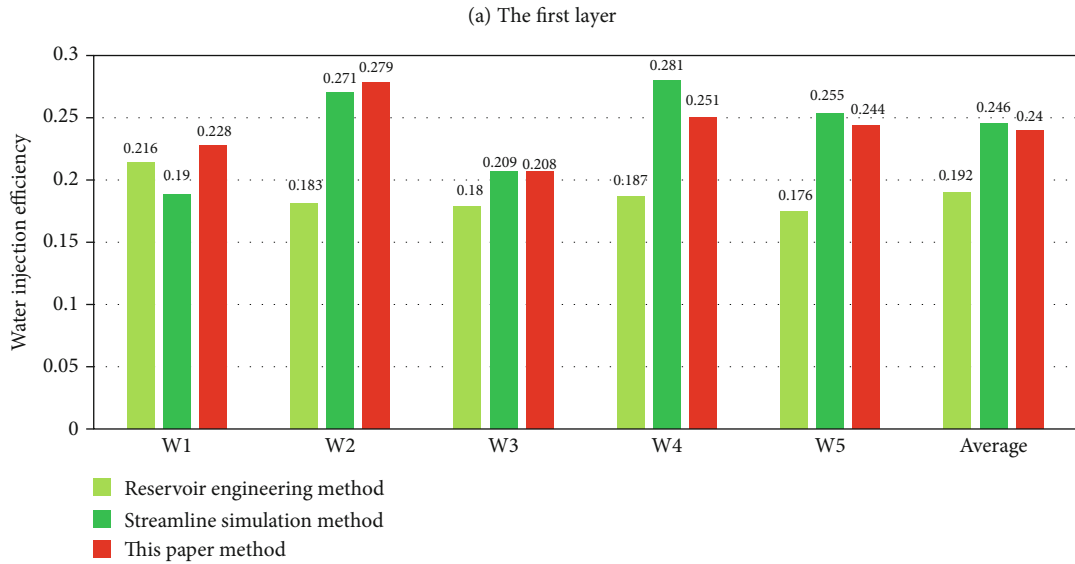
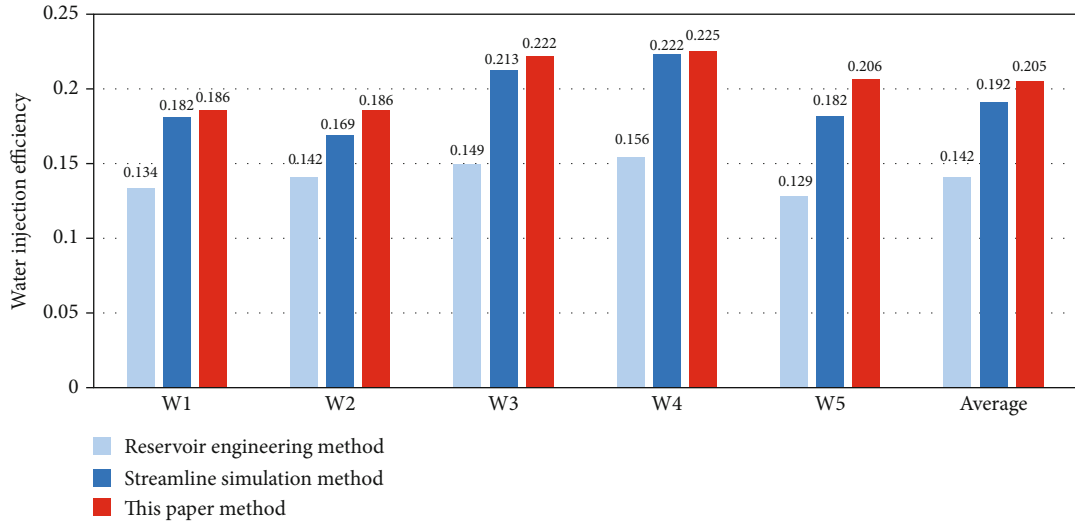


FIGURE 8: The water injection efficiency of injectors in three different methods.

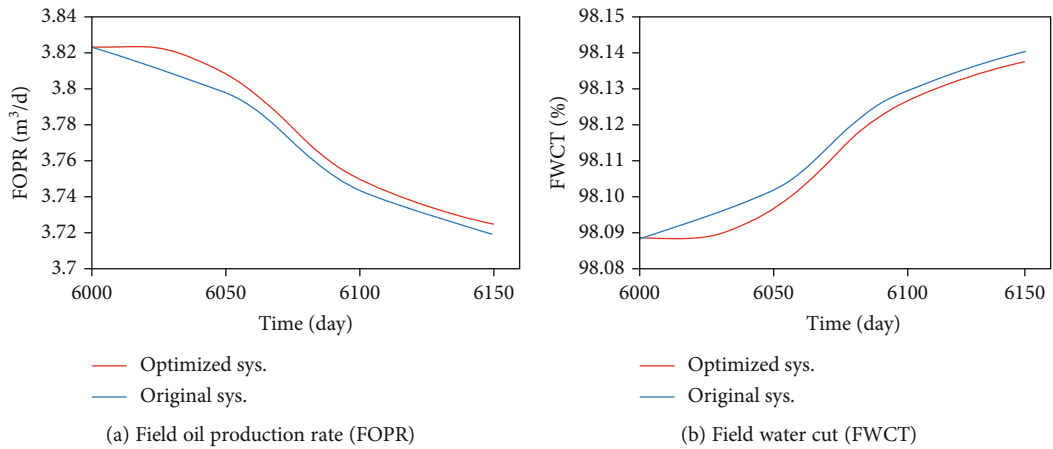


FIGURE 9: The comparison of optimized and original production systems.

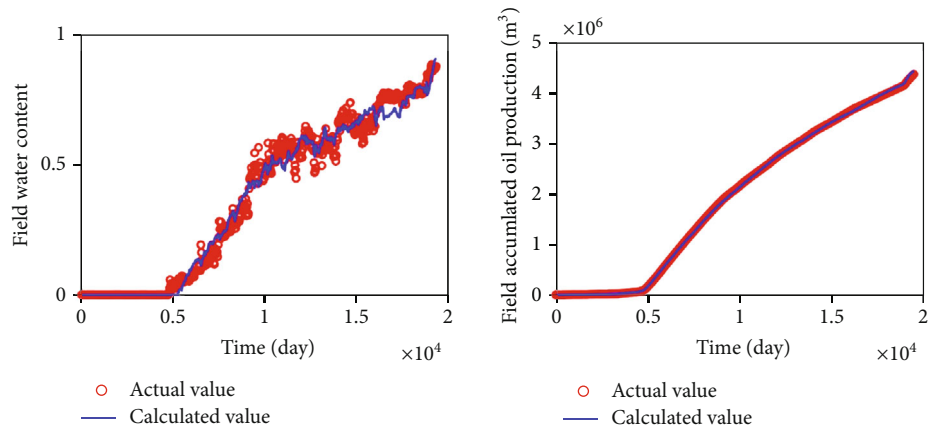


FIGURE 10: History matching results of the field water cut and total field oil production.

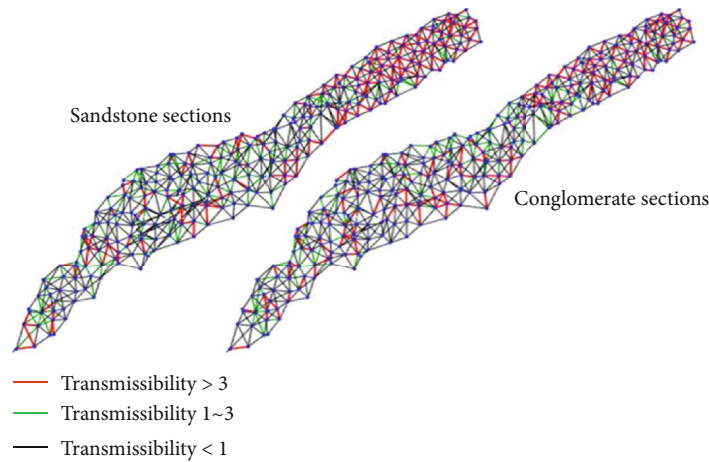


FIGURE 11: Reservoir interwell connectivity field.

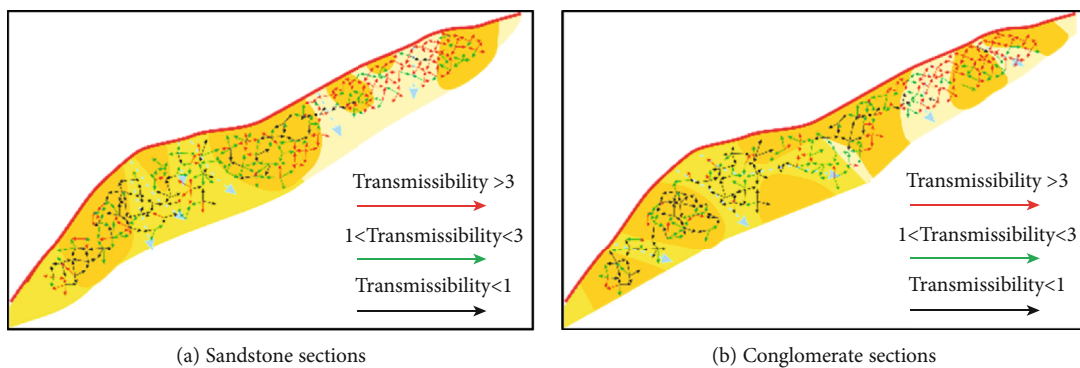


FIGURE 12: Interwell connectivity and sedimentary facies.

the plane, affected by source direction, the interwell connectivity from the southwest to the northeast improves and the permeability increases.

Combining the interwell connectivity with the sedimentary facies at the well nodes, the distribution pattern of the characteristics is obtained as shown in Table 1, which divides the interwell connectivity into four major categories and

twelve subcategories. The four types include the middle channel, the side of channel, the middle of the channel bar, and the side of the channel bar. Since the porosity of different sedimentary facies of the same section in this tight oil reservoir is not much different, the connection volume is mainly affected by the well spacing, and different types of connection units cannot be accurately distinguished. Therefore, when

TABLE 1: The interwell connection structure pattern.

Categories	Types	Connection types	Structure	Transmissibility	
Channel	Middle	Strong connection		>3	
		Medium-strength connection		1 ~ 3	
		Weak connection		<1	
		Strong connection		<1	
		Medium-strength connection		>3	
		Weak connection		1-3	
	Channel bar	Middle	Strong connection		>3
			Medium-strength connection		>3
			Weak connection		1-3
		Side	Strong connection		<1
			Medium-strength connection		>3
			Weak connection		1-3
Channel-channel bar	Side	Medium-strength connection		<1	
		Weak connection		>3	

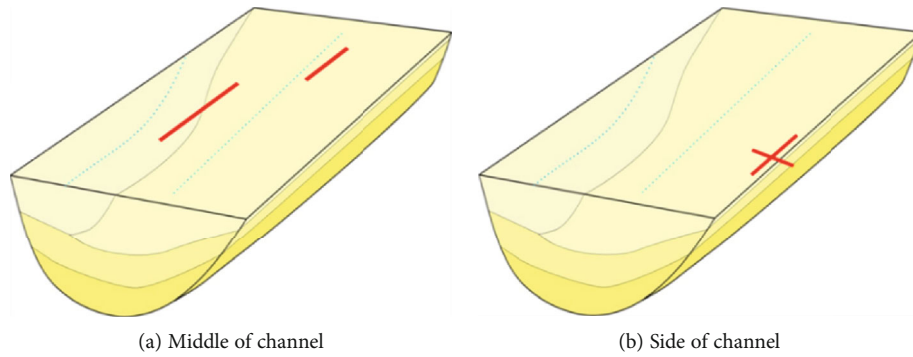


FIGURE 13: Channel sedimentary structure.

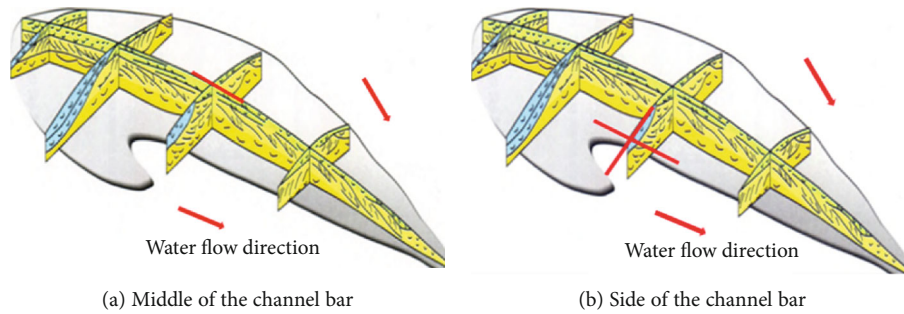


FIGURE 14: Channel bar sedimentary structure.

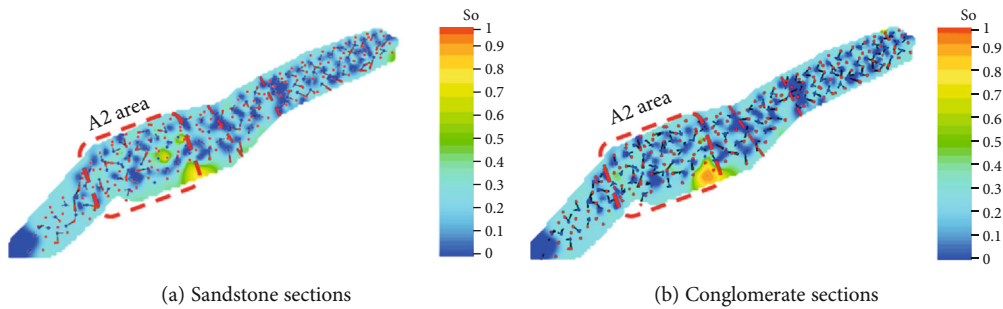


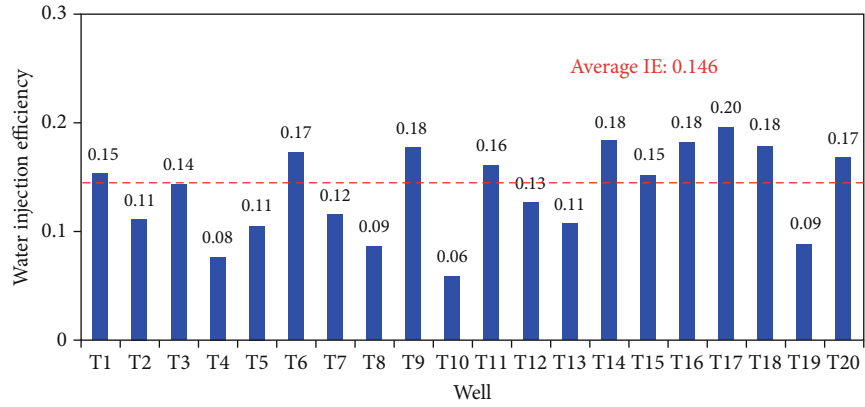
FIGURE 15: Oil saturation field.

dividing the types of interwell connection units, only choose the transmissibility and divide it into three types as the criteria for connectivity classification. The three types of connectivity classification include $T_{ij} > 3$, $1 < T_{ij} < 3$, and $T_{ij} < 1$, which, respectively, indicate strong, medium, and weak connectivity of the interwell transmissibility based on the proportion of each subtype in the different types of sedimentary facies. In the middle channel, the interwell is well connected and exhibits anisotropy. In the side of the channel, the interwell has a partial connection, with significant anisotropy. In the middle of the channel bar, the interwell is connected, and there is a large difference between the channel bars. In the side of the channel bar, the interwell is connected in some directions, and the physical properties are relatively worse.

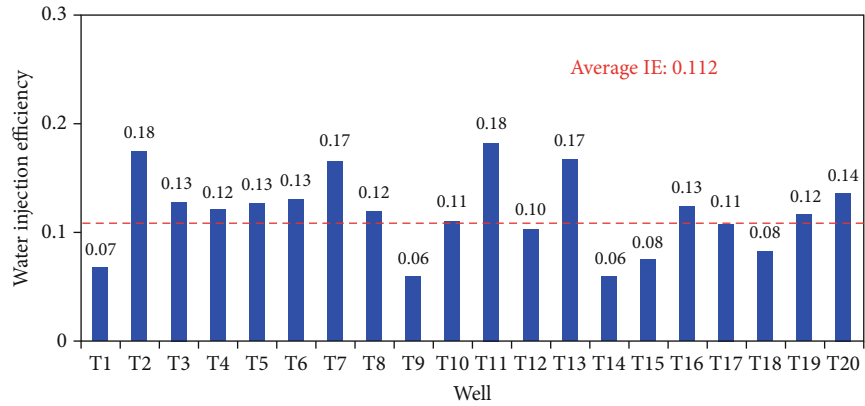
The sedimentary structure of the middle channel is shown in Figure 13(a). The middle channel has a thick channel sediment with good properties. When the two wells are

connected parallel to the source direction, the connectivity between the wells is good and may develop a dominant seepage channel. As shown in Figure 13(b), the sedimentary period changes quickly to the side of the channel and the sediment thickness of a single period decreases. Correspondingly, the flow barriers between sand bodies are more developed. Furthermore, the flow barriers cause the properties of the reservoir to become worse than those of the middle channel. The interwell connectivity is without change, and the dominant seepage channel is infrequent. In general, the connectivity of the parallel source direction is better than that of the vertical source direction.

As shown in Figure 14(a), the central area of the channel bar is dominated by parallel interlayers. The parallel interlayers of sand bodies between wells in the central area are uniformly distributed, with good connectivity in all directions. Additionally, the dominant seepage channels are developed.



(a) Sandstone sections



(b) Conglomerate sections

FIGURE 16: Water injection efficiency of injectors.

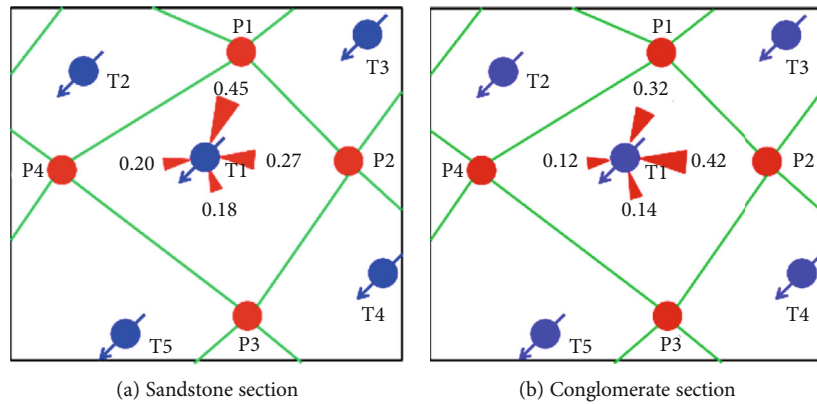


FIGURE 17: The dividing coefficient diagram of the T1 well group.

TABLE 2: Tracer test results of the T1 well group.

Injector	Tracer type & inject date	Tracer well	Tracer breakthrough date	Tracer breakthrough time (day)	Tracer peak concentration (ng/ml)	Duration (day)
T1	Er 3/19/2019	P1	4/14/2019	26	148.66	41
		P2	5/11/2019	54	126.31	30
		P4	5/19/2019	62	97.04	36

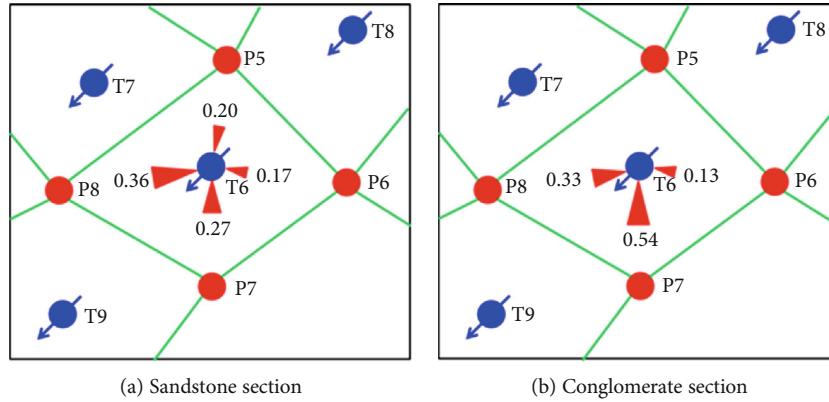


FIGURE 18: Dividing the coefficient diagram of the T6 well group.

TABLE 3: Tracer test results of the T6 well group.

Injector	Tracer type & inject date	Tracer well	Tracer breakthrough date	Tracer breakthrough time (day)	Tracer peak concentration (ng/ml)	Duration (day)
T6	Gd 3/20/2019	P8	5/9/2019	50	52.4	30
		P7	5/17/2019	58	97.01	26
		P8	4/25/2019	41	82.41	21

As shown in Figure 14(b), the side of the channel bar is affected by river erosion. Locally inclined interlayers develop, which worsen the connectivity between wells. The water injection has a poor development, and substantial oil remains in this area. In the parallel source connectivity direction, when the interlayer distribution is more consistent with the source direction, the interwell connectivity is better, and the seepage channel is more developed. When the interlayer distribution is inconsistent with the source direction, the interwell connectivity is poor. In the vertical source direction connectivity, the interwell connection becomes poor due to the changes in the sand body contact relationships and permeability. There is no obvious dominant seepage channel in this area.

Based on the study of the remaining oil enrichment area and the connectivity characteristics of each layer, the A2 area in Figure 15 with higher remaining oil saturation and complex connection relationship is preferred as the adjustment area for the water injection efficiency evaluation. The water injection efficiency of injectors in A2 area is shown in Figure 16.

4.2. The Optimization of the Production System and Implementation Effect. Targeting the problem of dominant seepage channels in some directions of the well group in area A2 that caused the dividing coefficient to be concentrated, this study combined the automatic optimization method of the injector and producer working system to form three sets of adjustment plans.

The first plan is a liquid volume adjustment plan for water injection volume. Comparing the average water injection efficiency with the efficiency of different layers in different wells, there is an increase in water injection volume in the higher efficiency layer and conversely, the injection is reduced. For the connected producers, calculating the change

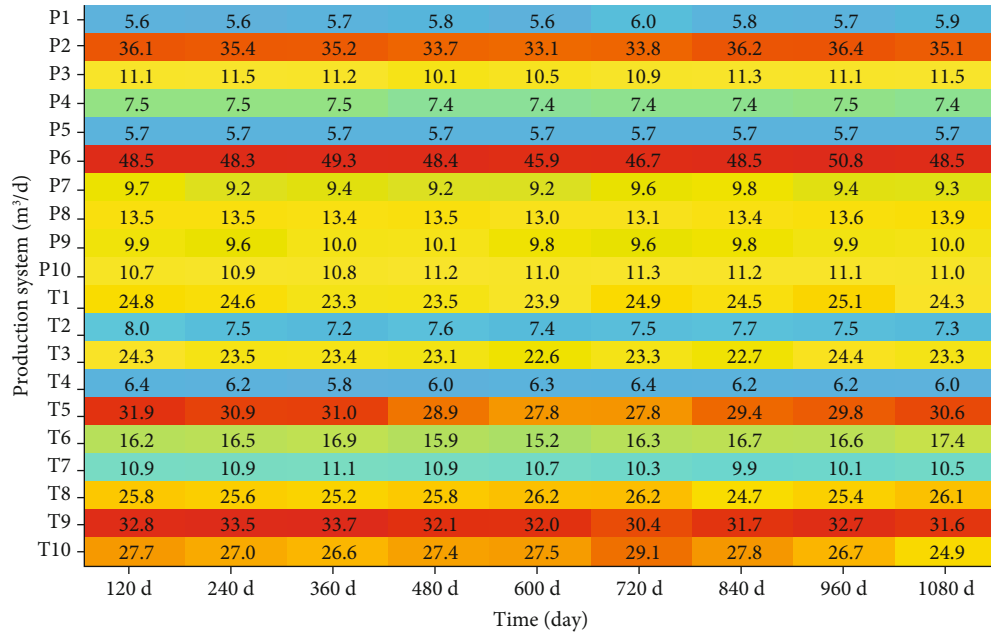
in injected water volume in each direction according to the dividing coefficient and summing all as the liquid volume adjustment of the producers. The second plan is a reservoir property adjustment plan. The measures include profile control for inefficient injectors, as well as sealing, backflow, and well function reassignment for strong connectivity, large dividing coefficient, high water cut producers.

To ensure accurate and effective measures, the dividing direction and tracer test data of key well groups were verified.

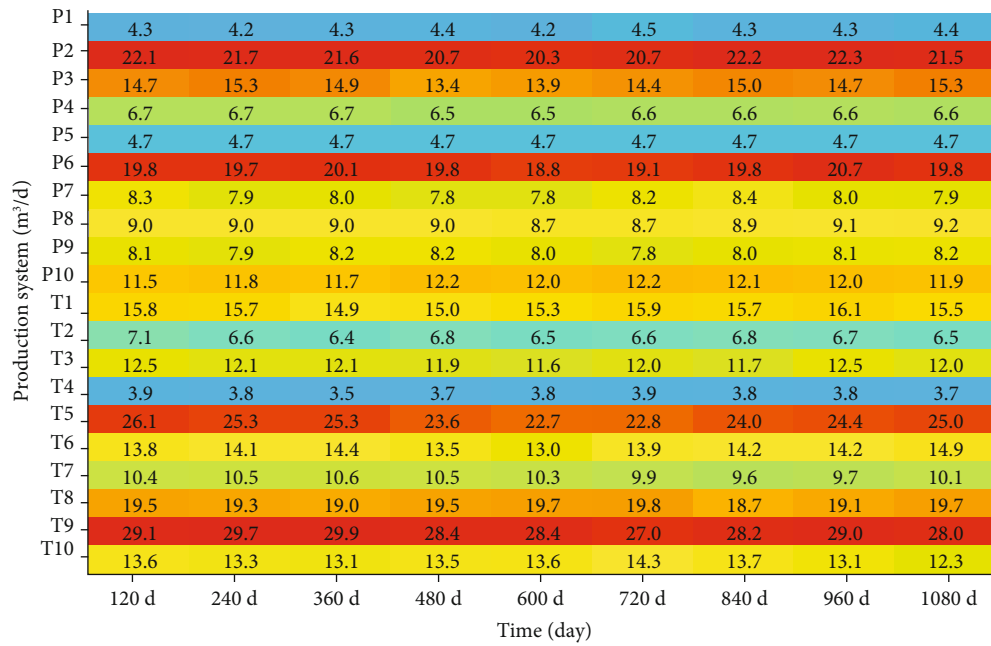
In Figure 17, the plane dividing coefficient of injector T1 shows that the producers P1 and P2 of the same well group are the main dividing directions, with 45% and 27% of injected water diverted on the sandstone section, respectively, and 32% and 42% on the conglomerate section, respectively. Table. 2 shows a good correspondence among the three wells; the tracer test data from the T1 well group shows that P1 has the longest sustained dose time (41 days) and the highest peak tracer concentration (148.66 ng/ml); P2 has a continuous tracer time of 30 days and the peak tracer concentration 126.31 ng/ml; no tracer reaction was seen in P3; P4 continued to be seen for 36 days, and the peak tracer concentration was 97.04 ng/ml.

The water injection efficiency of T1 in the sandstone section was 0.15, and the water injection efficiency of the conglomerate section was 0.07; the water injection efficiency in the sandstone section was higher than the average water injection efficiency. The injection volume of T1 in the sand and conglomerate sections changed to 4.2 m³ and 7.5 m³, respectively.

In Figure 18, the horizontal dividing coefficient of T6 shows that the producers, P7 and P8, in the same well group are the main dividing directions, with 36% and 27% of the injected water diverted in the sandstone section, and 33%



(a) Sandstone sections



(b) Conglomerate sections

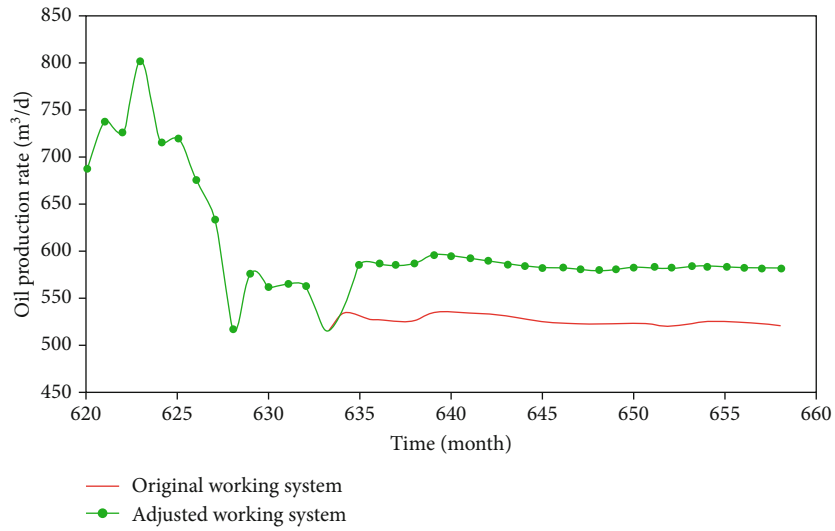
FIGURE 19: Adjusted production system.

and 54% in the conglomerate section, respectively. The tracer test data in Table 3 shows a good correspondence among the three wells. The tracer test data of the T6 well group shows that P7 lasted 26 days, and the peak tracer concentration was the highest (97.01 ng/ml). Two kinds of tracers were seen in P8, and the peak tracer concentrations were 52.4 ng/ml and 82.41 ng/ml, while no tracer reaction was seen in P5 and P6.

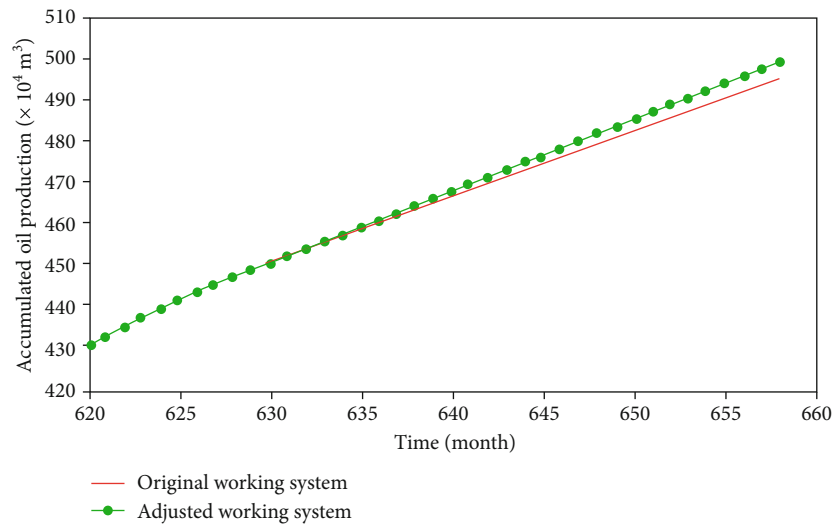
The water injection efficiency of T6 in the sandstone section was 0.17, and the water injection efficiency of the conglomerate section was 0.13. The water injection efficiency in

both was higher than the average water injection efficiency. The injection fluid volume of the T6 increased to 5.0 m³ in the sandstone section and increased to 3.5 m³ in the conglomerate section.

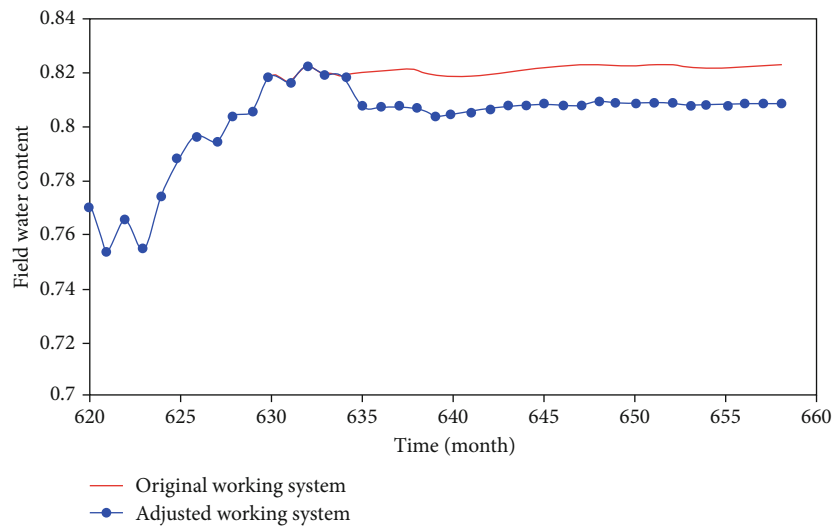
After a three-year production simulation of the adjusted production system in Figure 19 and with comparisons to the original system, the daily oil production in the field increased by 15.5%; the cumulative oil production in the field increased by 4.24 × 10⁴ t; the comprehensive water cut decreased by 1.39%, and the effect of the adjustment is obviously shown in Figure 20.



(a) Field daily oil production



(b) Field cumulative oil production



(c) Field water cut

FIGURE 20: The comparison of adjustment effect.

5. Conclusion

A layered water-injection efficiency evaluation method based on INSIM is proposed in this study by accurately adding virtual well points to characterize the actual geological connectivity of glutenite reservoirs and a well-to-well conductivity of the fitted connectivity model. Combined with the location of the sedimentary facies at the well point, a classification standard for interwell connectivity of glutenite was established, and the interwell connectivity was divided into four major categories and twelve subcategories. On this basis, to determine the injection water splitting quantity, the layered water injection efficiency of the injection well which is the basic knowledge to adjust the injection-production schedule was evaluated.

The method determines the vertical and horizontal water injection split coefficients by calculating data, such as connectivity parameters, pressure difference, and production index, and identifies the injection-production correspondence relationship and the effect of water injection. The calculation speed and the calculation result of the water injection efficiency are more reliable than the reservoir engineering method.

Based on this method, three types of liquid volume adjustment plans were formulated for an actual oilfield: injection-production structure adjustment, injection-production measurement adjustment, and comprehensive adjustment. It is predicted that after two years of implementation of the liquid volume adjustment measures for 20 water injection well groups in the A2 area, the daily oil production rate in the block will increase by 15.5%; the cumulative oil production in the block will increase by 4.24×10^4 t; the comprehensive water cut will decrease by 1.39%, and the effect of increasing oil precipitation will be obvious.

Nomenclature

A :	Dividing coefficient
b :	Feature parameter matrix
b_r :	Initial estimation of feature parameter matrix
C_t :	Total compressibility, MPa^{-1}
e :	Water injection efficient
e_x :	Average water injection efficient
f_w :	Water cut
G_B :	Covariance matrix of the model parameters
G_D :	Initial estimation covariance matrix of the model parameters
\bar{h} :	Average interwell reservoir thickness, m
$h(b)$:	Initial numerical simulation observation values
J :	Production index
K :	Layer average permeability, $10^{-3} \mu\text{m}^2$
\bar{K} :	Interwell average permeability, $10^{-3} \mu\text{m}^2$
K_r :	Relative permeability, $10^{-3} \mu\text{m}^2$
k_{obs} :	Observation values
L :	Well spacing, m
N_I :	Number of reservoir layers
N_{IC} :	Number of connected injectors
N_w :	Number of connected wells
O :	Objective function for history matching

p :	Flowing bottom hole pressure, MPa
q :	Production or injection volume, m^3
r :	Wellbore radius, m
s :	skin factor
S_w :	Water saturation
T :	Transmissibility, $\text{m}^3/\text{d}\cdot\text{MPa}^{-1}$
V :	Pore volume, m^3
η :	Liquid volume adjustment coefficient
λ :	Mobility, $10^{-3} \mu\text{m}^2/(\text{mPa}\cdot\text{s})$
μ :	Viscosity, $\text{mPa}\cdot\text{s}$

Subscripts

i :	Well-node index
ij :	Parameters between well i and well j
j :	Well-node index
k :	Layer index
max:	Parameter maximum
min:	Parameter minimum
o :	Oil phase
w :	Water phase

Superscript

N : Timestep.

Data Availability

Data is available on request.

Conflicts of Interest

The authors declare that they have no conflicts of interest.

Acknowledgments

This study is sponsored by the China Petroleum Science and Technology Major Project (No. 2016B-1106).

References

- [1] L. Sun, X. Wu, W. Zhou, X. Li, and P. Han, "Technologies of enhancing oil recovery by chemical flooding in Daqing oilfield, NE China," *Petroleum Exploration and Development*, vol. 45, no. 4, pp. 673–684, 2018.
- [2] H. N. Al-Saedi and R. E. Flori, "Enhanced oil recovery of low salinity water flooding in sandstone and the role of clay," *Petroleum Exploration and Development*, vol. 45, no. 5, pp. 927–931, 2018.
- [3] A. A. Yousef, S. H. al-Saleh, A. al-Kaabi, and M. S. al-Jawfi, "Laboratory investigation of the impact of injection-water salinity and ionic content on oil recovery from carbonate reservoirs," *SPE Reservoir Evaluation & Engineering*, vol. 14, no. 5, pp. 578–593, 2013.
- [4] S. E. Buckley and M. C. Leverett, "Mechanism of fluid displacement in sands," *Transactions of AIME*, vol. 146, no. 1, pp. 107–116, 2013.
- [5] G. Sheng, H. Zhao, Y. Su et al., "An analytical model to couple gas storage and transport capacity in organic matter with non-circular pores," *Fuel*, vol. 268, article 117288, 2020.

- [6] Y. Zhao, L. Zhang, Y. Xiong, Y. Zhou, Q. Liu, and D. Chen, "Pressure response and production performance for multi-fractured horizontal wells with complex seepage mechanism in box-shaped shale gas reservoir," *Journal of Natural Gas Science & Engineering*, vol. 32, pp. 66–80, 2016.
- [7] Z. Deliang, Z. Liehui, G. Jingjing, Z. Yuhui, and Z. Yulong, "Research on the production performance of multistage fractured horizontal well in shale gas reservoir," *Journal of Natural Gas Science & Engineering*, vol. 26, pp. 279–289, 2015.
- [8] R. Zhang, G. S. Li, and J. C. Guo, "Experimental research into fracture propagation of complex lithologies in fractured tight oil reservoirs," *Petroleum Science Bulletin*, vol. 1, no. 3, pp. 353–362, 2016.
- [9] H. Yu, Z. Yang, T. Ma, Z. Lei, S. Cheng, and H. Chen, "The feasibility of asynchronous injection alternating production for multistage fractured horizontal wells in a tight oil reservoir," *Petroleum Science Bulletin*, vol. 3, no. 1, pp. 32–44, 2018.
- [10] J. M. Fan, C. Wang, X. F. Qu, L. B. Cheng, and T. Xue, "Development and practice of water flooding huff-puff in tight oil horizontal well, Ordos Basin: a case study of Yanchang formation Chang 7 oil layer," *Acta Petrolei Sinica*, vol. 40, no. 6, pp. 706–715, 2019.
- [11] Z. Meng, S. L. Yang, L. Wang, Z. Wang, and W. Han, "Investigation on numerical simulation of co₂ huff and puff in tight oil reservoirs," *Journal of Petrochemical Universities*, vol. 29, no. 6, pp. 39–42, 2016.
- [12] R. P. Batycky, M. J. Blunt, and M. R. Thiele, "A 3D field-scale streamline-based reservoir simulator," *SPE Reservoir Engineering*, vol. 12, no. 4, pp. 246–254, 2013.
- [13] R. O. Baker, F. Kuppe, S. Chugh, R. Bora, S. Stojanovic, and R. Batycky, "Full-field modeling using streamline-based simulation: four case studies," *SPE Journal*, vol. 5, no. 2, pp. 126–134, 2002.
- [14] M. R. Thiele and R. P. Batycky, "Using streamline-derived injection efficiencies for improved waterflood management," *Society of Petroleum Engineers*, vol. 9, no. 2, pp. 187–196, 2013.
- [15] H. Hoteit and A. Firoozabadi, "Numerical modeling of two-phase flow in heterogeneous permeable media with different capillarity pressures," *Advances in Water Resources*, vol. 31, no. 1, pp. 56–73, 2008.
- [16] A. M. Yousef, P. H. Gentil, J. L. Jensen, and L. W. Lake, "A capacitance model to infer interwell connectivity from production and injection rate fluctuation," *SPE Reservoir Evaluation & Engineering*, vol. 9, no. 6, pp. 630–646, 2013.
- [17] M. Sayarpour, C. S. Kabir, and L. W. Lake, "Field applications of capacitance-resistance models in waterfloods," *SPE Reservoir Engineering*, vol. 12, pp. 853–864, 2009.
- [18] D. Weber, T. F. Edgar, L. Lake, L. S. Lasdon, S. Kawas, and M. Sayarpour, "Improvements in capacitance-resistive modeling and optimization of large scale reservoirs," in *SPE Western Regional Meeting*, pp. 369–385, San Jose, CA, USA, 2009.
- [19] A. Shabani, H. R. Jahangiri, and A. Shahrabadi, "Data-driven approach for evaluation of formation damage during the injection process," *Journal of Petroleum Exploration and Production Technology*, vol. 10, no. 2, pp. 699–710, 2020.
- [20] H. Zhao, Z. Kang, X. Zhang, H. Sun, L. Cao, and A. C. Reynolds, "INSIM: a data-driven model for history matching and prediction for waterflooding monitoring and management with a field application," in *SPE Reservoir Simulation Symposium*, vol. 1, pp. 431–461, Houston, TX, USA, 2015.
- [21] Z. Guo, A. C. Reynolds, and H. Zhao, "Waterflooding optimization with the INSIM-FT data-driven model," *Computational Geosciences*, vol. 22, no. 3, pp. 745–761, 2018.
- [22] Z. Guo and A. C. Reynolds, "INSIM-FT in three-dimensions with gravity," *Journal of Computational Physics*, vol. 380, pp. 143–169, 2019.
- [23] H. Zhao, L. Xu, Z. Guo, Q. Zhang, W. Liu, and X. Kang, "Flow-path tracking strategy in a data-driven interwell numerical simulation model for waterflooding history matching and performance prediction with infill wells," *SPE Journal*, vol. 25, no. 2, pp. 1007–1025, 2020.
- [24] H. Zhao, L. Xu, Z. Guo et al., "A new and fast waterflooding optimization workflow based on INSIM-derived injection efficiency with a field application," *Journal of Petroleum Science and Engineering*, vol. 179, pp. 1186–1200, 2019.
- [25] G. Sheng, Y. Su, and W. Wang, "A new fractal approach for describing induced-fracture porosity/permeability/ compressibility in stimulated unconventional reservoirs," *Journal of Petroleum Science and Engineering*, vol. 179, pp. 855–866, 2019.
- [26] M. Thiele and R. Batycky, "Water injection optimization using a streamline-based workflow," in *SPE Annual Technical Conference and Exhibition*, pp. 521–526, Denver, CO, USA, 2003.
- [27] L. Zhang, Y. Zhou, L. Zhao, and D. Zhang, "Finite element method using a characteristic-based split for numerical simulation of a carbonate fracture-cave reservoir," *Journal of Chemistry*, vol. 2015, Article ID 815051, 13 pages, 2015.

Research Article

A Digital Twin for Unconventional Reservoirs: A Multiscale Modeling and Algorithm to Investigate Complex Mechanisms

Tao Zhang ¹, Yiteng Li,¹ Jianchao Cai,^{2,3} Qingbang Meng ⁴, Shuyu Sun ^{1,2}
and Chenguang Li⁵

¹Computational Transport Phenomena Laboratory, Division of Physical Science and Engineering, King Abdullah University of Science and Technology, Thuwal 23955-6900, Saudi Arabia

²Institute of Geophysics and Geomatics, China University of Geosciences, Wuhan 430074, China

³State Key Laboratory of Petroleum Resources and Prospecting, China University of Petroleum, Beijing 102249, China

⁴Key Laboratory of Tectonics and Petroleum Resources, Ministry of Education, China University of Geosciences, Wuhan 430074, China

⁵China National Oil and Gas Exploration and Development Company Limited, China

Correspondence should be addressed to Shuyu Sun; shuyu.sun@kaust.edu.sa

Received 9 July 2020; Revised 8 September 2020; Accepted 15 September 2020; Published 2 November 2020

Academic Editor: Jinze Xu

Copyright © 2020 Tao Zhang et al. This is an open access article distributed under the Creative Commons Attribution License, which permits unrestricted use, distribution, and reproduction in any medium, provided the original work is properly cited.

The special mechanisms underneath the flow and transport behaviors in unconventional reservoirs are still challenging an accurate and reliable production estimation. As an emerging approach in intelligent manufacturing, the concept of digital twin has attracted increasing attentions due to its capability of monitoring engineering processes based on modeling and simulation in digital space. The application potential is highly expected especially for problems with complex mechanisms and high data dimensions, because the utilized platform in the digital twin can be easily extended to cover more mechanisms and solve highly complicated problems with strong nonlinearity compared with experimental studies in physical space. In this paper, a digital twin is designed to numerically model the representative mechanisms that affect the production unconventional reservoirs, such as capillarity, dynamic sorption, and injection salinity, and it incorporates multiscale algorithms to simulate and illustrate the effect of these mechanisms on flow and transport phenomena. The preservation of physical laws among different scales is always the first priority, and simulation results are analyzed to verify the robustness of proposed multiscale algorithms.

1. Introduction

The successes in the commercial exploitation of unconventional resources, such as shale gas and tight oil, in North America have already changed the current world energy market, and the growing public concerns on the depletion of conventional oil and gas resources in the foreseeable future also stimulates more efforts in both academia and industry to investigate unconventional reservoirs [1, 2]. A large number of technical studies have been carried on for a better characterization of oil and gas storage in either or both adsorbed or free states and a clearer description of the rock properties including porosity and permeability [3–5]. On the other

hand, environmental issues have challenged the development of the unconventional oil and gas resources. As a consequence of hydraulic fracturing and shale gas production, groundwater pollution has become a serious issue that haunts oil companies. Earthquake and gas explosion, the other two problems often criticized due to unconventional reservoir production, are increasingly arising public concerns. In order to achieve a better balance between recovery efficiency and environmental impacts, we need to pay more efforts for a thorough understanding of the special mechanisms that control the storage, flow, and transport of unconventional resources in subsurface reservoir in order to meet the growing global energy demands in an environmentally

friendly and economical approach. For instance, the classical viewpoint that transient linear flow dominates the flow regime for multifractured horizontal wells is challenged by the anomalous diffusion behavior, which also enlightens us that our understanding of the complex mechanisms and flow behaviors in unconventional reservoirs still needs to be improved [6].

Numerical modeling and simulation have become a popular approach in the study of unconventional reservoirs, mainly due to their significant superiority on efficiency and flexibility [3]. In practice, experimental studies are limited to time and space scale and also restricted by field or laboratory conditions. However, these constraints can be avoided by well-designed numerical simulation. Moreover, numerical schemes can be further verified through experimental analysis, and some key parameters are tuned from experimental results. After continual improvement and optimization, such mathematical model is believed to be “realistic” and is reliable to be applied to solve practical problems in much larger time and space scale in order to guide or suggest engineering practice. As one of the cutting-edge techniques, digital twins have been extensively used in automatic production, predictive maintenance, and complete-cycle management. Digital twins, also known as DT, can be defined as a simulation process or simulation-based system that integrates multidiscipline, multiphysics, and multiscale numerical methods to make full use of physical models, sensor data, operation history, and other information and to complete mapping in virtual space so as to reflect the whole life cycle of a corresponding process or equipment in physical space [7]. The concept of digital twins was first proposed in the field of advanced manufacturing, along with the application of state-of-the-art information technologies in industrial processes [8, 9]. With the arrival of the big data era, the entire product life cycle produces plenty of data in the aspect of designing, manufacturing, marketing, and service. These data can be transferred into the digital models for simulation and analysis, and in turn, the numerical results can provide supports to improve practical manufacturing. The data obtained in physical reality is often fragmented and isolated, but well-designed numerical schemes in virtual space can describe the underneath physical or chemical correlations among the data. Thus, the intelligence and efficiency of industrial manufacturing are constantly improved to achieve intelligent production and management. The similar idea can be applied to reservoir simulation in which data of the reservoir geology, fluid properties, and environmental and operation conditions can all feed into the model in virtual space.

In this paper, we will combine several promising numerical models and algorithms that describe the special mechanisms behind the flow and transport behaviors in unconventional reservoirs in different scales as an exploratory investigation to construct the digital twin. A thermodynamically consistent flash calculation scheme is designed to consider the effect of capillary pressure on phase equilibria, and the dynamic sorption is included in the particle distribution function to establish a delicate Lattice Bhatnagar-Gross-Krook (LBGK) scheme to simulate the shale gas flow and transport using Lattice Boltzmann Method (LBM). Multi-

component ion exchange and double-layer expansion, both directly relevant to fluid salinity, are also modeled in different scales. Simulation results are presented to show the effectiveness of the proposed algorithms for the investigated mechanisms. The remainder of this paper is organized as follows. In Section 2, several important mechanisms in unconventional reservoirs are modeled, and the corresponding simulation algorithms and results are illustrated in Section 3. Conclusive remarks are provided in Section 4.

2. Design of the Digital Twin

A digital twin is expected to realize interaction and integration between physical space and virtual world due to its feasibility on real-time synchronization, real mapping, and high fidelity. In order to create the virtual model of physical entity in unconventional reservoirs, the fluid flow and transport process in realistic reservoir conditions are mathematically described in the digital space, while data is transferred into the twin and information is fed back from the twin. The procedures and processes in physical entity are expected to be enabled or expanded with new capabilities based on the feedback, which may be obtained via various approaches, such as data fusion analysis and decision iteration optimization. In this section, a digital twin for unconventional reservoirs is designed to bridge the physical space and digital world, with focus on several selected mechanisms which affect the complete cycle of evaluation and production. As shown in Figure 1, some processes are extracted first from the physical space, such as reserve prediction, recovery evaluation, hydraulic fracturing, and environmental effect. To provide more effective, real-time, and intelligent improvement and optimization schemes to these processes, the digital twin is designed with three parts: models on reservoir geometry, Darcy’s scale fluid flow, and pore scale fluid flow. Each part is decomposed further with representative techniques and research topics. It should be noted that phase equilibrium calculations are conventionally investigated in pore scale, but in [10], Darcy’s scale phase equilibrium was studied.

In this paper, we will start to model capillarity and dynamic sorption, both of which play significant roles in unconventional reservoirs and affect many engineering processes in practice. The widespread nanopores are often considered as the main cause of significant capillary effect and confinement effect. The strong interactions between gas molecules and rock surface result into the dynamic sorption, and the related concepts of Knudsen diffusion, Knudsen layer, and Knudsen number are introduced. The large amount of water needed for hydraulic fracturing is often questioned by the local communities, and seawater or produced water after proper treatment is expected as an alternative to save fresh water. Water salinity, one of the key factors affecting injection and fracturing performance, has also attracted numerous attentions. In this section, thermodynamic equilibrium modeling for multicomponent fluid mixtures in unconventional reservoirs is used to describe phase behaviors and properties. A delicate LBGK model is constructed to take into account the effect of dynamic sorption on particle

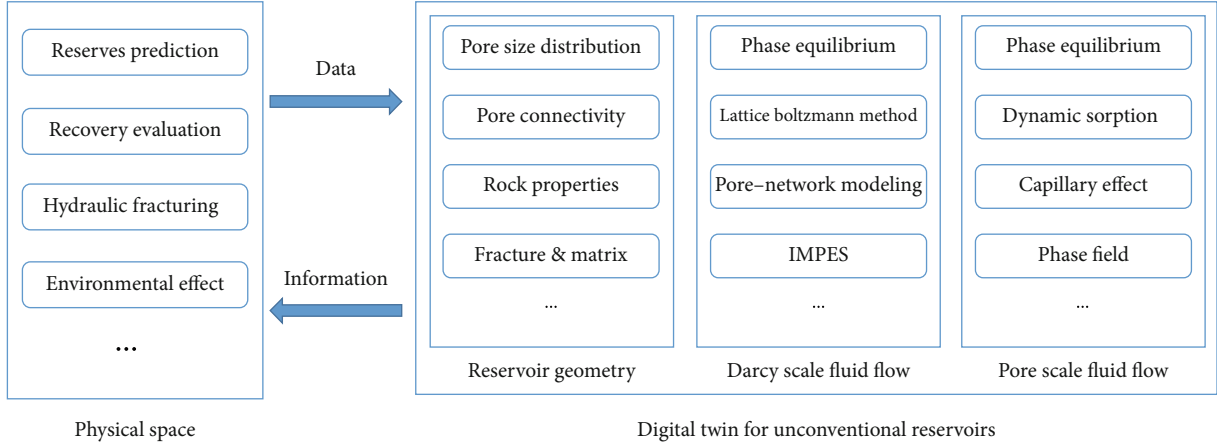


FIGURE 1: Design of a digital twin for unconventional reservoirs.

distribution functions. For the two processes directly relevant to salinity, the electrical interaction process is represented by multicomponent ion exchange equations and the electrostatic forces in a double-layer expansion process needed for numerical simulation are calculated using the DLVO-type theory, short for Derjaguin–Landau–Verwey–Overbeek theory.

2.1. Capillarity Modeling. The presence of capillary pressure could significantly deviate the phase behaviors of reservoir fluids in unconventional reservoirs from their bulk properties. Therefore, the capillary effect has to be taken into account in order to accurately estimate phase amounts and compositions of unconventional reservoir fluids at geological conditions. Defined as the pressure difference between wetting phase and nonwetting phase, $p_c = p_n - p_w$, the effect of capillary pressure can be concluded as moving the interface toward the nonwetting phase due to a positive capillary pressure and conversely due to a negative capillary pressure. The work done by capillary pressure can be formulated as

$$\frac{dW}{dt} = -p_n \frac{dV_n}{dt} - p_w \frac{dV_w}{dt} = -p_n \frac{dV_n}{dt} + p_w \frac{dV_n}{dt} = -p_c \frac{dV_n}{dt}, \quad (1)$$

where p_c is assumed to be constant along the interface between nonwetting and wetting fluids. Here, the Young-Laplace equation is used to calculate the capillary pressure as

$$p_c = \frac{2\sigma \cos \theta}{r}, \quad (2)$$

with the interfacial tension σ , in the unit of N/M, being estimated by the Weinaug-Katz correlation

$$\sigma = \left[\sum_{i=1}^M [\mathbf{P}]_i (\mathbf{n}_{i,w} - \mathbf{n}_{i,n}) \right]^4. \quad (3)$$

2.2. Dynamic Sorption Modeling. Usually, shale gas can exist as three states, including dissolved gas, adsorbed gas, and free

gas, and the dominant reserve is made up of the adsorbed gas, which has been reported in [11] that the adsorbed gas covers up to 80% of the total gas reservation. The dynamic balance between adsorption and desorption, as a result of shale structures and fluidity, can provide helpful knowledge to design and optimize fracturing and recovery processes. Such critical information is of significant importance to evaluate the reservoir and predict the well production. A large number of studies have been reported to analyze and model the dynamic sorption in unconventional reservoirs. Molecular accumulation, as a consequence of surface energy minimization, is often considered the main cause of adsorption on shale surface, while the van der Waals force is leading the physical sorption in potential theory. The sorption capacity is dependent on temperature, pressure, and other geochemical properties, such as the TOC content, also known as total organic carbon. Generally, if there are more organic matters in shale, a higher gas adsorption amount can be detected together with a higher surface area, total pore volume, and porosity. Moreover, permeability, which is the key factor relevant to flow and transport in porous media, is also affected by the adsorption and desorption process in gas production. For example, pressure drop facilitates gas desorption from kerogen, and on the other hand, the free gas production further decreases the pore pressure. As a result, pressure difference between the pores and bulk matrix will reinforce the desorption on the matrix surface. Plenty of isotherm models have been developed to mathematically describe the sorption mechanism, among which the most commonly used one is the Langmuir's model

$$V = \frac{V_L P}{P_L + P}, \quad (4)$$

where V denotes adsorbate volume, P denotes pressure, and P_L and V_L denote the Langmuir pressure and Langmuir volume, respectively. Other isotherm models, including Freundlich model, D-R model, BET model, and Toth model, are proposed later so that the estimations of these models get closer to the experimental results. In this paper, the following

equation is selected to model the dynamic sorption balance between adsorption and desorption

$$\frac{\partial V}{\partial t} = k_a C(V_m - V) - k_d V, \quad (5)$$

where k_a and k_d are the adsorption and desorption coefficients, respectively, with the unit of S^{-1} , and V_m denotes the saturated adsorption capacity. The gas concentration C can be calculated from the deformed advection-diffusion LB scheme:

$$\frac{\partial C}{\partial t} + \nabla \cdot (Cu) = \nabla \cdot (D_{\text{eff}} \nabla C) + S. \quad (6)$$

In the above equation, the total gas concentration at certain location can be calculated as the summation of distribution functions in all the directions:

$$C = \sum g c_i, \quad (7)$$

where $g c_i$ denotes the distribution function in convection-diffusion problems and the source term S ; in distribution balance equation, see Equation [eq: eq (6)], which represents the effect of dynamic sorption which is determined by

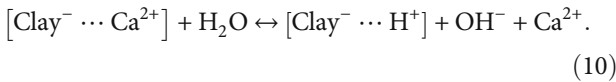
$$S = \omega_i V_s \delta_t. \quad (8)$$

Correspondingly, the macroscopic velocity can be formulated as

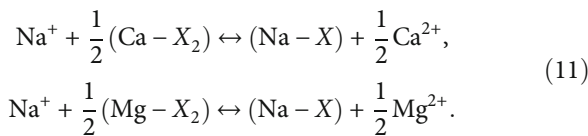
$$\sum (f_i - z \times S_i) = \rho u, \quad (9)$$

where S_i denotes the adsorbed amount in the site of the i th direction and z denotes a coefficient balancing the units.

2.3. Multicomponent Ion Exchange Modeling. The process of multicomponent ion exchange can be modeled as (using Ca^{2+} as an example of divalent cations)



A generalized model has been proposed in [12] for different ions, e.g., sodium, calcium, and magnesium cations, which are commonly seen in reservoir brine and rocks.

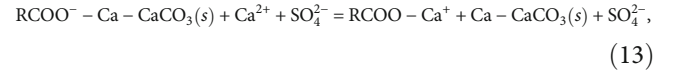


Two coefficients are presented in their study to model the ion exchange selectivity as

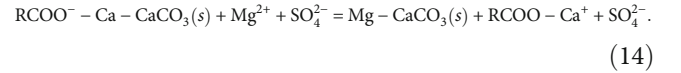
$$\begin{aligned} K'_{\text{Na/Ca}} &= \frac{\zeta(\text{Na} - X) [m(\text{Ca}^{2+})]^{0.5}}{[\zeta(\text{Ca} - X_2)]^{0.5} m(\text{Na}^+)} \times \frac{[\gamma(\text{Ca}^{2+})]^{0.5}}{\gamma(\text{Na}^+)}, \\ K'_{\text{Na/Mg}} &= \frac{\zeta(\text{Na} - X) [m(\text{Mg}^{2+})]^{0.5}}{[\zeta(\text{Mg} - X_2)]^{0.5} m(\text{Na}^+)} \times \frac{[\gamma(\text{Mg}^{2+})]^{0.5}}{\gamma(\text{Na}^+)}. \end{aligned} \quad (12)$$

The $\zeta(\text{MI} - X)$ term in the above equations represents the equivalent fraction of the cations on the exchanger, and MI denotes Na^+ , Ca^{2+} , or Mg^{2+} .

The wettability alteration is considered to result from ion adsorptions and corresponding surface charge change, which can be modeled as [13]



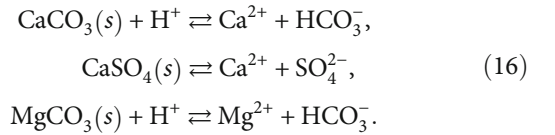
where SO_4^{2-} serves as a catalyst increasing Ca^{2+} ion concentration. A similar formula can be applied to brine containing Mg^{2+} ions



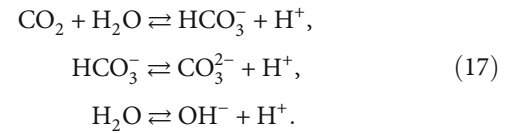
In high salinity injection, pH reversal may occur and the ion exchange can be modeled as



Dissolution and precipitation can happen with the interaction of injected brine and rock



The HCO_3^- in Equation [eqim] is also obtained from the interaction in the aqueous phase as



2.4. Double-Layer Expansion Modeling. The modified DLVO theory, which describes electrostatic forces, is commonly used to model and calculate the double-layer expansion process [14, 15], and the results can be used in numerical simulation of the low salinity waterflooding process [16]. Force contributions can be modeled as

$$\Pi(h) = \Pi_{\text{VDW}}(h) + \Pi_{\text{EDL}}(h) + \Pi_{\text{STR}}(h), \quad (18)$$

where the disjoining pressure is a summation of contributions from London van der Waals force, electrostatic force,

and structural force, all of which are functions of the wetting film thickness h . This formulation can be used in wettability calculation, as the following augmented Young-Laplace equation uses disjoining pressure to express the interaction equilibrium in oil/brine/rock system [15]:

$$p_c = \Pi(h) + \frac{2\sigma_{ow} \cos \theta}{r}, \quad (19)$$

where p_c is capillary pressure. The contact angle θ is given by [17]

$$\cos \theta = 1 + \frac{1}{\sigma_{ow}} I. \quad (20)$$

It can be referred from Equation [eqca] that if $I > 0$, the water film is unconditionally stable due to the constant contact angle $\theta = 0^\circ$. If the rock is water-wet, implying $90 > \theta > 0^\circ$ or $0 < I < -\sigma_{ow}$, then the water film is meta-stable; otherwise, it is oil-wet with $180 > \theta > 90^\circ$ or $-\sigma_{ow} < I < -\sigma_{ow}$.

The van der Waals force Π_{VDW} in Equation [eqfo] can be calculated by [18]

$$\Pi_{VDW}(h) = \frac{-A}{6\pi h^3}, \quad (21)$$

where A is the Hamaker constant. The electrostatic double-layer force in Equation [eqfo] can be modeled using a bounded estimation of the Poisson-Boltzmann equation [19]

$$\frac{d^2 \psi}{dx^2} = \frac{en_b}{z\varepsilon_0 \varepsilon_r} e^{-(ze\psi/k_B T)}, \quad (22)$$

where ε_0 denotes the dielectric constant of vacuum, ε_r denotes the relative dielectric constant of the aqueous medium, k_B denotes the Boltzmann constant, T denotes the absolute temperature (K), and z denotes the ion valence. An upper limit of the estimation can be established with a constant potential assumption that attraction between the plates with the same charge but unequal potential always exists

$$\Pi_{EDL}(h) = n_b k_B T \left(\frac{2\psi_{r1} \psi_{r2} \cosh(\kappa h) - \psi_{r1}^2 - \psi_{r2}^2}{(\sinh(\kappa h))^2} \right). \quad (23)$$

On the contrary, if a repulsion force is assumed to exist between the plates,

$$\Pi_{EDL}(h) = n_b k_B T \left(\frac{2\psi_{r1} \psi_{r2} \cosh(\kappa h) + \psi_{r1}^2 + \psi_{r2}^2}{(\sinh(\kappa h))^2} \right). \quad (24)$$

The term ψ_{ri} in the above two equations is defined as the reduced potential of i th plate, and it can be calculated by

$$\psi_{ri} = \frac{ze\zeta_i}{k_B T}. \quad (25)$$

The above approximation model is called the analytical compression approximation (CA) model, which is suitable for cases with low to intermediate electrostatic potential. A linear superposition approximation (LSA) is proposed, also called weak overlap approximation (WOA), as a correct answer between the two extremes as [20]

$$\Pi_{EDL}(h) = 64n_b k_B T \tanh\left(\frac{\zeta_1}{4}\right) \tanh\left(\frac{\zeta_2}{4}\right) \exp(-\kappa h), \quad (26)$$

where ζ_i is the zeta potential on the i th surface of each plate. It is proved in [19] that the LSA model is more favorable to fit the force measurement on surface experiments. κ in the above models are defined as the Debye-Hückel reciprocal length and determined by the following expression:

$$\kappa = \sqrt{\frac{2e^2 z^2 n_b}{\varepsilon_0 \varepsilon_r k_B T}}. \quad (27)$$

The hydration force can be calculated by [21]

$$\Pi_{STR}(h) = C_1 e^{h/\xi_1} + C_2 e^{-h/\xi_2}, \quad (28)$$

where C is the force coefficient relevant with the boundary conditions and h is the clay length. The hydrophobic force near the surface can be calculated using

$$\Pi_{BR}(h) = -\frac{A\delta^6}{7560} \left[\frac{8r_p + h}{(2r_p + h)^7} + \frac{6r_p + h}{h^7} \right]. \quad (29)$$

A more general form has been proposed in [22] to calculate the structural forces for all the cases.

$$\prod_{\text{structure}} = A_k \exp\left(-\frac{h}{h_s}\right). \quad (30)$$

3. Simulation and Results

All the aforementioned mechanisms, such as capillarity, sorption, and salinity, have challenged the conventional continuum modeling and simulation using Navier-Stokes equations. Consequently, modifications and improvements have to be introduced to account for these mechanisms so that the governing systems are generated in order to obey the physical laws as well as realistic conditions. Thermodynamic equilibrium schemes are reconstructed to account for capillary effect and to meet the first and second laws of thermodynamics. The calculated equilibrium solutions can ensure a good initial estimate for multiphase multicomponent flow simulation, and the new energy and entropy balance formulations can lead to a stable convergence while tolerating a relatively much larger time step. Mesoscopic numerical approaches, representative of LBM [23] and Pore Network Method [24], are widely employed in the direct simulation of flow and transport in porous media, and some simple

but effective terms can be added to take such special mechanisms into account. The new mass and momentum conservation properties can be proved rigorously, which further promote such delicate numerical approaches. However, there is still not a comprehensive model or simulation approach covering all the effect of capillarity, sorption, and salinity. In another words, more investigations are expected to develop a reliable and practical scheme to simulate engineering processes, and the concept of a digital twin can be a potential platform to cover as much mechanisms as we want. With conservation equations governing fluid flow through porous media, Darcy's scale simulation can be performed to model the migration and transport of oil and gas and predict the oil production. Pore scale simulation is conducted to investigate the detailed mechanisms of surface interactions and to show the correlation between the microscopic details in a single pore, thermal equilibrium conditions, and macroscopic flow and transport properties. Mesoscopic simulations, like LBM and pore network modeling, are used as a bridge to link between micromechanism and macrophenomena.

3.1. Darcy's Scale Simulation. A mass balance equation for immiscible incompressible oil-water two phase flow can be written as [25]

$$\begin{aligned} \phi \frac{\partial s}{\partial t} + \frac{\partial u_w}{\partial x} &= 0, \\ \phi \frac{\partial (1-s)}{\partial t} + \frac{\partial u_o}{\partial x} &= 0, \end{aligned} \quad (31)$$

where u_o and u_w denote the velocity of oil phase and water phase, respectively. The extended Darcy's law for aqueous and oil phases can be modeled as follows if gravity is ignored:

$$\begin{aligned} u_w &= -\frac{kk_{rw}(s, \gamma, \sigma_s)}{\mu_w} \frac{\partial p_w}{\partial x}, \\ u_o &= -\frac{kk_{ro}(s, \gamma)}{\mu_o} \frac{\partial p_o}{\partial x}, \end{aligned} \quad (32)$$

where p_o and p_w represent the pressure of oil phase and water phase, k_{ro} and k_{rw} are the oil and water relative permeability, respectively. A commonly used model to account for the effect of salinity on relative permeability and capillary pressure has been proposed in [26] as

$$\begin{aligned} k_{rw} &= \theta \times k_{rw}^{HS}(S^*) + (1-\theta) \times k_{rw}^{LS}(S^*), \\ k_{ro} &= \theta \times k_{ro}^{HS}(S^*) + (1-\theta) \times k_{ro}^{LS}(S^*), \\ p_{cow} &= \theta \times p_{cow}^{HS}(S^*) + (1-\theta) \times p_{cow}^{LS}(S^*), \end{aligned} \quad (33)$$

where

$$\begin{aligned} \theta &= \frac{(S_{orw} - S_{orw}^{LS})}{(S_{orw}^{HS} - S_{orw}^{LS})}, \\ S^* &= \frac{(S_o - S_{orw})}{(1 - S_{wr} - S_{orw})}. \end{aligned} \quad (34)$$

In the above system, p_{cow} denotes the oil-water capillary pressure, θ is a scaling factor, and S_{orw} denotes the residual oil saturation after waterflooding. The superscripts HS and LS denote the high salinity water and low salinity water, respectively. It is a simple model capable of predicting the oil recovery using low salinity waterflooding at field-scale studies or single-well tests. An obvious dependency of capillary pressure and relative permeability on injection salinity is expressed in the formulas, regarding the salt species in brine only as an additional single lumped component in the aqueous phase. A balance between the two extreme conditions, lower salinity limit and upper salinity limit, is conducted using the scaling factor.

A more comprehensive model is proposed in [27] which starts from the classical Corey equations [28]

$$\begin{aligned} k_{rw} &= k_{rw}^0 (S_w^*)^{n_w}, \\ k_{ro} &= k_{ro}^0 (1 - S_w^*)^{n_o}, \end{aligned} \quad (35)$$

where

$$\begin{aligned} S_w^* &= \frac{S_w - S_{wr}}{1 - S_{wr} - S_{or}}, \\ P_c &= \frac{c_w}{((S_w - S_{wi})/(1 - S_{wi}))^{a_w}} - \frac{c_o}{((1 - S_w - S_{or})/(1 - S_{or}))^{a_o}}. \end{aligned} \quad (36)$$

The first modification is assuming the residual oil saturation is a function of salinity only.

$$S_{or}(X_c) = S_{or}^{LS} + \frac{X_c - X_c^{LS}}{X_c^{LS} - X_c^{HS}} (S_{or}^{LS} - S_{or}^{HS}). \quad (37)$$

An additional modification introduces the salinity effect on the end-point water relative permeability

$$k_{rw}(X_c) = k_{rw}^{LS} + \frac{X_c - X_c^{LS}}{X_c^{LS} - X_c^{HS}} (k_{rw}^{LS} - k_{rw}^{HS}). \quad (38)$$

Next, the effect of salinity is also applied to the exponent of oil relative permeability

$$n_o(X_c) = n_o^{LS} + \frac{X_c - X_c^{LS}}{X_c^{LS} - X_c^{HS}} (n_o^{LS} - n_o^{HS}). \quad (39)$$

The salinity is denoted by X_c in the above equations, and the two thresholds of high salinity and low salinity are represented by the superscript HS and LS.

A dimensionless system to model the macroscopic flow of low salinity waterflooding can be written as [29, 30]

$$\begin{aligned} \frac{\partial s}{\partial t_D} + \frac{\partial f(s, \gamma)}{\partial x_D} &= 0, \\ S_s &= (S_{a0} - S_{cr}(\gamma))A_s(s, \gamma), f(s, \gamma) = f(s, \gamma, S_s(\gamma)), \\ \frac{\partial \gamma s}{\partial t_D} + \frac{\partial \gamma f(s, \gamma)}{\partial x_D} &= 0, \\ 1 &= -\lambda(s, \gamma) \frac{\partial P}{\partial x_D}, \lambda(s, \gamma) = \frac{k_{rw}(s, \gamma, S_s)\mu_o}{\mu_w} + k_{ro}(s, \gamma), \end{aligned} \quad (40)$$

where the subscript D in the above system stands for dimensionless and s denotes the saturation. The initial condition is provided as reservoir saturation and formation water salinity (γ) before injection [31]

$$t_D = 0 : s = s_I, \gamma = \gamma_I. \quad (41)$$

Several popular industrial software has been developed to calculate the mechanisms related with injection salinity. PHREEQC is an industry-standard geochemistry software which has been successfully applied in the study of low salinity waterflooding, with emphasis on the electrostatic reaction, ion exchange, and mineral dissolution [32, 33], and used to verify new models and approaches [12]. UTCHEM simulator is another widely accepted software in petroleum industry, developed by the University of Texas at Austin, to predict the effect of injected brine with various ion compositions, and the injected low salinity water is described using the integrated tool, UTCHEM-IPHREEQC [34]. IPHREEQC is also a state-of-art geochemical engine, and UTCHEM-IPHREEQC is an accurate, robust, and flexible tool that enables to model low salinity waterflooding and many other enhanced oil recovery techniques with respect to geochemistry. Later, another three-dimensional equation-of-state-based compositional simulator, also developed by the University of Texas at Austin, UTCOMP, is coupled with IPHREEQC and the effect of hydrocarbon components soluble in the aqueous phase on the pH buffering and other related reactions in the oil/brine/rock system [35].

3.2. Mesoscopic Simulation. In addition to LBM mentioned in Section 2, another representative mesoscopic approach, pore network modeling, has also shown promising potentials in simulating the flow and transport behaviors in unconventional reservoirs. By constructing a porous network in which pore bodies are connected through pore throats, such a model could represent highly irregular structure from the perspective of topology and geometry. After selecting certain distribution functions and key parameters to control the size of pore body and pore throat, the network is connected and a double permeability media is then constructed for further investigation. As explained in [11], the two structures, pore body and pore throat, can be treated as fracture and matrix, respectively, and this body-throat connection can be easily extended to carry on the streaming and collision process of distribution functions.

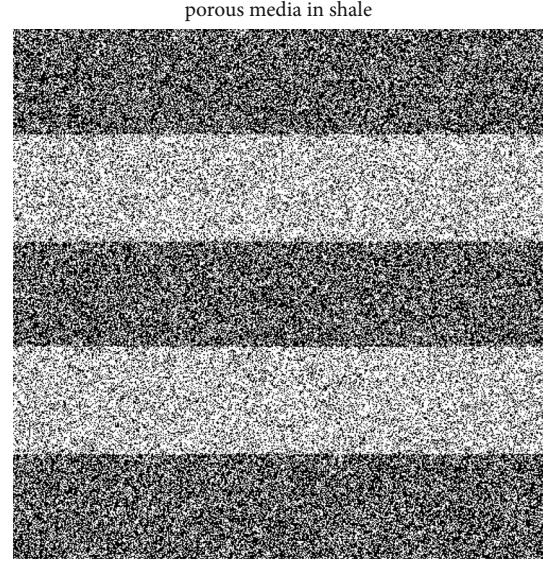


FIGURE 2: A porous media generated using pore network model with a designed structure.

TABLE 1: Parameters for pore network modeling.

Parameter	Media 1	Media 2	Unit
Min. pore body inscribed radius	0.0372	0.0625	mm
Max. pore body inscribed radius	0.254	0.366	mm
Mean. pore body inscribed radius	0.125	0.246	mm
Standard deviation	0.128	0.187	mm

A network constituting of 500×500 pore bodies is constructed as shown in Figure 2, where the black band represents matrix and white band represent fracture. It can be easily referred that this porous structure is generated by two sets of pore parameters, and the corresponding porosity and fluidity is different in these layers. The parameters of two types of media are listed in Table 1, and it can be stated that the three layers of Media 1 contain more matrix compared with the two layers of Media 2. Furthermore, a better mobility is expected in the two layers of Media 2, and more resistance may occur in the three layers of Media 1.

After constructing the porous media using pore network modeling, the detailed mesoscopic algorithm can be described as follows:

- (1) Generate the optimized LBGK scheme with sorption coefficients, weight matrix, medium structure, and flow scenario. Determine the inclusive parameters
- (2) Apply the free flow distribution function in fractures and transport distribution function in matrix. The dynamic sorption is then calculated, while at the first iteration, this adsorption is set to be zero. The free flow distribution function for fractured porous media reads as

$$F = -\frac{\phi v}{K} u - \frac{\varepsilon F \phi}{\sqrt{K}} |u| u + \phi G, \quad (42)$$

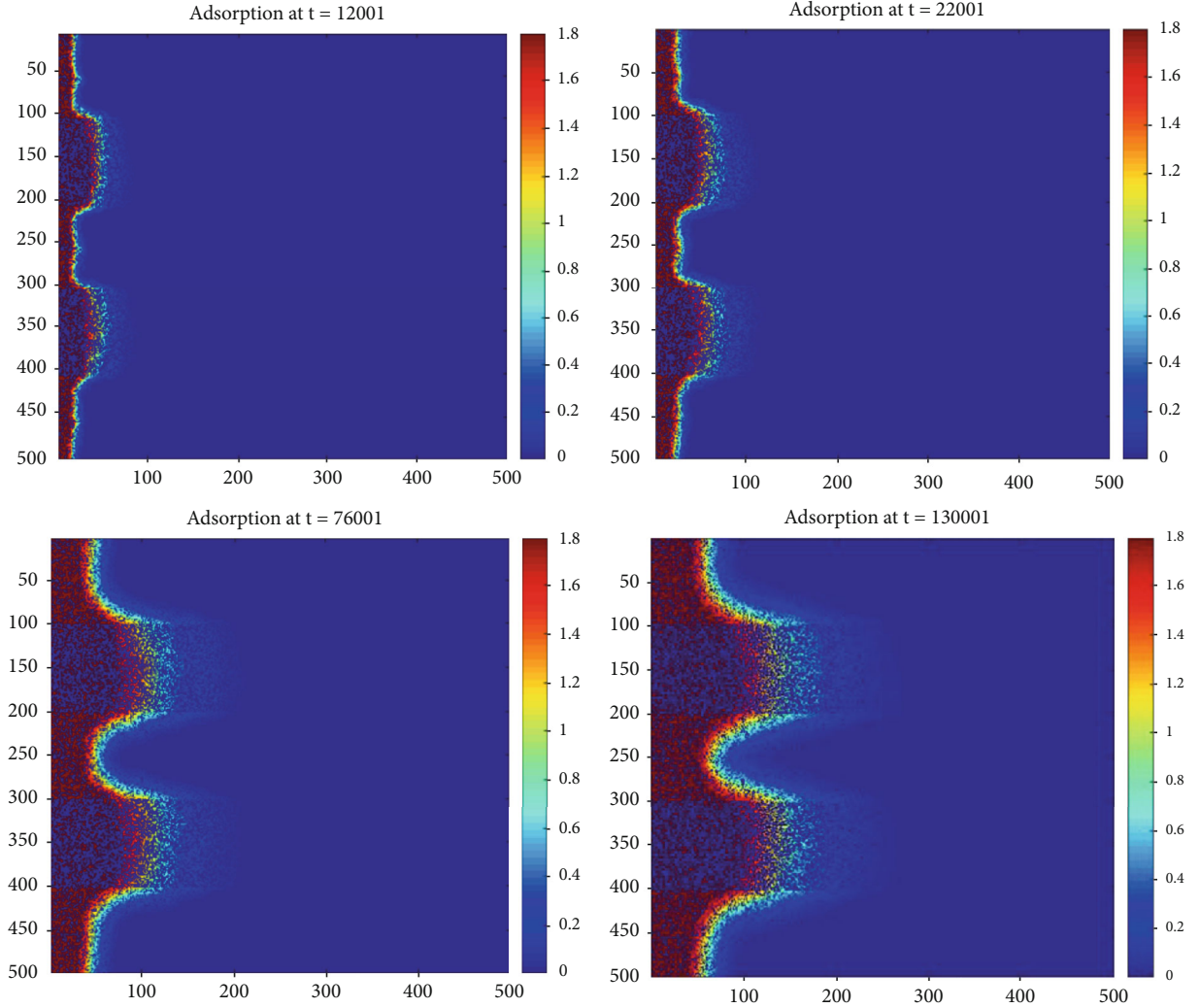


FIGURE 3: Adsorption distribution at time steps 12000, 22000, 76000, and 130000.

and the distribution function at equilibrium state is

$$f_i^{eq} = \rho w_i \left[1 + \frac{e_i \cdot u}{\phi c_s^2} + \frac{uu : (e_i e_i - c_s^2 I)}{2\phi c_s^4} \right]. \quad (43)$$

- (3) Use this calculated adsorption amount to update the free flow simulation, and further calculate the diffusion and transport process

This two-scale LBM can be easily recovered back into Navier-Stokes equation and advection-diffusion equation, respectively, for fracture and matrix scale LBGK scheme by Chapman-Enskog expansion [36]. The effectiveness of this algorithm with proper modifications on the general advection-diffusion LBGK scheme and the coupling of scales using the free flow velocity can be verified with the following example with constant gas injection on the left boundary of Figure 2. The adsorption distribution at different time step is

illustrated in Figure 3. It can be seen free flow is much faster in Media 2 with more fracture, while adsorption amount is much larger in Media 1 with more matrix. The black color in Figure 3 corresponds to the “fracture” structure. The result is reasonable in both scales, and it can be concluded that more adsorption in the matrix may be due to higher saturation sorption amount or adsorption coefficient (referred from Langmuir-type isothermal models) and can lead to smaller free flow velocity in fractures. On the contrary, the result of our scheme is reasonable in both media and the effect of dynamic sorption on free flow region is illustrated. The effect of porosity in both two scales, fracture and matrix, and the effect of sorption parameters in a Langmuir-type isothermal sorption model are all tested and analyzed. Generally, the increasing adsorbed amount in the matrix due to the higher adsorption coefficient or saturation sorption amount will result in a slower velocity in the free flow scale. However, if the increase of adsorbed gas amount is the result of larger matrix porosity, then the free flow velocity could be accelerated as the total resistance in the media has been decreased.

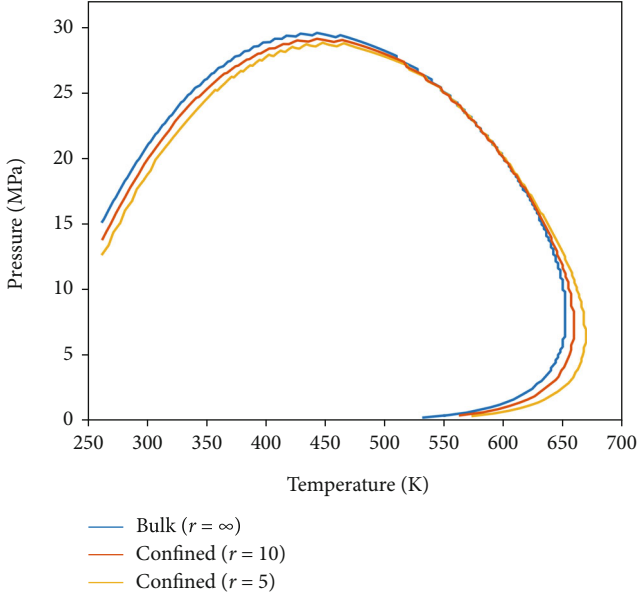


FIGURE 4: Phase envelope for an Eagle Ford oil considering capillarity at different pore radii.

3.3. Pore Scale Simulation. Phase equilibrium calculation is essentially needed for generating a physical-meaningful initial phase distribution benefiting further multiphase flow simulation. The following fugacity equation can be used to establish thermodynamic equilibrium, which can be calculated based on various equations of state (EOS), for example, Peng-Robinson EOS [37, 38]:

$$g_i \equiv f_{ig} - f_{io} = 0, \quad i = 1, \dots, n_m. \quad (44)$$

Generally, volume constraint is also needed for a complete conservation relation, which could be described as

$$\sum_q \left(\frac{N_q^{n+1}}{\rho_q^{n+1}} \right) - \varphi^{n+1} = 0, \quad q = g, w, o, \quad (45)$$

where N denotes the mole density, ρ denotes the mass density, and φ is the constitutive equation. Unconditional stability, the most essential property determining algorithm robustness and applicability in practice, is preserved by using the convex-concave splitting scheme on chemical potential. In details, the chemical potential $\mu_i(\mathbf{n})$ is supposed to have two components $\mu_i^{\text{convex}}(\mathbf{n})$ and $\mu_i^{\text{concave}}(\mathbf{n})$ and the counterpart splitting can be written as

$$\mu_i^{\text{convex}}(\mathbf{n}) = \frac{\partial f^{\text{convex}}}{\partial n_i} = \frac{\partial f^{\text{attraction}}}{\partial n_i} - \lambda \frac{\partial f^{\text{ideal}}}{\partial n_i}. \quad (46)$$

The unconditional stability of the above semi-implicit scheme has been proved in details in [37]. The evolution equations of mole and volume can be formulated based on

Onsager's reciprocal principle as

$$\frac{\partial N_i^G}{\partial t} = \sum_{j=1}^M \psi_{i,j} (\mu_j^G - \mu_j^L) + \psi_{i,M+1} (p^L - p^G), \quad (47)$$

$$\frac{\partial V^G}{\partial t} = \sum_{j=1}^M \psi_{M+1,j} (\mu_j^G - \mu_j^L) + \psi_{M+1,M+1} (p^L - p^G).$$

The computational efficiency and reliability require an energy stable system consistent with the second law of thermodynamics. Regarding the Onsager coefficient matrix Ψ , it can be divided into 4 submatrices, shown as below

$$\Psi = \begin{bmatrix} A & B \\ B^T & C \end{bmatrix}. \quad (48)$$

Here, $A = \partial(\mu_{i,2} - \mu_{i,1})/\partial N_{i,1}$, $B = \partial(\mu_{i,2} - \mu_{i,1})/\partial V_1 = \partial(p_1 - p_2)/\partial N_{i,1}$, and $C = \partial(p_1 - p_2)/\partial V_1$. It is essential to ensure the positive definition of the Onsager coefficient matrix; otherwise, a modified Cholesky factorization will be introduced to preserve its positive definiteness. Generally, $\Psi + \mathbf{E}$ should be sufficiently positive and \mathbf{E} is added as a diagonal matrix with suitable positive entries. This positive property can keep the continuous increasing of entropy in the iterations, which will ensure to reach the local maximum using the Newton-Raphson method. The effect of capillarity can be illustrated by the difference in tangent-plane distance (TPD) function and phase envelope of fluid mixtures in porous media with various pore radius. As shown in Figure 4, the TPD function with respect to temperature range [250,700] K and overall molar density range [0, 10000] mol/m³ is plotted for an EagleFord oil in two cases either with or without capillary effect. Within the specified molar density and temperature intervals, there is a single two-phase region and the phase boundary between single-phase and two-phase states is drawn in red and blue for the case with and without capillary effect, respectively. It can be seen that capillary pressure can significantly reshape the bulk phase envelope by suppressing the bubble point curve and meanwhile expanding the dew point curve.

The effect of pore radius on the work done by capillary pressure can be explained in Figure 5. If capillary pressure is taken into account, the dew point pressure will be decreased in the lower branch and the suppression of dew point pressure becomes significant as pore radius decreases. Moreover, dew point pressure increases in the upper branch and deviates more significantly from the dew point curve of the bulk phase where the capillary effect is negligible. The overall effect of the dew point pressure increasing in the upper branch and decreasing in the lower branch enlarges the vapor-liquid region compared with bulk phase envelope.

The effect of multicomponent ion exchange on relative permeability can be modeled as [39]

$$k_r(S, \beta_{Ca}, \beta_{Mg}) = F(\beta_{Ca}, \beta_{Mg}) k_r^{\text{HS}}(S) + [1 - F(\beta_{Ca}, \beta_{Mg})] k_r^{\text{LS}}(S), \quad (49)$$

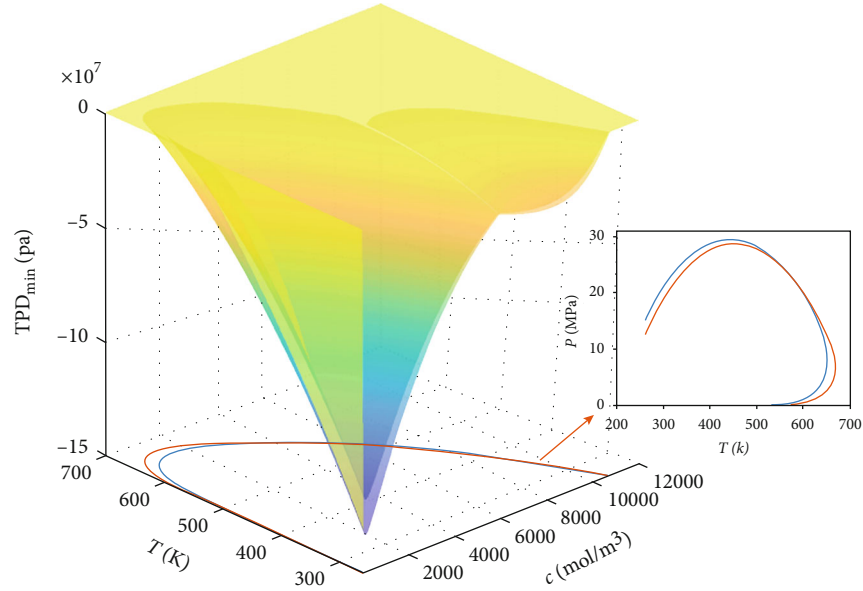


FIGURE 5: Global minimum of TPD function, as well as corresponding phase envelope, as a function of the overall molar density and temperature for an Eagle Ford oil with (red line) or without (blue line) capillarity.

where β is the absorbed cations and the subscripts Ca and Mg represent the calcium and magnesium ion, respectively. The scaling function, F , is dependent on the divalent ion adsorption conditions in the precipitation and dissolution processes.

The microscopic displacement efficiency as a function of trapping number is proposed in [40], using ionic strength (I_s) calculation as

$$I_s = \frac{1}{2} \sum_i Z_i^2 m_i, \quad (50)$$

where z_i and m_i denote the charge and molarity of the fluid species i , respectively. The thickness of double electric layer is then determined by

$$\kappa^{-1} = \sqrt{\frac{\epsilon_r \epsilon_0 k_B T}{2 N_A e^2 I}}, \quad (51)$$

where ϵ_r and ϵ_0 denote the relative permeability and the permeability of the free phase, respectively. A clay mineral model is built in [41] in terms of composition, structure, and charge density on the clay surface. Various salinity conditions, ranging from freshwater to seawater, have been considered, and system wetness can be either oil-wet or water-wet in that study.

4. Conclusion and Remarks

Due to the tight formations and related special mechanisms often met in unconventional reservoirs, there are still nonnegligible public concerns on the economic efficiency, production safety, and environmental friendship. As an effective approach to describe the flow and transport behaviors in sub-

surface reservoirs, a digital twin is designed in this paper to cover the purposes of media construction, mechanism investigation, and production estimation in physical entity. Representative mechanisms, such as capillarity, sorption, and injection salinity, have been mathematically characterized in details, and multiscale algorithms are developed to simulate the effect of these mechanisms. Physical reservations and equivalence between various scales can be preserved in the generated schemes, and several results are illustrated to prove the reliability and robustness.

More models and algorithms are expected to be included in the digital twin in the future to construct a more comprehensive numerical platform capable of simulating realistic engineering cases efficiently and accurately. Extensions to a wider range of applications are easy to perform as long as the physical correlations can be described numerically in the virtual space. Field scale studies can be enabled by the usage of parallel computing, bound-preserving, reduced-space methods and many other scale coupling techniques [42]. Molecular dynamics simulation and Monte Carlo simulation can also be added into this twin to lay a more solid theoretical foundation on fundamental microscopic mechanisms [43]. Accelerated flash calculations using deep learning algorithms have also been carried out by many researchers [44, 45], while the pore-scale flash calculation schemes have been extended to solve related engineering problems including carbon dioxide sequestration [46]. Hydraulic fracturing and rock properties are directly relevant with the exploitation of unconventional reservoirs, where numerous models have been developed to simulate the observations [47, 48]. Gathering and transportation are the connection between reservoir exploitation and market utilization, where the flow and transport in pipelines can also be modeled to resolve the engineering problem including scaling and corrosion [49,

50]. The next step is to find the proper connectors that link the many aspects of mechanisms, models, and algorithms to establish a comprehensive digital twin.

Data Availability

Data are available on request via email sent to tao.zhang.1@kaust.edu.sa.

Conflicts of Interest

The authors declare that they have no known competing financial interests or personal relationships that could have appeared to influence the work reported in this paper.

Acknowledgments

The work of Tao Zhang, Yiteng Li, and Shuyu Sun was supported by funding from the National Natural Scientific Foundation of China (Grants Nos. 51874262 and 51936001) and King Abdullah University of Science and Technology (KAUST) through the Grant no. BAS/1/1351-01-01.

References

- [1] Y. Shen, H. Ge, X. Zhang, L. Chang, D. Liu, and J. Liu, "Impact of fracturing liquid absorption on the production and water-block unlocking for shale gas reservoir," *Advances in Geo-Energy Research*, vol. 2, no. 2, pp. 163–172, 2018.
- [2] J. Cai, D. Lin, H. Singh, W. Wei, and S. Zhou, "Shale gas transport model in 3D fractal porous media with variable pore sizes," *Marine and Petroleum Geology*, vol. 98, pp. 437–447, 2018.
- [3] H. Wang, L. Chen, Z. Qu et al., "Modeling of multi-scale transport phenomena in shale gas production—a critical review," *Applied Energy*, vol. 262, article 114575, 2020.
- [4] D. Wang, X. Wang, H. Ge, D. Sun, and B. Yu, "Insights into the effect of spontaneous fluid imbibition on the formation mechanism of fracture networks in brittle shale: an experimental investigation," *ACS Omega*, vol. 5, no. 15, pp. 8847–8857, 2020.
- [5] G.-p. Zhu, J. Yao, H. Sun et al., "The numerical simulation of thermal recovery based on hydraulic fracture heating technology in shale gas reservoir," *Journal of Natural Gas Science and Engineering*, vol. 28, pp. 305–316, 2016.
- [6] R. Christopher, "Anomalous diffusion or classical diffusion in an anomalous reservoir? Evaluation of the impact of multiphase flow on reservoir signatures in unconventional reservoirs," in *Unconventional Resources Technology Conference*, pp. 22–24, Denver, Colorado, July 2019.
- [7] S. Sun and T. Zhang, "A 6M digital twin for modeling and simulation in subsurface reservoirs," *Advances in Geo-Energy Research*, vol. 4, no. 4, pp. 349–351, 2020.
- [8] F. Tao, J. Cheng, Q. Qi, M. Zhang, H. Zhang, and F. Sui, "Digital twin-driven product design, manufacturing and service with big data," *The International Journal of Advanced Manufacturing Technology*, vol. 94, no. 9–12, pp. 3563–3576, 2018.
- [9] S. Boschert and R. Rosen, "Digital twin—the simulation aspect," in *Mechatronic futures*, pp. 59–74, Springer International Publishing, 2016.
- [10] S. Sun, "Darcy-scale phase equilibrium modeling with gravity and capillarity," *Journal of Computational Physics*, vol. 399, article 108908, 2019.
- [11] T. Zhang, S. Sun, and H. Song, "Flow mechanism and simulation approaches for shale gas reservoirs: a review," *Transport in Porous Media*, vol. 126, no. 3, pp. 655–681, 2019.
- [12] C. Dang, L. Nghiem, N. Nguyen, Z. Chen, and Q. Nguyen, "Mechanistic modeling of low salinity water flooding," *Journal of Petroleum Science and Engineering*, vol. 146, pp. 191–209, 2016.
- [13] P. Zhang, M. T. Tweheyo, and T. Austad, "Wettability alteration and improved oil recovery by spontaneous imbibition of seawater into chalk: impact of the potential determining ions Ca^{2+} , Mg^{2+} , and SO_4^{2-} ," *Colloids and Surfaces A: Physicochemical and Engineering Aspects*, vol. 301, no. 1–3, pp. 199–208, 2007.
- [14] H. Ding and S. Rahman, "Experimental and theoretical study of wettability alteration during low salinity water flooding—an state of the art review," *Colloids and Surfaces A: Physicochemical and Engineering Aspects*, vol. 520, pp. 622–639, 2017.
- [15] Z. Jalili and V. A. Tabrizy, "Mechanistic study of the wettability modification in carbonate and sandstone reservoirs during water/low salinity water flooding," *Energy and Environment Research*, vol. 4, no. 3, 2014.
- [16] P. C. Myint and A. Firoozabadi, "Thin liquid films in improved oil recovery from low-salinity brine," *Current Opinion in Colloid & Interface Science*, vol. 20, no. 2, pp. 105–114, 2015.
- [17] S. Basu and M. M. Sharma, "Measurement of critical disjoining pressure for dewetting of solid surfaces," *Journal of Colloid and Interface Science*, vol. 181, no. 2, pp. 443–455, 1996.
- [18] H. C. Hamaker, "The London—van der Waals attraction between spherical particles," *physica*, vol. 4, no. 10, pp. 1058–1072, 1937.
- [19] J. N. Israelachvili, *Intermolecular and surface forces*, Academic press, 2015.
- [20] J. Gregory, "Interaction of unequal double layers at constant charge," *Journal of Colloid and Interface Science*, vol. 51, no. 1, pp. 44–51, 1975.
- [21] J. A. Molina-Bolivar and J. L. Ortega-Vinuesa, "How proteins stabilize colloidal particles by means of hydration forces," *Langmuir*, vol. 15, no. 8, pp. 2644–2653, 1999.
- [22] G. J. Hirasaki, "Wettability: fundamentals and surface forces," *SPE Formation Evaluation*, vol. 6, no. 2, pp. 217–226, 1991.
- [23] H. Wang, X. Yuan, H. Liang, Z. Chai, and B. Shi, "A brief review of the phase-field-based lattice Boltzmann method for multiphase flows," *Capillarity*, vol. 2, no. 3, pp. 33–52, 2019.
- [24] A. Golparvar, Y. Zhou, K. Wu, J. Ma, and Z. Yu, "A comprehensive review of pore scale modeling methodologies for multiphase flow in porous media," *Advances in Geo-Energy Research*, vol. 2, no. 4, pp. 418–440, 2018.
- [25] L. W. Lake, R. Johns, W. Rossen, and G. Pope, *Fundamentals of Enhanced Oil Recovery*, Prentice Hall, Englewood Cliffs, NJ, 2014.
- [26] G. R. Jerauld, K. J. Webb, C.-Y. Lin, and J. Seccombe, "Modeling low-salinity waterflooding," in *SPE Annual Technical Conference and Exhibition*, pp. 24–27, San Antonio, Texas, USA, 2006.
- [27] I. Tripathi and K. K. Mohanty, "Instability due to wettability alteration in displacements through porous media," *Chemical Engineering Science*, vol. 63, no. 21, pp. 5366–5374, 2008.

- [28] M. Delshad and G. A. Pope, "Comparison of the three-phase oil relative permeability models," *Transport in Porous Media*, vol. 4, no. 1, pp. 59–83, 1989.
- [29] A. Zeinijahromi, T. K. P. Nguyen, and P. Bedrikovetsky, "Mathematical model for fines-migration-assisted waterflooding with induced formation damage," *SPE Journal*, vol. 18, no. 3, pp. 518–533, 2013.
- [30] F. Hussain, A. Zeinijahromi, P. Bedrikovetsky, A. Badalyan, T. Carageorgos, and Y. Cinar, "An experimental study of improved oil recovery through fines-assisted waterflooding," *Journal of Petroleum Science and Engineering*, vol. 109, pp. 187–197, 2013.
- [31] S. Borazjani, A. Behr, L. Genolet, A. van der Net, and P. Bedrikovetsky, "Effects of fines migration on low-salinity waterflooding: analytical modelling," *Transport in Porous Media*, vol. 116, no. 1, pp. 213–249, 2017.
- [32] D. A. Afekare and M. Radonjic, "From mineral surfaces and coreflood experiments to reservoir implementations: comprehensive review of low-salinity water flooding (LSWF)," *Energy & Fuels*, vol. 31, no. 12, pp. 13043–13062, 2017.
- [33] A. Kazemi Nia Korrani, G. R. Jerauld, and K. Sepehrnoori, "Mechanistic modeling of low-salinity waterflooding through coupling a geochemical package with a compositional reservoir simulator," *SPE Reservoir Evaluation & Engineering*, vol. 19, no. 1, pp. 142–162, 2016.
- [34] K. N. Korrani, K. S. Aboulghasem, and M. Delshad, "A novel mechanistic approach for modeling low salinity water injection," in *SPE Annual Technical Conference and Exhibition*, New Orleans, Louisiana, USA, 2013.
- [35] A. K. N. Korrani, G. R. Jerauld, and K. Sepehrnoori, "Coupled geochemical-based modeling of low salinity waterflooding," in *SPE Improved Oil Recovery Symposium*, Tulsa, Oklahoma, USA, 2014.
- [36] T. Zhang and S. Sun, "A coupled Lattice Boltzmann approach to simulate gas flow and transport in shale reservoirs with dynamic sorption," *Fuel*, vol. 246, pp. 196–203, 2019.
- [37] J. Kou and S. Sun, "Thermodynamically consistent simulation of nonisothermal diffuse-interface two-phase flow with Peng–Robinson equation of state," *Journal of Computational Physics*, vol. 371, pp. 581–605, 2018.
- [38] J. Kou and S. Sun, "A stable algorithm for calculating phase equilibria with capillarity at specified moles, volume and temperature using a dynamic model," *Fluid Phase Equilibria*, vol. 456, pp. 7–24, 2018.
- [39] A. V. Omekeh, H. A. Friis, I. Fjelde, and S. Evje, "Modeling of ion-exchange and solubility in low salinity water flooding," in *SPE Improved Oil Recovery Symposium*, Tulsa, Oklahoma, USA, 2012.
- [40] E. W. Al-Shalabi, K. Sepehrnoori, G. Pope, and K. Mohanty, "A fundamental model for predicting oil recovery due to low salinity water injection in carbonate rocks," in *SPE Energy Resources Conference*, Port of Spain, Trinidad and Tobago, 2014.
- [41] T. Underwood, V. Erastova, P. Cubillas, and H. C. Greenwell, "Molecular dynamic simulations of montmorillonite–organic interactions under varying salinity: an insight into enhanced oil recovery," *The Journal of Physical Chemistry C*, vol. 119, no. 13, pp. 7282–7294, 2015.
- [42] H. Yang, S. Sun, Y. Li, and C. Yang, "A scalable fully implicit framework for reservoir simulation on parallel computers," *Computer Methods in Applied Mechanics and Engineering*, vol. 330, pp. 334–350, 2018.
- [43] Y. Yang, A. K. Narayanan Nair, and S. Sun, "Adsorption and diffusion of carbon dioxide, methane, and their mixture in carbon nanotubes in the presence of water," *The Journal of Physical Chemistry C*, vol. 124, no. 30, pp. 16478–16487, 2020.
- [44] K. Wang, J. Luo, Y. Wei, K. Wu, J. Li, and Z. Chen, "Artificial neural network assisted two-phase flash calculations in isothermal and thermal compositional simulations," *Fluid Phase Equilibria*, vol. 486, pp. 59–79, 2019.
- [45] T. Zhang, Y. Li, Y. Li, S. Sun, and X. Gao, "A self-adaptive deep learning algorithm for accelerating multi-component flash calculation," *Computer Methods in Applied Mechanics and Engineering*, vol. 369, article 113207, 2020.
- [46] Y. Li, Z. Qiao, S. Sun, and T. Zhang, "Thermodynamic modeling of CO₂ solubility in saline water using NVT flash with the cubic-Plus-association equation of state," *Fluid Phase Equilibria*, vol. 520, article 112657, 2020.
- [47] S. Al-Rbeawi, "The performance of complex-structure fractured reservoirs considering natural and induced matrix block size, shape, and distribution," *Journal of Natural Gas Science and Engineering*, vol. 81, article 103400, 2020.
- [48] S. Al-Rbeawi and J. F. Owayed, "Fluid flux throughout matrix-fracture interface: discretizing hydraulic fractures for coupling matrix Darcy flow and fractures non-Darcy flow," *Journal of Natural Gas Science and Engineering*, vol. 73, article 103061, 2020.
- [49] H. Bai, "Mechanism analysis, anti-corrosion techniques and numerical modeling of corrosion in energy industry," *Oil & Gas Science and Technology—Revue d'IFP Energies nouvelles*, vol. 75, 2020.
- [50] T. Zhang, Y. Li, C. Li, and S. Sun, "Effect of salinity on oil production: review on low salinity waterflooding mechanisms and exploratory study on pipeline scaling," *Oil & Gas Science and Technology—Revue d'IFP Energies nouvelles*, vol. 75, 2020.

Research Article

Investigation on the Secondary Generation of Natural Gas Hydrates in Horizontal Wellbore Caused by Pressure Jump during the Depressurization Development of Hydrate Bearing Layers

Qingjun Du,^{1,2} Yongge Liu,^{1,2} Jian Hou,^{1,2,3} Lina Shi ,^{1,2} Wenbin Wang,^{1,2} and Kang Zhou^{1,2}

¹Key Laboratory of Unconventional Oil & Gas Development (China University of Petroleum (East China)), Ministry of Education, Qingdao 266580, China

²School of Petroleum Engineering, China University of Petroleum (East China), Qingdao 266580, China

³Laboratory for Marine Mineral Resources, Qingdao National Laboratory for Marine Science and Technology, Qingdao 266237, China

Correspondence should be addressed to Lina Shi; shilina@upc.edu.cn

Received 1 July 2020; Revised 22 September 2020; Accepted 27 September 2020; Published 20 October 2020

Academic Editor: Wei Wei

Copyright © 2020 Qingjun Du et al. This is an open access article distributed under the Creative Commons Attribution License, which permits unrestricted use, distribution, and reproduction in any medium, provided the original work is properly cited.

When the depressurization development of a hydrate-bearing layer is initiated, the temperature of the near-wellbore formation quickly decreases to near the equilibrium temperature due to the dissociation of natural gas hydrate. Therefore, the secondary generation of natural gas hydrates in the wellbore easily occurs if pressure jumps to a high value due to the changes of production rates or shutdown of the well. Though hydrate generation in the process of high-pressure drilling and gas and water transportation has been widely investigated, the secondary generation of natural gas hydrates caused by pressure jump during the depressurization development process is not fully understood. In this study, the multiphase pipe flow of a horizontal well, the Vyniauskas-Bishnoi generation dynamics of natural gas hydrate, and a decomposition dynamics model developed by Kim and Bishnoi are combined to build a set of horizontal well gas-liquid-solid three-phase flow models, which consider the phase transition in the wellbore and distinguished the secondary hydrate generation area in the wellbore under different temperature and pressure conditions. The results show that when the toe-end pressure is 7 MPa and the environment temperature is 6.4°C, the secondary hydrate generation exists in the horizontal section of the horizontal well, and the maximum hydrate flow velocity in the wellbore is 0.044 m³/d. A high toe-end pressure, low environment temperature, and high gas output will result in a greater hydrate generation in the wellbore, and the wellbore pressure will have a remarkable influence on the amount generated and its range.

1. Introduction

Natural gas hydrate is an ice-like substance existing in high-pressure and low-temperature environments and is widely distributed in deep-sea sediment and land permafrost. Its reserves are extremely large, i.e., approximately twice as much as conventional fossil energy [1, 2]. The USA, Canada, Japan, and China have successfully carried out a trial production of natural gas hydrate reservoirs, concurrent with the gradual increase in global energy consumption and a reduc-

tion in fossil energy reserves. Natural gas hydrate has been regarded as one of the most promising new energy sources during the 21st century and has received heavy attention [3–5]. Natural gas hydrate is in a solid form in a reservoir and has no flowability, and its existence requires special temperature and pressure conditions. The current method of development is to decompose the hydrate by artificially destabilizing its conditions [6–8]. The state of gas hydrate generally varies dynamically during the exploitation process. The produced natural gas can react with the residing water

and reform hydrate. At present, the main development methods of natural gas hydrate reservoirs include depressurization, thermal activation, CO₂ displacement, and chemical injection [9–12]. Compared to thermal activation, CO₂ displacement, and chemical injection, depressurization can achieve a level of production without injecting fluid into the reservoir, which incurs the lowest development cost. Meanwhile, its technical feasibility has been proven by the successful development of the Messoyakha Gas Reservoir of the former Soviet Union; thus, depressurization has been the most studied development method in this field [13–15]. The decomposition of natural gas hydrate is an endothermic process, the reservoir temperature during the depressurization development process gradually decreases, and a secondary generation of hydrate is apt to occur in the near-wellbore area. Myshakin et al. established 2D and 3D models to simulate and analyze the rules of secondary hydrate generation and ice blockage during the depressurization development process [16, 17]. Ruan et al. established a three-phase three-component core-scale hydrate depressurization simulation model and studied the influences of the hydrate secondary generation and permeability change on the development of depressurization [18]. Gaddipati and Anderson found that after one year of depressurization development, the secondary generation of hydrate occurs in the near-wellbore formation, and the results show an increased potential for the formation of secondary hydrate and the appearance of a lag time for the production rates as the reservoir size increases [19]. Using a horizontal or inclined well can increase the contact area between the wellbore and reservoir, and much higher decomposition and production rates of natural gas can thus be realized. Owing to the lengthy contact, the temperature near the wellbore will decrease after the decomposition of the natural gas hydrate, thus decreasing the temperature in the wellbore, which enhances the regeneration of the hydrates.

In fact, during conventional gas and water pipeline transportation and underbalanced drilling studies in the petroleum industry, it has been discovered that if the temperature and pressure conditions in the transportation pipe or drilling wellbore meet the hydrate generation condition, the hydrate will tend to gather at the pipe wall to cause a flow area. Numerous researchers have targeted the multiphase flow issue in a transportation pipe and drilling wellbore. Experimentally, Grasso et al. observed that hydrate sedimentary phenomena exist in the pipe flow and proposed three hydrate sedimentation mechanisms [20]. Joshi et al. adopted a 95-m-long pipe to study the hydrate blockage mechanism in a high water content system; the results showed that the hydrate generation process can be divided into three phases, i.e., the hydrate is evenly distributed in the aqueous phase when the hydrate content is low during the original phase, the hydrate starts to aggregate when the hydrate amount increases to a certain level, and the aggregated hydrate starts to deposit and eventually block the wellbore during the last phase [21]. Natural gas hydrates have been proposed as a means to capture the associated gas produced on offshore oil platforms. In this regard, Andersson and Gudmundsson adopted a circulation pipe experiment to study the viscosity and rheological properties of hydrate in water slurries and found that as the concentration of the hydrate increases,

the viscosity of the water slurries increases [22]. Ding et al. adopted a high-pressure flow loop to observe the hydrate generation process when the gas and liquid mix and flow in the pipe; they found that the generation of hydrate has a significant influence on the flow type of the gas and liquid [23]. Nicholas et al. conducted a measurement of the adhesion force existing between the hydrate and the metal wall. The results showed that the hydrate entrained in the flow will not adhere to the metal wall, whereas the hydrate is directly generated on the pipe wall during the hydrate aggregation and thickening [24].

To investigate the mechanisms of the secondary generation of gas hydrate and flowability, studies have been conducted to build a simulation model to predict the generation of gas hydrates during the drilling process. In terms of mathematical modeling, Jassim et al. established a hydrate sedimentary model targeting a gas-dominated flowline; simulations were conducted on the hydrate particle size and hydrate sedimentary location [25]. Nicholas et al. established a hydrate sedimentation prediction model in a liquid condensate system according to the laws of the conservation of energy and mass and compared the resulting pressure and temperature curves [26]. Wang et al. studied a hydrate sedimentary model in a gas-dominated system with free water and conducted a simulation and prediction of the hydrate layer thickness distribution in a horizontal pipe [27–29].

The flow environment in a horizontal wellbore during the depressurization process of natural gas hydrate is quite different from that found in a conventional drilling wellbore [30]. Because hydrate dissociation is an endothermic process, the temperature of the near well region decreases to the equilibrium temperature quickly. At this time, if the pressure jumps to a high value due to the shutdown of the well or the adjustment of depressurization amplitude, natural gas hydrates will form in the wellbore and the following production of gas and water will be greatly hindered. Till now, the secondary generation of natural gas hydrates in horizontal wellbore caused by pressure jump during the depressurization development of hydrate-bearing layers has not been fully investigated. For this reason, the present study combines a mass variable flow in a horizontal well with the generation of natural gas hydrate and a decomposition dynamical model to establish a set of three-phase (i.e., gas, water, and hydrate) mass variable mathematical models for a horizontal well, which consider the hydrate phase transition in the wellbore, adopting a node analysis method to solve the model and conduct the example verification, which distinguishes the generation area of secondary hydrate under different temperature, pressure, and gas output conditions. The results of this study can provide a certain theoretical basis for the temperature and pressure control of a horizontal well in terms of the depressurization development of the hydrate reservoir and a hydrate prevention in the wellbore.

2. Mathematical Model

Figure 1 shows a schematic diagram of the depressurization development of a natural gas hydrate reservoir in a horizontal well. The water and methane produced through hydrate

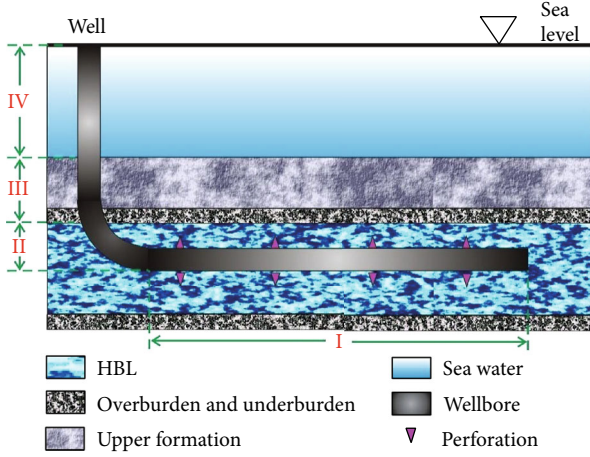


FIGURE 1: Natural gas hydrate reservoir horizontal well depressurization development.

decomposition will enter into a horizontal wellbore owing to the pressure difference. A hydrate generation will be triggered if the temperature and pressure condition in the wellbore meet the required conditions of the hydrate generation. If the anticoagulant and wellbore heating measures are not taken under the hydrate generating conditions, the hydrate aggregation and blockage are likely to occur by influencing the production. At this part, the mass conservation equations of the three-phase gas–water–natural gas hydrate and the momentum and energy conservation equations of the system are first established and are then combined with the Vysniauskas and Bishnoi generation dynamics model and the Kim and Bishnoi decomposition dynamical model. In addition, a three-phase mass variable mathematical model for a horizontal well considering the hydrate phase transition is established. Considering that the wellbore length is much larger than the well radius, the fluid flow in the wellbore is often seen as one-dimensional flow in the current researches and commercial software [31, 32]. In this paper, the flow is also assumed as one-dimensional, and only the flowing properties along the wellbore are investigated.

2.1. Conservation Law. Assume that the flow of each phase in a wellbore is in a stable state, for the gas and liquid phases, the changes in mass when flowing in the horizontal wellbore are mainly the amount of inflow from the hydrate reservoir to the wellbore, and the mass caused or consumed through the hydrate generation or decomposition. For the hydrate phase, because there is no inflow amount, the change in mass only equals the generation or decomposition mass. Thus, the mass conservation equations of the three phases are as follows:

$$\begin{cases} \frac{\partial(\rho_g v_g E_g A)}{\partial s} = q_g - x_g R_H, \\ \frac{\partial(\rho_w v_w E_w A)}{\partial s} = q_w - (1 - x_g) R_H, \\ \frac{\partial(\rho_H v_H E_H A)}{\partial s} = R_H, \end{cases} \quad (1)$$

where ρ_g , ρ_w , and ρ_H are the densities of the gas, water, and hydrate phases (kg/m^3); v_g , v_w , and v_H are the velocities of the gas, water, and hydrate phases (m/s); and E_g , E_w , and E_H are the volume fractions of the gas, water, and hydrate phases, respectively.

Based on the momentum theorem, the momentum equations of a mathematical model for a three-phase pipe flow can be obtained as follows:

$$\begin{aligned} \frac{\partial}{\partial s} (AE_g \rho_g v_g^2 + AE_w \rho_w v_w^2 + AE_H \rho_H v_H^2) \\ = -\frac{d(AF_r)}{ds} - A_g \sin \alpha (E_g \rho_g + E_w \rho_w + E_H \rho_H), \end{aligned} \quad (2)$$

where α is the angle between the wellbore and the horizontal direction ($^\circ$), F_r is the frictional resistance of the fluid during the wellbore flow process (P_a), and P is the wellbore pressure (P_a).

The energy change in the fluid for each phase during the wellbore flow process mainly includes the heat carried by the injecting gas and water, the heat exchange between fluids in the wellbore and reservoir, and the heat released or absorbed through the hydrate generation and decomposition, and thus, the energy conservation equation of the system is as follows:

$$\begin{aligned} \frac{\partial}{\partial s} \left[w_g \left(C_g T + \frac{1}{2} v_g^2 - g \cdot s \cdot \sin \alpha \right) \right. \\ \left. + w_w \left(C_w T + \frac{1}{2} v_w^2 - g \cdot s \cdot \sin \alpha \right) \right] = \frac{d(q_g C_g T_e + q_w C_w T_e)}{ds} \\ - 2\pi \frac{T - T_e}{Rt} - \frac{R_H \Delta H_H}{M_H} \end{aligned} \quad (3)$$

where w_g and w_w are the mass flow of the gas and liquid phases, respectively (kg/s), C_g and C_w are the specific heat of the gas and liquid phases ($\text{J}/(\text{kg} \cdot ^\circ\text{C})$), T is the temperature in the wellbore ($^\circ\text{C}$), T_e is the environment temperature ($^\circ\text{C}$), Rt is the pipe thermal resistance, ΔH_H is the decomposition heat of the hydrate (J/mol), and M_H is the average molecular weight of the natural gas hydrate (kg/mol).

2.2. Supplementary Conditions. The biggest difference between a mathematical model and a conventional gas–water variable mass flow model of a horizontal wellbore is that a mathematical model includes the natural gas hydrate generation and decomposition dynamics, whereas the aspects of the high-pressure physical properties, state equation, and flow type judgment of the gas are the same as in a conventional model. The natural gas state equation used in this paper is a P-R equation, and the flow-type judgment adopts the classical Beggs–Brill model.

As for the calculation of the hydrate decomposition rate, this paper adopts the most commonly used Kim–Bishnoi

dynamics model, the expression of which is as follows [33]:

$$r_H = A a_s \exp\left(\frac{\Delta E_a}{RT}\right) \exp\left(-\frac{a}{\Delta T^b}\right) \cdot P^\gamma, \quad (4)$$

where A is the composite preindex constant, $A = 4.554 \times 10^{-26} \text{cm}^3/\text{cm}^2 \cdot \text{min} \cdot \text{bar}^\gamma$; ΔE_a is the activation energy, $\Delta E_a = 106204 \text{J/mol}$; R is the gas constant, $R = 8.314 \text{J}/(\text{mol} \cdot \text{K})$; γ , a , and b are the test constants, where $\gamma = 2.986$, $a = 0.0778 \text{K}^b$, and $b = 2.411$; ΔT is the subcooled temperature (K), $\Delta T = T_{eq} - T$; T_{eq} is the phase equilibrium temperature; P is the pressure (kPa); and a_s is the area of the gas-liquid interface, $a_s = 67.1 \text{cm}^2$.

As for the calculation of the hydrate generation rate, this study adopts the Vysniauskas-Bishnoi dynamics model, the

expression of which is as follows [34]:

$$\frac{dn_H}{dt} = k A_s \exp\left(-\frac{\Delta E}{RT}\right) (P_{eq} - P_g), \quad (5)$$

where k is the decomposition rate constant, $k = 1.24 \times 10^{11} \text{mol}/(\text{m}^2 \text{MPa} \cdot \text{s})$; ΔE is the hydrate decomposition activation energy, $\Delta E = 78300 \text{J/mol}$; R is the gas constant, $R = 8.314 \text{J}/(\text{mol} \cdot \text{K})$; T is the temperature (K); P_g is the pressure (MPa); P_{eq} is the pressure balance corresponding to the temperature T (MPa); and A_s is the total surface area of the hydrate particles (m^2). Based on the phase equilibrium line of the hydrate, the judgments of the hydrate generation, and the decomposition, the phase equilibrium line adopted by this study is the regression form proposed by Moridis in 2003 [35]:

$$\begin{aligned} T \geq 273.2 \text{K} \quad \ln P_e &= \begin{cases} -1.94138504464560 \times 10^5 + 3.31018213397926 \times 10^3 T \\ -2.25540264493806 \times 10^1 T^2 + 7.67559117787059 \times 10^{-2} T^3, \\ -1.30465829788791 \times 10^{-4} T^4 + 8.6065316687571 \times 10^{-8} T^5 \end{cases} \\ T \geq 273.2 \text{K} \quad \ln P_e &= \begin{cases} -4.38921173434628 \times 10^1 + 7.76302133739303 \times 10^{-1} T \\ -7.27291427030502 \times 10^{-3} T^2 + 3.85413985900724 \times 10^{-5} T^3, \\ -1.03669656828834 \times 10^{-7} T^4 + 1.09882180475307 \times 10^{-10} T^5 \end{cases} \end{aligned} \quad (6)$$

where T is the temperature (K) and P_e is the pressure balance corresponding to T (MPa).

2.3. Boundary Conditions. The inlet pressure of the wellbore, external environment temperature, horizontal well length, gas production index, and liquid production index are included as follows:

$$\begin{cases} P(L) = P_L, \\ T(L) = T_L, \end{cases} \quad (7)$$

$$T_e = T_e(h), \quad (8)$$

$$\begin{cases} E_i(L) = 0 \\ v_j(L) = 0 \end{cases} \quad j = g, w, H, \quad (9)$$

where h is the wellbore depth (m), T_e is the environment temperature (K), T_e is the linear function of the wellbore depth (h), and P_L and T_L are the horizontal well toe-end pressure and temperature.

The main difference between the model in this paper and those for well drilling and gas transportation is that the gas and water will flow into the horizontal wellbore through the perforations during the development of the hydrate-bearing layer. Therefore, the fluid flow in the wellbore is variable mass flow, and the gas and liquid production indices are used

to determine the inflow rate of gas and water as follows:

$$\begin{cases} J_g = I, \\ J_w = J, \end{cases} \quad (10)$$

where I and J are the gas production index and liquid production index and L is the horizontal well length (m).

3. Solution and Verification of Model

3.1. Solution of Model. The node method is adopted to solve the model, which divides the horizontal well into N sections, and $N + 1$ nodes will be generated in total, where $i = 0, 1, \dots, N - 1, N$. Based on the flow direction, where $i = 0$ is located at the toe-end of the horizontal well, the model is then solved from the toe-end toward the heel end, deflecting the horizontal and vertical section successively. Figure 2 shows a flow chart of the calculation. The following takes any two nodes i and $i + 1$ in the wellbore as an example to describe the details of the calculation process. Assume that the parameters of the node i are known quantities used to calculate the values of each parameter at node $i + 1$.

- (1) Assume that the pressure and temperature of node $i + 1$ are P_{i+1} and T_{i+1} , respectively
- (2) Utilize the state equation to calculate the properties of each phase at node $i + 1$ and calculate the inflow

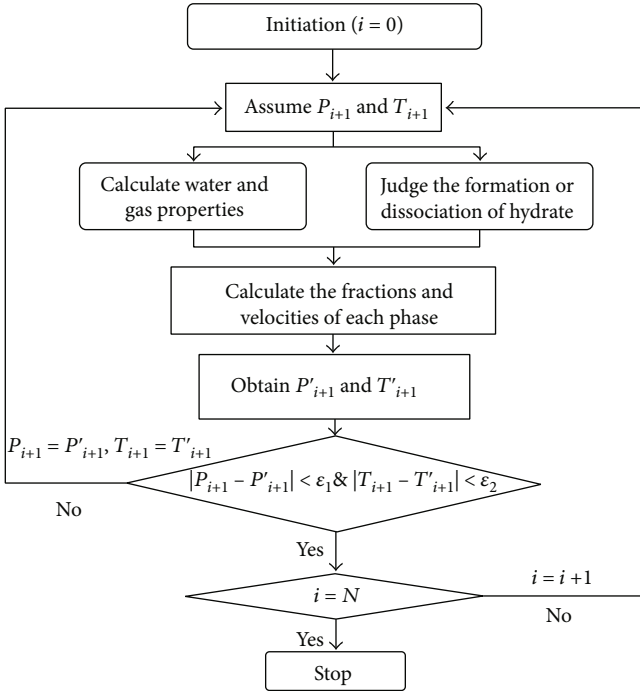


FIGURE 2: Calculation workflow.

terms of gas $q_{g,i+1}$ and water $q_{w,i+1}$ based on the gas output and liquid output indexes

- (3) Base on the pressure and temperature conditions at node $i + 1$ to judge whether the hydrate is generated; if the hydrate generation condition is met, the amount of hydrate generated is $R_{H,i+1}$, and the corresponding reaction heat can then be calculated. By contrast, if the hydrate decomposition condition is met, we can then judge whether the hydrate first exists. The calculation is not required if the hydrate does not exist, and if the hydrate does exist, the hydrate decomposition amount $R_{H,i+1}$ corresponding to the reaction heat can then be calculated
- (4) The continuity equation is used to solve the apparent rate of each phase v_{i+1}
- (5) The Beggs–Brill method is utilized to judge the flow type and determine the liquid holdup E_{wj+1}
- (6) The volume fractions of the hydrate phase E_{Hj+1} and gas phase E_{gj+1} are calculated, and the apparent rate is then utilized to solve the fluid velocities of each phase v_{j+1}
- (7) Substitute the determined parameters into the momentum and energy equations to solve the new P_{i+1} and T_{i+1}
- (8) If the obtained pressure and temperature are within the allowable error, i.e., $|P_{i+1} - P'_{i+1}| < \epsilon_1$, $|T_{i+1} - T'_{i+1}| < \epsilon_2$, then stop calculating the $i + 1$ node;

otherwise, return to step (1) to reestimate until the condition becomes true

- (9) Judge whether the $i + 1$ node is the last node; if not, take the parameters of $i + 1$ as the known conditions for the calculation of the next node and repeat the above steps. The entire calculation of the wellbore is then complete, and the calculation is finished
- (10) The parameters of all nodes in the wellbore can be calculated through the above steps

3.2. Model Verification. No detailed measurement data of the fluids in the wellbore of a natural gas hydrate reservoir with a recent trial production were available, and thus, the model verification in this study is simply for a vertical wellbore gas–liquid two-phase flow mode. The measured data in 14 actual water-and-gas producing wells in a Chinese gas field are shown in Table 1 [36]. In this study, a wellbore gas–liquid two-phase flow model was established, as described in Section 2.1, to calculate the flowing bottom-hole pressures of the 14 wells. We then compared them with the measured data, as shown in Figure 3. According to Figure 3, the relative error between the calculation results of the model established by this study and the measured data is between 0.6% and 8.4%, which means that the goodness of fit is generally high, and thus, the model established through this study is reliable.

The model in this paper is verified with field data from the well testing operations on a deepwater gas well: M-3, see refer [37]. The temperature profile along the wellbore is calculated. The ambient temperature profile is the same as in the reference. The calculated data and the measured data are shown in Figure 4. It shows that the calculated data is consistent with the testing temperature.

4. Results and Discussions

4.1. Temperature-Pressure Distribution and Hydrate Generation in Wellbore. Taking the basic information of the natural gas hydrate reservoir of the Shenhu Sea area of the South China Sea as a reference to conduct a parameter selection, the main parameters are as shown in Table 2 [38–41]. We assume the original pressure and temperature of a hydrate reservoir to be 10 MPa and 11°C, respectively. During the depressurization development process, excessive depressurization will readily lead to a fast air and water flow and the production of sand; therefore, the depressurizing range will generally not exceed 50% [42]. The depressurization range of a horizontal well is selected to be 5 MPa, which means that the horizontal well produces a pressure of 5 MPa at a flowing bottom hole. Based on the hydrate phase equilibrium line, which was regressed by Moridis, the hydrate phase equilibrium temperature corresponding to 5 MPa is approximately 6.4°C; considering that the depressurization will first lead to a fast hydrate decomposition in the near-wellbore area, the temperature of the near-wellbore formation will decrease to near the equilibrium temperature. At this moment, if the pressures of the wellbore and near-wellbore

TABLE 1: Measured data in gas wells.

Well no.	Well depth	Gas output, 10^4 m ³ /d	Water output, m ³ /d	Wellhead temperature, °C	Well-bottom temperature, °C	Wellhead pressure, MPa	Well-bottom pressure, MPa
1	3260	5.3	15.7	34	106.5	20.402	27.704
2	3260	4.3	7	33	106	24.088	32.234
3	3260	3	3.5	32	108	30.137	39.195
4	2520	6.5	48	43	89	7.436	13.077
5	2520	5.2	33	41	96	7.482	13.164
6	2520	4	29	40	99	7.301	13.122
7	2520	3.5	38	39	98	7.012	13.155
8	2330	2.4	50	35	85	9.002	17.363
9	2330	2	45	35	84	8.679	17.597
10	2800	2	35	35	100	4.989	11.454
11	2800	1	11.3	35	97	8.367	14.185
12	3260	4.5	12	24	106	16.392	23.911
13	2860	2.5	49	31	107.6	4.394	10.592
14	2800	2	33	30	101.9	6.433	12.024

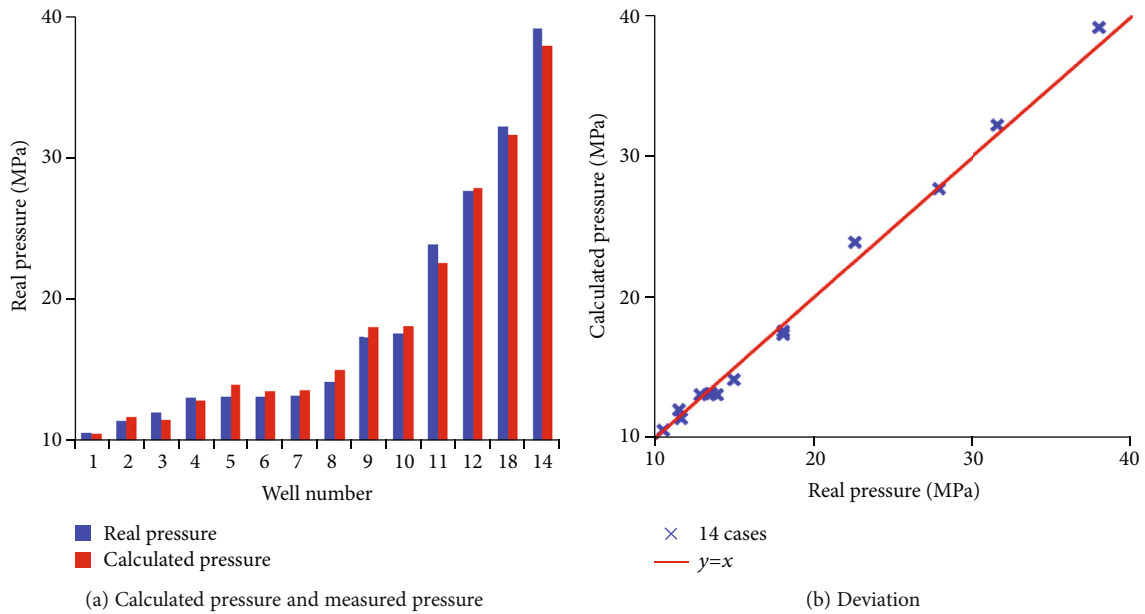


FIGURE 3: Comparison between calculated results and measured data of flowing bottom-hole pressure.

formation increase owing to a change in production and other factors, a secondary hydrate generation will easily occur in the near-wellbore formation and wellbore. Assume that the toe-end pressure increases to 7 MPa, the differential pressure of the production is 2 MPa, and thus, the pressure of the near-wellbore formation is 9 MPa.

Figure 5 shows the original temperature and pressure distribution along with the wellbore formation. The original temperature and pressure curves of the formation can be divided into four parts: Section I is the horizontal section of a horizontal well; the formation pressure in this section decreases to 9 MPa owing to the depressurization

development, and the pressure in the near-wellbore formation decreases to approximately 6.4°C owing to the endothermic decomposition of the near-wellbore hydrate. Section II is the hydrate layer section; the vertical deep span of this section is 30 m, and the wellbore length in this section is approximately 80 m owing to the deflecting section. According to the radial flow principle, the formation temperature and pressure will gradually restore to the original formation temperature and pressure in a logarithmic form as the vertical distance between this section and the horizontal well increases. Section III is the original formation section, and the temperature and pressure in this

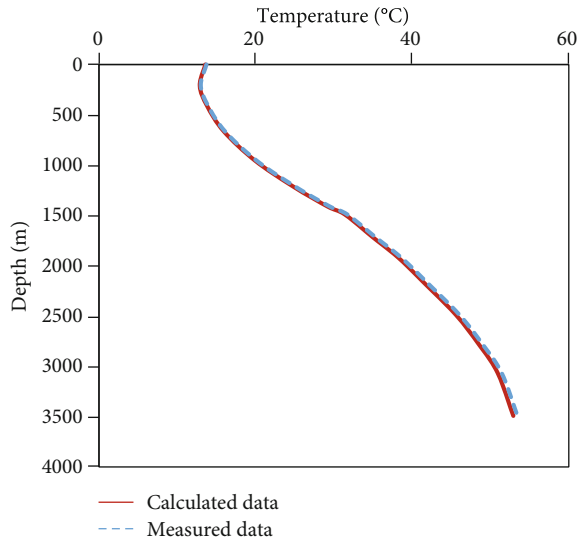


FIGURE 4: Comparison between the calculated temperature and measured temperature (M-3 well: gas production rate = $30 \times 10^4 \text{ m}^3/\text{d}$; water flow rate = $10 \text{ m}^3/\text{d}$).

section are the temperature and pressure of the original formation, where the temperature gradually decreases as the depth decreases. When the flow reaches the bottom of the ocean, the temperature is 5°C and the pressure is 8 MPa. Section IV is the seawater section, and the temperature and pressure in this section increase linearly as the well length increases. When it finally reaches the ground, the temperature is 25°C , whereas the pressure is 0.1 MPa.

Figure 6 shows the temperature and pressure distribution in the wellbore. It should be noted that the dotted line in Figure 6(b) denotes the equilibrium temperature at the corresponding pressure in the wellbore. Figure 7 shows the gas and water output profiles of the horizontal section at the corresponding standard ground temperature and pressure, and the hydrate flow velocity curve in the wellbore. As indicated in Figure 6, in the horizontal section, namely, Section I, the changes in the wellbore temperature and pressure are small, mainly because the viscosities of gas and water are low and the pressure loss caused by frictional resistance is also small, whereas the pressure is mainly consumed during a lift in the inclining and vertical sections; similarly, the temperatures of the inflow gas and water are the same as the formation environment temperature; meanwhile, the influences of the heat conduction and convection can be analyzed by comparing Figures 5 and 6(b). The two changing trends of the wellbore fluid temperature and the environment temperature are consistent after the entrance of the fluid into the deflecting section. The formation temperature is higher than the wellbore fluid temperature, and thus, the fluid temperature will continually increase. However, as the depth decreases, the formation temperature continually decreases, and therefore, the wellbore fluid temperature will decrease continually and the temperature will reach the lowest point at the bottom of the sea section; after

entering the seawater section, the seawater temperature increases as the depth decreases, and the wellbore fluid temperature increases continually. The shaded area in Figure 6(b) indicates that the wellbore fluid temperature is lower than the equilibrium temperature in the wellbore section; the temperatures in Sections I–IV are lower than the equilibrium temperature, and thus, different levels of hydrate are generated. By considering Figure 7(b) as well, the hydrate flow rates in these three sections continually increase, the hydrate generation rate is high, and the increasing amplitude of the flow rate is large when the difference between the wellbore temperature and equilibrium temperature is significant; when fluid enters Section III, the hydrate generation rate slows down and the increase in the amplitude of flow rate correspondingly decreases as the wellbore fluid temperature increases. As the fluid enters Section IV, the seawater section, and migrates upward, the wellbore fluid temperature continually increases, finally exceeding the hydrate equilibrium temperature. The hydrate in the wellbore turns from a generation to decomposition, and because the decomposition rate is much faster than the generation rate, as shown in Figure 7(b), the hydrate flow rate will decrease rapidly until a full decomposition occurs, and the flow rate is zero. Numerically, the maximum hydrate flow rate in the wellbore is $0.044 \text{ m}^3/\text{d}$ because the diameter of the wellbore is small and the tubing volume per unit length is only $7.85 \times 10^{-3} \text{ m}^3$. If the generated hydrate has a certain amount of pipe wall deposition, it easily causes the effective diameter of the wellbore to decrease and even block the wellbore, and thus, wellbore heating and other measures should be adopted to prevent the hydrate generation in the wellbore and ensure a smooth production. According to Figure 7(a), the wellbore pressures from the toe-end to the heel-end are slightly decreased owing to a friction resistance, and thus, the differential pressure corresponding to the toe-end is the largest. The gas and water output rates are also the greatest at this point; however, the heterogeneity of the formation is not considered in this scheme because the frictional resistance is relatively small, the difference in the inflow profile throughout the entire wellbore is relatively small, and the water and gas outputs under the ground obtained through accumulation are 1.38×10^4 and $91.7 \text{ m}^3/\text{d}$, respectively.

4.2. Analysis of Influencing Factors. Hydrate generation is closely related to the temperature and pressure in the wellbore. In this section, we investigate the influences of the environment temperature and wellbore pressure on the hydrate generation and inflow performance.

4.2.1. Wellbore Pressure. Each parameter is kept consistent with the basic scheme, whereas the toe-end pressure is changed to 6 MPa (corresponding to a difference in production pressure of 3 MPa) and 8 MPa (corresponding to a difference in production pressure of lower than 1 MPa). Figure 8 shows a comparison diagram of the on-way pressure, temperature, hydrate flow rate, total gas, and water output under different toe-end pressures. Among them,

TABLE 2: Basic parameters.

Basic parameters	Value	Basic parameters	Value
Horizontal section length, m	500	Wellhead environment temperature, °C	25
Submarine environment temperature, °C	5	Submarine section length, m	800
Horizontal well burial depth, m	1,000	Deflecting section length, m	150
Sea temperature gradient, °C/100 m	-2.5	Formation temperature gradient, °C/100 m	3
Gas output index, kg/(MPa·m·s)	0.0001	Water output index, kg/(MPa·m·s)	0.001
Hydrate reservoir pressure, MPa	10	Thermal conductivity of formation, W/m/°C	3.92
Radius of tubing, m	0.05	Tubing thickness, m	0.01
Radius of casing, m	0.1	Casing thickness, m	0.01
Radius of cement sheath, m	0.15	Cement sheath thickness, m	0.05
Thermal conductivity of cement, W/m/°C	19.4	Thermal conductivity of casing and tubing, W/m/°C	45
Hydrate formation rate, mole/(MPa·s·m ²)	2.9×10^3	Hydrate dissociation rate, mole/(Pa·s·m ²)	1.24×10^{11}
Activation energy, J/mole	81084.2	Reaction enthalpy, J/mole	51858

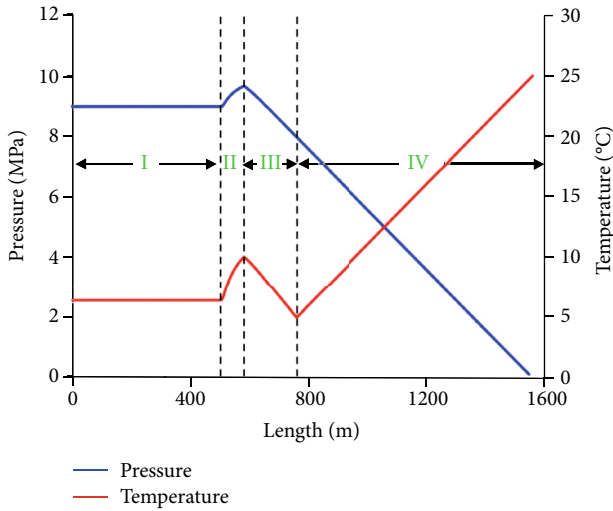


FIGURE 5: The original temperature and pressure distribution along with wellbore.

the dotted line in Figure 8(b) denotes the hydrate phase equilibrium temperature (EqT) of the corresponding wellbore pressure. According to Figure 8(a), the changing trends of the wellbore pressure under different toe-end pressures are the same, and the change in the differential pressure in the horizontal section is small; in addition, a decrease in the main pressure occurs in the fluid lifting of the vertical wellbore. The lower the toe-end pressure is, the lower the on-way pressure will be in the wellbore. Thus, the equilibrium temperature in Figure 8(b) corresponding to the toe-end pressure of 6 MPa is the lowest point; the fluid temperature in the wellbore will rapidly increase to above the equilibrium temperature after the fluid enters the deflecting section. The hydrate starts to decompose at this time, as shown in Figure 8(c). The hydrate flow rate in the wellbore will rapidly decrease. When the toe-end pressures reach 7 and 8 MPa, respec-

tively, owing to the relatively high hydrate phase equilibrium temperatures, the temperature will increase to above the equilibrium temperature only when the wellbore fluid reaches the wellbore of the seawater section. According to Figure 8(c), the hydrate peak flows corresponding to 6, 7, and 8 MPa are 0.016, 0.044, and 0.085 m³/d, respectively. According to the comparison results between the gas and water outputs (Figure 8(d)), the lower the wellbore pressure is, the greater the corresponding production differential pressure will be, and the larger the gas and water outputs that will occur without a change in the gas and liquid production indexes. Overall, the wellbore pressure has a significant influence on the hydrate generation and the generation area; in addition, the amount of hydrate flow in the wellbore increases as the toe-end pressure increases, and thus, the pressure in the wellbore should be closely monitored during the actual development of a hydrate reservoir to prevent hydrate generation and wellbore blockage.

4.2.2. Environment Temperature in the Horizontal Section. During the depressurization process of a horizontal well, the temperature of the near-wellbore formation continually decreases because of the hydrate endothermic decomposition. It should be noted that the toe-end pressure in this section is assumed to be 7 MPa. To simulate the hydrate generation in the wellbore under different environment temperatures, the environment temperatures of the horizontal section are set to 5.4°C, 6.4°C, and 7.4°C, respectively. Because the differential pressure and gas and water production indexes during production are constant, it can be seen that the pressure and gas and water inflows in the wellbore of the three schemes are basically the same. Figure 8 only compares and analyzes the temperature and amount of hydrate flow in the wellbore; at the same time, because the pressure change is small, the three schemes in Figure 9(a) only plot one hydrate phase equilibrium line corresponding to the wellbore pressure. According to Figure 9(a), the difference among the

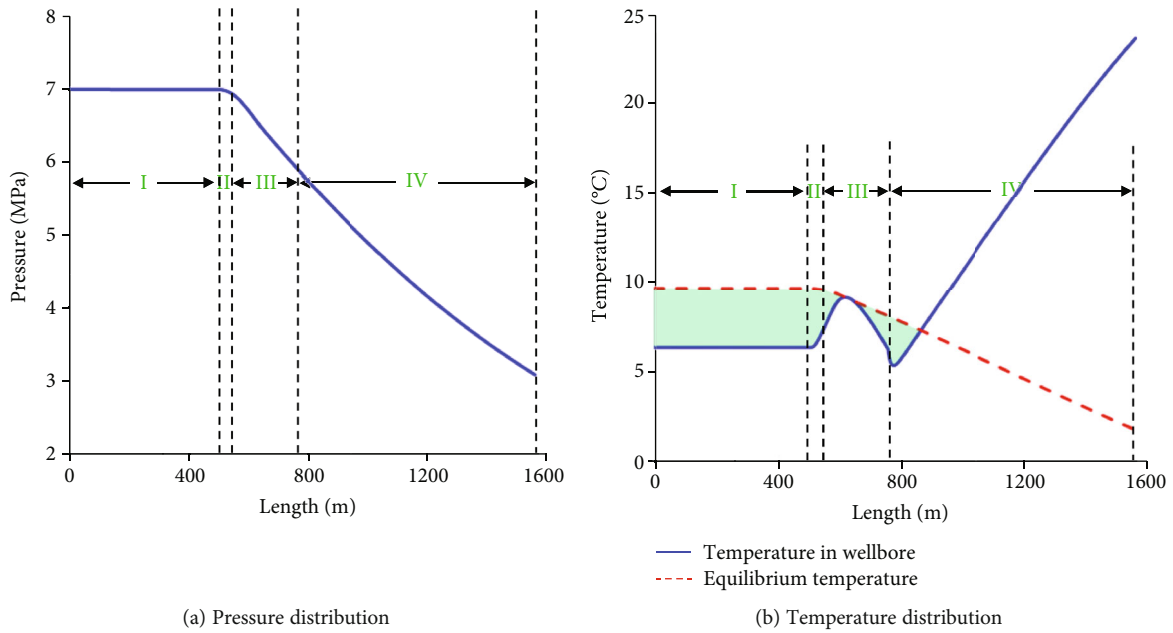


FIGURE 6: Temperature and pressure distribution in the wellbore.

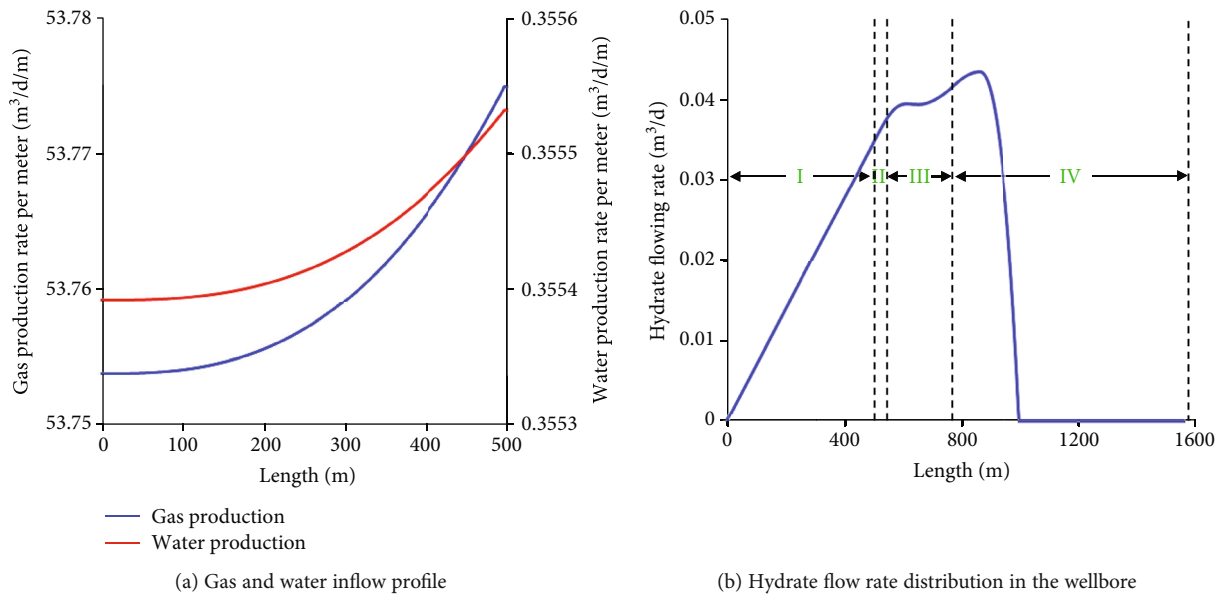


FIGURE 7: Gas and water inflow profile and hydrate flow rate distribution in the wellbore.

wellbore temperature distributions corresponding to the three schemes is only reflected in the horizontal and deflecting sections; the lower the environment temperature is, the lower the fluid temperature will be in a horizontal section. For the deflecting section, the fluid temperature in the wellbore will rapidly increase because of the increase in the environmental temperature. The temperatures in the wellbore for the three schemes are gradually approaching each other. According to Figure 9(b), the

lower the temperature is in the horizontal section, the faster the hydrate generation rate will be, and the maximum hydrate flow rates corresponding to environment temperatures of 5.4°C, 6.4°C, and 7.4°C are 0.036, 0.044, and 0.048 m³/d, respectively, which means that a lower wellbore temperature will lead to a faster hydrate generation rate; however, because the hydrate decomposition rate is much faster than its generation rate, the hydrate will rapidly decompose when the temperature in the wellbore is

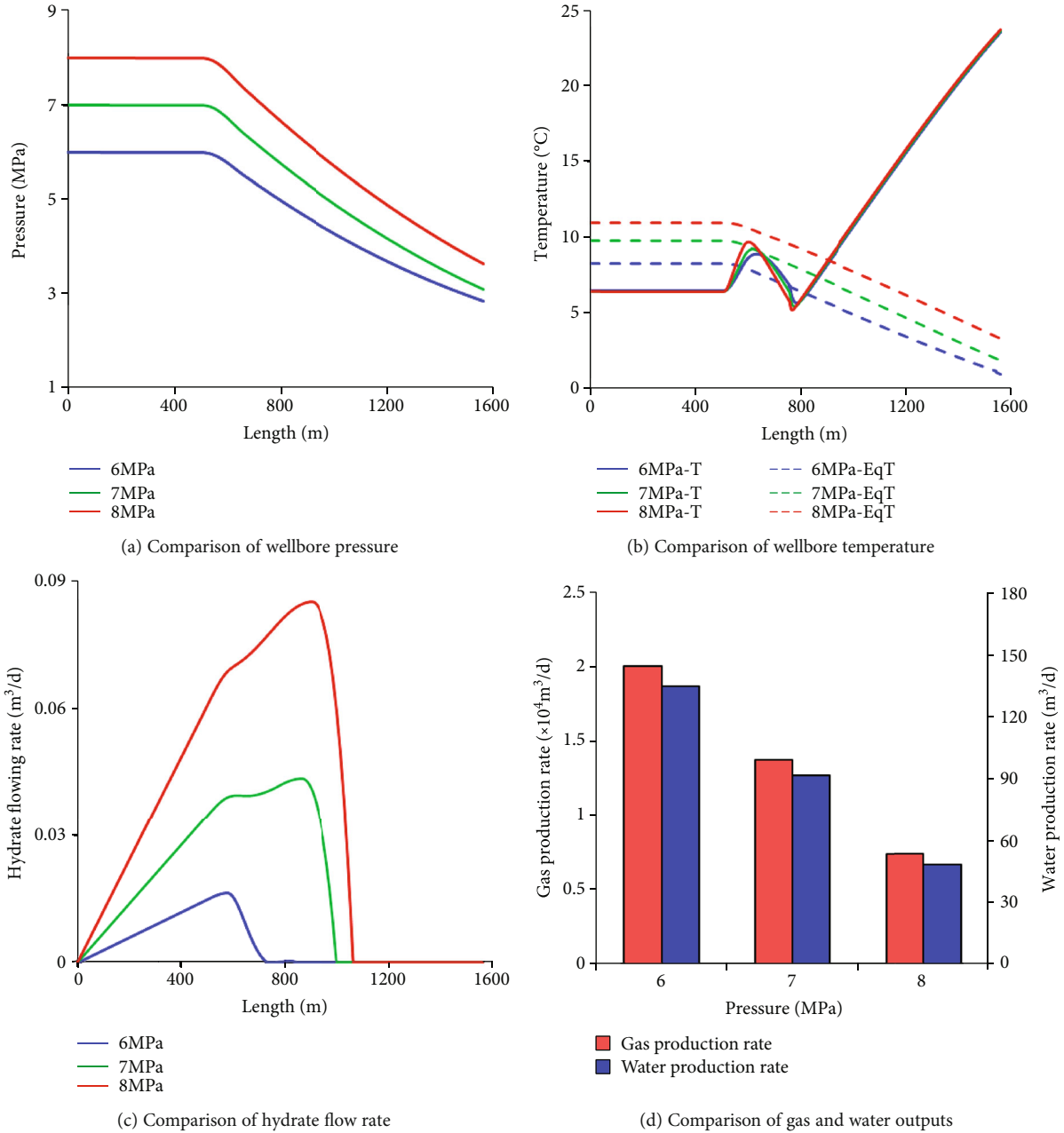


FIGURE 8: Comparison of each wellbore parameter under different toe-end pressures.

higher than the hydrate phase equilibrium temperature, and the differences among the hydrate generation areas in the three schemes are slight.

4.2.3. Influence of Gas Output. To investigate the influence of the gas output on hydrate generation in the wellbore, assuming the toe-end pressure and environment temperature as 7 MPa and 6.4°C, respectively, the gas output index is set as $0.5 \times 10^{-4} \text{ kg}/(\text{MPa} \cdot \text{m} \cdot \text{s})$, $1 \times 10^{-4} \text{ kg}/(\text{MPa} \cdot \text{m} \cdot \text{s})$, and $1.5 \times 10^{-4} \text{ kg}/(\text{MPa} \cdot \text{m} \cdot \text{s})$ for the three schemes, respectively. Figure 10 shows a comparison diagram of the on-way pressure, temperature, hydrate flow rate, and total gas

and water outputs under different gas outputs. It can be seen from the figure that, because the frictional resistance of the wellbore is small, the difference among the fluid pressures in the horizontal wellbore under different gas outputs is slight. For the vertical wellbore, the gas holdup increases because, owing to a large gas output, the density of the gas-water mixture decreases, and thus, the differential pressure in the vertical section under a large gas output is small. According to Figure 10(b), although the difference among the fluid pressures in the wellbore under different gas outputs is slight, the pressures in the vertical wellbore under different gas outputs are different, and the corresponding phase

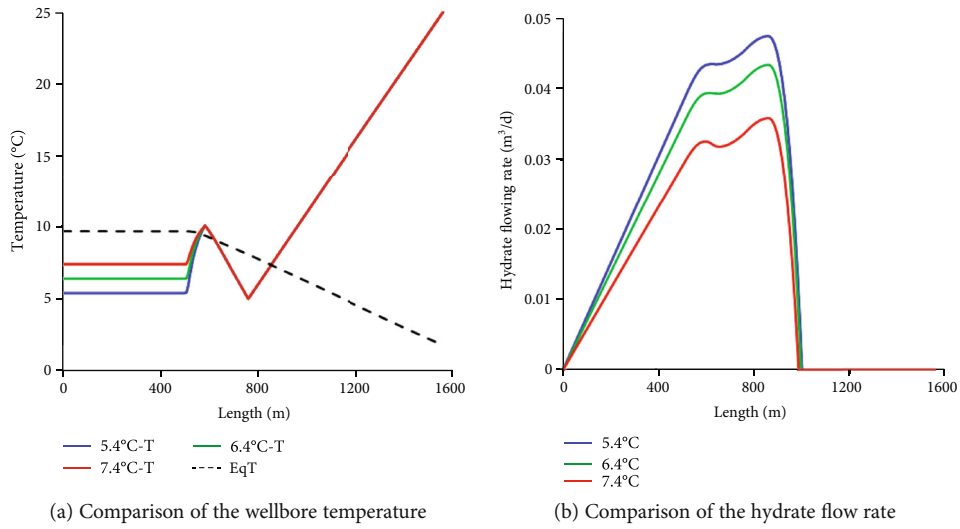


FIGURE 9: Comparison of wellbore temperature and hydrate flow rate under different horizontal well environment temperatures.

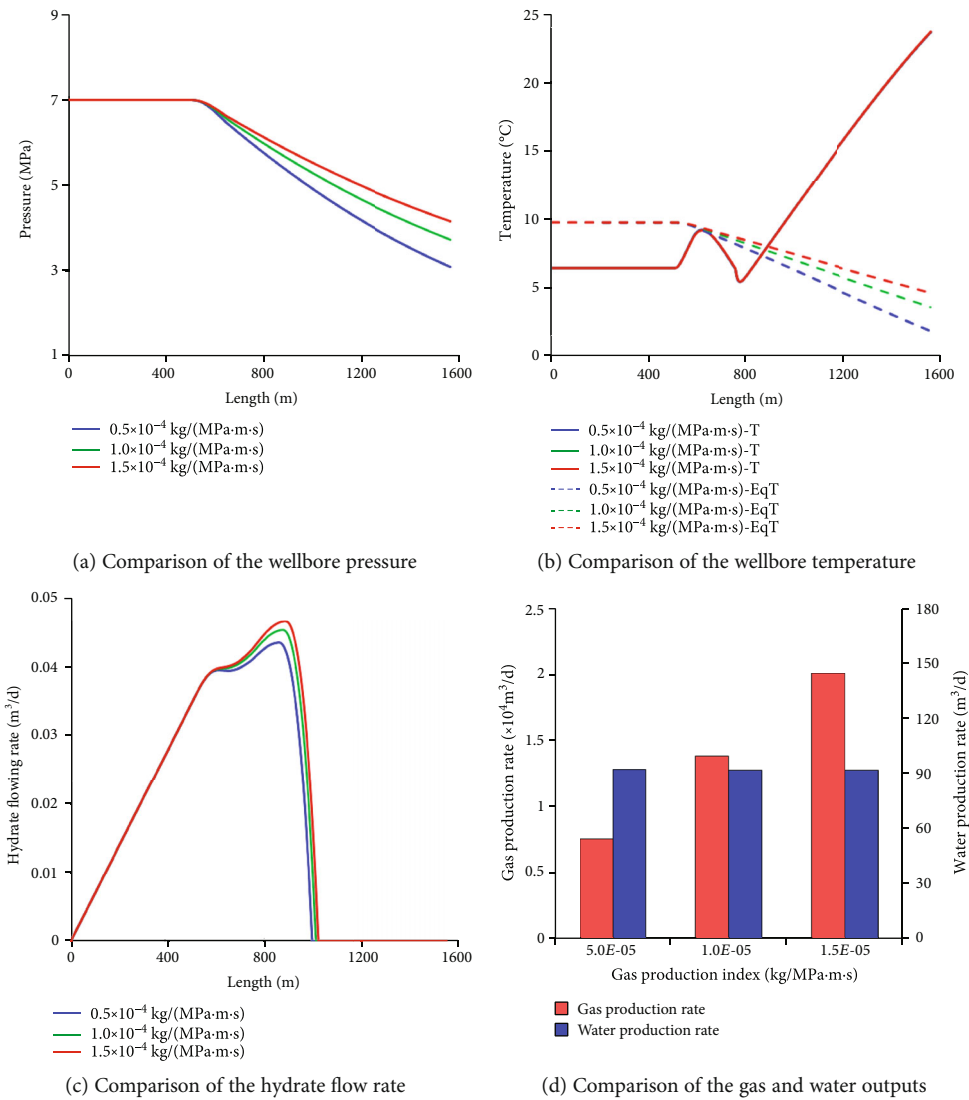


FIGURE 10: Comparison of each wellbore parameter under different gas output indexes.

equilibrium pressures also have some differences, i.e., the larger the gas output, the higher the equilibrium temperature of the corresponding vertical section will be. At the same time, according to Figure 10(c), the higher gas output corresponds to a larger hydrate generation area and hydrate generation amount, although the differences among the three schemes are generally small. Because only the gas production index is changed, and according to Figure 10(d), the liquid outputs of the three schemes are basically the same; the gas outputs increase as the gas output indexes increase.

5. Conclusions

In this study, a multiphase pipe flow of a horizontal well was combined with natural gas hydrate generation and a decomposition dynamics model to establish a set of gas–liquid–solid three-phase flow models of a horizontal well when considering the phase transition in the wellbore. Based on this model, the temperature and pressure distribution and hydrate secondary generation rule are analyzed in the wellbore. The main conclusions obtained are as follows:

- (1) The viscosities of gas and water are low, the pressure loss in the horizontal section caused by frictional resistance is small, and the fluid pressure in the horizontal section is almost the same. If the toe-end pressure is higher than the equilibrium pressure of the hydrate phase, the hydrate generation condition will be met within the entire horizontal section
- (2) The fluid pressure loss in a wellbore is mainly consumed in the fluid lifting of the deflecting section and the vertical section after it reaches the deflecting section; when the environment temperature changes, the changing trends of wellbore fluid temperature and environment temperature are the same. Because the temperatures of the sea-bottom and the subbottom formation are relatively low, the horizontal wellbore area mainly concentrates on the horizontal section of the horizontal well, the sea-bottom formation section, and the subsea area if the hydrate generation condition is met in a horizontal wellbore
- (3) For the case described herein, the fastest hydrate flow in the wellbore is $0.044 \text{ m}^3/\text{d}$. If the generated hydrate has certain amounts of pipe wall deposition, it may block the wellbore and cause a decrease in its effective diameter. Heating and other measures should be adopted to prevent hydrate generation in the wellbore to ensure a smooth production
- (4) Pressure in the wellbore has a significant influence on the secondary hydrate generation. In addition, the hydrate generation area and flow amount in the wellbore increase as the toe-end pressure increases, and thus, to prevent a hydrate generation and wellbore blockage, the pressure in the wellbore should be closely monitored during the actual development of a hydrate reservoir. A lower wellbore temperature and higher gas output index will lead to a greater

amount of hydrate generated, and the influences of these two factors on the secondary hydrate generation will be much smaller than the influence of the wellbore pressure

The three-phase mass variable mathematical model of a horizontal well considers the hydrate phase transition, which is a stable state model. During the depressurization development process of a natural gas hydrate reservoir, the pressure, temperature, and gas and water indexes of the near-wellbore formation are continuously changing as the development progresses. At different development stages, the gas–water flow state and hydrate secondary generation situation in the wellbore are different, and the influence of the hydrate generated in the wellbore on the reservoir development is the study category of the instable model. Subsequent studies need to couple the established stable state model with a natural gas hydrate reservoir depressurization development model and utilize the coupled instability model to confirm the above studies.

Data Availability

The data used to support the findings of this study are available from the corresponding author upon request.

Conflicts of Interest

The authors declare that there are no conflicts of interest regarding the publication of this paper.

Acknowledgments

This work was financially supported by the National Natural Science Foundation of China (Grant No. 51804324), the National Science Foundation for Distinguished Young Scholars of China (Grant No. 51625403), the Major Scientific and Technological Projects of CNPC (ZD2019-184-002), Natural Science Foundation of Shandong Province (Grant No. ZR2017QEE008, ZR2018BEE004), the Indigenous Innovation Program of Qingdao (Grant No. 16-5-46-jch), and the Fundamental Research Funds for the Central Universities (Grant No. 18CX02169A).

References

- [1] Z. R. Chong, S. H. B. Yang, P. Babu, P. Linga, and X. S. Li, "Review of natural gas hydrates as an energy resource: prospects and challenges," *Applied Energy*, vol. 162, pp. 1633–1652, 2016.
- [2] J. B. Klauda and S. I. Sandler, "Global distribution of methane hydrate in ocean sediment," *Energy & Fuels*, vol. 19, no. 2, pp. 459–470, 2005.
- [3] A. Demirbas, "Methane hydrates as potential energy resource: part 2 – methane production processes from gas hydrates," *Energy Conversion & Management*, vol. 51, no. 7, pp. 1562–1571, 2010.
- [4] G. J. Moridis, T. S. Collett, R. Boswell et al., "Toward production from gas hydrates: current status, assessment of resources, and simulation-based evaluation of technology and potential,"

- SPE Reservoir Evaluation & Engineering*, vol. 12, pp. 745–771, 2009.
- [5] L. L. Liu, X. B. Lu, X. H. Zhang, C. L. Liu, and B. Du, “Numerical simulations for analyzing deformation characteristics of hydrate-bearing sediments during depressurization,” *Advances in Geo-Energy Research*, vol. 1, no. 3, pp. 135–147, 2017.
- [6] L. Huang, Z. Su, N. Y. Wu, and J. W. Chen, “Analysis on geologic conditions affecting the performance of gas production from hydrate deposits,” *Marine and Petroleum Geology*, vol. 77, pp. 19–29, 2017.
- [7] X. S. Li, C. G. Xu, Y. Zhang, X. K. Ruan, G. Li, and Y. Wang, “Investigation into gas production from natural gas hydrate: a review,” *Applied Energy*, vol. 172, pp. 286–322, 2016.
- [8] G. J. Moridis, T. S. Collett, S. R. Dallimore, T. Satoh, S. Hancock, and B. Weatherill, “Numerical simulation studies of gas production scenarios from hydrate accumulations at the Mallik Site, Mackenzie Delta, Canada,” in *Presented at 4th International Conference on Gas Hydrates, Yokohama Symposium*, Yokohama, Japan, May 2002.
- [9] Y. Liu, J. Hou, H. Zhao, X. Liu, and Z. Xia, “A method to recover natural gas hydrates with geothermal energy conveyed by CO₂,” *Energy*, vol. 144, pp. 265–278, 2018.
- [10] J. Sun, L. Zhang, F. Ning et al., “Production potential and stability of hydrate-bearing sediments at the site GMGS3-W19 in the South China Sea: a preliminary feasibility study,” *Marine and Petroleum Geology*, vol. 86, pp. 447–473, 2017.
- [11] Y. Liu, J. Hou, H. Zhao, X. Liu, and Z. Xia, “Numerical simulation of simultaneous exploitation of geothermal energy and natural gas hydrates by water injection into a geothermal heat exchange well,” *Renewable and Sustainable Energy Reviews*, vol. 109, pp. 467–481, 2019.
- [12] X. Zang, D. Liang, and N. Wu, “Investigation of CO₂ separation from synthesis CO₂/CH₄ mixture utilizing tetra-n-butyl ammonium bromide semi-hydrate,” *Canadian Journal of Chemical Engineering*, vol. 94, no. 9, pp. 1792–1800, 2016.
- [13] M. Pooladi-Darvish, “Gas production from hydrate reservoirs and its modeling,” *Journal of Petroleum Technology*, vol. 56, pp. 65–71, 2004.
- [14] J. Hou, E. Zhao, Y. Liu et al., “Pressure-transient behavior in class III hydrate reservoirs,” *Energy*, vol. 170, pp. 391–402, 2019.
- [15] G. Moridis, “Numerical studies of gas production from class 2 and class 3 hydrate accumulations at the Mallik Site, Mackenzie Delta, Canada,” *SPE Reservoir Evaluation & Engineering*, vol. 7, pp. 175–183, 2004.
- [16] E. M. Myshakin, M. Gaddipati, K. Rose, and B. J. Anderson, “Numerical simulations of depressurization-induced gas production from gas hydrate reservoirs at the Walker Ridge 313 site, northern Gulf of Mexico,” *Marine & Petroleum Geology*, vol. 34, no. 1, pp. 169–185, 2012.
- [17] E. M. Myshakin, T. Ajayi, B. J. Anderson, Y. Seol, and R. Boswell, “Numerical simulations of depressurization-induced gas production from gas hydrates using 3-D heterogeneous models of L-Pad, Prudhoe Bay Unit, North Slope Alaska,” *Journal of Natural Gas Science & Engineering*, vol. 35, pp. 1336–1352, 2016.
- [18] X. Ruan, Y. Song, J. Zhao, H. Liang, M. Yang, and Y. Li, “Numerical simulation of methane production from hydrates induced by different depressurizing approaches,” *Energies*, vol. 5, no. 2, pp. 438–458, 2012.
- [19] M. Gaddipati and B. Anderson, “3D reservoir modeling of depressurization-induced gas production from gas hydrate reservoirs at the walker ridge site, Northern Gulf of Mexico,” *Critical Care Medicine*, vol. 30, pp. 290–296, 2012.
- [20] G. A. Grasso, E. D. Sloan, C. A. Koh, and A. K. Sum, “Hydrate deposition mechanisms on pipe walls,” in *Presented at the Offshore Technology Conference*, Houston, TX, USA, May 2014.
- [21] S. V. Joshi, G. A. Grasso, P. G. Lafond et al., “Experimental flowloop investigations of gas hydrate formation in high water cut systems,” *Chemical Engineering Science*, vol. 97, pp. 198–209, 2013.
- [22] V. Andersson and J. S. Gudmundsson, “Flow properties of hydrate-in-water slurries,” *Annals of the New York Academy of Science*, vol. 912, no. 1, pp. 322–329, 2000.
- [23] L. Ding, B. Shi, X. Lv et al., “Investigation of natural gas hydrate slurry flow properties and flow patterns using a high pressure flow loop,” *Chemical Engineering Science*, vol. 146, pp. 199–206, 2016.
- [24] J. W. Nicholas, L. E. Dieker, E. D. Sloan, and C. A. Koh, “Assessing the feasibility of hydrate deposition on pipeline walls—adhesion force measurements of clathrate hydrate particles on carbon steel,” *Journal of Colloid and Interface Science*, vol. 331, no. 2, pp. 322–328, 2009.
- [25] E. Jassim, M. A. Abdi, and Y. Muzychka, “A new approach to investigate hydrate deposition in gas-dominated flowlines,” *Journal of Natural Gas Science and Engineering*, vol. 2, no. 4, pp. 163–177, 2010.
- [26] J. W. Nicholas, C. A. Koh, E. D. Sloan, L. Nuebling, H. He, and B. Horn, “Measuring hydrate/ice deposition in a flow loop from dissolved water in live liquid condensate,” *AIChE Journal*, vol. 55, no. 7, pp. 1882–1888, 2009.
- [27] Z. Wang, Y. Zhao, B. Sun, L. Chen, J. Zhang, and X. Wang, “Modeling of hydrate blockage in gas-dominated systems,” *Energy & Fuels*, vol. 30, no. 6, pp. 4653–4666, 2016.
- [28] Z. Wang, J. Zhang, B. Sun, L. Chen, Y. Zhao, and W. Fu, “A new hydrate deposition prediction model for gas-dominated systems with free water,” *Chemical Engineering Science*, vol. 163, pp. 145–154, 2017.
- [29] Z. Wang, J. Zhang, L. Chen et al., “Modeling of hydrate layer growth in horizontal gas-dominated pipelines with free water,” *Journal of Natural Gas Science and Engineering*, vol. 50, pp. 364–373, 2018.
- [30] H. Zambrano, L. D. G. Sigalotti, J. Klapp, F. Peña-Polo, and A. Bencomo, “Heavy oil slurry transportation through horizontal pipelines: experiments and CFD simulations,” *International Journal of Multiphase Flow*, vol. 91, pp. 130–141, 2017.
- [31] N. Wang, B. Sun, Z. Wang, J. Wang, and C. Yang, “Numerical simulation of two phase flow in wellbores by means of drift flux model and pressure based method,” *Journal of Natural Gas Science and Engineering*, vol. 36, pp. 811–823, 2016.
- [32] V. Oballa and L. Buchanan, *Flexible Wellbore Model Coupled to Thermal Reservoir Simulator*, Presented at World Heavy Oil congress, Puerto La cruz, Venezuela, 2009.
- [33] H. C. Kim, P. R. Bishnoi, R. A. Heidemann, and S. S. H. Rizvi, “Kinetics of methane hydrate decomposition,” *Chemical Engineering Science*, vol. 42, no. 7, pp. 1645–1653, 1987.
- [34] A. Vysniauskas and P. R. Bishnoi, “A kinetic study of methane hydrate formation,” *Chemical Engineering Science*, vol. 38, no. 7, pp. 1061–1072, 1983.

- [35] G. J. Moridis, "Numerical studies of gas production from methane hydrates," *SPEJ*, vol. 8, pp. 359–370, 2002.
- [36] Y. Jin, "Numerical simulation of two-phase gas-liquid flow in pipes," Ph.D. Thesis, Southwest Petroleum University, 2005.
- [37] Z. Wang, Y. Zhao, J. Zhang, S. Pan, J. Yu, and B. Sun, "Flow assurance during deepwater gas well testing: hydrate blockage prediction and prevention," *Journal of Petroleum Science and Engineering*, vol. 163, pp. 211–216, 2018.
- [38] G. Li, G. J. Moridis, K. Zhang, and X. S. Li, "The use of huff and puff method in a single horizontal well in gas production from marine gas hydrate deposits in the Shenhu Area of South China Sea," *Journal of Petroleum Science and Engineering*, vol. 77, no. 1, pp. 49–68, 2011.
- [39] K. Zhang, G. J. Moridis, N. Y. Wu, X. S. Li, and M. T. Reagan, "Evaluation of Alternative Horizontal Well Designs for Gas Production From Hydrate deposits in the Shenhu Area, South China Sea," in *International Oil and Gas Conference and Exhibition in China*, Beijing China, 2010.
- [40] C. L. Liu, Q. G. Meng, G. W. Hu et al., "Characterization of hydrate-bearing sediments recovered from the Shenhu area of the South China Sea," *Interpretation-A Journal of Subsurface Characterization*, vol. 5, pp. SM13–SM23, 2017.
- [41] Z. Su, G. J. Moridis, K. Zhang, R. Yang, and N. Y. Wu, "SS - Gas Hydrate: Numerical investigation of gas production strategy for the hydrate deposits in the Shenhu area," in *Offshore Technology Conference*, Houston, TX, USA, 2010.
- [42] Y. Liu, Y. Bai, Z. Xia, and J. Hou, "Parameter optimization of depressurization-to-hot-water-flooding in heterogeneous hydrate bearing layers based on the particle swarm optimization algorithm," *Journal of Natural Gas Science and Engineering*, vol. 53, pp. 403–415, 2018.

Research Article

Study on a New Rock Fracability Evaluation Model of Shale Gas Reservoir

Fei Wang ¹, Yonghao Zhang,² Xin Li,² and Xue Han²

¹College of Geology Engineering and Geomatics, Chang'an University, Xi'an 710054, China

²China Petroleum Logging Co. Ltd., Xi'an 710077, China

Correspondence should be addressed to Fei Wang; wangfeijlu-147@163.com

Received 20 March 2020; Revised 4 September 2020; Accepted 21 September 2020; Published 19 October 2020

Academic Editor: Wen-Dong Wang

Copyright © 2020 Fei Wang et al. This is an open access article distributed under the Creative Commons Attribution License, which permits unrestricted use, distribution, and reproduction in any medium, provided the original work is properly cited.

Shale gas is an important unconventional energy resource that needs large-scale fracturing to form industrial deliverability. The evaluation of reservoir fracability plays a key role in the optimization of the sweet spot, the design of multistage fracturing, and the prediction of economic benefit. Based on volumetric fracturing, the study proceeded from the fracture complexity of the fractured core, and the bursting pressure experiment technology using the constant strain rate method was established. After the core has fractured, the fracture morphology was extracted and the fracture parameters including fracture area ratio and fracture declination dispersion were calculated to construct the fracture complexity of the pressed core. Combined with the core strength, the fracability index of the core was determined to evaluate the reservoir fracability. This method can represent not only the fracturing effect but also the fracturing difficulty. Compared with the monitoring data of hydrofracture-induced microseism of the sample well, the core fracturing index was found to be in good agreement with the actual fracturing effect. This method is more reasonable than the traditional brittleness index method and rock mechanics parameter method.

1. Introduction

There are lots of shale gas resources in China. With the development of shale gas exploration and evaluation, several basins/areas with shale reservoirs in China (such as Fuling, Changning, Weiyuan, and Yanchang) have been industrially exploited, and they show promising prospects for exploration. However, due to the characteristics of shale gas reservoirs such as low porosity, low permeability, and low abundance, the single-well production rate is generally low and declines rapidly. One of the key factors restricting the recoverability of shale gas is the accurate prediction of the fracability of shale oil and gas reservoirs. The concept of the “brittleness index” introduced in shale gas development in North America has become the most important parameter in fracability evaluation of shale gas reservoirs. Different subjects and fields have different understandings of brittleness, so there is no widely accepted definition of brittleness and accurate calculation method. In the field of earth science, it is generally accepted that rocks show little or no plastic deformation before bursting, and it is characterized by brittleness.

In the study of shale reservoir brittleness evaluation, Jarvie et al. (2007) believed that the brittleness of reservoir rock was the characteristic parameter of rock fracture ability, which was the result of the comprehensive action of lithology, mineral composition, effective stress, reservoir temperature, pressure, pore fluid property, and total organic carbon [1]. Currently, the studies published for evaluating brittleness are mainly based on rock mineral composition, elastic parameters, and stress-strain tests. For the mineral composition method, Jarvie et al. (2007), Rickman et al. (2008), and Huiyuan et al. (2019) believed that the higher the content of brittle minerals in rocks, the more brittle the rocks would be [1–4]. For the rock mechanics parameter method, Rickman et al. (2008) and Goodway et al. (2010) believed that the rock brittleness index was closely related to Young's modulus and Poisson's ratio, and the brittleness would become greater when the Young's modulus gets larger and the Poisson's ratio gets smaller [3, 5]; Liu and Sun (2015) and Bai (2016) considered that different minerals have different brittleness, and they constructed a new elastic parameter, i.e., brittleness factor, which could better explain the

brittleness change in reservoir rocks [6, 7]. For the stress-strain method, the stress-strain curve of the rock which reflects the whole process of rock deformation, cracking, and ultimate loss of bearing capacity under external load is the most intuitive and effective method for qualitative evaluation of rock brittleness [8–10]. Jin et al. (2014), Bishop (1967), Tarasov and Potvin (2013), Munoz et al. (2016), and Ge et al. (2020) constructed the evaluation models of reservoir brittleness index based on their understandings of the stress-strain curve [11–15].

Currently, the brittleness index calculated based on mineral composition and rock mechanics parameters is a commonly used brittleness evaluation method in fracturing reconstruction. Despite the advantages in ease of use and high parameter accessibility, their theoretical defects and application limitations prevent them meeting the needs of unconventional reservoir development [16–18]. On the other side, the brittleness index characterized by the stress-strain curve of rock galloped ahead in recent years. The stress-strain curve theoretically illustrates a deformation-to-destruction process of the rock under external force, each part of the curve is of clear physical significance, but the entire curve is not in comprehensive use. Thus, to build a complete simplified model to describe an actually complex stress-strain curve is one of the obstacles for its wide application.

The existing methods of brittleness evaluation are generally based on certain properties of the rock itself. The brittleness index was proposed by studying the influence of these properties on the rock brittleness. However, it lacks quantitative evaluation on the effect of brittle fracture. For fracturing, the ultimate goal is to fracture the rock to form a complex network and maximize the contact volume of the reservoir. Therefore, from the perspective of the fracturing effect, a quantitative description of the brittle fracture degree is needed to study the relationship between fracture effect and rock properties. The establishment of a rock brittleness index for the quantitative description of the fracturing effect will be a more useful method for unconventional reservoir brittleness evaluation in the future. Based on rock volumetric fracturing, the fracturing difficulty and fracturing effect of the rock were comprehensively considered, and the fracture pressure test technology of the constant strain rate method was established in this study. Through this experiment, the fracture information of the fractured core was collected, and the fracture complexity was calculated. After combining them with the standard strength of the rock, a new core fracability evaluation model was constructed and was applied in the study area which has achieved satisfactory results.

2. Experimental Method

We tested the black shale of Wufeng-Longmaxi's formation of the upper Ordovician and lower Silurian in Sichuan basin as the research target and carried out the fracability test research of the mud shale reservoir based on volumetric fracturing. We established a new set of evaluation indexes of reservoir fracability and provided new ideas and methods for

fracability evaluation of shale gas reservoirs. The instrument used in this experiment was AutoLab 1500.

2.1. Experimental Samples. The samples selected in this study were from the black shale of Wufeng-Longmaxi formation in the Zhaotong area, Sichuan Basin, which is gray-black or dark black in color. With the low-speed diamond linear cutting technology, the core was processed into standard plunger samples with a diameter of 2.5 cm and length of about 4.8 cm. Finally, 16 samples which met the experimental requirements were processed.

The results from X-ray diffraction analysis of 16 rock samples from Wufeng-Longmaxi formation in the Zhaotong area are shown in Table 1. The change characteristics of lithology and mineral composition showed that the shale reservoir of Wufeng-Longmaxi formation is highly heterogeneous in the longitudinal direction, and the total organic matter content (TOC) ranges from 0.48 to 79% with average of 2.73%. The average of brittle minerals (quartz, feldspar, pyrite, and calcium carbonate) was found to be 57.9%, and the average of clay was 27.8%.

3. Principle of the Rock Fracability Measurement Based on Volumetric Fracturing

3.1. The Experimental Scheme. First the triaxial compressive experiment was performed to the core; the core was fractured and followed by optical scanning or X-ray CT scanning, and then the parameters of each fracture were collected and extracted. Fracture area ratio (or fracture porosity) and discrete degree of fracture inclination were calculated, and their average was taken after normalization. This average was just the fracture complexity of the fractured core. The higher the fracture complexity and the lower the core strength, the easier the core is to be fractured. The strength of the rock can be obtained by correcting the triaxial compressive strength to eliminate the size effect. The ratio of fracture complexity to rock strength after fracture is defined as the fracability index of the rock. The rationality of this method can be verified by the comparison between the core fracturing index and the monitoring data of hydrofracture-induced microseism. The key of this model is to use the constant strain rate method to control the fracturing degree of the mud shale and the accuracy of 2D and 3D fracture parameters extraction. The specific research scheme is shown in Figure 1.

3.2. Triaxial Compression Test of the Constant Strain Rate Method. Constant strain rate method is a common method of the triaxial compression test. In this study, the core fracturing is needed to be controlled on the same degree. During the fracturing experiment, the test confining pressure was loaded to the effective pressure condition of the reservoir, then the pressure front was controlled to drop at a constant speed, and the axial pressure was kept increasing. After the core fractured, the pressure front continued to drop at a uniform speed until the residual strength was confirmed, and then, the pressure was stopped. The process of constant strain rate method is shown in Figure 2.

TABLE 1: Shale mineral composition characteristics of Wufeng-Longmaxi formation.

Sample	Formation	Depth (m)	TOC (%)	Quartz (%)	K-feldspar (%)	Plagioclase (%)	Calcite (%)	Dolomite (%)	Pyrite (%)	Ankerite (%)	Clay mineral (%)
1	Longmaxi	1399.47	0.94	32.9	2.6	6.6	10.3	9.8	0.9	4.4	32.5
2	Longmaxi	1875.68	0.48	13.9	0	4.3	40.8	7.6	0.9	9.1	23.4
3	Longmaxi	1934.25	0.52	24.6	1.3	4.2	21.8	8.6	0.8	6.6	32.2
4	Longmaxi	2054.63	5.45	47	0	3.4	13	11.2	1.8	5.6	18
5	Longmaxi	2062.88	2.40	30.2	1	2.4	27.8	6	0	6.1	26.6
6	Longmaxi	2164.24	1.92	35.9	1	6.3	6.9	3.2	1.9	3.1	41.7
7	Longmaxi	2174.36	2.71	34	1.2	2.8	13.1	3.3	1.4	0	44.1
8	Longmaxi	2177.01	2.50	41.5	0	1.9	14.3	0	1.9	0	40.5
9	Wufeng	2200.92	7.79	47.1	0	6.6	7.6	5.8	1.8	4.5	26.6
10	Wufeng	2205.24	3.28	54.2	0	1.6	12.5	2.9	0	2.8	26
11	Wufeng	2285.55	2.81	25.3	1.1	2	28.3	19.3	2.6	13.3	8.2
12	Wufeng	2287.34	1.74	25.7	0.8	1.7	30.7	12.3	2.6	10.2	16
13	Baota	2293.97	0.90	20.1	1.7	5.8	26.6	1.9	0.9	4.2	38.7
14	Longmaxi	2507.35	—	—	—	—	—	—	—	—	—
15	Longmaxi	2508.57	—	—	—	—	—	—	—	—	—
16	Wufeng	2512.11	4.85	27.3	1	4.8	24.2	14.4	2.3	12.1	14

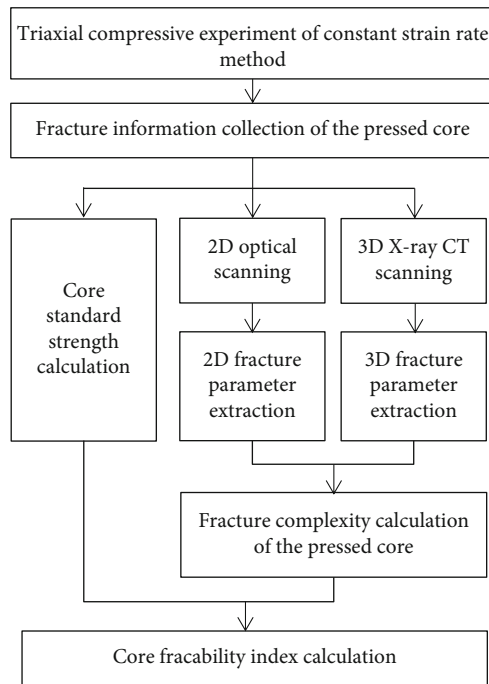


FIGURE 1: Technical flow of the shale fracability experiment analysis method based on quantitative FRAC of the fractured core.

It can be seen from Figure 2 that the axial pressure increased to the peak value at about 1000 s and then decreased which indicating the rock sample to be broken. After about 1150 seconds, the falling speed of axial pressure decreased, and the curve gradually formed an inflection point (of which the corresponding axial pressure is the residual strength of the rock sample). After about 1180 seconds, the

inflection point was confirmed, then the falling of curve was terminated, and the experiment was completed.

The 2D optical scanner and 3D CT scanner were used to scan the core fractures after being pressed. The results of the core fractures is shown in Figure 3(a) and 3(b).

4. Quantitative Evaluation Method of Fracability of the Shale Oil Reservoir Core

4.1. Fracture Analysis of the Pressed Core

4.1.1. Morphology Analysis of the 2D Core Surface Fracture. The lateral surface of the core can be roller scanned to obtain the fracture distribution image. The fracture morphology can be characterized by four parameters: fracture extension, fracture penetration, fracture width, and fracture inclination angle. The fracture extension is the length of the fracture on the side surface. Fracture penetration is the depth of the surface fracture entering into the core. The fracture width is the opening degree of the fracture. The fracture inclination angle is the angle between the fracture and the core axis.

Fractures can be divided into four levels based on the fracture morphology of the core. The characteristics are shown in Table 2. The fractures at all levels were manually retraced, and the treatment effect of the fracture image on the side surface is shown in Figure 4(a). The fracture extraction results of pressed cores are shown in Figure 4(b). The 2D fracture images of the pressed core in the test are shown in Figure 5.

After retracing the fractures, the length of each fracture and the length and width of fracture inscribed rectangle were extracted in pixels, which should be converted into the actual length when applied. The calculation method is shown in formula (1):

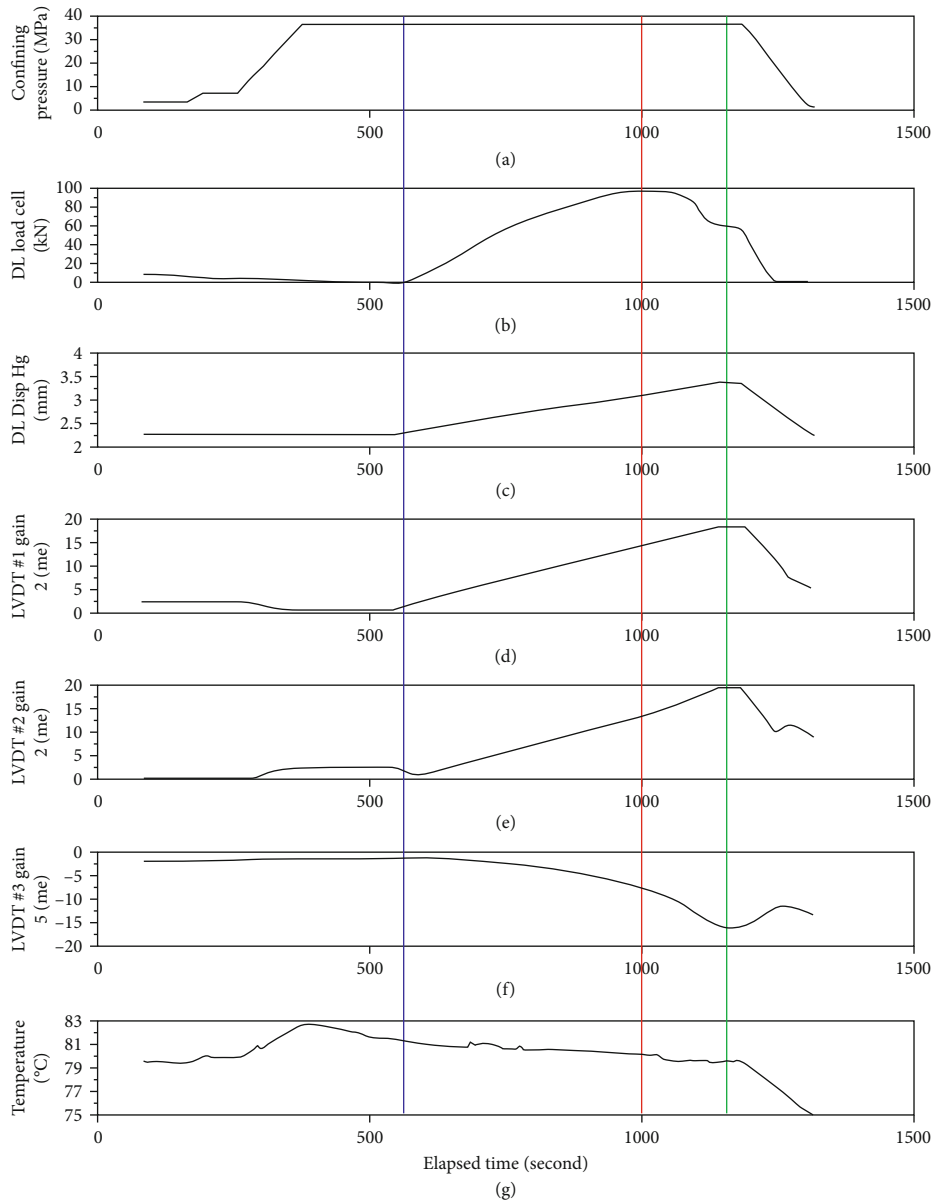
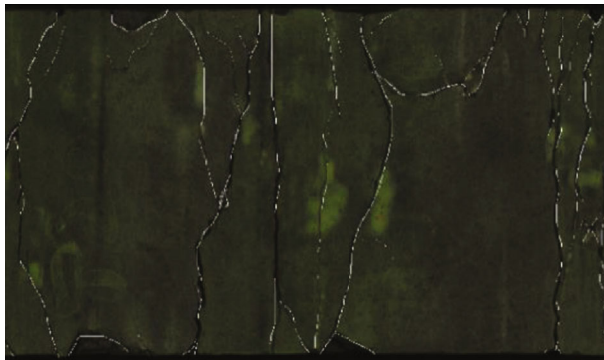
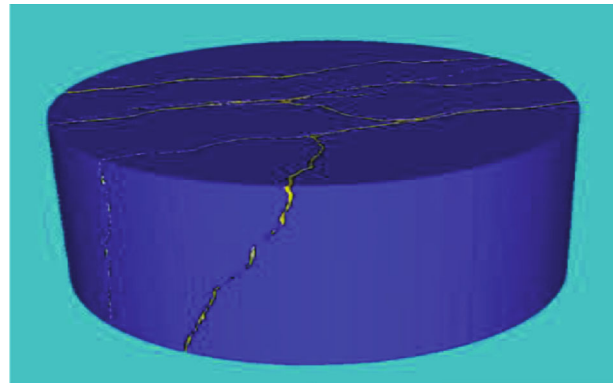


FIGURE 2: Bursting pressure experiment process of the constant strain rate method.



(a) Side view of the 2D optical scanning



(b) Fracture image of the 3D CT scanning

FIGURE 3: The 2D optical scan and the 3D CT scan of the shale samples.

TABLE 2: Fracture classification table of the pressed core.

Level	Name	The main characteristics
Level I	Main fracture	The longest and widest extension runs through the core, most cores have only one main fracture.
Level II	Secondary fracture	The extension and width are large, but the penetration degree is poor, and there are no symmetrical fractures on the plane graph.
Level III	Branch fracture	The extension and penetration are poor, but have a certain width; it is very obvious in the image. The occurrence is not consistent with the main and secondary fracture.
Level IV	Associated fracture	Small fractures have low extension, penetration, and width.

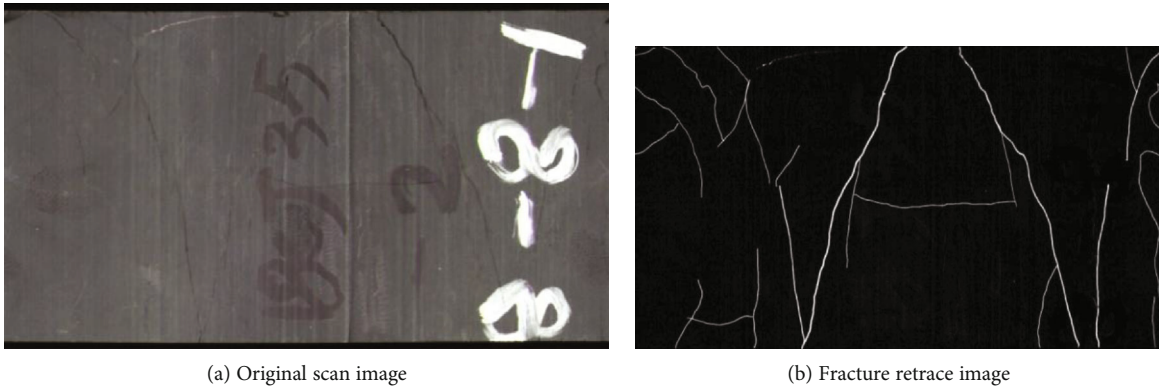


FIGURE 4: Side surface fracture images of the pressed core.

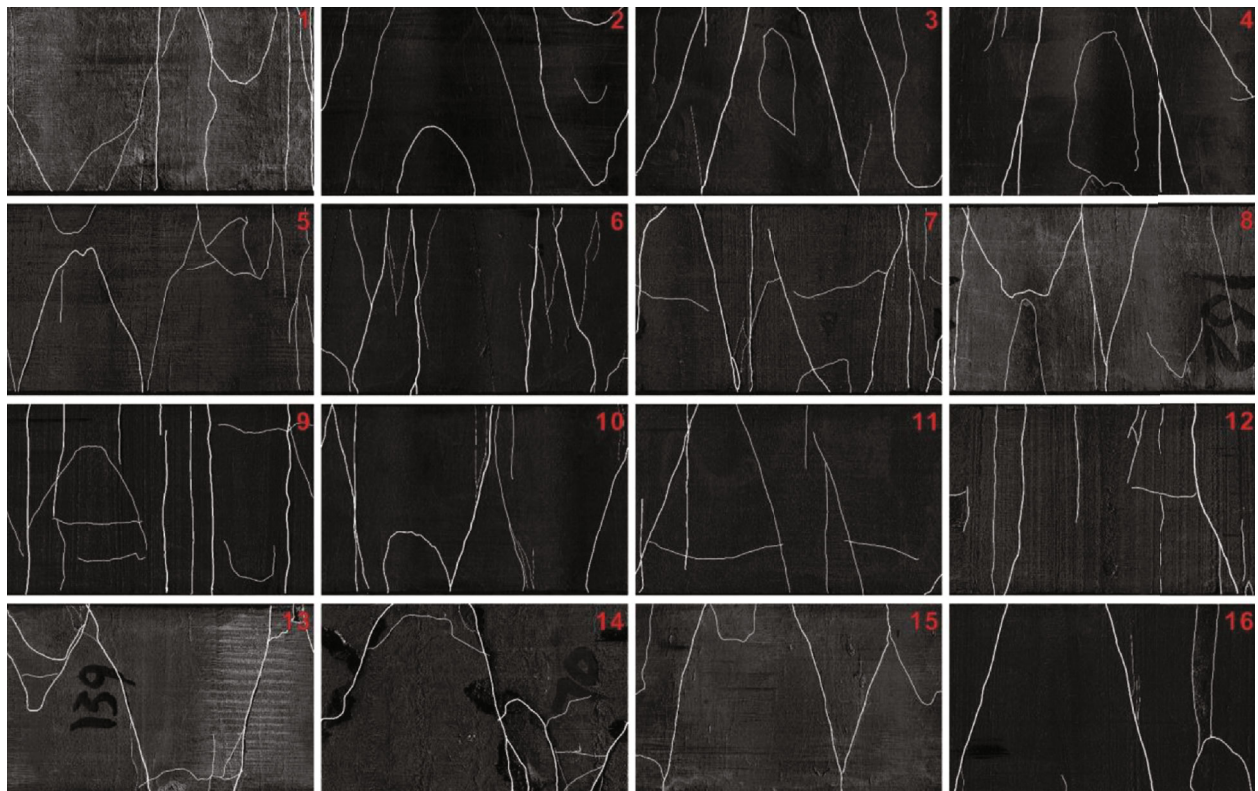


FIGURE 5: 2D fracture images of the pressed core.

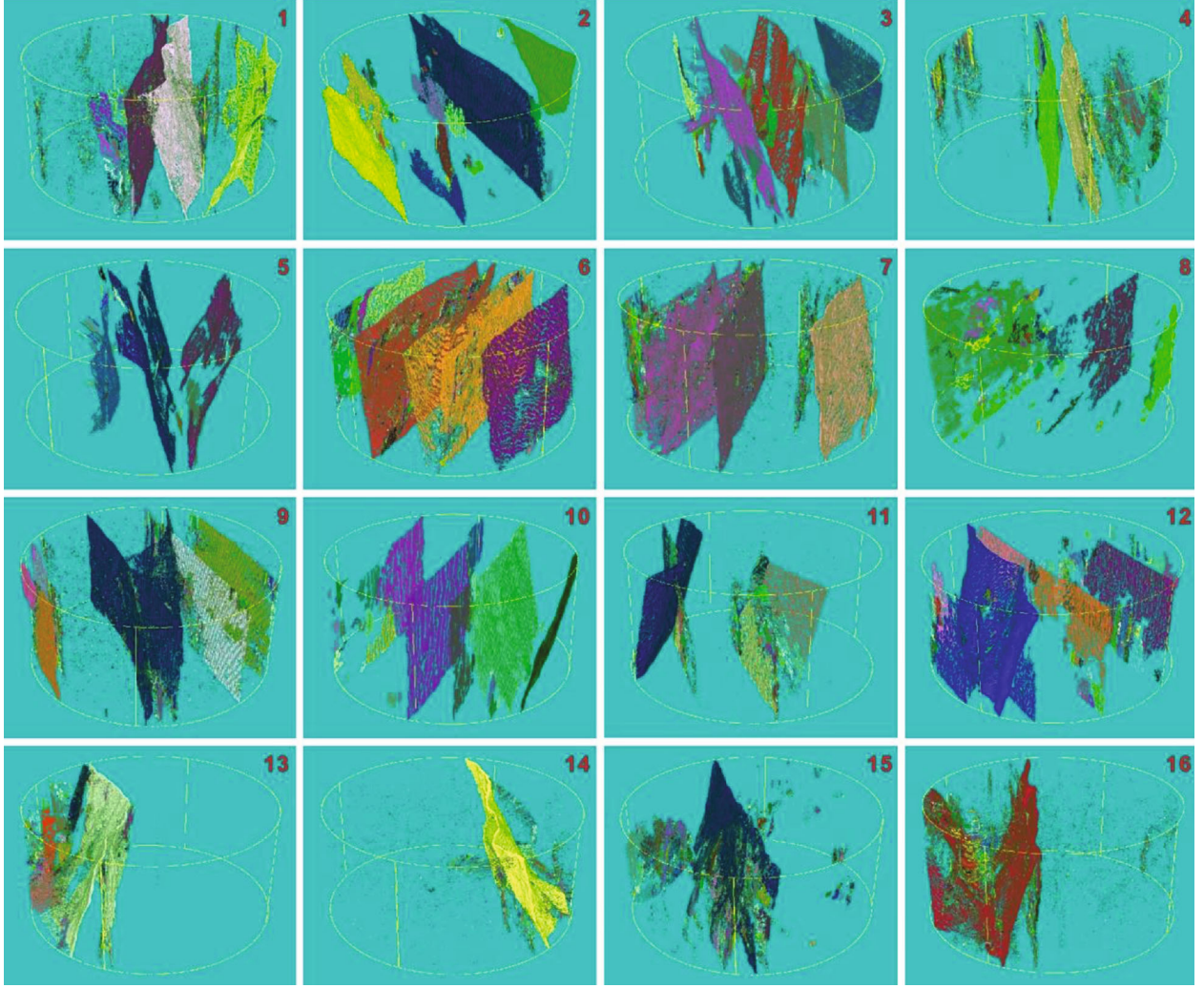


FIGURE 6: 3D fracture images after the core being pressed.

$$l_i = l_p \times \frac{h}{h_p}, \quad (1)$$

where l_i is the actual length of the fracture i , in mm; l_p is the pixel length of the fracture, in pixel; h is the actual height of the rock sample, in mm; h_p is the pixel height of the rock sample, in pixel. The calculation method of fracture inclination is shown in formula (2).

$$A = \arctan \frac{H}{W}. \quad (2)$$

In the formula, A is the crack inclination angle, the unit is degree; H and W are the height and width of the fracture's inscribed rectangle, both units are in pixel. The fracture inclination angle is calculated from formula (2), and the value of A is between 0° and 90° .

4.1.2. X-CT Fracture Analysis of the 3D Pressed Core. Based on real rock samples, digital core technology digitizes the core through a series of image processing technologies and

numerical algorithms to construct a 3D digital core. In this study, CT scanning images were used to construct digital cores and quantitatively characterize fracture information of shale cores before and after fracturing (Sinha 2006).

CT scanning images can be converted into a series of 2D images of core cross-sections through the reconstruction algorithm, and these images are combined to obtain the three-dimensional gray image of the core. From these images, 3D digital core construction and fracture parameter extraction were carried out for the core as shown in Figure 6.

The characteristics of the fractures in the CT scanning image are high grayscale, strong continuity, and a long and narrow line or dendritic distribution. Therefore, the 3D shape factor F can be used to describe the target morphology [15, 16].

$$F = 36\pi \frac{V_p}{S_p}, \quad (3)$$

where F represents the sphericity factor of the target; V_p is the target volume; S_p is the target surface area; when F

approaches 1, the target shape is close to a sphere; when F approaches 0 ($F < 0.05$), the target shape is planar in three-dimensional space.

The crack has ductility in 3D space; thus, the shape and ductility of the target can be characterized by the equivalent sphere radius R_{eq} and the minimum external sphere radius R_{min} . R_{eq} refers to the sphere radius that equals the volume of the target, which is only related to the target volume. R_{min} is closely related to the extensibility of the target in space. When R_{min} and R_{eq} of the target are close, the extension line of the equivalent sphere in all directions is similar. On the contrary, when $(R_{min}/R_{eq}) > 3$, it indicates that the extensibility only exists in a certain direction.

4.2. Calculation of Fracture Complexity after the Core Being Pressed. After the size and inclination of each fracture were obtained, the complexity of the fracture was studied. Regardless of two-dimensional or three-dimensional, the description of fracture complex degree should include two aspects: one is the size of the fracture which should include the number of fractures and each size of the fracture (2D for the fracture area, 3D for the fracture volume); another is the form of the fracture, which can be described by fracture dispersion. The higher the fracture dispersion, the closer the fracture gets to the reticulation. Fracture size can be represented by surface fracture rate (2D) or fracture porosity (3D), and the complexity of fracture form can be represented by fracture inclination dispersion.

Fracture area ratio is the ratio of the total area of all fractures to the lateral surface area of the core.

$$R_f = \sum_{i=1}^n \frac{l_i \times b_i}{S_1} \times 100, \quad (4)$$

where R_f is the fracture area ratio, dimensionless; l_i and b_i are the length and width of the fracture i , in mm; S_1 is the lateral surface area of the core and the unit is mm^2 .

Fracture porosity is the ratio of all fracture volumes in the 3D image divided by the total volume in the 3D reconstruction area of the core.

$$\varphi_f = \sum_{i=1}^n \frac{V_i}{V_t} \times 100, \quad (5)$$

where φ_f is the fracture porosity, dimensionless; V_i is the volume occupied by the space of fracture i in the 3D image; V_t is the total volume of 3D core reconstruction area.

The dispersion of fracture inclination angle is expressed as the variance of all fracture inclination angles:

$$D_a = \sqrt{\frac{\sum_{i=1}^n (A_i - \bar{A})^2}{n}} \times 100, \quad (6)$$

where D_a is the dispersion of fracture inclination angle, and the unit is degree; \bar{A} is the average inclination angle; A_i is the inclination angle of fracture i , both are in degrees.

Considering that the contribution of fractures in different sizes to the formation of a fracture network is different, each fracture and its corresponding inclination angle should be weighted when calculating the fracture complexity.

$$A'_i = A_i \times \frac{S_i}{S_f} \text{ (two-dimensional),} \quad (7)$$

$$A'_i = A_i \times \frac{V_i}{V_f} \text{ (three-dimensional),}$$

where A'_i is the weighted inclination angle of fracture i ; A_i is the original inclination angle, and the units are both degrees; S_i (V_i) is the area (volume) of the fracture; and \bar{S}_f (\bar{V}_f) is the average of all fracture areas (volume) of the rock sample.

In order to facilitate the comparison and subsequent analysis of different rock samples, the fracture area ratio (fracture porosity) and inclination dispersion are normalized.

$$R_{fn} = \frac{R_f - R_{f_{min}}}{R_{f_{max}} - R_{f_{min}}} \text{ (two-dimensional),}$$

$$\varphi_{fn} = \frac{\varphi_f - \varphi_{f_{min}}}{\varphi_{f_{max}} - \varphi_{f_{min}}} \text{ (three-dimensional),} \quad (8)$$

$$D_{an} = \frac{D_a - D_{a_{min}}}{D_{a_{max}} - D_{a_{min}}},$$

where R_{fn} (φ_{fn}) and D_{an} are normalized fracture area ratio (fracture porosity) and inclination dispersion of the pressed core after fracture analysis, which are dimensionless; the subscripts max and min are maximum and minimum, respectively.

The complexity of fractures of the pressed core is represented by the size and morphology of fractures. Therefore, the average value of the normalized fracture area ratio (fracture porosity) and the normalized fracture inclination dispersion can be used to characterize the fracture complexity:

$$F_c = \frac{(R_f - R_{f_{min}})/(R_{f_{max}} - R_{f_{min}}) + (D_a - D_{a_{min}})/(D_{a_{max}} - D_{a_{min}})}{2} \text{ (two-dimensional),}$$

$$F_c = \frac{(\varphi_f - \varphi_{f_{min}})/(\varphi_{f_{max}} - \varphi_{f_{min}}) + (D_a - D_{a_{min}})/(D_{a_{max}} - D_{a_{min}})}{2} \text{ (three-dimensional),} \quad (9)$$

where F_c is the complexity of fracture after the core is pressed.

The 2D and 3D fracture complexity of the pressed core are shown in Table 3. We can see that there is a good correlation between the fracture complexity of the 2D core pressing and the 3D core pressing.

The rock brittleness index and fracture complexity after pressure were calculated by the mineral content method and the rock elastic mechanics parameter method, respectively. They were performed on samples no. 11 and no. 7. The calculated results are shown in Table 4. It can be seen

TABLE 3: Comparison of the 2D and 3D fracture complexity analysis results after the core being pressed.

Test no.	Normalized fracture inclination dispersion	Normalized fracture area ratio	2D fracture complexity	2D fracability index	Normalized fracture porosity	Normalized fracture inclination dispersion	3D fracture complexity	3D fracability index
1	45.3	55.2	50.3	32.8	36.6	13.7	25.1	17.7
2	12.5	55.6	34.1	24.3	24.8	32.9	28.9	11.1
3	50.9	58.6	54.7	30.8	23.5	44.0	33.7	14.9
4	53.4	55.5	54.5	35.5	25.9	34.8	30.4	17.9
5	48.2	58.4	53.3	29.2	16.0	46.9	31.4	14
6	58.8	58.3	58.6	27.8	70.0	27.0	48.5	12.9
7	54.9	75.7	65.3	27.3	56.3	32.5	44.4	14.3
8	34.5	58.2	46.4	30.7	10.0	33.8	21.9	18.8
9	67.8	76.3	72.1	29.9	17.2	46.5	31.9	17
10	75.1	60.7	67.9	39.6	24.9	32.5	28.7	18
11	50.7	56.1	53.4	25.5	8.7	42.6	25.7	13.8
12	69.4	44.3	56.8	22.3	16.5	32.8	24.7	11.4
13	65.4	48.3	56.8	21.9	4.7	45.7	25.2	10.7
14	54.2	43.7	49.0	18.9	2.1	40.5	21.3	8.7
15	13.3	46.0	29.7	13.4	3.9	29.7	16.8	6
16	85.5	41.6	63.6	34.5	2.9	19.0	10.9	17.1

TABLE 4: Comparison of brittleness index and fracture complexity after the rock being pressed.

Sample number	11	7
Brittleness index of the mineral content method	60.9	41.3
Brittleness index of the Poison-Yang method	66.3	63.6
Fracture complexity after the core being pressed	10.9	33.7

from Table 4 that the brittleness index of sample no. 11 calculated by the mineral content method is larger than that of sample no. 7. The brittleness index of sample no. 11 calculated by the rock mechanics parameter method is slightly different than that of sample no. 7. Brittleness index of sample no. 11 calculated by the fracability index method is smaller than that of sample no. 7, and the difference is obvious. As seen from the CT scanning before and after the core being pressed, the fracture generated in sample no. 7 is more complex than that of the core in sample no. 11, as shown in Figures 7 and 8. The fracture effect is consistent with the fracture complexity after the core being pressed.

4.3. Calculation of the Core Standard Strength. The fracturing difficulty of the rock can be characterized by its compressive strength, which is related to the sample size. In order to use the peak pressure in the bursting pressure experiment of the constant strain rate method to represent the fracturing difficulty of the core, the effect of size should be eliminated.

In this study, half of the triaxial compressive strength obtained in the bursting pressure experiment was taken as the initial value of the standard compressive strength to estimate the size impact coefficient and to correct the peak pressure. The specific formula is

$$S_s = S_i \left(\frac{h}{d} \right)^{-[-0.085 \times \ln(S_i/2) + 0.5421]} \quad (10)$$

where S_s is the standard strength of the core; S_i is the peak pressure in the bursting pressure experiment of the constant strain rate method; h and d are the height and diameter of the core, respectively.

4.4. Construction of the Core Fracability Index. For the full characterization of mud shale reservoir core fracability, full consideration of the fracture complexity, and standard strength of the core, the core fracability index expression F was presented.

$$F = f(F_c, S_s), \quad (11)$$

where F , the core fracability index, is the comprehensive reflection of the core fracability; F_c is the fracture complexity after the core being pressed, representing the fracture network complexity of the rock being pressed; S_s is the core standard strength, representing the force required to fracture the rock; B_i is the core brittleness coefficient, representing the rock fracture opening speed and width after being pressed.

The higher the fracture complexity of the pressed core, then the lower the standard strength, thus the better the core fracability is. The fracability index F of the shale reservoir core is defined as follows:

$$F = \frac{F_c}{S_s}, \quad (12)$$

where F_c is the fracture complexity of the pressed core, dimensionless; S_s is the standard compressive strength of the core, in MPa; F is the fracability index of the core, in

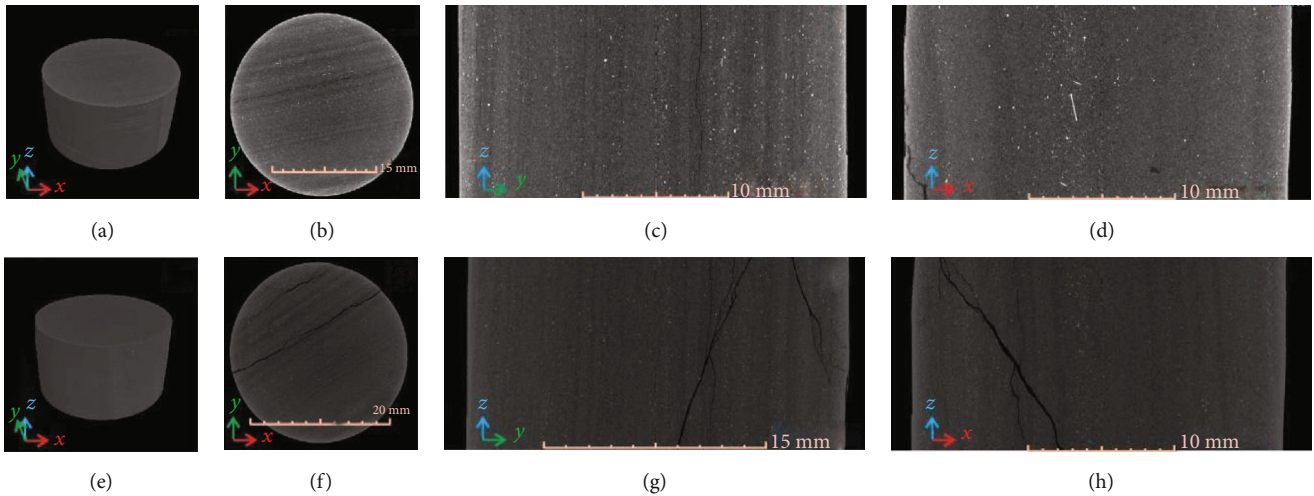


FIGURE 7: 3D CT images before sample 11 being pressed and after being pressed. (a–d) 3D CT images before sample 11 being pressed. (e–h) 3D CT images after sample 11 being pressed.

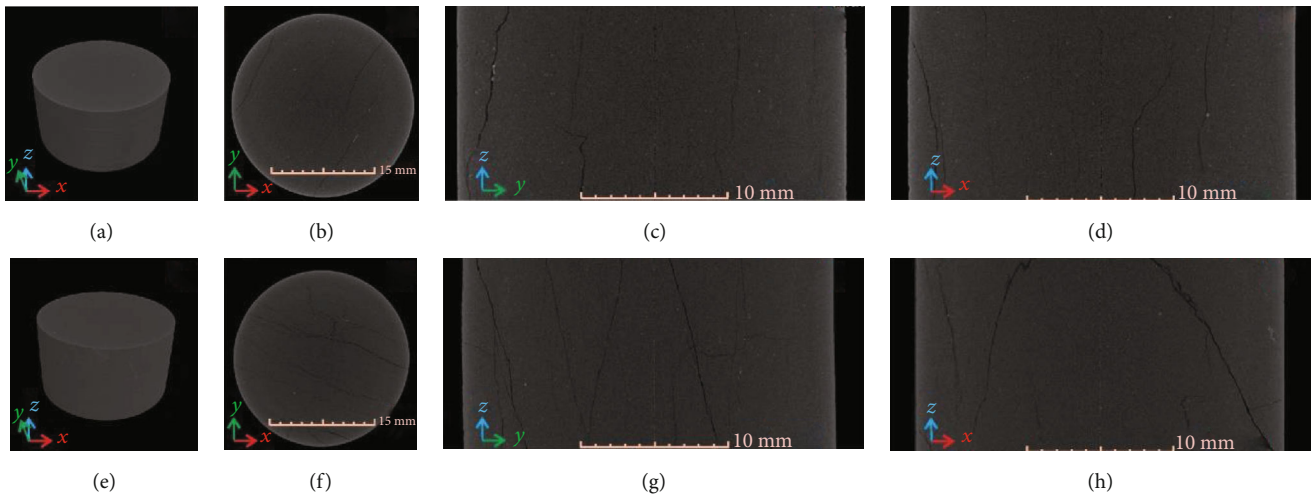


FIGURE 8: 3D CT images of sample 7 before being pressed and after being pressed. (a–d) 3D CT images of sample 7 before being pressed. (e–h) 3D CT images of sample 7 after being pressed.

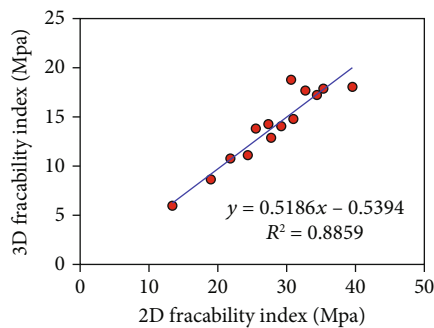


FIGURE 9: Comparison between the 2D core fracability index and the 3D core fracability index.

MPa^{-1} , and the physical significance is the fracture complexity generated from pressure 1 MPa.

According to the fracture complexity of the pressed core and the standard core strength test, the core fracability index

was obtained. The 2D core fracability index obtained from the core testing was compared with the 3D fracability index, as shown in Figure 9. The 2D core fracability index is correlated with that of the 3D index. Thus, in the actual data processing, the 2D core fracability index can represent the evaluation effect of the reservoir fracturing.

5. Actual Data Processing

The core fracability index of the shale reservoir takes full account of the fracturing effect and the fracturing difficulty. The microseismic data can effectively verify its evaluation effect.

Figure 10(a) shows the microseismic monitoring results during the fracturing in the X well. In the figure, the vertical coordinate is the depth direction, and the horizontal coordinate is the east direction. Every point in the figure represents a microseismic event, i.e., the generation of a fracture. The

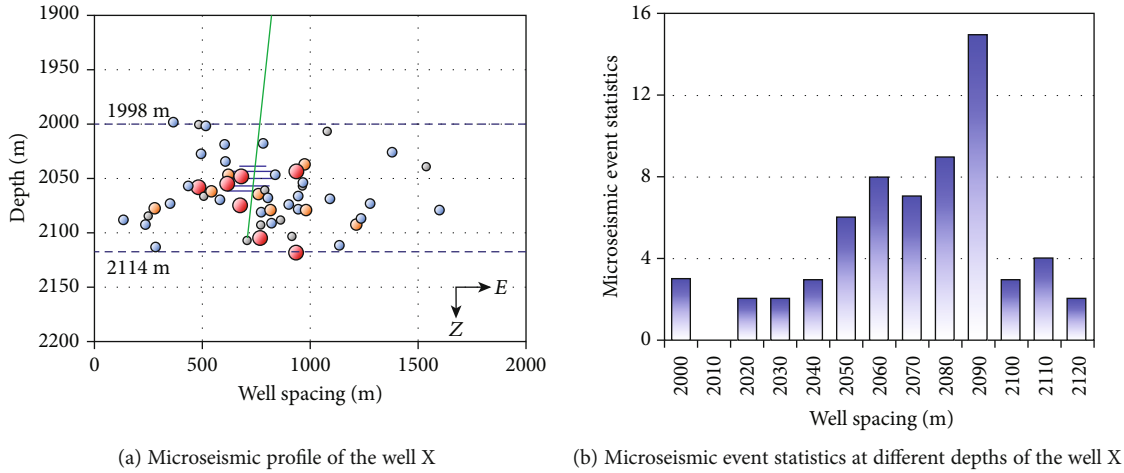


FIGURE 10: Modeling correctness verification using microseismic data.

TABLE 5: Information of the three rock samples from the well X and the results of fracability analysis.

Sample no.	Depth (m)	Lithology	Standard strength (MPa)	Fracability index (2D)	Fracability index (3D)
7	2054.63	Ash black mud shale	278.3	21.1	21.8
5	2062.88	Ash black shale	200.6	21.6	25.4

denser the point, the more fractures are generated in the interval that indicates better fracability.

All the points in Figure 10(a) are projected onto the vertical coordinate, indicating the microearthquakes detected at each depth, and the statistical histogram (Figure 10(b)) is performed with a step size of 10 meters. The statistics of microearthquakes at different depths can be roughly seen. As it is shown in Figure 10(b), the fracturing section of the well X is between 1999 m and 2114 m. Two cores in the well have been experimentally analyzed for their fracability (shown in Table 5).

As it is shown in Table 5, the 2D and 3D fracability indexes of cores 5 and 7 are relatively high, and there are a large number of microearthquakes at the depths of these cores. The core fracability index has a good correlation with the number of microearthquakes. It means that the core analysis fracability index can indicate the formation fracability.

6. Conclusions

The evaluation of reservoir fracability plays a key role in sweet spot optimization, multistage fracturing design, and economic benefit prediction. In this study, the rock samples were fractured through the triaxial compression test, and the fracability of rock samples was characterized by the fracability index which achieved excellent results. Conclusions are drawn as follows:

- (1) The traditional brittleness index method based on mineral composition and rock mechanics parameters cannot meet the developmental needs of the unconventional reservoirs because it does not take

the influence of pore fluid, pore structure, reservoir temperature, and pressure into account. The influence of dynamic and static elastic modulus difference of rocks is also ignored

- (2) Based on the fracture complexity after pressure which is defined by the brittleness index proposed in the shale gas development, a set of experimental analysis methods was established, and the core fracability index was proposed. This method represents not only the fracturing effect but also the fracturing difficulty. Comparing with the monitoring data of hydrofracture-induced microseism of the sample well, the core fracability index is in good agreement with the actual fracturing effect. In addition, the core fracability index method is more reasonable to characterize reservoir fracturing compared with the traditional brittleness index method. Due to the high correlation between the two-dimensional and the three-dimensional core fracability index, it is enough to use the two-dimensional core fracability index in the actual data processing to represent the evaluation of reservoir fracability

Data Availability

The data used to support the findings of this study are available from the corresponding author upon request.

Conflicts of Interest

The authors declare that they have no conflicts of interest.

Acknowledgments

This work was supported by the Fundamental Research Funds for the Central Universities, CHD (300102260107); Natural Science Basic Research Plan in Shaanxi Province of China (Grant no. 2020JQ-747); Scientific Research Plan Projects of Shaanxi Education Department (Grant no. 18JK0517); and Major Science and Technology Project of China National Petroleum Corporation (2019 A-3611).

References

- [1] D. M. Jarvie, R. J. Hill, T. E. Ruble, and R. M. Pollastro, "Unconventional shale-gas systems: the Mississippian Barnett Shale of north-central Texas as one model for thermogenic shale-gas assessment," *AAPG Bulletin*, vol. 91, no. 4, pp. 475–499, 2007.
- [2] R. Rickman, M. J. Mullen, J. E. Petre, W. V. Grieser, and D. Kundert, "A practical use of shale petrophysics for stimulation design optimization: all shale plays are not clones of the Barnett Shale," in *SPE Annual Technical Conference and Exhibition*, Denver, Colorado, USA, 2008.
- [3] B. Huiyuan, F. Wang, Z. Chengen et al., "A new model between dynamic and static elastic parameters of shale based on experimental studies," *Arabian Journal of Geosciences*, vol. 12, no. 19, p. 609, 2019.
- [4] K. K. Chong, W. V. Grieser, A. Passman, H. C. Tamayo, N. Modeland, and B. E. Burke, "A completions guide book to shale-play development: a review of successful approaches toward shale-play stimulation in the last two decades," in *Canadian Unconventional Resources and International Petroleum Conference*, Calgary, Alberta, Canada, 2010.
- [5] B. Goodway, M. Perez, J. Varsek, and C. Abaco, "Seismic petrophysics and isotropic-anisotropic AVO methods for unconventional gas exploration," *The Leading Edge*, vol. 29, no. 12, pp. 1500–1508, 2010.
- [6] Z. Liu and Z. Sun, "New brittleness indexes and their application in shale/clay gas reservoir prediction," *Petroleum Exploration and Development*, vol. 42, no. 1, pp. 129–137, 2015.
- [7] M. Bai, "Why are brittleness and fracability not equivalent in designing hydraulic fracturing in tight shale gas reservoirs," *Petroleum*, vol. 2, no. 1, pp. 1–19, 2016.
- [8] H. Zhang, H. Huang, Z. Li, and M. Liu, "Oil physical status in lacustrine shale reservoirs – a case study on Eocene Shahejie Formation shales, Dongying Depression, East China," *Fuel*, vol. 257, article 116027, 2019.
- [9] K. Elwegaa, H. Emadi, M. Soliman, T. Gamadi, and M. Elsharafi, "Improving oil recovery from shale oil reservoirs using cyclic cold carbon dioxide injection – an experimental study," *Fuel*, vol. 254, article 115586, 2019.
- [10] X. Jin, S. Shah, J. Roegiers, and B. Zhang, "Fracability evaluation in shale reservoirs: an integrated petrophysics and geomechanics approach," in *SPE Hydraulic Fracturing Technology Conference*, The Woodlands, TX, USA, 2014.
- [11] X. Jin, S. N. Shah, J. C. Roegiers, and B. Zhang, "An integrated petrophysics and geomechanics approach for fracability evaluation in shale reservoirs," *SPE Journal*, vol. 20, no. 3, pp. 518–526, 2015.
- [12] A. W. Bishop, "Progressive failure-with special reference to the mechanism causing it," in *Proceedings of the Geotechnical Conference*, vol. 2, pp. 142–150, Oslo, 1967.
- [13] B. Tarasov and Y. Potvin, "Universal criteria for rock brittleness estimation under triaxial compression," *International Journal of Rock Mechanics and Mining Sciences*, vol. 59, pp. 57–69, 2013.
- [14] H. Munoz, A. Taheri, and E. K. Chanda, "Rock drilling performance evaluation by an energy dissipation based rock brittleness index," *Rock Mechanics and Rock Engineering*, vol. 49, no. 8, pp. 3343–3355, 2016.
- [15] X. Ge, Y. Xiao, Y. Fan, J. Liu, and Y. Zhang, "Laboratory investigation of the relationship between static rock elastic parameters and low field nuclear magnetic resonance data," *International Journal of Rock Mechanics and Mining Sciences*, vol. 127, article 104207, 2020.
- [16] S. K. Sinha and P. W. Fieguth, "Automated detection of cracks in buried concrete pipe images," *Automation in Construction*, vol. 15, no. 1, pp. 58–72, 2006.
- [17] H. Sui, W. Gao, and R. Hu, "A new evaluation method for the fracability of a shale reservoir based on the structural properties," *Geofluids*, vol. 2019, Article ID 2079458, 14 pages, 2019.
- [18] B. Hou, Y. Zeng, M. Fan, and D. Li, "Brittleness evaluation of shale based on the Brazilian splitting test," *Geofluids*, vol. 2018, Article ID 3602852, 11 pages, 2018.

Research Article

The Determination of a Damage Model for Mudstone under Uniaxial Loading in Acidic Conditions

K. Cao,^{1,2} L. Ma ,¹ Y. Wu,² A. J. S. (Sam) Spearing,¹ Naseer Muhammad Khan,^{1,3} and Y. Xie⁴

¹School of Mines, China University of Mining and Technology, Xuzhou, 221116 Jiangsu, China

²State Key Laboratory for Geomechanics and Deep Underground Engineering, China University of Mining and Technology, Xuzhou, 221116 Jiangsu, China

³Department of Mining Engineering, Balochistan University of Information Technology Engineering and Management Sciences, Quetta, Pakistan

⁴Xutuan Mine, Huaibei Coal Mining Group Co., Ltd., Mengcheng, 233500 Anhui, China

Correspondence should be addressed to L. Ma; ckma@cumt.edu.cn

Received 29 March 2020; Revised 26 August 2020; Accepted 5 September 2020; Published 8 October 2020

Academic Editor: Wen-Dong Wang

Copyright © 2020 K. Cao et al. This is an open access article distributed under the Creative Commons Attribution License, which permits unrestricted use, distribution, and reproduction in any medium, provided the original work is properly cited.

The influence of acid solutions was investigated on the mechanical properties of mudstone. Uniaxial compression tests on mudstone samples were conducted to determine the variations of relative mass, porosity, deformation, and strength characteristics of mudstone subjected to acidic solutions with different pH values. The change of pH, relative mass, and porosity of mudstone in the process of acid solution immersion was monitored during soaking. The mechanism of hydrochemical corrosion of mudstone samples was preliminarily discussed. The damage parameter was introduced based on the porosity rate. The results show that with increased solution acidity, the peak stress and elastic modulus decreased to different levels, while the peak strain increases in the rock samples. The increased chemical damage parameters reduce the mechanical parameters and increased the deformation parameters. On the basis of the mechanical test, considering the stress-strain relationship of rock in the compaction stage, a segmented damage constitutive model of rock based on chemical damage parameters is established, and the test results are verified. The results show that the correlation coefficient between the theoretical curve and the experimental data is as high as 0.98, and the model is suitable for the analysis of chemically corroded rock under the uniaxial compression test. The results provide a reference for the analysis and design of coal-bed methane wells where the rocks frequently become acidic during the production of methane.

1. Introduction

Coal-bed methane (CBM) is a clean and efficient energy source associated with coal seams [1–3]. More than 50% of China's coal seams are rich in coal-bed methane, with a total of 35 trillion m³ of coal-bed methane in the mines, which is the third largest coal-bed methane storage in any country after Russia and Canada. During the process of coal-bed methane well drainage and gas production, the groundwater continuously changes into acidic or alkaline water [4–7]. The coal and rock of the reservoir are affected due to this corrosion. The hydrochemical solution produces pore water pressure, which reduces the effective stress that the rock skeleton can bear, thus reducing the effective strength of the

rock. Furthermore, a hydrochemical solution has certain adverse chemical effects on the mineral composition of the rock and the cementing properties between the mineral particles. This chemical effect plays a significant role in changing the original structure of the rock and can even produce new minerals [8–11]. This in turn affects the process of desorption, diffusion, and seepage interaction of coal-bed methane in the reservoir. Whether coal-bed methane can produce gas and whether it can produce high productive yield depends on the degree and range of desorption of coal-bed methane [4]. Therefore, it is of great significance to study the physical and mechanical properties of the rock corroded by chemical water in order to ensure the efficient exploitation of coal-bed methane.

In recent years, much progress has been made in understanding the influence of hydrochemical solutions on rock mechanical properties. Tang et al. [12] studied the rock mechanics and environmental effects under the action of hydrochemistry and obtained the results of a three-point bending test and uniaxial rock compression test under the action of different hydrochemistry solutions. Feng and Ding [13] studied the characteristics of crack propagation of prefabricated rock samples under various chemical solution corrosion and uniaxial compression conditions by using the independently developed stress-percolation-chemical coupling mechanics system. Wang et al. [11] carried out corrosion tests on sandstone under the action of different pH aqueous chemical solutions. The type and degree of water-rock chemical interaction in different aqueous chemical environments are different, which leads to different changes in the microstructure of rock. The neutral solution loss of cementing materials in rock and large-size mineral aggregates in the acid solution would also undergo a lot of dissolution. Ding et al. [14] carried out dissolution kinetic experiments and analysis on rocks soaked in different aqueous chemical solutions, analyzed the dissolution characteristics of rocks in different aqueous chemical solutions, and obtained the corresponding erosion dissolution kinetics equations. Li et al. [15] and Xu et al. [16] conducted shear tests on the mudstone corroded by chemical solution. They studied the influence of hydrochemical solution on the shear strength of mudstone, established the relationship between porosity and shear strength index, and obtained the influenced role of chemical solution corrosion on the crack opening, failure, and expansion direction of mudstone. Han et al. [17] carried out wave velocity tests and conventional triaxial compression tests on mudstones corroded by aqueous chemical solution with different electrolyte pH values, compositions, and varying concentrations of calcium and magnesium ions in the solution. He concluded that the decrease of mechanical properties of mudstones after chemical corrosion was closely related to the change of porosity.

The study of the mechanical properties of rock can provide a basis for the design of rock excavations, while the construction of the constitutive rock model can provide a theoretical basis for the prediction of the stability of the rock. In terms of the constitutive rock model, Kang [18] analyzed the influence of water on rock strength and deformation based on damage mechanics. They used the volume change caused by rock dilatancy to characterize damage variables and established the evolution equation of damage variables for saturated rock. Hu et al. [19] analyzed the influence of water on the mechanical properties of rock under uniaxial compression and deduced the statistical model of rock damage considering the influence of water content. Based on the Weibull distribution, Zhang et al. [20] established a statistical damage constitutive model that can reflect multiple test curves by using the relationship between peak strength and elastic modulus in addition to the relationship between water content and rock damage constitutive model parameters. Chen et al. [21] based on the principle of effective stress assumed that the damage of rock was caused by the effective stress of particles and the effective stress of body structure.

According to the condition of stress balance, the stress relation equation under the two effective stresses is obtained, and on this basis, the damage evolution equation of saturated rock under uniaxial compression is established.

The constitutive damage models of rock established in the past however only consider the influence of water content, and the constitutive damage model of rock after chemical solution corrosion was seldom reported. Due to the corrosion of a chemical solution, the initial compaction stage of the rock stress-strain curve is more significant. The compaction stage of stress-strain curve drawn by the traditional statistical damage constitutive model is quite different from the experimental curve. In this paper, the mechanical properties of mudstone after chemical corrosion were analyzed. Chemical damage parameters were introduced to quantitatively characterize the mechanical parameters of rocks, and the compaction stage and subsequent stage were innovatively expressed separately. This allowed a rock segmental damage statistical constitutive model with chemical damage parameter interface to be built. The research results are expected to enrich the rock mechanics theory of underground engineering and provide a theoretical reference for the more efficient mining of coal-bed methane.

2. Experimental Design

2.1. Preparation of Acidic Solutions. The complex composition of water ions in nature makes it impossible to consider the effects of all the various ions on rocks. Considering the high content of Na^+ , K^+ , and Cl^- ions typically found in groundwater therefore, a solution of NaCl and KCl was selected as the electrolyte solute to configure the hydrochemical solution [11]. The mine water collected from the rock is mainly acidic, with a pH range of 2.0-6.5; therefore, this research considers mostly the influence of the acidity of the solution on the rock characteristics and properties. The interaction between water and rock is a slow process in situ, so due to time constraints, four different acidic solutions with high solution concentration and increasing the pH value were selected. This was to reflect the water chemistry and solution corrosion effect in a relatively short time on the mudstone samples. The chemical solutions prepared for this research are shown in Table 1. Electrolyte solutions with pH values of 1.3, 3.3, 5.3, and 7.3 with a concentration of 0.1 mol/L NaCl and KCl were used in this research experiment. The pH value of the acid solution was adjusted by adding 68% HNO_3 into the mix. The procedure was first to add NaCl and KCl into the distilled water, stir with a glass rod to make it fully dissolved, then take 68% HNO_3 , dilute with 100 ml distilled water, and add it to the electrolyte solution drop by drop. During the gradual acid introduction, a pH meter was used to monitor the pH change of the solution in real time until the predetermined pH value was reached.

2.2. Sample Preparation. The representative sandy mudstone samples collected from a coal mine in Shandong Province, China, were used in this research study. The X-ray diffractometer was used for the mineralogical composition of representative samples. The result shows quartz (35.7%), feldspar

TABLE 1: Preparation of chemical solutions.

Group	Solution type	Solution composition	Solution concentration (Mol/L)	pH value
A	Acidic solution	NaCl, KCl	0.1	1.3
B	Acidic solution	NaCl, KCl	0.1	3.3
C	Acidic solution	NaCl, KCl	0.1	5.3
D	Neutral solution	NaCl, KCl	0.1	7.3

(16.3%), calcite (6.4%), dolomite (4.2%), mica (3.4%), and clay mineral content (34%). The main mineral composition was kaolinite, illite, chlorite, and carbonate.

The rock samples were collected from the mine at the same location. The core was extracted from the same block of mudstone to keep similar and uniformed mechanical properties and minimize any mineralogical and size effect. The prepared rectangular-sized specimens had precise dimensions of $50 \times 50 \times 100$ mm. The edge angles were kept strictly at 90° to ensure that the lateral pressure could be loaded smoothly and evenly on the rock sample sides. The nonparallelism of the two ends of the test piece was less than 0.005 mm, and the grinding flatness of the end face was less than 0.02 mm. A total of 20 samples were prepared and divided into five groups: A, B, C, D, and E. E group samples were kept completely dry as a control.

The size and weight of the finished samples were recorded after vacuumed and dried for 48 hrs at 108°C . The rock sample from groups A, B, C, and D was soaked in each chemical solution, as described in Table 1. In order to reduce the dispersion of experimental data, and the peak strength of each group of rock samples is removed from the one that deviates from the average value. Therefore, a total of 15 rock samples left having three specimens from each group were used for subsequent data analysis.

2.3. Experimental Procedure. In this research, the previous experimental research procedure was followed [11]. 1.5 litres of each pH solution was used for each sample. It was found that the H^+ in the solution having pH 3.3 and 5.3 was consumed by chemical reaction with the minerals in the rock, after the rock sample was soaked for about 30 days. Therefore, all rock samples were soaked for 30 days in a full immersion solution container in an open environment. The samples were immersed in the solution and regularly agitated to reflect the real occurrence environment of rock. During the soaking of the samples, the solution pH and rock samples' mass and porosity samples' change were noted. The pH of the solution and rock mass were measured every two hours in the early stage and once daily when it reached a stable stage. During the soaking process, the measurement interval was based on the change rate of the pH value of the solution. It is considered that the water-rock interaction reached a steady state when the change of the pH value remained stable

for a period of time. All rock samples were tested using the conventional uniaxial loading method with the displacement rate of 0.1 mm/min, after soaking.

3. Experiment Results

3.1. Interaction between the Hydrochemical Solution and Mudstone

3.1.1. pH Change of Solution. The pH value of the solution was monitored over time during the experiment, as shown in Figure 1. With the neutral solution having pH = 7.3, the pH value increased slowly with soaking time and then remained constant. With the acidic solution having pH = 5.3, pH showed a trend of rapid increase, slow growth, and stable with the increase of soaking time. The pH value began to increase to 6.8 from 0 to 115 hours, and then slowly increased to 7.7 from 115 to 591 hours, and then became stable and remained constant. With the solution having pH = 3.3, the pH value increased with the increase of soaking time and reached pH value to 7.4 maximum, and the solution was stable with soaking time 720 hours. The pH value of the solution with pH = 1.3 had almost no change with the increase of immersion time, because the content of H^+ in the solution with pH = 1.3 was more, and only a small proportion of H^+ is consumed when a chemical reaction occurs with rocks. When the pH is 3.3 and 5.3 solutions begin to soak, the pH shows a rapid growth trend. This is because the concentration of H^+ in the initial stage of rock soaking was high, and the chemical reaction rate was fast. With the increase of soaking time, the concentration of H^+ decreases, resulting in the slow chemical reaction rate.

3.1.2. Change of Masses of Mudstone Samples. In the process of soaking, the samples were taken out every day; sample surface water was wiped with a cotton cloth to make it free of surface liquid. The sample was placed in a dry location for 5 minutes to ensure that the liquid on the surface of the sample volatilizes completely and then weighed on an electronic scale. According to the difference between the measured mass and the initial mass of the sample, the relative mass change rate of the sample at different times is [11, 17]

$$\omega = \frac{m - m_{\text{NS}}}{m_{\text{NS}}} \times 100\%, \quad (1)$$

where m_{NS} and m are the mass of the sample in the initial state and after soaking condition, respectively.

Figure 2 shows the curve of the change rate of the relative mass of the sample with the immersion time, which indirectly reflects the degree of water-rock interaction. As observed from Figure 2, the relative mass change rate of the soaked samples in the solution with pH = 7.3, pH = 5.3, pH = 3.3, and pH = 1.3 increases rapidly at the initial stage of immersion. Thus, the water absorption on the rock surface at the initial stage of immersion is much higher than the mineral consumption due to chemical reaction. After a prolonged soaking time, samples in an acid solution having pH 5.3, 3.3, and 1.3 show a decreased trend while samples having pH = 7.3 show an increasing trend due to the neutral

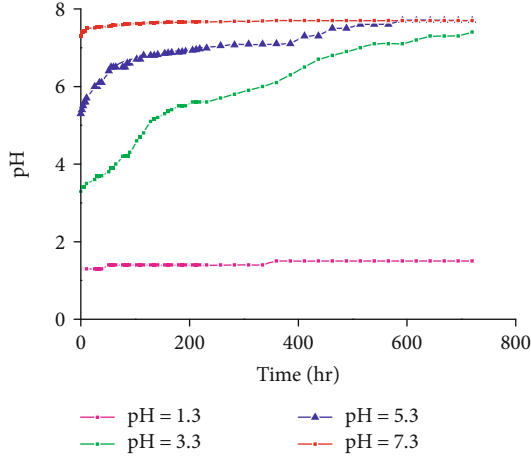


FIGURE 1: pH value of solution with time.

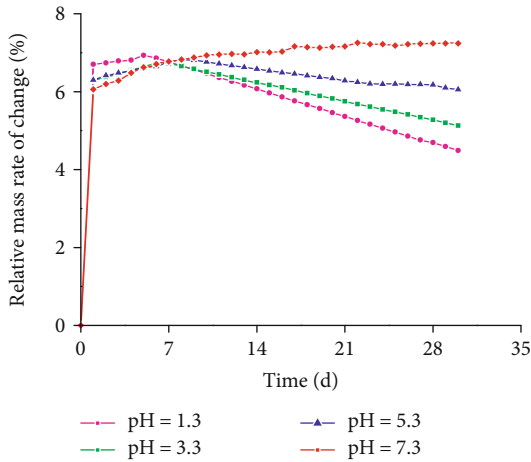


FIGURE 2: Change rate of relative mass of sample with soaking time.

solution; no chemical reaction occurred with rock mineral. Initially, during the soaking of samples, solution diffusion was dominant in the acid rock reaction, and water absorption increased the mass of the samples. During prolonged soaking, the rock samples are saturated, and chemical corrosion plays an active role. The mudstone mineral components are hydrolyzed and dissolved, which decreased the mass of the sample. The relative mass change rate of samples in pH = 5.3, 3.3, and 1.3 solutions show a downward trend, and the lower the pH value is, the faster the decline speed. The trends show that the stronger the acidity of the solution, the stronger the reaction between the sample and the solution, and the faster the corrosion rate.

3.1.3. Porosity. Mudstone is a porous medium with microcracks and pores. The porosity of the sample in this experiment is its total porosity (including two parts of open and closed pores), and the calculation formula is [17]

$$n = \left(1 - \frac{\rho_g}{\rho}\right) \times 100\%, \quad (2)$$

where n is the total porosity of the specimen, ρ_g is the bulk density of the specimen, and ρ is the particle density of the specimen.

The bulk density is determined by the following formula:

$$\rho_g = \rho_V \times \frac{m_0}{m_1 - m_2}, \quad (3)$$

where m_0 is the mass of the dry sample in air (g), m_1 is the mass of the saturated sample in air (g), m_2 is the mass of the saturated sample in water (g), and ρ_V is the density of water at room temperature (g/cm^3).

When testing the total porosity before corrosion, the dried rock samples of groups A-D were tested in the air first and then soaked in water for 14 days to test the mass of rock samples in the air and water, respectively. Finally, the rock samples of groups A-D are baked in a dryer for 48 hours, cooled naturally to room temperature, and soaked in chemical solution.

The particle density is determined by the following formula:

$$\rho = \rho_V \times \frac{m_3}{m_4 + m_3 - m_5}, \quad (4)$$

where m_3 is the mass of rock powder in the air (g), m_4 is the mass of a density bottle containing distilled water (g), and m_5 is the mass of a density bottle containing rock powder and water (g).

Three parts of rock powder are produced by rolling the fragments of dry rock samples under uniaxial loading, and the average of the three parts of rock powder particle density is taken as the particle density of rock.

In this paper, the porosity rate reflects the variations of porosity in the mudstone specimens; the calculating formula is [17]

$$\eta = \frac{n_t - n_0}{n_0} \times 100\%, \quad (5)$$

where n_0 and n_t is the total porosity of the specimen before and after corrosion, respectively.

Table 2 shows the statistics of porosity and porosity change rate of mudstone before and after corrosion. The porosity change rate of group A is 7.77%, group B is 6.27%, group C is 4.38%, and group D is 1.89%. Furthermore, the rate of porosity increased with acidity, which shows porosity is strongly influenced by acidity. The porosity change rate of group A is 4.11 times than that of group D.

3.2. Mechanical Properties. The comparison of the results of the parallel tests revealed that the prepeak stress-strain curves of each group of three tests have a good similarity. The post-peak stress-strain curves of the three tests are different due to the differences of the individual samples, showing a particularly distinct type. The main mechanical parameters of rock samples are determined by the stress-strain prepeak curve, so it can be considered that the uniaxial loading test of mudstone soaked by acid water is repeatable.

TABLE 2: Rock porosity and chemical damage parameters.

Sample number	Initial porosity (%)	Porosity after corrosion (%)	Rate of porosity change (%)	Chemical damage parameter (%)
A ₁	15.74	16.95	7.69	1.44
A ₂	16.01	17.24	7.68	1.47
A ₃	15.88	17.14	7.94	1.50
B ₁	16.33	17.38	6.43	1.25
B ₂	15.92	16.92	6.28	1.19
B ₃	16.04	17.02	6.11	1.17
C ₁	16.21	16.93	4.44	0.85
C ₂	15.85	16.56	4.48	0.84
C ₃	16.08	16.76	4.23	0.81
D ₁	15.77	16.07	1.90	0.36
D ₂	15.80	16.12	2.03	0.38
D ₃	16.17	16.45	1.73	0.33

The stress-strain curve of mudstone after soaking in acid water is shown in Figure 3. It includes the loading processes of all rock samples' progress through four stages: compaction, elastic, plastic (stable crack propagation and unstable crack propagation), and postpeak. As the acidity of the solution increases, the range of the stress-strain curve in the compaction stage increases, the range of the elastic stage decreases, and the plastic stage becomes more significant. In this paper, "axial stress method" is used to analyze the proportion of the compression stage of the specimen after immersion in acid water from the stress-strain curve before peak stress. Several points are selected in the straight-line section (linear elastic deformation stage) of the stress-strain curve, and the best fitting straight line of the linear elastic deformation stage is obtained. Since the slopes of the compaction stage and the elastic stage are different, the bifurcation point of the fitting line and the stress-strain curve is defined as the endpoint of the compaction stage as shown in Figure 4, and the corresponding stress value is the compaction stress [22]. The crack initiation stress and crack damage stress are determined by the crack volume strain curve and the volume strain curve, respectively [23–25]; the volumetric strain calculation formula is as follows:

$$\varepsilon_v = \varepsilon_1 + 2\varepsilon_2, \quad (6)$$

where ε_v is the volumetric strain, ε_1 is the axial strain, and ε_2 is the lateral strain.

The crack volume strain of the rock will change due to the crack deformation in the process of the primary microcrack closing and expanding and then new crack initiation and development. For rock under uniaxial loading, the formula of crack volume strain can be expressed as follows:

$$\varepsilon_{ve} = \varepsilon_v - \frac{1 - 2\mu}{E} \sigma_1, \quad (7)$$

where ε_{ve} is the crack volume strain, σ_1 is the axial stress, μ is the Poisson ratio, and E is the elastic modulus.

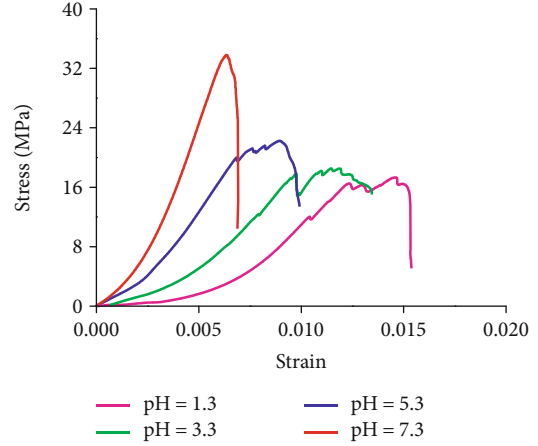


FIGURE 3: Stress strain of rock after soaking at different pH.

Figure 4 shows the evolution curve of rock volume strain and crack volume strain, in which the turning point of the crack volume strain from rising to horizontal is the end point of compaction stage, the turning point from horizontal to falling is the crack initiation point, and the turning point of volume strain curve from rising to falling is the crack damage point.

The ratio of compaction stress to peak stress of each specimen is shown in Table 3. According to Table 3, the ratio of the rock compaction stress to peak stress decreases with the increase of pH. The average ratio of compaction stress to peak stress in groups: A is 0.378, B is 0.333, C is 0.314, D is 0.305, and E (control group) is 0.253. The results revealed that acidity significantly increases the proportion of rock compaction stage.

The three kinds of mechanical parameters of mudstone soaked in acid water were obtained from the uniaxial compressive test data. These parameters were peak stress, elastic modulus, and peak strain. The trend of peak stress, peak strain, and modulus of elasticity of rock with pH is shown in Figures 5–7. The peak stress and elastic modulus linearly have a positive correlation with pH variation, while peak strain and pH have a linearly negative correlation. When pH increased by 1, the peak stress and elastic modulus increased by 2.21 MPa and the 0.96 GPa, respectively, while the peak strain decreased by 0.0016.

The mechanical properties of mudstone change with the changes in the pH value of the acid solution. At the same time, the acid solution will also affect the macroscopic failure pattern of mudstone. The failure patterns of mudstone samples were recorded by photographing, and the failure patterns were sketched. Due to the space limitation, a typical rock sample was selected for analysis in each group. Figure 8 shows the failure pattern and sketch of mudstone under uniaxial loading after soaking in acid solution. As shown in Figure 8, rock samples C₂ and D₁ were damaged by a single tensile crack. Two main tensile cracks appeared on the surface of the rock sample A₃, with the bifurcation cracks distributed in the area near the main crack, and shear cracks appeared in the upper area of the rock sample. The rock sample B₂ is shear failure, and two tensile cracks

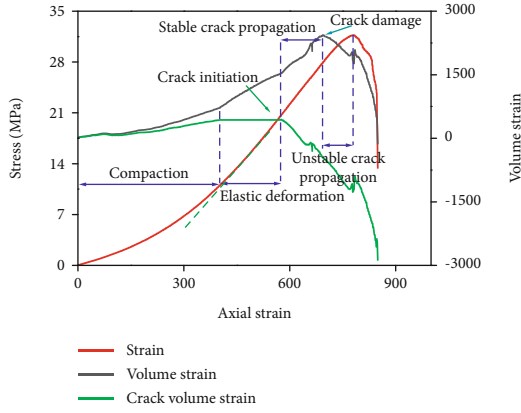


FIGURE 4: The curve of volumetric strain and crack volumetric strain of rock.

TABLE 3: Rock mechanical parameters.

Sample number	Peak stress (MPa)	Peak strain	Compressive stress (MPa)	Ratio	Elastic Modulus (GPa)
A ₁	17.33	0.0146	6.92	0.399	2.11
A ₂	18.61	0.0177	6.91	0.371	2.31
A ₃	17.51	0.0153	6.37	0.364	1.92
B ₁	21.59	0.0119	7.99	0.370	3.64
B ₂	21.54	0.0118	7.09	0.329	3.06
B ₃	22.11	0.0123	6.61	0.299	3.40
C ₁	26.87	0.00896	9.30	0.346	5.69
C ₂	27.01	0.0090	8.18	0.303	4.60
C ₃	26.25	0.00896	7.69	0.293	4.79
D ₁	30.41	0.00613	8.48	0.279	8.07
D ₂	31.70	0.00638	10.4	0.328	7.68
D ₃	30.77	0.00609	9.48	0.308	8.22
E ₁	50.14	0.00498	10.6	0.211	10.5
E ₂	43.28	0.00537	12.5	0.288	9.87
E ₃	46.97	0.00521	12.2	0.259	9.93

appeared near the main shear crack. In other words, the number of cracks in the process of rock failure increases with the increase of acidity, and the failure pattern tends to be complex. This is due to the stress concentration that occurred around the pores and microcracks during the crack stable development stage of rock, which will cause the pores and microcracks to generate new cracks and stably expand. The acid solution will increase the porosity of mudstone and then promote the formation of more new cracks and stable propagation of microcracks. In the crack unstable development stage of rock, more microcracks will expand irregularly, and the deformation will be more complex and severe. When the microcracks gather to form the local weakening of macro critical scale, more microcracks will be generated on the rock surface. Therefore, with the increase of acidity, the number of cracks after rock failure increases and hence, the failure morphology tends to be more complex, and the peak strain increases.

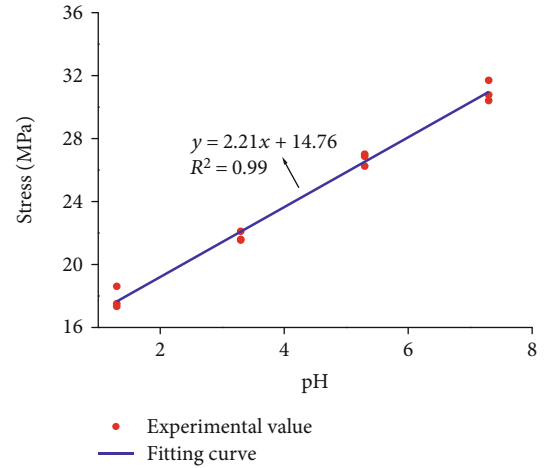


FIGURE 5: Variation trend of peak stress with pH.

4. Constitutive Model Development

4.1. Chemical Corrosion. The mudstone damage caused by chemical corrosion is mainly due to the dissolution of soluble cementitious materials and chemical reactions within the mineral composition. The chemical corrosion correspondingly changes the microstructure of mudstone continuously and causes damage, which reduces the mechanical properties of mudstone. In this paper, porosity is selected as a parameter representing damage. Porosity reflects the corrosion damage degree of solution chemical corrosion to mudstone. The selected chemical damage parameter, D_{ch} , is calculated as follows [17]:

$$D_{ch} = \left(1 - \frac{1 - n_t}{1 - n_0}\right) \times 100\%, \quad (8)$$

where n_t is the porosity after chemical corrosion and n_0 is the porosity before chemical corrosion.

The microstructure and mineral composition of mudstone samples were changed to different degrees after corroded by an aqueous chemical solution. The corrosion caused damage to the samples and resulted in the macroscopic mechanical parameters of the samples to decrease. According to Equation (8), the corresponding chemical damage variable D_{ch} of mudstone samples after corrosion by an acidic solution is calculated, and the relationship between D_{ch} and physical mechanical parameters of mudstone samples is obtained. The fitting curve results are shown in Figures 9–11.

The peak strength and elastic modulus of mudstone samples decreased with the increase of damage variables, while the peak strain increases with the increase of damage variables. Furthermore, acidity affects the macroscopic physical and mechanical parameters of mudstone samples and decreases with the increase of acidity. The deformation parameters however increased with the increase of acidity. Based on the results, therefore, the relationships between peak strength, peak strain, elastic modulus, and chemical damage parameter were fitted by using the first-order

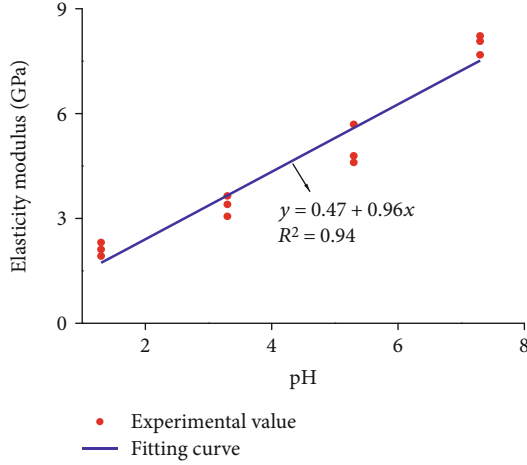


FIGURE 6: Variation trend of elastic modulus with pH.

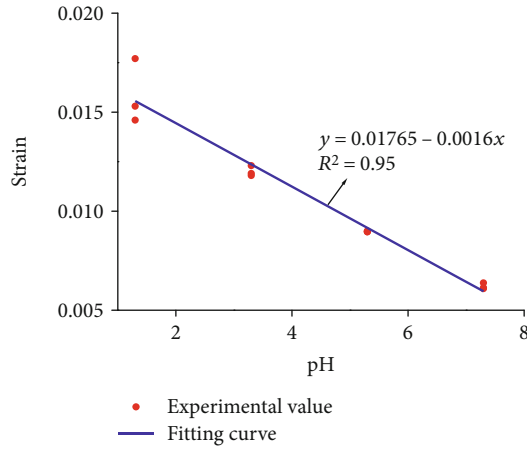


FIGURE 7: Variation trend of peak strain with pH.

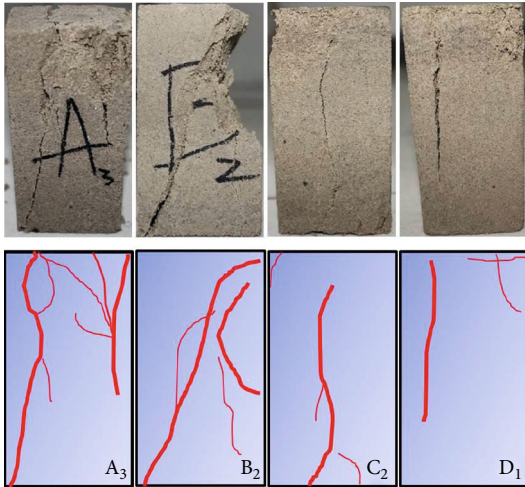


FIGURE 8: Failure pattern and sketch of mudstone under uniaxial loading after acidic solution corrosion.

function relationship, and all of them had a good fitting degree with a correlation coefficient from 0.92 to 0.97. The expressions of mudstone peak strength, peak strain, elastic

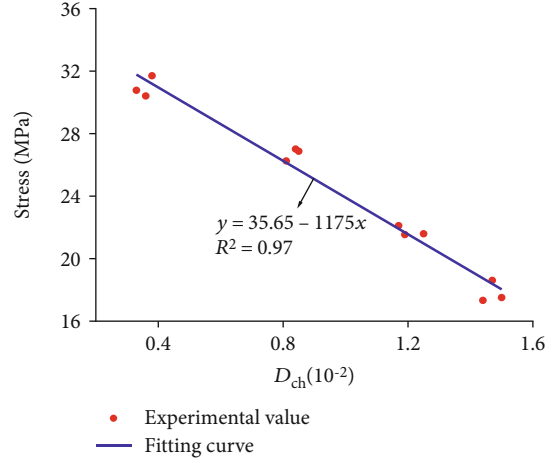


FIGURE 9: Chemical damage parameters and peak stress.

modulus, and chemical damage parameters D_{ch} after soaking in acid water are as follows:

$$\begin{cases} \sigma_c = a - bD_{ch}, \\ \varepsilon_c = c + dD_{ch}, \\ E = e - fD_{ch}. \end{cases} \quad (9)$$

4.2. *Damage Variables under Stress.* According to the equivalent strain hypothesis proposed by Lemaitre [26], the effective stress is equal to the deformation of the damaged material; that is, the strain caused by the stress of rock is equivalent to the strain caused by the effective stress of rock without damage. It is only necessary to replace the nominal stress with the effective stress, and the constitutive damage equation of the rock is

$$[\sigma] = [\sigma^*](I - [D]) = [H][\varepsilon](I - [D]), \quad (10)$$

where $[\sigma]$ and $[\sigma^*]$ are nominal stress and effective stress, respectively, I is the identity matrix, $[D]$ is the damage variable matrix, $[H]$ is the elastic modulus matrix, $[\varepsilon]$ is the strain matrix. Assuming that rock damage is isotropic, the one-dimensional damage constitutive relation of rock can be expressed as

$$\sigma = \sigma^*(1 - D) = E\varepsilon(1 - D), \quad (11)$$

where D is the damage variable.

From the above, the compaction stage of uniaxial stress-strain curve of rock under acid water immersion can be clearly identified, and the proportion of compaction increases with the increase of acidity. The traditional continuous damage constitutive model does not consider the compaction stage of rock. Therefore, in this paper, the uniaxial compressive stress-strain curve of rock soaked in acid water is divided into the compaction stage and subsequent damage expansion stage, and therefore, a separate damage constitutive model is established.

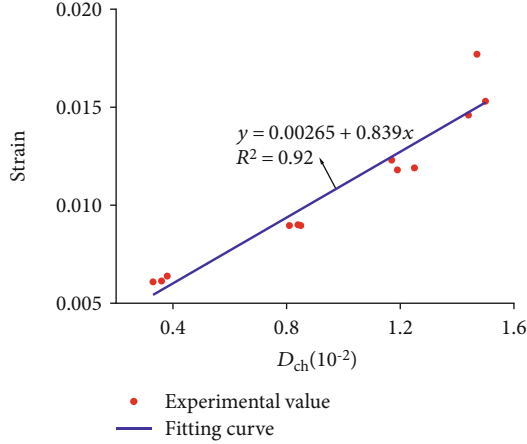


FIGURE 10: Chemical damage parameters and peak strain.

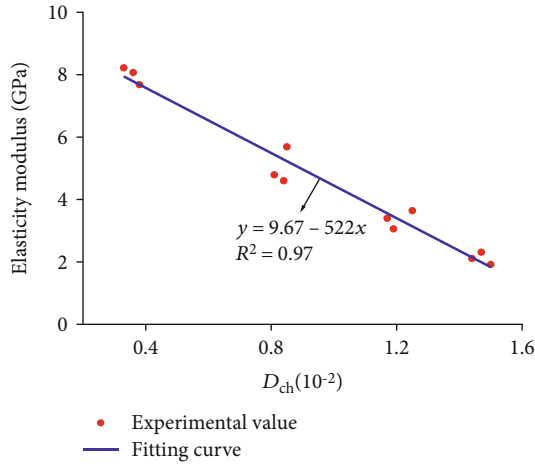


FIGURE 11: Chemical damage parameters and elastic modulus.

It is assumed that the pores and fissures of the rock are compacted in the compaction stage without damage expansion, and continuous damage occurs in the elastic (linear), plastic, and postpeak stages. According to the results of Lu's research [27], the stress-strain relationship in the rock compaction stage can be expressed as

$$\sigma = \sigma_A \left(\frac{\varepsilon}{\varepsilon_A} \right)^2, \quad (12)$$

where σ is stress and ε is strain, in the process of uniaxial loading, while σ_A is the maximum stress and ε_A is the maximum strain in the compaction stage.

The rock material is heterogeneous and contains a variety of defects, which greatly affect mechanical properties. The distribution of defects is random, so the resulting damage is also distributed randomly in the rock material. It can therefore be considered that the rock strength is a random variable. Weibull distribution is used to describe the law of random statistical distribution of rock strength, so the probability density function of the failure of microelements of rock material is [28, 29]

$$P(F) = \frac{m}{F} \left(\frac{\varepsilon}{F} \right)^{m-1} \exp \left[- \left(\frac{\varepsilon}{F} \right)^m \right], \quad (13)$$

where m and F are two constants, characterizing the brittleness (nonuniformity) of materials, reflecting the different response characteristics of rock materials to external loads, and both are nonnegative numbers. F is the random distribution variable of the microelement intensity, m is the shape factor of the distribution function. If the damage variable D is defined as the ratio of N_f of material damage to the total number of elements N , the range is 0~1. Then, the damage variable of rock material is

$$\begin{aligned} D &= \frac{N_f}{N} = \frac{N \int_0^{\varepsilon} (m/F) (x/F)^{m-1} \exp[-(x/F)^m] dx}{N} \\ &= 1 - \exp \left[- \left(\frac{\varepsilon}{F} \right)^m \right]. \end{aligned} \quad (14)$$

Substituting Equation (14) into Equation (11), the stress-strain relationship under uniaxial loading of mudstone can be obtained as

$$\sigma = E\varepsilon \exp \left[- \left(\frac{\varepsilon}{F} \right)^m \right]. \quad (15)$$

The m and F of the damage statistical constitutive model can be determined by the peak strength point (ε_c, σ_c) of the stress-strain curve under the uniaxial loading of mudstone after soaking in acid water. The slope at the peak strength point (ε_c, σ_c) is 0. When $\varepsilon = \varepsilon_c$, there are

$$\frac{d\sigma}{d\varepsilon} = E \left[1 - m \left(\frac{\varepsilon_c}{F} \right)^m \right] \exp \left[- \left(\frac{\varepsilon_c}{F} \right)^m \right] = 0. \quad (16)$$

Meanwhile, the peak intensity point (ε_c, σ_c) satisfies

$$\sigma_c = E\varepsilon_c \exp \left[- \left(\frac{\varepsilon_c}{F} \right)^m \right]. \quad (17)$$

According to Equations (16) and (17), the following can be obtained:

$$m = [\ln (E\varepsilon_c/\sigma_c)]^{-1}, \quad (18)$$

$$F = \varepsilon_c [\ln (E\varepsilon_c/\sigma_c)]^m. \quad (19)$$

In combination with Equations (12) and (15), we can obtain the constitutive damage model of mudstone soaked by segmental acid water:

$$\sigma = \begin{cases} \sigma_A (\varepsilon/\varepsilon_A)^2 (\varepsilon \leq \varepsilon_A), \\ \sigma_A + E(\varepsilon - \varepsilon_A) \exp \left[- \left(\frac{\varepsilon - \varepsilon_A}{F} \right)^m \right] (\varepsilon \geq \varepsilon_A). \end{cases} \quad (20)$$

The authors used formula (20) to do the model curve and found that the peak strength of all rock samples was lower than the experiment value. Thus, the damage variable is defined based on the fact that all the bearing capacity of the rock is lost after the failure. In fact, although the bearing

capacity of the rock after the failure is reduced, it can still bear part of compressive stress and shear stress; that is, the rock still has residual strength after the failure. For this reason, some scholars put forward a modified damage variable characterized by critical damage value [30]:

$$D' = D_u \cdot D, \quad (21)$$

where D_u is the critical loss value and D' is the modified damage variable.

$$D_u = 1 - \sigma_p / \sigma_c, \quad (22)$$

where σ_p is the residual strength.

It can be seen from Equation (14) that the damage variable of rock is actually related to $\exp[-(\varepsilon/F)^m]$. If Equation (21) is used to deduce the damage constitutive model of rock, the derivation process and the final expression will be complicated. In order to make the curve drawn by the model consistent with the experiment curve and simplify the damage constitutive model of rock. In this paper, the reciprocal of the critical damage value is substituted into Equation (17), and the revised statistical damage model of rock is

$$\sigma_c = E\varepsilon_c \frac{1}{D_u} \exp\left[-\left(\frac{\varepsilon_c}{F}\right)^m\right]. \quad (23)$$

The damage constitutive model of mudstone after acidic water corrosion can be obtained by combining Equations (12), (19), and (23):

$$\sigma = \begin{cases} \sigma_A (\varepsilon/\varepsilon_A)^2 (\varepsilon \leq \varepsilon_A), \\ \sigma_A + E \frac{1}{D_u} (\varepsilon - \varepsilon_A) \exp\left[-\frac{1}{m} \left(\frac{\varepsilon - \varepsilon_A}{\varepsilon_c - \varepsilon_A}\right)^m\right] (\varepsilon \geq \varepsilon_A). \end{cases} \quad (24)$$

Equation (9) of compressive strength, peak strain, elastic modulus, and chemical damage parameters of mudstone

$$\sigma = \begin{cases} 6.92(\varepsilon/0.00852)^2 (\varepsilon \leq 0.00852), \\ 6.92 + \frac{35.65 - 1175 * 0.0144}{35.65 - 1175 * 0.0144 - 5.13} (9.67 - 522 * 0.0144) * 1000*, \\ (\varepsilon - 0.00852) \exp\left[-\frac{1}{1.74} \left(\frac{\varepsilon - 0.00852}{0.0146 - 0.00852}\right)^{1.74}\right] (\varepsilon \geq 0.00852). \end{cases} \quad (27)$$

After that, the strain data obtained by the test were substituted into Equation (27) to obtain the corresponding stress value, so as to determine the stress-strain curve of the model. Other rock samples are similar to drawing model curves. Figure 12 shows the experiment curve and model curve of the uniaxial loading of rock after soaking in acidic

soaked in acid water is substituted into Equation (18), Equations (9) and (22) are substituted into Equation (24), and the segmented damage constitutive model of mudstone soaked in acid water characterized by chemical damage parameters is obtained:

$$m = \{\ln [(e - fD_{ch})(c + dD_{ch})/(a - bD_{ch})]\}^{-1}, \quad (25)$$

$$\sigma = \begin{cases} \sigma_A (\varepsilon/\varepsilon_A)^2 (\varepsilon \leq \varepsilon_A), \\ \sigma_A + \frac{a - bD_{ch}}{a - bD_{ch} - \sigma_p} (e - fD_{ch})(\varepsilon - \varepsilon_A) \exp\left[-\frac{1}{m} \left(\frac{\varepsilon - \varepsilon_A}{\varepsilon_c - \varepsilon_A}\right)^m\right] (\varepsilon \geq \varepsilon_A). \end{cases} \quad (26)$$

5. Model Verification

Based on the results of the uniaxial loading tests and the above theoretical assumptions, a piecewise statistical constitutive damage model of mudstone soaked in acid water is established in this paper. In order to further verify the rationality of the model, the fitting curve data was used for analysis. This included the maximum stress σ_A and maximum strain ε_A in the compaction stage, peak strain, and residual strength of mudstone soaked in acid water that can be obtained from the measured test data. According to Figures 9-11, parameters $a = 35.65$, $b = 1175$, $c = 0.00265$, $d = 0.839$, $e = 9.67$, and $f = 522$. The statistical constitutive parameter m is calculated from Equation (25). By taking the above parameters into Equation (26), the constitutive model of piecewise statistical damage of mudstone after acid water corrosion can be calculated.

Taking rock sample A₁ as an example to illustrate how to do the curve of the model, the residual strength of rock sample A₁ after failure is 5.13 MPa, the peak strain is 0.0146, the compressive stress and strain are 6.92 MPa and 0.00852, respectively, and the chemical damage parameter is 0.0144. The above parameters were substituted into Equation (25) to obtain the value of m which is 1.74, and then, all parameters were substituted into Equation (26) to obtain the piecework damage constitutive model of rock sample A₁ which is

water. The model curve in this paper is consistent with the experimental curve, and the correlation coefficient is as high as 0.98 before the peak stress.

The traditional continuous damage constitutive model, due to the significant deviation in the initial compaction stage, leads to the poor fitting between the estimated curve

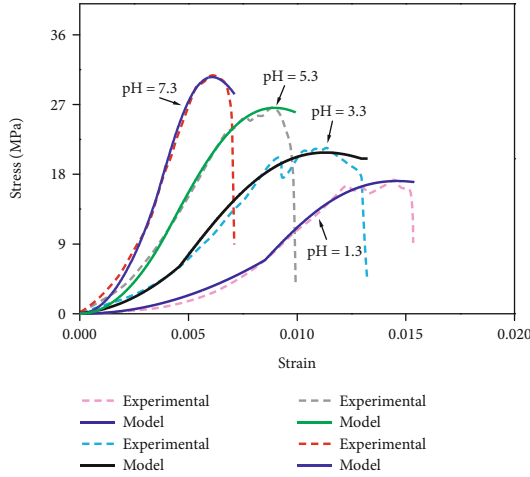


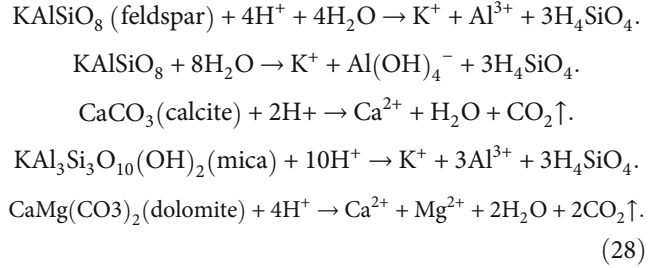
FIGURE 12: Uniaxial loading test curve and model curve of rock after acid water immersion.

and the rock stress-strain curve. The segmented statistical constitutive model of rock damage is expressed in the compaction stage and the subsequent stage separately. The advantages of the rock damage model from the elastic (linear) stage overcome the problem of a large deviation of the estimated curve from the experiment curve. Furthermore, the degree of the fitting is high and is more suitable for the analysis of rock uniaxial compression stress-strain after chemical solution corrosion.

6. Corrosion Mechanism of Acid Water on Mudstone

In acidic solutions, the initial H^+ content of the solution is relatively high. In the early stage of soaking, the water-rock chemistry is mainly the ion exchange reaction between H^+ and mineral components. The reaction causes the replacement of the cation of mineral crystals, dissolution, and deterioration of mineral components. As consumption of H^+ and hence its depletion occurs, the water-rock chemical reaction gradually changed to mineral hydrolysis and the reaction rate slowed down. The chemical interaction between water and rock caused both physical and chemical changes in the rock specimens. In terms of physical action, the dissolution of water on the rock leads to the decrease of interparticle relay and friction and thus produces a splitting action on the micropores. In terms of chemical action, the chemical action of water and rock not only causes the change of rock mineral composition but also leads to the change of fine microstructure such as particle size and shape, pore, and fissure morphology. The combined action of these two affects finally leads to the change of physical and mechanical properties of rock. The solubility of clay mineral in the acidic solution will also be greatly increased. Feldspar solubility in the acidic solution will greatly increase, and the solubility increases with the decrease of pH. The corrosion degree of calcite, dolomite, and other carbonate minerals increased significantly at normal pressure and temperature. During different hydrochemical solutions, minerals such as feldspar, calcite,

mica, and dolomite in mudstone have the following series of chemical reactions with the H^+ ions in the solutions:



In addition to the above chemical reactions, there is also dissolution in the solution. Some minerals in the mudstone are easily soluble in the chemical solution, such as some chlorides and some oxides (iron, aluminum oxides, etc.), which are lost along with the chemical corrosion. This results in the increase of porosity of the rock and the softening of the rock structure. After the above series of hydrochemical reactions occurring between water and rocks, the reaction products were lost with the solution, resulting in the increase of porosity and softening of the sample, and some particles on the sample surface were detached. From the microscopic view, the corrosion of the hydrochemical solution to the mudstone sample causes changes in its composition and structure, which leads to an increase in its porosity. On the macro level, it is the deterioration of the mechanical characteristics of mudstone samples, which is closely related to porosity. From the analysis of the test results, it is concluded that in the process of chemical corrosion, the greater relative mass change and porosity change rate of mudstone samples, the greater the deterioration degree of rock.

7. Conclusions

The following are the conclusions of the research:

- (1) The peak stress and elastic modulus of rock samples decrease to different degrees with the increases of solution acidity, but the peak strain increases with the increase of solution acidity, and the proportion of compaction stage increases with the increase of acidity
- (2) There is a close relationship between the physical parameters of mudstone and its chemical parameters after chemical corrosion. The greater the chemical damage parameter, the greater the reduction of its mechanical parameters, and the stronger the softening effect of deformation parameters
- (3) A segmental rock damage statistical constitutive model based on chemical damage parameters has been developed. This overcomes the problem of large deviation between the fitting curve and the test curve before the peak, with the correlation coefficient as high as 0.98, which is suitable for the analysis of the uniaxial compressive stress-strain problem of rock soaked in acid water

Data Availability

All data are given in the paper and if further data were in need, it will be provide in Annexure.

Conflicts of Interest

We declare that we do not have any commercial or associative interest that represents a conflict of interest in connection with the work submitted.

Acknowledgments

This paper was supported by the National Natural Science Foundation of China (51874280) and the Priority Academic Program Development of Jiangsu Higher Education Institutions (PAPD).

References

- [1] X. Liu, C. Liu, and G. Liu, "Dynamic behavior of coalbed methane flow along the annulus of single-phase production," *International Journal of Coal Science & Technology*, vol. 6, no. 4, pp. 547–555, 2019.
- [2] C. Wu, C. Yuan, G. Wen, L. Han, and H. Liu, "A dynamic evaluation technique for assessing gas output from coal seams during commingling production within a coalbed methane well: a case study from the Qinshui basin," *International Journal of Coal Science & Technology*, vol. 7, no. 1, pp. 122–132, 2020.
- [3] W. Zhao, K. Wang, R. Zhang, H. Dong, Z. Lou, and F. An, "Influence of combination forms of intact sub-layer and tectonically deformed sub-layer of coal on the gas drainage performance of boreholes: a numerical study," *International Journal of Coal Science & Technology*, 2020.
- [4] A. H. Liu, *Dynamic change features of water chemistry during coal reservoir drainage and physical simulation of CBM desorption at fixed pressures and flow in southern qinshui basin*, Chin U Min Technol, 2013.
- [5] Y. Yu and L. Ma, "Application of roadway backfill mining in water-conservation coal mining: a case study in northern Shaanxi, China," *Sustainability*, vol. 11, no. 13, p. 3719, 2019.
- [6] I. Beentjes, J. T. Bender, A. J. Hawkins, and J. W. Tester, "Chemical dissolution drilling of barre granite using a sodium hydroxide enhanced supercritical water jet," *Rock Mechanics and Rock Engineering*, vol. 53, no. 2, pp. 483–496, 2020.
- [7] T. Al-Bazali, "A novel experimental technique to monitor the time-dependent water and ions uptake when shale interacts with aqueous solutions," *Rock Mechanics and Rock Engineering*, vol. 46, no. 5, pp. 1145–1156, 2013.
- [8] O. Sho, Y. Hideaki, K. Naoki, C. Dae-Sung, and K. Kiyoshi, "Modeling of coupled thermal-hydraulic-mechanical-chemical processes for predicting the evolution in permeability and reactive transport behavior within single rock fractures," *International Journal of Rock Mechanics and Mining Sciences*, vol. 107, pp. 271–281, 2018.
- [9] T. Han, J. Shi, and X. Cao, "Fracturing and damage to sandstone under coupling effects of chemical corrosion and freeze–thaw cycles," *Rock Mechanics and Rock Engineering*, vol. 49, no. 11, pp. 4245–4255, 2016.
- [10] Y. Lin, F. Gao, K. Zhou, and R. G. Gao, "Mechanical properties and statistical damage constitutive model of rock under a coupled chemical-mechanical condition," *Geofluids*, vol. 2019, Article ID 7349584, 17 pages, 2019.
- [11] W. Wang, X. H. Li, Q. Z. Zhu, C. Shi, and W. Y. Xu, "Experimental study of mechanical characteristics of sandy slate under chemical corrosion," *Rock and Soil Mechanics*, vol. 9, pp. 2559–2566, 2017.
- [12] L. Tang, P. Zhang, and S. Wang, "Experimental study on the macroscopic mechanical effects of water-rock chemistry on rocks," *Chinese Journal of Rock Mechanics and Engineering*, vol. 21, no. 4, pp. 526–531, 2002.
- [13] X. Feng and W. Ding, "Experimental study of limestone micro-fracturing under a coupled stress, fluid flow and changing chemical environment," *International Journal of Rock Mechanics and Mining Sciences*, vol. 44, no. 3, pp. 437–448, 2007.
- [14] W. Ding, J. Chen, T. Xu, H. Chen, and H. Wang, "Study on mechanical and chemical dissolution characteristics of limestone under chemical solution erosion," *Rock and Soil Mechanics*, vol. 36, no. 7, pp. 1825–1830, 2015.
- [15] P. Li, J. Liu, and G. Li, "Study on the influence of hydrochemistry on shear strength characteristics of sandstone," *Rock and Soil Mechanics*, vol. 32, no. 2, pp. 380–386, 2011.
- [16] J. Xu, H. Wu, L. Cheng, J. Liu, and W. Zhou, "Experimental study on shear failure characteristics of sandstone under acidic conditions," *Chinese Journal of Rock Mechanics and Engineering*, vol. 31, no. 2, pp. 3898–3903, 2012.
- [17] T. Han, Y. Chen, J. Shi, C. Yu, and M. He, "Experimental study on the influence of hydrochemical corrosion on mechanical properties of sandstone," *Chinese Journal of Rock Mechanics and Engineering*, vol. 32, no. 2, pp. 3065–3072, 2013.
- [18] H. P. Kang, "The damage of water to rock," *Hydrogeology and Engineering Geology*, vol. 3, pp. 39–41, 1994.
- [19] X. Hu, B. Hong, and Y. Meng, "Statistical damage model of red sandstone with effect of water ratio considered," *Journal of China University of Mining and Technology*, vol. 36, no. 5, pp. 609–613, 2007.
- [20] E. Zhang, G. Yang, L. Tang, Q. Yang, and Z. Xie, "Study on influence of water content to damage and degradation laws of argillaceous siltstone," *Coal Science & Technology*, vol. 47, no. 2, pp. 19–25, 2019.
- [21] Y. L. Chen, W. Shao, and Y. C. Zhou, "The elastoplastic damage constitutive model of water saturated concrete under uniaxial compression," *Engineering Mechanics*, vol. 28, no. 11, pp. 59–063, 2011.
- [22] H. Wang, T. H. Yang, H. L. Liu, and Y. C. Zhao, "Deformation and acoustic emission characteristics of dry and saturated sandstone under cyclic loading," *Journal of Northeast Normal University(Natural Science Edition)*, vol. 37, p. 1165, 2016.
- [23] X. F. Li, H. B. Li, L. W. Liu, Y. Q. Liu, M. H. Ju, and J. Zhao, "Investigating the crack initiation and propagation mechanism in brittle rocks using grain-based finite-discrete element method," *International Journal of Rock Mechanics and Mining Sciences*, vol. 127, p. 104219, 2020.
- [24] C. D. Martin and N. A. Chandler, "The progressive fracture of Lac du Bonnet granite," *International Journal of Rock Mechanics and Mining Sciences*, vol. 31, no. 6, pp. 643–659, 1994.
- [25] G. K. Zhang, H. B. Li, M. Y. Wang, and X. F. Li, "Crack initiation of granite under uniaxial compression tests: a comparison study," *Journal of Rock Mechanics and Geotechnical Engineering*, vol. 12, no. 3, pp. 656–666, 2020.

- [26] J. Lemaitre, "How to use damage mechanics," *Nuclear Engineering and Design*, vol. 80, no. 2, pp. 233–245, 1984.
- [27] Z. D. Lu, *Experimental and theoretical analysis on mechanical properties of fractured rock under water-rock interaction*, Institute of Rock and Soil Mechanics, Wuhan, 2010.
- [28] J. A. Sanchidrián, F. Ouchterlony, P. Segarra, and P. Moser, "Size distribution functions for rock fragments," *International Journal of Rock Mechanics and Mining Sciences*, vol. 71, pp. 381–394, 2014.
- [29] K. Shin, K. Sugawara, and S. Okubo, "Application of weibull's theory to estimating in situ maximum stress σ_H by hydrofracturing," *International Journal of Rock Mechanics and Mining Sciences*, vol. 38, no. 3, pp. 413–420, 2001.
- [30] Y. R. Zhang, C. J. Deng, and J. L. Wang, "The study of slip line field and upper bound method based on the non-associated flow rule," *Engineering and Science*, vol. 12, no. 8, pp. 56–69, 2010.

Research Article

Gas Transport in Shale Nanopores with Miscible Zone

Xiang Li ¹, Sai Xu ², Youzhi Hao ¹, Daolun Li ³, and Detang Lu ¹

¹Department of Modern Mechanics, University of Science and Technology of China, Hefei, Anhui 230027, China

²Key Laboratory of Tectonics and Petroleum Resources, Ministry of Education, China University of Geosciences, Wuhan 430074, China

³School of Mathematics, Hefei University of Technology, Hefei, Anhui 230009, China

Correspondence should be addressed to Detang Lu; dtlu@ustc.edu.cn

Received 16 February 2020; Revised 8 June 2020; Accepted 20 July 2020; Published 7 October 2020

Academic Editor: Wen-Dong Wang

Copyright © 2020 Xiang Li et al. This is an open access article distributed under the Creative Commons Attribution License, which permits unrestricted use, distribution, and reproduction in any medium, provided the original work is properly cited.

Based on the results of molecular dynamics simulation, in a gas-water miscible zone, the velocity profiles of the flowing water film do not increase monotonously but increase first and then decrease, which is due to the interaction between water and gas molecules. This exhibits a new physical mechanism. In this paper, we firstly propose a gas-water flow model that takes into account the new physical phenomena and describes the distribution of gas-water velocity in the whole pore more accurately. In this model, a decreasing factor for water film in the gas-water miscible zone is used to describe the decrease of water velocity in the gas-water miscible zone, which leads to the gas velocity decrease correspondingly. The new flow model considers the interaction among gas and water molecules in the miscible zone and can provide more accurate velocity profiles compared with the flow models not considering the miscible region. Comparison calculation shows that the previous model overestimates the flow velocity, and the overestimation increases with the decrease of the pore radius. Based on the new gas-water flow model, a new permeability correction factor is deduced to consider the interaction among gas and water molecules.

1. Introduction

Shale formation is a great energy source. As a result of rising energy demand and prices, research into unconventional oil and gas is deepening, and successful development of shale formation in the United States has led to a boom in research and development [1]. Nowadays, there are about 213 tcm of recoverable shale gas reserves in the world [2]. Shale gas is a very important unconventional energy, and its exploitation capacity is mainly determined by gas storage and flow capacity [3, 4]. Shale gas has a big advantage over other energy sources in terms of carbon dioxide emissions and prices and is becoming a bigger and bigger part of total energy production [5, 6]. However, because shale is mainly stored in natural fractures, micropores, nanopores, and other complex and relatively impermeable shale formations, its exploitation has many technical and flow mechanism problems [1, 7–9]. Therefore, it is important to study the flow mechanism in shale formation in order to provide more theoretical support for the improvement of mining technology and efficiency.

Shale formation pores are mainly nanoscale. The pore radius varies widely and is mainly on the nanometer scale, which is quite different from the transport mechanism in conventional formation and has a significant effect on the gas flow performance [1, 7]. When considering the transport of single-phase gas in the nanometer pore channel, there is slip effect on the wall surface due to the interaction between solid and gas molecules [10]. Surface diffusion of adsorbed gas cannot be neglected in smaller pores and increases significantly with the increase of the maximum adsorption capacity [11]. By defining the ratio of the average free path of gas to the characteristic dimension as the Knudsen number K_n , the gas transport mechanism can be divided into viscous flow, slip flow, transition flow, and molecular free flow [12–14]. Therefore, when establishing the flow equation, the flow boundary cannot be regarded as a nonslip boundary, and it needs to be corrected by adding gas slip [15]. Based on the Knudsen number K_n , two kinds of models are established: continuity equation obtained by converting the boundary condition to nonslip boundary [16], several transport

mechanisms combined by weight coefficients with a unified gas transport equation [17, 18]. Based on a unified diffusion coefficient, Cai et al. [19] proposed an apparent permeability model of shale which investigated the gas transport mechanism in a shale nanopore by considering convective flow, gas diffusion, and surface diffusion. However, the above results only apply to single-phase gas transport. In a real shale reservoir, the injection of fracturing fluid and initial water saturation make the real pore flow more than a single-phase gas flow [20]. Therefore, when studying nanopores, the gas-water two-phase velocity model should be established, which makes the model more consistent with the actual situation.

In order to establish a more accurate gas flow model in nanometer pores, a lot of literatures have discussed gas and water flow models. Li et al. [21] proposed an analytical method based on the Hagen-Poiseuille formula and capillary pressure curve to model and analyze the gas-water relative permeability of nanopores with interface effect. Singh and Cai [8] proposed a new method which predicts permeability of fractured shale by discretizing the medium into matrix and can estimate permeability at any scale of interest and is used to predict relative permeability estimates of two-phase flow in fractured shale samples. Li et al. [22] proposed an analytical model to consider the flowing water film by changing the boundary conditions of the gas-liquid interface and the solid-liquid interface. The model has two different nanoscale characteristic sizes of crack hole and circular hole and is in good agreement with the experimental data, which proves that the high-viscosity flowing water film can improve the flow capacity of gas.

However, the gas-water two-phase flow in nanopores is more complex than the above literatures. Molecular dynamics simulation plays an important role in studying the mechanism of gas-water flow in pores. Xu et al. [23] performed a comprehensive study on the two-phase transport characteristics of shale gas and water through hydrophilic and hydrophobic nanopores combined with molecular dynamics (MD) simulation and analysis model. Hao et al. [24] used nonequilibrium molecular dynamics to simulate the mixed flow behavior of water and methane gas in shale pores. Based on Hao et al.'s research, we found that the velocity profiles of the gas-water in the nanometer pore are different from the previous studies, as shown in Figure 1. At the gas-water interface, due to the interaction between gas and water molecules, the water film velocity profile has an obvious downward trend near the gas-water interface, which is partly enlarged as shown in Figure 1(a), but the water velocity profile in a previous paper is increasing monotonically as shown in Figure 1(b) [25]. Based on the molecular dynamics results, there are gas and water molecules in a zone near the gas-water interface which is called the miscible zone in the next section. The effect of the miscible zone on flow behavior is not considered in the above-mentioned models. This shows that there are some physical mechanisms that are not considered in previous papers.

Based on the research gap, in this paper, a gas-water two-phase model was proposed to study the influence of the miscible zone at the gas-water interface. The flow model takes a

decreasing factor into account to describe the effect of the miscible zone on flow behaviors.

2. Model Establishment

2.1. Miscible Zone. Figure 2 gives the density distribution of gas and water molecules in pores, the density 2D distribution of gas and water molecules, and an elevation of water and gas at equilibrium in a pore in Hao et al.'s molecular dynamics simulation results [20]. As shown in Figure 2(a), at the gas-water interface, there is a region where gas-water molecules coexist. Figures 2(b) and 2(c) show the density 2D distribution of gas and water molecules. Near the pore wall are all water molecules, and in the middle of the pore are all gas molecules. At the gas-water interface, there is a region where the density of gas and water molecules is not zero, and in this region, the gas and water molecules coexist. In order to show the region where gas-water molecules coexist clearly, the 1D density distribution of gas and water is shown in Figures 2(d) and 2(e), which show that there are three zones: zone 1, zone 2, and zone 3. Only water molecules are in zone 1, which represents the water film. In zone 2, there are gas and water molecules at the same time. The number of water molecules decreases while gas molecules increase (indicated by the shaded part). Combined with the analysis of 1D and 2D density distribution of gas-water molecules, water and gas molecules form interfacial regions with the 1-99 thickness (1%-99% of bulk gas density) around 0.3 nm [23, 26], and we call the interfacial regions as the miscible zone (zone 2). In zone 3, the water molecule number of zone 3 becomes less and is about five or six times less than that in zone 2, but the number of gas molecules reaches its maximum. Therefore, in zone 3, gas molecules are those that dominated and it is considered as pure gas phase flow.

Figure 2(b) shows that the density distribution of water and gas molecules is not strictly symmetrical. In order to model the flow behavior, Figure 2 is simplified to Figure 3, in which there are three flow zones in the circular pore.

They are a high-viscosity water film zone near the wall, a gas zone in the middle, and a miscible zone between the gas zone and the water film zone. Hao et al.'s results show that due to the gas-water molecule interaction, the farther away from the wall of the pore, the slower the velocity of water, as shown in Figure 2. In this paper, we use a decreasing factor β to describe the effect of molecule interaction in the miscible region on the water velocity as follows:

$$\beta = \begin{cases} 1 + 4.5 \ln \frac{r}{r_0 - h_w + h_m}, & r \in [r_0 - h_w, r_0 - h_w + h_m], \\ 1, & r \in [r_0 - h_w + h_m, r_0], \end{cases} \quad (1)$$

where h_m and h_w are the thickness of the miscible zone and water film zone, respectively, and r_0 is the pore radius.

2.2. Mobile High-Viscosity Water Film. The walls of the nanopores are mainly composed of hydrophilic or hydrophobic materials [27]. However, because of the diversity of wall

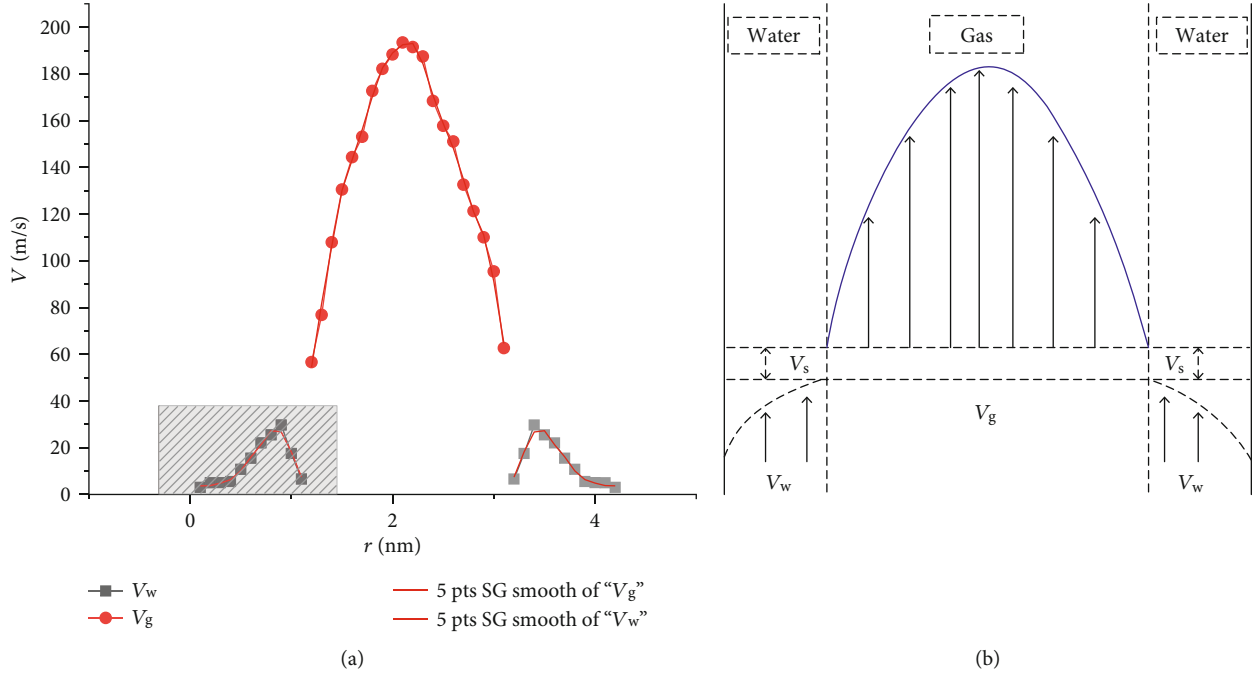


FIGURE 1: Comparison of velocity profile between molecular dynamics simulation results and the results only considering the slip velocity of gas and water. (a) Molecular dynamics simulation results of gas and water velocity in nanometer pores. $T = 333.15$ K, $P = 207$ MPa, $r_0 = 2$ nm, $L = 7.23$ cm, $\theta = 30^\circ$. (b) Schematic view of the gas and water velocity which considers the slip velocity of gas and water. v_s is the gas slip velocity.

materials, hydrophobic substances will also be doped. Due to the solid attraction of the hydrophilic channel wall, the water molecules are trapped on the surface of the hydrophilic solid and arranged in an orderly manner within a few molecular diameters near the channel wall [27, 28]. A large number of molecular dynamics simulation results and experimental data illustrate that the thickness of water film is about 0.7 nm [29–31]. When the pressure gradient in the pores reaches a certain height, the water film will flow. Such a water film will show the characteristics of high viscosity and slow flow rate, which is of great significance in establishing the gas-liquid two-phase velocity model in nanometer pores.

Because of the interaction of gas and water molecule, the real slip of confined water can be calculated as [22]

$$l_s = \frac{C}{(\cos \theta + 1)^2}, \quad (2)$$

where θ is the contact angle, l_s is the slip length, and C is assigned to be 0.41, dimensionless.

2.3. Flow Equation. This model is based on the Hagen-Poiseuille equation for steady-state laminar flow through circular pores. As shown in Figure 3, the high-viscosity water film is distributed on the pore surface evenly, and the miscible zone exists at the gas-water interface. Based on the model of Mattia and Calabrò [25], gas and water velocity are, respectively,

$$\begin{cases} V_g = -\frac{\Delta P}{4\mu_g L} r^2 + C_1, & r \in [0, r_0 - h_w], \\ V_w = \beta \left(-\frac{\Delta P}{4\mu_w L} r^2 + C_2 \right), & r \in [r_0 - h_w, r_0], \end{cases} \quad (3)$$

where μ_w and μ_g are viscosity of water and gas, respectively; L is the length of the pore; and ΔP is the pressure difference between entrance and exit.

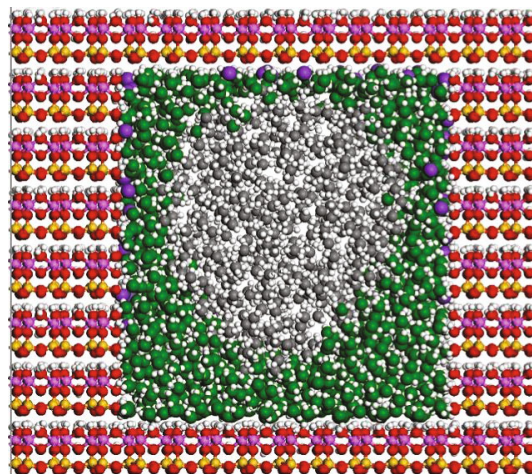
The boundary conditions for velocity continuity are as follows:

$$\begin{cases} \frac{\partial V_g}{\partial r}(r=0) = 0, \\ V_w(r=r_0) = -l_s \frac{\partial V_w}{\partial r}(r=r_0), \\ V_g(r=r_0 - h_w) = V_w(r=r_0 - h_w) - v_s(r=r_0 - h_w), \end{cases} \quad (4)$$

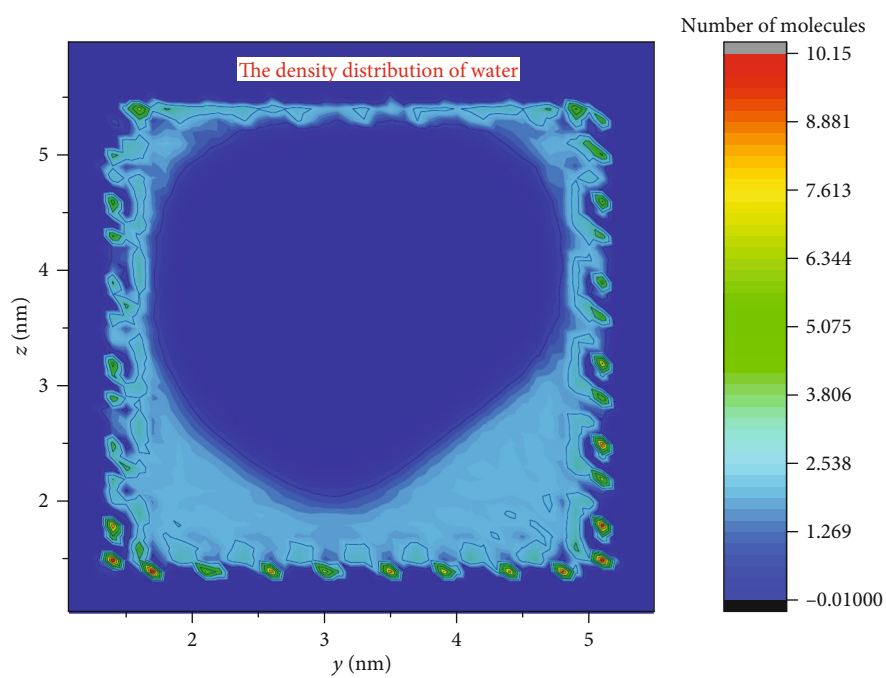
where v_s describes the gas-water momentum transport and the interaction between gas molecules, which can be defined as [32]

$$v_s = \frac{2 - \sigma_v}{\sigma_v} \frac{\lambda}{1 - b\lambda} \left(\frac{\partial v_g}{\partial r} \right), \quad (5)$$

where v_s is the slip velocity between water and gas, σ_v is the tangential momentum accommodation coefficient, b



(a)



(b)

FIGURE 2: Continued.

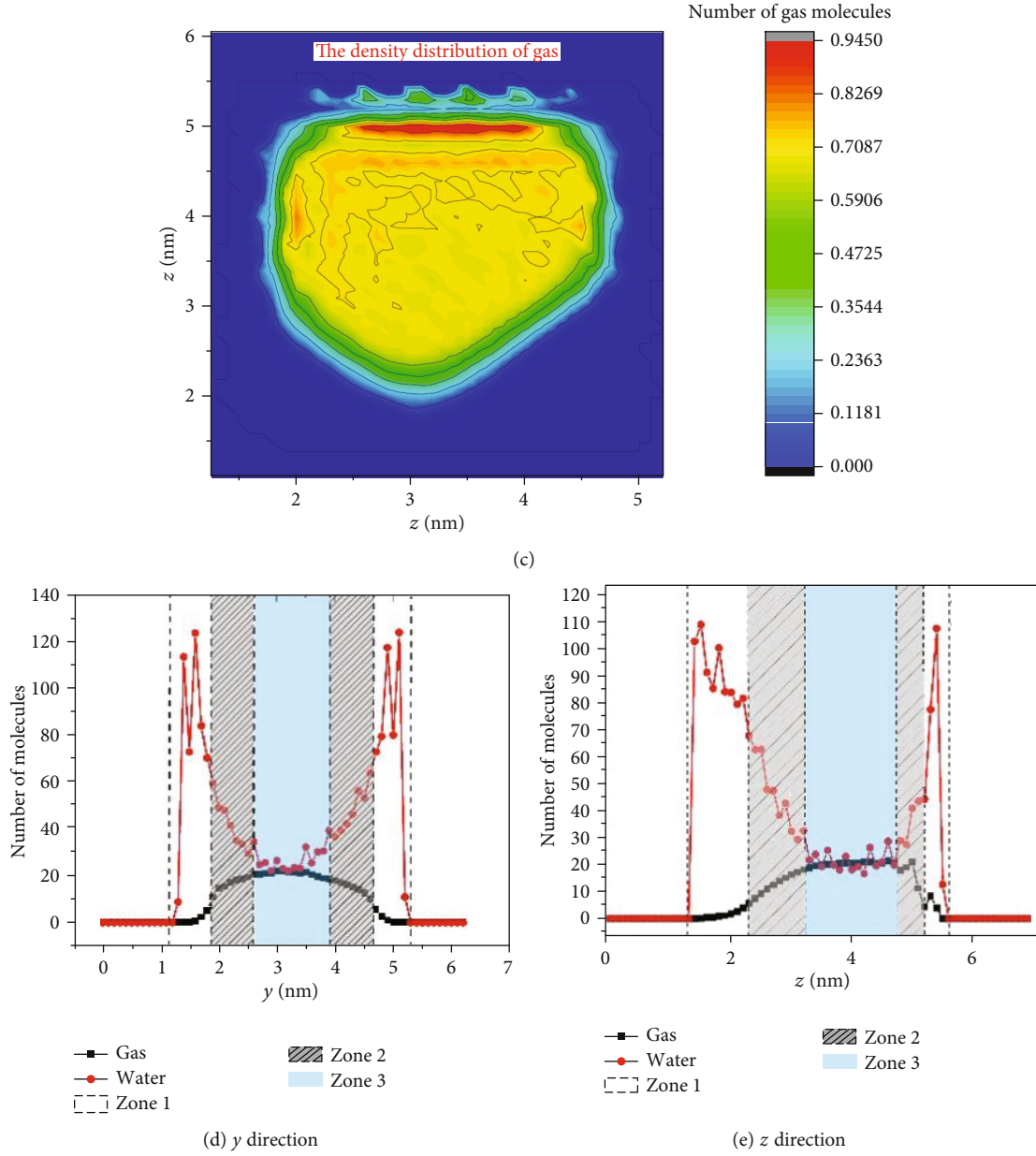


FIGURE 2: The elevation of water and gas at equilibrium in a pore, the density 2D distribution of gas and water molecules, and an average density distribution curve of gas and water in the yz plane under a static equilibrium state of equilibrium molecular dynamics [24]. (a) The elevation of water and gas at equilibrium in a pore. The gray ball represents the carbon atoms in the methane molecule, which can represent gas molecules. The green ball represents the oxygen atoms in the water molecule, which can represent water molecules. (b) The density 2D distribution of gas. (c) The density 2D distribution of water. (d) The density distribution curve of water and gas molecules along the y direction, and (e) is the density distribution curve of water and gas along the z direction. The shaded areas are estimated to be highly interactive between the gas and water molecules.

is a slip coefficient, and λ is the mean free path, which can be defined as

$$\lambda = \frac{\mu_g}{P} \sqrt{\frac{\pi ZRT}{2M}}, \quad (6)$$

where R is the gas constant, M is the molecular weight, T is the temperature, and Z is the gas compressibility factor, which is calculated [22]:

$$\begin{aligned} Z = & 0.702 \left(\frac{P}{P_c}\right)^2 e^{-2.5T/T_c} - 5.524 \left(\frac{P}{P_c}\right) e^{-2.5T/T_c} \\ & + 0.044 \left(\frac{T}{T_c}\right)^2 - 0.164 \frac{T}{T_c} + 1.15, \end{aligned} \quad (7)$$

where T_c is the critical temperature and P_c is the critical pressure.

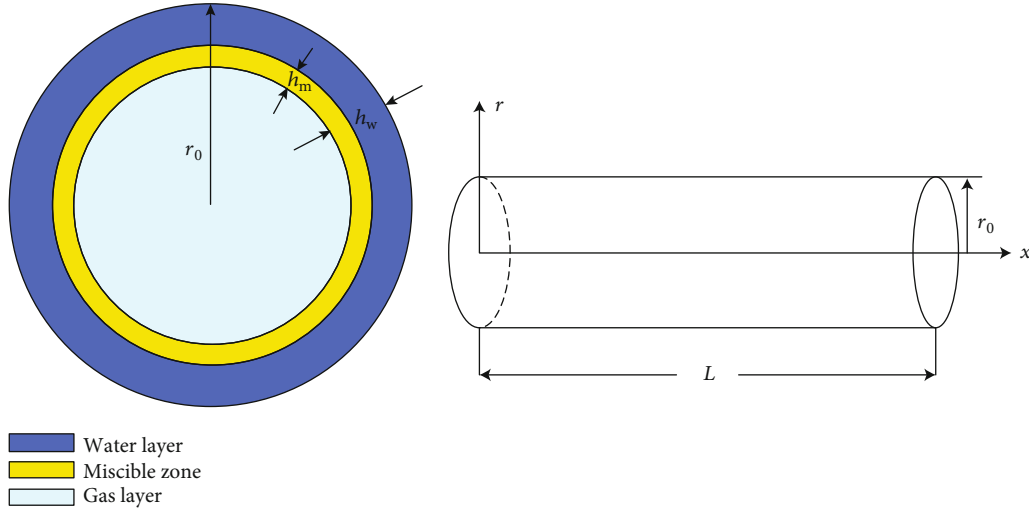


FIGURE 3: Schematic view of the model.

By the combination of Equations (3) and (4), the velocity profiles are obtained:

$$V_g = \frac{\Delta P}{4\mu_g L} [(r_0 - h_w)^2 - r^2] + \beta \frac{\Delta P}{4\mu_w L} (2r_0 h_w - h_w^2 + 2l_s r_0) + \frac{2 - \sigma_v}{\sigma_v} \frac{\lambda}{1 - b\lambda} \frac{\Delta P}{2\mu_g L} (r_0 - h_w). \quad (8)$$

By integrating Equation (8) along the r direction, the gas flow equation can be further deduced as

$$Q_g = -\frac{\Delta P \pi}{8\mu_g L} (r_0 - h_w)^4 + \beta \frac{\Delta P \pi}{4\mu_g L} (r_0 - h_w)^2 (2r_0 - h_w) + \frac{\Delta P \pi}{2\mu_w L} l_s r_0 (r_0 - h_w)^2 + \frac{2 - \sigma_v}{\sigma_v} \frac{\lambda}{1 - b\lambda} \frac{\Delta P \pi}{\mu_g L} (r_0 - h_w)^3, \quad (9)$$

where Q_g is the flow rate of gas in nanopores.

In Darcy's equation, the flow rate Q_d of gas is as follows:

$$Q_d = \frac{K_{Ag} (r - h_w)^2 \pi \Delta P}{\mu_g L}. \quad (10)$$

The flow rate of porous media is modified by the ratio of tortuosity to porosity [22]:

$$Q_d = \frac{\phi_g}{\tau} Q_g. \quad (11)$$

Substituting Equations (9) and (10) into Equation (11) to

get the formula for calculating the gas apparent permeability,

$$K_{Ag} = \frac{\phi_g}{\tau} \left[\frac{(r_0 - h_w)^2}{8} + \beta \frac{\mu_g}{4\mu_w} (2r_0 h_w - h_w^2 + 2l_s r_0) + \frac{2 - \sigma_v}{\sigma_v} \frac{\lambda}{1 - b\lambda} \frac{(r_0 - h_w)}{2} \right], \quad (12)$$

where K_{Ag} is the gas apparent permeability when considering the flow of water film in the nanopores.

When the miscible zone and flowing water film with high viscosity are not considered, it reduces to a single gas flow model, and its boundary condition is given as follows:

$$\begin{cases} \frac{\partial V_g}{\partial r}(r=0) = 0, \\ V_g(r=r_0 - h_w) = -V_s(r=r_0 - h_w). \end{cases} \quad (13)$$

Using the same derivation process in the formula of velocity profile and apparent permeability of gas without considering the miscible zone and flowing high-viscosity water film can be deduced as follows:

$$V_{Agi} = \frac{\Delta P}{4\mu_g L} [(r_0 - h_w)^2 - r^2] + \frac{2 - \sigma_v}{\sigma_v} \frac{\lambda}{1 - b\lambda} \frac{\Delta P}{2\mu_g L} (r_0 - h_w),$$

$$K_{Agi} = \frac{\phi_g}{\tau} \left[\frac{(r_0 - h_w)^2}{8} + \frac{2 - \sigma_v}{\sigma_v} \frac{\lambda}{1 - b\lambda} \frac{r_0 - h_w}{2} \right], \quad (14)$$

where V_{Agi} is the gas velocity in the nanometer pores without considering the miscible zone and the mobile water film and K_{Agi} is the apparent permeability without considering the miscible zone and the high-viscosity flowing water film.

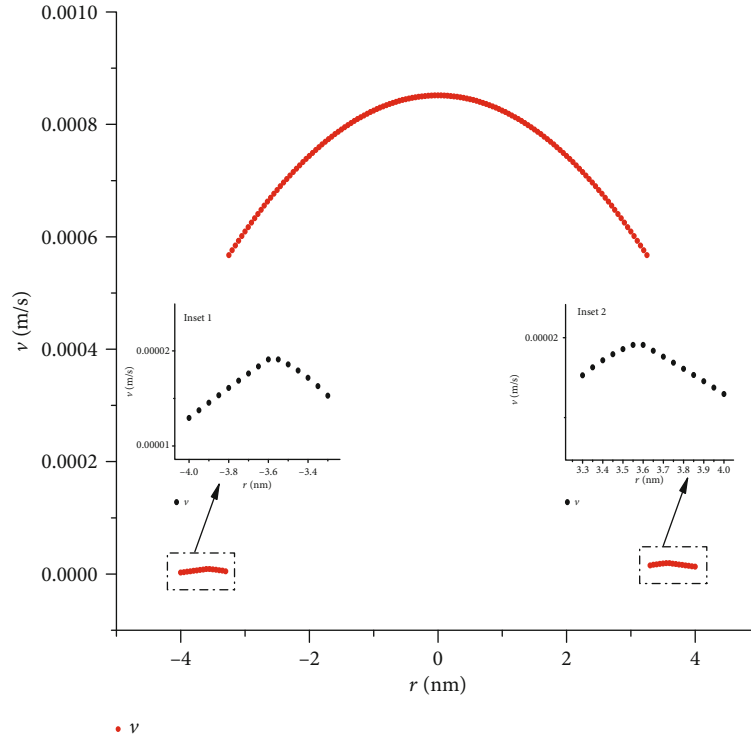


FIGURE 4: Gas and water velocity profile of the proposed model, and the insets show the enlargement of the water film velocity on the left and right. $P = 50$ MPa, $T = 350$ K, $\varnothing = 0.9$, $h_w = 0.7$ nm, $h_m = 0.3$ nm, $L = 7.23$ cm, $\theta = 30^\circ$, $r_0 = 4$ nm.

3. Model Validation

In order to verify the model in this paper, a comparison was made between the velocity profile of gas-water calculated by the proposed model and the result obtained by molecular dynamics simulation. Figure 4 shows the velocity profile of gas and water in a pore that contains a local magnification of the velocity of the water film on the left and right sides. The velocity profile of the gas in the middle of the pore is parabolic, while the velocity of the water film near the pore wall first rises and then falls at the gas-water interface. Comparing Figure 1 with Figure 4, the overall velocity distribution trend is consistent with the results of molecular dynamics simulation. This shows that the proposed model can correctly reflect the simulation results. Through the comparison of velocity profile between the model in this paper and Li et al.'s model, it can be found that when the model in this paper does not consider the miscible zone, it is the model proposed in Li et al.'s paper. This also indirectly verifies the correctness of the model in this paper.

4. Results and Discussion

4.1. Comparison between the Proposed Model and Single Gas Model

4.1.1. Gas Velocity Profile. The gas velocity profile depends on whether the flow of water film and miscible zone are considered. Figures 5(a)–5(c) give the gas flow velocity for the single gas flow (with static water film and without miscible zone)

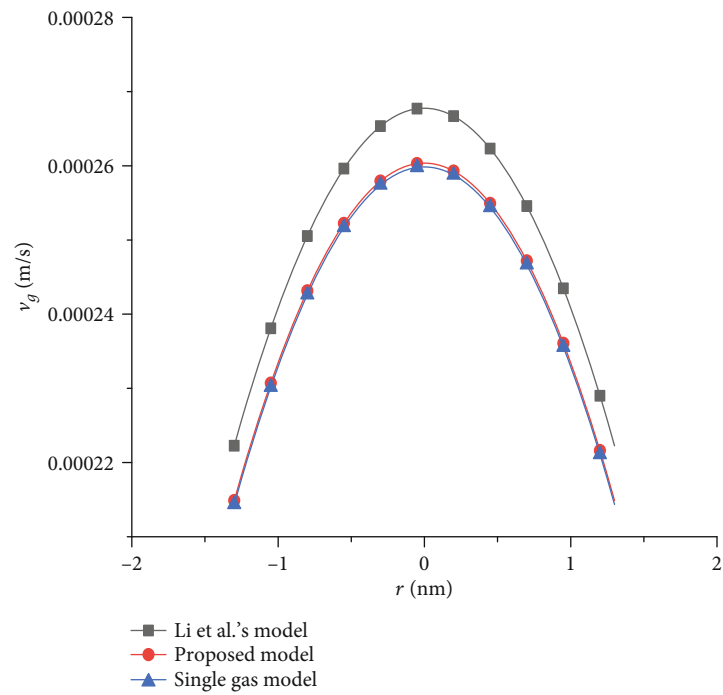
and the proposed model in this paper with the pore radius of 2 nm, 3 nm, and 5 nm, respectively. It shows that gas flow velocity of the single gas model is smaller than that of the proposed gas-water flow model.

We can see that when the pore radius increases, the difference of gas velocity profile between the proposed model and single gas flow becomes larger. When the pore radius is 2 nm, their gas velocity is approximately equal. For the smaller nanopores, although the water film thickness occupies a relatively large pore radius and enhances gas velocity at the interface of water film and gas, the miscible zone reduces the gas velocity, so that the combined effect is not obvious.

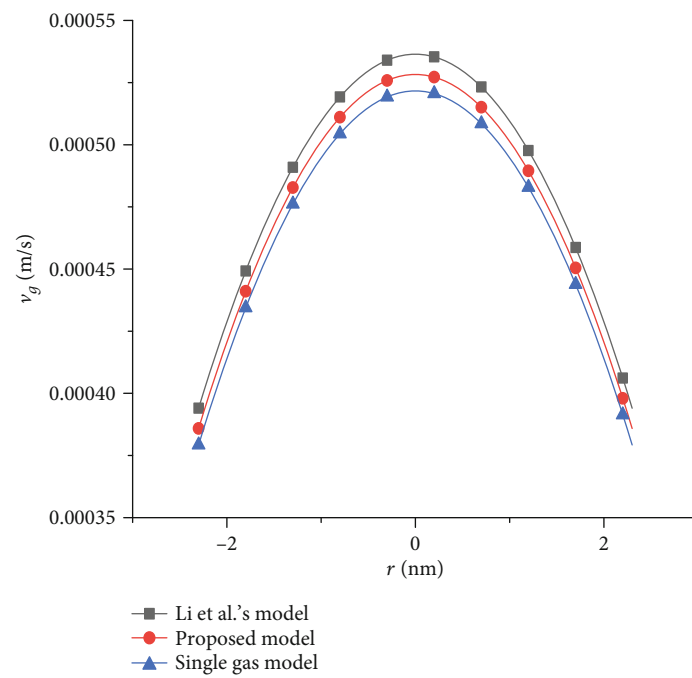
However, when the pore radius is 5 nm, the difference of gas velocity profile between the proposed model and single gas flow model becomes more obvious. According to Equation (1), we know that the value of the decreasing factor at the interface of water film and gas increases with the increase of the pore radius. The mobile water film increases the gas flow capacity bigger, which leads to larger gas velocity profile.

4.1.2. Gas Transport Capacity. In this paper, the ratio of K_{Ag} to K_{Ag_i} which is defined as the apparent permeability enhancement factor K_c , is used to evaluate the enhanced gas flow capacity by considering the miscible zone and high-viscosity flowing water film compared with the single gas model.

Figure 6(a) shows that the value of K_c is always larger than 1 and that K_c increases with the increase of the pressure,



(a)



(b)

FIGURE 5: Continued.

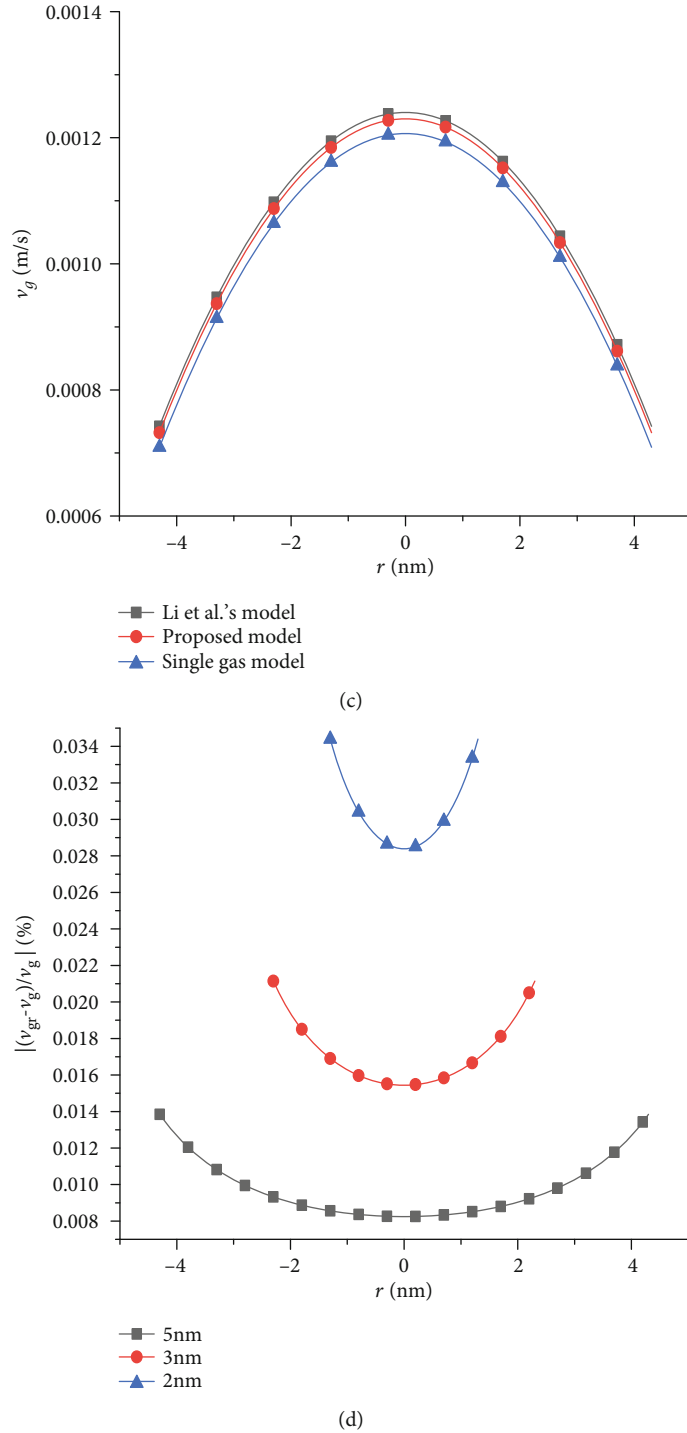


FIGURE 5: Comparison between the proposed model, single gas model, and Li et al.'s model [22] at different pore radii of 1 nm, 2 nm, and 4 nm. v_{gr} is the velocity in Li et al.'s paper. $P = 50$ MPa, $T = 350$ K, $\varnothing = 0.9$, $h_w = 0.7$ nm, $h_m = 0.3$ nm, $L = 7.23$ cm, $\theta = 30^\circ$ in all cases. (a) Gas velocity profile comparison at $r_0 = 2$ nm; (b) gas velocity profile comparison at $r_0 = 3$ nm; (c) gas velocity profile comparison at $r_0 = 5$ nm; (d) the relative differences between Li et al.'s model and the proposed model.

which means that the gas transport capacity is underestimated if the miscible zone and mobile water film are not considered.

Figure 6(b) shows that K_c is smaller for larger pore radius. When flowing water film and miscible zones are con-

sidered coherently, enhancement factor K_c is very small, for example, $K_c = 1.013$ for $r_0 = 50$ nm. The mobile water film leads to the increase of the apparent permeability enhancement factor. The miscible zone lowers the apparent permeability enhancement factor. The two factors are canceled

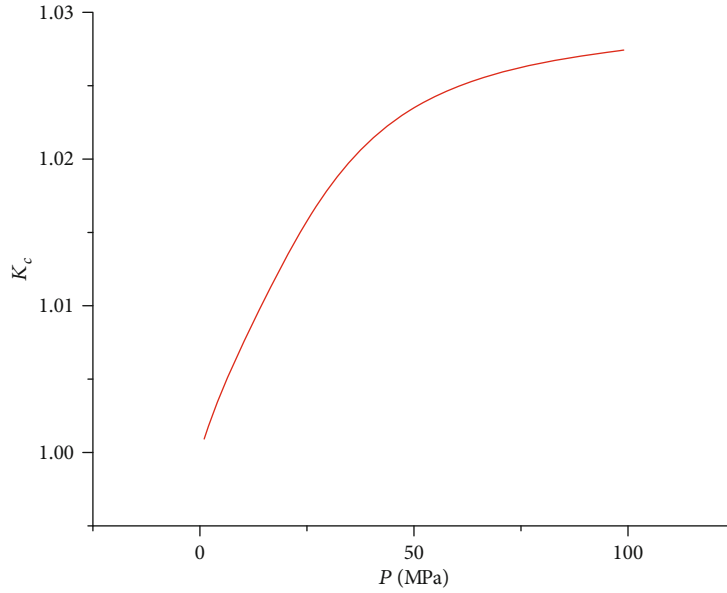
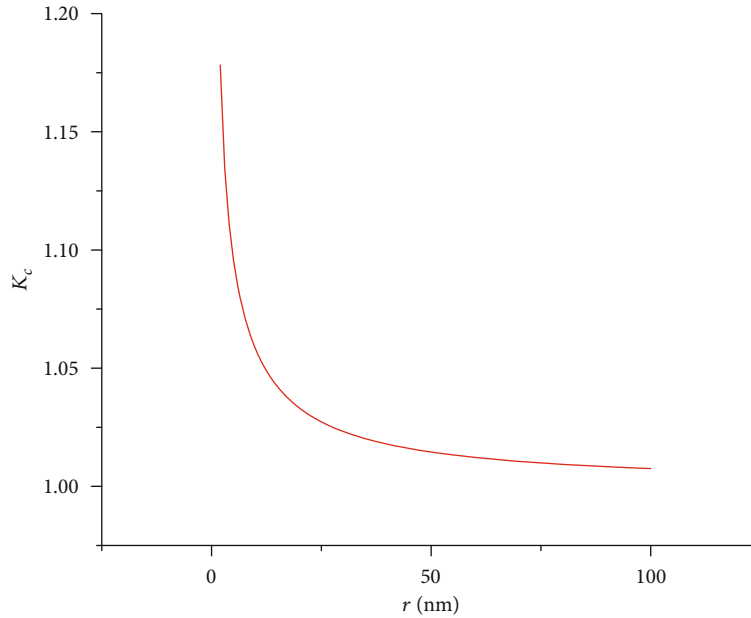
(a) Relationship between P and K_C (b) Relationship between r and K_C

FIGURE 6: Effect of the miscible zone and high-viscosity flowing water film on gas transport capacity. (a) $T = 300$ K, $h_w = 0.7$ nm, $h_m = 0.3$ nm, $\theta = 30^\circ$, $r_0 = 4$ nm; (b) $T = 300$ K, $h_w = 0.7$ nm, $h_m = 0.3$ nm, $p = 50$ MPa, $L = 7.23$ cm, $\theta = 30^\circ$.

out, which leads to a small apparent permeability enhancement factor in total.

4.2. Comparison between the Proposed Model and Li et al.'s Model. When the miscible zone is neglected, the flow model is described by Li et al.'s model [22].

4.2.1. Gas Velocity Profile. The miscible zone has effect on the gas velocity profile. Figures 5(a)–5(c) also give the gas flow velocity for Li et al.'s model and the proposed model under the pore radius of 2 nm, 3 nm, and 5 nm, respectively. It shows that gas flow velocity calculated by the proposed model is smaller than the gas flow velocity of Li et al.'s model

[22]. The reason is that the miscible zone lowers the gas velocity and thus lowers the apparent permeability enhancement factor.

We can see that when the pore radius increases, the difference of gas velocity profile between the proposed model and Li et al.'s model becomes smaller. This means that for the smaller nanopores, the miscible zone has larger effect on the gas velocity.

Figure 5(d) gives the relative differences of gas velocity between Li et al.'s model and the proposed model in this paper. It clearly shows that error would increase for the smaller nanopores when the miscible zone is neglected. At the centerline, the differences are 2.85%, 1.5%, and 0.82%

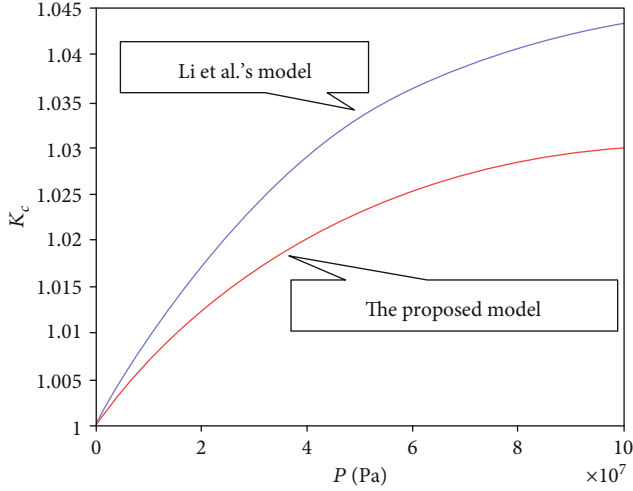


FIGURE 7: Comparison of gas apparent permeability enhancement factor K_C with Li et al.'s model [22]. $T = 300\text{ K}$, $h_w = 0.7\text{ nm}$, $h_m = 0.3\text{ nm}$, $r_0 = 5\text{ nm}$, $L = 0.0723\text{ m}$, $\theta = 30^\circ$.

for the pore radius of 2 nm, 3 nm, and 5 nm, respectively. The results also show that Li et al.'s model overestimates the gas velocity.

4.2.2. Apparent Permeability Enhancement Factor. In order to exhibit the effect of the miscible zone on permeability correction under the mobile water film, Figure 7 gives the comparison of the flow enhancement factor between with and without consideration of the miscible zone. When the miscible zone is neglected, the gas velocity will be larger at the interface of mobile water film and gas. This leads to a larger flow enhancement factor as shown in Figure 7.

4.2.3. Gas Flow Comparison. In order to exhibit the effect of the miscible zone on the gas flow rate under the flowing water film, Figure 8 gives the comparison of the gas flow rate between the proposed model and Li et al.'s model. It shows that the gas flow rate Q_g calculated by the proposed model is less than that of Li et al.'s model. The gas flow rate of Li et al.'s model is 5% higher than that of the model in this paper. This again shows that the miscible zone reduces the flow ability.

4.2.4. Gas Velocity Profile. In order to exhibit the effect of the miscible zone on gas velocity profile under the flowing water film, Figure 5 gives the water velocity profile comparison between with and without consideration of the miscible zone. The gas velocity at the center line is the highest, and the overall gas velocity is parabolic. The gas velocity profile comparison in Figure 5 shows that gas velocity is smaller when the miscible zone is considered. The reason is that when the miscible zone is considered, the water velocity profile near the boundary increases first and then decreases (Figure 1(b)) and is like a parabola. According to boundary conditions in Equation (13), the gas velocity at the boundary will be smaller compared with the velocity of that not considering the miscible zone, which will lead to a smaller gas velocity profile.

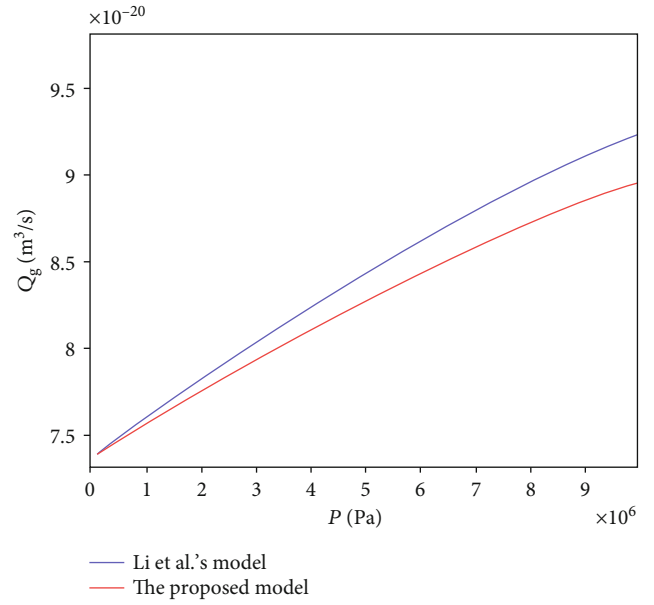


FIGURE 8: Comparison of gas flow rate Q_g with Li et al.'s model [22]. $T = 300\text{ K}$, $h_w = 0.7\text{ nm}$, $h_m = 0.3\text{ nm}$, $r_0 = 5\text{ nm}$, $L = 0.0723\text{ m}$, $\theta = 30^\circ$.

4.2.5. Water Flow Rate. In order to exhibit the effect of the miscible zone on the water flow rate under the flowing water film, Figure 9 gives the gas velocity comparison between with and without consideration of the miscible zone. As shown in Figure 9, the water flow rate in the proposed model is smaller than that in Li et al.'s paper, but all of them increase with the increase of pressure. In this paper, we use the proposed model to describe the velocity distribution of water film, which is different from Li et al.'s model. Due to the existence of the miscible zone, there is an obvious downward trend around the gas-water interface instead of a monotonic rise. Therefore, the average velocity of water film in this paper is less than the average velocity of water film not considering the miscible zone in Li et al.'s paper. This indicates that the water flow rate of the proposed model is smaller than that of Li et al.'s model. This means that the water flowback ratio is smaller due to the existence of the miscible zone.

4.3. Comparison among Proposed Model

4.3.1. Single Gas Flow Model and Li et al.'s Model. Figures 4(a)–4(c) give the gas flow velocity for the single gas flow, Li et al.'s model, and the proposed model in this paper with the pore radius of 2 nm, 3 nm, and 5 nm, respectively. It shows that gas flow velocity of the single gas model is smallest caused by neglecting the water film flow and that gas flow velocity of Li et al.'s model is largest caused by neglecting the miscible zone. The gas flow velocity considering the miscible zone is between the two.

As to the water flow rate, the water flow calculated by Li et al.'s model is largest. The water flow calculated by the single-phase gas model is zero due to the neglect of the flow of water film. The water flow rate calculated by the proposed model is between them.

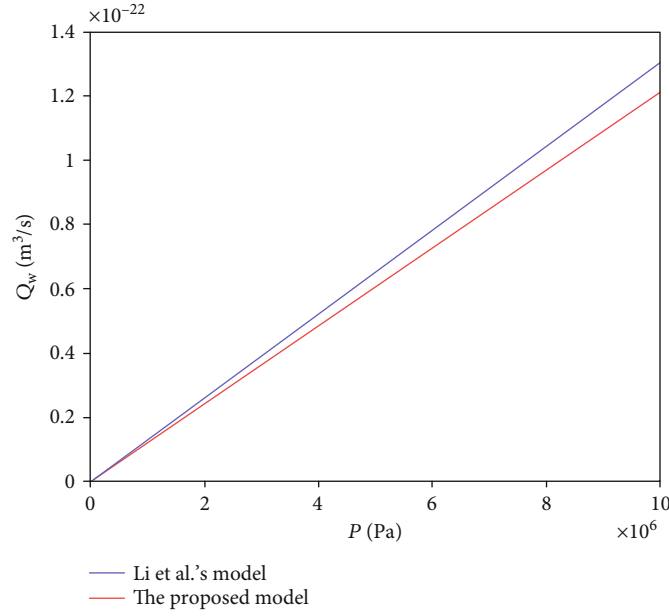


FIGURE 9: Comparison of water flow rate Q_w with Li et al.'s model [22]. $T = 300$ K, $h_w = 0.7$ nm, $h_m = 0.3$ nm, $r_0 = 5$ nm, $L = 0.0723$ m, $\theta = 30^\circ$.

5. Conclusions

In shale nanopores, the miscible zone and mobile high-viscosity water film are potential influencing factors for gas transport. Inspired by the results of molecular dynamics simulation, the miscible zone is considered into the gas flow model in this paper. The calculation results of Li et al.'s model are compared to verify that the model in this paper is more comprehensive. According to the results of the study and discussion, the following conclusions are drawn:

- (1) Simulating the gas flow pattern in actual shale formations, miscible zones should be taken into account. Ignoring the influence of miscible regions leads to an overestimation of the velocity of the gas in the pores. If the flow of water film and miscible zone are ignored, the velocity of gas in pores will be underestimated
- (2) The flow enhancement factor reflects the transport capacity of shale gas under different conditions, which can be concluded as follows: in the case of larger pressure and smaller pores, the enhancement factor is larger and the flow enhancement is more significant
- (3) By comparing with Li et al.'s paper and single gas model in the aspects of velocity, gas flow rate, water flow rate, and enhancement factor, it is verified that ignoring the miscible zone and only considering the mobile high-viscosity water film will overestimate the flow rate of water and gas and the flow capacity of gas will also be overestimated in the calculation process

The above results show that proposing the miscible zone has a significance in modifying the gas flow model. In the

study of the miscible zone, the paper only discusses the indirect influence on gas velocity through the influence on water film velocity and the value of the thickness cannot be used to every situation. Therefore, the specific mechanism of action of the miscible zone needs to be explained, and the calculation of the thickness of the miscible zone needs to be more accurate which will be the focus of the next work.

Nomenclature

b :	Slip coefficient, dimensionless
C :	Constant, dimensionless
h_m :	Thickness of the miscible zone (m)
h_w :	Thickness of the water film zone (m)
K_{Ag} :	Gas apparent permeability with the miscible zone and mobile high-viscosity water film (m^2)
K_{Agi} :	Gas apparent permeability with the static high-viscosity water film (m^2)
K_c :	Enhancement factor, dimensionless
L :	Length of the pore model (m)
l_s :	True slip length (m)
M :	Molecular weight (kg/mol)
P_c :	Critical pressure (Pa)
ΔP :	Pressure difference between the entrance and exit (Pa)
Q_d :	Darcy rate of gas flow (m^3/s)
Q_g :	Flow rate of gas (m^3/s)
r_0 :	Pore radius (m)
R :	Gas constant (8.314 J/(K · mol))
T :	Temperature (K)
T_c :	Critical temperature (K)
V_{Agi} :	Gas velocity with the static high-viscosity water film (m/s)
v_s :	Gas slip velocity (m/s)
Z :	Gas compressibility factor, dimensionless
λ :	Mean free path (m)

μ_g :	Viscosity of gas
μ_w :	Viscosity of water
τ :	Pore tortuosity, dimensionless
ϕ_g :	Porosity occupied by gas, dimensionless
β :	Decreasing factor, dimensionless
θ :	Contact angle ($^\circ$)
σ_v :	Tangential momentum accommodation coefficient, dimensionless.

Data Availability

The data used to support the findings of this study are available from the corresponding author upon request.

Conflicts of Interest

The authors declare that there is no conflict of interest regarding the publication of this paper.

Acknowledgments

This work is supported by the National Science and Technology Major Project of China (Grant No. 2017ZX05009005-002) and the Fundamental Research Funds for the Central Universities (China University of Geosciences, Wuhan) (Grant No. CUGGC04).

References

- [1] H. L. Li, "Development state and countermeasure research on China shale gas industry and technology equipment," *Unconventional Oil and Gas*, vol. 1, no. 2, pp. 78–82, 2014.
- [2] W. Shen, X. Li, A. Cihan, X. Lu, and X. Liu, "Experimental and numerical simulation of water adsorption and diffusion in shale gas reservoir rocks," *Advances in Geo-Energy Research*, vol. 3, no. 2, pp. 165–174, 2019.
- [3] X. Tang, N. Ripepi, K. Luxbacher, and E. Pitcher, "Adsorption models for methane in shales: review, comparison and application," *Energy & Fuels*, vol. 31, no. 10, pp. 10787–10801, 2017.
- [4] H. Yu, Y. B. Zhu, X. Jin, H. Liu, and H. A. Wu, "Multiscale simulations of shale gas transport in micro/nano-porous shale matrix considering pore structure influence," *Journal of Natural Gas Science and Engineering*, vol. 64, pp. 28–40, 2019.
- [5] J. M. Carey, *Surprise side effect of shale gas boom: a plunge in US greenhouse gas emissions*, Forbes Magazine, 2012.
- [6] L. Zhang, B. Shan, Y. Zhao, and Z. Guo, "Review of micro seepage mechanisms in shale gas reservoirs," *International Journal of Heat and Mass Transfer*, vol. 139, pp. 144–179, 2019.
- [7] R. G. Loucks, R. M. Reed, S. C. Ruppel, and D. M. Jarvie, "Morphology, genesis, and distribution of nanometer-scale pores in siliceous mudstones of the Mississippian Barnett shale," *Journal of sedimentary research*, vol. 79, no. 12, pp. 848–861, 2009.
- [8] H. Singh and J. Cai, "A feature-based stochastic permeability of shale: part 1—validation and two-phase permeability in a Utica shale sample," *Transport in Porous Media*, vol. 126, no. 3, pp. 527–560, 2019.
- [9] Z. X. Xu, S. B. Guo, H. Qiao, and H. M. Li, "Research on fractal characteristics of micro pore structure for shale gas," *Unconventional Oil and Gas*, vol. 1, no. 2, pp. 20–25, 2014.
- [10] R. A. Millikan, "Coefficients of slip in gases and the law of reflection of molecules from the surfaces of solids and liquids," *Physical Review*, vol. 21, no. 3, pp. 217–238, 1923.
- [11] J. Cai, D. Lin, H. Singh, W. Wei, and S. Zhou, "Shale gas transport model in 3D fractal porous media with variable pore sizes," *Marine and Petroleum Geology*, vol. 98, pp. 437–447, 2018.
- [12] M. T. Cantisano, D. P. Restrepo, S. Cespedes et al., "Relative permeability in a shale formation in Colombia using digital rock physics," *Unconventional Resources Technology Conference*, 2013, pp. 909–915, August 2013.
- [13] A. Salama, M. F. E. Amin, K. Kumar, and S. Sun, "Flow and transport in tight and shale formations: a review," *Geofluids*, vol. 2017, Article ID 4251209, 21 pages, 2017.
- [14] Y. Yuan, W. Yan, F. Chen, J. Li, Q. Xiao, and X. Huang, "Numerical simulation for shale gas flow in complex fracture system of fractured horizontal well," *International Journal of Nonlinear Sciences and Numerical Simulation*, vol. 19, no. 3-4, pp. 367–377, 2018.
- [15] D. Li, L. Zhang, J. Y. Wang, and D. Lu, "Composition-transient analysis in shale-gas reservoirs with consideration of multi-component adsorption," *SPE Journal*, vol. 21, no. 2, pp. 648–664, 2016.
- [16] F. Javadpour, D. Fisher, and M. Unsworth, "Nanoscale gas flow in shale gas sediments," *Journal of Canadian Petroleum Technology*, vol. 46, no. 10, 2007.
- [17] G. P. Brown, A. Dinardo, G. K. Cheng, and T. K. Sherwood, "The flow of gases in pipes at low pressures," *Journal of Applied Physics*, vol. 17, no. 10, pp. 802–813, 1946.
- [18] D. S. Scott and F. A. L. Dullien, "Diffusion of ideal gases in capillaries and porous solids," *AIChE Journal*, vol. 8, no. 1, pp. 113–117, 1962.
- [19] J. Cai, D. Lin, H. Singh, S. Zhou, Q. Meng, and Q. Zhang, "A simple permeability model for shale gas and key insights on relative importance of various transport mechanisms," *Fuel*, vol. 252, pp. 210–219, 2019.
- [20] Y. Hao, X. Jia, Z. Lu, D. Lu, and P. Li, "Water film or water bridge? Influence of self-generated electric field on coexisting patterns of water and methane in clay nanopores," *The Journal of Physical Chemistry C*, vol. 123, no. 36, pp. 22656–22664, 2019.
- [21] T. Li, H. Song, J. Wang, Y. Wang, and J. Killough, "An analytical method for modeling and analysis gas-water relative permeability in nanoscale pores with interfacial effects," *International Journal of Coal Geology*, vol. 159, pp. 71–81, 2016.
- [22] R. Li, K. Wu, J. Li, J. Xu, and Z. Chen, "Gas transport in shale nanopores with mobile high-viscosity water film," *Industrial & Engineering Chemistry Research*, vol. 57, no. 32, pp. 11219–11228, 2018.
- [23] Y. H. Xu, H. Yu, J. C. Fan, Y. B. Zhu, F. C. Wang, and H. A. Wu, "Two-phase transport characteristic of shale gas and water through hydrophilic and hydrophobic nanopores," *Energy & Fuels*, vol. 34, no. 4, pp. 4407–4420, 2020.
- [24] Y. Z. Hao, D. T. Lu, X. T. Jia, and P. C. Li, "Mixture flow of water and methane through shale nanopore by molecular dynamics simulation," *Scientia Sinica Physica, Mechanica & Astronomica*, vol. 48, no. 9, article 094707, 2018.
- [25] D. Mattia and F. Calabrò, "Explaining high flow rate of water in carbon nanotubes via solid-liquid molecular interactions,"

- Microfluidics and Nanofluidics*, vol. 13, no. 1, pp. 125–130, 2012.
- [26] G. Galliero, “Lennard-Jones fluid-fluid interfaces under shear,” *Physical Review E*, vol. 81, no. 5, article 056306, 2010.
- [27] C. Neto, D. R. Evans, E. Bonaccorso, H.-J. Butt, and V. S. J. Craig, “Boundary slip in Newtonian liquids: a review of experimental studies,” *Reports on Progress in Physics*, vol. 68, no. 12, pp. 2859–2897, 2005.
- [28] K. Liu and M. Ostadhassan, “The impact of pore size distribution data presentation format on pore structure interpretation of shales,” *Advances in Geo-Energy Research*, vol. 3, no. 2, pp. 187–197, 2019.
- [29] R. J. Mashl, S. Joseph, N. R. Aluru, and E. Jakobsson, “Anomalous immobilized water: a new water phase induced by confinement in nanotubes,” *Nano Letters*, vol. 3, no. 5, pp. 589–592, 2003.
- [30] M. Neek-Amal, F. M. Peeters, I. V. Grigorieva, and A. K. Geim, “Commensurability effects in viscosity of nanoconfined water,” *ACS Nano*, vol. 10, no. 3, pp. 3685–3692, 2016.
- [31] Z. Qin and M. J. Buehler, “Nonlinear viscous water at nanoporous two-dimensional interfaces resists high-speed flow through cooperativity,” *Nano Letters*, vol. 15, no. 6, pp. 3939–3944, 2015.
- [32] G. E. M. Karniadakis, A. Beskok, and M. Gad-el-Hak, “Micro flows: fundamentals and simulation,” *Applied Mechanics Reviews*, vol. 55, no. 4, pp. B76–B76, 2002.

Research Article

Verification of Fracture Reorientation and Analysis of Influence Factors in Multiple Fracturing Treatment

Mingjing Lu ^{1,2,3,4}, Yuliang Su,¹ Marte Gutierrez,⁴ Yaohua Zhan,⁵ Kai Chen,² and Bintao Zheng²

¹China University of Petroleum (East China), China

²Petroleum Engineering Technology Research Institute of Shengli Oilfield, SINOPEC, China

³Postdoctoral Scientific Research Working Station of Shengli Oilfield, SINOPEC, China

⁴Colorado School of Mines, USA

⁵CNOOC, Shenzhen, China

Correspondence should be addressed to Mingjing Lu; lumingjing001@126.com

Received 11 February 2020; Revised 9 September 2020; Accepted 15 September 2020; Published 25 September 2020

Academic Editor: Jianchao Cai

Copyright © 2020 Mingjing Lu et al. This is an open access article distributed under the Creative Commons Attribution License, which permits unrestricted use, distribution, and reproduction in any medium, provided the original work is properly cited.

A fracture will be initiated and propagated along the direction of maximum horizontal stress in fracturing treatment; however, in refracturing stimulation, the new fracture may be initiated and propagated along a different direction from the initial one. This is defined as a fracture reorientation. It is difficult to predict fracture reorientation due to the variation of formation properties after long-term production. To verify the existence of fracture reorientation and analyze its influencing factors in multiple fracturing treatment, experimental and numerical simulations are presented in this paper. Firstly, multiple fracturing stimulation is carried out with a self-assembled large true triaxial apparatus, and the fracture reorientation is successfully induced by changing the injection pressure and initial stresses in multiple fracturing processes. Then, numerical coupled hydromechanical modeling of the actual field production and injection well pattern is performed. In particular, the stress reversal region, which indicates the distance of fracture reorientation, and the factors that influence the reorientation are analyzed. The laboratory experiment and numerical simulation results show that the fracture reoriented angle obtained can be perpendicular to the initial fracture. Stress field and formation pressure are the two main factors that influence the fracture reorientation. With higher pressure differences and lower initial horizontal stress differences, the area in which it is possible to initiate reoriented fracture will be larger. The fractures of wells in the early production stage are hard to reorient due to the high formation and borehole pressure difference, and the fracture reorientation area will be expanded until the pressure difference is low to a certain value. This research result can guide oilfield stimulation treatments.

1. Introduction

Unconventional reservoir formations are considered to be with low permeability and porosity, and underground liquid seepage is hard to achieve during the producing process. Profitable productivity can be obtained only by implementing stimulation treatment [1, 2]. However, after long-term production, the productivity of wells with initial fracturing treatment will decrease due to improper or small-scale fracturing treatment, closure of initial fracture, fines plugging, deformation and cracking of proppants, and borehole contamination

[3, 4]. In this situation, refracturing treatment is an effective stimulation method for wells to regain productivity. Initial fractures will be reopened, surface flushed, or proppant refilled in multiple fracturing treatment, and flow capacity will then be restored or even enhanced by extending the geometry of initial fractures. Additionally, by applying proper fracturing materials and large-scale fracturing treatment, fracture reorientation will be induced and new fractures will be initiated and extended to the direction different from the former one. This is the best scenario in field treatment because the fractures will penetrate regions with more residual oil and higher pressure.

Fracture reorientation is monitored in multiple fracturing stimulation in field treatments. Many researchers have studied the influencing factors that lead to fracture reorientation. Stress field changes are considered to be the leading factor of fracture reorientation in refracturing treatment [5]. By analyzing pressure data of refracturing field cases, it was shown that stress field changes due to propped initial fractures and depleted porous pressure is the main reason for fracture reorientation [6, 7]. With theoretical analysis, it is concluded that the in-situ stress field would be altered in the production process from an existing initial fracture, resulting in new fractures that would be initiated and propagated to the direction perpendicular to the former one [8]. The initial reservoir stress field is steady before development; however, this status will be changed after well drilling, fracturing, liquid injection, and withdrawal. Regions of stress reversals caused by stress field alternation were observed in both vertical wells and horizontal wells [9, 10]. For complicated well patterns, well injection and production make the stress field alternation difficult to predict. It was pointed out that fracture reorientation was always common in water flooding reservoirs due to the change of formation pressure after water injection [11]. It is difficult to evaluate stress field changes for those wells with complicated interference due to dynamic pore pressure change in the production and injection processes. With the development of fracturing technology, results of field and laboratory cases indicate that fracture reorientation can be induced by proper fracturing techniques and methods [12]. It has been verified that fracture reorientation can be easily induced by setting the direction of the perforation and controlling the horizontal stress difference in well completion and stimulation process. This can be done while the fracture initiation and propagation can be artificially guided to certain directions [13].

Mechanisms of fracture reorientation are identified and classified since it has become a research priority in restimulation treatments. For a fractured well, liquid production and injection will cause formation pressure change, and then, the stress field will be altered due to the increase or decrease of porous pressure. Meanwhile, it has been shown by numerical models that the stress field is an important factor that influences pressure and production performance [14]. Both the initial minimum and maximum horizontal stresses will be changed to some extent that the minimum can exceed the maximum one. The induced stress change will finally form an area where the directions of the initial stresses are totally reversed. This area is defined as the stress reversal region where fracture reorientation will exist. New fractures will be initiated at the direction perpendicular to the initial fractures in a reversal region [15]. Basic theories and models are applied to determine the mechanisms and influencing factors of fracture reorientation in multiple fracturing treatments.

In 1995, fracture reorientation caused by stress field change induced by production was first presented and explained based on the poroelasticity theory [16]. Since then, many models have been presented to deeply study the mechanisms and influence factors of fracture reorientation. Analytical and numerical models were built to calculate the

stress changes from wells after fracturing treatment, and then, the influencing factors of the fracture length were discussed in refracturing treatment [17]. It was verified that there existed a stress reversal region around infilled wells after researching the stress changes induced by water flooding wells [18]. Coupled models were built and in situ stress changes due to well production were investigated, and models were applied to determine the right time for refracturing treatment. Meanwhile, factors that influence the existence of fracture reorientation were analyzed [19]. A heterogeneous, two-dimensional coupled model was presented to study the stress field changes due to production, and geological parameters that influence stress reversal were discussed [20]. Numerical models were presented to verify the possibility of fracture reorientation, and the relationship between enhanced oil recovery and fracture reorientation region was also discussed by Benedict and Wegner [21].

Based on a literature review, many theoretical studies and field tests have been done to study the mechanism of fracture reorientation in refracturing treatment. However, due to the difficulty of restoring reservoir conditions and simulating the complicated processes of multiple fracturing treatment, there are fewer researches on physical simulation in the laboratory to achieve fracture propagation. Therefore, fracture propagation in refracturing treatment can only be monitored by indirect ways in field tests, which are difficult to visually observe.

In this paper, the whole process of multiple fracturing treatment is completed on a self-assembled true triaxial apparatus that can apply three independent confining stresses, and fractured samples are sliced to directly observe the complicated fracture propagation. Then, numerical hydraulic-mechanic coupled modeling for a production and injection well pattern is simulated based on the poroelasticity and porous media fluid theories. The main factors that impact fracture reorientation are further studied based on numerical models. Research results may guide field engineers in predicting the possibility of fracture reorientation before operating field treatment.

2. Fracture Reorientation in Laboratory Tests

Experiments were performed in the laboratory using a true triaxial apparatus, and multiple fracturing treatment was completed under three independent confining stresses applied to simulate realistic underground conditions. By applying various confining stresses and injecting fracturing liquids at different pressures, fracture reorientation is successfully induced and can be directly observed by slicing the test samples after finishing the experiments.

2.1. Test Samples and Equipment

2.1.1. Test Sample. The $30 \times 30 \times 30 \text{ cm}^3$ cubic samples were an artificial sandstone made from nonshrink grout/cement and sand that passes the # 40 or 0.42 mm opening mesh. The cement and sand were mixed with water in a concrete mixer and placed in a cubic mold to cure and dry. Two cubical samples were prepared and hydraulically fractured under

different stages. The properties of the artificial sandstone are shown in Table 1, where ρ is sample density, ϕ is the porosity, k is the permeability, UCS is the unconfined compressive strength, BTS is the Brazilian Tensile Strength, and E is the Young's modulus. Tap water and hydrate pump oil were used as fracturing fluids.

2.1.2. Test Equipment. The true triaxial apparatus used in the laboratory simulation of fracture reorientation in cubical samples was designed and fabricated at Colorado School of Mines specifically for fracturing simulation studies. The apparatus is composed of five parts, namely, the true triaxial cell, hydraulic pumps to apply the three principal confining stresses, a digital data acquisition system, an acoustic emission monitoring system, and a miniature drilling rig. The main part is the true triaxial cell which consists of a rigid cylindrical frame with rigid plate lids on top and bottom. The confining pressure is applied via three dog-bone flat jacks hydraulically pressurized by manual pumps and are resisted by three rigid plates at the opposing sides of the flat jacks. Fracturing is induced through a miniaturized casing to a bottom-hole well that is partly uncompleted. Fracturing pressure is applied by two Isco micropumps working in tandem. Figure 1 shows a schematic diagram of the assembled true triaxial fracturing system with multiple well locations. Detailed information on the design and operation of the true triaxial system can be found in Lu et al. [22] and Frash et al. [23].

2.2. Experimental Procedures. The experimental procedures to simulate fracture reorientation in rocks include four main steps for one simulation stage: (1) sample preparation and equipment assembly, (2) simulation of reservoir conditions by applying confining pressures to the three sample faces, (3) simulation of the fracturing treatment by increasing pressure in the injection well using the Isco pumps, and (4) post-test analysis by slicing the samples into thin cuts and imaging the induced fracture(s). The fracture initiation and propagation processes are monitored in real-time from the injection pump pressure and by acoustic emission sensors. Initial stresses applied to the samples and locations of the acoustic sensors are shown in Figure 2. S_1 – S_6 are the six AE sensors; σ_h , σ_H , and σ_v are the minimum horizontal stress, maximum horizontal stress, and vertical stress, respectively.

Five boreholes were drilled in sample 1 under the following test procedures: (1) the vertical, maximum horizontal, and minimum horizontal stresses were set to 16, 12, and 8 MPa, respectively. Then, the middle well was fractured with water at a flow rate of 0.5 mL/min. The injection pump is stopped when a pressure drop was observed, which indicated that fracture has been initiated, or when the acoustic emissions indicated fracture initiation. (2) The flow rate was increased to 30 mL/min to refracture the sample. (3) The fracturing fluid is injected into the four edge wells with a constant bottom-hole pressure to prevent the fracture from extending to the corner wells. A high-viscosity oil is then injected into the middle well, and the pump was kept running until the fracture propagated close to the edge of the sample. (4) The major and minor horizontal stresses were rotated 90°,

TABLE 1: Material properties of the test samples.

Samples	ρ kg/m ³	ϕ %	K 10 ⁻³ μm^2	UCS MPa	BTS MPa	E GPa
1	1950	25.8	0.15	59.7	2.4	10.4
2	1980	25.2	0.13	58.9	2.4	10.8

and the middle well injection flow rate was increased to 20 mL/min. Figure 3 shows the pressure change with time during the three-stage fracturing process.

Three boreholes were drilled in sample 2 using the following procedures: (1) the three principal stresses were set to the same magnitudes as in sample 1. Then, the corner wells were pressurized at a constant flow rate of 0.5 mL/min. The pump was kept running until fractures were fully propagated. (2) The injection fluid was changed to a high viscosity fluid. The middle well was fractured with a high constant flow rate of 30 mL/min, and the pump was stopped as soon as fracture initiation occurred based on a well pressure drop or acoustic emissions; then, the well pressure was released. (3) The fracturing fluid was injected into the middle well at constant pressure to maintain a constant bottom-hole pressure, and then, another corner well is fractured. Figure 4 shows the pressure change with time during the multiple fracturing process.

2.3. Experimental Results and Analysis. After the fracturing tests, the samples were sliced into thin horizontal sections about 2.75 cm in thickness to observe the induced fractures directly. The sliced sections showed direct evidences of fracture reorientation induced by changing the initial stress field and the injection pressure. For sample 1, the fracture initiated in the first fracturing treatment and then propagated in the secondary fracturing treatment. By rotating the orientations of the initial horizontal stresses, a second fracture initiated at the direction perpendicular to the initial fracture and then propagated as shown in Figure 5. Fracture propagation was also located by acoustic emission as shown in the 3D scatter diagram, which shows a high correspondence of the AE signals with the orthogonal-induced fractures. Spots of different colors show the fracture location of every fracturing treatment. Backpressure applied to the corner wells showed that the fracture intersected the corner wells.

The acoustic emission events for fracture location in the sample during multiple fracturing indicate fracture initiation and propagation of every fracturing treatment, which agrees with the observations from the sliced samples.

As shown in Figure 6, multiple tiny fractures are initiated around the middle well, and the initiated directions of these fractures are complicated by fracturing at a high flow rate. To observe the fractures, pressure is released as soon as possible after fracture initiation to avoid the main fracture intersecting with the tiny fractures. Fracture propagation located by acoustic emission is shown by the 3D scatter diagram. With the same stress field, well 2 was fractured before well 1, and the fracture propagates along the initial maximum horizontal stress. However, the fracture propagation of well 1 is different with that of well 2 because of the applied

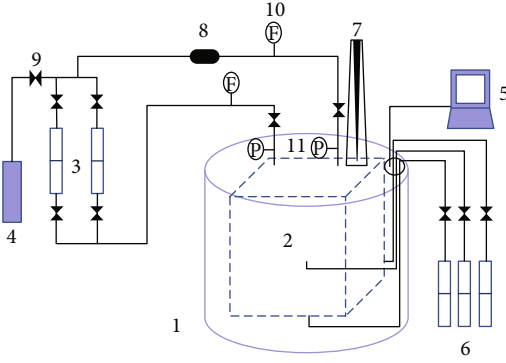


FIGURE 1: Diagram of the assembled true triaxial fracturing system. 1. Hardened steel cell. 2. Block sample. 3. Syringe pumps. 4. Pump liquid reservoir. 5. Acoustic emission receiver. 6. Hydraulic pump for stresses. 7. Drilling system. 8. Filter. 9. Isolated valves. 10. Flow transducer. 11. Pressure transducer.

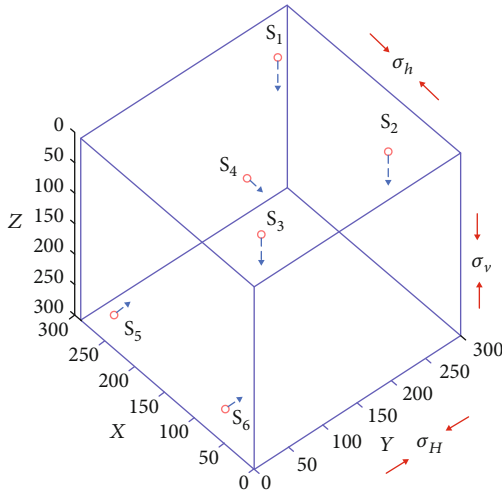


FIGURE 2: Independent confining stresses applied and locations of sensors on the sample.

backpressure of well 1 and altered stress field. It is a complicated process because the fracture initiated and the propagated direction can be impacted by so many factors.

2.4. Fracture Reorientation Mechanism Analysis. It can be verified from the experiments that fracture reorientation occurred in the process of refracturing operation, and new fractures could initiate at angles different from that of the initial one. In refracturing treatment, injected pressure, bottom-hole stress distribution, and well interference are all important factors that determine the initiated direction of new fractures. In the refracturing process, the pore pressure around the bottom well will be increased sharply with high-pressure liquid injected. However, due to the existence of an initial fracture, the pore pressure at the parallel direction with the initial fracture is increased more than that at perpendicular direction, which leads to an unbalanced increase of the minimum and maximum horizontal stresses. As shown in Figure 7, the inner stress reversal region is formed which determines the initiation direction of fracture reorientation.

However, it is not enough for field applications only to have new fractures initiated and reoriented. It is important that fractures must propagate and extend to the far field away from the well bottom. The propagation distance of fracture reorientation is determined by the stress fields around and far away from the well bottom. This stress reversal region is determined by the stress field far away from the well bottom-hole which is induced by liquid production and injection, and the outer elliptical stress reversal region determines the extended distance of fracture reorientation as shown in Figure 7.

Based on the above interpretation of the experimental results and the fracture reorientation mechanism, it can be shown that new fractures will be initiated around the well bottom-hole during the process of refracturing treatment. By applying a high flow rate of injected liquid and changing the in situ stress field in a small-scale sample in laboratory tests, it is easier to create new reoriented fractures. Oriented perforation is one common technique in field treatment, but it is difficult to simulate in small-scale cubic samples in the laboratory, especially in refracturing treatment. However, it can be inferred that with oriented perforating technology in field treatment, fractures will be easily reoriented in the initiation period. As analyzed above, if the outer stress reversal region is small or even nonexistent, new fractures will propagate along the original direction. In order to identify the distance of the reoriented fractures, it is necessary to study the far stress field distribution which will be varied due to long-term production and injection, which is known as stress variation induced by a poroelastic effect. Since it is impossible to simulate samples that are large enough for poroelastic effect research, numerical simulation is used in the following to extend the experimental results.

3. Coupled Hydromechanical Modeling

As mentioned above, the formation of liquid withdrawal and injection will lead to pressure change and will cause variation of the stress field; the formation stress field determines the direction of fracture initiation and propagation in refracturing treatment. Meanwhile, the area of the reversal stress region determines the distance of fracture propagation. Therefore, research on the stress field induced by pore pressure is an important task before multiple fracturing treatments. To further study the induced stress distribution after initial fracturing treatment, numerical coupled hydro-mechanical models of production and injection well patterns are simulated to study the factors that influence the stress reversal region.

3.1. Poroelastic Model. The deformation of porous media saturated with liquid is controlled by the applied effective stresses. The relationship between the strain tensor and the volumetric strain for porous media can be expressed as:

$$\varepsilon = \frac{1}{2} [\nabla u + [\nabla u]^T], \quad (1)$$

$$\varepsilon_v = \text{tr}(\varepsilon) = \nabla \cdot u, \quad (2)$$

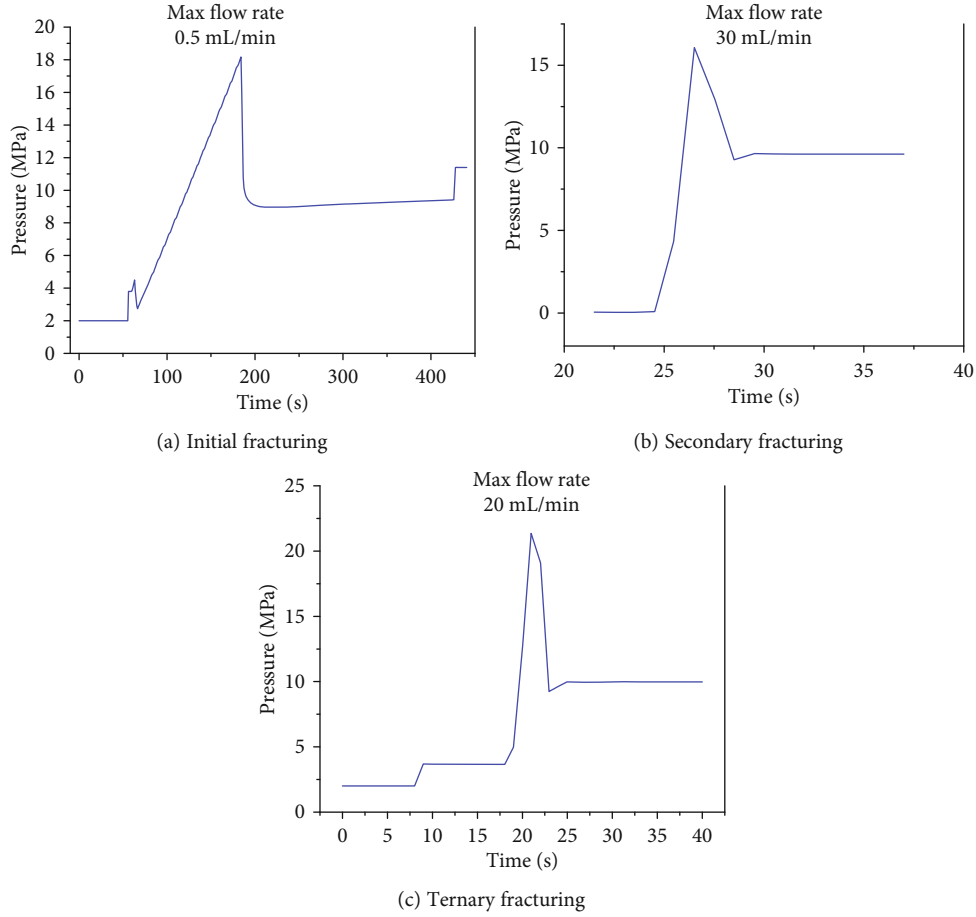


FIGURE 3: Pressure versus time from multiple-stage fracturing of sample 1.

where ε is strain tensor of porous media, u is the displacement of porous media, ε_v is the volumetric strain for porous media, and $\text{tr}(\varepsilon)$ is the trace of the strain tensor ε .

For linear poroelastic media, based on the effective stress principle, the relationship of the effective strain, the overall stress, and the pore pressure can be expressed as:

$$\sigma' = \sigma - a(pI), \quad (3)$$

where σ' is the effective stress tensor (in MPa), σ is total stress tensor (in MPa), p is the pore pressure of the porous media (in MPa), a is Biot's poroelastic constant, and I is second-order identity matrix.

The momentum equation for the motion of elastic porous media can be obtained from equilibrium:

$$\frac{\partial^2(\rho u)}{\partial t^2} - \nabla \cdot \sigma' = 0. \quad (4)$$

When the rock reaches the state of mechanical equilibrium, the velocity of the point of mass is zero, so the first expression of the equation is zero. By combining Eq. (3), the above equation can be expressed as:

$$-\nabla \sigma' = a(\nabla p) - \nabla \sigma = 0. \quad (5)$$

Then, associating Eq. (1) and Eq. (2) with the above equation yields:

$$\nabla \left[G \nabla u + G(\nabla u)^T + \lambda \text{tr}(\nabla u)I \right] - a \nabla p = 0 \quad (6)$$

where G is the shear modulus of porous media, $G = E/(2(1 + \nu))$ (in MPa), ν is Poisson's ratio, and λ is the Lamé constant (in MPa) defined as $\lambda = E\nu/(1 + \nu)(1 - 2\nu)$.

3.2. Model for Fluid Flow in Porous Media. In this paper, the hydraulic response of a reservoir is modeled as a two-phase immiscible fluid flow. The model is applied to reveal pore pressure changes in the reservoir during fluid injection and production processes. Considering the deformation of the porous media during water flooding, the kinematic velocity of the porous media skeleton and the actual velocity of the pore fluids in porous media is the sum of the flow velocity of liquid and deformation velocity of porous media.

$$U = U_r + v_s = \frac{v}{\phi s_j} + v_s = \frac{v}{\phi s_j} + \frac{\partial u}{\partial t}, j = o, w, \quad (7)$$

where U is the fluid seepage velocity in the porous medium (in m/s), U_r is the relative velocity between liquid and porous medium (in m/s), v_s is the velocity caused by

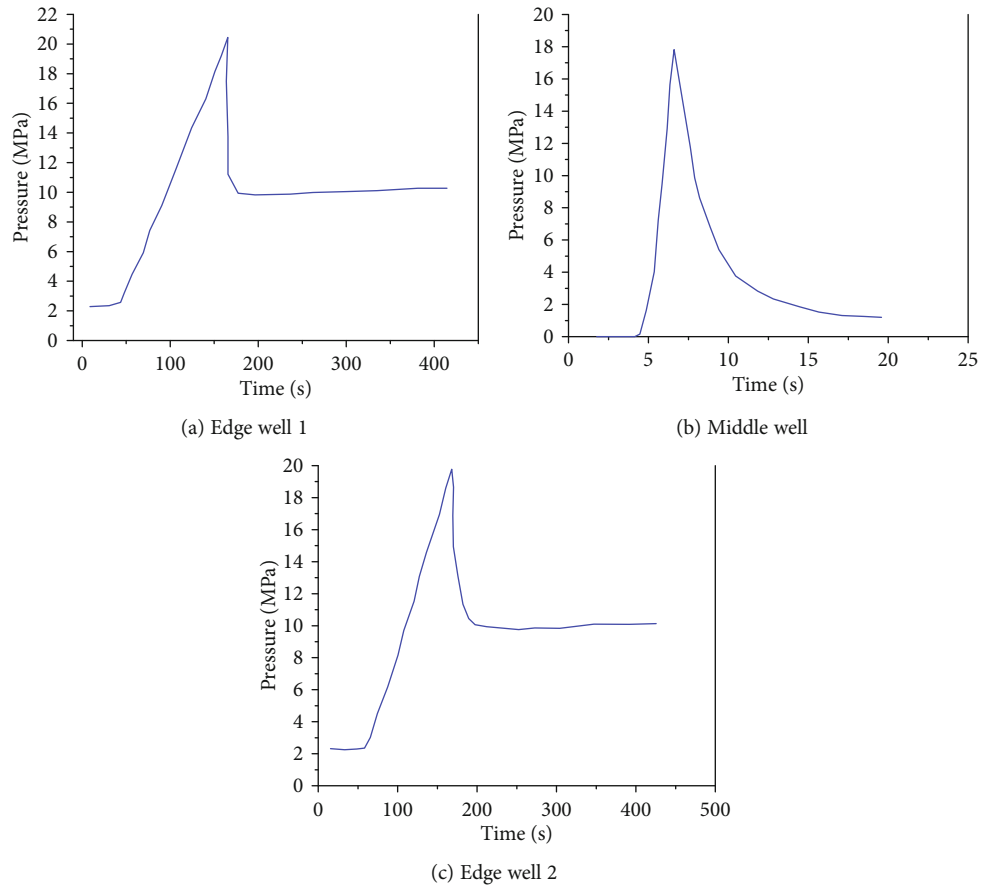


FIGURE 4: Pressure versus time from multiple fracturing of sample 2.

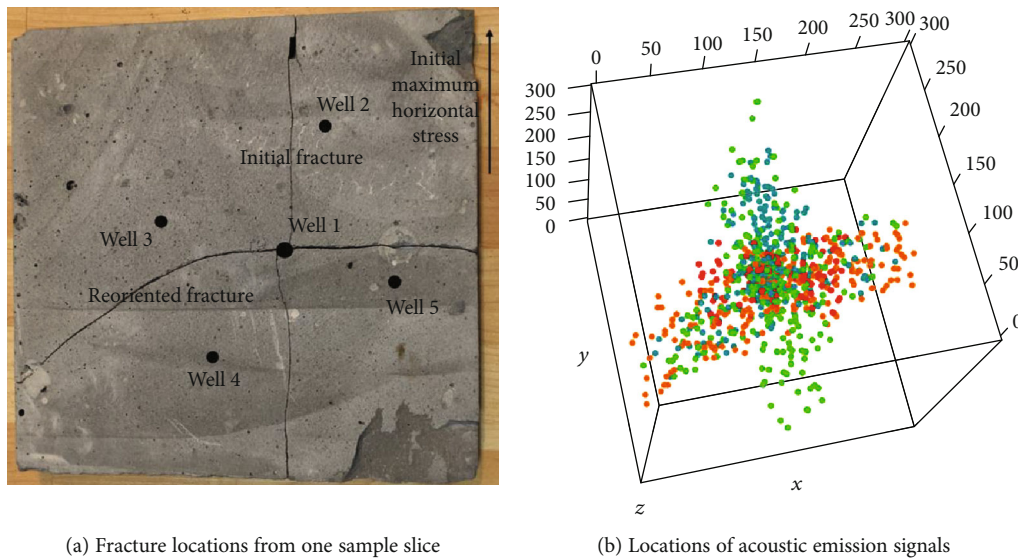


FIGURE 5: Image of induced orthogonal fractures from a horizontal slice of the sample (30 cm × 30 cm) and 3D scatter diagram of acoustic emission locations for sample 1 (30 cm × 30 cm × 30 cm).

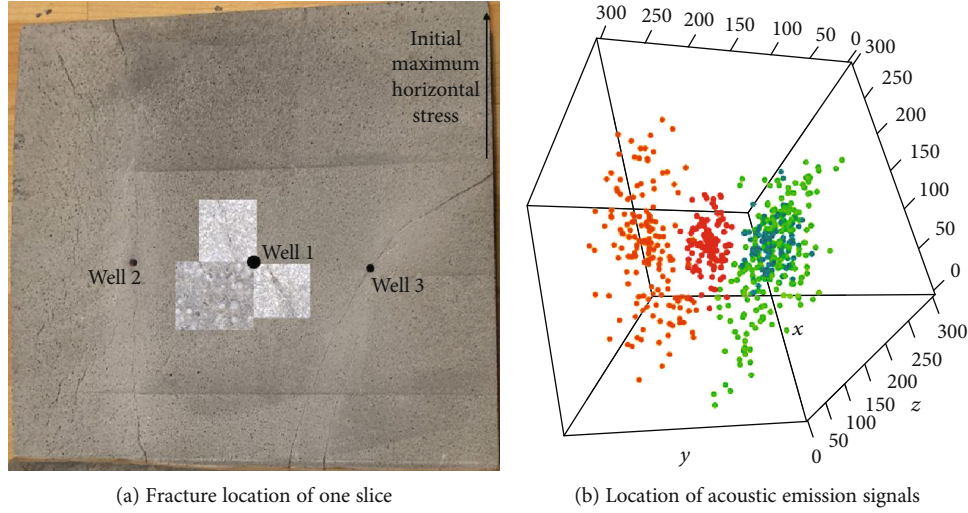


FIGURE 6: Diagram of fracture propagation in one slice (30 cm × 30 cm) and 3D scatter diagram of acoustic emission location of sample 2 (30 cm × 30 cm × 30 cm) stereoscope images of tiny fractures around well 1 in the sliced sample under digital microcamera.

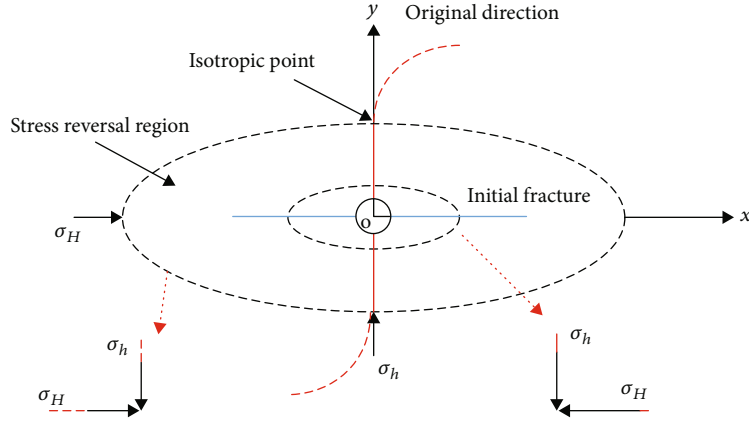


FIGURE 7: Diagram of stress reversal region and fracture reorientation in refracturing treatment.

the deformation of the porous medium (in m/s), v is the Darcy seepage velocity of the fluid (in m/s), and s_j is the saturation of the liquid phase j .

Therefore, the absolute velocity of liquid phase j in the coupled hydromechanical models can be expressed as:

$$v_j^{\text{real}} = \phi s_j U = v + \phi s_j \frac{\partial u}{\partial t}. \quad (8)$$

Based on the law of mass conservation, the equation of continuity for the two-phase oil/water seepage can be expressed as:

$$\frac{\partial}{\partial t} \left[\frac{\phi s_j}{B_j} \right] + \nabla \cdot \left[\frac{v_j^{\text{real}}}{B_j} \right] - Q_j = 0, \quad j = o, w, \quad (9)$$

where B_j is the volume factor of liquid phase j (in m^3/m^3) and Q_j is the flow rate of the injected or produced liquid at standard condition (in m^3/d).

Combining Eq. (8) and Eq. (9) yields:

$$\nabla \cdot \left(\frac{\lambda_j}{B_j} \nabla p \right) - \frac{\phi s_j}{B_j} \frac{\partial \varepsilon_v}{\partial t} + Q_j = \frac{\partial}{\partial t} \left(\frac{\phi s_j}{B_j} \right) \quad j = o, w, \quad (10)$$

where μ_j is the viscosity of liquid phase j (in $\text{mPa}\cdot\text{s}$) and λ_j is the mobility of liquid phase j (in $10^{-3} \mu\text{m}^2/(\text{mPa}\cdot\text{s})$) and is defined as $\lambda_j = k k_j / \mu_j$.

The above equation can be expanded as:

$$\frac{\partial}{\partial t} \left(\frac{\phi s_j}{B_j} \right) = \frac{\phi}{B_j} \frac{\partial s_j}{\partial t} + \frac{s_j}{B_j} \frac{\partial \phi}{\partial t} - \frac{\phi s_j}{B_j^2} \frac{\partial B_j}{\partial t}. \quad (11)$$

The compressibility factors of the rock pore volume, oil, and water and can be defined, respectively, as:

$$C_m = \frac{1}{\phi} \frac{\partial \phi}{\partial p} \quad C_o = -\frac{1}{B_o} \frac{\partial B_o}{\partial p_o} \quad C_w = -\frac{1}{B_w} \frac{\partial B_w}{\partial p_w}. \quad (12)$$

From the continuity equation for the porous medium, the relationship between the strain and displacement can be obtained as:

$$\frac{d\phi}{dt} = (1 - \phi) \frac{d(\nabla u)}{dt} \quad (13)$$

Combining Eq. (11), Eq. (12), and Eq. (13) with Eq. (10) and multiplying by B_j give the saturation equation of liquid phase j :

$$\nabla \cdot (\lambda_j \nabla p) + B_j Q_j = \phi \frac{\partial s_j}{\partial t} + s_j \frac{\partial(\nabla u)}{\partial t} + \phi c_j s_j \frac{\partial p}{\partial t}. \quad (14)$$

The pressure equation can be obtained by combining the oil phase of Eq. (10).

$$\nabla \cdot (\lambda_o \nabla p) + \nabla \cdot (\lambda_w \nabla p) + B_o Q_o + B_w Q_w = \frac{\partial(\nabla u)}{\partial t} + \phi c_t \frac{\partial p}{\partial t}. \quad (15)$$

The relationship of oil saturation and water saturation can be shown as:

$$s_o + s_w = 1. \quad (16)$$

The coupled hydromechanical model described by the above equations can be discretely solved by a finite element method.

3.3. Model Coupling and Boundary Conditions

3.3.1. Coupling of Stress and Seepage in the Artificial Fracture Region. The relationship between the fracture width and stress can be expressed as [24]:

$$w_f = \frac{K_n w_{fi}^2}{K_n w_{fi} + \sigma_n}, \quad (17)$$

where w_f is the width of the artificial fracture (in m), w_{fi} is the initial width of artificial fracture (in m), K_n is the normal stiffness of artificial fracture (in MPa/m), and σ_n' is effective normal stress acting across the fracture surface.

Based on the seepage model of two flat plates, the relationship between the fracture permeability and fracture width can be expressed by using the parallel-plate law as:

$$k_f = \frac{1}{12} w_f^2. \quad (18)$$

A dimensionless fracture conductivity $R_{\text{conductivity}}$ can be defined as the ratio of real-time fracture conductivity and initial fracture conductivity.

$$R_{\text{conductivity}} = \frac{k_f w_f}{k_{fi} w_{fi}}. \quad (19)$$

3.3.2. Coupling of Stress and Seepage Field in the Rock Matrix Region. The porosity of the porous medium is defined as:

$$\phi_m = \frac{V - V_s}{V}, \quad (20)$$

where V is the total volume of porous media (in m^3) and V_s is the skeleton volume of porous media (in m^3). Combining with volumetric strain, dynamic porosity can be defined as:

$$\phi_m = \frac{(V_b + V_b \varepsilon_v) - V_s}{V_b + V_b \varepsilon_v} = \frac{\phi_{m0} + \varepsilon_v}{1 + \varepsilon_v}. \quad (21)$$

Based on the capillary bundle model, dynamic permeability can be defined as:

$$k_m = \frac{k_{m0}}{1 + \varepsilon_v} \left(1 + \frac{\varepsilon_v}{\phi_{m0}} \right)^3. \quad (22)$$

3.3.3. Boundary Conditions. The boundary conditions of the poroelastic model include the displacement boundary conditions and stress boundary conditions. The displacement boundary conditions at the initial time of the reservoir can be shown as:

$$u|_{\Omega} = \vec{u}. \quad (23)$$

The stress boundary conditions at the initial time of the reservoir can be shown as:

$$\sigma \cdot n|_{\Omega} = \vec{\sigma}, \quad (24)$$

where n is the stress in the normal direction, $\vec{\sigma} = \begin{bmatrix} \sigma_{x0} \\ \sigma_{y0} \end{bmatrix}$, MPa.

Based on the seepage theory, the boundary conditions for the seepage model include the initial time conditions and boundary conditions. The initial time conditions of the seepage model can be shown as:

$$\begin{aligned} p_m|_{t=0} &= p_f|_{t=0} = p_i, \\ s_w|_{t=0} &= s_{wi}. \end{aligned} \quad (25)$$

The interior and exterior boundary conditions include the Dirichlet and Neumann conditions. The Dirichlet boundary condition is applied when the liquid pressure is known at the boundary, and the Neumann boundary condition is applied as the liquid pressure gradient at the normal direction of the exterior boundary.

$$\begin{aligned} p_f &= p_m = \bar{p}, \\ \frac{k}{\mu} \cdot n \nabla p_m &= C. \end{aligned} \quad (26)$$

3.4. Model Implementation and Basic Parameters. The model assumptions include the Darcy flow in porous media,

neglecting the capillary force and the gravity, neglecting the temperature change, and only linear elastic deformation for the rocks and without the fracturing occurring during the producing process.

COMSOL Multiphysics is applied for discretizing and implementing the coupled hydromechanical model [20]. All data used in the simulation were collected from a typical low permeability reservoir, and the basic parameters used in the model are shown in Table 2.

The rhombus inverted nine-spot well pattern is widely applied in the development of low permeability reservoir, and for the convenience of numerical simulation and research on the well interference of target wells, this approach is played in choosing wells for numerical simulation, as shown in Figure 8. Two wells with different locations are set as target wells for detailed research; P3 is an edge well and P5 is a corner well.

4. Results and Parametric Analysis

4.1. Model Results. To investigate the formation stress variation of fractured vertical wells in the water flooding reservoir, the models of the well pattern are simulated for producing 3000 days. Change of maximum horizontal stress, in situ stress, and strains at the direction of the initial minimum and maximum horizontal stresses (x and y axis) are analyzed with different field development periods. Figure 9 shows the maximum stress distribution in different development periods. Figure 10 shows the minimum stress distribution in different development periods. Figure 11 shows the shear stress distribution in different development periods.

By analyzing the stress distributions in different locations, it is found that stress changes are mainly around oil wells and water wells. The low-stress region is formed around fractured oil wells due to the pressure drop caused by liquid production, while the high-stress region is formed around water wells due to high pressure caused by water injection. The stress gradient is high around fractured oil wells and water wells. By analyzing the stress distribution in different development periods, stresses change with development, which increases around water wells and decreases around oil wells.

The maximum stress directions in different development periods are shown in Figure 12, and the direction at the initial time is along the propagation of the fracture. In the early period, the direction of stress varies sharply around all oil wells, the changed direction of stress is reversed to be perpendicular to the initial direction, and the stress direction is changed to the radial direction of the wellbore. In the mid-period, the stress reversal region expands while the area of the middle well is bigger than that of the edge wells. In the late period, the stress change around water wells is dominant and expands at the radial direction of the wellbore, the stress reversal region decreases and then gets steady for the edge wells, while it increases and then gets steady for the middle well.

4.2. Parametric Analysis. The effects of the initial in situ stresses and fluid pressures, which are considered to be the

TABLE 2: Basic parameters used in numerical simulation.

Parameter	Value
Minimum horizontal stress/MPa	20
Maximum horizontal stress/MPa	16
Poisson's ratio of rock	0.25
Density of rock/($\text{kg} \cdot \text{m}^{-3}$)	2000
Young's modulus/GPa	10
Biot coefficient	0.70
Porosity	0.1
Permeability/($10^{-3} \mu\text{m}^2$)	1
Fracture porosity	0.2
Reservoir pressure/MPa	15
Produced well pressure/MPa	6
Injected well pressure/MPa	30
Oil density/($\text{kg} \cdot \text{m}^{-3}$)	800
Water density/($\text{kg} \cdot \text{m}^{-3}$)	1000
Oil viscosity/($\text{mPa} \cdot \text{s}$)	50
Water viscosity/($\text{mPa} \cdot \text{s}$)	1
Fluid compressibility/ MPa^{-1}	0.0003
Fracture half-length/m	100

dominant factors that influence the fracture propagation and stress reversal region, will be analyzed separately in this paper.

4.2.1. Initial Horizontal Stresses. To investigate the influence of stresses on fracture reorientation, the models with different ratios of maximum and minimum horizontal stress of 1.02, 1.04, 1.06, and 1.12 are simulated. In this paper, the dimensionless fracture reorientation factor (L_a) is defined as the ratio of the equivalent radius of the reversal region and half-length of the initial fracture. The results are shown in the following figures. Figures 13 and 14 show dimensionless fracture reorientation factor changing with different initial horizontal stress ratio for the edge well and the middle well, respectively.

It can be seen that for edge wells, the dimensionless fracture reorientation factor increases to a maximum and then decreases with time, while decreases with the increasing initial horizontal stress ratio. It means the initial horizontal stress ratio has less influences on the time when the stress reversal region gets to be steady, while influences more on stress reversal distance. For the middle well, the dimensionless fracture reorientation factor increases and then slows down with time, and it also decreases with the increasing initial horizontal stress ratio. A small horizontal stress ratio is more conducive to fracture reorientation.

4.2.2. Fluid Pressure. The pressure difference between the reservoir formation and the well bottom is determined by injection pressure and production pressure at the well bottom. Simulations are performed where bottom pressures are set as 6 MPa with injection pressures of 30, 25, and 20 MPa. Another set of simulations were performed using an injection pressure of 30 MPa with a bottom pressure of 6, 7, and

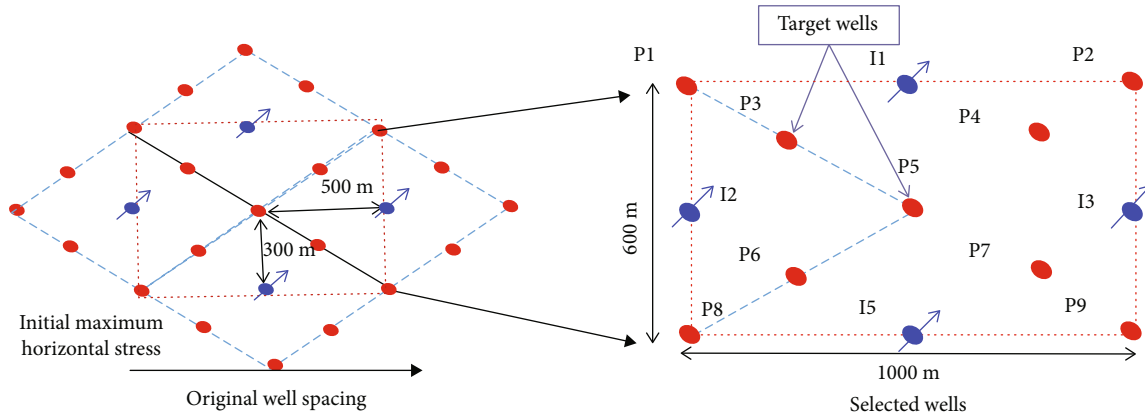


FIGURE 8: Diagram of the well pattern for numerical simulation.

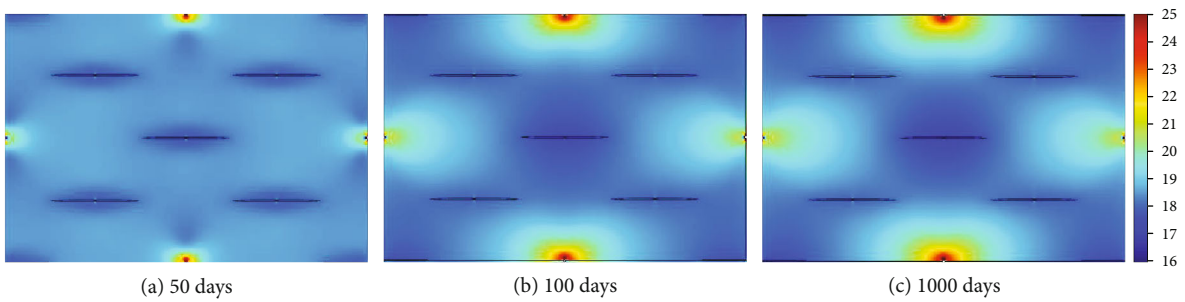


FIGURE 9: Maximum stress distribution in different development periods.

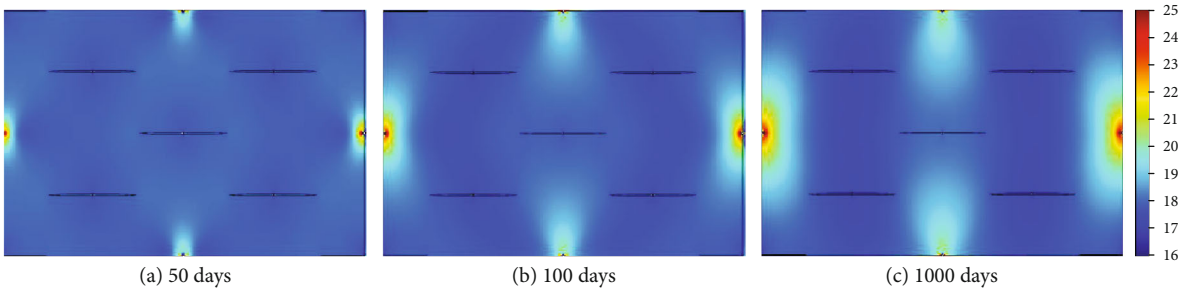


FIGURE 10: Minimum stress distribution in different developing periods.

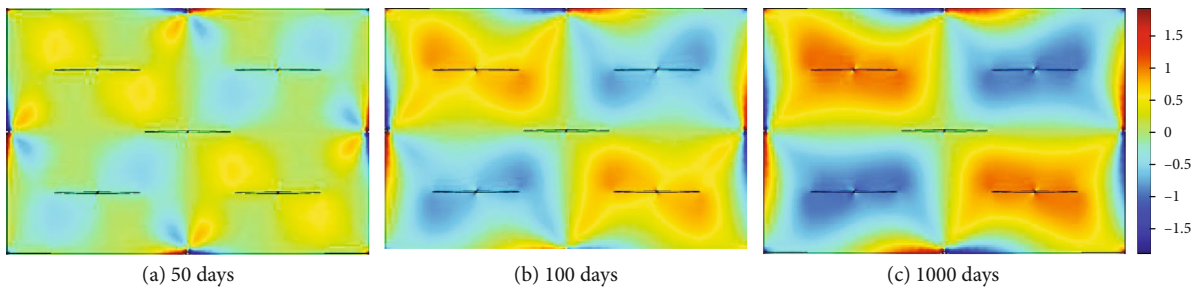


FIGURE 11: Shear stress distribution in different developing periods.

8 MPa. Figures 15 and 16 show the dimensionless fracture reorientation factor changing with different production pressure difference for the edge well and middle well, respectively.

For the middle well, with the same bottom pressure, dimensionless reversal distance increases with higher injection

pressure, when the bottom pressure is lower than 25 MPa. The reservoir pressure depletes, and the pressure gradient is small in the development process, which causes that dimensionless reversal distance to increase and then decrease gradually. For the edge wells, dimensionless reversal

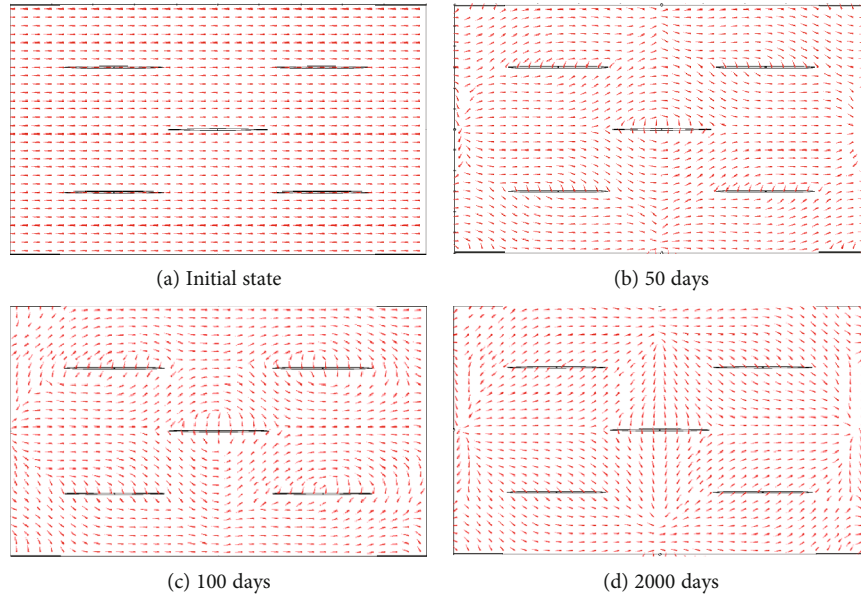


FIGURE 12: Maximum stress direction in different developing periods.

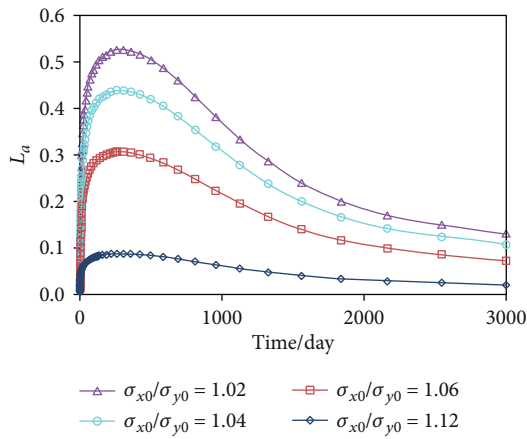


FIGURE 13: Initial horizontal stress ratio versus L_a of edge well.

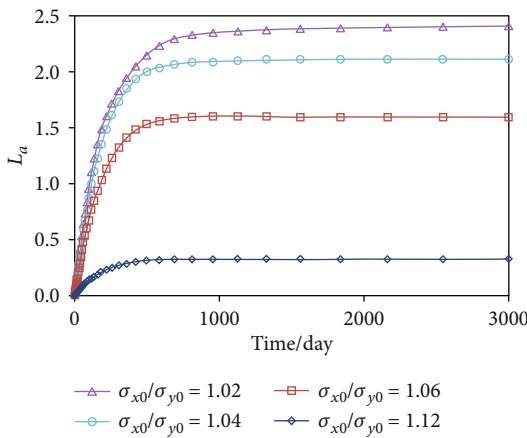


FIGURE 14: Initial horizontal stress ratio versus L_a of the middle well.

distance increases and then decreases with time. The same parameter increases with higher injection pressure, which means with higher producing pressure difference, stress variation induced by production is bigger, and fracture reorientation is easier due to high horizontal stress difference.

With the same injection pressure, for the middle well, dimensionless stress reversal distance increases with high producing bottom pressure at the same development period. With higher bottom pressure over 8 MPa, it is difficult for stress reversal to occur due to the low pressure difference around the producing well (with initial reservoir pressure of 9 MPa), and the stress reversal region expands until the production time of 900 days. For the edge well, the dimensionless stress reversal distance increases and then decreases with time. The same parameter increases with the decreasing bottom pressure of the producing well. With the higher bottom pressure of over 8 MPa, it is difficult for stress reversal until producing time of 100 days. The results indicate that the stress change for the edge well is faster than that of the middle well.

5. Conclusions

The mechanisms of fracture reorientation in refracturing treatment are studied, and the concept of the two stress reversal regions is proposed. With physical laboratory tests and numerical simulation, the fracture reorientation is verified to be existed around the well bottom, and influence factors that impacted fracture extended distance are analyzed.

- (1) Two stress reversal regions that impacted fracturing treatment in refracturing treatment are proposed: the inner one is highly influenced by fracturing parameters during the refracturing process, and the outer one is impacted by the development of the reservoir

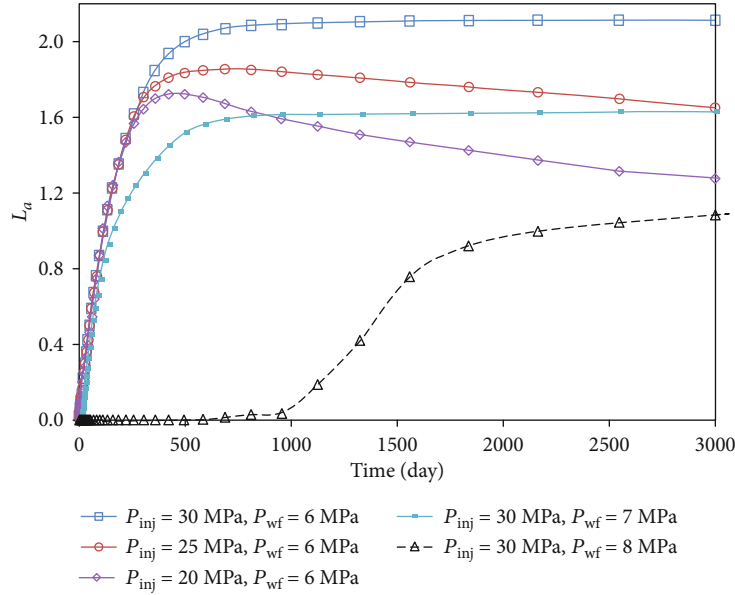


FIGURE 15: Effect of production pressure difference on L_a of the edge well.

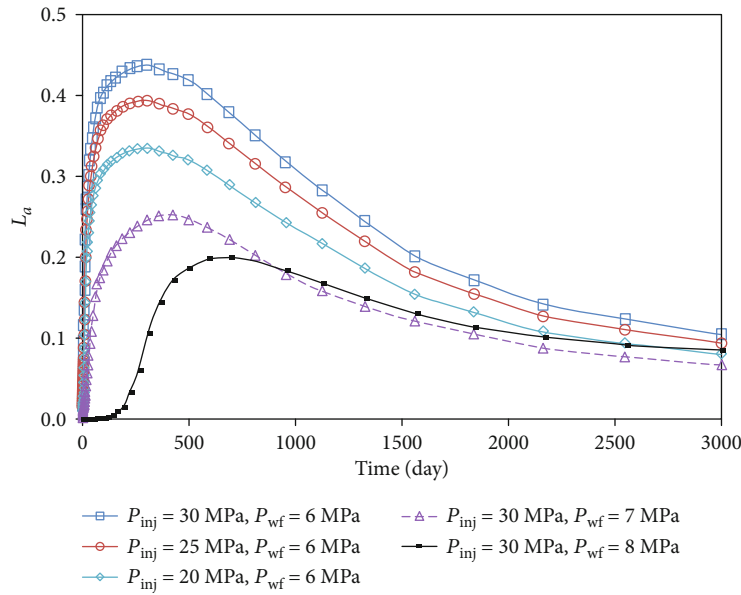


FIGURE 16: Effect of production pressure difference on L_a of the middle well.

- (2) Fracture reorientation is induced by changing the initial stress field and the injection pressure in laboratory tests on the true triaxial fracturing system. The direction of reoriented fracture can reach to be perpendicular to the initial fracture
- (3) In the refracturing treatment, new fractures are easily initiated and reoriented around the well bottom by controlling fracturing parameters, which is verified by experimental results
- (4) The propagation distance of the reoriented fracture is determined by poroelastic effect, the initial stress field will change with pore pressure varies, and the outer

stress reversal region is formed which determines the fracture reoriented distance in the fracturing treatment

- (5) The stress field and the injected and produced pressures are the main factors that influence the stress reversal region, and the propagation of the reoriented fractures will be varied due to different well location

Data Availability

The data used to support the findings of this study are available from the corresponding author upon request.

Conflicts of Interest

The authors declare no competing interest.

Acknowledgments


This study was supported by the Major National Science and Technology Project (2017ZX05009-001, 2017ZX05069, 2017ZX05072).

References

- [1] G. Sheng, Y. Su, and W. Wang, "A new fractal approach for describing induced-fracture porosity/permeability/ compressibility in stimulated unconventional reservoirs," *Journal of Petroleum Science and Engineering*, vol. 179, pp. 855–866, 2019.
- [2] M. C. Vincent, "Restimulation of unconventional reservoirs: when are refracs beneficial," *Journal of Canadian Petroleum Technology*, vol. 50, pp. 36–52, 2011.
- [3] M. Lu, Y. Su, S. Zhan, and A. Almrabat, "Modeling for reorientation and potential of enhanced oil recovery in refracturing," *Advances in Geo-Energy Research*, vol. 4, no. 1, pp. 20–28, 2020.
- [4] M. C. Vincent and M. R. Besler, "Declining frac effectiveness-evidence that propped fractures lose conductivity, surface area, and hydraulic continuity," in *Unconventional Resources Technology Conference*, pp. 696–710, Denver, Colorado, USA, 2013.
- [5] N. R. Warpinski and P. T. Branagan, "Altered stress-fracturing," *Journal of Petroleum Technology*, vol. 41, pp. 990–997, 1989.
- [6] J. L. Elbel and M. G. Mack, "Refracturing: observations and theories," in *SPE Production Operations Symposium*, Oklahoma City, Oklahoma, 1993.
- [7] E. P. Lolon, M. J. Mayrhofer, and I. Garcia, "Integrated fracture and production-modeling study in the bossier sands, North Louisiana," in *SPE Annual Technical Conference and Exhibition*, Denver, Colorado, USA, 2008.
- [8] I. D. Palmer, "Induced stresses due to propped hydraulic fracture in coalbed methane wells," in *Low Permeability Reservoirs Symposium*, Denver, Colorado, USA, 1993.
- [9] N. P. Roussel and M. M. Sharma, "Quantifying transient effects in altered-stress refracturing of vertical wells," *SPE Journal*, vol. 15, no. 3, pp. 770–782, 2013.
- [10] N. P. Roussel and M. M. Sharma, "Optimizing fracture spacing and sequencing in horizontal-well fracturing," *SPE Production & Operations*, vol. 26, no. 2, pp. 173–184, 2011.
- [11] C. A. Wright, R. A. Conant, G. M. Golich, P. L. Bondor, A. S. Murer, and C. A. Dobie, "Hydraulic fracture orientation and production/injection induced reservoir stress changes in diatomite waterfloods," in *SPE Western Regional Meeting*, pp. 8–10, Bakersfield, California, USA, 1995.
- [12] P. Li, "Theoretical study on reorientation mechanism of hydraulic fractures," Society of Petroleum Engineers, 2008.
- [13] G. Zhang and M. Chen, "Dynamic fracture propagation in hydraulic re-fracturing," *Journal of Petroleum Science and Engineering*, vol. 70, no. 3-4, pp. 266–272, 2010.
- [14] K. Zhao and P. Du, "Performance of horizontal wells in composite tight gas reservoirs considering stress sensitivity," *Advances in Geo-Energy Research*, vol. 3, no. 3, pp. 287–303, 2019.
- [15] M. T. Hecker, M. E. Houston, and J. D. Dumas, "Improved completion designs in the Hugoton field utilizing multiple gamma emitting tracers," in *SPE Annual Technical Conference and Exhibition*, Dallas, Texas, USA, 1995.
- [16] K. Fisher, B. M. Robinson, and G. W. Voneiff, "A comprehensive study of the analysis and economic benefits of radioactive tracer engineered stimulation procedures," in *SPE Annual Technical Conference and Exhibition*, Dallas, Texas, USA, 1995.
- [17] E. Siebrits, J. L. Elbel, E. Detournay et al., "Parameters affecting azimuth and length of a secondary fracture during a refracture treatment," in *SPE Annual Technical Conference and Exhibition*, New Orleans, USA, 1998.
- [18] N. P. Roussel, H. Florez, and A. A. Rodriguez, "Hydraulic fracture propagation from infill horizontal wells," in *SPE Annual Technical Conference and Exhibition*, New Orleans, Louisiana, USA, 2013.
- [19] G. Zhang and M. Chen, "Study of the optimal timing for refracturing," *Petroleum Science and Technology*, vol. 27, no. 10, pp. 969–983, 2009.
- [20] B. Hagemann, J. Wegner, and L. Ganzer, "Investigation of hydraulic fracture re-orientation effects in tight gas reservoirs," *Presented at COMSOL Conference*, pp. 379–388, 2013.
- [21] D. Benedict and J. L. Miskimins, "The effects of hydraulic fracture reorientation," in *SPE Hydraulic Fracturing Technology Conference*, The Woodlands, Texas, 2009.
- [22] M. Lu, Y. Su, M. Gutierrez, W. Wang, Y. Gan, and A. Almrabat, "Laboratory investigation of fracture propagation in multiple fracturing with complex well interference," in *SPE Hydraulic Fracturing Technology Conference and Exhibition*, Woodlands, Texas, USA, 2020a.
- [23] L. P. Frash, M. Gutierrez, J. Hampton, and J. Hood, "Laboratory simulation of binary and triple well EGS in large granite blocks using AE events for drilling guidance," *Geothermics*, vol. 55, pp. 1–15, 2015.
- [24] N. Barton, S. Bandis, and K. Bakhtar, "Strength, deformation and conductivity coupling of rock joints," *International Journal of Rock Mechanics and Mining Sciences & Geomechanics Abstracts*, vol. 22, no. 3, pp. 121–140, 1985.

Research Article

A New Model to Calculate Oil-Water Relative Permeability of Shaly Sandstone

Huiyuan Bian ^{1,2}, Kewen Li^{3,4}, Binchi Hou,⁵ and Xiaorong Luo⁶

¹College of Geology & Environment, Xi'an University of Science and Technology, Xi'an, Shaanxi 710054, China

²Key Laboratory of Coal Resources Exploration and Comprehensive Utilization, MLR, Xi'an, Shaanxi 710021, China

³School of Energy Resources, China University of Geosciences, Beijing, China

⁴Stanford University, USA

⁵Research Institute of Shaanxi Yanchang Petroleum (Group) Co., LTD, China

⁶Tuha Branch of China National Petroleum Corporation Logging, Tuha, Xinjiang 839009, China

Correspondence should be addressed to Huiyuan Bian; bianhuiyuan@xust.edu.cn

Received 29 May 2020; Revised 5 August 2020; Accepted 7 September 2020; Published 24 September 2020

Academic Editor: Wen-Dong Wang

Copyright © 2020 Huiyuan Bian et al. This is an open access article distributed under the Creative Commons Attribution License, which permits unrestricted use, distribution, and reproduction in any medium, provided the original work is properly cited.

Oil-water relative permeability curves are the basis of oil field development. In recent years, the calculation of oil-water relative permeability in sandstone reservoirs by resistivity logging data has received much attention from researchers. This article first analyzed the existing mathematical models of the relationship between relative permeability and resistivity and found that most of them are based on Archie formula, which assumes the reservoir is clean sandstone. However, in view of the fact that sandstone reservoir is commonly mixed with shale contents, this research, based on the dual water conductivity model, Poiseuille's equation, Darcy's law, and capillary bundle model, derived a mathematical model (DW relative permeability model) for shaly sandstone reservoir, which calculates the oil-water relative permeability with resistivity. To test and verify the DW relative permeability model, we designed and assembled a multifunctional core displacement apparatus. The experiment of core oil-water relative permeability and resistivity was designed to prove the effectiveness of the DW relative permeability model in shaly sandstone reservoirs. The results show that the modified Li model can well express the transformational relation between resistivity and relative permeability in sandstone reservoir with low clay content. Compared with the modified Li model and the Pairoys model, the DW relative permeability model is more helpful to collect better results of relative permeability in shaly sand. These findings will play a significant role in the calculation of oil-water relative permeability in reservoirs based on resistivity logging data and will provide important data and theory support to the shaly sandstone reservoir characterized oil field development.

1. Introduction

The evaluation of tight reservoir has always been an important part of petroleum geology research, while oil-water relative permeability, which is vital to the evaluation of fluid flow in porous media, is used in all aspects of the reservoir engineering [1, 2]. Traditionally, relative permeability is obtained in laboratory. However, in many cases, especially in low permeability reservoirs, or when phase transformation or mass transfer happens with the change of pressure, oil-water relative permeability experiments are difficult, expensive, and time consuming simultaneously [3, 4]. Alternately, it is diffi-

cult to maintain the samples the same as in the reservoirs; moreover, relative permeability is almost impossible to obtain in real time. Despite all these difficulties, experiment serves as the main method to calculate relative permeability curves for oil fields.

Conventional resistivity logging data, which is the basic information of oil and gas well standard logging, is in large amount and available. In recent years, more and more scholars indicated that there is a relationship between relative permeability and resistivity [5–9]. Cai et al. [10] presented a review of the electrical conductivity models using fractal, percolation, and effective medium theories. In another article,

Cai et al. [11] proposed a combined model including pore-throat ratio, tortuosity, and connectivity, exactly estimating the influence of complex pore structure on the transport behavior associated with electrical parameters. Li [12] based on Archie formula put forward a mathematical model that uses resistivity to calculate the relative permeability of gas-water, and Li verified the model with experimental data. Li et al. [13, 14] conducted a lot of research on this field. Li together with Horne and Williams worked out methods to calculate two-phase relative permeability with resistivity logging data in uniform medium. Mohammed and Birol [15] modified Li model by taking the fluid viscosity and the average water saturation at the time of water breakthrough into consideration. Alex et al. [16] proposed a method using resistivity to calculate relative permeability in dual porosity model, but the model has not been verified experimentally. Pairoys et al. [17] verified the Li model and Brooks-Corey model [6] with gas-water relative permeability experiments and found that the Li model works better than Brooks-Corey model in that situation. Then, the Li model is modified by replacing the pore size distribution index λ to index saturation exponent n Li model [18]. Pairoys [19] analyzed the change of resistivity under different frequency in the process of unsteady two-phase flow displacement, based on which the Li model was verified again with gas-water relative permeability experimental data and oil flooding data by Bian and Li [20]. The above-modified models based on the Li model were established under the condition of homogeneous clean sandstone reservoir. However, most real sandstone reservoirs contain shale contents, which influence rock resistivity and relative permeability significantly.

This study, based on the dual water conductivity model, Poiseuille's equation, Darcy's law, and capillary bundle model, proposed and verified a mathematical model (DW relative permeability model) to calculate relative permeability using resistivity. To improve the Li model, a new model named "dual water relative permeability model (DW model)" was proposed in the consideration of better expressing the transformational relations between resistivity and relative permeability in the shaly sand reservoir. According to experiments, the DW model achieved the goal of reflecting the relation between resistivity and relative permeability in a better way than the modified Li model and Pairoys model, which is helpful in both the calculation of oil-water relatively permeability in shaly sand reservoir based on resistivity and the oil field development.

2. Mathematical Background

2.1. Relationship between Water Saturation and Relative Permeability. There exist many relationship models between water saturation and relative permeability, among which the most common one is as shown below [20]:

$$k_{rw} = k_{rw\max} (S_w^f)^{n_w}, \quad (1)$$

$$k_{rnw} = k_{rnw\max} (1 - S_w^f)^{n_{nw}}, \quad (2)$$

$$S_w^f = \frac{S_w - S_{wr}}{1 - S_{wr} - S_{nwr}}, \quad (3)$$

where k_{rw} and k_{rnw} are relative permeabilities of the wetting and nonwetting phase, S_w and S_{wr} are the saturation and the irreducible saturation of wetting phase, $k_{rw\max}$ is the maximum k_{rw} when $S_w = 1 - S_{nwr}$, $k_{rnw\max}$ is the maximum k_{rnw} when $S_w = S_{wr}$, S_{nwr} is the residual saturation of nonwetting phase, and S_w^f is the normalized saturation of wetting phase.

2.2. Li Model for the Relationship between Relative Permeability and Resistivity. Fluid flow in porous media is similar to current flow in conductive media [13]. According to the Li model, gas/water relative permeability is calculated using resistivity.

$$S_w^* = \frac{S_w - S_{wr}}{1 - S_{wr}}, \quad (4)$$

$$k_{rw}^* = S_w^* \frac{1}{I}, \quad (5)$$

$$k_{rw}^* = (S_w^*)^{(2+\lambda)/\lambda}, \quad (6)$$

$$k_{rnw}^* = (1 - S_w^*)^2 \left[1 - (S_w^*)^{(2+\lambda)/\lambda} \right], \quad (7)$$

where I is the resistivity index, and k_{rw}^* is the wetting-phase normalized relative permeability.

2.3. Pairoys Model. Many modified models grew out of the Li model that is suitable for gas-water two-phase flow and oil flooding, but not for water flooding. Pairoys worked out the following model after analyzing water flooding situation [19].

$$S_w' = \frac{S_w - S_{wc}}{1 - S_{wc} - S_{or}}, \quad (8)$$

$$k_{rw}^* = \frac{S_w'}{I}, \quad (9)$$

$$k_{rnw}^* = \left(1 - S_w' \right) \frac{I}{I_{\max}}, \quad (10)$$

where S_w is the saturation of the wetting phase, S_{wc} is the irreducible saturation of the wetting phase, S_{or} is the residual saturation of the nonwetting phase, S_w' is the normalized saturation of the wetting phase, I is the resistivity index, when $S_w = 1 - S_{or}$, and k_{rw}^* and k_{rnw}^* are normalized relative permeabilities of the wetting and nonwetting phases I_{\max} is the resistivity index.

2.4. Modified Li Model. Based on the Li model, Bian and Li proposed a model for the relationship between resistivity and oil-water relative permeability of water wet sandstone reservoirs with low shaly contents [20].

$$S_w' = \frac{S_w - S_{wc}}{1 - S_{wc} - S_{or}}, \quad (11)$$

$$k_{rw}^* = S_w' \frac{R_{or}}{R_t}, \quad (12)$$

$$k_{ro}^* = \left(1 - S_w'\right)^2 (1 - k_{rw}), \quad (13)$$

where R_{or} is the formation resistivity when $S_w = 1 - S_{or}$ and k_{rw}^* and k_{ro}^* are normalized relative permeabilities of the water and oil phases.

3. Relationship between Resistivity and Relative Permeability of Shaly Sand Reservoir

The relationship models of resistivity and relative permeability mentioned above all assume that the reservoirs are homogeneous and pure sandstone. However, in reality, most sandstone reservoirs contain shale contents. Therefore, in order to calculate the relative permeability in shaly sand reservoirs accurately, a new model suitable for shaly sandstone should be established.

The cross-sectional area, length, and volume of the water wet shaly sandstone are A , L , and V , respectively (as shown in Figure 1(a)). The effective pore space of rock is considered to be composed of n large bore capillary columns with equal cross-sectional area and m small bore capillary columns with equal cross-sectional area. The large columns are filled with movable water and oil, while the small columns are filled with immovable water (irreducible water) and residual oil. The cross-sectional area, cross-section radius, length, and volume of the large bore capillary columns are A_a , r_a , L_a , and V_{a-j} , while those of the small columns are A_b , r_b , L_b , and V_{b-j} , respectively (as shown in Figure 1(b)).

When the water saturation of the rock is S_w , in the i^{th} ($i = 1, 2, \dots, n$) large capillary columns, the oil cross-sectional area and oil cross-section radius are A_{of} and r_{of} , while the cross-sectional area, length, and volume of the movable water are A_{wf} , L_{wf} , and V_{wf-j} , respectively. In the j^{th} ($j = 1, 2, \dots, m$) small capillary columns, the oil cross-sectional area and oil cross-section radius are A_{or} and r_{or} , while the cross-sectional area, length, and volume of the immovable water are A_{wc} , L_{wc} , and V_{wc-j} , respectively. Due to the existence of shale contents, it is assumed that the immobile water in the small capillary columns contains clay water. The cross-sectional area, length, and volume of the clay water are A_{wb} , L_{wb} , and V_{wb-j} , respectively (as shown in Figure 1(c)).

When the core sample is saturated with water, according to Poiseuille flow formula, the liquid flow in the i^{th} ($i = 1, 2, \dots, n$) large capillary column q_{a-i} is calculated as follows.

$$q_{a-i} = \frac{\pi r_a^4 \Delta p}{8 \mu L_a}, \quad (14)$$

where Δp is the pressure difference, and μ is the fluid viscosity.

The total flow of water in the rock q is

$$q = \sum_{i=1}^n \frac{\pi r_a^4 \Delta p}{8 \mu L_a} + \sum_{j=1}^m \frac{\pi r_b^4 \Delta p}{8 \mu L_b}. \quad (15)$$

According to Darcy's formula,

$$Q = k \frac{A \Delta p}{\mu L}. \quad (16)$$

Suppose that the length of the large capillary column is equal to that of the small capillary column. The permeability k is obtained as follows.

$$k = \frac{1}{8} \left(\varphi_a \frac{r_a^2}{\tau_a^2} + \varphi_b \frac{r_b^2}{\tau_b^2} \right). \quad (17)$$

Similarly, when the water saturation is S_w ($S_{wc} \leq S_w \leq 1 - S_{or}$), the small capillary columns are filled with bound water and residual oil, while the large capillary columns are filled with movable water and movable oil.

According to the Poiseuille flow formula, the total flow of movable water in the rock q_{wf} is

$$q_{wf} = \sum_{i=1}^n \frac{A_{wf}^2 \Delta p}{8 \pi \mu L_{wf}}. \quad (18)$$

According to Darcy's formula,

$$Q_{wf} = k_w \frac{A \Delta p}{\mu L}. \quad (19)$$

So, the permeability k_w is

$$k_w = \frac{1}{8} \varphi S_{wf} \frac{(r_a^2 - r_{of}^2)}{\tau_{wf}^2}. \quad (20)$$

And the water relative permeability k_{rw} is obtained as follows.

$$k_{rw} = \frac{\varphi S_{wf} (r_a^2 - r_{of}^2)}{\tau_{wf}^2 (\varphi_a (r_a^2 / \tau_a^2) + \varphi_b (r_b^2 / \tau_b^2))}. \quad (21)$$

The electrical conductivity of the model is analyzed below. The resistivity of free water is R_w , while the resistivity of clay water is R_{wb} . In the j^{th} ($j = 1, 2, \dots, m$) small capillary columns, the cross-sectional area, length, and volume of the bound free water are A_{wz} , L_{wz} , and V_{wz-j} , respectively. When the core sample is saturated with

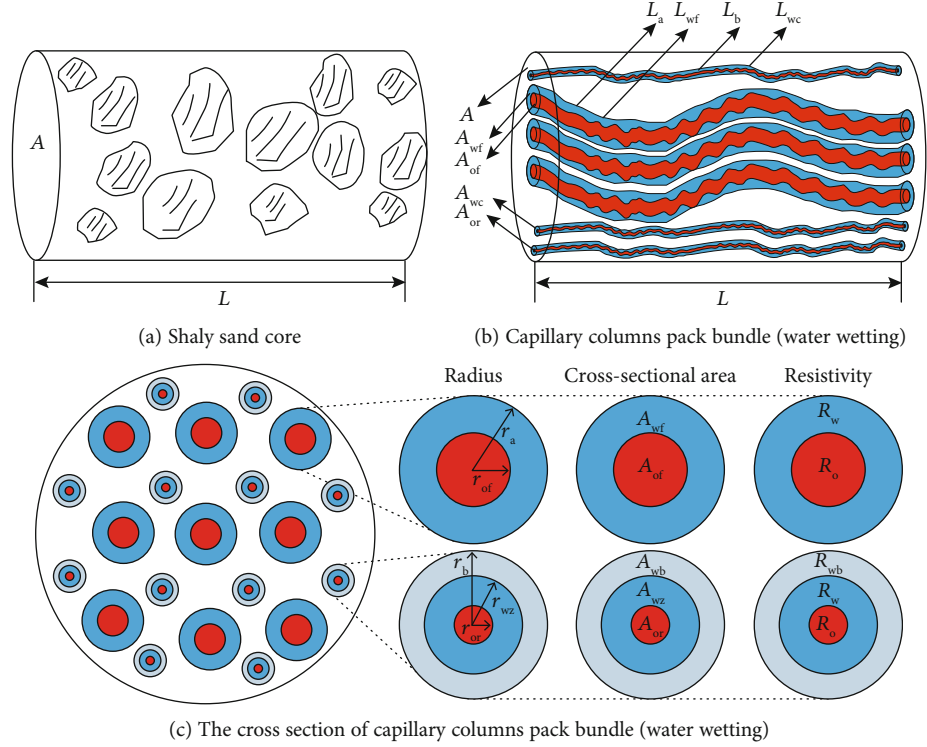


FIGURE 1: Capillary bundle model.

water, the resistivity is R_0 . When the saturation is S_w and the resistivity is R_t , there is the following equation.

$$\frac{1}{R_t(L/A)} = \sum_{i=1}^n \frac{1}{R_w(L_{wf}/A_{wf})} + \sum_{j=1}^m \frac{1}{R_w(L_{wz}/(A_b - A_{wb}))} + \sum_{j=1}^m \frac{1}{R_{wb}(L_{wb}/A_{wb})}. \quad (22)$$

Assuming that all the capillary columns have the same length,

$$L_a = L_b = L_A, \quad (23)$$

$$L_{wf} = L_{wc} = L_{wz} = L_{wb} = L_w. \quad (24)$$

The resistivity index I is

$$I = \frac{R_t}{R_0}. \quad (25)$$

So, the water relative permeability k_{rw} can be obtained.

$$k_{rw} = \frac{(S_w - S_{wc})^2}{(1 - S_{wc} - S_{or})^2 + (S_{wc} + S_{or})^2} \frac{\tau_A^2}{\tau_w^2}. \quad (26)$$

Define the resistivity R_b .

$$\frac{S_{wc}}{R_b} = \frac{S_{wc} - S_{wb}}{R_w} + \frac{S_{wb}}{R_{wb}}. \quad (27)$$

Define SR can be calculated as follows.

$$SR = \frac{R_b}{R_w} \frac{1 - S_{or} - S_{wc}}{S_{wc}}. \quad (28)$$

Therefore, the normalized water relative permeability in the dual water relative permeability model can be expressed as follows:

$$k_{rw}^* = \frac{k_{rw}}{k_{rw}(S_w = 1 - S_{or})}, \quad (29)$$

$$k_{rw}^* = \left(S_w'\right)^2 \frac{(R_{or}/R_0)(SR + 1) - 1}{I(SRS_w' + 1) - 1}. \quad (30)$$

When $S_w = S_{wc}$, $k_{rw}^* = 0$. When $S_w = 1 - S_{or}$, $S_w' = 1$ and $k_{rw}^* = 1$, which satisfies the boundary condition.

When the clay water content is 0 ($S_{wb} = 0$), the model is simplified to a clean sandstone model, and the normalized water relative permeability is as follows.

$$k_{rw}^* = \left(S_w'\right)^2 \frac{R_{or}(1 - S_{or}) - R_0 S_{wc}}{R_t S_w - R_0 S_{wc}}. \quad (31)$$

3.1. Determination of the Parameters in the DW Relative Permeability Model

3.1.1. Calculation of the Resistivity of Clay Water R_{wb} . Diffusion factor of Na^+ ion diffusion layer α is calculated as follows [21]:

$$\alpha = \begin{cases} 1, & \text{when } P_w > P_{wo}, \\ \sqrt{\frac{P_{wo}}{P_w}}, & \text{when } P_w \leq P_{wo}, \end{cases} \quad (32)$$

where P_w is the salinity of formation water, P_{wo} is the salinity of formation water when $x_d = x_{dH}$, and x_d is the thickness of Na^+ ion diffusion layer (10^{-8} cm).

The pore volume occupied by clay water V_Q when $Q_v = 1 \text{ mmol/cm}^3$ is calculated as follows:

$$V_Q = \frac{1}{2.853 + 0.019T(^{\circ}\text{C})}. \quad (33)$$

The equivalent conductivity β of compensation Na^+ ion in clay water (S/m) (mmol/L) is calculated as follows:

$$\beta = 0.0857T(^{\circ}\text{C}) - 0.143. \quad (34)$$

The clay water resistivity R_{wb} is calculated as follows:

$$R_{wb} = \frac{\alpha V_Q}{\beta}, \quad (35)$$

$$R_{wb} = \alpha \frac{0.0857T(^{\circ}\text{C}) - 0.143}{2.853 + 0.019T(^{\circ}\text{C})}. \quad (36)$$

It can be seen from the above formula that the resistivity of formation water is affected by both α and temperature T . When the water salinity is high, $\alpha = 1$. Therefore, the resistivity of clay water R_{wb} is independent from the equilibrium cation concentration and clay types.

3.1.2. Calculation of the Clay Water Saturation S_{wb} .

$$S_{wb} = \alpha V_Q Q_v. \quad (37)$$

Substitute equation (33) into equation (37),

$$S_{wb} = \frac{\alpha Q_v}{2.853 + 0.019T(^{\circ}\text{C})}. \quad (38)$$

From the above formula, it can be seen that the clay water saturation S_{wb} increases with the increase of α . As the temperature T increases, S_{wb} decreases. With the increase of Q_v , S_{wb} increases.

3.1.3. Calculation of the Resistivity R_b .

$$\frac{S_{wc}}{R_b} = \frac{S_{wc} - S_{wb}}{R_w} + \frac{S_{wb}}{R_{wb}}. \quad (39)$$

3.1.4. Calculation of the Parameter SR .

$$SR = \frac{R_b}{R_w} \frac{1 - S_{or} - S_{wc}}{S_{wc}}. \quad (40)$$

3.1.5. Calculation of the Normalized Water Saturation S'_w .

$$S'_w = \frac{S_w - S_{wc}}{1 - S_{wc} - S_{or}}. \quad (41)$$

3.1.6. Calculation of the Normalized Water Relative Permeability k_{rw}^* .

$$k_{rw}^* = \left(S'_w\right)^2 \frac{(R_{or}/R_0)(SR + 1) - 1}{I(SRS'_w + 1) - 1}. \quad (42)$$

In conclusion, the DW relative permeability model can be expressed as follows.

$$\left\{ \begin{array}{l} (1) \alpha = \begin{cases} 1, & \text{when } P_w > P_{wo}, \\ \sqrt{\frac{P_{wo}}{P_w}}, & \text{when } P_w \leq P_{wo}, \end{cases} \\ (2) R_{wb} = \alpha \frac{0.0857T(^{\circ}\text{C}) - 0.143}{2.853 + 0.019T(^{\circ}\text{C})}, \\ (3) S_{wb} = \frac{\alpha Q_v}{2.853 + 0.019T(^{\circ}\text{C})}, \\ (4) \frac{S_{wc}}{R_b} = \frac{S_{wc} - S_{wb}}{R_w} + \frac{S_{wb}}{R_{wb}}, \\ (5) SR = \frac{R_b}{R_w} \frac{1 - S_{or} - S_{wc}}{S_{wc}}, \\ (6) S'_w = \frac{S_w - S_{wc}}{1 - S_{wc} - S_{or}}, \\ (7) k_{rw}^* = \left(S'_w\right)^2 \frac{(R_{or}/R_0)(SR + 1) - 1}{I(SRS'_w + 1) - 1}, \\ (8) k_{ro}^* = \left(1 - S'_w\right)^2 (1 - k_{rw}^*). \end{array} \right. \quad (43)$$

3.2. Sensitivity Analysis of Parameters of DW Model of Shaly Sandstone

3.2.1. The Effect of Irreducible Water Saturation S_{wc} on k_{rw}^* . Suppose that $S_{or} = 0.2$, $S_{wb} = 0.05$, $R_0 = 30 \Omega \cdot \text{m}$, $R_{or} = 35 \Omega \cdot \text{m}$, $R_w = 0.5 \Omega \cdot \text{m}$, and $R_{wb} = 0.1 \Omega \cdot \text{m}$, oil-water relative permeability curves under different irradiated water saturation S_{wc} are shown in Figure 2. It indicates that the normalized water relative permeability k_{rw}^* decreases while S_{wc} increases. The reason is that the movable water saturation S_{wf} decreases under the same normalized water saturation S'_w as S_{wc} increases, thus the normalized relative permeability of water phase k_{rw}^* decreases.

3.2.2. The Effect of Residual Oil Saturation S_{or} on k_{rw}^* . Suppose that $S_{wc} = 0.2$, $S_{wb} = 0.05$, $R_0 = 30 \Omega \cdot \text{m}$, $R_{or} = 35 \Omega \cdot \text{m}$, $R_w = 0.5 \Omega \cdot \text{m}$, and $R_{wb} = 0.1 \Omega \cdot \text{m}$, the oil-water relative permeability curves under different residual oil saturation S_{or} are shown in Figure 3. It illustrates that the normalized water relative permeability k_{rw}^* decreases with the increase of S_{or} .

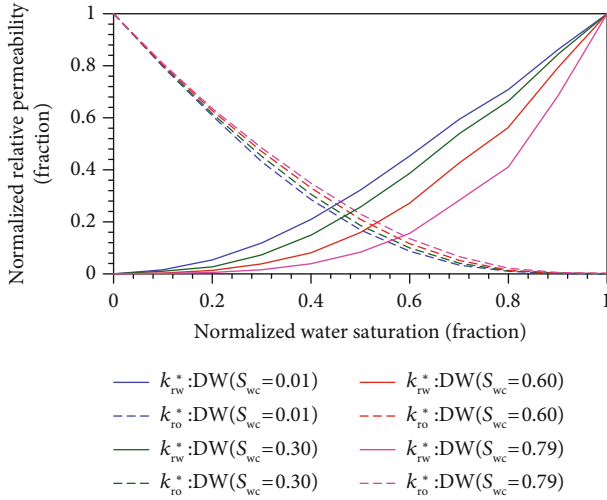


FIGURE 2: Normalized oil-water relative permeability curves under different S_{wc} .

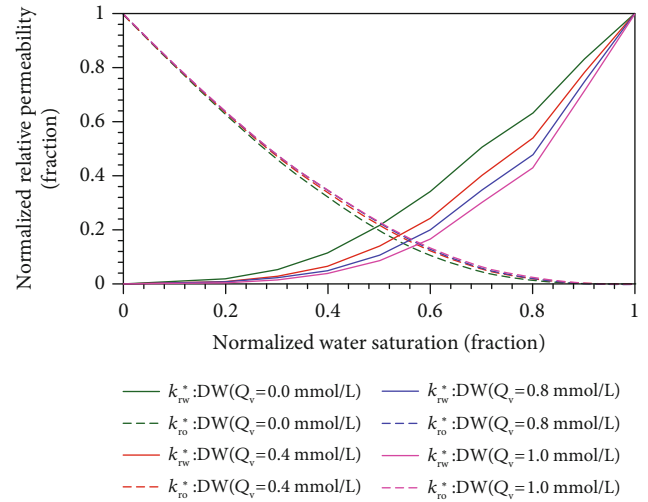


FIGURE 4: Normalized oil-water relative permeability curves under different Q_v .

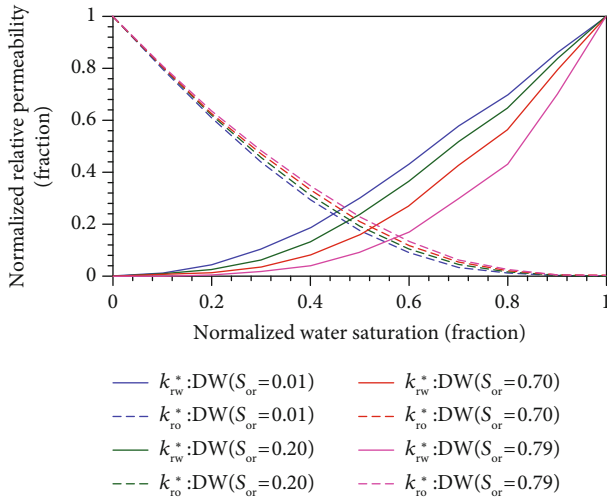


FIGURE 3: Normalized oil-water relative permeability curves under different S_{or} .

because the movable water saturation S_{wf} decreases under the same normalized water saturation S_w^l when S_{or} increases, which leads to the decrease of normalized relative permeability of water phase k_{rw}^* .

3.2.3. The Effect of Cation Exchange Capacity Q_v on k_{rw}^* . Suppose that there are a set of cores with the same parameters as follows. $T = 20^\circ\text{C}$, $P_w = 8000$ ppm, $S_{wc} = 0.5$, $S_{or} = 0.2$, $R_w = 5 \Omega \cdot \text{m}$, $R_0 = 33 \Omega \cdot \text{m}$, and $R_{or} = 35 \Omega \cdot \text{m}$. Normalized oil-water relative permeability curves under different Q_v are shown in Figure 4. It illustrates that the normalized water relative permeability k_{rw}^* decreases with the increase of Q_v .

Studies [22–24] show that clay mineral content is one of the main factors affecting the shape of oil-water relative permeability curve of rock. When water is injected into the core sample, it first enters into larger pores, where the relative permeability of the water phase increases rapidly. Soon after the

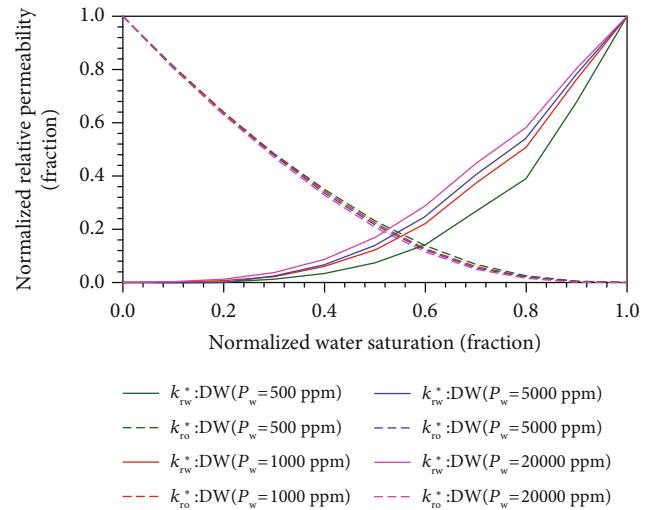
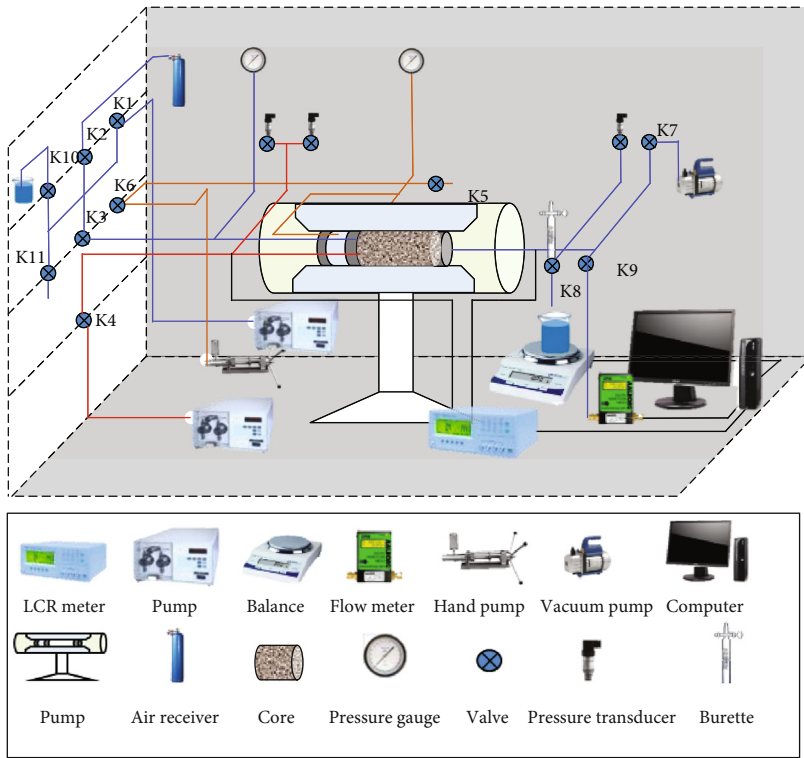


FIGURE 5: Normalized oil-water relative permeability curves under different P_w .

injection, water gradually enters into small pores, where the flow resistance increases. At the same time, the oil in large pore paths is separated into small oil droplets by the water. If the oil droplets migrate to the vicinity of the pore throat, the so-called “liquid resistance effect” will emerge when the diameter of the oil droplets is similar to that of the pore throat. In this case, the capillary force of the orifice throat must be overcome if the oil droplets want to move [25, 26]. The hydrophilic particles in the pores will move to the pore throat and cause blockage. With the increase of water saturation S_w , the amount of plugging particles will increase, and the relative permeability of water phase will decrease accordingly.

3.2.4. The Effect of Total Salinity P_w on k_{rw}^* . Suppose that $T = 20^\circ\text{C}$, $Q_v = 0.25$ mmol/L, $S_{wc} = 0.5$, and $S_{or} = 0.3$. Figure 5



(a) Schematic of the apparatus used for the simultaneous measurements



(b) Experimental apparatus

FIGURE 6: Multifunctional core displacement experimental apparatus.

TABLE 1: The basic physical parameters of core samples.

No.	Samples	L (cm)	D (cm)	φ (%)	$k_w (\times 10^{-3} \mu\text{m}^2)$	Q_v (mmol/mL)
Group I	A-7	5.158	2.552	26.61	548.22	0.068
	A-8	7.572	2.555	23.53	51.80	0.097
	A-9	6.724	2.549	24.83	349.98	0.062
	B-1	5.150	2.554	17.62	14.06	0.100
	B-9	7.363	2.554	27.33	647.10	0.103
	B-10	6.697	2.580	30.70	250.67	0.092
Group II	A-1	7.224	2.556	27.66	123.36	0.155
	A-3	6.325	2.535	27.42	119.43	0.168
	A-5	7.424	2.551	24.64	58.09	0.514
	A-10	7.871	2.549	26.86	1200.05	0.857
	B-7	7.063	2.566	24.87	33.02	0.142
	B-8	6.737	2.548	24.31	42.38	0.240

shows the normalized oil-water relative permeability curves under different P_w . It illustrates that the normalized water relative permeability k_{rw}^* increases with increased P_w .

In shaly sand reservoir, with the decrease of salt content in free water, the salinity in free water decreases, clay mineral crystal layer expands, and the formation permeability continues to decline, which is called the salt-sensitive phenomenon (Meng, 2012). There are a large number of clay minerals in shaly sand reservoir. Therefore, with the decrease of free water salinity, the salt content in free water decreases, the

salt-sensitive phenomenon gets worse, and the relative permeability of water phase goes down.

4. Experimental Verification of DW Relative Permeability Model

4.1. Experiments. In order to verify the relationship between resistivity and relative permeability in DW Model, a multifunctional core displacement experiment device was designed

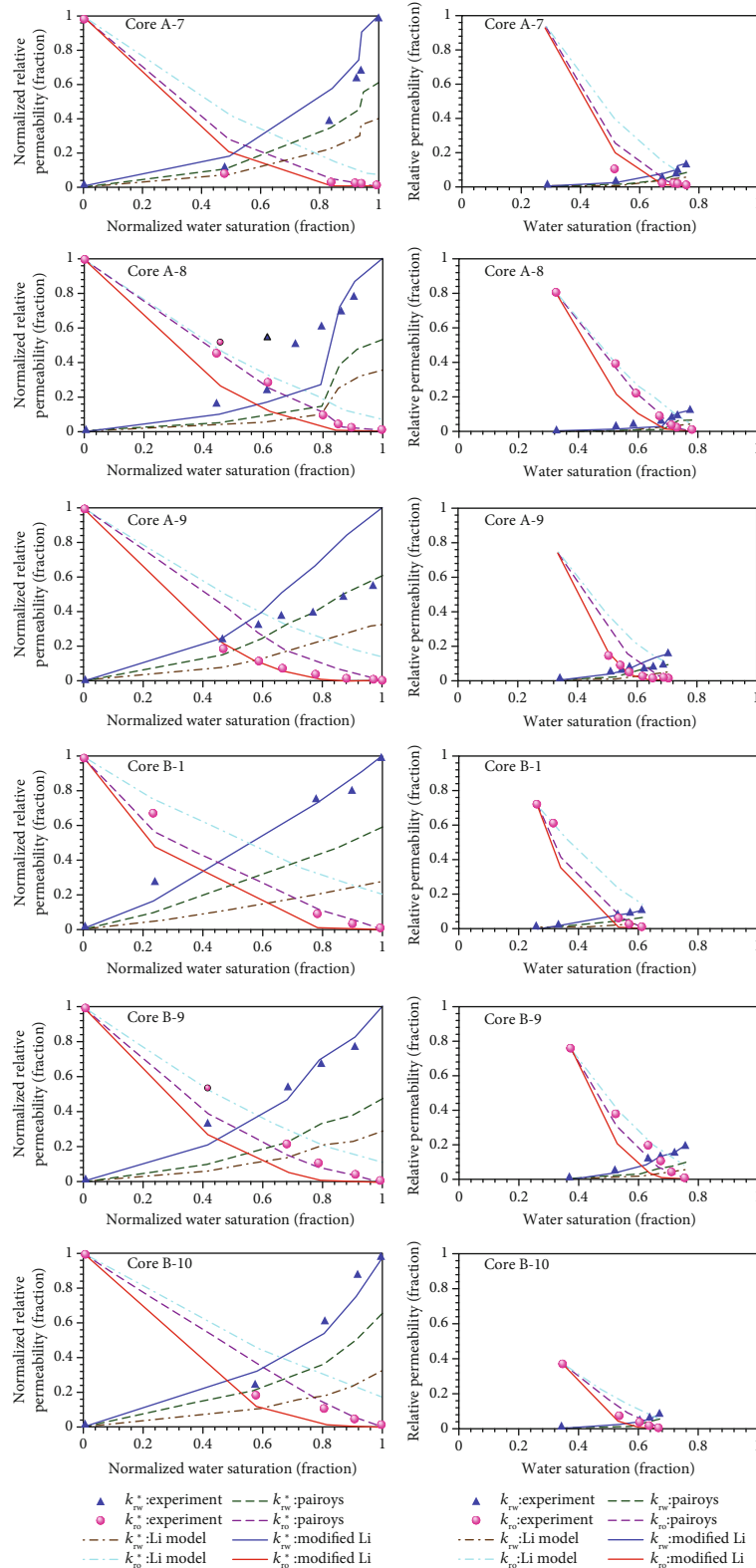


FIGURE 7: Comparison of relative permeability curves in sandstone reservoir.

(Figure 6). The resistivity and relative permeability of core samples with different water saturations were measured.

Core samples from Wells A and B are tested to explore the relationship between resistivity and relative permeabil-

ity. Core samples are divided into two groups. Group I contains less clay and smaller Q_v than group II. The basic physical parameters of cores are shown in Table 1. The salinity of formation water in wells A and B are

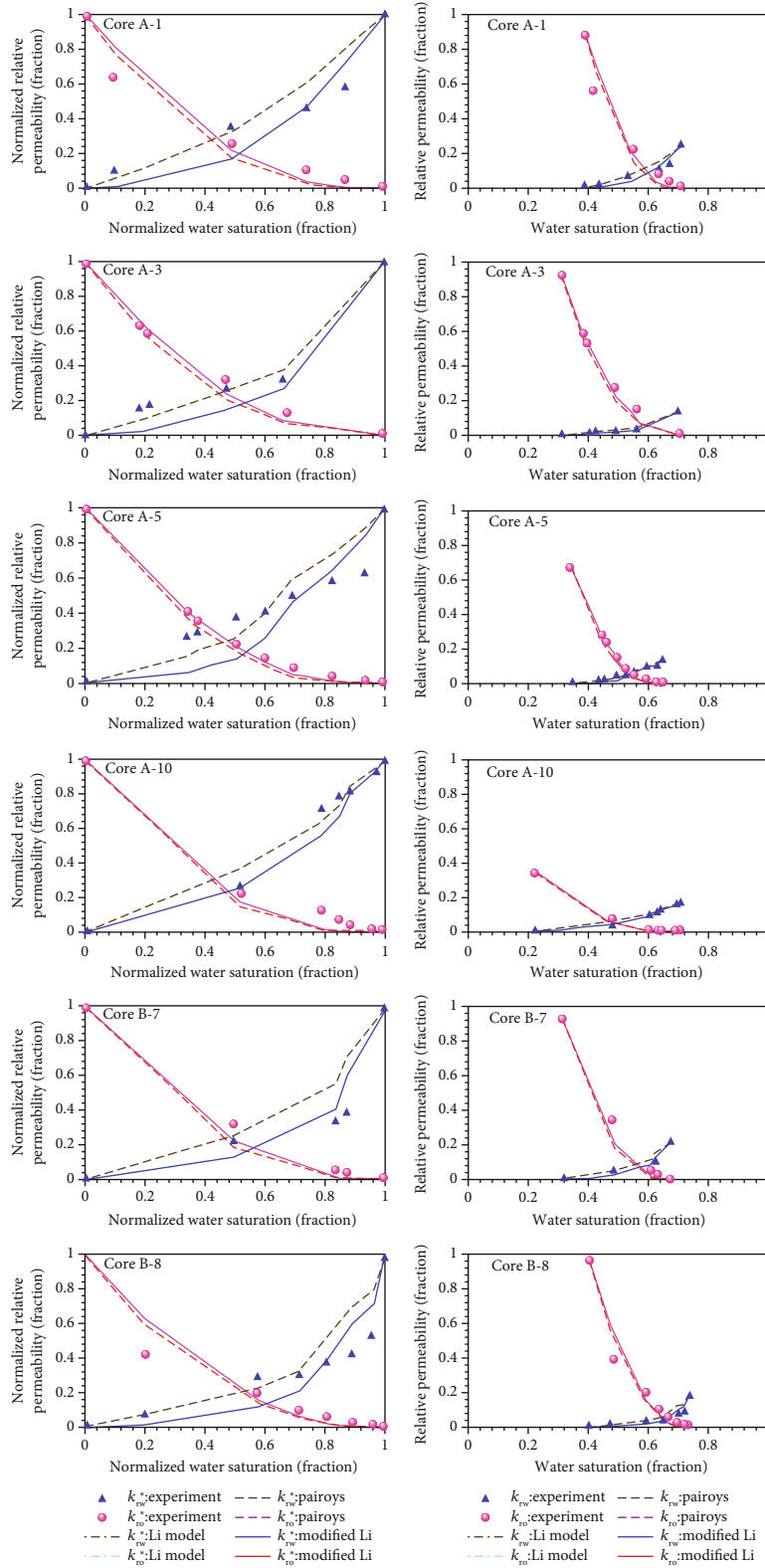


FIGURE 8: Comparison of relative permeability curves in shaly sand reservoir.

7500 ppm and 8000 ppm, respectively. The density of brine used is 1.02 g/cm³. The oil viscosity in both wells is 8.8 mPa s at 20°C, and its density is 0.845 g/cm³.

4.2. Verification of Relationship Models between Resistivity and Relative Permeability of Sandstone. The Li model, modified Li model, and Pairoys model are verified with the

experimental data of core samples in group I. Figure 7 shows the oil-water relative permeability curves of group I cores. In Figure 7(a), the solid blue triangular and pink dots are the normalized water and oil relative permeability obtained from the water displacing oil experiment, respectively; the brown and sky blue chain dotted lines are the normalized water and oil relative permeability calculated with resistivity based on the Li model; the green and purple broken line are the normalized water and oil relative permeability calculated with resistivity based on Pairoys model; and the blue and red solid line are the ones calculated with resistivity based on the modified Li model. Figure 7(a) indicates that the Li model does not work well in the data process of water flooding. The problems of Pairoys model is that the normalization oil relative permeability it calculates is nonnegligibly larger than the experimental value. However, the normalization water and oil relative permeabilities calculated by the modified Li model are in good agreement with experimental data.

Figure 7(b) shows the oil-water relative permeability curve of cores in group I. The water relative permeabilities calculated by the Li model and Pairoys model are smaller than the experimental data, while the oil relative permeabilities are larger. The oil and water relative permeabilities calculated by the modified Li model fit well with the experimental data in sandstone reservoir with less shale contents.

4.3. Verification of Relationship Models between Resistivity and Relative Permeability of Shaly Sandstone. Experiment is designed to measure the resistivity and relative permeability of shaly sandstone samples in group II. Figure 8 shows the comparison of the experimental results and the model calculated results.

Figure 8(a) shows the normalized relative permeability curves, and Figure 8(b) shows the relative permeability curves. The filled dots are the unsteady oil-water relative permeability experiment data, the broken lines are the relative permeability curves calculated with resistivity by the modified Li model, and the solid lines are calculated with resistivity by the DW model. As shown in Figure 8, the Li model, the water relative permeability calculated by the modified Li model fits well with the experimental data, but the calculated oil relative permeability curve is smaller than the experimental data. Meanwhile, the relative permeability curves of oil and water calculated by the DW relative permeability model better fit the experimental data.

5. Conclusions

This study established the relationship model between the resistivity and oil-water relative permeability of the shaly sandstone reservoir based on the rock physics experiment and the logging response of the shaly sandstone reservoir. According to existing research results, the following main conclusions can be drawn.

- (1) In view of the influence of shale, the DW relative permeability model, suitable for shaly sandstone reservoir, was derived to calculate oil-water relative permeability using resistivity based on the dual water

conductivity model, Poiseuille's equation, and Darcy's law.

- (2) According to the sensitivity analysis, with other conditions being the same, the relative permeability of water phase will decrease as the irreducible water saturation increases, residual oil saturation increases, cation exchange capacity of rock increases, or free water salinity decreases.
- (3) With the core water flooding experimental device, the resistivity and oil-water relative permeability of two groups of sandstone samples with different shale contents were tested. The experimental results show that the modified Li model is suitable for clean sandstone reservoirs, and the DW relative permeability model is suitable for shaly sandstone reservoirs.

Data Availability

The data used to support the findings of this study are available from the corresponding author upon request.

Conflicts of Interest

The authors declared that they have no conflicts of interest to this work.

Acknowledgments

The study has been supported by the National Major Science and Technology Projects of China (No. 2017ZX05030-002), by the Natural Science Basic Research Plan in Shaanxi Province of China (Grant no. 2020JQ-747), and by the Scientific Research Plan Projects of Shaanxi Education Department (Grant no. 18JK0517).

References

- [1] M. T. Szabo, "New methods for measuring imbibition capillary pressure and electrical resistivity curves by centrifuge," *Society of Petroleum Engineers Journal*, vol. 14, no. 3, pp. 243–252, 2013.
- [2] G. I. Barenblatt and A. A. Gil'Man, "Nonequilibrium counterflow capillary impregnation," *Journal of Engineering Physics*, vol. 52, no. 3, pp. 335–339, 1987.
- [3] J. Toth, T. Bodi, P. Szucs, and F. Civan, "Direct determination of relative permeability from nonsteady-state constant pressure and rate displacements," *Proceedings of the SPE Production and Operations Symposium*, Oklahoma City, Oklahoma, 2001.
- [4] E. C. Kumbur, K. V. Sharp, and M. M. Mench, "Validated Leverett approach for multiphase flow in PEFC diffusion media," *Journal of The Electrochemical Society*, vol. 154, no. 12, pp. B1295–B1304, 2007.
- [5] A. T. Corey, "The interrelation between gas and oil relative permeabilities," *Producers Monthly*, vol. 19, no. 1, pp. 38–41, 1954.
- [6] R. H. Brooks and A. T. Corey, "Properties of porous media affecting fluid flow," *Journal of the Irrigation and Drainage Division*, vol. 92, no. 2, pp. 61–88, 1966.

- [7] J. F. App and J. E. Burger, "Experimental determination of relative permeabilities for a rich gas/condensate system using live fluid," *SPE Reservoir Evaluation & Engineering*, vol. 12, no. 2, pp. 263–269, 2013.
- [8] W. Wei, J. C. Cai, X. Y. Hu, and Q. Han, "An electrical conductivity model for fractal porous media," *Geophysical Research Letters*, vol. 42, no. 12, pp. 4833–4840, 2015.
- [9] K. Li, B. Hou, H. Bian, H. Liu, C. Wang, and R. Xie, "Verification of model for calculating capillary pressure from resistivity using experimental data," *Fuel*, vol. 252, pp. 281–294, 2019.
- [10] J. C. Cai, W. Wei, X. Y. Hu, and D. A. Wood, "Electrical conductivity models in saturated porous media: a review," *Earth-Science Reviews*, vol. 171, pp. 419–433, 2017.
- [11] J. Cai, Z. Zhang, W. Wei, D. Guo, S. Li, and P. Zhao, "The critical factors for permeability-formation factor relation in reservoir rocks: pore-throat ratio, tortuosity and connectivity," *Energy*, vol. 188, p. 116051, 2019.
- [12] G. E. Archie, "The electrical resistivity log as an aid in determining some reservoir characteristics," *Transaction of American Institute of Mining, Metallurgical, and Petroleum Engineers*, vol. 146, no. 2, pp. 54–62, 1942.
- [13] K. Li and R. N. Horne, "Comparison of methods to calculate relative permeability from capillary pressure in consolidated water-wet porous media," *Water resources research*, vol. 42, no. 6, pp. W06405.1–W06405.9, 2006.
- [14] K. Li and W. Williams, "Determination of capillary pressure function from resistivity data," *Transport in Porous Media*, vol. 67, no. 1, pp. 1–15, 2007.
- [15] I. A. Mohammed and D. Birol, "An improved relative permeability model to match displacement experiments," *International Journal of Applied Science and Technology*, vol. 1, no. 2, pp. 41–58, 2011.
- [16] A. Valdes-Perez, H. Pulido, H. Cinco-Ley, and G. Galicia-Muñoz, "Discretization of the resistivity, capillary pressure and relative permeability for naturally fractured reservoirs. Proceedings," *Proceedings of the Thirty-Seventh Workshop on Geothermal Reservoir Engineering*, Stanford, California, 2012.
- [17] F. Pairoys, A. Al-Zoukani, and A. Keskin, "Interrelationship between resistivity and relative permeability of a carbonate rock during drainage and imbibition experiments," *Proceedings of the International Symposium of the Society of Core Analysts*, Napa Valley, California, USA, 2013.
- [18] K. Li and R. N. Horne, "A semianalytical method to calculate relative permeability from resistivity well logs," *Proceedings of the SPE Annual Technical Conference and Exhibition*, Dallas, Texas, 2005.
- [19] F. Pairoys, "Two-phase semi-dynamic method with electrical measurements: determination of relative permeability and capillary pressure from a single experiment," *Proceedings of the International Symposium of the Society of Core Analysts*, Avignon, France, 2014.
- [20] H. Y. Bian and K. Li, "A modified method and experimental verification for estimating relative permeability from resistivity logging data," *Proceedings of the International Petroleum Technology Conference*, Kuala Lumpur, 2014.
- [21] H. Q. Xia, X. H. Zhang, and X. J. Liu, "A new approach to calculate clay bound water volume and cation exchange capacity," *Journal of Southwest Petroleum Institute*, vol. 22, no. 1, pp. 55–58, 2000.
- [22] R. Zhang, "An approach to the origin of anomalous shape of oil-water relative permeability curves in sandstone and conglomerate reservoirs," *Petroleum Exploration and Development*, vol. 23, no. 2, pp. 79–83, 1996.
- [23] H. M. Gao, H. Q. Jiang, M. F. Chen, and Y. F. He, "Microscopic simulation of the effect of microscopic reservoir parameters on oil-water relative permeability," *Petroleum Exploration and Development*, vol. 33, no. 6, pp. 734–737, 2007.
- [24] G. M. Lin-peng, Z. S. Guo-hua, and L. F. Li-xia, "Feature controls and influence for petroleum development of relative permeability curve in low permeable sandstone reservoirs," *Acta Sedimentologica Sinica*, vol. 26, no. 3, pp. 445–451, 2008.
- [25] H. Z. Cui, G. Q. Yao, and F. D. Zhou, "Type and the variety characteristics of relative permeability curve in low permeable glutenite oil reservoirs," *Geological Science and Technology Information*, vol. 22, no. 1, pp. 88–91, 2003.
- [26] J. M. He, "Influencing factors of abnormal oil/water relative permeability curve," *Petroleum Geology and Recovery Efficiency*, vol. 16, no. 2, pp. 74–76, 2009.

Research Article

Multifractal Analysis of Pore Structure and Evaluation of Deep-Buried Cambrian Dolomite Reservoir with Image Processing: A Case from Tarim Basin, NW China

Xiaojun Zhang,^{1,2} Haodong Han ,³ Jun Peng ,⁴ and Yingchun Gou^{1,2}

¹Research Institute of Petroleum Exploration & Development-Northwest, Petrochina, Lanzhou 730020, China

²Key Laboratory of Reservoir Characterization, CNPC, Lanzhou 730020, China

³Chengdu Center of China Geological Survey, Chengdu 610081, China

⁴College of Geosciences and Technology, Southwest Petroleum University, Chengdu 610500, China

Correspondence should be addressed to Haodong Han; hanhaodong@163.com

Received 17 December 2019; Revised 6 July 2020; Accepted 10 July 2020; Published 21 September 2020

Academic Editor: Wei Wei

Copyright © 2020 Xiaojun Zhang et al. This is an open access article distributed under the Creative Commons Attribution License, which permits unrestricted use, distribution, and reproduction in any medium, provided the original work is properly cited.

Reservoir pore space assessment is of great significance for petroleum exploration and production. However, it is difficult to describe the pore characteristics of deep-buried dolomite reservoirs with the traditional linear method because these rocks have undergone strong modification by tectonic activity and diagenesis and show significant pore space heterogeneity. In this study, 38 dolostone samples from 4 Cambrian formations of Tarim Basin in NW China were collected and 135 thin section images were analyzed. Multifractal theory was used for evaluation of pore space heterogeneity in deep-buried dolostone based on thin section image analysis. The physical parameters, pore structure parameters, and multifractal characteristic parameters were obtained from the digital images. Then, the relationships between lithology and these parameters were discussed. In addition, the pore structure was classified into four categories using *K*-means clustering analysis based on multifractal parameters. The results show that the multifractal phenomenon generally exists in the pore space of deep-buried dolomite and that multifractal analysis can be used to characterize the heterogeneity of pore space in deep-buried dolomite. For these samples, multifractal parameters, such as α_{\min} , α_{\max} , $\Delta\alpha_L$, $\Delta\alpha_R$, Δf , and AI, correlate strongly with porosity but only slightly with permeability. However, the parameter $\Delta\alpha$, which is usually used to reveal heterogeneity, does not show an obvious link with petrophysical properties. Of dolomites with different fabrics, fine crystalline dolomite and medium crystalline dolomite show the best petrophysical properties and show significant differences in multifractal parameters compared to other dolomites. More accurate porosity estimations were obtained with the multifractal generalized fractal dimension, which provides a new method for porosity prediction. The various categories derived from the *K*-means clustering analysis of multifractal parameters show distinct differences in petrophysical properties. This proves that reservoir evaluation and pore structure classification can be accurately performed with the *K*-means clustering analysis method based on multifractal parameters of pore space in deep-buried dolomite reservoirs.

1. Introduction

Deep-buried dolomite reservoirs have strong heterogeneity and complex pore structure [1]. Their pore geometry and structure are strongly influenced by tectonic factors, diagenesis, and chemical reactions between rock and different fluids [2, 3]. And they generally show various types of pore space, complex pore structure, and strong reservoir heterogeneity [1]. It will increase the difficulty of characterization on pore

structure, feature description, and reservoir evaluation of deep-buried dolomite reservoirs.

It is well known that microscopic pore structure features control the reservoir quality. Therefore, clarifying the microscopic characteristics and heterogeneity of pore structure is very important for understanding the macroscopic characteristics of a reservoir [4]. However, it is difficult to characterize micropores' heterogeneity with traditional Euclidean geometry. Fortunately, fractal geometry,

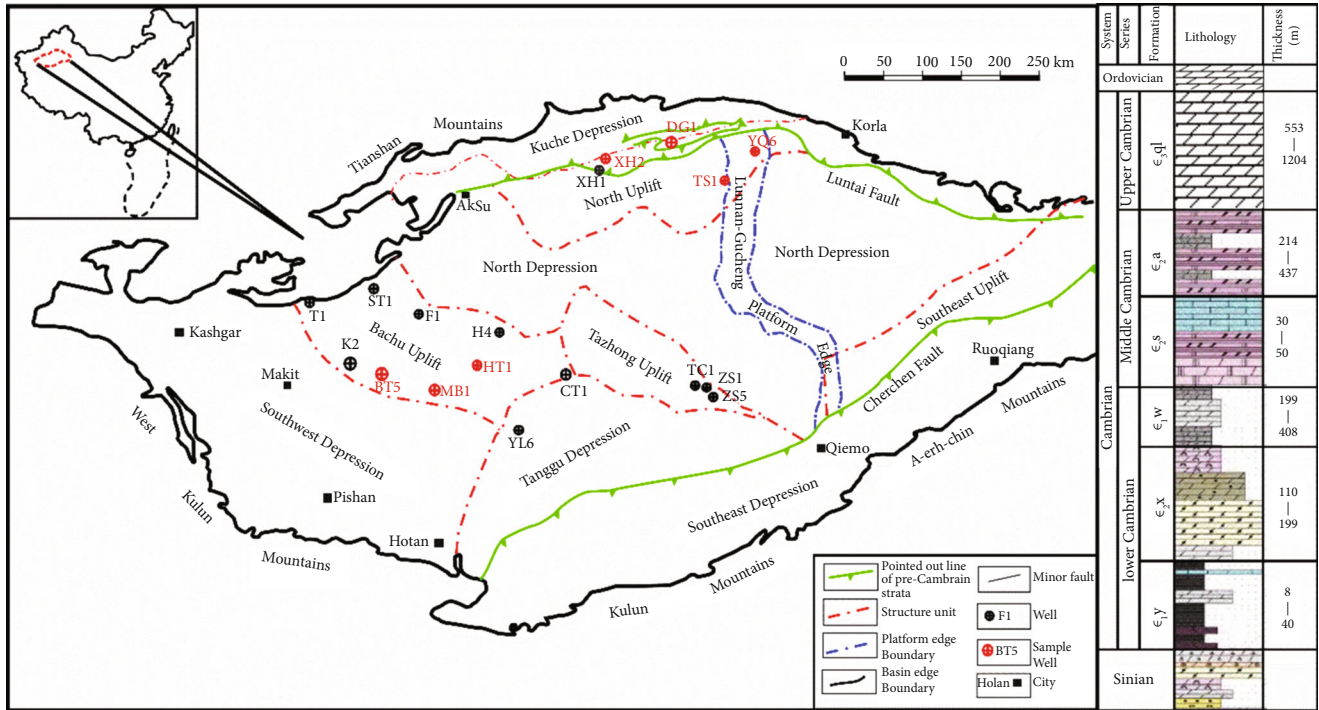


FIGURE 1: Basic information of the study area and distribution of the sampling well.

created by Mandelbrot [5], has been introduced into analyses of the pore distribution properties of sedimentary rocks, and it plays an important role in characterization of heterogeneity and self-similarity [6–8]. Compared to classical geometry, fractal geometry reveals the deterministic and stochastic unity laws of regularity and chaos in pore structure [9–14]. Furthermore, multifractal analysis is a multiscale method based on power-law relationships and can describe local irregular fluctuations more effectively than the monofractal method [15–17]. In multifractal analysis, the self-similarity measure can be regarded as the singularity strength and parameters of the multifractal spectrum through scale decomposition of interrelated fractal series [17–20]. To date, multifractal analysis has been widely used to depict the statistical properties of scale variation for studies in soil science, geosciences, and materials due to its advantage in heterogeneity analysis [21–27].

Fractal and multifractal behavior has been observed in sedimentary rocks and soil from scanning electron microscopy (SEM) [6, 28, 29], X-ray computed tomography (CT) [12, 30], nuclear magnetic resonance (NMR) [18, 31, 32], and mercury intrusion analysis of core plugs [23, 33–36]. Fractal geometry and the multifractal method have been widely used to describe the porosity and permeability of porous media and clastic rocks [37–40]. However, only a few of these studies have focused on carbonate rocks [16, 20, 41–44], and research on deep-buried dolomite is even more limited. Accordingly, further study on deep-buried dolomites within the framework of multifractal theory is needed in an attempt to expand and deepen the application of this powerful mathematics tool in different fields of the earth sciences. Meanwhile, a new evaluation method based

on multifractal theory is proposed to study the characteristics of pore space and pore structure in dolomite reservoirs.

This section analysis is an easy way to determine the two-dimensional topological properties of pore space and pore throat size in rocks, despite its lower resolution and magnitude compared to SEM and CT. In this study, multifractal analysis and digital image analysis of thin section images were used to extract quantitative information reflecting the distribution of pore space and the pore structure characteristics. Thirty-eight Cambrian dolomite core plug samples from Tarim Basin in northwestern China were chosen as the study objects, and casting thin section images were obtained. Then, based on image analysis, the multifractal behavior of pore space in deep-buried dolomite and the application of multifractal theory for heterogeneity evaluation were analyzed, and the relationships between multifractal parameters and the physical properties of different lithologies were studied. Finally, classification of the pore structure was accomplished with *K*-means clustering analysis of multifractal parameters. The results are of great significance for quantitative heterogeneity characterization, pore structure evaluation, and petroleum exploration in deep-buried dolomite reservoirs.

2. Methodology

2.1. Study Area and Sampling. Tarim Basin located in northwestern China is the largest inland basin with total area of $53 \times 10^4 \text{ km}^2$ in China. It is bounded by West Kunlun Mountains, Tianshan Mountains, Kunlun Mountains, and Altun Mountains (Figure 1). For detailed geological setting and stratigraphic column of the basin, the reader can refer to Du and

Pan [45]. In the study, up to 38 dolostone samples were collected from different formations of the Cambrian strata in 7 wells to estimate the petrophysical properties. These samples were made into a plunger for the petrophysical test and molded into thin section for image processing, respectively. The information of each sample could be seen in Table 1.

2.2. Experiments. Helium porosity and permeability were measured by CMS-300 Automated Permeameter (Core Measurement Systems) under confining pressure of 34.5 MPa. For image analysis, casting thin sections were produced with the following procedure: (1) set samples in a glass tube at constant temperature of 100°C for 2 h; (2) reduce the glass tube to a vacuum with pressure 0.09 MPa and keep samples in it for 1 h; (3) inject blue epoxy resin into samples at pressure of 8 MPa and temperature of 100°C for 12 h; and (4) after natural cooling, polish the samples into thin sections with thickness 20 μm , and mount each chip on a glass slide. Therefore, pore spaces in thin section were filled by blue epoxy resin and could be easily distinguished from matrix under the microscope. For image and multifractal analyses, chromo-photographs were captured from representative views of each thin section. These collected images with different magnifications, such as 25x, 50x, 100x, and 400x, can reveal both macropores and micropores. All images were obtained using the transmission mode of BX51 microscope in State Key Laboratory of Oil and Gas Reservoir Geology and Exploitation, Southwest Petroleum University, China.

2.3. Image Analysis. Casting thin section observation is an inexpensive tool for characterizing pore structure in rocks and has been widely used in heterogeneity of rock microscopic pores [44]. By image processing on thin section image, the pore type, pore shape, pore scale, and pore throat type could be acquired. The image analysis consists of image filtering, image segmentation, connected domain identification, and statistics of pore size distribution (PSD). First, median filtering was used to eliminate noise in images. The K -nearest neighbor (KNN) classification algorithm is implemented in image segmentation for getting binary image, where the pixel values one and zero represent pore and matrix, respectively. Then, the coordinates and area of each pore were obtained with the connected domain identification method [46]. Finally, parameters such as total porosity (φ), PSD, average pore radius (r_b), average pore throat radius (r_t), and permeability (K) value were calculated with the following formulas [47–50].

$$\varphi = \frac{A_{\text{pore}}}{A_{\text{total}}}, \quad (1)$$

$$r_b = \frac{\sum_{i=1}^{\text{Num}} r_i A_i}{A_{\text{total}}}, \quad (2)$$

$$r_t = \frac{\sum_{i=1}^{\text{Num}} r_{ti} A_i}{A_{\text{total}}}, \quad (3)$$

where A_{pore} is the pore area in the image, A_{total} is the total area of the image, r_i is the mean radius of each pore, A_i is the area of i th pore, Num is the total number of pores, and r_{ti} is the minimum radius of each pore.

According to the values of φ , r_b , and r_t , the permeability value K could be obtained with the following formula [51]:

$$K = \frac{\varphi r_b^2}{\tau^2} \cdot \frac{[\ln(r_b/r_t)]^2}{[(r_b/r_t)^2 - 1] \cdot [(r_b/r_t)^2 - (r_t/r_b)^2]}, \quad (4)$$

where τ is pore tortuosity in samples, and here, its value was assumed to be 1. The estimated values of porosity and permeability are shown in Table 1.

2.4. Multifractal Analysis. For multifractal analysis, a cubic box of size δ was used to cover the pore space. Assuming that there are m_i pore pixels in the i^{th} box ($1 \leq i \leq n(\delta)$), $n(\delta)$ denotes the number of boxes required to cover the pore space at the scale of δ and the total number of pixels in the pore space is M . The measurement $\mu_i(\delta)$, which denotes the local probability of finding a box to cover the pore space at the scale of δ , can be defined as follows [52]:

$$\mu_i = \frac{m_i}{M}. \quad (5)$$

With respect to the fluctuation in local porosity, a local crowding index α_i can be defined for the i^{th} box, i.e., the singularity exponent, and it holds that

$$\mu_i(\delta) \propto \delta^{\alpha_i}. \quad (6)$$

Two approaches are available to compute the multifractal spectrum: the moment method and the direct method [52]. In both methods, a weighted sum over all boxes must be performed to yield the partition function $\chi(q, \delta)$ as follows:

$$\chi(q, \delta) = \sum_i [\mu_i(\delta)]^q = \sum_i \left(\frac{m_i}{M}\right)^q, \quad (7)$$

where the variable q denotes the order of moment for μ_i ; it is clear to note that different q values actually allow probing of the contribution to $\chi(q, \delta)$ from boxes with different μ_i . In particular, at negative q values, $\chi(q, \delta)$ is dominated by boxes with small μ_i , while at positive q values, $\chi(q, \delta)$ is dominated by boxes with large μ_i . For a multifractal measure, it holds that

$$\chi(q, \delta) \propto \delta^{\tau(q)}, \quad (8)$$

where the mass exponent $\tau(q)$ is a nonlinear function of q but independent on δ ; the singularity exponent α and the Hausdorff dimension $f(\alpha)$ can be determined with the Legendre transformation:

$$\alpha(q) = \frac{d\tau(q)}{dq}, \quad (9)$$

TABLE 1: Basic information, petrophysical data from helium porosimetry, and image analysis of samples in the study.

Sample	Well	Depth	Formation	Lithology	Image Number	φ (%)	φ_I (%)	φ_M (%)	K (mD)	K_I (mD)
S1	BT5	4812.9	ϵ_3 ql	MD	4	0.80	2.99	0.79	0.001	0.809
S2	BT5	5782.08	ϵ_1 x	MD	6		7.48	2.01		0.889
S3	BT5	5783.95	ϵ_1 x	MD	4	4.30	8.56	2.83	0.540	3.072
S4	BT5	5784.8	ϵ_1 x	MD	6	2.50	10.20	2.74	0.01	0.558
S5	BT5	5785.12	ϵ_1 x	FD	4	3.30	14.87	4.29	1.160	7.365
S6	BT5	5785.95	ϵ_1 x	FD	6		7.24	3.07		1.703
S7	DG1	6216.87	ϵ_3 ql	SD	3	1.00	2.06	2.27	0.020	0.011
S8	DG1	6217.99	ϵ_3 ql	GD	2	1.00	0.96	0.97	0.020	0.059
S9	DG1	6256.34	ϵ_3 ql	FD	4	2.70	12.25	3.17	22.600	3.587
S10	DG1	6295.28	ϵ_3 ql	FD	3		5.46	1.73		0.644
S11	DG1	6297.6	ϵ_3 ql	FD	2		1.83	0.81		0.531
S12	HT1	6163.85	ϵ_2 a	GD	2	0.90	0.86	0.48	20.877	0.013
S13	XH2	5350.45	ϵ_3 ql	FD	5	4.80	18.40	5.24	4.050	2.977
S14	XH2	5355.3	ϵ_3 ql	SD	4		13.98	5.78		1.627
S15	XH2	5515.87	ϵ_3 ql	SD	3		3.36	0.79		0.439
S16	XH2	5517.68	ϵ_3 ql	FD	5		4.32	2.17		0.153
S17	XH2	5590.4	ϵ_3 ql	DM	2		0.83	1.13		0.002
S18	XH2	5590.9	ϵ_3 ql	DM	2		1.38	1.74		0.005
S19	XH2	5595.76	ϵ_3 ql	GD	5		4.43	1.76		0.527
S20	YQ6	7059.35	ϵ_3 ql	CD	3		3.50	2.42		0.240
S21	YQ6	7060.43	ϵ_3 ql	CD	3		2.43	1.48		0.364
S22	YQ6	7061.07	ϵ_3 ql	CD	5	1.80	2.21	1.77	1.350	0.099
S23	YQ6	7062.3	ϵ_3 ql	MD	3	0.30	1.43	0.51	0.060	0.132
S24	YQ6	7118.5	ϵ_3 ql	MD	5	2.20	11.45	3.52	0.450	1.187
S25	YQ6	7118.78	ϵ_3 ql	FD	3	2.90	3.58	1.28	0.130	0.590
S26	YQ6	7119.3	ϵ_3 ql	MD	3	2.70	2.69	1.46	0.020	0.327
S27	YQ6	7119.42	ϵ_3 ql	FD	4	0.80	1.32	1.08	0.700	0.006
S28	YQ6	7119.93	ϵ_3 ql	FD	4	2.80	5.03	2.82	0.070	1.552
S29	YQ6	7314.05	ϵ_3 ql	SD	3	0.60	1.11	0.55	0.003	0.033
S30	YQ6	7313.74	ϵ_3 ql	SD	3	0.60	2.13	0.42	0.003	0.331
S31	BT5	4811.6	ϵ_3 ql	FD	3	0.20	1.57	1.08		0.034
S32	MB1	6002.98	ϵ_2 s	SD	3	2.40	5.07	3.58	12.800	0.089
S33	MB1	6008.59	ϵ_2 s	SD	3	5.80	5.55	6.42	3.170	0.097
S34	MB1	6009.07	ϵ_2 s	GD	3	3.20	1.70	1.44	0.740	0.024
S35	TS1	7105.43	ϵ_3 ql	DM	3	0.6	1.04	1.16	0.6	0.913
S36	TS1	7268.10	ϵ_3 ql	FD	2	3.7	2.92	1.73	0.03	2.677
S37	TS1	7875.60	ϵ_3 ql	FD	4	3.7	8.09	4.39	34.14	3.772
S38	TS1	8407.56	ϵ_3 ql	SD	3	9.10	15.32	8.90	4.160	2.270

The abbreviation “ ϵ_3 ql” represents Lower Qulitage Formation of Upper Cambrian; “ ϵ_2 s” represents Shayilik Formation of Middle Cambrian; and “ ϵ_1 x” represents Sholbrak Formation of Lower Cambrian. φ_I is the porosity obtained with Equation (1), φ_M is the porosity obtained with Equation (16), and K_I is the permeability computed from Equations (2)–(4) with images.

$$f(\alpha(q)) = q \cdot \alpha(q) - \tau(q). \quad (10)$$

The multifractal generalized dimensions D_q of the q^{th} order are defined as

$$D_q = \frac{1}{q-1} \lim_{\delta \rightarrow 0} \frac{\ln [\chi(q, \delta)]}{\ln (\delta)}. \quad (11)$$

When $q = 1$, the above equation can be expressed as

$$D_1 = \lim_{\delta \rightarrow 0} \left(\frac{\sum_{i=1}^{N(\delta)} \mu_i(\delta) \ln (\mu_i(\delta))}{\ln (\delta)} \right). \quad (12)$$

The multifractal generalized dimensions D_q are related to the mass exponent $\tau(q)$ by

$$\tau(q) = (q-1)D_q. \quad (13)$$

The $q-D_q$, $q-\alpha$, and $\alpha-f(\alpha)$ construct the powerful tool for characterizing the heterogeneity of pore structure.

2.5. Porosity Estimation Based on Multifractal Analysis. It is clear that the porosity of dolomite can be estimated using the total number and area of boxes as follows:

$$\phi = \frac{N(\delta) \cdot \delta^2}{A_{\text{total}}}, \quad (14)$$

where $N(\delta)$ is the box number for pores, δ is the size of the box, and A_{total} is the total area of the image. Using the box-counting method for fractal and multifractal theory, the total number of boxes covering the pore space can be expressed as the following formula:

$$N(\delta) \propto \delta^{-D_0}, \quad (15)$$

where D_0 is the capacity dimension obtained from Equation (11) when q is equal to zero. Then, the porosity can be calculated with the box size δ and the capacity dimension D_0 as follows:

$$\phi \propto \frac{\delta^{2-D_0}}{A_{\text{total}}}. \quad (16)$$

In order to facilitate the calculation, A_{total} was assumed to be 1, and δ was set as the reciprocal of the pixel number for each column of the image. Therefore, the porosity can be estimated with the pixel number in the image and the capacity dimension.

3. Results

3.1. Porosity, Permeability, and Micropore Characteristics of Dolomite. Dolomite is widespread in Cambrian strata of Tarim Basin. According to classification and nomenclature schemes of carbonate rocks suggested by Dunham [53], the dolomite in the study area can be divided into dolomicrite (DM), crystalline dolomite, and grain dolomite (GD). In addition, crystalline dolomites are subdivided into silty crystalline dolomite (SD), fine crystalline dolomite (FD), medium crystalline dolomite (MD), and coarse crystalline dolomite (CD) in accordance with the crystal size.

The porosity determined from the helium porosimetry test shows that these samples have low porosity values ranging from 0.2% to 9.1% (Table 1) and wide permeability values ranging from 0.003 mD to 34.14 mD. The Cambrian dolomite contains a variety of reservoir spaces such as vugs, intergranular pores, intergranular dissolved pores, and fractures. Intergranular or intercrystal dissolved pores are mainly developed in the silty, fine, and medium crystalline dolomites; intercrystalline pores mainly existed in the silty and fine crystalline dolomites; and fractures are widely distributed in various types of dolomites. Typically, intergranular dissolved pores are connected by microfractures or flat pore

throats. In addition, some throats and pores filled by bitumen indicate that the rocks have experienced oil and gas accumulation and filling.

The shape and size of intergranular or intercrystal dissolved pores are mainly controlled by the crystal structure and morphology. In general, compared to the other dolomites, the fine crystalline dolomite and medium crystalline dolomite with high reservoir quality and permeability are the most favorable reservoir rocks. As shown in Figure 2, there are obvious differences in pore type and porosity between the various dolomite types constituting the Cambrian dolomite formations of Tarim Basin.

The microcrystalline dolomite is mainly formed in tidal flat environment with arid climate at the pencontemporaneous stage. It formed from the Mg^{2+} rich in brine replacing Ca^{2+} in marl sediment. Due to the relatively fast crystallization speed and without being affected by later diagenesis, microcrystalline dolomites are usually with fine, poor euhedral crystals and close contact. Its porosity and permeability are poor and with average value of 2.1% and 0.175 mD, respectively (Table 1). The microcrystalline dolomite often shows the structure of laminae and bird eyes and develops a small amount of cracks and sutures mostly filled by calcite, quartz, gypsum, and anhydrite (Figure 2(a)). Thus, it is difficult to become an effective reservoir.

Silty dolomite formed from the recrystallization of microcrystalline dolomite in shallow burial environment. It performs as small crystal size, poor subhedral crystal, dirty crystal surface, and with contact each other. Cloudy centers and clear borders can be seen in some silty dolomite crystals. In this type of dolomite, dissolved pores and intercrystalline and look like pinhole and with dense distribution. The pore space performs as irregular harbor and with homogeneous pore size (Figure 2(b)).

3.2. Pore Characteristics. Sedimentation is the most important factor, which provides the material foundation for the primary porosity and pore development in dolomite. Typically, carbonates with high primary porosity form in high-energy environments, such as granular beaches and microbial mounds. However, tectonic activity also plays an important role in modifying porosity and pore space in dolomite. For example, as a result of tectonic uplift, buried carbonate rocks may be exposed at the surface and dissolved by atmospheric freshwater or karstification, such that large amounts of intergranular dissolved pores form in reservoir rocks. Alternatively, in the vicinity of tectonic fault zones, intensive formation of concentrated fracture networks may provide channels for geofluid flow. Acids contained in these fluids can dissolve carbonate minerals, form pores along fractures, and increase the porosity. Finally, the comprehensive transformation and alteration by various diagenetic processes in dolomite determine the final state of the pore space and porosity in reservoir rocks.

The image analysis results show that significant differences in porosity and pore size distribution exist in deep-buried dolomites with different crystal sizes and the pore size distribution reveals strong heterogeneity. As shown in Figure 3, the samples numbered S2, S32, and S22 are fine

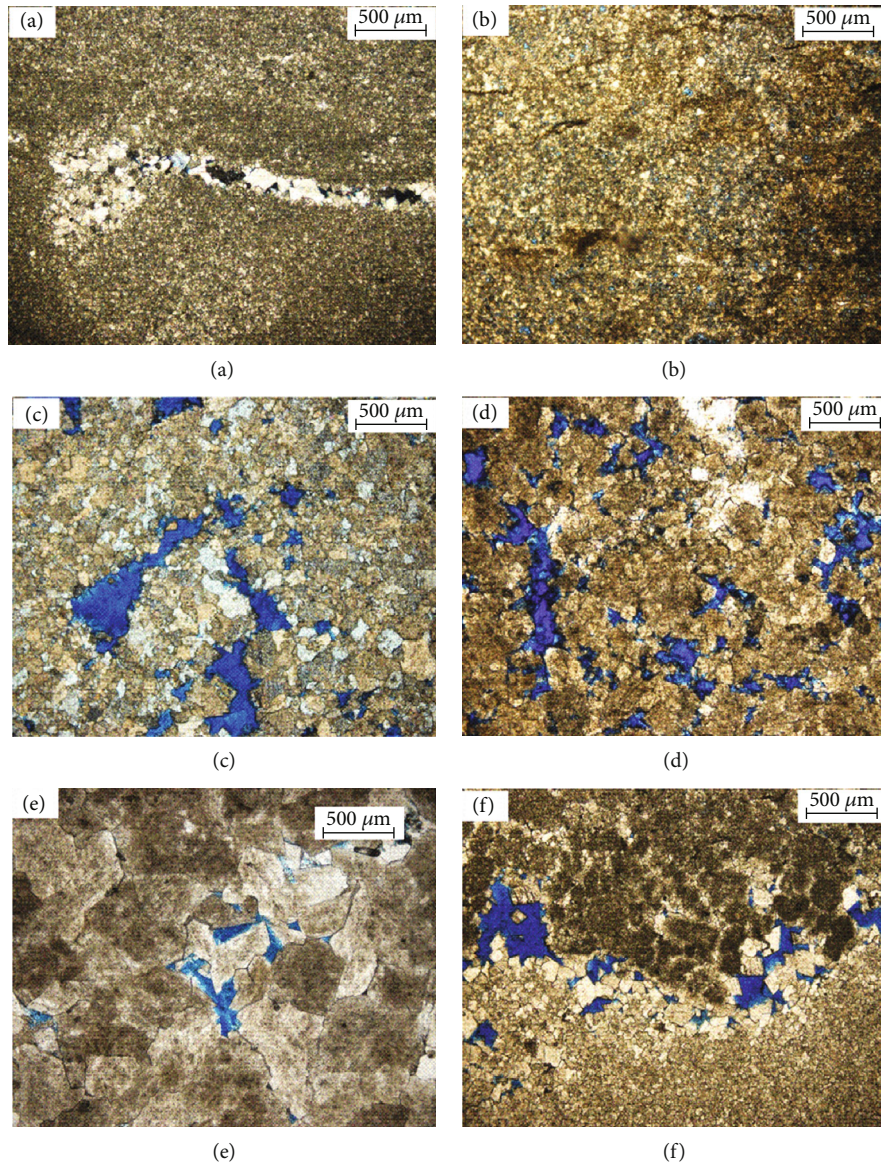


FIGURE 2: The thin section images of different types of dolomite. (a) Thin section image of MD sample S18 with low porosity value 1.38%. It shows that the intergranular pores are not developed and the fractures are filled with quartz, asphalt, and other minerals. (b) Image of SD sample S32 with porosity 5.07%. The pore space consists of medium and small intergranular pores and dissolved pores. (c) Image of FD sample S5 with porosity 14.87%. The pores are mainly larger intergranular dissolved pores. (d) Image for MD sample S4 with porosity 10.2%. Intergranular pores and intergranular dissolved pores with large size mainly develop in such type of dolomite. (e) Image of CD sample S22 with porosity 2.21%. The intergranular pores were slightly developed. (f) Image of GD sample S19 with porosity 4.43%. Dolarenite was recrystallized as fine crystalline dolomite. The intergranular dissolved pore with medium scale distributes along fractures.

crystalline dolomite, silty crystalline dolomite, and medium crystalline dolomite, respectively.

In the fine crystalline dolomite sample (S2), with porosity of 9.5%, large intercrystalline pores are well developed. In the silty crystalline dolomite sample (S32), with porosity of 5.1%, intercrystalline pores are well developed due to dissolution and dolomitization in the seepage-reflux model. As indicated by sample S32, the silty crystalline dolomite evolved from lagoon sediments containing gypsum deposited during evaporation. During the syngenetic period, the silty dolomite formed due to evaporation pump dolomitization. When sea level fell, the silty crystalline dolomite formation was exposed

at the surface and underwent dissolution by freshwater, which formed the intergranular dissolved pores and gypsum mold pores. During the later burial stage, fractures formed due to tectonic activity and were filled by organic acid and asphalt from pyrolysis of hydrocarbons. The organic acid dissolved residual gypsum and soluble calcite, which increased the intergranular dissolved pores. In other words, the early gypsum and small dolomite crystal size determine the pore size ranging from small to medium scale. However, in the medium crystalline dolomite sample (S22) with a low porosity value of 2.3%, only a few intergranular pores and microfractures were developed. Due to hydrothermal filling,

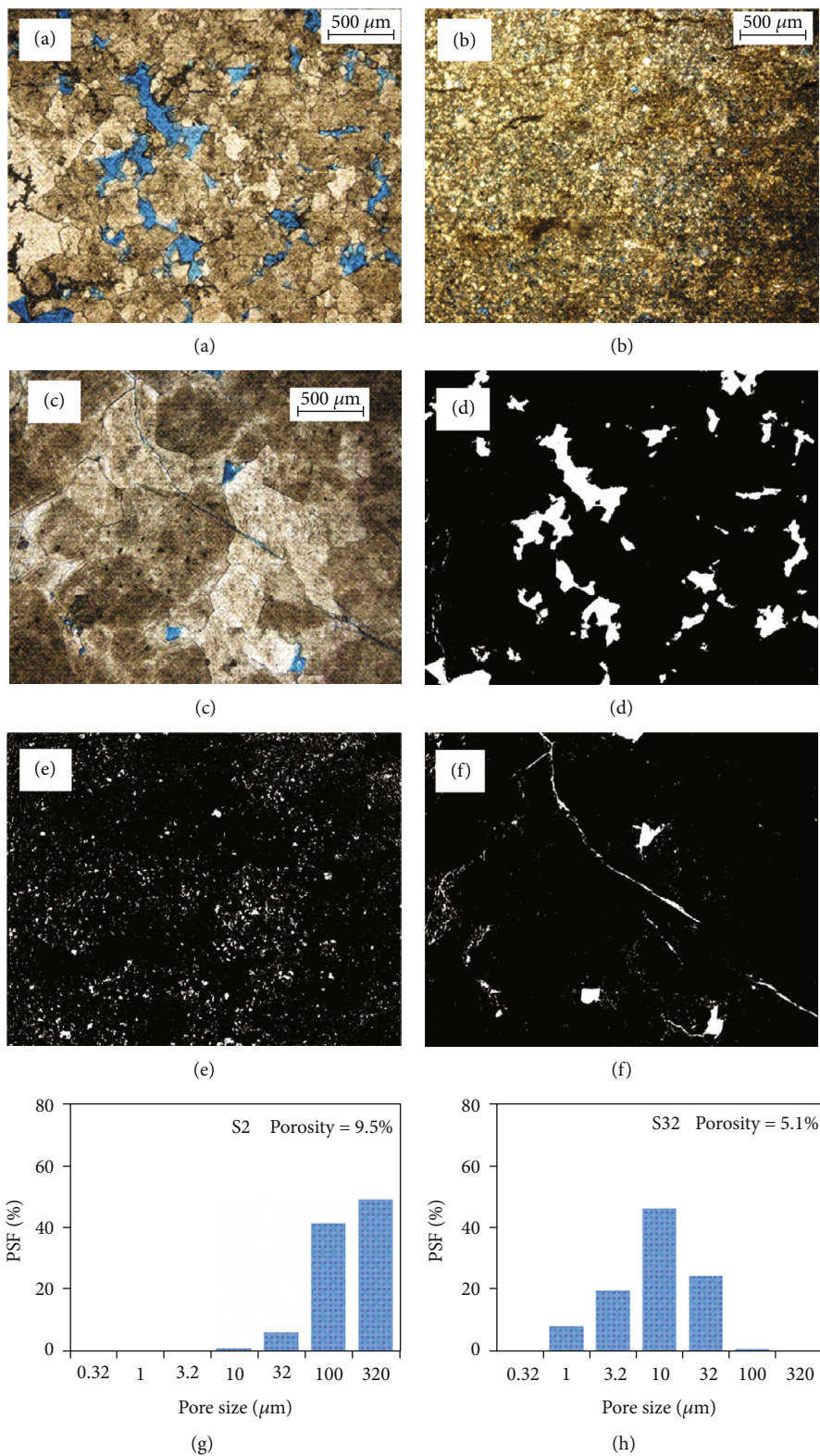


FIGURE 3: Continued.

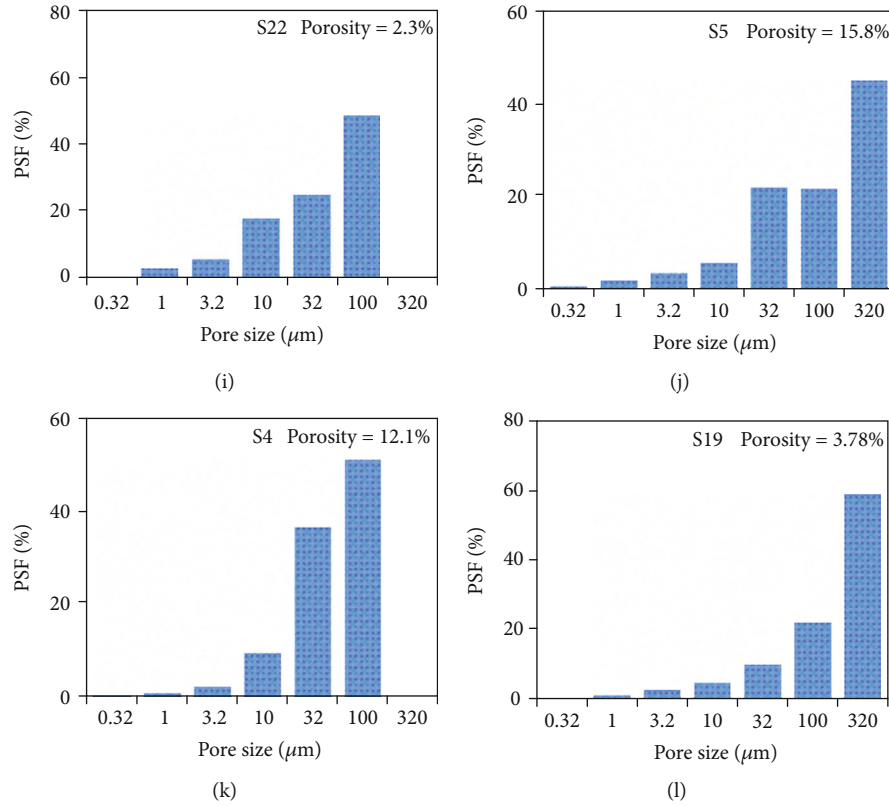


FIGURE 3: Thin section images, binary images, and pore size distribution of dolomite samples. (a) Inter-crystalline pores and inter-crystal dissolved pores in sample S2, well BT5, 5782.08 m, ϵ_{1x} , medium crystalline dolomite. (b) Inter-crystal dissolved pores in sample S32, well MB1, 6002.98 m, ϵ_{2s} , silty crystalline dolomite. (c) Fracture and inter-crystal dissolved pores in sample S22, well YQ6, 7061.07 m, ϵ_{3ql} , coarse crystalline dolomite. (d–f) The binary image of samples S2, S32, and S22, where the white and black pixel represents pore and solid matrix, respectively. (g–l) The pore size distribution and porosity of samples S2, S32, S22, S5, S4, and S19 corresponding to images in Figure 2 and this figure.

pores in the coarse crystalline dolomite were filled by large saddle dolomite crystals and were severely diminished. Only a few fine pores and fractures remained. These fractures and dissolved pores were formed under late stress conditions and were distributed along the grain boundaries.

The pore size distributions in samples S22 and S32 show a wide scale range and stronger heterogeneity than that in sample S2. The tiny crystals in sample S32 determine the pore scale, producing small- and medium-scale pores, whereas in the coarse crystalline dolomite, the coarse crystals are more difficult to dissolve completely but easily form fractures and dissolved pores along the crystal edges under stress action and dissolution (Figure 3).

3.3. Multifractal Analysis on Pores of Dolomite. In this study, the order of moment q is selected from -5 to 5 with steps of 0.5. The value of $\chi(q, \delta)$ at q of $\pm 5, \pm 4, \pm 3, \pm 2, \pm 1$, and 0 are shown in Figure 4(a). The values $\tau(q)$, the slope of these $\chi(q, \delta) - q$ lines, can be determined with the least square fitting method, as shown in Figure 4(b). Therefore, the singularity exponent $\alpha(q)$ and multifractal spectrum $f(\alpha)$ can be obtained with the direct method via Equations (9) and (10), and results are shown in Figures 4(c) and 4(d). The program for calculating the fractal dimension,

singularity exponent, mass exponent, and multifractal spectrum of pores in dolomite from thin section images has been designed. The characteristic parameters of multifractal spectra were extracted from binary images with a batch process using this software, and the spectrum plots $\alpha(q) - q$, $D(q) - q$, $\tau(q) - q$, and $f(\alpha) - \alpha$ for each image were exported in batch.

The most popular parameters for pore structure characterization are D_q , $f(\alpha)$, $\tau(q)$, and $\Delta\alpha$. In general, D_q increases with increasing pore structure complexity [19]. $\Delta\alpha$ is often used as an indicator of the heterogeneity and is positively correlated with heterogeneity. Corresponding to $q = 0, 1$, and 2, the generalized dimension D_q is the capacity dimension, information dimension, and correlation dimension, respectively.

In multifractal analysis, the singularity exponent α and the multifractal spectrum can be used to describe local material features. The continuous distribution of α may be used to depict the pore structure of rocks, with the parameters α_{\min} and α_{\max} corresponding to the maximum and minimum pore sizes, respectively, as shown in Figure 4(c). The width of the multifractal spectrum ($\Delta\alpha = \alpha_{\max} - \alpha_{\min}$) reflects the irregularity strength of the probability measure for a physical quantity in the whole fractal structure and reveals fractal

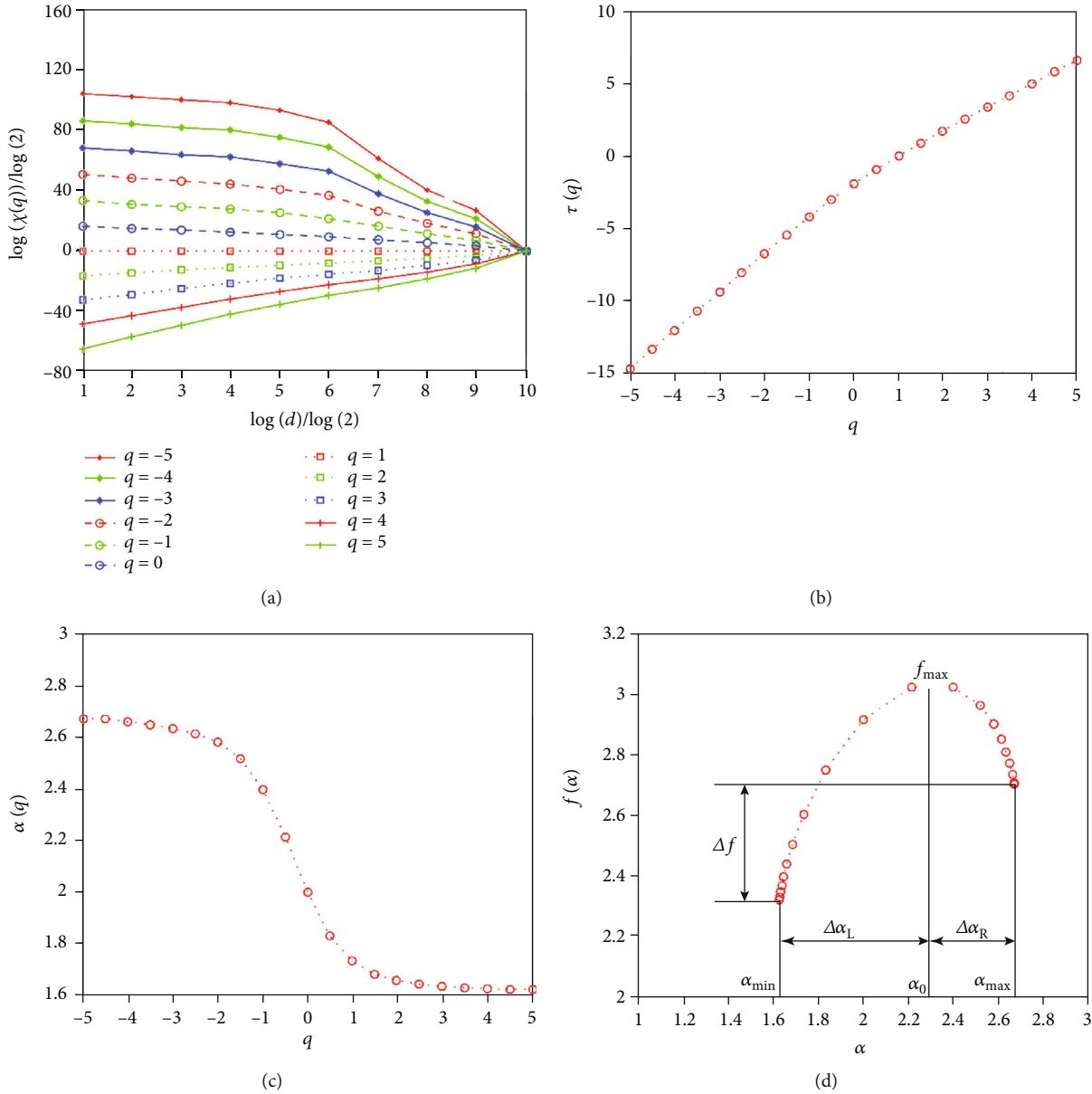


FIGURE 4: Procedures of multifractal analysis on pore space in dolomites. (a) The partition function of probability to cover the pore space at different q values. (b) The mass exponent τ varying with the moment q . (c) The singularity exponent α computed from the direct method. (d) The multifractal spectrum.

characteristics at different scales and local conditions. The wider the $f(\alpha) - \alpha$ spectrum, the higher the heterogeneity in the local scaling indices of the studied variable and vice versa. Thus, a higher value of $\Delta\alpha$ indicates a more heterogeneous distribution of the probability measure for a physical quantity. The parameter Δf is the amplitude difference between the values of function $f(\alpha)$ at α_{\max} and α_{\min} and indicates the morphological characteristics of the multifractal spectrum and the proportion between the maximum and minimum singularity, as shown in Figure 4(d). The value $\Delta\alpha_L$ is the difference between α_{\min} and α_0 , which is the width of the left half of the multifractal spectrum from α_{\min} to α_0 , and the value $\Delta\alpha_R$ is the right half width. Similarities and differences of pore distribution in rocks can be also be examined

with the help of the asymmetrical index (AI), which is the ratio between $(\Delta\alpha_L - \Delta\alpha_R)$ and $(\Delta\alpha_L + \Delta\alpha_R)$, ranging from -1 to 1, and shows the deviation of the multifractal spectrum to the left or to the right. All the above parameters extracted from multifractal analysis of 38 dolostone samples are shown in Table 2.

The multifractal analysis results of samples with different pore structure are shown in Figure 5, respectively. For all the samples, the spectrum $\alpha - q$ of pore distribution is an anti-“S” shape. With increasing q , the singularity exponent α is reduced with q and tends to be constant at the minimum and maximum values of q (Figure 5(a)). The mass exponent spectrum $\tau(q) - q$, which increases with the addition of q but not at a constant gradient, shows that the pore space

TABLE 2: Petrophysical properties and parameters of multifractal analysis on dolostone samples.

Sample	α_L	α_R	$\Delta\alpha$	$\Delta\alpha_L$	$\Delta\alpha_R$	AI	Δf	D_0	D_1	D_2
S1	1.246	1.706	0.460	1.246	0.251	-0.109	0.101	1.360	1.298	1.270
S2	1.358	1.862	0.504	1.358	0.294	-0.193	0.104	1.483	1.429	1.400
S3	1.455	1.861	0.406	1.455	0.321	-0.565	0.336	1.528	1.476	1.460
S4	1.425	1.943	0.518	1.425	0.334	-0.288	0.177	1.524	1.475	1.453
S5	1.527	2.020	0.493	1.527	0.352	-0.455	0.315	1.584	1.544	1.532
S6	1.379	1.902	0.523	1.379	0.264	-0.011	0.066	1.539	1.466	1.425
S7	1.215	1.710	0.495	1.215	0.141	0.427	-0.393	1.499	1.429	1.365
S8	1.125	1.559	0.434	1.125	0.099	0.570	-0.358	1.386	1.309	1.245
S9	1.466	1.967	0.501	1.466	0.333	-0.351	0.245	1.544	1.496	1.479
S10	1.287	1.795	0.508	1.287	0.232	0.085	-0.056	1.464	1.391	1.348
S11	1.179	1.672	0.493	1.179	0.189	0.234	-0.054	1.363	1.266	1.216
S12	1.044	1.493	0.448	1.044	0.122	0.466	-0.346	1.293	1.222	1.169
S13	1.511	2.032	0.520	1.511	0.349	-0.346	0.185	1.610	1.569	1.548
S14	1.489	2.039	0.549	1.489	0.335	-0.213	0.102	1.623	1.569	1.538
S15	1.201	1.626	0.425	1.201	0.178	0.163	-0.038	1.359	1.293	1.253
S16	1.307	1.806	0.499	1.307	0.221	0.111	-0.082	1.493	1.421	1.374
S17	1.130	1.543	0.414	1.130	0.096	0.537	-0.560	1.407	1.365	1.324
S18	1.159	1.642	0.483	1.159	0.124	0.487	-0.459	1.464	1.401	1.336
S19	1.272	1.766	0.495	1.272	0.199	0.190	-0.080	1.466	1.382	1.329
S20	1.347	1.778	0.431	1.347	0.204	0.012	-0.016	1.508	1.450	1.410
S21	1.239	1.727	0.488	1.239	0.186	0.230	-0.115	1.443	1.359	1.306
S22	1.300	1.686	0.386	1.300	0.149	0.242	-0.113	1.466	1.408	1.369
S23	1.127	1.654	0.527	1.127	0.303	-0.150	0.192	1.302	1.251	1.204
S24	1.475	1.912	0.437	1.475	0.262	-0.249	0.139	1.557	1.525	1.497
S25	1.293	1.674	0.382	1.293	0.180	0.067	0.041	1.424	1.364	1.330
S26	1.271	1.722	0.451	1.271	0.188	0.162	-0.053	1.441	1.367	1.323
S27	1.174	1.647	0.474	1.174	0.165	0.296	-0.202	1.401	1.325	1.267
S28	1.369	1.833	0.464	1.369	0.224	0.047	-0.004	1.528	1.468	1.429
S29	1.073	1.531	0.458	1.073	0.135	0.413	-0.254	1.312	1.232	1.171
S30	1.185	1.583	0.398	1.185	0.258	-0.346	0.204	1.277	1.241	1.221
S31	1.267	1.654	0.387	1.267	0.172	0.068	-0.028	1.401	1.340	1.307
S32	1.457	1.979	0.522	1.457	0.216	0.171	-0.221	1.560	1.542	1.513
S33	1.469	2.017	0.548	1.469	0.259	0.056	-0.126	1.597	1.622	1.576
S34	1.235	1.605	0.371	1.235	0.110	0.460	-0.301	1.439	1.388	1.347
S35	1.167	1.588	0.421	1.167	0.102	0.510	-0.318	1.410	1.338	1.282
S36	1.250	1.631	0.381	1.250	0.090	0.527	-0.073	1.463	1.366	1.315
S37	1.496	1.846	0.350	1.496	0.165	-0.028	0.012	1.586	1.556	1.520
S38	1.447	1.840	0.393	1.447	0.170	0.115	-0.013	1.680	1.520	1.478

distributions have multifractal properties (Figure 5(b)). On the multifractal spectrum $f(\alpha) - \alpha$, f increases with increasing α when α is less than α_0 but decreases when α is greater than α_0 . The shape of spectrum $f(\alpha) - \alpha$ displays a “left hook,” “right hook,” or a symmetric parabola (Figure 5(c)).

3.4. Reservoir Heterogeneity Evaluation of Dolomite with Multifractal Analysis. Multifractal theory has been widely used in sandstone reservoir evaluation, pore structure analysis, porosity prediction, and heterogeneity studies [11, 17–19]. Based on multifractal analysis, this work includes esti-

mation of porosity for deep-buried dolomite, evaluation of heterogeneity for different types of dolomite, and classification of pore structure for dolostone samples using clustering analysis method and multifractal parameters.

3.4.1. Porosity Estimated with Multifractal Analysis. The crossplot in Figure 6 shows the relationship between the porosity calculated with the capacity dimension and porosity values obtained from core plug helium porosimetry. The results indicated that the porosity values predicted by the capacity dimension are very close to the measured values.

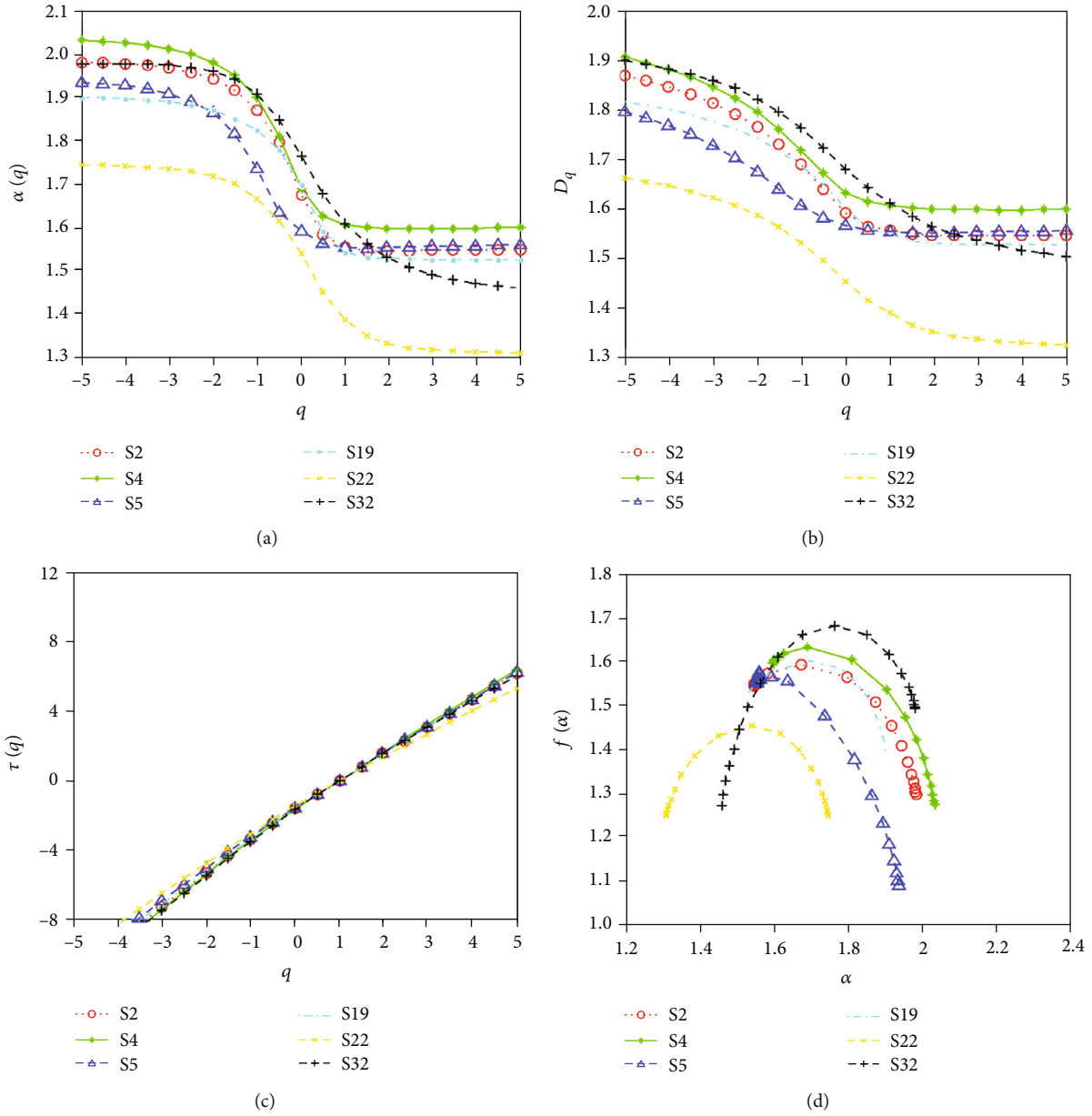


FIGURE 5: Multifractal analysis of pores in dolomite for samples S2, S4, S5, S19, S22, and S32. (a) Plots of singularity exponents against moments q . For each sample, the $\alpha(q)$ decreases against the increase of q . (b) Plots of D_q changing with q . (c) Plots of mass exponent varying with the moment q . (d) Multifractal spectrum of the Hausdorff dimension $f(\alpha)$ changing with singularity exponent α .

Although there is a deviation between the predicted and measured values in two points that may be caused by the selected domain for image from thin section or the heterogeneity of pore space, the predicted porosity is still strongly correlated with measured values with multiple correlation coefficient value 0.865. Thus, the generalized fractal dimension obtained by multifractal analysis can provide a new method for the porosity prediction of dolomite.

3.4.2. Multifractal Characteristics of Different Types of Dolomite. In order to compare the multifractal characteristics and physical properties of pore spaces in dolomite samples with different crystal sizes, the average values of the multi-

fractal and physical parameters extracted from image analysis of each sample were calculated from the data listed in Table 2, and the heterogeneity and physical characteristics of dolomites with different crystal sizes were analyzed. Statistical analyses of these parameters clearly show the differences between various dolomite types. As shown in Table 3, the fine and medium crystalline dolomites have higher values of porosity, permeability, average pore radius, and average pore throat radius than coarse crystalline, silty crystalline, and microcrystalline dolomites. In addition, the multifractal parameters obtained from the fine and medium crystalline dolomite samples are significantly different to those from dolomites with other crystal sizes; e.g., the characteristics of

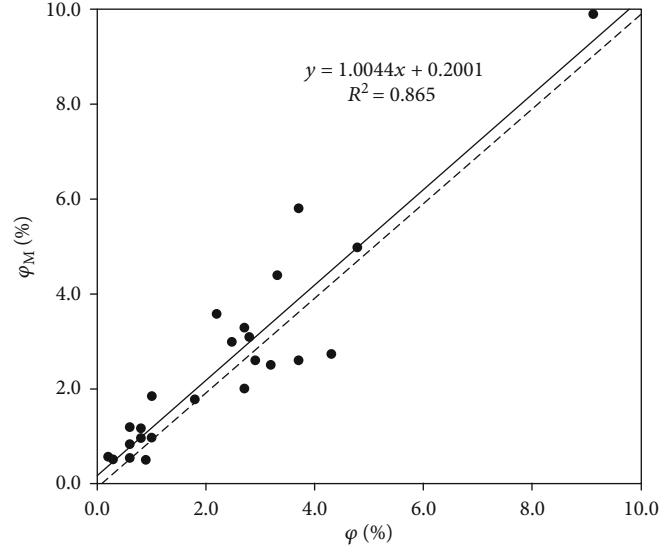


FIGURE 6: Comparison of total porosity values obtained from core plug helium porosimetry (horizontal axis) and porosity obtained from multifractal analysis on digital image.

TABLE 3: Average value of physical properties and multifractal parameters corresponding to different types of dolomites.

Lithology	φ_l (%)	R_b (μm)	R_l (μm)	K_l (mD)	α_L	α_R	$\Delta\alpha$	$\Delta\alpha_L$	$\Delta\alpha_R$	AI	Δf	D_0
DM	1.08	54.21	23.34	0.31	1.15	1.59	0.44	0.33	0.11	0.51	-0.43	1.42
SD	4.62	79.15	20.90	0.50	1.27	1.74	0.47	0.27	0.20	0.16	-0.10	1.46
FD	7.93	138.95	32.56	1.97	1.37	1.85	0.47	0.23	0.25	-0.05	0.05	1.52
MD	7.53	120.00	30.50	1.00	1.37	1.84	0.47	0.19	0.28	-0.21	0.14	1.49
CD	2.53	44.65	11.40	0.23	1.30	1.71	0.42	0.25	0.17	0.19	-0.09	1.47
GD	1.99	70.15	19.16	0.16	1.17	1.61	0.437	0.30	0.16	0.33	-0.27	1.40

higher $\Delta\alpha$ and D_0 values, negative AI value, and positive Δf value demonstrate that they show stronger heterogeneity and comparatively well-developed macropores.

4. Discussion

4.1. Magnification Effect on Multifractal Analysis. In addition, the fractal law will be affected by image magnification due to the image zoom setting, and the multifractal parameters will vary with image magnification [26, 43, 44, 54]. It can be observed that the fractal dimension and multifractal spectrum change irregularly when the image resolution is changed [26]. In other words, a rock may show complete multifractal or local multifractal characteristics. Multifractality may be found in pore space or in solid matrix. These complex properties may lead to difficulty in identifying the fractal structure from rock images [43, 44].

Before conducting multifractal analysis on images, the size of these images should be kept constant by image resampling because the number of pixels influences the results of multifractal analysis. Due to dependence of the minimum distinguished pore scale on the image resolution, the accurate determination of porosity will be directly affected by the pixels of the image if the field of view has been confirmed. In other words, some pores cannot be distinguished at low

resolutions, such that the porosity will be lower because the indistinguishable pores are not calculated. In addition, the multifractal spectrum will be different when the number of pixels in the image is changed. In fact, the magnification effect has a direct influence on multifractal analysis [43, 44]. Therefore, in order to compare the multifractal characteristics of pores in different reservoirs, the image scale and number of pixels should be maintained at the same magnification and size.

4.2. Relationship between Petrophysical Properties and Multifractal Parameters. The pore structure can be described by a continuous distribution series of singularity exponents α . Therefore, the values α_{\min} and α_{\max} correspond to the maximum and minimum pore sizes, respectively. In Figure 7(a), there is a strong positive correlation between porosity and the value of α_{\min} and α_{\max} , where the value of α_{\min} and α_{\max} increases gradually with increasing porosity. Figure 8(a) shows a slightly nonlinear correlation between permeability and α_{\min} and α_{\max} .

The value of $\Delta\alpha$, as a comprehensive parameter for evaluating the heterogeneity of the spatial distribution of pores, reflects the degree of aggregation in pore scale. The higher the value of $\Delta\alpha$, the more dispersive the pore size distribution, which indicates strong heterogeneity of the pore space

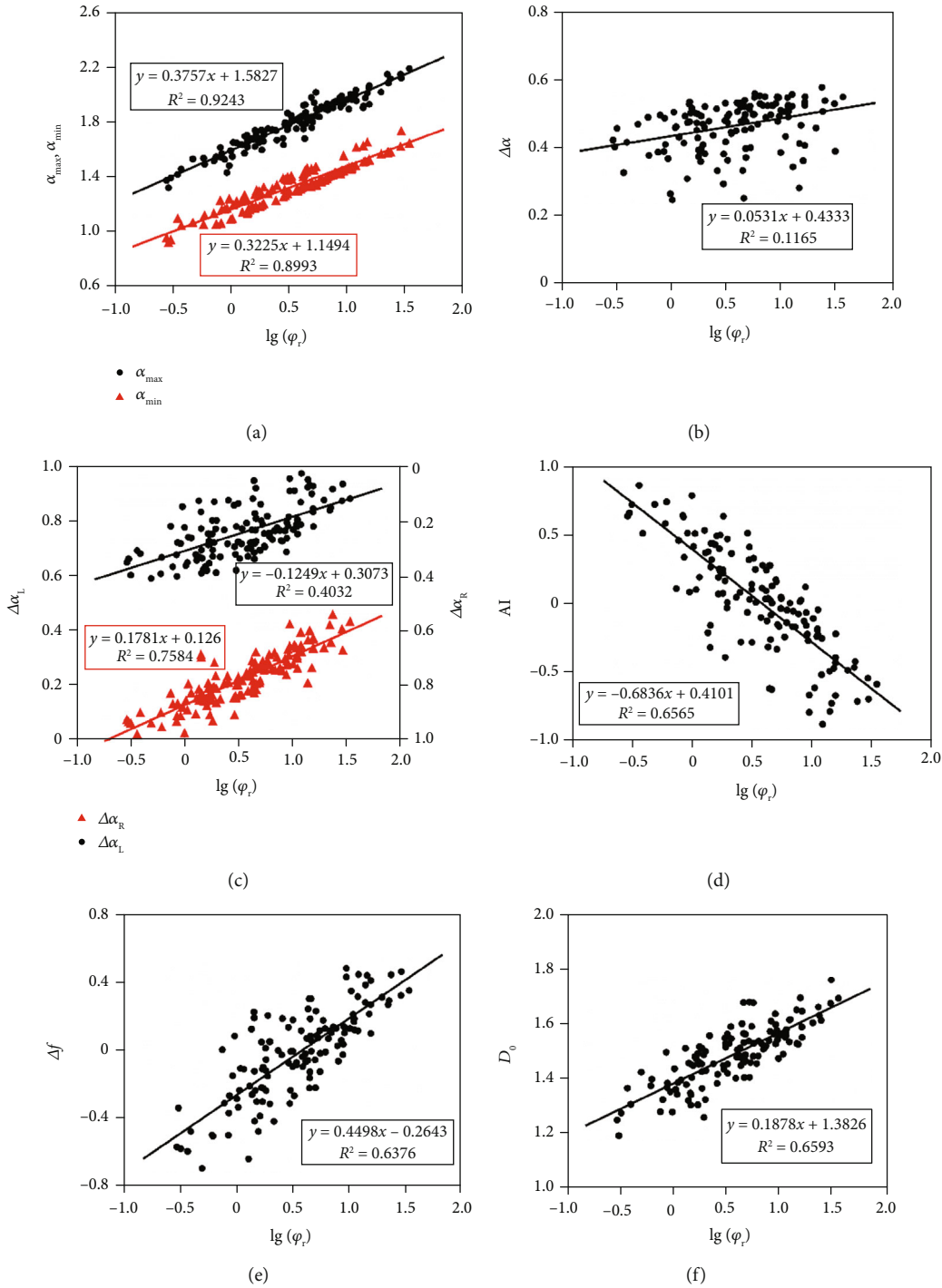


FIGURE 7: The crossplots of porosity values and multifractal parameters. (a) The relationship between singularity exponents α_{\min} and α_{\max} and porosity from image analysis. (b) The relationship between $\Delta\alpha$ and porosity from image analysis. (c) The relationship between $\Delta\alpha_L$, $\Delta\alpha_R$, and porosity from image analysis. (d) The relationship between AI and porosity. (e) The relationship between Δf and porosity. (f) The relationship between D_0 and porosity.

in dolomite. In addition, as there are no significant correlations between the porosity, permeability, and value of $\Delta\alpha$, it indicates that the influence of reservoir heterogeneity on petrophysical properties is complex and cannot be described with a simple linear formula (Figures 7(b) and 8(b)). However, there is a positive correlation between $\Delta\alpha_L$ and porosity but a strong negative correlation between

$\Delta\alpha_R$ and porosity, which indicates higher porosity and pores concentrated in a larger pore size range (Figures 7(c) and 8(c)). Nevertheless, there is only a slightly linear relationship between $\Delta\alpha_L$, $\Delta\alpha_R$, and permeability.

The asymmetrical index (AI), as a parameter to describe the regularity of the multifractal spectrum, is determined by the difference between the values of $\Delta\alpha_L$ and $\Delta\alpha_R$. A positive

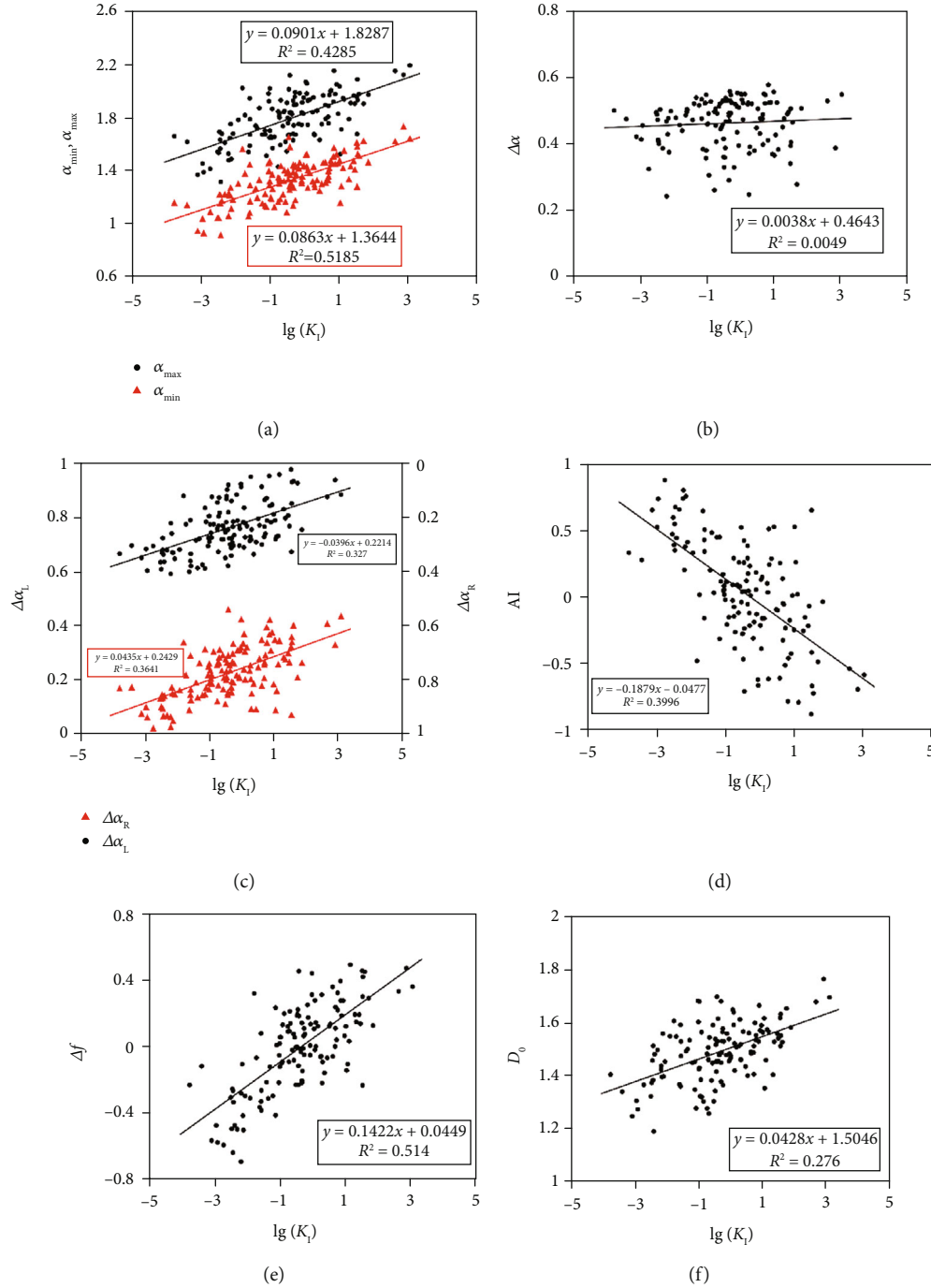


FIGURE 8: The crossplots of permeability values and multifractal parameters. (a) The relationship between singularity exponents α_{\min} and α_{\max} and permeability from image analysis. (b) The relationship between $\Delta\alpha$ and permeability from image analysis. (c) The relationship between $\Delta\alpha_L$, $\Delta\alpha_R$, and permeability from image analysis. (d) The relationship between AI and permeability. (e) The relationship between Δf and permeability. (f) The relationship between D_0 and permeability.

value of AI indicates that the pores are scattered dispersively in the large-scale range but concentrated in the small-scale range, and vice versa. Generally, the corresponding value of porosity is larger when the pore size distribution is concentrated in the large-scale range. Therefore, a significant negative correlation is presented in the AI-porosity crossplot but there is a slightly negative correlation between AI and K_1 in the AI-permeability crossplot (Figures 7(d) and 8(d)).

The Δf parameter reflects the morphological characteristics of the multifractal spectrum. When the value of Δf is positive, the $f(\alpha) - \alpha$ curve will display as a “left hook,” and vice versa, it will display as a “right hook.” As shown in Figures 7(e) and 8(e), the higher the value of Δf , the higher the porosity will be. This is mainly because macropores will engender a larger contribution and influence on the value of porosity if they play a dominant role in the reservoir space

TABLE 4: The statistical results of porosity and permeability in different classes based on K -means clustering analysis with multifractal parameters.

Type	Porosity (%)			Permeability (mD)		
	Maximum	Minimum	Average	Maximum	Minimum	Average
I	3.6	1.4	2.4	0.809	0.034	0.395
II	8.1	2.2	5.2	3.772	0.089	1.013
III	18.4	7.5	12.1	7.365	0.558	2.658
IV	2.9	0.8	1.4	2.677	0.001	0.373

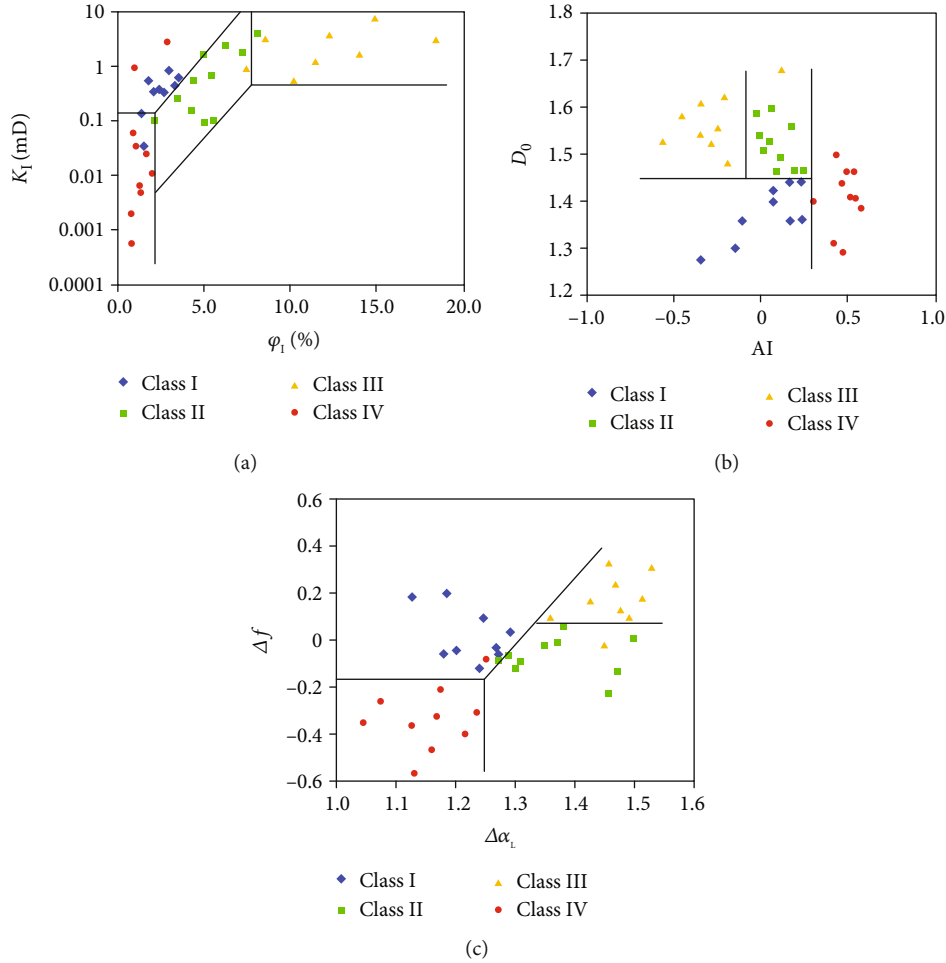


FIGURE 9: Crossplot of porosity and permeability and multifractal feature parameters of dolomites in different categories from K -means clustering analysis based on multifractal parameters.

of a rock. In addition, there is a correlation preference between the value of D_0 and porosity, but not with permeability (Figures 7(f) and 8(f)).

4.3. Reservoir Evaluation Based on K -Means Clustering with Multifractal Parameters. In this study, K -means clustering analysis was introduced to fully exploit the reservoir implications of multifractal parameters obtained from the multifractal analysis of digital images.

According to the multifractal parameters of each sample, the K -means clustering method was used to classify these samples into four categories. The statistics of physical prop-

erties for each category show significant differences between them. As shown in Table 4 and Figure 9, class III corresponds to the best physical reservoir properties, the porosity of which is greater than 7.5% with an average value of 12.1% and the permeability of which is generally greater than 0.56 mD with an average value of 2.66 mD. For class II, the porosity ranges from 2.2% to 8.1% with an average value of 5.2%, while the permeability ranges from 0.089 mD to 3.772 mD with an average value of 1.01 mD. Classes I and IV, characterized by low porosity and low permeability pore structure types, have average porosity values of 2.4% and 1.4%, respectively. Based on the multifractal characteristic parameters, the K -means

clustering analysis method can be used to classify reservoirs and provide a new method for reservoir evaluation and classification of pore structure.

Based on the parameters such as D_0 , AI, $\Delta\alpha_L$, and Δf , we attempted to construct the criteria of pore structure, with purpose of pore structure classification by multifractal analysis. Figure 9 shows the crossplot of porosity and permeability, D_0 and AI, and $\Delta\alpha_L$ and Δf . We establish the discrimination criteria for pore typing, which are expressed as follows:

Pore structure class I: $AI < 0.24$ and $D_0 \leq 1.44$ and $\Delta f > -0.11$.

Pore structure class II: $-0.03 < AI < 0.24$, $D_0 > 1.44$, $\Delta f < 0.07$, and $\Delta\alpha_L > 1.27$.

Pore structure class III: $AI \leq -0.03$, $D_0 > 1.44$, $\Delta f \geq 0.07$, and $\Delta\alpha_L \geq 1.36$.

Pore structure class IV: $AI \geq 0.24$, $\Delta f < -0.11$, and $\Delta\alpha_L \leq 1.27$.

5. Conclusions

In this study, multifractal analysis was used to evaluate the pore space in dolomite reservoirs. Then, the relationship between the statistical multifractal characteristic parameters and the physical properties of dolomite was analyzed. Finally, the pore structure of dolomite was classified by K -means clustering analysis with multifractal parameters. The conclusions can be summarized as follows:

- (1) The porosity and permeability of deep-buried dolomite are closely related to the multifractal characteristic parameters. There are strong correlations between porosity, permeability, and multifractal parameters, such as α_{\min} , α_{\max} , $\Delta\alpha_R$, $\Delta\alpha_L$, AI, and Δf . The porosity can be accurately predicted on the basis of the multifractal generalized dimension, and this provides a new method for porosity estimation of dolomite reservoirs from thin section images
- (2) Significant divergence in porosity, permeability, and multifractal parameters has been found between dolomites with different crystal sizes, since the rock type and crystallization degree control the reservoir performance and permeability of dolomite to a certain extent
- (3) K -means clustering analysis of multifractal feature parameters can be used for quantitative pore structure classification and precise reservoir evaluation. The discrimination criteria for pore typing can be expressed with AI, D_0 , Δf , and $\Delta\alpha_L$

Data Availability

The data used to support the findings of this study are included within the article.

Conflicts of Interest

The authors declare that they have no conflicts of interest.

Acknowledgments

Funding for this research was provided by Key Laboratory of Reservoir Characterization, CNPC. The samples and thin sections are obtained with help from Exploration and Development Research Institute of Sinopec Northwest Oilfield Company. The image collection and data analysis were completed in State Key Laboratory of Oil and Gas Reservoir Geology and Exploitation, Southwest Petroleum University, China. We also thank Professor Cai Jianchao, China University of Geosciences (Wuhan), for his examining of the manuscript and precious revision suggestions.

References


- [1] J. Lai, S. Wang, C. Zhang et al., "Spectrum of pore types and networks in the deep Cambrian to Lower Ordovician dolostones in Tarim Basin, China," *Marine and Petroleum Geology*, vol. 112, article 104081, 2020.
- [2] J. Lai, S. Wang, G. Wang et al., "Pore structure and fractal characteristics of Ordovician Majiagou carbonate reservoirs in Ordos Basin, China," *AAPG Bulletin*, vol. 103, no. 11, pp. 2573–2596, 2019.
- [3] J. H. Norbistrath, G. P. Eberli, B. Laurich, G. Desbois, R. J. Weger, and J. L. Urai, "Electrical and fluid flow properties of carbonate microporosity types from multiscale digital image analysis and mercury injection," *AAPG Bulletin*, vol. 99, no. 11, pp. 2077–2098, 2015.
- [4] J. Lai, G. Wang, Z. Fan et al., "Insight into the pore structure of tight sandstones using NMR and HPMI measurements," *Energy & Fuels*, vol. 30, no. 12, pp. 10200–10214, 2016.
- [5] B. B. Mandelbrot and J. A. Wheeler, "The fractal geometry of nature," *American Journal of Physics*, vol. 51, no. 3, pp. 286–287, 1983.
- [6] A. J. Katz and A. H. Thompson, "Fractal sandstone pores: implications for conductivity and pore formation," *Physical Review Letters*, vol. 54, no. 12, pp. 1325–1328, 1985.
- [7] H. Pape, L. Riepe, and J. R. Schopper, "Theory of self-similar network structures in sedimentary and igneous rocks and their investigation with microscopical and physical methods," *Journal of Microscopy*, vol. 148, no. 2, pp. 121–147, 1987.
- [8] A. H. Thompson, A. J. Katz, and C. E. Krohn, "The microgeometry and transport properties of sedimentary rock," *Advances in Physics*, vol. 36, no. 5, pp. 625–694, 1987.
- [9] J. W. Crawford and N. Matsui, "Heterogeneity of the pore and solid volume of soil: distinguishing a fractal space from its non-fractal complement," *Geoderma*, vol. 73, no. 3–4, pp. 183–195, 1996.
- [10] J. Lai and G. Wang, "Fractal analysis of tight gas sandstones using high-pressure mercury intrusion techniques," *Journal of Natural Gas Science and Engineering*, vol. 24, pp. 185–196, 2015.
- [11] Z. Song, G. Liu, W. Yang, H. Zou, M. Sun, and X. Wang, "Multi-fractal distribution analysis for pore structure characterization of tight sandstone—a case study of the Upper Paleozoic tight formations in the Longdong District, Ordos Basin," *Marine and Petroleum Geology*, vol. 92, pp. 842–854, 2018.
- [12] X. Chen, G. Yao, J. Cai, Y. Huang, and X. Yuan, "Fractal and multifractal analysis of different hydraulic flow units based on micro-CT images," *Journal of Natural Gas Science and Engineering*, vol. 48, pp. 145–156, 2017.

- [13] Y. Xia, J. Cai, E. Perfect, W. Wei, Q. Zhang, and Q. Meng, "Fractal dimension, lacunarity and succolarity analyses on CT images of reservoir rocks for permeability prediction," *Journal of Hydrology*, vol. 579, article 124198, 2019.
- [14] Y. Wu, P. Tahmasebi, C. Lin et al., "A comprehensive study on geometric, topological and fractal characterizations of pore systems in low-permeability reservoirs based on SEM, MICP, NMR, and X-ray CT experiments," *Marine and Petroleum Geology*, vol. 103, pp. 12–28, 2019.
- [15] B. B. Mandelbrot, "Multifractal measures, especially for the geophysicist," *Pure and Applied Geophysics*, vol. 131, no. 1-2, pp. 5–42, 1989.
- [16] S. Xie, Q. Cheng, Q. Ling, B. Li, Z. Bao, and P. Fan, "Fractal and multifractal analysis of carbonate pore-scale digital images of petroleum reservoirs," *Marine and Petroleum Geology*, vol. 27, no. 2, pp. 476–485, 2010.
- [17] X. Ge, Y. Fan, J. Li, and M. Aleem Zahid, "Pore structure characterization and classification using multifractal theory—an application in Santanghu basin of western China," *Journal of Petroleum Science and Engineering*, vol. 127, pp. 297–304, 2015.
- [18] P. Zhao, Z. Wang, Z. Sun, J. Cai, and L. Wang, "Investigation on the pore structure and multifractal characteristics of tight oil reservoirs using NMR measurements: Permian Lucaogou Formation in Jimusaer Sag, Junggar Basin," *Marine and Petroleum Geology*, vol. 86, pp. 1067–1081, 2017.
- [19] J. Peng, H. Han, Q. Xia, and B. Li, "Evaluation of the pore structure of tight sandstone reservoirs based on multifractal analysis: a case study from the Kepingtage Formation in the Shuntuoguole Uplift, Tarim Basin, NW China," *Journal of Geophysics and Engineering*, vol. 15, no. 4, pp. 1122–1136, 2018.
- [20] P. Zhao, X. Wang, J. Cai et al., "Multifractal analysis of pore structure of Middle Bakken formation using low temperature N₂ adsorption and NMR measurements," *Journal of Petroleum Science and Engineering*, vol. 176, pp. 312–320, 2019.
- [21] J. Piñuela, A. Alvarez, D. Andina, R. J. Heck, and A. M. Tarquis, "Quantifying a soil pore distribution from 3D images: multifractal spectrum through wavelet approach," *Geoderma*, vol. 155, no. 3-4, pp. 203–210, 2010.
- [22] F. San José Martínez, M. A. Martín, F. J. Caniego et al., "Multifractal analysis of discretized X-ray CT images for the characterization of soil macropore structures," *Geoderma*, vol. 156, no. 1-2, pp. 32–42, 2010.
- [23] J. A. Lafond, L. Han, S. E. Allaire, and P. Dutilleul, "Multifractal properties of porosity as calculated from computed tomography (CT) images of a sandy soil, in relation to soil gas diffusion and linked soil physical properties," *European Journal of Soil Science*, vol. 63, no. 6, pp. 861–873, 2012.
- [24] Y. Gao, J. Jiang, G. de Schutter, G. Ye, and W. Sun, "Fractal and multifractal analysis on pore structure in cement paste," *Construction and Building Materials*, vol. 69, no. 11, pp. 253–261, 2014.
- [25] A. Dathe and P. Baveye, "Dependence of the surface fractal dimension of soil pores on image resolution and magnification," *European Journal of Soil Science*, vol. 54, no. 3, pp. 453–466, 2003.
- [26] A. Dathe, A. M. Tarquis, and E. Perrier, "Multifractal analysis of the pore- and solid-phases in binary two-dimensional images of natural porous structures," *Geoderma*, vol. 134, no. 3-4, pp. 318–326, 2006.
- [27] E. Vidal-Vázquez, O. A. Camargo, S. R. Vieira et al., "Multifractal analysis of soil properties along two perpendicular transects," *Vadose Zone Journal*, vol. 12, no. 3, pp. 1–13, 2013.
- [28] C. E. Krohn, "Fractal measurements of sandstones, shales, and carbonates," *Journal of Geophysical Research*, vol. 93, no. B4, pp. 3297–3305, 1988.
- [29] J. Muller, O. K. Huseby, and A. Saucier, "Influence of multifractal scaling of pore geometry on permeabilities of sedimentary rocks," *Chaos Solitons & Fractals*, vol. 5, no. 8, pp. 1485–1492, 1995.
- [30] S. Karimpouli and P. Tahmasebi, "3D multi-fractal analysis of porous media using 3D digital images: considerations for heterogeneity evaluation," *Geophysical Prospecting*, vol. 67, pp. 1082–1093, 2018.
- [31] L. Zhou and Z. Kang, "Fractal characterization of pores in shales using NMR: a case study from the Lower Cambrian Niutitang Formation in the Middle Yangtze Platform, Southwest China," *Journal of Natural Gas Science and Engineering*, vol. 35, pp. 860–872, 2016.
- [32] P. Zhao, X. Hu, X. Ge, Z. Wang, and J. Cai, *Multifractal Analysis of Pore Structure of Tight Oil Reservoirs Using Low-Field NMR Measurements*, Elsevier: Petrophysical Characterization and Fluids Transport in Unconventional Reservoirs, 2019.
- [33] L. Luo and H. Lin, "Lacunarity and fractal analyses of soil macropores and preferential transport using micro-X-ray computed tomography," *Vadose Zone Journal*, vol. 8, no. 1, pp. 233–241, 2009.
- [34] J. He, W. Ding, A. Li et al., "Quantitative microporosity evaluation using mercury injection and digital image analysis in tight carbonate rocks: a case study from the Ordovician in the Tazhong Palaeouplift, Tarim Basin, NW China," *Journal of Natural Gas Science and Engineering*, vol. 34, pp. 627–644, 2016.
- [35] P. Li, M. Zheng, H. Bi, S. Wu, and X. Wang, "Pore throat structure and fractal characteristics of tight oil sandstone: a case study in the Ordos Basin, China," *Journal of Petroleum Science and Engineering*, vol. 149, pp. 665–674, 2017.
- [36] J. Chen, E. Li, and J. Luo, "Characterization of microscopic pore structures of rock salt through mercury injection and nitrogen absorption tests," *Geofluids*, vol. 2018, Article ID 927361, 7 pages, 2018.
- [37] B. Yu and J. Li, "Some fractal characters of porous media," *Fractals*, vol. 9, no. 3, pp. 365–372, 2011.
- [38] G. S. Padhy, C. Lemaire, E. S. Amirtharaj, and M. A. Ioannidis, "Pore size distribution in multiscale porous media as revealed by DDIF-NMR, mercury porosimetry and statistical image analysis," *Colloids and Surfaces A-Physicochemical and Engineering Aspects*, vol. 300, no. 1-2, pp. 222–234, 2007.
- [39] P. Xu and B. Yu, "Developing a new form of permeability and Kozeny-Carman constant for homogeneous porous media by means of fractal geometry," *Advances in Water Resources*, vol. 31, no. 1, pp. 74–81, 2008.
- [40] Z. Zhang and A. Weller, "Fractal dimension of pore-space geometry of an Eocene sandstone formation," *Geophysics*, vol. 79, no. 6, pp. D377–D387, 2014.
- [41] J. Cai, D. Lin, H. Singh, S. Zhou, Q. Meng, and Q. Zhang, "A simple permeability model for shale gas and key insights on relative importance of various transport mechanisms," *Fuel*, vol. 252, pp. 210–219, 2019.

- [42] J. Muller, "Characterization of the North Sea chalk by multifractal analysis," *Journal of Geophysical Research*, vol. 99, no. B4, pp. 7275–7280, 1994.
- [43] M. S. Jouini, S. Vega, and E. A. Mokhtar, "Multiscale characterization of pore spaces using multifractals analysis of scanning electronic microscopy images of carbonates," *Nonlinear Processes in Geophysics*, vol. 18, no. 6, pp. 941–953, 2011.
- [44] S. Vega and M. S. Jouini, "2D multifractal analysis and porosity scaling estimation in Lower Cretaceous carbonates," *Geophysics*, vol. 80, no. 6, pp. 575–586, 2015.
- [45] J. Du and W. Pan, "Accumulation conditions and play targets of oil and gas in the Cambrian subsalt dolomite, Tarim Basin, NW China," *Petroleum Exploration and Development*, vol. 43, no. 3, pp. 327–339, 2016.
- [46] J.-P. Yan, Q. Liang, Z.-Z. Li, B. Geng, X.-P. Kou, and Y. Hu, "A connected domain identification method and its application in quantitatively pickup information of caves using electric imaging logging," *Chinese Journal of Geophysics*, vol. 59, no. 12, pp. 4759–4770, 2016.
- [47] S. A. Flavio, S. Luthi, and G. P. Eberli, "Quantitative characterization of carbonate pore systems by digital image analysis," *AAPG Bulletin*, vol. 82, no. 10, pp. 1815–1836, 1998.
- [48] Y. Wu, P. Tahmasebi, C. Lin, and C. Dong, "Process-based and dynamic 2D modeling of shale samples: considering the geology and pore-system evolution," *International Journal of Coal Geology*, vol. 218, article 103368, 2020.
- [49] Y. Wu, P. Tahmasebi, C. Lin, L. Ren, and C. Dong, "Multiscale modeling of shale samples based on low- and high-resolution images," *Marine and Petroleum Geology*, vol. 109, pp. 9–21, 2019.
- [50] Y. Wu, P. Tahmasebi, C. Lin, M. J. Munawar, and V. Cnudde, "Effects of micropores on geometric, topological and transport properties of pore systems for low-permeability porous media," *Journal of Hydrology*, vol. 575, pp. 327–342, 2019.
- [51] E. Müller-Huber and J. Schön, "Carbonates with complex pore systems-modeling of permeabilities and application of modified capillary tube models," in *SEG Technical Program Expanded Abstracts 2013*, pp. 2587–2591, Society of Exploration Geophysicists, 2013.
- [52] A. Chhabra and R. V. Jensen, "Direct determination of the $f(\alpha)$ singularity spectrum," *Physical Review Letters*, vol. 62, no. 12, pp. 1327–1330, 1989.
- [53] R. J. Dunham, "Classification of carbonate rocks according to depositional texture," *AAPG Bulletin*, vol. 1, pp. 108–121, 1962.
- [54] Z. Liu, B. Shi, H. I. Inyang, and Y. Cai, "Magnification effects on the interpretation of SEM images of expansive soils," *Engineering Geology*, vol. 78, no. 1-2, pp. 89–94, 2005.

Research Article

Investigation of Multistage Hydraulic Fracture Optimization Design Methods in Horizontal Shale Oil Wells in the Ordos Basin

Suotang Fu,^{1,2} Jian Yu,³ Kuangsheng Zhang,^{1,2} Hanbin Liu,^{1,2} Bing Ma ,^{1,2} and Yuliang Su⁴

¹CNPC Changqing Oilfield, Xi'an Shaanxi, China 710018

²State Key Laboratory for Exploration and Development of Low Permeability Oil & Gas Fields, Xi'an Shaanxi, China 710018

³CNPC Changqing Oilfield Exploration Institute, Xi'an Shaanxi, China 710018

⁴School of Petroleum Engineering, China University of Petroleum (East China), No. 66, Changjiang West Road, Huangdao District, Qingdao, China 266580

Correspondence should be addressed to Bing Ma; 18823354@qq.com

Received 7 April 2020; Revised 19 June 2020; Accepted 27 June 2020; Published 21 September 2020

Academic Editor: Wei Wei

Copyright © 2020 Suotang Fu et al. This is an open access article distributed under the Creative Commons Attribution License, which permits unrestricted use, distribution, and reproduction in any medium, provided the original work is properly cited.

Based on the analysis of the typical Ordos well groups, this study began with the accurate characterization of the fracture geometry by adopting advanced laboratory experiment methods and monitoring techniques. Then, with the integration of fracture geometry characterization and in situ stress distributions, fracture optimizations of the target wells were performed through numerical simulations methods. Finally, this study established a sweet spot prediction and identification method for long horizontal shale oil wells and constructed a set of optimization design methods for multistage hydraulic fracturing. This investigation revealed that the hydraulic fractures in Chang-7 terrestrial shale oil reservoirs exhibited the belt pattern, and the primary fractures generated the secondary fractures, which activated the natural fractures and induced shear failure. Macroscopic fractures were found to be perpendicular to the direction of the minimum principal stress. Secondary fractures and activated natural fractures were distributed around the primary fracture in the form of fracture types I and II. Multicluster perforation optimization techniques, which were based on shale reservoir classification and evaluation, and aimed at activating multiclusters and determining fracture sweet spots, were developed. These were successfully applied to the field operation and achieved production enhancement performance.

1. Introduction

Ordos Basin Chang-7 shale oil specifically refers to the oil in the 7th member of the Triassic Yanchang Formation, which is generated and accumulated within the tight sandstone and shale source rock without covering long migration distances [1]. Compared to other domestic shale oils in China, Chang-7 shale oil has low pressure and poor reservoir properties; however, it also has low viscosity and shallow buried depth. Compared to the Permian Basin shale oil, Chang-7 shale oil features low brittleness index, pressure gradient, and undeveloped natural fractures [1, 2]. These characters lead to drilling and stimulation challenges in the economic and effective development of Chang-7 shale oil. Hydraulic fracturing is the primary method to increase oil recovery of shale reservoirs. The region filled with a complex fracture

network during hydraulic fracturing stimulation is created, which is defined as the stimulated reservoir volume (SRV). Research proves that the SRV area is the main contribution of production in unconventional reservoirs [3]. The two main challenges are the difficulties in maximizing the SRV due to a low brittleness index and large horizontal stress differences, along with the rapid production decline due to low reservoir pressure. Therefore, it is essential to conduct an investigation on multiscale fracture characterization and fracture design optimization in order to promote efficient oilfield development.

Large-scale laboratory experiment simulations of hydraulic fracturing have played a vital role in understanding the mechanism of complex fracture propagation and simulating field operations [3]. As understanding the complexity of hydraulic fractures is challenging [4, 5], laboratory

experiments can be performed to better control the experimental conditions, gradually understand the complexity of artificial fractures, evaluate the effectiveness of fracture monitoring methods, and provide a basis for guiding on-site hydraulic fracturing. Methods of direct observation and indirect study can be adopted to examine fracture propagations. Direct observation mainly refers to study of the post-frac core samples and fracture visualizations, such as PMMA for direct observation of fracture propagation process [6, 7]. Indirect study is the indirect analysis of fracture characteristics by detecting the signals generated during fracture propagation, mainly including acoustic emission (AE) and acoustic wave technology, CT scanning, DIC technology, fiber optic measurement technology, and electromagnetic signal monitoring [8]. Acoustic emission technology can detect the acoustic signals of rock fractures, while acoustic wave technology inverts the shape of fractures by actively transmitting acoustic signals and then receiving the reflected signals. Acoustic emission localization is a common method to study acoustic emission activities of rocks, and it is also the most developed method to monitor the fracture propagations [9, 10]. Acoustic waves were first applied to detect the laboratory hydraulic fracture propagations by researchers from the University of Delft, who also detected the fracture tips, fluid edges, and fracture widths. However, this method has limitations in field applications [11, 12]. Synchrotron X-ray microtomography is applied to observe the three-dimensional (3D) real-time fracture propagations and investigate the effects of microfractures, grain boundaries, and pore sizes on fracture toughness and propagation directions [13]. AlTammar and Sharma employed DIC technology to observe the displacement field changes around fractures and changes in pore pressure field changes caused by fracturing fluid filtration [14]. Because fiber optic materials have the characteristics of antielectromagnetic interference, antienvironmental noise, electrical insulation, and robust safety performance, they have been widely used in harsh environments for downhole measurement, and they have also begun to be applied in hydraulic fracturing monitoring [15, 16]. During hydraulic fracture propagations, ions in the reservoir continue to dissolve into the fracturing fluid to form a current and generate a magnetic signal, which can reflect the propagation of the fractures. However, due to the high detection accuracy requirements of this technology, no field applications have been carried out [17].

Accurate identification of sweet spots in shale reservoirs is the basic prerequisite to improve the effect of shale reservoir stimulations. The classification and evaluation of engineering sweet spots in the Ordos Basin is important for guiding fracture stage selections for multistage fractures in shale oil reservoirs. The determination of sweet spots is closely related to rock brittleness, fracture toughness, natural fractures, and in situ stress, which can be measured using fracability and brittleness index. Chong et al. summarized the hydraulic fractures in the Barnett shale in Texas and defined fracability as the property that the reservoir can be effectively fractured to obtain increased production capacity [18]. Mullen and Enderlin posited that fracability is not only

associated with geomechanical properties and proposed the complex fracability index model, which integrated rock properties, geomechanics, fracture toughness, and natural fractures into a single index [19]. The higher the complex fracability index value, the easier it is to generate a complex fracture network. Fang and Amro compared the fracability of the terrestrial and marine shale, determining that the fracability of the former is more complicated [20]. The effects of the brittleness index, mineral content, natural fracture, diagenesis, and sedimentation on fracability were studied, and it was concluded that the fracability calculation methods should be further improved. Hu et al. [21] examined the effect of confining pressure on shale compressive strength, Young's modulus, Poisson's ratio, and number of microcracks, introducing fracture toughness and establishing a new brittleness calculation model [21]. Jin et al. [22] integrated the critical energy release rate with the brittleness and proposed a fracability index model, which provided a reference for distinguishing the fracture target zone and optimized horizontal well trajectory and perforation cluster spacing [22]. Xu and Sonnenberg [23] described the geomechanical properties of the Bakken shale based on well logging data, triaxial tests, rebound impact tests, and X-ray data, and proposed a new mineralogy-based brittleness index and proved the significant positive correlation between mineralogy and the brittleness index model [23].

Combining shale oil reservoir engineering-based sweet spot identification with geological sweet spot descriptions to determine optimal fracturing programs is the current trend of shale oil development [24]. Liu et al. [25] optimized the multistage fracture spacing and perforation locations based on the analysis of reservoir and engineering combined sweet spots [25]. Wigger et al. [26] applied the similar method and optimized the development plan for Eagle Ford shale reservoir [26]. Brittleness index and fracability have been extensively studied; however, the studied brittleness index and fracability models are limited in applicability to specific reservoirs.

In addition to laboratory experiments, fiber optic materials were first used in this study to reflect fracture propagation. Based on the specific fracture network, the fracture optimizations of the target wells are performed through numerical simulations methods. Finally, a suitable method to determine the sweet spots and design the fracture program is proposed to develop the shale oil reservoirs in the Ordos Basin.

2. Laboratory Experimental Investigation

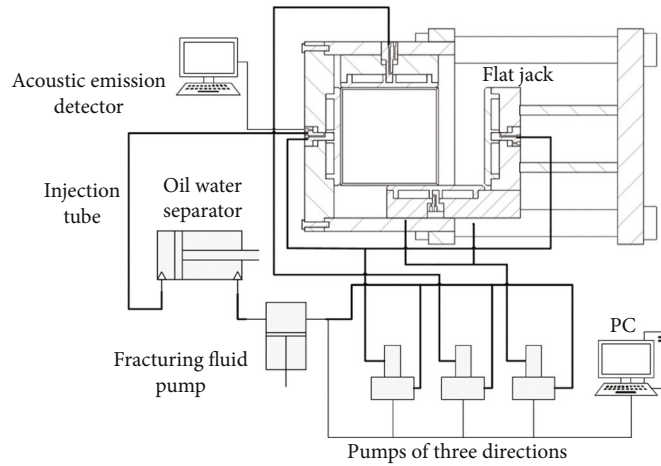
2.1. Experiment Equipment and Setup. This experimental study used the High Temperature High Pressure (HTHP) Fracture Simulation System, and 50 MPa triaxial stresses are applied to the $30 \times 30 \times 30 \text{ cm}^3$ specimen under 100°C (Figure 1).

The specimen is composed of 40–70 mesh quartz sand mixed with composite Portland Cement in a 1:1 ratio. The mechanical properties of the specimen are shown in Table 1.

Twelve AE sensors are placed on the four sides of the specimen (Figure 2(a)) and fixed in the AE hole during the



(a)



(b)

FIGURE 1: Schematics of (a) the HTHP fracture system and (b) the experiment setup.

TABLE 1: Mechanical properties of the artificial cement specimen.

Parameters	Value
Fracture toughness ($\text{MPa}\sqrt{\text{m}}$)	0.7
Uniaxial compressive strength (MPa)	27.98 ± 1
Tensile strength (MPa)	3.55 ± 0.2
Poisson's ratio	0.17
Elastic modulus (GPa)	24.6

experiment (Figure 2(b)). The threshold of the AE analysis system is set to 40 dB and the sampling frequency is 10 MHz. The experiment simulated the open-hole multistage fracture beginning from the toe, and the hole length is 15 cm.

2.2. Experiment Program. In order to study the acoustic emission distribution during fracture propagation, two stress differences of 5 MPa and 10 MPa were set. The experiment fluid is 2% guar fluid with a viscosity of 106 cp. The parameters used in the experiment are listed in Table 2.

2.3. Fracture Network Characterization and Controlling Factors. The specimens are cut off after the experiment to observe the fracture geometry. As shown in Figure 3, the red surface represents the fracture surface. Due to the stress concentration at the bottom of the hole, the fracture propagates along the inclined surface in an elliptical shape (Figure 3(a)). As the stress difference increases, the fracture surface becomes a plane fracture nearly perpendicular to the minimum in situ stress (Figure 3(b)).

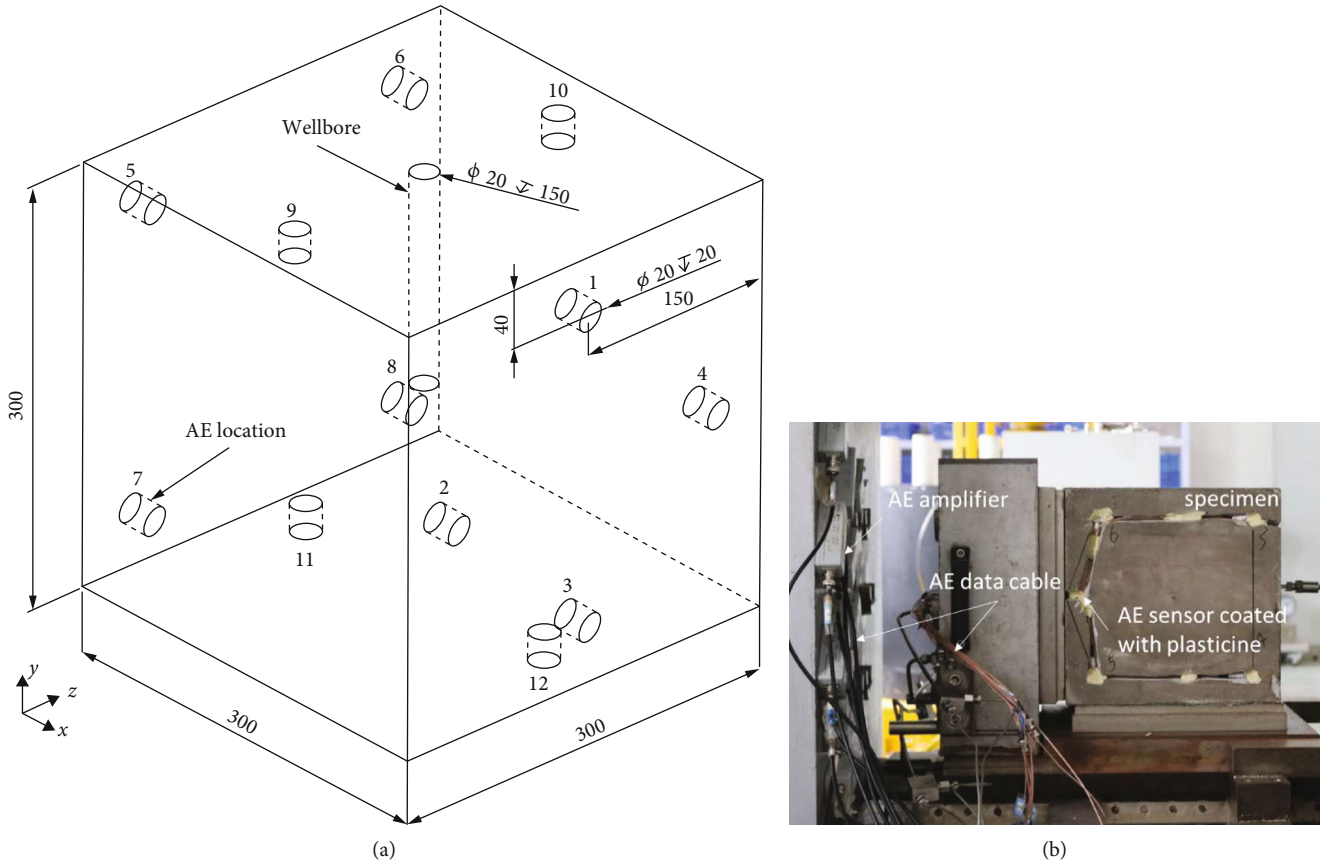


FIGURE 2: Schematic of the AE hydraulic fracturing system.

TABLE 2: Experimental parameters for water-based fracturing.

No. of specimens	Fluid	$\sigma_v - \sigma_H - \sigma_h$ (MPa)	Rate (mL/min)
1#	Water + guar	32-26-21	2
2#		32-26-16	

The energy of the acoustic emission signal is divided into three categories. Red represents the highest energy level of the acoustic emission event, followed by blue, while the green energy level is the smallest. The highest energy level represents the main fracture trajectory, as shown in Figure 4. A large number of high-level and low-level acoustic emission events are gathered around the primary fracture, indicating the existence of secondary fractures around the primary fracture. The width of the fracture generated in the lab experiment is 8–10 cm.

As the stress difference increases, the number of acoustic emission events decrease, and the acoustic emission events are more dispersed, as shown in Figure 5. The increased stress difference results in a single form of the fracture; hence, acoustic emission is mainly distributed on the primary fracture surface. Moreover, the fracture network is not formed, i.e., the fracture zone is not obvious.

In order to analyze the microfracture morphology, the fracture surface of specimen #1 was selected to undergo scanning electron microscopy (Figure 6). When hydraulic fractures extend to the grain particle boundary, fractures tend to extend along the particle boundary, which lead to fracture reorientation or generation of fracture branches. This phenomenon is difficult to observe on the macrofracture surface. The generation of microfractures is in line with the band-shaped distribution of acoustic emission events, i.e., there are a large number of acoustic emission signals around the primary fractures.

The band-distributed acoustic emission events and microfracture distribution indicated the hydraulic fractures as fracture zones with a certain width. According to the in situ stress state and reservoir mechanical properties of Chang-7 shale reservoir, the experiment results indicated that the hydraulic fractures in Chang-7 reservoir would follow a fractured band pattern, which is different from that of the currently used multistage fracture models in the Ordos Basin. In the band-shaped fractures, the primary fracture generated the secondary fractures, which further activated the natural fractures and induced shear failure. Macrofractures are perpendicular to the direction of the minimum principal stress. Secondary fractures and activated natural fractures are distributed around the primary fracture in the form of type I and II failures.

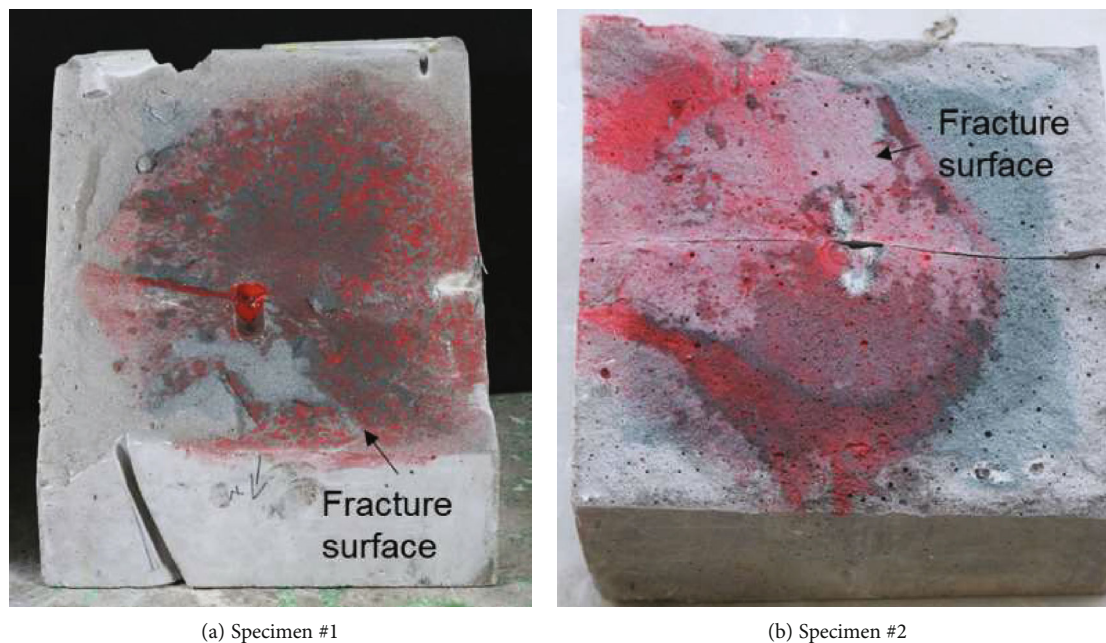


FIGURE 3: Hydraulic fracture shape of the specimens.

3. Investigation of 3D In Situ Stress and Fracture Parameter Optimizations

3.1. 3D Reservoir Geomechanics. The magnitude and orientation of in situ stress have an important influence on the design, implementation, and evaluation of hydraulic fracturing. The 3D geomechanical modeling begins with the geological model, integrates multiwell 1D geomechanical models and adopts the 3D geomechanical workflow established specifically for shale reservoirs. The finite element analysis (VISAGE) was used to establish a three-dimensional geomechanical model to more accurately determine the three-dimensional spatial distribution of the geostress field. It combined seismic, geological, well logging, core, imaging, and 1D geomechanical models, comprehensively characterized by the reservoir heterogeneity, anisotropic stress field, and other key 3D engineering parameters. This study selected a rectangular area of 2680 m × 5460 m from X platform as the research target.

3.1.1. 3D FEM Gridblocks. To avoid the interference of the boundary effect on the simulation results of the reservoir stress field, the geomechanical grid needs to be extended in the horizontal direction, generally 2 to 3 times the plane size of the geological model; in order to ensure the stability of the FEM simulation, the extended gridblock of the underlying formation is basically consistent with the overlying formation. In addition to the extended grids, this study also added the overlying rock layer, the underlying rock layer, and the lateral rock layer, covering the range from the ground to a depth of approximately 4200 m. The total number of elements is 10.53 million, the horizontal accuracy of the target layer grid is 20 m, and the vertical accuracy is approximately

0.5 m. The grid sizes of the overburden, underburden, and lateral rock layers outside the reservoir site gradually transition to the coarse grid.

3.1.2. 3D Geomechanical Parameters. The well logging data and 1D geomechanical data of 3 vertical wells and 12 horizontal wells were used to perform 3D attribute interpolation. First, the 3D model is interpolated to obtain the *P*-wave time difference, *S*-wave time difference, and density attribute volume. On this basis, dynamic elastic parameters are calculated, including dynamic Young's modulus and dynamic Poisson's ratio, and static and dynamic transformations are performed to obtain static elastic parameters. Rock strength parameters were calculated according to the formula obtained in the 1D geomechanical study, including uniaxial compressive strength (UCS), tensile strength (TSTR), and internal friction angle (FANG), as shown in Figure 7.

Figure 8 showed the comparison of 1D (red) and 3D geomechanical parameters (colored), from left to right, as Young's modulus and Poisson's ratio. It can be seen that the 1D and 3D geomechanical parameters have good consistency, thus verifying the reliability of the mechanical parameters in the 3D model.

3.1.3. Boundary Conditions. The value of horizontal in situ stress is mainly affected by overlying stress, pore pressure, and tectonic events. The effect of overburden stress is reflected in the model by the density and gravity of the overburden. The effect of pore pressure will be reflected by the input 3D pore pressure attribute volume in the FEM simulation. In the VISAGE simulation, the effect of tectonic events is reflected as the boundary conditions using the structural strain method (tectonic stress coefficient), which is used

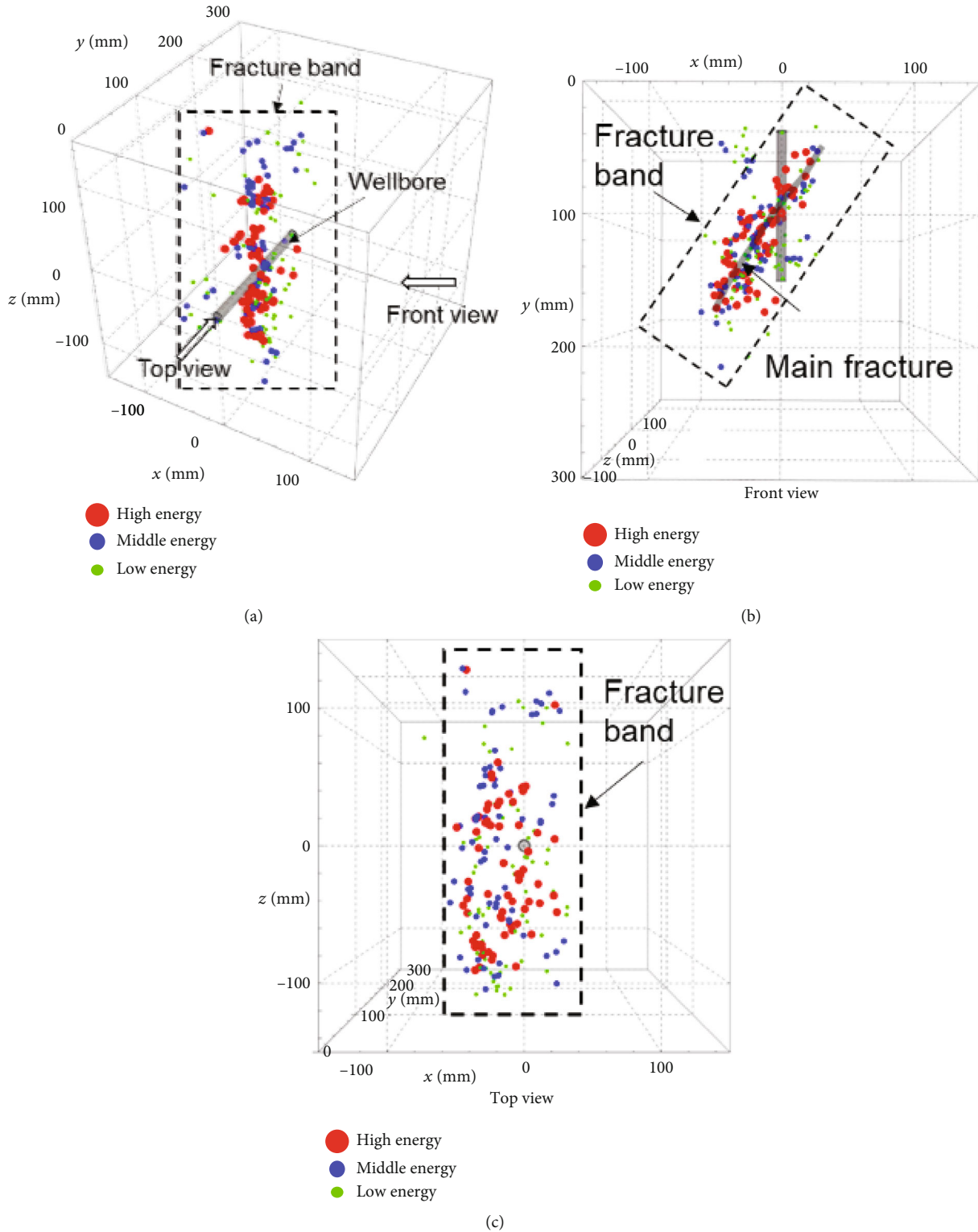


FIGURE 4: Different views of AE localization of specimen #1.

to apply rock deformation caused by tectonic action on the boundary around the model. Similar to the 1D geomechanical model, the 3D model is based on long-term geomechanical research experience in Longdong area and uses 0.00012 and 0.00242 as the tectonic strain values in the

direction of the minimum and maximum horizontal principal stress, respectively.

3.1.4. *Simulation Results of In Situ Stress.* Figure 9 showed the comparison of the 1D (black line) and 3D (colored) in

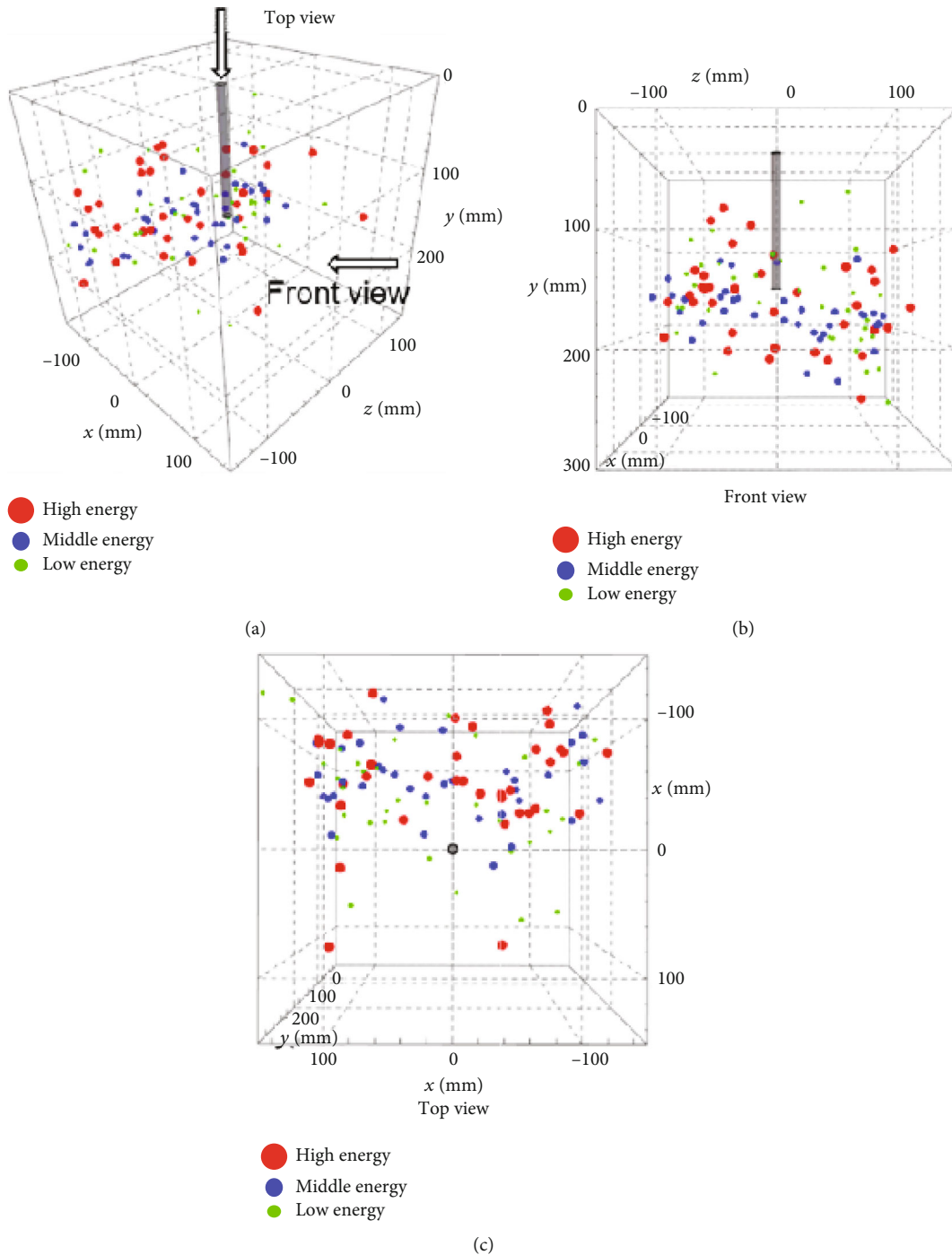


FIGURE 5: Different views of the AE localization of specimen #2.

situ stress results for some horizontal wells. From left to right, the overlying stress and the minimum and maximum horizontal principal stress are listed in order. It can be seen that the 1D and 3D in situ stress models show good consistency.

The 3D distribution of the X platform is shown in Figure 10. The 3D in situ stress distribution has a significant correlation with lithology. The stress of the mudstone layer is

high, and it is simple to control fracture propagation. The minimum horizontal principal stress of sandstone is approximately 32 MPa and that of mudstone is approximately 40 MPa.

3.2. Hydraulic Fracture Parameter Optimizations. Due to the unique sedimentary characteristics of shale oil reservoirs in the Ordos Basin, the sand bodies exhibit strong

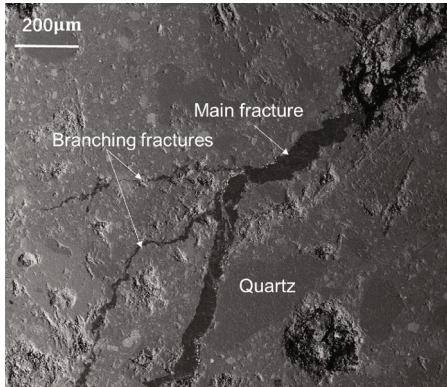


FIGURE 6: Microfracture morphology under a scanning electron microscope.

heterogeneity and well-developed natural fractures. Twelve horizontal wells are drilled on the X platform in the targeted zones of Chang-7₁² and Chang-7₂¹ with a well spacing of 200–400 m. Optimizations are conducted by considering the following factors: post-frac production control, influences of natural fractures, stress shadow and cluster spacing, stage length, well length, mudstone fracability, vertical stress shielding fluid system, and fluid/proppant volumes. Based on the previous research on the distribution of in situ stress, the “stress shadow” effect is introduced into the research of multicluster fracture initiation and expansion. This effect more accurately characterizes the competition between close-range hydraulic fracturing fractures.

3.2.1. Fracture Propagations under Different Cluster Spacing. A 50 m horizontal section with good petrophysical properties are selected for well Y. The fracture propagations of cluster spacings of 2.5 m, 5 m, 10 m, 15 m, and 20 m are examined under fixed fluid and proppant volume. The perforation location and study results are shown in Figure 11.

Figure 11 shows that the smaller the cluster spacing, the more obvious the stress interference between the fractures, and the length of the fractures in some perforated clusters is very limited, while some cannot even initiate cracks. However, after the cluster spacing is increased, the stress interference between perforated clusters becomes significantly smaller, fracture extension is guaranteed, and the length is increased. The simulated hydraulic fracture geometric parameters are shown in Table 3.

3.2.2. Productions under Different Cluster Spacing. The production forecast is conducted using the Petrel-IX simulator based on the fracture simulation results (Figure 12). It can be seen that as the fracture length increases, the pressure drawdown area increases. The pressure drawdown area further grows under increased number of fractures.

Under a fixed 400 m well spacing, the 1-year, 3-year, and 5-year cumulative production of different cluster spacings are plotted in Figure 13, which revealed that a 5 m cluster spacing resulted in the highest cumulative produc-

tion, and hence, it is the optimum cluster spacing under given conditions.

Under a fixed 200 m well spacing, the 1-year, 3-year, and 5-year cumulative production of different cluster spacings are plotted in Figure 14, which revealed that the 5 m cluster spacing result in the highest cumulative production, and hence, it is the optimum cluster spacing under given conditions.

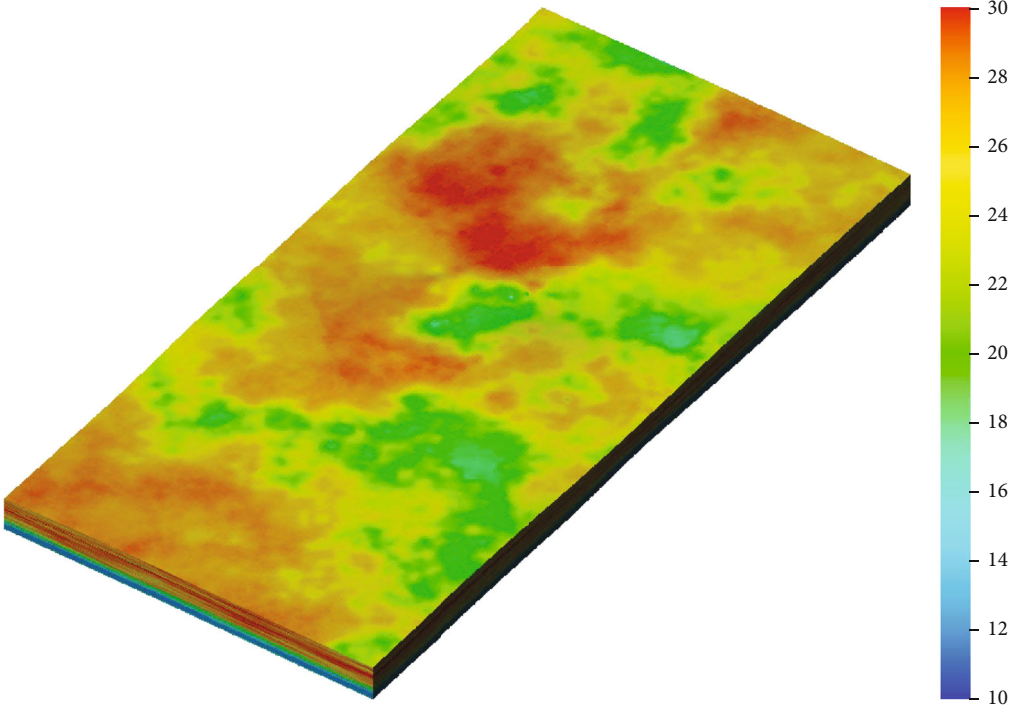
3.2.3. Stage Length and Number of Clusters. According to previous global unconventional oil and gas development experience, as the number of single-stage perforating clusters increases, the percentage of perforations that do not contribute to production increases. The perforation cluster of 4, 5, and 6 will result in the average effective production contribution clusters of 2.8, 3.8, and 3.1, respectively. In general, when the perforation clusters are more than 5, the effective perforation clusters are between 3 and 4 clusters on average, and the number of effective perforation clusters does not increase with the increase of the total perforation clusters (Figure 15). Therefore, the number of single-stage perforation clusters in Chang-7 shale reservoir stimulation is suggested to be no more than 5.

4. Optimization Design Methods of Multistage Fractures considering Engineering Sweet Spots

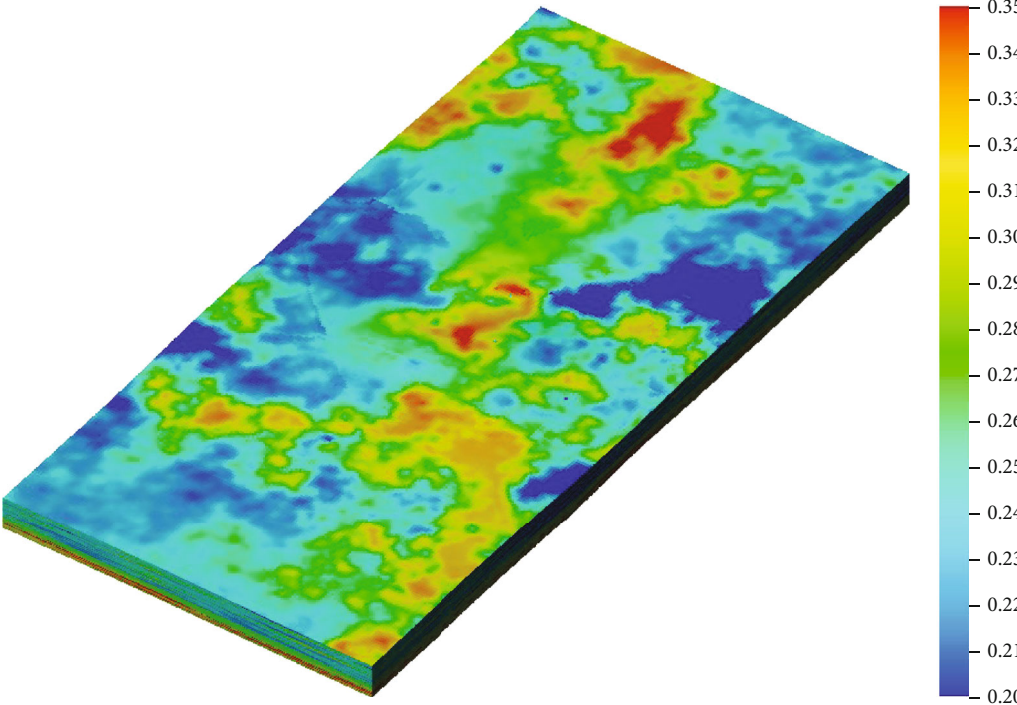
4.1. Controlling Factors and Identification of Engineering Sweet Spots. The purpose of the engineering sweet spot evaluation is to select the optimum horizon section for hydraulic fracturing to achieve the optimal reservoir treatment. The identification of the geology and engineering integrated sweet spots in the Ordos Basin is conducted by fully utilizing the well logging data for the basic parameters [16]; the flow-chart is as follows:

- (1) Basic well logging data interpretation, including mud content, porosity, permeability, oil saturation, in situ stress, and rock mechanical properties
- (2) Identification of geological sweet spots by interpreting mud content, porosity, permeability, and oil saturation
- (3) Identification of engineering sweet spots by analyzing the minimum principle stress, brittleness index, and other mechanical parameters
- (4) Statistical study of the parameters of geological and engineering sweet spots and establish classification criteria
- (5) Comprehensively evaluate the geological and engineering sweet sport to determine the integrated sweet spots for hydraulic fracturing

The integrated sweet spot identification is performed based on the interpretation of logging and production data of 213 oil wells, as shown in Table 4, wherein type I, II, and III sweet spots are marked in red, yellow, and white,

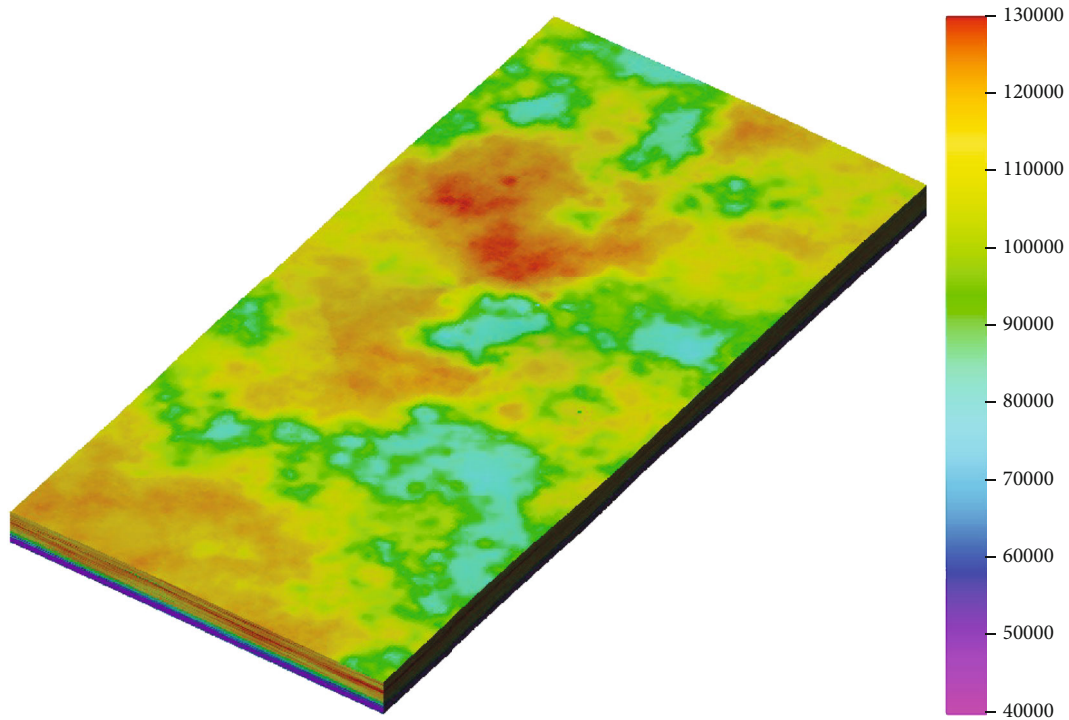


(a) Young's modulus

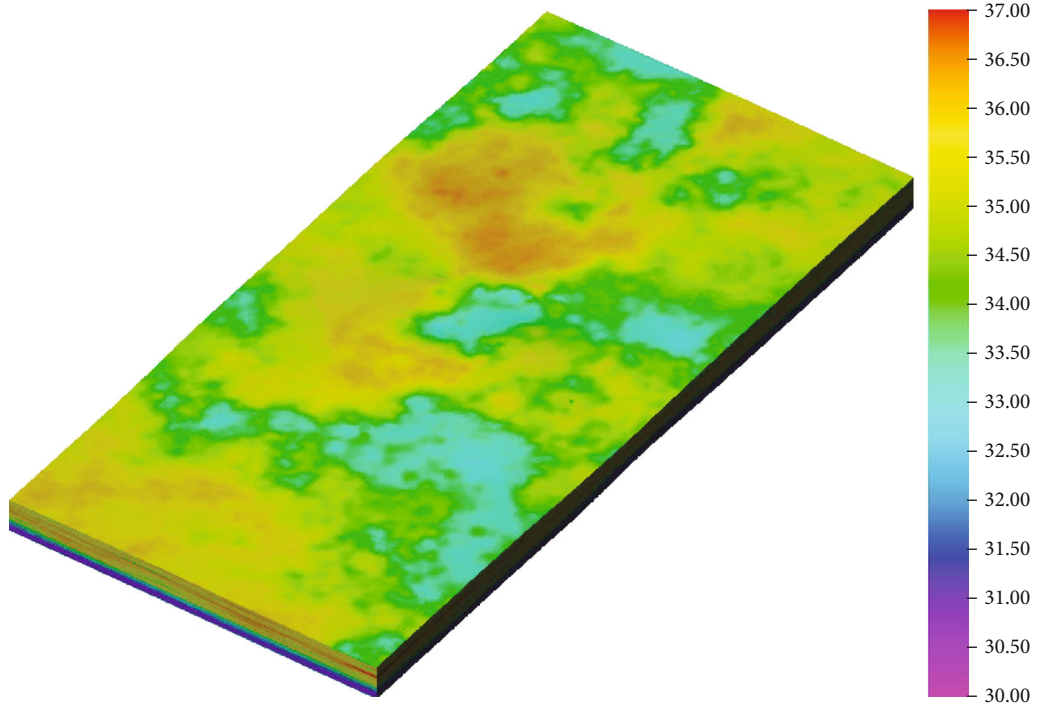


(b) Poisson's ratio

FIGURE 7: Continued.



(c) Uniaxial compressive strength



(d) Internal friction angle

FIGURE 7: 3D mechanical properties in this study.

respectively. The symbols Φ_e , S_o , σ_h , BI, and Sh represent effective porosity, oil saturation, minimum horizontal stress, brittleness index, and mud content, respectively. The identification method is applied to well Y, and the identification results are shown in Figure 16.

4.2. Optimization of Perforation in Multistage Hydraulic Fracturing. Perforation optimization is one of the major factors in multistage hydraulic fracturing, and the key is to achieve the optimum match for perforation and reservoir fracability. The perforation optimization requires a

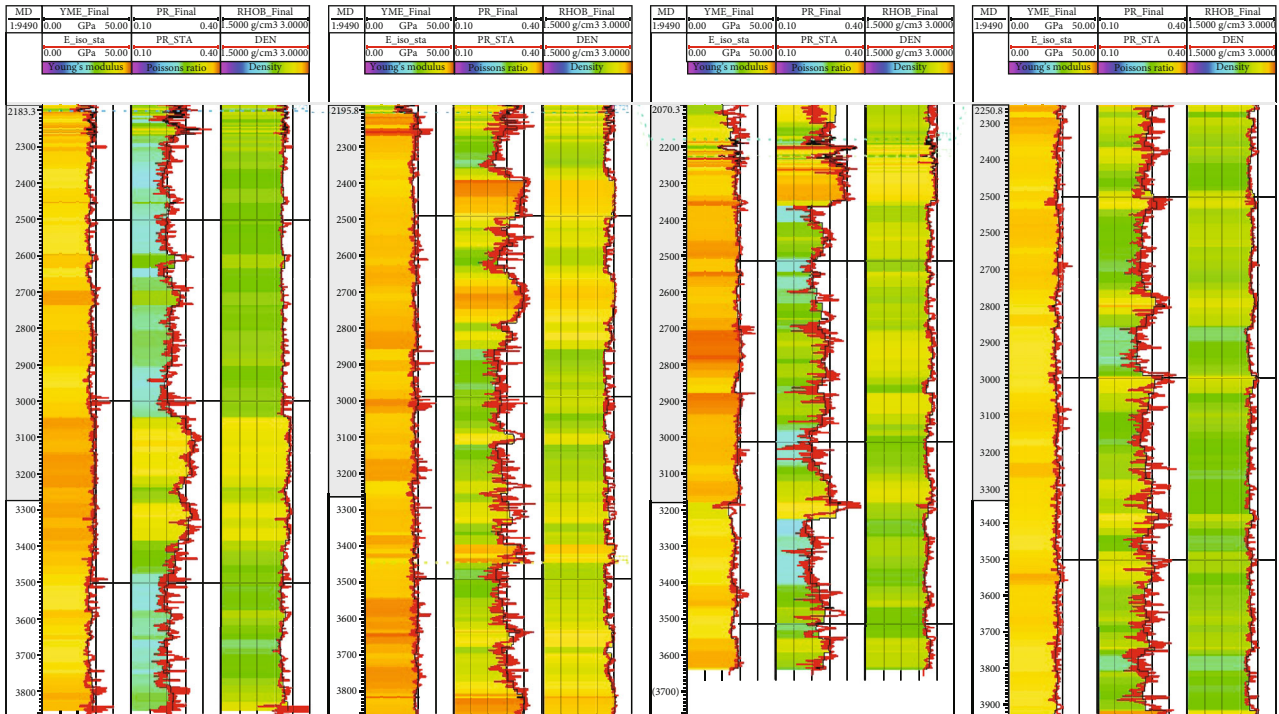


FIGURE 8: Comparisons of 1D (red line) and 3D (colored) mechanical properties in this study.

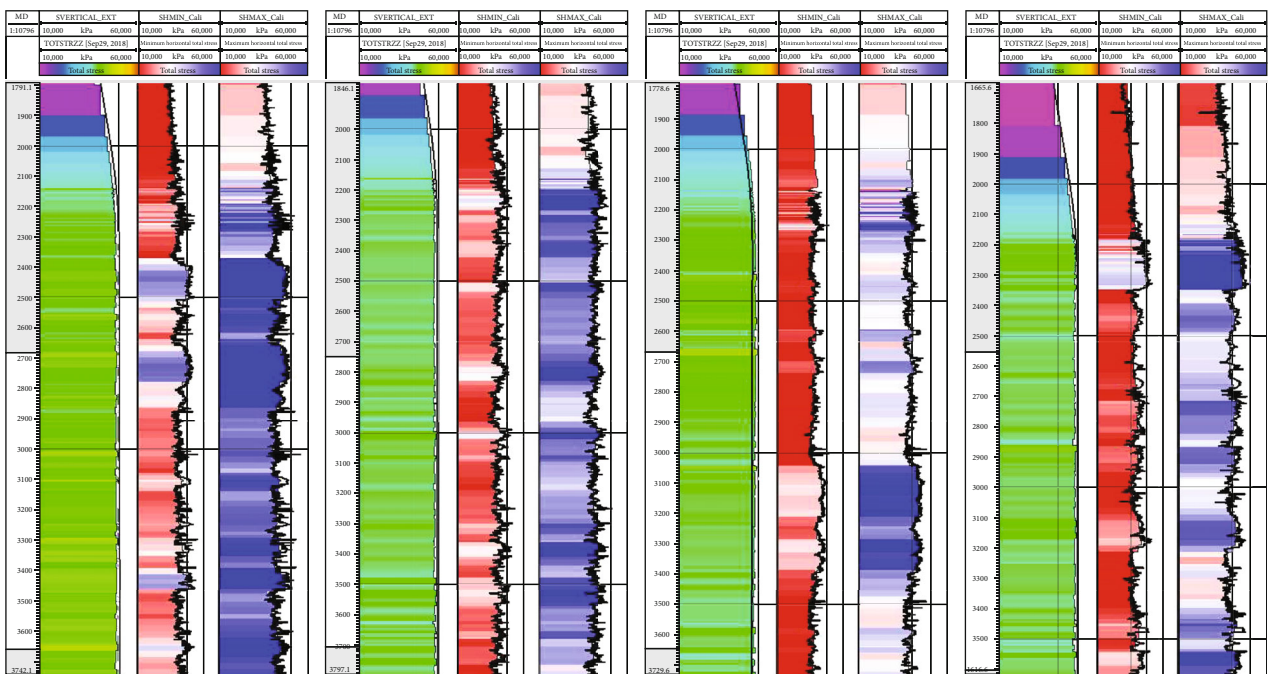


FIGURE 9: Comparison of the 1D (black line) and 3D (colored) in-situ stress results for some horizontal wells.

reasonable design for cluster spacing, cluster location, and number of holes, in order to ensure optimum reservoir stimulation. The operators proposed a perforation design specifically customized to the reservoir properties of Chang-7 reservoir.

- (1) Based on the integrated geological and engineering sweet spot, the cluster spacing is differentiated. The 5–7 m cluster spacing is designed for the type I sweet spots, while the 8–12 m cluster spacing is designed for the type II sweet spots

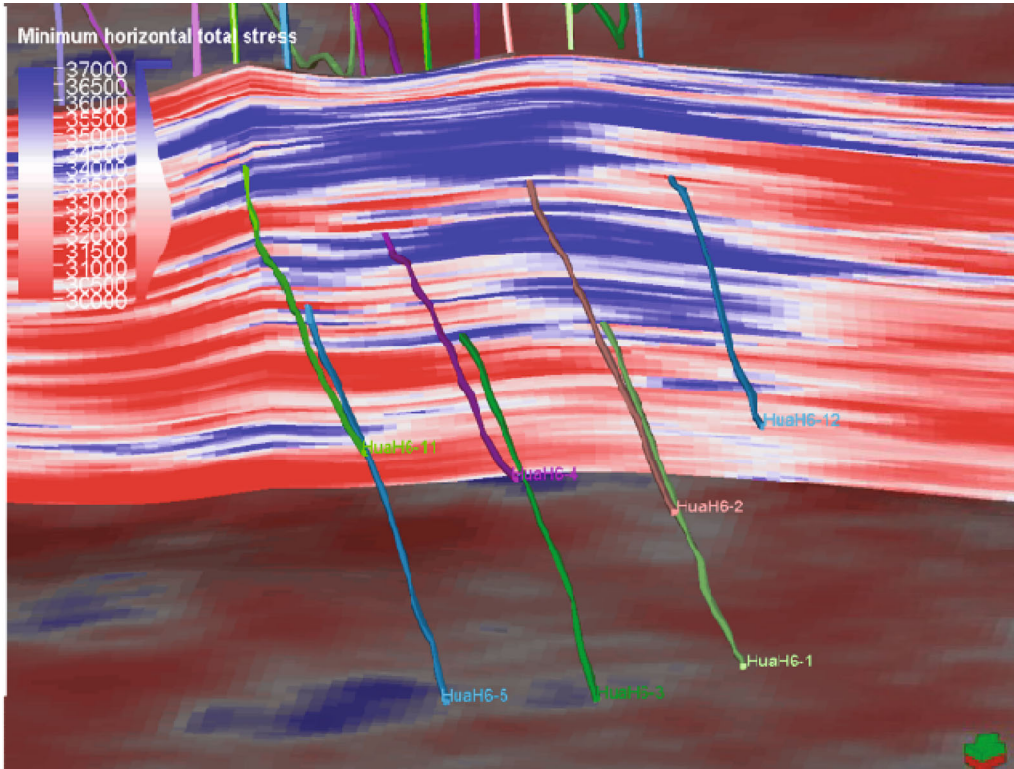


FIGURE 10: 3D distribution of the X platform.

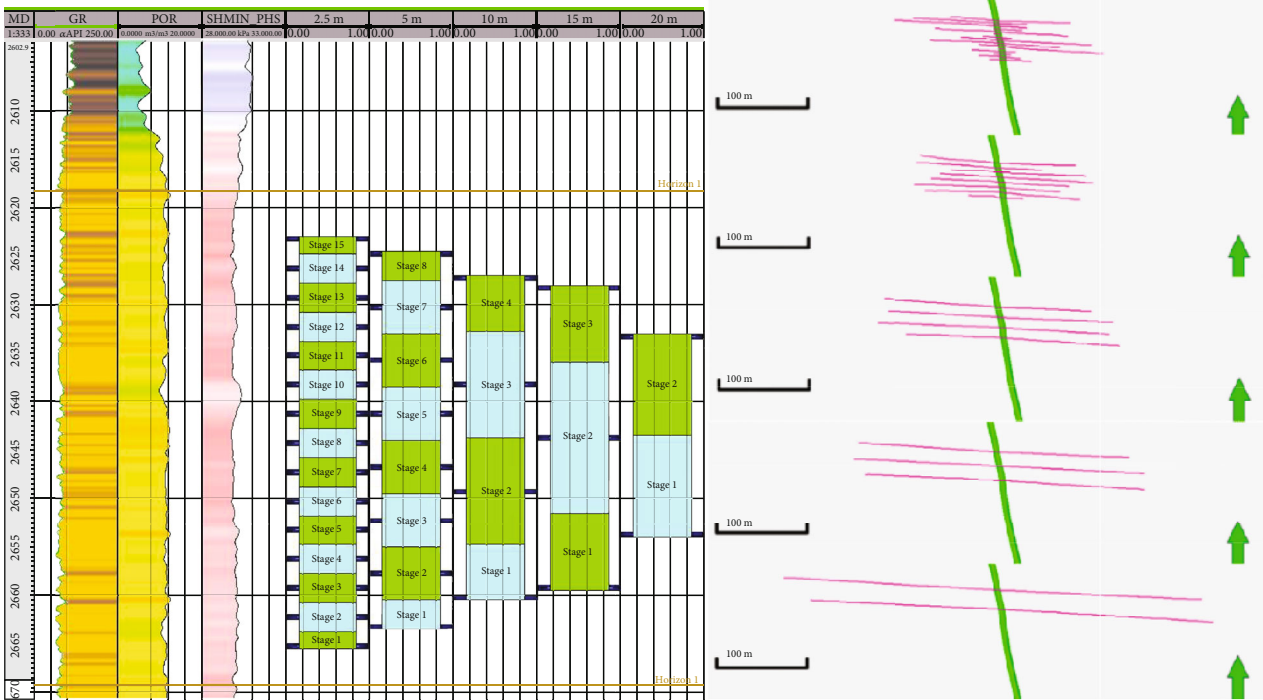


FIGURE 11: Locations of perforations and the fracture geometries.

(2) Considering the influence of mechanical properties and in situ stress differences on the simultaneous initiation of multicluster perforation, limited entry

perforation technology is used to achieve effective initiation of multicluster fractures. Number 36–45 holes are placed in one cluster of perforation

TABLE 3: Parameters of the hydraulic fracture geometries under different cluster spacings.

Cluster spacing (m)	2.5	5	10	15	20
Cluster number	15	8	4	3	2
Average half length (m)	33.8	67.1	113.6	146.0	217.5
Average fracture conductivity (md.m)	837	818	945	1041	1013

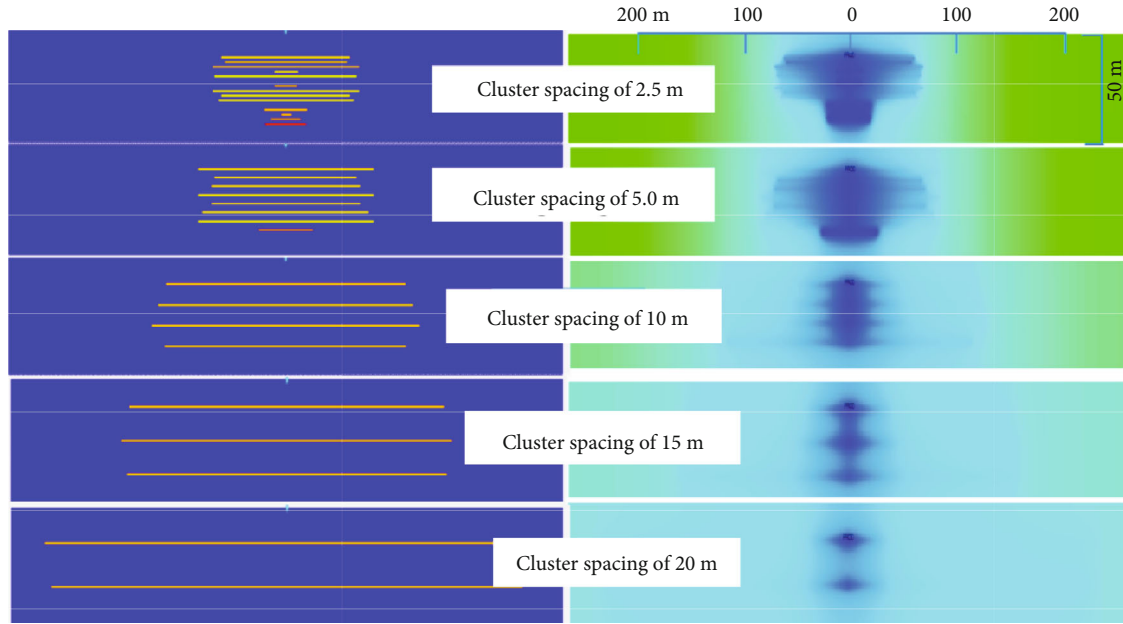


FIGURE 12: Pressure drawdown under different cluster spacings.

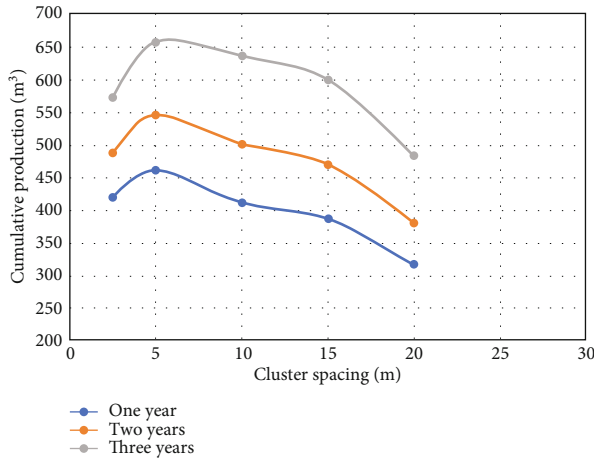


FIGURE 13: Cumulative production under different cluster spacings at 400 m well spacing.

The designing of a multi-cluster perforation scheme begins with dividing the horizontal section into stages, followed by the selection of the perforation methods. The perforation locations are first determined by the examination of geological sweet spots, adjustment according to the engineering sweet spots, and optimization of hole numbers.

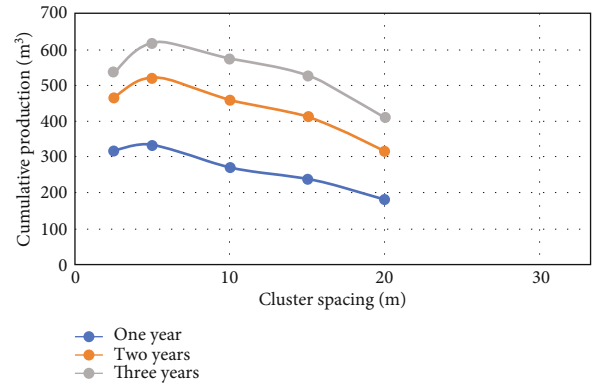


FIGURE 14: Cumulative production under different cluster spacings at 200 m well spacing.

A typical perforation optimization example of well Y is shown in Figure 17.

5. Field Application and Result Evaluation

The proposed optimization method is applied to 174 wells, which have an average lateral length of 1706 m, divided into 22 stages with 94 clusters. The average fracture fluid volume

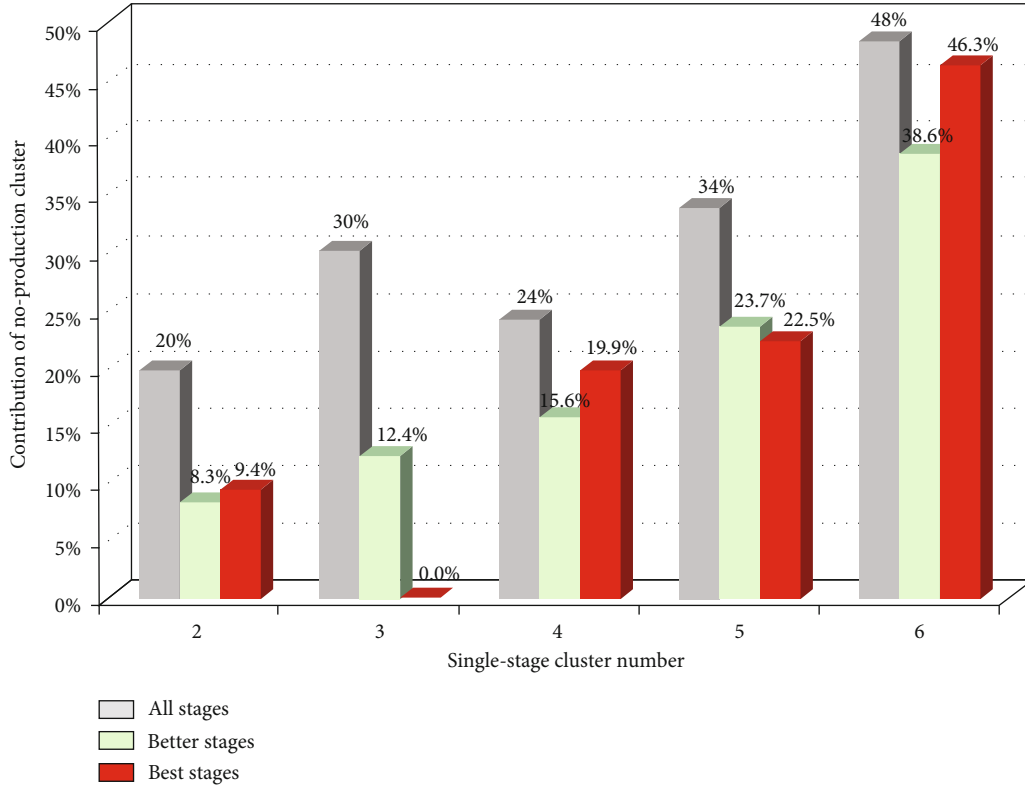


FIGURE 15: Comparison of single-stage cluster and effective clusters in Marcellus, Haynesville, Eagleford, Fayetteville, Barnett, and Woodford shales [27].

TABLE 4: Integrated sweet spot identification criteria.

		Geological sweet spots			Nonreservoir
		I	II	III	
Engineering sweet spots	I	$\Phi_e \geq 5\%$ $S_o \geq 70\%$ $\sigma_h \leq 30 \text{ MPa}$ $BI \geq 50$	$3 \leq \Phi_e < 5\%$ $50 \leq S_o < 70\%$ $\sigma_h \leq 30 \text{ MPa}$ $BI \geq 50$	$\Phi_e < 3\%$ $S_o < 50\%$ $\sigma_h \leq 30 \text{ MPa}$ $BI \geq 50$	
	II	$\Phi_e \geq 5\%$ $S_o \geq 70\%$ $30 < \sigma_h \leq 34 \text{ MPa}$ $40 \leq BI < 50$	$3 \leq \Phi_e < 5\%$ $50 \leq S_o < 70\%$ $30 < \sigma_h \leq 34 \text{ MPa}$ $40 \leq BI < 50$	$\Phi_e < 3\%$ $S_o < 50\%$ $30 < \sigma_h \leq 34 \text{ MPa}$ $40 \leq BI < 50$	$S_h > 40\%$
	III	$\Phi_e \geq 5\%$ $S_o \geq 70\%$ $\sigma_h > 34 \text{ MPa}$ $BI < 40$	$3 \leq \Phi_e < 5\%$ $50 \leq S_o < 70\%$ $\sigma_h > 34 \text{ MPa}$ $BI < 40$	$\Phi_e < 3\%$ $S_o < 50\%$ $\sigma_h > 34 \text{ MPa}$ $BI < 40$	

is 28294 m³, pumping at 10–15 m³/min, with proppant usage at 3146 m³. The fracture spacing is 5–15 m, with a fracture density of 7.8 fracture/100 m. The most fractured stages are 48 with 248 clusters, and the highest fluid and proppant volumes are 72000 m³ and 12000 ton, respectively. Microseismic monitoring indicated the minimized unstimulated reservoir volume and that the reservoir is largely stimulated at more than 90% SRV. The initial post-frac production increased from 10 ton/day to 16.8 ton/day. The first-year cumulative production reached 4680 ton, and the decline rate dropped from 42.5% to 27.8%. The cumulative production in the

third year is estimated at 8766 ton. Horizontal wells with a lateral length of 1500 m and well spacing of 400 m could produce a EUR of 24000 ton/well with an investment return rate of 9.11%.

6. Conclusion

- (1) Band-shaped fractures are created in Chang-7 shale oil reservoir stimulations. The primary fracture generated the secondary fractures, which further activated the natural fractures and induced shear failure.

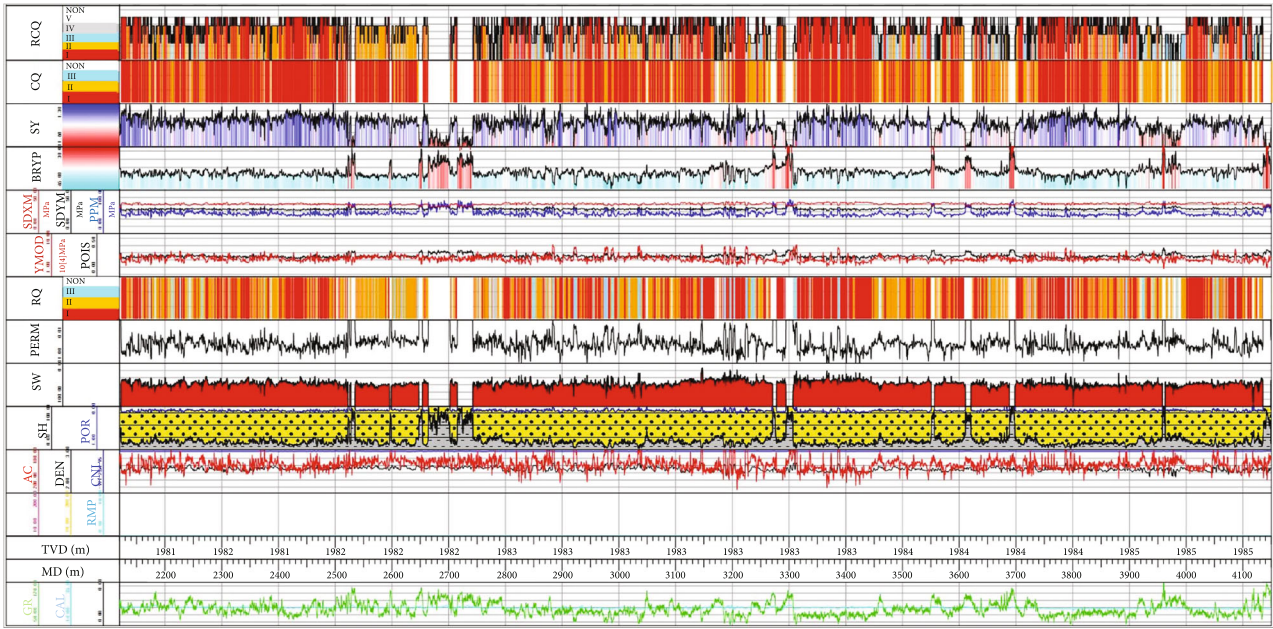


FIGURE 16: Integrated sweet spot identification in well Y.

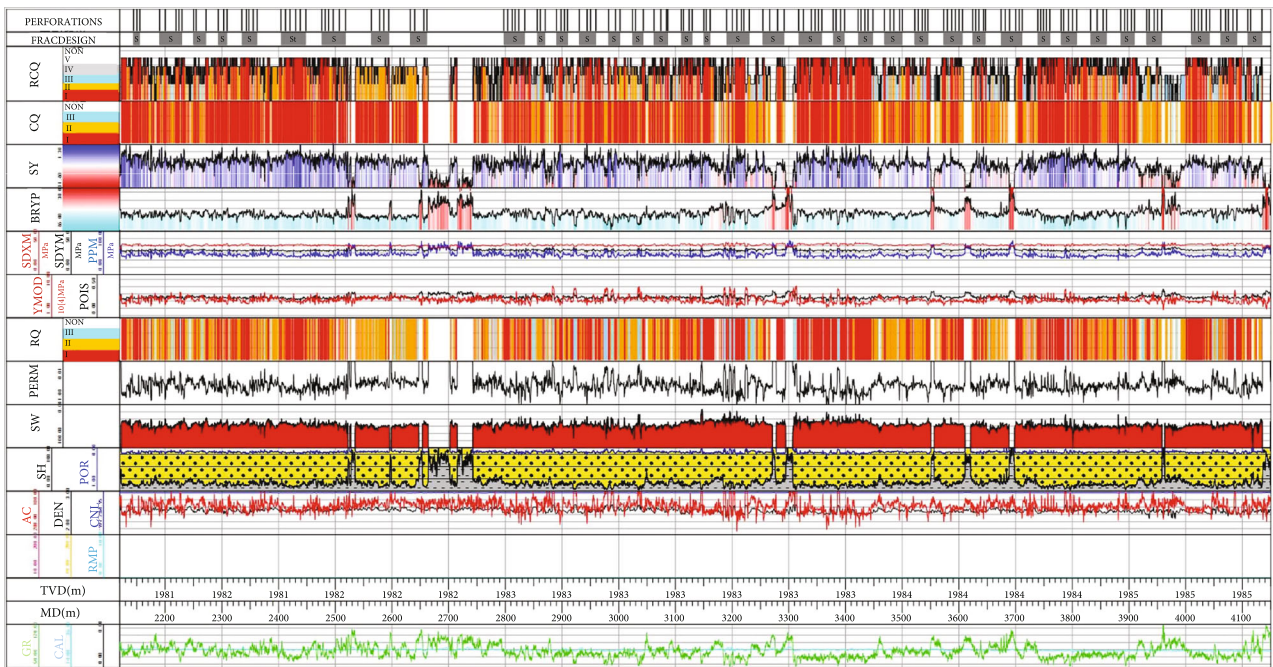


FIGURE 17: Perforation optimization example of well Y.

- (2) The current fracturing design scheme for the efficient development of Chang-7 reservoir has been formed according to the fracture parameter optimization and the design basis of shale oil reservoir treatment
- (3) Based on the shale reservoir classification and evaluation, this study established a multicluster perforation optimization technology for horizontal wells in shale reservoirs with the goal of fully initiating multiple clusters and fully utilizing the fracture sweet spots
- (4) The proposed optimization methods are applied to the field operations and great production enhancements are achieved

Data Availability

Data are available on request.

Conflicts of Interest

The authors declare that there is no conflict of interest regarding the publication of this paper.

Acknowledgments

This study is sponsored by the “Demonstration Project of Tight Oil Development in the Ordos Basin” (2017ZX05069), “Demonstration Project of Low Permeability Reservoir Development in the Ordos Basin” (2016ZX05050), and “Tight Oil Accumulation, Exploration and Development” (2016ZX05046).

References

- [1] L. Mu, Z. Zhao, X. Li et al., “Fracturing technology of stimulated reservoir volume with subdivision cutting for shale oil horizontal wells in Ordos Basin,” *Oil and Gas Geology*, vol. 40, pp. 626–635, 2019.
- [2] G. Sheng, H. Zhao, Y. Su et al., “An analytical model to couple gas storage and transport capacity in organic matter with non-circular pores,” *Fuel*, vol. 268, p. 117288, 2020.
- [3] G. Sheng, Y. Su, and W. Wang, “A new fractal approach for describing induced-fracture porosity/permeability/ compressibility in stimulated unconventional reservoirs,” *Journal of Petroleum Science and Engineering*, vol. 179, pp. 855–866, 2019.
- [4] J. Ciezobka, J. Courtier, and J. Wicker, “Hydraulic fracturing test site (HFTS) project overview and summary of results,” *SPE/AAPG/SEG Unconventional Resources Technology Conference*, 2018, Houston, TX, United States, July 2018, 2018Unconventional Resources Technology Conference (URTEC).
- [5] J. F. W. Gale, S. J. Elliott, and S. E. Laubach, “Hydraulic fractures in core from stimulated reservoirs: core fracture description of HFTs slant core, Midland Basin, West Texas,” *SPE/AAPG/SEG Unconventional Resources Technology Conference*, 2018, Houston, TX, United States, July 2018, 2018Unconventional Resources Technology Conference (URTEC).
- [6] A. P. Bunger, “A photometry method for measuring the opening of fluid-filled fractures,” *Measurement Science and Technology*, vol. 17, no. 12, pp. 3237–3244, 2006.
- [7] D. Zhou, G. Zhang, P. Zhao, Y. Wang, and S. Xu, “Effects of post-instability induced by supercritical CO₂ phase change on fracture dynamic propagation,” *Journal of Petroleum Science and Engineering*, vol. 162, pp. 358–366, 2018.
- [8] D. Zhou, G. Zhang, Y. Wang, and Y. Xing, “Experimental investigation on fracture propagation modes in supercritical carbon dioxide fracturing using acoustic emission monitoring,” *International Journal of Rock Mechanics and Mining Sciences*, vol. 110, pp. 111–119, 2018.
- [9] Y. Chitrana, C. Moreno, C. Sondergeld, and C. Rai, “An experimental investigation into hydraulic fracture propagation under different applied stresses in tight sands using acoustic emissions,” *Journal of Petroleum Science and Engineering*, vol. 108, pp. 151–161, 2013.
- [10] G. Dresen, S. Stanchits, and E. Rybacki, “Borehole breakout evolution through acoustic emission location analysis,” *International Journal of Rock Mechanics and Mining Sciences*, vol. 47, no. 3, pp. 426–435, 2010.
- [11] J. Groenenboom and D. B. Van Dam, “Monitoring hydraulic fracture growth: laboratory experiments,” *Geophysics*, vol. 65, no. 2, pp. 603–611, 2000.
- [12] D. B. Van Dam, C. J. De Pater, and R. Romijn, “Analysis of hydraulic fracture closure in laboratory experiments,” *Proceedings of the 1998 SPR/ISRM Rock Mechanics In Petroleum Engineering, EUROCK. Part 1 (of 2)*, 1998, Trondheim, Norway, July 1998, 1998Soc Pet Eng (SPE).
- [13] F. Renard, D. Bernard, J. Desrues, and A. Ougier-Simonin, “3D imaging of fracture propagation using synchrotron X-ray microtomography,” *Earth and Planetary Science Letters*, vol. 286, no. 1-2, pp. 285–291, 2009.
- [14] M. J. AlTammar and M. M. Sharma, “Effect of borehole pressurization scheme on breakdown pressure,” *Rock Mechanics and Rock Engineering*, vol. 52, no. 8, pp. 2709–2715, 2019.
- [15] P. A. Sookprasong, R. S. Hurt, C. C. Gill, and R. F. Lafollette, “Fiber optic DAS and DTS in multicluster, multistage horizontal well fracturing: Interpreting hydraulic fracture initiation and propagation through diagnostics,” *SPE Annual Technical Conference and Exhibition*, 2014, Amsterdam, Netherlands, October 2014, 2014Society of Petroleum Engineers (SPE).
- [16] X. Yang, G. Zhang, X. Du et al., “Measurement and implications of the dynamic fracture width in hydraulic fracturing using FBG strain sensors,” *51st US Rock Mechanics / Geomechanics Symposium*, 2017, San Francisco, CA, United States, June 2017, 2017American Rock Mechanics Association (ARMA).
- [17] N. H. Cuevas, *Electrokinetic coupling in hydraulic fracture propagation*, ProQuest LLC, 2009.
- [18] K. K. Chong, W. V. Grieser, A. Passman, C. H. Tamayo, N. Modeland, and B. Burke, “A completions guide book to shale-play development: a review of successful approaches towards shale-play stimulation in the last two decades,” *Society of Petroleum Engineers - Canadian Unconventional Resources and International Petroleum Conference 2010*, 2010, Calgary, Alberta, Canada, October 2010, 2010.
- [19] M. Mullen and M. Enderlin, “Fracability index - more than just calculating rock properties,” *SPE Annual Technical Conference and Exhibition 2012: Unconventional Wisdom*, 2012, San Antonio, TX, United States, October 2012, 2012Society of Petroleum Engineers (SPE).
- [20] C. Fang and M. Amro, “Influence factors of fracability in non-marine shale,” *European Unconventional Resources Conference and Exhibition 2014: Unlocking European Potential*, vol. 2, 2014, pp. 1196–1202, Vienna, Austria, February 2014, Society of Petroleum Engineers.
- [21] Y. Hu, M. E. G. Perdomo, K. Wu et al., “A novel model of brittleness index for shale gas reservoirs: confining pressure effect,” *SPE Asia Pacific Unconventional Resources Conference and Exhibition*, 2015, Brisbane, QLD, Australia, November 2015, 2015Society of Petroleum Engineers.
- [22] X. Jin, S. N. Shah, J.-C. Roegiers, and B. Zhang, “An integrated petrophysics and geomechanics approach for fracability evaluation in shale reservoirs,” *SPE Journal*, vol. 20, no. 3, pp. 518–526, 2015.
- [23] J. Xu and S. Sonnenberg, “Brittleness and rock strength of the Bakken formation, Williston basin, North Dakota,” *SPE/AAPG/SEG Unconventional Resources Technology*

Conference 6, 2016, San Antonio, TX, United States, August 2016, 2016Unconventional Resources Technology Conference (URTEC).

- [24] C. Cipolla, X. Weng, H. Onda, T. Nadaraja, U. Ganguly, and R. Malpani, "New algorithms and integrated workflow for tight gas and shale completions," *SPE Annual Technical Conference and Exhibition*, vol. 4, 2011, pp. 2950–2967, Denver, CO, United States, October–November 2011, Society of Petroleum Engineers (SPE).
- [25] H. Liu, Y. Luo, X. Li et al., "Advanced completion and fracturing techniques in tight oil reservoirs in ordos basin: a workflow to maximize well potential," *International Petroleum Technology Conference 2013: Challenging Technology and Economic Limits to Meet the Global Energy Demand*, 2013, Beijing, China, March 2013, 2013.
- [26] E. Wigger, A. Viswanathan, K. Fisher, R. Slocombe, P. Kaufman, and C. Chadwick, "Logging solutions for completion optimization in unconventional resource plays," *European Unconventional Resources Conference and Exhibition: Unlocking European Potential*, 2014, Vienna, Austria, February 2014, 2014Society of Petroleum Engineers.
- [27] C. Miller, G. Waters, and E. Rylander, "Evaluation of production log data from horizontal wells drilled in organic shales," *Society of Petroleum Engineers - SPE Americas Unconventional Gas Conference 2011, UGC 2011, Society of Petroleum Engineers (SPE)*, 2011, pp. 623–645, The Woodlands, Texas, USA, June 2011.

Research Article

Analysis of Dynamic Damage-Induced Porosity Changes of Granites in Leaching Mining Technique Based on SHPB Test

Yichen Miao ^{1,2}, Changwu Liu ^{2,3}, Zhiliang He,^{1,2,4} Yuanjun Ma,^{2,3} Haikuan Wu,^{2,3} and Ding Wang⁵

¹Institute of Disaster Management and Reconstruction, Sichuan University-The Hong Kong Polytechnic University, Chengdu, China

²State Key Laboratory of Hydraulics and Mountain River Engineering, Sichuan University, Chengdu, China

³College of Water Resource and Hydropower, Sichuan University, Chengdu, China

⁴School of Environment and Resource, Southwest University of Science & Technology, Mianyang, China

⁵School of Civil Engineering and Architecture, Southwest University of Science & Technology, Mianyang, China

Correspondence should be addressed to Changwu Liu; liuchangwu@scu.edu.cn

Received 16 July 2020; Revised 25 July 2020; Accepted 27 August 2020; Published 9 September 2020

Academic Editor: Stefan Iglauer

Copyright © 2020 Yichen Miao et al. This is an open access article distributed under the Creative Commons Attribution License, which permits unrestricted use, distribution, and reproduction in any medium, provided the original work is properly cited.

In situ leaching was a very important technical approach in ion-adsorption rare earth mining, because it can effectively avoid the geological hazards, protect the environment, and reduce the mining costs. The critical issue of this mining technique was to increase the permeability of ion-adsorption rare earth deposits. Due to the close relationship between the permeability and the porosity, in this paper, several experiments were conducted to find the dynamic characteristics of the granite deposit and the relationship between the dynamic characteristics and the porosity. Moreover, the SHPB test system was equipped to conduct the dynamic test, and the ultrasonic wave detector with high precision was employed to obtain the damage factor of granites. The test results showed that the failure mode under dynamic load and static load was close, and they both had splitting failure. Besides, when cyclic dynamic loading velocity was between 5.8 m/s and 8.4 m/s, the specimen was not a failure, but it caused the damage and changed the porosity. And the dynamic thresholds of failure stress and damage stress were found. Finally, a linear relationship between the porosity and the damage factor was found, which would help to analyze and predict the change of porosity under different dynamic loading velocities.

1. Introduction

The rare earth elements (REE) are valuable mineral resources, being widely used in advanced electronics, lighting, power generation, and military application. The rare earth elements were first discovered at the end of the 18th century in Sweden [1, 2]. Until now, China's rare earth reserves are 18 million tonnes, accounting for 23% of global reserves, which dominated all aspects of supply chains of rare earth minerals in the international markets [3–5]. Chinese and rest-of-world mine production of rare earths is shown in Figure 1.

In 1970, ion-adsorption rare earth deposits were first discovered in Ganzhou, China. These deposits were formed by chemical weathering decomposition and dissolution of granites, which contained relatively high abundance of rare earth elements [7]. Ion-adsorption rare earth reserves only accounted for 2.9% of the total rare earth reserves in China, and they were sparsely distributed throughout seven adjacent provinces of southern China, which were rarely found anywhere else in the world [8, 9]. Recently, in situ leach mining was widely used in ion-adsorption rare earth mining, because of lower cost and more environmental protection. Extraction of rare earths from ore deposits was

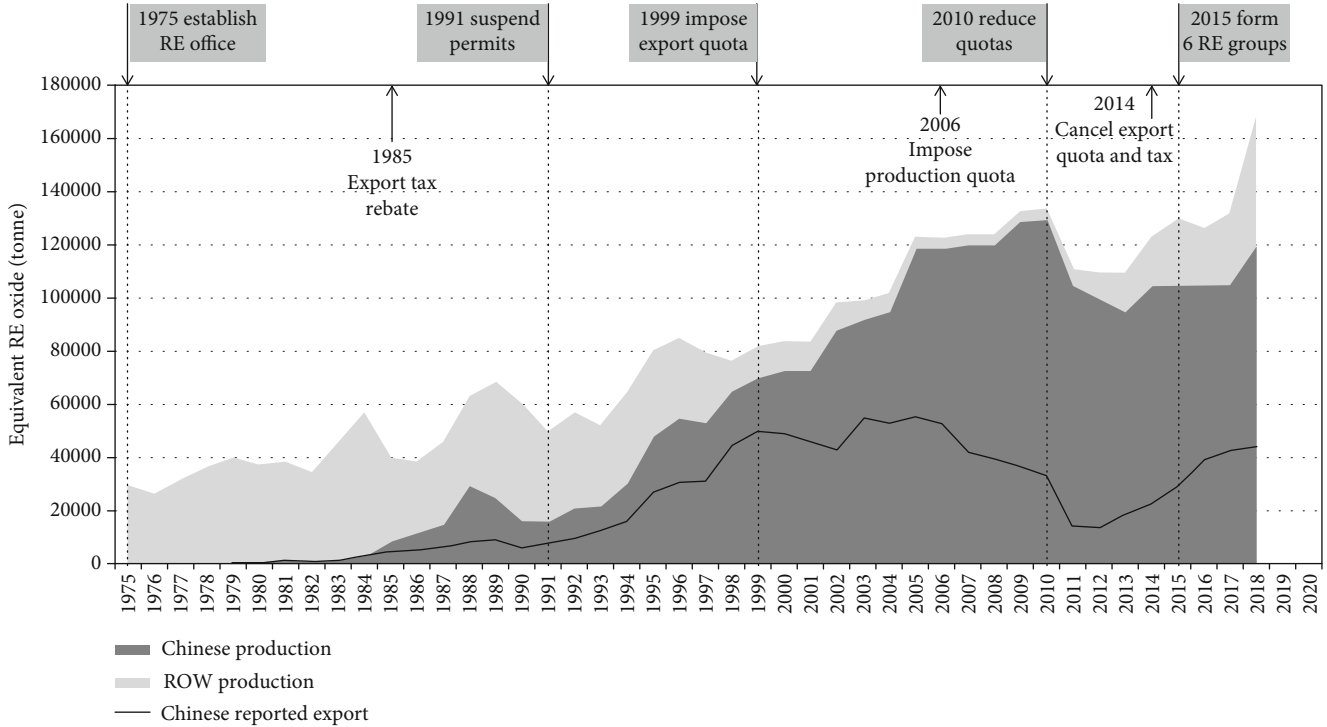
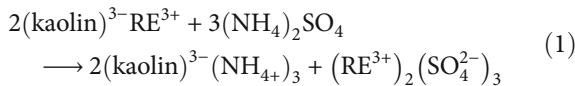


FIGURE 1: Chinese and rest-of-world mine production of rare earths [6]. This figure is reproduced from Shen et al. (2020) (under the Creative Commons Attribution License/public domain).

accomplished with aqueous electrolyte solution (ammonium sulfate $((\text{NH}_4)_2\text{SO}_4)$). The ion exchange reaction between kaolinite and $(\text{NH}_4)_2\text{SO}_4$ can be chemically represented as [10]



Many scholars had made some contributions to in situ leach mining technology. Larson summarized the information of in situ leach mining in the United States [11]. Mudd tested the technique of in situ leach mining in Australia, and he conducted the research on the issues related to chemistry and the environment [12]. Taylor et al. argued that the process of ISL (in situ leach) had considerably less environmental impact than other conventional mining techniques [13]. Parker and Jupe indicated that the technique of energy recovery from HDR (Hot Dry Rock) should be applied to leaching mining investigations [14]. Al-Harashseh and Kingman summarized the methods of leaching mining assisted by microwaves, in which the microwave technology had great potential to improve the extraction efficiency [15]. Xunzhong and Maonan made an introduction to the technical process of in situ leaching of ion-absorbed rare earth minerals, and they proved that this type of in situ leaching had many advantages [16]. Based on the principle of pollution control, Zhu et al. proposed six pollution control measures to serve as reference for mine design, pollution management, and research work [17]. Li et al. reviewed the development of techniques on the protection of resource

and environment during the exploitation process and proposed an environmental engineering model for ion-absorbed rare earth mining [18]. In the cyclic impact times, with the increase of repeated action times of impact loads, Zhu et al. indicated that the deformation modulus and yield stress of granite decreased and yield strain increased [19]. Under cyclic impaction, Jin et al. established an evolution model of damage accumulation of rocks, which was like the S-shaped growth curve [20]. Yan et al. found the relationship between dynamic load properties and porosity based on the dynamic load test of weakly weathered granites, which could help to improve the permeability of granites [21, 22]. Therefore, the permeability of granite deposits was a critical issue affecting the mining cost and environmental protection.

It is of great significance to study the dynamic mechanical properties of granites in ion-adsorption rare earth deposits. Finding the relationship between the variation of porosity and dynamic loads should be the key point to improve the permeability of granites in ore deposits. Besides, establishing the connection between the quantified damage level and the porosity greatly made sense for leaching mining and environmental protection. However, the current research results lacked the research on the above issues, especially for ion-adsorption rare earth ores under the condition of in situ leaching mining. In this paper, the split Hopkinson pressure bar (SHPB) test system was equipped to conduct the dynamic uniaxial loading test. And the longitudinal wave velocity of rock samples can be recorded by the ultrasonic wave detector, helping to reduce the dispersion of rock samples and to quantify the damage degree of granites under dynamic loading. The test results offered an opportunity to analyze the

dynamic behavior and porosity properties of granites under SHPB test, which would effectively improve the permeability of granites in ion-adsorption rare earth deposits.

2. Experimental Work

2.1. Granite Specimen Preparation. This experiment used granites in northern areas of Sichuan province, China. The geology stratum was composed of the Bikou Group and the overlying Sinian and Paleozoic sedimentary rocks, and there were more Indochina granites in the Bikou Group. The granite was off-white medium-fine-grained feldspar granite, which was grayish-white, with medium-fine-to-fine granite structure and massive. The main mineral components were (1) quartz, other-shaped granular, content about 22.9%; (2) plagioclase, self-shaped columnar, content 53.9%; (3) potash feldspar, irregular plate shape, content 17.6%; and (3) dark-colored minerals, mainly biotite, semi-self-flaky, polychromatic, content 5.6%, with hornblende being rare. (4) The secondary minerals are mainly sphene and apatite, followed by zircon, sphene, and magnetite. The XRD diffraction spectrum of granite is shown in Figure 2.

According to Standard for test methods of engineering rock mass, 2013 (GB/T 50266–2013, China), the double-sided grinding machine was used for fine processing to ensure that the parallelism error was less than 0.05 mm, and the error of the height and diameter of the specimen was not more than 0.3 mm. There were two sizes of specimens in this experiment. One size was made for uniaxial loading test, with the diameter of 50 mm and the height of 100 mm, and the other was for dynamic loading test, with the diameter of 50 mm and the height of 50 mm.

2.2. Split Hopkinson Pressure Bar (SHPB) Test System. A conventional SHPB test system was employed to conduct high strain-rate compression tests on rock specimens. The SHPB system consisted of an air gun, a striker bar, a barrel, an incident bar, a transmitted bar, a stopper, two strain gauges, a strain amplifier, and a computer, which is shown in Figure 3. In this paper, bars of SHPB used in this experiment were 40Cr alloy steel. The density was 7.81 g/cm³, the elastic wave velocity was 5410 m/s, and the diameter of the bars was 50 mm. The lengths of the incident bar and the transmitted bar were 2 m and 1.5 m, respectively. The system can achieve the dynamic loading from 0 to 500 MPa. The oscilloscope (DL850) was produced by Yokogawa Electric Co., Ltd. to monitor the strain changes of bars, which is shown in Figure 4.

In the equations below [23, 24], the following symbols were used in this paper: (1) incident wave (I), (2) transmitted wave (T), (3) reflected wave (R), (4) rock specimen (s), (5) density of bars (ρ), (6) elastic modulus of bars (E), (7) velocity of waves in bars (c), (8) cross-sectional area of bars (A), (9) cross-sectional area of specimens (A_s), and (10) length of specimens (l_0). If the specimen deformed uniformly, the strain rate $\dot{\epsilon}_s$ was calculated as follows (Figure 5):

$$\dot{\epsilon}_s = \frac{d\epsilon_s}{dt} = \frac{v_1(t) - v_2(t)}{l_0}. \quad (2)$$

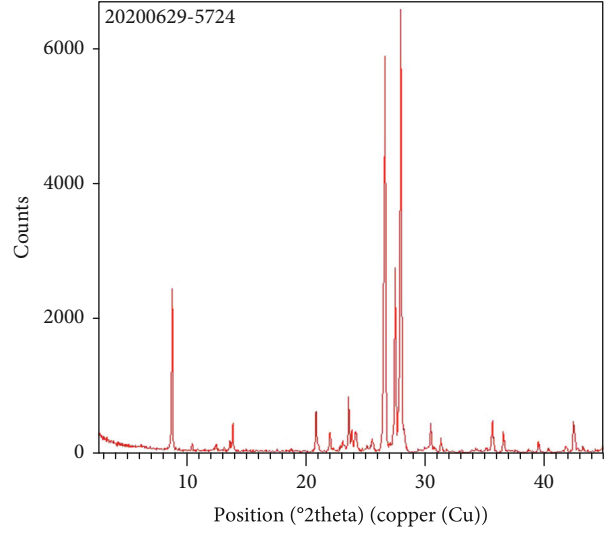


FIGURE 2: XRD diffraction spectrum of granite.

The velocity at interface 1 (v_1) and interface 2 (v_2) can be written as follows:

$$v_1(t) = c(\epsilon_I(t) - \epsilon_R(t)), \quad v_2(t) = c\epsilon_T(t). \quad (3)$$

By substituting these interface velocities into Equation (2),

$$\dot{\epsilon}_s = \frac{c[\epsilon_I(t) - \epsilon_R(t) - \epsilon_T(t)]}{l_0}. \quad (4)$$

Stresses at the ends of the specimen were

$$\begin{aligned} \sigma_1(t) &= \frac{EA}{A_s} [\epsilon_I(t) + \epsilon_R(t)], \\ \sigma_2(t) &= \frac{EA}{A_s} \epsilon_T(t). \end{aligned} \quad (5)$$

If the specimen was in dynamic stress equilibrium,

$$\epsilon_I(t) + \epsilon_R(t) = \epsilon_T(t). \quad (6)$$

Then, the stress, strain rate, and strain were given by .

$$\begin{aligned} \sigma_s(t) &= \frac{\sigma_1(t) + \sigma_2(t)}{2} = \frac{EA}{A_s} [\epsilon_I(t) + \epsilon_R(t)], \\ \dot{\epsilon}_s(t) &= \frac{-2c}{l_0} \epsilon_R(t), \\ \epsilon_s &= \frac{-2c}{l_0} \int \epsilon_R(t) dt. \end{aligned} \quad (7)$$

2.3. Ultrasonic Wave Detector. The detector named V-Meter MK IV was produced by the NDT Company. In this paper, the longitudinal P-wave was used as a measurement method. The P-wave velocity was calculated using the transmission travel time of an acoustic pulse along the axial direction of

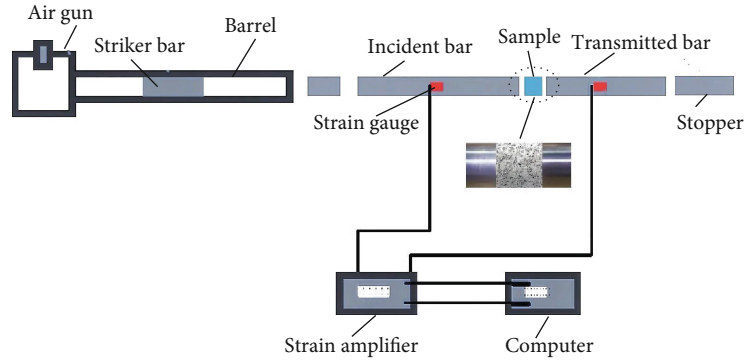


FIGURE 3: Schematic of the split Hopkinson pressure bar system.



FIGURE 4: (a) SHPB test system and (b) the oscilloscope.

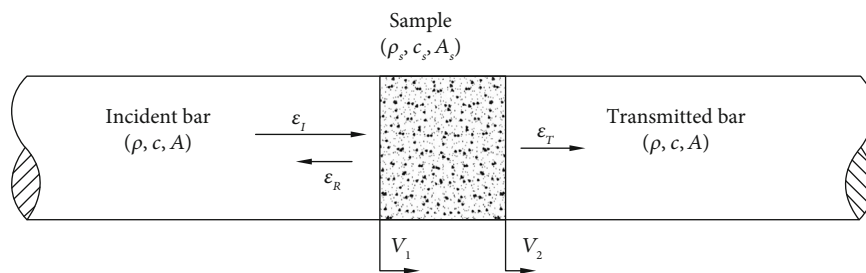


FIGURE 5: Symbols describing the parameters for the incident and transmitted bars and the specimen interface velocities [24].

the samples [25]. The experimental setup includes a waveform generator; two piezoelectric transducers, with a resonant frequency of 540 kHz; and a numerical oscilloscope board connected to a computer. A constant pressure by hand was applied to ensure tight contact between the rock specimen and the transducers. And Vaseline was used as the coupling agent. Checks were performed to ensure the sensitivity of the P-wave velocity measurement. Usually, two piezoelectric transducers were directly contacted for the error test, and the

error was from 0 to 0.1 μ s. In addition, the damage factor can be calculated as follows:

$$D = 1 - \left(\frac{v_1}{v_2} \right)^2, \quad (8)$$

where v_1 is the ultrasonic wave velocity after rock damage and v_2 is the ultrasonic wave velocity before rock damage. The ultrasonic wave detector is shown in Figure 6.



FIGURE 6: Ultrasonic wave detector.

2.4. Porosity Test Method and Device. The porosity of granites was measured by the saturation weighing method. The specific steps of this measurement method are as follows: (1) dry the specimen for 24 h at 105°C; (2) place the specimen in a vacuum device filled with water and evacuate for 4 h, with the vacuum pressure of 0.1 MPa; (3) put the specimen in water for 24 h; and (4) weigh the saturated specimen. In order to minimize the error of weighting after the specimen was saturated, the electronic scale was calibrated with a standard weight of 500 g before each weighing. Finally, porosity test devices are shown in Figure 7.

2.5. Experimental Process

- (1) Firstly, the main mineral components were analyzed, and the XRD diffraction spectrum of the granite was obtained. Secondly, some specimens with a diameter of 50 mm and a height of 100 mm were used for the conventional uniaxial static tests. Some basic mechanical properties were obtained after this process
- (2) Based on the SHPB test system, extensive dynamic uniaxial compression tests on natural granites were conducted to find the dynamic characteristics of granites under different impact velocities. And granite specimens had a diameter of 50 mm and a height of 50 mm. Then, multiple cyclic dynamic loading tests were conducted to find the threshold which causes the initial damage of granites under the impact of equal velocity
- (3) Cyclic dynamic loading tests for granites were conducted. At the same time, P-wave velocities of granites were obtained by using an ultrasonic wave detector. Meanwhile, the porosity of granites was obtained by weighing saturated specimens. Before weighing, specimens need to be vacuumed and saturated for 4 h and were then soaked in water for 24 h

3. Results and Analysis

3.1. Static Mechanical Properties of Granites. The static compression loading test was conducted on natural specimens of

granites. And the MTS 815.03 test system was used to conduct the uniaxial compression test. The mechanical properties of granites are shown in Table 1. Moreover, axial and lateral stress-strain curves of granites and the failure type of granites are shown in Figure 8.

Based on the test results, the failure mode of granites was splitting failure, which is shown in Figure 8(b), because under the axial pressure, tensile stress was generated in the lateral direction. Then, the lateral tensile stress eventually exceeded the tensile limit of granites and caused failure. The main fracture was initiated near the center of specimens and spread along the vertical diameter. While the fracture ran through the entire height of the specimen, a secondary fracture emerged near the loading plate and formed some new microfractures.

In order to find out the cracking stress (σ_{ci}) and the damaging stress (σ_{cd}), the lateral strain response (LSR) method was used [26–28]. And the methodology can be summarized as follows, and the test results are shown in Figure 9.

- (1) Determine the onset of unstable crack growth where total volumetric strain reversal occurs, which can find damaging stress (σ_{cd}) (Figure 9(a))
- (2) Determine the linear lateral strain reference line (Figure 9(b))
- (3) Find the change (Δ LSR) between the lateral line and the linear reference line in the lateral strain curve (Figure 9(b))
- (4) Plot the axial stress versus change in the lateral strain (Δ LSR) (Figure 9(c))
- (5) Determine the maximum change in the lateral strain difference and the associated axial stress, which can find the cracking stress (σ_{ci}) (Figure 9(c))

3.2. Dynamic Mechanical Properties of Granites. Using the SHPB test system, there were two purposes which needed to be achieved. The first was to obtain the dynamic mechanical properties of granites under different loading velocities. The second was to find the threshold which caused the initial damage of granites. During the test, the compressive strain, associated with the transmitted wave, was recorded by strain gauges on the transmitted bar. These three elastic stress pulses in the incident and transmitted bars are recorded with the strain gauges and denoted as the incident strain $\varepsilon_I(t)$, reflected strain $\varepsilon_R(t)$, and transmitted strain $\varepsilon_T(t)$, as shown in Figure 10. The relationship between stresses and strains is shown in Figure 11. And dynamic mechanical properties of granites are illustrated in Table 2.

Many dynamic loading tests were conducted to analyze the dynamic mechanical properties of granites, and the results were as follows:

- (1) In this paper, the test data with loading velocity between 9 m/s and 13 m/s were selected for processing and analysis. Under the same loading velocity, the waveform diagram corresponded to the stress-strain curve one by one. At the same time, within



FIGURE 7: (a) Drying oven, (b) vacuum saturation device, and (c) electronic scale.

TABLE 1: Mechanical properties of granites.

Density (kg/m^3)	Elastic modulus (GPa)	Static strength (MPa)	Porosity (%)
2.59	15.73	89.12	0.91

the range of loading velocities, the samples were destroyed under one dynamic load. It can be found from Figure 10 that the greater the loading velocity, the larger the amplitudes of the incident wave, the reflected wave, and the transmitted wave

- (2) It can be seen from Figure 11 that the magnitude of dynamic strength and strain rate depended on the magnitude of the loading velocity. The greater the loading velocity, the larger the dynamic strength, the elastic modulus, and the strain rate were getting. At the same time, when the loading velocity increased, the higher the energy was released, and the number of granite fragments increased. From the perspective of the granite's failure form, the frac-

ture surface of the granite was mostly parallel to the loading direction, the specimen mainly underwent the splitting failure, and there were multiple splitting cracks that penetrated the rock

Based on a large number of test results, when the loading velocity was between 8 m/s and 9 m/s, the rock needed to be repeatedly loaded at the same rate once or twice before failure. In addition, when the loading velocity was between 7 m/s and 8 m/s, the granite specimens needed to undergo 2 to 4 dynamic loading tests before failure. Moreover, when the loading velocity was between 6 m/s and 7 m/s, the granite needed to be subjected to 4 to 6 times of loading tests before failure. However, when the loading velocity was lower than 5.8 m/s, after more than 30 cycles of loading test, the specimens cannot be damaged or even destroyed. The cyclic dynamic loading test results are shown in Table 3.

Based on the above analysis, there was indeed a stress threshold for granite failure at the lowest dynamic loading velocity. Obviously, the lowest velocity was 9.0 m/s, and the stress threshold for failure was 60.49 MPa. However, the threshold for cracking damage under cyclic dynamic loading

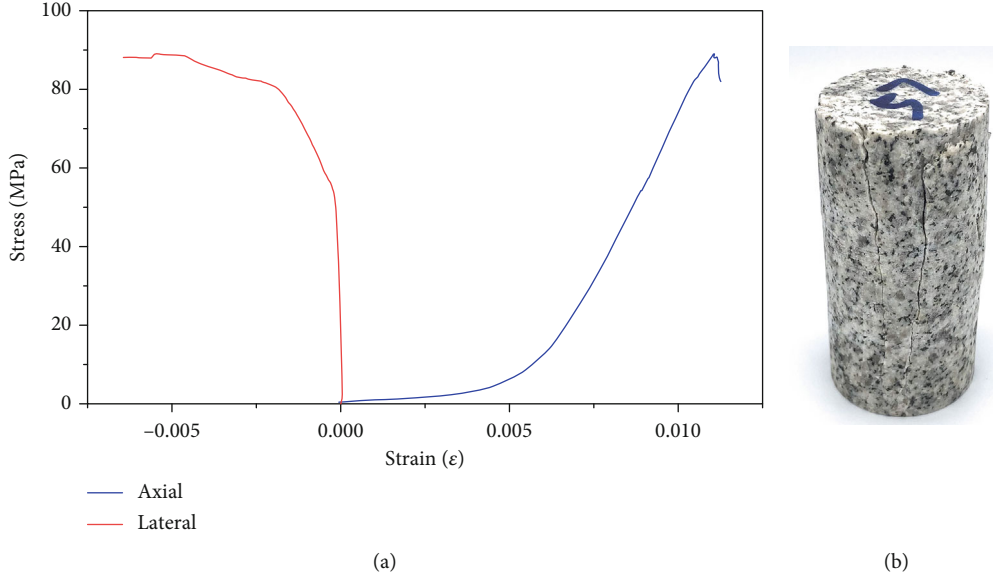


FIGURE 8: (a) The uniaxial stress-strain curves of granites and (b) the failure type of granites.

needs more analysis. Liang et al. indicated that there was no obvious correlation between the ratio of initiation stress and peak strength and strain rate in rock specimens [29]. Based on Liang et al.'s theory, the following equations can be obtained to predict the threshold for damage under dynamic loading:

$$\frac{\sigma_{ci}^d}{\sigma_c^d} = \alpha \frac{\sigma_{ci}}{\sigma_c}, \tag{9}$$

$$\frac{\sigma_{cd}^d}{\sigma_c^d} = \beta \frac{\sigma_{cd}}{\sigma_c},$$

where σ_{ci}^d , σ_{cd}^d , and σ_c^d are the cracking stress, damage stress, and ultimate strength under dynamic loading, respectively, and σ_{ci} , σ_{cd} , and σ_c are the cracking stress, damage stress, and ultimate strength under static loading, respectively. α and β are related coefficients.

Due to the uncertainty of the dynamic ultimate strength under different strain rates, this article assumed that the dynamic ultimate strength was equal to the static ultimate strength ($\sigma_c^d = \sigma_c$). Thus, the dynamic cracking stress σ_{ci}^d was 39.62 MPa, and the dynamic damage stress σ_{cd}^d was 55 MPa. Based on Table 3, when the dynamic ultimate strength of the specimen was close to the dynamic damage stress, the sample needed to be impacted more times to failure. Therefore, under constant-cyclic dynamic loading, the lowest velocity was 5.8 m/s, and the stress threshold for failure was 55.1 MPa, which was very close to the damage stress under static loading.

3.3. Analysis of Granite Porosity and Damage Degree under Cyclic Loading. As mentioned in the previous section, when the loading velocity was greater than 9 m/s, the granite would fail by one time of the loading test. When the loading velocity was less than 5.8 m/s, no obvious damage and destruction

had occurred in the sample after more than 30 times of the loading test. Therefore, this paper mainly worked on the damage characteristics and porosity changes of granites under the loading velocities from 5.8 m/s to 8.4 m/s. The following figure shows the change of wave velocities of granites under cyclic dynamic loading.

In Figure 12, at a loading rate of 8.4 m/s, the ultrasonic wave velocity of D7 decreased faster, and the increment of the damage factor was also higher. And a significant longitudinal penetrating fissure appeared on the surface of the sample. This showed that the damage level of the sample was very serious, and it was close to the critical condition of failure. At a loading velocity of 7.2 m/s, the ultrasonic wave velocity of D10 gradually decreased, and the magnitude of the decrease gradually increased. At a loading velocity of 5.8 m/s, the wave velocity of D40 reduced slowly, which reduced fast in the last three impacts. Generally speaking, the greater the loading velocity, the greater the damage of the sample would be. But when the loading velocity was below a certain threshold, the sample would not be damaged.

In Figure 13(a), at a loading velocity of 8.4 m/s, the porosity of D7 increased rapidly from 0.94% to 1.41% after the single loading. Under the loading velocity of 5.8 m/s, after 12 cyclic loading tests, the porosity of the sample gradually increased from 0.98% to 1.44%, and the growth rate gradually increased with the increase of the number of cycles, which can be seen as an exponential growth.

To describe the relationship between the damage factor and the porosity, Figure 13(b) was made to analyze this phenomenon. Through linear fitting, to some extent, there was a linear relationship between the damage factor and the porosity. That is to say, under the loading velocity from 5.8 m/s to 8.4 m/s, the change of porosity can be predicted by the damage factor. Because of the development of a microfissure in rock specimens, the porosity had increased gradually. And the damage factor was a quantitative indicator that can well reflect the development of the microfissure in

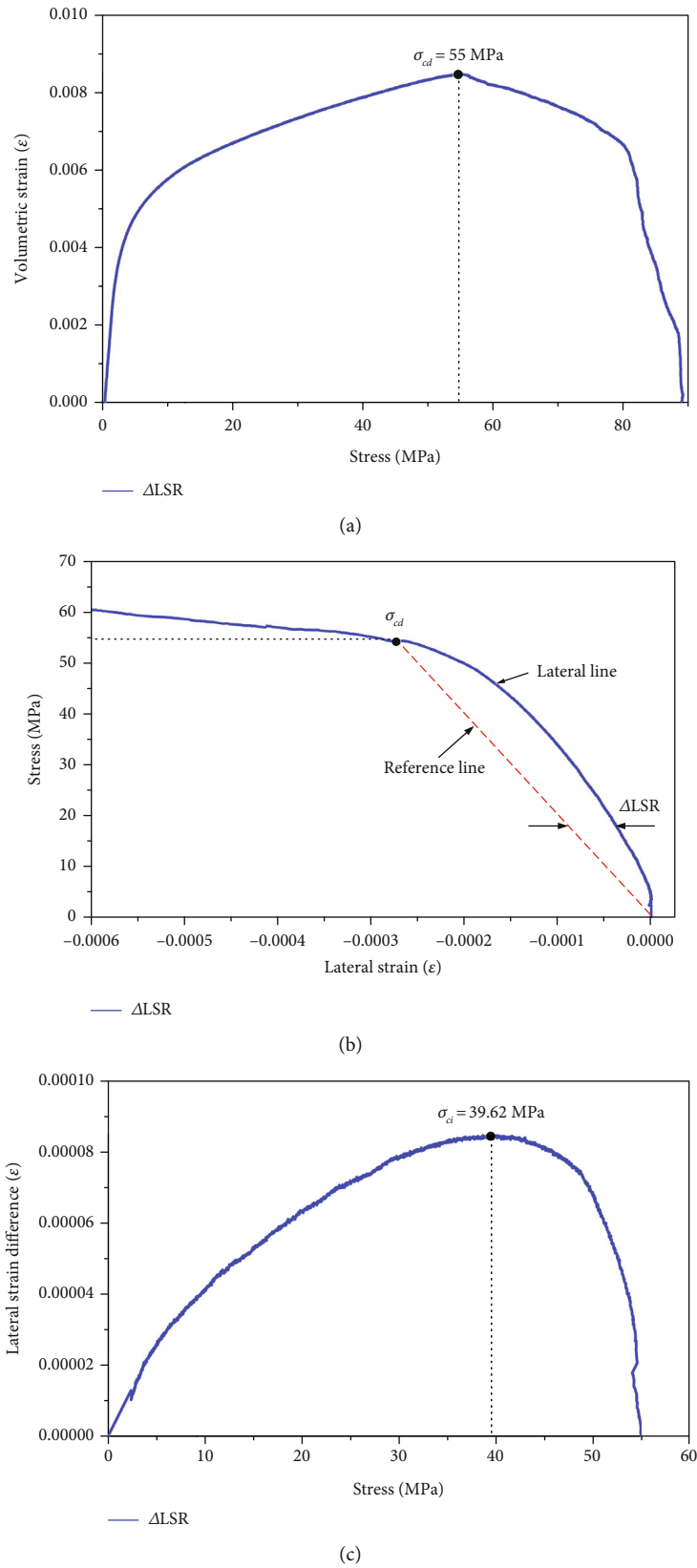


FIGURE 9: Example of the methodology used to establish the cracking stress (σ_{ci}) using the lateral strain response (LSR).

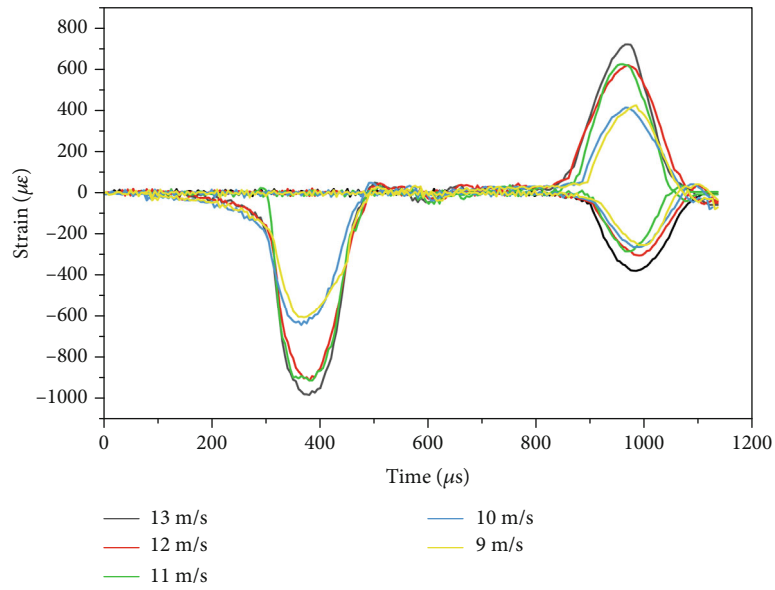
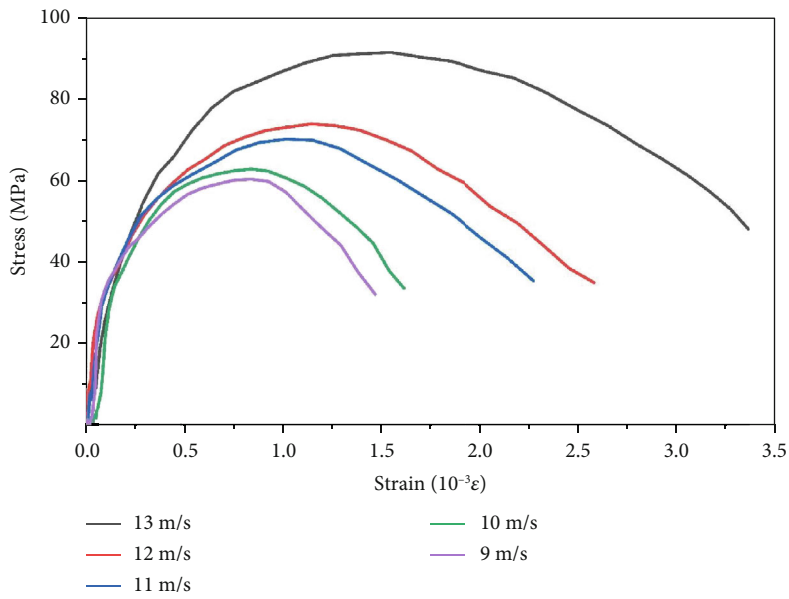


FIGURE 10: Some examples of incident, reflected, and transmitted strain signals under different loading velocities.



(a)



(b)

FIGURE 11: (a) Stress and strain change of granites under dynamic loading and (b) the failure types of granites with the impact velocity of 13 m/s, 12 m/s, 11 m/s, 10 m/s, and 9 m/s, respectively.

TABLE 2: Dynamic mechanical properties of granites.

Specimen number	Length to diameter ratio	Initial wave velocity (m/s)	Striker velocity (m/s)	Strength (MPa)	Strain rate (s^{-1})	Number of broken rocks
D33	1.021	3597	12.8	91.59	74.99	10
D32	1.034	3543	11.7	74.02	70.43	6
D57	1.016	3623	10.6	71.63	64.19	4
D52	1.025	3649	9.6	62.99	18.86	3
D23	1.031	3672	9.0	60.49	18.86	2

TABLE 3: Constant-velocity cyclic dynamic loading test.

Specimen number	Ultrasonic wave velocity in saturation (m/s)	Average loading velocity (m/s)	Loading times	Ultimate strength (MPa)
D7	4524	8.4	2	58.8
D10	4944	7.2	4	57.4
D43	4665	6.9	5	56.9
D40	4978	5.8	13	55.5
D35	4653	6.3	7	56.1
D50	4841	5.5	30	55.1

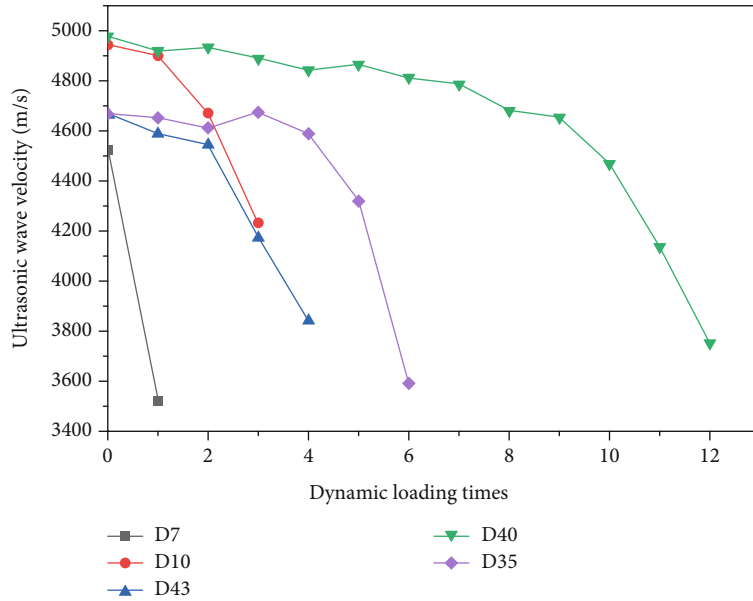


FIGURE 12: Relationship between the dynamic loading times and the ultrasonic wave velocity.

the rock. Therefore, in engineering practice, the porosity of rocks can be measured indirectly by the ultrasonic wave detector.

4. Conclusion

This paper presented the dynamic mechanical properties of granites based on the SHPB test system and the ultrasonic wave detector. The uniaxial dynamic mechanical properties with different loading velocities and the relationship between

the dynamic mechanical properties and the porosity were analyzed as follows:

- (1) Based on many tests, the failure mode of granites under static uniaxial compression load was very similar to its failure mode under dynamic uniaxial compression load. The fracture surface of the granite was mostly parallel to the loading direction, and the specimen mainly underwent the splitting failure. Moreover, according to test results, when the dynamic loading velocity was higher than 9 m/s,

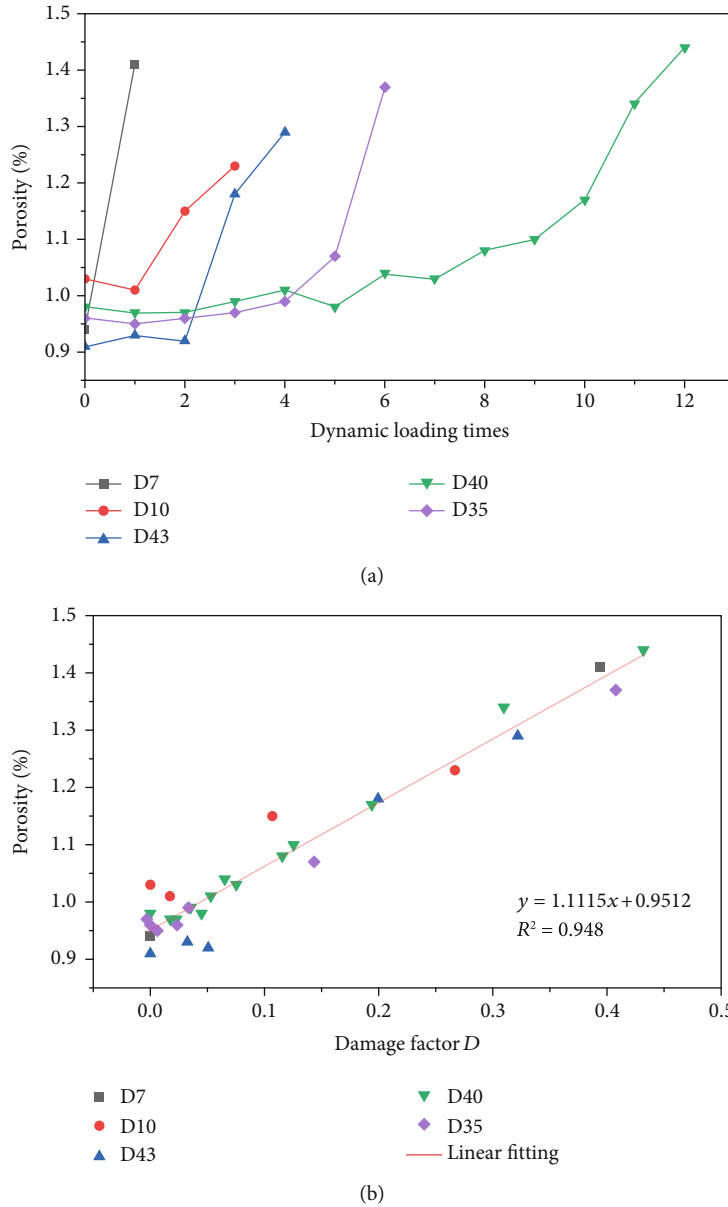


FIGURE 13: (a) Relationship between dynamic loading times and the porosity under different loading velocities and (b) relationship between the damage factor and the porosity.

granite specimens failed under one impact load. And when the dynamic loading velocities were from 5.8 m/s to 8.4 m/s, granites had varying degrees of damage instead of failure

- (2) Based on the test results, the minimum dynamic loading velocity causing granite failure was 9 m/s, in which the dynamic strength was 60.49 MPa. Moreover, under the cyclic dynamic loading, the minimum dynamic loading velocity causing granite failure was 5.8 m/s, in which the dynamic strength was 55.5 MPa. Based on Liang et al.'s theory, under the cyclic dynamic loading, when the dynamic strength was close to the static damage stress, granites needed to undergo more cyclic loads before failure occurred. When the dynamic strength of granites

was very close to the static damage stress, it was almost impossible to cause any damage or failure for granites after 30 dynamic loads. Therefore, according to test results, static damage stress can be used to predict the dynamic threshold of initial damage under cyclic dynamic loading

- (3) The changes of the porosity depended on the loading velocity and the number of dynamic loading. At the loading velocity of 8.4 m/s, the porosity grew fast, but the granite specimen was prone to failure; therefore, it was hard to control the change of the porosity under this velocity. At the loading velocity of 5.8 m/s, the porosity grew slowly. And it may take more time to control the porosity. Therefore, when the loading velocity was between 5.8 m/s and 8.4 m/s, it can

effectively control the porosity of granites. Moreover, this paper found the linear relationship between the change of the porosity and the damage factor, which would help to quantify and control the porosity changes in engineering practice

Data Availability

The data used to support the findings of this study are available from the corresponding author upon request.

Conflicts of Interest

The authors declare that they have no conflicts of interest.

Acknowledgments

The authors are grateful for the financial support from Sichuan University.

References

- [1] C. Preinfalk and G. Morteani, "The industrial applications of rare earth elements," in *in Lanthanides, tantalum and niobium*, pp. 359–370, Springer, 1989.
- [2] J. H. L. Voncken, *The Rare Earth Elements: An Introduction*, Springer, 2016.
- [3] Anonymous, *On Promoting Sustainable and Healthy Development of Rare Earth Industry*. State Council of the People's Republic of China, State Council of the People's Republic of China, 2011.
- [4] S. Massari and M. Ruberti, "Rare earth elements as critical raw materials: focus on international markets and future strategies," *Resources Policy*, vol. 38, no. 1, pp. 36–43, 2013.
- [5] G. Gunn, *Critical Metals Handbook*, John Wiley & Sons, 2014.
- [6] Y. Shen, R. Moomy, and R. G. Eggert, "China's public policies toward rare earths, 1975–2018," *Mineral Economics*, vol. 33, no. 1–2, pp. 127–151, 2020.
- [7] X. J. Yang, A. Lin, X.-L. Li, Y. Wu, W. Zhou, and Z. Chen, "China's ion-adsorption rare earth resources, mining consequences and preservation," *Environmental Development*, vol. 8, pp. 131–136, 2013.
- [8] W. Su, *Economic and Policy Analysis of China's Rare Earth Industry*, China Financial and Economic Publishing House, Beijing, 2009.
- [9] J. Voncken, *The Rare Earth Elements - An Introduction*, Springer International Publishing, 2016.
- [10] X. Tang and M. Li, "In-situ leach mining of ion-absorbed rare earth mining," *Mining research and development*, vol. 17, pp. 1–4, 1997.
- [11] W. C. Larson, *Uranium in situ leach mining in the United States*. Information circular, Department of the Interior, Bureau of Mines, 1978.
- [12] G. Mudd, "Critical review of acid in situ leach uranium mining: 1. USA and Australia," *Environmental Geology*, vol. 41, no. 3–4, pp. 390–403, 2001.
- [13] G. Taylor, V. Farrington, P. Woods, R. Ring, and R. Molloy, "Review of environmental impacts of the acid in-situ leach uranium mining process," *CSIRO Land and Water Client Report*, CSIRO Clayton, Victoria, 2004.
- [14] R. H. Parker and A. Jupe, "In situ leach mining and hot dry rock (HDR) geothermal energy technology," *Minerals Engineering*, vol. 10, no. 3, pp. 301–308, 1997.
- [15] M. Al-Harashsheh and S. W. Kingman, "Microwave-assisted leaching—a review," *Hydrometallurgy*, vol. 73, no. 3–4, pp. 189–203, 2004.
- [16] T. Xunzhong and L. Maonan, "In-situ leach mining of ion-absorbed rare-earth mineral," *Mining research and development*, vol. 2, 1997.
- [17] Y. Zhu, L. Zhou, and Q. Li, "Water pollution prevention method for in-situ leach mining of ion-absorbed rare-earth mineral," *Nonferrous Metals (Mineral Processing Section)*, vol. 6, pp. 46–49, 2011.
- [18] Y.-x. Li, L. Zhang, and X.-m. Zhou, "Resource and environment protected exploitation model for ion-type rare earth deposit in southern of China," *Chinese Rare Earths*, vol. 31, no. 2, pp. 80–85, 2010.
- [19] J. J. Zhu, X. B. Li, F. Q. Gong, and S. M. Wang, "Dynamic characteristics and damage model for rock under uniaxial cyclic impact compressive loads," *Chinese Journal of Geotechnical Engineering*, vol. 35, no. 3, pp. 531–539, 2013.
- [20] J. Jin, X. Li, C. Qiu et al., "Evolution model for damage accumulation of rock under cyclic impact loadings and effect of static loads on damage evolution," *Chinese Journal of Rock Mechanics and Engineering*, vol. 33, no. 8, pp. 1662–1671, 2014.
- [21] L. Yan, L. Liu, S. Zhang, D. Lan, and J. Liu, "Testing of Weakly Weathered Granites of Different Porosities Using a Split Hopkinson Pressure Bar Technique," *Advances in Civil Engineering*, vol. 2018, Article ID 5267610, 11 pages, 2018.
- [22] L. Yan, W. Yi, L. Liu, J. Liu, and S. Zhang, "Blasting-Induced Permeability Enhancement of Ore Deposits Associated with Low-Permeability Weakly Weathered Granites Based on the Split Hopkinson Pressure Bar," *Geofluids*, vol. 2018, Article ID 4267878, 14 pages, 2018.
- [23] M. A. Kaiser, *Advancements in the Split Hopkinson Bar Test*, Virginia Tech, 1998.
- [24] S. Demirdag, K. Tufekci, R. Kayacan, H. Yavuz, and R. Altindag, "Dynamic mechanical behavior of some carbonate rocks," *International Journal of Rock Mechanics and Mining Sciences*, vol. 47, no. 2, pp. 307–312, 2010.
- [25] M. Takarli, W. Prince, and R. Siddique, "Damage in granite under heating/cooling cycles and water freeze–thaw condition," *International Journal of Rock Mechanics and Mining Sciences*, vol. 45, no. 7, pp. 1164–1175, 2008.
- [26] T. Stacey, "A simple extension strain criterion for fracture of brittle rock," in *International Journal of Rock Mechanics and Mining Sciences & Geomechanics Abstracts*, pp. 469–474, Elsevier, 1981.
- [27] M. S. Diederichs, "The 2003 Canadian Geotechnical Colloquium: Mechanistic interpretation and practical application of damage and spalling prediction criteria for deep tunnelling," *Canadian Geotechnical Journal*, vol. 44, no. 9, pp. 1082–1116, 2007.
- [28] M. Nickislar and C. D. Martin, "Evaluation of methods for determining crack initiation in compression tests on low-porosity rocks," *Rock Mechanics and Rock Engineering*, vol. 45, no. 4, pp. 607–617, 2012.
- [29] C. Y. Liang, X. Li, S. X. Wang, S. D. Li, J. M. He, and C. F. Ma, "Experimental investigations on rate-dependent stress-strain characteristics and energy mechanism of rock under uniaxial compression," *Chinese Journal of Rock Mechanics and Engineering*, vol. 31, no. 9, pp. 1830–1838, 2012.

Research Article

Permeability Characteristics of Coal after Supercritical CO₂ Adsorption at Different Temperatures

Xueying Liu ^{1,2}, Jin Yu ¹, Di Wu ², and Xiaochun Xiao ²

¹Fujian Research Center for Tunneling and Urban Underground Space Engineering, Huaqiao University, Xiamen 361021, China

²School of Mechanics and Engineering, Liaoning Technical University, Fuxin, Liaoning 123000, China

Correspondence should be addressed to Jin Yu; bugyu0717@163.com

Received 9 July 2020; Revised 3 August 2020; Accepted 27 August 2020; Published 9 September 2020

Academic Editor: Stefan Iglauer

Copyright © 2020 Xueying Liu et al. This is an open access article distributed under the Creative Commons Attribution License, which permits unrestricted use, distribution, and reproduction in any medium, provided the original work is properly cited.

CO₂ storage in coal seams has become one effective method to reduce CO₂ emission and help exploit coalbed methane (CBM). The permeability is a key parameter for CBM extraction. In deep coal seams (>800 m), CO₂ exists in the supercritical state. In the present work, permeability tests were performed on briquettes before and after supercritical CO₂ (SC-CO₂) adsorption at various temperatures to investigate the effects of SC-CO₂ adsorption on the permeability. Experimental results show that SC-CO₂ adsorption leads to volumetric expansion and permeability augment. The permeability enhancement decreases continuously at 35°C, while it initially increases and reduces at pressures exceeding 9 or 10 MPa at 45 or 55°C, respectively. Besides, the permeability enhancement ratio shows a linear increase with the expansion. The research provides a basis for further research on the enhanced coalbed methane (ECBM) recovery.

1. Introduction

The emission of CO₂ has been increasing over the years, and carbon capture and storage (CCS) has been considered to mitigate greenhouse effects [1]. Among various storage options (oil reservoirs, saline aquifers, and coal seams), storage in coal seams is promising because of advantages: firstly, there are plenty of unmineable coal resources because of limited recovery, and potential reserves of CBM in China ranks third in the world [2]; secondly, due to greater affinity of CO₂ to coal than CH₄, it contributes to ECBM recovery. Researchers from America, Japan, and China have performed pilot experiments for ECBM feasibility [3–5]. Specifically, when the temperatures and pore pressures are above the critical point (31.06°C, 7.38 MPa), CO₂ exists in a supercritical state in coal seams with a depth under 800 m [6]. SC-CO₂ has the characteristics of strong diffusion, low viscosity, and surface tension.

Research has been carried out on ECBM through experiments and numerical simulations [7–10]. When CO₂ is pressurized into coal seams, gas transport mainly includes diffusion, seepage, and competitive adsorption [11]. Adsorption of CO₂ has been investigated from the subcritical state to

the supercritical state [12, 13], and various adsorption models have been assessed, such as Langmuir, Dubinin-Astakhov (D-A), and Dubinin-Radushkevich (D-R) models [14]. The adsorption could induce swelling [15, 16] and change the pore distribution, surface area, and function groups of coal [17, 18], leading to the variation in the seepage characteristics and mechanical properties [19, 20]. Pores are classified as micropores (<2 nm) for adsorption, mesopores (2–50 nm), and macropores (>50 nm) for seepage, and changes in pore structures have been investigated to reveal the mechanism. Sampath et al. compared the effects of short-term and long-term CO₂ interaction on pore structures [21]. Considered the existence of water in coal seams, Ni et al. [22] and Liu et al. [23] investigated the interaction with SC-CO₂ and water, indicating that the chemical reaction also influences pore structures.

The permeability is a key parameter for gas exploitation, and it is influenced by the effective stress and CO₂ adsorption, occasionally along with extraction and dissolution. Although previous studies have focused on permeability variation, however, the specific influence of each factor is uncertain, especially in the supercritical state. In the present

work, a series of permeability tests were performed before and after SC-CO₂ adsorption under nonconfining conditions at different temperatures. The effect of CO₂ adsorption on the permeability is investigated, and porosity differences between specimens are reduced by using briquettes. Results can provide a basis for further field application of ECBM.

2. Experimental Specimens and Apparatus

2.1. Specimens. The porosity of specimens drilled from the same block may be different, and this difference can influence the permeability characteristics and adsorption capacity. Therefore, the briquettes are selected as the specimens because of homogeneity and controllable porosity.

Blocks are extracted from Xinqiu Mine, Fuxin, Liaoning Province. The blocks are crushed and sieved until the diameter is below 0.25 mm. 255 g pulverized coal and 5 g rosin are put together into a cylinder with a thick wall, and a briquette is shaped in the cylinder with a loading of 460 kN as shown in Figure 1. The diameter and length are 50 mm and 100 mm, respectively. All specimens are dried at the temperature of 105°C for 24 hours. The average porosity is 0.31 by comparing the apparent density of specimens and the true density of powdered coal, and it can be considered that there is no difference between specimens.

2.2. Experimental System. The experiments include two parts, permeability tests and adsorption experiments. Based on Darcy's law, transient and steady-state methods are frequently used to determine permeability [24–26]. In the present work, the latter method is used because of the relatively high permeability of briquettes. The experimental system for permeability tests consists of the injection part (N₂ cylinder), a seepage and reference cell, a pump with a regulator, and a flow meter as shown in Figure 2. After being vacuumed, confining pressures are applied by the pump firstly. N₂ is pressured into the reference cell, and once the pressure is stable, N₂ is injected into the seepage cell to start the test. The flow meter is used to measure the flow rate of N₂, and the permeability is determined by [27]

$$k = \frac{2\mu P_2 L Q}{(P_1^2 - P_2^2) A}, \quad (1)$$

where μ is the viscosity of N₂, Q is the flow rate. P_1 and P_2 are the upstream and downstream pressures, respectively, and L and A are the length and cross-sectional area, respectively.

The main parts of the experimental system for adsorption are the reference cell and adsorption cell. The adsorption amount is measured by the volumetric method, and the void volume is estimated by injecting He according to the national standard. The diameter and length of a specimen at several positions are measured with a vernier caliper to calculate the volume before and after the experiment, and volumetric expansion can be determined by

$$S = \frac{(V - V_0)}{V_0} \times 100\%, \quad (2)$$

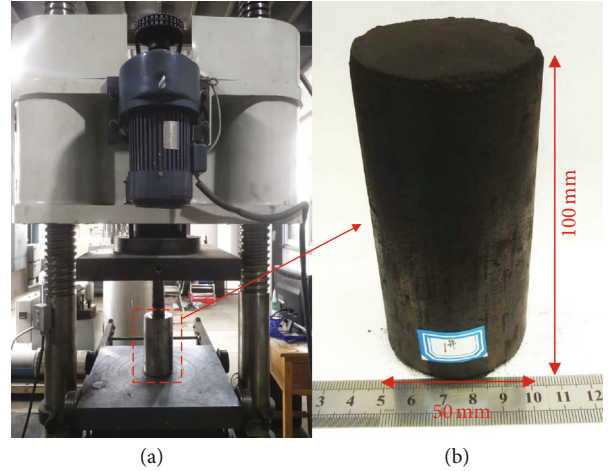


FIGURE 1: The process of making a specimen.

where S is volumetric swelling and V_0 and V are the initial and final volume of the specimen, respectively.

According to the measurement in Wu et al. [13], the adsorption amount can be determined by

$$n = \frac{1}{mRT} \left[V_R \left(\frac{P_{R1}}{Z_{R1}} - \frac{P_{R2}}{Z_{R2}} \right) - \left(\frac{V_{A1} P_{A1}}{Z_{A1}} - \frac{V_{A2} P_{A2}}{Z_{A2}} \right) \right], \quad (3)$$

where n is the excessive adsorption amount per unit of a specimen. m is the weight of a specimen. R , the universal gas constant, is 8.314 J/(g·mol·K). T is the equilibrium temperature. V_R and V_A are the void volumes of reference and adsorption cells, and P_R and P_A are respective pressures of two cells. Subscripts 1 and 2 refer to the initial and final state, respectively. Z_{R1} , Z_{R2} , Z_{A1} , and Z_{A2} are compressibility factors corresponding to P_{R1} , P_{R2} , P_{A1} , and P_{A2} , respectively, at the temperature of T .

2.3. Experimental Procedures. The experimental procedures cover three stages, determining the permeability, CO₂ adsorption, and measuring the permeability after CO₂ desorption.

Stage one: a series of permeability tests are performed on a briquette placed in the seepage cell using N₂ with the injection pressure of 2 MPa and confining pressure of 12 MPa at 35°C

Stage two: the specimen is taken out from the seepage cell and placed in the adsorption cell. Experiments of CO₂ adsorption are conducted without confinement at the pressure of 8 MPa and temperature of 35°C. The experiment lasts for 24 hours according to the national standard, and the pressure reduction and deformation are recorded

Stage three: after desorption for 12 hours, permeability tests are repeated three times to investigate the variation and determine the effect of adsorption on the permeability.

A new specimen is replaced in the adsorption cell, and the second and third stages are repeated at CO₂ pressures of 9, 10, 11, 12, and 13 MPa. Subsequently, the temperature is increased to 45 or 55°C; this series of experiments are repeated.

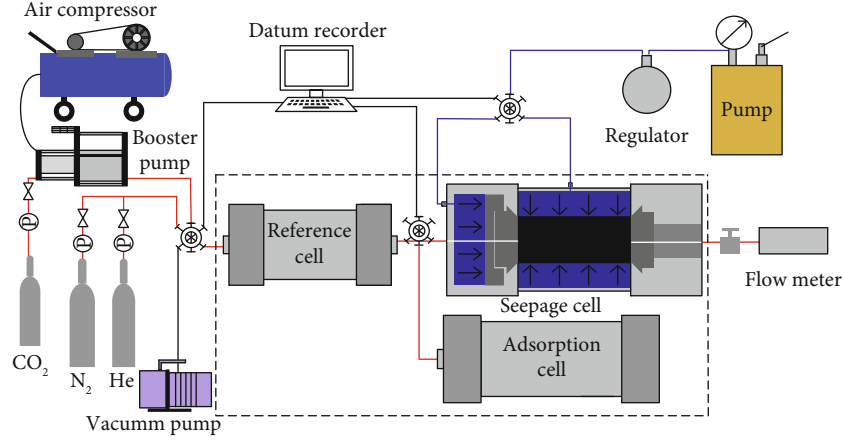


FIGURE 2: Experimental system.

3. Experimental Results and Discussion

3.1. Permeability Characteristics before and after SC-CO₂ Adsorption. Figure 3 shows that the permeability enhances remarkably after SC-CO₂ adsorption at different temperatures. After the adsorption, the permeability decreases by 0.4 mD with pressures ranging from 8 MPa to 9 MPa, and it reduces by approximately 0.7 mD at pressures increasing from 9 MPa to 13 MPa at 35°C. Nevertheless, the permeability after CO₂ adsorption increases slightly initially and subsequently decreases moderately with the increase of CO₂ pressures at 45 and 55°C, and peaks are observed obviously at the pressures of 9 MPa at 45°C. Compared with the initial permeability, the permeability enhancement ratio, η , can be determined by

$$\eta = \frac{(k - k_0)}{k_0} \times 100\%, \quad (4)$$

where k_0 and k are permeability values before and after CO₂ adsorption, respectively.

To reveal the variation of η with temperatures, the ratio is replotted as shown in Figure 4. The ratio decreases by approximately 13% at the pressure of 8 MPa, while it increases by 10% before decreasing at 9 MPa. When pressures are in the range of 10–13 MPa, the proportion increases slightly with temperatures ranging from 35 to 45°C, and it continues rising moderately with the increase of temperatures to 55°C.

3.2. Adsorption and Deformation. Figure 5 demonstrates that CO₂ adsorption induces various swelling at different pressures and temperatures. The volumetric swelling reduces by 4% at 35°C, while the expansion increases slightly before 9 MPa and subsequently decreases by 3.5% and 1.2% at 45 and 55°C, respectively. When pressures exceed 10 MPa, the expansion at 55°C is greater than that at other temperatures.

Although the Langmuir model is generally applied to estimate the adsorption amount and deformation, however, it is poorly applied to adsorption at pressures exceeding 6 MPa mainly due to the assumption of monolayer adsorp-

tion. Alternatives such as the modified D-R model have been found more suitable to fit with the adsorption amount and swelling [28, 29]. In this model, gas densities replace the pressures and adsorbed densities replace the saturated vapor pressures, which avoids the limitation of saturated vapor pressure in the supercritical state, as shown in

$$S = S_{\max} \exp\left(-D \ln^2 \frac{\rho_a}{\rho}\right) + a\rho, \quad (5)$$

where S_{\max} is the maximum swelling. For adsorption amount, D is related to the adsorption heat and affinity of the gas to the sorbent, while for swelling it is possibly regarded as an empirical parameter. ρ , CO₂ density, varies with temperatures and pressures and is obtained from the website of the US National Institute of Standards and Technology (NIST), as shown in Figure 6. ρ_a , the density of the adsorbed phase, is considered as 1000 kg/m³ [28, 29].

The deformations of specimens at three temperatures are fitted with the modified D-R model with a great determination as shown in Figure 7 and Table 1. S_{\max} decreases by 13% with temperatures ranging from 35 to 55°C, while it does not vary significantly with the temperatures in the previous study [29]. This difference is mainly because the briquette structure is loose, while the structure of raw coal specimens is dense. The adsorbed density of CO₂ is approximately close to liquid CO₂ density, revealing that the adsorbed CO₂ requires less volume than gaseous CO₂. The a term is related to CO₂ solubility, and this term can be used to describe the compression at great pressures.

3.3. Adsorption and Swelling. Figure 8 demonstrates that the swelling of specimens decreases linearly by 1.5% with the increase of adsorption amount by 1 mmol/g, which is shown in the previous study [13]. Studies reported an increase in deformation with the augment of absolute adsorption, along with a stable trend at CO₂ pressures approaching 10 MPa [15, 29]. The process of CO₂ adsorption and specimen deformation is from the disequilibrium state to the dynamic equilibrium state. With CO₂ injection, CO₂ diffuses due to pressure differences and it is absorbed by the matrix. CO₂ acts as the

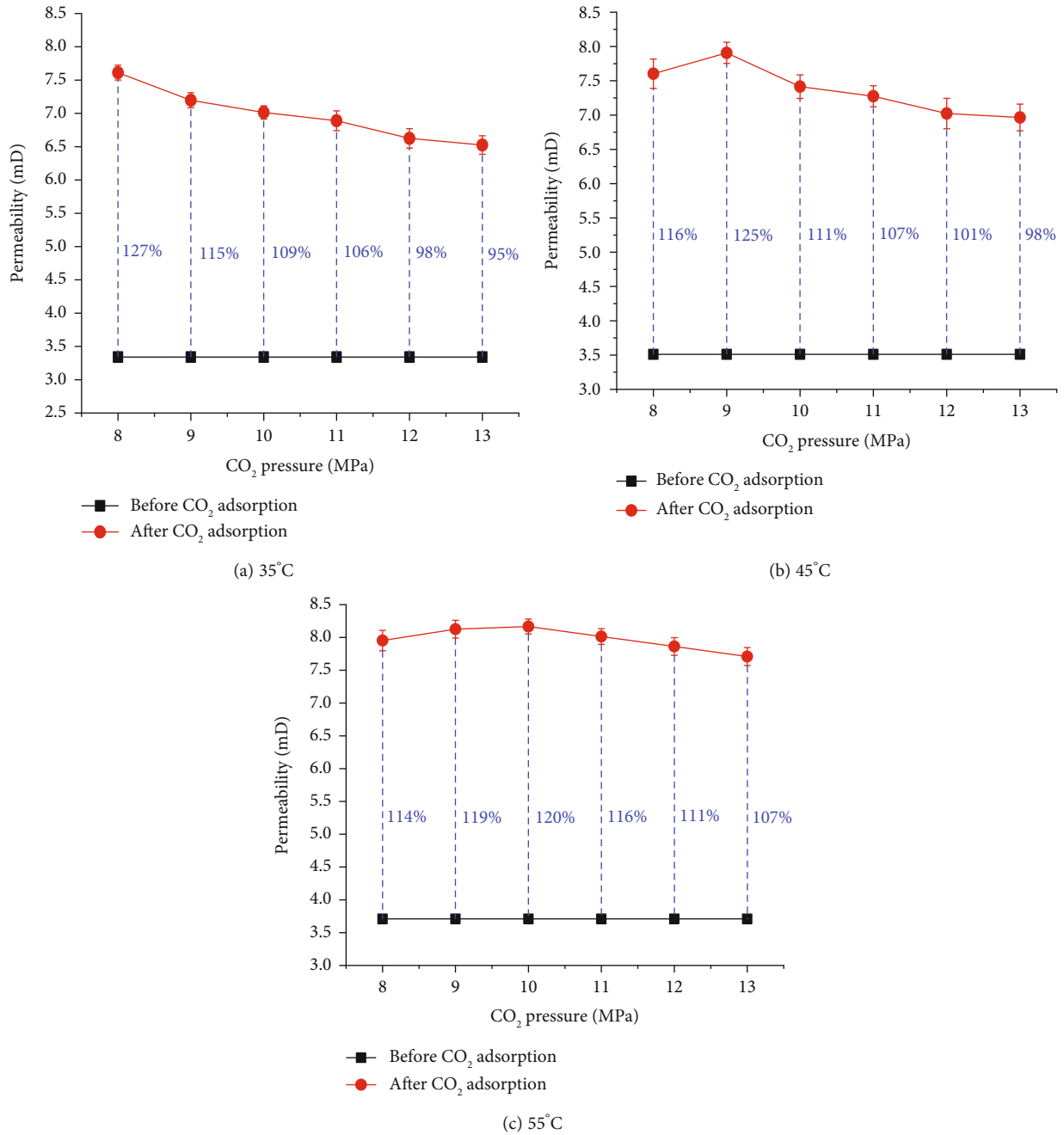


FIGURE 3: Permeability enhancement at different temperatures.

plasticizer and enables coal structure rearrangement, reducing the softening temperatures [30]. CO₂ adsorption can reduce the surface energy of the coal and weak mechanical properties. These are the main reasons that matrix swells significantly after adsorption. High-pressure CO₂ can constrain matrix swelling and the expansion shows a downward trend when CO₂ pressures exceed 10 MPa.

3.4. Analysis of the Permeability Changes Induced by CO₂. The permeability ratio shows a linear augment with the volumetric swelling as shown in Figure 9. It is noted that the proportion at 55°C is slightly lower than that at other

temperatures. The adsorption-induced swelling indicates greater porosity and wider seepage channels, and therefore, permeability is enhanced. This reveals that the permeability enhancement under nonconfinement is influenced mostly by the adsorption.

For CO₂ geological storage in deep coal seams, where strata pressures restrict the swelling, the permeability variation after CO₂ interaction is a coupled result of CO₂ adsorption and effective stresses, along with extraction or dissolution. For CO₂ adsorption in the confined stress, due to gas injection, both the reduction in effective stresses and CO₂ adsorption induce matrix expansion (equations (6) and (7)). Under the

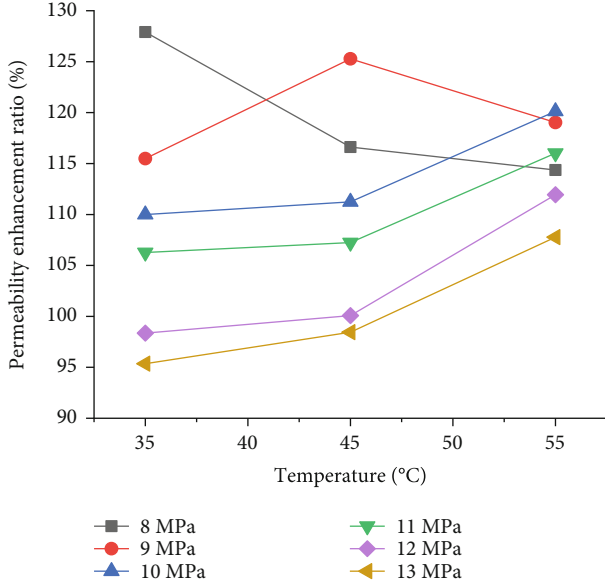


FIGURE 4: Permeability enhancement ratio with the increase of temperatures.

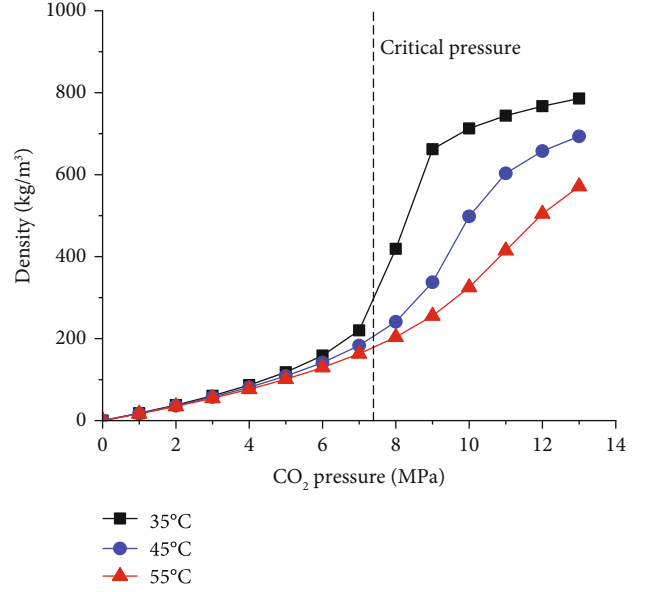


FIGURE 6: CO₂ density at different temperatures and pressures.

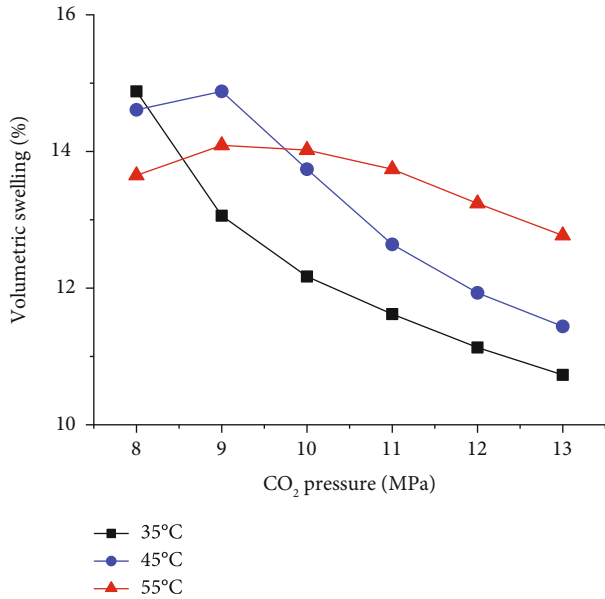


FIGURE 5: Volumetric swelling at different pressures and temperatures.

great confinement, the coal matrix expands inward and cleats narrow, leading to permeability reduction. Ranathunga et al. observed shrinkage in macropores with the help of scanning electron microscopy (SEM) [31]. All microcleats, the main channels of gas seepage, can be observed closely by micro-CT scanning after SC-CO₂ injection, and permeability decreases drastically by 2 orders of magnitude [32]. After CO₂ adsorption under a constraint pressure, the permeability reduction ratio augments linearly with the increase of swelling [33].

$$\varepsilon = \varepsilon_e + S, \quad (6)$$

$$\varepsilon_e = -\frac{\sigma - P}{3K}, \quad (7)$$

where ε is the total deformation induced by effective stresses and adsorption. ε_e is the volumetric deformation caused by effective stresses, namely, $\sigma - P$, and K is the bulk modulus. In equation (7), the minus indicates compression.

As a solvent, SC-CO₂ can extract organic minerals and alter the pore surface, tarnishing the surface. Li et al. observed permeability augment after CO₂ cycling adsorption and desorption under a constraint pressure, along with the expansion in macro- and mesopores but few changes in micropores [34]. Because of noticeable fractures on the surface, the extraction is attributed to the remarkable permeability improvement. The solubility varies with CO₂ density, and therefore, it is difficult to quantify the effects of extraction.

Another influencing factor is the chemical reaction. Water exists in coal seams, and the interaction of CO₂ and water can dissolve the carbonate minerals. CO₂ could dissolve in water forming an acid solution, in which calcite is dissolved. The interaction of water and SC-CO₂ causes an increment in pores, and the permeability is improved [23]. Nevertheless, some silicate minerals could form precipitation and block pore connections, reducing the permeability [22].

3.5. Discussion for CO₂-ECBM. CO₂-ECBM is injecting CO₂ through wells into deep coal seams at a certain injection pressure. The permeability is the key factor during gas production. Although the permeability becomes greater at high pressures without considering the Klinkenberg effect [7], however, increasing CO₂ pressures cannot be effective for improving exploitation efficiency according to the previous analysis. Among the four factors, the effect of extraction and solution on permeability is limited and estimated difficultly. Swelling decreases gradually with the increase of CO₂ pressure. Besides, injecting high-pressure CO₂ is liable

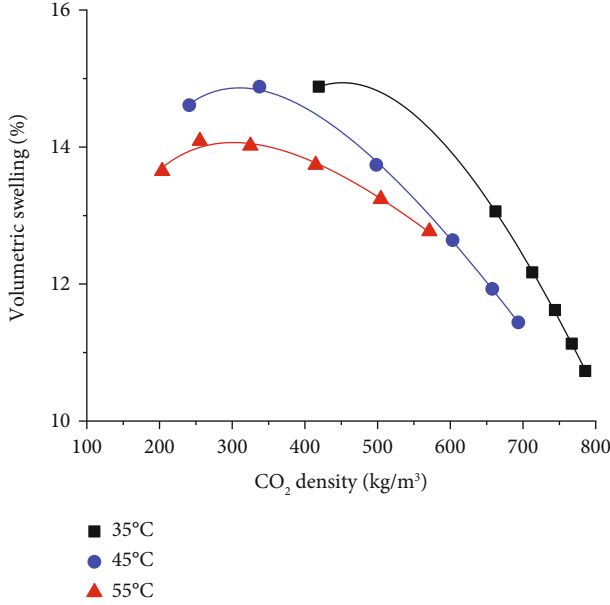
FIGURE 7: Expansion fits with CO₂ densities.

TABLE 1: Fitting parameters for the modified D-R model.

Temperature (°C)	S_{\max}	D	a
35	0.32	0.28	-2.7×10^{-4}
45	0.23	0.11	-1.6×10^{-4}
55	0.19	0.07	-1.1×10^{-4}

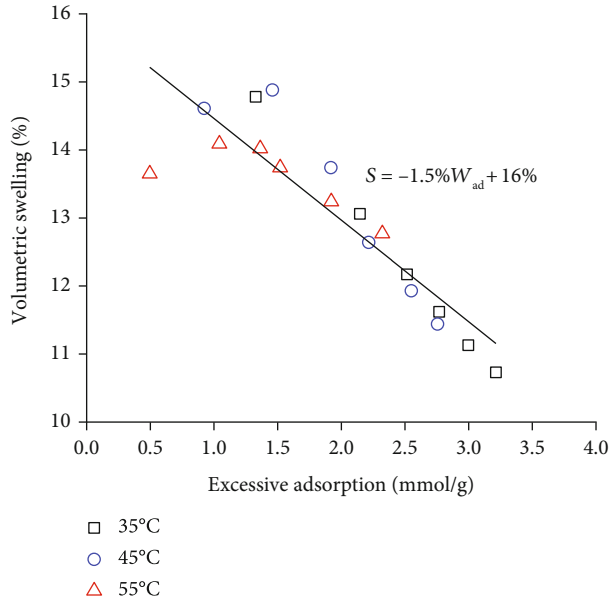


FIGURE 8: Volumetric swelling with excessive adsorption.

to induce disasters and weaken the mechanical properties. Therefore, the permeability could be not enhanced significantly by only increasing CO₂ pressures.

According to the national standard, numerous adsorption experiments last for 24 hours, after which the surface area decreases, while the surface area augments remarkably

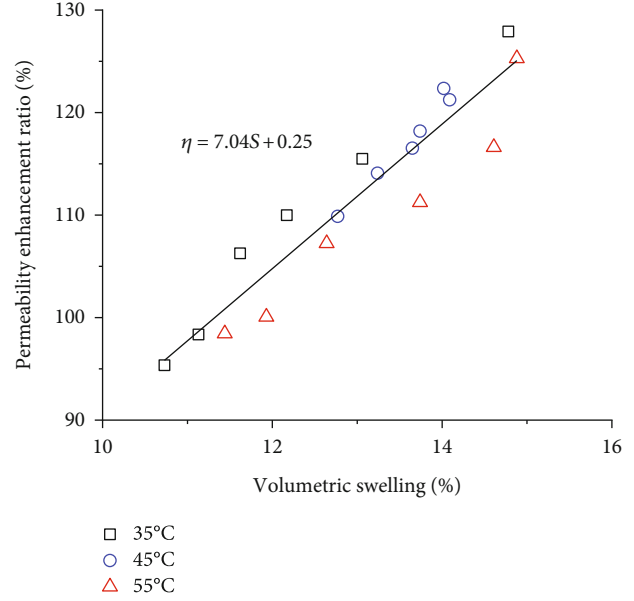


FIGURE 9: Permeability enhancement ratio with volumetric swelling.

after 7 days and 14 days [21]. Kutchko et al. summarized no significant variations in macropores after 104 days considering the offset [35]. Due to limited observation, SEM images cannot reflect total surface changes, while those changes can be estimated in other methods such as CT and nuclear magnetic resonance (NMR) [36, 37]. The interaction time should be taken into consideration, and further studies are required to investigate the long-term changes and mechanical behavior for coal of different ranks.

4. Conclusions

Permeability characteristics were investigated on briquettes before and after SC-CO₂ adsorption under nonconfinement. The main results are as follows:

- (1) Permeability enhances significantly after CO₂ adsorption in briquettes. The permeability enhancement reduces continuously with the increase of CO₂ pressure at 35°C, while it augments slightly before decreasing moderately at 45 and 55°C
- (2) CO₂ adsorption could cause volumetric swelling, and expansion is fitted well with the modified D-R model at the considering temperatures
- (3) The permeability enhancement ratio is a linear function with swelling. The permeability enhancement under nonconfinement is influenced mainly by SC-CO₂ adsorption
- (4) For CO₂ storage in coal seams, the permeability is influenced by four factors, effective stresses, dsorption, extraction, and solution, and the limited effects of extraction and solution are difficult to quantify. Further research is required to study long-term variations in permeability and mechanical properties

Notations

k :	Permeability, mD
μ :	Viscosity, $\mu\text{Pa}\cdot\text{s}$
Q :	Flow rate, cm^3/s
P_1 :	Upstream pressure, MPa
P_2 :	Downstream pressure, MPa
L :	Length, cm
A :	Cross-sectional area, cm^2
S :	Volumetric expansion
V :	Initial volume of the specimen, cm^3
V_0 :	Final volume of the specimen, cm^3
n :	Adsorption amount per unit of a specimen, mol/g
m :	Weight, g
T :	Equilibrium temperature, K
V_R :	Volume of the reference cell, cm^3
P_{R1} :	Initial pressure of the reference cell, MPa
P_{R2} :	of the reference cell, MPa
Z_{R1} :	Compressibility factor corresponding to P_{R1}
Z_{R2} :	Compressibility factor corresponding to P_{R2}
V_{A1} :	Initial void volume of the adsorption cell, cm^3
V_{A2} :	Final void volume of the adsorption cell, cm^3
P_{A1} :	Initial pressure of adsorption cell, MPa
P_{A2} :	Final pressures of adsorption cell, MPa
Z_{A1} :	Compressibility factor corresponding to P_{A1}
Z_{A2} :	Compressibility factor corresponding to P_{A2}
η :	Permeability enhancement ratio
k_0 :	Permeability before CO_2 adsorption, mD
S_{max} :	Maximum swelling
D :	Empirical parameter
ρ_a :	density of adsorbed CO_2 , kg/m^3
ρ :	CO_2 density, kg/m^3
a :	Empirical parameter
ε :	Total deformation of a specimen
ε_e :	Volumetric deformation caused by effective stresses
σ :	Volume stress, MPa
P :	Pore pressure, MPa
K :	Bulk modulus, MPa.

Data Availability

The data used to support the findings of this study are available from the corresponding author upon request.

Conflicts of Interest

The authors declare that there is no conflict of interest regarding the publication of this paper.

Acknowledgments

This study was supported by the National Natural Science Foundation of China (No. 51874144 and No. 51679093) and Scientific and Technology Plan Projects in Xiamen (No. 3502z20193040).

References

- [1] R. S. Haszeldine, "Carbon capture and storage: how green can black be?," *Science*, vol. 325, no. 5948, pp. 1647–1652, 2009.
- [2] J. Yun, F. Xu, L. Liu, N. Zhong, and X. Wu, "New progress and future prospects of CBM exploration and development in China," *International Journal of Mining Science and Technology*, vol. 22, no. 3, pp. 363–369, 2012.
- [3] S. R. Reeves, "The Coal-Seq project: key results from field, laboratory, and modeling studies," in *Greenhouse Gas Control Technologies* 7, pp. 1399–1403, Elsevier, 2005.
- [4] J. Q. Shi, S. Durucan, and M. Fujioka, "A reservoir simulation study of CO_2 injection and N_2 flooding at the Ishikari coalfield CO_2 storage pilot project, Japan," *International Journal of Greenhouse Gas Control*, vol. 2, no. 1, pp. 47–57, 2008.
- [5] J. Ye, S. Feng, Z. Fan et al., "Micro-pilot test for enhanced coalbed methane recovery by injecting carbon dioxide in south part of Qinshui Basin," *Acta Petrolei Sinica*, vol. 28, no. 4, pp. 77–80, 2007.
- [6] R. Span and W. Wagner, "A new equation of state for carbon dioxide covering the fluid region from the triple-point temperature to 1100 K at pressures up to 800 MPa," *Journal of Physical and Chemical Reference Data*, vol. 25, no. 6, pp. 1509–1596, 1996.
- [7] D. Wu, X. Liu, B. Liang, K. Sun, and X. Xiao, "Experiments on displacing methane in coal by injecting supercritical carbon dioxide," *Energy & Fuels*, vol. 32, no. 12, pp. 12766–12771, 2018.
- [8] V. Vishal, T. N. Singh, and P. G. Ranjith, "Influence of sorption time in CO_2 -ECBM process in Indian coals using coupled numerical simulation," *Fuel*, vol. 139, pp. 51–58, 2015.
- [9] V. Vishal, B. Mahanta, S. P. Pradhan, T. N. Singh, and P. G. Ranjith, "Simulation of CO_2 enhanced coalbed methane recovery in Jharia coalfields, India," *Energy*, vol. 159, pp. 1185–1194, 2018.
- [10] Y. Fan, C. Deng, X. Zhang, F. Li, X. Wang, and L. Qiao, "Numerical study of CO_2 -enhanced coalbed methane recovery," *International Journal of Greenhouse Gas Control*, vol. 76, pp. 12–23, 2018.
- [11] S. Harpalani and R. A. Schraufnagel, "Shrinkage of coal matrix with release of gas and its impact on permeability of coal," *Fuel*, vol. 69, no. 5, pp. 551–556, 1990.
- [12] R. Wang, Q. Wang, Q. Niu, J. Pan, H. Wang, and Z. Wang, " CO_2 adsorption and swelling of coal under constrained conditions and their stage-change relationship," *Journal of Natural Gas Science and Engineering*, vol. 76, p. 103205, 2020.
- [13] D. Wu, X. Liu, K. Sun, X. Xiao, and L. Xin, "Experiments on supercritical CO_2 adsorption in briquettes," *Energy Sources, Part A: Recovery, Utilization, and Environmental Effects*, vol. 41, no. 8, pp. 1005–1011, 2018.
- [14] H. Liu, S. Sang, S. Liu et al., "Supercritical- CO_2 adsorption quantification and modeling for a deep coalbed methane reservoir in the southern Qinshui Basin, China," *ACS Omega*, vol. 4, no. 7, pp. 11685–11700, 2019.
- [15] J. Jia, S. Sang, L. Cao, and S. Liu, "Characteristics of CO_2 /supercritical CO_2 adsorption-induced swelling to anthracite: an experimental study," *Fuel*, vol. 216, pp. 639–647, 2018.
- [16] H. Liu, B. Lin, and W. Yang, "Theoretical models for gas adsorption-induced coal deformation under coal seam field conditions," *Energy Science & Engineering*, vol. 7, no. 5, pp. 1504–1513, 2019.
- [17] K. Zhang, Y. Cheng, K. Jin et al., "Effects of supercritical CO_2 fluids on pore morphology of coal: implications for CO_2 geological sequestration," *Energy & Fuels*, vol. 31, no. 5, pp. 4731–4741, 2017.

- [18] K. Zhang, Y. Cheng, W. Li, D. Wu, and Z. Liu, "Influence of supercritical CO₂ on pore structure and functional groups of coal: implications for CO₂ sequestration," *Journal of Natural Gas Science and Engineering*, vol. 40, pp. 288–298, 2017.
- [19] M. A. Pirzada, M. Zoorabadi, H. Lamei Ramandi, I. Canbulat, and H. Roshan, "CO₂ sorption induced damage in coals in unconfined and confined stress states: a micrometer to core scale investigation," *International Journal of Coal Geology*, vol. 198, pp. 167–176, 2018.
- [20] M. S. A. Perera and K. H. S. M. Sampath, "Modelling of free and adsorbed CO₂-induced mechanical property alterations in coal," *International Journal of Coal Geology*, vol. 217, p. 103348, 2020.
- [21] K. H. S. M. Sampath, I. Sin, M. S. A. Perera, S. K. Matthai, P. G. Ranjith, and L. Dong-yin, "Effect of supercritical-CO₂ interaction time on the alterations in coal pore structure," *Journal of Natural Gas Science and Engineering*, vol. 76, p. 103214, 2020.
- [22] X. Ni, Q. Li, Y. Wang, and S. Gao, "Permeability variation characteristics of coal after injecting carbon dioxide into a coal seam," *International Journal of Mining Science and Technology*, vol. 25, no. 4, pp. 665–670, 2015.
- [23] C. Liu, S. Sang, X. Fan et al., "Influences of pressures and temperatures on pore structures of different rank coals during CO₂ geological storage process," *Fuel*, vol. 259, p. 116273, 2020.
- [24] J. Yu, X. Chen, H. Li, J. Zhou, and Y. Cai, "Effect of freeze-thaw cycles on mechanical properties and permeability of red sandstone under triaxial compression," *Journal of Mountain Science*, vol. 12, no. 1, pp. 218–231, 2015.
- [25] J. Yu, X. Chen, Y. Cai, and H. Li, "Triaxial test research on mechanical properties and permeability of sandstone with a single joint filled with gypsum," *KSCE Journal of Civil Engineering*, vol. 20, no. 6, pp. 2243–2252, 2016.
- [26] J. Yu, W. Yao, K. Duan, X. Liu, and Y. Zhu, "Experimental study and discrete element method modeling of compression and permeability behaviors of weakly anisotropic sandstones," *International Journal of Rock Mechanics and Mining Sciences*, vol. 134, p. 104437, 2020.
- [27] J. Yu, S. Chen, X. Chen, Y. Zhang, and Y. Cai, "Experimental investigation on mechanical properties and permeability evolution of red sandstone after heat treatments," *Journal of Zhejiang University-SCIENCE A*, vol. 16, no. 9, pp. 749–759, 2015.
- [28] R. Sakurovs, S. Day, S. Weir, and G. Duffy, "Application of a modified Dubinin-Radushkevich equation to adsorption of gases by coals under supercritical conditions," *Energy & Fuels*, vol. 21, no. 2, pp. 992–997, 2007.
- [29] S. Day, R. Fry, and R. Sakurovs, "Swelling of Australian coals in supercritical CO₂," *International Journal of Coal Geology*, vol. 74, no. 1, pp. 41–52, 2008.
- [30] J. W. Larsen, "The effects of dissolved CO₂ on coal structure and properties," *International Journal of Coal Geology*, vol. 57, no. 1, pp. 63–70, 2004.
- [31] A. S. Ranathunga, M. S. A. Perera, P. G. Ranjith, and H. Bui, "Super-critical CO₂ saturation-induced mechanical property alterations in low rank coal: an experimental study," *The Journal of Supercritical Fluids*, vol. 109, pp. 134–140, 2016.
- [32] Y. Zhang, M. Lebedev, M. Sarmadivaleh, A. Barifcani, and S. Iglauer, "Swelling-induced changes in coal microstructure due to supercritical CO₂ injection," *Geophysical Research Letters*, vol. 43, no. 17, pp. 9077–9083, 2016.
- [33] Q. Niu, L. Cao, S. Sang, X. Zhou, and S. Liu, "Experimental study of permeability changes and its influencing factors with CO₂ injection in coal," *Journal of Natural Gas Science and Engineering*, vol. 61, pp. 215–225, 2019.
- [34] W. Li, Z. Liu, E. Su, and Y. Cheng, "Experimental investigation on the effects of supercritical carbon dioxide on coal permeability: implication for CO₂ injection method," *Energy & Fuels*, vol. 33, no. 1, pp. 503–512, 2018.
- [35] B. G. Kutchko, A. L. Goodman, E. Rosenbaum, S. Natesakhawat, and K. Wagner, "Characterization of coal before and after supercritical CO₂ exposure via feature relocation using field-emission scanning electron microscopy," *Fuel*, vol. 107, pp. 777–786, 2013.
- [36] B. Mahanta, P. G. Ranjith, T. N. Singh, V. Vishal, W. Duan, and M. Sazid, "Digital rock physics and application of high-resolution micro-CT techniques for geomaterials," in *Deep Rock Mechanics: From Research to Engineering* pp. 299–307, Taylor Francis Group, London.
- [37] Y. Cai, J. Yu, G. Fu, and H. Li, "Experimental investigation on the relevance of mechanical properties and porosity of sandstone after hydrochemical erosion," *Journal of Mountain Science*, vol. 13, no. 11, pp. 2053–2068, 2016.

Research Article

Permeability of the Hydrated Shale under Cyclic Loading and Unloading Conditions

Liu Xianshan ^{1,2}, Li Man,^{1,2} Xu Ming,^{1,2} and Kang Zhiyong^{1,2}

¹Key Laboratory of New Technology for Construction of Cities in Mountain Area (Chongqing University), Ministry of Education, Chongqing 400045, China

²School of Civil Engineering, Chongqing University, Chongqing 400045, China

Correspondence should be addressed to Liu Xianshan; lzmoumou@163.com

Received 9 June 2020; Revised 28 July 2020; Accepted 8 August 2020; Published 7 September 2020

Academic Editor: Wei Wei

Copyright © 2020 Liu Xianshan et al. This is an open access article distributed under the Creative Commons Attribution License, which permits unrestricted use, distribution, and reproduction in any medium, provided the original work is properly cited.

The hydrated shales under cyclic loading and unloading conditions are common for the shale reservoir development; corresponding mechanical properties and permeability evolution are very significant and should be deeply researched. Firstly, the experiments of the hydrated shales under the above conditions are discussed, showing that the peak strength is lower and corresponding permeability is higher for more days of hydrating treatment. Secondly, the damage theory is proposed to analyze the shale permeability evolution due to hydromechanical damage and get permeability variation under initial loading and unloading conditions, observing that the permeability in the loading process decreases with increasing confining pressure and increases in the unloading process with decreasing confining pressure; however, the former changes much greater than the latter considering the same confining pressure, indicating that the irreversible damage for the hydrated shales in this cyclic condition has resulted in obvious difference of the permeability. Furthermore, the curves between the permeability and confining pressure based on the experimental data are fitted as negative exponential functions under initial loading conditions and power functions under more cyclic loading conditions, showing that more loading process will change the permeability evolution model. However, the permeability while unloading changes smoothly and can be fitted as a power function with the confining pressure. And in addition, the loss ratio and recovery ratio of the permeability have been deeply researched under five cyclic loading and unloading conditions, thoroughly explaining the permeability decreasing variation with more cyclic processes. Finally, the sensitive coefficients of the permeability have been investigated to observe the largest coefficients under initial cyclic conditions and less and less with more cyclic processes, especially the coefficients while loading which are more sensitive to lower confining pressure and smaller while unloading, which is in accordance with the shale permeability loss and recovery variation, revealing the permeability evolution of the hydrated shale under complex extracted environment.

1. Introduction

China Mineral Resources (2018) has reported that accumulated proven geological reserves of shale gas from 2015 to 2017 are, respectively, 5441, 7643, and 9168 billion cubic meters, and corresponding productions are, respectively, 45, 78.82, and 100 billion cubic meters. The shale gas production in China has gradually increased in recent years, but the recovery efficiency is still lower than that in America; the reservoir permeability as an important index is significant for deeply understanding the exploration mechanism. However, the shale reservoir influenced by deposition and the tectonic

movement includes orientated clay mineral and different pore structures, causing significant anisotropy and heterogeneity [1] for extracting gas more difficult. As for the drilling process, the drilling fluid hydrating the shale repeatedly will weaken the mechanical parameters and enlarge the seepage channels, resulting in instability of the well wall. Note that the failure of reservoir shale and corresponding permeability variation in the process [2, 3] is a potential instance considered in the gas engineering. Especially, the noted hydration effect will cause vague variation of the mechanical and permeable properties of the shales, drastically enhancing the difficulty of shale gas development. Therefore, deep research on

the permeability of hydrated shale under complex extracting circumstances has attracted attentions by many researchers.

In recent years, a few researches about the hydrated shale with the help of the advanced equipment have been investigated. Shi and Xia [4] observed the variation of the shale structure by XRD, SEM, and CT, indicating that the water weakening minerals caused crack propagation, and Ma and Chen [5] conducted hydration experiment by CT and observed that obvious damage was mainly in the initial hydrated stage; also, Liu et al. [6] used SEM to observe the microcrack propagation to form the large fractures when hydrating much more time. Massat et al. [7] carried out experiments to research on hydration influence on the shale structures and pore distribution, mainly causing the crack propagation, and Liu et al. [8] pointed out that arranged mineral particles provided channels for shale absorbing water when hydrating to change corresponding structures. The above experiments show that hydration greatly changes the shale microstructure to influence on its mechanical characteristics, so the issue about the properties of the hydrated shale should be solved in detail. Zhang and Sheng [9] analyzed the crack propagation and gave the relationship of the hydration expansion stress and seepage parameters. Teng et al. [10] researched the elastic modulus and strength decreasing variation with long hydrating time. Zhu et al. [11] explained that mechanical parameters of the hydrated shale decreased because of corresponding clay structures changing into flocculent fabrics. Roshan et al. [12] also carried out physical and chemical analysis to illuminate the mineral hydration influence on the shale permeability. Zhang and Sheng [13] compared the shale permeability variation considering water and KCL treatment, showing that water hydration affected the shale permeability more greatly. The above studies indicate that the hydration effect on the mechanical and permeable properties in laboratory conditions and in situ compression tests should not be ignored, and deep investigations about complex load combination on the hydromechanical behavior of the reservoir shales should be deeply conducted.

In decades, some researchers have paid more attentions to the rock permeability under different loading conditions. Tan et al. [14] determined the relationship of the rock permeability and corresponding axial strain in the process of the progressive failure, indicating the complex hydromechanical coupled behavior of low porous rocks; Zhou et al. [15] discussed the shale permeability evolution considering different combinations of the shale structures and different confining pressures; Liu [16] analyzed the shale deformation and corresponding permeability variation and proposed a permeability model considering rock damage evolution; and Yu et al. [17] conducted the permeability tests under loading and unloading conditions, showing that the permeability after unloading sharply increased and the value reached to the maximum considering unloading confining pressure at the prepeak. The above researches about the permeability evolution under single loading or unloading condition give supports to investigate the permeability variation under cyclic loading and unloading conditions. And also, some researches have been implemented. Yu et al. [18] conducted the seepage experi-

ments to describe the permeability variation of sandstones under freeze-thaw loading conditions; Yin et al. [19]; Xu et al. [20], and Pan et al. [21] researched the coal permeability under a combination of the axial and confining pressure and gave the theoretical analysis; and Kong et al. [22] found out that the permeability evolution curve under loading conditions could not match that in the process of unloading. Zhang et al. [23] conducted the periodic seepage tests of the sandstones in the Three Gorges Reservoir, showing that permeability is approaching a stable value under four cyclic loading and unloading conditions. Sun et al. [24] determined the dynamic permeability model considering cyclic axial stress. Wang et al. [25] carried out the three-axial cyclic loading tests to investigate the relationship of the coal permeability and damage energy. Therefore, researches about the permeability characteristics of the reservoir shale under complex loading and unloading conditions should be deeply investigated. Sun et al. [26] and Yan et al. [27] carried out the seepage tests to reveal the strong relationship of shale permeability and real-time damage, providing useful information for research on the permeability characteristics of hydrated shale under cyclic loading and unloading conditions.

Therefore, taking a reservoir shale as a case study, considering the shale structures and hydration effect, corresponding permeability experiments under cyclic loading and unloading conditions are conducted to investigate the relationship of crack propagation and permeability of reservoir shales. And also, the damage analysis has been proposed to analyze the shale damage evolution and corresponding permeability variation, revealing the permeability characteristics caused by progressive damage considering the hydromechanical coupling effect. Furthermore, some models describing the permeability loses, permeability recoveries, and corresponding stress-sensitive coefficients are proposed to indicate the permeability evolution under cyclic loading and unloading conditions, revealing the permeability evolution mechanism of the hydrated shale under complex conditions.

2. Seepage Experiments of the Hydrated Shale

2.1. Sample Preparation. To investigate the permeability characteristics of hydrated reservoir shales under cyclic loading and unloading conditions, the testing shales are the outcrop taken from Longmaxi in Chongqing Shizhu county, which are selected for the permeability experiments. Firstly, the mineral composition of the pulverized shale should be analyzed based on XRD to get the diffraction pattern as Figure 1(a), showing the minerals of Quartz, orthoclase, plagioclase, calcite, dolomite, illite, montmorillonite, chlorite, and kaolinite. And according to the method by the International Society for Rock Mechanics (ISRM), the size of all tested specimens is cylindrical with 50 mm diameter and 100 mm length approximately, shown in Figure 1(b). It is observed from Figure 1(b) that the shales are black with obvious bedding. Furthermore, acoustic emissions from all specimens are detected and received by the nonmetallic acoustic detector RSM-SY5 in order to illuminate that every group of reservoir sandstone specimens is uniform to avoid the

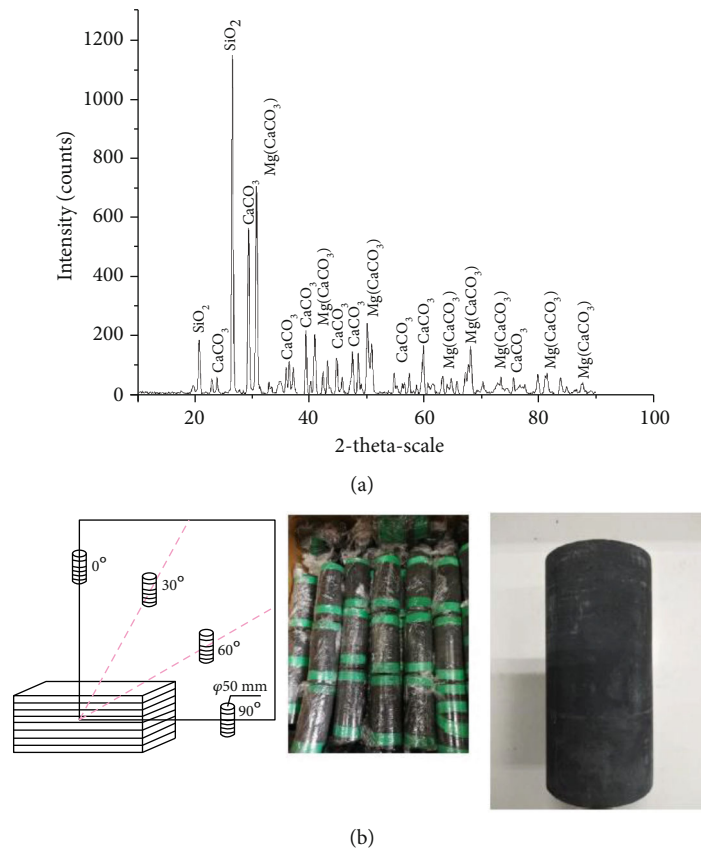


FIGURE 1: The shale samples and corresponding XRD. The labels are in Figure 1 as follows, Fig.1(a) Diffraction pattern of the shale based on XRD. Fig.1(b) Arranged shale samples.

specimen heterogeneity influencing on the experimental efficiency and accuracy.

2.2. Apparatus for Shale Seepage Experiments. All the seepage experiments will be conducted in Geotechnical Test Center of Chongqing University, and a rock servo-controlled triaxial equipment named Rock 600-50HT PLUS manufactured by TOP-INDUSTRIE in France is arranged for all the tests.

The experimental apparatus consists of a hydraulic pressure transfer system, a pressure chamber equipment, a hydraulic pressure system, and an automatic data collection system; performing triaxial compression tests at confining pressures (P2) up to 60 MPa, with increasing deviatoric stress (P1) up to 500 MPa and with an increasing transducer, has a resolution of 0.01 MPa. And the system can handle the constant-head, constant flow-rate, and transient-pulse permeability tests under low or high confining and water pressures. Also, different fluids can be chosen as the testing fluid and the servo-controlled fluid pump can regulate the pore pressure up to 60 MPa (P3/P4) according to the experimental target.

This apparatus can perform mechanical tests, seepage tests, and hydromechanical tests by computer and robotized operations, ensuring that all the testing data can be analyzed safely, timely, and accurately. The apparatus can be used to deal with hydrostatic pressure tests, triaxial seepage tests, etc. Four kinds of loading modes including displacement loading, stress loading, strain loading, and flow loading are

employed to satisfy different experimental requirements. And the apparatus can automatically record all the real-time data every 5 seconds.

2.3. Testing Theory and Design. Firstly, the hydrated shales have been treated with 0 days (no hydration), 2 days, 5 days, and 10 days, shown in Figure 2, and obvious cracks are observed on the shale surface with more hydrated days. When conducting the shale seepage tests, the shale specimens are enclosed in a 3 mm thick Viton rubber jacket and then placed in the sample assembly. When testing, the axial displacement is measured with two displacement LVDTs, and the circumferential deformation is measured with a circumferential sensors. Considering the temperature influencing on the shale deformation and seepage characteristics, all the tests are conducted at room temperature ($25 \pm 2^\circ\text{C}$).

And then, corresponding tests of the hydrated shales under different load combinations are performed. For obtaining the damage variation and permeability characteristics of the hydrated shale, the samples are firstly conducted with desired confining pressure, and the axial stress is proportionally increased to the value of the confining pressure to ensure an initial isotropic stress or zero deviatoric stress. In addition, the upstream pressure (P3) and downstream pressure (P4) are balanced for the hydrated shales to ensure the fluid in a single phase. Afterwards, the deviatoric stress is increased stepwise and the seepage testing is invoked for measurements of the rock permeability. For this seepage

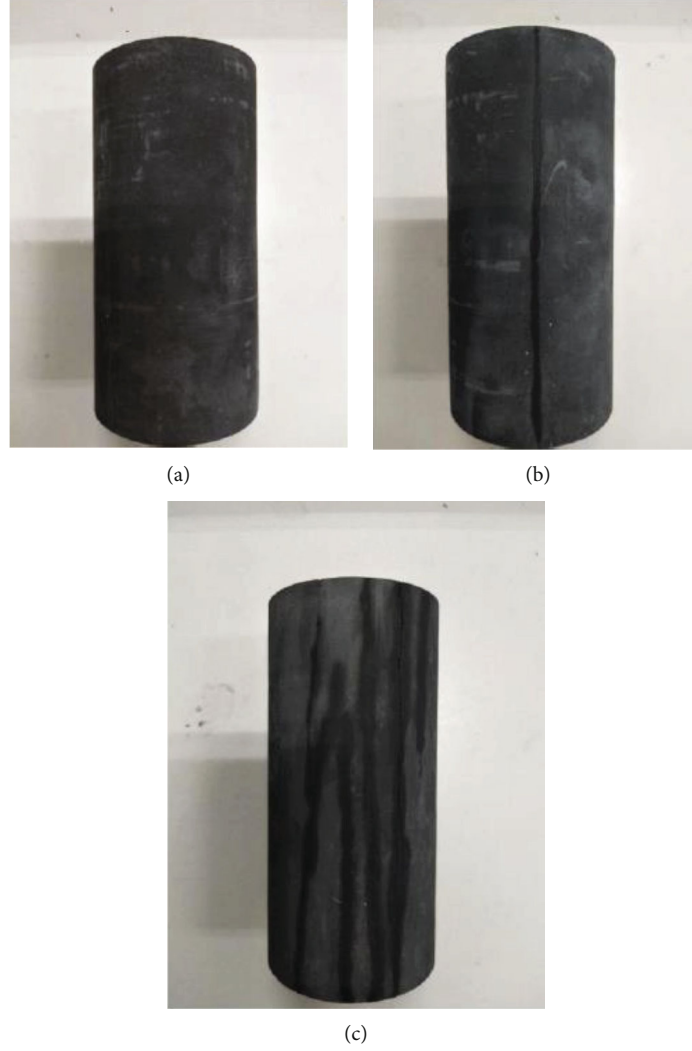


FIGURE 2: The shale samples with different hydrating days. The labels in Fig.2 are as follows, (a)No hydration (b) 2days (c)5 days (d) 10days.

testing procedure, the permeability of the samples can be calculated by measuring the fluid volume from the pump in a period of time and written by [16]

$$k = \frac{\mu LV}{A \Delta p \Delta t}, \quad (1)$$

where k is the shale permeability (m^2), μ is the fluid dynamic viscosity (water at $T = 20^\circ\text{C}$, $1 \times 10^{-3} \text{ Pa} \cdot \text{s}$), L is the shale specimen height (m), V is the fluid volume (m^3) from the pump in time Δt , A is the cross-sectional area (m^2), Δp is the fluid pressure difference (Pa), and Δt is the flow time(s).

As for the seepage tests under cyclic loading and unloading conditions, the detailed design is listed in Table 1. The design considers seepage pressure 4 MPa and axial pressure 5 MPa and confining pressure loading from 5 MPa to 11 MPa and unloading from 11 MPa to 5 MPa (increment of 1 MPa) for five times, and permeability of the hydrated shales under different stages can be measured, describing the permeability variation with different hydrated days under designed load conditions.

TABLE 1: The seepage tests of the hydrated shale under cyclic loading and unloading conditions.

Seepage pressure (MPa)	Axial pressure (MPa)	Hydration time (d)	Confining pressure (MPa)							
			5	6	7	8	9	10	11	
4	5	0	Cyclic loading and unloading condition							
		2								
		5								
		10								

3. Permeability Analysis of the Shale with Different Hydrated Time

3.1. Mechanical Characteristics and Permeability Variation of the Hydrated Shale. In order to describe the mechanical characteristics and corresponding permeability variation of the hydrated shale with different days (2 days, 5 days, and 10 days), the curves of the deviatoric stress and strain and

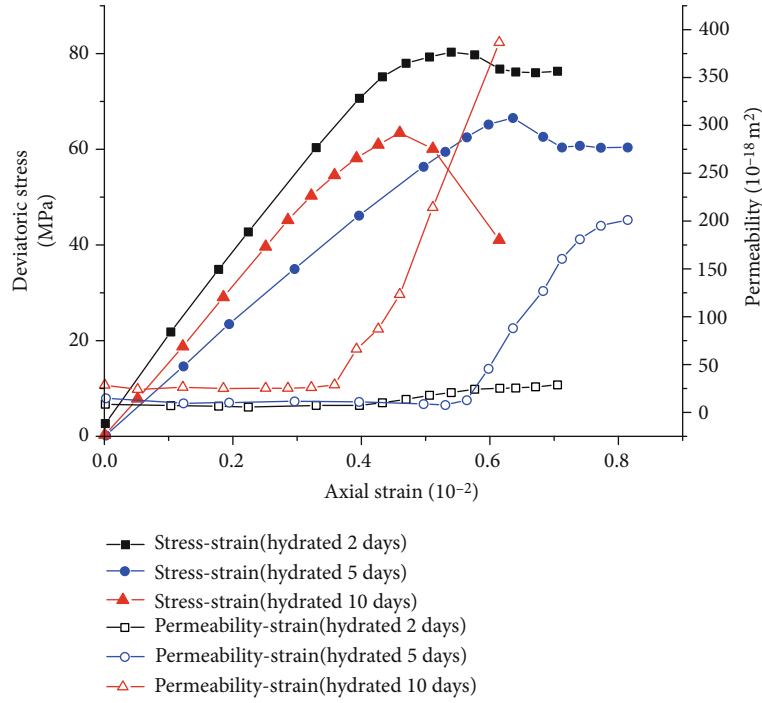


FIGURE 3: The curves of stress and permeability variation.

permeability and strain considering the load combination of seepage pressure 4 MPa and confining pressure 5 MPa are shown in Figure 3. It can be seen that the variation patterns of the deviatoric stress and strain are similar; however, the shale treated by more hydrated days shows lower peak strength. According to the hydrated characteristic shown in Figure 2, it can be concluded that there is more water absorption into the shale with more hydrated days, causing the mineral expansion and separation to generate the flocculent fabrics and larger pore structure, so the water can flow into the pores and fractures more and more to enlarge the shale damage. Therefore, the shale specimen with more hydrated days generated more cracks quickly to propagate under progressive loading conditions [28], especially the shale bedding which was softened and lubricated to weaken the rock strength and failed more easily.

Furthermore, the permeability evolution under different combinations of confining pressure and different water pressures is plotted in Figure 3, showing that given the same loading conditions, the permeability of given hydrated days decreased in the initial loading stage and then increased with increasing loads; the variation was in accordance with the above stages of the shale crack propagation and permeability evolution in reference [26], deeply calibrating the synchronism of the permeability evolution with the crack initiation and propagation. Also, it can be seen from Table 2 that the initial permeability of the shale with hydration for 0 days, 2 days, 5 days, and 10 days, respectively, $6.63 \times 10^{-18} \text{ m}^2$, $8.69 \times 10^{-18} \text{ m}^2$, $14.65 \times 10^{-18} \text{ m}^2$, and $26.58 \times 10^{-18} \text{ m}^2$, indicating that the permeability of the shale with more hydrated days in the initial compaction stage is larger because of more cracks mentioned in Figure 2. And increasing ratio of shale

TABLE 2: The permeability considering hydraulic pressure with different confining pressures (10^{-18} m^2).

Hydrated days (day)	0	2	5	10
Initial permeability	6.63	8.69	14.65	26.58
Minimum permeability	3.31	3.52	6.49	12.54
Maximum permeability	29.57	39.54	201.55	386.71

permeability considering hydrated days from 0 days to 2 days, 2 days to 5 days, and 5 days to 10 days is, respectively, 31.07%, 68.58%, and 81.43%, the comparison showing that the permeability is more sensitive to the hydrated period. So the permeability variation can explain that long-time hydration causes much more pores and propagated cracks to enlarge the seepage channels, resulting in the permeability increasing greatly. Therefore, observations from the above data indicate that the hydration should not be ignored for the reservoir drilling and hydraulic fracturing in the process of shale gas extraction.

And also, corresponding minimum permeability of shales with no hydration, hydrated 2 days, 5 days, and 10 days under the same load condition, respectively, with values $3.31 \times 10^{-18} \text{ m}^2$, $3.52 \times 10^{-18} \text{ m}^2$, $6.49 \times 10^{-18} \text{ m}^2$, and $12.54 \times 10^{-18} \text{ m}^2$, is also listed in Table 2. It can be observed that the minimum permeability of shales also increased with more hydrated days, showing that more and greater cracks of shales with long period of hydration still dominate. In addition, the corresponding maximum permeability is listed in Table 2, and the corresponding values are $29.57 \times 10^{-18} \text{ m}^2$, $39.54 \times 10^{-18} \text{ m}^2$, $201.55 \times 10^{-18} \text{ m}^2$, and $386.71 \times 10^{-18} \text{ m}^2$ considering no hydration and hydrated 2 days, 5 days, and 10 days,

showing that the permeability considering hydrated 10 days is 13.1 times of no hydration, which concludes that greater fractures are generated for this kind of shale with more days of hydration under the same condition.

Therefore, the curves of permeability variation can be summarized into that more hydrated days cause much more pores and fractures to enlarge larger seepage channels, and the water is speeded up to flow in the cracks resulting in corresponding permeability of shales with more hydrated days which increases more obviously under the above same load combination. The main reason for the hydration enlarging the crack aperture and quantities is crack propagating and new cracks initiating among the inorganic minerals, and the crack widening between the banded organic materials and inorganic minerals. And also, the ion such as Na^+ , K^+ , and Ca^{2+} will be dissolved; once the water is drained out, the ion will gather on the clay surface causing the wider crack. Therefore, the crack should be connected to form larger cracks, and corresponding permeability will increase greatly.

3.2. Permeability Characteristics of Hydrated Shale Induced. To comprehensively characterize the permeability change of reservoir rocks, an important index named damage variable D describing the defect variation closely related to the microcrack growth and microstructural evolution was proposed. Based on the research in the literature [16], it is assumed that the strength of rock microelements obeys Weibull stochastic distribution; accordingly, the damage variable D can be described by

$$D = 1 - \exp \left[- \left(\frac{F}{F_0} \right)^m \right], \quad (2)$$

where m and F_0 are the Weibull parameters and F is the random strength variables of rock microelements.

Suppose $F = f(\tilde{\sigma}')$, where $\tilde{\sigma}'$ is the effective stress tensors, so the rock failure criteria can be written by

$$F = f(\tilde{\sigma}') - k_0 = 0, \quad (3)$$

where k_0 is constant related to cohesion and friction angle considering the rock yielding; $F = f(\tilde{\sigma}') \geq k_0$ represents the rock yielding or failing. And the rock failure criteria may be described based on Drucker-Prager criteria

$$F = \alpha \tilde{I}'_1 + \sqrt{\tilde{J}'_2}, \quad (4)$$

$$\alpha = \frac{\sin \varphi}{\sqrt{9 + 3 \sin^2 \varphi}}, \quad (5)$$

where φ is the friction angle; \tilde{I}'_1 is first invariant of effective stress tensor, and \tilde{J}'_2 is the second invariant of effective stress tensor.

Suppose the stress-strain of rocks obeys the Generalized Hook's Law, the principle stress-stain can be written by

$$\tilde{\varepsilon}'_1 = \frac{1}{E} \left[\tilde{\sigma}'_1 - \mu (\tilde{\sigma}'_2 + \tilde{\sigma}'_3) \right], \quad (6)$$

where E is the elastic module and μ is Poisson's ratio.

Considering $\sigma_1 > \sigma_2 = \sigma_3$ in triaxial tests and $\varepsilon_1 = \tilde{\varepsilon}'_1$, substituting the expression $\tilde{\sigma}'_{ij} = (\sigma_{ij} - p_w \delta)_{ij} / (1 - D)$ into Equation (6) gives

$$\sigma_1 = E \varepsilon_1 (1 - D) + 2\mu \sigma_3 + (1 - 2\mu) p_w \quad (7)$$

And also, the measured axial deviatoric stress σ_{1t} and real axial stain ε_1 should be shown in Equation (8) and Equation (9).

$$\sigma_{1t} = \sigma_1 - \sigma_3 \quad (8)$$

$$\varepsilon_1 = \varepsilon_{1t} + \varepsilon_{10} \quad (9)$$

Therefore, the statistical damage constitutive model [16] considering pore pressure can be written by

$$\begin{aligned} \sigma_{1t} &= [E \varepsilon_{1t} + (1 - 2\mu)(\sigma_3 - p_w)] \exp \left[- \left(\frac{F}{F_0} \right)^m \right] + (2\mu - 1)(\sigma_3 - p_w) \\ F &= \frac{[E \varepsilon_{1t} + (1 - 2\mu)(\sigma_3 - p_w)]}{\sigma_{1t} + (1 - 2\mu)(\sigma_3 - p_w)} \cdot \left[\frac{\sin \varphi (\sigma_{1t} + 3\sigma_3 - 3p_w)}{\sqrt{9 + 3 \sin^2 \varphi}} + \frac{\sigma_{1t}}{\sqrt{3}} \right], \\ \frac{\sigma_{1t} - (2\mu - 1)(\sigma_3 - p_w)}{E \varepsilon_{1t} + (1 - 2\mu)(\sigma_3 - p_w)} &= \exp \left(- \left(\frac{F}{F_0} \right)^m \right), \end{aligned} \quad (10)$$

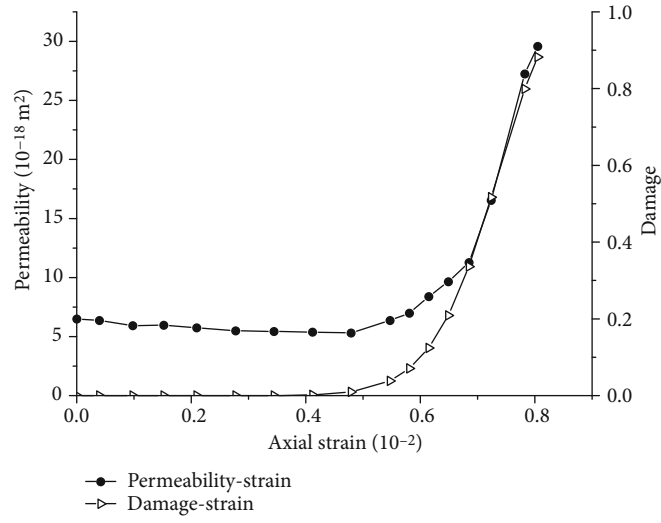
where E is elastic module, ε_{1t} is deviatoric strain; σ_{1t} is deviatoric stress, σ_3 is confining pressure, p_w is permeable pressure, φ is internal frictional angle, and μ is Poisson's ratio.

And then, Equation (5) may be changed as below:

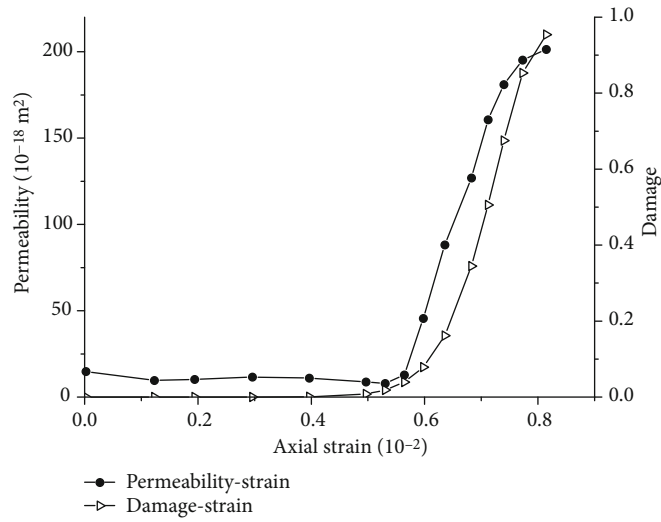
$$\begin{aligned} \frac{\sigma_{1t} - (2\mu - 1)(\sigma_3 - p_w)}{E \varepsilon_{1t} + (1 - 2\mu)(\sigma_3 - p_w)} &= \exp \left(- \left(\frac{F}{F_0} \right)^m \right), \\ \ln \left\{ \ln \left[\frac{\sigma_{1t} - (2\mu - 1)(\sigma_3 - p_w)}{E \varepsilon_{1t} + (1 - 2\mu)(\sigma_3 - p_w)} \right] \right\} &= m \ln F - B, \\ Y &= mX - B, \end{aligned} \quad (11)$$

in which, $X = \ln F$; $Y = \ln \{ \ln [(E \varepsilon_{1t} + (1 - 2\mu)(\sigma_3 - p_w)) / (\sigma_{1t} + (1 - 2\mu)(\sigma_3 - p_w))] \}$; B is the fitting parameter; and F_0 can be calculated by $F_0 = \exp(B/m)$ according to the fitting analysis.

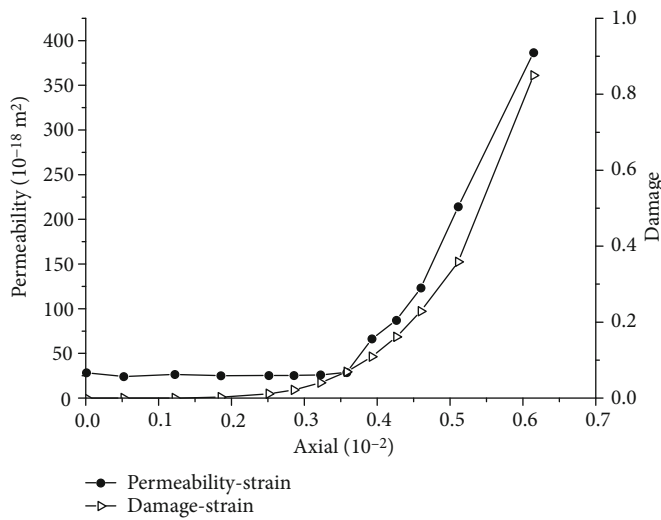
Based on above derived formula, the curves of shale damage and strain and permeability and strain can be calculated and are shown in Figures 4(a)–4(c). The comparison of the permeability and corresponding damage variation about the shales with different hydrated days present similar variations. However, it was observed from Figure 4 that shale with hydration of 10 days has greater damage and larger permeability with the same strain, indicating that more fractures and cracks representing greater damage have generated for this shale with more days of hydration. As for the shale



(a)



(b)



(c)

FIGURE 4: The permeability and damage coefficient of the shale rocks vs. axial strain considering hydrated days. The labels in Fig.4 are as follows,(a) 2 days (b) 5 days (c) 10 days.

samples with the same hydrated days, it can be seen that the variation patterns of the damage and permeability variation are similar to the deviatoric stress variation in Figure 3, indicating that increasing loads enlarge the shale damage and permeability, so the damage variation rate can be considered to describe the crack propagation and permeability development.

Therefore, the permeability related to the damage variable D can be written by Equation (12) using the testing data of hydrated 2 days, 5 days, and 10 days, shown in Figures 5(a)–5(c). It can be seen from the fitting curves that the relationship of the permeability and corresponding damage variable can be expressed by exponential functions with the correlation coefficient exceeding 0.97, indicating that the gradual damage is the key to describe the permeability evolution.

$$k = \zeta \exp(a + bD + cD^2), \quad (12)$$

where k is the permeability, D is damage variable, ζ is a parameter valued 10^{-18} , and a, b, c are fitting parameters based on the experimental data.

And also, it can be observed that the shale permeability increases with greater damage variable, indicating that the shale damage variation can represent inner crack propagation, and the permeability evolution is closely related to the crack propagation, so the permeability evolution is considered to be synchronized with the damage evolution. In addition, the curves $k \sim D$ in Figures 5(a)–5(c) show that the shale permeability in Figure 5(c) with 10-day hydrated days is the greatest under the same loading conditions compared with other shales with less hydrated days; the main reason is concluded that initial damage is the greatest for 10-day hydrated shales resulting in the greatest initial permeability and it was kept the greatest even with the same damage variable, explaining the effect of hydration on the shale permeability.

4. The Permeability of the Shale under Loading and Unloading Conditions

4.1. The Permeability Variation under the First Loading and Unloading Conditions

4.1.1. The Permeability Variation under the First Loading Conditions. It can be observed from the black solid lines in Figures 6(a)–6(d) that the permeability variation decreased sharply with increasing confining pressure in the initial loading stage; however, the value decreased smoothly with greater confining pressure. The reason is that the shale bedding with initial confining pressure may be closed and caused larger deformation, so the fracture aperture closed much more and formed less seepage channel to show smaller permeability. While the confining pressure was increased significantly, the pores and fractures cannot be compacted more easily, and the permeability changes very slowly. Therefore, the confining pressure dominated the permeability variation considering the same

seepage pressure. As seen from the solid black lines in Figures 6(a)–6(d) considering the confining pressure increasing from 5 MPa to 11 MPa, the shale permeability with no hydration and hydrated 2 days, 5 days and 10 days decrease from $6.2 \times 10^{-18} \text{ m}^2$, $8.58 \times 10^{-18} \text{ m}^2$, $14.88 \times 10^{-18} \text{ m}^2$, and $24.45 \times 10^{-18} \text{ m}^2$ to $0.58 \times 10^{-18} \text{ m}^2$, $0.77 \times 10^{-18} \text{ m}^2$, $1.127 \times 10^{-18} \text{ m}^2$, and $1.49 \times 10^{-18} \text{ m}^2$. The changes for the shale permeability indicate that the permeability considering larger confining pressure is not sensitive to the load increment.

Therefore, considering the same seepage pressure and axial pressure, the shale permeability decreased more smoothly with increasing confining pressure. In addition, the relationship of the permeability and confining pressure can be fitted as power function, exponential function, and quadratic polynomial function for the first loading conditions listed in Table 3 [22], and it can be seen that the fitting curves under the first loading condition based on the above testing data can be expressed by an exponential function with relation coefficient of 0.97, showing that corresponding fitting coefficients of shales considering more hydrated days are greater.

4.1.2. The Permeability Variation under the First Unloading Conditions. It can be seen from the dotted lines in Figures 6(a)–6(d) that the permeability variation in the initial unloading stage increased more smoothly with confining pressure decreasing; however, the permeability increased relatively more sharply with smaller confining pressure. And also, when considering the confining pressure decreases from 11 MPa to 5 MPa, the shale permeability of no hydration and hydrated 2 days, 5 days, and 10 days increases from $0.42 \times 10^{-18} \text{ m}^2$, $0.61 \times 10^{-18} \text{ m}^2$, $0.70 \times 10^{-18} \text{ m}^2$, and $1.12 \times 10^{-18} \text{ m}^2$ to $1.54 \times 10^{-18} \text{ m}^2$, $1.38 \times 10^{-18} \text{ m}^2$, $2.5 \times 10^{-18} \text{ m}^2$, and $4.90 \times 10^{-18} \text{ m}^2$. It can be concluded that considering the same seepage pressure and axial pressure, the shale permeability increases much more with decreasing confining pressure. In addition, the fitting curves under the unloading condition based on the above testing data can be expressed by an exponential function with relation coefficient of 0.95 listed in Table 3.

Therefore, as observed from the figures and tables about the permeability variations under the first loading and unloading conditions, it can be seen that the permeability under the same confining pressure in the loading stage is larger than that in the unloading stage, especially that the permeability cannot recover to the original value even if the confining pressure reaches to the origin condition. For example, the permeability of the shale with 2-day hydration is $8.6 \times 10^{-18} \text{ m}^2$ with confining pressure 11 MPa in the loading stage, otherwise the permeability is $1.4 \times 10^{-18} \text{ m}^2$ in the unloading stage even if the confining pressure is unloaded to the original value, and the permeability just recovers to 20% of the original value. The main reason is that loading process generates irreversible damage inside the shales and cannot recover again in the unloading process. Thus, the curves of shale permeability cannot coincide in the loading and unloading stage.

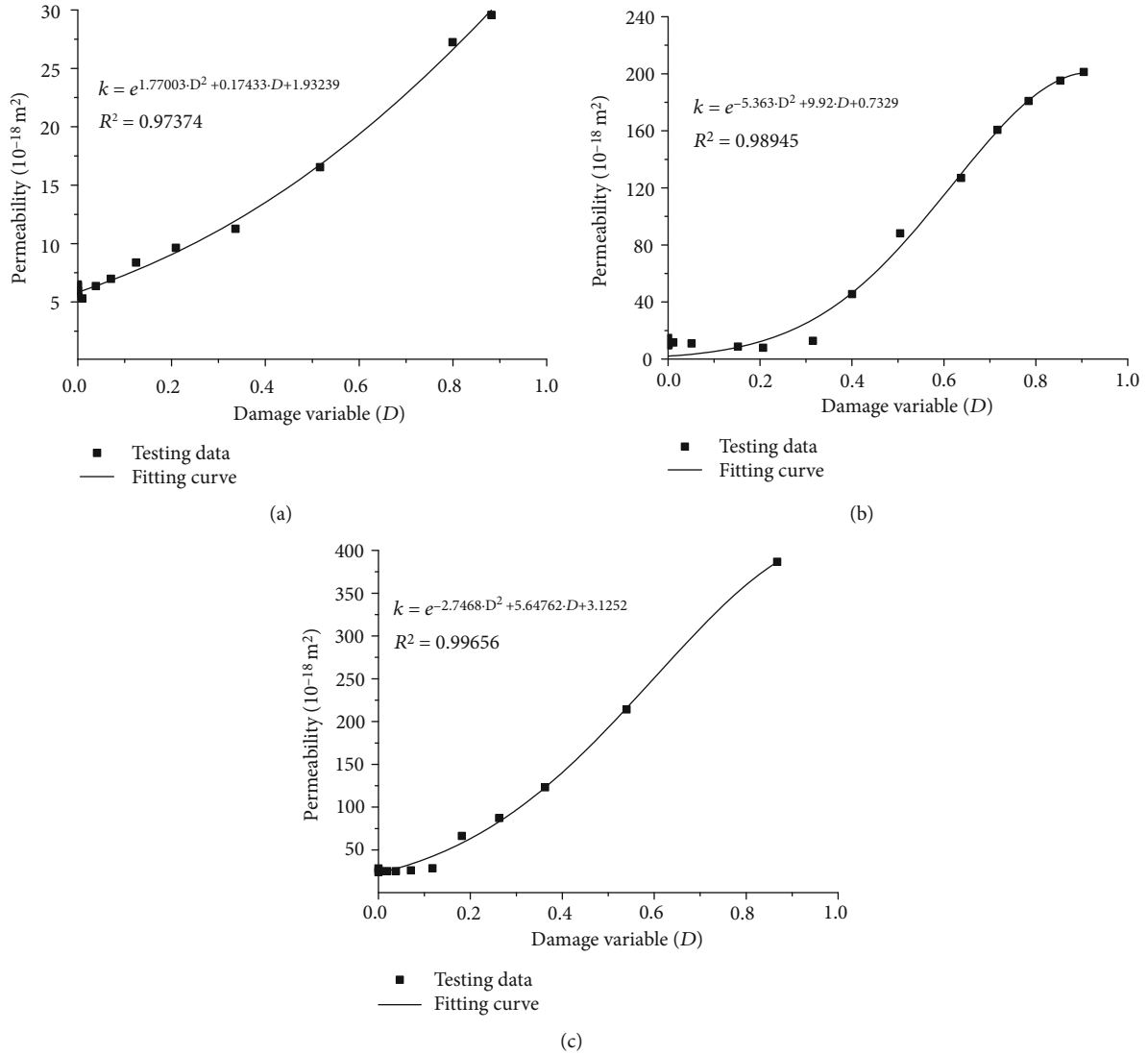


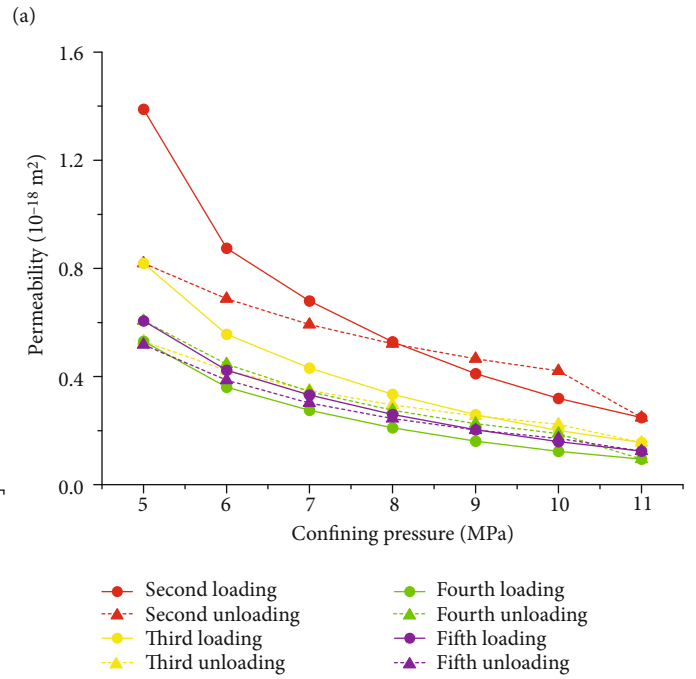
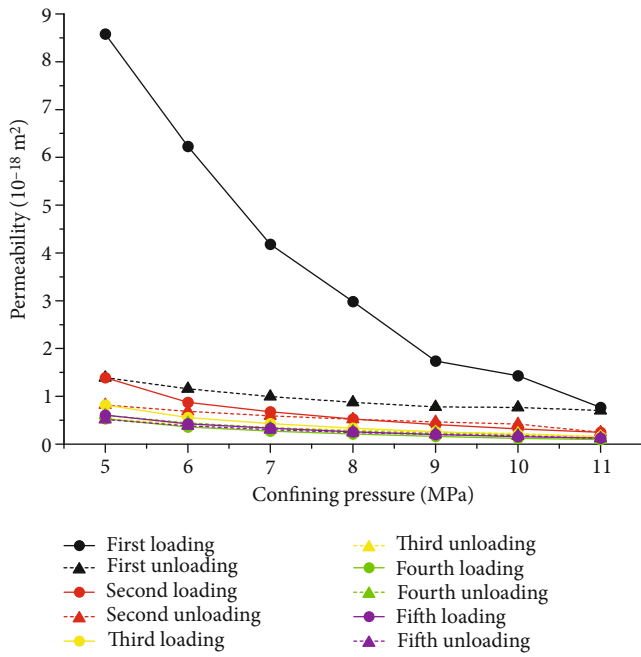
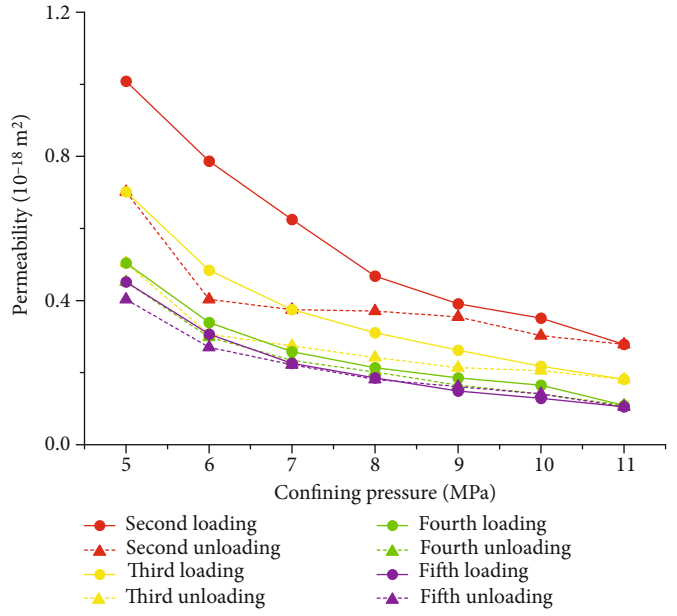
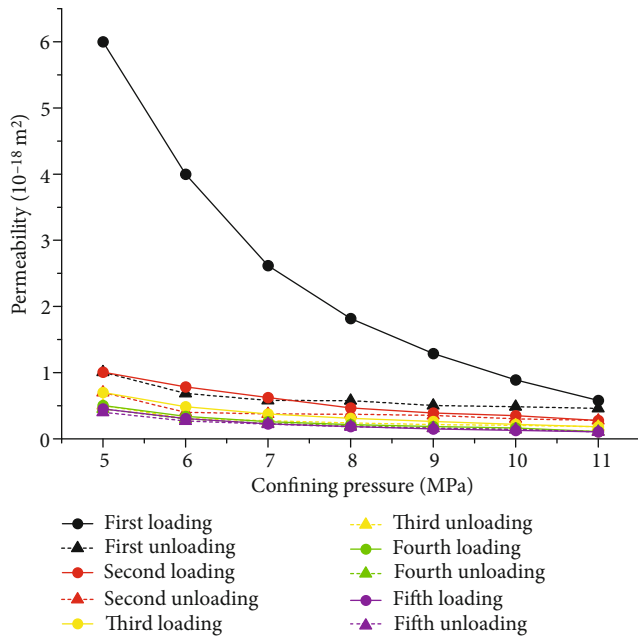
FIGURE 5: The relationship of the permeability and damage variation considering hydrated days. The labels in Fig.5 are as follows,(a) 2 days (b) 5 days (c) 10 days.

4.2. *The Permeability Variation under Cyclic Loading and Unloading Conditions.* In order to describe the permeability evolution under cyclic loading and unloading conditions, the curves considering five cycles shown in Figures 6(a)–6(d) have been compared in detail. The comparisons indicate that the variation patterns of the shale permeability are similar to the variation considering the first loading and unloading conditions. And it can be clearly seen from the curves in Figure 6(a) ② representing the magnified four cycles that considering the confining pressure increasing from 5 MPa to 11 MPa in the second cyclic loading and unloading process, the shale permeability with no hydration and hydrated 2 days, 5 days, and 10 days decreases from $1.54 \times 10^{-18} \text{ m}^2$, $1.39 \times 10^{-18} \text{ m}^2$, $2.5 \times 10^{-18} \text{ m}^2$, and $4.9 \times 10^{-18} \text{ m}^2$ to $0.28 \times 10^{-18} \text{ m}^2$, $0.25 \times 10^{-18} \text{ m}^2$, $0.69 \times 10^{-18} \text{ m}^2$, and $0.4 \times 10^{-18} \text{ m}^2$. And also, when considering the confining pressure decreases from 11 MPa to 5 MPa, the shale permeability of no hydration and hydrated 2 days, 5 days, and 10 days increases from $0.21 \times 10^{-18} \text{ m}^2$, 0.25

$\times 10^{-18} \text{ m}^2$, $0.69 \times 10^{-18} \text{ m}^2$, and $0.4 \times 10^{-18} \text{ m}^2$ to $0.7 \times 10^{-18} \text{ m}^2$, $0.82 \times 10^{-18} \text{ m}^2$, $1.74 \times 10^{-18} \text{ m}^2$, and $2.58 \times 10^{-18} \text{ m}^2$.

Also, as seen from the curves in Figure 6(b) ② considering the confining pressure increasing from 5 MPa to 11 MPa in the third cyclic loading and unloading process, the shale permeability with no hydration, hydrated 2 days, 5 days and 10 days decreases from $0.7 \times 10^{-18} \text{ m}^2$, $0.82 \times 10^{-18} \text{ m}^2$, $1.74 \times 10^{-18} \text{ m}^2$, and $2.58 \times 10^{-18} \text{ m}^2$ to $0.18 \times 10^{-18} \text{ m}^2$, $0.56 \times 10^{-18} \text{ m}^2$, $0.45 \times 10^{-18} \text{ m}^2$, and $0.31 \times 10^{-18} \text{ m}^2$. And also, when considering the confining pressure decreases from 11 MPa to 5 MPa, the shale permeability of no hydration and hydrated 2 days, 5 days, and 10 days increases from $0.18 \times 10^{-18} \text{ m}^2$, $0.16 \times 10^{-18} \text{ m}^2$, $0.27 \times 10^{-18} \text{ m}^2$ and $0.31 \times 10^{-18} \text{ m}^2$ to $0.54 \times 10^{-18} \text{ m}^2$, $0.61 \times 10^{-18} \text{ m}^2$, $1.25 \times 10^{-18} \text{ m}^2$ and $1.74 \times 10^{-18} \text{ m}^2$.

And it is observed from the curves in Figure 6(c) ② considering the confining pressure increasing from 5 MPa to



(b)

FIGURE 6: Continued.

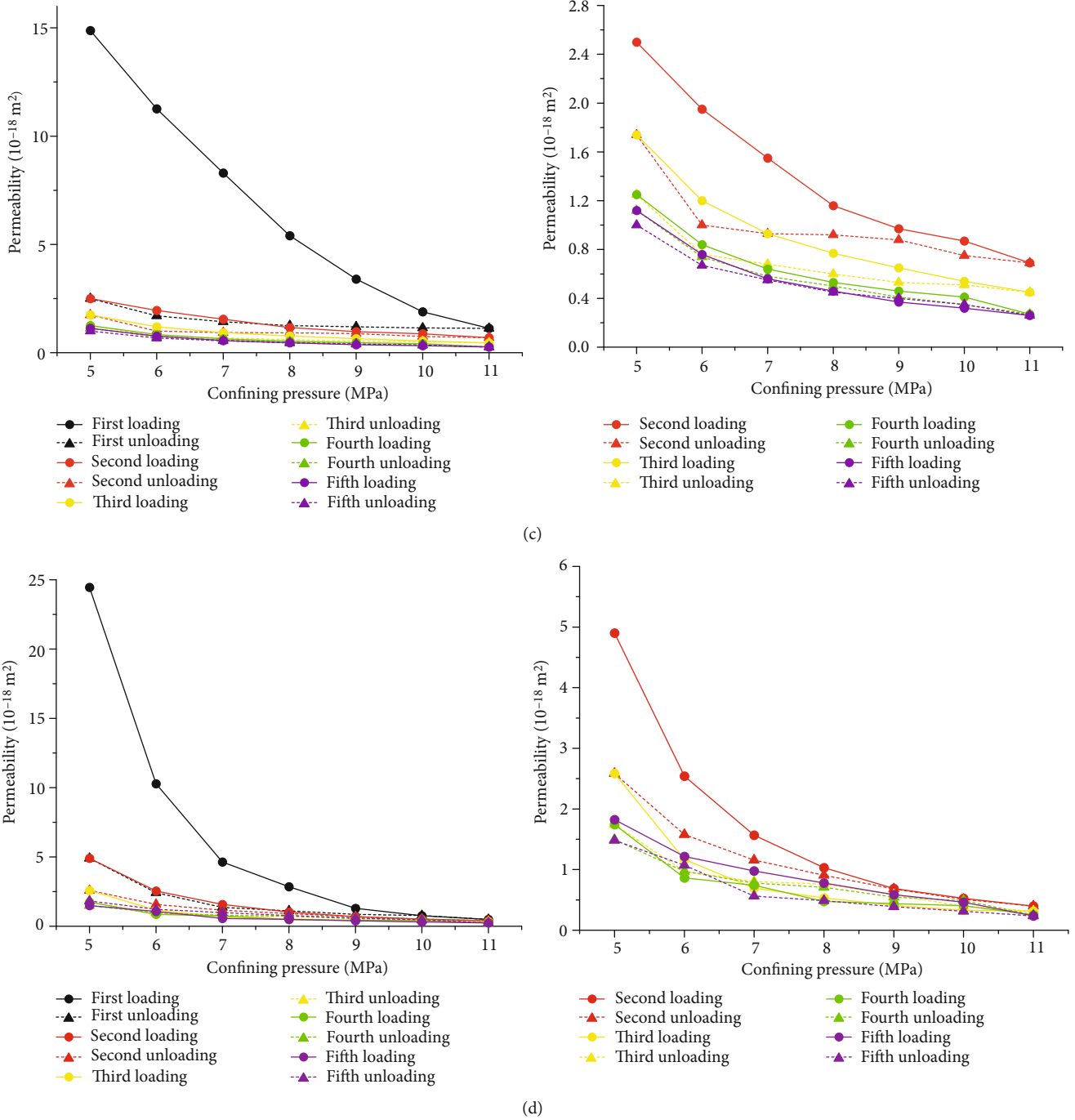


FIGURE 6: The permeability variation of the hydrated shale considering cycling loading and unloading conditions. The labels in Fig.6 are as follows, (a) No hydration (b) 2days (c) 5 days (d) 10 days.

11 MPa in the fourth cyclic loading and unloading process, the shale permeability with no hydration and hydrated 2 days, 5 days, and 10 days decreases from $0.51 \times 10^{-18} \text{ m}^2$, $0.61 \times 10^{-18} \text{ m}^2$, $1.25 \times 10^{-18} \text{ m}^2$, and $1.74 \times 10^{-18} \text{ m}^2$ to $0.11 \times 10^{-18} \text{ m}^2$, $0.09 \times 10^{-18} \text{ m}^2$, $0.27 \times 10^{-18} \text{ m}^2$, and $0.25 \times 10^{-18} \text{ m}^2$. And also, when considering the confining pressure decreases from 11 MPa to 5 MPa, the shale permeability of no hydration and hydrated 2 days, 5 days, and 10 days increases from $0.11 \times 10^{-18} \text{ m}^2$, $0.12 \times 10^{-18} \text{ m}^2$, $0.45 \times$

10^{-18} m^2 , and $0.25 \times 10^{-18} \text{ m}^2$ to $0.45 \times 10^{-18} \text{ m}^2$, $0.53 \times 10^{-18} \text{ m}^2$, $1.12 \times 10^{-18} \text{ m}^2$, and $1.49 \times 10^{-18} \text{ m}^2$.

Furthermore, as seen from the curves in Figures 6(d) representing the magnified four cycles considering the confining pressure increasing from 5 MPa to 11 MPa in the fifth cyclic loading and unloading process, the shale permeability with no hydration and hydrated 2 days, 5 days, and 10 days decreases from $0.46 \times 10^{-18} \text{ m}^2$, $0.53 \times 10^{-18} \text{ m}^2$, $1.1 \times 10^{-18} \text{ m}^2$, and $1.5 \times 10^{-18} \text{ m}^2$ to $0.10 \times 10^{-18} \text{ m}^2$, $0.12 \times 10^{-18} \text{ m}^2$, $0.26 \times$

TABLE 3: Curves of permeability and confined pressure of hydrated shale rocks.

Hydrated days	Cycles	Loading			Unloading		
		F_S	Fitting curves (y represents permeability k ; x represents confining pressure P_c)	Relation coefficient R^2	F_m	Fitting curves (y represents permeability k ; x represents confining pressure P_c)	Relation coefficient R^2
0	1	0.9	$y = 47.667\exp(-0.41x)$	0.99	0.181	$y = 4.163x^{(-0.97)}$	0.99
	2	0.21	$y = 2.95 \exp(-0.212x)$	0.98	0.089	$y = 2.735x^{(-0.962)}$	0.98
	3	0.08	$y = 9.74x^{(-1.657)}$	0.97	0.065	$y = 2.792x^{(-1.16)}$	0.97
	4	0.065	$y = 8.073x^{(-1.744)}$	0.98	0.054	$y = 6.448x^{(-1.681)}$	0.98
	5	0.057	$y = 7.882x^{(-1.802)}$	0.99	0.051	$y = 4.6972x^{(-1.556)}$	0.99
2	1	0.91	$y = 55.492\exp(-0.370x)$	0.99	0.092	$y = 4.163x^{(-0.97)}$	0.99
	2	0.13	$y = 40.556x^{(-2.107)}$	0.98	0.071	$y = 2.735x^{(-0.962)}$	0.98
	3	0.07	$y = 22.95x^{(-2.058)}$	0.97	0.059	$y = 2.792x^{(-1.16)}$	0.97
	4	0.056	$y = 17.271x^{(-2.145)}$	0.98	0.046	$y = 6.448x^{(-1.681)}$	0.98
	5	0.05	$y = 13.697x^{(-1.965)}$	0.99	0.044	$y = 4.6972x^{(-1.556)}$	0.99
5	1	0.924	$y = 92.738\exp(-0.359x)$	0.99	0.074	$y = 10.181x^{(-0.962)}$	0.9
	2	0.121	$y = 35.39x^{(-1.629)}$	0.98	0.071	$y = 6.78x^{(-0.962)}$	0.95
	3	0.086	$y = 24.145x^{(-1.657)}$	0.97	0.057	$y = 6.92x^{(-1.159)}$	0.97
	4	0.066	$y = 20.014x^{(-1.744)}$	0.98	0.054	$y = 15.988x^{(-1.681)}$	0.98
	5	0.056	$y = 19.543x^{(-1.802)}$	0.99	0.05	$y = 11.646x^{(-1.556)}$	0.99
10	1	0.95	$y = 1397.26 \exp(-0.811x)$	0.99	0.072	$y = 316.21x^{(-2.691)}$	0.99
	2	0.18	$y = 775.56x^{(-3.177)}$	0.98	0.067	$y = 103.7x^{(-2.305)}$	0.98
	3	0.092	$y = 141.97x^{(-2.634)}$	0.97	0.056	$y = 39.639x^{(-1.979)}$	0.97
	4	0.061	$y = 50.236x^{(-2.176)}$	0.98	0.043	$y = 32.695x^{(-1.908)}$	0.98
	5	0.051	$y = 60.482x^{(-2.311)}$	0.99	0.042	$y = 81.857x^{(-2.309)}$	0.99

10^{-18} m^2 , and $0.24 \times 10^{-18} \text{ m}^2$. And also, when considering the confining pressure decreases from 11 MPa to 5 MPa, the shale permeability of no hydration and hydrated 2 days, 5 days, and 10 days increases from $0.10 \times 10^{-18} \text{ m}^2$, $0.09 \times 10^{-18} \text{ m}^2$, $0.26 \times 10^{-18} \text{ m}^2$, and $0.24 \times 10^{-18} \text{ m}^2$ to $0.40 \times 10^{-18} \text{ m}^2$, $0.52 \times 10^{-18} \text{ m}^2$, $1.0 \times 10^{-18} \text{ m}^2$, and $1.42 \times 10^{-18} \text{ m}^2$. However, it can be concluded from Figures 6(a) ②–6(d) ② that the variation rate of the shale permeability is more smooth after 3 cyclic loading and unloading processes, indicating that the shale permeability is mainly sensitive to the first load combination.

And also, the fitting curves of the shale permeability under 5 cyclic loading and unloading conditions are described by main power functions listed in Table 3. For deeply investigating the cyclic loading and unloading conditions influencing on the shale permeability variation, the permeability loss in the loading condition and permeability recovery in the unloading condition are introduced to describe the permeability evolution under complex conditions. The permeability based on the tests is normalized as

$$F = \frac{k_i}{k_0} \times 100\%, \quad (13)$$

where F is the dimensionless factor of the permeability, k_i is the permeability under loading or unloading condition, and k_0 is the original permeability.

According to formula (13), the loss rate F_S in the loading condition is defined as the ratio of the permeability in the beginning stage and permeability in the ending stage as $F_S = F_0 - F_t$, in which F_0 is the dimensionless factor of the permeability in the beginning loading stage and F_t is the dimensionless factor of the permeability in the ending loading stage. As for the unloading stage, the recovery is defined as $F_m = F_C - F_t$, where F_C is the dimensionless factor of the permeability considering the confining pressure unloading to the original value. Based on the permeability under different load conditions, the loss rate and recovery rate are calculated and listed in Table 3. It can be seen from Table 3 that for the shale with no hydration, the permeability loss rate in the first cyclic condition is larger than 90%, 21% in the second cycle, 8% in the third cycle, 6.5% in the fourth cycle, and 5.7% in the fifth cycle. As for the shale specimens with hydration of 2 days, the permeability loss rate in the first cyclic condition is larger than 91%, 13% in the second cycle, 7.7% in the third cycle, 5.6% in the fourth cycle, and 5.0% in the fifth cycle. As for

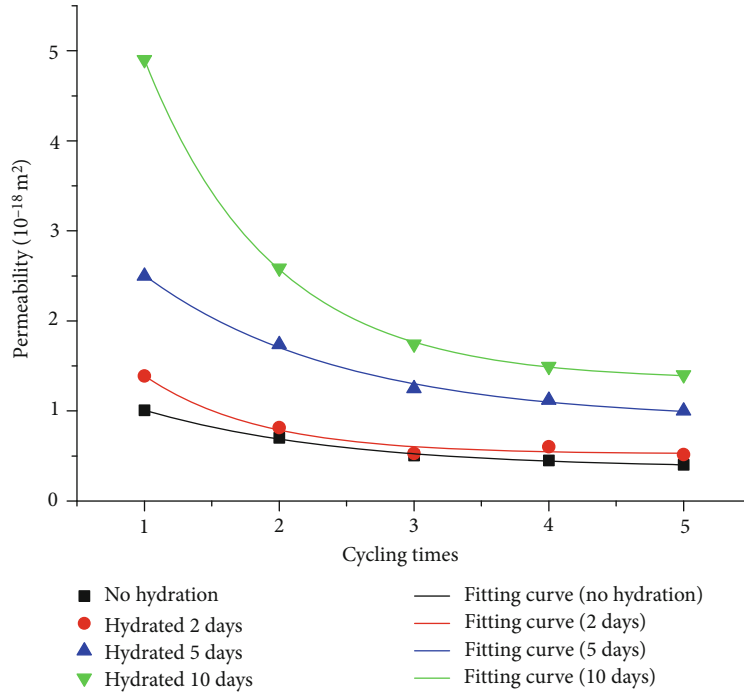


FIGURE 7: Comparison of permeability of hydrated shale under 5 cyclic loading and unloading conditions.

the shale with hydration of 5 days, the permeability loss rate in the first cyclic condition is larger than 92.4%, 12.1% in the second cycle, 8.6% in the third cycle, 6.6% in the fourth cycle, and 5.6% in the fifth cycle. As for the shale with hydration of 10 days, the permeability loss rate in the first cyclic condition is larger than 95.0%, 18.0% in the second cycle, 9.2% in the third cycle, 6.1% in the fourth cycle, and 5.1% in the fifth cycle. The permeability losses for different conditions indicate that the permeability loss rate decreases more smoothly considering more load cycles considering the same hydrated days. However, the hydrated days enlarge the permeability loss rate for the former three cycles, showing that the hydration effect cannot be ignored in the shale permeability research.

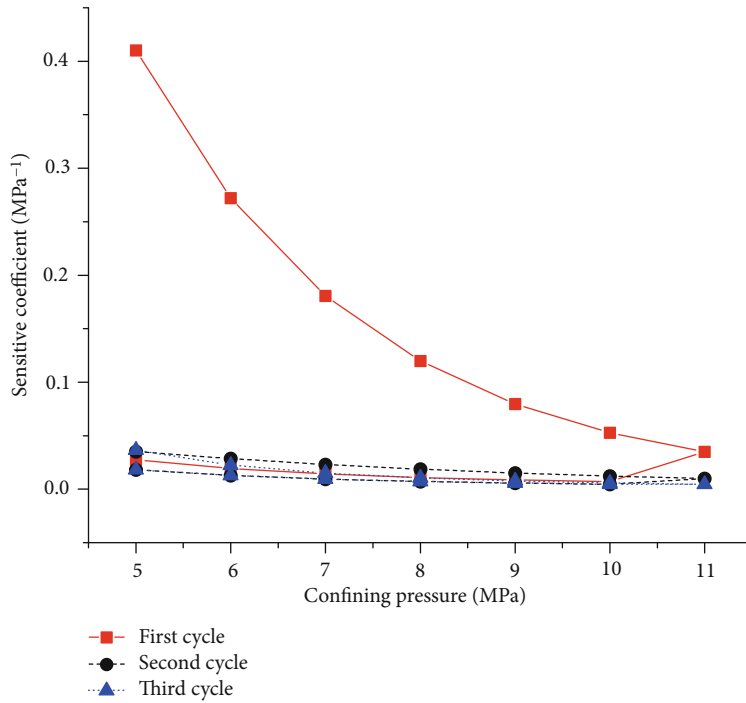
And also, the permeability in the unloading stage is smaller than that in the loading stage because of the irreversible deformation, so the permeability recovery listed in Table 3 is relatively smaller. The results indicate that for the shale with no hydration, the permeability recovery rate in the first cyclic condition is 18.1%, 8.9% in the second cycle, 6.5% in the third cycle, 5.4% in the fourth cycle, and 5.1% in the fifth cycle. As for the shale with hydration of 2 days, the permeability recovery rate in the cyclic condition is 9.2%, 7.1% in the second cycle, 5.9% in the third cycle, 4.6% in the fourth cycle, and 4.4% in the fifth cycle. As for the shales with hydration of 5 days, the permeability recovery rate in the cyclic condition is 7.4%, 7.1% in the second cycle, 5.7% in the third cycle, 5.4% in the fourth cycle, and 5.0% in the fifth cycle. As for the shale with hydration of 10 days, the permeability recovery rate in the cyclic condition is 7.2%, 6.7% in the second cycle, 5.6% in the third cycle, 4.3% in the fourth cycle, and 4.2% in the fifth cycle. The permeability recovery rate is less than 20% after the first unloading, indicating that the shale permeability with obvious

irreversible deformation under loading condition is difficult to be recovered to the original value.

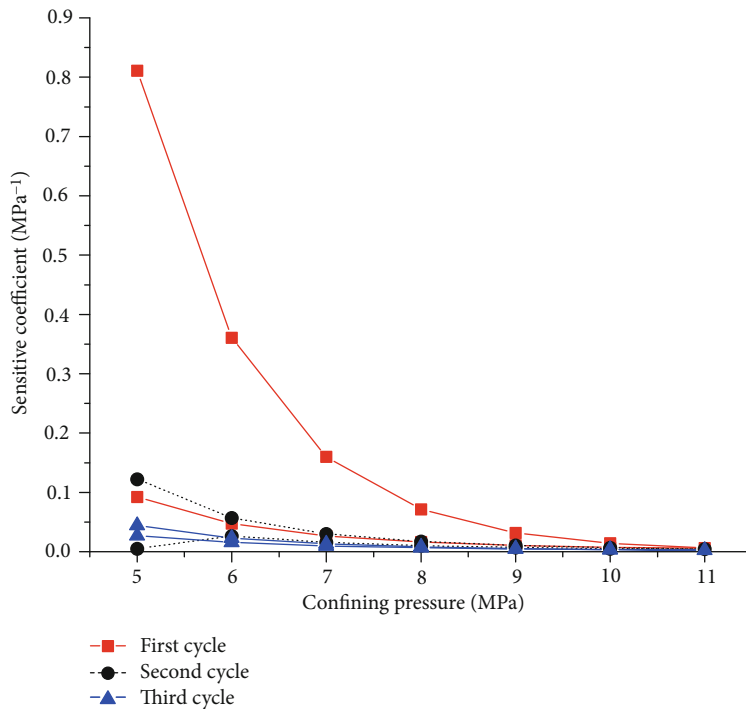
In addition, the comparison listed in Table 3 shows that the permeability loss rate and recovery rate is related to the hydration days, indicating that the loss rate is greater and the recovery rate is less with more hydration days, indicating the permeability in the loading stage is sensitive to the confining pressure, but insensitive to the confining pressure in the unloading condition. Thus, the permeability in the end of the every cycle is given by Figure 7, indicating that for the shale considering certain hydrated days, more cycles cause the permeability to change smoothly and reduce the sensibility of the permeability, and the permeability is greater with more hydrated days considering the same load combination, indicating permeability with more hydration is more sensitive to the cycles.

4.3. *The Sensibility of the Shale Permeability on the Stress under Cyclic Loading and Unloading Conditions.* For describing the relationship of the permeability and the confining pressure under cyclic loading and unloading conditions, the sensibility coefficient is defined to investigate the shale permeability variation. The larger coefficient indicates the permeability is more sensitive to the stress. According to references [29, 30], the sensibility coefficient c_k can be written by formula (14), where k_0 is the initial permeability for different hydrated shale samples, and corresponding permeability is $6.63 \times 10^{-18} \text{ m}^2$, $8.69 \times 10^{-18} \text{ m}^2$, $14.65 \times 10^{-18} \text{ m}^2$, and $26.58 \times 10^{-18} \text{ m}^2$ for the shale with no hydration and hydrated 2 days, 5 days, and 10 days.

$$c_k = -\frac{1}{k_0} \frac{\partial k}{\partial p}. \quad (14)$$



(a)



(b)

FIGURE 8: Permeability-stress-sensitive coefficient of reservoir shale with different hydrated days. The labels in Fig.8 is as follows, (a) No hydration (b) 10 days.

Combined with the permeability expressions in Table 3, the sensibility coefficient c_k can be calculated for the shale with no hydration and hydrated 10 days. And c_k are compared using the testing data based on three cyclic loads to research on the sensibility variation. It can be observed from

Figure 8 that in the loading condition, c_k decreases with increasing confining pressure, has a larger variation rate under lower confining pressure, shows stronger sensibility, and presents insensitivity to the larger confining pressure, indicating that increasing confining pressure compresses

the shale fractures and the same pressure increment cannot greatly change the permeability to reduce the sensibility. As for the unloading condition, c_k may recover smoothly with decreasing confining pressure. It can be concluded that the irreversible deformation cannot recover to the original stage, and corresponding c_k is smaller than that under the same confining pressure condition in the loading stage, which is in accordance with the variation of the permeability loss rate and recovery rate. Compared with the coefficient c_k of the shale with no hydration and hydrated 10 days, c_k in the latter condition is quite larger, emphasizing the hydration effect on the shale damage and permeability.

5. Conclusions

The hydrated reservoir shale as a case study and the permeability evolution under cyclic loading and unloading conditions are researched using the experiments and theoretical analysis, and the corresponding permeability loss rate, recovery rate, and stress sensibility are deeply investigated to reveal the evolution mechanism of the shale permeability considering the hydration and cyclic loading and unloading conditions. The main conclusions are obtained as below:

- (1) The curves of stress and strain have the same variation, and lower peak strength and greater permeability are obtained with more hydrated days. Then, the permeability evolution based on the damage theory shows that permeability is simultaneous to the damage variation, greater damage greater permeability
- (2) In the primary loading stage, the shale permeability increases with more hydrated days and decreases with increasing confining pressure, indicating that larger confining pressure makes the shale pores and fractures more compacted to form less seepage channels. In the unloading stage, the permeability under the same confining pressure is smaller than that in the loading stage. And the curves of the permeability under loading and unloading conditions cannot coincide. As for 5 cyclic loading and unloading conditions, the relationship of the permeability and the confining pressure in the first loading stage is a negative exponent function and then the power functions, and in the unloading stage, the relationship is power function
- (3) The permeability loss rate and the permeability recovery rate less than 20% decreases with more cyclic loading and unloading conditions. And the loss rate and recovery rate are very obvious in the first stage, indicating that both rates are sensitive to the first load combination
- (4) The sensibility of the permeability and the stress indicates that in the loading stage, the permeability is more sensitive under smaller confining pressure, and increasing confining pressure reduces the sensibility, and in the unloading stage, the sensitive coefficient

is smaller than that under the same confining pressure in the loading stage, indicating the irreversible deformation cannot recover to the original condition, which is in accordance with the permeability loss rate and recovery rate

Data Availability

The data in this manuscript is based on the lab experiments and applicable.

Conflicts of Interest

The authors declare that there are no conflicts of interest regarding the publication of this paper.

Acknowledgments

The research is financially supported by the National Natural Science Foundation of China No. 51779021 and the Fundamental Research Funds for the Central Universities No. 2020CDCGJ021.

References

- [1] H. Sone and M. D. Zoback, "Mechanical properties of shale-gas reservoir rocks-part 1: static and dynamic elastic properties and anisotropy," *Geophysics*, vol. 78, pp. 381–392, 2013.
- [2] J. P. Liu and J. S. Sun, "Borehole wall collapse and control in shale gas well drilling," *Drilling Fluid and Completion Fluid*, vol. 33, pp. 25–29, 2016.
- [3] H. Xue, S. Zhou, Y. Jiang, F. Zhang, Z. Dong, and W. Guo, "Effects of hydration on the microstructure and physical properties of shale," *Petroleum Exploration and Development*, vol. 45, no. 6, pp. 1146–1153, 2018.
- [4] B. Z. Shi and B. R. Xia, "The variation of microstructures in the hard brittle shale hydration process," *Journal of Daqing Petroleum University*, vol. 35, pp. 28–34, 2011.
- [5] T. Ma and P. Chen, "Study of meso-damage characteristics of shale hydration based on CT scanning technology," *Petroleum Exploration and Development*, vol. 41, no. 2, pp. 249–256, 2014.
- [6] X. Liu, W. Zeng, L. Liang, and J. Xiong, "Experimental study on hydration damage mechanism of shale from the Longmaxi Formation in southern Sichuan Basin, China," *Petroleum*, vol. 2, no. 1, pp. 54–60, 2016.
- [7] L. Massat, O. Cuisinier, I. Bihannic et al., "Swelling pressure development and inter-aggregate porosity evolution upon hydration of a compacted swelling clay," *Applied Clay Science*, vol. 124–125, pp. 197–210, 2016.
- [8] X. J. Liu, J. Xiong, and L. X. Liang, "Hydration experiment of hard brittle shale of the Longmaxi Formation," *Journal of Southwest Petroleum University (Science and Technology Edition)*, vol. 38, pp. 178–186, 2016.
- [9] S. Zhang and J. J. Sheng, "Study of the propagation of hydration-induced fractures in Mancos Shale using computerized tomography," *International Journal of Rock Mechanics and Mining Sciences*, vol. 95, pp. 1–7, 2017.
- [10] H. W. Teng, S. Ren, and D. Y. Jiang, "Experimental study of mechanical properties of water-saturated weak shale in

- Gonghe tunnel,” *Chinese Journal of Rock Mechanics and Engineering*, vol. 29, Supplement 1, pp. 2657–2662, 2010.
- [11] B. L. Zhu, X. N. Li, X. Y. Wu, and Y. J. Wang, “Experimental study of mechanical properties of water-saturated weak shale,” *Chinese Journal of Rock Mechanics and Engineering*, no. S2, pp. 3896–3905, 2015.
- [12] H. Roshan, S. Ehsani, C. E. Marjo, M. S. Andersen, and R. I. Acworth, “Mechanisms of water adsorption into partially saturated fractured shales: an experimental study,” *Fuel*, vol. 159, pp. 628–637, 2015.
- [13] S. Zhang and J. J. Sheng, “Effect of water imbibition on hydration induced fracture and permeability of shale cores,” *Journal of Natural Gas Science and Engineering*, vol. 45, pp. 726–737, 2017.
- [14] X. Tan, H. Konietzky, and T. Frühwirt, “Laboratory observation and numerical simulation of permeability evolution during progressive failure of brittle rocks,” *International Journal of Rock Mechanics and Mining Sciences*, vol. 68, pp. 167–176, 2014.
- [15] T. Zhou, S. Zhang, L. Yang, X. Ma, Y. Zou, and H. Lin, “Experimental investigation on fracture surface strength softening induced by fracturing fluid imbibition and its impacts on flow conductivity in shale reservoirs,” *Journal of Natural Gas Science and Engineering*, vol. 36, pp. 893–905, 2016.
- [16] X. Liu, M. Xu, and K. Wang, “Mechanism of permeability evolution for reservoir sandstone with different physical properties,” *Geofluids*, vol. 2018, Article ID 5327895, 16 pages, 2018.
- [17] J. Yu, X. Chen, Y. Y. Cai, and H. Li, “Triaxial test research on mechanical properties and permeability of sandstone with a single joint filled with gypsum,” *KSCE Journal of Civil Engineering*, vol. 20, no. 6, pp. 2243–2252, 2016.
- [18] J. Yu, X. Chen, H. Li, J. W. Zhou, and Y. Y. Cai, “Effect of freeze-thaw cycles on mechanical properties and permeability of red sandstone under triaxial compression,” *Journal of Mountain Science*, vol. 12, no. 1, pp. 218–231, 2015.
- [19] G. Z. Yin, W. P. Li, M. H. Li, X. Li, B. Z. Deng, and C. B. Jiang, “Permeability properties and effective stress of raw coal under loading-unloading conditions,” *Journal of China Coal Society*, vol. 39, no. 8, pp. 1497–1503, 2014.
- [20] J. Xu, B. B. Li, T. Zhou, D. Liu, J. Cao, and G. B. Ye, “Experimental study of deformation and seepage characteristics of coal under cyclic loading,” *Chinese Journal of Rock Mechanics and Engineering*, vol. 33, no. 2, pp. 225–234, 2014.
- [21] R. K. Pan, Y. P. Cheng, J. Dong, and H.-D. Chen, “Research on permeability characteristics of layered natural coal under different loading and unloading,” *Journal of China Coal Society*, vol. 39, no. 3, pp. 473–477, 2014.
- [22] Q. Kong, H. L. Wang, and W. Y. Xu, “Experimental study on permeability and porosity evolution of sandstone under cyclic loading and unloading,” *Chinese Journal of Geotechnical Engineering*, vol. 37, no. 10, pp. 1893–1900, 2015.
- [23] Z. H. Zhang, Q. C. Sun, D. Z. Li, M. P. Du, and H. Y. Yao, “Experimental study on permeability characteristics of red sandstone under cyclic seepage pressures,” *Rock and Soil Mechanics*, vol. 5, pp. 937–943, 2015.
- [24] G. Z. Sun, Y. B. Jing, R. L. Zhang, and L. G. Wang, “Permeability of coal samples containing methane under cyclic loading-unloading of axial stresses,” *Chinese Journal of Rock Mechanics and Engineering*, vol. 35, no. 5, pp. 928–938, 2016.
- [25] X. Y. Wang, H. W. Zhou, J. C. Zhong, L. Zhang, C. Wang, and L. An, “Study on energy evolution and permeability characteristics of deep coal damage under triaxial cyclic loading and unloading conditions,” *Chinese Journal of Rock Mechanics and Engineering*, vol. 12, pp. 2676–2684, 2018.
- [26] W. J. B. Sun, Y. J. Zuo, Z. H. Wu, and Y. F. Xu, “Experimental study on seepage-damage evolution of shale,” *China Mining Magazine*, vol. 26, no. 3, pp. 142–145, 2017.
- [27] C. Yan, Y. Cheng, F. Deng, and J. Tian, “Permeability change caused by stress damage of gas shale,” *Energies*, vol. 10, no. 9, pp. 1350–1360, 2017.
- [28] X. P. Zhou, H. Cheng, and Y. F. Feng, “An experimental study of crack coalescence behaviour in rock-like materials containing multiple flaws under uniaxial compression,” *Rock Mechanics and Rock Engineering*, vol. 47, no. 6, pp. 1961–1986, 2014.
- [29] Y. Z. Huang and E. Z. Wang, “Experiment study on coefficient of sensitiveness between percolation and effective for low pressure for low permeability rock,” *Chinese Journal of Rock Mechanics and Engineering*, vol. 26, no. 2, pp. 410–414, 2007.
- [30] D. S. Yang, W. Wang, W. Z. Chen et al., “Investigation on stress sensitivity of permeability in a natural fractured shale,” *Environmental Earth Sciences*, vol. 78, no. 55, pp. 1–10, 2019.

Research Article

Apparent Permeability Prediction of Coal Matrix with Generalized Lattice Boltzmann Model considering Non-Darcy Effect

Zhigao Peng^{1,2}, Shenggui Liu,³ Yingjun Li,⁴ and Qi Yao¹

¹College of Civil Engineering, Hunan City University, Yiyang 413000, China

²Key Laboratory of Key Technologies of Digital Urban-Rural Spatial Planning of Hunan Province, Hunan City University, Yiyang 413000, China

³School of Mechanics & Civil Engineering, China University of Mining and Technology (Beijing), Beijing 100083, China

⁴State Key Laboratory for Geomechanics and Deep Underground Engineering, China University of Mining and Technology (Beijing), Beijing 100083, China

Correspondence should be addressed to Zhigao Peng; pengzhgg@163.com

Received 17 June 2020; Revised 30 July 2020; Accepted 10 August 2020; Published 1 September 2020

Academic Editor: Stefan Iglauer

Copyright © 2020 Zhigao Peng et al. This is an open access article distributed under the Creative Commons Attribution License, which permits unrestricted use, distribution, and reproduction in any medium, provided the original work is properly cited.

Methane flow in coal is associated with the content of both organic matter (OM) and inorganic matter (IOM). Coal matrix contains nanopores ranging in size from a few to hundreds of nanometers, which leads to a non-Darcy effect where the measured permeability of a gas (apparent permeability) is higher than that of a liquid (intrinsic permeability). In this study, a generalized Lattice Boltzmann model (GLBM) is employed for gas flow through the reconstructed coal matrix consisting of OM, IOM, and fractures. The apparent permeability model is proposed to calculate the total flow flux accounting for multiple transport mechanisms including viscous flow, slip flow, transitional flow, and the Knudsen diffusion. The impact of effective pore radius and gas surface diffusion on permeability in the gas adsorption-desorption process is also considered in the model. What's more, the weighting factors are adopted to adjust the contribution of the viscous flow and the Knudsen flow. The effect of total organic/inorganic content and the development of fractures on the apparent permeability of the reconstructed coal matrix is also studied. It is found that the apparent permeability is extremely low when a fracture is nonexistent, and varies almost linearly with the total organic/inorganic content. A fracture plays a significant role in determining apparent permeability and the velocity distribution of the coal matrix.

1. Introduction

Permeability is a key factor in the exploitation of coalbed methane, which directly determines whether the target coal reservoir is valuable for mining. For a long time, people evaluated the permeability of the coal reservoir based on Darcy's law. However, recent extensive studies [1–4] show that the non-Darcy effect at the pore scale has a great contribution to the gas flow flux. If the influence is ignored, the permeability obtained will have a great deviation.

Coal is a typical tight porous medium, with a wide distribution of pore size, which is distributed in the range of 1–100 nm [5, 6]. Therefore, gas flow in coal in the form

of a multiscale flow process includes viscous flow, slip flow, transition flow, and the Knudsen diffusion (free molecular flow). Under the exploitation of coalbed methane, the dominant flow mechanism also changes with the reservoir pressure [7]. Specifically, the adsorbed gas in the nanopore of the matrix is desorbed as free gas when the pressure drops in the process of drilling and drainage, and the resulting pressure difference then leads the free gas to diffuse into the fracture system. After the gas pressure tends to be stable, gas flows in the form of viscous flow in the wellbore, macropore, or fracture network under a pressure gradient. However, due to the small pore throat of the coal matrix, when the average free path of gas molecules is close to the pore

size, the gas molecules have a nonzero velocity on the wall, which will result in the occurrence of gas slippage [8]. In addition to the discontinuous effect causing the apparent permeability of the gas to be higher than the intrinsic permeability, the concentration difference of the adsorbed gas on the pore surface will also make the gas diffuse to the low concentration area; this phenomenon is called surface diffusion [9, 10]. Previous studies [11, 12] have confirmed that the total amount of adsorbed gas is more than 85% in coal reservoirs; therefore, the surface diffusion of adsorbed gas is also an important transfer mechanism [9, 13–15].

The coal seam is a kind of low permeability reservoir. According to well test data [16], the permeability of most CBM reservoirs is less than 1 mD, and permeability is one of the main control factors limiting the productivity of CBM. Villazon et al. [17] established a permeability model that took into consideration the non-Darcy effect and employed a lognormal distribution as pore size distribution. However, the model only considered the effect of gas slippage, and other involved flow mechanisms were not taken into account. Based on this model, Xiong et al. [18] proposed a fully coupled, free and adsorptive phase transport permeability model taking into consideration the impact of the effective pore radius and the non-Darcy gas flow. This model linearly superimposed the flow flux contributed by gas slippage and surface diffusion, and took into account the effect of adsorbed gas molecules on the pore space, but did not regard the influence of the Knudsen diffusion. Wu et al. [19] proposed the weighting factor for automatically adjusting the contribution of viscous flow and the Knudsen diffusion to the total flow flux by the Kn within different pore size ranges and reservoir pressures.

The maceral composition of coal consists of organic matter (OM) and inorganic matter (IOM) [11, 12]. The basic organic components of coal that can be identified under an optical microscope are called organic macerals, which are macerals converted from plant residues. Inorganic macerals are the minerals in coal observed under a microscope. The IOM in coal is usually finely dispersed in OM. Zhao et al. [6] tested six groups of coal samples based on the American Society for Testing and Materials (ASTM 2009-D5142) and found that the contents of mineral components were 2.6%, 3.0%, 5.7%, 7.7%, 13.9%, and 17.5%, respectively. Therefore, the process of methane migration in the coal matrix involved complicated multiscale gas flows in porous media, which can be assumed to divide into three parts: (1) gas flow with non-Darcy effect and gas adsorption in OM, (2) gas flow with non-Darcy effect in IOM, and (3) gas free flow in microfractures.

In recent years, the Lattice Boltzmann Method (LBM) on fluid flow in porous media attracted wide attention [20]. LBM was naturally suitable for pore-scale modeling, since it can easily deal with fluid flow in a channel [21, 22]. However, understanding the fluid dynamics in porous media and predicting effective transport properties (permeability, effective diffusivity, etc.) is of paramount importance for practical applications. It is essential to establish a model capable of dealing with the fluid flow at a larger scale. Guo and Zhao [20] developed a generalized Lattice Boltzmann model

(GLBM) for fluid flow through porous media, then the properties such as porosity and permeability were introduced into each site of the porous media. GLBM is suitable for REV-scale modeling, which is capable of handling fluid flow in porous media with permeable and impermeable matter and channel. Chen et al. [23] first established a model considering Klinkenberg's effect and introduced the apparent permeability as a parameter into the GLBM. Wang et al. [10] proposed a DGM-GMS (i.e., the dusty gas model and the generalized Maxwell-Stefan model) coupled permeability model based on the GLBM, which takes into consideration the permeability of OM and IOM at the REV scale, respectively.

In this paper, based on previous studies, we proposed a GLBM model for predicting coalbed methane permeability. This model included the following sections: (1) The generalized Lattice Boltzmann method was employed to solve the generalized Navier-Stokes equations, which was applied to the calculation and prediction of local permeability at representative elementary volume (REV) scale. (2) The fully coupled viscous flow, slip flow, transition flow, and the Knudsen diffusion were considered in the simulation, and the contribution of these flow mechanisms to the total flow flux was automatically adjusted by the weight factor. (3) The impact of adsorbed gas molecules on the pore space and the contribution of surface diffusion to the total flow flux were taken into consideration. (4) The separate evolution of the local permeability of OM and IOM in the coal matrix was taken into consideration.

2. Generalized Model for Fluid Flow in Porous Media

For isothermal flows of incompressible fluids in porous media at the REV scale, the generalized Navier-Stokes equations which were proposed by Nithiarasu [24] are capable of the simulation.

2.1. Generalized Navier-Stokes Equations. The governing equations of mass and momentum for the generalized Navier-Stokes equations can be given by

$$\nabla \cdot \mathbf{u} = 0, \quad (1)$$

$$\frac{\partial \mathbf{u}}{\partial t} + (\mathbf{u} \cdot \nabla) \left(\frac{\mathbf{u}}{\varepsilon} \right) = -\frac{1}{\rho} \nabla(\varepsilon p) + \nu_e \nabla^2 \mathbf{u} + \mathbf{F}, \quad (2)$$

where ε is the porosity, $\nu_e = \nu J$ is the effective viscosity, J_e is the viscosity ratio, and \mathbf{F} represents the total body force including both medium resistance and external forces and can be given by

$$\mathbf{F} = -\frac{\varepsilon \nu}{K} \mathbf{u} - \frac{\varepsilon F_\varepsilon}{\sqrt{K}} |\mathbf{u}| \mathbf{u} + \varepsilon \mathbf{G}, \quad (3)$$

where ν is the kinematic viscosity of the fluid and \mathbf{G} is the external body force. F_ε is the geometric function and K is the permeability of porous media; both these two parameters are related to the porosity. For a porous medium

composed of solid particles with diameter d_p , the Ergun correlation [25] gives

$$F_\varepsilon = \frac{1.75}{\sqrt{150\varepsilon^3}}, \quad (4)$$

$$K = \frac{\varepsilon^3 d_p^2}{150(1-\varepsilon)^2}. \quad (5)$$

Note that equation (4) was the original permeability of the GLBM; as for three-component porous media, there are three sets of permeability that should be decided: OM, IOM, and fractures. The permeability of fractures can be calculated directly by equation (4) with a porosity of 1, then the GLBM recovered to the LBM and the region of the fracture naturally becomes a channel. The apparent permeability of OM and IOM will be proposed in Section 3, which can be substituted into equation (3).

2.2. LB Model for Generalized Navier-Stokes Equations. Guo and Zhao [20] constructed a LB model which can be used to solve the generalized Navier-Stokes equations, and the corresponding evolution equation of the particle distribution function is

$$f_i(x + \mathbf{e}_i \delta_t, t + \delta_t) - f_i(x, t) = -\frac{1}{\tau} [f_i(x, t) - f_i^{\text{eq}}(x, t)] + \delta_t F_i, \quad (6)$$

where

$$f_i^{\text{eq}} = \rho \omega_i \left[1 + \frac{\mathbf{e}_i \cdot \mathbf{u}}{c_s^2} + \frac{\mathbf{u} \mathbf{u} : (\mathbf{e}_i \mathbf{e}_i - c_s^2 I)}{2\varepsilon c_s^4} \right], \quad (7)$$

$$F_i = \rho \omega_i \left(1 - \frac{1}{2\tau} \right) \left[\frac{\mathbf{e}_i \cdot \mathbf{F}}{c_s^2} + \frac{\mathbf{u} \mathbf{F} : (\mathbf{e}_i \mathbf{e}_i - c_s^2 I)}{\varepsilon c_s^4} \right],$$

where f_i is the discrete density distribution function, f_i^{eq} is the local equilibrium equation, \mathbf{e}_i is the discrete velocity of particles, δ_t is the time step, τ is the relaxation time, and ω_i is the weighting coefficient.

As in the standard LB model, the density and velocity of flow are defined as

$$\rho = \sum_i f_i, \quad (8)$$

$$\rho \mathbf{u} = \sum_i f_i \mathbf{e}_i + \frac{\delta_t}{2} \rho \mathbf{F}.$$

Because the force \mathbf{F} also contains the flow velocity \mathbf{u} , the velocity can be explicitly given by

$$\mathbf{u} = \frac{\mathbf{v}}{c_0 + \sqrt{c_0^2 + c_1 |\mathbf{v}|}}, \quad (9)$$

where \mathbf{v} is a temporary velocity defined by

$$\rho \mathbf{v} = \sum_i f_i \mathbf{e}_i + \frac{\delta_t}{2} \varepsilon \rho \mathbf{G}, \quad (10)$$

and the parameters c_0 and c_1 are given by

$$c_0 = \frac{1}{2} \left(1 + \varepsilon \frac{\delta_t \nu}{2K} \right), \quad (11)$$

$$c_1 = \varepsilon \frac{\delta_t F_\varepsilon}{2\sqrt{K}}.$$

By using the Chapman-Enskog technique with the pressure $p = c_s^2 \rho / \varepsilon$, and the effective viscosity $\nu_e = c_s^2 (\tau - 0.5) \delta_t$, the generalized LB model can recover to equation (1) and equation (2) in the incompressible limit.

3. The Apparent Permeability Model of CBM Taking Multiple Flow Mechanisms into Consideration

The pores of OM in coal are usually less than 100 nm in diameter and have a large amount of gas adsorbed on their surfaces [26, 27]. In nanopores, the probability of gas molecules colliding with the pore wall is significantly increased, which provides a nonnegligible momentum source for gas transfer near the pore wall. The flux contribution of gas slip to the total flow increases, which is a significant deviation from Darcy's law. For the nanopores in OM, the presence of the adsorbed gas molecules adds another complication. Firstly, the gas molecules adsorbed on the pore surface will transfer along the wall due to the concentration difference. Secondly, the gas adsorption amount increases with the pressure; thus, the adsorption efficiency of the pore space constituted by the reshaped channel will be related to the pressure.

According to Poiseuille's law, for capillary tubes with a radius r , the intrinsic permeability (i.e., the absolute permeability, which is the viscous flow permeability of an unreactive ideal fluid) can be expressed as

$$K_\infty = \frac{r^2}{8}. \quad (12)$$

The volume flux of gas viscous flow is

$$Q_\infty = \pi r^2 \frac{K_\infty dp}{\mu dx}, \quad (13)$$

where μ is the dynamic viscosity coefficient of the gas (Pa·s), p is the pressure (Pa), and Q_∞ is the volume flow flux (m³/s).

As gas molecules adsorbed on the inner surface of a capillary, the loss of the cross-sectional area for free gas transmission may be large [18]. Let us assume that the gas adsorption conforms to the Langmuir monolayer adsorption theory. When the gas adsorption amount of specific sites in the capillary tube reaches saturation, the section of the capillary tube should subtract the molecular diameter of

the adsorbed gas molecules. Therefore, the effective radius of the capillary tube allowing free gas to pass through can be written as

$$r_{\text{eff}} = r - d_m. \quad (14)$$

The gas adsorption amount is a function of pressure. When the reservoir pressure is p , the coverage of adsorbed molecules on the inner surface of the capillary tube should be considered. Therefore, based on the Langmuir single-layer adsorption theory [28], the effective radius can be modified to

$$r_{\text{eff}} = r - d_m \frac{p}{p + p_L}. \quad (15)$$

Then, the relationship between effective porosity and initial porosity is

$$\frac{\varepsilon_{\text{eff}}}{\varepsilon_0} = \phi = \frac{r_{\text{eff}}^2}{r_0^2}. \quad (16)$$

After considering the reduction effect of gas adsorption to the pore space, the volume flow flux can be rewritten as

$$Q_{a,\infty} = \pi r_{\text{eff}}^2 \frac{r_{\text{eff}}^2 dp}{8\mu dx} = \pi r^2 \phi \frac{r_{\text{eff}}^2 dp}{8\mu dx}. \quad (17)$$

Consequently, the permeability involving gas adsorption becomes a function of pressure:

$$K_{a,\infty} = \phi(p) \frac{r_{\text{eff}}^2(p)}{8}. \quad (18)$$

The Navier-Stokes equations with appropriate slip boundary conditions are sufficient for modeling gas flow in the slip flow regime [29]. However, since the mean free path of the gas molecules is comparable to the pore size in the transitional flow regime, momentum transfer between gas molecules and between the gas molecules and the wall is significant. Therefore, the combined effect of viscous flow and the Knudsen diffusion should be considered simultaneously in the transitional flow regime [14, 15].

Klinkenberg [30] proposed the apparent permeability equation, which gave the linear relationship between the apparent permeability and the reciprocal of the pore pressure, as follows:

$$K = K_{\infty} f(Kn) = K_{\infty} \left(1 + \frac{b_k}{p} \right), \quad (19)$$

where $f(Kn)$ is the correction coefficient and Klinkenberg's correction is the first-order correction; Beskok and Karniadakis [8] give a second-order correction, which is suitable for describing gas flow in four flow regimes (includes viscous flow, slip flow, transition flow, and free molecular flow):

$$f(Kn) = (1 + \alpha Kn) \left(1 + \frac{4Kn}{1 - bKn} \right), \quad (20)$$

where b is the gas slippage coefficient, generally $b = -1$; α is a gas rarefied coefficient. Civan [31] gives

$$\alpha = \frac{1.358}{1 + 1.70Kn^{0.4348}}. \quad (21)$$

The Knudsen number is defined as the ratio of the mean free path of molecules to the characteristic pore size of porous media:

$$Kn = \frac{\lambda}{r}. \quad (22)$$

The mean free path is defined as

$$\lambda = \frac{\mu}{p} \sqrt{\frac{\pi RT}{2M}}. \quad (23)$$

Considering the impact of the effective pore size and gas slippage on apparent permeability, the effective radius r_{eff} should be employed instead of the pore radius in equation (19), and the corresponding permeability should be corrected to

$$K_a = K_{a,\infty}(p) f(Kn'). \quad (24)$$

The mass flow flux with the gas slippage taken into consideration is

$$m_a = \rho \pi r_{\text{eff}}^2 \frac{K_a dp}{\mu dx} = \rho \pi r^2 \phi \frac{K_a dp}{\mu dx}. \quad (25)$$

As the Knudsen number is in the range of $10^{-3} < Kn < 10^{-1}$, the collision between gas molecules is dominant in the process of gas transport, and the probability of collision between gas molecules and the wall is relatively small, but it cannot be ignored. When the velocity of gas molecules near the wall is nonzero, gas slippage will occur, which can be described by the ideal gas slip flow equation [14]. If $Kn > 10$, the collision between gas molecules and the nanopore wall is dominant, and the behavior of gas transfer can be described as the Knudsen diffusion. According to Fick's law, the flux contributed by the Knudsen diffusion can be written as

$$J_{Kn} = -D_{Kn} \frac{\partial C}{\partial x}. \quad (26)$$

The corresponding volume flow flux is

$$Q_{Kn} = D_{Kn} \frac{M}{RT} \frac{dC}{dx}, \quad (27)$$

where D_{Kn} is the Knudsen diffusion coefficient for gas flow in a single capillary, which can be defined as [2].

$$D_{Kn} = \frac{2r_{eff}}{3} \sqrt{\frac{8RT}{\pi M}}. \quad (28)$$

Then, the mass flow flux contributed by the Knudsen diffusion is

$$m_{Kn} = \pi r_{eff}^2 D_{Kn} \frac{M}{RT} \frac{dp}{dx} = \pi r^2 \phi D_{Kn} \frac{M}{RT} \frac{dp}{dx}. \quad (29)$$

Due to the different concentrations of adsorbed gas in each site on the inner surface of a nanopore, surface diffusion makes a significant role in gas transport. The adsorbed gas and the bulk flow gas can be connected by the relationship of the Langmuir isotherm adsorption equation:

$$J_s = -D_s \frac{\partial C_a}{\partial x} = -D_s \frac{C_{max} p_L}{(p + p_L)^2} \frac{dp}{dx}. \quad (30)$$

The mass flow flux contributed by surface diffusion is

$$m_s = D_s \frac{M C_{max} p_L}{(p + p_L)^2} \pi (r^2 - r_{eff}^2) \frac{dp}{dx} = \pi r^2 D_s \frac{M C_{max} p_L}{(p + p_L)^2} (1 - \phi) \frac{dp}{dx}. \quad (31)$$

In the viscous flow regime, the probability of intermolecular collisions dominates the total collisions, which occur under high-pressure conditions or in systems without boundaries. For the Knudsen diffusion, only the collision between the gas molecules and the solid walls is considered, which occurs in systems with near-vacuum pressure or extreme restriction [10]. Due to the restriction of gas molecules in coal pores, both viscous flow and the Knudsen diffusion cannot be neglected under high pressure. Therefore, the combined effect of viscous flow and the Knudsen diffusion should be considered in gas transport. Besides, both viscous flow and the Knudsen diffusion are considered in the same computational region; it is necessary to determine the reasonable weighting coefficients of each and their respective contributions to the overall phase transport [19]. The combination of gas slippage and the Knudsen diffusion has been established by Darabi et al. [2, 32] using different weighting coefficients and linear summing. Based on the analysis of collision frequencies between molecules and between molecules and pore walls, the weighting factors that distinguish the contribution of these two flow mechanisms to the total flow can be obtained [9, 15]

$$\begin{aligned} \omega_v &= \frac{1}{1 + Kn}, \\ \omega_k &= \frac{1}{(1 + 1/Kn)}, \\ \omega_v + \omega_k &= 1. \end{aligned} \quad (32)$$

TABLE 1: Roy et al.'s experimental condition and fluid parameters.

Physical parameters	Value
Mean pore radius (r/nm)	100
Porosity	0.2
Tortuosity	1
Temperature (K)	300
Molar mass (kg/mol)	39.948
Gas dynamic viscosity (Pa · s)	2.22×10^{-5}
Length of porous media (μm)	60
Constant pressure at outlet (kPa)	4.8

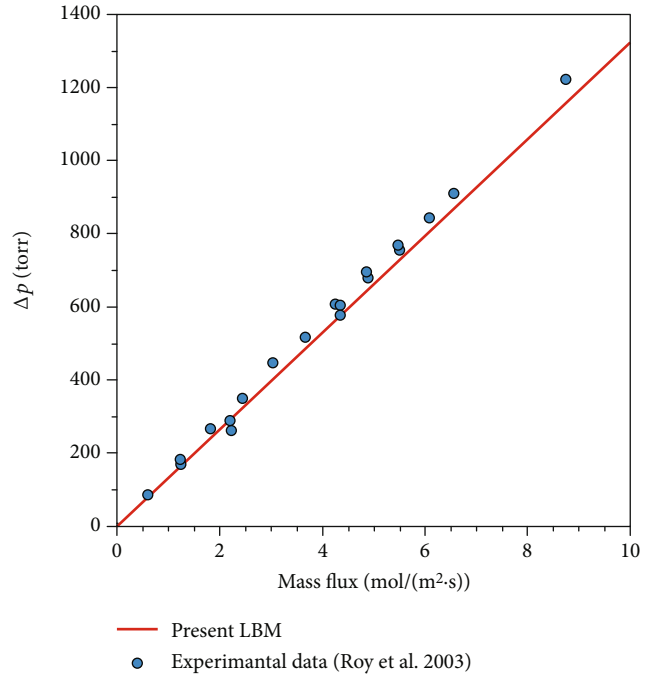


FIGURE 1: Comparison of LB simulation results and experimental data.

Considering the influence of porosity and tortuosity of porous media, the total flux can be expressed as

$$\begin{aligned} m &= \omega_v m_v + \omega_k m_{Kn} + m_s \\ &= \frac{\rho \pi r^2}{\mu} \left[\frac{1}{1 + Kn} \frac{\phi \varepsilon_0}{\tau} K_a + \frac{1}{1 + 1/Kn} \frac{\mu \phi \varepsilon_0}{\rho \tau} D_{Kn} \frac{M}{RT} \right. \\ &\quad \left. + D_s \frac{\mu M C_{max} p_L \varepsilon_0}{\rho (p + p_L)^2 \tau} (1 - \phi) \right]. \end{aligned} \quad (33)$$

The total mass flow of gas transport in the coal matrix can be considered as a combination of viscous flow (includes the slip flow and transition flow), the Knudsen diffusion, and surface diffusion. In this paper, based on the combined effects

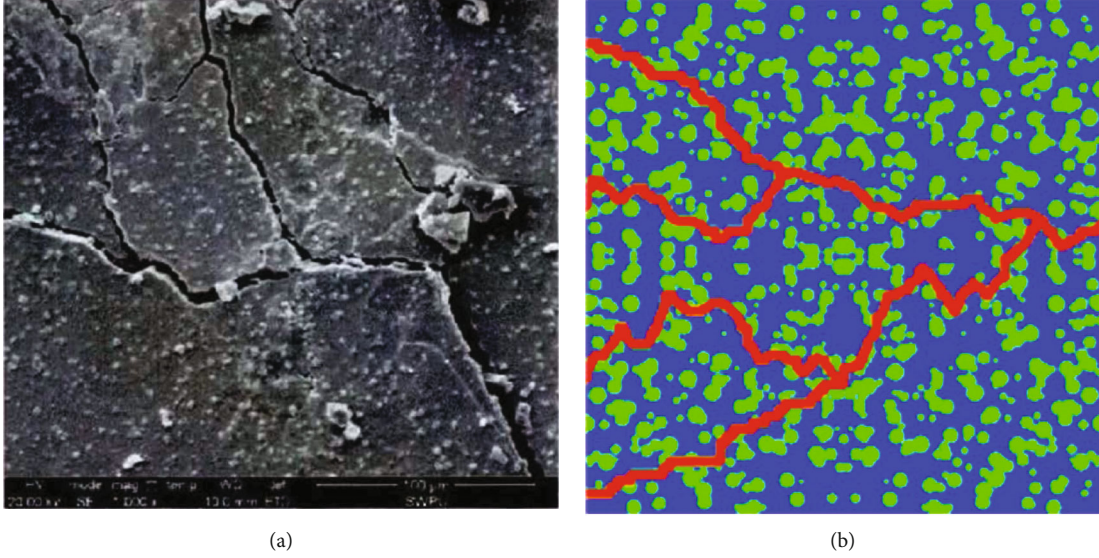


FIGURE 2: Schematic diagram of coal and the 2D reconstructed image.

of viscous flow, the Knudsen diffusion, and surface diffusion, the apparent permeability of OM is obtained:

$$K_{\text{app,om}} = \frac{1}{1 + Kn} \frac{\phi \varepsilon_0}{\tau} K_a + \frac{1}{1 + 1/Kn} \frac{\mu \phi \varepsilon_0}{\rho \tau} D_{Kn} \frac{M}{RT} + D_s \frac{\mu M C_{\text{max}} \rho_L \varepsilon_0}{\rho (p + p_L)^2 \tau} (1 - \phi). \quad (34)$$

Nanopores are also distributed in the IOM of coal, which may have a certain adsorption effect on gas molecules, but they can be ignored compared to the strong adsorption effect of OM. Therefore, it is assumed that the pores of IOM only serve as channels for fluid percolation. According to equation (34), we can get the apparent permeability of IOM:

$$K_{\text{app,iom}} = \frac{1}{1 + Kn} \frac{\varepsilon_0}{\tau} K_{\infty} f(Kn) + \frac{1}{1 + 1/Kn} \frac{\mu \varepsilon_0}{\rho \tau} D_{Kn} \frac{M}{RT}. \quad (35)$$

4. Results and Discussion

4.1. Model Validation. As in Appendix A [33], the simulation results of GLBM had been compared with the theoretical solutions to confirm the accuracy of the model. To further verify the obtained model, we compared the numerical results with existing experimental data. Under the experimental conditions shown in Table 1, Roy et al. [34] measured the mass flow of argon through a homogeneous porous medium composed of long tubes and straight cylindrical nanopores. The conditions set by the GLBM simulation are consistent with the experiment as detailed in Table 1, and the simulation results are shown in Figure 1. It can be found that the simulation results are in good agreement with the experimental data. It is noteworthy that the pore size was approximately 200 nm; thus, the effect of surface diffusion was weak and ignored in the simulation.

Therefore, the model proposed in this paper can accurately describe the coalbed methane in the nanopores in the real state.

4.2. The Impact of Component Content and Fracture on Permeability. Figure 2(a) shows the microstructure of the coal reproduced from the previous study [35]. It can be observed that coal is a three-component porous medium composed of OM, IOM, and fracture. Among them, OM accounts for the majority of the total volume and is randomly divided into irregular shapes by the fracture, and IOM is finely dispersed in the OM. There are many methods for porous medium random reconstruction. Chen et al. [23] reconstructed shale matrix reconstruction images based on the Quartet Structure Generation Set (QSGS). However, from Figure 2(a), we can find that the dispersed IOM is roughly circular, and there are overlaps in many positions, which makes the distribution form more complex and increases the difficulty of reconstruction. According to the morphology and distribution characteristics of the three components, we reconstructed a three-component porous medium, as shown in Figure 2(b), which roughly represents the microstructure of the coal composed of microfracture (red), OM (blue), and IOM (green). Besides, due to the limitation of observation technology, both OM and IOM contain a large number of pores that cannot be shown in the figure. These pores play an important role in methane migration, which should be considered in the model.

Zhao et al. [6] tested the macerals of six groups of coal samples following ASTM 2009-d5142 and found that the contents of IOM were 2.6%, 3.0%, 5.7%, 7.7%, 13.9%, and 17.5%, respectively. The results show that the content of OM and IOM in coal is markedly different, and IOM has a wide range of contents.

To explore the influence of the volume fraction of OM and IOM on permeability, we reconstructed 8 groups of porous media with the random distribution of OM and

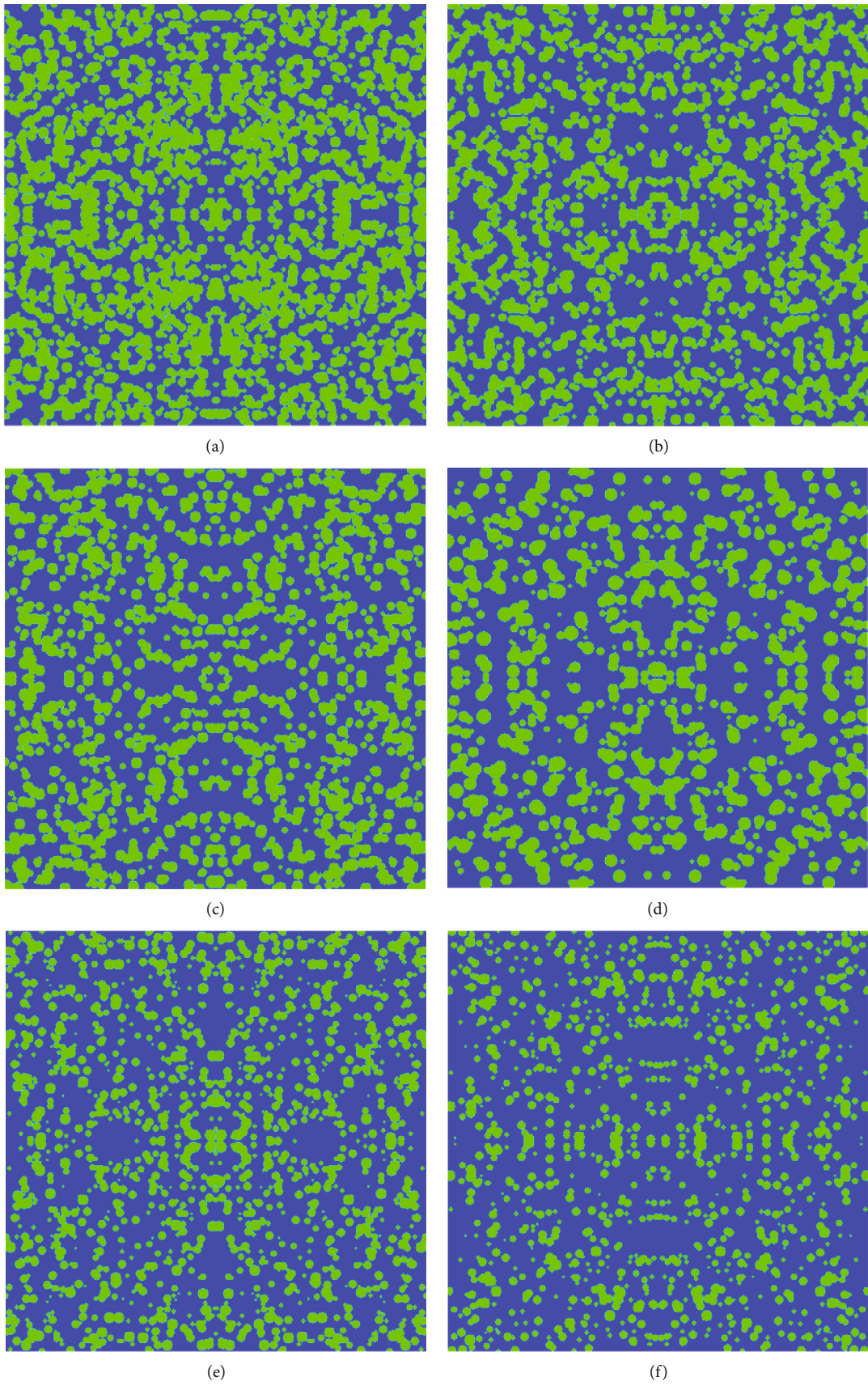


FIGURE 3: Continued.

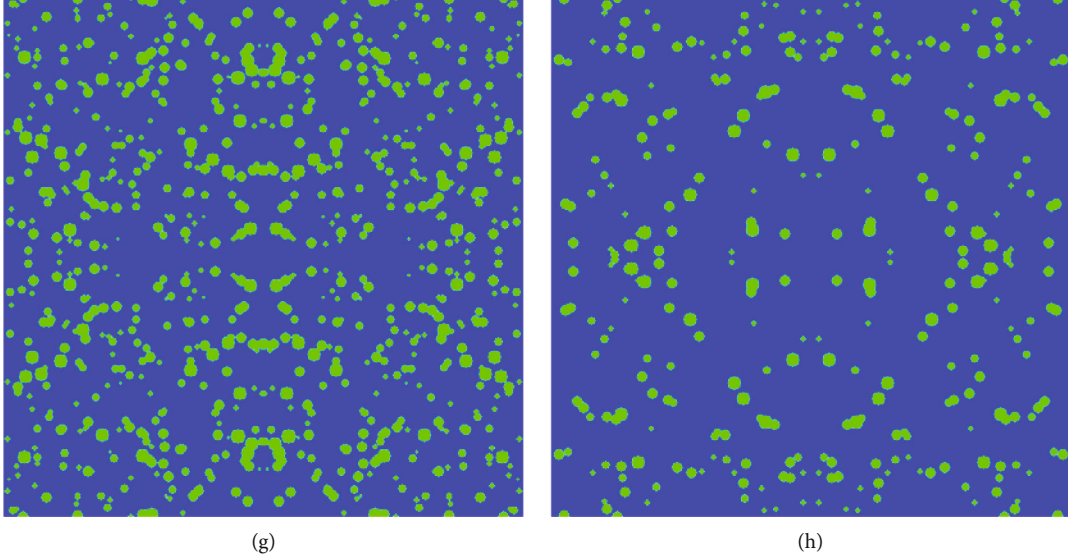


FIGURE 3: Random reconstruction images of coal matrix with different contents of OM and IOM. The volume fractions of OM and IOM are (a) [0.48, 0.52], (b) [0.59, 0.41], (c) [0.62, 0.38], (d) [0.66, 0.34], (e) [0.72, 0.28], (f) [0.80, 0.20], (g) [0.85, 0.15], and (h) [0.93, 0.07], respectively.

TABLE 2: The physical parameters for simulation in three-component porous media.

Groups Physical parameters	Inorganic matter (IOM)	Organic matter (OM)
Simulation region size ($\mu\text{m} \times \mu\text{m}$)	400 \times 400	
Temperature (K)	303.15	
Mean pressure (MPa)	6	
Gas density (kg/m^3)	43.6089	
Gas dynamic viscosity ($\text{Pa} \cdot \text{s}$)	1.26×10^{-5}	
Tortuosity	4	
Porosity (%)	20	5
Adsorption capacity (m^3/t)	—	20
Langmuir pressure (Mpa)	—	2
Median (nm)	10	3
σ (nm)	0.8	0.35

IOM, as shown in Figure 3. In this part, the influence of fracture is not considered. The volume fractions of OM and IOM are (a) [0.48, 0.52], (b) [0.59, 0.41], (c) [0.62, 0.38], (d) [0.66, 0.34], (e) [0.72, 0.28], (f) [0.80, 0.20], (g) [0.85, 0.15], and (h) [0.93, 0.07], respectively, as shown in Figure 3. To ensure the generality of the research, the content of IOM in the reconstructed porous media covers from 7% to 52%. Other parameters used in the simulation are shown in Table 2. A global permeability is employed to evaluate the impact of the content of each component on the permeability. The global permeability can be obtained according to Darcy's law,

$$\bar{u} = -\frac{K_{\text{global}}}{\mu} \nabla p, \quad (36)$$

where \bar{u} is the mean fluid velocity (m/s) and ∇p is the pressure gradient (Pa/m).

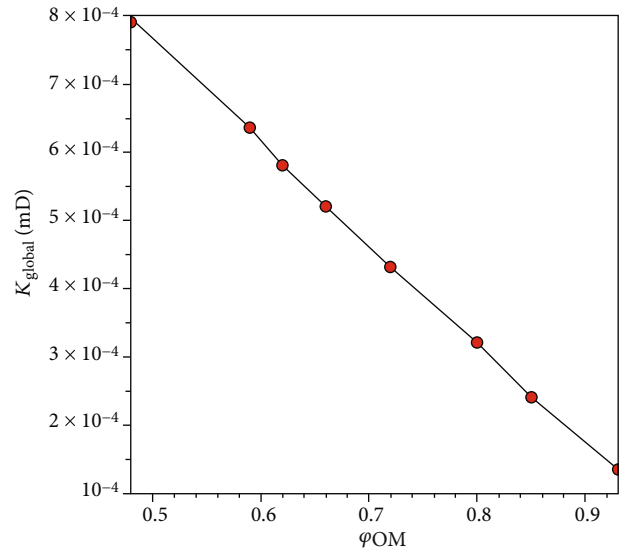


FIGURE 4: Changes of global permeability with OM content.

As shown in Figure 4, with the variation of the volume fraction of OM, global permeability K_{global} shows a near-linear change despite the random distribution of OM and IOM. The overall trend follows that K_{global} decreases with an increase in OM content. This indicates that IOM may have a great contribution to gas transport due to its wide distribution of mesopores and macropores. It is worth mentioning that the results based on IOM are finely dispersed in the OM assumption. The porosity/permeability of IOM itself is not certainly greater than that of OM, but in the state of dispersion, the interface between inorganic particles or between inorganic particles and organic particles will increase the probability of macropores. As the coal matrix is characterized by a strong heterogeneity, it may also contain a large volume

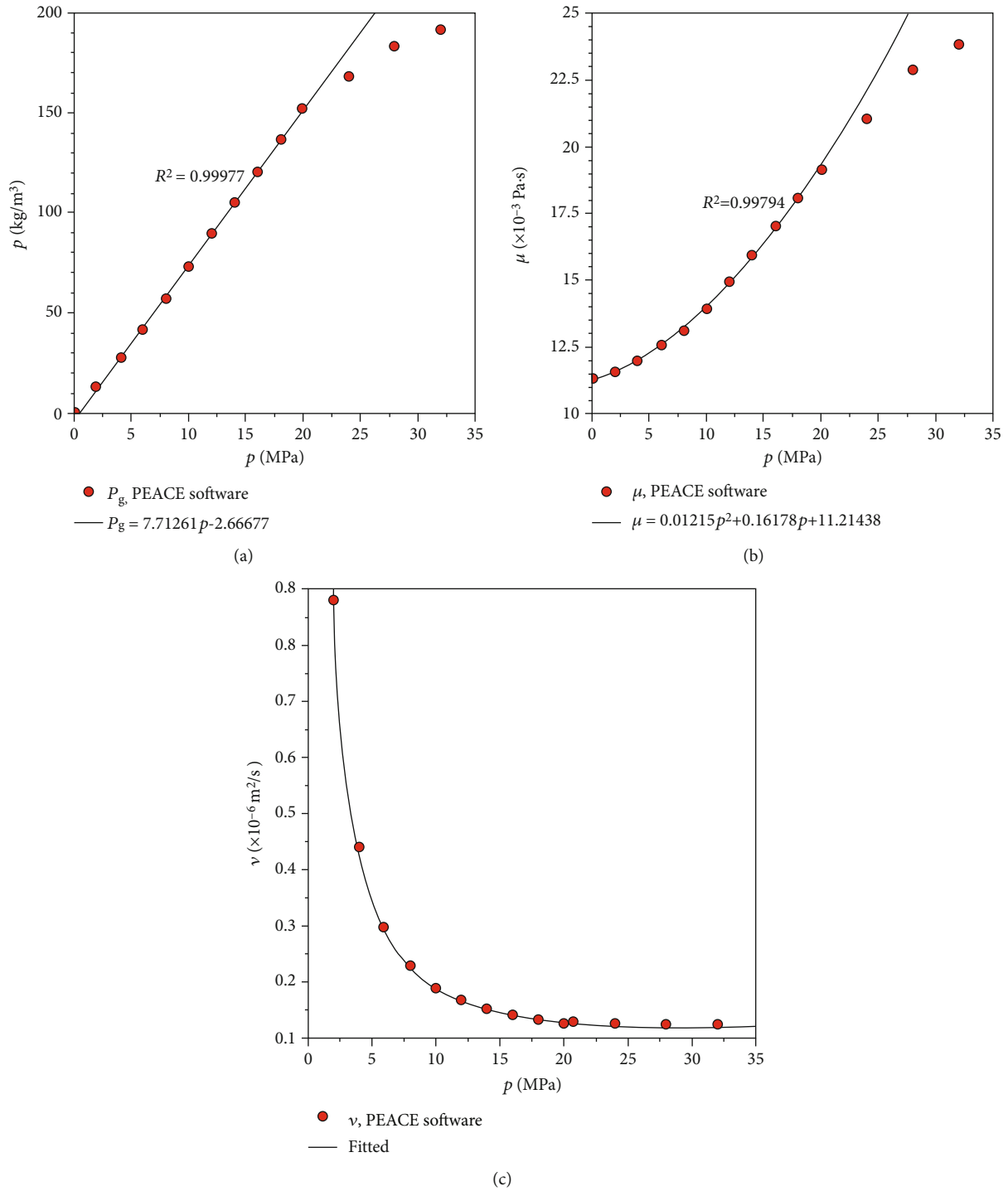


FIGURE 5: Methane density, viscosity coefficient, and the corresponding fitting function under different pressure conditions ((a) density, (b) dynamic viscosity, and (c) kinematic viscosity).

of inorganic crystals, and the porosity and permeability will be considerably lower than that of OM.

In fact, in the process of coalbed methane mining, we are more concerned about the data of the whole production cycle. However, due to the nature of LBM and the limited range of pressure (density) fluctuation in the simulation, the results obtained directly from the real parameters of the coal reservoir may not be correct. In this part, the density

and viscosity coefficient of coalbed methane under different pressures are used to calculate the global permeability, and the results are summarized to indirectly obtain the data of the whole pressure drop process. It should be noted that the density and viscosity coefficients of methane are discrete under different conditions. We employed an online calculation software (<http://www.peacesoftware.de/einigewerte/methan.html>) to calculate the corresponding parameters

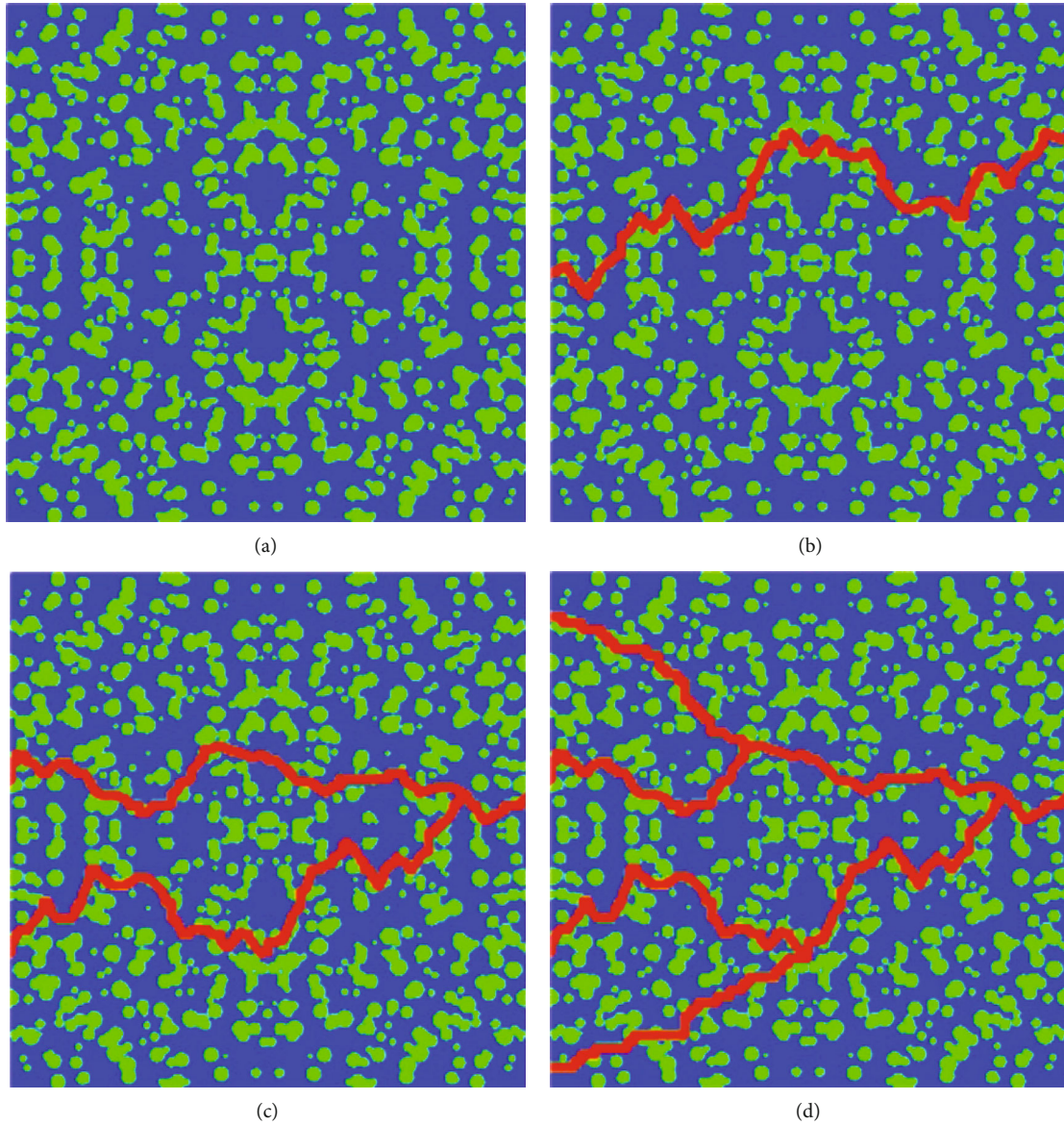


FIGURE 6: The reconstructed coal matrix with different fracture development.

according to different pressures (the temperature is maintained at 303.15 K). Through observation, when the pressure is below 20 MPa, the relationship between the pressure and density of methane is close to linear, as shown in Figure 5(a). Similarly, the relationship between pressure and dynamic viscosity can be fitted by a quadratic polynomial, as shown in Figure 5(b). Figure 5(c) shows the fitting relationship between kinematic viscosity and pressure, which is a vital parameter in LBM. The pressure-matched parameters are used in the following simulation. Reservoir temperature may have a great influence on the physical properties of the gas in the process of exploitation; however, the temperatures do have some connections with other sides, e.g., gas adsorption. Therefore, we only consider the isothermal conditions at the present research.

There is a kind of double-pore structure composed of pores and fractures, in which fractures are common in coal.

As can be seen from Figure 2(a), the morphology of fractures is “tree-like,” with many branches, which connect all parts of the coal.

To further explore the impact of fractures on permeability, four groups of three-component porous media are reconstructed in this part, as shown in Figure 6. The distribution and content of OM and IOM remain unchanged in the following research. In the four groups of porous media, the fracture distributions are as follows: (a) no fracture, (b) fractal dimension $D_f = 2.36$ (the volume fraction of the fracture is 3.5%), (c) $D_f = 2.43$ (the volume fraction of the fracture is 5.9%), and (d) $D_f = 2.50$ (the volume fraction of the fracture is 8.4%). According to the relationship between density and the viscosity coefficient shown in Figure 6, the simulation is carried out under different pressures. The calculation input parameters are shown in Table 2, and the simulation results are shown in Figures 7 and 8.

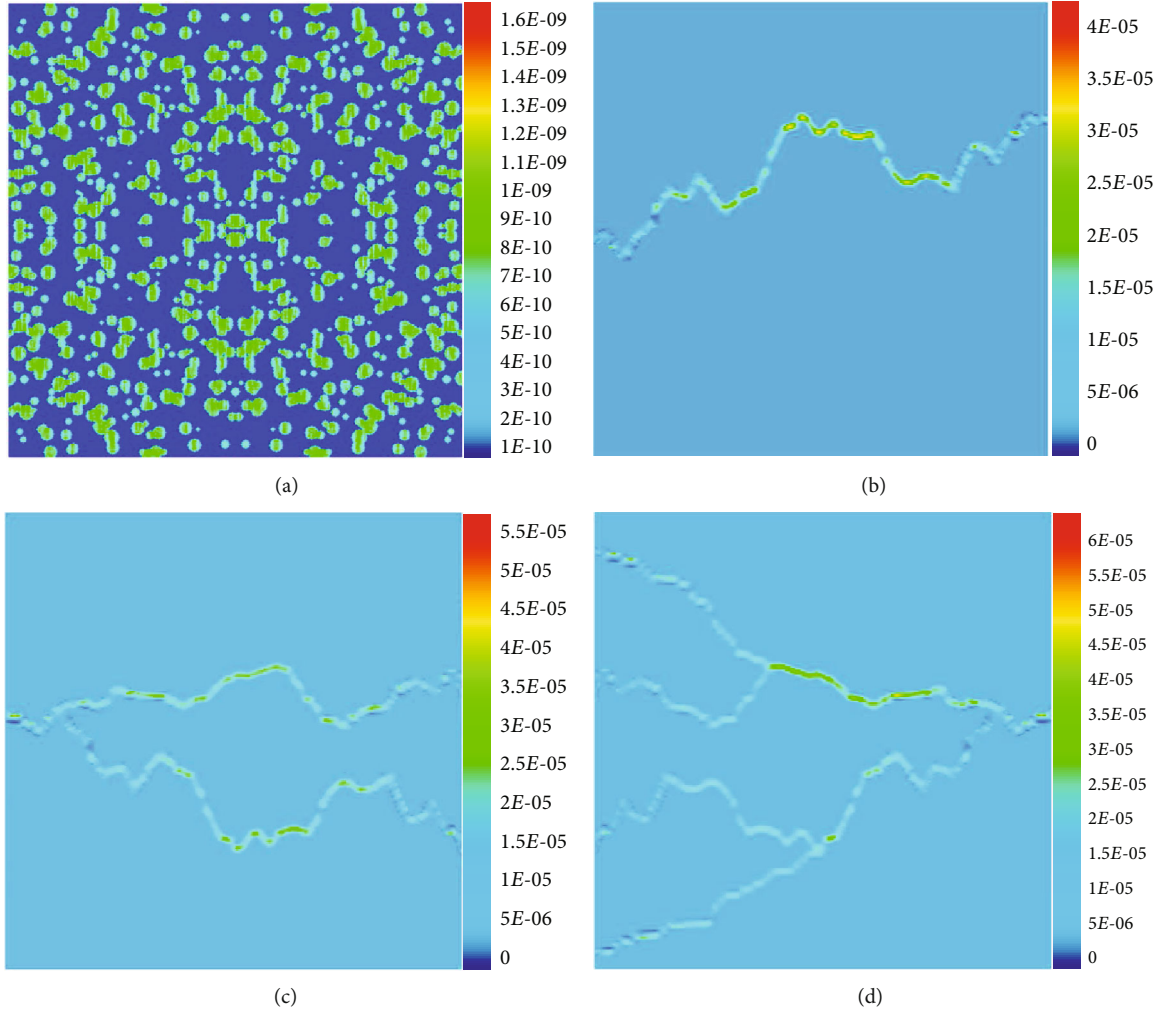


FIGURE 7: Velocity distribution in different fracture development.

Figure 7(a) shows that the fluid velocity is very slow when no fracture exists in the matrix, and the fluid velocity in IOM is significantly higher than that in OM. With the existence of a fracture in the matrix, as shown in Figures 7(b)–7(d), the velocity in the fracture is several orders of magnitude higher than that in the matrix, which indicates that the contribution of fractures to the gas transport capacity is large; besides, the fluid velocities in IOM and OM are also significantly increased, which dramatically enhances the gas flow. Moreover, the trend in Figures 7(b)–7(d) suggests that with the increase of the content of the fracture (or the fractal dimension), the magnitude of the fluid velocity grows up, effectively improving the gas flow.

Figure 8 summarizes global permeability under different pressures and fracture development. It can be found that with the increase of the content of the fracture, the trend of global permeability variation is similar, which increases with the decrease of pressure. When no fracture exists completely in the matrix, the global permeability is in the order of 10^{-4} mD in the pressure drop range, which is extremely low permeability; the results were verified by the Finite Element Method as can be seen in Appendix B. In practice, the reservoir with such a small permeability has no value for exploita-

tion. However, when the matrix contains a fracture with a width of about $10\ \mu\text{m}$, the permeability is greatly stimulated, and the permeability reaches 0.4 mD as the reservoir pressure is 5 MPa. The global permeability increases with the enlargement of the content of the fracture, and when the volume fraction is at 8.4%, the permeability exceeds 0.85 mD. Figure 8(e) collects the results of Figures 8(a)–8(d) and shows that the existence of fractures is crucial for improving the permeability of a coal reservoir, and it also indicates the necessity of reservoir stimulation techniques such as hydraulic fracturing. According to the statistical results of the permeability tests of previous studies [5, 6, 12, 16], the permeability of coal reservoirs in China is basically in the range of $1 \times 10^{-3} \sim 1$ mD, which shows that the permeability prediction results are reliable.

5. Conclusion

In this paper, we established a GLBM model for predicting coalbed methane permeability in the REV scale, which was fully coupled with the viscous flow, slip flow, transition flow, and the Knudsen diffusion. The model also considered the impact of the effective pore radius and surface adsorption

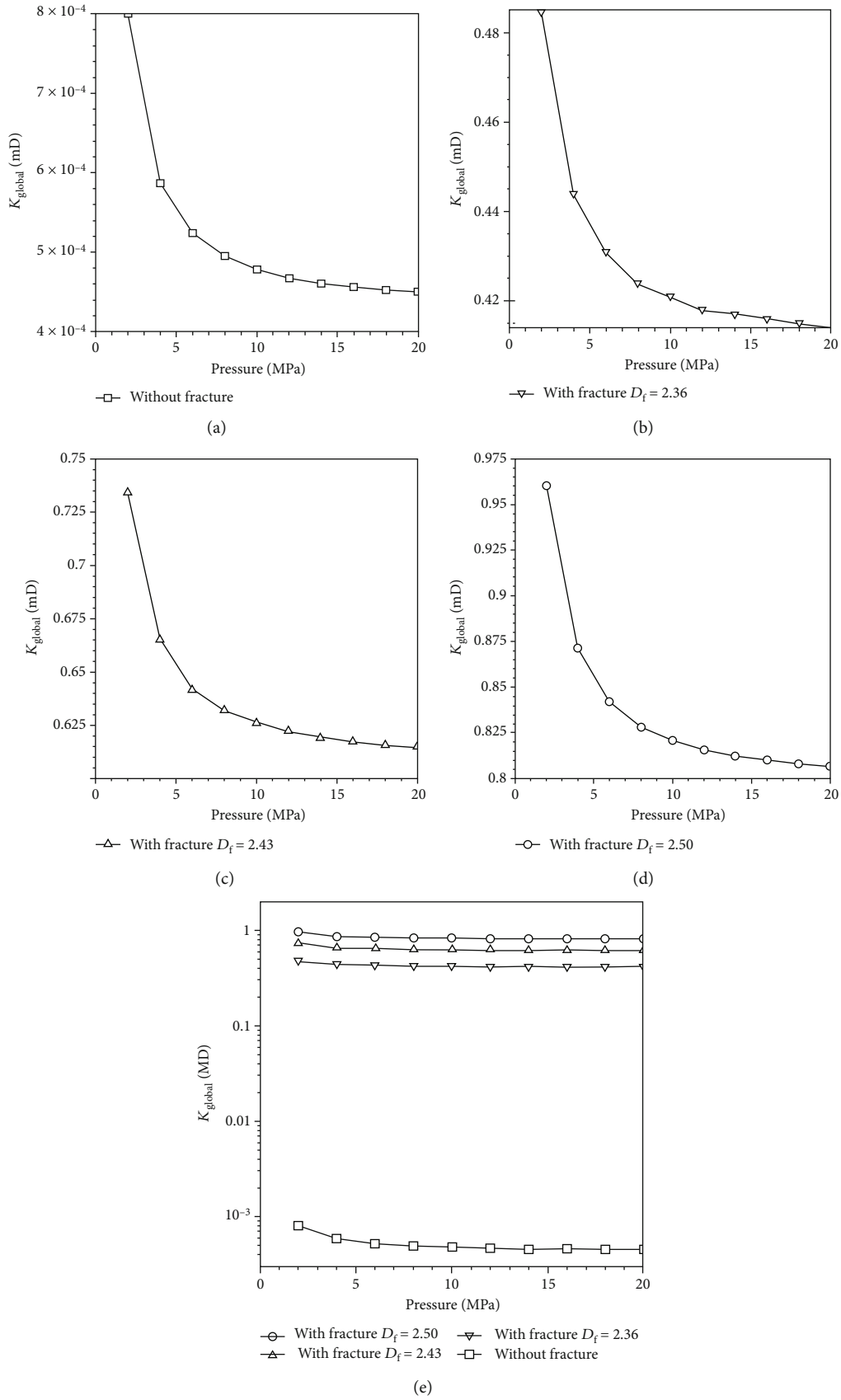


FIGURE 8: The impact of fracture development on permeability.

and adopted the weighting factors to automatically adjust the contribution of viscous flow and the Knudsen diffusion to the total gas flow. Besides, based on the morphology and distribution characteristics of OM, IOM, and fractures in the coal matrix, a random reconstruction algorithm of three-component porous media is developed. For the accuracy of the simulation, we adopted a series of pressure-matched parameters.

The results are as follows: (1) Due to the wide range of pore size distribution, the distribution of mesopores and macropores is relatively large, which makes the contribution of IOM to the gas transport capacity also relatively large. (2) The permeability of the coal matrix itself is extremely low, and the contribution of a fracture to gas permeability is very large. (3) The greater the content of the fracture (or the fractal dimension), the larger the permeability; it is necessary to employ reservoir stimulation techniques such as hydraulic fracturing in the development process of coalbed methane.

Data Availability

The data used to support the findings of this study are included within the article.

Conflicts of Interest

The authors declare that they have no conflicts of interest.

Acknowledgments

This work was supported by a project of the Education Department of Hunan (Grant No. 19C0370) and the Youth Project of Natural Science Foundation of Hunan Province (Grant No. 2020JJ5023).

Supplementary Materials

In Appendix A, we simulated the fluid flow between two parallel plates filled with a porous medium to verify the GLBM with the proposed apparent permeability model. In Appendix B, the results of methane flow in the coal matrix containing OM and IOM were verified by the finite element software COMSOL Multiphysics. (*Supplementary Materials*)

References

- [1] T. Huang, L. Cao, C. Yuan, and P. Chen, "A novel numerical model of gas transport in multiscale shale gas reservoirs with considering surface diffusion and Langmuir slip conditions," *Energy Science & Engineering*, vol. 7, no. 4, pp. 1315–1332, 2019.
- [2] F. Javadpour, "Nanopores and apparent permeability of gas flow in mudrocks (shales and siltstone)," *Journal of Canadian Petroleum Technology*, vol. 48, no. 8, pp. 16–21, 2013.
- [3] Y. Ning, S. He, H. Liu, H. Wang, and G. Qin, *Permeability Boltzmann simulations on multi-scale reconstructed digital rocks*, 2016.
- [4] Y. Zhang, D. Li, X. Sun, Z. Song, D. Shi, and Y. Su, "A new model for calculating the apparent permeability of shale gas in the real state," *Natural Gas Industry B*, vol. 5, no. 3, pp. 245–252, 2018.
- [5] Y. Zhao, Y. Sun, S. Liu, Z. Chen, and L. Yuan, "Pore structure characterization of coal by synchrotron radiation nano-CT," *Fuel*, vol. 215, pp. 102–110, 2018.
- [6] Y. Zhao, S. Liu, D. Elsworth, Y. Jiang, and J. Zhu, "Pore structure characterization of coal by synchrotron small-angle X-ray scattering and transmission electron microscopy," *Energy & Fuels*, vol. 28, no. 6, pp. 3704–3711, 2014.
- [7] A. Sakhaee-Pour and S. Bryant, "Gas permeability of shale," *SPE Reservoir Evaluation and Engineering*, vol. 15, pp. 401–409, 2013.
- [8] A. Beskok and G. E. Karniadakis, "Report: a model for flows in channels, pipes, and ducts at micro and nano scales," *Micro-scale Thermophysical Engineering*, vol. 3, pp. 43–77, 1999.
- [9] K. Wu, X. Li, C. Guo, C. Wang, and Z. Chen, "A unified model for gas transfer in nanopores of shale-gas reservoirs: coupling pore diffusion and surface diffusion," *SPE Journal*, vol. 21, no. 5, pp. 1583–1611, 2016.
- [10] J. Wang, L. Chen, Q. Kang, and S. S. Rahman, "Apparent permeability prediction of organic shale with generalized Lattice Boltzmann model considering surface diffusion effect," *Fuel*, vol. 181, pp. 478–490, 2016.
- [11] T. A. Moore, "Coalbed methane: a review," *International Journal of Coal Geology*, vol. 101, pp. 36–81, 2012.
- [12] X. Fu, Y. Qin, and Z. Wei, *Coalbed Methane Geology*, China University of Mining and Technology Press, Xuzhou, China, 2007, September 2018, <http://opac.its.csu.edu.cn/NTRdrBookRetrInfo.aspx?BookRecno=482536>.
- [13] K. Wu, X. Li, C. Wang, Z. Chen, and W. Yu, "Apparent permeability for gas flow in shale reservoirs coupling effects of gas diffusion and desorption," *Proceedings of the 2nd Unconventional Resources Technology Conference*, pp. 2328–2345, 2014.
- [14] F. Javadpour, D. Fisher, and M. Unsworth, "Nanoscale gas flow in shale gas sediments," *Journal of Canadian Petroleum Technology*, vol. 46, 2013.
- [15] K. Wu, Z. Chen, X. Li, C. Guo, and M. Wei, "A model for multiple transport mechanisms through nanopores of shale gas reservoirs with real gas effect–adsorption-mechanic coupling," *International Journal of Heat and Mass Transfer*, vol. 93, pp. 408–426, 2016.
- [16] Z. Meng, Y. Tian, and G. Li, *Theory and Method of Coalbed Methane Development Geology*, Science Press, Beijing, China, 2010, September 2018, http://webpac.lib.tongji.edu.cn/opac/item.php?marc_no=0001990933.
- [17] M. Villazon, G. German, R. F. Sigal, F. Civan, and D. Devegowda, "Parametric investigation of shale gas production considering nano-scale pore size distribution, formation factor, and non-Darcy flow mechanisms," in *SPE Annual Technical Conference and Exhibition*, Denver, Colorado, USA, November 2011.
- [18] X. Xiong, D. Devegowda, M. Villazon, G. German, R. F. Sigal, and F. Civan, "A fully-coupled free and adsorptive phase transport model for shale gas reservoirs including non-Darcy flow effects," in *SPE Annual Technical Conference and Exhibition*, San Antonio, Texas, USA, October 2012.
- [19] K. Wu, X. Li, C. Wang, W. Yu, and Z. Chen, "Model for surface diffusion of adsorbed gas in nanopores of shale gas reservoirs," *Industrial and Engineering Chemistry Research*, vol. 54, no. 12, pp. 3225–3236, 2015.

- [20] Z. Guo and T. S. Zhao, "Lattice Boltzmann model for incompressible flows through porous media," *Physical Review E*, vol. 66, no. 3, article 036304, 2002.
- [21] Z. Guo and C. Shu, *Lattice Boltzmann Method and Its Applications in Engineering*, World Scientific, Singapore, 2013.
- [22] Y. He, Y. Wang, and Q. Li, *Lattice Boltzmann Method: Theory and Applications*, Science Press, Beijing, China, 2009.
- [23] L. Chen, W. Fang, Q. Kang, J. De'Haven Hyman, H. S. Viswanathan, and W. Q. Tao, "Generalized Lattice Boltzmann model for flow through tight porous media with Klinkenberg's effect," *Physical Review. E, Statistical, Nonlinear, and Soft Matter Physics*, vol. 91, no. 3, article 033004, 2015.
- [24] K. S. P. Nithiarasu, "Natural convective heat transfer in a fluid saturated variable porosity medium," *International Journal of Heat and Mass Transfer*, vol. 40, no. 16, pp. 3955–3967, 1997.
- [25] S. Ergun, "Fluid flow through packed columns," *Chemical Engineering Progress*, vol. 48, pp. 89–94, 1952.
- [26] S. Hou, X. Wang, X. Wang, Y. Yuan, S. Pan, and X. Wang, "Pore structure characterization of low volatile bituminous coals with different particle size and tectonic deformation using low pressure gas adsorption," *International Journal of Coal Geology*, vol. 183, pp. 1–13, 2017.
- [27] Y. Li, C. Zhang, D. Tang et al., "Coal pore size distributions controlled by the coalification process: an experimental study of coals from the Junggar, Ordos and Qinshui basins in China," *Fuel*, vol. 206, pp. 352–363, 2017.
- [28] I. Langmuir, "The adsorption of gases on plane surfaces of glass, mica and platinum," *Journal of the American Chemical Society*, vol. 40, no. 9, pp. 1361–1403, 1918.
- [29] Q. Li, Y. L. He, G. H. Tang, and W. Q. Tao, "Lattice Boltzmann modeling of microchannel flows in the transition flow regime," *Microfluidics and Nanofluidics*, vol. 10, no. 3, pp. 607–618, 2011.
- [30] L. J. Klinkenberg, "The Permeability of Porous Media to Liquids and Gases," *Proceedings of "OilGasScientificResearch-Projects" Institute, SOCAR*, 2012.
- [31] F. Civan, "Effective correlation of apparent gas permeability in tight porous media," *Transport in Porous Media*, vol. 82, no. 2, pp. 375–384, 2010.
- [32] H. Darabi, A. Ettehad, F. Javadpour, and K. Sepehrnoori, "Gas flow in ultra-tight shale strata," *Journal of Fluid Mechanics*, vol. 710, pp. 641–658, 2012.
- [33] Z. Peng, S. Liu, S. Tang, Y. Zhao, and Y. Li, "Multicomponent Lattice Boltzmann simulations of gas transport in a coal reservoir with dynamic adsorption," *Geofluids*, vol. 2018, 13 pages, 2018.
- [34] S. Roy, R. Raju, H. F. Chuang, B. A. Cruden, and M. Meyyappan, "Modeling gas flow through microchannels and nanopores," *Journal of Applied Physics*, vol. 93, no. 8, pp. 4870–4879, 2003.
- [35] D. Chen, *Influence of Gas Adsorption on Seepage and Mechanical Properties of Coal*, Southwest Petroleum University, Chengdu, China, 2014.

Research Article

Representative Elementary Volume of Rock Using X-Ray Microcomputed Tomography: A New Statistical Approach

Taufiq Rahman,¹ Hamed Lamei Ramandi ,² Hamid Roshan,² and Stefan Iglauer³

¹Department of Petroleum Engineering, Curtin University, WA 6151, Australia

²School of Minerals and Energy Resources Engineering, UNSW Sydney, NSW 2052, Australia

³School of Engineering, Edith Cowan University, WA 6027, Australia

Correspondence should be addressed to Hamed Lamei Ramandi; h.lameiramandi@unsw.edu.au

Received 1 April 2020; Revised 6 August 2020; Accepted 7 August 2020; Published 1 September 2020

Academic Editor: Jianchao Cai

Copyright © 2020 Taufiq Rahman et al. This is an open access article distributed under the Creative Commons Attribution License, which permits unrestricted use, distribution, and reproduction in any medium, provided the original work is properly cited.

Rock heterogeneity is a key parameter influencing a range of rock properties such as fluid flow and geomechanical characteristics. The previously proposed statistical techniques were able to rank heterogeneity on a qualitative level to different extents; however, they need to select a threshold value for determination of representative elementary volumes (REV), which in turn makes the obtained REV subjective. In this study, an X-ray microcomputed tomography (μ CT) technique was used to obtain images from different porous media. A new statistical technique was then used to compute REV, as a measure of heterogeneity, without the necessity of defining a threshold. The performance of the method was compared with other methods. It was shown that the calculated sum of the relative errors of the proposed method was lowest compared to the other statistical techniques for all tested porous media. The proposed method can be applied to different types of rocks for more accurate estimation of a REV.

1. Introduction

Accurate determination of rock heterogeneity is critical for a variety of industrial applications; for instance, it plays a key role in determining the reservoir's ability to recover oil and gas [1–4], carbon geostorage efficiency [5–8], contaminant mitigation and natural source zone depletion [9, 10], water discharge and extraction rates [11, 12], or geothermal energy production feasibility [13–15]. It is thus essential to understand rock heterogeneity in detail so that reliable predictions can be made and the targeted processes can be further optimised.

Heterogeneity is formed as a result of a verity of geological processes such as deposition, diagenesis, erosion, and structural deformation that ultimately control the geometry of sedimentary deposits [11]. Heterogeneity, thus, is a multi-scale phenomenon that reflects the complexity of a geological formation. It is significant at different length scales: from submicron subgrain scale, which may include biogeochemical features such as skeleton structures of biological species

forming limestone [16, 17] or grain distribution effects [18, 19], to micrometre heterogeneities induced by different grain shapes and sizes [20], to eventually millimetre to centimetre fractures in the rock generated by geomechanical processes [21, 22] or at even larger scale faults, which have been created by tectonic movements [17, 23].

Knowledge of flow in micrometre pore scale is required to understand macroscopic characteristics of flow in porous media; thus, prior to performing upscaling exercises of petrophysical properties [24–27], the accurate characterisation of the porous media at pore scale is crucial for quantifying the heterogeneity of a large system. The pore-scale properties can then be upscaled to core scale or even larger scales. Several works have been conducted to deal with upscaling nonadditive properties of heterogeneous porous media, such as permeability, from the pore scale to the core scale, for example, applying dual-scale pore network models linking pores at different length scales [28] or a direct numerical simulation method for coupling pores at different length scales [4, 29].

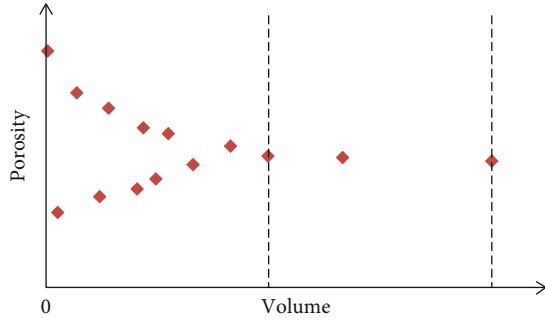


FIGURE 1: Definition of the representative elementary volume (REV): the point at which the petrophysical parameter (here porosity) turns constant is the minimum REV (the area between the two discontinues lines).

One of the methods for quantifying the heterogeneity is using the representative elementary volume (REV), which has been applied to different rock types [30–32]. The REV is defined as the minimum volume of a rock that is representative of any larger volume, provided that the next level of heterogeneity at a larger scale has not been reached [33]. This concept is visualised in Figure 1 by plotting porosity against rock volume. The point at which the parameter, i.e., porosity in Figure 1, becomes constant identifies the REV. While a practical REV is required for performing reservoir simulations and providing geological and fluid dynamical predictions, due to experimental limitations originated partly from rock heterogeneity, a constant value cannot be generally obtained. Statistical methods such as direct observation analysis and nonlinear regression modellings, which employ standard deviation of porosity, coefficient of variation of porosity, or relative gradient error of porosity as predictors [20, 33–35], are therefore used to provide an estimate of REV. Nevertheless, these methods have some limitations in finding the value of REV. Visual observation, as discussed by Costanza-Robinson et al. [20], has the least accuracy, and the other three methods highly depend on the way of choosing their threshold values [34, 35].

In this work, an X-ray microcomputed tomography (μ CT) technique is employed to acquire high-resolution 3D images from different porous media for observing detailed pore morphology at micrometre to millimetre scale. These digital porous media were then subsampled, and their REVs were computed using different methods and compared with a new method proposed in this study. The proposed method uses linear regression to determine the volume at which the standard deviation of porosity is minimised. A weighted regression is then employed in which the estimated REV is imputed, and the corresponding porosity is estimated.

2. Methodology

2.1. Samples. Five porous media with different level of heterogeneities, as presented in Table 1, were selected including a highly homogeneous glass bead pack as a benchmark, a sand

pack, two outcrop sandstones (Bentheimer and St. Bees), and one outcrop carbonate (Mount Gambier). In the case of the outcrop rocks, cylindrical core plugs of approximately 5 mm in diameter and 5–10 mm in length were cored from larger blocks. The unconsolidated materials were packed in hollow plastic cylinders.

2.2. X-Ray Microcomputed Tomography Imaging. The samples were imaged in a dry state with an Xradia Versa XRM500T μ CT instrument at a resolution of $\sim 4 \mu\text{m}^3$. The subvolumes of the samples ($\sim 3 \text{mm}^3$) were imaged to minimise beam hardening, i.e., to improve image quality [36]. The raw images were then filtered using a 3D nonlocal means filter [37] and segmented with a watershed algorithm [38], as shown in Figure 2.

2.3. Digital Measurements. The porosity was calculated by the ratio of the number of voxels in the void phase (pore space) to the total number of voxels (bulk volume) in the segmented image. As shown in Figure 1, the porosity (ϕ_i) can vary with sample volume (V) because of heterogeneity. The images were randomly subsampled into a number of different subvolumes (subsamples), with the condition of no overlap. Figures 3 and 4 exemplify the subsampling method and illustrate the pore space of the digital Bentheimer subsamples with different sizes. Table 2 provides the size of different subsamples. In total, 105 subsamples were acquired. The subsamples ranged from 100^3 voxels to $300 \times 600 \times 600$ voxels, which corresponded to a volume range of $\sim 0.04 \text{mm}^3$ to $\sim 10.38 \text{mm}^3$ for the subsamples with different image resolutions (voxel sizes).

3. Results and Discussion

3.1. Visual Interpretation. One of the simplest techniques to determine REV is plotting porosity values against sample volume, as suggested by Bear [33]. Application of this method to the digital porous media is displayed in Figure 5. It is seen that (a) there is a notable variance of porosity associated with the samples from the smallest volume, which is related to heterogeneity [34], and (b), as expected, this variance narrows with the increase of volume. This implies that a REV can be estimated at sufficiently low variance. In terms of point (a), the variance is particularly significant for volumes smaller than 0.1mm^3 , and it ranges from $\pm 10\%$ for the highly homogeneous glass bead pack to $\pm 100\%$ for the highly heterogeneous carbonate. The variance of porosity can be thus used as a qualitative indicator for rock heterogeneity.

The results of REV assessment, using Figure 5, by visual inspection, is provided in Table 3. The average porosity (Figure 5) follows the trend described by Bear [33]. However, this is a highly subjective analysis. In particular, the technique of looking at the data points does not provide a clear indication of where exactly the REV need to be placed.

3.2. Standard Deviation Analysis. Another method for identifying the cut-off (i.e., the REV value) is applying a mathematical criterion. The unbiased standard deviation s , Equation

TABLE 1: Details of the digital porous media.

Porous medium	Resolution (μm)	Volume (voxels)	Volume (mm^3)
Glass bead pack	3.40	$646 \times 726 \times 906$	16.70
Sand pack	4.09	$682 \times 691 \times 879$	28.34
Bentheimer sandstone	4.58	$657 \times 667 \times 682$	28.73
St. Bees sandstone	3.78	$675 \times 694 \times 816$	20.65
Mount Gambier carbonate	4.58	$663 \times 706 \times 701$	31.54

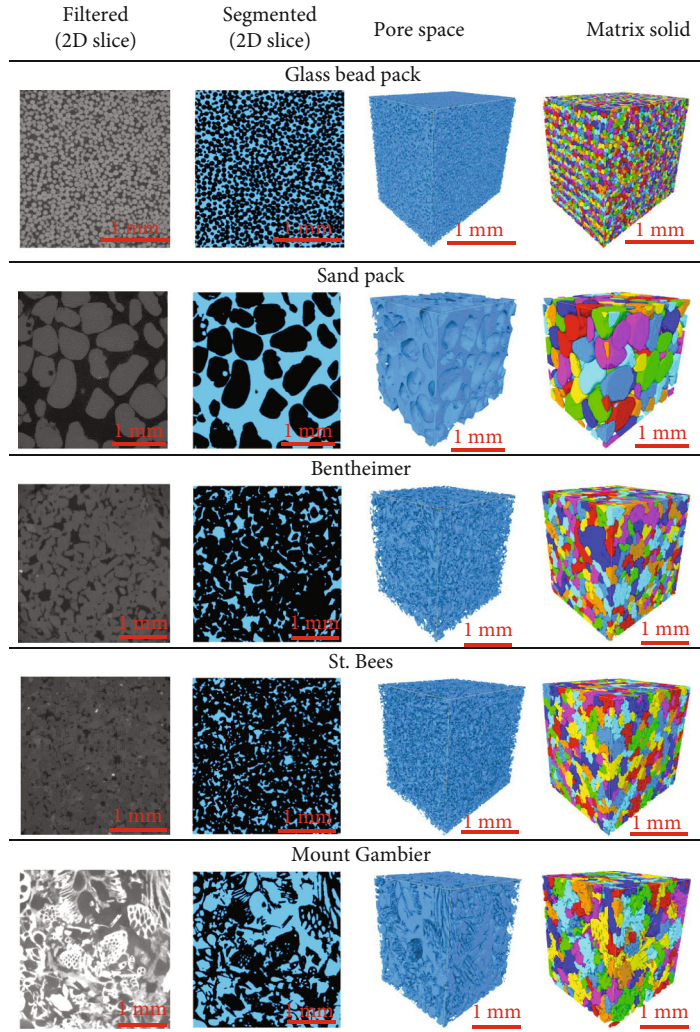


FIGURE 2: From left to right: raw 2D image slice through each porous medium (dark = pore space; grey and white = solid phase), segmented 2D image slice (blue = pore space and black = solid phase), 3D pore spaces (blue = pore space and transparent = solid phase), and 3D rock matrix (different colours indicate different grain sizes).

(1), [39] was used to perform the analysis on the samples. Recalling that the sample volume was subsampled into the i^{th} size,

$$s = \sqrt{\frac{\sum_{i=1}^k (\phi_i - \bar{\phi})^2}{N - 1}}, \quad (1)$$

where s is the standard deviation (unbiased estimate), ϕ_i is the porosity measured for the i^{th} subvolume ($i = 1, 2, 3, \dots, k$), $\bar{\phi}$ is the arithmetic average of the porosity of the i^{th} subvolume, N is the total number of subsamples taken, i is the smallest subsample, and k is the largest subsample; the porosity variance as a function of volume can then be assessed by plotting s_i versus subsample volume (Figure 6).

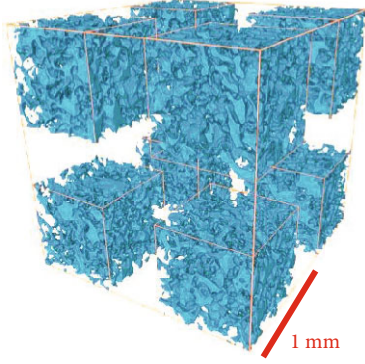


FIGURE 3: Illustration of the subsampling method in the digital Bentheimer sample. Subsample volumes shown are 300^3 voxels (1 mm^3). Only eight corner subsamples are shown in blue for better visualisation.

As seen in Figure 6, the standard deviation rapidly drops with increasing subvolume, but the slope of the decay also rapidly decreases, approximately following a power-law relation $s = AV^b$, where A and b are the least square nonlinear regression fitting parameters and V is the subsample volume (Table 4). While the power-law exponents b are all in the range (0.5 ± 0.2) , coefficient A causes the largest difference in terms of REV. Note that the most homogenous sample, i.e., the glass bead pack, has the smallest coefficient and exponent, and the most heterogeneous sample, i.e., the carbonate, has the largest coefficient A . The exponent b is likely related to the grain size as the sand pack has the largest b and the largest grains.

The standard deviation curves in general give a good indication of heterogeneity, and different samples can be readily compared. However, a threshold value is required to determine the REV. Table 5 shows that a smaller threshold value resulted in a larger REV. At the same time, a smaller threshold had higher accuracy. REV thus strongly depends on the required accuracy. The experimental accuracy of a standard helium pycnometer, $\pm 0.5\%$ [40], was used as a threshold value, Figure 6 (dashed black line). It was found that the glass bead pack consistently had the smallest REV (0.4 mm^3 at 0.5% threshold) indicating that the sample was very homogenous, in contrast to Mt. Gambier, which always had the highest REV and thus was a very heterogeneous rock.

The results were consistent with data reported by Zhang et al. [35], who measured a REV of 5 mm^3 for Brent Triassic sandstone and a REV of 2 mm^3 for a crushed glass bead pack (0.5% threshold), and Stroeven et al. [39] conclude that the REV for a densely packed system is significantly lower than for a less dense pack, as presented in Figure 2 and Table 5. It was found that the grain size had likely a major impact on REV, which was also reflected in the relatively high REV values of the sand pack (Table 5); even though the sand pack was comparatively significantly more symmetrically formed, it had large grains.

3.3. Coefficient of Variation. The coefficient of variation, CV, Equation (2) [41], is unitless and therefore useful when comparing variation between datasets with substantial differences in their means. CV can be used for a REV analysis in a similar way as s .

$$\text{CV} = \frac{s}{\phi}. \quad (2)$$

The plot of CV as a function of subvolume (Figure 7) shows that CV rapidly decreases with increasing sample volume. The CV values again can be approximated using power-law relations (Table 6), similar to s , as CV and s are closely related (Equations (1) and (2)). The exponents and the ratios between the coefficients of CV (Table 6) and s (Table 4) fitting equations are similar, although the nominal values are different. Similar to the standard deviation analysis, a cut-off value needs to be selected to obtain REV. Three thresholds (Table 7) were tested, and it was again observed that REV strongly depended on the threshold value.

Table 7 indicates that the carbonate rock had the largest heterogeneity as expected, followed by St. Bees sandstone, while the glass bead pack was the most homogeneous media. By looking at the μCT images, it seemed that the Bentheimer was more homogeneous than St. Bees because of its more symmetrical structure. However, the grain size in St. Bees was substantially smaller than in Bentheimer, as seen in Figure 2; thus, the grain size was a key factor, which strongly influenced REV.

Zhang et al. [35] measured a REV of 0.02 mm^3 for a Brent Triassic sandstone (porosity = 15.2%) at a CV = 0.2. Their result is consistent with the observations in this study; nevertheless, using CV = 0.05 delivers results that are more compatible with pycnometric measurements (Table 7). The consequence of using such a CV cut-off is, however, noticeable; REV increases ~ 100 -fold, assuming the sandstones are somewhat similar, which seems likely. This threshold value can thus considerably change the REV and has to be selected carefully, and it needs to be compatible with any subsequent analysis, e.g., NMR measurements, which can observe individual atoms [42], and may need a different accuracy level than for instance capillary pressure-water saturation measurements where volume balances in core plugs are considered [43].

3.4. Relative Gradient Error Criterion. An alternative method for determining REV is the relative gradient error (ϵ_g) analysis, Equation (3) [20]:

$$\epsilon_g = \frac{|\phi^{i+1} - \phi^{i-1}|}{\phi^{i+1} + \phi^{i-1}} \frac{1}{\sqrt[3]{V}}, \quad (3)$$

where ϕ is the porosity, i is the subsample number, and V is the volume of the subsample.

Figure 8 presents the plot of computed ϵ_g for all samples versus sample volume; again, it is seen that ϵ_g rapidly drops with increasing subvolume, and the data are much closer to

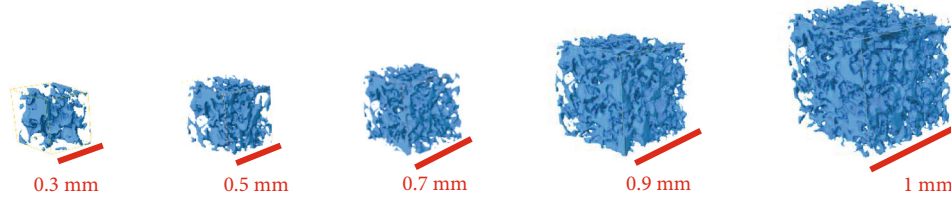


FIGURE 4: Pore space visualisations of digital Bentheimer subsamples. From left to right: the following subvolumes are shown: $\sim 0.04 \text{ mm}^3$, $\sim 0.13 \text{ mm}^3$, $\sim 0.31 \text{ mm}^3$, $\sim 0.61 \text{ mm}^3$, and 1 mm^3 (100^3 , 150^3 , 200^3 , 250^3 , and 300^3 voxels).

TABLE 2: Size of the subsamples analysed.

Subsample size (voxels)	Number of subsamples	Volume (mm^3)				
		Glass beads	Sand pack	Bentheimer	St. Bees	Mount Gambier
$300 \times 600 \times 600$	2	4.25	7.39	10.38	5.83	10.38
$200 \times 600 \times 600$	3	2.83	4.93	6.92	3.89	6.92
$150 \times 600 \times 600$	4	2.12	3.70	5.19	2.92	5.19
$250 \times 300 \times 600$	4	1.77	3.08	4.33	2.43	4.33
$100 \times 600 \times 600$	6	1.42	2.46	3.46	1.94	3.46
$200 \times 250 \times 600$	6	1.18	2.05	2.88	1.62	2.88
$300 \times 300 \times 300$	8	1.06	1.85	2.60	1.46	2.60
$200 \times 200 \times 600$	8	0.94	1.64	2.31	1.30	2.31
$150 \times 250 \times 600$	8	0.88	1.54	2.16	1.22	2.16
$250 \times 250 \times 250$	8	0.61	1.07	1.50	0.84	1.50
$150 \times 150 \times 600$	10	0.53	0.92	1.30	0.73	1.30
$200 \times 200 \times 200$	10	0.31	0.55	0.77	0.43	0.77
$150 \times 150 \times 150$	12	0.13	0.23	0.32	0.18	0.32
$100 \times 100 \times 100$	20	0.04	0.07	0.10	0.05	0.10

each other especially after 1 mm^3 subvolume. This is also reflected in the statistical fits through the data points (Table 8), where generally high power-law exponents (~ -0.5 to -2.2 with a median b value of -1.6) were calculated.

Similar to the other statistical methods, to determine REV, a threshold value had to be selected, which similarly showed a significant influence of the threshold value (Table 9). This influence was, however, smaller than where s or CV analysis was used, mainly because of the lower sensitivity of ε_g analysis, i.e., more similar numbers and curves generally need to be compared in the ε_g analysis. For instance, the glass bead pack had ε_g values smaller than 0.1 mm^3 for all thresholds tested while the REV of the other four samples could hardly be accurately distinguished with the ε_g approach. Note that Costanza-Robinson et al. [20] prescribed $\varepsilon_g < 0.2$ as a threshold value, which, however, led to low accuracy in this case (Table 8). It, therefore, seems that the s and CV analysis are both superior to the ε_g method while the relative gradient error method is still superior to the visual method, consistent with Costanza-Robinson et al. [20].

3.5. Regression Modelling. To avoid the threshold choice in the above methods and therefore have a unique solution to REV value, a new method to estimate the volume of each rock is proposed in this study, at which point the variance of the porosity is minimised. To achieve this, a linear regression model is used, where volume is modelled as a function of the standard deviation of porosity. The standard deviations of the smallest subvolumes are identified as outliers and excluded from the model as they added unnecessary noise. To ensure the normality of the residual errors, the volume is modelled as $\log_e(\text{Volume})$:

$$\log_e y = \beta_0 + \beta_1 x + \epsilon, \quad (4)$$

where y is the volume, x is the standard deviation of the corresponding volume, β_0 is the constant, β_1 is the slope parameters, and ϵ is the error term of the regression equation.

To minimise the standard deviation in this equation, it is assumed to have a theoretical value of zero. When x is zero, the equation becomes $\log_e y = \beta_0$, and therefore, the volume

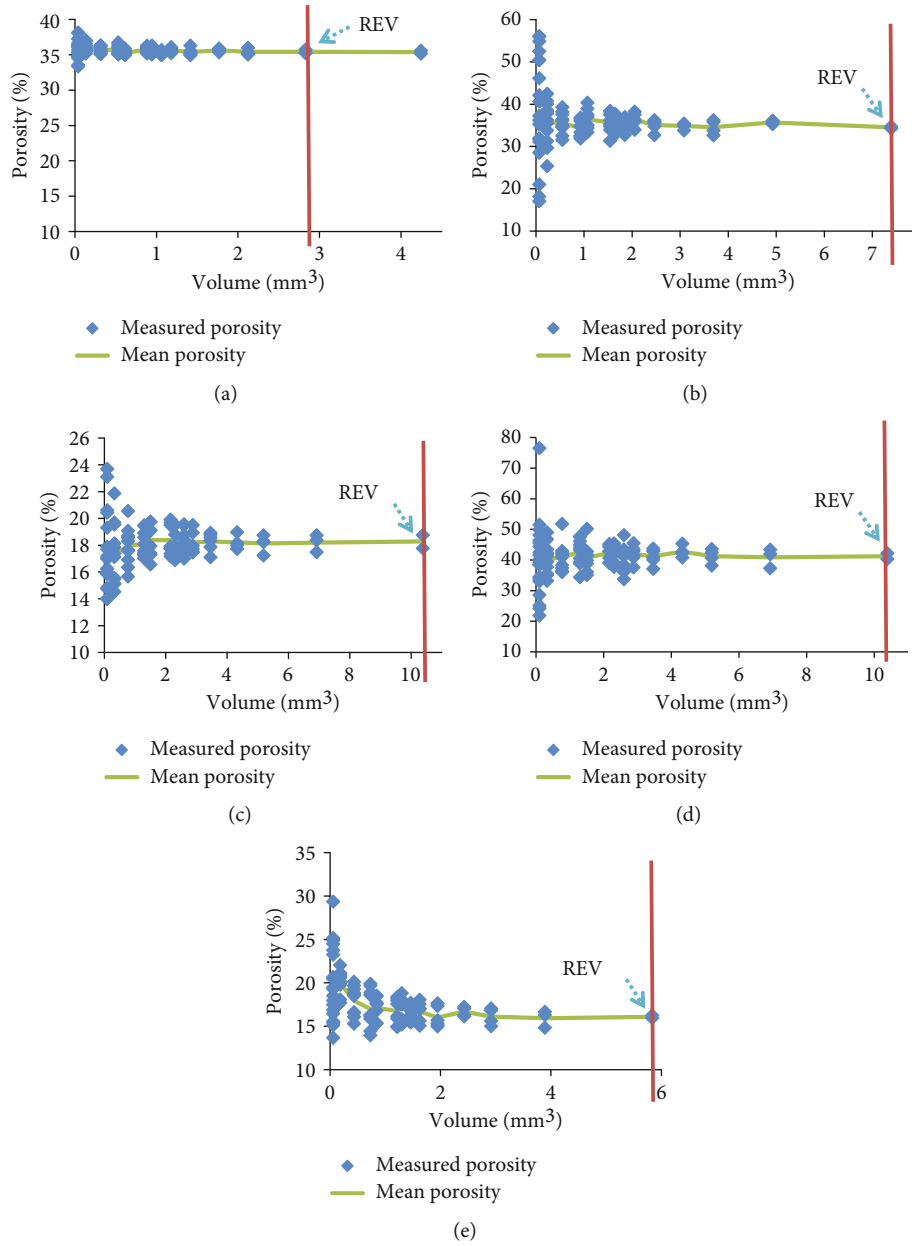


FIGURE 5: Empirical porosity variation (blue points) in the subvolumes of the five samples examined: (a) glass bead pack, (b) sand pack, (c) Bentheimer sandstone, (d) Mount Gambier carbonate, and (e) St. Bees sandstone. The green line indicates the arithmetically averaged porosity of the sample. The vertical red line indicates the REV found by visual inspection.

TABLE 3: Porosities and REV properties of the five samples analysed.

Porous medium	Porosity sample* (%)	Variation**	REV*** (mm ³)
Glass bead pack	35.35	±10%	2.8
Sand pack	35.18	±67%	4.9
Bentheimer sandstone	18.07	±30%	>10
St. Bees sandstone	16.27	±100%	>7.5
Mt. Gambier carbonate	40.54	±100%	>10

*Of the largest volume investigated. **Porosity variation for 0.1 mm³ subvolumes. ***By visual inspection.

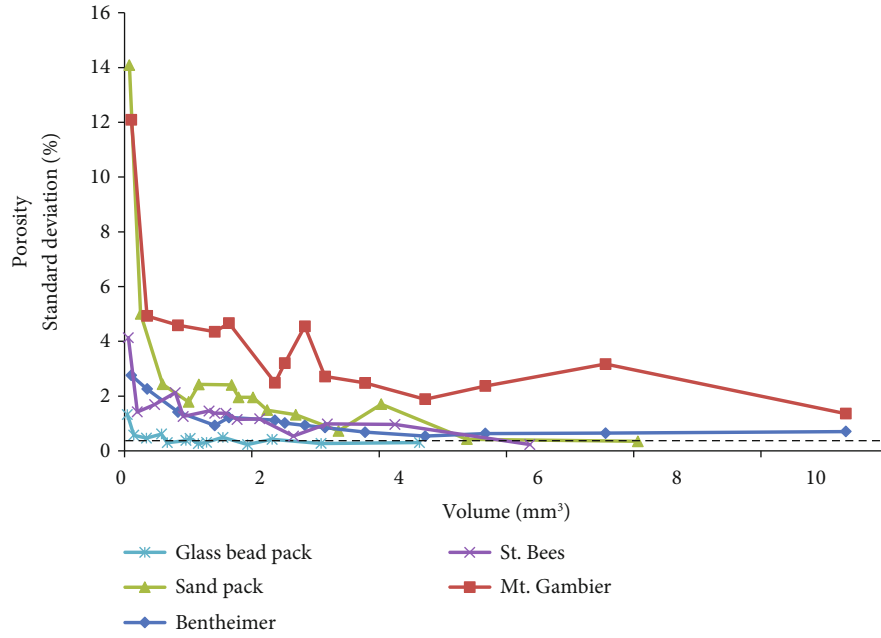


FIGURE 6: Porosity standard deviations of the five samples versus subvolume size. The dashed horizontal black line is the 0.5% threshold. The power-law fit for Mt. Gambier is indicated as a thin black line.

TABLE 4: Fitting equations for the REV analysis using the standard deviation approach.

Porous medium	Fitting equation	<i>A</i>	<i>b</i>
Glass bead pack	$s = 0.3785 V^{-0.298}$	0.3785	-0.298
Sand pack	$s = 2.1761 V^{-0.744}$	2.1761	-0.697
Bentheimer sandstone	$s = 1.2637 V^{-0.362}$	1.2637	-0.362
St. Bees sandstone	$s = 1.2302 V^{-0.421}$	1.2302	-0.421
Mt. Gambier carbonate	$s = 4.3488 V^{-0.382}$	4.3488	-0.382

TABLE 5: Influence of threshold value on REV, standard deviation technique. Associated equations are listed in Table 4.

Porous medium	Threshold (% porosity)	REV (mm ³) from data curve	REV (mm ³) from fitting equation
Glass bead pack	0.5	0.3	0.40
Sand pack	0.5	4.85	7.40
Bentheimer	0.5	4.3	10.40
St. Bees sandstone	0.5	5.1	>6
Mt. Gambier carbonate	0.5	>10.5	>10.5
Glass bead pack	1	0.07	0.05
Sand pack	1	2.85	3.10
Bentheimer	1	2.3	2.00
St. Bees sandstone	1	2.1	1.60
Mt. Gambier carbonate	1	>10.5	>10.5
Glass bead pack	2	0.05	0.05
Sand pack	2	0.8	1.13
Bentheimer	2	0.45	0.29
St. Bees sandstone	2	0.15	0.32
Mt. Gambier carbonate	2	4.1	7.50

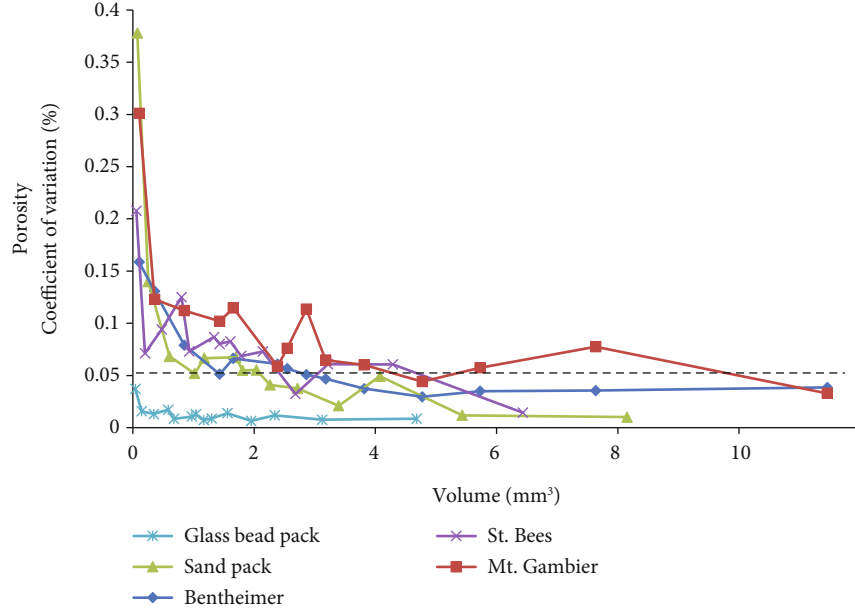


FIGURE 7: Coefficient of variation of the five samples plotted versus sample volume. The dashed horizontal black line is the 0.05 threshold. The power-law fit for Mt. Gambier is indicated as a thin black line.

TABLE 6: Fitting equations for the REV analysis using the CV approach.

Porous medium	Fitting equation	A	b
Glass bead pack	$CV = 0.0106 V^{-0.295}$	0.0106	-0.295
Sand pack	$CV = 0.0611 V^{-0.686}$	0.0611	-0.686
Bentheimer sandstone	$CV = 0.0705 V^{-0.374}$	0.0705	-0.374
St. Bees sandstone	$CV = 0.0716 V^{-0.366}$	0.0716	-0.366
Mt. Gambier carbonate	$CV = 0.1058 V^{-0.389}$	0.1058	-0.389

at which the standard deviation of the porosity is minimised is e^{b_0} , i.e., the exponential of the y -intercept. While this provides an estimated REV, the percent porosity of which the REV corresponds to is also calculated by employing a weighted linear regression of present porosity as a function of $\log_e(\text{Volume})$:

$$p = \alpha_0 + \alpha_1 \log_e(\text{Volume}) + \epsilon, \quad (5)$$

where p is the percent porosity, α_0 represent the constant, α_1 is the slope term of this model, and ϵ is the error term.

The regression is weighted by the reciprocal of the standard deviation at each volume. Once the constant and slope terms are calculated, the REV for that particular rock is substituted into the equation, thus returning its corresponding percent porosity. The results for each rock are presented in Table 10 in their untransformed original units. The back-transformed regression equations are then shown visually in Figure 9.

3.6. Comparison of the Techniques. Sum of the relative errors (unitless ratio) of regression [44], obtained from each technique, is used to compare the above techniques appropriately:

$$\text{Re} = \sum_1^n \text{abs} \left[\frac{f_i - Y_i}{Y_i} \right], \quad (6)$$

where abs is the absolute value, Re is the sum of the relative error of regression, f_i is the model estimate, and Y_i is the exact value.

Table 11 lists the sum of relative errors obtained from each model fit. As seen in Table 11, the proposed regression technique presented the lowest errors of the regression. Note that the average porosity was used in the model to have only one measurement per subvolume to be consistent with other techniques. In addition, in the majority of cases, the proposed method predicted a REV larger than the other methods. However, the comparison of the estimates with the plotted data indicated that the proposed regression method was very sensible both in terms of prediction and error propagation. Many of the subsamples from the rocks still showed a considerable variation of the porosity at the estimates of REV obtained by other techniques. A notable advantage of the proposed method is that it removes the subjectivity of either visually estimating REV or choosing a threshold to estimate REV.

TABLE 7: Influence of CV threshold value on REV. Associated equations are listed in Table 6.

Porous medium	Threshold (-)	REV (mm ³) from data curve	REV (mm ³) from fitting equation
Glass bead pack	0.025	0.09	0.05
Sand pack	0.025	2.95	3.55
Bentheimer	0.025	>10.50	>10.50
St. Bees sandstone	0.025	5.40	>6.00
Mt. Gambier carbonate	0.025	>10.50	>10.50
Glass bead pack	0.050	0.01	0.01
Sand pack	0.050	1.95	1.33
Bentheimer	0.050	2.70	2.50
St. Bees sandstone	0.050	2.23	2.70
Mt. Gambier carbonate	0.050	4.00	6.90
Glass bead pack	0.075	0.01	0.01
Sand pack	0.075	0.50	0.74
Bentheimer	0.075	0.85	0.85
St. Bees sandstone	0.075	0.18	0.85
Mt. Gambier carbonate	0.075	1.95	2.45

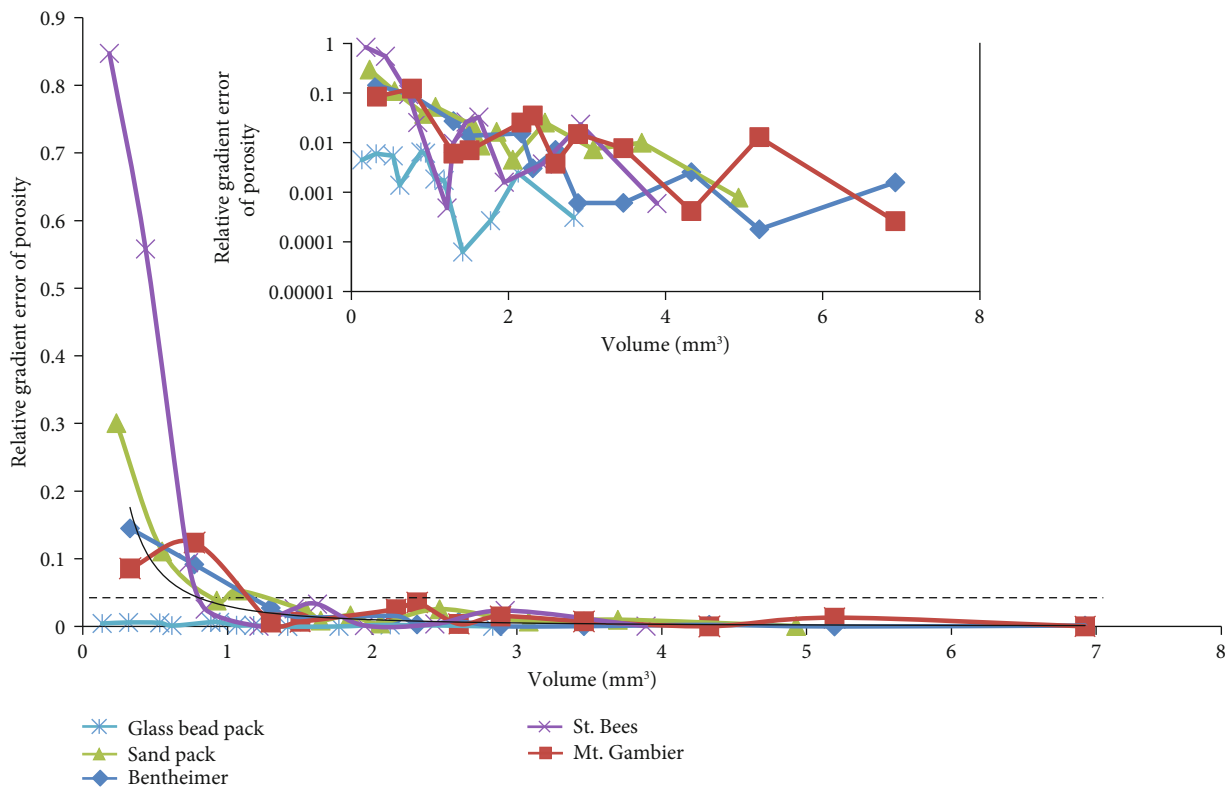


FIGURE 8: Relative gradient error of the five samples plotted versus sample volume. The dashed black line is the 0.05 threshold value.

4. Conclusion

Quantification of rock heterogeneity can be accomplished using a REV, i.e., the larger the REV, the higher the heterogeneity. A range of porous media was imaged using

the μ CT technique and then subsampled (105 subsamples for each porous medium, a total of 525 subsamples). Different statistical methods with which REV can be estimated, including visual interpretation, standard deviation analysis, coefficient of variation analysis, and relative gradient error

TABLE 8: Fitting equations for the REV analysis by a relative gradient error.

Porous medium	Fitting equation	A	b
Glass bead pack	$\varepsilon_g = 0.0014 V^{-1.675}$	0.0014	-1.675
Sand pack	$\varepsilon_g = 0.0124 V^{-1.629}$	0.0124	-1.629
Bentheimer sandstone	$\varepsilon_g = 0.0102 V^{-0.591}$	0.0102	-0.591
St. Bees sandstone	$\varepsilon_g = 0.0083 V^{-2.195}$	0.0083	-2.195
Mt. Gambier carbonate	$\varepsilon_g = 0.0100 V^{-1.573}$	0.0100	-1.573

TABLE 9: Influence of threshold value on REV; ε_g analysis. Associated equations are shown in Table 8 and associated data in Figure 8.

Porous medium	Threshold (-)	REV (mm ³) from data curve	REV (mm ³) from fitting equation
Glass bead pack	0.025	0.10	0.10
Sand pack	0.025	1.50	1.25
Bentheimer	0.025	1.35	2.25
St. Bees sandstone	0.025	0.85	1.00
Mt. Gambier carbonate	0.025	1.22	1.28
Glass bead pack	0.050	0.10	0.10
Sand pack	0.050	0.85	0.82
Bentheimer	0.050	1.10	0.74
St. Bees sandstone	0.050	0.80	0.72
Mt. Gambier carbonate	0.050	1.10	0.71
Glass bead pack	0.075	0.10	0.10
Sand pack	0.075	0.72	0.65
Bentheimer	0.075	0.92	0.61
St. Bees sandstone	0.075	0.76	0.60
Mt. Gambier carbonate	0.075	0.99	0.56

TABLE 10: Estimates of REV and its corresponding porosity as calculated using the linear regression models. Estimates are presented in original units.

Rock	Estimated REV (mm ³)	Porosity (%) estimate at estimated REV
Glass beads	6.2	35.3
Sand pack	6.1	35.0
Bentheimer	14.9	18.6
St. Bees	6.9	15.3
Mt. Gambier	19.1	42.3

criterion analysis, were tested on the subsamples and compared with the new regression method proposed in this study.

The results indicate that the visual inspection approach is the least accurate approach. The relative gradient error, the standard deviation, and the coefficient of variation analyses have a higher degree of accuracy than the visual inspection approach. However, the results highly depend on the selected threshold values. Furthermore, it is not possible to determine a true REV in a theoretical sense or base on selecting threshold values. The proposed regres-

sion modelling method, however, does not rely on a visual inspection and threshold value selection. The sum of relative errors of regression is also the lowest using the proposed technique. The method gives larger REV, which is satisfactory as many of the subsamples from different rocks show considerable variation in porosity at the estimated REV obtained by other techniques. In addition, it is shown that the grain size has a profound impact on REV, i.e., the larger the grains, the larger the REV, and the samples with a very ordered and symmetric structure can have a large REV if they contain large grains.

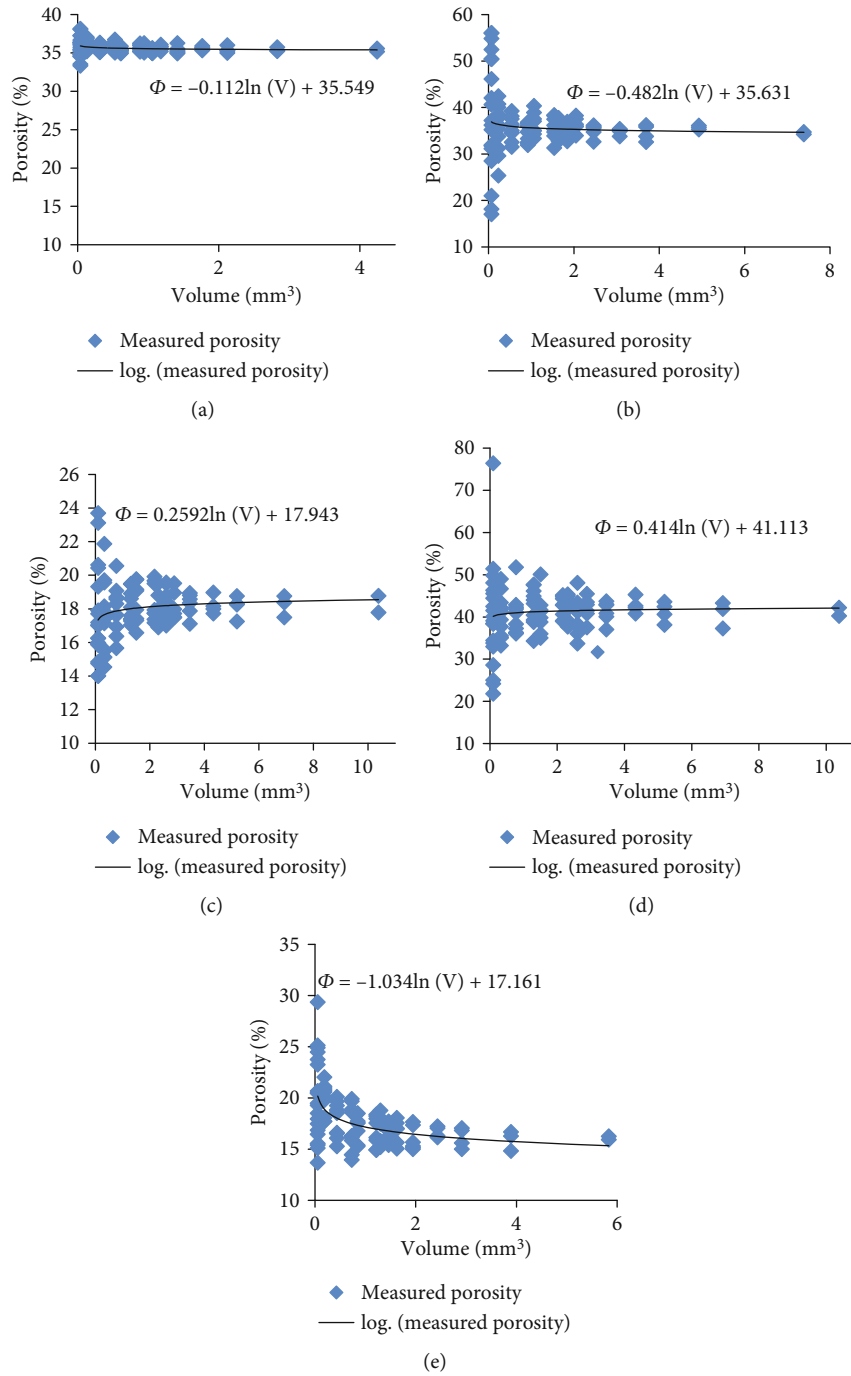


FIGURE 9: Volume plotted against porosity (%), with a back-transformed regression line. (a) Glass bead pack, (b) sand pack, (c) Bentheimer sandstone, (d) St. Bees sandstone, and (e) Mount Gambier carbonate.

TABLE 11: Sum of relative error of regression obtained from each model fit.

Porous medium	Standard deviation (s)	Coefficient of variation (CV)	Relative gradient error (ϵ_g)	Regression modelling (p)
Glass bead pack	3.3116	3.2842	22.7227	0.0552
Sand pack	3.9485	3.8569	7.6258	0.1872
Bentheimer sandstone	2.9153	2.9482	9.5289	0.2919
St. Bees sandstone	4.737	4.9612	40.5122	0.2660
Mt. Gambier carbonate	2.6284	2.6821	19.769	0.3842

Data Availability

The data supporting the conclusions of the study is already presented in the manuscript, and readers can download from the paper or can contact the authors.

Conflicts of Interest

There are no conflicts of interest.

Acknowledgments

The authors wish to acknowledge the financial assistance provided through the Australian National Low Emissions Coal Research and Development (ANLEC R&D), project 3-0911-0155. ANLEC R&D is supported by Australian Coal Association Low Emissions Technology Limited and the Australian Government through the Clean Energy Initiative. The μ CT measurements were performed using the μ CT system courtesy of the National Geosequestration Laboratory (NGL) of Australia. The NGL is a collaboration between Curtin University, CSIRO, and the University of Western Australia established to conduct and deploy critical research and development to enable commercial-scale carbon storage options. Funding for this facility was provided by the Australian Federal Government.

References

- [1] N. R. Morrow, *Interfacial Phenomena in Petroleum Recovery*, CRC Press, 1991.
- [2] M. Blunt, F. J. Fayers, and F. M. Orr Jr., "Carbon dioxide in enhanced oil recovery," *Energy Conversion and Management*, vol. 34, no. 9-11, pp. 1197–1204, 1993.
- [3] S. Du, S. Pang, and Y. Shi, "Quantitative characterization on the microscopic pore heterogeneity of tight oil sandstone reservoir by considering both the resolution and representativeness," *Journal of Petroleum Science and Engineering*, vol. 169, pp. 388–392, 2018.
- [4] S. Norouzi Apourvari and C. H. Arns, "Image-based relative permeability upscaling from the pore scale," *Advances in Water Resources*, vol. 95, pp. 161–175, 2016.
- [5] J.-C. Perrin and S. Benson, "An experimental study on the influence of sub-core scale heterogeneities on CO₂ distribution in reservoir rocks," *Transport in Porous Media*, vol. 82, no. 1, pp. 93–109, 2009.
- [6] S. C. M. Krevor, R. Pini, L. Zuo, and S. M. Benson, "Relative permeability and trapping of CO₂ and water in sandstone rocks at reservoir conditions," *Water Resources Research*, vol. 48, no. 2, 2012.
- [7] T. Rahman, M. Lebedev, A. Barifcani, and S. Iglauer, "Residual trapping of supercritical CO₂ in oil-wet sandstone," *Journal of Colloid and Interface Science*, vol. 469, pp. 63–68, 2016.
- [8] N. Wei, M. Gill, D. Crandall et al., "CO₂ flooding properties of liujiagou sandstone: influence of sub-core scale structure heterogeneity," *Greenhouse Gases: Science and Technology*, vol. 4, no. 3, pp. 400–418, 2014.
- [9] K. Sookhak Lari, G. B. Davis, J. L. Rayner, T. P. Bastow, and G. J. Puzon, "Natural source zone depletion of Inapl: a critical review supporting modelling approaches," *Water Research*, vol. 157, pp. 630–646, 2019.
- [10] K. Sookhak Lari, J. L. Rayner, and G. B. Davis, "Towards characterizing Inapl remediation endpoints," *Journal of Environmental Management*, vol. 224, pp. 97–105, 2018.
- [11] C. E. Koltermann and S. M. Gorelick, "Heterogeneity in sedimentary deposits: a review of structure-imitating, process-imitating, and descriptive approaches," *Water Resources Research*, vol. 32, no. 9, pp. 2617–2658, 1996.
- [12] J. C. Maréchal, S. Lanini, B. Aunay, and P. Perrochet, "Analytical solution for modeling discharge into a tunnel drilled in a heterogeneous unconfined aquifer," *Groundwater*, vol. 52, no. 4, pp. 597–605, 2014.
- [13] Q. Zhou, J. T. Birkholzer, C.-F. Tsang, and J. Rutqvist, "A method for quick assessment of CO₂ storage capacity in closed and semi-closed saline formations," *International Journal of Greenhouse Gas Control*, vol. 2, no. 4, pp. 626–639, 2008.
- [14] T. R. Elliot, T. A. Buscheck, and M. Celia, "Active CO₂ reservoir management for sustainable geothermal energy extraction and reduced leakage," *Greenhouse Gases: Science and Technology*, vol. 3, no. 1, pp. 50–65, 2013.
- [15] T. Dewers, P. Eichhubl, B. Ganis et al., "Heterogeneity, pore pressure, and injectate chemistry: control measures for geologic carbon storage," *International Journal of Greenhouse Gas Control*, vol. 68, pp. 203–215, 2018.
- [16] J. R. Jones, G. Poologasundarampillai, R. C. Atwood, D. Bernard, and P. D. Lee, "Non-destructive quantitative 3d analysis for the optimisation of tissue scaffolds," *Biomaterials*, vol. 28, no. 7, pp. 1404–1413, 2007.
- [17] K. Bjorlykke, *Petroleum Geoscience: From Sedimentary Environments to Rock Physics*, Springer Science & Business Media, 2010.
- [18] R. Al-Raoush and A. Papadopoulos, "Representative elementary volume analysis of porous media using x-ray computed tomography," *Powder Technology*, vol. 200, no. 1-2, pp. 69–77, 2010.
- [19] Y. Bazaikin, B. Gurevich, S. Iglauer et al., "Effect of CT-image size and resolution on the accuracy of rock property estimates," *Journal of Geophysical Research: Solid Earth*, vol. 122, no. 5, pp. 3635–3647, 2017.
- [20] M. S. Costanza-Robinson, B. D. Estabrook, and D. F. Fouhey, "Representative elementary volume estimation for porosity, moisture saturation, and air-water interfacial areas in unsaturated porous media: data quality implications," *Water Resources Research*, vol. 47, no. 7, 2011.
- [21] S. Iglauer, S. Wang, and V. Rasouli, "X-ray micro-tomography measurements of fractured tight sandstone," in *SPE Asia Pacific Oil and Gas Conference and Exhibition*, Society of Petroleum Engineers, 2011.
- [22] J. P. Morris, R. L. Detwiler, S. J. Friedmann, O. Y. Vorobiev, and Y. Hao, "The large-scale geomechanical and hydrogeological effects of multiple CO₂ injection sites on formation stability," *International Journal of Greenhouse Gas Control*, vol. 5, no. 1, pp. 69–74, 2011.
- [23] E. Dombrádi, D. Sokoutis, G. Bada, S. Cloetingh, and F. Horváth, "Modelling recent deformation of the pannonian lithosphere: lithospheric folding and tectonic topography," *Tectonophysics*, vol. 484, no. 1-4, pp. 103–118, 2010.
- [24] S. Rolland du Roscoat, M. Decain, X. Thibault, C. Geindreau, and J. F. Bloch, "Estimation of microstructural properties from synchrotron x-ray microtomography and determination of the rev in paper materials," *Acta Materialia*, vol. 55, no. 8, pp. 2841–2850, 2007.

- [25] T. Kanit, F. N’Guyen, S. Forest, D. Jeulin, M. Reed, and S. Singleton, “Apparent and effective physical properties of heterogeneous materials: representativity of samples of two materials from food industry,” *Computer Methods in Applied Mechanics and Engineering*, vol. 195, no. 33-36, pp. 3960–3982, 2006.
- [26] M. J. King, P. R. King, C. A. McGill, and J. K. Williams, “Effective properties for flow calculations,” *Transport in Porous Media*, vol. 20, no. 1-2, pp. 169–196, 1995.
- [27] O. Rozenbaum and S. R. du Roscoat, “Representative elementary volume assessment of three-dimensional x-ray microtomography images of heterogeneous materials: application to limestones,” *Physical Review E*, vol. 89, no. 5, 2014.
- [28] A. Moctezuma, S. Bekri, C. Laroche, and O. Vizika, “A dual network model for relative permeability of bimodal rocks: application in a vuggy carbonate,” in *Proceedings of the International Symposium of the Society of Core Analysts*, pp. 1–13, Pau, France, 2003.
- [29] S. N. Apourvari and C. H. Arns, “An assessment of the influence of micro-porosity for effective permeability using local flux analysis on tomographic images,” in *IPTC 2014: International Petroleum Technology Conference: European Association of Geoscientists & Engineers*, Pau, France, 2014.
- [30] S. M. Shah, J. P. Crawshaw, F. Gray, J. Yang, and E. S. Boek, “Convex hull approach for determining rock representative elementary volume for multiple petrophysical parameters using pore-scale imaging and Lattice–Boltzmann modelling,” *Advances in Water Resources*, vol. 104, pp. 65–75, 2017.
- [31] J. O. Adeleye and L. T. Akanji, “Pore-scale analyses of heterogeneity and representative elementary volume for unconventional shale rocks using statistical tools,” *Journal of Petroleum Exploration and Production Technology*, vol. 8, no. 3, pp. 753–765, 2018.
- [32] S. Jackson, Q. Lin, and S. Krevor, “Representative elementary volumes, hysteresis, and heterogeneity in multiphase flow from the pore to continuum scale,” *Water Resources Research*, vol. 56, no. 6, article e2019WR026396, 2020.
- [33] J. Bear, *Dynamics of Fluids in Porous Media*, Courier Corporation, 2013.
- [34] M. Halisch, “The rev challenge—estimating representative elementary volumes and porous rock inhomogeneity from high resolution micro-ct data sets,” in *Proceedings of International Symposium of the Society of Core Analysts, Napa Valley, California, USA*, 2013.
- [35] D. Zhang, R. Zhang, S. Chen, and W. E. Soll, “Pore scale study of flow in porous media: scale dependency, rev, and statistical rev,” *Geophysical Research Letters*, vol. 27, no. 8, pp. 1195–1198, 2000.
- [36] S. R. Stock, *Microcomputed Tomography*, CRC Press, 2018.
- [37] A. Buades, B. Coll, and J. M. Morel, “A non-local algorithm for image denoising,” in *2005 IEEE Computer Society Conference on Computer Vision and Pattern Recognition (CVPR’05)*, IEEE, vol. 2, pp. 60–65, San Diego, CA, June 2005.
- [38] S. Schlüter, A. Sheppard, K. Brown, and D. Wildenschild, “Image processing of multiphase images obtained via x-ray microtomography: a review,” *Water Resources Research*, vol. 50, no. 4, pp. 3615–3639, 2014.
- [39] M. Stroeven, H. Askes, and L. J. Sluys, “Numerical determination of representative volumes for granular materials,” *Computer Methods in Applied Mechanics and Engineering*, vol. 193, no. 30-32, pp. 3221–3238, 2004.
- [40] S. Iglauer, M. A. Fernø, P. Shearing, and M. J. Blunt, “Comparison of residual oil cluster size distribution, morphology and saturation in oil-wet and water-wet sandstone,” *Journal of Colloid and Interface Science*, vol. 375, no. 1, pp. 187–192, 2012.
- [41] M. G. Vangel, “Confidence intervals for a normal coefficient of variation,” *The American Statistician*, vol. 50, no. 1, pp. 21–26, 1996.
- [42] O. Talabi, S. AlSayari, S. Iglauer, and M. J. Blunt, “Pore-scale simulation of nmr response,” *Journal of Petroleum Science and Engineering*, vol. 67, no. 3-4, pp. 168–178, 2009.
- [43] C. H. Pentland, R. El-Maghraby, S. Iglauer, and M. J. Blunt, “Measurements of the capillary trapping of super-critical carbon dioxide in Berea sandstone,” *Geophysical Research Letters*, vol. 38, no. 6, 2011.
- [44] M. ÇİMEN, “Estimation of daily suspended sediments using support vector machines,” *Hydrological Sciences Journal*, vol. 53, no. 3, pp. 656–666, 2009.

Research Article

Experiments and Modeling on the Influence of Interfacial Tension on Imbibition Height of Low-Permeability Reservoir

Xiaoxia Ren ^{1,2}, Aifen Li,³ Piyang Liu,¹ and Bingqing He³

¹Qingdao Key Laboratory for Geomechanics and Offshore Underground Engineering, School of Science, Qingdao University of Technology, Qingdao 266525, China

²Shandong Key Laboratory of Oilfield Chemistry, China University of Petroleum (East China), Qingdao 266580, China

³School of Petroleum Engineering, China University of Petroleum (East China), Qingdao 266580, China

Correspondence should be addressed to Xiaoxia Ren; renxiaoxia1010@163.com

Received 8 July 2020; Revised 6 August 2020; Accepted 11 August 2020; Published 25 August 2020

Academic Editor: Wei Wei

Copyright © 2020 Xiaoxia Ren et al. This is an open access article distributed under the Creative Commons Attribution License, which permits unrestricted use, distribution, and reproduction in any medium, provided the original work is properly cited.

Low-permeability reservoirs have tiny pores with winding and complicated pore throats. The oil recovery efficiency of low-permeability reservoirs can be enhanced through the displacement of reservoir oil through imbibition. In the present study, experiments were conducted to investigate variations in the imbibition height of hydrophilic and weakly-hydrophilic rock samples under different interfacial tensions. An imbibition model considering imbibition resistance and bending of pore throats was established based on fractal theory. According to the experimental results, variations in the imbibition height of low-permeability rock samples with time can be divided into three stages. In the first stage, the capillary force plays a dominant role, while the viscous force and gravity have very slight effects. The imbibition height first increases rapidly and then levels off to a constant rate. With the increase in interfacial tension, the imbibition rate in the first stage increases, the ultimate imbibition height increases initially and then decreases, and the contribution of the imbibition height in the first stage to the ultimate imbibition height becomes greater. There is an optimal interfacial tension that causes the ultimate imbibition height to reach its maximum. The calculated results obtained from the proposed imbibition model are consistent with the experimental results, indicating that the model can accurately reflect the change in the imbibition height in low-permeability reservoirs in the first stage.

1. Introduction

Abundant oil and gas resources are present in low-permeability reservoir formations, which are widely distributed all over the world. Low-permeability reservoirs have small pore radii, few effective pores, and complicated pore throats with abundant microcracks [1]. It is difficult for traditional water-flooding to displace crude oil from capillary tubes in such a system [2]. Therefore, methods for the efficient development of low-permeability reservoirs have been widely studied in the petroleum industry [3].

Research and practice indicate that the displacement of oil through imbibition can significantly enhance the recovery of fractured reservoirs [4]. Generally, imbibition refers to diffusion under the action of capillary force, as the wetting-phase fluid enters the pore throat of rock spontaneously and displaces the nonwetting-phase fluid in the pore [5].

Studying the imbibition characteristics of low-permeability reservoirs and understanding the mechanisms of imbibition displacement can provide an effective method to enhance the recovery of low-permeability reservoirs.

According to current research findings, the interfacial tension of the fluid has a significant effect on the imbibition. Laboratory studies and field practices have yielded both positive and negative observations. The general principle is that surfactants trigger imbibition by either interfacial tension reduction or wettability alteration [6]. Standnes et al. [7] experimentally compared the oil recovery from oil-wet reservoir cores using different surfactant solutions and found that cationic surfactant C12TAB had high efficiency of imbibition. Alshehri et al. [8] found that a reduction in the interfacial tension can decrease the imbibition resistance of the oil-wet core and improve the imbibition effect. Sun et al. [9] reported that the reduction in interfacial tension could

effectively decrease the work of adhesion, which is conducive to improving recovery through imbibition. Santanna et al. [10] performed static imbibition experiments and found that the imbibition rate and the oil recovery factor were higher when an ionic surfactant was used. It has been reported that the wettability change is the primary cause of improving the imbibition recovery rate using surfactants [11]. Babadagli [12] found that nonionic surfactant solution increased the recovery rate and ultimate recovery of heavy oil in water-wet sandstones. This effect was attributed to the change in wettability due to the addition of surfactant. Sun et al. [9] found that the imbibition effects of hydrophilic and lipophilic cores were both influenced by wettability, and the surfactant has a significant effect on the recovery of the lipophilic core through imbibition. Alvarez and Schechter [13] found that the addition of an appropriate surfactant can improve oil recovery by altering wettability and interfacial tension. Shen et al. [14] studied the surfactant solution imbibition in porous media with subnanometer and nanometer capillaries using a mechanical model, and the simulated calculation showed that the change in wettability contributes more to the imbibition recovery of tight oil than lower interfacial tension. Gao et al. [15] found that the imbibition degree of strong water-wet cores was large when water was used for imbibition. Liu et al. [16] found through experiments that the oil recovery through imbibition is improved as the rock wetness is shifted from oil-wet to water-wet. Saputra et al. [17] performed laboratory-scale imbibition experiments and found that oil recovery is enhanced by the addition of surfactant as a result of wettability alteration, and the reservoir properties have a significant effect on the results of surfactant-assisted spontaneous imbibition. Liu et al. [18] found that the addition of surfactant mainly recovered oils in the macropores, whose surfaces can be easily altered to be water-wet by surfactant, while it had less effect on the recovery of oil in the micropores. Kumar and Mandal [19] found that using surfactant solutions as the imbibing fluid can recover oils from sandstone and carbonate samples, mainly due to the alteration of wettability. However, Keijzer and de Vries [20] held that the addition of surfactants would result in extremely low interfacial tension. Consequently, the capillary force would not be sufficient to drive imbibition, thereby influencing the recovery through imbibition. Tang et al. [21] found that the injected surfactant did not improve the displacement effect through pulse imbibition.

In order to analyze imbibition variations, researchers have also established different imbibition models, among which the Lucas-Washburn (LW) model, Terzaghi imbibition model, and Szekely model are frequently cited [22, 23]. The LW model (Equation (1)) can be used to calculate the relationship between imbibition height and imbibition time. However, in this model, the inertia force and gravity of the fluid during imbibition are ignored, thus affecting the accuracy in practical applications.

$$h = \sqrt{\frac{r\sigma \cos \theta}{2\eta} t}, \quad (1)$$

where h denotes the imbibition height of the fluid in the capillary tubes, m; r denotes the radius of the capillary tube, with the unit of m; σ denotes the interfacial tension of fluid, N/m; θ denotes the wetting angle, degrees; t denotes imbibition time, s; and η denotes fluid viscosity, Pa·s.

Zhmud et al. [24] found that the LW model was not suitable for describing the later stage of imbibition due to the influence of gravity and derived a long term model considering the gravitational acceleration:

$$h = \frac{2\sigma \cos \theta}{\rho g r} \left[1 - e^{-\rho^2 g^2 r^3 / 16\eta\sigma \cos \theta \lambda t} \right], \quad (2)$$

where g denotes the gravitational acceleration g (9.8 m/s^2), ρ denotes the fluid density, with the unit of kg/m^3 .

Based on the model proposed by Zhmud et al., Fries and Dreyer introduced the Lambert W function into the model and proposed a model with better accuracy [25]:

$$h(t) = \frac{a}{b} \left[1 + W\left(-e^{-1-b^2/a\lambda t}\right) \right], \quad (3)$$

where $a = \sigma r \cos \theta / 4\eta$, and $b = \rho g r^2 / 8\eta$.

These imbibition models based on LW model can directly calculate the imbibition height. In order to accurately describe the imbibition process, several studies have been performed to develop other kinds of improved models, which can predict the oil recovery rate or volume by imbibition. Cai et al. [26] derived analytical expressions for calculating the capillary rise of wetting liquid in a single tortuous capillary by introducing the tortuosity and fractal dimension for a tortuous capillary, respectively. After that, Cai et al. [27] discussed the effect of tortuosity on capillary imbibition in wet porous media based on the capillary model and fractal geometry and derived an analytical model for the time exponent for capillary imbibition in terms of fractal dimension for tortuous capillaries. Moreover, Cai et al. [28] proposed an analytical model for calculating the weight of wetting liquid imbibed into the porous media, and the predicting results are in good agreement with available experimental data published in the literature. Li and Zhao [29] derived a mathematical model using pore volume fractal dimension to predict the production rate by imbibition and found that there was almost no effect of wettability on the value of the fractal dimension function. Considering the effect of the high-permeability fracture network in the matrix rock, Andersen et al. [30] developed an imbibition model for oil recovery in fractured reservoirs. Considering the sizes and shapes of pores, the tortuosity of imbibition streamlines, and the initial wetting-phase saturation, Cai et al. [31] developed a more generalized spontaneous imbibition model, which can be used to characterize the imbibition behavior of different porous media. Subsequently, Andersen et al. [32] derived an exponential model for predicting the imbibition profile under the right conditions: disk with constant permeability, core with negligible capillary gradients, and constant capillary-pressure derivative in the saturation interval. Ashraf and Phirani [33] developed a one-dimensional model to

predict the position of the fluid fronts during imbibition in a multilayer porous medium.

In summary, the previous experimental studies on spontaneous imbibition mainly focused on the oil recovery volume and rate of imbibition. There are no unified conclusions regarding the effects of interfacial tension on the imbibition height of low-permeability reservoirs. The imbibition height can also directly indicate the imbibition characteristics and can help to understand the imbibition mechanism and select proper surfactants [34]. Therefore, it needs to be comprehensively studied. Actual low-permeability reservoirs have complicated characteristics [35], and the calculation results given by traditional imbibition models are quite different from the real cases. There is much room for improvement in the current models being applied in the field. Therefore, it is necessary to conduct experimental and modeling studies on the imbibition height to guide the enhanced oil recovery of low-permeability reservoirs.

In this paper, the effect of the interfacial tension of imbibition fluids on the imbibition height of hydrophilic and weakly-hydrophilic low-permeability rocks was experimentally studied. Considering the imbibition resistance and bending of pore throat during imbibition, a prediction model for the imbibition height was established based on fractal theory.

2. Materials and Methods

2.1. Preparation of the Imbibition Solution and Measurement of Physical Properties. To study the influence of interfacial tension and salinity on the imbibition height, NaCl and distilled water were used to prepare brine with various salinities: 0, 2500, 25000, and 70000 mg/L. Surfactant TOF-1 (provided by Changqing Oil Field) was selected for testing. TOF-1 has been widely used in Changqing Oil Field as a commercial cleanup additive for fracturing fluids. It is a liquid product whose main ingredient is a cationic fluorocarbon surfactant. The critical micelle concentration of TOF-1 is 3.5×10^{-2} mol/L. TOF-1 was added to prepare the imbibition solution with various volume fractions: 0.001%, 0.005%, 0.05%, 0.5%, and 5%. Next, the density of imbibition solution was measured using a densimeter, the viscosity was measured using a capillary viscometer, and the interfacial tension was tested using TX-500C Spinning Drop Interface Tensiometer. The contact angle was measured using the contact angle analyzer (Kruss DSA100) according to Standard SY/T 5153-2017 [36].

2.2. Preparation of Rock Samples with Different Wettability and Measurement of Physical Properties. Low-permeability outcrop rocks were cut into several cuboid rock samples with cross-sections of 2.5 cm \times 2.5 cm and cylindrical parallel rock samples with diameters of 2.5 cm. The samples were placed into a drying oven overnight. The porosity and permeability of the parallel rock samples were measured using a pulse porometer and pulse permeameter [37]. The porosities of prepared rock samples ranged from 14.2% to 14.5%, with an average of 14.3%. Permeability ranged from 0.170 to 0.175 mD, with an average of 0.172 mD. The maximum and

minimum diameters of capillary tube (λ_{\max} and λ_{\min}), and the equivalent radius of the capillary tube (r_c) were obtained by a high-pressure mercury injection capillary force curve [38].

In this paper, rock samples with different degrees of wettability were used for the experiments. Several of the cut rock samples were calcined at 800°C for 24 h in a muffle furnace and denoted as Group A. The unprocessed rock samples were denoted as Group B. Water-wet indices of the parallel samples in Groups A and B were measured by spontaneous imbibition method according to Standard SY/T5153—2017 “Measurement of reservoir rock wettability” [36]. The water-wet index of the samples in Group A ranged from 0.86 to 0.90, with an average value of 0.883, indicating that they belong to hydrophilic rock samples. The water-wet index of Group B ranged from 0.60 to 0.63, so they can be categorized as weakly hydrophilic rock samples.

2.3. Methods for Imbibition Experiments. Through several exploratory experiments, a direct measurement method for imbibition height was established with the experimental equipment shown in Figure 1. First, the dry rock sample was fixed in the support. To prevent water evaporation from occurring on the surface of the rock samples and affecting the experimental results, each rock sample was coated with a transparent hot-melt adhesive at 230°C before the experiment. After the samples cooled to room temperature, the bottom of the samples was then cut off so that the end of the sample was in direct contact with the imbibition solution. Imbibition solution was poured into a beaker until the surface of the liquid was in contact with the bottom end of the rock sample. This point was considered the beginning of the spontaneous imbibition process. During this spontaneous imbibition process, it was necessary to continuously add imbibition solution into the beaker to ensure that there was a solid-liquid contact surface. The entire process was recorded with a camera, and the imbibition height was analyzed. As the interface of the imbibed and unimbibed regions is usually not a horizontal line, the imbibition height was taken as the average of 3–5 height values.

3. Results and Discussion

3.1. Results on Imbibition Height Tests. At a constant temperature of 26°C, the rock samples of Groups A and B were placed in TOF-1 imbibition solution with different volume fractions, respectively, to analyze the change in imbibition height with time.

3.1.1. Variation in Imbibition Height of Rock Samples in Group a. Figure 2 shows the variations of imbibition height as a function of time for the imbibition solution with the salinity of 0 mg/L (deionized water). The imbibition process can be divided into three stages: Stage I is the initial stage of imbibition, in which imbibition height is positively correlated to time; Stage II is the metaphase of imbibition, in which imbibition height is still positively correlated to time, but the slope in this stage is less than that in the first stage and decreases continuously; in Stage III, imbibition height

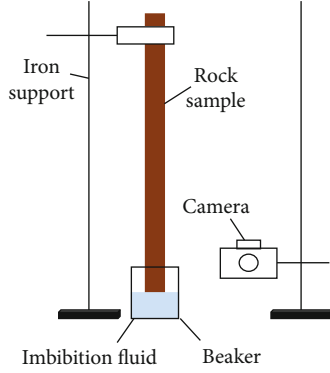


FIGURE 1: Flow chart of improved imbibition height experiment.

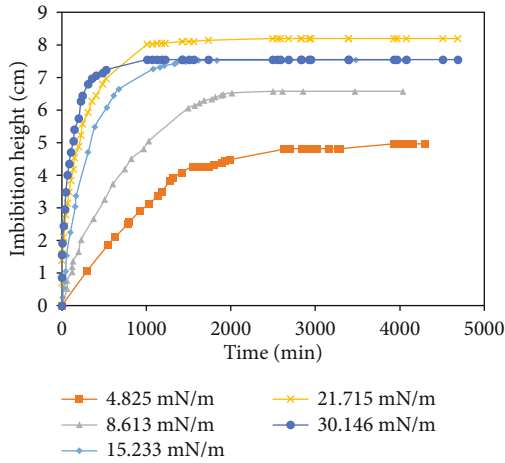


FIGURE 2: Change in imbibition height with time under different interfacial tensions with a salinity of 0 mg/L.

generally no longer changes, showing that the imbibition has essentially stopped. During the initial stage, the capillary force plays a dominant role and serves as the driving force, while the resistance effect of viscosity and gravity can be neglected [28]. Here, the imbibition height rapidly increases. After the imbibition lasts for several hours, gravity gradually increases, so the imbibition height increases at a lower rate. In the later stage, resistance has a more significant effect, and capillary force as a driving force for imbibition is no longer able to overcome resistance.

The ratio of imbibition height to the duration is defined as the growth rate of imbibition height during the first stage. It is abbreviated as imbibition rate. Table 1 shows the imbibition rates and ultimate imbibition heights under different interfacial tensions with a salinity of 0 mg/L. The imbibition height during Stage I has a higher contribution to the overall imbibition height. Especially under higher interfacial tension (0.001% TOF-1), the imbibition height during Stage I is closer to the ultimate imbibition height. With the increase in interfacial tension, the duration of Stage I reduces, the imbibition height increases, and the imbibition rate accelerates. This is because with the increase in interfacial tension, capillary force increases, which then facilitates imbibition [39]. However, a higher imbibition rate results in the earlier

TABLE 1: Results of imbibition experiments under different interfacial tensions with a salinity of 0 mg/L.

Interfacial tension [mN/m]	Time of stage I [min]	Imbibition height in stage I [mm]	Imbibition rate in stage I [mm/min]	Ultimate imbibition height [mm]
4.825	563	15.91	0.028	49.62
8.613	480	23.52	0.049	65.75
15.233	359	40.78	0.114	75.39
21.715	339	54.92	0.162	81.93
30.146	246	67.54	0.275	75.48

effect of gravity in the imbibition process, and an overall shorter Stage I. With the increase in interfacial tension, the ultimate imbibition height first increases and then decreases. The reason is that the increase in interfacial tension increases the capillary force which serves as the driving force, thus facilitating imbibition. However, the increasing imbibition rate causes the fluid to flow through the small pore throats instead of the large ones [40], thus increasing imbibition resistance. Furthermore, a higher imbibition rate results in the earlier effect of gravity on the imbibition process, and the imbibition height increases more slowly. Therefore, for a hydrophilic reservoir formation, there exists an optimal interfacial tension which allows the ultimate imbibition height to reach its maximum and represents the best case for displacing oil in the reservoir.

The overall results of the experiments with a salinity of 2500 mg/L are essentially the same as those with a salinity of 0 mg/L (Figure 3). With the increase in interfacial tension, the imbibition rate during stage I increases, and the ultimate imbibition height increases first and then decreases. The maximum is reached when the interfacial tension is 21.497 mN/m (0.005% TOF-1). Similarly, the experiments with salinities of 25000 mg/L and 70000 mg/L also show the same variation trend in imbibition, as shown in Figure 4. The ultimate imbibition height first increases and then decreases, and reaches its maximum when the interfacial tensions are 21.602 mN/m and 21.755 mN/m (0.005%TOF-1), respectively.

3.1.2. Variation in Imbibition Height of Rock Samples in Group B. In imbibition solutions with different TOF-1 volume fractions, the experimental results on the imbibition of rock samples in Group B are consistent with those in Group A, as shown in Table 2. With a salinity of 0–70000 mg/L and interfacial tension in the range of 4–30 mN/m, the duration of Stage I decreases with an increase in the interfacial tension. Moreover, the imbibition rate increases and the ultimate imbibition height first increases and then decreases.

Thus, for either hydrophilic rock samples or weakly-hydrophilic rock samples, there exists an optimal interfacial tension to achieve the maximum imbibition height, which represents the best imbibition effect. In these experiments, the imbibition solution with a TOF-1 volume fraction of 0.005% (with the interfacial tension of 21.497–21.755 mN/m) has the best imbibition effect.

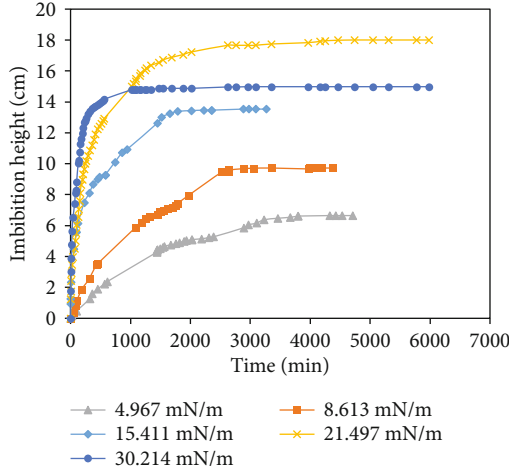


FIGURE 3: Change in imbibition height with time under different interfacial tensions with a salinity of 2500 mg/L.

According to the experimental results of the rock samples in Group A and Group B, the influence of the wettability of samples on imbibition height was further analyzed. The salinity of 2500 mg/L is taken as an example, as shown in Figure 5. During Stage I of imbibition, the growth rates of the imbibition height of hydrophilic and weakly hydrophilic samples both increase with the increase in interfacial tension, and under the same experimental conditions, the imbibition height of the hydrophilic samples increases more rapidly. The more hydrophilic rock samples show greater imbibition heights during both Stage I and Stage III. According to the analysis, a more hydrophilic rock sample results in a smaller wetting angle of the liquid-solid interface [41]. Also, a greater capillary force results in a faster increase in imbibition height and greater overall imbibition height.

3.2. Establishment of a Calculation Model for Imbibition Height. Flow resistance is an essential factor influencing the imbibition effect. However, the impact of flow resistance and the bending extent of pore throats are not adequately considered in the existing models. Thus, in this paper, a study was conducted to create a new imbibition model with consideration of flow resistance and the bending conditions of pore throats.

3.2.1. Model Establishment. Figure 6 shows a physical model for imbibition. The slender region in the middle is a capillary tube; the blue region is the imbibition solution; h denotes the imbibition height in the traditional capillary tube (Figure 6(a)); and h_s denotes the imbibition height in the improved model (Figure 6(b)). Considering the bending of pore throats, the capillary tube is curved, and the streamline of the imbibition solution is also a curve. In this paper, the fractal theory is used to describe the curved streamline.

The fractal theory describes the complexity and diversity of a research object through mathematical methods from the perspective of the fractal dimension. Due to self-similarity

and iterative generation between the parts and the whole of the fractal body, there is a scaling relationship between the physical quantity $M(\varepsilon)$ to be studied and the measurement scale ε of the object, as follows [42]:

$$M(\varepsilon) \sim \varepsilon^{D_f}, \quad (4)$$

where D_f is the fractal dimension, which is an important parameter that describes the characteristics of a fractal body.

Stratigraphic rocks are also fractal [43]. Hence, the pore fractures and fluid streamlines in rocks present fractal distributions [44], with the scaling relationship as follows:

$$h_f = \varepsilon^{1-D_f} h_s^{D_f}, \quad (5)$$

where h_f denotes the imbibition length, with the unit of m; and h_s denotes imbibition distance, with the unit of m.

When the above scaling relationship is used to describe the fluid streamline in the stratum, ε denotes the equivalent pore diameter λ_c . Therefore, the scaling relationship can also be expressed as:

$$h_f = \lambda_c^{1-D_f} h_s^{D_f}, \quad (6)$$

D_f denotes the property parameter of the fractal body [45]:

$$D_f = d - \frac{\ln \varphi}{\ln (\lambda_{\min} / \lambda_{\max})}, \quad (7)$$

where d denotes spatial dimensions, with the constant of 2 or 3; φ denotes the porosity of the rock samples, dimensionless; λ_{\max} and λ_{\min} denote the maximum and minimum diameters of capillary tube, respectively, with a unit of m.

According to Figure 6(b), using the Bernoulli equation, the change in energy of the imbibition solution when moving from the initial position to the final position is:

$$p_1 + \frac{1}{2} \rho v_{f1}^2 + \rho g h_1 = p_2 + \frac{1}{2} \rho v_{f2}^2 + \rho g h_2 + \omega, \quad (8)$$

where P_1 and P_2 denote the pressures at the initial and final positions, respectively, with a unit of Pa; ρ is the density of the imbibition solution, with a unit of kg/m^3 ; v_{f1} and v_{f2} denote the flow velocities of imbibition solution at the initial and final positions, respectively, with a unit of m/s; h_1 and h_2 denote the heights of the initial and final positions, with a unit of m; and ω denotes the pressure loss in the flow process of imbibition solution, with a unit of Pa.

The total energy loss of the fluid element in the imbibition process is:

$$E = 2\pi r \omega dr, \quad (9)$$

where r denotes the radius of the capillary tube, with a unit of mm.

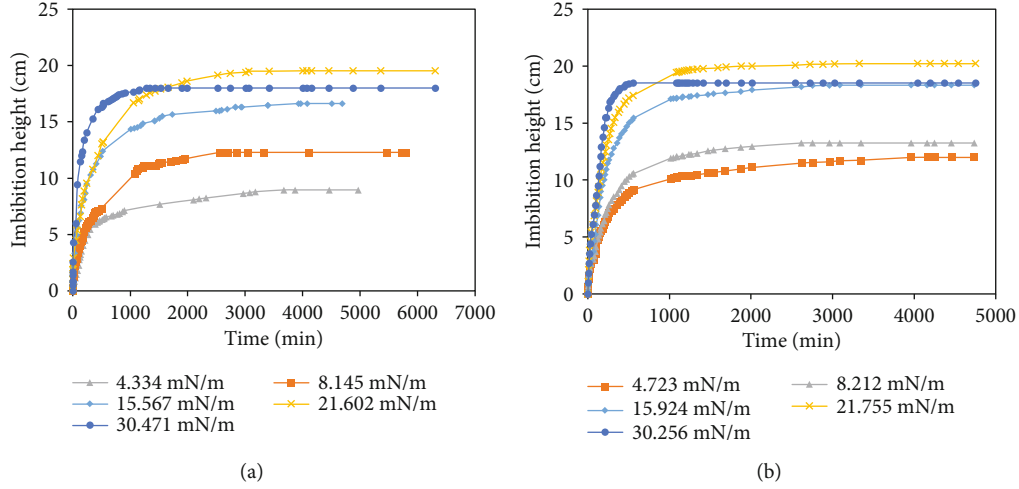


FIGURE 4: Change of imbibition height with time under different interfacial tensions. (a) With a salinity of 25000 mg/L. (b) With a salinity of 70000 mg/L.

TABLE 2: Results of imbibition experiments of rock samples in Group B.

Salinity (mg/L)	TOF-1 volume fraction [%]	Interfacial tension [mN/m]	Time of Stage I [min]	Imbibition height in Stage I [mm]	Imbibition rate in Stage I [mm/min]	Ultimate imbibition height [mm]
0	5	4.825	535	3.98	0.007	18.21
	0.5	8.613	462	15.07	0.033	19.92
	0.05	15.233	197	19.15	0.097	22.51
	0.005	21.715	175	19.46	0.111	24.03
	0.001	30.146	149	20.31	0.136	22.15
2500	5	4.967	492	12.75	0.026	21.15
	0.5	8.613	377	18.88	0.050	30.38
	0.05	15.411	170	22.64	0.133	43.15
	0.005	21.497	137	29.24	0.213	55.01
	0.001	30.214	125	30.15	0.241	35.07
25000	5	4.334	373	24.75	0.066	32.31
	0.5	8.145	353	25.36	0.072	44.48
	0.05	15.567	205	28.54	0.139	65.40
	0.005	21.602	127	35.75	0.281	80.59
	0.001	30.471	111	38.66	0.348	70.27
70000	5	4.723	347	33.99	0.098	84.23
	0.5	8.212	259	34.11	0.132	97.16
	0.05	15.924	223	88.94	0.399	135.28
	0.005	21.755	158	93.45	0.591	151.51
	0.001	30.256	105	95.92	0.914	148.78

The energy loss caused by internal friction in the imbibition process of the fluid element can be obtained through the formula for Newtonian internal friction:

$$W = -2\pi h_f \eta \frac{d}{dr} \left(r \frac{dv_f}{dr} \right), \quad (10)$$

where v_f denotes the flow velocity of the fluid in the axial direction of the capillary tube, with a unit of m/s; and η

denotes the viscosity of imbibition solution, with a unit of Pa·s.

At the initial stage of imbibition, gravity has less effect on imbibition and is negligible. Therefore, the energy loss within the flow is caused by internal friction, that is, $E = W$.

$$2\pi r \omega dr = -2\pi L_f \eta \frac{d}{dr} \left(r \frac{dv_f}{dr} \right). \quad (11)$$

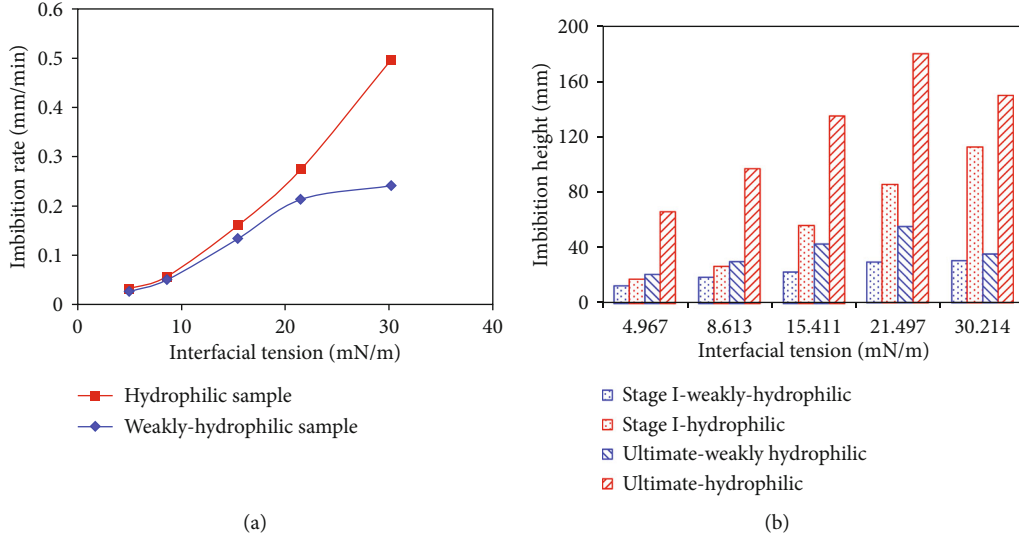


FIGURE 5: Effect of rock sample wettability on the imbibition rate and imbibition height. (a) Imbibition rate in Stage I. (b) Imbibition height.

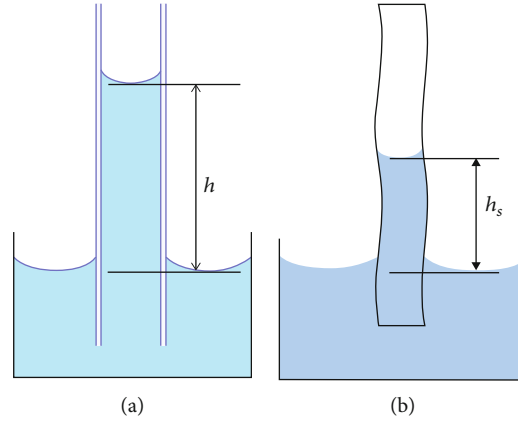


FIGURE 6: Imbibition models. (a) Traditional model. (b) New model.

Calculating the derivative of the imbibition height, the following equation can be obtained:

$$\frac{1}{\eta} \frac{\partial \omega}{\partial h_f} r dr = -\frac{d}{dr} \left(r \frac{dv_f}{dr} \right), \quad (12)$$

where $\partial \omega / \partial h_f$ is the pressure gradient of the capillary tube along the direction of imbibition, with a unit of Pa/s.

The boundary condition can be expressed as:

$$\begin{cases} r = 0, \frac{dv_f}{dr} = 0, \\ r = r_c, v_f = 0 \end{cases}, \quad (13)$$

where r_c denotes the equivalent radius of the capillary tube, with the unit of m.

After integrating Equation (13) through the boundary condition, the following equation can be obtained:

$$v_f = \frac{1}{4\eta} \frac{\partial \omega}{\partial h_f} (r_c^2 - r^2). \quad (14)$$

The derivative of r can be obtained as:

$$\frac{dv_f}{dr} = -\frac{r}{2\eta} \frac{\partial \omega}{\partial h_f}. \quad (15)$$

Using the average imbibition rate as the equivalent value of the flow velocity of the fluid along the axial direction of the capillary tube, the following equation can be obtained:

$$\bar{v}_f = \frac{1}{\pi r_c^2} \int_0^{r_c} 2\pi r v_f dr = \frac{1}{\pi r_c^2} \int_0^{r_c} \frac{1}{4\eta} \frac{\partial \omega}{\partial h_f} (r_c^2 - r^2) 2\pi r dr = \frac{r_c^2}{8\eta} \frac{\partial \omega}{\partial h_f}. \quad (16)$$

Substituting Equation (16) into Equation (15), the following equation can be obtained:

$$\frac{dv_f}{dr} = -\frac{r}{2\eta} \cdot \frac{8\eta\bar{v}_f}{r_c^2} = -\frac{4r\bar{v}_f}{r_c^2}. \quad (17)$$

Substituting Equation (17) into the formula for Newtonian internal friction, the internal friction is calculated as follows:

$$\tau = \eta \left. \frac{dv_f}{dr} \right|_{r=r_c} = -\eta \times \frac{4r_c\bar{v}_f}{r_c^2} = -\frac{4\bar{v}_f\eta}{r_c}. \quad (18)$$

Frictional force f (i.e., imbibition resistance) on the side of imbibition part of the capillary tube is calculated as:

$$f = 2\pi r_c h_f \tau = -8\pi\eta h_f \bar{v}_f. \quad (19)$$

The average imbibition rate \bar{v}_f is:

$$\bar{v}_f = \frac{dh_f}{dt}. \quad (20)$$

Therefore, the differential equation for the length of the imbibition effect is:

$$\frac{d}{dt} \left(\pi r_c^2 \rho h_f \frac{dh_f}{dt} \right) = 2\pi \sigma r_c \cos \theta - 8\pi \eta h_f \frac{dh_f}{dt}, \quad (21)$$

where t denotes imbibition time, with the unit of s; σ denotes interfacial tension of imbibition solution, with the unit of N/m; and θ denotes wetting angle, with the unit of $^\circ$.

After substituting Equation (6) into Equation (21), the formula for the change in imbibition height with time can be obtained by solving the equation:

$$h_s = \sqrt[2D_f]{\frac{\sigma r_c \cos \theta}{\eta \lambda_c^{2-2D_f}} \left[t - \frac{r_c^2}{8\eta} \left(1 - e^{-8\eta t / r_c^2} \right) \right]}. \quad (22)$$

As the influence of gravity is not taken into consideration in the model derivation process, h_s denotes the height of Stage I (gravity is negligible).

3.2.2. Model Verification. The imbibition model was verified with the experimental data on the rock samples in Group A under different interfacial tensions, with a salinity of 0 mg/L taken as the example. The parameters of the imbibition solution and rock samples are shown in Table 3, and the calculation results are shown in Figure 7. By taking the imbibition resistance and the bending condition of the pore throats into account, the new model is able to obtain calculated results that fit well with the experimental results. The coefficient of determination (goodness of fit) R^2 was used to analyze the fitting effectiveness [46]. For solutions with the surface tensions of 4.825, 8.613, 15.233, 21.715, and 30.146 mN/m, the R^2 values are 0.909, 0.927, 0.965, 0.954 and 0.933, respectively, indicating that the proposed model can predict the imbibition trend in the initial period of imbibition. Overall, during

TABLE 3: Basic parameters of cores and imbibition solution.

No.	R [μm]	D_f	ρ [kg/m^3]	σ [mN/m]	$\cos \theta$	η [$\text{mPa}\cdot\text{s}$]
1				4.825	0.80	3.8
2				8.613	0.72	1.8
3	0.22	1.105	1000	15.233	0.68	1.5
4				21.715	0.63	1.3
5				30.146	0.55	1.1

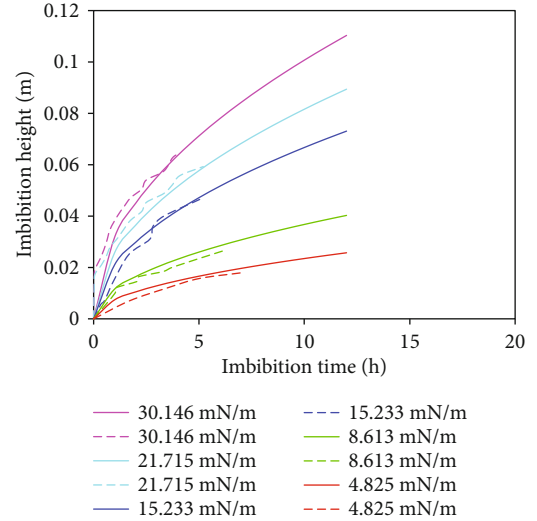


FIGURE 7: Comparison between the experimental results and calculation results obtained by the improved capillary model under different interfacial tensions. The dotted line indicates experimental results, and the solid line represents the calculated results.

Stage I, with the increase in imbibition time, the imbibition height rapidly increases while the imbibition rate gradually decreases. Also, at the same imbibition time, larger interfacial tension results in greater imbibition height.

4. Conclusions

In low-permeability reservoir formations, the increase in imbibition height with imbibition time can be divided into three stages. During Stage I, the capillary force, which serves as the driving force, plays a dominant role. The resistance of viscous force and gravity are negligible. Therefore, the imbibition height rapidly increases, followed by a slow increase. Interfacial tension has a significant effect on imbibition height. With the increase in interfacial tension, the imbibition rate during Stage I increases. The ultimate imbibition height first increases and then decreases, and the contribution of the imbibition height during the first stage to the ultimate imbibition height becomes greater. There is an optimal interfacial tension that allows the ultimate imbibition height to reach its maximum. The newly-established imbibition model takes into account the imbibition resistance and the bending of the pore throats, so it can reflect the change in imbibition height with time during Stage I. The calculation results are consistent with the experimental results, indicating

that the model is applicable for a low-permeability reservoir and would help predict the production results.

Data Availability

The data used to support the findings of this study are available from the first author upon request.

Conflicts of Interest

The authors declare that there are no conflicts of interest regarding the publication of this paper.

Acknowledgments

This work was supported by the Opening Fund of Shandong Key Laboratory of Oilfield Chemistry and the Fundamental Research Funds for the Central Universities.

References

- [1] C. R. Clarkson, M. Freeman, L. He et al., "Characterization of tight gas reservoir pore structure using USANS/SANS and gas adsorption analysis," *Fuel*, vol. 95, pp. 371–385, 2012.
- [2] P. Kathel and K. K. Mohanty, "Dynamic surfactant-aided imbibition in fractured oil-wet carbonates," *Journal of Petroleum Science and Engineering*, vol. 170, pp. 898–910, 2018.
- [3] N. Pal, N. Kumar, R. K. Saw, and A. Mandal, "Gemini surfactant/polymer/silica stabilized oil-in-water nanoemulsions: design and physicochemical characterization for enhanced oil recovery," *Journal of Petroleum Science and Engineering*, vol. 183, article 106464, 2019.
- [4] A. Javaheri, A. Habibi, H. Dehghanpour, and J. M. Wood, "Imbibition oil recovery from tight rocks with dual-wettability behavior," *Journal of Petroleum Science and Engineering*, vol. 167, pp. 180–191, 2018.
- [5] Y. Liu, J. Cai, M. Sahimi, and C. Qin, "A study of the role of microfractures in counter-current spontaneous imbibition by lattice Boltzmann simulation," *Transport in Porous Media*, vol. 133, no. 2, pp. 313–332, 2020.
- [6] J. Tu and J. J. Sheng, "Experimental and numerical study of surfactant solution spontaneous imbibition in shale oil reservoirs," *Journal of the Taiwan Institute of Chemical Engineers*, vol. 106, pp. 169–182, 2020.
- [7] D. C. Standnes, L. A. D. Nogaret, H.-L. Chen, and T. Austad, "An evaluation of spontaneous imbibition of water into oil-wet carbonate reservoir cores using a nonionic and a cationic surfactant," *Energy & Fuels*, vol. 16, no. 6, pp. 1557–1564, 2002.
- [8] A. J. Alshehri, E. Sagatov, and A. R. Kovscek, "Pore-Level Mechanics of Forced and Spontaneous Imbibition of Aqueous Surfactant Solutions in Fractured Porous Media," in *SPE Annual Technical Conference and Exhibition*, New Orleans, Louisiana, 2009.
- [9] L. Sun, W. Pu, J. Xin, and Y. Wu, "Influence of surfactant on high temperature imbibition of low permeability cores," *Journal of China University of Petroleum*, vol. 36, no. 6, pp. 103–107, 2012.
- [10] V. C. Santanna, T. N. C. Dantas, T. A. Borges, A. R. Bezerril, and A. E. G. Nascimento, "The influence of surfactant solution injection in oil recovery by spontaneous imbibition," *Petroleum Science and Technology*, vol. 32, no. 23, pp. 2896–2902, 2014.
- [11] H. Alkan, M. Szabries, N. Dopffel et al., "Investigation of spontaneous imbibition induced by wettability alteration as a recovery mechanism in microbial enhanced oil recovery," *Journal of Petroleum Science and Engineering*, vol. 182, article 106163, 2019.
- [12] T. Babadagli, "Analysis of Oil Recovery by Spontaneous Imbibition of Surfactant Solution," in *SPE International Improved Oil Recovery Conference in Asia Pacific*, Kuala Lumpur, Malaysia, 2003.
- [13] J. O. Alvarez and D. S. Schechter, "Wettability alteration and spontaneous imbibition in unconventional liquid reservoirs by surfactant additives," *SPE Reservoir Evaluation & Engineering*, vol. 20, no. 1, pp. 107–117, 2017.
- [14] A. Shen, Y. Liu, M. Bai et al., "Surfactant effects of wettability alteration and low IFT on countercurrent imbibition for tight oil formation," *Energy & Fuels*, vol. 32, no. 12, pp. 12365–12372, 2018.
- [15] L. Gao, Z. Yang, and Y. Shi, "Experimental study on spontaneous imbibition characteristics of tight rocks," *Advances in Geo-Energy Research*, vol. 2, no. 3, pp. 292–304, 2018.
- [16] J. Liu, J. J. Sheng, X. Wang, H. Ge, and E. Yao, "Experimental study of wettability alteration and spontaneous imbibition in Chinese shale oil reservoirs using anionic and nonionic surfactants," *Journal of Petroleum Science & Engineering*, vol. 175, pp. 624–633, 2019.
- [17] I. W. R. Saputra, K. H. Park, F. Zhang, I. A. Adel, and D. S. Schechter, "Surfactant-assisted spontaneous imbibition to improve oil recovery on the Eagle Ford and Wolfcamp shale oil reservoir: laboratory to field analysis," *Energy & Fuels*, vol. 33, no. 8, pp. 6904–6920, 2019.
- [18] J. Liu, J. J. Sheng, and W. Huang, "Experimental investigation of microscopic mechanisms of surfactant-enhanced spontaneous imbibition in shale cores," *Energy & Fuels*, vol. 33, no. 8, pp. 7188–7199, 2019.
- [19] A. Kumar and A. Mandal, "Critical investigation of zwitterionic surfactant for enhanced oil recovery from both sandstone and carbonate reservoirs: adsorption, wettability alteration and imbibition studies," *Chemical Engineering Science*, vol. 209, article 115222, 2019.
- [20] P. P. M. Keijzer and A. S. de Vries, "Imbibition of surfactant solutions," *SPE Advanced Technology Series*, vol. 1, no. 2, pp. 110–113, 1993.
- [21] H. Tang, D. Lu, J. Xie, and Y. Zhang, "Experiment study of water imbibition injection for daanzai fracturing reservoir," *Journal of Southwest Petroleum Institute*, vol. 27, no. 2, pp. 41–44, 2005.
- [22] E. W. Washburn, "The Dynamics of Capillary Flow," *Physical Review*, vol. 17, no. 3, pp. 273–283, 1921.
- [23] J. Szekely, A. W. Neumann, and Y. K. Chuang, "The rate of capillary penetration and the applicability of the Washburn equation," *Journal of Colloid & Interface Science*, vol. 35, no. 2, pp. 273–278, 1971.
- [24] B. V. Zhmud, F. Tiberg, and K. Hallstenson, "Dynamics of capillary rise," *Journal of Colloid & Interface Science*, vol. 228, no. 2, pp. 263–269, 2000.
- [25] N. Fries and M. Dreyer, "An analytic solution of capillary rise restrained by gravity," *Journal of Colloid and Interface Science*, vol. 320, no. 1, pp. 259–263, 2008.
- [26] C. Jian-Chao, Y. Bo-Ming, M. Mao-Fei, and L. Liang, "Capillary Rise in a Single Tortuous Capillary," *Chinese Physics Letters*, vol. 27, no. 5, article 054701, 2010.

- [27] J. Cai and B. Yu, "A discussion of the effect of tortuosity on the capillary imbibition in porous media," *Transport in Porous Media*, vol. 89, no. 2, pp. 251–263, 2011.
- [28] J. Cai, X. Hu, D. C. Standnes, and L. You, "An analytical model for spontaneous imbibition in fractal porous media including gravity," *Colloids and Surfaces A: Physicochemical and Engineering Aspects*, vol. 414, pp. 228–233, 2012.
- [29] K. Li and H. Zhao, "Fractal prediction model of spontaneous imbibition rate," *Transport in Porous Media*, vol. 91, no. 2, pp. 363–376, 2012.
- [30] P. O. Andersen, S. Evje, and H. Kleppe, "A model for spontaneous imbibition as a mechanism for oil recovery in fractured reservoirs," *Transport in Porous Media*, vol. 101, no. 2, pp. 299–331, 2014.
- [31] J. Cai, E. Perfect, C. L. Cheng, and X. Hu, "Generalized modeling of spontaneous imbibition based on Hagen–Poiseuille flow in tortuous capillaries with variably shaped apertures," *Langmuir*, vol. 30, no. 18, pp. 5142–5151, 2014.
- [32] P. O. Andersen, S. Evje, and A. Hiorth, "Modeling of spontaneous-imbibition experiments with porous disk—on the validity of exponential prediction," *SPE Journal*, vol. 22, no. 5, pp. 1326–1337, 2017.
- [33] S. Ashraf and J. Phirani, "A generalized model for spontaneous imbibition in a horizontal, multi-layered porous medium," *Chemical Engineering Science*, vol. 209, article 115175, 2019.
- [34] J. Xiao, Y. Luo, M. Niu et al., "Study of imbibition in various geometries using phase field method," *Capillarity*, vol. 2, no. 4, pp. 57–65, 2019.
- [35] M. Meng, R. Zhong, and Z. Wei, "Prediction of methane adsorption in shale: classical models and machine learning based models," *Fuel*, vol. 278, article 118358, 2020.
- [36] CPSC, "SY/T 5153-2017 Measurement of reservoir rock wettability," 2017.
- [37] M. Meng and Z. Qiu, "Experiment study of mechanical properties and microstructures of bituminous coals influenced by supercritical carbon dioxide," *Fuel*, vol. 219, pp. 223–238, 2018.
- [38] A. Li, *Petrophysics*, China university of Petroleum Press, Dongying, 2011.
- [39] A. S. Zelenev and Z. Grenoble, "Wettability of reservoir rocks having different polarity by a model nonionic surfactant: fluid imbibition study into crushed rock packs," *Energy & Fuels*, vol. 32, no. 2, pp. 1340–1347, 2018.
- [40] A. Kumar and A. Mandal, "Core-scale modelling and numerical simulation of zwitterionic surfactant flooding: designing of chemical slug for enhanced oil recovery," *Journal of Petroleum Science and Engineering*, vol. 192, article 107333, 2020.
- [41] P. Pillai and A. Mandal, "Wettability modification and adsorption characteristics of imidazole-based ionic liquid on carbonate rock: implications for enhanced oil recovery," *Energy & Fuels*, vol. 33, no. 2, pp. 727–738, 2019.
- [42] B. B. Mandelbrot, *The Fractal Geometry of Nature*, W. H. Freeman and Company, 1982.
- [43] K. Liu, O. Mehdi, and L. Kong, "Fractal and multifractal characteristics of pore throats in the Bakken shale," *Transport in Porous Media*, vol. 126, no. 3, pp. 579–598, 2019.
- [44] R. Guo, Q. Xie, X. Qu et al., "Fractal characteristics of pore-throat structure and permeability estimation of tight sandstone reservoirs: a case study of Chang 7 of the Upper Triassic Yanchang Formation in Longdong area, Ordos Basin, China," *Journal of Petroleum Science and Engineering*, vol. 184, article 106555, 2020.
- [45] B. Yu and J. Li, "Some fractal characters of porous media," *Fractals*, vol. 9, no. 3, pp. 365–372, 2001.
- [46] T. Tjur, "Coefficients of determination in logistic regression models—a new proposal: the coefficient of discrimination," *The American Statistician*, vol. 63, no. 4, pp. 366–372, 2009.

Research Article

Multiple Approaches to Quantifying the Effective Porosity of Lacustrine Shale Oil Reservoirs in Bohai Bay Basin, East China

Binyu Ma,^{1,2} Qinhong Hu ,³ Shengyu Yang ,^{1,2} Na Yin,¹ Hongguo Qiao,¹ Tao Zhang,¹ and Mianmo Meng¹

¹Key Laboratory of Deep Oil and Gas, China University of Petroleum (East China), Qingdao 266580, China

²Laboratory for Marine Mineral Resources, Qingdao National Laboratory for Marine Science and Technology, Qingdao 266071, China

³Department of Earth and Environment Sciences, University of Texas at Arlington, Arlington 76019, USA

Correspondence should be addressed to Qinhong Hu; maxhu@uta.edu and Shengyu Yang; s.yang@upc.edu

Received 2 April 2020; Revised 20 July 2020; Accepted 31 July 2020; Published 25 August 2020

Academic Editor: Jianchao Cai

Copyright © 2020 Binyu Ma et al. This is an open access article distributed under the Creative Commons Attribution License, which permits unrestricted use, distribution, and reproduction in any medium, provided the original work is properly cited.

An effective porosity is defined as the ratio of volume of interconnected pore space to total volume of a porous sample. It controls the magnitude of fluid flow and is a key parameter in the assessment of recoverable resources. However, its accurate measurement in tight formations is challenging, due to their complex pore structure and lithofacies heterogeneity. In this study, porosities of sixteen lacustrine shale samples from the second Member of the Kongdian Formation (Ek_2) in the Cangdong Sag, Bohai Bay Basin were measured and compared using multiple methods and sample sizes to compare and contrast the effective porosity results. The methods included helium pycnometry (HP; cubes of 1 cm^3 and grains at $500\text{--}841\ \mu\text{m}$), water immersion porosimetry (WIP; cubes), mercury intrusion porosimetry (MIP; cubes), and nuclear magnetic resonance (NMR; cubes). Finally, samples were completely sealed using paraffin for bulk density measurements to evaluate the extent of potential clay swelling in shale samples involving probing fluids. Results from the HP, WIP, and MIP methods for skeletal density, bulk density, and effective porosity with cubic samples were compared. While very similar skeletal densities were found for all three methods, a lower bulk density, and therefore lower porosity, from the MIP approach can be attributed to the experimental conditions (e.g., vacuum efficiency, applied pressure, wettability of water/helium vs. mercury) and the probable presence of pores with diameters larger than $50\ \mu\text{m}$ not measurable by MIP. Furthermore, the HP porosity of granular samples with $500\text{--}841\ \mu\text{m}$ grain sizes can be regarded as approaching the total porosity. The complicated relationship between WIP and NMR porosities may result from the heat-induced volatilization of moisture in pores during NMR tests, and countercurrent imbibition of water replacing the residual hydrocarbons during the saturation process for sample preparation in both tests. The swelling behavior of the lacustrine Ek_2 shale with water is not significant because of the low content of expansive clay minerals. In summary, the WIP and HP methods are recommended for effective porosity measurement, whereas the NMR and MIP methods are invaluable for the measurement of pore-size distribution, with additional information on the effective porosity.

1. Introduction

The commercial exploration and production of marine-sourced shale gas and oil in the United States [1–4] and marine shale gas in China [5, 6] has led to significant attention being paid to oil resources in lacustrine shale reservoirs in China. Examples include the Shahejie Formation in Bohai Bay Basin [7], Qingshankou Formation in Songliao Basin [8], Yanchang Formation in Ordos Basin [9], and Luocaogou

Formation in Jungar Basin [10]. However, several notable characteristics of lacustrine shales in China, such as lower thermal maturity, generation of fluids with higher viscosities and high wax contents, and limited geographical distributions, pose greater challenges to a cost-effective development compared to marine petroleum systems [11]. Thus, in addition to a direct extraction of tight oil, *in situ* conversion technology plays a significant role in the development of lacustrine shale oil in China [12]. An evaluation by the

Research Institute of Petroleum Exploration and Development of PetroChina suggested that the recoverable resources of lacustrine shale oil reservoirs in China, with a thermal maturity (R_o) less than 1.0%, in these areas are as large as $700\text{--}900 \times 10^8 t$ using *in situ* conversion technology [13].

For either extraction approaches, a porosity measurement is important because it not only significantly affects the accuracy of resource estimates of reservoirs, but also determines favorable target areas, in conjunction with the hydrocarbon saturation and brittleness of shale reservoirs [4]. At present, porosity measurements of shale can be generally divided into the following categories: (1) gas expansion porosimetry, such as helium pycnometry (HP) for skeletal density with additional information on bulk density for calculating the porosity [14], as well as low-pressure gas physisorption with N_2 or CO_2 [15]; (2) three dimensional (3D) imaging techniques, such as microcomputed tomography (micro-CT), nano-CT, and focused ion beam-scanning electron microscopy (FIB-SEM) [16, 17]; (3) fluid immersion porosimetry (FIP), such as FIP with water (WIP) or kerosene (KIP) and dual liquid porosimetry (DLP), as well as mercury intrusion porosimetry (MIP) [18–22]; and (4) radiation detection methods, such as nuclear magnetic resonance (NMR) and small angle neutron scattering (SANS) [23–25]. Note that the approaches involving a probing fluid (e.g., He, N_2 , CO_2 , H_2O , and Hg) measure the effective (or connected portion of pore space linked to sample surface) porosity, while CT, SEM, and SANS detect the total (both connected and non-connected) porosity; in addition, gas physisorption, MIP, and NMR also quantify the pore-size (throat) distribution.

The low-pressure gas physisorption approach is usually used to characterize both macropores (>50 nm; according to the pore classification proposed by IUPAC [26]) and mesopores (2–50 nm) with N_2 , or micropores (<2 nm) with CO_2 , but this only covers a portion of the total pore space in shales, which have a broad spectrum of nm to μm pores [7]. The imaging approaches (nano-CT and FIB-SEM) are usually employed to observe the pore types and 3D distribution of pore networks, since the porosities from 3D reconstructions are not representative due to lower spatial resolution of micro-CT, and small scale of nano-CT and FIB-SEM analyses of heterogeneous shales [16]. Finally, the SANS approach has been recently employed to detect the volume of total (including both connected and non-connected/isolated pores), but it is limited by sample size as well as availability of the instrumentation [25].

Kuila et al. [20] measured the porosity of shales and mudrocks using the WIP technique and concluded that measurements were reproducible with a low uncertainty, due to insignificant swelling related to the low content of smectite and mixed-layered illite-smectite (I/S) in the samples. Porosity from KIP is consistently lower than that of WIP due to incomplete pore saturation by kerosene, as the migration of kerosene is restricted by clay- and capillary-bound water in samples with a high content ($\sim 40\%$) of partially expandable I/S [21]. Thus, WIP is widely used in porosity measurement of shales with low contents of expandable clays, as commonly found in unconventional hydrocarbon shale reservoirs [27].

The MIP technique can obtain a range of pore structure information of shale, such as pore volume and surface area, bulk and particle densities, porosity, and pore-throat size distribution from the Washburn Equation [28]. Furthermore, Katz and Thompson's method [29] has been adopted by Gao and Hu [30] to obtain the permeability from MIP data. Although the MIP approach has been widely used in pore characterization of shales, some problems, such as the compressibility of shale samples at intrusion pressures higher than 10,000 psi (68.9 MPa), and conformance effect from the irregularities of sample surfaces, can affect the accuracy of MIP results [31, 32]. Moreover, the existence of ink bottle pores will lead to overestimation of the contribution of smaller pores [30], but this makes MIP approach to detect pore-throat size distribution which is directly relevant to fluid flow and mass transport.

NMR refers to the response of atomic nuclei in external magnetic fields to cause resonance phenomenon [33]. Two NMR relaxations, longitudinal relaxation (T_1) and transverse relaxation (T_2), where T_2 is always faster than T_1 , arise after the magnetization and resonance of fluid protons in porous materials [34]. Porosity of shale can be obtained by comparing T_2 signals before and after fluid saturation [24, 35]. Moreover, the NMR technique has advantages of being rapid, nondamaging to the samples, and repeatable, and therefore has been widely applied in shale reservoir studies for porosity and pore-size distribution, as well as the content and movability of oil and water [24].

All of these approaches use different-sized samples for porosity analyses, and porosities measured show a significant dependence on sample size, especially for low-porosity samples [36]. Sample crushing is needed for most of these approaches, to accelerate the intrusion of fluids (i.e., water for WIP, mercury for MIP, and helium for HP) into pore spaces and reduce the time needed for fluid saturation equilibrium [14]. However, significant discrepancies have been found from various sample sizes used in porosity measurements. Comisky et al. [37] studied the effects of sample size on porosity using the MIP method, and indicated that the effective porosity of Eagle Ford shale increased with decreasing sample sizes, because some isolated pores were opened up by the crushing process. Good agreement between MIP and HP porosities using 20–35 mesh (500–841 μm) samples suggested that this sample size is optimal for shale porosity measurements [37]. Working with the Longmaxi shale in China, Sun et al. [38] suggested that sample sizes smaller than 60 mesh (250 μm) may alter the integrity of the original particle size composition. Thus, in this work samples with 20–35 mesh (500–841 μm) were prepared to measure the porosity using HP method, whereas cube-shaped samples (~ 1 cm^3) were prepared for WIP, NMR, MIP, and HP measurements. The latter were analyzed at two sample sizes so that we could assess the effect of sample size on results.

Using HP, WIP, MIP, and NMR techniques on lacustrine shale samples from the actively explored Bohai Bay Basin in East China [39], the purpose of this study was to assess the effective porosity values from multiple approaches, explain the differences in them, and evaluate the impact of

experimental conditions and sample composition (e.g., clay swelling and organic matter contents) on these measurements.

2. Samples and Methods

2.1. Sample Preparation and Basic Geochemical Properties. The Paleogene-aged second Member of the Kongdian Formation (Ek₂) in the Cangdong Sag, Bohai Bay Basin, East China was deposited in a deep and semideep lacustrine environment and mainly consists of black shales and mudstones with thin dolomite and siltstone interlayers [39–41]. Sixteen shale samples were acquired from five wells: A well (4 samples), B well (4 samples), C well (6 samples), D well (1 sample), and E well (1 sample) (Figure 1). Sample IDs and their burial depths are presented in Table 1.

Each sample was processed into three different sizes for the associated tests: (1) cube-shaped samples (~1 cm × 1 cm × 1 cm) for multiple porosity and density measurements; (2) granular samples with a particle size of 500–841 μm for HP skeletal density measurement [14]; and (3) powdered samples with a particle size < 75 μm (< #200 mesh) for TOC (total organic carbon) and pyrolysis tests. Sample size reduction was performed by gentle crushing using a mortar and pestle, followed by stainless steel sieves under wet rinsing.

Organic matter richness and quality are always important parameters of shales, due to their significant influence on shale pore structure and reserve assessment [3, 4]. TOC and pyrolysis analyses were performed using a LECO CS230 instrument and Rock-Eval 6 Analyzer, respectively, following established procedures [42]. The pyrolysis test provides several useful geochemical parameters, such as thermally extractable hydrocarbon content (S₁), maturity (T_{max}), and remaining hydrocarbon potential (S₂). The hydrogen index (HI) is calculated as 100 × S₂/TOC.

2.2. HP Measurement. The Gas Research Institute (GRI) method developed by Luffel and Guldry [14] has been widely employed in porosity and permeability measurements of the shale matrix. Combining bulk density of intact (i.e., cubic) samples (e.g., measured by mercury immersion using Archimedes' Principle), and skeletal density of granular samples (500–841 μm) measured by HP after crushing and then solvent extraction and followed by drying in an oven, the GRI porosity can be calculated as follows:

$$\phi_{\text{GRI}} = \frac{\rho_{\text{s-Granular sample}} - \rho_{\text{b-Intact sample}}}{\rho_{\text{s-Granular sample}}} \times 100. \quad (1)$$

However, there are potential sources of errors in the GRI procedure, such as an artificial increase in porosity by removing some organic matter during solvent extraction and different choices of drying temperatures (60°C, 105°C, or 200°C) [20]. In this study, two sample types, namely ~10 g granular and cube-shaped samples, were first oven-dried at 60°C for 48 h to evaluate the effective (instead of total [12]) porosity, and then cooled to about 23°C in a desiccator. Samples were not solvent extracted. The samples were then analyzed for skeletal density using the HP technique with a G-DenPyc

2900 instrument. Then, the HP porosity ($\phi_{\text{HP-GRI}}$ for granular samples or $\phi_{\text{HP-Cube}}$ for cube-shaped samples) was calculated using equation (2) and the bulk density (from the WIP test):

$$\phi_{\text{HP-GRI}} \text{ (OR } \phi_{\text{HP-Cube}}) = \frac{\rho_{\text{s-GRI}} \text{ (OR } \rho_{\text{s-Cube}}) - \rho_{\text{b-WIP}}}{\rho_{\text{s-GRI}} \text{ (OR } \rho_{\text{s-Cube}})} \times 100. \quad (2)$$

2.3. WIP Measurement. For cubic samples, the bulk density, skeletal density, and porosity were determined by saturating samples with a liquid (deionized (DI) water) and calculating the pore volume from the weight difference between the dry and fully-saturated (assisted with vacuum pulling) samples, followed by bulk volume determination using Archimedes' Principle [20]. This technique is called water immersion porosimetry (WIP) when DI water is used as the saturation fluid.

In this study, 1 cm sided cubes saw-cut from each sample were polished with 2000-grit sandpaper to smooth out surface roughness (the measured roughness is reduced from 1.26 ± 0.025 μm for saw-cut samples to ~0.2 μm) which would otherwise increase the uncertainty of the results. The smooth samples were first oven dried at 60°C for 48 h to remove the moisture and volatile hydrocarbons in the pore space without influencing the clay-bound water and destroying the structure of clay minerals [43]. The weight of dry samples in air (DW_{Air}) was measured using a Radwag AS 82/220.R2 (readability 0.01 mg). Using a custom-designed saturation apparatus, the samples were evacuated under a vacuum of ~200 Pa for 15 h inside the saturator and then were saturated with DI water under 15 MPa pressure for 24 h. Subsequently, the weight of the saturated sample in air (SW_{Air}), after removing the excess surface water with a slightly damp Kimwipe, was obtained, along with the submerged weight of the saturated sample in DI water (SW_{Sub}).

The bulk and skeletal densities of the sample were calculated from Equations (3) and (4).

$$\rho_{\text{b-WIP}} = \frac{DW_{\text{Air}}}{SW_{\text{Air}} - SW_{\text{Sub}}} \times \rho_{\text{H}_2\text{O}}, \quad (3)$$

$$\rho_{\text{s-WIP}} = \frac{DW_{\text{Air}}}{DW_{\text{Air}} - SW_{\text{Sub}}} \times \rho_{\text{H}_2\text{O}}, \quad (4)$$

where $\rho_{\text{H}_2\text{O}}$ is the density of DI water at the experimental temperature (around 23°C). Following Haynes et al. [44], $\rho_{\text{H}_2\text{O}}$ is calculated using equation (5) as a function of temperature, which does not vary much:

$$\rho_{\text{H}_2\text{O}} = -0.0000053T^2 + 0.0000081T + 1.0001627, \quad (5)$$

where T is the temperature of DI water. The porosity (ϕ_{WIP}) of the sample measured by the WIP technique is then calculated using equation (6):

$$\phi_{\text{WIP}} = \frac{\rho_{\text{s-WIP}} - \rho_{\text{b-WIP}}}{\rho_{\text{s-WIP}}} \times 100. \quad (6)$$

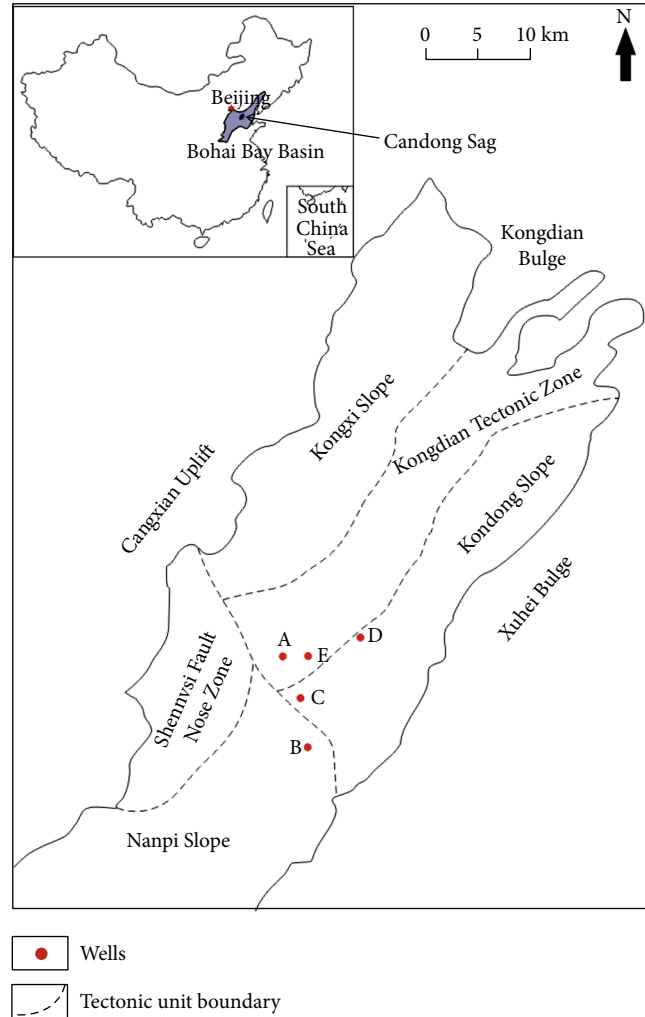


FIGURE 1: Map of Cangdong Sag in Bohai Bay Basin and location of five sampling wells (modified from [41]).

2.4. MIP Measurement. MIP analysis is one of the most efficient methods to characterize pore structure for a wide range of porous media [7, 22, 45], because mercury has a high surface energy and is nonwetting. Liquid mercury is injected into the pore networks by incrementally overcoming the capillary pressure. Assuming that pores are cylindrical in shape, the relationship between applied pressure and the pore-throat size can be described using the Washburn equation [27]. The incremental mercury intrusion volume is monitored at each applied pressure to obtain the cumulative pore volume. Combining the pore volume and sample volume, which is obtained by subtracting the mercury volume at a low applied pressure (just to envelop the sample surface, without mercury intrusion into the pore space, to obtain the bulk volume) from the volume of the penetrometer when empty, the porosity (ϕ_{MIP}) can be calculated. Then, the bulk density ($\rho_{\text{b-MIP}}$) and skeletal density ($\rho_{\text{s-MIP}}$) can be calculated from mercury weight (volume) at the beginning and end of MIP tests.

Before the MIP experiments, each smooth cube-shaped sample was oven dried at 60°C for at least 48 h. A Micromer-

tics AutoPore IV 9520 was utilized to measure porosity and pore-throat size distribution (not a focus of this work) under the intrusion pressures from 5 psi (0.034 MPa) to 60,000 psi (413 MPa), corresponding to pore-throat sizes from 50 μm to 2.8 nm using the modified Washburn equation of considering both the variable contact angle and surface tension of mercury in nm-sized pore throats [46]. At the beginning of the MIP tests, the samples were evacuated to 50 μm Hg pressure (6.7 Pa), and an equilibration time of 60 s was selected at each applied pressure point. The skeletal density obtained from the MIP measurement was used to compare with the same data from WIP and HP methods.

2.5. NMR Measurement. Porosity can be calculated from the T_2 spectrum in NMR tests, as the amplitude of T_2 is proportional to the number of hydrogen atoms, which is in turn used to determine the fluid (i.e., pore) volume within a sample [24]. In this study, the T_2 spectrum was measured successively in dry and water saturated samples using a MesoMR23-060H-I, NIUMAG Corporation. The porosity

was calculated based on the ΔT_2 between dry and saturated samples, to remove the influence of background signals from the presence of hydrogen-containing organic matter, clay-bound water, and structural water in shale [24]. The saturated sample was analyzed by NMR after the WIP measurement on that sample, which provides the bulk volume needed in the calculation of porosity from NMR data. In this work, the NMR experimental parameters were as follows: echo interval TE, 0.1 ms; waiting time TW, 3000 ms; number of scans, 32 times; number of echoes, 6000 times.

2.6. Bulk Density Measurements from Sample Envelopment. In addition to the abovementioned methods, the bulk density

of a sample can be measured using Archimedes' Principle after being totally sealed by a nonwetting material such as paraffin (following the Chinese National Standard GB/T 23561.3-2009) [47]. The cube-shaped samples were used to measure bulk density by this method after NMR measurement. Firstly, the air-dry sample was weighed in air (W_{Sample}). Then paraffin, with a measured density (ρ_{Paraffin}) of $0.9225 \text{ cm}^3/\text{g}$, was employed to seal the sample. After that, the sample with paraffin was weighed in air ($W_{\text{Sample+Paraffin}}$) and in DI water ($SW_{\text{Sample+Paraffin}}$). Finally, the bulk density of the sample ($\rho_{\text{b-Paraffin-sealing}}$) can be determined from equation. (7).

$$\rho_{\text{b-Paraffin-sealing}} = \frac{W_{\text{Sample}}}{(W_{\text{Sample+Paraffin}} - SW_{\text{Sample+Paraffin}})/\rho_{\text{H}_2\text{O}} - (W_{\text{Sample+Paraffin}} - W_{\text{Sample}})/\rho_{\text{Paraffin}}}. \quad (7)$$

Furthermore, a Micromeritics GeoPyc 1365 instrument was employed to measure the bulk density of oven-dried cubic samples with $\sim 100 \mu\text{m}$ diameter DryFlo[®] as the enveloping material [48]. The result can be compared with the results of the WIP and paraffin-sealing methods to evaluate the extent of swelling on shale samples from contact with water in WIP tests. To verify the effect of clay minerals, especially expandable smectite and mixed-layered illite-smectite, on sample swelling, the quantitative abundance of clay minerals was obtained by X-ray diffraction (XRD) analyses using powdered sample ($< 75 \mu\text{m}$).

3. Results

3.1. Total Organic Carbon (TOC) and Pyrolysis and Clay Minerals. TOC and pyrolysis data are given in Table 1. TOC values range from 0.44 to 8.20 wt.%, with an average of 2.93 wt.% and standard deviation of 1.98 wt.%. Most samples are organic-rich with TOC contents greater than 2 wt.%. The S_1 values obtained from pyrolysis tests range from 0.23 to 4.52 mg HC/g rock, with an average of 2.19 and standard deviation of 1.44 mg HC/g rock. HI values range from 109 to 681. All samples except for three have TOC $> 1.5\%$ and HI > 300 , suggesting they are good oil-prone source rocks. Two samples have TOC $< 0.5\%$ and HI < 150 , suggesting they are and always were poor source rocks. The T_{max} ranges from 442 to 450°C, indicating the samples are mature for oil generation, which is consistent with other studies [39, 40].

The clay mineral contents range from 3 to 45% ($N = 16$), with a mean value of 21% (Table 1). The relative concentrations of mixed-layered illite-smectite to total clay minerals average 41% and range between 7 to 82%, and the smectite contents range from 2 to 47%, with the values below detection for almost half of 16 samples.

3.2. Sample Densities

3.2.1. Bulk Density from WIP, Paraffin-Sealing, and DryFlo-Envelopment Methods. As shown in Table 2, the bulk density

values obtained from WIP tests range from 2.060 to 2.538 g/cm^3 ($2.425 \pm 0.119 \text{ g/cm}^3$; average \pm standard deviation), very close to these from the paraffin-sealing method at 2.070 to 2.549 g/cm^3 ($2.445 \pm 0.122 \text{ g/cm}^3$). A comparison of results for 16 samples from these two methods is shown in Figure 2, in which the bulk density of WIP measurement is similar to or smaller than that of samples sealed by paraffin. The relative difference in bulk density between the WIP and paraffin-sealing methods ranges from 0.125 to 1.47%; sample B-3834 has the highest relative difference of 3.10%. The results for five samples from DryFlo[®] envelopment are also shown in Table 2, and the comparison with WIP results is shown in Figure 2. The results with DryFlo[®] are slightly larger than those of WIP tests, with the range of relative difference from 0.14 to 1.40%.

3.2.2. Skeletal Density from HP, WIP, and MIP Methods. Skeletal density of cube-shaped samples was obtained from WIP, MIP, and HP measurements, whilst the HP test was also conducted on granular samples. Skeletal densities from these methods are shown in Table 2. The skeletal density of granular samples from HP ranges from 2.242 to 2.648 g/cm^3 ($2.550 \pm 0.093 \text{ g/cm}^3$), which is systematically larger than the results of all other measurements (Table 2; Figure 3). The results from WIP range from 2.175 to 2.629 g/cm^3 ($2.515 \pm 0.106 \text{ g/cm}^3$), whereas the skeletal density from MIP ranges from 2.187 to 2.608 g/cm^3 ($2.517 \pm 0.100 \text{ g/cm}^3$). Figure 3 shows the comparison of skeletal density results from WIP and MIP measurements (blue circles), which is seen clustering around the 1:1 line. A slight increase in HP densities of almost all cube-shaped samples compared with these of WIP tests is also shown in Figure 3 (red diamonds).

3.3. Effective Porosity of the Samples. Four different methods (HP, WIP, MIP, and NMR) were employed to measure the effective porosity of cube-shaped samples, and the results

TABLE 1: Basic information of Ek₂ samples employed in this study.

Sample	Depth (m)	TOC (%)	S ₁ (mg/g)	S ₂ (mg/g)	T _{max} (°C)	HI (mg/g)	Total clays (%)	Smectite (%)	Illite (%)	Mixed-layered illite-smectite (%)
A-3143	3143.87	2.49	1.28	18.08	443	726	20.64	33	22	22
A-3150	3150.23	1.66	0.81	9.68	442	583	12.41	5	22	59
A-3161	3161.47	1.56	0.54	9.62	444	617	20.23		13	82
A-3268	3268.09	6.44	2.61	43.83	446	681	44.75		13	80
B-3831	3831.92	0.48	0.29	0.59	445	123	43.70	2	24	44
B-3834	3834.15	0.44	0.23	0.48	450	109	32.34	2	27	41
B-3847	3847.25	2.79	3.93	10.81	446	387	17.82		21	10
B-3859	3859.39	4.72	3.87	22.73	446	482	9.90	37	5	19
C-4081	4081.55	2.6	3.39	14.55	450	560	12.51		44	51
C-4095	4095.27	1.79	4.52	6.67	442	373	16.05	32	20	13
C-4096	4096.66	2.02	4.02	8.46	443	419	13.99		20	77
C-4113	4113.26	2.2	1.6	9.33	447	424	13.51	20	21	1
C-4116	4116.29	3.37	3.03	8.01	443	238	3.36	10	20	18
C-4126	4126.07	2.4	2.47	9.11	445	380	11.77		21	75
D-2916	2916.19	3.7	0.45	21.15	443	572	33.90	47	3	25
E-2603	2603.31	8.2	1.94	53.76	446	656	34.91		13	39

TABLE 2: Results of bulk and skeletal densities from various methods.

Sample	HP		WIP		MIP	Sealed by paraffin	Enveloped by DryFlo
	Skeletal density (g/cm ³)	Skeletal density ¹ (g/cm ³)	Bulk density (g/cm ³)	Skeletal density (g/cm ³)	Skeletal density (g/cm ³)	Bulk density (g/cm ³)	Bulk density (g/cm ³)
A-3143	2.514 ± 0.002	2.552 ± 0.004	2.404 ± 0.012	2.491 ± 0.008	2.510	2.412	
A-3150	2.587 ± 0.003	2.594 ± 0.004	2.457 ± 0.018	2.585 ± 0.016	2.575	2.486	2.463
A-3161	2.595 ± 0.002	2.619 ± 0.004	2.454 ± 0.002	2.590 ± 0.002	2.565	2.451	2.489
A-3268	2.383 ± 0.002	2.435 ± 0.003	2.265 ± 0.001	2.381 ± 0.001	2.424	2.282	
B-3831	2.624 ± 0.007	2.648 ± 0.006	2.473 ± 0.003	2.629 ± 0.004	2.589	2.500	
B-3834	2.583 ± 0.005	2.598 ± 0.005	2.449 ± 0.004	2.586 ± 0.003	2.517	2.528	
B-3847	2.526 ± 0.009	2.547 ± 0.009	2.465 ± 0.025	2.506 ± 0.022	2.534	2.489	2.469
B-3859	2.501 ± 0.008	2.544 ± 0.008	2.420 ± 0.015	2.498 ± 0.016	2.502	2.440	2.454
C-4081	2.528 ± 0.002	2.549 ± 0.011	2.477 ± 0.009	2.526 ± 0.008	2.514	2.499	
C-4095	2.593 ± 0.005	2.605 ± 0.005	2.525 ± 0.004	2.591 ± 0.002	2.600	2.537	
C-4096	2.532 ± 0.004	2.545 ± 0.009	2.463 ± 0.006	2.528 ± 0.012	2.580	2.499	
C-4113	2.568 ± 0.007	2.578 ± 0.006	2.513 ± 0.009	2.566 ± 0.016	2.576	2.521	
C-4116	2.571 ± 0.006	2.618 ± 0.007	2.538 ± 0.001	2.566 ± 0.002	2.608	2.543	
C-4126	2.555 ± 0.004	2.605 ± 0.008	2.526 ± 0.004	2.563 ± 0.001	2.559	2.549	2.543
D-2916	2.468 ± 0.008	2.513 ± 0.004	2.305 ± 0.002	2.457 ± 0.007	2.433	2.316	
E-2603	2.177 ± 0.002	2.242 ± 0.010	2.060 ± 0.026	2.175 ± 0.028	2.187	2.070	

¹Data for granular samples; all other data are for cubic samples.

are shown in Table 3. The effective porosity of cube-shaped samples from HP tests, calculated using HP-derived skeletal density and WIP bulk density, ranges from 1.13 to 6.62%. The effective porosity of samples from WIP ranges from 1.10 to 6.20%, whereas the effective porosity from MIP and NMR measurements ranges from 0.41 to 3.55% and from 1.88 to 4.04%, respectively. In addition, the HP measurement

were also conducted on granular samples, and the results range from 2.52 to 8.30% (Table 3). The values of HP porosity ($4.93 \pm 1.91\%$) of the granular samples are the highest, in a decreasing order followed by the porosity values for cubes measured by HP ($3.77 \pm 1.69\%$), WIP ($3.60 \pm 1.70\%$), NMR porosity ($2.86 \pm 0.56\%$), and MIP ($2.05\% \pm 0.92\%$) (Table 3; Figure 4).

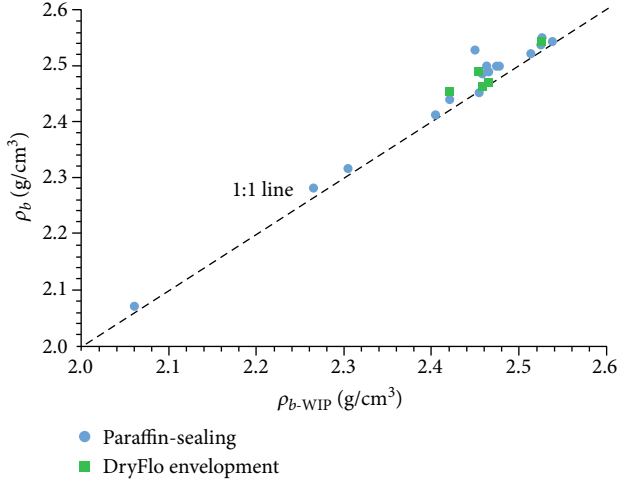


FIGURE 2: Comparison of bulk density measured from the WIP, paraffin-sealing, and DryFlo-enveloping techniques; the x -axis is for bulk density from the WIP method, and the y -axis from the paraffin-sealing and DryFlo-enveloping methods. The WIP bulk density is smaller than the other methods when the point is located above the 1 : 1 line.

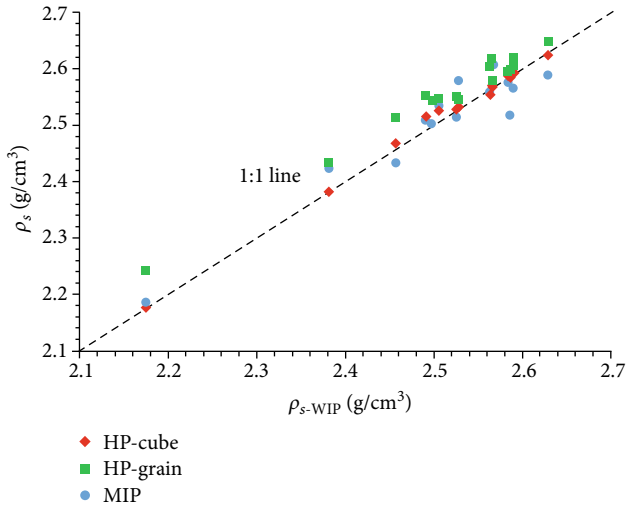


FIGURE 3: Comparison of skeletal density measured from the HP, WIP, and MIP techniques; the x -axis presents skeletal density from the WIP method and the y -axis from the HP and MIP methods, with smaller values from WIP than from the other methods indicated by the data located above the 1 : 1 line.

4. Discussion

4.1. WIP and NMR Methods Employing Water as the Probing Fluid. Shale is a unique hydrocarbon reservoir due to its pronounced heterogeneity with comingling composition such as organic matter and inorganic matrices [3, 4]. The same sample cubes were employed to measure the NMR porosity following the WIP measurement, to minimize the impact of shale heterogeneity when cutting $\sim 1 \text{ cm}^3$ sized cubes. Equally importantly, WIP provides the sample bulk volume to go with the calculation of porosity from NMR analyses. The

TABLE 3: Results of effective porosity from four methods.

Sample	HP porosity (%)		WIP porosity (%)	MIP porosity (%)	NMR porosity (%)
	Cube	GRI			
A-3143	4.357	5.776	3.480	0.917	2.697
A-3150	5.025	5.266	4.920	2.134	3.131
A-3161	5.422	6.288	5.224	2.696	3.363
A-3268	4.957	6.987	4.896	2.532	3.083
B-3831	5.737	6.607	5.916	2.790	3.406
B-3834	5.178	5.714	5.302	2.806	2.915
B-3847	2.398	3.187	1.603	2.750	1.957
B-3859	3.221	4.870	3.091	2.590	2.986
C-4081	2.025	2.847	1.944	1.067	2.812
C-4095	2.636	3.084	2.549	0.742	3.098
C-4096	2.737	3.234	2.595	2.910	2.572
C-4113	2.144	2.523	2.084	1.363	1.875
C-4116	1.291	3.055	1.097	1.109	2.194
C-4126	1.128	3.043	1.448	0.406	2.327
D-2916	6.623	8.295	6.198	2.402	4.042
E-2603	5.367	8.109	5.276	3.549	3.333

comparison between WIP and NMR effective porosity is shown in Figure 5, and three regions can be divided and marked according to the porosity range. In Region I with WIP porosity $< 2\%$, the NMR porosity is generally greater than the WIP porosity. This is the opposite of Region III, in which the WIP porosity is greater than the NMR porosity for WIP porosities greater than 4%. In the intermediate region, data plot on or close to the 1 : 1 line.

The difference between WIP and NMR porosities is probably due to an increase in experimental temperature inside the sample container during the analysis by NMR, which takes ~ 5 min for each sample analysis, that could result in a heat-induced loss of moisture in the samples, especially in macropores near the surfaces of the samples. In addition, a countercurrent imbibition may occur during the vacuum saturation process to displace some residual hydrocarbons from the as-received (i.e., not solvent cleaned) shale samples [49–51]; however, this will influence both the WIP and NMR results. Imbibition may influence the WIP results because the density of hydrocarbons ($0.86\text{--}0.89 \text{ g/cm}^3$ at 20°C) from Ek₂ shale reservoir is less than 0.998 g/cm^3 of DI water [39]. However, the heating pretreatment of samples may potentially result in an increase of density of residual hydrocarbons by removing some lighter components that would reduce the influence of imbibition on WIP results; it is reported that shale oil produced from the Ek₂ Formation has a high content of asphaltenes at 16–76%, with an average of 39% [52]. Thus, the values of difference in hydrogen index between residual hydrocarbons and DI water is quite higher than the values of density difference between hydrocarbons and DI water. Therefore, the imbibition may have greater influence on NMR porosity, especially the samples with lower porosity (e.g., Region I), in which the high proportion of small pores with large capillary forces may have a stronger imbibition effect [53].

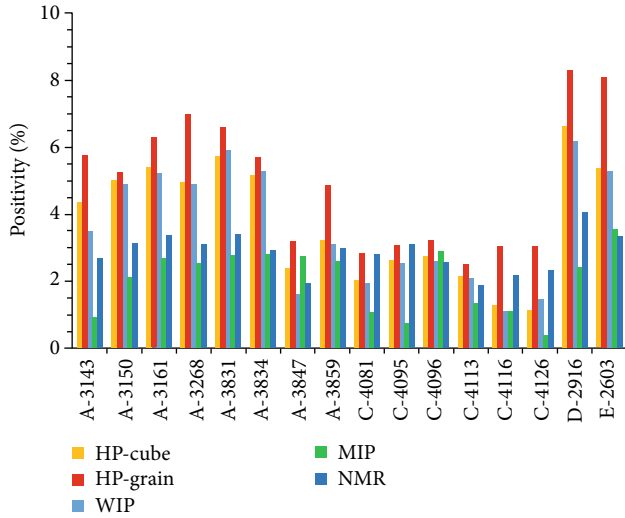


FIGURE 4: Histogram comparison of porosities from the four different methods for each sample.

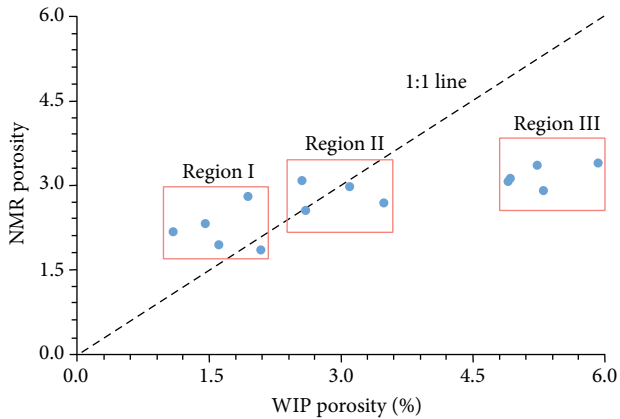


FIGURE 5: Comparison of porosities from WIP and NMR measurements. Three regions are divided according to absolute difference between porosities from two methods.

Furthermore, the experimental parameters play an extremely critical role in NMR measurements. In previous studies of shale samples, the echo interval TE usually ranges from 0.06 to 0.2 ms [24], and a shorter echo interval TE may potentially cause an enhancement of the T_2 spectrum amplitude of small pores but a reduction for large pores. In contrast, longer echo interval TE would lose some signals of small pores and cause a lower value of NMR porosity [24]. The porosity may be potentially underestimated by NMR due to the wide pore-size range of Ek₂ shale samples, in which abundant inorganic and organic pores are protected by a high proportion of brittle minerals from compaction [39]. In addition, a shorter waiting time TW may result in nonmagnetization of some of the atomic nuclei of fluids in large pores and therefore less detection of large pores. At the same time, the number of scans may cause varying results depending on the strength of resonance signals. Overall, in this study using the same cubic samples, we modified the parameters of waiting time TW and number of scans to

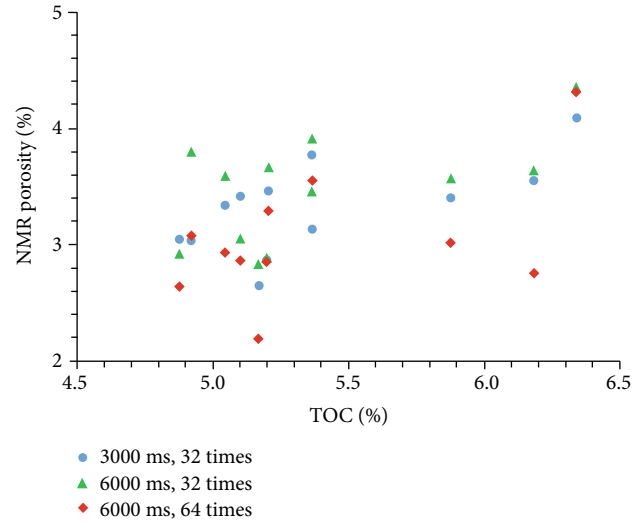


FIGURE 6: Porosities from NMR tests with different experimental parameters.

6000 ms and 64 times, respectively, to assess the influence of experimental parameters on NMR porosity. An increase in measured porosity is shown in Figure 6 as a result of the increase in waiting time TW for a given sample. However, with the number of scans changed from 32 to 64 times, an unexpected decrease in NMR porosity shows up in Figure 6; this may be due to the increase in water loss from samples because of the nearly doubled experimental time. Thus, controls of temperature and humidity during the NMR measurements are critical, as are the experimental parameters.

4.2. Multifluid Impact on HP, WIP, and MIP Methods. The HP technique is a very common method for skeletal density measurements due to the smaller molecular size of helium compared with water or other fluids, and its inertness towards organic matter and inorganic matrices increases its ability to access more pores. However, no significant difference is shown between HP and WIP skeletal densities for the same sample size (Figure 3). It is possible that some small pores may not be accessed by helium since it is likely to be a nonwetting phase for the as-received shale samples, whereas the shale samples adsorb more water due to the existence of hydrophilic minerals and bound water.

Although two different fluids, DI water and mercury, were employed in WIP and MIP measurements, the skeletal densities of samples from two methods are generally comparable (Table 2; Figure 3). In MIP, the highest pressure was up to 60,000 psi (413 MPa), which is much higher than the saturating pressure (15 MPa) applied in WIP. The higher vacuum used in MIP measurement (50 μ m Hg pressure or 6.7 Pa), compared with that of WIP measurement (200 Pa), contributes to the invasion of mercury into evacuated pore space [22]. Compared with mercury, DI water experiences less resistance to small pores during the invasion due to the existence of hydrophilic minerals and pores.

Effective porosities from WIP tend to be significantly higher than those from MIP (Table 3; Figure 4). This can

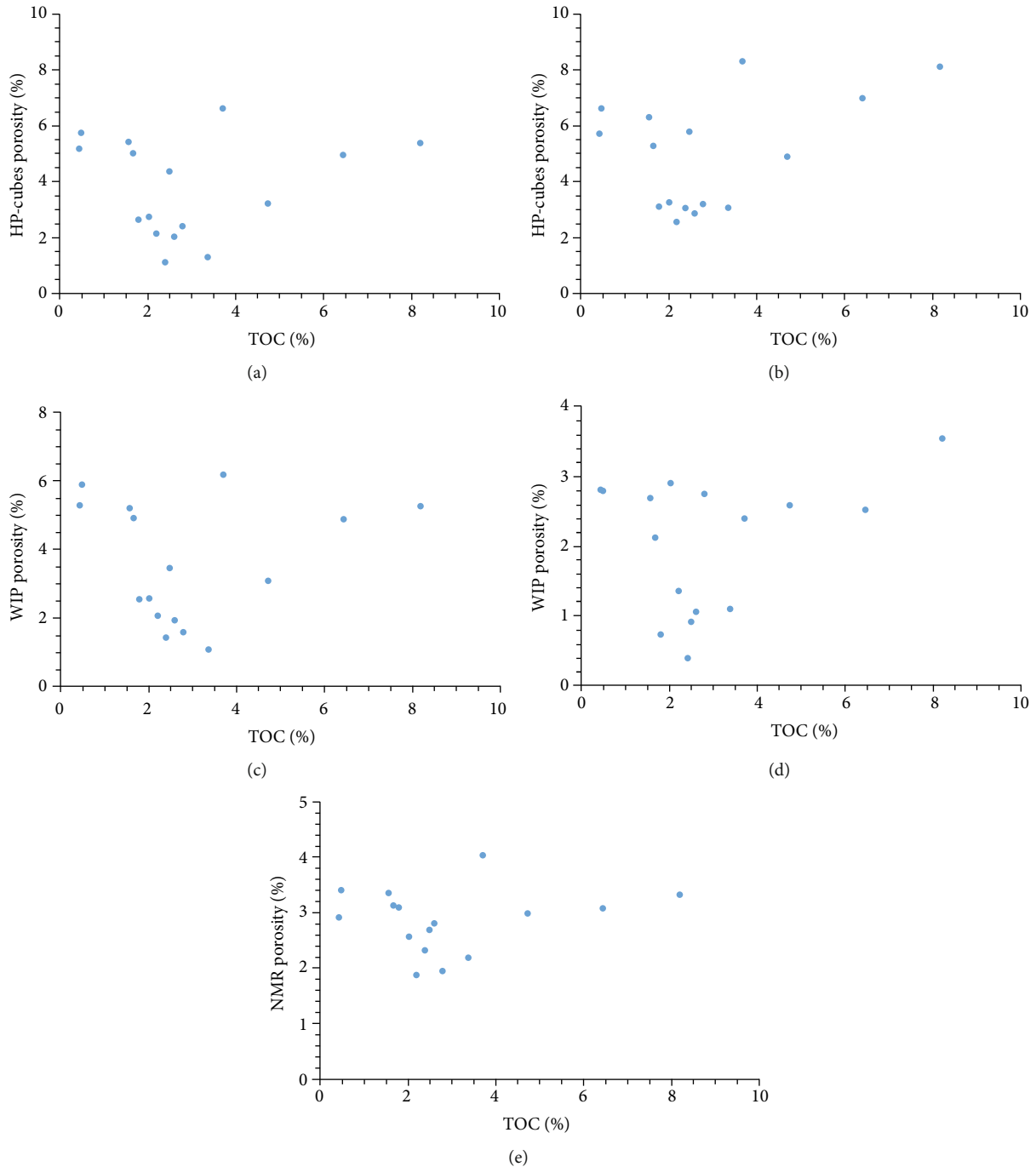


FIGURE 7: Relationships between TOC and porosities from different methods.

be attributed to undetected pore-throat diameter ranges larger than $50\ \mu\text{m}$ or smaller than $2.8\ \text{nm}$ in MIP. In addition, sample compressibility and fractures induced under high pressures are potential factors in MIP measurements that would influence both effective porosity and skeletal density data [30, 31]. The size and structure of clay minerals might impact effective porosity and permeability analyses of tight shale, due to the potential plugging of pore channels [54, 55].

Comparisons of the skeletal density and effective porosity values calculated using HP measurement on granular sam-

ples and WIP are shown in Figures 3 and 4. The reduced granular size systematically result in somewhat higher values of skeletal density and much higher values of porosity, because isolated pores in the larger samples are made accessible to the probing fluids when crushed to grains [37]; isolated pores are dominant in tight shale and the relative abundance is proportional to the sample size [36]. Thus, the HP porosity of granular samples at $500\text{-}841\ \mu\text{m}$ can be considered to be a good approximation of the “total” porosity, and the difference between HP and WIP porosities could indicate the extent of isolated porosity.

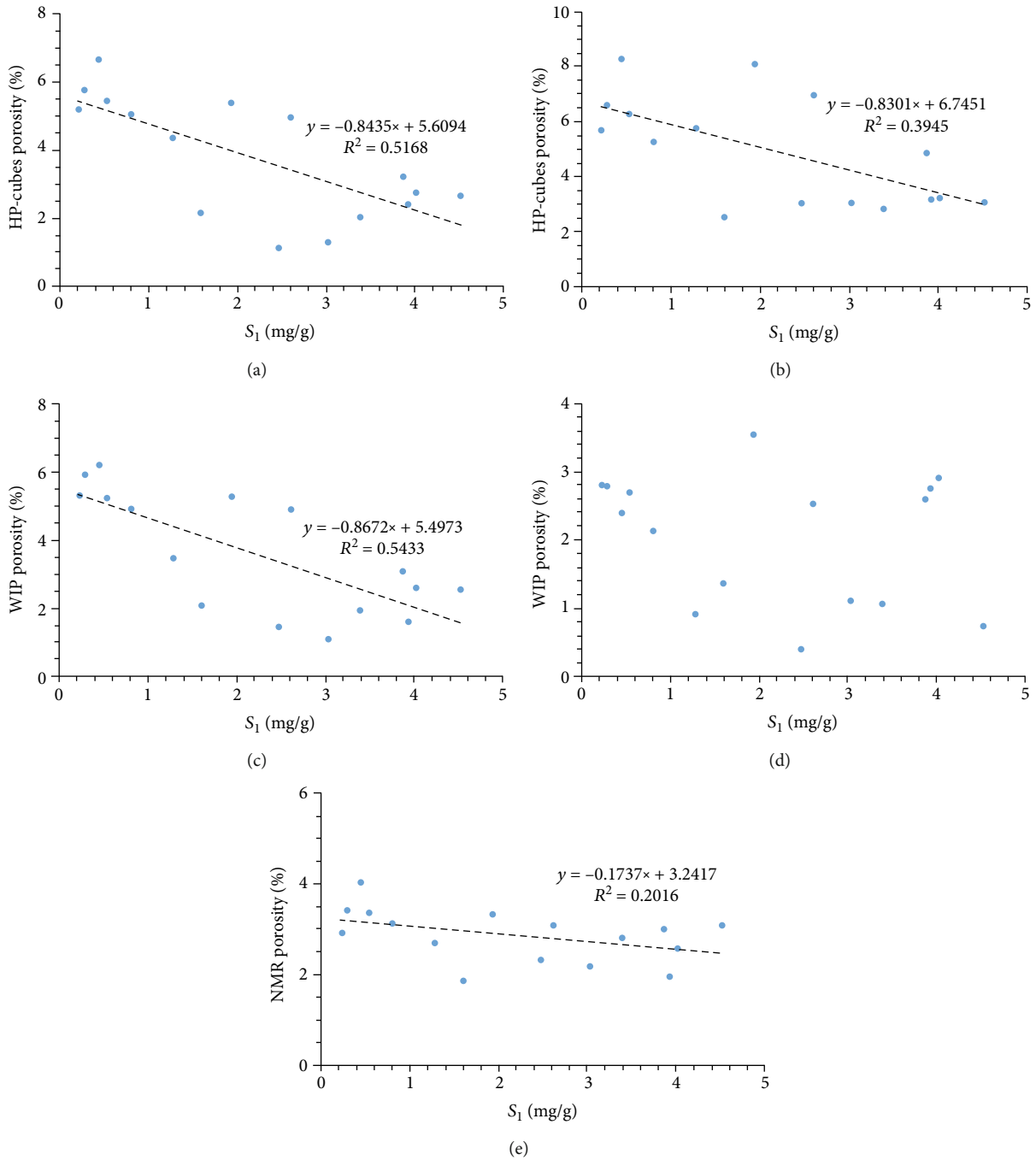


FIGURE 8: Relationships between S_1 and porosities from different methods.

4.3. Bulk Density Measurements Implicated by Clay Swelling.

In this study, three methods (WIP, paraffin-sealing, and DryFlo® envelopment) were used to measure the bulk density of samples (Section 3.2.1 and Table 2). The DryFlo method tended to give the highest densities, followed by WIP, then “sealed by paraffin” methods. A possible reason for the difference between the three methods could be the clay swelling ability of clay minerals, especially smectite and mixed-layered illite-smectite, during the saturation process with DI water. Ek₂ shale reservoirs have oil window thermal maturities, with the majority of smectite already transformed to mixed-layered illite-smectite and illite [39, 40]. Thus, the

relative difference in bulk density from WIP and the other two methods is less than 2% (Table 2). In addition, there is no clear relationship between clay minerals and relative difference in porosity, suggesting a minor effect of clay swelling in our results. Generally, a slight swelling of Ek₂ shale samples and the resulting experimental uncertainty is acceptable. In addition, a higher vacuum followed by a reduced time of saturation during the WIP tests could help to reduce the degree of sample swelling [21].

4.4. Effects of Organic Matter on Porosity Measurements.

Abundant pores in organic matter could make a significant

contribution to shale porosity, especially in gas shales at high thermal maturities [15]. In this work, no significant relationships are observed between TOC and effective porosities from HP, WIP, MIP, and NMR measurements. A very slight positive relationship between TOC and porosity of samples is shown in Figure 7, which suggests limited contributions of organic matter-hosted pore volumes to the porosity of samples.

Negative-to-no relationships between S_1 and porosities are shown in Figure 8, indicating that some pores might be occupied by bitumen and liquid hydrocarbons. Solvent extraction, which removes both liquid and solid (bitumen) hydrocarbons, has been shown to increase porosity in previous studies [56, 57]. In Figure 8(d), the complicated relationship between S_1 and MIP porosity may result from the residual hydrocarbons in pores pushed by mercury under high pressure to migrate at micro- to nanolevels [56].

5. Conclusions

In this study, sixteen lacustrine shale samples from Ek₂ in Cangdong Sag in Bohai Bay Basin in East China were studied to quantify the effective porosity and bulk and skeletal densities using HP, WIP, MIP, and NMR techniques. The porosities measured by WIP and NMR methods are noticeably different, which may potentially result from moisture loss in pores during NMR measurement (heat-controlling approaches have been developed and implemented for follow-on studies) and countercurrent imbibition during the saturation process. In addition, the experimental parameters used in NMR need to be considered to detect total effective pores without an underestimation from signal losses.

A slight increase of skeletal density is observed for HP compared with that of WIP, because of a small molecular size of helium and imperfect wetting to water of the shale, while the deviation of MIP skeletal densities can be attributed to the experimental conditions (e.g., vacuum efficiency, applied pressure, and wettability of water/helium vs. mercury). Porosities of granular samples measured by HP are the highest among the four methods, because more isolated pores can start to be liberated in smaller granular sizes (i.e., 500–841 μm), and so this can be considered as close to the “total” porosity. The HP method is versatile in dealing with a range of sample sizes, and we are currently using it for independent measurements of both skeletal and bulk densities for a wide range of granular sizes (from 2.54 cm diameter core plugs down to $\sim 30 \mu\text{m}$ granular samples) to identify when the “total porosity” is achieved. The difference between HP porosity of granular samples and WIP porosity of cube-shaped samples may indicate the extent of isolated porosity. Complementary approaches to quantifying the total (both effective/connected and nonconnected), such as SANS and FIB-SEM, are also ongoing.

Although clay swelling was suspected on Ek₂ shale samples, its effect on results from WIP measurements is insignificant because of the low content of clay minerals, especially with clay types of predominantly mixed-layered illite-smectite with a partial expandability but only a modest amount of much more expandable smectite. Therefore,

WIP could be employed to measure the porosity of samples with low contents of expandable clay minerals, and the HP tests are suitable for total effective porosity measurements. Whereas the NMR and MIP methods are best suited for analyzing the pore-size distribution, as well as providing ancillary values of porosity. While relevant to subsurface conditions, the porosity measurements of as-received samples with high residual shale oil contents in this work may have restricted usage in assessing total porosity for resource evaluation, due to the partial blockage of residual oil during the measurement, as suggested by a weak negative relationship between S_1 and porosities. The work of solvent extraction on these samples with the follow-on porosity quantification is ongoing.

Data Availability

All laboratory data used to support the findings of this study are included within the article.

Disclosure

We would also like to declare that the work in this manuscript is an original research that has not been published previously or submitted to another journal.

Conflicts of Interest

The authors declare that they have no known competing financial interests or personal relationships that could have appeared to influence the work reported in this paper.

Acknowledgments

This work was funded by the National Natural Science Foundation of China (Nos. 41830431 and 41802146) and the Key Laboratory of Unconventional Petroleum Geology, China Geological Survey (No. 30200018-19-ZC0613-0065). The authors would like to thank Dagang Oilfield Company of China National Petroleum Corporation (CNPC) for providing the core samples used in this work.

References

- [1] K. A. Bowker, “Barnett Shale gas production, Fort Worth Basin: issues and discussion,” *AAPG Bulletin*, vol. 91, no. 4, pp. 523–533, 2007.
- [2] R. G. Loucks and S. C. Ruppel, “Mississippian Barnett Shale: lithofacies and depositional setting of a deep-water shale-gas succession in the Fort Worth Basin, Texas,” *AAPG Bulletin*, vol. 91, no. 4, pp. 579–601, 2007.
- [3] C. R. Clarkson, J. L. Jensen, and S. Chipperfield, “Unconventional gas reservoir evaluation: what do we have to consider?,” *Journal of Natural Gas Science and Engineering*, vol. 8, pp. 9–33, 2012.
- [4] D. M. Jarvie, “Shale resource systems for oil and gas: part 2—shale-oil resource systems,” *AAPG Memoir*, vol. 97, pp. 89–119, 2012.
- [5] L. Chen, L. Zuo, Z. Jiang et al., “Mechanisms of shale gas adsorption: evidence from thermodynamics and kinetics study

- of methane adsorption on shale,” *Chemical Engineering Journal*, vol. 361, pp. 559–570, 2019.
- [6] R. Yang, Q. Hu, S. He et al., “Wettability and connectivity of overmature shales in the Fuling gas field, Sichuan Basin (China),” *AAPG Bulletin*, vol. 103, no. 3, pp. 653–689, 2019.
- [7] Q. Hu, Y. Zhang, X. Meng, Z. Li, Z. Xie, and M. Li, “Characterization of micro-nano pore networks in shale oil reservoirs of Paleogene Shahejie Formation in Dongying Sag of Bohai Bay Basin, East China,” *Petroleum Exploration and Development*, vol. 44, no. 5, pp. 720–730, 2017.
- [8] B. Liu, J. Shi, X. Fu et al., “Petrological characteristics and shale oil enrichment of lacustrine fine-grained sedimentary system: a case study of organic-rich shale in first member of Cretaceous Qingshankou Formation in Gulong Sag, Songliao Basin, NE China,” *Petroleum Exploration and Development*, vol. 45, no. 5, pp. 884–894, 2018.
- [9] X. Tang, J. Zhang, X. Wang, B. Yu, W. Ding, and L. Zhang, “Geochemical characteristics and estimation of gas content of the low-middle mature continental shales: a case study from the Ordos Basin,” *2013 AAPG Annual Convention and Exhibition*, vol. 10517, p. 35, 2013.
- [10] S. Zhang, C. Liu, H. Liang et al., “Paleoenvironmental conditions, organic matter accumulation, and unconventional hydrocarbon potential for the Permian Lucaogou Formation organic-rich rocks in Santanghu Basin, NW China,” *International Journal of Coal Geology*, vol. 185, pp. 44–60, 2018.
- [11] B. Katz and F. Lin, “Lacustrine basin unconventional resource plays: key differences,” *Marine and Petroleum Geology*, vol. 56, pp. 255–265, 2014.
- [12] Y.-H. Sun, F.-T. Bai, X.-S. Lü et al., “A novel energy-efficient pyrolysis process: Self-pyrolysis of oil shale triggered by topochemical heat in a horizontal fixed bed,” *Scientific Reports*, vol. 5, no. 1, p. 8290, 2015.
- [13] W. Zhao, H. Suyun, L. Hou et al., “Types and resource potential of continental shale oil in China and its boundary with tight oil,” *Petroleum Exploration and Development*, vol. 47, no. 1, pp. 1–11, 2020.
- [14] D. L. Luffel and F. K. Guldry, “New core analysis methods for measuring reservoir rock properties of Devonian shale,” *Journal of Petroleum Technology*, vol. 44, pp. 1184–1190, 2013.
- [15] R. Yang, S. He, Q. Hu, D. Hu, S. Zhang, and J. Yi, “Pore characterization and methane sorption capacity of over-mature organic-rich Wufeng and Longmaxi shales in the southeast Sichuan Basin, China,” *Marine and Petroleum Geology*, vol. 77, pp. 247–261, 2016.
- [16] G. Wang, H. Yu, and B. De Man, “An outlook on X-ray CT research and development,” *Medical Physics*, vol. 35, no. 3, pp. 1051–1064, 2008.
- [17] X. Tang, Z. Jiang, S. Jiang, and Z. Li, “Heterogeneous nanoporosity of the Silurian Longmaxi Formation shale gas reservoir in the Sichuan Basin using the QEMSCAN, FIB-SEM, and nano-CT methods,” *Marine and Petroleum Geology*, vol. 78, pp. 99–109, 2016.
- [18] Q. Hu, T. J. Kneafsey, R. C. Trautz, and J. S. Y. Wang, “Tracer penetration into welded tuff matrix from flowing fractures,” *Vadose Zone Journal*, vol. 1, no. 1, pp. 102–112, 2002.
- [19] Q. Hu, X. Gao, Z. Gao, R. Ewing, S. Dultz, and J. Kaufmann, “Pore accessibility and connectivity of mineral and kerogen phases in shales,” *Unconventional Resources Technology Conference*, vol. 1922943, p. 17, 2014.
- [20] U. Kuila, D. K. McCarty, A. Derkowski, T. B. Fischer, and M. Prasad, “Total porosity measurement in gas shales by the water immersion porosimetry (WIP) method,” *Fuel*, vol. 117, pp. 1115–1129, 2014.
- [21] T. Topór, A. Derkowski, U. Kuila, T. B. Fischer, and D. K. McCarty, “Dual liquid porosimetry: a porosity measurement technique for oil- and gas-bearing shales,” *Fuel*, vol. 183, pp. 537–549, 2016.
- [22] M. G. Kibria, Q. Hu, H. Liu, Y. Zhang, and J. Kang, “Pore structure, wettability, and spontaneous imbibition of Woodford Shale, Permian Basin, West Texas,” *Marine and Petroleum Geology*, vol. 91, pp. 735–748, 2018.
- [23] M. Sun, B. Yu, Q. Hu et al., “Pore structure characterization of organic-rich Niutitang shale from China: Small angle neutron scattering (SANS) study,” *International Journal of Coal Geology*, vol. 186, pp. 115–125, 2018.
- [24] J. Li, S. Lu, G. Chen, M. Wang, S. Tian, and Z. Guo, “A new method for measuring shale porosity with low-field nuclear magnetic resonance considering non-fluid signals,” *Marine and Petroleum Geology*, vol. 102, pp. 535–543, 2019.
- [25] Y. Zhang, Q. Hu, S. Long et al., “Mineral-controlled nm- μ m-scale pore structure of saline lacustrine shale in Qianjiang Depression, Jiangnan Basin, China,” *Marine and Petroleum Geology*, vol. 99, pp. 347–354, 2019.
- [26] IUPAC, “Manual of symbols and terminology,” *Pure and Applied Chemistry*, vol. 31, p. 578, 1972.
- [27] M. J. Wilson, M. V. Shalaby, and L. Wilson, “Clay mineralogy and unconventional hydrocarbon shale reservoirs in the USA. I. Occurrence and interpretation of mixed-layer R3 ordered illite/smectite,” *Earth-Science Reviews*, vol. 158, pp. 31–50, 2016.
- [28] E. W. Washburn, “Note on a method of determining the distribution of pore sizes in a porous material,” *Proceedings of the National Academy of Sciences of the United States of America*, vol. 7, no. 4, pp. 115–116, 1921.
- [29] A. J. Katz and A. H. Thompson, “Quantitative prediction of permeability in porous rock,” *Physical Review B*, vol. 34, no. 11, pp. 8179–8181, 1986.
- [30] Z. Gao and Q. Hu, “Estimating permeability using median pore-throat radius obtained from mercury intrusion porosimetry,” *Journal of Geophysics and Engineering*, vol. 10, no. 2, article 025014, 2013.
- [31] H. Giesche, “Mercury porosimetry: a general (practical) overview,” *Particle and Particle Systems Characterization*, vol. 23, no. 1, pp. 9–19, 2006.
- [32] R. F. Sigal, “A methodology for blank and conformance corrections for high pressure mercury porosimetry,” *Measurement Science and Technology*, vol. 20, no. 4, article 045108, 2009.
- [33] G. Coates, L. Xiao, and M. Prammer, “NMR logging: principles and applications,” *Haliburton Energy Services*, vol. 234, 1999.
- [34] N. Bloembergen, E. M. Purcell, and R. V. Pound, “Relaxation effects in nuclear magnetic resonance absorption,” *Physical Review*, vol. 73, no. 7, pp. 679–712, 1948.
- [35] E. Rylander, P. M. Singer, T. Jiang, R. Lewis, R. McLin, and S. Sinclair, “NMR T2 distributions in the Eagle Ford shale: reflections on pore size,” *SPE USA Unconventional Resources Conference 2013*, pp. 426–440, 2013.
- [36] Q. Hu, “Quantifying effective porosity of oil and gas reservoirs,” *AAPG Search and Discovery Article*, vol. 70376, 2018.
- [37] J. T. Comisky, M. Santiago, B. McCollom, A. Buddhala, and K. E. Newsham, “Sample size effects on the application of

- mercury injection capillary pressure for determining the storage capacity of tight gas and oil shales,” *Society of Petroleum Engineers - Canadian Unconventional Resources Conference 2011*, pp. 2103–2125, 2011.
- [38] J. Sun, X. Dong, J. Wang et al., “Measurement of total porosity for gas shales by gas injection porosimetry (GIP) method,” *Fuel*, vol. 186, pp. 694–707, 2016.
- [39] X. Zhao, L. Zhou, X. Pu et al., “Development and exploration practice of the concept of hydrocarbon accumulation in rifted-basin troughs: A case study of Paleogene Kongdian Formation in Cangdong sag, Bohai Bay Basin,” *Petroleum Exploration and Development*, vol. 45, no. 6, pp. 1166–1176, 2018.
- [40] X. Pu, L. Zhou, W. Han et al., “Geologic features of fine-grained facies sedimentation and tight oil exploration: a case from the second Member of Paleogene Kongdian Formation of Cangdong Sag, Bohai Bay Basin,” *Petroleum Exploration and Development*, vol. 43, no. 1, pp. 24–33, 2016.
- [41] K. Chen, X. Liu, J. Liu, C. Zhang, M. Guan, and S. Zhou, “Lithofacies and pore characterization of continental shale in the second Member of the Kongdian Formation in the Cangdong Sag, Bohai Bay Basin, China,” *Journal of Petroleum Science and Engineering*, vol. 177, pp. 154–166, 2019.
- [42] F. Behar, V. Beaumont, B. Penteado, and H. De, “Rock-Eval 6 technology: Performances and developments,” *Oil & Gas Science and Technology*, vol. 56, no. 2, pp. 111–134, 2001.
- [43] L. E. Flint, “Characterization of hydrogeologic units using matrix properties, Yucca Mountain, Nevada,” *Water-Resources Investigations Report*, vol. 98, p. 4243, 1998.
- [44] W. M. Haynes, D. R. Lide, and T. Bruno, *CRC Handbook of Chemistry and Physics 2012–2013*, vol. 93, pp. 7–9, 2012.
- [45] N. Zhang, M. He, B. Zhang, F. Qiao, H. Sheng, and Q. Hu, “Pore structure characteristics and permeability of deep sedimentary rocks determined by mercury intrusion porosimetry,” *Journal of Earth Science*, vol. 27, no. 4, pp. 670–676, 2016.
- [46] S. Wang, F. Javadpour, and Q. Feng, “Confinement correction to mercury intrusion capillary pressure of shale nanopores,” *Scientific Reports*, vol. 6, 2016.
- [47] H. Tian, L. Pan, X. Xiao, R. W. T. Wilkins, Z. Meng, and B. Huang, “A preliminary study on the pore characterization of Lower Silurian black shales in the Chuandong Thrust Fold Belt, southwestern China using low pressure N₂ adsorption and FE-SEM methods,” *Marine and Petroleum Geology*, vol. 48, pp. 8–19, 2013.
- [48] F. Rabier, M. Temmerman, T. Böhm et al., “Particle density determination of pellets and briquettes,” *Biomass and Bioenergy*, vol. 30, no. 11, pp. 954–963, 2006.
- [49] M. Q. Hu, P. Persoff, and J. S. Y. Wang, “Laboratory measurement of water imbibition into low-permeability welded tuff,” *Journal of Hydrology*, vol. 242, no. 1–2, pp. 64–78, 2001.
- [50] M. Meng, H. Ge, W. Ji, Y. Shen, and S. Su, “Monitor the process of shale spontaneous imbibition in co-current and counter-current displacing gas by using low field nuclear magnetic resonance method,” *Journal of Natural Gas Science and Engineering*, vol. 27, pp. 336–345, 2015.
- [51] Q. Meng, Z. Cai, J. Cai, and F. Yang, “Oil recovery by spontaneous imbibition from partially water-covered matrix blocks with different boundary conditions,” *Journal of Petroleum Science and Engineering*, vol. 172, pp. 454–464, 2019.
- [52] X. Liu, Q. Liu, J. Liu, Q. Dong, M. Guan, and H. Li, “Geochemical characteristics of organic-rich shales of the second Member of Kongdian Formation in Cangdong Sag, Huanghua Depression,” *Lithologic Reservoirs*, vol. 27, no. 6, pp. 15–22, 2015.
- [53] L. L. Handy, “Determination of effective capillary pressures for porous media from imbibition data,” *Transactions of the AIME*, vol. 219, no. 1, pp. 75–80, 2013.
- [54] D. Xiao, S. Jiang, D. Thul, S. Lu, L. Zhang, and B. Li, “Impacts of clay on pore structure, storage and percolation of tight sandstones from the Songliao Basin, China: implications for genetic classification of tight sandstone reservoirs,” *Fuel*, vol. 211, pp. 390–404, 2018.
- [55] R. Wang, W. Shi, X. Xie et al., “Clay mineral content, type, and their effects on pore throat structure and reservoir properties: insight from the Permian tight sandstones in the Hangjinqi area, north Ordos Basin, China,” *Marine and Petroleum Geology*, vol. 115, p. 104281, 2020.
- [56] J. J. Valenza, N. Drenzek, F. Marques, M. Pagels, and M. Mastalerz, “Geochemical controls on shale microstructure,” *Geology*, vol. 41, no. 5, pp. 611–614, 2013.
- [57] L. Chen, Z. Jiang, Q. Liu et al., “Mechanism of shale gas occurrence: insights from comparative study on pore structures of marine and lacustrine shales,” *Marine and Petroleum Geology*, vol. 104, pp. 200–216, 2019.

Research Article

A New Upscaling Method for Fluid Flow Simulation in Highly Heterogeneous Unconventional Reservoirs

Qi Zhang,^{1,2} Huibin Yu ,¹ Xiaofeng Li,¹ Tiesheng Liu,^{1,2} and Junfeng Hu¹

¹Institute of Oceanographic Instrumentation, Qilu University of Technology (Shandong Academy of Sciences), China

²Shandong Technological Center of Oceanographic Instrumentation, China

Correspondence should be addressed to Huibin Yu; yuhuibin2019@163.com

Received 8 January 2020; Revised 9 July 2020; Accepted 27 July 2020; Published 25 August 2020

Academic Editor: Wei Wei

Copyright © 2020 Qi Zhang et al. This is an open access article distributed under the Creative Commons Attribution License, which permits unrestricted use, distribution, and reproduction in any medium, provided the original work is properly cited.

High heterogeneity and nonuniformly distributed multiscale pore systems are two characteristics of the unconventional reservoirs, which lead to very complex transport mechanisms. Limited by inadequate computational capability and imaging field of view, flow simulation cannot be directly performed on complex pore structures. The traditional methods usually coarsen the grid to reduce the computational load but will lead to the missing microstructure information and inaccurate simulation results. To develop a better understanding of flow properties in unconventional reservoirs, this study proposed a new upscaling method integrated gray lattice Boltzmann method (GLBM) and pore network model (PNM), accounting for the fluid flow in heterogeneous porous media. This method can reasonably reduce the computational loads while preserving certain micropore characteristics. Verifications are conducted by comparing the simulation and experimental results on tight sandstones, and good agreements are achieved. The proposed method is proven to be capable of estimating bulk properties in highly heterogeneous unconventional reservoirs. This method could contribute to the development of multiscale pore structure characterizations and enhance the understandings of fluid flow mechanisms in unconventional reservoirs.

1. Introduction

With the advanced technology and growing demand for oil and gas, increasing attention has been paid to the development of unconventional oil and gas resources [1]. Unconventional reservoirs have multiple types of pore spaces, complex pore structures, and various mineral compositions and usually feature a high degree of heterogeneity and multiscale characteristics [2–4]. The flow mechanisms in unconventional reservoirs are greatly affected by microscale effects, and it is very challenging to describe the complex pore structures accurately and transmission characteristics of such porous media [5].

At present, there are two main methods to obtain and describe the complex pore structure and morphology of unconventional reservoirs: laboratory methods and high-precision imaging analysis methods. High-precision imaging analysis methods include the methods of scanning electron microscopy (SEM), micro-nano CT X-ray scanning, and dual-beam scanning electron microscopy (FIB-SEM) [6, 7].

However, due to the limitation of the imaging field of view, the entire high-precision pore space of the core cannot be obtained by one imaging; therefore, the multiscale characterization of the flow characteristics should fully consider the interaction between different scale pores in the heterogeneity reservoirs.

Microsimulation methods can accurately describe microscale fluid flow mechanisms. However, it is difficult to consider microscale flow effects in core-scale flow simulation analysis, limited by the method applicability and computational power. Worldwide, scholars have developed simulation methods for highly heterogeneous rocks at different scales, such as the pore network model method, lattice Boltzmann method (LBM), and molecular simulation method [8]. With topology of the pore space, the three-dimensional pore network model can not only characterize the pore structure parameters (pore radius, roaring channel radius, and coordination number) [9, 10] but also provide the basis of research for microscopic flow simulation of porous media. The 3D PNM can reduce the cost of experiments, shorten

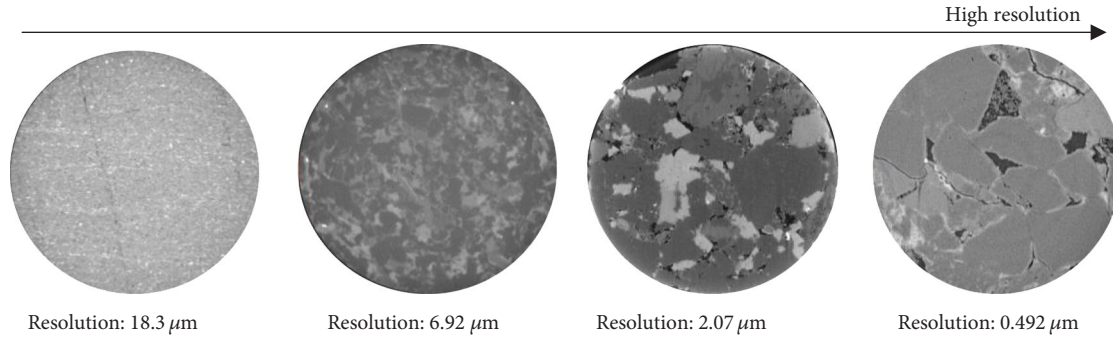


FIGURE 1: CT images of highly heterogeneous unconventional reservoirs.

experimental data obtaining time, and get experimental data that are difficult to measure in the laboratory.

In recent years, the simulation methods of pore network models have also continued to be refined. Martin et al. further divided the pore systems and proposed a generalized PNM method, which eliminated the effects of model parameters on simulation results [11, 12]. Jiang et al. obtained an equivalent multiscale PNM by analyzing the correlation between the statistical characteristics and geometric structure parameter variables of pore network models at different scales [13]. The lattice Boltzmann method is suitable for pore-scale or representative elementary volume (REV) scale studies. However, due to the pore size distribution and connectivity, the LBM involves a sufficient number of meshes and calculations, which requires a large number of computing resources and space storage. It also leads to the limited size of the simulation space. Walsh et al. proposed the gray lattice Boltzmann method based on the partial bounce, which corrected the effect of microstructure on model permeability by adding the net flow particle ratio [14]. Ma et al. improved the convergence of the algorithm by limiting the direction of flow bounce and carried out an ideal model simulation [15]. Chenchen et al. further optimized the GLB method and carried out the 2D heterogeneous model flow simulation. The simulation results have a high consistency with the analytical solution [16, 17].

In fractured and heterogeneous tight cores, the flow patterns of oil and gas in fractures and micro-nano pores are distinct, and single-scale governing equations or flow simulation methods cannot accurately reveal the fluid flow in these porous media [18]. Therefore, scale upgrade methods are currently used for shale structure characterization and flow simulation studies, such as homogenization theory and volume average method [19]. Homogenization theory is mostly used in porous materials with a relatively regular pore structure and periodic distribution [20]. The volume averaging method is generally upgraded on the REV scale using smoothing and spatial averaging formulas [21]. At present, traditional scale upgrading methods are mostly ideal models based on periodic assumptions, which cannot fully consider the differences in real core pore space. They are difficult to apply to the flow simulation of complex and highly heterogeneous shales.

This paper employs multiple imaging techniques to analyze the interaction between pore structure and fluid flow at

different scales. At the same time, the pore structure parameters and flow parameters are coupled and iterated using the pore network model and the gray lattice Boltzmann method. The results are of great significance for finely characterizing the complex multiscale pore structure and flow mechanism of unconventional reservoirs.

2. Methodologies

2.1. Multiscale Pore Space Modeling. The pore radius of unconventional reservoir cores is mainly at the nanometer and micrometer scales [22–24], and high heterogeneity exists in pore numbers, volumes, and distributions, which causes anisotropy and greatly increases the complexity of flow simulation [25, 26]. The complexity of pore space mainly lies in the following aspects. First, there are various types of pore structures, which are poorly sortable and difficult to determine the size of REV, including organic pores, inorganic pores, natural microcracks, and artificial cracks. Secondly, the pore size distribution is complex, and nano-micron-millimeter-level pore structures are well developed. The effects of strong compaction, cementation, and clay transformation result in small pore spaces, narrow pore throats, complicated structures, and poor connectivities. The pore sizes in the cores are quite diverse, including large intragranular pores formed by dissolution, and numerous intercrystalline micropores formed by clay minerals, and these differences lead to diverse oil and gas fluid patterns. Due to the existence of multiscale and interconnected pore space, heterogeneity in unconventional reservoirs is very strong (Figure 1). A scanning electron microscope (SEM), field emission electron microscope, atomic force microscope, and nano-CT can visually and intuitively analyze the micro-nano pore morphology, distribution location, connectivity, and degree of pore development in pore space. However, due to the limitation of a single observation field of vision, only combining multiple imaging technologies can effectively observe the complex pore space (Figure 2).

Because the REV scale of digital core image processing is far beyond the computational capability, and the traditional method of directly coarsening the grid will lose numerous microscopic pore structure information, reducing the simulation accuracy, this paper proposed low-precision and high-resolution subscale imaging technology (Figure 3). First, the low-precision imaging data are classified based on

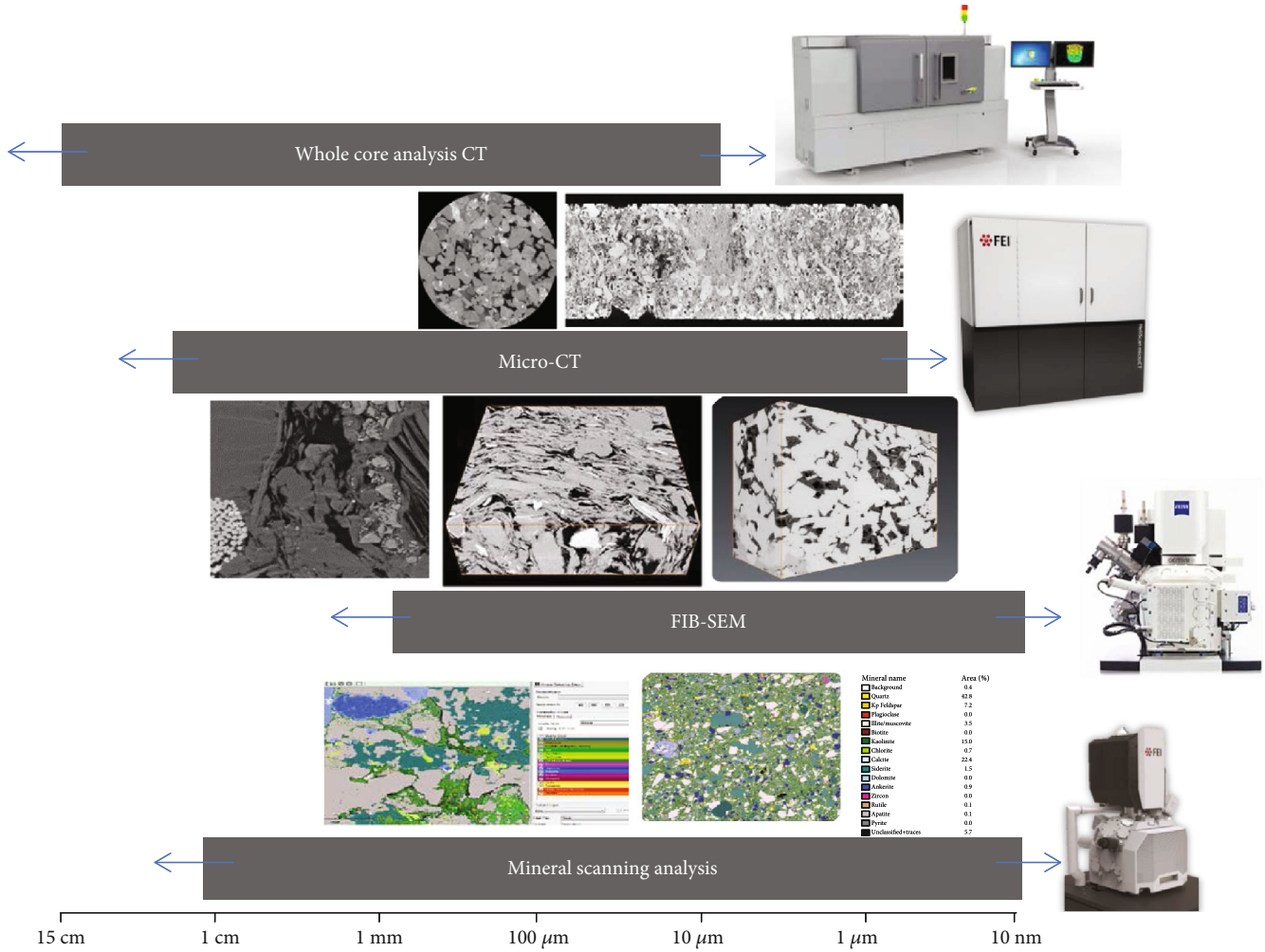


FIGURE 2: The applicable scope of imaging technology ([27]).

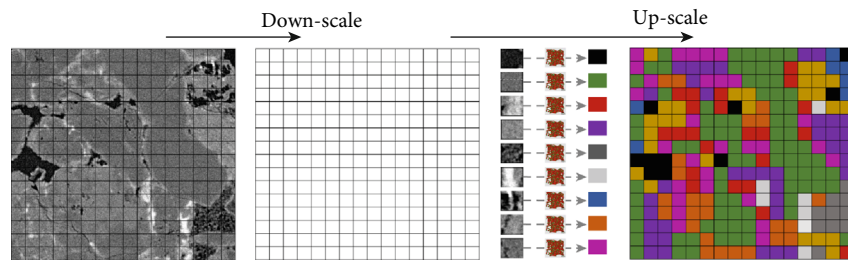


FIGURE 3: The schematic flow of multiscale modeling.

the selection of rock physical properties, and a coarse mesh model is established to reduce the calculation requirement. A position in the pore structure is selected for high-precision scanning to obtain the micro-nano pore information of core pore space and for multiscale flow simulation. The CT scanning method uses the attenuation law of X-ray intensity to obtain a three-dimensional structure data of the pore space inside the core [28]. One of the advantages is CT can provide gray data (electron density map) containing massive pore structure information of the sample. The core structure can be divided into pores and matrix by the binary method through the gray map. Moreover, there are much

other information that can be obtained from grayscale CT images, such as local porosity and mass concentration of the transported component ([29]):

$$\epsilon_{(x,y,z)} = \frac{CT_{\text{saturated}(x,y,z)} - CT_{\text{dry}(x,y,z)}}{CT_{\text{saturated}} - CT_{\text{air}}} \quad (1)$$

The local porosity can be calculated using the above formula by analyzing the change of the gray value of two different materials in the pore space, in which $\epsilon_{(x,y,z)}$ is the porosity of (x, y, z) and $CT_{\text{saturated}(x,y,z)}$ and $CT_{\text{dry}(x,y,z)}$ represent the

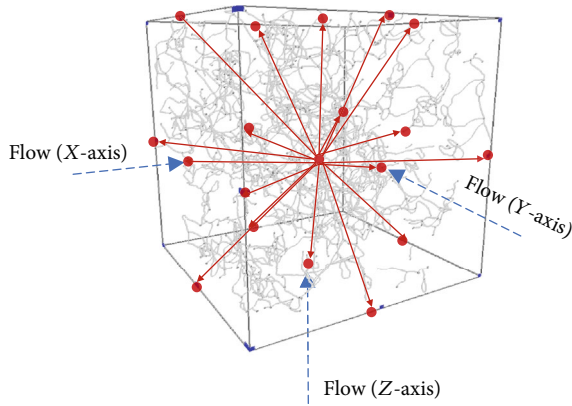


FIGURE 4: Medial axis of pore space.

saturated and dry gray values of (x, y, z) . Imaging the core using appropriate resolution, the pore distribution pattern can be observed and the gray map can be obtained. On the gray map, the gray value of each point contains certain information of the pore space structure of the region. Since porosity is one of the most important factors affecting the fluid flow, local porosity, which can be calculated by the above equation, is taken as the basis for grouping the core zones. According to different porosity value ranges, core data are divided into groups, each with a different label, and a specific location in each category is selected for high-precision scanning. By means of high-precision scanning, the pore information of the typical pore structure in each type of porosity range can be obtained, consequently establishing and coupling the model at both scales.

2.2. Pore Network Model. Since Fatt (1956) constructed the first pore network model composed of unequal diameter cylindrical capillaries, the refinement of the pore network model has been continuously improved, which can not only describe pore structure characteristics more accurately but also make great progress in flow simulation [30]. In this paper, the medial axis method [31], which is commonly used in the construction of the pore network model, was adopted to obtain the positions of the pores and the pore throats by identifying the intersection of the central axis.

2.2.1. Extraction of the Medial Axis of Pore Space. The medial axis of the pore space is the skeleton curve that connects the center of each pore space, and it could reflect the basic topological characteristics of the real pore space simply and compactly. To get the central axis, the first step is to obtain the Euclidean distance map of pore space by distance transformation. The local maximum value (ridge points) was accounted to represent the topological skeleton of pore space. Secondly, pore points (object points) were defined as 26-adjacency, and matrix points (background points) were defined as 6-adjacency. Based on the Euclidean distance map and calculation of the Euler number, thinning procedure which is iteratively deleting pore points and searching the skeleton points can be used without changing the original image topology. At last, we would obtain the medial axis of pore space which is only a single voxel wide. The voxels in

the medial axis can be distinguished as three types according to how many neighbours they have: regular points, end-points, and junction points. The connectivity would be one of the key considerations during construction of the network model.

2.2.2. Recognition of Nodes (Pore Elements) and Bonds (Throat Elements). An essential step in constructing the pore network model is to divide the digital core pore space into pores and throats in a general sense. In this paper, the node with a coordination number greater than 2 on the central axis is defined as the pore center, and the pore region is defined by the maximum incised sphere region. Parameters such as pore radius are obtained by the method of spherical isometric expansion. After removing the pore space classified above, the remaining pore space is the pore throat space. Combined with the pore node information, the corresponding throat structural characteristics are statistically analyzed.

2.2.3. Pore Structure Characteristics and Permeability Calculation. As we can assume that relatively homogenous areas exist in the heterogeneous pore space, the pore network model is helpful to better analyze the characteristics of the pore structure in the different areas. General geometric and topological properties of the pores and throats including pore (or throat) size distribution, shape factor, and coordination number can be calculated and analyzed. The pore-scale network model can be used to model flow in pore space and get flow parameters based on mathematical description of conductance and threshold pressure. And the permeability would then be used in the iteration of the GLB model. Meanwhile, each individual lattice in the GLB model is not isolated which means that there were flows between lattices in different directions (Figure 4). Correspondingly, flow capacity of the pore network model should be affected by the flows in $x y z$ directions. Triaxial permeabilities could separately calculate with different settings of the inlet and outlet of the medial axis, which will provide a data basis for subsequent GLB simulation.

2.3. GLBM-Based Multiscale Flow Capacity Characterization. Using the classified grid model as the base model for GLBM simulation, and coupling the microscopic triaxial permeability obtained from PNM, the pore structure upgrading and downgrading can be integrated, so that the computational loads can be reasonably reduced on the premise of preserving certain microscopic pore characteristics. The LBM method is a set of models for simulating the movement of microparticles based on molecular dynamics. It has the characteristics of entirely independent time, space, and interaction. It is a fully parallel algorithm that can carry out numerical simulation of complex fluid problems, widely used in petroleum, chemical, energy, water conservancy, machinery, and other fields. Traditional LBM only distinguishes flow lattice from nonflow lattice (Figure 5), while GLBM thoroughly considered the effects of anisotropy and heterogeneity of the porous media, and the semiflowing gray lattice was added, in which there are collisions between fluid particles and solid matrix, representing the effect of the solid scattering degree in the lattice on the flow. Generally speaking, when the fluids flow

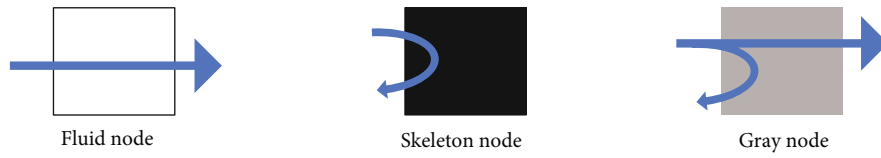


FIGURE 5: Flow mechanism in different kinds of GLB lattices.

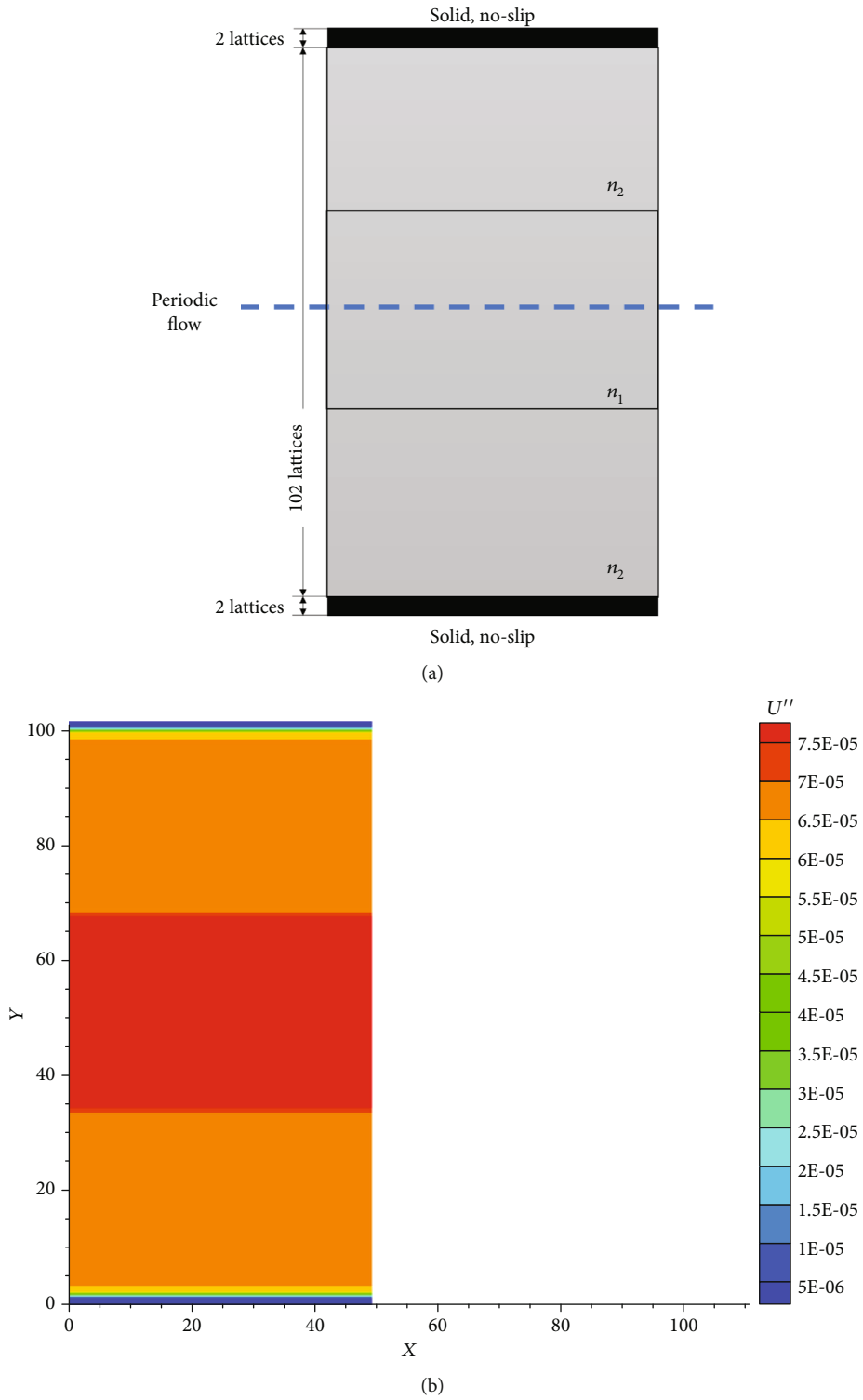


FIGURE 6: (a) Theoretical model. (b) Velocity profile of $n_{s1} = 0.44$ and $n_{s2} = 0.41$.

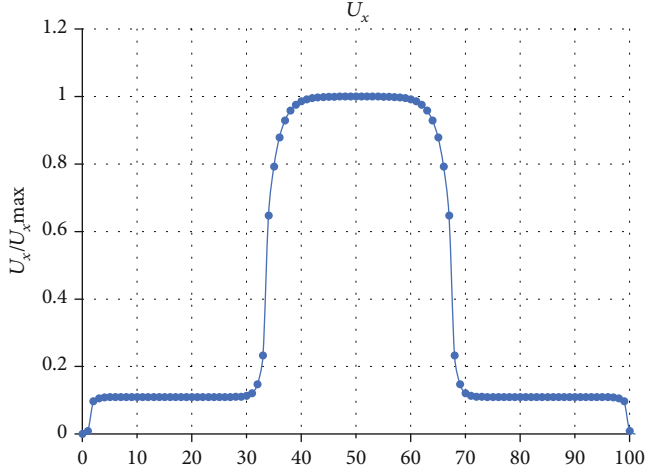


FIGURE 7: Velocity distribution curve along the y -axis of $n_{s1} = 0.091$ and $n_{s2} = 0.44$.

through the pore space, part of it is bounced back through the rock particles, which means that the flow field includes the sum of penetrating the pore space and the nonpenetrating bounced back fluid (Figure 5).

The governing equation can be expressed as

$$f_i(x + c_i \delta_i, t + \delta_i) - f_i(x, t) = -\frac{1}{\tau} [f_i(x, t) - f_i^{eq}(x, t)] + \Delta_i(x, t). \quad (2)$$

Different from the traditional LBM, the simulation of fluid flow can be divided into three processes:

(1) Collision:

$$\tilde{f}_\alpha^c(\tilde{r}, \tilde{t}) = \tilde{f}_\alpha(\tilde{r}, \tilde{t}) - \frac{\tilde{f}_\alpha(\tilde{r}, \tilde{t}) - \tilde{f}_i^{eq}(\tilde{r}, \tilde{t})}{\tilde{\tau}^*} + F_\alpha, \quad (3)$$

in which F is the internal driving force in the lattice [32], $F_\alpha = (\tilde{F} \cdot (e_\alpha - \tilde{u})/\tilde{\theta})\Gamma_\alpha(\tilde{u})$, and $\Gamma_\alpha(\tilde{u}) = w_\alpha[1 + e_\alpha \cdot \tilde{u}/\tilde{\theta} + (e_\alpha \cdot \tilde{u})^2/2\tilde{\theta}^2 + \tilde{u}^2/2\tilde{\theta}]$

(2) Practical bounce-back [15]:

$$\tilde{f}_\alpha^{\text{out}}(\tilde{r}, t^{**}) = (1 - n_s)\tilde{f}_\alpha^c(\tilde{r}, t^{**}) + n_s\tilde{f}_\alpha^c(\tilde{r}, \tilde{t}^*) \quad (4)$$

(3) Flow:

$$\tilde{f}_\alpha(\tilde{r} + e_\alpha, \tilde{t} + 1) = \tilde{f}_\alpha^c(\tilde{r}, \tilde{t}) \quad (5)$$

The effective viscosity is $(2n_s(6\tilde{\tau}^*\tilde{\tau}^* - 8\tilde{\tau}^* + 1) - 12n_s^2\tilde{\tau}^*(\tilde{\tau}^* - 1) + (2\tilde{\tau}^* - 1))/(6[1 + 2n_s(\tilde{\tau}^* - 1)](1 - 2n_s))$.

During the partial bounce-back process, n_s represents the bounce-back coefficient when the fluids flow through the porous media, and it is the average scattering density of solid lattice points ranging from 0 to 0.5. It characterizes the solid

structure of the porous media and is related to local solid weight in the gray lattice.

It is assumed that Figure 6 is the profile of a $50 \times 102 \times 102$ heterogeneous theoretical model. There are two solid boundaries in the positive and negative directions of y and z , and the fluid flows along the x -axis. The flow area is divided into upper, middle, and lower parts, in which the upper and lower parts have the bounce-back coefficient $n_{s1} = 0.44$, and the bounce-back coefficient of the middle part is $n_{s2} = 0.41$. Key parameters are set as follows: the grid size is equal to 1; the timestep is 1; and the values of ρ_0 , τ , Vf , and F are set as 1, 2, 0.5, and $0.0001 \times \rho$, 0, 0, respectively. Since the flow is nonhomogeneous, by using the surface boundary calculation method, the velocity profile along the y -axis can be obtained as follows in Figure 2, and it conforms to the basic flow law.

Based on the analysis of the flow field of the porous medium, the general N-S equation is deduced in the pore space. The flow field of partial bounce-back coefficients is explained as

$$n_s \delta f = n_s [f_\alpha(x, t) - f_\alpha^c(x, t)]. \quad (6)$$

By solving the Brinkman equation flow field, n_s is related to the permeability of the local flow field:

$$k = \frac{(1 - 2n_s)v_f}{2n_s}. \quad (7)$$

During upscaling, the permeability in the typical core pore network model is treated as the permeability of the local flow field in the GLB model grid. By coupling permeability and partial bounce-back coefficient, the relationship between microstructure and complex multiscale porous media flow features can be established, so that the multiscale permeability of the entire core can be characterized and the upgrade is completed.

3. Results and Discussion

Tight sand cores from unconventional reservoirs are selected as the experimental sample for multiscale characterizations. The cylindrical core sample is 25 mm long with a 30 mm diameter. The permeability and porosity is 4.16 mD and 6.98%, respectively. The CT images with different resolutions are shown in Figure 7, the general trend of pore space can be analyzed based on the grayscale distribution, and the few macropores can be seen with low-resolution images. The observational field at this resolution equates with the traditional laboratory test of permeability. However, the connectivity between visible pores is very poor, so it is not suitable of carrying out pore network model modeling and flow simulation. Some large connected pores with the pore radius range of 10 to 70 μm can be extracted at high resolution, and the tiny pores and microfractures which have significant influence on fluid flow in multiscale pore space would be captured when the scanning resolution reaches 0.545 μm .

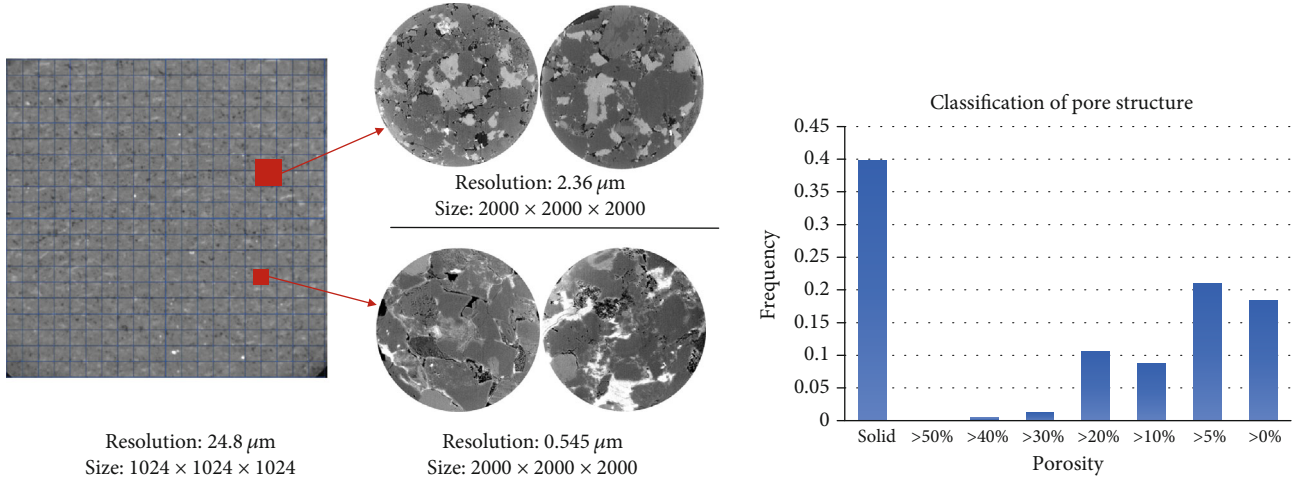


FIGURE 8: CT images of tight sandstone and classification of pore structure.

The raw CT images with a resolution of $24.8\ \mu\text{m}$ were downsampled to build a $100 \times 100 \times 100$ GLB model, so each lattice contains information of $10 \times 10 \times 10$ voxels. There were three kinds of lattice: solid, pore, and gray lattice. Based on the grayscale analysis on the heterogeneous pore structure of tight sandstone, the scanning porosity of pore space was roughly classified into 8 ranges (Figure 8). About 40% lattices in the model were defined as solid which means that there were no flows. For the rest of the area, lattices with porosity less than 5% constitute most of the flow area. Therefore, the multiscale GLB model should be built by combining pore structure characteristics at different scales. The gray lattice in the GLB model which represents these areas can add more microscopic properties to help the flow simulation more accurately.

By further high-precision observation on the selected core region, relatively complete and effectively connected pore space can be observed. Each gray lattice is, respectively, represented by subvolume A (size: $100 \times 100 \times 100$) with a resolution of $2.36\ \mu\text{m}$ and subvolume B (size: $450 \times 450 \times 450$) with a resolution of $0.545\ \mu\text{m}$. Affected by scanning view, the morphology of the large pore can be seen clearer and more complete. So, we used subvolume A to analyze lattices with porosity greater than 30%. These areas usually have good percolation ability and high permeability based on the Poiseuille equation and pore network model. The pore space structure becomes a little more complex when the porosity of lattice is lower than 30%. There are 9 kinds of pore structures extracted from the CT images with high resolution during porosity between 0 and 30%. The pore structure parameters of all these types of pore structures are shown in Table 1. Besides the traditional pore with different sizes, microporous clusters generated by clay mineral dissolution and interconnected microfractures are the most common pore structure. As shown in Table 1, the porosity of porous clusters usually distributes between 5% and 30% with a pore radius of about $1.75\ \mu\text{m}$; their gray value is relatively focused and slightly lower than pores. There are enough flow channels in the porous cluster so that the permeability could reach hundreds

of millidarcies. Meanwhile, permeability is only 0.07 mD in the area where pores poorly develop. Compared with the microfracture network which has higher permeability in all directions, the individual microfractures usually have low permeability on two axes and no flows on the other axis. All of these microscale pore structures impacted the flow simulation in a significant way.

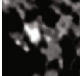
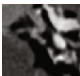
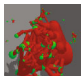


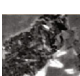
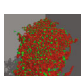

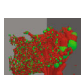
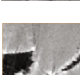
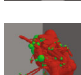

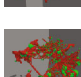

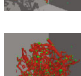
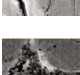
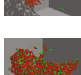

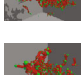

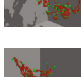
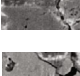
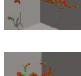
Limited by the porosity measured in the lab, the lattices of the GLB model, respectively, are associated with the corresponding type of the pore network model based on the porosity of the lattice and dispersion degree of the grayscale distribution of the voxels (Figure 9). The upscaling process was carried out through assigning the permeability parameters of each pore network model to the partial bounce-back coefficient of lattice in the GLB model (Figure 2).

The simulation results are shown in Table 2. Besides sample 1# which is used for imaging, we also choose two other samples 2# and 3# from the same block to analyze and model. Their CT images with low resolution have similar distribution range of grayscale map, so the pore network models extracted from sample 1# can match their downscale GLB model directly. Even if there comes an error in either of the simulation and experimental method, the results were basically the same. Using the method described in this paper, multiscale pore structure characteristics can be considered into flow simulation. The 12 types of pore network model were all extracted from connected pore space in the high-resolution images; this may be the reason why the simulation result is higher than the permeability measured in lab.

4. Conclusion

- (1) The influence of the core microscopic pore structure and its heterogeneity on core physical property cannot be ignored. With the limited observing field of imaging techniques, the modeling area of pore space only represented a certain range of pore/throat size

TABLE 1: Pore structure of different pore space types.

Porosity	Pore space image	PNM	Permeability x -axis (mD)	Permeability y -axis (mD)	Permeability z -axis (mD)
>50%			Poiseuille equation	Poiseuille equation	Poiseuille equation
40%-50%			6880.5	7112.1	6499.6
30%-40%			2997.2	3390.3	4252.25
			130.538	667.9	536.35
20%-30%			319.884	325.73	452.6
			83.1	11146.4	58.21
10%-20%			52.532	214.1	720.5
			13.257	290	247.7
5%-10%			10.558	14.27	113.82
			0.07	0.085	301.41
			0.2	0.201	0
0%-5%			0.316	10.102	0.792

which is decided by imaging resolution. Based on the combination of the downscale method and upscale method, a new upscaling method is proposed to effectively describe the characterization of multiscale pore space

- (2) Imaging data with low resolution usually showed disconnected pore space, which means that the areas identified as "skeleton" under low resolution actually have a lot of micropores. To solve the problem, we used gray lattice besides the pore to represent the multiscale pore space and got its microscopic pore structure information by means of high-precision

scanning. And based on classification using local porosity, the imaging steps can be able to simplify to a finite number while not affecting the model accuracy

- (3) By combining the pore network model and the GLB model, the new method can be a practical option to carry out flow simulation in highly heterogeneous unconventional reservoirs. Permeability of gray lattices calculated from the pore network model with high resolution would be assigned to a partial bounce-back coefficient of the gray lattices in the GLB model to solve the problem that connection

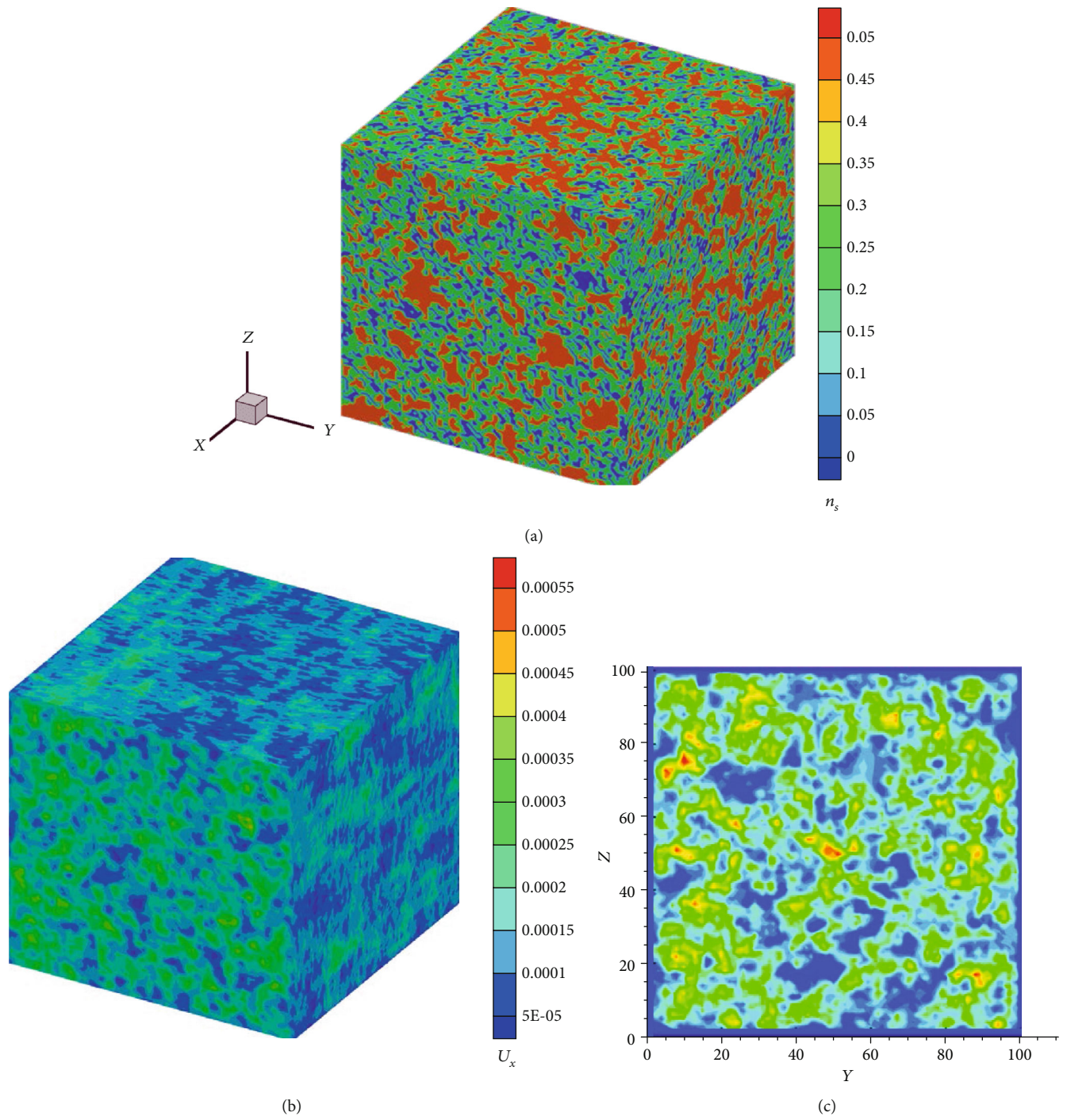


FIGURE 9: Simulation result: (a) GLB model; (b) x -axis velocity distribution; (c) cross-section of x -axis velocity distribution.

TABLE 2: Result comparison using GLBM.

No.	Core size	Permeability ^a	Porosity ^b	Simulation result	Error
Sample 1#	25 × 25 × 25 mm	4.16 mD	6.98%	4.59 mD	10.3%
Sample 2#	25 × 25 × 25 mm	3.97 mD	6.03%	4.41 mD	11.1%
Sample 3#	25 × 25 × 25 mm	4.89 mD	8.34%	5.42 mD	10.8%

^aMeasured at 297.15 K using nitrogen. ^bMeasured at 297.15 K.

between different scales of pores can be barely obtained. And we also consider putting the pore network model in the loop iteration of the GLB model to further increase accuracy in future work

Data Availability

The data used to support the findings of this study are available from the first author upon request.

Conflicts of Interest

The authors declare that they have no conflicts of interest.

Acknowledgments

We would like to express appreciation to the following financial support: Shandong Province Natural Science Foundation (ZR2019PEE039 and ZR2018BEE008), National Natural Science Foundation of China (51804328), and Production-study-research Innovation Foundation of Shandong Academy of Sciences (YDLH41903CZ, YDLH41906CZ, and YDLH41901CZ).

References

- [1] J. Li, B. Guo, and M. Zheng, "Main types, geological features and resource potential of tight sandstone gas in China," *Natural Gas Geoscience*, vol. 23, pp. 607–615, 2012.
- [2] G. R. L. Chalmers and R. M. Bustin, "The organic matter distribution and methane capacity of the Lower Cretaceous strata of Northeastern British Columbia, Canada," *International Journal of Coal Geology*, vol. 70, no. 1-3, pp. 223–239, 2007.
- [3] F. P. Wang, R. M. Reed, and E. Geology, *SPE 124253 pore networks and fluid flow in gas shales*, 2009.
- [4] L. Wang, Y. He, X. Peng, H. Deng, Y. Liu, and W. Xu, "Pore structure characteristics of an ultradeep carbonate gas reservoir and their effects on gas storage and percolation capacities in the Deng IV member, Gaoshiti-Moxi Area, Sichuan Basin, SW China," *Marine and Petroleum Geology*, vol. 111, pp. 44–65, 2020.
- [5] M. Wang and Z. Wang, "Multiscale simulation and analysis for gas flow in deep-seated micronano pore," *Diqiu Kexue Zhongguo Dizhi Daxue Xuebao/earth Science Journal of China University of Geosciences*, vol. 43, pp. 1792–1816, 2018.
- [6] B. Bai, M. Elgmati, H. Zhang, and M. Wei, "Rock characterization of Fayetteville shale gas plays," *Fuel*, vol. 105, pp. 645–652, 2013.
- [7] F. Javadpour, "Nanopores and apparent permeability of gas flow in mudrocks (shales and siltstone)," *Journal of Canadian Petroleum Technology*, vol. 48, no. 8, pp. 16–21, 2013.
- [8] S. Lu, B. Shen, C. Xu, G. Chen, and X. He, "Study on adsorption behavior and mechanism of shale gas by using GCMC molecular simulation," *Diqiu Kexue - Zhongguo Dizhi Daxue Xuebao/Earth Science - Journal of China University of Geosciences*, vol. 43, pp. 1783–1791, 2018.
- [9] M. J. Blunt, B. Bijeljic, H. Dong et al., "Pore-scale imaging and modelling," *Advances in Water Resources*, vol. 51, pp. 197–216, 2013.
- [10] W. B. Lindquist, S. M. Lee, D. A. Coker, K. W. Jones, and P. Spanne, "Medial axis analysis of void structure in three-dimensional tomographic images of porous media," *Journal of Geophysical Research Solid Earth*, vol. 101, no. B4, pp. 8297–8310, 1996.
- [11] A. Q. Raeini, B. Bijeljic, and M. J. Blunt, "Generalized network modeling: network extraction as a coarse-scale discretization of the void space of porous media," *Physical Review E*, vol. 96, no. 1, article 013312, 2017.
- [12] A. Q. Raeini, B. Bijeljic, and M. J. Blunt, *Generalized network modelling: capillary-dominated two-phase flow - model description*, 2017.
- [13] X. Li, Z. Jiang, J. Ma, and X. Wang, "A Pore-skeleton-based method for calculating permeability and capillary pressure," *Transport in Porous Media*, vol. 124, no. 3, pp. 767–786, 2018.
- [14] S. D. C. Walsh, H. Burwinkle, and M. O. Saar, "A new partial-bounceback lattice-Boltzmann method for fluid flow through heterogeneous media," *Computers & Geosciences*, vol. 35, no. 6, pp. 1186–1193, 2009.
- [15] J. Zhu and J. Ma, "An improved gray lattice Boltzmann model for simulating fluid flow in multi-scale porous media," *Advances in Water Resources*, vol. 56, pp. 61–76, 2013.
- [16] C. Chen, L. Li, R. Mei, and J. F. Klausner, "Chapman–Enskog analyses on the gray lattice Boltzmann equation method for fluid flow in porous media," *Journal of Statistical Physics*, vol. 171, no. 3, pp. 493–520, 2018.
- [17] I. Ginzburg, "Comment on "An improved gray lattice Boltzmann model for simulating fluid flow in multi-scale porous media": intrinsic links between LBE Brinkman schemes," *Advances in Water Resources*, vol. 88, pp. 241–249, 2016.
- [18] C. R. Clarkson, J. L. Jensen, and S. Chipperfield, "Unconventional gas reservoir evaluation: what do we have to consider?," *Journal of Natural Gas Science & Engineering*, vol. 8, pp. 9–33, 2012.
- [19] M. Zhang, J. Yao, H. Sun et al., "Triple-continuum modeling of shale gas reservoirs considering the effect of kerogen," *Journal of Natural Gas Science & Engineering*, vol. 24, pp. 252–263, 2015.
- [20] J. B. Keller, *Darcy's law for flow in porous media and the two-space method*, 1980.
- [21] M. Quintard, B. Ladevie, and S. Whitaker, "Effect of homogeneous and heterogeneous source terms on the macroscopic description of heat transfer in porous media," *JAMA the Journal of the American Medical Association*, vol. 260, pp. 3171–3175, 2000.
- [22] C. R. Clarkson, N. Solano, R. M. Bustin et al., "Pore structure characterization of North American shale gas reservoirs using USANS/SANS, gas adsorption, and mercury intrusion," *Fuel*, vol. 103, pp. 606–616, 2013.
- [23] C. R. Clarkson, J. L. Jensen, P. K. Pedersen, and M. Freeman, "Innovative methods for flow-unit and pore-structure analyses in a tight siltstone and shale gas reservoir," *AAPG Bulletin*, vol. 96, no. 2, pp. 355–374, 2012.
- [24] R. G. Loucks, R. M. Reed, S. C. Ruppel, and D. M. Jarvie, "Morphology, genesis, and distribution of nanometer-scale pores in siliceous mudstones of the Mississippian Barnett Shale," *Journal of Sedimentary Research*, vol. 79, no. 12, pp. 848–861, 2009.
- [25] X. Gu, D. R. Cole, G. Rother, D. F. R. Mildner, and S. L. Brantley, "Pores in Marcellus shale: a neutron scattering and FIB-SEM study," *Energy & Fuels*, vol. 29, no. 3, pp. 1295–1308, 2015.
- [26] Wenk, V. L. R. Loon, Voltolini, Mazurek, and Vinsot, "Preferred orientations and anisotropy in shales: Callovo-

- Oxfordian shale (France) and Opalinus clay (Switzerland),” *Clays and Clay Minerals*, vol. 56, no. 3, pp. 285–306, 2008.
- [27] Scientific TF, <https://www.fei.com/>.
- [28] D. F. Swinehart, “The Beer-Lambert law,” *Journal of Chemical Education*, vol. 39, no. 7, p. 333, 1962.
- [29] Y. Zhang, P. Mostaghimi, and R. T. Armstrong, “On the challenges of greyscale-based quantifications using X-ray computed microtomography,” *Journal of Microscopy*, vol. 275, no. 2, pp. 82–96, 2019.
- [30] T. Bultreys, W. De Boever, and V. Cnudde, “Imaging and image-based fluid transport modeling at the pore scale in geological materials: a practical introduction to the current state-of-the-art,” *Earth-Science Reviews*, vol. 155, pp. 93–128, 2016.
- [31] Z. Jiang, K. Wu, G. Couples, M. I. J. V. Dijke, K. S. Sorbie, and J. Ma, “Efficient extraction of networks from three-dimensional porous media,” *Water Resources Research*, vol. 43, pp. 2578–2584, 2007.
- [32] X. He, X. Shan, and G. D. Doolen, “Discrete Boltzmann equation model for nonideal gases,” *Physical Review E*, vol. 57, no. 1, pp. R13–R16, 1998.

Research Article

Multifractal Analysis of Acoustic Emissions during Hydraulic Fracturing Experiments under Uniaxial Loading Conditions: A Niutitang Shale Example

Jingqiang Tan ^{1,2}, Jun Xie ^{1,2}, Lei Li ^{1,2}, Qiao Lyu ^{1,2}, Jianqiang Han ^{3,4}, and Zhengguang Zhao ⁵

¹Key Laboratory of Metallogenic Prediction of Nonferrous Metals and Geological Environment Monitoring (Central South University), Ministry of Education, Changsha 410083, China

²School of Geosciences and Info-Physics, Central South University, Changsha 410083, China

³Institute of Acoustics, Chinese Academy of Sciences, Beijing 100190, China

⁴Beijing Engineering Research Center for Offshore Drilling Exploration and Measurement, Beijing 100190, China

⁵School of Earth and Environmental Sciences, The University of Queensland, Brisbane QLD 4072, Australia

Correspondence should be addressed to Jingqiang Tan; tanjingqiang@aliyun.com

Received 2 June 2020; Revised 13 July 2020; Accepted 14 July 2020; Published 10 August 2020

Academic Editor: Wei Wei

Copyright © 2020 Jingqiang Tan et al. This is an open access article distributed under the Creative Commons Attribution License, which permits unrestricted use, distribution, and reproduction in any medium, provided the original work is properly cited.

Fracture characterization is essential for estimating the stimulated reservoir volume and guiding subsequent hydraulic fracturing stimulations in shale reservoirs. Laboratory fracturing experiments can help provide theoretical and technical guidance for field operations. In this study, hydraulic fracturing experiments on the shale samples from Niutitang Formation in Hunan Province (China) under a uniaxial loading condition are conducted. The multifractal method is used to analyze the acoustic emission (AE) signals and characterize fracture initiation and propagation. The hydraulic fracturing process can be divided into three stages based on the characteristics of AE signals: the initial stage, the quiet stage, and the fracturing stage. The multifractal analysis results showed that: (1) the value of the spectrum width, $\Delta\alpha$, continues to increase as the energy accumulates until the fracturing stage starts; and (2) the difference in the multifractal spectrum values, Δf , reflects the relationship between small and large signal frequencies and can quantify the fracture scale, i.e., the lower the Δf , the larger the fracture scale and vice versa. The results were further verified using a time-frequency analysis of the AE signals and micro-CT scanning of the samples. This study demonstrates that the multifractal method is feasible for quantitatively characterizing hydraulic fractures and can aid field hydraulic fracturing operations.

1. Introduction

The shale gas revolution in North America has affected the world energy market and greatly promoted the process of global shale gas exploration and production [1, 2]. Shale gas is usually stored as adsorbed or free gas in organic-rich mud shale, which has (extremely) low porosity and permeability [3, 4]. Hydraulic fracturing (HF) improves reservoir permeability by injecting high-pressure fluid into the ground to form a fracture network that is effectively connected to the wellbore

[5–7]. Microseismic monitoring is generally implemented as a routine technology to monitor the development and expansion of fracturing networks in real time [8, 9]. Additionally, microseismic monitoring technology has also been widely used for monitoring in other fields, including geothermal production, mining, carbon dioxide storage, and other industrial fields [10, 11].

However, in-field microseismic monitoring, underground geological conditions are quite complex, such as the unknown distribution of natural/preexisting fractures and heterogeneous

stress conditions. To effectively control the variables and focus when studying the evolution mechanism of HF, a feasible and important strategy is to simulate field-scale HF monitoring using laboratory-scale experiments with acoustic emission (AE) monitoring [12, 13]. AE is primarily related to the initiation and expansion of cracks. The frequency of laboratory- and small-scale acoustic emissions is generally in a range between several kHz to MHz. By analyzing the AE characteristics of rock fractures, it is helpful to understand the rock fracturing mechanism and provide a theoretical and technical basis for field HF monitoring [14]. Numerous studies have reported laboratory-scale rock fracture analysis using AE monitoring, including the rupture process of brittle rock [15, 16], the mechanical and acoustic properties of shale rocks [17, 18], the characteristics of fracture propagation with bedding planes at different directions [19], and the focal mechanism of AEs during laboratory-scale HF experiments [20, 21].

The processes of rock cracking and propagation have self-similarity and can be described by the fractal method (e.g., fractal dimension) [22]. There are many studies that have characterized rock fracture evolution using the fractal or multifractal analyses of the accompanying AE signals [23–26]. For example, Kong et al. [26] analyzed the fractal characteristics of AE parameters of methane-containing coal samples in triaxial compression experiments. The results of the correlation dimension revealed that the fractal dimension could describe the propagation of a crack. Compared with the conventional fractal method, the multifractal theory has the potential to describe the rock rupture evolution state comprehensively [27, 28]. Kong et al. [29] used the multifractal method to study the AE characteristics of sandstone subjected to thermal treatment. The AE time series had multifractal features, and the fractal dimension followed an increasing-decreasing trend against the temperature. Kong et al. [30] applied the multifractal theory to analyze the AE characteristics of coal samples subjected to uniaxial compression. The results revealed that the time-varying multifractal characteristics could describe the AE mechanisms and the difference in strong and weak AE signals. Tan et al. [31] studied the multifractal characteristics of shale acoustic emission energy in uniaxial experiments under different immersion conditions. The results showed that the multifractal spectrum of the AE parameters was influenced by soaking times, which was directly related to changes in the pores and cracks of the shale samples. However, most of the above studies have focused on conventional compression experiments with intact samples. Therefore, quantitative multifractal analysis of AE parameters that results from shale hydraulic fracturing experiments requires further study.

In this study, the characteristics of AE events in hydraulic fracturing experiments under a uniaxial loading condition are analyzed to evaluate shale fracturing at different stages. The AE signals are quantified using multifractal analysis to study the rupture scale and energy characteristics. Finally, the reliability of the results is further verified using a time-frequency analysis and X-ray computed tomography (CT) scanning. The multifractal analysis can help provide quantitative guidance for fracture characterization during field hydraulic fracturing operations.

2. Materials and Methods

2.1. Sample Preparation. The samples were collected from outcrop shale samples of Niutitang Formation in Yiyang, Hunan Province, China. The outcrop shales were cored into cylindrical samples (size of 50×100 mm) with errors of less than 0.5 mm, and small cylindrical holes (size of 3×55 mm) were drilled at the center of the samples. The size and other physical properties of the six samples are shown in Table 1. Three of the six samples had horizontal bedding characteristics (the direction of bedding plane is parallel to the axial direction), which are termed as H1, H2, and H3. The other three samples were characterized by vertical bedding (the direction of bedding plane is perpendicular to the axial direction), which are termed as T1, T2, and T3. There were no visible fractures at the surface of the samples. The mineral components of the shale samples were quartz, with an average value of 74.2%; feldspar, with an average value of 14.3%; and clay minerals, with an average value of 7.8%. The samples tested were brittle rock and were not influenced by weathering. During the experiment, six acoustic emission (AE) sensors were placed at heights of 15 mm, 50 mm, and 85 mm, as shown in Figure 1(a).

2.2. Experimental System and Scheme. Compared with the true triaxial experiments in field applications, there is no confining pressure under uniaxial loading conditions. It is no doubt that the confining pressure affects the characteristics of both the propagation of the fractures and the accompanying AE events. [32–34]. However, hydraulic fracturing experiments under uniaxial loading conditions can better control associated variables and focus on the mechanism of fracture evolution. Besides, it can also clarify the fracture formation characteristic under different conditions, and reveal the fracture microscopic morphology in guiding field hydraulic fracturing [12]. Hydraulic fracturing experiments under uniaxial loading conditions are used to analyze AE characteristics associated with fracture propagation in various fields including geothermal production, salt well mining, and shale gas exploitation [35, 36].

The uniaxial compressive loading and hydraulic fracturing experiments were conducted using a servo-hydraulically controlled deformation apparatus, the GCTS RTR-2000 rock mechanic system at the Institute of Acoustics, Chinese Academy of Sciences. The system can provide a maximum axial force of 4600 kN and a maximum confining pressure of 210 MPa. Figure 1 shows the experimental system and setup for the shale samples. The PAC AE monitoring system was used for the experiments, which is made by the Physical Acoustic Corporation Ltd., USA for the real-time monitoring of AE signals during hydraulic fracturing (HF) experiments. The components of the acoustic emission monitoring system include AE sensors, preamplifiers, and a central system with recording, processing, and display units (Figure 1(d)). The sampling rate of the AE acquisition was 1 MHz, and the band-pass filter was set to 125–750 kHz. The threshold value of the AE signals was set to 35 dB. The two primary parameters obtained using the AE monitoring system included the AE counts and energy, which can reflect the deformation and fracture process of rock samples. The number of times that the signal exceeded the threshold was the AE counts, and the

TABLE 1: Physical properties of the six shale samples.

Sample ID	Bedding direction	Mass (g)	Diameter (mm)	Height (mm)	Density (g/cm ³)	P-wave velocity (m/s)
T-1	Vertical	461.5	49.81	99.46	2.38	/
T-2		459.1	49.96	99.54	2.35	3805
T-3		463.4	49.9	99.67	2.38	3780
H-1	Horizontal	482.5	49.84	100.33	2.47	4457
H-2		492.4	49.91	100.21	2.51	4450
H-3		500.3	49.94	99.08	2.58	4620

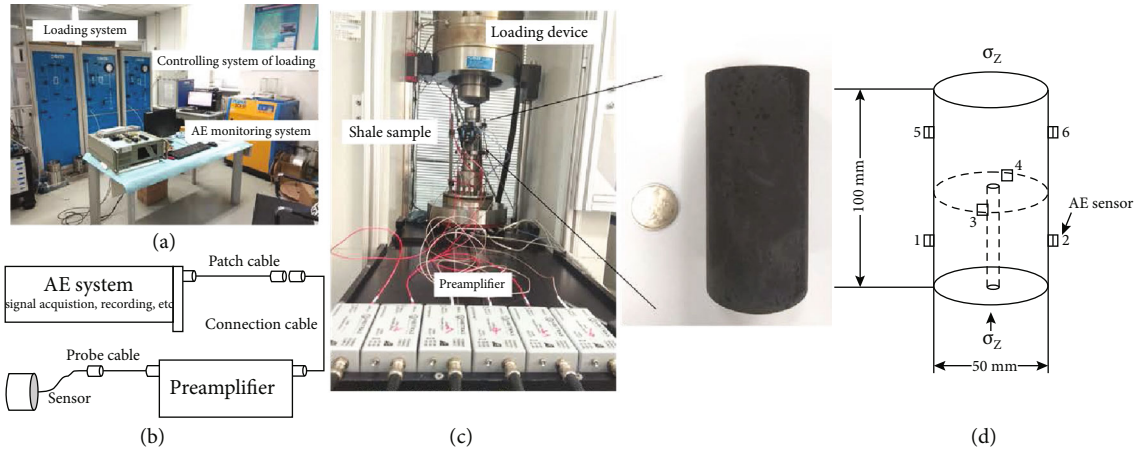


FIGURE 1: The GCTS RTR-2000 rock mechanic system and the experimental setup. (a) The experimental loading system, controlling system, and acoustic emission (AE) monitoring system. (b) The principle sketch of the AE monitoring system. (c) The loading device and preamplifiers. (d) The sample parameters and the sensor arrangement.

total area of the envelope for the AE waveform was defined as the AE energy. Other AE parameters and a typical AE waveform along with the time-frequency characteristics are shown in Figure 2.

The experimental scheme included the following five main steps:

- (1) Sealing Wellbore. A 50 mm long steel pipe was inserted into the injection hole (Figure 1(a)). Epoxy resin was used to seal the injection section of the shale sample. The sealed sample was preserved for 24 hours to ensure a stable sealing.
- (2) Sensor Installation. The heat shrinkage tube was closely bonded to the shale sample, and the AE sensors were placed on the tube surface using honey (Figures 1(a) and 1(c)).
- (3) Axial Loading. The specimen was loaded in the axial direction, and the axial stress value was set to 35 MPa, referring to the measured minimum compressive strength. The axial loading rate was 2 MPa/min.
- (4) Fluid Injection. Water was injected into the borehole at a rate of 2 MPa/min. When a sudden drop in pore pressure (injection pressure) occurred, this would indicate a break or damage of the sample and the system would shut down.

- (5) CT Scanning. After the HF experiments, the fractured samples were removed for micro-CT scanning that produced both 3D images and 2D slices of the cross sections.

2.3. *Multifractal Method.* The fractal method is used to describe the self-similarity of different local features in irregular phenomena in nature, and it is generally represented by the fractal dimension [37, 38]. Fractal analysis has been successfully applied to many branches in petrology and rock physics, such as characterizing the pores and fracture networks in rocks [39–41]. To better quantitatively describe the spatial distribution characteristics of complex systems, the multifractal method has been proposed and utilized [27]. For example, the observed AE signals from rock samples could be multifractal. Hence, there is a need for more than one scaling exponent to characterize AE signals and related fractures [42]. The multifractal method has been used to describe the structural characteristics of rock samples using the generalized fractal dimension and multifractal spectrum [5]. In addition, many studies have adopted multifractal theory to study the AE activity of rock fracturing [26, 30]. In this study, the box-counting method was used to analyze the multifractal characteristics of the time series of the AE parameters [31, 43]. The detailed calculation process of the multifractal spectrum of the AE time series is as follows [31]:

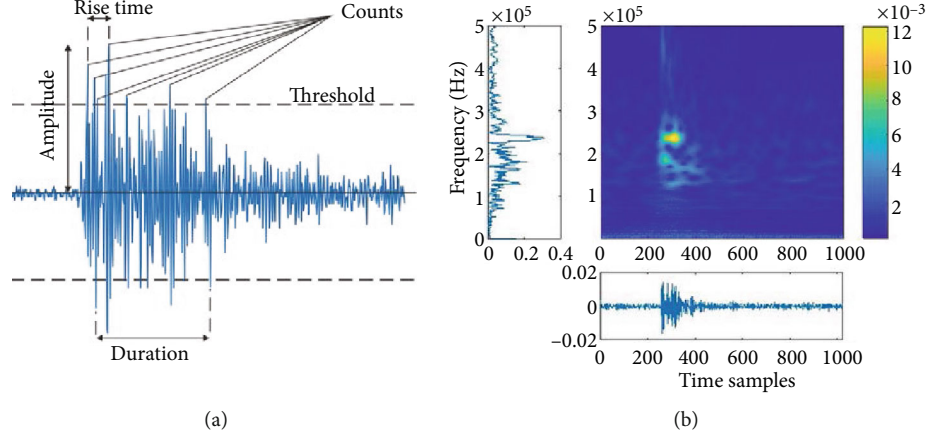


FIGURE 2: AE signals: (a) a sample AE event; and (b) the time-frequency characteristics of a sample AE event.

First, a box with a width of L was used to divide the time series into N subsets. The normalized probability of each subset is $\{P_i(L); i = 1, 2, 3, \dots, N\}$, and the singularity strength is defined as:

$$P_i(L) \sim L^{\alpha_i} \dots \quad (1)$$

When the time series has multifractal regularity, the following relationship can be obtained:

$$N_\alpha(L) \sim L^{-f(\alpha)}, \quad (2)$$

where $f(\alpha)$ is the multifractal spectrum function, which can be also roughly defined as the fractal dimension with the same singularity subset. For calculating the multifractal spectrum of a time series, the following spectrum function was generally used:

$$X(q, L) = \sum_{i=1}^N P_i^q \sim L^{\tau(q)}, \quad (3)$$

where $\tau(q)$ is the quality index, $q \in (-\infty, +\infty)$; and the quality index, $\tau(q)$, is the slope of the relationship of $\ln(X(q, L))$ and $\ln L$ under double logarithmic coordinates. Also, $\tau(q)$ can determine the fractal characteristics of the time series: if the value of $\tau(q)$ changes with q , the AE time series has multifractal characteristics. If it is a constant value for a certain q , the time series has a single regularity. Chhabra and Jensen [43] proposed the normalized single parameter measurement cluster as:

$$\mu_i(q, L) = \frac{[P_i(L)]^q}{\sum_j [P_j(L)]^q}. \quad (4)$$

The multifractal spectrum function, $f(a)$, and singularity strength, $a(q)$, can be computed by:

$$f(q) = -\lim_{N \rightarrow \infty} \frac{\sum_{i=1}^N \mu_i(q, L) \ln \mu_i(q, L)}{\ln N} = \lim_{L \rightarrow 0} \frac{\sum_{i=1}^N \mu_i(q, L) \ln \mu_i(q, L)}{\ln L},$$

$$\alpha(q) = -\lim_{N \rightarrow \infty} \frac{\sum_{i=1}^N \mu_i(q, L) \ln P_i(q, L)}{\ln N} = \lim_{L \rightarrow 0} \frac{\sum_{i=1}^N \mu_i(q, L) \ln P_i(q, L)}{\ln L}. \quad (5)$$

When the value of q is determined, $a(q)$ and $f(a)$ can be calculated, and we can obtain the multifractal spectrum $f(a) - a(q)$ of the time series. The heterogeneity of the time series can be indicated by the spectrum width $\Delta\alpha = \alpha_{\max} - \alpha_{\min}$ [30, 44]. The larger $\Delta\alpha$ is, the greater the difference between the large and small signals is. In addition, the value of $f(a)$ represents the frequency at which the singularity strength, $a(q)$, occurs in the time series. Therefore, $\Delta f = f(a_{\max}) - f(a_{\min})$ indicates the frequency of occurrence of the large and small signals: $\Delta f < 0$ means the large-amplitude signals dominate, and the larger-scale fractures dominate the fracture system. In contrast, $\Delta f > 0$ means the amplitude/energy of most AE signals is small, and small-scale fractures dominate the fracture system.

3. Results and Discussion

3.1. Mechanical Behaviors. During the fluid injection process, the pore pressure and AE signals were recorded. Table 2 lists the vertical stress and pore pressure loading on the shale samples. Figure 3 shows the relation of the pore pressure and loading time. The curves of the vertical samples were shifted 400s horizontally to present a clear comparison between the horizontal and vertical samples. The maximum pore pressures of the horizontal samples were 14.52 MPa, 16.78 MPa, and 18.27 MPa, while those of the vertical samples were 26.53 MPa, 27.98 MPa, and 29.04 MPa, which are approximately double compared with the horizontal samples. Since the mineral composition was basically the same and the samples had no visible preexisting fractures, the results suggest that the bedding structure played a controlling role on the process of rock deformation and fracturing. The results are consistent with Lin et al. [45], and it showed the effects of the anisotropy on fracture propagation in shale samples. As

TABLE 2: Vertical stress and pore pressure loading on the six shale samples.

Samples	Vertical stress (MPa)	Injection rate (MPa/min)	Maximum pore pressure (MPa)
H1	35	2	14.52
H2	35	2	16.78
H3	35	2	18.27
T1	35	2	26.53
T2	35	2	27.98
T3	35	2	29.04

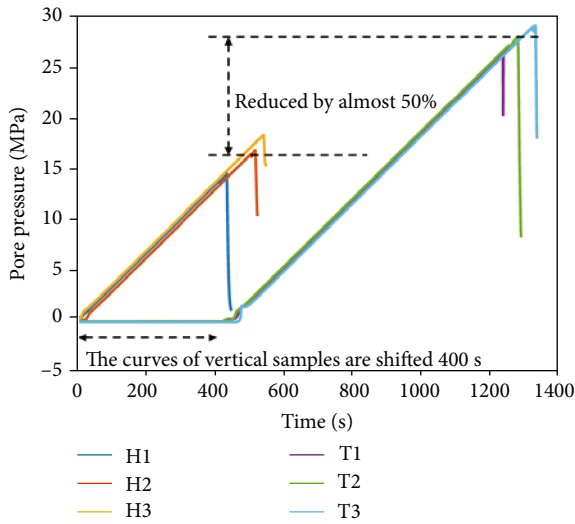


FIGURE 3: Time history of the pore pressures.

the pore pressure increased, the effective normal stress decreased continuously. Once the breakdown pressure was reached, the fracture initiated along the direction of the minimum principal stress and propagated along that of the maximum principal stress, which was in the vertical direction here. The bedding direction of the horizontal samples was parallel to the axial direction, and lower pore pressures were required to break the samples compared with the vertical samples. In addition, the bedding direction of which was nearly perpendicular to the direction of the fracture propagation [46–49]. The results are also consistent with the principle of the extensively-used horizontal well drilling technology in shale gas exploitation in which wells are drilled along the bedding direction (horizontal) to achieve a smaller breakdown pressure and a larger contacting volume with the target layer [50]. It is worth mentioning that shale anisotropy also has important effects on the field fracturing operation [51]. In the current study, we only focus on testing and validating the effectiveness of the multifractal method, without considering the shale anisotropy. We believe that further studies are required to address the anisotropic issues when generalizing the method to the field scale.

3.2. *Multifractal Analysis of AE Signals.* There are several studies that have classified the fracturing process based on fracturing experiments. Damani et al. [52] reported that the

fracture pressure response can be divided into six broad regions according to the pump pressure and cumulative AE events. Jiang et al. [53] divided the shale supercritical CO₂ fracturing process into the fracture initiation stage and the fracture propagation stage according to the AE parameter curves.

Figure 4 shows the relationship of the AE counts, the AE energy, and the loading pore pressure for the horizontal samples (H1, H2, H3). Figure 5 shows the corresponding results of the vertical samples (T1, T2, T3). It is obvious that the AE counts and the AE energy shared a similar trend in all of the samples. In addition, the accumulative counts and energy steadily increased with the loading pore pressure. There is a difference between the detailed plots of the different samples, which was largely caused by the heterogeneity of the samples. As the loading pore pressure increased, the effective normal stress inside the rock sample decreased continuously. When the Mohr stress circle reached the rupture envelope surface, the rock broke down and generated a large amount of AE events [5, 54, 55]. Therefore, the hydraulic fracturing process can be roughly divided into three stages based on these plots [52, 53, 56]. First is the initial stage, which corresponds to the beginning of the water injection, where a small number of AE events occurred as the pore pressure increased instantaneously. Then, the quiet stage in which the fracturing system tended to be stable and the AE activity was inactive (“quiet”). Finally, the fracturing stage indicated the breakdown of the rocks and a sudden increase in the AE counts and energy. An important difference between the horizontal and vertical samples was the duration of the quiet stage. According to the dashed green lines in Figures 4 and 5, the duration of the quiet stage (stage II) for the horizontal and vertical samples was approximately 400 s and 700 s, respectively. This is consistent with the larger pore pressure required for the fracturing of vertical sample, which was largely caused by the direction of the bedding planes and discussed in the above section.

The multifractal method was used to further quantify the AE characteristics associated with the hydraulic fracturing experiments. It has been demonstrated that the time series of the AE parameters has multifractal characteristics [31]. The multifractal spectrum of the AE counts and energy time series throughout all stages is shown in Figure 6. The complete results for both the individual and overall stages are listed in Table 3. The results are closely related with the characteristics of fracture evolution. The values of the spectrum width, $\Delta\alpha$, of the AE counts for the six rock samples vary between two and four, which means the dispersion of the AE signals was relatively obvious. The primary reason is that the fracturing process can produce both large and small AE events/signals. The multifractal spectrum of the AE energy showed that the $\Delta\alpha$ values were between three and five, which shows a consistent result of the AE counts. The entire process of shale hydraulic fracturing can be divided into different stages, including the initiation stage, the quiet stage, and the fracturing stage, and these naturally produce AE events with varying characteristics (e.g., counts and energy).

The different $\Delta\alpha$ values of the samples with the same bedding direction partially revealed the heterogeneity of the AE parameters/signals and that of the shales. In sample T3

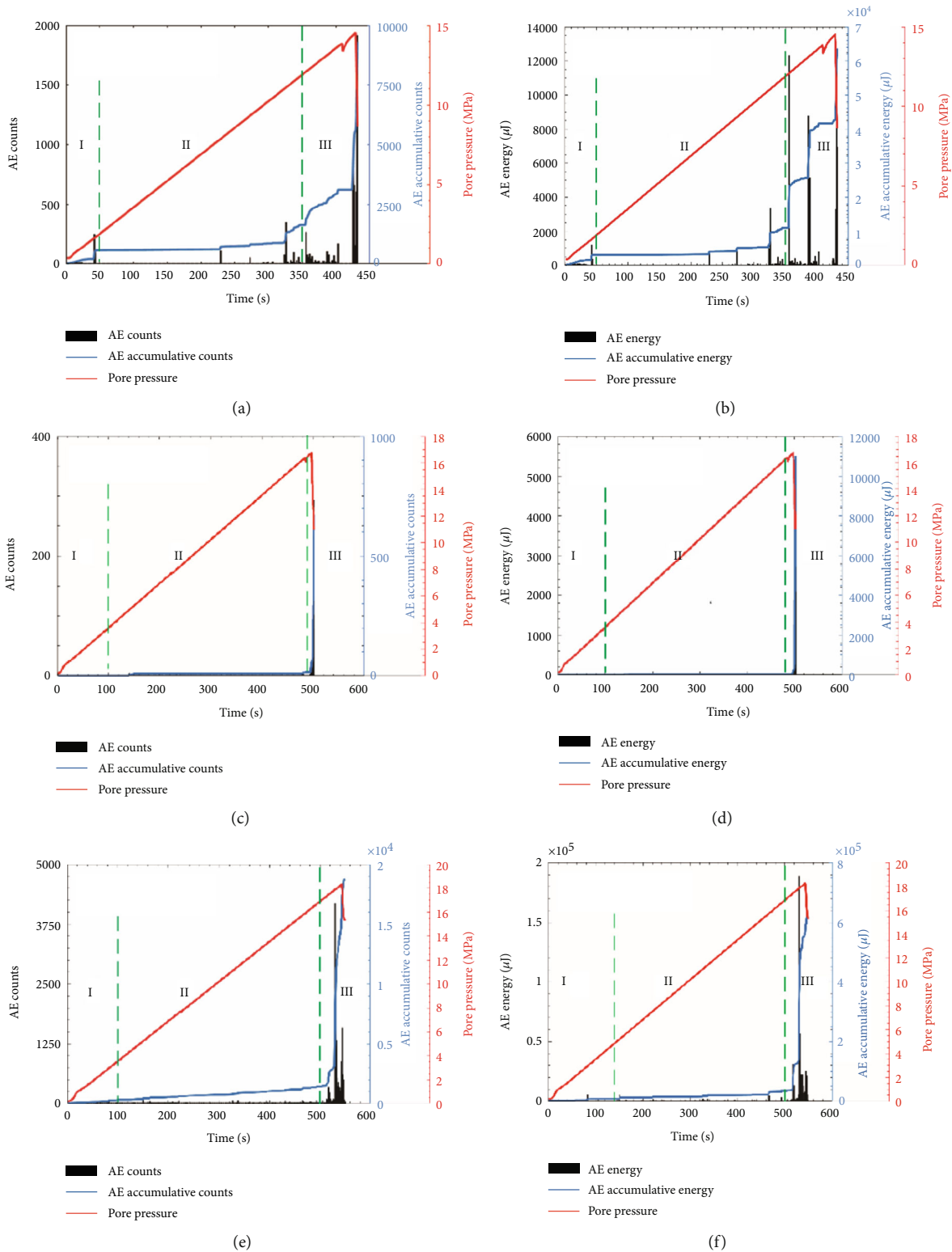
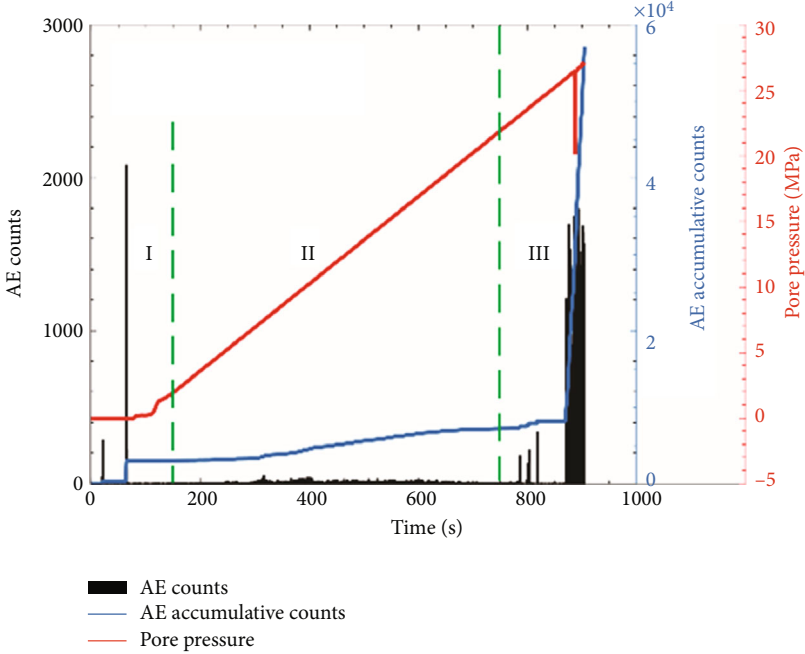


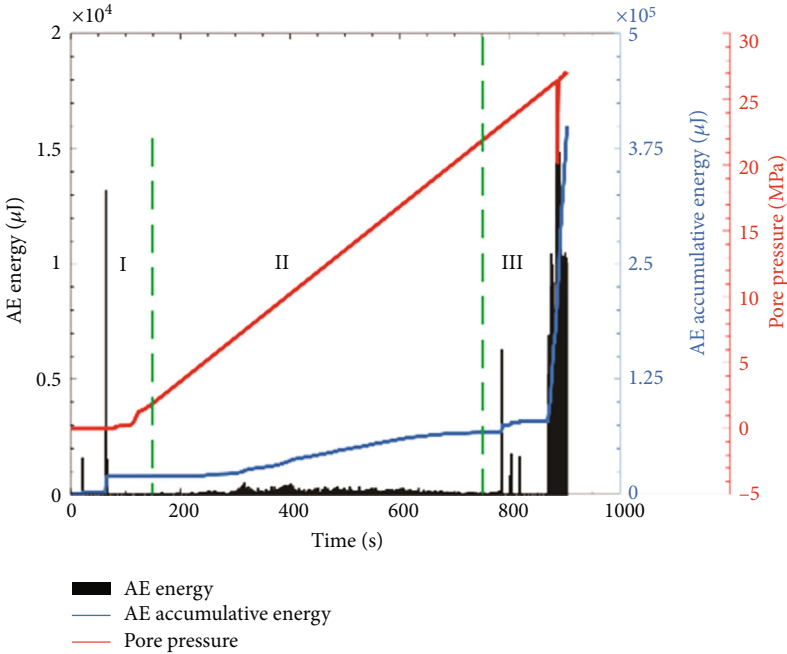
FIGURE 4: Plots of the relationship between the AE counts/accumulative counts, AE energy/accumulative energy, and loading pore pressures for the horizontal samples H1, H2, H3. (a, b) Plots of the sample H1. (c, d) Plots of the sample H2. (e, f) Plots of the sample H3. The green dashed lines roughly indicate the three stages (I: initial stage; II: quiet stage; and III: fracturing stage) of the fracturing process.

for example, the $\Delta\alpha$ values of the AE count and energy for all of the stages were 2.140 and 3.261, respectively. The values were relatively smaller than those of the other samples, indi-

cating a small difference in the AE activities and/or fracture scales during the different stages. The difference in the multi-fractal spectrum values, Δf , reflects the amplitude/energy of

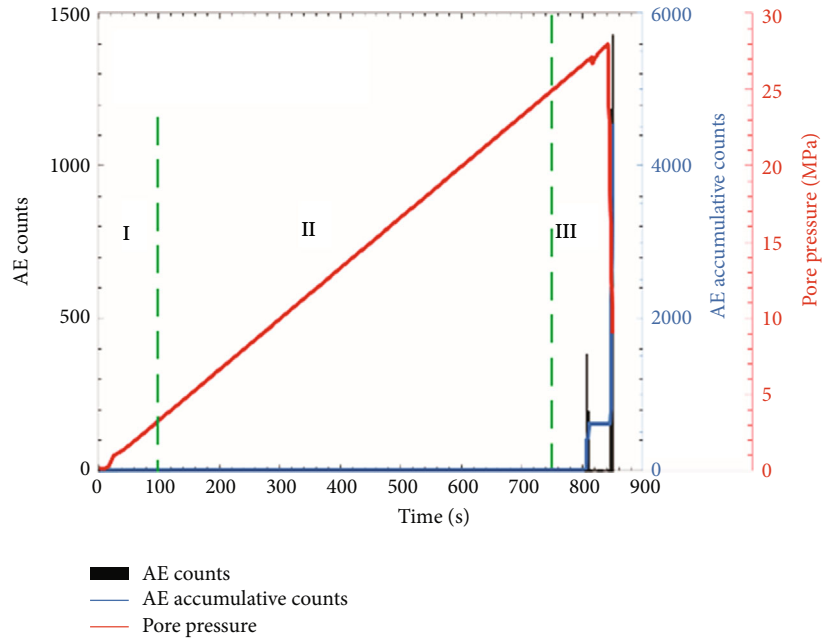


(a)

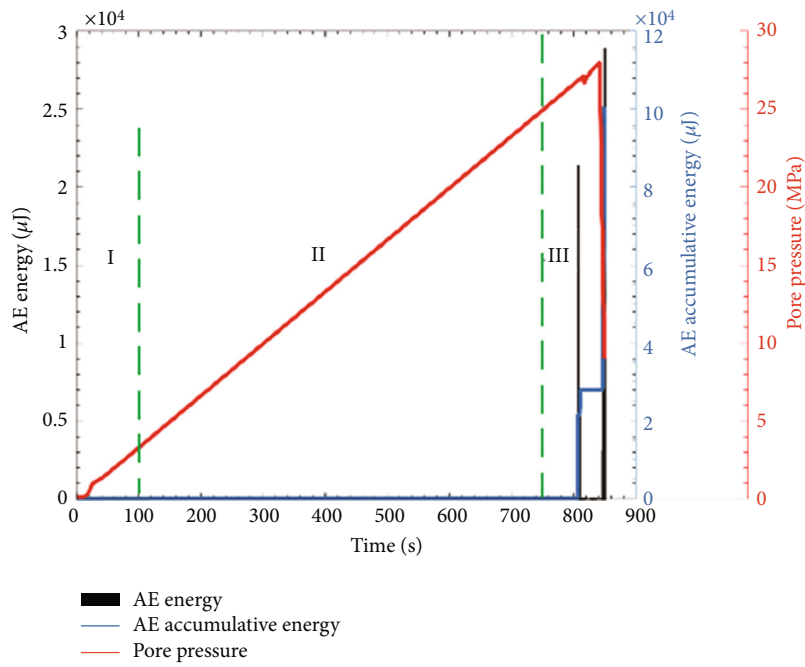


(b)

FIGURE 5: Continued.



(c)



(d)

FIGURE 5: Continued.

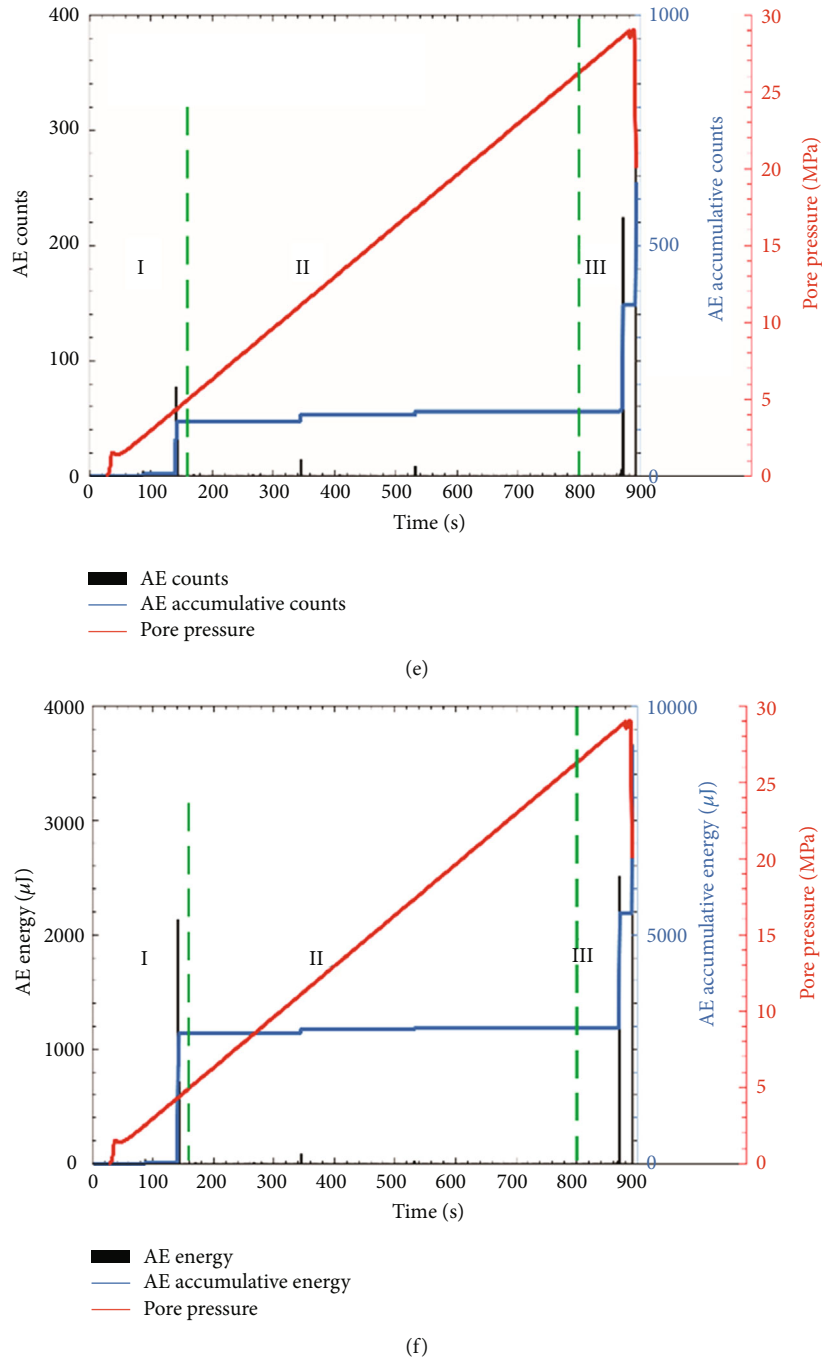


FIGURE 5: Plots of the relationship of AE counts/accumulative counts, AE energy/accumulative energy, and loading pore pressures for the vertical samples T1, T2, T3. (a, b) Plots of sample T1. (c, d) Plots of sample T2. (e, f) Plots of sample T3. The green dashed lines roughly indicate the three stages (I: initial stage; II: quiet stage; and III: fracturing stage) of the fracturing process.

the AE events and the scale of the fractures. Most of the Δf values of the horizontal samples were positive values, which means the fracturing process was dominated by small-scale fractures. The Δf values of the AE count and energy for sample H2 were 1.643 and 1.639, respectively. The values were larger than those of the other two horizontal samples, and subsequent CT scanning results also showed several small-scale fractures (see Figures 7 and 8). However, the AE count and AE energy Δf values of the vertical sample, T2, for all the stages were negative, and these were -1.884 and

-1.839 for the AE count and energy, respectively. The CT scanning results of sample T2 showed large-scale fractures (see Figures 9 and 10) that resulted from the relatively large injection pressure and the connection between new fractures and weak bedding planes (preexisting fractures). More detailed discussions of the time-frequency analysis and CT scanning are presented in later sections.

Figure 11 shows the variations in $\Delta\alpha$ and Δf values for the different samples at different stages. For the horizontal samples, $\Delta\alpha$ increased along with loading times and stages.

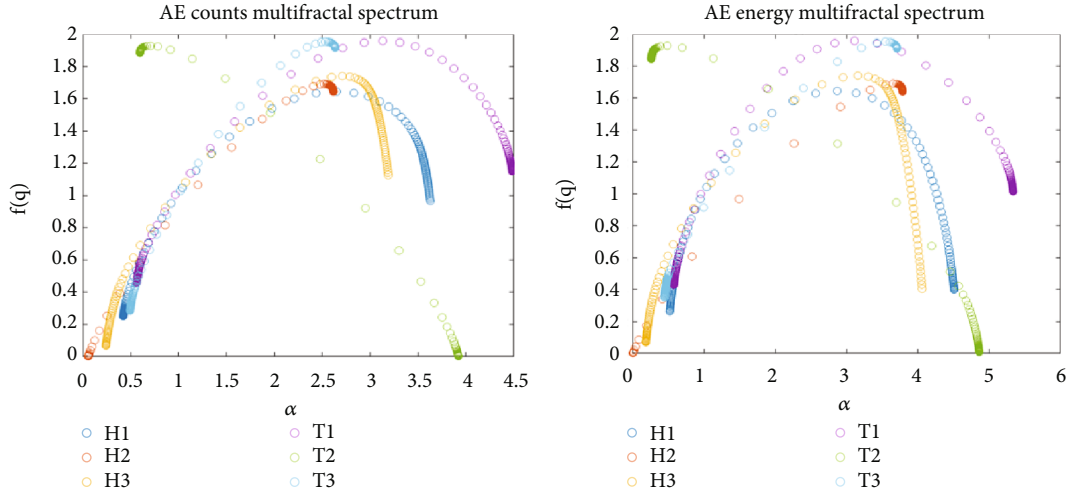


FIGURE 6: The multifractal spectrum $f(\alpha) - \alpha$ of time series of AE counts and energy for all the stages.

TABLE 3: Values of $\Delta\alpha$ and Δf for different samples at different stages.

Sample		Counts				Energy			
		Stage I	Stage II	Stage III	All stages	Stage I	Stage II	Stage III	All stages
H1	$\Delta\alpha$	1.296	2.440	3.291	3.208	1.113	3.243	4.024	3.986
	Δf	0.007	0.607	-0.147	0.714	-0.029	0.301	-0.262	0.135
H2	$\Delta\alpha$	0.006	1.197	2.574	2.557	0.006	1.555	3.800	3.780
	Δf	-0.003	-0.430	0.264	1.643	-0.003	-0.090	0.282	1.639
H3	$\Delta\alpha$	0.841	1.076	2.291	2.946	2.008	2.374	3.493	3.874
	Δf	0.142	-0.180	0.129	1.060	0.061	0.035	-0.001	0.336
T1	$\Delta\alpha$	3.151	1.608	3.927	3.921	3.966	1.738	4.764	4.756
	Δf	0.993	-0.336	0.255	0.690	0.804	-0.357	0.297	0.586
T2	$\Delta\alpha$	0.004	1.177	3.133	3.329	0.521	1.839	4.402	4.596
	Δf	0.002	0.552	0.000	-1.884	-0.537	0.214	0.011	-1.839
T3	$\Delta\alpha$	2.154	1.631	1.804	2.140	3.287	2.379	3.192	3.261
	Δf	0.567	-0.073	1.143	1.631	0.667	0.046	1.121	1.562

During the initial stage, the injection pressure was small and only excited small AE events. As the injection pressure increased, the strain energy continuously accumulated. At the fracturing stage, small fractures were extended and connected to form large-scale fractures. Therefore, both small and large AE events were generated, and the difference between small and large signals increased. Several previous studies also revealed that the $\Delta\alpha$ value rose gradually along with hydraulic fracturing [30, 44]. However, for the vertical samples, the results were more complex. A possible reason was the inconsistency in the directions of the principal stress and the bedding planes. And there were few AE events at the quiet stage and led to low $\Delta\alpha$ values. For samples H2 and T2, the values of $\Delta\alpha$ during different stages varied greatly, revealing a difference in the AE activity and/or fracture scales throughout all the stages. In addition, most large-scale fractures and AE events occurred during the final fracturing stage.

3.3. Time-Frequency Analysis. AE waveforms and frequencies contain important information during hydraulic fracturing, including internal fracture size and fracture type [21, 57, 58]. The microscopic evolution characteristics can be inferred by statistically analyzing the time-frequency characteristics of the AE signals during the fracturing process [35, 59]. First, the time domain AE signal was converted into the time-frequency spectrum using a wavelet transform to obtain the main frequency of its signal. AE events were classified to four types: low amplitude in low frequency band (LL), high amplitude in low frequency band (HL), low amplitude in high frequency band (LH), and high amplitude in high frequency band (HH) (Table 4). The maximum amplitudes and main frequency contents are statistically summarized in Figure 12. It can be seen that a small number of LL-type and LH-type AE events were generated during the initial stage of hydraulic fracturing, and the amplitude was on the order of 10^{-2} . As the

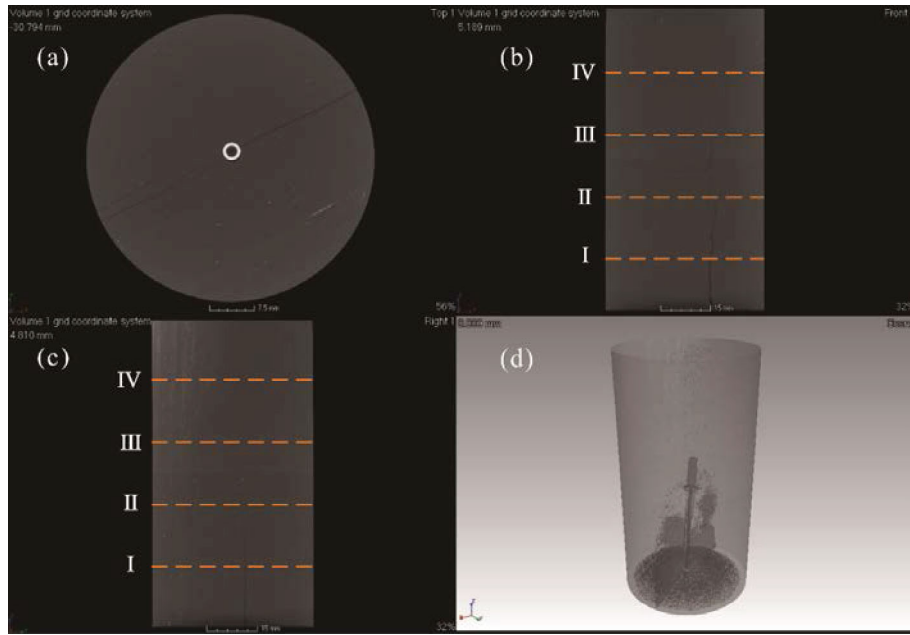


FIGURE 7: Micro-CT scanning results of rock sample H2. (a) A horizontal slice. (b, c) Two vertical slices near the sample center and are cut roughly perpendicular to the fractures, and I-IV correspond to the horizontal slices at heights of 20 mm, 40 mm, 60 mm, and 80 mm. (d) The 3D view of the scanning result.

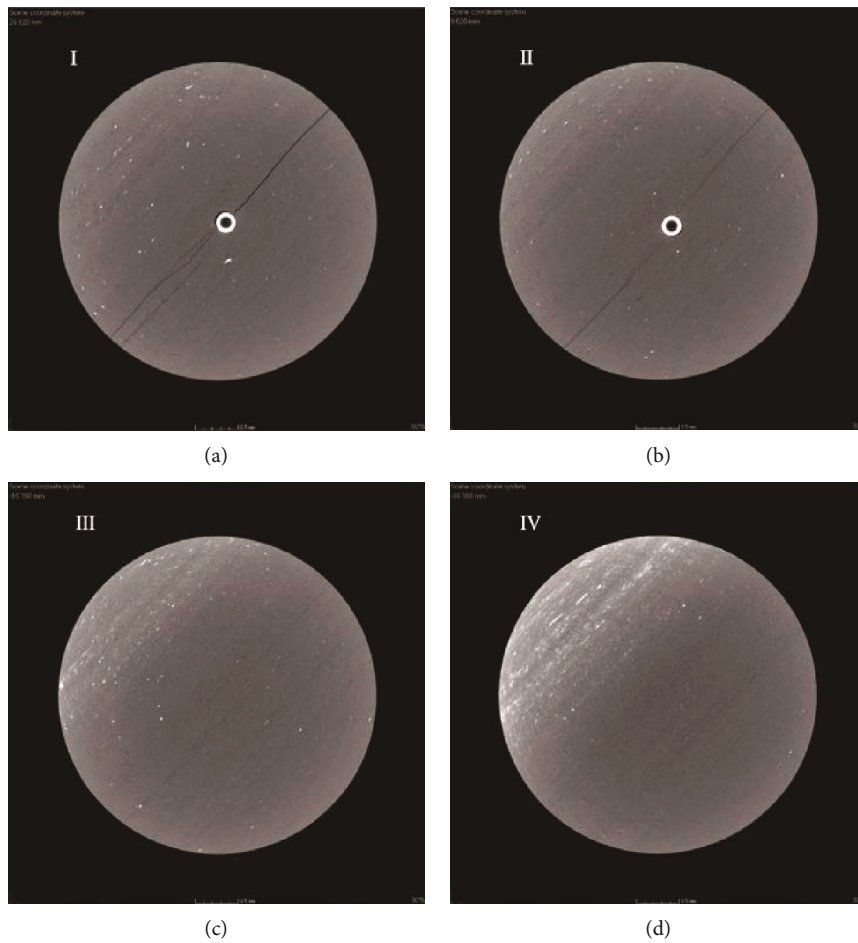


FIGURE 8: Four horizontal slices of the micro-CT scanning results of rock sample H2. (a–d) Correspond to the horizontal slices at heights of 20 mm, 40 mm, 60 mm, and 80 mm, respectively.

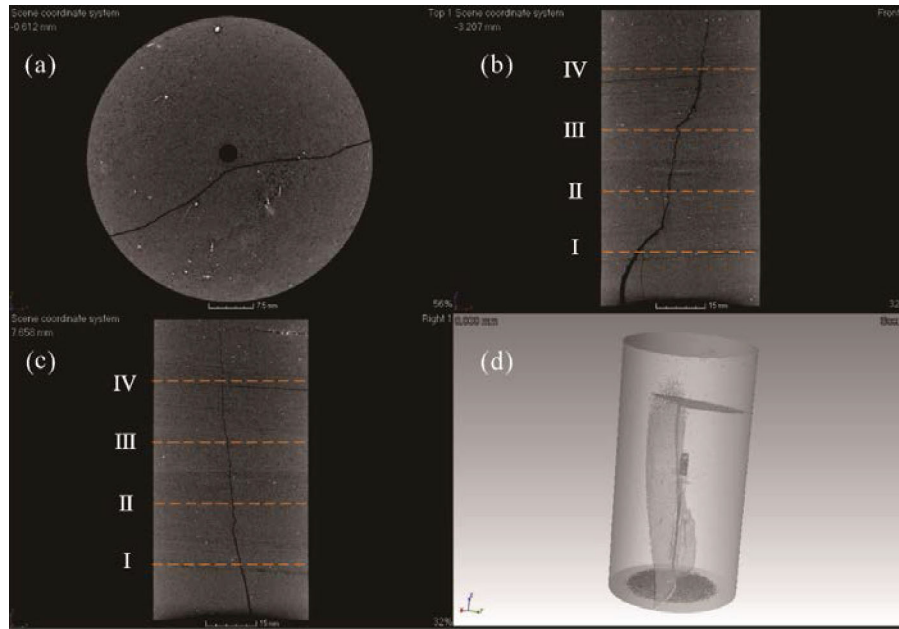


FIGURE 9: Micro-CT scanning results of rock sample T2. (a) A horizontal slice. (b, c) Two vertical slices near the sample center and are cut roughly perpendicular to the fractures, and I-IV correspond to the horizontal slices at heights of 20 mm, 40 mm, 60 mm, and 80 mm. (d) The 3D view of the scanning result.

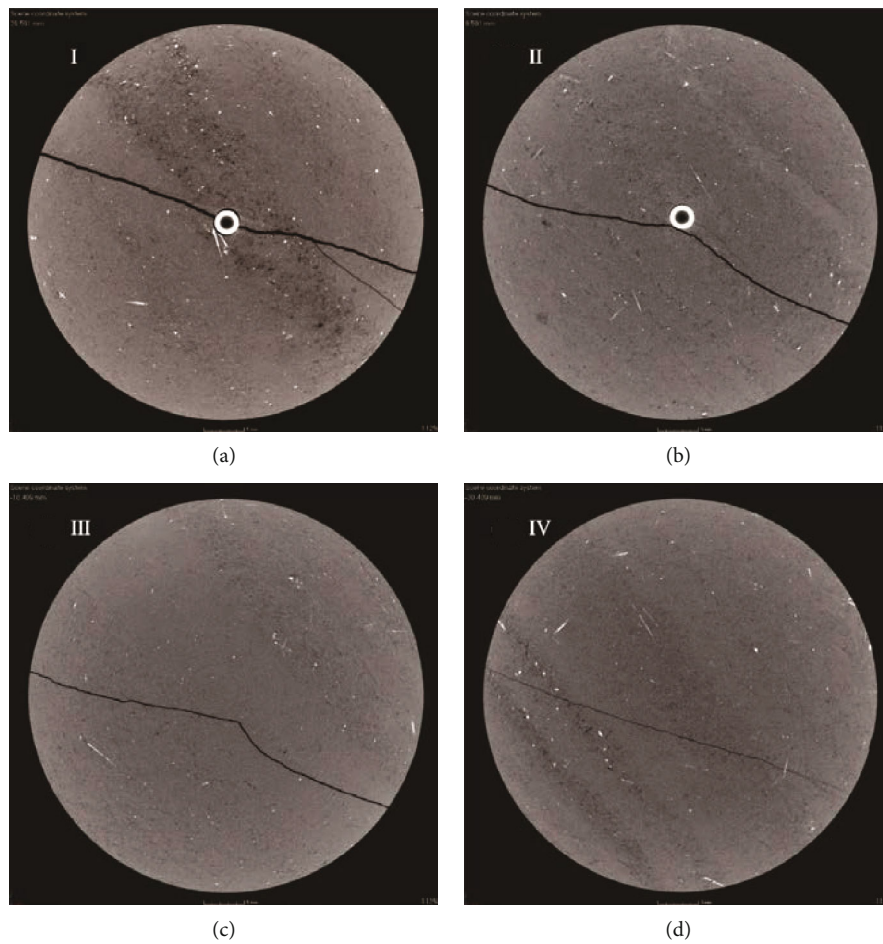


FIGURE 10: Four horizontal slices of the micro-CT scanning results of rock sample T2. (a-d) Correspond to the horizontal slices at heights of 20 mm, 40 mm, 60 mm, and 80 mm, respectively.

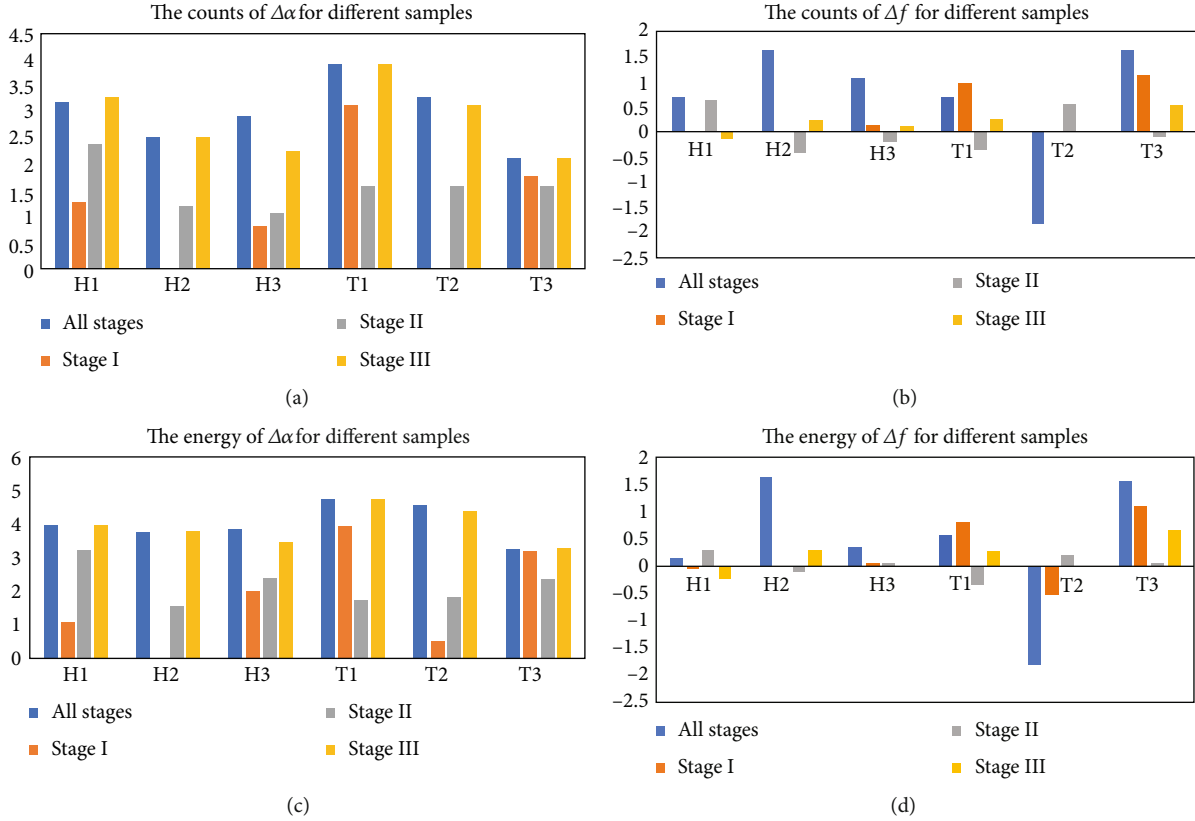


FIGURE 11: Values of $\Delta\alpha$ and Δf for the different samples at different stages. (a, b) Corresponding to $\Delta\alpha$ and Δf of the AE counts. (c, d) correspond to $\Delta\alpha$ and Δf of the AE energy.

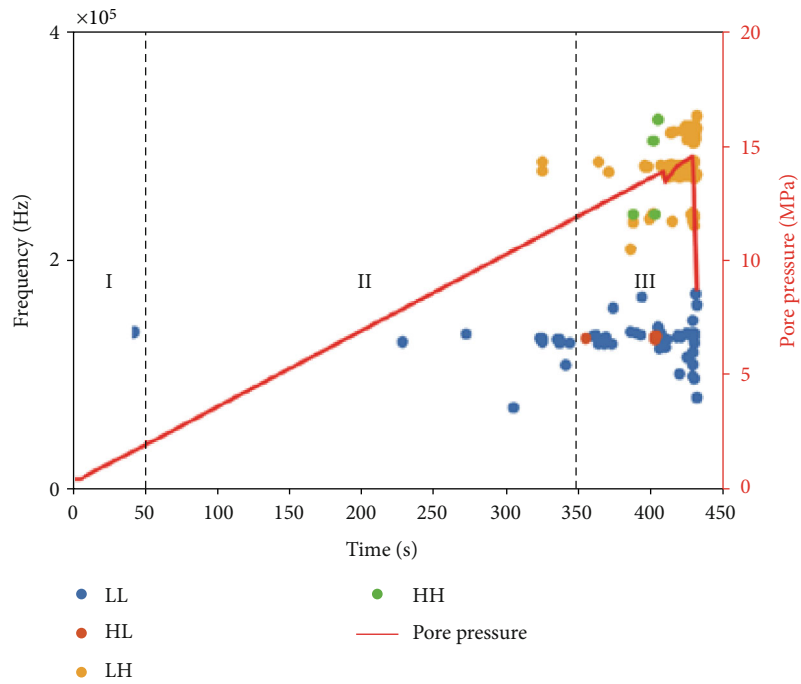
TABLE 4: Types of time-frequency characteristics of AE signals.

	Low amplitude (0-0.1)	High amplitude (0.1-5)
Low frequency band (0-200 kHz)	Low amplitude in low frequency band (LL)	High amplitude in low frequency band (HL)
High frequency band (200-400 kHz)	Low amplitude in high frequency band (LH)	High amplitude in high frequency band (HH)

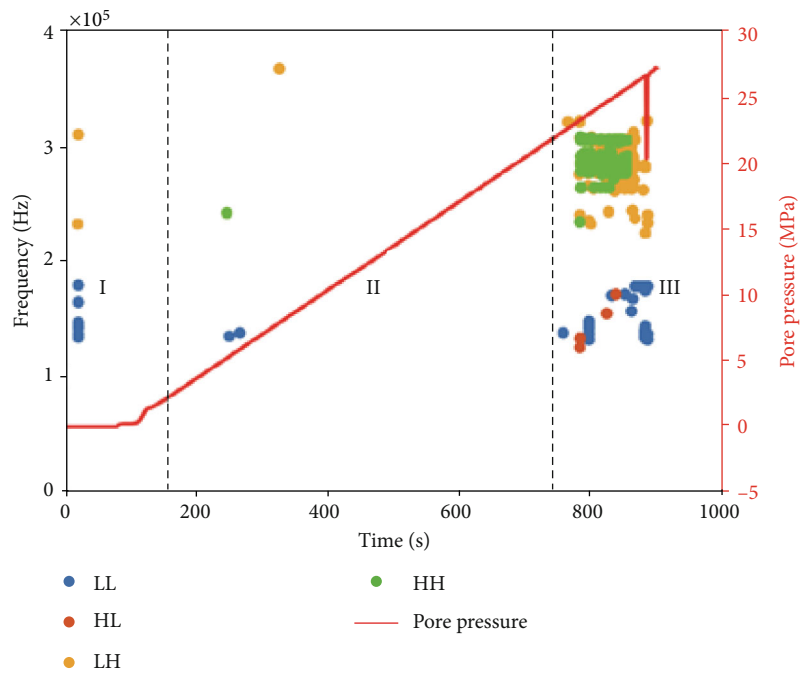
injection pressure gradually increased, the effective principal stress decreased continuously, and strain energy was accumulated. LL-type AE events were continuously generated during this stage. Once the breakdown pressure was reached, the crack initiated and propagated to form small-scale fractures, producing more LH-type AE events. Simultaneously, small-scale cracks might have been connected to each other, forming large-scale fractures and producing HL type AE signals. Therefore, large-scale and small-scale fractures coexisted simultaneously during the fracturing stage. This was consistent with the variations of the multifractal spectrum values Δf at different stages and further verified the reliability of the results. And the HL- and LH-type AE signals were used as precursors before samples cracking [35]. Though the mineral composition of the rock samples is almost the same, the maximum pore pressures of the vertical and horizontal rock samples are also in the same range; the energy and the count values of AE events show a large difference. It is obvious that the anisotropy of shale seriously affects its physical properties. For the two horizontal rock samples H2 and H3, the number of events in the first and second stages is relatively small. How-

ever, in the third stage, the HH-type and the HL-type AE events of rock sample H3 are much larger than those of H2.

3.4. CT Scanning. The internal structural characteristics of the horizontal sample H2 and the vertical sample T2 were studied using micro-CT scanning. Figures 7 and 9 show the overview of the micro-CT scanning results of rock samples H2 and T2. Figures 8 and 10 show four horizontal slices of the scanning results. The fractures initiated in the vicinity of the injection hole and continuously propagated along the axial direction (the vertical direction, which is also the direction of the maximum principal stress). The fractures were finally connected and formed a fracture plane, which was also nearly parallel to the axial direction. The morphological characteristics of the fractures are closely related to the confining pressure. When the axial pressure is much greater than the confining pressure, the fracture will propagate perpendicular to the direction of the local minimum principal stress, along with the borehole wall [60, 61]. The different scales of the cracks of the two samples were also consistent with the results of the multifractal spectrum values.

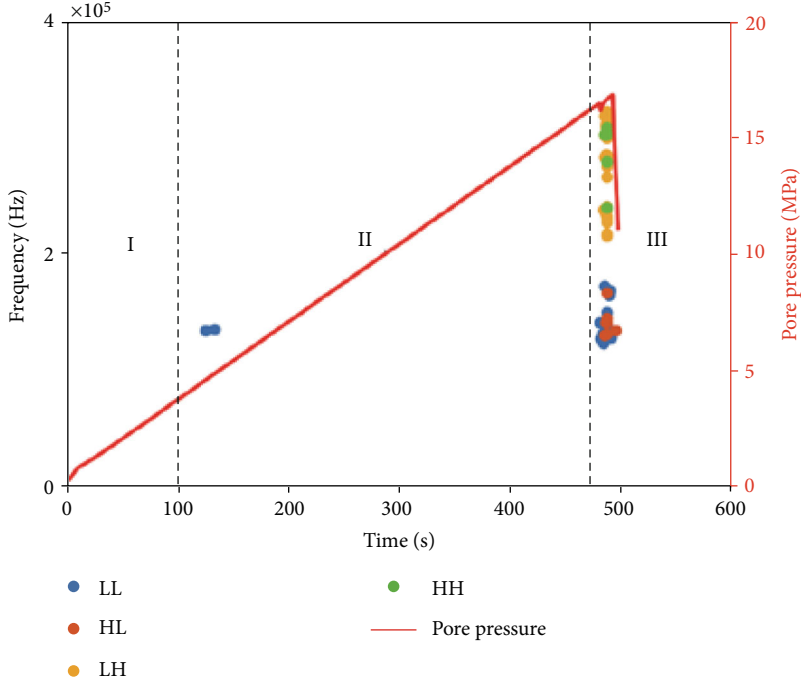


(a)

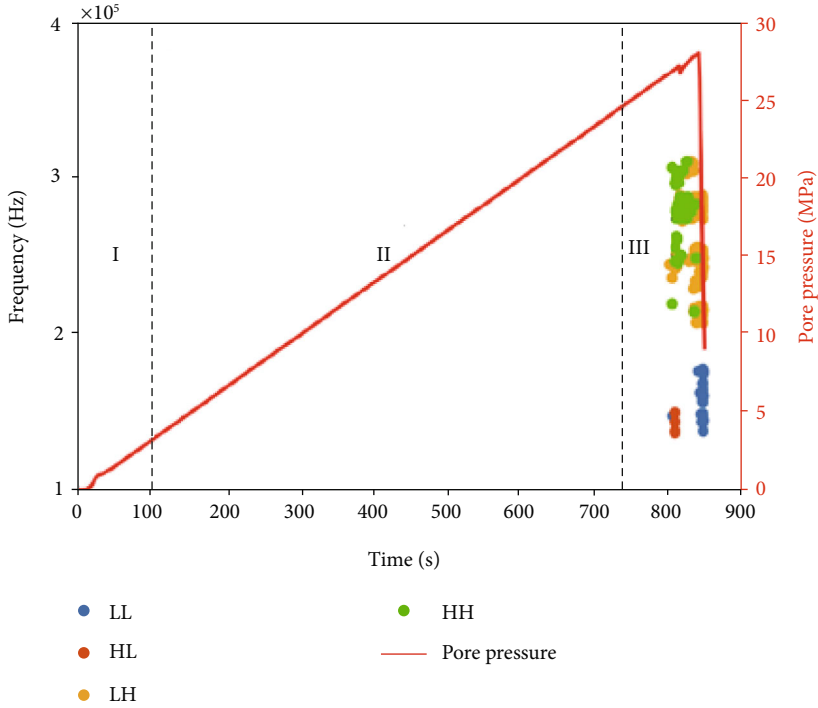


(b)

FIGURE 12: Continued.



(c)



(d)

FIGURE 12: Continued.

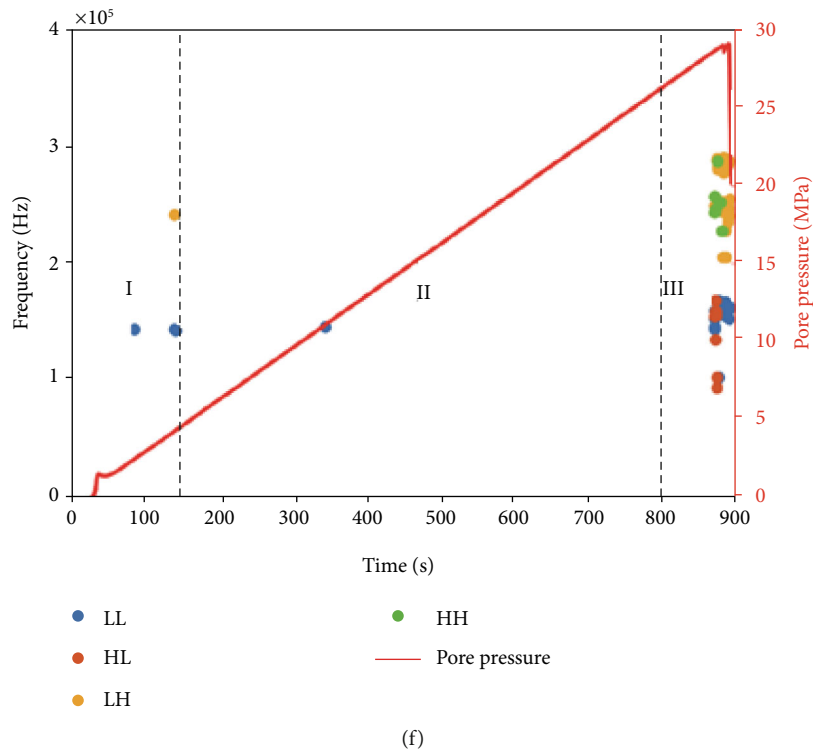
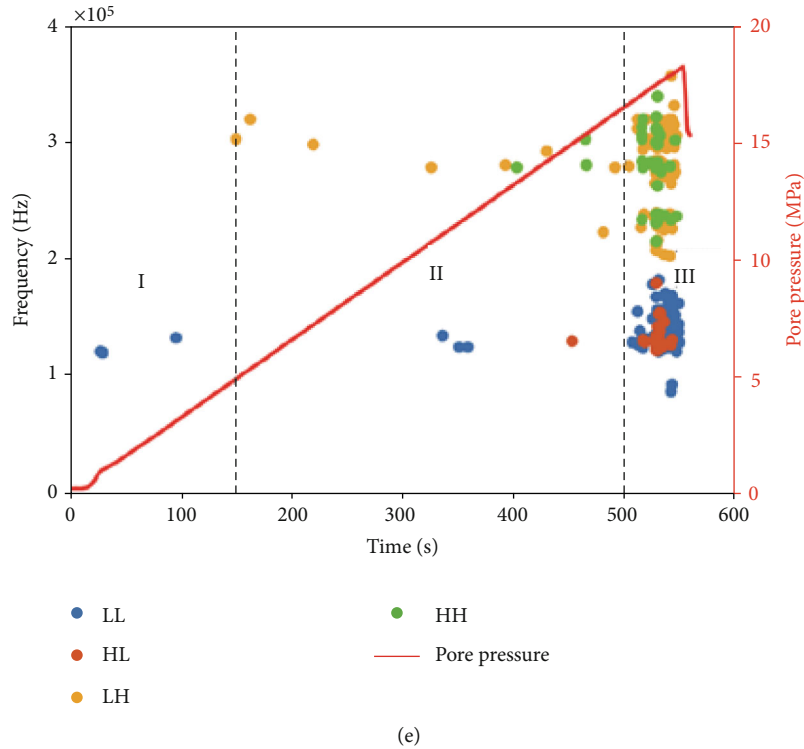


FIGURE 12: Time-frequency characteristics of the AE signals. (a–f) correspond to the results of H1, T1, H2, T2, H3, and T3, respectively.

For the horizontal sample H2, the scale of the fractures was small, and only a few fractures were visible. The fractures remained in the vicinity of the injection hole and did not propagate vertically far away from the injection hole (see Figure 8). The fracture widths corresponded to heights of 20 mm and 40 mm and were relatively large, being 0.1–

0.15 mm and 0–0.1 mm, respectively [62]. There were no visible fractures in the horizontal slices corresponding to the heights of 60 mm and 80 mm. A possible reason is that the injection (pore) pressure was small, and only small-scale fractures were produced. To quantitatively study the morphological characteristics of the fractures, an image

TABLE 5: Characteristics of visible fractures of rock samples H2 and T2.

	Direct length (mm)	Length (mm)	Width (mm)	Tortuosity	
H2	I	47.50	47.69	0-0.15	1.00
	II	47.62	48.11	0-0.15	1.01
	III	/	/	/	/
	IV	/	/	/	/
T2	I	48.90	49.68	0.10-0.40	1.02
	II	47.90	48.80	0.20-0.30	1.02
	III	46.88	48.47	0.10-0.20	1.03
	IV	47.36	47.83	0.05-0.15	1.01

processing software (Image J) was used to calculate the length and curvature of the visible fractures in the horizontal slices. The detailed results are listed in Table 5. The tortuosity was defined as the ratio of the total fracture length to the two direct lengths of the ends of the fracture [63]. The tortuosity of the visible fractures was small, and the fractures penetrated the rocks nearly straightly.

For the vertical sample T2, the fracture width and scale were larger than those of horizontal sample H2. This was a result of the relatively larger maximum injection pressure. Fracture width gradually decreased from the bottom (0 mm) to the top (100 mm). The reason was that the fractures initiated at the bottom portion of the sample, where the injection hole was located. Another important and distinct characteristic was the nearly horizontal fracture plane at a height of approximately 80 mm, which was potentially caused by weakness of the bedding planes and/or nonvisible preexisting fractures. The fracture length, width, and tortuosity of samples H2 and T2 are quite different. The horizontal sample H2 is dominated by small-scale fractures, while the vertical sample T2 is dominated by large-scale fractures.

4. Conclusions

Hydraulic fracturing experiments were conducted under a uniaxial loading condition on shale samples from the Niutitang Formation in Yiyang, Hunan Province (China). The AE signals were recorded during the fracturing process, and the multifractal method was used to characterize fracture initiation and propagation. The study indicated that the multifractal method can be used to quantitatively characterize hydraulic fracturing and can contribute to optimize in situ hydraulic fracturing operations. The results were further verified using a time-frequency analysis of the AE signals and micro-CT scanning of the samples. The primary conclusions are listed below.

- (1) The direction of the bedding planes largely affected the required injection pressure that fractured the rock. The required pressure needed for rocks with bedding planes parallel to the direction of maximum principal stress was less (nearly half) than those with vertical bedding planes under essentially the same conditions.

- (2) The hydraulic fracturing process could be divided into three stages based on the characteristics of AE signals: an initial stage, the quiet stage, and the fracturing stage. During the initial stage, a small number of AE events were excited due to the instantaneous change in pore pressure. Also, the strain energy accumulated and a few AE events occurred during the quiet stage. During the fracturing stage, the fractures initiated and propagated promptly and produced a large amount of AE events. A multifractal analysis of the time series of the AE counts and energy quantitatively characterized the heterogeneity of the AE signals during hydraulic fracturing. The value of spectrum width, $\Delta\alpha$, continued to increase as the energy accumulated until the fracturing stage began. The Δf value reflects the relationship between small and large signal frequencies and quantifies the fracture scale. Hence, the lower the Δf , the larger the fracture scale, and vice versa.
- (3) The time-frequency analysis and CT scanning results further demonstrated the different magnitudes and scales of the AE signals and the fractures. Most AE events and large fractures were produced during the fracturing stage. The required fracturing pressure for the vertical samples was larger, while more large-scale fractures and complex fracture planes might be generated due to the existence of bedding planes that vertically or obliquely cross the maximum principal stress. The time-frequency characteristics can verify the change of the multifractal spectrum parameter $\Delta\alpha$. And the LH- and HL-type AE signals can be used as precursors of rock failure. CT scanning results were consistent with the multifractal spectrum parameter Δf . These results further verified the stage classification and multifractal results of the AE signals.

Data Availability

The data used to support the findings of this study are available from the corresponding author upon request.

Conflicts of Interest

The authors declare that there is no conflict of interest regarding the publication of this paper.

Acknowledgments

The work is sponsored by the National Natural Science Foundation of China (grant no. 41872151), the National Thousand Young Talents Program (Jingqiang Tan, grant no. 413170110), the Innovation-driven Project of Central South University (grant no. 502501005), Hunan Provincial Natural Science Foundation of China (grant no. 2019JJ50762), the China Postdoctoral Science Foundation (grant no. 2019M652803), the Graduate Research Innovation Project of Central South University (grant no. 2020zzts661), and the Open Research Fund Program of State Key Laboratory of Acoustics, Chinese Academy of Sciences (grant no. SKLA201911).

References

- [1] R. W. Howarth, A. Ingraffea, and T. Engelder, "Should fracking stop?," *Nature*, vol. 477, no. 7364, pp. 271–275, 2011.
- [2] J. D. Hughes, "A reality check on the shale revolution," *Nature*, vol. 494, no. 7437, pp. 307–308, 2013.
- [3] C. Wang, L. Hong, R. Gao et al., "Status-quo and challenges of enhanced oil recovery in low permeability reservoirs," *Unconventional Oil & Gas*, vol. 5, no. 3, pp. 102–108, 2018.
- [4] B. Liu, Y. Yang, J. Li, Y. Chi, J. Li, and X. Fu, "Stress sensitivity of tight reservoirs and its effect on oil saturation: A case study of Lower Cretaceous tight clastic reservoirs in the Hailar Basin, Northeast China," *Journal of Petroleum Science and Engineering*, vol. 184, article 106484, 2020.
- [5] K. Liu, D. Gao, Y. Wang, and Y. Yang, "Effect of local loads on shale gas well integrity during hydraulic fracturing process," *Journal of Natural Gas Science and Engineering*, vol. 37, pp. 291–302, 2017.
- [6] L. Wang, Y. Tian, X. Yu et al., "Advances in improved/enhanced oil recovery technologies for tight and shale reservoirs," *Fuel*, vol. 210, pp. 425–445, 2017.
- [7] P. Jian, Z. Zhuang, X. Tang, W. Duan, C. Guo, and T. Lin, "Comprehensive analysis for hydrocarbon accumulation main control factors and enrichment of unconventional oil and gas," *Unconventional Oil & Gas*, vol. 4, no. 3, pp. 110–118, 2017.
- [8] S. C. Maxwell and T. Urbancic, "The role of passive microseismic monitoring in the instrumented oil field," *The Leading Edge*, vol. 20, no. 6, pp. 636–639, 2001.
- [9] L. Li, J. Tan, D. A. Wood et al., "A review of the current status of induced seismicity monitoring for hydraulic fracturing in unconventional tight oil and gas reservoirs," *Fuel*, vol. 242, pp. 195–210, 2019.
- [10] M. Weingarten, S. Ge, J. W. Godt, B. A. Bekins, and J. L. Rubinstein, "High-rate injection is associated with the increase in U.S. mid-continent seismicity," *Science*, vol. 348, no. 6241, pp. 1336–1340, 2015.
- [11] F. Grigoli, S. Cesca, E. Priolo et al., "Current challenges in monitoring, discrimination, and management of induced seismicity related to underground industrial activities: a European perspective," *Reviews of Geophysics*, vol. 55, no. 2, pp. 310–340, 2017.
- [12] M. S. Paterson and T. Wong, *Experimental Rock Deformation—The Brittle Field*, Springer, Berlin; New York, 2nd edition, 2005.
- [13] C. Grosse and M. Ohtsu, *Acoustic Emission Testing*, Springer Berlin Heidelberg, Berlin, Heidelberg, 2008.
- [14] X. Lei, K. Masuda, O. Nishizawa et al., "Detailed analysis of acoustic emission activity during catastrophic fracture of faults in rock," *Journal of Structural Geology*, vol. 26, no. 2, pp. 247–258, 2004.
- [15] S. Stanchits, A. Surdi, P. Gathogo, E. Edelman, and R. Suarez-Rivera, "Onset of hydraulic fracture initiation monitored by acoustic emission and volumetric deformation measurements," *Rock Mechanics and Rock Engineering*, vol. 47, no. 5, pp. 1521–1532, 2014.
- [16] Z. Moradian, H. H. Einstein, and G. Ballivy, "Detection of cracking levels in brittle rocks by parametric analysis of the acoustic emission signals," *Rock Mechanics and Rock Engineering*, vol. 49, no. 3, pp. 785–800, 2016.
- [17] Y. Liang, Q. Li, Y. Gu, and Q. Zou, "Mechanical and acoustic emission characteristics of rock: effect of loading and unloading confining pressure at the postpeak stage," *Journal of Natural Gas Science and Engineering*, vol. 44, pp. 54–64, 2017.
- [18] J. Clarke, L. Adam, J. Sarout, K. van Wijk, B. Kennedy, and J. Dautriat, "The relation between viscosity and acoustic emissions as a laboratory analogue for volcano seismicity," *Geology*, vol. 47, no. 6, pp. 499–503, 2019.
- [19] Y. Wang, C. H. Li, and Y. Z. Hu, "Experimental investigation on the fracture behaviour of black shale by acoustic emission monitoring and CT image analysis during uniaxial compression," *Geophysical Journal International*, vol. 213, no. 1, pp. 660–675, 2018.
- [20] E. Aker, D. Kühn, V. Vavryčuk, M. Soldal, and V. Oye, "Experimental investigation of acoustic emissions and their moment tensors in rock during failure," *International Journal of Rock Mechanics and Mining Sciences*, vol. 70, pp. 286–295, 2014.
- [21] B. Zhang, X. Tian, B. Ji, J. Zhao, Z. Zhu, and S. Yin, "Study on microseismic mechanism of hydro-fracture propagation in shale," *Journal of Petroleum Science and Engineering*, vol. 178, pp. 711–722, 2019.
- [22] H. P. Xie, *An Introduction of Fractal Methods on Rock Mechanics*, Science Press, Beijing, 1996.
- [23] H. P. Xie, J. F. Liu, Y. Ju, J. Li, and L. Z. Xie, "Fractal property of spatial distribution of acoustic emissions during the failure process of bedded rock salt," *International Journal of Rock Mechanics and Mining Sciences*, vol. 48, no. 8, pp. 1344–1351, 2011.
- [24] X. Z. Wu, X. X. Liu, Z. Z. Liang, X. You, and M. Yu, "Experimental study of fractal dimension of AE serials of different rocks under uniaxial compression," *Rock & Soil Mechanics*, vol. 33, no. 12, pp. 3561–3569, 2012.
- [25] R. Zhang, F. Dai, M. Z. Gao, N. W. Xu, and C. P. Zhang, "Fractal analysis of acoustic emission during uniaxial and triaxial loading of rock," *International Journal of Rock Mechanics and Mining Sciences*, vol. 79, pp. 241–249, 2015.
- [26] X. Kong, E. Wang, S. Hu, R. Shen, X. Li, and T. Zhan, "Fractal characteristics and acoustic emission of coal containing methane in triaxial compression failure," *Journal of Applied Geophysics*, vol. 124, pp. 139–147, 2016.
- [27] R. Lopes and N. Betrouni, "Fractal and multifractal analysis: a review," *Medical Image Analysis*, vol. 13, no. 4, pp. 634–649, 2009.
- [28] A. N. Pavlov and V. S. Anishchenko, "Multifractal analysis of complex signals," *Physics-Uspekhi*, vol. 50, no. 8, p. 819, 2007.
- [29] B. Kong, E. Wang, Z. Li, X. Wang, L. Chen, and X. Kong, "Nonlinear characteristics of acoustic emissions during the deformation and fracture of sandstone subjected to thermal treatment," *International Journal of Rock Mechanics and Mining Sciences*, vol. 90, pp. 43–52, 2016.
- [30] X. Kong, E. Wang, X. He, D. Li, and Q. Liu, "Time-varying multifractal of acoustic emission about coal samples subjected to uniaxial compression," *Chaos, Solitons & Fractals*, vol. 103, pp. 571–577, 2017.
- [31] J. Tan, C. Hu, Q. Lyu et al., "Multi-fractal analysis for the AE energy dissipation of CO₂ and CO₂+ brine/water treated low-clay shales under uniaxial compressive tests," *Fuel*, vol. 246, pp. 330–339, 2019.
- [32] Z. Cheng, Y. Fu, and C. Tang, "Confining pressure effect on acoustic emissions during rock failure," *Chinese Journal of Rock Mechanics and Engineering*, vol. 16, no. 1, pp. 65–70, 1997.

- [33] T. Xu, C. Tang, S. Wang, and Y. Zhang, "Numerical tests on confining pressure effect in rock failure process," *Journal of Central South University(Science and Technology)(China)*, vol. 35, no. 5, pp. 840–844, 2004.
- [34] Y. Li, B. Wang, L. Song, J. Liu, J. Zuo, and D. Liu, "Ultrasonic wave propagation characteristics for typical anisotropic failure modes of shale under uniaxial compression and real-time ultrasonic experiments," *Journal of Geophysics and Engineering*, vol. 17, no. 2, pp. 258–276, 2020.
- [35] G. Chen, X. Sun, J. Wang, D. Wang, and Z. Zhu, "Detection of cracking behaviors in granite with open pre-cut cracks by acoustic emission frequency spectrum analysis," *Arabian Journal of Geosciences*, vol. 13, no. 6, p. 258, 2020.
- [36] J. Yang, Z.-L. Mu, and S.-Q. Yang, "Experimental study of acoustic emission multi-parameter information characterizing rock crack development," *Engineering Fracture Mechanics*, vol. 232, article 107045, 2020.
- [37] B. B. Mandelbrot, "Fractals: form, chance, and dimension," *Physics Today*, vol. 32, no. 5, pp. 65–66, 1979.
- [38] C. C. Barton and P. R. PointeLa, Eds., *Fractals in the Earth Sciences*, Springer US, Boston, MA, 1995.
- [39] R. Liu, Y. Jiang, N. Huang, and S. Sugimoto, "Hydraulic properties of 3D crossed rock fractures by considering anisotropic aperture distributions," *Advances in Geo-Energy Research*, vol. 2, no. 2, pp. 113–121, 2018.
- [40] A. Sakhaee-Pour and W. Li, "Fractal dimensions of shale," *Journal of Natural Gas Science and Engineering*, vol. 30, pp. 578–582, 2016.
- [41] Y. Xia, J. Cai, E. Perfect, W. Wei, Q. Zhang, and Q. Meng, "Fractal dimension, lacunarity and succolarity analyses on CT images of reservoir rocks for permeability prediction," *Journal of Hydrology*, vol. 579, article 124198, 2019.
- [42] L. Telesca, V. Lapenna, and M. Macchiato, "Multifractal fluctuations in earthquake-related geoelectrical signals," *New Journal of Physics*, vol. 7, pp. 214–214, 2005.
- [43] A. Chhabra and R. V. Jensen, "Direct determination of the $f(\alpha)$ singularity spectrum," *Physical Review Letters*, vol. 62, no. 12, pp. 1327–1330, 1989.
- [44] S. Hu, E. Wang, Z. Li, R. Shen, and J. Liu, "Time-varying multifractal characteristics and formation mechanism of loaded coal electromagnetic radiation," *Rock Mechanics and Rock Engineering*, vol. 47, no. 5, pp. 1821–1838, 2014.
- [45] C. Lin, J. He, X. Li, X. Wan, and B. Zheng, "An experimental investigation into the effects of the anisotropy of shale on hydraulic fracture propagation," *Rock Mechanics and Rock Engineering*, vol. 50, no. 3, pp. 543–554, 2017.
- [46] E. Detournay, "Propagation regimes of fluid-driven fractures in impermeable rocks," *International Journal of Geomechanics*, vol. 4, no. 1, pp. 35–45, 2004.
- [47] A. P. Bunger, E. Detournay, and D. I. Garagash, "Toughness-dominated hydraulic fracture with leak-off," *International Journal of Fracture*, vol. 134, no. 2, pp. 175–190, 2005.
- [48] D. Xu, R. Hu, W. Gao, and J. Xia, "Effects of laminated structure on hydraulic fracture propagation in shale," *Petroleum Exploration and Development*, vol. 42, no. 4, pp. 573–579, 2015.
- [49] X. Zhang, Y. Lu, J. Tang, Z. Zhou, and Y. Liao, "Experimental study on fracture initiation and propagation in shale using supercritical carbon dioxide fracturing," *Fuel*, vol. 190, pp. 370–378, 2017.
- [50] M. J. Economides and K. G. Notte, *Reservoir Stimulation*, Wiley, Chichester, UK, 3rd edition, 2000.
- [51] M. Naoi, Y. Chen, K. Nishihara et al., "Monitoring hydraulically-induced fractures in the laboratory using acoustic emissions and the fluorescent method," *International Journal of Rock Mechanics and Mining Sciences*, vol. 104, pp. 53–63, 2018.
- [52] A. Damani, C. H. Sondergeld, and C. S. Rai, "Experimental investigation of in situ and injection fluid effect on hydraulic fracture mechanism using acoustic emission in Tennessee sandstone," *Journal of Petroleum Science and Engineering*, vol. 171, pp. 315–324, 2018.
- [53] Y. Jiang, C. Qin, Z. Kang et al., "Experimental study of supercritical CO₂ fracturing on initiation pressure and fracture propagation in shale under different triaxial stress conditions," *Journal of Natural Gas Science and Engineering*, vol. 55, pp. 382–394, 2018.
- [54] M. Cacace, G. Blöcher, N. Watanabe et al., "Modelling of fractured carbonate reservoirs: outline of a novel technique via a case study from the Molasse Basin, southern Bavaria, Germany," *Environmental Earth Sciences*, vol. 70, no. 8, pp. 3585–3602, 2013.
- [55] Y. Zheng, J. Liu, and Y. Lei, "The propagation behavior of hydraulic fracture in rock mass with cemented joints," *Geofluids*, vol. 2019, 15 pages, 2019.
- [56] S. D. Goodfellow, N. Tisato, M. Ghofranitabari, M. H. B. Naseri, and R. P. Young, "Attenuation properties of Fontainebleau sandstone during true-Triaxial deformation using active and passive Ultrasonics," *Rock Mechanics and Rock Engineering*, vol. 48, no. 6, pp. 2551–2566, 2015.
- [57] P. J. de Groot, P. A. M. Wijnens, and R. B. F. Janssen, "Real-time frequency determination of acoustic emission for different fracture mechanisms in carbon/epoxy composites," *Composites Science and Technology*, vol. 55, no. 4, pp. 405–412, 1995.
- [58] K. Ohno and M. Ohtsu, "Crack classification in concrete based on acoustic emission," *Construction and Building Materials*, vol. 24, no. 12, pp. 2339–2346, 2010.
- [59] J. Zhang, "Investigation of relation between fracture scale and acoustic emission time-frequency parameters in rocks," *Shock and Vibration*, vol. 2018, 14 pages, 2018.
- [60] X. Li, Z. Feng, G. Han et al., "Breakdown pressure and fracture surface morphology of hydraulic fracturing in shale with H₂O, CO₂ and N₂," *Geomechanics and Geophysics for Geo-Energy and Geo-Resources*, vol. 2, no. 2, pp. 63–76, 2016.
- [61] B. Zhang, B. Ji, and W. Liu, "The study on mechanics of hydraulic fracture propagation direction in shale and numerical simulation," *Geomechanics and Geophysics for Geo-Energy and Geo-Resources*, vol. 4, no. 2, pp. 119–127, 2018.
- [62] J. Tan, R. Hu, W. Wang, and J. Dick, "Palynological analysis of the late Ordovician - early Silurian black shales in South China provides new insights for the investigation of pore systems in shale gas reservoirs," *Marine and Petroleum Geology*, vol. 116, article 104145, 2020.
- [63] J. He, C. Lin, X. Li, Y. Zhang, and Y. Chen, "Initiation, propagation, closure and morphology of hydraulic fractures in sandstone cores," *Fuel*, vol. 208, pp. 65–70, 2017.

Research Article

Transient Flow Theory of Multiple-Fractured Horizontal Wells with Complex Mechanisms in Shale Gas Reservoirs

Dianfa Du ^{1,2}, Genkai Zhang,^{1,2} Yanwu Zhao,^{1,2} Xiaofei Sun,^{1,2} and Bin Zhang^{1,2}

¹Key Laboratory of Unconventional Oil & Gas Development (China University of Petroleum (East China)), Ministry of Education, Qingdao 266580, China

²School of Petroleum Engineering, China University of Petroleum (East China), Qingdao 266580, China

Correspondence should be addressed to Dianfa Du; dudf@upc.edu.cn

Received 7 February 2020; Revised 26 May 2020; Accepted 11 July 2020; Published 3 August 2020

Academic Editor: Wei Wei

Copyright © 2020 Dianfa Du et al. This is an open access article distributed under the Creative Commons Attribution License, which permits unrestricted use, distribution, and reproduction in any medium, provided the original work is properly cited.

Shale reservoirs have the characterizations of low porosity, low permeability, and hydrocarbon organic matter self-generation and self-storage, resulting in its complex flow mechanisms. Compared with fractured vertical wells, multiple-fractured horizontal wells are widely used due to their advantages of effectively increasing the well control range and further expanding the drainage area. To further study the multiscale flow mechanisms of shale gas, a flow model was established that considered viscous flow in microfractures and inorganic pores, the diffusion of Knudsen in nanoscale porosity, the coexistence of slippage, adsorption-desorption effects under infinity, and closed outer boundary conditions; based on the continuous point source solution, a multiple-fractured horizontal well flow model was established and solved by MATLAB programming. Then, the effects of various factors were investigated. The results show that the Knudsen diffusion and slippage coefficients mainly affect the apparent permeability of the matrix pores. The more the Knudsen diffusion and slippage coefficients are, the earlier the turbulent flow occurs and the higher the gas production is.

1. Introduction

The revolution of shale gas in the United States of America (USA) is changing the energy structure of the world [1, 2]. Based on its various forms in the reservoir, the shale gas can be divided into free shale gas, adsorbed shale gas, and dissolved shale gas. Most of the shale gas is deposited in pores and microfractures in a free state, and the proportion of the gas adsorbed on the surface of organic matter and clay mineral particles [3] could generally reach more than 50% [4]. The dissolved gas exists in liquid hydrocarbons or adsorbed on the surface of other substances in the kerogen [5–7] as shown in Figure 1. Through tank degassing experiments, Cheng et al. [8] observed the diffusion of gas from the kerogen or clay particles to the surface of the pores.

Scholars have committed to the research on shale gas flow models since a decade ago. In 2009, a mathematical model was developed for horizontal wells with triple media branches [9], and the bottom well pressure solution of the horizontal well with the triple media branches in Laplace

space was solved by using the point source function theory. Soon, a pressure calculation formula for any point in a stratum with fractures at different inclinations in a fractured horizontal well was developed based on the same theory [10]. Then, Ozkan et al. [11] applied the trilinear flow model to fractured horizontal wells, which is suitable for shale reservoirs with a matrix permeability of only micron-scale Darcy and nanoscale Darcy. This model assumes that the artificial vertical fractures are formed after fracturing, and the surrounding of the fractures is considered to be a dual medium.

In the same year, Stalgorova and Mattar [12] proposed a trilinear flow model to analyze the production dynamics of conventional reservoirs and fractured horizontal wells in unconventional gas reservoirs. In this model, the entire reservoir was divided into three regions (the external reservoir, the internal reservoir, and the hydraulic fracture). The flow of gas between the three regions was assumed to be linear in this model. The results indicated that the most effective way to increase the productivity of unconventional gas reservoirs is to increase the fracture density. The effects of fracture

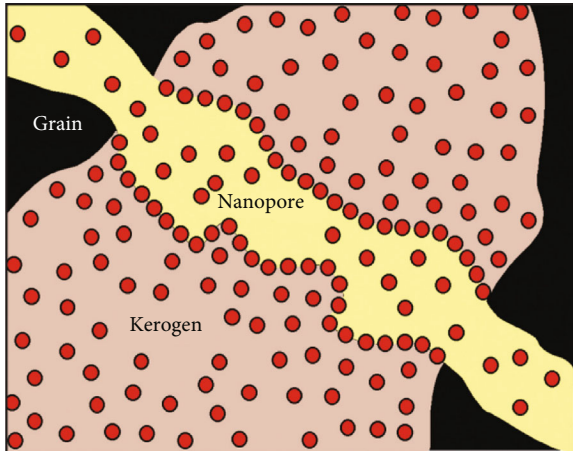


FIGURE 1: Schematic diagram of gas molecule in a small part of a kerogen grain pore system of a mudrock.

permeability on productivity are not obvious. Then, a new trilinear flow model [13] was proposed based on Ozkan's model. Similarly, the model divided the entire reservoir into three parts: the fractured zone, the unreformed zone, and the artificial fracture. The results studied by this model points out that due to the multiple factors such as rock properties and ground stress, the hydraulic fractures formed during the fracturing process are not necessarily perpendicular to the horizontal wellbore but form a certain fracture network structure. In 2014, Dejam et al. [14] established a fractured horizontal well flow model for shale gas reservoirs based on the triple-porosity four-linear flow model, which considers the effects of gas adsorption and desorption effect of gas in the matrix. The model mainly studies the quasisteady state turbulence of the matrix to the microfracture medium and the large-fracture medium. In 2017, the unsteady flow regimes of a slightly compressible fluid under the linear and radial pre-Darcy flow conditions are modeled and the corresponding highly nonlinear diffusivity equations are solved analytically by aid of a generalized Boltzmann transformation technique [15]. The influence of pre-Darcy flow on the pressure diffusion for homogeneous porous media is studied in terms of the nonlinear exponent and the threshold pressure gradient. In addition, the pressure gradient, flux, and cumulative production per unit area are compared with the classical solution of the diffusivity equation based on the Darcy flow. In 2018, a two-phase flowback model is developed with multiscale diffusion mechanisms, and it is found that the two-phase flowback and the flow consistency between the matrix and fracture network have significant influences on cumulative gas production. The multiscale diffusion mechanisms in different zones should be carefully considered in the flowback model [16]. In 2019, a model considering convective flow, gas diffusion, and surface diffusion was established to investigate gas transport mechanism, and a common practice in modeling shale gas permeability is to use Knudsen diffusion coefficient when calculating diffusive flux, but the use of Knudsen diffusion coefficient would be incorrect if the shale gas flow regime is lying in either the transition diffusion or Fick's diffusion, in which case the dif-

fusion coefficient must correspond to that regime [17]. Then, a series of shale gas adsorption and desorption experiments are conducted [18]. Desorption and adsorption curves are not coincident, with the former located above the latter, which suggests that adsorption hysteresis also occurs in shale gas.

A multiple-fractured horizontal well (MFHW) is extensively applied to develop the shale gas reservoirs, which makes the production of unconventional reservoirs economically and practically feasible [19]. After massive fracturing, the complex fracture network will exist around the horizontal wellbore. To model the flow behavior more rigorously, the fractures within the network should be represented explicitly rather than idealized as dual-porosity media around the wellbore. A mathematical model considering the stress sensitivity of the reservoir permeability, Darcy flow, diffusion, and adsorption and desorption in shale gas reservoirs is developed, and the numerical nonlinear production decline equations are derived and obtained. Subsequently, the model is verified by a simplified model, and production decline curves for a MFHW with discrete fracture networks in shale gas reservoirs are plotted [20]. An analytical solution is developed for the shale gas productivity of a multiple-fractured horizontal well based on a diffusion model and a trilinear flow pattern. The shale gas reservoir is divided into three flow regions: hydraulic-fracture region, microfracture network or dual-porosity region, and pure-matrix region. For the pure-matrix region, a transient diffusion equation is solved based on our previous diffusivity model developed for the shale matrix. For the microfracture network region, a modified dual-porosity model is proposed wherein both the free and adsorbed gases in the shale matrix flow into the microfracture network through a pseudosteady diffusion process. A dimensionless solution is obtained for the bottom-hole pressure in the Laplace domain considering the skin effect. An analytical solution is obtained for the gas production rate in a real-time domain through a partial Taylor series simplification and Laplace inverse transform. This analytical solution is compared with the field data of the shale gas produced from a fractured horizontal well located in southwestern China, and a good agreement is observed [21]. A semianalytical model of finite-conductivity multiple-fractured horizontal wells in LC gas reservoirs is established based on the Laplace-space superposition principle and fracture discrete method. The proposed model is validated against a commercial numerical simulator. Type curves are obtained to study pressure characteristics and identify flow regimes. The effects of some parameters on type curves are discussed [22].

Different models are featured in different aspects, so there are many problems at present. (1) The migration mechanisms of shale gas in the pores are not clear. In addition, the equation describing the flow of shale gas in the pores is mostly derived under the conditions of single capillary and ideal gas. (2) The effects of flow law are not considered comprehensively in the existing models, and the models do not fit well with the actual conditions; it is difficult for the model to fully describe the Darcy flow, Knudsen diffusion, adsorption-desorption, Fick diffusion, and other mechanisms. (3) The

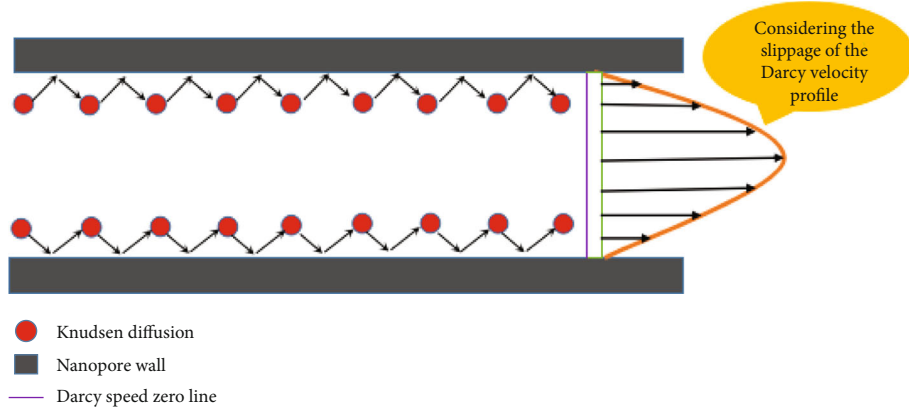


FIGURE 2: Migration of single component gas in nanoscale pores.

research results and methods of shale gas in microcosmic are difficult to be used in macroscopic research. The research results between microcosmic flow and macroscopic flow are not closely related.

First, the shale gas multiscale flow mechanisms are presented. Then, a flow model was established that considered viscous flow in microfractures and inorganic pores, the diffusion of Knudsen in nanoscale porosity, the coexistence of slippage, and adsorption-desorption effects under infinity and closed outer boundary conditions; based on the continuous point source solution, a multiple-fractured horizontal well flow model was established and solved by MATLAB programming, and the effects of various factors were investigated.

2. Shale Gas Multiscale Flow Mechanisms

Unlike conventional reservoirs, shale gas reservoirs have the characteristics of low porosity, low permeability, self-generation, and self-storage of hydrocarbon organics. The spatial structure of the reservoir is a typical multiscale feature. The migration of shale gas in the reservoir is a typical multiscale flow usually including the following three stages: (1) free gas flows from pores to the wellbore; (2) after the pore pressure drops, the adsorbed gas on the pore wall surface begins to desorb into the pores and then become free gas; and (3) dissolved gas in organic matter diffuses to the pore surface [23–25].

2.1. Flow in Fractures and Macropores. The flow of shale gas in natural fractures and large matrix pores satisfies Darcy's law, which is

$$v = -\frac{k_1}{\mu} \nabla p. \quad (1)$$

v is the gas flow velocity in m/s, k_1 is the medium permeability in μm^2 , μ is the gas viscosity in mPa-s, and ∇ is the gradient operator, $\nabla = (\partial/\partial x)\vec{i} + (\partial/\partial y)\vec{j} + (\partial/\partial z)\vec{k}$.

During the development of shale gas reservoirs, natural fractures and matrix systems exhibit stress-sensitive effects as formation pressures decrease. The permeability k_1 is a function of formation pressure at this time, which is

$$k_1 = k_1(p_1). \quad (2)$$

p_1 is the medium system pressure in Pa.

2.2. Flow in Nanoscale Pores. In shale reservoirs, nanoscale pores are mainly organic pores, of which the velocity of gas molecules is not zero at the wall surface, and both the slip flow and the Knudsen effect exist in pores, as shown in Figure 2.

There would be slippage when the fluid flowed in porous media [26]. Therefore, the following formula was proposed to calculate the apparent gas permeability of reservoir rocks:

$$k_a = k_m \left(1 + \frac{b}{\bar{p}} \right), \quad (3)$$

where k_a is the apparent permeability in μm^2 , k_m is the equivalent liquid permeability in μm^2 , b is the slip factor which depends on the gas type and pore throat characteristics in Pa, and \bar{p} is the average pressure of the flow path in Pa.

There are many models of visual permeability in shale nanoscale pores, which are summarized in Table 1, and the slip coefficient expressions of various scholars are obtained. It is noteworthy that these models only consider the slippage mechanism. The Knudsen diffusion terms must be added if these models are applied to nanoscale pores.

In this paper, the expression of the coefficient of permeability correction F [27] considering slippage effect and Knudsen is as follows:

$$F = [1 + \alpha(Kn)Kn] \left[1 + \frac{4Kn}{1 - b_0Kn} \right]. \quad (4)$$

$\alpha(Kn)$ is the sparse function related to Kn ; it can be expressed as follows:

$$\alpha(Kn) = \alpha_0 \frac{2}{\pi} \tan^{-1}[c_1 Kn^{c_2}]. \quad (5)$$

When the flow pattern of shale gas in the nanoscale pores is slippage, $b_0 = -1$, $\alpha_0 = 64/15\pi$, $c_1 = 4$, and $c_2 = 0.4$.

TABLE 1: Various calculation formulas for slip factor.

Serial number	Expression of b	Author
1	$b = \frac{4c\lambda\bar{p}}{r}$	Klinkenberg [25]
2	$b = \frac{(8\pi RT/M_g)^{0.5} \mu_g}{r(2/a-1)}$ R (J/mol/K), T (K), M (kg/mol), μ_g (Pa · s), b (Pa)	Javadpour [23]
3	$b = \mu_g \sqrt{\frac{\pi RT \phi}{\tau M_g K_\infty}}$ R (J/mol/K), T (K), M (kg/mol), μ_g (Pa · s), k (mD), b (Pa)	Civan [26]

2.3. *Gas Desorption on Organic Surface.* A large amount of shale gas is absorbed on the surface of organic matter under actual formation conditions, and desorption occurs mainly during mining [28–32]. There are many factors affecting the desorption of shale gas, such as organic matter content, organic matter maturity, temperature, and pressure [33–35]. The relationship between various factors is complicated.

In the establishment of the flow model, the instantaneous desorption model is used to characterize the shale gas. The expression of the Langmuir isotherm equation is as follows:

$$V = V_m \frac{p}{p_L + p}. \quad (6)$$

The mass flow of desorption per unit volume of shale gas reservoir per unit of time during extraction is

$$q_{\text{des}} = \rho_{\text{gsc}} \frac{\partial V}{\partial t}, \quad (7)$$

where q_{des} is the shale gas mass flow desorbed from a unit volume of reservoir rock in kg/s and ρ_{gsc} is the shale gas density under standard conditions in kg/m³.

Substituting Equation (6) into Equation (7),

$$q_{\text{des}} = \rho_{\text{gsc}} V_m \frac{p_L}{(p_L + p)^2} \frac{\partial p}{\partial t}. \quad (8)$$

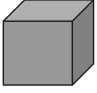
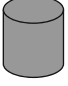
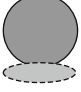
If the Langmuir equation is expressed in pseudopressure form, the above equation can be changed to

$$q_{\text{des}} = \rho_{\text{gsc}} V_m \frac{\psi(p_L)}{[\psi(p_L) + \psi(p)]^2} \frac{\partial \psi(p)}{\partial t}. \quad (9)$$

At this point, Equations (8) and (9) can be used to express the instantaneous amount of desorption gas, and then the instability flow model of shale gas wells can be studied.

2.4. *Diffusion in Porous Kerogen (Organic Matter).* There are two forms of diffusion: steady state diffusion and nonsteady state diffusion. When the gas consistence in the porous kerogen is independent of the spatial position and only related to time, it is called pseudosteady state diffusion and can be

TABLE 2: Shale organic form factors and geometric factors of different shapes.

Organic shape	Schematic	Feature length	Values of F_s	Values of F_g
Block		Thickness, $2h$	2	$\pi^2/4h^2$
Cylinder		Cylindrical radius, R	4	$5.7832/R^2$
Sphere		Sphere radius, R	6	π^2/R^2

described by Fick's first diffusion law; when the gas concentration in organic matter is related to both time and space coordinates, it is called nonsteady state diffusion and can be described by Fick's second diffusion law.

2.4.1. *Pseudosteady State Diffusion.* The derivative of shale gas consistence in the matrix with respect to time is proportional to the consistence difference of gas inside and outside the organic matter, which can be expressed as

$$\frac{dC_o}{dt} = DF_s [C_E(p) - C_o]. \quad (10)$$

Therefore, the diffusion gas flow from the unit volume of shale organic matter to the nanoscale pores is

$$q_F = M_g F_g \frac{dC_o}{dt}, \quad (11)$$

where C_o is the molar concentration of shale gas in organic matter under pseudosteady state conditions in mol/m³; C_E is the molar concentration of gas at organic wall in mol/m³; p is the nanoscale pore pressure; F_s is the shape factor in 1/m², determined by the shape of the organic matter; D is the Fick diffusion coefficient in m²/s; t is the time in s; q_F is the Fick mass flow in kg/(m³·s); and F_g is the geometric

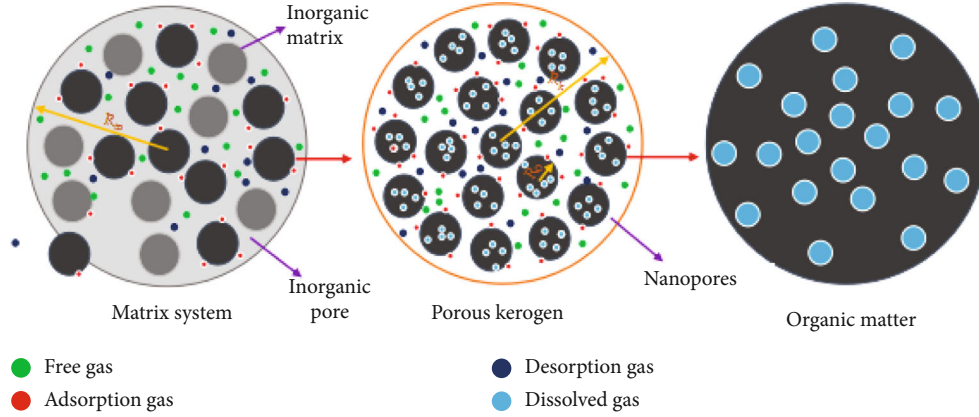


FIGURE 3: Matrix part of the quad medium model for shale gas reservoirs.

factor; it is determined by the organic shapes that are listed in Table 2.

2.4.2. Nonsteady State Diffusion. The diffusion of dissolved gas in organic matter is usually an unsteady state diffusion. If there is a stable and continuous diffusion source, the pseudo-steady diffusion rule will be met. Based on theory of uniformity, this paper assumes that the organic matter is spheres of equal size with radius of R_o . The physical model is shown in Figure 3.

According to the unsteady diffusion theory, the dissolved gas consistence C_o is a function of time and spatial position. For the spherical matrix model, it is assumed that the gas consistence on the outer surface of the organic matter is in dynamic equilibrium with the free gas in the nanoscale pores. The gas consistence change in the organic matter can be described by the following mathematical model:

$$\frac{\partial C_o}{\partial t} = \frac{1}{r_o^2} \frac{\partial}{\partial r_o} \left(D r_o^2 \frac{\partial C_o}{\partial r_o} \right), \quad (12)$$

where C_o is the volumetric consistence of shale gas in organic matter under unsteady conditions in mol/m^3 and r_o is the radial coordinates of spherical organic rock mass in m.

Before a gas reservoir is put into production, the pressure at each point in the reservoir is the original formation pressure p_i , and the gas concentration at each point in the organic matter is related to its internal pressure. Furthermore, it is assumed that the rate of change in gas concentration at the center of the organic matter is zero, and the gas concentration at the outer boundary of the organic matter is the same as the gas concentration in the nanoscale pores. Therefore, the initial boundary conditions for the nonsteady state diffusion in the organic matter satisfy the following process:

$$\begin{aligned} C_o(t=0, r_o) &= C_o(p_i), \\ \frac{\partial C_o(t, r_o=0)}{\partial r_o} &= 0, \\ C_o(t, r_o=R_o) &= C_o(p), \end{aligned} \quad (13)$$

where p_i is the reservoir original formation pressure in MPa, p is the nanoscale pore pressure connected to the outer sur-

face of organic matter in MPa, and R_o is the spherical organic radius in m.

According to the above model and the corresponding definite conditions, the dissolved gas concentration distribution in the organic rock mass can be obtained, and then the mass diffusion of gas per unit volume of organic matter can be determined according to

$$q_F = M_g \frac{3D}{R_o} \frac{\partial C_o}{\partial r_o} \Big|_{r_o=R_o}. \quad (14)$$

q_F is the Fick mass flow in $\text{kg}/(\text{m}^3 \cdot \text{s})$.

3. Establishment and Point Source Solutions for Flow Model

3.1. Characterization of the Microscopic Flow Model. Strictly speaking, the shale reservoirs should be divided into four parts of organic matter that existed which are microfracture systems, inorganic pores, nanoscale pores, and gas dissolved organic matter [36, 37]. A comprehensive flow model is proposed in this section that considers multiple porous media, including the viscous flow in microfractures and inorganic pores, the diffusion of Knudsen in nanoscale porosity, the coexistence of slippage, adsorption-desorption effects, and the diffusion of dissolved gases in organic matter [38, 39].

3.1.1. Dissolved Gas Diffusion in Porous Kerogen. The diffusion of dissolved gas in porous kerogen can be described by the nonsteady state Fick diffusion law:

$$\frac{1}{r_o^2} \frac{\partial}{\partial r_o} \left(r_o^2 D_o \frac{\partial C}{\partial r_o} \right) = \frac{\partial C}{\partial t}. \quad (15)$$

3.1.2. Flow in Nanoscale Pores in Kerogen. There are three sources of gas in organic pores, namely, free gas in pores, desorption gas on the surface of organic matter, and dissolved gas diffused from kerogen. The flow equation in the pores of spherical kerogen is as follows:

$$\begin{aligned}
-\frac{1}{r_k^2} \frac{\partial}{\partial r_k} (r_k^2 \rho_k v_k) + q_{ck} + q_{bk} &= \frac{\phi_k}{f_k} \frac{\partial \rho_k}{\partial t}, \\
v_k &= -\frac{k_{\text{kapp}}}{\mu} \frac{\partial p_k}{\partial r_k}, \\
k_{\text{kapp}} &= \left[1 + \frac{\alpha_0}{1 + AK_n^{-B}} K_n \right] \left[1 + \frac{4K_n}{1 - bK_n} \right] k_{\infty},
\end{aligned} \tag{16}$$

where r_k is the radial radius of kerogen in nanoscale pores in m, ρ_k is the gas density in kerogen nanoscale pores in kg/m^3 , v_k is the gas permeation velocity in kerogen nanoscale pores in m/s, f_k is the ratio of kerogen volume to rock volume, k_{∞} is the inherent permeability of kerogen nanoscale pores in mD, q_{ck} is the gas mass rate desorbed from organic pore in kg/s , q_{bk} is the mass rate of gas diffused from organic matter in kg/s , V_{Lk} is the Langmuir volume in kerogen in kg/s , and p_{Lk} is the Langmuir pressure in kerogen in MPa.

$$\begin{aligned}
q_{ck} &= -\rho_{sc} V_{Lk} \frac{p_{Lk}}{(p_k + p_{Lk})^2} \frac{\partial p_k}{\partial t}, \\
q_{bk} &= -\left(1 - \frac{\phi_k}{f_k} \right) \frac{3}{R_o} \rho_{sc} D_o \frac{\partial C}{\partial r_o} \Big|_{r_o=R_o, r_k}.
\end{aligned} \tag{17}$$

The correction coefficients of permeability can be taken as follows: $b = 1.000$, $\alpha_0 = 1.358$, $A = 0.170$, and $B = 0.435$.

3.1.3. Flow in Matrix Macropore. The flow equation of matrix macropore in spherical coordinates can be written as

$$\begin{aligned}
-\frac{1}{r_m^2} \frac{\partial}{\partial r_m} (r_m^2 \rho_m v_m) + q_{km} &= \phi_m \frac{\partial \rho_m}{\partial t}, \\
v_m &= -\frac{k_m}{\mu} \frac{\partial p_m}{\partial r_m}, \\
q_{km} &= -\frac{3}{R_m} f_m \rho_m \frac{k_{\text{kapp}}}{\mu} \frac{\partial p_k}{\partial r_k} \Big|_{r_k=R_k, r_m}.
\end{aligned} \tag{18}$$

3.1.4. Flow in Microfracture System. The mass conservation equation of the microfracture system is

$$\begin{aligned}
-\frac{1}{r_f^2} \frac{\partial}{\partial r_f} (r_f^2 \rho_f v_f) + q_{mf} &= \phi_f \frac{\partial \rho_f}{\partial t}, \\
v_f &= -\frac{k_f}{\mu} \frac{\partial p_f}{\partial r_f}, \\
q_{mf} &= -\frac{3}{R_m} \rho_m \frac{k_m}{\mu} \frac{\partial p_m}{\partial r_m} \Big|_{r_m=R_m}.
\end{aligned} \tag{19}$$

3.2. The Solution of Microscopic Flow Model. The general equation of flow for the corresponding microfracture system under various flow models is as follows:

TABLE 3: Definitions of dimensionless parameters.

Dimensionless time	$t_D = \frac{k_f t}{(\phi \mu_i C_{ii})_{f+m+k} L_{\text{ref}}^2}$
Dimensionless radial radius of kerogen in nanoscale pores	$r_{kD} = \frac{r_k}{R_k}$
Dimensionless matrix radial radius	$r_{mD} = \frac{r_m}{R_m}$
Storage coefficient of the kerogen	$\omega_k = \frac{(\phi \mu C_{tk})_i}{(\phi \mu_i C_{ii})_{f+m+k}}$
Storage coefficient of the matrix	$\omega_m = \frac{(\phi \mu C_{tm})_i}{(\phi \mu_i C_{ii})_{f+m+k}}$
Storage coefficient of the fracture system	$\omega_f = \frac{(\phi \mu C_{tf})_i}{(\phi \mu_i C_{ii})_{f+m+k}}$
Dimensionless Fick diffusion coefficient	$D_{oD} = \frac{(\phi \mu_i C_{ii})_{f+m+k} R_o^2}{k_{\text{koo}} R_o^2}$
Transfer coefficient from the matrix to the fracture	$\lambda_{mf} = \frac{k_m L_{\text{ref}}^2}{k_f R_m^2}$
Transfer coefficient from kerogen to matrix	$\lambda_{km} = \frac{k_{\text{koo}} R_m^2}{k_m R_k^2}$

$$\frac{1}{r_D^2} \frac{\partial}{\partial r_D} \left(r_D^2 \frac{\partial \Delta \bar{m}_f}{\partial r_D} \right) = f(s) \Delta \bar{m}_f, \tag{20}$$

where $f(s)$ is the corresponding parameter and s is the Laplace variable.

The developed microscopic flow model divides shale reservoirs into four parts: the microfracture system, inorganic pores, nanoscale porosity pores, and organic matter with dissolved gas. A flow model that is a comprehensive consideration of porous media was established, including viscous flow in microfractures and inorganic pores, Knudsen diffusion in nanoscale porosity, coexistence of slippage, adsorption-desorption effects, and dissolved gas diffusion in organic matter. The solution processes of the various microscopic flow mechanism model are in the appendix.

The dimensionless variables are defined in Table 3.

The resulting expression $f(s)$ is as follows:

$$f(s) = \omega_f s + \lambda_m - \frac{\lambda_m^2}{\lambda_k \omega_k s / (\lambda_k + \omega_k s) + \lambda_m + \omega_m s}. \tag{21}$$

So far, we have gotten the expressions of dimensionless pseudopressure of microfractures under various flow mechanisms of shale gas reservoirs and given their unified form in spherical coordinates.

3.3. Continuous Point Source Solution of Circular Boundary Shale Gas Reservoir

3.3.1. Flow Model. In this section, the continuous point source solution at any point in an anisotropic circular gas reservoir with a closed upper and lower boundary is derived. The physical model is shown in Figure 4. The main

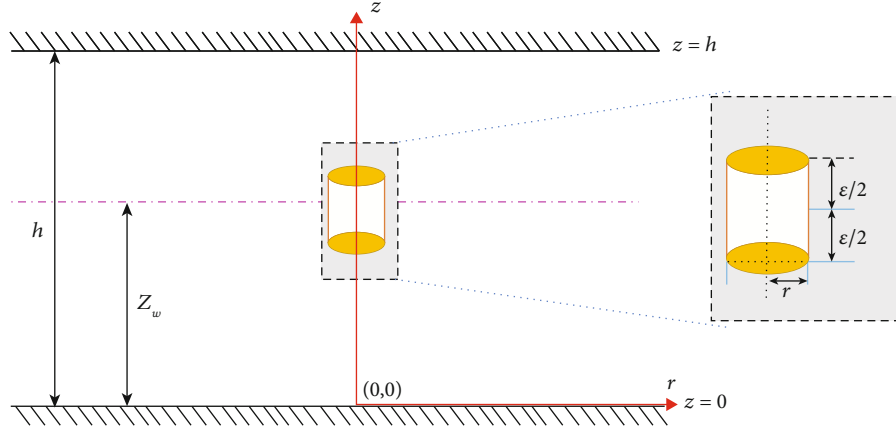


FIGURE 4: Schematic diagram of a continuous point source physical model in the gas reservoir with closed boundary on top and bottom.

assumptions in the model are as follows: (1) the gas reservoir is homogeneous, the thickness is h , the initial pressure is p_i ; (2) the permeability of the gas reservoir in the horizontal and vertical directions are k_{fh} and k_{fz} , respectively; (3) the middle distance of the gas reservoir is the lower boundary z_w , where exists a cylindrical source sink. The radius of the microelement cylinder is r and the height is ϵ . (4) The source and sink strength of the cylinder is q_{scins} , and (5) the gas flow in the gas reservoir meets the Darcy flow, and the effects of capillary pressure and gravity on the flow are ignored.

According to the flow theory of oil and gas reservoirs, the continuity equation of gas flow is

$$\frac{1}{r} \frac{\partial (r \rho_g v_r)}{\partial r} + \frac{\partial (\rho_g v_z)}{\partial z} = - \frac{\partial (\rho_g \phi_f)}{\partial t}, \quad (22)$$

where ρ_g is the density of gas in crack systems in kg/m^3 , v_r is the radial flow velocity of gas in m/s , v_z is the flow velocity of gas in the vertical direction in m/s , ϕ_f is the porosity of the fracture system, r/z is the radial and vertical coordinates, and t is the production time in s .

The flow equations of gas flow in the transverse and longitudinal directions are as follows:

$$\begin{aligned} v_r &= - \frac{k_{fh}}{\mu_g} \frac{\partial p_f}{\partial r}, \\ v_z &= - \frac{k_{fz}}{\mu_g} \frac{\partial p_f}{\partial z}, \end{aligned} \quad (23)$$

where k_{fr} is the permeability of the reservoir fracture system in the horizontal direction in m^2 , k_{fz} is the permeability of the reservoir fracture system in the vertical direction in m^2 , p_f is the crack system pressure in Pa , and μ_g is the gas viscosity in $\text{Pa}\cdot\text{s}$.

According to the state equation of real gas, the density of gas can be expressed as follows:

$$\rho_g = \frac{p_f M_g}{ZRT}, \quad (24)$$

where M_g is the gas molar mass in kg/mol , T is the absolute temperature of the gas in K , and Z is the gas compression factor.

According to the definition of rock compressibility, the following relationship exists between the porosity of the rock fracture system and the pressure of the fracture system:

$$c_f = \frac{1}{\phi_f} \frac{\partial \phi_f}{\partial p_f}, \quad (25)$$

where c_f is the fracture pore compression factor.

For the inner boundary conditions, it is assumed that gas enters mainly from the side of the cylinder, and as the radius of the microelement tends to 0, it can be considered as a continuous point sink, and its inner boundary expression is [38]

$$\lim_{\epsilon \rightarrow 0} \left[\lim_{r \rightarrow 0} \int_{z_w - \epsilon/2}^{z_w + \epsilon/2} \frac{2\pi r k_{fh}}{B_g \mu_g} \frac{\partial p_f}{\partial r} dz_w \right] = \begin{cases} 0, & |z - z_w| > \frac{\epsilon}{2}, \\ q_{scins}, & |z - z_w| \leq \frac{\epsilon}{2}. \end{cases} \quad (26)$$

Among them, the volume coefficient of gas B_g is as follows:

$$B_g = \frac{p_{sc} Z T}{p_f T_{sc}}. \quad (27)$$

The upper and lower boundaries of the gas reservoir are all closed. Therefore, the upper and lower boundary conditions can be described as

$$\left. \frac{\partial p_f}{\partial z} \right|_{z=0} = 0, \quad \left. \frac{\partial p_f}{\partial z} \right|_{z=h} = 0. \quad (28)$$

The outer boundary conditions can be described as

$$r \frac{\partial p_f}{\partial r} \Big|_{r=r_e} = \vartheta p_f \Big|_{r=r_e}. \quad (29)$$

Introducing the following proposed pressure,

$$\psi(p_f) = 2 \int_{p_i}^{p_f} \frac{p}{\mu_g Z} dp. \quad (30)$$

Substituting the gas density, volumetric coefficient, and pseudopressure definition into the flow equation of the fracture system,

$$\frac{1}{r} \frac{\partial}{\partial r} \left(r \frac{\partial \psi_f}{\partial r} \right) + \frac{k_{fz}}{k_{fh}} \frac{\partial^2 \psi_f}{\partial z^2} = \frac{\phi_f \mu_g c_{fg}}{k_{fh}} \frac{\partial \psi_f}{\partial t}, \quad (31)$$

$$\lim_{\varepsilon \rightarrow 0} \left[\lim_{r \rightarrow 0} \int_{z_w - \varepsilon/2}^{z_w + \varepsilon/2} r \frac{\partial \psi_f}{\partial r} dz_w \right] = \begin{cases} 0, & |z - z_w| > \frac{\varepsilon}{2}, \\ \frac{p_{sc} T}{\pi k_{fh} T_{sc} h} q_{scins}, & |z - z_w| \leq \frac{\varepsilon}{2}. \end{cases} \quad (32)$$

For the above continuity equation, the viscosity and compressibility of the gas are all functions of pressure. In order to obtain the analytical solution of the equation, the viscosity and compressibility of the part are usually regarded as the values in the original state.

$$\mu_g = \mu_{gi}, C_g = C_{gi}. \quad (33)$$

Several dimensionless variables are defined in Table 4.

Substituting the above dimensionless quantities into Equations (30) and (31), the flow equation of the fracture system becomes as follows:

$$\frac{1}{r_D} \frac{\partial}{\partial r_D} \left(r_D \frac{\partial \Delta \psi_f}{\partial r_D} \right) + \frac{1}{h_D^2} \frac{\partial^2 \Delta \psi_f}{\partial z_D^2} = \frac{\partial \Delta \psi_f}{\partial t_D}. \quad (34)$$

The inner boundary condition becomes as follows:

$$\lim_{\varepsilon \rightarrow 0} \left[\lim_{r_D \rightarrow 0} \int_{z_D - \varepsilon/2}^{z_D + \varepsilon/2} r_D \frac{\partial \Delta \psi_f}{\partial r_D} dz_{wD} \right] = \begin{cases} 0, & |z_D - z_{wD}| > \frac{\varepsilon}{2}, \\ -\frac{p_{sc} T}{\pi k_{fh} T_{sc} h} q_{scins}, & |z_D - z_{wD}| \leq \frac{\varepsilon}{2}. \end{cases} \quad (35)$$

The upper and lower boundary conditions become as follows:

$$\frac{\partial \Delta \psi_f}{\partial z_D} \Big|_{z_D=0} = 0, \quad \frac{\partial \Delta \psi_f}{\partial z_D} \Big|_{z_D=1} = 0. \quad (36)$$

TABLE 4: Definitions of dimensionless parameters.

Dimensionless microfracture radial distance	$r_D = r/L_{ref}$
Dimensionless outer boundary radius	$r_{eD} = r_e/L_{ref}$
Dimensionless time	$t_D = k_{fh} t / \phi_f \mu_{gi} C_{gi} L_{ref}^2$
Dimensionless distance from the lower boundary	$z_D = z/h$
Dimensionless height of the gas reservoir	$h_D = (h/L_{ref}) \sqrt{k_{fh}/k_{fz}}$
Dimensionless pressure	$\Delta \psi_f = \psi_{fi} - \psi_f$

The outer boundary condition becomes as follows:

$$r_D \frac{\partial \Delta \psi_f}{\partial r_D} \Big|_{r_D=r_{eD}} = \vartheta \Delta \psi_f \Big|_{r_D=r_{eD}}. \quad (37)$$

3.3.2. The Solution of the Flow Model. Since there are many derivation formulas for solving similar flow models (appendix), this section does not carry out long derivation but directly gives the general solution of the model; as shown in Equation (38), the solution process requires Laplace transform and Fourier cosine transform.

$$\begin{aligned} \Delta \bar{\psi}_f = & \frac{p_{sc} T \bar{q}_{scins}}{\pi k_{fh} h T_{sc}} \{K_0(\xi_0 r_D) + C_n I_0(\xi_0 r_D) \\ & + 2 \sum_{n=1}^{\infty} [K_0(\xi_n r_D) + C_n I_0(\xi_n r_D)] \cos(n\pi z_{wD}) \cos(n\pi z_D)\}, \end{aligned} \quad (38)$$

where $r_D = \sqrt{(x_D - x_{wD})^2 + (y_D - y_{wD})^2}$, $\xi_n = \sqrt{f(s) + (n\pi)^2/h_D^2}$ ($n = 0, 1, 2, 3 \dots$), and $C_n = (r_{eD} \xi_n K_1(\xi_n r_{eD}) + \vartheta K_0(\xi_n r_{eD})) / (r_{eD} \xi_n I_1(\xi_n r_{eD}) - \vartheta I_0(\xi_n r_{eD}))$.

3.3.3. The Continuous Point Source Solution under Different Outer Boundary Conditions. Above, we have solved the hybrid outer boundary model. However, the outer boundary of a gas reservoir has the following two situations: infinite and closed boundaries. Therefore, the continuous point source solutions were analyzed in these two cases.

(1) *Infinity Outer Boundary.* When the outer boundary of a gas reservoir is infinite, the outer boundary equation is as follows:

$$\lim_{r_D \rightarrow 0} \frac{\partial \Delta \psi_f}{\partial r_D} \Big|_{r_D=r_{eD}} = 0. \quad (39)$$

Therefore,

$$C_n = 0. \quad (40)$$

Substituting Equation (40) into Equation (39), we obtain a continuous point source solution with closed top and bottom boundaries and infinite outer boundary:

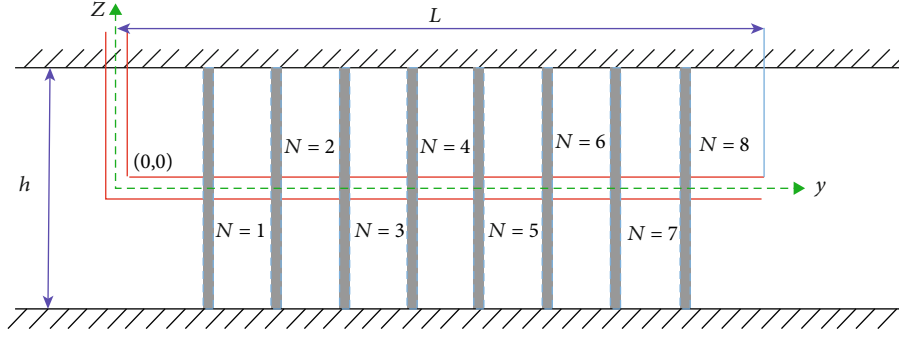


FIGURE 5: Schematic diagram of multiple-fractured horizontal well model for shale gas reservoir.

$$\Delta\bar{\psi}_f = \frac{p_{sc} T \bar{q}_{scins}}{\pi k_{fh} h T_{sc}} \left\{ K_0(\xi_0 r_D) + 2 \sum_{n=1}^{\infty} K_0(\xi_n r_D) \cos(n\pi z_{wD}) \cos(n\pi z_D) \right\}. \quad (41)$$

The source intensity q_{scins} for a continuous point is a constant. Thus, the above equation can be written as follows:

$$\Delta\bar{\psi}_f = \frac{p_{sc} T q_{scins}}{\pi k_{fh} h T_{sc} S} \left\{ K_0(\xi_0 r_D) + 2 \sum_{n=1}^{\infty} K_0(\xi_n r_D) \cos(n\pi z_{wD}) \cos(n\pi z_D) \right\}. \quad (42)$$

(2) *Closed Outer Boundary.* When the outer boundary is closed, it is known from the closed boundary conditions:

$$C_n = \frac{K_1(\xi_n r_{eD})}{I_1(\xi_n r_{eD})}. \quad (43)$$

When the outer boundary is closed, the continuous point source solution is as follows:

$$\Delta\bar{\psi}_f = \frac{p_{sc} T \bar{q}_{scins}}{\pi k_{fh} h T_{sc}} \left\{ K_0(\xi_0 r_D) + \frac{K_1(\xi_n r_{eD})}{I_1(\xi_n r_{eD})} I_0(\xi_0 r_D) + 2 \sum_{n=1}^{\infty} \left[K_0(\xi_n r_D) + \frac{K_1(\xi_n r_{eD})}{I_1(\xi_n r_{eD})} I_0(\xi_n r_D) \right] \cdot \cos(n\pi z_{wD}) \cos(n\pi z_D) \right\}. \quad (44)$$

4. Study on Unsteady Flow Rules of Circular Boundary Multiple-Fractured Horizontal Wells

4.1. *The Establishment of a Physical Model.* A model diagram of a multiple-fractured horizontal well in a circular shale gas reservoir is shown in Figure 5. The following assumptions are given:

- (1) The gas reservoir is homogeneous, horizontal, and equal in thickness. The upper and lower boundaries are closed. The lateral direction is infinite or closed and the reservoir thickness is h
- (2) The horizontal well is located in the center of the gas reservoir and its length is L

- (3) The pressure drop caused by fluid flowing in the wellbore is ignored, and the hydraulic fractures supply fluid to the wellbore, regardless of the flow of the reservoir fluid directly to the wellbore
- (4) The number of hydraulic fractures is N , and it is a fully cracked fracture with infinite flow conductivity. The fracture is regarded as a 2D surface source rather than a 3D volume source
- (5) Fracture cracks are symmetrical bifurcations distributed at equal intervals along the horizontal wellbore
- (6) The flow process is an isothermal flow, regardless of the effects of fluid gravity and capillary forces

4.2. *Mathematical Model Establishment and Solution.* As shown in Figure 5, the direction of the wellbore along the horizontal well is the y -axis, the vertical upward direction is the z -axis direction, and the direction along the fracture surface is the x -axis direction. For multistage fracturing horizontal wells, the flow process of fluids in the reservoir is quite complicated. Not only is the mutual interference between the seams and the fractures, but the flow on the fracture surface is also uneven. Therefore, the solution method for continuing to use the fracturing vertical wells does not work. We can first divide the crack into several units, and it is assumed that the flow on each section is evenly distributed, but the flow in the cracks on different units is different. By solving the pressure response expressions at each fracture cell and combining the bottom hole pressure with the normalized production conditions, the expressions of the bottom hole pressures in multistage fracturing horizontal wells in shale gas reservoirs are solved.

In this study, the fractures are infinitely inducing flow cracks that are completely fracturing. According to the continuous point source solution of the circular reservoir obtained, it is integrated along the longitudinal direction that we can obtain a continuous linear source solution. For a continuous line source with an intensity of q_{scL} , there is an infinite atmospheric boundary:

$$\Delta\bar{\psi}_{fL} = \frac{p_{sc} T q_{scins}}{\pi k_{fh} h T_{sc} S} \int_0^h K_0(\xi_0 r_D) + 2 \sum_{n=1}^{\infty} K_0(\xi_n r_D) \cos(n\pi z_{wD}) \cos(n\pi z_D) dz_w, \quad (45)$$

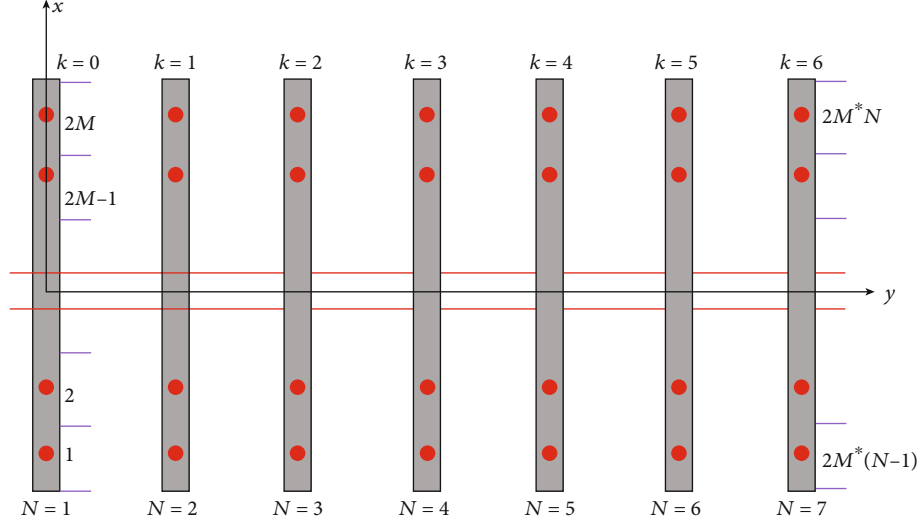


FIGURE 6: Crack discrete grid.

where $r_D = \sqrt{(x_D - x_{wD})^2 + (y_D - y_{wD})^2}$ and $\xi_n = \sqrt{f(s) + (n\pi)^2 h_D^2}$ ($n = 0, 1, 2, 3 \dots$).

The continuous line source intensity and continuous point source intensity have the following relationship:

$$q_{scL} = q_{scins} h. \quad (46)$$

The definition of the dimensionless distance z_{wD} is as follows:

$$z_{wD} = \frac{z_w}{h}. \quad (47)$$

Substituting Equations (46) and (47) into Equation (45), we can obtain a continuous linear source solution for an infinite boundary shale gas reservoir with a circular outer boundary:

$$\Delta \bar{\psi}_{fL} = \frac{p_{sc} T q_{scL}}{\pi k_{fh} h T_{sc} s} K_0(\xi_0 r_D). \quad (48)$$

In the same way, the solution of a continuous line source can be obtained when the gas reservoir boundary is closed:

$$\Delta \bar{\psi}_{fL} = \frac{p_{sc} T q_{scL}}{\pi k_{fh} h T_{sc} s} \left[K_0(\xi_0 r_D) + \frac{K_1(\xi_0 r_{eD})}{I_1(\xi_0 r_{eD})} I_0(\xi_0 r_D) \right]. \quad (49)$$

The predecessors have basically formed a set of theoretical systems for the crack dispersion and superposition principle to solve the pressure response. The following is a brief introduction. In the hypothetical part of the model in this section, the number of fractures is N , the length of horizontal wells is L , and each fracture is equally divided into $2M$ units as shown in Figure 6.

From the discrete fracture schematic, the node coordinates of each segment in the fracture can be obtained. The

crack node coordinates in the negative direction of the x -axis can be obtained by the following equation:

$$\begin{cases} x_i = - \left[M - (i - k * 2M) + \frac{1}{2} \right] \Delta L_{fL_i}, & 1 \leq i - k * 2M \leq M, \\ y_i = y_{k+1}. \end{cases} \quad (50)$$

The coordinates of the crack node in the positive direction of the x -axis can be obtained by the following equation:

$$\begin{cases} x_i = \left[(i - k * 2M) - M - \frac{1}{2} \right] \Delta L_{fL_i}, & M + 1 \leq i - k * 2M \leq 2M, \\ y_i = y_{k+1}, \end{cases} \quad (51)$$

where x_i is the abscissa of the i -th crack cell in m, y_i is the ordinate of the i -th crack cell, and ΔL_{fL_i} is the section i -th crack length.

For the crack unit length, since each crack is divided into $2M$ parts, the length of the i -th crack cell is

$$\Delta L_{fL_i} = \frac{L_{fL_i}}{M}. \quad (52)$$

As mentioned earlier, it has been assumed that the flow distribution of each fracture cell is uniform, so that the pseudopressure drop formed at any point (x, y) in the formation at the i -th crack cell is

$$\Delta \bar{\psi}_{fi} = \int_r \Delta \bar{\psi}_{fL} dl. \quad (53)$$

Since the cracks are all parallel to the x -axis, the above curve integrals can be directly converted into coordinate integrals. When the outer boundary of the reservoir is infinite, Equation (49) is substituted into Equation (53), where the

coordinates of the i -th node are substituted into, we can get the following equation:

$$\Delta\bar{\psi}_{fi} = \int_{x_i - \Delta L_{fi}/2}^{x_i + \Delta L_{fi}/2} \frac{p_{sc} T q_{scL_i}}{\pi k_{fh} h T_{sc} S} K_0 \left(\xi_0 \sqrt{(x_D - x_{wDi})^2 + (y_D - y_{wDi})^2} \right) dx_w. \quad (54)$$

Since the flow is uniformly distributed on the discrete units of the fracture, assuming that the i -th discrete unit is q_{sci} , the following relationship can be satisfied between the line flow and the unit flow:

$$q_{scL} = q_{scL_i} \Delta L_{fi}. \quad (55)$$

Introducing the following dimensionless pressure and dimensionless production:

$$\psi_{fD} = \frac{\pi k_{fh} h T_{sc}}{p_{sc} T q_{sc}} \Delta\psi_f, \quad (56)$$

$$q_{Di} = \frac{q_{sci}}{q_{sc}}. \quad (57)$$

Substituting Equations (56) and (57) into Equation (54),

$$\Delta\bar{\psi}_{fDi} = \frac{q_{Di}}{s \Delta L_{fDi}} \int_{-(\Delta L_{fDi}/2)}^{\Delta L_{fDi}/2} K_0 \left(\xi_0 \sqrt{(x_D - x_{wDi} - \alpha)^2 + (y_D - y_{wDi})^2} \right) d\alpha, \quad (58)$$

where ΔL_{fDi} is the dimensionless length of the i -th crack unit.

According to the superposition principle of the potential, the total pressure response generated at each position of the crack in the N cracks at any position in the reservoir is

$$\bar{\psi}_D(x_D, y_D) = \sum_{i=1}^N \bar{\psi}_{fDi}(x_D, y_D). \quad (59)$$

According to the previous assumption,

$$\bar{\psi}_{wD} = \bar{\psi}_D(x_{Dj}, y_{Dj}) = \sum_{i=1}^N \bar{\psi}_{fDi}(x_{Dj}, y_{Dj}), \quad (60)$$

where (x_{Dj}, y_{Dj}) is the intersection point of the j -th section of a fracture and the wellbore.

When a horizontal well is produced at a given production volume, the production of the well is numerically equal to the sum of the flow of all cracks. Therefore, we have the following equation:

$$q_{sc} = \sum_{i=1}^{N \times 2M} (q_{scLi} \Delta L_{fi}). \quad (61)$$

Substituting Equation (61) into Equation (57), there are the following normalization conditions:

$$\sum_{i=1}^{N \times 2M} q_{Di} = 1. \quad (62)$$

In Figure 6, we separate the cracks into $N \times 2M$ units and solve the pseudopressure at each unit, so we can have $N \times 2M$ equations, which, plus the normalized equation for production, total $N \times 2M + 1$ equations, while the unknowns include the flow rate and bottom hole pressure of each fracture cell, which is also $N \times 2M + 1$. The equations are closed and there is a unique solution. For ease of understanding, this set of equations is written in the following matrix form:

$$\begin{bmatrix} A_{1,1} & \cdots & A_{1,n} & \cdots & A_{1,2M \times N} & -1 \\ \cdots & \cdots & \cdots & \cdots & \cdots & -1 \\ A_{n,1} & \cdots & A_{n,n} & \cdots & A_{n,2M \times N} & \cdots \\ \cdots & \cdots & \cdots & \cdots & \cdots & -1 \\ A_{2M \times N,1} & \cdots & A_{2M \times N,n} & \cdots & A_{2M \times N,2M \times N} & -1 \\ 1 & \cdots & 1 & \cdots & 1 & 0 \end{bmatrix} \begin{bmatrix} q_{D1} \\ q_{D2} \\ \cdots \\ \cdots \\ q_{D,2M \times N} \\ \bar{\psi}_{wD} \end{bmatrix} = \begin{bmatrix} 0 \\ 0 \\ \cdots \\ \cdots \\ 0 \\ 1 \end{bmatrix}. \quad (63)$$

The expression of $A_{i,j}$ is as follows:

$$A_{i,j} = \frac{1}{s \Delta L_{fDj}} \int_{-(\Delta L_{fDj}/2)}^{\Delta L_{fDj}/2} K_0 \left(\xi_0 \sqrt{(x_{Di} - x_{Dj} - \alpha)^2 + (y_{Di} - y_{Dj})^2} \right) d\alpha. \quad (64)$$

The above formula is the fracturing horizontal well production and pressure calculation formula under the condition of the infinite outer boundary. If the boundary of the gas reservoir is closed, the formula can be simplified to Equation (64):

$$A_{i,j} = \frac{1}{s \Delta L_{fDj}} \int_{-(\Delta L_{fDj}/2)}^{\Delta L_{fDj}/2} \left[K_0(\xi_0 r_D) + \frac{K_1(\xi_0 r_{eD})}{I_1(\xi_0 r_{eD})} I_0(\xi_0 r_D) \right] d\alpha. \quad (65)$$

4.3. Gas Well Bottom Pressure Dynamic Curve Analysis. So far, we have obtained the unstable pressure of multiple-fractured horizontal wells in circular reservoirs considering a variety of complex flow mechanisms. According to the expression, the computer programming and Stehfest numerical inversion techniques [38] were used to obtain pressure and production dynamic curves of shale gas reservoir fractured.

Figure 7 shows the typical pressure response curves of multistage fracturing horizontal wells in shale reservoirs with different outer boundary conditions. Multiple concaves appear in the dynamic curve, reflecting the effects of various flow mechanisms on the pressure response. As the pressure wave propagates in the formation, different pore media rich in shale gas begin to flow, causing the pressure of the porous media to fall.

According to Figure 7, we can divide the flow of horizontal wells into the following stages:

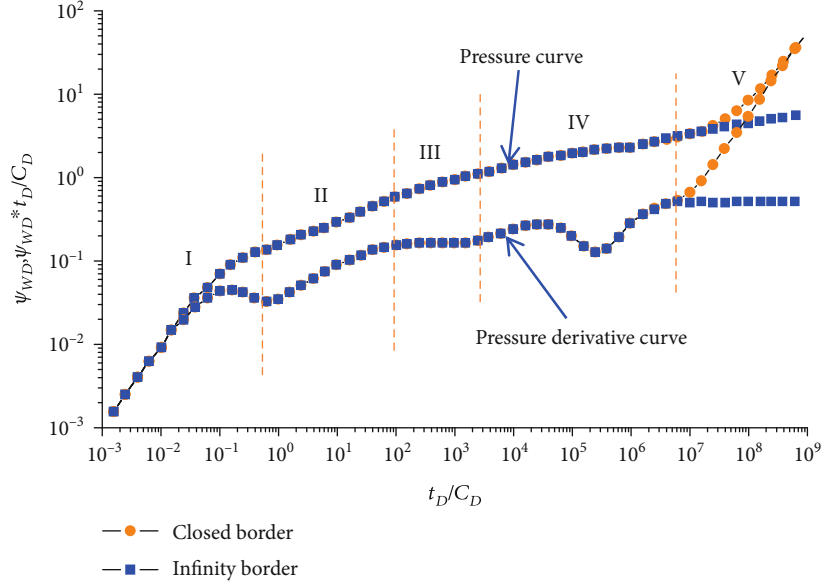


FIGURE 7: Pressure response curves of multiple-fractured horizontal wells in shale reservoirs with different outer boundary conditions under double logarithmic coordinates.

Stage I: the wellbore storage and subsequent transitional flow stages. In the wellbore storage phase, the pressure and pressure derivative curves coincide with each other with a slope of 1

Stage II: the early linear flow stage perpendicular to the fracturing fracture. After the completion of the well storage phase, the free gas in the reservoir flowed first in the direction perpendicular to the fracture surface, and there was no mutual interference between the fractures. In this flow stage, the slope of the pressure derivative curve is $1/2$

Stage III: early radial flow stage. The pressure derivative curve shows a horizontal line with a slope of $1/(2N)$

Stage IV: the turbulence stage. This stage corresponds to the linear flow stage from the formation to the entire fracturing zone. The concave character appears on the pressure derivative curve

Stage V: the boundary control stage. The characteristics of the boundary flow are exhibited after the pressure wave spreads to the boundary. For the closed boundary, when the pressure wave spreads to the boundary, the pressure will increase faster; combined with the continuous line source solution Equation (49) under the closed boundary, the pressure and pressure derivative curves coincide and the slope is 1

The parameters used in the mechanistic model are listed in Table 5.

The pressure curves for different slippage coefficients under double logarithmic coordinates are shown in Figure 8. Making the slippage coefficient b equals 1, 8, and 16, it can be seen that as the slippage coefficient b increases and the turbulence trough appears earlier and earlier. According to the knowledge of flow mechanics, when the shale gas desorbed from the organic pore, slippage appears, so the slippage coefficient b affects the turbulence stage the most. The greater the slippage coefficient b is, the more obvi-

TABLE 5: Parameters in the following models.

Parameter	Value
Original pressure, p_i (MPa)	25
Formation thickness, h (m)	40
Crack number	5
Initial gas compression factor, C_{gi} (MPa $^{-1}$)	0.02
Microfracture permeability, k_f (mD)	0.01
Horizontal well length, L (m)	1000
Well storage coefficient, C_D	10^{-5}
Gas reservoir boundary radius, r_e (m)	5000
Temperature, T (K)	335.15
Half length of crack, x_f (m)	40
Relative gas density	0.65
Microfracture porosity	0.02
Gas well production, q_{sc} (m 3 /d)	1.2×10^4
Skin factor, S_{kin}	0.1

ous is the slippage effect, and the larger the apparent permeability of the matrix is, so that the turbulence of matrix pores to the fracture system is more serious, and eventually, the time of turbulence appears earlier. Naturally, a larger slippage coefficient will increase the production of shale gas wells.

Figure 9 shows the influence of different Knudsen diffusion coefficients on the pressure response of multiple-fractured horizontal wells. It is not difficult to see from the figure that the influence of Knudsen diffusion coefficient D_K (m 2 /s) on the pressure dynamics and the gas slippage effect on the well test curve of gas wells are similar. With the increase of D_K (m 2 /s), the turbulence troughs appear

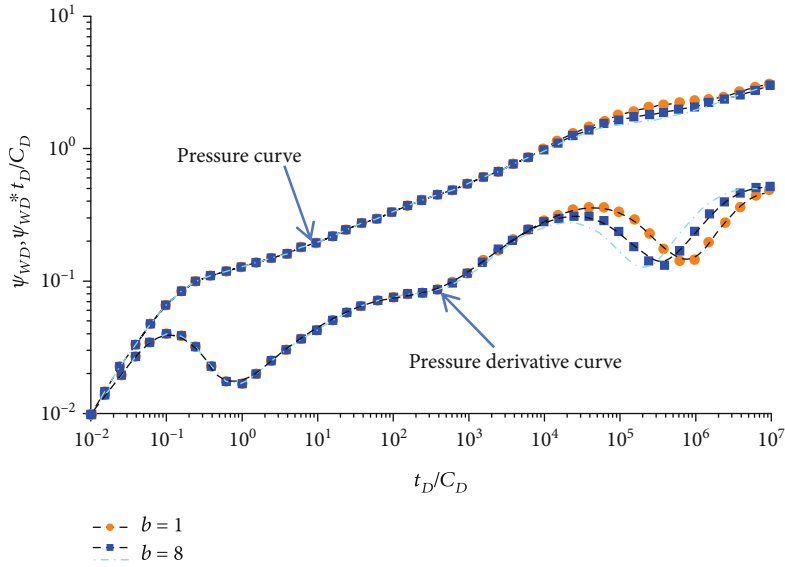


FIGURE 8: Pressure dynamic curves of multistage fracturing horizontal wells with different slip coefficients (infinity border).

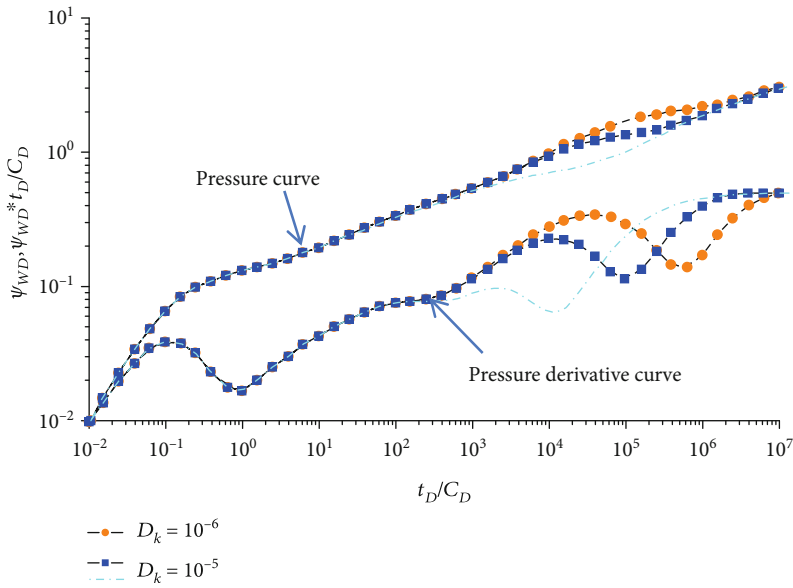


FIGURE 9: Pressure dynamic curves of multiple-fractured horizontal wells with different Knudsen diffusion coefficients under double logarithmic coordinates (infinity border).

earlier and the pressure and pressure derivative curves are getting lower and lower, so the production of gas wells will also increase.

5. Summary and Conclusions

- (1) A flow model for shale gas reservoirs considering flow in microfractures and inorganic pores, the diffusion of Knudsen in nanoscale porosity, the coexistence of slippage, established adsorption-desorption effects, and the continuous point source solution of the flow mechanisms model were obtained under closed and infinity outer boundaries

- (2) Based on the continuous point source solution, a circular boundary multiple-fractured horizontal well flow model was established, and the gas well bottom pressure dynamic curve and the relevant sensitivity factors are analyzed with the help of MATLAB programming
- (3) The results of the sensitivity analysis show that the Knudsen diffusion and slippage coefficients mainly affect the apparent permeability of the matrix pores. The more the Knudsen diffusion and slippage coefficients are, the earlier the turbulent flow occurs and the higher the gas production is

Appendix

A. The Diffusion of Dissolved Gas in Porous Kerogen

The diffusion of dissolved gas in porous kerogen can be described by the nonsteady state Fick diffusion law:

$$\frac{1}{r_o^2} \frac{\partial}{\partial r_o} \left(r_o^2 D_o \frac{\partial c_o}{\partial r_o} \right) = \frac{\partial c_o}{\partial t}. \quad (\text{A.1})$$

The internal boundary conditions:

$$\frac{\partial c_o(t, r_o = 0)}{\partial r_o} = 0. \quad (\text{A.2})$$

The outer boundary conditions:

$$c_o|_{r_o=R_o, r_k} = k_H p_k|_{r_k}. \quad (\text{A.3})$$

The initial conditions:

$$c_o(r_o, t) = k_H p_i. \quad (\text{A.4})$$

The following dimensionless variables were defined as follows:

$$\begin{aligned} t_D &= \frac{k_f t}{\Delta L_{\text{ref}}^2}, \\ r_{oD} &= \frac{r_o}{R_o}, \\ D_{oD} &= \frac{\Delta D_o R_k^2}{k_{k\infty} R_o^2}, \\ \lambda_{mf} &= \frac{k_m L_{\text{ref}}^2}{k_f R_m^2}, \\ \lambda_{km} &= \frac{k_{k\infty} R_m^2}{k_m R_k^2}, \\ c_D &= c_i - c. \end{aligned} \quad (\text{A.5})$$

Firstly, the aforementioned equations become dimensionless, then the Laplace transformation was conducted:

$$\begin{aligned} \frac{1}{r_{oD}^2} \frac{\partial}{\partial r_{oD}} \left(r_{oD}^2 \frac{\partial \bar{c}_{oD}}{\partial r_{oD}} \right) &= \frac{1}{D_{oD} \lambda_{km} \lambda_{mf}} s \bar{c}_{oD}, \\ \frac{\partial \bar{c}_{oD}(s, r_{oD} \rightarrow 0)}{\partial r_{oD}} &= 0, \\ \bar{c}_{oD}(s, r_{oD} = 1) &= k_H \bar{p}_i - k_H \bar{p}_k. \end{aligned} \quad (\text{A.6})$$

Ordering $M = \bar{c}_{oD} r_{oD}$, we can get

$$\begin{aligned} \frac{d^2 M}{dr_{oD}^2} - \frac{1}{D_{oD} \lambda_{km} \lambda_{mf}} s M &= 0, \\ \bar{c}_{oD} &= k_H \frac{\sinh \left(\sqrt{s/(D_{oD} \lambda_{km} \lambda_{mf})} r_{oD} \right)}{\sinh \left(\sqrt{s/(D_{oD} \lambda_{km} \lambda_{mf})} r_{oD} \right)} \left(\frac{p_i}{s} - \bar{p}_k|_{r_k} \right), \\ \frac{\partial \bar{C}_{mD}}{\partial r_{mD}} \Big|_{r_{mD}=1} &= -\frac{k_H \mu_g Z}{P \xi} \left[\sqrt{\lambda s} \coth \left(\sqrt{\lambda s} - 1 \right) \right] \Delta \bar{\psi}_f. \end{aligned} \quad (\text{A.7})$$

B. Flow in Nanoscale Pores in Kerogen

The flow equation in the pores of spherical kerogen is as follows:

$$\begin{aligned} \frac{1}{r_k^2} \frac{\partial}{\partial r_k} \left(r_k^2 \rho_k \frac{k_{\text{kapp}}}{\mu} \frac{\partial p_k}{\partial r_k} \right) + q_{ck} + q_{bk} &= \frac{\phi_k}{f_k} \frac{\partial \rho_k}{\partial t}, \\ k_{\text{kapp}} &= \left[1 + \frac{\alpha_0}{1 + AK_n^{-B}} K_n \right] \left[1 + \frac{4K_n}{1 - bK_n} \right] k_{\infty}, \\ q_{ck} &= -\rho_{sc} V_{Lk} \frac{p_{Lk}}{(p_k + p_{Lk})^2} \frac{\partial p_k}{\partial t}, \\ q_{bk} &= -\left(1 - \frac{\phi_k}{f_k} \right) \frac{3}{R_o} \rho_{sc} D_o \frac{\partial C}{\partial r_o} \Big|_{r_o=R_o, r_k}. \end{aligned} \quad (\text{B.1})$$

According to the research of Javadpour [23]

$$k_{\text{kapp}} = \alpha_k k_{\infty}, \quad (\text{B.2})$$

where

$$\alpha_k = \left(1 + \frac{1.358}{1 + 0.17K_n^{-0.4348}} K_n \right) \left(1 + \frac{4K_n}{1 - K_n} \right). \quad (\text{B.3})$$

The internal boundary conditions of the porous kerogen are

$$4\pi r_k^2 \frac{k_{\text{kapp}}}{\mu} \frac{\partial p_k}{\partial r_k} \Big|_{t, r_k \rightarrow 0} \cdot \rho_k = 0. \quad (\text{B.4})$$

The outer boundary conditions:

$$p_k|_{r_k=R_k, r_k} = p_m|_{r_m}. \quad (\text{B.5})$$

The initial conditions:

$$p_k|_{t=0, 0 \leq r_k \leq R_k} = p_i. \quad (\text{B.6})$$

The following dimensionless variables were defined:

$$\begin{aligned} r_{kD} &= \frac{r_k}{R_k}, \\ \omega_k &= \frac{(\phi\mu C_{tk})_i}{\Lambda}, \\ \Lambda &= (\phi\mu_i C_{ti})_{f+m+k}, \\ k_{HD} &= \left(1 - \frac{\phi_k}{f_k}\right) \frac{\mu_i Z_i}{p_i} \frac{3p_{sc} T}{T_{sc} \Lambda} k_H, \\ \psi_D &= \frac{\pi k_f h T_{sc}}{q_{sc} p_{sc} T} \Delta\psi, \end{aligned} \quad (\text{B.7})$$

$$\sigma_k = (p_{sc} T / \Lambda T_{sc}) (V_{Lk} p_{Lk} / (p_k + p_{Lk})^2) (\mu_i Z_i / p_i).$$

Firstly, the aforementioned equations become dimensionless, and then the Laplace transformation was conducted:

$$\begin{aligned} \frac{1}{r_{kD}^2} \frac{\partial}{\partial r_{kD}} \left(r_{kD}^2 \frac{\partial \bar{\psi}_{kD}}{\partial r_{kD}} \right) &= f_1(s) \bar{\psi}_{kD}, \\ r_{kD}^2 \frac{\partial \bar{\psi}_{kD}}{\partial r_{kD}} \Big|_{r_{kD}=0} &= 0, \\ \bar{\psi}_{kD} \Big|_{r_{kD}=1, r_{mD}} &= \frac{\alpha_k}{\alpha_m} \bar{\psi}_{mD} \Big|_{r_{mD}} = \frac{k_{kapp}}{k_{koo}} \bar{\psi}_{mD} \Big|_{r_{mD}} \quad (\alpha_m = 1). \end{aligned} \quad (\text{B.8})$$

The general form of the equation:

$$\bar{\psi}_{kD} = \alpha_k \frac{sh\left(\sqrt{f_1(s)} r_{kD}\right)}{r_{kD} sh\left(\sqrt{f_1(s)}\right)} \bar{\psi}_{mD} \Big|_{r_{mD}}. \quad (\text{B.9})$$

C. Flow in Matrix Macropore

The macropore flow control equation of the matrix under the spherical coordinates can be written as follows:

$$\begin{aligned} -\frac{1}{r_m^2} \frac{\partial}{\partial r_m} (r_m^2 \rho_m v_m) + q_{km} &= \phi_m \frac{\partial p_m}{\partial t}, \\ v_m &= -\frac{k_m}{\mu} \frac{\partial p_m}{\partial r_m}, \\ q_{km} &= -\frac{3}{R_k} f_k \rho_k \frac{k_{kapp}}{\mu} \frac{\partial p_k}{\partial r_k} \Big|_{r_k=R_k, r_m}. \end{aligned} \quad (\text{C.1})$$

The internal boundary conditions:

$$4\pi r_m^2 \frac{k_{am}}{\mu} \frac{\partial p_m}{\partial r_m} \Big|_{t, r_m \rightarrow 0} \cdot \rho_m = 0. \quad (\text{C.2})$$

The outer boundary conditions:

$$p_m \Big|_{r_m=R_m, r_f} = p_f \Big|_{r_f}. \quad (\text{C.3})$$

The initial conditions:

$$p_m \Big|_{t=0, 0 \leq r_m \leq R_m} = p_i. \quad (\text{C.4})$$

The following dimensionless variables were defined:

$$\begin{aligned} r_{mD} &= \frac{r_m}{R_m}, \\ \omega_m &= \frac{(\phi\mu C_{tm})_i}{\Lambda}. \end{aligned} \quad (\text{C.5})$$

Dimensionless form:

$$\begin{aligned} \frac{1}{r_{mD}^2} \frac{\partial}{\partial r_{mD}} \left(r_{mD}^2 \frac{\partial \psi_{mD}}{\partial r_{mD}} \right) &= \frac{(\omega_m + f_c \sigma_m)}{\alpha_m \lambda_{mf}} \frac{\partial \psi_{mD}}{\partial t_D} \\ &+ 3f_k \alpha_k \lambda_{km} \left[\sqrt{f_1(s)} \coth\left(\sqrt{f_1(s)}\right) - 1 \right] \psi_{mD}. \end{aligned} \quad (\text{C.6})$$

Laplace transformation:

$$\begin{aligned} \frac{1}{r_{mD}^2} \frac{\partial}{\partial r_{mD}} \left(r_{mD}^2 \frac{\partial \bar{\psi}_{mD}}{\partial r_{mD}} \right) &= f_2(s) \bar{\psi}_{mD}, \\ r_{mD}^2 \frac{\partial \bar{\psi}_{mD}}{\partial r_{mD}} \Big|_{r_{mD}=0} &= 0, \\ \bar{\psi}_{mD} \Big|_{r_{mD}=1, r} &= \bar{\psi}_{fD} \Big|_r. \end{aligned} \quad (\text{C.7})$$

The general form of the equation:

$$\bar{\psi}_{mD} = \alpha_m \frac{sh\left(\sqrt{f_2(s)} r_{kD}\right)}{r_{mD} sh\left(\sqrt{f_2(s)}\right)} \bar{\psi}_{fD} \Big|_{r_D}, \quad (\text{C.8})$$

where

$$f_2(s) = \frac{s(\omega_m + f_c \sigma_m)}{\alpha_m \lambda_{mf}} + 3f_k \alpha_k \lambda_{km} \left[\sqrt{f_1(s)} \coth\left(\sqrt{f_1(s)}\right) - 1 \right]. \quad (\text{C.9})$$

D. Flow in Microfracture System

The mass conservation equation for natural fracture systems is as follows:

$$\begin{aligned} -\frac{1}{r_f^2} \frac{\partial (r_f^2 \rho_f v_f)}{\partial r_f} + q_{mf} &= \phi_f \frac{\partial \rho_f}{\partial t}, \\ v_f &= -\frac{k_f}{\mu} \frac{\partial p_f}{\partial r_f}, \\ q_{mf} &= -\frac{3}{R_m} \rho_m \frac{k_m}{\mu} \frac{\partial p_m}{\partial r_m} \Big|_{r_m=R_m}. \end{aligned} \quad (D.1)$$

The internal boundary conditions:

$$2\pi r_f h \frac{k_{af}}{\mu} \frac{\partial p_f}{\partial r_f} \Big|_{r_f \rightarrow 0} \cdot \rho_f = \rho_{gsc} \tilde{q}. \quad (D.2)$$

The outer boundary conditions:

$$p_f \Big|_{r_f \rightarrow \infty} = p_i. \quad (D.3)$$

The initial conditions:

$$p_f \Big|_{t=0} = p_f. \quad (D.4)$$

The following dimensionless variables were defined:

$$\begin{aligned} \omega_f &= \frac{(\phi \mu C_{if})_i}{\Lambda}, \\ r_{fD} &= \frac{r_f}{L_{ref}}. \end{aligned} \quad (D.5)$$

Dimensionless form:

$$\begin{aligned} \frac{1}{r_{fD}^2} \frac{\partial}{\partial r_{fD}} \left(r_{fD}^2 \frac{\partial \bar{\psi}_{fD}}{\partial r_{fD}} \right) &= f(s) \bar{\psi}_{fD}, \\ r_{fD} \frac{\partial \bar{\psi}_{fD}}{\partial r_{fD}} \Big|_{r_{fD} \rightarrow 0} &= -\frac{\bar{q}}{q_{sc}}, \\ \bar{\psi}_{fD} \Big|_{r_{fD} \rightarrow \infty} &= 0, \\ \bar{\psi}_{fD} &= AI_0 \left(\sqrt{f(s)} r_{fD} \right) + BK_0 \left(\sqrt{f(s)} r_{fD} \right). \end{aligned} \quad (D.6)$$

Substituting internal and outer boundary conditions into the above general form:

$$\bar{\psi}_{fD} = \frac{\bar{q}}{q_{sc}} K_0 \left(\sqrt{f(s)} r_{fD} \right), \quad (D.7)$$

where

$$f(s) = s\omega_f + 3\alpha_f \lambda_{mf} \left[\sqrt{f_2(s)} \coth \left(\sqrt{f_2(s)} \right) - 1 \right]. \quad (D.8)$$

Data Availability

This article does not have any underlying data.

Conflicts of Interest

The authors declare that they have no conflicts of interest.

References

- [1] F. Bilgili, E. Koçak, Ü. Bulut, and M. N. Sualp, "How did the US economy react to shale gas production revolution? An advanced time series approach," *Energy*, vol. 116, pp. 963–977, 2016.
- [2] G. Yuan, S. Luo, and J. Zheng, "Policies on promoting the development of China's shale gas industry," *Science & Technology Review*, vol. 36, no. 4, pp. 8–11, 2018.
- [3] X.-C. Lu, F.-C. Li, and A. T. Watson, "Adsorption measurements in Devonian shales," *Fuel*, vol. 74, no. 4, pp. 599–603, 1995.
- [4] S. Roy, R. Raju, H. F. Chuang, B. A. Cruden, and M. Meyyappan, "Modeling gas flow through microchannels and nanopores," *Journal of Applied Physics*, vol. 93, no. 8, pp. 4870–4879, 2003.
- [5] N. S. Alharthy, M. A. Kobaisi, H. Kazemi, and R. M. Graves, *Physics and Modeling of Gas Flow in Shale Reservoirs*, Society of Petroleum Engineers, 2012.
- [6] D. G. Hill and C. R. Nelson, "Gas productive fractured shales—an overview and update," *Gas Transport in Porous Media*, vol. 6, no. 2, 2000.
- [7] F. Javadpour, D. Fisher, and M. Unsworth, "Nanoscale gas flow in shale gas sediments," *Journal of Canadian Petroleum Technology*, vol. 46, no. 10, 2007.
- [8] S. Cheng, L. Zhang, and X. Li, "Test analysis of trilateral medium branch horizontal well," *Hydrodynamics Research and Progress*, vol. 24, no. 2, pp. 127–132, 2009.
- [9] D. Fan, J. Yao, and Z. Wang, "Well test interpretation of fracturing horizontal wells based on different dip angles," *Hydrodynamics Research and Progress*, vol. 24, no. 6, pp. 705–712, 2009.
- [10] M. L. Brown, E. Ozkan, and R. S. Raghavan, "Practical solutions for pressure transient response of fractured horizontal wells in unconventional reservoirs," in *SPE Reservoir Evaluation & Engineering*, pp. 4–7, Society of Petroleum Engineers, 2009.
- [11] E. Ozkan, M. Brown, and R. Raghavan, "Comparison of fractured horizontal well performance in conventional and unconventional reservoirs," *Dermatologic Surgery*, vol. 27, no. 8, pp. 703–708, 2009.
- [12] M. Stalgorova, "Practical analytical model to simulate production of horizontal wells with branch fractures," in *SPE Canadian Unconventional Resources Conference*, p. 17, Calgary, Alberta, Canada, 2012.
- [13] D. Obembe and M. E. Hossain, "A new pseudo-steady triple-porosity model for naturally fractured shale gas reservoir," in

- SPE Annual Technical Conference and Exhibition*, p. 14, Houston, TX, USA, 2015.
- [14] M. Dejam, H. Hassanzadeh, and Z. Chen, "Pre-Darcy flow in porous media," *Water Resources Research*, vol. 53, no. 10, pp. 8187–8210, 2017.
- [15] H. Wang, J. G. Wang, F. Gao, and X. Wang, "A two-phase flowback model for multiscale diffusion and flow in fractured shale gas reservoirs," *Geofluids*, vol. 2018, Article ID 5910437, 15 pages, 2018.
- [16] J. Cai, D. Lin, H. Singh, S. Zhou, Q. Meng, and Q. Zhang, "A simple permeability model for shale gas and key insights on relative importance of various transport mechanisms," *Fuel*, vol. 252, pp. 210–219, 2019.
- [17] L. He, H. Mei, X. Hu, M. Dejam, Z. Kou, and M. Zhang, "Advanced flowing material balance to determine original gas in place of shale gas considering adsorption hysteresis," *SPE Reservoir Evaluation and Engineering*, vol. 22, no. 4, pp. 1282–1292, 2019.
- [18] M. Wei, Y. Duan, M. Dong, Q. Fang, and M. Dejam, "Transient production decline behavior analysis for a multi-fractured horizontal well with discrete fracture networks in shale gas reservoirs," *Journal of Porous Media*, vol. 22, no. 3, pp. 343–361, 2019.
- [19] J. Liu, J. G. Wang, F. Gao, Y. Ju, and X. Wang, "Analytical solution for shale gas productivity of a multiple-fractured horizontal well based on a diffusion model," *Arabian Journal for Science and Engineering*, vol. 43, no. 5, pp. 2563–2579, 2018.
- [20] J. Ren, Y. Y. Gao, Q. Zheng, P. Guo, and D. L. Wang, "Pressure transient analysis of a finite-conductivity multiple fractured horizontal well in linear composite gas reservoirs," *Journal of Central South University*, vol. 27, no. 3, pp. 780–796, 2020.
- [21] M. B. Asadi, M. Dejam, and S. Zendehboudi, "Semi-analytical solution for productivity evaluation of a multi-fractured horizontal well in a bounded dual-porosity reservoir," *Journal of Hydrology*, vol. 581, no. 1, article 124288, 2020.
- [22] E. S. Carlson and J. C. Mercer, "Devonian shale gas production: mechanisms and simple models," *Journal of Petroleum Technology*, vol. 43, no. 4, pp. 476–482, 2013.
- [23] F. Javadpour, "Nanopores and apparent permeability of gas flow in mudrocks," *Journal of Canadian Petroleum Technology*, vol. 48, no. 8, pp. 16–21, 2009.
- [24] H. Sondergeld, K. E. Newsham, and J. T. Comisky, "Petrophysical considerations in evaluating and producing shale gas resources," in *SPE Unconventional Gas Conference*, p. 34, Pittsburgh, PA, USA, 2010.
- [25] L. J. Klinkenberg, "The permeability of porous media to liquids and gases," in *API Drilling and Production Practice*, p. 14, New York, NY, USA, 1941.
- [26] F. Civan, "Effective correlation of apparent gas permeability in tight porous media," *Transport in Porous Media*, vol. 82, no. 2, pp. 375–384, 2010.
- [27] K. Mosher, Y. Liu, and J. Wilcox, *The impact of pore size on methane and CO₂ desorption in carbon*, Stanford University, 2011.
- [28] A. C. Bumb and C. R. McKee, "Gas well testing in the presence of desorption for coalbed methane and Devonian shale," *SPE Formation Evaluation*, vol. 3, no. 1, pp. 179–185, 1988.
- [29] A. Beskok, G. E. Karniadakis, and W. Trimmer, "Rarefaction and compressibility effects in gas microflows," *Journal of Fluids Engineering*, vol. 118, no. 3, pp. 448–456, 1996.
- [30] S. A. Mengal and R. A. Wattenbarger, "Accounting for adsorbed gas in shale gas reservoirs," in *SPE Middle East Oil and Gas Show and Conference*, p. 15, Manama, Bahrain, 2011.
- [31] G. Sheng, Y. Su, and W. Wang, "A new fractal approach for describing induced-fracture porosity/permeability/compressibility in stimulated unconventional reservoirs," *Journal of Petroleum Science and Engineering*, vol. 179, no. 8, pp. 855–866, 2019.
- [32] D. J. K. Ross and R. M. Bustin, "The importance of shale composition and pore structure upon gas storage potential of shale gas reservoirs," *Marine and Petroleum Geology*, vol. 26, no. 6, pp. 916–927, 2009.
- [33] R. M. Bustin, A. M. Bustin, and A. Cui, "Impact of shale properties on pore structure and storage characteristics," in *SPE Shale Gas Production Conference*, Fort Worth, TX, USA, 2008.
- [34] H. L. Liu and H. Y. Wang, "The use of source and Green's functions in solving unsteady-flow problems in reservoirs," *Natural Gas Industry*, vol. 32, no. 9, pp. 5–9, 2012.
- [35] G. Sheng, H. Zhao, Y. Su et al., "An analytical model to couple gas storage and transport capacity in organic matter with non-circular pores," *Fuel*, vol. 268, no. 1, p. 117288, 2020.
- [36] C. Chen, "Multiscale imaging, modeling, and principal component analysis of gas transport in shale reservoirs," *Fuel*, vol. 182, pp. 761–770, 2016.
- [37] M. Dejam, H. Hassanzadeh, and Z. Chen, "Semi-analytical solutions for a partially penetrated well with wellbore storage and skin effects in a double-porosity system with a gas cap," *Transport in Porous Media*, vol. 100, no. 2, pp. 159–192, 2013.
- [38] H. Stehfest, "Algorithm 368: numerical inversion of Laplace transforms [D5]," *Communications of the ACM*, vol. 13, no. 1, pp. 47–49, 1970.

Research Article

Investigating the Influences of Pore-Scale Characteristics on Tight Oil Migration by a Two-Phase Pore Network Model

Jianhui Zeng ^{1,2}, Yongchao Zhang ^{3,4}, Jingsheng Ma ⁵, Changling Liu ^{3,4}
and Zhe Cao ^{1,2}

¹State Key Laboratory of Petroleum Resources and Prospecting, China University of Petroleum, Beijing 102249, China

²College of Geosciences, China University of Petroleum, Beijing 102249, China

³The Key Laboratory of Gas Hydrate, Ministry of Natural Resources, Qingdao Institute of Marine Geology, Qingdao 266071, China

⁴Laboratory for Marine Mineral Resources, Pilot National Laboratory for Marine Science and Technology, Qingdao 266071, China

⁵Institute of Petroleum Engineering, Heriot-Watt University, Edinburgh EH14 4AS, UK

Correspondence should be addressed to Yongchao Zhang; yongchao.zhang@hotmail.com

Received 11 February 2020; Revised 28 May 2020; Accepted 18 July 2020; Published 1 August 2020

Academic Editor: Stefan Iglauer

Copyright © 2020 Jianhui Zeng et al. This is an open access article distributed under the Creative Commons Attribution License, which permits unrestricted use, distribution, and reproduction in any medium, provided the original work is properly cited.

The migration of expelled hydrocarbon from source rock into unconventional tight reservoirs is subject to different pore-scale fluid transport mechanisms as opposed to the conventional counterparts and therefore plays a crucial role in controlling the hydrocarbon distribution and accumulation in the former. One of the different mechanisms is related to the formation of a more viscous boundary layer (BL) of brine, i.e., wetting phase fluid on pore surfaces, giving rise to the so-called BL effect. In this work, a two-phase pore network model (PNM) that considers this BL effect is developed to study the influences of pore-scale characteristics on the oil migration process, manifested through the BL effect in tight-sandstone media. Good agreements are reached between experimentally derived relative permeability curves and predicted ones, by applying this model to the pore-network networks extracted from the same samples. Then, this validated model was used to evaluate the impacts of the following factors on the oil migration process: pore radius, coordination number, aspect ratio, brine viscosity, and wettability. The results show that all factors can influence the oil migration process but at different magnitudes. The applicability and significance of the developed tight oil migration PNM are discussed in this work.

1. Introduction

Following the shale gas breakthrough in the United States, tight oil has become the next focus of unconventional petroleum exploration worldwide [1, 2]. Tight oil from the Bakken Formation has accounted for more than 10% of the United States daily oil production in 2017 [3]. Unlike conventional reservoirs, tight oil reservoirs are usually characterized by low porosity, low permeability, complicated pore-throat structures, and strong heterogeneity ([4–6]). The hydrocarbon migration is a process in which hydrocarbon expelled from low-permeability source rocks finds tortuous porous paths through carrier beds into the traps where hydrocarbon can accumulate to form reservoirs in the geological time-

frame [7]. Of many factors that control this process and therefore the resultant reservoirs in terms of their sizes, fluid saturations, and fluid properties within them, which are of crucial importance for hydrocarbon exploration and exploitation [8, 9], the tightness of pore space within carrier and reservoir rocks is of pivotal importance. Compared with conventional reservoirs, oil migration behaves distinctively in tight reservoirs in the following aspects [5, 10]: (1) there is no clear demarcation between the primary migration and secondary migration process, (2) the migration distance is typically short which induces hydrocarbon inner source accumulation or near-source accumulation, and (3) the impact of capillary pressure is significantly important during the migration process while the effect of buoyancy is limited.

1.1. Relationships between Pore-Scale Characteristics and Oil Migration. The significance of pore-scale characteristics for the oil migration process has been assessed using experimental and geological methods in previous literature. Lai et al. [11] analyzed the pore-structure characteristics of tight sandstones in the Sichuan Basin, China, by using experimental data and basin-scale inferential methods. They concluded that the complex pore systems in tight sandstones are associated with the original depositional environments and subsequent diagenesis alteration; the coexistence of different types of pores results in the polymodal distribution of pore sizes. Relationships between the pore-structure characteristics and diagenesis alteration effects are concluded in their published review paper [12]. Similar work was reported by Xiong et al. [13]. They classified the pore system of tight sandstone into four types: intergranular pores, dissolution pores, clay-aggregated pores, and microfractures, the sizes of which are distributed in the different ranges varying from nano- to microscale. The flow potential during the oil migration process and the oil storage capacity in terms of oil migration and accumulation are contributed by the pores with different sizes. Cao et al. [14] further identified the key geological controlling factors of microscale oil distribution during oil migration and accumulation by geochemical approaches combined with mesoscale petrophysical methods, which includes porosity, pore throat radius, and hydrocarbon generation capacity. Zhang et al. [15] conducted and analyzed hydrocarbon charging experiments using natural tight sandstones samples. The experimental results show that the starting pressure of oil migration and terminal oil saturation values both show good logarithmic relationships with the sample permeability. However, the growth curves of oil saturation (S_o) with charging pressure are irregular and distinctive for different samples, such characteristics cannot be explained without sufficient pore-scale information of rock samples. To get a better understanding of the oil migration critical conditions and controlling factors at the pore scale, further investigations were completed in our previous works [16–18] by using a series of microscopic observation methods including CT (X-ray computed tomography), SEM (scanning electron microscopy), NMR (nuclear magnetic resonance), and casting thin section techniques. Several concluding remarks obtained from these works are as follows: (1) there exists a critical pore radius threshold for oil migration in tight cores, which ranges from 0.035 to 0.627 μm ; (2) the oil-charging curves of tight reservoirs could be classified into four types, where the pore-structure factors play crucial roles; and (3) the surface areas of effective pores/throats, pore quantity density, and coordination number are proved to be important factors controlling the oil migration process.

Despite some qualitative relationships and critical conditions obtained from these existing experiments, the influencing mechanisms of the pore-scale characteristics on the microscale oil migration behaviors are not clearly understood. Besides, due to the complex interactions of different factors and high costs of the forced fluid displacement experiments, the quantitative relationship between any single pore-scale parameter and oil migration cannot be achieved experimentally.

1.2. Pore Network Modeling of Physical Processes at the Pore Scale. PNM (pore network modeling) is referred to any analytical and/or numerical models of physiochemical processes prescribed on pore networks composed of pore elements that are connected through throat elements. Since pore networks can be constructed to resemble geometric and topologic characteristics of pore space of realistic porous sample, PNM has been proved to be able to capture the manifestation of pore-scale processes, through simulation, on sample scales and predict macroscopic transport properties in porous media [19, 20]. Fatt [21] pioneered PNM and proposed a 2D regular network model for predicting capillary pressure and relative permeability of the primary drainage process in which the radii of pores were randomly assigned. Dullien et al. [22] extended that method to the 3D network model with more realistic pore-scale representation. The subsequent development of PNM has allowed the packing of grains with different sizes and shapes to be modeled, simulating a wide range of flow processes in different porous sedimentary rocks [23–26]. The readers are referred to the reviews [13, 27] for a summary of the recent advances in PNM models applied to various processes. Recently, PNM has been applied to tight formations. Riepe et al. [28] presented a case history of combining CT imaging and PNM to establish a relationship between microscale structures and petrophysical properties of tight clastic rocks in Oman. That application shows the promise of an alternative approach for the evaluation of unconventional reservoirs. Ruspini et al. [29] introduced a multiscale pore network modeling workflow to compute the transport properties of clay-rich tight sandstone samples with wide pore size distributions. The representative network is composed of macropores, defined as completely resolved porosity, and micropores which are defined as unresolved porosity and treated as the equivalent continuum. Wang and Sheng [30, 31] proposed a quasistatic PNM model to simulate the drainage process in shale and tight porous formations. The liquid non-Darcy flow mechanism was incorporated into the proposed PNM model using an empirical equation obtained from experiments [32]. Based on their simulations, Wang and Sheng concluded that the non-Darcy flow behaviors show significant influences on the absolute permeability predictions, but not on the relative permeability results.

PNM models have been developed for modeling the oil migration process in conventional formations, but not suitable for directly studying the oil migration process in tight formations. Compared with medium- or high-permeability media, the fluid flow in tight media shows obvious non-Darcy flow (NDF) behaviors [33, 34], which is the flow velocity of fluid being not linearly dependent on the charging pressure gradient. Some researchers [35–37] proposed that these NDF behaviors were attributed to the existence of the boundary layer (BL) of water attached to the pore surface where the viscosity is much larger than the fluid in the pore center. The BL with different thicknesses in pores significantly reduces the effective seepage radius, which results in the NDF behaviors in tight media. In recent works, a parametric model of BL thickness of BL (see Equation (1)) was proposed by Cheng's group [14, 38, 39] based on the

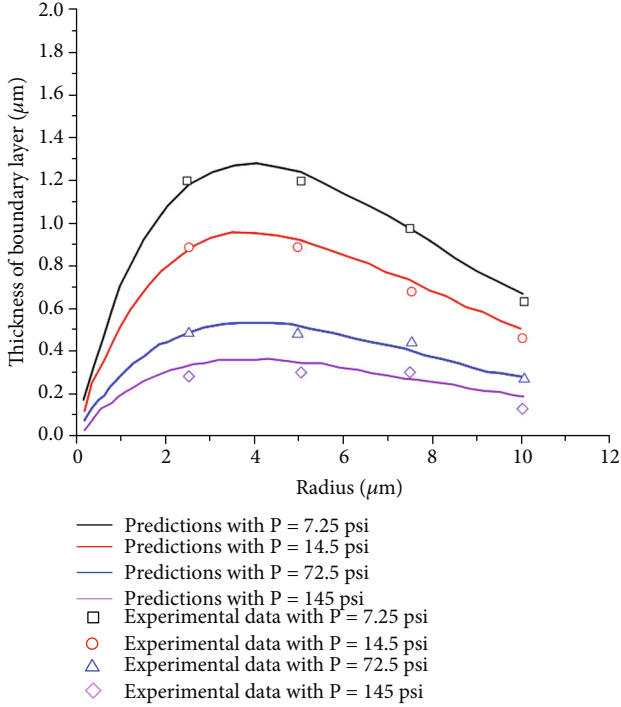


FIGURE 1: A comparison between calculation results of BL thickness using Equation (1) and microtube experimental results (reproduced from [39]).

experiments where coefficients are fitted using the particle swarm optimization algorithm [40]. The calculation equation is given as

$$\frac{\delta}{r} = h_1 \cdot \mu_w \cdot e^{h_2 r} \cdot (\nabla p)^{h_3}, \quad (1)$$

where δ is the thickness of BL, μ_w is the brine viscosity, and ∇p is the pressure difference between inlet and outlet per unit length. The three coefficients (h_1 , h_2 , and h_3) are determined to be 0.258, -0.261, and -0.419. The proposed method shows good predictions of BL thickness of numerous microtube experiment results conducted by Li et al. (2011) as shown in Figure 1. These experiments are conducted through simulating the pore-throat system with microfused silica capillary tubes, the radius of which ranges from 2.5 μm to 10 μm . The influence of BL thickness on the fluid NDF is analyzed by measuring the flow rate, pressure gradient, and viscosity experimentally.

A PNM for simulating the oil migration behaviors is developed in this work, considering NDF behavior due to BL of water. Equation (1) is employed to calculate BL thicknesses in the network elements to account for the NDF behaviors during tight oil migration. We are aware that the developed model employed the BL theory may be neither universally applicable nor accurate for all the cases of tight formations. The principal objectives of this work are as follows: (1) to extend the application of PNM to analyze the oil migration in tight formations; (2) to study the influences of pore-scale characteristics on oil migration using PNM method, which includes the radius of pores, average coordi-

nation number, aspect ratio (the average diameter ratio of pores to throats), brine viscosity, and wettability conditions; and (3) to discuss the significances and limitations of the conducted PNM simulations.

2. A Quasistatic Two-Phase PNM with BL for Modeling the Oil Migration in Tight Formation

In this section, a quasistatic two-phase pore-network model with BL is developed for modeling oil migration in tight formation, by adapting a well-established quasistatic PNM model for the primary drainage process. This newly developed model is implemented to support a simulation workflow to be discussed in a later section.

2.1. The Model Development. The oil migration into initially water-filled water-wet pore networks occurs in forms of piston-like displacement [41]. When the driving force of oil phase exceeds the capillary entry pressure (P_{entry}) of the neighboring water-filled network elements, oil will displace water in pores/throats. We add a BL of immobile water of finite thickness, δ , to each network element whose radius and volume available to oil phase are reduced proportionally. So, as a result, we should expect higher capillary entry pressure at any oil pressure and higher oil relative permeability and lower water relative permeability at any water saturation.

The capillary entry pressure, for a cylindrical throat, is calculated as follows:

$$P_{\text{entry}} = P_{\text{wetting_phase}} - P_{\text{nonwetting_phase}} = \frac{2\sigma}{r - \delta} \cos \theta, \quad (2)$$

where σ is the interfacial tension between the oil and water, θ is the contact angle that quantifies the wettability property, and r is the pore radius. For an angular pore element, the capillary entry pressure can be adapted from that of Øren [42] as follows:

$$P_{\text{entry}} = \frac{\sigma \left(1 + 2\sqrt{\pi G}\right)}{r - \delta} F_d(\theta, G) \quad (3)$$

$$F_d(\theta, G) = \frac{1 + \sqrt{1 + 4GD/\cos^2\theta}}{1 + 2\sqrt{\pi G}}, \quad (4)$$

$$D = \pi \left(1 - \frac{3\theta}{\pi}\right) + 3 \sin \theta \cos \theta - \frac{\cos^2\theta}{4G}. \quad (5)$$

The parameter G in Equations (3) and (4) is the shape factor for the network element, which can be calculated through Equation (6):

$$G = \frac{A}{S^2}, \quad (6)$$

where A is the cross-sectional area and S is the perimeter of the element.

To calculate permeability of each connected phase from the inlet to outlet faces of a PNM model, the single-phase flow between two neighboring pore elements is given by a Poiseuille-type law [43]:

$$Q_{ij} = g_{ij}(P_i - P_j), \quad (7)$$

where P_i and P_j are the pressure values of pore i and pore j and g_{ij} is the conductance between the two pores, which can be determined through the following Equation (8).

$$\frac{L_{ij}}{g_{ij}} = \frac{L_i}{g_i} + \frac{L_t}{g_t} + \frac{L_j}{g_j}. \quad (8)$$

Here, g_i , g_j , and g_t are the conductances of pores i and j and the throat connecting the pores.

In this work, the conductance of network elements is calculated following the functional form in the "3Rs" approach [44, 45] but takes into consideration BL, and it is expressed as

$$g = \bar{A}\pi(r - \delta)^\lambda \frac{10^{6\lambda-24}}{8\mu L}, \quad (9)$$

where \bar{A} is the conductance constants, λ is the conductance exponent, L is the length of the element. μ in Equation (9) is the average viscosity of the fluids in the pores and calculated by

$$\mu = f_o\mu_o + f_w\mu_w, \quad (10)$$

where f_o and f_w are the fractions of oil and water in the calculation element. Based on the calculations of Equation (7), the pressure field of the network model can be calculated by applying the mass conservation at each pore element:

$$\sum Q_{ij} = \sum g_{ij}(P_i - P_j) = 0. \quad (11)$$

When the pressure field for a phase in the network is obtained, we can calculate the relative permeability of each phase (oil or water phase) as follows:

$$K_{rp} = \frac{q_p\mu_p L}{A\Delta P_p}, p = o, w, \quad (12)$$

The new model is implemented on an earlier version of the open-source PNM code (https://github.com/ahboujelben/numSCAL_basic) by extending its quasistatic two-phase model. For technical details in that code, the reader is referred to Regaieg et al. [46] and Boujelben et al. [47].

2.2. Simulation Procedure. Simulations are carried according to the procedure illustrated by Figure 2. For a given pore network that may be extracted from X-ray CT images of real rock samples or stochastically generated, (1) it is initialized 100% water saturation (S_w) at a reference pressure while wettability condition is applied to each network element; (2)

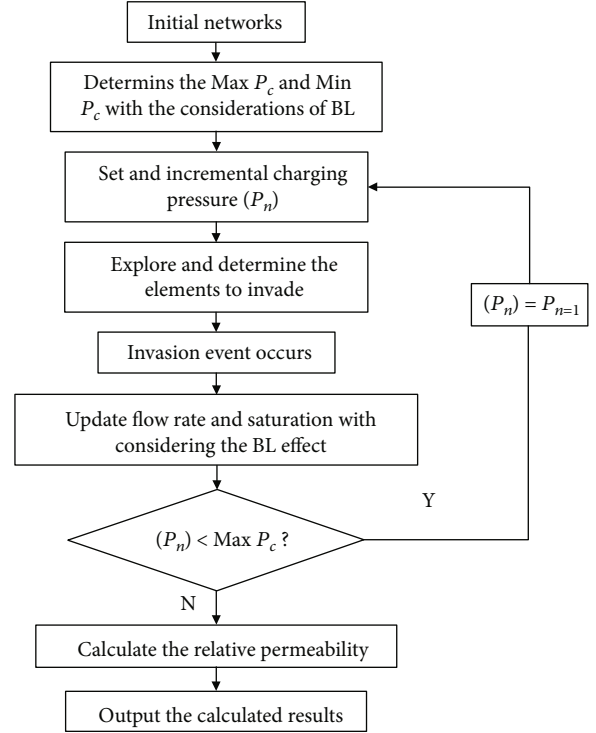


FIGURE 2: A workflow for quasistatic flow modeling of oil migration with consideration of the BL effects.

explore the minimum and maximum radius (Min R and Max R) of elements, then calculate the corresponding maximum and minimum entry capillary pressure (Max P_c and Min P_c) with considering the BL effect. The calculations of Max P_c and Min P_c were realized by the iterative method; (3) set an incremental charging pressure (P_n) which increases from Min P_c to Max P_c . The incremental step is set by (Max P_c - Min P_c) / simulation steps; (4) explore for and determine the elements to invade. An invasion event occurs when the charging pressure overcomes the entry pressure of element. The entry pressure of each element is calculated by Equations (3)–(5). (5) Update phase saturation and flow rate with the consideration of BL effect. (6) Check the terminal condition whether the charging pressure is larger than Max P_c . If no, increase the charging pressure by step and do loop for steps (4) to (6). If yes, output the phase saturation and calculate relative permeability for each phase.

3. Model Validations

Model validation has been conducted by making comparisons between the predicted relative permeability and experimental results for a Berea sandstone sample and two tight sandstone samples (Samples S5 and S6). The relative permeability data measured on the Berea sample and its matched CT image data can be downloaded from the Imperial College database (the website address is <http://www.imperial.ac.uk/earth-science/research/research-groups/perm/research/pore-scale-modelling/>). Samples S5 and S6 are taken from the Chang-7 members of the Yangchang Formation in the Ordos Basin, a typical tight oil basin in northwest China.

TABLE 1: Properties of the three experimental samples.

Properties	Berea	Sample S5	Sample S6
Porosity (%)	19.50	9.72	10.47
Permeability (mD)	1106.00	0.83	1.45
Coordination no.	4.20	3.10	3.30
Mean pore radius (μm)	19.20	4.20	4.40
Maximum radius (μm)	73.60	12.20	15.80
Minimum radius (μm)	3.60	1.00	1.00

Oil charging experiments are carried out by using Samples S5 and S6 to simulate the physical process of oil migration in tight media. Experimental apparatus, experimental procedures, and the properties of used water/oil have been described in our previous work [15, 48]. Both tight samples are scanned to obtain CT images using Zeiss Xradia-500 Versa with a resolution of $0.99\ \mu\text{m}$, at the Stata Key Laboratory of Petroleum Resources and Respecting, China. Raw CT images are preprocessed and reconstructed to 16-bit grey images using a multi-threading software package “tomoRecon” [49]. The image filtering and phase segmentation are completed by using Avizo 9.7 software. An interactive thresholding module is used to segment the phases by selecting values of image intensity ranges for each phase [50]. The properties of the three experimental samples are shown in Table 1. It shows that the porosity, permeability, and pore connectivity of the tight sandstone samples (S5 and S6) are much smaller than those of the Beria sample. The pore size ranges of the tight samples are distributed in smaller and narrower scope compared to the Beria sample. Note that the lower limit of pore radius for tight samples is limited by the solution of CT images which means some pores with radius smaller than $1\ \mu\text{m}$ may not be detected by CT scanning. More information concerning the pore-structure features in the tight formations of the Ordos Basin can be found in our previous work [17, 18].

A modified maximal ball (MB) method developed by Dong and Blunt [51] was applied to extract pore networks from 3D CT images. The modified MB method explore and build an inscribed sphere at each void voxel of images first by a two-step searching algorithm, then remove those included in others. The rest spheres (MBs) are defined as pores and throats followed the clustering rule of family trees sorted by their size and rank. Geometrical properties are calculated for each pore and throat, including the size of pore and throat, volume, and shape factor. For more details of the pore network extraction, the readers are referred to Dong and Blunt’s original publication [51]. In our work, pore networks of tight sandstone samples were extracted using an open-source software package (website for download: <https://github.com/aliraeini/pnextract>) that implements those mentioned techniques. The flow modeling of these three samples is conducted followed the steps in Sections 2.1 and 2.2. For the three samples, the predicted relative permeability curves from the newly developed model with consideration of BL effect are compared with those without BL effect, while both the model predictions are compared to experimental data (Figures 3 and 4). Figure 3 indicates that both the PNM models with and

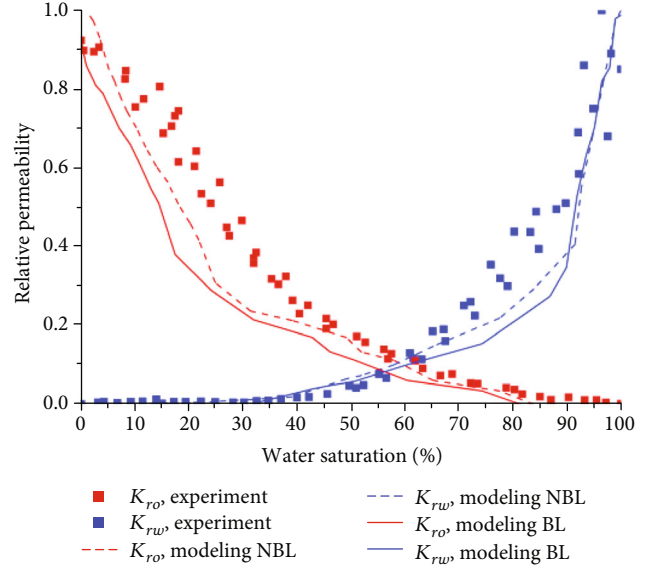


FIGURE 3: Predicted relative permeability of Berea sandstone (lines) compared to the experimental data by Oak [52] (square). The oil relative permeability data are marked with red, while the water relative permeability data are marked with blue. Data modeling NBL/BL means that the calculations using the model without/with BL consideration, respectively.

without BL consideration show good agreements with the experimental data, which in turn partly proves that Equation (1) for BL calculation is basically reasonable for the pore size distribution in natural samples. Figure 4 shows that the predictions of the BL model are in better agreement with the experimental data than that without BL effect in tight sandstone samples. Compared to the model without BL effect, the BL model shows lower permeability predictions for each phase of which locates in a narrower and higher S_w range. The differences between NBL and BL models are mainly attributed to the decrease of pore radius and connectivity in BL model caused by the existence of BL. Specific impacts of the single influencing factor on relative permeability predictions are further discussed in Sections 4 and 5.

4. Sensitivity Analyses of Five Pore-Scale Factors

Stochastically synthetic pore networks were constructed for the sensitivity analysis, with respect to five featured pore-scale factors (i.e., the radius of pores, average coordination number, aspect ratio, brine viscosity, and wettability), on their impacts on the oil migration. The changing scopes of these factors are determined by considering the pore-structure characteristics of tight formations and referring to the measured results in several published works [4, 10, 53]. The resultant relative permeability curves are employed for showing the relative fluid flow capability during the oil migration, while oil charging curves for explaining the oil content accumulated. Technically, the water in the BL is simplified as dead water without flowing but count for S_w in the calculation of relative permeability and S_o . Note that each pore network is generated as a regular lattice network first and throats were then removed randomly to match the

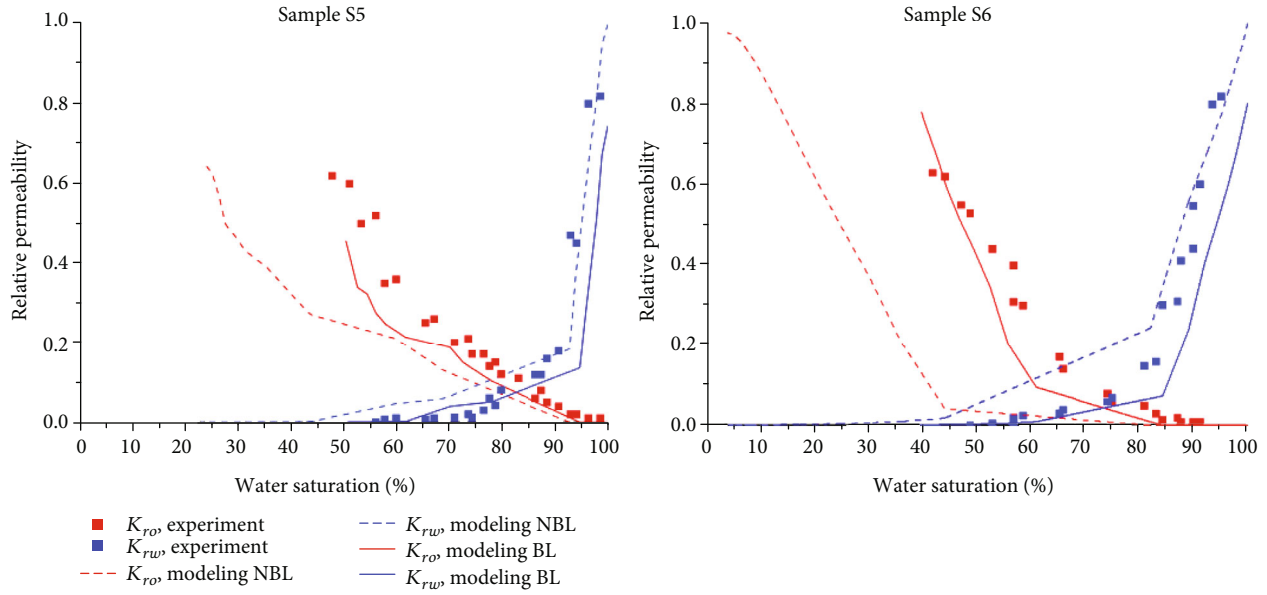


FIGURE 4: Predicted relative permeability of S5 and S6 tight sandstone (lines) compared to the experimental results (square). The oil relative permeability data are marked with red, while the water relative permeability data are marked with blue. Data modeling NBL/BL means that the calculations using the model without/with BL consideration, respectively.

TABLE 2

Models	Model size ($N_x \times N_y \times N_z$)	Radius setting	Coord. NO.	A. ratio	Viscosity of brine (mPa·s)	Wettability
Run. 1~3	$25 \times 25 \times 25$	Run1: $R_{\min} = 0.1, R_{\max} = 1$ Run2: $R_{\min} = 0.1, R_{\max} = 2$ Run3: $R_{\min} = 0.1, R_{\max} = 5$	Coord. no. = 3.0	A.ratio = 2	Viscosity = 1	CA. = 0°
Run. 4~6	$25 \times 25 \times 25$	$R_{\min} = 0.1, R_{\max} = 2$	Run4: Coord. no. = 2.5; Run5: Coord. no. = 3.0; Run6: Coord. no. = 3.5;	A.ratio = 2	Viscosity = 1	CA. = 0°
Run. 6~9	$25 \times 25 \times 25$	$R_{\min} = 0.1, R_{\max} = 2$	Coord. no. = 3.0	Run6: A.ratio = 1; Run7: A.ratio = 2; Run8: A.ratio = 3;	Viscosity = 1	CA. = 0°
Run. 10~12	$25 \times 25 \times 25$	$R_{\min} = 0.1, R_{\max} = 2$	Coord. no. = 3.0	A.ratio = 2	Run 10: viscosity = 1; Run 11: viscosity = 2; Run 12: viscosity = 3;	CA. = 0°
Run. 13~15	$25 \times 25 \times 25$	$R_{\min} = 0.1, R_{\max} = 2$	Coord. no. = 3.0	A.ratio = 2	Viscosity = 1	Run 13: CA. = 0° Run 14: CA. = 30° Run 15: CA. = 60°

prescribed average coordination number. The size of pore elements follows a uniform distribution in the prescribed size range. Pore networks and their parameters set for sensitivity analysis are given in Table 2.

Runs 1~3 are used to assess the impact of radius on relative permeability and oil charge where the coordination number remains the same but the upper limits of pore size ranges increase from 1 to 5 μm with a constant lower limit of 0.1 μm . The calculated absolute permeabilities of the models are 0.001 mD, 0.03 mD, and 0.9 mD. Figure 5 shows that with the decrease of upper limit pore radius range the maximums of the oil/water phase relative permeability decrease. Meanwhile, the endpoints of K_{rw} at the S_w axis increase from 3.5% to 20.8%. The predicted K_{ro} with small

pores at the low S_w (less than 35%) is higher than that with large pores but turns to be lower at a high S_w condition. The predicted K_{rw} shows an opposite trend within the corresponding saturation range. The S_w at the intersection points of K_{rw} and K_{ro} curves stayed constant for Runs 1~3. The oil charging curves in Figure 6 show that the calculated S_o of models increases gradually with increasing charging pressure and terminates at the S_o of 96.5%, 86.5%, and 79.2% for Runs 1~3, respectively. The required charging pressure for 0.1 ~ 1 μm model is much larger than that with 0.1 ~ 5 μm .

4.1. The Impact of Average Coordination Number. The coordination number (Z) is defined as the average number of throats connected with each pore body, which quantifies

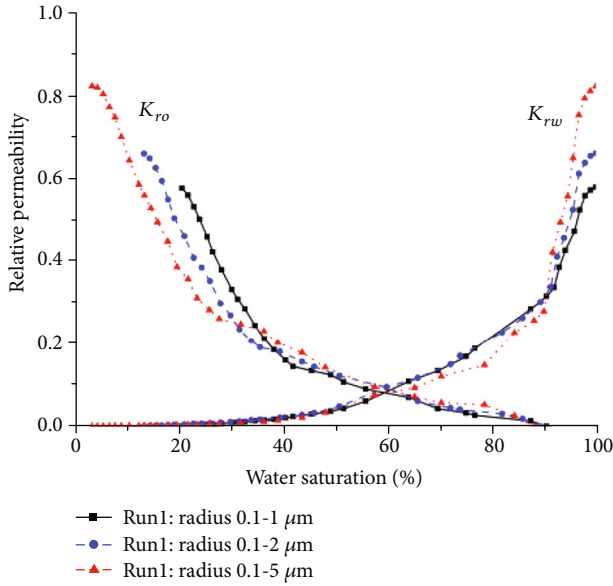


FIGURE 5: Effect of pore radius on relative permeability.

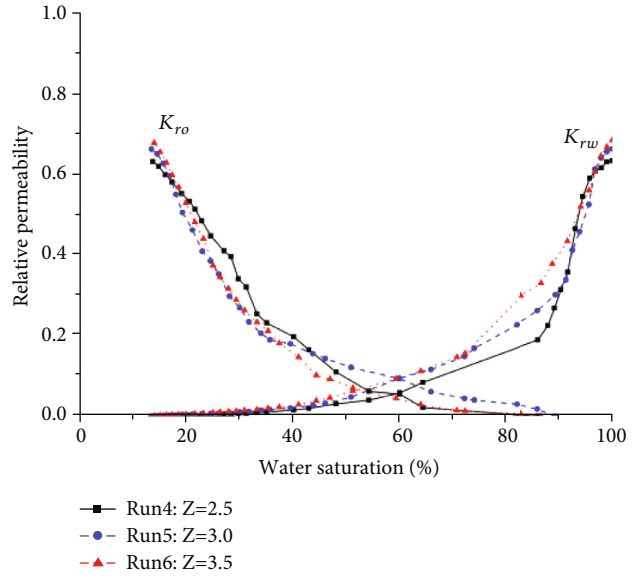


FIGURE 7: Effect of coordination number on relative permeability.

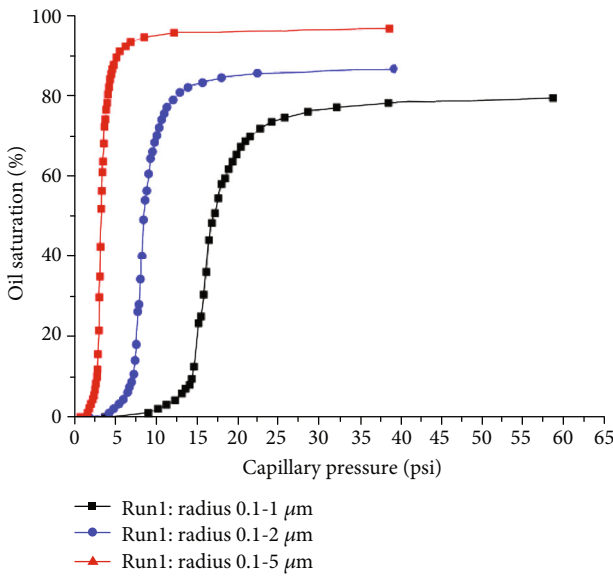


FIGURE 6: Effect of pore radius on oil charging curves.

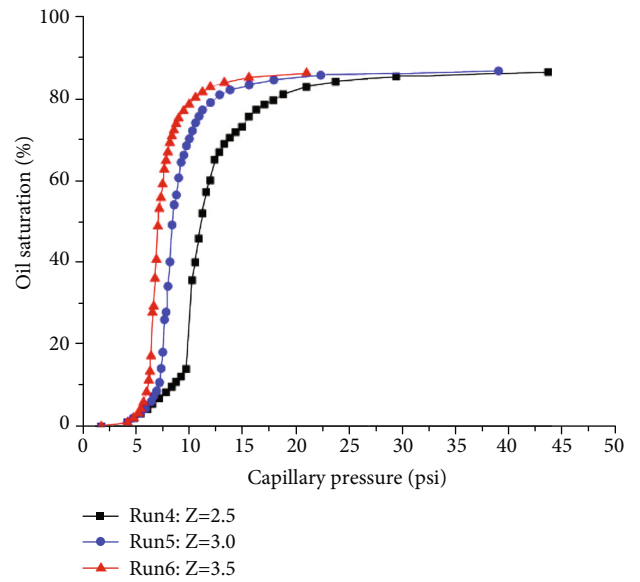


FIGURE 8: Effect of coordination number on oil charging curves.

the connectivity of the networks [54, 55]. A higher coordination number means a better connection condition of the pores in the network. Runs 4~6 set with different coordination numbers (i.e., $Z = 2.5$, $Z = 3$, and $Z = 3.5$) are used to evaluate the impact of coordination number on oil migration behaviors. The calculated absolute permeabilities of the models are 0.01 mD, 0.03 mD, and 0.06 mD. Figure 7 shows that the maximums of oil/water phase relative permeability decrease with the decreasing Z values. Meanwhile, the endpoints of K_{rw} curves at the S_w axis are kept constant ($S_w = 13.5\%$) for different simulations. The calculated K_{ro} in the poor connectivity model (Run 4) is slightly higher than that in the better connectivity models (Runs 5 and 6) at a low S_w condition but turns to be lower at a high S_w condition. The

predicted K_{rw} curve shows an opposite trend. The corresponding X -axis values at the intersection points of K_{rw} and K_{ro} curves stayed constant while the corresponding Y -axis values decrease with the decrease of Z values. The oil charging curves in Figure 8 show that the calculated S_o of all three models increase with the charging pressure and terminates the same $S_o = 86.5\%$. However, the required charging pressure reaching the maximum S_o decreases with the increasing Z of the networks.

4.2. *The Impact of Aspect Ratio.* The impact of aspect ratio on oil migration is realized by increasing the pore radius while keeping the throat radius constant. Runs 7~9 with different aspect ratios are built and calculated in this section of whom

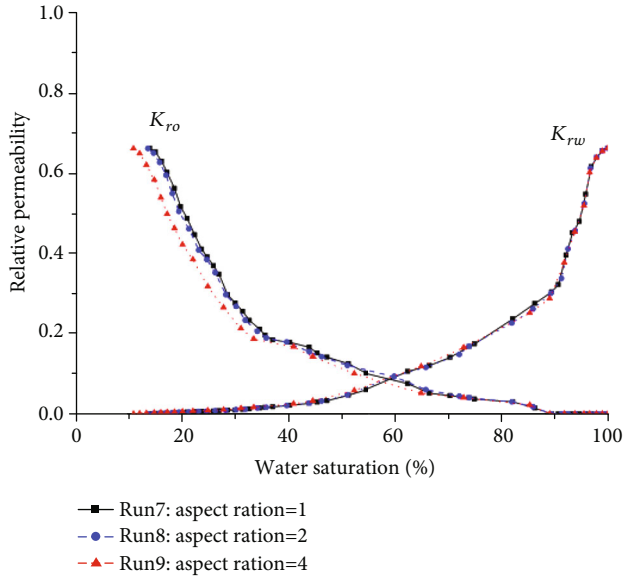


FIGURE 9: Effect of aspect ratio on relative permeability.

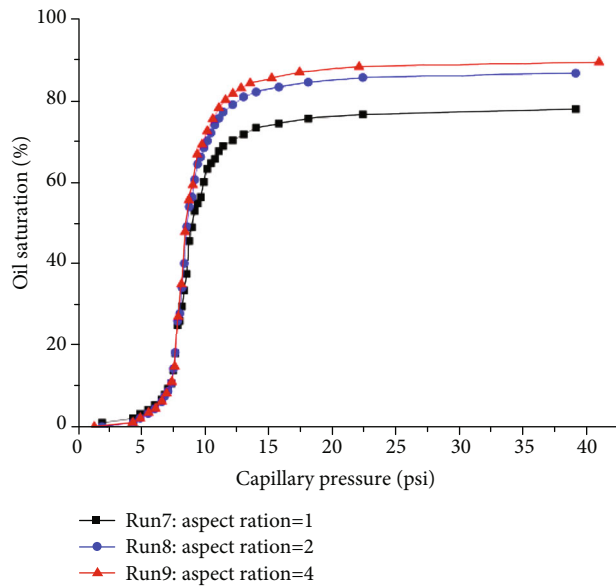


FIGURE 10: Effect of aspect ratio on oil charging curves.

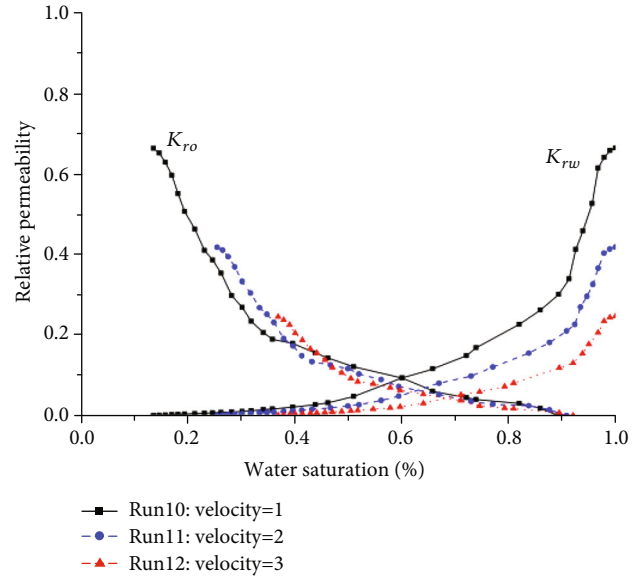


FIGURE 11: Effect of brine viscosity on relative permeability.

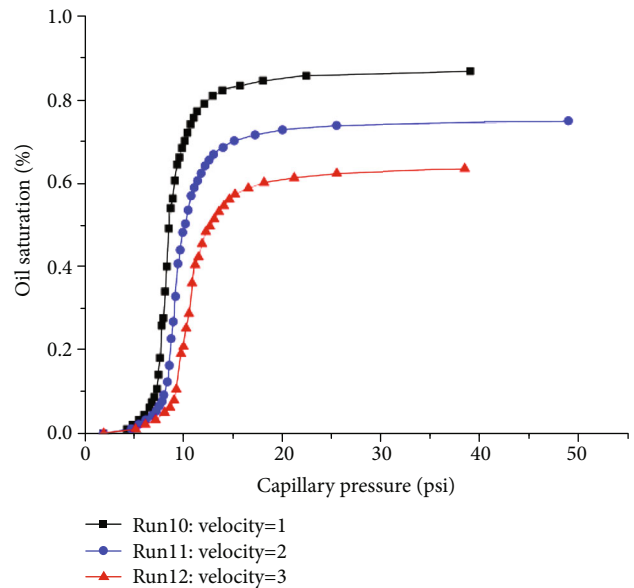


FIGURE 12: Effect of brine viscosity on oil charging curves.

the calculated absolute permeabilities are all 0.03 mD for the throat radii of models remain unchanged. Figure 9 shows that the influence of aspect ratio on relative permeability is relatively weak; the predicted K_{ro} of Run 9 is slightly lower than others (Runs 7~8) within a limited water saturation range of 0~35%. The oil charging curves in Figure 10 show that the maximums of S_o in Runs 7~9 are 77.8%, 86.5%, and 89.2%, respectively. The required charging pressure reaching the maximum S_o for three models are equal.

4.3. The Impact of Brine Viscosity. Runs 10~12 with different viscosity (μ) settings are used to assess the impact of brine viscosity on oil migration behaviors. The calculated relative permeability results in Figure 11 show that the predicted

K_{ro} and K_{rw} values both decrease with the increasing brine viscosity; under the condition of high water saturation, the impact of brine viscosity on relative permeability is more obvious which induces that the intersections point of K_{rw} and K_{ro} shift towards the bottom-right area of the coordinates. The oil charging curves in Figure 12 show that the S_o of all three models increase with the charging pressure and terminates the maximum S_o of 63.2%, 74.6%, and 86.5%. The required charging pressure reaching the maximum S_o for three models are equal.

4.4. The Impact of Wettability Condition. Sensitivity simulations of the wettability effects in conventional reservoir media have been performed in previous works [56, 57]. The

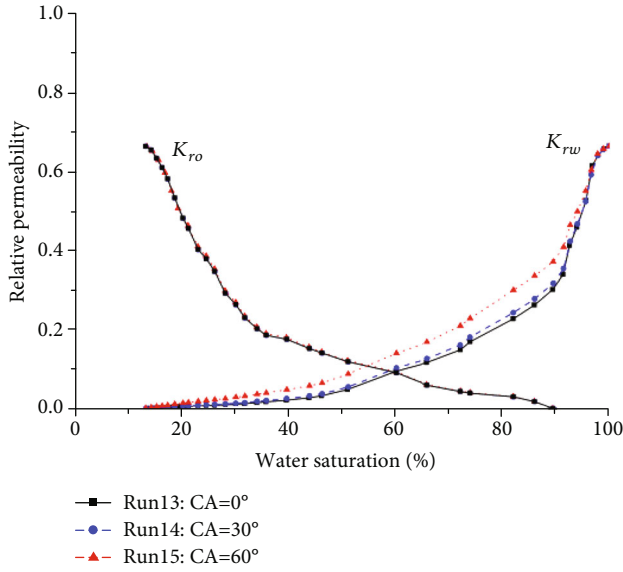


FIGURE 13: Effect of wettability conditions on relative permeability.

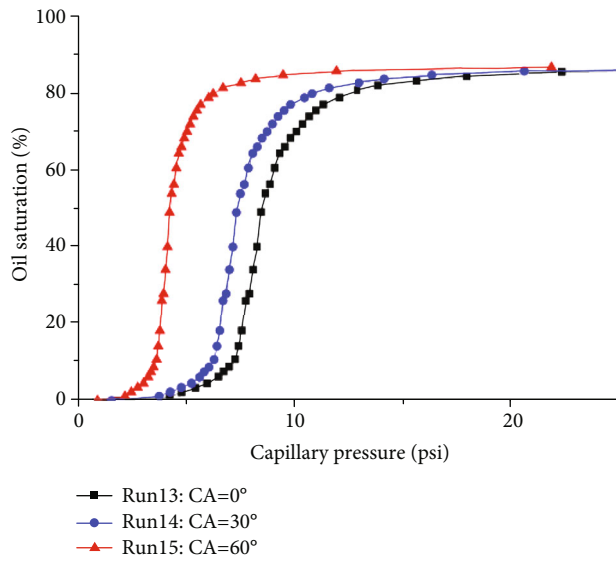


FIGURE 14: Effect of wettability conditions on oil charging curves.

wettability condition before the hydrocarbon migration process is assumed to be water wet. In our simulations, contact angle (CA) is used for qualifying the wettability of rock surface [58, 59]. Three models with different wettability settings (CA = 0°, Run 13; CA = 30°, Run 14; and CA = 60°, Run 15) are modeled to assess the influence of wettability on oil migration, where CA is assigned to be uniformly distributed in the pores and throats. Figure 13 shows that the calculated K_{rw} becomes larger when CAs increase from 0° to 60°, while the wettability setting has little influence on the K_{ro} predictions. Figure 14 shows that S_o of the three networks grow and terminate at the same maximum S_o value of 86.7% with the increase of charging pressure. The required charging pressure reaching the maximum S_o decreases with the increasing CA under the limited water-wet condition.

5. Discussions

5.1. The Applicability and Limitations of the Developed PNM Model. Numerous models have been developed in the past decades to simulate the fluid flow processes in porous media. The forces set in these models mainly involve capillary pressure, viscous force, and gravity force. These network models simulating the two-phase flow system can be divided into two types: quasistatic model and dynamic model. The quasistatic model is suitable to simulate the fluid flow when the capillary pressure is dominating while the viscous force is negligible. When the nonnegligible viscous force is present; however, a dynamic model needs to be considered. When the capillary number is less than 10^4 , the simulations of the quasistatic model are believed to be accurate enough [19]. In conventional reservoir formations, oil migration can also be divided into two types: steady oil migration and episodic oil migration [60]. The oil flow under the steady oil migration mode is assumed to be governed by capillary pressure, and the flow in the episodic migration is governed by viscous pressure while the natural buoyancy plays a role in the fluid flow. However, for the low-permeability reservoir (e.g., tight reservoir and shale reservoir), whether both the steady oil migration and episodic oil migration can be identified to explain the flow phenomena in low-permeability media is still a question. A common consensus is that the effect of buoyancy on fluid flow can be neglected because of the extremely small size of pores in tight formations [61, 62]. Due to the same reason, the effect of capillary pressure becomes significantly important, which means the fluid flow in tight media is more likely to follow the steady migration mode. This is the reason why the quasistatic method is employed in our present work. However, some other scholars [63] also proposed that present day reservoirs may not represent the conditions of the reservoir during the time of hydrocarbon expulsion and migration, indicating that the viscous force may have been the main controlling factor, and buoyancy may have been an important force forming the hydrocarbon distribution in tight oil/gas migrates and accumulates.

Some other limitations of the PNM methods should be noticed here. (1) The fluid inside the networks is considered incompressible and immiscible. (2) The real pore-throat system of the rock is simplified as simple 3D geometric shapes following the pore-network generation rules. (3) The chemical interactions between the fluids and solid matrix are neglected. (4) The wettability conditions are set as constantly distributed, which may not exactly match the real condition in nature [64]. (5) The gravity forces and influence of microfracture in the pore-throat system are not considered in the developed model. For these limitations, the PNM model may not provide precise predictions for the actual geological conditions.

The permeability of the tested tight samples may be slightly larger than the permeability scope of tight sandstone by generally speaking. But the upper limit of tight media permeability is not standard. In some literature, tight oil is defined as oil resource reserved in very low permeability formation which cannot be produced at economic rates unless the formation is simulated by large hydraulic fracture

treatments or produced by the use of horizontal wellbores [65]. The main reason we select these two samples with larger permeability is that the forced displacement experiments are hard to implement when the permeability of the sample is smaller than 0.5 mD. For the same reason, a complete series of experiments using different samples cannot be completed. Furthermore, the BL theory is employed in this work to explain the non-Darcy flow phenomenon in tight media. This theory is merely one of the numerous non-Darcy theories. Some other theory such as threshold pressure gradient theory can be also used for explaining the non-Darcy flow [66]. It may be acceptable to use the BL theory under most conditions, although the range of application, prediction accuracy, and limiting conditions of this theory remains to be further investigated.

5.2. The Simulation Results and Their Significances. Based on the reservoir exploration and production experiences, previous literature has concluded that the migration of tight oil behaves differently from the conventional reservoirs (as described in the Introduction). Some of these behaviors could be explained using the obtained simulation results in this work. For example, the initial water saturation (S_{wi} , the measured water saturation before the well drilling) in tight reservoirs is reported to be much higher than that in the conventional reservoirs [63]. Seen from the simulation results in Sections 4.1 and 4.2, the S_{wi} increases dramatically with the decrease of pore size and pore connectivity. The calculated S_{wi} with the pore size of $0.1 \sim 1 \mu\text{m}$ (absolute permeability $K = 0.01 \text{ mD}$) is 20.8% and the calculated S_{wi} with the pore size of $0.1 \sim 5 \mu\text{m}$ (absolute permeability $K = 0.9 \text{ mD}$) is only 3.5%. Note that the low S_{wi} here does not mean most of water could be replaced by the injected oil during the oil migration process in the natural system, which is only an idealized calculation value under the ideal hypothesis conditions.

The influential mechanisms of several factors on relative permeability and oil saturation during the oil migration are analyzed as follows. The decrease of pore radius leads to the decreases of both oil and water relative permeability and the increase of BL thickness. This increase of BL thickness further results in a higher irreducible water saturation and a lower effective seepage radius. Thus, the two-phase seepage zone in the relative permeability curves decreases with the decreasing pore size; the maximum of oil saturation which corresponds to the irreducible water saturation in the oil saturation curves also shows a decreasing trend with the decrease of pore radius. Under the condition of the same pore radius distribution, the scope of two-phase seepage remains unchanged with the change of pore connectivity. However, the decrease of coordination number will reduce the seepage area of the media which leads to the decrease of relative permeability for oil and water. Besides, under the condition of poor connectivity, water phase is easy to stay in the corner of the networks. This phenomenon may cause relative permeability to move towards the high water saturation direction. The changes of connectivity of the pore systems may change the pore space volume and water/oil content by absolute values but show no influence on the irreducible water saturation. Therefore, the maximum of oil saturation would

keep constant at a high injection pressure. The differences between the relative permeability curves of Berea sample and tight samples (Figures 3 and 4) are mainly attributed to these aforementioned two factors. The impact of brine viscosity on oil migration is relatively simple. The thickness of the BL would increase with the increase of brine viscosity which causes the decrease of effective seepage radius for oil and water phases as well as the increase of irreducible water saturation. Meanwhile, a higher brine viscosity would directly reduce the permeability of water phase, which causes the decreasing trend of water relative permeability in Figure 11 to be much more obvious than that of oil with the increasing brine viscosity. Overall, the simulated five factors all show influence on the relative permeability and S_o , but with different sensitivities. Compared with aspect ratio and hydrophilia of the rock, the pore radius, pore connectivity, and brine viscosity play more important roles in controlling the oil migration behaviors.

The improved oil migration PNM provides a new solution for analyzing the effects of complex pore-scale characteristics on tight oil migration and accumulation. Combining the quantitative results obtained from models and traditional geological analysis methods may be more helpful for studying the mechanisms of tight oil reservoir formation and evolution.

6. Conclusions

To better understand and quantitatively analyze the relationship between the oil migration characteristics and pore structures in tight formations, a two-phase PNM with consideration of the BL effect is developed in this work. Several conclusions are drawn as follows:

- (1) This work proves that PNM method with consideration to the BL effect is applicable and effective for tight oil migration analyses, which shows better prediction accuracy than that without the BL effect
- (2) Five important factors including pore radius, coordination number, aspect ratio, brine viscosity, and wettability show influences on the tight oil migration, but sensitivities of these factors on oil migration are different
- (3) Based on the simulations, the influences of pore radius, coordination number, and brine viscosity on oil migration are more pronounced while the influences of aspect ratio and hydrophilia of the rock surface are relatively weak
- (4) With the decrease of pore radius, coordination number or the increase of brine viscosity in the oil-phase relative permeability is weakened, which induces less oil accumulation in the pore system

Data Availability

The experimental and simulation data used to support the findings of this study have been deposited in the Mendeley

repository (the download address is <https://data.mendeley.com/datasets/j3467gsr3k/1>). The data is also available on request.

Conflicts of Interest

The author(s) declare(s) that they have no conflicts of interest.

Acknowledgments

This work was financially supported by the National Natural Science Foundation of China (grants 41972147 and 41330319). Y. Zhang would show his sincere thanks to the Heriot-Watt University, UK, for hosting his academic visit during which the work reported here was carried out in part. Ma thanks UK NERC (grant NE/R018022/1) for financial support.

References



- [1] J. Boak and R. Kleinberg, "Shale gas, tight oil, shale oil and hydraulic fracturing," *Future Energy*, vol. 67-95, 2020.
- [2] J. D. Hughes, "a reality check on the shale revolution," *Nature*, vol. 494, no. 7437, pp. 307-308, 2013.
- [3] BP Energy, *BP Energy Outlook*, Energy, BP, 2018.
- [4] J. Cai and X. Hu, *Petrophysical Characterization and Fluids Transport in Unconventional Reservoirs*, Elsevier, 2019.
- [5] C. R. Clarkson and K. Pedersen, "Production analysis of Western Canadian unconventional light oil plays," in *Proceedings Canadian Unconventional Resources Conference*, Calgary, Alberta, Canada, November, 2011 Society of Petroleum Engineers.
- [6] P. H. Nelson, "Pore-throat sizes in sandstones, tight sandstones, and shales," *AAPG Bulletin*, vol. 93, no. 3, pp. 329-340, 2009.
- [7] T. T. Schowalter, "Mechanics of secondary hydrocarbon migration and entrapment," *AAPG Bulletin*, vol. 63, no. 5, pp. 723-760, 1979.
- [8] X. Luo, "Simulation and characterization of pathway heterogeneity of secondary hydrocarbon migration," *AAPG Bulletin*, vol. 95, no. 6, pp. 881-898, 2011.
- [9] P. Ungerer, J. Burrus, B. P. Y. C. Doligez, P. Y. Chenet, and F. Bessis, "Basin evaluation by integrated two-dimensional modeling of heat transfer, fluid flow, hydrocarbon generation, and migration," *AAPG Bulletin*, vol. 74, no. 3, pp. 309-335, 1990.
- [10] C. Zou, *Unconventional petroleum geology*, Elsevier, 2017.
- [11] J. Lai, G. Wang, Z. Fan et al., "Insight into the pore structure of tight sandstones using NMR and HPMI measurements," *Energy & Fuels*, vol. 30, no. 12, pp. 10200-10214, 2016.
- [12] J. Lai, G. Wang, Z. Wang et al., "A review on pore structure characterization in tight sandstones," *Earth Science Reviews*, vol. 177, pp. 436-457, 2018.
- [13] Q. Xiong, T. G. Baychev, and A. P. Jivkov, "Review of pore network modelling of porous media: experimental characterisations, network constructions and applications to reactive transport," *Journal of Contaminant Hydrology*, vol. 192, pp. 101-117, 2016.
- [14] Z. Cao, G. Liu, H. Zhan, Y. Kong, Z. Niu, and D. Zhao, "Geological control factors of micro oil distribution in tight reservoirs," *Marine and Petroleum Geology*, vol. 77, pp. 1193-1205, 2016.
- [15] Y. Zhang, J. Zeng, Z. Dai et al., "Experimental investigation on oil migration and accumulation in tight sandstones," *Journal of Petroleum Science Engineering*, vol. 160, pp. 267-275, 2018.
- [16] X. Feng, J. Zeng, S. Tao, J. Yang, S. Feng, and Z. Pang, "Oil-charging pore-throat radius threshold of tight reservoirs: a comparison on multi-method calculation results," *Journal of Nanoscience and Nanotechnology*, vol. 17, no. 9, pp. 6067-6076, 2017.
- [17] J. Qiao, J. Zeng, X. Feng, Z. Yang, Y. Zhang, and S. Feng, "Characteristics of nano-micro pore networks and petroleum microscopic occurrence state in ultra-low permeability (tight) sandstone reservoir," *Journal of Nanoscience and Nanotechnology*, vol. 17, no. 9, pp. 6039-6050, 2017.
- [18] J. Zeng, X. Feng, S. Feng, Y. Zhang, J. Qiao, and Z. Yang, "Influence of tight sandstone micro-nano pore-throat structures on petroleum accumulation: evidence from experimental simulation combining X-ray tomography," *Journal of Nanoscience and Nanotechnology*, vol. 17, no. 9, pp. 6459-6469, 2017.
- [19] M. J. Blunt, *Multiphase Flow in Permeable Media: A Pore-Scale Perspective*, Cambridge University Press, 2017.
- [20] J. Ma, X. Zhang, Z. Jiang, H. Ostadi, K. Jiang, and R. Chen, "Flow properties of an intact MPL from nano-tomography and pore network modeling," *Fuel*, vol. 136, pp. 307-315, 2014.
- [21] I. Fatt, "The network model of porous media: capillary pressure characteristics," *Transactions of the AIME*, vol. 207, no. 1, pp. 144-181, 2013.
- [22] F. A. L. Dullien, I. Chatzis, and M. S. El Sayed, "Modeling transport phenomena in porous media by networks consisting of non-uniform capillaries," in *Proceedings SPE Annual Fall Technical Conference and Exhibition*, New Orleans, Louisiana, October, 1976 Society of Petroleum Engineers.
- [23] M. J. Blunt, B. Bijeljic, H. Dong et al., "Pore-scale imaging and modelling," *Advances in Water Resources*, vol. 51, pp. 197-216, 2013.
- [24] J. Ma, J. P. Sanchez, K. Wu, G. D. Couples, and Z. Jiang, "A pore network model for simulating non-ideal gas flow in micro- and nano-porous materials," *Fuel*, vol. 116, pp. 498-508, 2014.
- [25] H. Sun, L. Duan, L. Liu et al., "The influence of micro-fractures on the flow in tight oil reservoirs based on pore-network models," *Energies*, vol. 12, no. 21, p. 4104, 2019.
- [26] D. Wang, C. Wang, C. Li et al., "Effect of gas hydrate formation and decomposition on flow properties of fine-grained quartz sand sediments using X-ray CT based pore network model simulation," *Fuel*, vol. 226, pp. 516-526, 2018.
- [27] V. Joekar-Niasar and S. M. Hassanizadeh, "Analysis of fundamentals of two-phase flow in porous media using dynamic pore-network models: a review," *Critical Reviews in Environmental Science and Technology*, vol. 42, no. 18, pp. 1895-1976, 2012.
- [28] L. Riepe, M. H. Suhaimi, M. Kumar, and M. A. Knackstedt, "Application of high resolution micro-CT-imaging and pore network modeling (PNM) for the petrophysical characterization of tight gas reservoirs-a case history from a deep clastic tight gas reservoir in Oman," in *Proceedings SPE Middle East Unconventional Gas Conference and Exhibition*, Muscat, Oman, 2011 Society of Petroleum Engineers.

- [29] L. Ruspini, G. Lindkvist, S. Bakke, L. Alberts, A. Carnerup, and P. E. Øren, "A multi-scale imaging and modeling workflow for tight rocks," in *Proceedings SPE Low Perm Symposium*, Denver, Colorado, USA, 2016 Society of Petroleum Engineers.
- [30] X. Wang and J. J. Sheng, "Pore network modeling of the non-Darcy flows in shale and tight formations," *SPE Journal*, vol. 163, pp. 511–518, 2018.
- [31] X. Wang and J. J. Sheng, "Spontaneous imbibition analysis in shale reservoirs based on pore network modeling," *Journal of Petroleum Science and Engineering*, vol. 169, pp. 663–672, 2018.
- [32] X. Wang and J. J. Sheng, "Effect of low-velocity non-Darcy flow on well production performance in shale and tight oil reservoirs," *Fuel*, vol. 190, pp. 41–46, 2017.
- [33] J. Cai, E. Perfect, C. L. Cheng, and X. Hu, "Generalized modeling of spontaneous imbibition based on Hagen-Poiseuille flow in tortuous capillaries with variably shaped apertures," *Langmuir*, vol. 30, no. 18, pp. 5142–5151, 2014.
- [34] Z. Zeng and R. Grigg, "A criterion for non-Darcy flow in porous media," *Transport in Porous Media*, vol. 63, no. 1, pp. 57–69, 2006.
- [35] Y. Huang, Z. Yang, Y. He, and X. Wang, "An overview on non-linear porous flow in low permeability porous Media," *Theoretical and Applied Mechanics Letters*, vol. 3, no. 2, article 022001, 2013.
- [36] B. Zeng, L. Cheng, and C. Li, "Low velocity non-linear flow in ultra-low permeability reservoir," *Journal of Petroleum Science and Engineering*, vol. 80, no. 1, pp. 1–6, 2011.
- [37] Y. Yang, K. Wang, Q. Lv et al., "Flow simulation considering adsorption boundary layer based on digital rock and finite element method," *Petroleum Science*, 2020.
- [38] M. Chen, L. Cheng, R. Cao, C. Lv, J. Wu, and H. Liu, "A pore network model for studying boundary layer effect on fluid flow in tight formation (Russian)," in *Proceedings SPE Annual Caspian Technical Conference and Exhibition*, Baku, Azerbaijan, November, 2017 Society of Petroleum Engineers.
- [39] X. Tian, L. Cheng, Y. Yan, H. Liu, W. Zhao, and Q. Guo, "An improved solution to estimate relative permeability in tight oil reservoirs," *Journal of Petroleum Exploration and Production Technology*, vol. 5, no. 3, pp. 305–314, 2015.
- [40] A. E. Bakyani, H. Sahebi, M. M. Ghiasi et al., "Prediction of CO₂-oil molecular diffusion using adaptive neuro-fuzzy inference system and particle swarm optimization technique," *Fuel*, vol. 181, pp. 178–187, 2016.
- [41] P. H. Valvatne and M. J. Blunt, "Predictive pore-scale modeling of two-phase flow in mixed wet media," *Water Resources Research*, vol. 40, no. 7, 2004.
- [42] P. E. Oren, S. Bakke, and O. J. Arntzen, "Extending predictive capabilities to network models," in *Proceedings SPE Annual Technical Conference and Exhibition*, San Antonio, Texas, October 1997 Society of Petroleum Engineers..
- [43] J.-C. Cai, "A fractal approach to low velocity non-Darcy flow in a low permeability porous medium," *Chinese Physics B*, vol. 23, no. 4, article 044701, 2014.
- [44] I. Bondino, S. R. McDougall, and G. Hamon, "Pore-scale Modelling of the effect of viscous pressure gradients during heavy oil depletion experiments," *Journal of Canadian Petroleum Technology*, vol. 50, no. 2, pp. 45–55, 2013.
- [45] J. Cruickshank, S. R. McDougall, and K. S. Sorbie, "Anchoring methodologies for pore-scale network models: application to relative permeability and capillary pressure prediction," *Petrophysics*, vol. 43, p. 04, 2002.
- [46] M. Regaieg, S. R. McDougall, I. Bondino, and G. Hamon, "Finger thickening during extra-heavy oil waterflooding: simulation and interpretation using pore-scale modeling," *PLoS One*, vol. 12, no. 1, article e0169727, 2017.
- [47] A. Boujelben, S. McDougall, M. Watson, I. Bondino, and N. Agenet, "Pore network modelling of low salinity water injection under unsteady-state flow conditions," *Journal of Petroleum Science and Engineering*, vol. 165, pp. 462–476, 2018.
- [48] J. Zeng, Y. Zhang, S. Zhang, J. Qiao, X. Feng, and S. Feng, "Experimental and theoretical characterization of the natural gas migration and accumulation mechanism in low-permeability (tight) sandstone cores," *Journal of Natural Gas Science Engineering*, vol. 33, pp. 1308–1315, 2016.
- [49] M. L. Rivers, "tomoRecon: high-speed tomography reconstruction on workstations using multi-threading," in *Developments in X-Ray Tomography VIII*, vol. 8506, International Society for Optics and Photonics, 2012, 85060U.
- [50] C. Lore, *User's Guide-Avizo 9.7*, 2018, <https://assets.thermofisher.com/TFS-Assets/MSD/Product-Guides/user-guide-avizo-software.pdf>.
- [51] H. Dong and M. J. Blunt, "Pore-network extraction from micro-computerized-tomography images," *Physical Review*, vol. 80, no. 2, article 036307, 2009.
- [52] M. J. Oak, "Three-phase relative permeability of water-wet Berea," in *Proceedings SPE/DOE Enhanced Oil Recovery Symposium*, Tulsa, Oklahoma, April 1990 Society of Petroleum Engineers.
- [53] H. Zhao, Z. Ning, Q. Wang et al., "Petrophysical characterization of tight oil reservoirs using pressure-controlled porosimetry combined with rate-controlled porosimetry," *Fuel*, vol. 154, pp. 233–242, 2015.
- [54] H. J. Vogel and K. Roth, "Quantitative morphology and network representation of soil pore structure," *Advances in Water Resources*, vol. 24, no. 3–4, pp. 233–242, 2001.
- [55] Y. Yang, Y. Li, J. Yao et al., "Formation damage evaluation of a sandstone reservoir via pore-scale X-ray computed tomography analysis," *Journal of Petroleum Science and Engineering*, vol. 183, p. 106356, 2019.
- [56] M. J. Blunt, "Pore level modeling of the effects of wettability," *SPE Journal*, vol. 2, no. 4, pp. 494–510, 1997.
- [57] S. Zou, R. T. Armstrong, J. Y. Arns, C. H. Arns, and F. Hussain, "Experimental and theoretical evidence for increased ganglion dynamics during fractional flow in mixed-wet porous media," *Water Resources Research*, vol. 54, no. 5, pp. 3277–3289, 2018.
- [58] J. S. Buckley, "Effective wettability of minerals exposed to crude oil," *Current Opinion in Colloid & Interface Science*, vol. 6, no. 3, pp. 191–196, 2001.
- [59] Y. Zhang, J. Zeng, J. Qiao, X. Feng, and Y. Dong, "Investigating the effect of the temperature and pressure on wettability in crude oil-brine-rock systems," *Energy & Fuels*, vol. 32, no. 9, pp. 9010–9019, 2018.
- [60] J. Zeng and Z. Jin, "Experimental investigation of episodic oil migration along fault systems," *Journal of Geochemical Exploration*, vol. 78–79, pp. 493–498, 2003.
- [61] L. Chen, X. Zhu, L. Wang, H. Yang, D. Wang, and M. Fu, "Experimental study of effective amphiphilic graphene oxide flooding for an ultralow-permeability reservoir," *Energy & Fuels*, vol. 32, no. 11, pp. 11269–11278, 2018.

- [62] J. Ma, K. Wu, Z. Jiang, and G. D. Couples, "SHIFT: An implementation for lattice Boltzmann simulation in low-porosity porous media," *Physical Review E*, vol. 81, no. 5, article 056702, 2010.
- [63] W. K. Camp, "Pore-throat sizes in sandstones, tight sandstones, and shales: discussion," *AAPG Bulletin*, vol. 95, no. 8, pp. 1443–1447, 2011.
- [64] Y. Liu, S. Iglauer, J. Cai, M. A. Amooie, and C. Qin, "Local instabilities during capillary-dominated immiscible displacement in porous media," *Capillarity*, vol. 2, no. 1, pp. 1–7, 2019.
- [65] S. Holditch, "Tight gas sands," *Journal of Petroleum Technology*, vol. 58, no. 6, pp. 86–93, 2006.
- [66] G. Han, Y. Liu, K. Nawnit, and Y. Zhou, "Discussion on seepage governing equations for low permeability reservoirs with a threshold pressure gradient," *Advances in Geo-Energy Research*, vol. 2, no. 3, pp. 245–259, 2018.

Research Article

Pore Structure Fractal Characterization and Permeability Simulation of Natural Gas Hydrate Reservoir Based on CT Images

Hang Bian,^{1,2} Yuxuan Xia,³ Cheng Lu ,^{1,2,4,5} Xuwen Qin ,^{1,2} Qingbang Meng,⁶ and Hongfeng Lu^{1,2}

¹Guangzhou Marine Geological Survey, China Geological Survey, Guangzhou 510075, China

²Southern Marine Science and Engineering Guangdong Laboratory, Guangzhou 511458, China

³Institute of Geophysics and Geomatics, China University of Geosciences, Wuhan 430074, China

⁴Center of Oil & Natural Gas Resource Exploration, China Geological Survey, Beijing 100083, China

⁵School of Energy Resources, China University of Geosciences, Beijing 100083, China

⁶Key Laboratory of Tectonics and Petroleum Resources, Ministry of Education, China University of Geosciences, Wuhan 430074, China

Correspondence should be addressed to Cheng Lu; jaluch@126.com and Xuwen Qin; cgs_qin@aliyun.com

Received 26 December 2019; Accepted 19 March 2020; Published 21 July 2020

Academic Editor: Wen-Dong Wang

Copyright © 2020 Hang Bian et al. This is an open access article distributed under the Creative Commons Attribution License, which permits unrestricted use, distribution, and reproduction in any medium, provided the original work is properly cited.

The gas-water two-phase seepage process is complex during the depressurization process of natural gas hydrate in a clayey silt reservoir in the South China Sea, the transport mechanism of which has not been clarified as it is affected by the pore structure. In this study, we select six clayey silt samples formed after the dissociation of natural gas hydrate in the South China Sea, employing CT scanning technology to observe the pore structure of clayey silt porous media directly. The original CT scanning images are further processed to get the binarized images of the samples, which can be used for simulation of the porosity and absolute permeability. Based on the fractal geometry theory, pore structures of the samples are quantitatively characterized from the aspect of pore distribution, heterogeneity, and anisotropy (represented by three main fractal geometric parameters: fractal dimension, lacunarity, and succolarity, respectively). As a comparison, the binarized CT images of two conventional sandstone cores are simulated with the same parameters. The results show that the correlation between porosity and permeability of the hydrate samples is poor, while there is a strong correlation among the succolarity and the permeability. Fractal dimension (represents complexity) of clayey silt samples is higher compared with conventional sandstone cores. Lacunarity explains the difference in permeability among samples from the perspective of pore throat diameter and connectivity. Succolarity indicates the extent to which the fluid in the pore is permeable, which can be used to characterize the anisotropy of pore structures. Therefore, these three fractal parameters clarify the relationship between the microstructure and macroscopic physical properties of clayey silt porous media.

1. Introduction

Natural gas hydrate refers to one kind of ice-like crystalline compound formed by a methane-based hydrocarbon gas and water in a stable domain controlled by a certain temperature and pressure condition [1]. In the field of exploration and development of the natural gas hydrate, especially in hydrate classification, extraction, dissociation, experimental simulation, productivity evaluation method, etc., the work has become a research hotspot pursued by scientific research

institutions, experts, and scholars [2–8]. The first offshore natural gas hydrate production test was conducted by China Geological Survey at Shenhu Area in South China Sea in 2017 [9]. During the depressurization process of production, the solid hydrate is decomposed into methane gas and water. The two-phase flow passes through the formation and then flows into the wellbore. In the initial stage, the flow rate is stable. However, as production progresses, the flow rate is going to be greatly reduced, resulting in a significant decrease in production. The above-mentioned multiphase flow within

pore space is extremely complicated, and its seepage mechanism is not yet clear. It is speculated to be related to pore structure and mineral composition of the hydrate reservoir.

The differences of porosity, connectivity, and topology of pore space always determine the macroscopic seepage properties [10, 11]. The pore space of the reservoir core can be obtained by multi-laboratory test methods [12–15]. The obtained pore space images and parameters can also lay the foundation for calculation of permeability [16–18]. Many numerical simulation methods [19–21] were used to obtain permeability of the reservoir, which greatly promotes understanding of the relationship between reservoir porosity and permeability, and the formulation of reservoir development programs.

Fractal geometry theory, as the powerful tool for quantification of complex space, has been used by many scholars in the study of characterization of the pore structure and modelling of transport phenomena in conventional and unconventional reservoirs. Yu and Cheng [22] established the fractal permeability model for the bidispersed porous media and introduced the algorithm of pore space fractal dimension and tortuosity fractal dimension based on the box-counting method. Cai et al. [23] established a fractal permeability model for creeping microstructures under different pressure conditions based on the data of water flooding experiment combined with CT scanning [24] for clayey silt sediments. Liu et al. [25] used fractal dimensions to establish a fractal theory-based relative permeability model of hydrate-bearing sediments. N'Diaye et al. [26] computed fractal dimension, lacunarity, and succolarity to provide a precise description of porosity and pore characteristics. Xia et al. [27] proposed that succolarity can be used to predict the permeability of low permeable sandstone reservoirs. Therefore, fractal geometry theory has been proved to be a good method to characterize the reservoir microstructure and to study the macroscopic differences in physical properties of reservoirs. In the study of clayey silt porous media, the macroscopic changes of reservoir physical properties can also be explained from the perspective of microstructure based on fractal geometry theory. However, few studies have used fractal quantitative parameters to characterize the microporous structure of clayey silt porous media and further used to study the change of permeability.

In this study, pore structure images of six hydrate reservoir samples were firstly acquired by micro-CT scanning. Then, the porosity, permeability, and fractal parameters were obtained based on the binarized pore images. Finally, how microporous structures affect the permeability of clayey silt reservoir samples was analyzed according to the relationship between permeability and pore structure parameters.

2. Materials and Facility

2.1. Hydrate Reservoir Samples. Six clayey silt samples are taken from the field of the first offshore natural gas hydrate production test, which is located at Shenhu Area in the South China Sea [9]. There are eight natural gas hydrate deposits, among which the W11-17 deposit (Figure 1) is selected as the optimal target for the production test. The lithology of

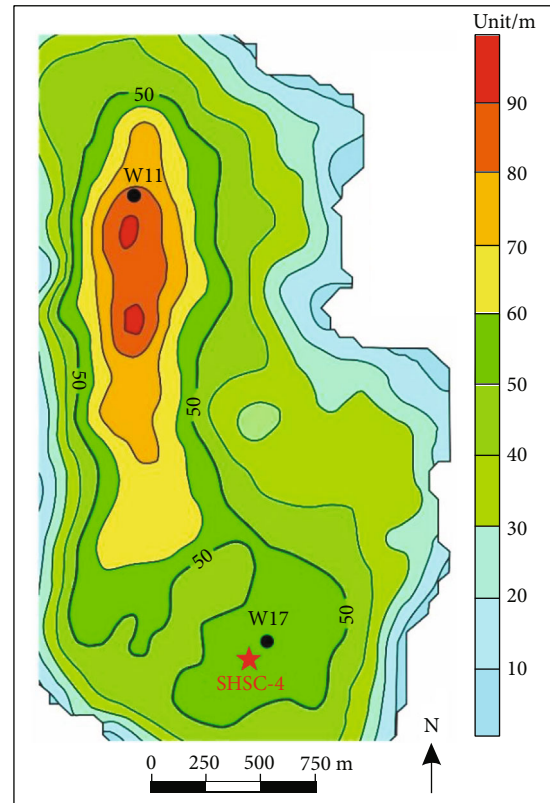


FIGURE 1: The deposit of W11-17 of the natural gas hydrate reservoir in Shenhu Area.

the reservoir is clayey silt, of which the clay mineral content is high (26%-30%), mainly composed of montmorillonite and illite. The average median diameter of the sample particle is $12\ \mu\text{m}$. The average values of effective porosity and hydrate saturation are 33% and 31%, respectively. Pore space of the reservoir is filled with three phases: solid hydrate, free gas, and water. Detailed geological, ore body, seismic, and logging information of reservoir can be found in literature [9].

2.2. CT (Computed Tomography) Scanner. Six clayey silt samples taken from the hydrate reservoir are subjected to CT scanning by a MicroSCT-200 micron CT scanner. The scanning voltage and power are 95 kV and 10 W, respectively. The scanning mode is focused scanning, and all clayey silt samples are 5 mm in diameter and 5 mm in length, so the pixel number and pixel resolution for CT images of all clayey silt samples are $2000 \times 2000 \times 1500$ and $\sim 1\ \mu\text{m}$, separately.

3. Methods

After the original CT scanning images obtained, a series of preprocessing including extraction, filtering, and binarization [28] is conducted to acquire the binarized pore space structure images. Based on the binarized images, a variety of data such as sample porosity, permeability, and fractal structural parameters can be acquired and then can be used

to construct a relational model between pore structure and physical properties.

3.1. Porosity Calculation. Porosity ϕ refers to the ratio of the pore volume to the total volume of the rock. It is an important parameter to quantitatively describe the rock reservoir capacity. The expression is shown below:

$$\phi = \frac{V_p}{V_b} = \frac{V_p}{V_p + V_s}, \quad (1)$$

where V_p is the pore volume, V_b is the total volume of the rock, and V_s is the total volume of the skeleton.

In microscopic sample images, the pore volume and the rock skeleton volume correspond to the pixel volume of different color regions. Since the size represented by each pixel is uniform in all images of the same resolution, Equation (1) can be transformed to

$$\phi = \frac{N_p}{N_b} = \frac{N_p}{N_p + N_s}, \quad (2)$$

where N_p is the number of pore pixels, N_b is the total number of pixels of the sample image, and N_s is the number of sample skeleton pixels. The resulting binarized image is converted into an array matrix as displayed in Figure 2(b), and the sample image is represented by the pixel value of each pixel in the image. A sample image of a cube corresponds to a three-dimensional array matrix. By counting the number “0” and “1” in the matrix, the number of pore pixels and rock skeleton pixels can be obtained, respectively.

3.2. Fractal Structural Parameters Calculation. In the fractal geometry theory, fractal dimension, lacunarity, and succolarity are the main parameters of fractal analysis. Fractal dimension is used as the basic parameter of fractal quantitative characterization. Among plentiful research results, the box-counting method is a widely used and accurate method by which the fractal dimension of pore distribution can be obtained based on the structural images of the tested sample. In this study, all fractal dimensions are calculated based on the box-counting method as well. In the box-counting method, the image is covered by boxes with scale r , and the number of the boxes N covered with the pores is recorded. The expression is as follows:

$$N = r^{-D}. \quad (3)$$

Therefore, the negative value of the slope of the linear fit for the box-number and scale of double logarithmic plots in the self-similar interval is the pore space fractal dimension D .

Lacunarity analysis is a popular analytical tool of fractal microstructure in recent years. It can quantitatively analyze the degree of fractal clustering and characterize the changes of natural images and can consequently distinguish different structures with the same fractal dimension. Lacunarity characterizes the distribution of the observed objects in the image and measures the frequency and magnitude of observed

objects. The larger the lacunarity, the more intensive the distribution of the observed object.

The gliding box-counting method is a general measurement method of lacunarity. The value of lacunarity can be defined as a statistical moment function when $q = 2$ divided by the squared value of $q = 1$ [29, 30]:

$$\Lambda(r) = \frac{Z_Q^{(2)}(r)}{\left[Z_Q^{(1)}(r)\right]^2}, \quad (4)$$

$$\Lambda^*(r) = \frac{\Lambda(r) - \Lambda_{\min}}{\Lambda_{\max} - \Lambda_{\min}} = \phi \frac{\Lambda(r) - 1}{1 - \phi}. \quad (5)$$

Equation (5) is used to normalize lacunarity, which can exclude the influence of porosity.

Succolarity is one of the crucial parameters of fractal geometry, which indicates the ability of fluid flowing inside the medium, that is, the extent to which the fluid in the pore is permeable or flowing. It can be used to measure the connectivity of the patterns or structures in different directions.

The algorithm of succolarity is also based on the box-counting method, which evaluates the fluid flow ability in different flow directions by applying a virtual pressure field. The value of succolarity can be characterized as the pressure coverage value divided by the maximum possible coverage value [31]:

$$\text{Su}(\text{BS}(k), \text{dir}) = \frac{\sum_{k=1}^n \text{OP}(\text{BS}(k)) \times \text{PR}(\text{BS}(k), \text{pc})}{\sum_{k=1}^n \text{OP}(\text{BS}(k)) \times \max \text{PR}(\text{BS}(k), \text{pc})}. \quad (6)$$

3.3. Permeability Calculation. In order to study the relationship between complex microstructure and macroscopic seepage property of the gas hydrate reservoir, we selected the absolute permeability, which is associated with the sample structure, as the research object. Absolute permeability k of the rock core is the permeability measured when only one fluid (single phase) flows through the pores of the rock, the fluid does not react with the rock, and the flow of fluid is based on Darcy’s law of linear percolation. When a single-phase fluid with viscosity μ flows through a porous medium whose cross-section is A , length is L , and pressure difference is ΔP , the amount of fluid Q flowing through the rock pores within a unit time is

$$Q = \frac{Ak\Delta P}{\mu L}. \quad (7)$$

Based on Equation (7), the absolute permeability of the six samples was simulated using the finite volume method (FVM) [32]. Avizo® 9 software is employed to convert the six binary graphic models into FVM models for the absolute permeability simulation. Simulation work is done with the Avizo XLab Hydro Extension module which assumes that the fluid was laminar and the viscosity was 0.001 Pa·s. The velocity-pressure coupling solver is used, and the absolute convergence factor is 1×10^{-4} . The fluid flow governing

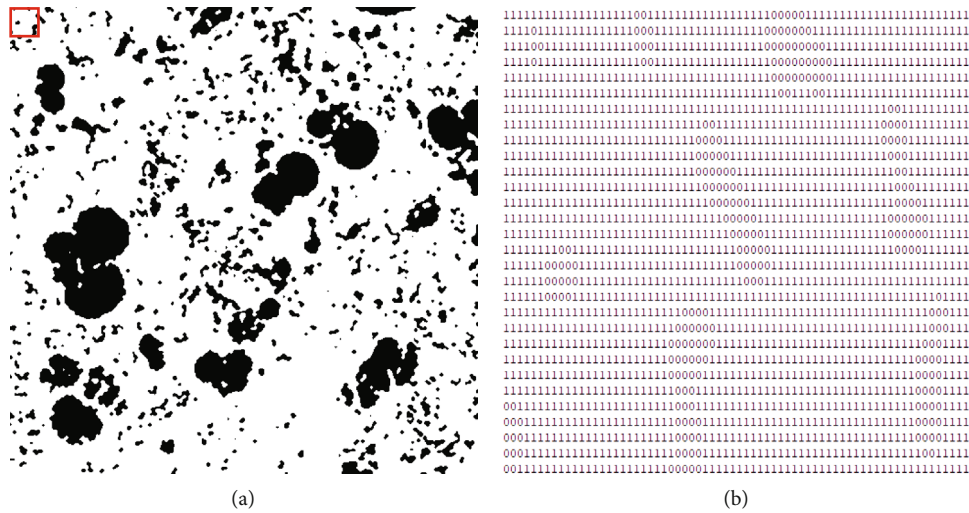


FIGURE 2: (a) Binarized image; (b) numerical image of the portion inside the red line.

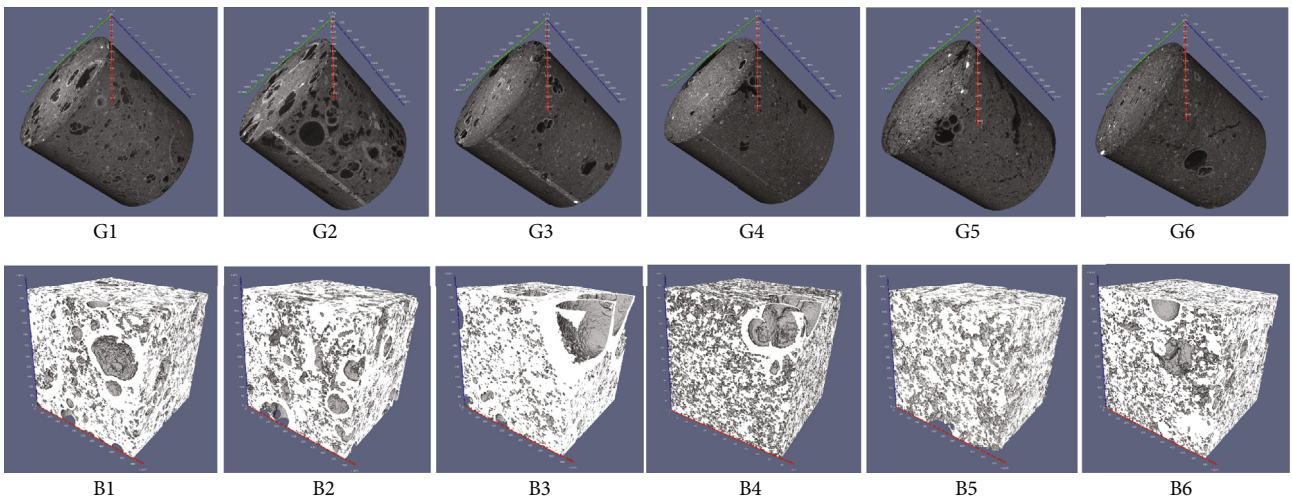


FIGURE 3: Original grayscale images (G) and binarized images (B, 512^3 pixels) of six hydrate reservoir samples. In the binarized images, the gray portion indicates the pores, and the white part indicates the solid.

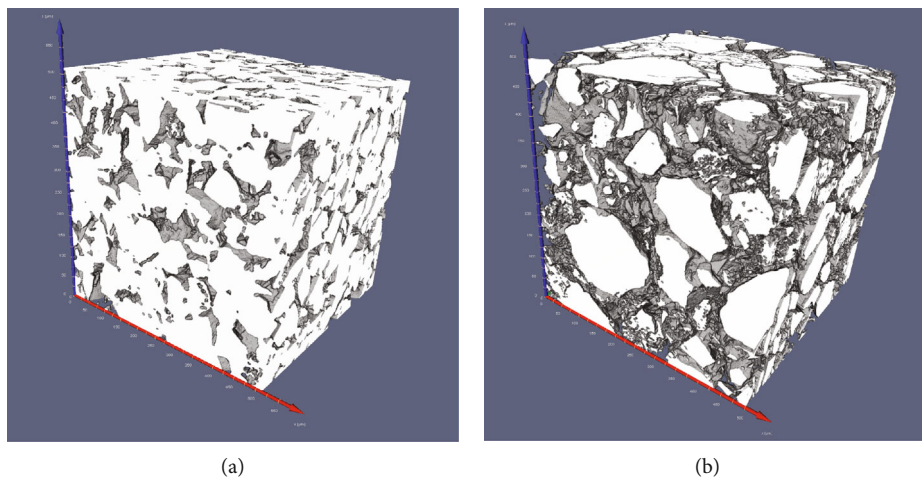


FIGURE 4: The three-dimensional images of conventional sandstone reservoir cores (Cores a and b) used for comparison. The gray portion indicates the pores, and the white part indicates the solid.

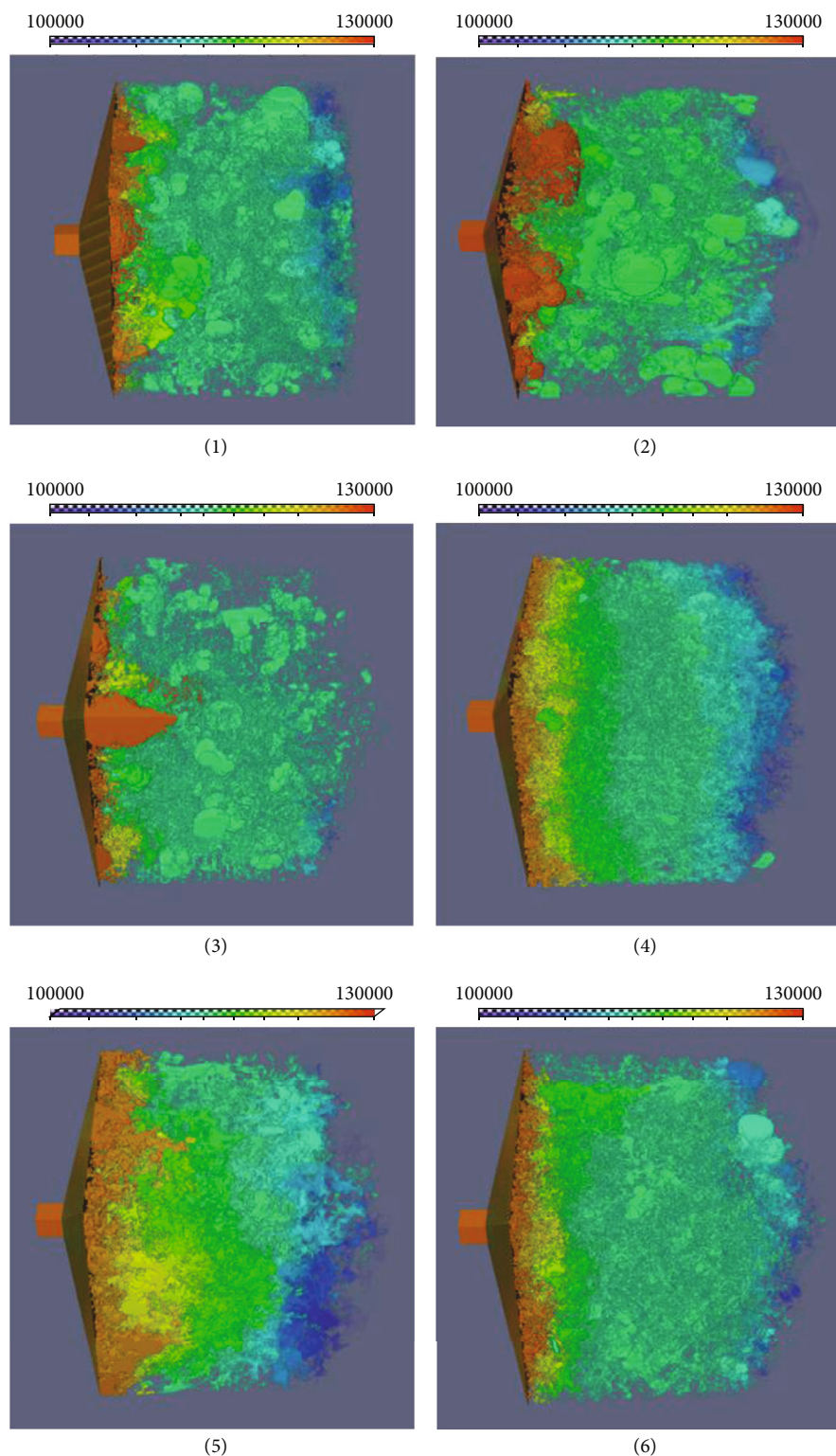


FIGURE 5: The pressure field (Pa) distributed on y direction of the permeability simulation of the six hydrate samples.

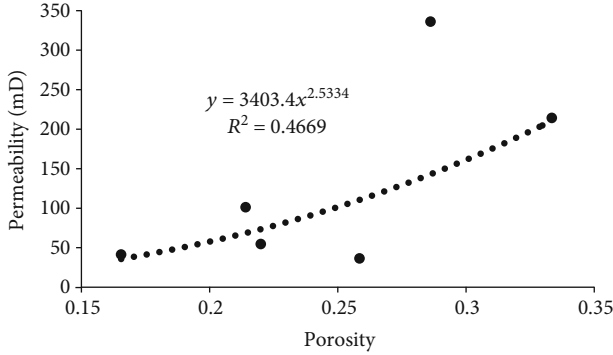
equation is the Navier-Stokes (N-S) equation with the pressure gradient along the direction of calculated permeability. Fluid circulates only in the core, and the core boundary is non-circulating. After completion of the iterations, the flow at the outlet can be obtained. Then, the permeability of each rock sample can be calculated by Darcy's law.

4. Results and Discussion

Figure 3 (G1-G6) shows original grayscale images of the six samples. The pores of the hydrate reservoir samples in Shenhu Area possess ring-like boundaries, which are derived from microorganisms such as diatoms. After a series of

TABLE 1: Calculated physical properties of hydrate samples and sandstone cores on three directions.

Physical properties	Samples							
	1	2	3	4	5	6	Core a	Core b
Porosity	0.22	0.26	0.17	0.33	0.29	0.21	0.18	0.39
Permeability (mD)								
x	—	51.09	36.84	260.81	130.45	94.62	196.53	1497.73
y	54.65	36.40	41.35	214.13	336.14	101.18	118.68	1433.94
z	23.67	18.48	—	200.55	278.47	—	175.53	1496.86

FIGURE 6: Fitting schematic diagram of porosity and permeability of six hydrate samples (permeability is taken on y direction).

preprocessing procedures conducted, the binarized pore structure images of the six samples are obtained, which are expressed in Figure 3 (B1-B6).

In order to better illustrate the special physical properties of hydrate reservoir samples, we selected two conventional sandstone cores for comparison. The pixel number and pixel resolution for CT images of sandstone cores shown in Figure 4 are 512^3 and $\sim 1 \mu\text{m}$. According to Figures 3 and 4, unlike the irregular intergranular pores of conventional sandstone reservoirs, the pore morphology of the hydrate reservoir mostly turns out to be spherical and uniform in the image. The reason is that the hydrate reservoirs are mainly composed of fine silt particles with good sorting, so that the intergranular pores are consequently regular. In addition, the hydrate reservoir is greatly affected by microbial processes during diagenesis, which leads to the existence of spheroidal bioclastics and interdental pores.

4.1. Porosity and Permeability. After the binarized images shown in Figures 3 and 4 obtained, porosity and permeability can be calculated based on these images. Figure 5 illustrates the pressure field distributed on y direction of permeability simulation of the six hydrate samples. Table 1 shows the porosity and absolute permeability of hydrate Samples 1-6 and conventional sandstone Cores a and b. The ranges of porosity and absolute permeability of eight samples and cores are 0.17~0.39 and 18.48~1497.73 mD, respectively. The simulation results on Core 1 x , Core 3 z , and Core 6 z express that the pressure field and the velocity field are opposite in direction, which results in the inability to calculate the permeability. And the cause of this condition is presumed to be the absence of connected pores on these directions.

According to the data in Table 1, the hydrate sample exhibits higher porosity and lower permeability compared with the conventional sandstone core, and the porosity and permeability are poorly correlated (as shown in Figure 6, the correlation coefficient is only 0.4669). That is, the porosity of Sample 1, 2, and 3 is 0.22, 0.26, and 0.17, respectively, but the absolute permeability is much smaller than that of sandstone Core a, whose porosity is 0.18. The porosity of hydrate Sample 4 and Sample 5 has reached a high level at about 0.3, but the permeability is only an average of 200 mD. When the porosity of conventional sandstone Core b is greater than 0.3, the permeability can reach more than 1000 mD. As for Sample 6, although the porosity is also approximately 0.2, its permeability is more than twice of that of Sample 1, 2, and 3. In summary, the permeability of the hydrate sample is lower than that of the conventional sandstone core and the distribution is complex, having poor correlation with the porosity. It is necessary to carry out further analysis for the microscopic pore structure of the sample by using fractal theory to find out the seepage mechanism.

4.2. Fractal Dimension and Permeability. The 3D fractal dimensions of hydrate samples and sandstone cores are calculated by the box-counting method based on Equation (3). The range of 3D fractal dimension of eight samples and cores is 2.70~2.85. The fractal dimension characterizes a complex feature of the overall pore distribution, which is generally affected by many factors, especially porosity. The larger the porosity, the larger the fractal dimension, and the more complex the pore space distribution develops. From this perspective, in the case of low porosity, hydrate samples exhibit a high fractal dimension compared with conventional sandstone cores (Samples 1, 2, 3, and 6 > Core a and Sample 4 > Core b), which proves that the distribution of pore space of the hydrate sample is more complicated than that of the conventional sandstone cores (Table 2).

4.3. Lacunarity and Permeability. In order to observe lacunarity (heterogeneity) of different samples and cores more intuitively, medians of the normalized values at different scales are listed in Table 3. The range of lacunarity midvalue of eight samples and cores is 0.168~0.447. Among the hydrate samples with smaller porosity, it can be seen that though the porosities of Sample 1, 2, 3, and 6 are similar, permeability of Sample 6 is almost double of that of Sample 1, 2, and 3. The results indicate that with the heterogeneity of sample increases, the permeability decreases. The reason is that when porosity is small, permeability of the hydrate

TABLE 2: Calculated 3D fractal dimensions of six hydrate samples and two sandstone cores.

Parameter	Samples						Core a	Core b
	1	2	3	4	5	6		
Fractal dimension	2.77	2.79	2.71	2.85	2.81	2.78	2.70	2.85

TABLE 3: Midvalue of 3D lacunarity of six hydrate samples and two sandstone cores under different-scale normalizations.

Parameter	Samples						Core a	Core b
	1	2	3	4	5	6		
Lacunarity midvalue	0.348	0.447	0.443	0.168	0.293	0.204	0.409	0.401

TABLE 4: Calculated 3D succolarity value of six hydrate samples on different directions.

Direction	Succolarity					
	Sample 1	Sample 2	Sample 3	Sample 4	Sample 5	Sample 6
x-positive	0.0924	0.1335	0.0296	0.3293	0.2754	0.1710
x-negative	0.0917	0.1685	0.0149	0.3009	0.2366	0.1585
y-positive	0.1051	0.1498	0.0439	0.3149	0.2635	0.1405
y-negative	0.0902	0.1566	0.0432	0.3218	0.2568	0.1830
z-positive	0.0949	0.1595	0.0024	0.3312	0.2486	0.1603
z-negative	0.0897	0.1784	0.0385	0.2962	0.2692	0.1683

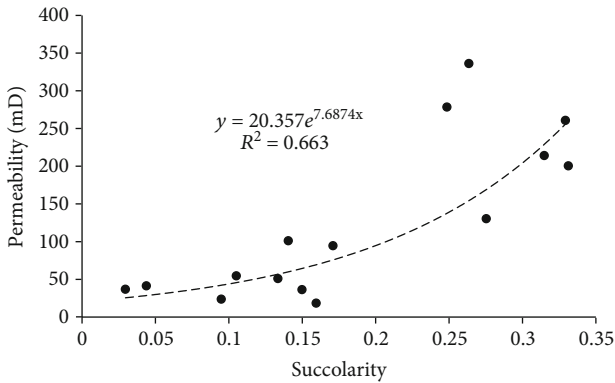


FIGURE 7: The fitting curve of succolarity and permeability for six hydrate samples on different positive directions.

sample with uniform pore distribution depends on the connectivity of pore throats. That is, the stronger the pore distribution heterogeneity of the hydrate sample, the worse the connectivity of the pore throats, and the smaller the permeability in consequence. Therefore, for a hydrate sample with a small porosity, the smaller the calculated lacunarity (the weaker the heterogeneity), the easier it is to exhibit a larger permeability. That is, the stronger the pore distribution heterogeneity of the hydrate sample, the worse the pore throat connectivity, and the smaller the permeability consequently. Therefore, for a hydrate sample with small porosity, the smaller the calculated lacunarity (the weaker the heterogeneity), the more likely it is to possess higher permeability.

On the other hand, hydrate samples with larger porosity and sandstone cores show that the stronger the heterogeneity, the higher the permeability. Namely, Core a is more heterogeneous in the case of possessing smaller porosity, and its

permeability is basically not lower than Samples 4 and 5; Sample 5 has a lower porosity than Sample 4, but it is highly heterogeneous, and the permeabilities in two directions are greater than Sample 4. The reason is that in the hydrate samples with larger porosity and sandstone cores, the distribution of pore space has already formed pore throats for fluid flow. Currently, the greater the heterogeneity of the pore distribution, the larger the diameter of the pore throats, which consequently leads to the higher permeability. Therefore, in hydrate samples with large porosity and all sandstone cores, the larger the calculated lacunarity (the stronger the heterogeneity), the greater the permeability.

4.4. *Succolarity and Permeability.* Table 4 shows the calculated value of the 3D succolarity on six directions of six hydrate samples. The range of the results is 0.0024~0.3312. It can be seen that, except for Sample 3, hydrate samples have little difference in succolarity values on all directions. Since succolarity can characterize the physical significance of the anisotropic characteristics of core pore structure distribution, the hydrate sample pore structure has no obvious anisotropic characteristics. For Sample 3, the extremely small succolarity value on z direction also indicates that there is no connected pores in this direction, which explains why the permeability cannot be calculated.

Figure 7 is a schematic diagram showing the fitting of succolarity and permeability on different positive directions of six hydrate samples (except Sample 1 x, Sample 3 z, and Sample 6 z, on which direction the permeability cannot be calculated). It can be seen that, succolarity values of the hydrate samples show a good correlation with the permeabilities (correlation coefficient is 0.663). The cause of the incomplete fitting is that the pore radius of Sample 5 is larger (Figure 5), which results in a higher permeability, however

the effect of pore radius has not been considered by succolarity. Even so, compared with porosity, succolarity can be used to fit the permeability and establish a prediction model, which gives a certain theoretical guidance to the changing rule of hydrate reservoir permeability.

5. Conclusions

In this study, six natural gas hydrate samples are conducted with CT scanning to get the pore structure, which are used to calculate the porosity, permeability, and fractal parameters. The results show that the fractal parameter can quantitatively characterize the pore structure and analyze the change of permeability of the hydrate reservoir. The following conclusions can be derived:

- (a) Compared with the conventional sandstone cores, the hydrate samples show higher porosity and lower permeability, and the correlation between porosity and permeability is poor
- (b) From the comparison results of the fractal dimension, hydrate samples possess higher fractal dimension than conventional sandstone cores and the structural development is more complicated
- (c) From the results of lacunarity calculation, it turns out that for hydrate samples with smaller porosity, with the lacunarity of pore distribution (the weaker the heterogeneity) decreases, the permeability increases; for the hydrate samples with larger porosity and sandstone cores, with the lacunarity of pore distribution (the stronger the heterogeneity) increases, the permeability increases
- (d) According to calculation results of succolarity, hydrate samples basically show nonanisotropic development characteristics. It is clear that the correlation between the succolarity value and the permeability value is high. Therefore, a predictive model of permeability can be built to provide theoretical support for hydrate reservoir development

Data Availability

The data used to support the findings of this study are available from the corresponding author upon request.

Conflicts of Interest

The authors declare that they have no conflicts of interest.

Acknowledgments

This research was funded by the National Natural Science Foundation of China (No. 51991365), China Geological Survey Project (No. DD20190232), Key Special Project for Introduced Talents Team of Southern Marine Science and Engineering Guangdong Laboratory (Guangzhou) (GML2019ZD0105), and Key Program of Marine Economy Development (Six

Marine Industries) Special Foundation of Department of Natural Resources of Guangdong Province [2020]047.

References

- [1] E. D. Sloan Jr., "Fundamental principles and applications of natural gas hydrates," *Nature*, vol. 426, no. 6964, pp. 353–359, 2003.
- [2] J. Cai, Y. Xia, S. Xu, and H. Tian, "Advances in multiphase seepage characteristics of natural gas hydrate sediments," *Chinese Journal of Theoretical and Applied Mechanics*, vol. 52, pp. 208–223, 2020.
- [3] S. Fan, C. Yu, X. Lang, Y. Wang, and J. Chen, "Micro-nano-scale studies on occurrence and gas production and storage technology of marine gas hydrates," *Earth Science*, vol. 43, pp. 1542–1548, 2018.
- [4] X. Ge, J. Liu, Y. Fan, D. Xing, S. Deng, and J. Cai, "Laboratory investigation into the formation and dissociation process of gas hydrate by low-field NMR technique," *Journal of Geophysical Research: Solid Earth*, vol. 123, no. 5, pp. 3339–3346, 2018.
- [5] M. R. Islam, "A new recovery technique for gas production from Alaskan gas hydrates," *Journal of Petroleum Science and Engineering*, vol. 11, no. 4, pp. 267–281, 1994.
- [6] K. A. Kvenvolden, "Gas hydrates—geological perspective and global change," *Reviews of Geophysics*, vol. 31, no. 2, pp. 173–187, 1993.
- [7] X. Liu, H. Liu, L. Xing, Y. Yin, and J. Wang, "Seismic low-frequency shadow beneath gas hydrate in the Shenhu area based on the stereoscopic observation system," *Journal of Earth Science*, vol. 29, no. 3, pp. 669–678, 2018.
- [8] L. Zhang, C. Zhang, K. Zhang et al., "Pore-scale investigation of methane hydrate dissociation using the lattice Boltzmann method," *Water Resources Research*, vol. 55, no. 11, pp. 8422–8444, 2019.
- [9] J. Li, J. L. Ye, X. W. Qin et al., "The first offshore natural gas hydrate production test in South China Sea," *China Geology*, vol. 1, no. 1, pp. 5–16, 2018.
- [10] J. Cai, E. Perfect, C. L. Cheng, and X. Hu, "Generalized modeling of spontaneous imbibition based on Hagen-Poiseuille flow in tortuous capillaries with variably shaped apertures," *Langmuir*, vol. 30, no. 18, pp. 5142–5151, 2014.
- [11] J. Qiao, J. Zeng, S. Jiang, and Y. Wang, "Impacts of sedimentology and diagenesis on pore structure and reservoir quality in tight oil sandstone reservoirs: implications for macroscopic and microscopic heterogeneities," *Marine and Petroleum Geology*, vol. 111, pp. 279–300, 2020.
- [12] B. Hazra, D. A. Wood, V. Vishal, A. K. Varma, D. Sakha, and A. K. Singh, "Porosity controls and fractal disposition of organic-rich Permian shales using low-pressure adsorption techniques," *Fuel*, vol. 220, pp. 837–848, 2018.
- [13] Y. Yao and D. Liu, "Comparison of low-field NMR and mercury intrusion porosimetry in characterizing pore size distributions of coals," *Fuel*, vol. 95, pp. 152–158, 2012.
- [14] X. Zhao, M. J. Blunt, and J. Yao, "Pore-scale modeling: effects of wettability on waterflood oil recovery," *Journal of Petroleum Science and Engineering*, vol. 71, no. 3–4, pp. 169–178, 2010.
- [15] C. Zou, D. Dong, S. Wang et al., "Geological characteristics and resource potential of shale gas in China," *Petroleum Exploration and Development*, vol. 37, no. 6, pp. 641–653, 2010.

- [16] P. C. Carman, "Fluid flow through granular beds," *Transactions Institute of Chemical Engineers*, vol. 15, pp. 150–167, 1997.
- [17] P. C. Carman, "The determination of the specific surfaces of powders I," *Journal of the Society of the Chemical Industrialists*, vol. 57, pp. 225–234, 1938.
- [18] H. A. Nooruddin and M. E. Hossain, "Modified Kozeny–Carmen correlation for enhanced hydraulic flow unit characterization," *Journal of Petroleum Science and Engineering*, vol. 80, no. 1, pp. 107–115, 2011.
- [19] M. J. Blunt, B. Bijeljic, H. Dong et al., "Pore-scale imaging and modelling," *Advances in Water Resources*, vol. 51, pp. 197–216, 2013.
- [20] C. Manwart, U. Aaltosalmi, A. Koponen, R. Hilfer, and J. Timonen, "Lattice-Boltzmann and finite-difference simulations for the permeability for three-dimensional porous media," *Physical Review E*, vol. 66, no. 1, pp. 16702–16713, 2002.
- [21] L. Zhang, W. Jing, Y. Yang et al., "The investigation of permeability calculation using digital core simulation technology," *Energies*, vol. 12, no. 17, article 3273, 2019.
- [22] B. Yu and P. Cheng, "A fractal permeability model for bi-dispersed porous media," *International Journal of Heat and Mass Transfer*, vol. 45, no. 14, pp. 2983–2993, 2002.
- [23] J. Cai, Y. Xia, C. Lu, H. Bian, and S. Zou, "Creeping micro-structure and fractal permeability model of natural gas hydrate reservoir," *Marine and Petroleum Geology*, vol. 115, article 104282, 2020.
- [24] C. Lu, Y. Xia, X. Sun et al., "Permeability evolution at various pressure gradients in natural gas hydrate reservoir at the Shenhu area in the South China Sea," *Energies*, vol. 12, no. 19, article 3688, 2019.
- [25] L. Liu, S. Dai, F. Ning, J. Cai, C. Liu, and N. Wu, "Fractal characteristics of unsaturated sands – implications to relative permeability in hydrate-bearing sediments," *Journal of Natural Gas Science and Engineering*, vol. 66, pp. 11–17, 2019.
- [26] M. N'Diaye, C. Degeratu, J. M. Bouler, and D. Chappard, "Biomaterial porosity determined by fractal dimensions, succolarity and lacunarity on microcomputed tomographic images," *Materials Science and Engineering: C*, vol. 33, no. 4, pp. 2025–2030, 2013.
- [27] Y. Xia, J. Cai, E. Perfect, W. Wei, Q. Zhang, and Q. Meng, "Fractal dimension, lacunarity and succolarity analyses on CT images of reservoir rocks for permeability prediction," *Journal of Hydrology*, vol. 579, article 124198, 2019.
- [28] H. Dong and M. J. Blunt, "Pore-network extraction from micro-computerized-tomography images," *Physical Review E*, vol. 80, no. 3, article 036307, 2009.
- [29] C. Allain and M. Cloitre, "Characterizing the lacunarity of random and deterministic fractal sets," *Physical Review A*, vol. 44, no. 6, pp. 3552–3558, 1991.
- [30] A. Roy, E. Perfect, W. M. Dunne, N. Odling, and J.-W. Kim, "Lacunarity analysis of fracture networks: evidence for scale-dependent clustering," *Journal of Structural Geology*, vol. 32, no. 10, pp. 1444–1449, 2010.
- [31] R. H. C. de Melo and A. Conci, "How succolarity could be used as another fractal measure in image analysis," *Telecommunication Systems*, vol. 52, no. 3, pp. 1643–1655, 2013.
- [32] N. Ahmad, J. Rappaz, J.-L. Desbiolles et al., "Numerical simulation of macrosegregation: a comparison between finite volume method and finite element method predictions and a confrontation with experiments," *Metallurgical and Materials Transactions A*, vol. 29, no. 2, pp. 617–630, 1998.

Research Article

Maximum Sizes of Fluid-Occupied Pores within Hydrate-Bearing Porous Media Composed of Different Host Particles

Lele Liu ^{1,2}, Nengyou Wu ^{1,2}, Changling Liu ^{1,2}, Qingguo Meng,^{1,2} Haitao Tian,³ Yizhao Wan,^{1,2} and Jianye Sun^{1,2}

¹Key Laboratory of Gas Hydrate, Ministry of Natural Resources, Qingdao Institute of Marine Geology, Qingdao 266071, China

²Laboratory for Marine Mineral Resources, Qingdao National Laboratory for Marine Science and Technology, Qingdao 266071, China

³Institute of Geophysics and Geomatics, China University of Geosciences, Wuhan 430074, China

Correspondence should be addressed to Nengyou Wu; wuny@ms.giec.ac.cn and Changling Liu; qdluchangling@163.com

Received 16 March 2020; Revised 26 May 2020; Accepted 4 June 2020; Published 15 July 2020

Academic Editor: Wei Wei

Copyright © 2020 Lele Liu et al. This is an open access article distributed under the Creative Commons Attribution License, which permits unrestricted use, distribution, and reproduction in any medium, provided the original work is properly cited.

Hydraulic properties of hydrate-bearing sediments are largely affected by the maximum size of pores occupied by fluids. However, effects of host particle properties on the maximum size of fluid-occupied pores within hydrate-bearing sediments remain elusive, and differences in the maximum equivalent, incircle, and hydraulic diameters of fluid-occupied pores evolving with hydrate saturation have not been well understood. In this study, numerical simulations of grain-coating and pore-filling hydrate nucleation and growth within different artificial porous media are performed to quantify the maximum equivalent, incircle, and hydraulic diameters of fluid-occupied pores during hydrate formation, and how maximum diameters of fluid-occupied pores change with hydrate saturation is analyzed. Then, theoretical models of geometry factors for incircle and hydraulic diameters are proposed based on fractal theory, and variations of fluid-occupied pore shapes during hydrate formation are discussed. Results show that host particle properties have obvious effects on the intrinsic maximum diameters of fluid-occupied pores and introduce discrepancies in evolutions of the maximum pore diameters during hydrate formation. Pore-filling hydrates reduce the maximum incircle and hydraulic diameters of fluid-occupied pores much more significantly than grain-coating hydrates; however, hydrate pore habits have minor effects on the maximum equivalent diameter reduction. Shapes of fluid-occupied pores change little due to the presence of grain-coating hydrates, but pore-filling hydrates lead to much fibrous shapes of fluid-occupied pores.

1. Introduction

Natural gas hydrates vastly stored in marine sediments along the continental margins have a great potential to become one of global unconventional hydrocarbon energy resources [1–3]. Currently, the exploitation of this potential energy resource is still not economically feasible and requires innovative production methods and techniques [4, 5]. New methods and techniques should be well evaluated by numerical simulators prior to field applications, and results of these numerical evaluations largely depend on proper characterizations of coupled processes and appropriate quantifications of physical properties of hydrate-bearing sediments [6–9].

Hydraulic properties of hydrate-bearing sediments are quite crucial [10–12], and they still represent an ongoing research issue although great effort has been made [13–16].

Hydraulic properties (e.g., saturated water permeability, water retention curve, and relative permeability to water and gas) of hydrate-bearing sediments are inherently governed by pore-scale structures of the solid matrix and pores [17–20]. The pore space occupied by water and/or gas within hydrate-bearing sediments shrinks due to solid hydrate formation, and structures of fluid-occupied pores can be highly diverse due to different hydrate pore habits (e.g., grain-coating and pore-filling) even though hydrate saturations are identical. These diverse pore structures are experimentally

observed, and how they change during hydrate formation or dissociation has been quantified by using varieties of parameters with clear physical significances. Examples include porosity, shape factor, Euler characteristic of individual hydrate cluster, fractal dimensions, pore surface, and pore volume and size [21–24]. Various pore sizes (e.g., the critical, mean, and maximum pore sizes) have been correlated to the hydraulic permeability of porous media, and larger pore sizes generally lead to higher values of the hydraulic permeability [25–27]. Hydraulic properties of porous media are significantly affected by the maximum pore size [27–29], and the maximum pore size is experimentally and theoretically correlated with porosity, permeability, and particle size [30–33]. Grain sizes of marine sediments hosting natural gas hydrates are of a wide range from clays and silts to coarse-grained sands, and sand particle shapes are generally different [34–36]. Effects of host sediments properties (e.g., porosity, grain size, and shape) on the maximum size of fluid-occupied pores within hydrate-bearing sediments remain elusive, although papers have been published to clarify how the maximum size of fluid-occupied pores evolve with hydrate saturation during hydrate formation and dissociation [23, 37].

Pores and fluid channels within most porous media in nature are generally nonspherical and noncircular [38–40]. For these irregularly shaped pores, several definitions of pore diameter are applied to quantify pore sizes. Examples include the equivalent diameter [41], the incircle diameter, and the hydraulic diameter [42]. The equivalent diameter λ_e is a diameter of a circle having an area equal to the pore area. The incircle diameter λ_i is determined by using the maximum ball method [43], and it is widely applied to pore network extractions from porous media [16, 24, 44]. The hydraulic diameter λ_h is defined as $\lambda_h = 4A/P$, where A is the cross-sectional area and P is the wetted perimeter of the cross-section. The hydraulic diameter is commonly used to simplify fluid flow in noncircular tubes and channels as round pipe flow [17, 45, 46]. For fluid-occupied pores within hydrate-bearing sediments, the maximum pore size is expected to decrease with increasing hydrate saturation. However, similarities and differences in the maximum equivalent, incircle, and hydraulic diameters of fluid-occupied pores evolving with hydrate saturation have not been well understood.

This study is aimed at clarifying the effects of host particle properties on the maximum size of fluid-occupied pores within hydrate-bearing porous media and further the understanding of different maximum pore diameters evolving with hydrate saturation. Grain-coating and pore-filling hydrates are randomly nucleated and grew within different artificial porous media to quantify the maximum equivalent, incircle, and hydraulic diameters of fluid-occupied pores at selected hydrate saturations, followed by analyses of maximum fluid-occupied pore diameters changing due to the presence of gas hydrates. Then, theoretical models for incircle and hydraulic diameter-related geometry factors are proposed based on the fractal theory, and these proposed models are further applied to provide insights into the hydrate saturation and morphology-dependent pore shape changes during hydrate formation.

2. Methods

Ten square images of artificial porous media shown in Figure 1(a) are generated by using the method of [47] for further numerical simulations of hydrate nucleation and growth in this study. Each of these porous media is constructed by randomly placing black particles with unrestricted overlap into a white square image until the desired porosity has been reached. The porosity is calculated as the ratio of white over total pixel numbers in a square image, and the square image has a side length of 300 pixels. The shape of a solid particle is characterized by using a concept of sphericity which is defined as $S = 2\sqrt{\pi A_s}/P_s$, where A_s is the area and P_s is the perimeter of the solid particle [48]. Particle sphericity values are normally no bigger than 1, and $S = 1$ represents a circular solid particle. In addition, $S = 0.86$ stands for an elliptical solid particle with a major over minor diameter ratio of 2, and $S = 0.76$ for a diameter ratio of 3. Sphericity and size values of solid particles used for porous media constructions are summarized in Figure 1(b), and Figure 1(c) shows the intrinsic porosity and median particle diameter map for those artificial porous media.

Random nucleation and growth of grain-coating and pore-filling hydrates within artificial porous media is numerically simulated by using the method of [37]. These numerical simulations continually calculate minimum distances d_s of fluid-occupied pore pixels to solid particle and hydrate pixels, and fluid-occupied pore pixels are selectively turned into hydrate pixels until the desired hydrate saturation S_h has been reached. Different nucleation and growth preferences represent different hydrate pore habits. Grain-coating hydrate nucleation and growth is simulated by stochastically changing candidate pore pixels with $d_s = 1$ px into hydrate pixels. Pore-filling hydrate nucleation and growth is modeled by preferentially seeding hydrate in candidate pore pixels with the highest d_s , followed by randomly changing hydrate-touched pore pixels into hydrate pixels, and the value of the growth parameter is set to be 0.7 in this study. Each case of numerical simulations is 100 times performed to obtain probabilistically acceptable results. For more details, please refer to our previous paper [37].

The maximum equivalent λ_e , incircle λ_i , and hydraulic λ_h diameters of fluid-occupied pores within hydrate-bearing porous media are quantified from $S_h = 0$ to $S_h = 0.8$ at intervals of $S_h = 0.1$. When a preselected hydrate saturation is reached, fluid-occupied pores are extracted from hydrate-bearing porous media by using the function named “bwlable” with $n = 4$ (i.e., 4 connected pixels) in MATLAB 2016Ra, followed by calculations of the area and perimeter for all the fluid-occupied pores. Calculated values of the area and perimeter are further used to determine values of equivalent λ_e and hydraulic λ_h diameters, and the incircle diameter λ_i is quantified by using minimum distance d_s values. Assuming that there is a rectangular fluid-occupied pore with side lengths of 5 px and 6 px in hydrate-bearing porous media (Figure 2(a)), the equivalent diameter is calculated to be $\lambda_e = 6.2$ px, the incircle diameter $\lambda_i = 5.0$ px, and the hydraulic diameter $\lambda_h = 5.5$ px according to their definitions (Figure 2(b)). Values of the maximum equivalent, incircle,

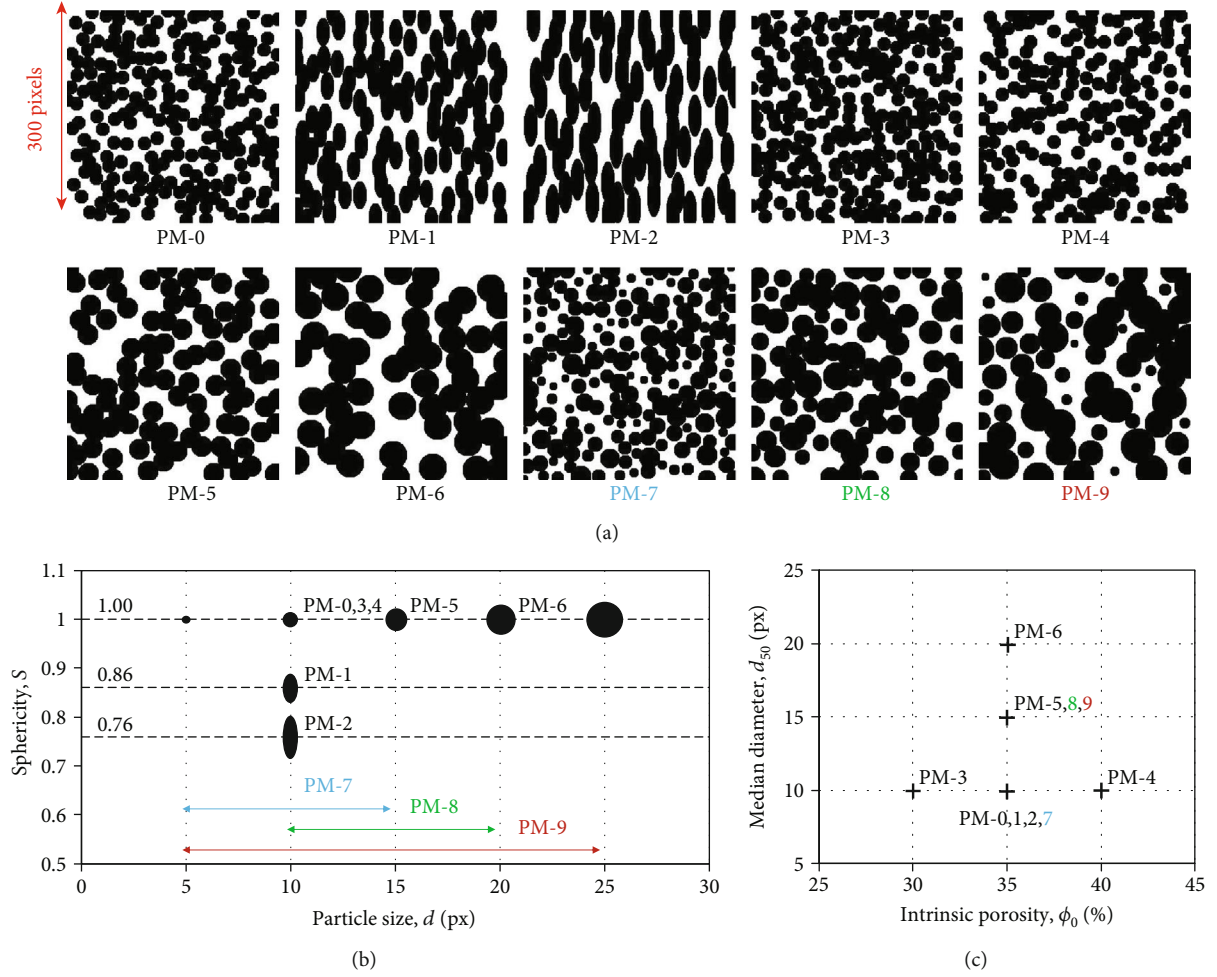


FIGURE 1: Artificial porous media for further numerical simulations of hydrate nucleation and growth in this study. (a) Square images of artificial porous media constructed by randomly placing and freely overlapping particles. The side length of square images is 300 px. Black color represents solid particles, and white color stands for fluid-occupied pores. (b) Size d and sphericity S of solid particles used for porous media constructions. (c) Intrinsic porosity ϕ_0 of artificial porous media and median diameter d_{50} of solid particles.

and hydraulic diameters of pores within hydrate-free porous media are determined and summarized in Figure 2(c) as intrinsic maximum pore diameters.

3. Results

The maximum equivalent Λ_e , incircle Λ_i , and hydraulic Λ_h diameters of fluid-occupied pores within ten images of porous media containing gas hydrates are shown in Figure 3, and all the pore diameters decrease with increasing hydrate saturation S_h . The average value of intrinsic maximum equivalent diameters Λ_{e0} of fluid-occupied pores within ten porous media (Figure 1(a)) is 154.7 ± 41.1 px with a confidence interval of 95.4% (the same below), and it decreases to 29.7 ± 16.7 px (19.2% of the intrinsic value) and 5.6 ± 1.3 px (3.6% of the intrinsic value) when hydrate saturation S_h is 0.8 for grain-coating (Figure 3(a)) and pore-filling (Figure 3(b)) hydrates, respectively. The average value of intrinsic maximum incircle diameters Λ_{i0} of fluid-occupied pores within ten porous media is 47.8 ± 23.3 px, and it decreases to 28.0 ± 16.7 px (58.6% of the intrinsic

value) for grain-coating hydrates (Figure 3(c)) and 1.0 ± 0.0 px (2.1% of the intrinsic value) for pore-filling hydrates (Figure 3(d)) when $S_h = 0.8$. The average value of intrinsic maximum hydraulic diameters Λ_{h0} of fluid-occupied pores within ten porous media is 19.7 ± 9.1 px, and it decreases to 10.7 ± 3.7 px (54.3% of the intrinsic value) and 4.7 ± 0.6 px (23.9% of the intrinsic value) when $S_h = 0.8$ for grain-coating (Figure 3(e)) and pore-filling (Figure 3(f)) hydrates, respectively. It is obvious that pore-filling hydrates reduce values of the maximum equivalent, incircle, and hydraulic diameters more efficiently than grain-coating hydrates when $S_h = 0.8$, and the maximum hydraulic diameter is the least sensitive to hydrate saturation.

Host particle properties (e.g., intrinsic porosity, particle size, and sphericity) obviously affect the intrinsic maximum equivalent Λ_{e0} , incircle Λ_{i0} , and hydraulic Λ_{h0} diameters of fluid-occupied pores (Figure 2(c)) and introduce diversities (41.1 px for Λ_{e0} , 23.3 px for Λ_{i0} , and 9.1 px for Λ_{h0}) in values of the intrinsic maximum pore diameter. All the intrinsic diversities decrease due to the presence of gas hydrates, and this implies that effects of host particle properties decrease

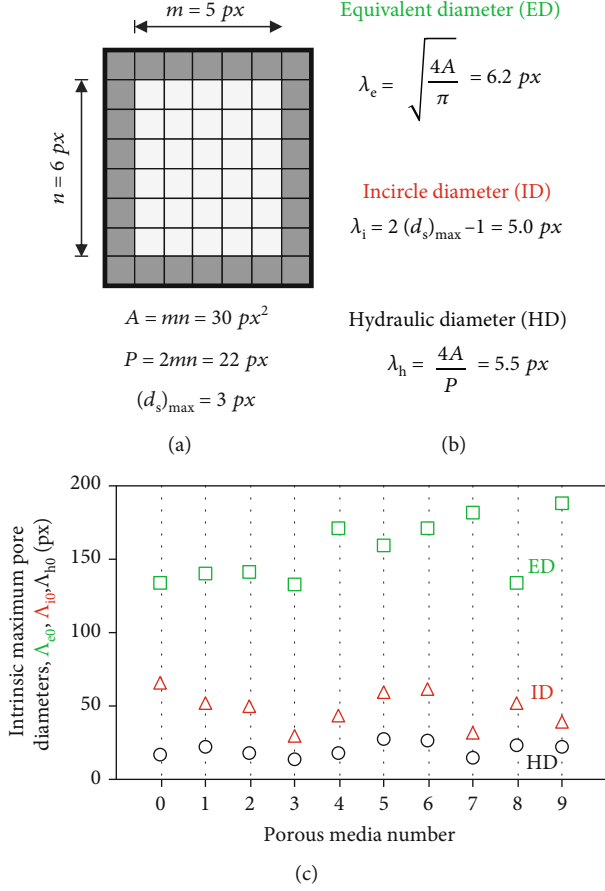


FIGURE 2: Equivalent, incircle, and hydraulic diameters of fluid-occupied pores within hydrate-bearing and hydrate-free porous media. (a) A pixel map of a rectangular pore occupied by fluids within hydrate-bearing porous media. Light gray pixels stand for the fluid-occupied pore with side lengths of 5 and 6 px, while dark gray pixels represent solid particle and hydrate pixels. Area A of the pore is 30 px^2 , and perimeter P is 22 px. Symbol d_s represents the minimum distances of pore pixels to solid particle and hydrate pixels, and the maximum value $(d_s)_{\max}$ in the rectangular pore is 3 px. (b) Values of equivalent λ_e , incircle λ_i , and hydraulic λ_h diameters for the rectangular pore shown in (a). (c) Values of intrinsic maximum equivalent Λ_{e0} , incircle Λ_{i0} , and hydraulic Λ_{h0} diameters in hydrate-free artificial porous media shown in Figure 1(a).

with increasing hydrate saturation. In addition, pore-filling hydrates (Figures 3(b), 3(d), and 3(f)) have more significant effects on the intrinsic diversity reductions than grain-filling hydrates (Figures 3(a), 3(c), and 3(e)) when $S_h = 0.8$.

In order to obtain further understandings of hydrate saturation and morphology-dependent maximum equivalent, incircle, and hydraulic diameters, Figure 4 shows normalized maximum equivalent Λ_e^* , incircle Λ_i^* , and hydraulic Λ_h^* diameters of fluid-occupied pores within hydrate-bearing porous media. Normalized maximum pore diameters are defined as ratios of maximum pore diameters within hydrate-bearing over hydrate-free porous media. All the values of normalized maximum equivalent diameters Λ_e^* of fluid-occupied pores within porous media containing

grain-coating (Figure 4(a)) and pore-filling (Figure 4(b)) hydrates generally fall into the region between upper $\Lambda_e^* = \sqrt{1 - S_h}$ and lower $\Lambda_e^* = 1 - \sqrt{S_h}$ curves, with Λ_e^* values partially lower than $1 - \sqrt{S_h}$ when hydrate saturation is lower (i.e., $S_h < 0.5$) for grain-coating hydrates and higher (i.e., $S_h > 0.5$) for pore-filling hydrates. These two models are derived based on the assumption that gas hydrates uniformly grow into all pores with different sizes, and for their derivations, refer to [29, 37]. Pore-filling hydrates reduce normalized maximum incircle (Figure 4(d)) and hydraulic (Figure 4(f)) diameters of fluid-occupied pores more significantly than grain-coating hydrates (Figures 4(c) and 4(e)). Normalized maximum incircle and hydraulic diameters of fluid-occupied pores decreasing due to the presence of grain-coating hydrates (Figures 4(c) and 4(e)) can be generally described by using $\Lambda_{i,e}^* = \sqrt{1 - S_h}$. Normalized maximum incircle diameter Λ_i^* of fluid-occupied pores within porous media containing pore-filling hydrates decreases with increasing hydrate saturation as $\Lambda_i^* = (1 - \sqrt{S_h})/2$ when $S_h > 0$ in a general trend (the blue dot curve in Figure 4(d)), and normalized maximum hydraulic diameter can be generally depicted by using $\Lambda_h^* = 1 - \sqrt{S_h}$ (Figure 4(f)).

An empirical model $\Lambda_{e,i,h}^* = 1 - (1 - m)\sqrt{S_h} - mS_h^n$ [23, 37] is applied to fit values of different normalized maximum pore diameters, and values of empirical parameters are summarized in Figure 4(g). The empirical model is an alternative form for the weighted average of theoretical models $1 - \sqrt{S_h}$ for pore-filling hydrates and $\sqrt{1 - S_h}$ for grain-coating hydrates [23]. Values of empirical parameters m and n are largely controlled by hydrate pore habits. For grain-coating hydrates, the normalized maximum equivalent diameter of fluid-occupied pores can be described by setting $m = 0.067$ and $n = 70.6$, normalized maximum incircle diameter by setting $m = 0.71$ and $n = 5.98$, and normalized maximum hydraulic diameter by setting $m = 0.51$ and $n = 19.4$. For pore-filling hydrates, the normalized maximum equivalent diameter of fluid-occupied pores can be described by setting $m = 0.95$ and $n = 0.70$, normalized maximum incircle diameter by setting $m = 0.55$ and $n = 0.10$, and normalized maximum hydraulic diameter by setting $m = 0.50$ and $n = 0.79$.

4. Discussion: Pore Shape Changes due to Hydrate Formation

Fractal theory is widely used to characterize pore-scale structures and investigate various physical (e.g., hydraulic and electrical) properties of porous media [49, 50]. In these investigations, pores within porous media are treated as circles with equivalent areas in the two-dimensional space, and the maximum equivalent diameter Λ_e can be calculated as [50]

$$\Lambda_e = \sqrt{\frac{4}{\pi} \frac{2 - D_f}{D_f} \frac{\phi}{1 - \phi} A_{\text{tot}}}, \quad (1)$$

where A_{tot} is the total area of porous media, ϕ is porosity, and D_f is pore-size fractal dimension [28] which can be determined by using the box-counting method [51].

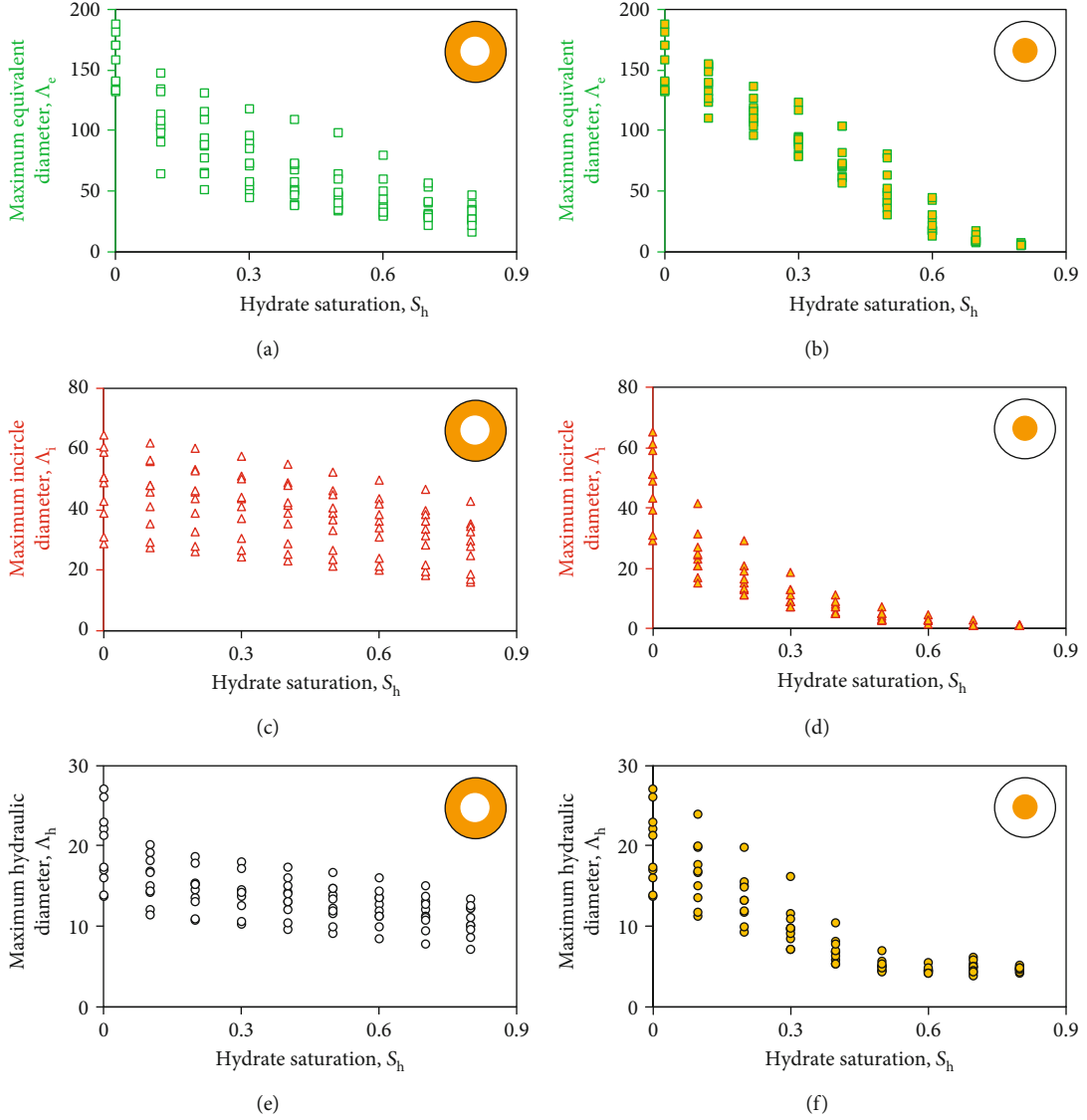


FIGURE 3: The maximum equivalent Λ_e , incircle Λ_i , and hydraulic Λ_h diameters of fluid-occupied pores within hydrate-bearing porous media evolving with hydrate saturation S_h . The maximum equivalent diameter Λ_e for grain-coating (a) and pore-filling (b) hydrates. The maximum incircle diameter Λ_i for grain-coating (c) and pore-filling (d) hydrates. The maximum hydraulic diameter Λ_h for grain-coating (e) and pore-filling (f) hydrates.

For the case that size of a pore within porous media is quantified by using incircle diameter λ_i (Figure 5(a)), area A_p of the pore can be calculated as

$$A_p = c_i \pi \left(\frac{\lambda_i}{2} \right)^2, \quad (2)$$

and c_i is a geometry factor for incircle diameter. For references, the geometry factor for incircle diameter $c_i = 4/\pi$ for square-shaped pores, $c_i = (3\sqrt{2})/\pi$ for regular triangle-shaped pores, and $c_i = 1$ for circular pores. Then, the maximum incircle diameter Λ_i can be easily calculated as

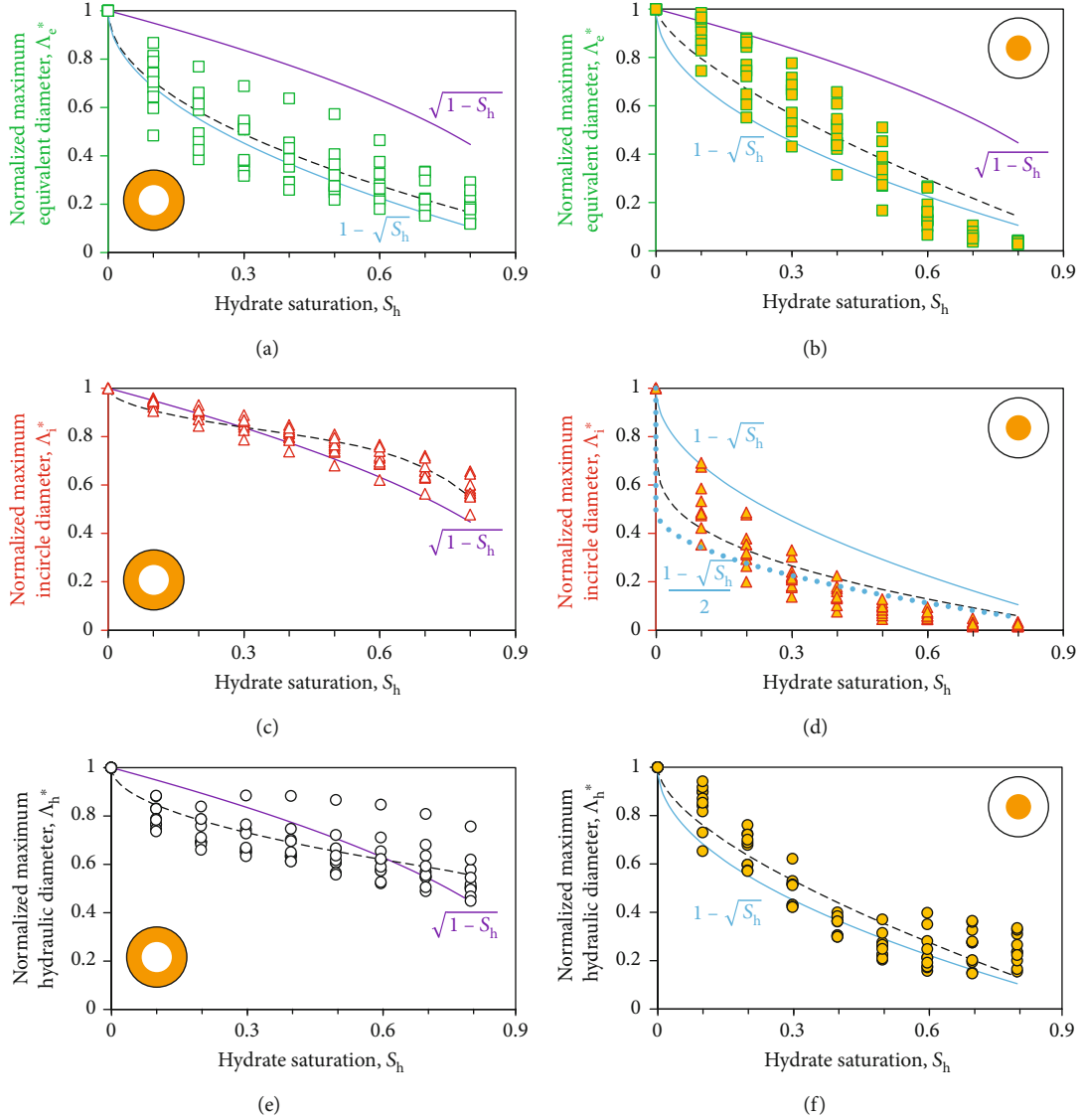
$$\Lambda_i = \sqrt{\frac{1}{c_i} \frac{4}{\pi} \frac{2 - D_f}{D_f} \frac{\phi}{1 - \phi} A_{\text{tot}}}. \quad (3)$$

If hydraulic diameter λ_h is used to quantify sizes of pores within porous media (Figure 5(a)), area A_p of an individual pore can be calculated as

$$A_p = c_h \pi \left(\frac{\lambda_h}{2} \right)^2, \quad (4)$$

and c_h is a geometry factor for hydraulic diameter. For references, the geometry factor for hydraulic diameter $c_h = 4/\pi$ for square-shaped pores, $c_h = (3\sqrt{3})/\pi$ for regular triangle-shaped pores, and $c_h = 1$ for circular pores. Then, the maximum hydraulic diameter Λ_h can be easily calculated as

$$\Lambda_h = \sqrt{\frac{1}{c_h} \frac{4}{\pi} \frac{2 - D_f}{D_f} \frac{\phi}{1 - \phi} A_{\text{tot}}}. \quad (5)$$



Fitting model	$\Lambda^* = 1 - (1 - m)\sqrt{S_h} - mS_h^n$					
Hydrate behaviors	Grain-coating hydrates			Pore-filling hydrates		
Model parameters	m	n	R^2	m	n	R^2
Equivalent diameter	0.067	70.6	0.8817	0.95	0.70	0.8832
Incircle diameter	0.71	5.98	0.9148	0.55	0.10	0.9340
Hydraulic diameter	0.51	19.4	0.7158	0.50	0.79	0.8784

(g)

FIGURE 4: Normalized maximum equivalent Λ_e^* , incircle Λ_i^* , and hydraulic Λ_h^* diameters of fluid-occupied pores within hydrate-bearing porous media evolving with hydrate saturation S_h . Normalized maximum equivalent diameter Λ_e^* for grain-coating (a) and pore-filling (b) hydrates. Normalized maximum incircle diameter Λ_i^* for grain-coating (c) and pore-filling (d) hydrates. The blue solid dot curve in (d) is drawn by $\Lambda_i^* = (1 - \sqrt{S_h})/2$ when $S_h > 0$ and $\Lambda_i^* = 1$ when $S_h = 0$. Normalized maximum hydraulic diameter Λ_h^* for grain-coating (e) and pore-filling (f) hydrates. (g) A fitting model and its parameter values for descriptions of different pore diameters changing with hydrate saturation. The fitting model is drawn as black dashed curves in (a–f).

If grain-coating hydrates uniformly grow in pores with different sizes and do not alter the shape of fluid-occupied pores (Figure 5(b)), area A_{pc} , incircle λ_{ic} , and hydraulic λ_{hc}

diameters of these pores decrease with increasing hydrate saturation S_h as $A_{pc} = A_{p0}(1 - S_h)$, $\lambda_{ic} = \lambda_{i0}\sqrt{1 - S_h}$, and $\lambda_{hc} = \lambda_{h0}\sqrt{1 - S_h}$, respectively. In these equations, subscript 0

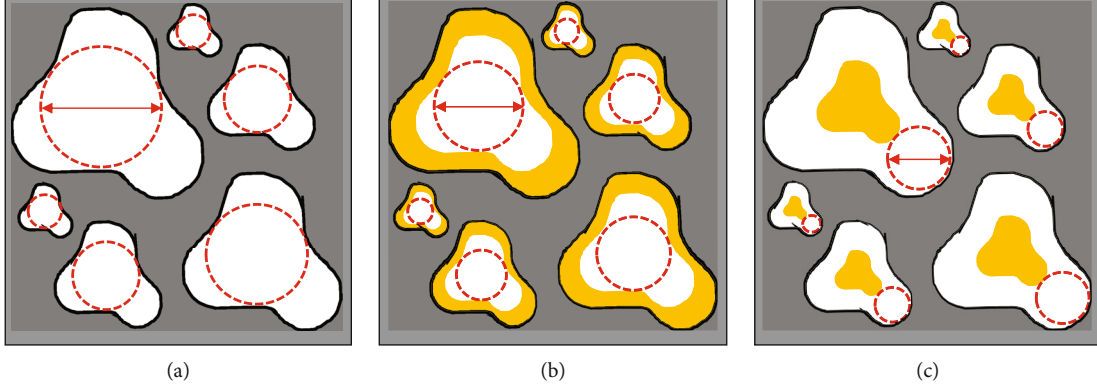


FIGURE 5: Irregularly shaped pores within hydrate-free and hydrate-bearing porous media. Gray color stands for solid particle, white for fluid-occupied pores, and yellow for gas hydrates. Red dashed circles represent incircles quantifying fluid-occupied pores. (a) Irregularly shaped pores with different sizes in hydrate-free porous media. (b) Irregularly shaped pores in porous media containing grain-coating hydrates. Gas hydrates uniformly grow in all pores with different sizes, and the shape of fluid-occupied pores before and after hydrate formation is unchanged. (c) Irregularly shaped pores in porous media containing pore-filling hydrates. Gas hydrates uniformly grow in all pores with different sizes, and the shape of solid hydrates is identical with that of intrinsic pores within porous media.

represents the intrinsic (i.e., hydrate-free) condition and subscript c stands for grain-coating hydrates. Then, it is easy to obtain

$$c_{ic} = c_{i0}, \quad (6)$$

according to Equation (2), and

$$c_{hc} = c_{h0}, \quad (7)$$

based on Equation (4). Normalized geometry factor c_{ic}^* for incircle diameter in porous media containing grain-coating hydrates can be defined as

$$c_{ic}^* = \frac{c_{ic}}{c_{i0}} = 1, \quad (8)$$

according to Equation (6), and normalized geometry factor c_{hc}^* for hydraulic diameter as

$$c_{hc}^* = \frac{c_{hc}}{c_{h0}} = 1, \quad (9)$$

according to Equation (7).

If pore-filling hydrates uniformly grow in pores with different sizes and the hydrate shape is identical with the intrinsic pore shape (Figure 5(c)), area A_{pf} , incircle λ_{if} , and hydraulic λ_{hf} diameters of these pores decrease with increasing hydrate saturation S_h as $A_{pf} = A_{p0}(1 - S_h)$, $\lambda_{if} = \lambda_{i0}(1 - \sqrt{S_h})/2$, and $\lambda_{hc} = \lambda_{i0}(1 - \sqrt{S_h})$, respectively. In these equations, subscript f represents pore-filling hydrates. Then, it is easy to obtain

$$c_{if} = \frac{4(1 + \sqrt{S_h})}{1 - \sqrt{S_h}} c_{i0}, \quad (10)$$

according to Equation (2), and

$$c_{hf} = \frac{1 + \sqrt{S_h}}{1 - \sqrt{S_h}} c_{h0}, \quad (11)$$

based on Equation (4). Equation (10) is applicable for $S_h > 0$, and $c_{if} = c_{i0}$ when $S_h = 0$. Normalized geometry factor c_{if}^* for incircle diameter in porous media containing pore-filling hydrates can be defined as

$$c_{if}^* = \frac{c_{if}}{c_{i0}} = \frac{4(1 + \sqrt{S_h})}{1 - \sqrt{S_h}}, \quad S_h > 0, \quad (12)$$

according to Equation (10), and normalized geometry factor c_{hf}^* for hydraulic diameter as

$$c_{hf}^* = \frac{c_{hf}}{c_{h0}} = \frac{1 + \sqrt{S_h}}{1 - \sqrt{S_h}}, \quad (13)$$

according to Equation (11).

Values of the pore-size fractal dimension for fluid-occupied pores within porous media containing grain-coating and pore-filling hydrates are summarized in Tables 1 and 2, respectively. The pore diameter ratio β defined as the ratio of the minimum over maximum pore diameters can be calculated by [52]

$$\beta = \phi^{1/(2-D_f)}, \quad (14)$$

and values of the pore diameter ratio within porous media containing grain-coating and pore-filling hydrates are shown in Figure 6. It is obvious that all the β values are generally smaller than 1.0×10^{-2} , and the fractal theory can be used to analyze properties of porous media containing gas hydrates in this study [52].

Values of geometry factor c_i for incircle diameter within hydrate-bearing porous media can be calculated by using Equations (3), where $A_{tot} = 300 \times 300 \text{ px}^2$. Geometry factors

TABLE 1: Pore-size fractal dimensions of fluid-occupied pores in porous media containing grain-coating hydrates.

S_h	Porous media number									
	PM-0	PM-1	PM-2	PM-3	PM-4	PM-5	PM-6	PM-7	PM-8	PM-9
0	1.7912 ± 0.0000	1.7777 ± 0.0000	1.7774 ± 0.0000	1.7619 ± 0.0000	1.8171 ± 0.0000	1.7706 ± 0.0000	1.7580 ± 0.0000	1.7916 ± 0.0000	1.7709 ± 0.0000	1.7677 ± 0.0000
0.1	1.7775 ± 0.0001	1.7646 ± 0.0000	1.7652 ± 0.0000	1.7486 ± 0.0001	1.8036 ± 0.0000	1.7563 ± 0.0000	1.7432 ± 0.0000	1.7788 ± 0.0000	1.7569 ± 0.0001	1.7539 ± 0.0000
0.2	1.7614 ± 0.0001	1.7484 ± 0.0001	1.7497 ± 0.0001	1.7329 ± 0.0001	1.7873 ± 0.0001	1.7393 ± 0.0001	1.7256 ± 0.0001	1.7638 ± 0.0001	1.7403 ± 0.0001	1.7375 ± 0.0001
0.3	1.7420 ± 0.0001	1.7289 ± 0.0001	1.7311 ± 0.0001	1.7144 ± 0.0002	1.7681 ± 0.0001	1.7189 ± 0.0001	1.7041 ± 0.0001	1.7461 ± 0.0001	1.7209 ± 0.0001	1.7181 ± 0.0001
0.4	1.7186 ± 0.0001	1.7051 ± 0.0001	1.7084 ± 0.0001	1.6924 ± 0.0002	1.7448 ± 0.0001	1.6938 ± 0.0001	1.6774 ± 0.0001	1.7247 ± 0.0001	1.6973 ± 0.0001	1.6943 ± 0.0001
0.5	1.6896 ± 0.0002	1.6755 ± 0.0001	1.6800 ± 0.0001	1.6654 ± 0.0003	1.7164 ± 0.0001	1.6621 ± 0.0002	1.6438 ± 0.0002	1.6984 ± 0.0001	1.6680 ± 0.0001	1.6647 ± 0.0002
0.6	1.6521 ± 0.0002	1.6373 ± 0.0002	1.6435 ± 0.0002	1.6308 ± 0.0003	1.6797 ± 0.0002	1.6205 ± 0.0002	1.6007 ± 0.0002	1.6647 ± 0.0002	1.6298 ± 0.0002	1.6273 ± 0.0002
0.7	1.6005 ± 0.0003	1.5855 ± 0.0003	1.5936 ± 0.0003	1.5842 ± 0.0004	1.6302 ± 0.0002	1.5634 ± 0.0003	1.5446 ± 0.0003	1.6193 ± 0.0002	1.5779 ± 0.0003	1.5772 ± 0.0003
0.8	1.5227 ± 0.0004	1.5085 ± 0.0005	1.5187 ± 0.0004	1.5142 ± 0.0006	1.5569 ± 0.0003	1.4775 ± 0.0004	1.4666 ± 0.0004	1.5513 ± 0.0003	1.4995 ± 0.0004	1.5042 ± 0.0004

TABLE 2: Pore-size fractal dimensions of fluid-occupied pores in porous media containing pore-filling hydrates.

S_h	Porous media number									
	PM-0	PM-1	PM-2	PM-3	PM-4	PM-5	PM-6	PM-7	PM-8	PM-9
0	1.7912 ± 0.0000	1.7777 ± 0.0000	1.7774 ± 0.0000	1.7619 ± 0.0000	1.8171 ± 0.0000	1.7706 ± 0.0000	1.7580 ± 0.0000	1.7916 ± 0.0000	1.7709 ± 0.0000	1.7677 ± 0.0000
0.1	1.7719 ± 0.0001	1.7591 ± 0.0001	1.7595 ± 0.0001	1.7449 ± 0.0001	1.7990 ± 0.0001	1.7511 ± 0.0001	1.7372 ± 0.0001	1.7765 ± 0.0001	1.7533 ± 0.0001	1.7500 ± 0.0001
0.2	1.7551 ± 0.0001	1.7419 ± 0.0001	1.7427 ± 0.0001	1.7290 ± 0.0002	1.7828 ± 0.0001	1.7318 ± 0.0002	1.7158 ± 0.0002	1.7613 ± 0.0001	1.7364 ± 0.0001	1.7317 ± 0.0002
0.3	1.7386 ± 0.0001	1.7247 ± 0.0002	1.7258 ± 0.0002	1.7137 ± 0.0002	1.7662 ± 0.0001	1.7128 ± 0.0003	1.6946 ± 0.0002	1.7457 ± 0.0002	1.7184 ± 0.0002	1.7127 ± 0.0002
0.4	1.7221 ± 0.0001	1.7073 ± 0.0002	1.7087 ± 0.0003	1.6979 ± 0.0002	1.7491 ± 0.0002	1.6938 ± 0.0003	1.6731 ± 0.0003	1.7297 ± 0.0002	1.7002 ± 0.0002	1.6934 ± 0.0003
0.5	1.7046 ± 0.0002	1.6890 ± 0.0002	1.6907 ± 0.0003	1.6812 ± 0.0002	1.7311 ± 0.0002	1.6743 ± 0.0004	1.6515 ± 0.0004	1.7126 ± 0.0002	1.6813 ± 0.0003	1.6732 ± 0.0004
0.6	1.6847 ± 0.0002	1.6689 ± 0.0003	1.6708 ± 0.0003	1.6610 ± 0.0002	1.7110 ± 0.0002	1.6532 ± 0.0004	1.6283 ± 0.0004	1.6926 ± 0.0003	1.6606 ± 0.0004	1.6518 ± 0.0004
0.7	1.6548 ± 0.0002	1.6405 ± 0.0003	1.6422 ± 0.0003	1.6292 ± 0.0002	1.6819 ± 0.0002	1.6261 ± 0.0004	1.6022 ± 0.0004	1.6615 ± 0.0003	1.6326 ± 0.0003	1.6248 ± 0.0004
0.8	1.6046 ± 0.0003	1.5920 ± 0.0003	1.5939 ± 0.0003	1.5771 ± 0.0003	1.6326 ± 0.0002	1.5790 ± 0.0003	1.5579 ± 0.0004	1.6103 ± 0.0002	1.5843 ± 0.0004	1.5778 ± 0.0004

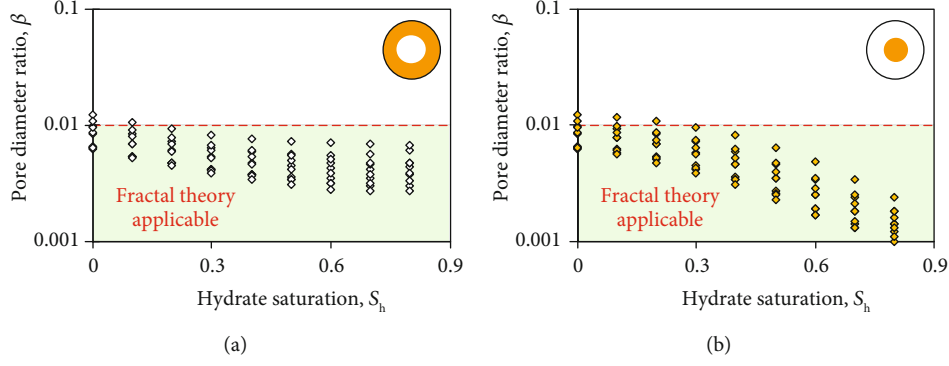


FIGURE 6: Pore diameter ratio β changing due to the presence of grain-coating (a) and pore-filling (b) hydrates within porous media. Regions colored in light green represent fractal theory applicable conditions (i.e., $\beta < 1.0 \times 10^{-2}$).

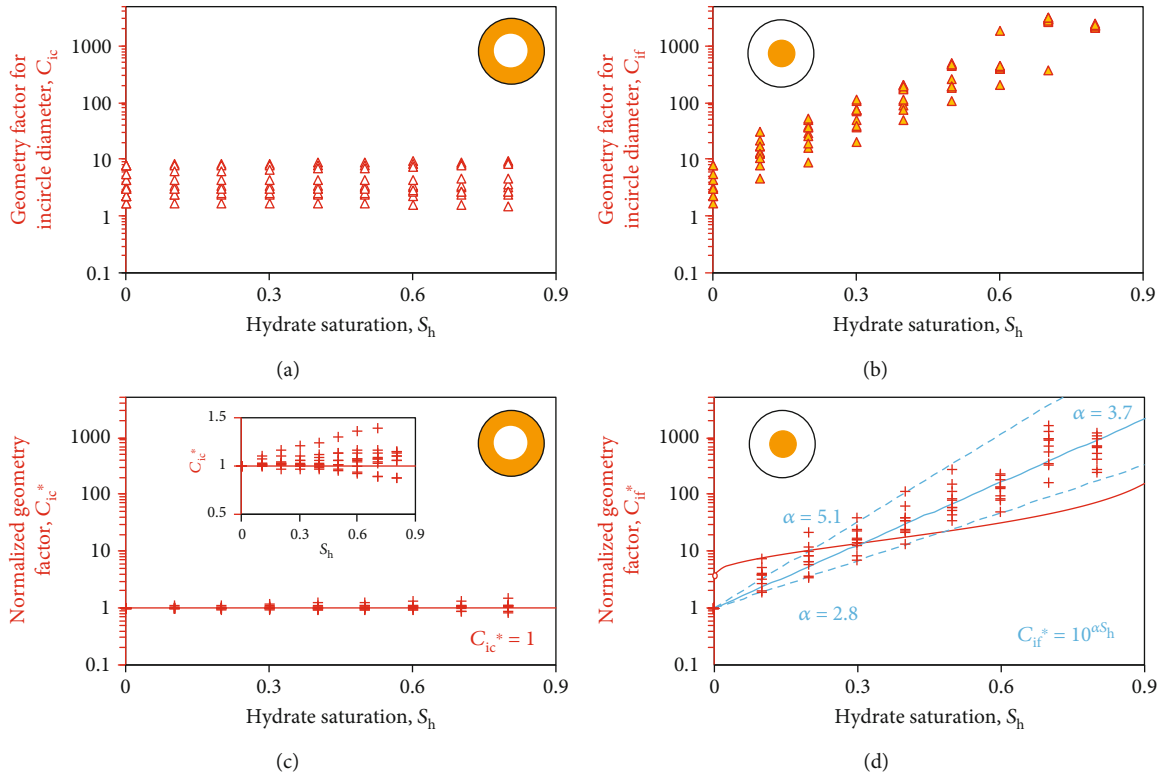


FIGURE 7: Geometry factors c_i and normalized geometry factors c_i^* for incircle diameter evolving with hydrate saturation S_h . (a) Geometry factor for incircle diameter c_{ic} in porous media containing grain-coating hydrates. (b) Geometry factor for incircle diameter c_{if} in porous media containing pore-filling hydrates. (c) Normalized geometry factor for incircle diameter c_{ic}^* in porous media containing grain-coating hydrates. (d) Normalized geometry factor for incircle diameter c_{if}^* in porous media containing pore-filling hydrates. The red curve is drawn by $c_{if}^* = 4(1 + \sqrt{S_h})/(1 - \sqrt{S_h})$ when $S_h > 0$, and $c_{if}^* = 1$ at $S_h = 0$.

for incircle diameter changing due to the presence of grain-coating and pore-filling hydrates are shown in Figures 7(a) and 7(b), respectively. It is obvious that hydrate saturation S_h has little effects on c_{ic} values compared with c_{if} values. The normalized geometry factor for incircle diameter changing due to the presence of grain-coating hydrates is shown in Figure 7(c) and pore-filling hydrates in Figure 7(d). It is shown that c_{ic}^* values generally stay close to the horizontal red line $c_{ic}^* = 1$ (Figure 7(c)), and c_{if}^* values go through an evolutionary process from below to above the red curve $c_{if}^* = 4(1 + \sqrt{S_h})/1 - \sqrt{S_h}$ (Figure 7(d)). These discrepancies

between numerical simulated $c_{ic,f}^*$ data and corresponding theoretical models (i.e., Equations (8) and (12)) are mainly due to differences in hydrate pore habits since grain-coating and pore-filling hydrate growths can hardly follow the uniform and self-similar way (Figure 5) strictly. Based on simulated data, an empirical model is proposed as

$$c_{if}^* = 10^{\alpha S_h}, \quad (15)$$

to depict how c_{if}^* values evolve with hydrate saturation. Equation (15) with $\alpha = 3.7$ can capture the essential physics of pore

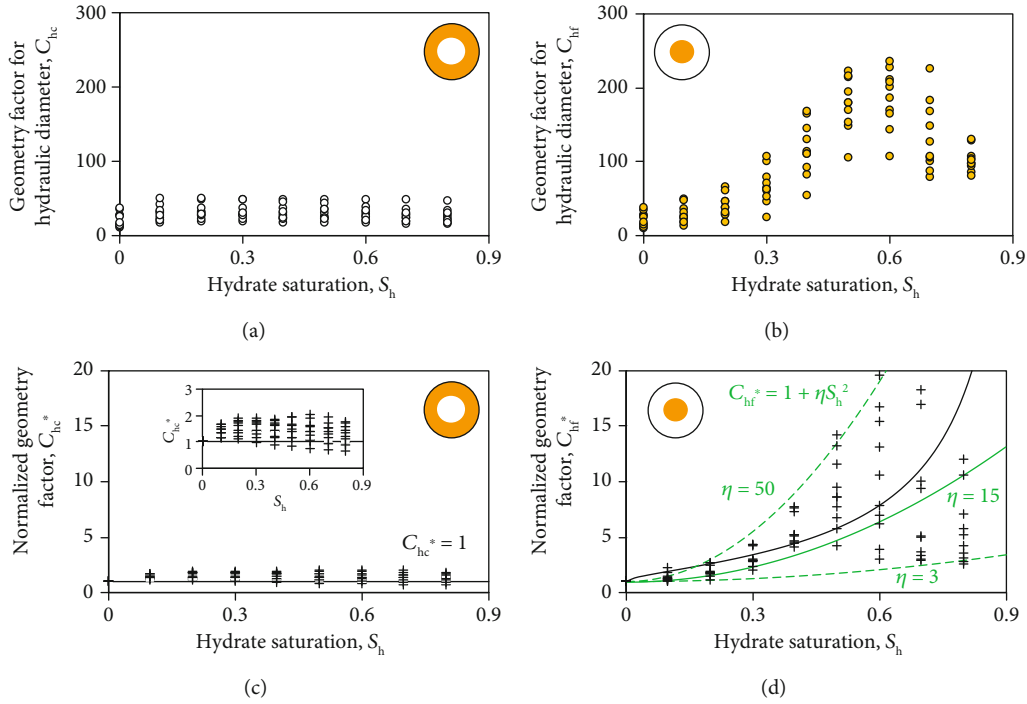


FIGURE 8: Geometry factors c_h and normalized geometry factors c_h^* for hydraulic diameter evolving with hydrate saturation S_h . (a) Geometry factor for hydraulic diameter c_{hc} in porous media containing grain-coating hydrates. (b) Geometry factor for hydraulic diameter c_{hf} in porous media containing pore-filling hydrates. (c) Normalized geometry factor for hydraulic diameter c_{hc}^* in porous media containing grain-coating hydrates. (d) Normalized geometry factor for hydraulic diameter c_{hf}^* in porous media containing pore-filling hydrates. The black curve is drawn by $c_{hf}^* = (1 + \sqrt{S_h}) / (1 - \sqrt{S_h})$.

shape changes in hydrate-bearing porous media during hydrate formation, while $\alpha = 2.8$ and $\alpha = 5.1$ set the lower and upper bounds.

Geometry factors c_h and normalized geometry factors c_h^* for hydraulic diameter evolving with hydrate saturation S_h are shown in Figure 8. It is obvious that hydrate saturation and morphology effects on c_i and c_i^* values are similar with those on c_h and c_h^* values. Normalized geometry factor c_{hc}^* for hydraulic diameter in porous media containing grain-coating hydrates changes much more mildly compared with normalized geometry factor c_{hf}^* . The black curve in Figure 8(d) drawn by using Equation (13) agrees well with the general trend of c_{hf}^* values increasing due to the presence of pore-filling hydrates. Based on simulated data, another empirical model is proposed for the normalized geometry factor c_{if}^* prediction, which is

$$c_{hf}^* = 1 + \eta S_h^2, \quad (16)$$

with $\eta = 15$ describing the general trend, $\eta = 3$ setting the lower bound, and $\eta = 50$ setting the upper bound.

In general, grain-coating hydrates barely change while pore-filling hydrates significantly enhance c_{ic}^* and c_{hc}^* values, and perimeters of fluid-occupied pores decrease with an increase in grain-coating hydrate saturations but increase due to the presence of pore-filling hydrates according to their definitions. This implies that shapes of fluid-occupied pores do not obviously change due to the presence of grain-

coating hydrates, but they alter to be more fiber-shaped when pore-filling hydrates occur.

5. Conclusions

This study numerically simulates random nucleation and growth of grain-coating and pore-filling hydrates within artificial two-dimensional porous media to quantify the maximum equivalent, incircle, and hydraulic diameters of fluid-occupied pores, and how maximum pore diameters evolve due to the presence of gas hydrates is analyzed. Theoretical and empirical models of geometry factors for incircle and hydraulic diameters of fluid-occupied pores are proposed based on fractal theory, and these proposed models together with simulated data are further applied to discuss effects of hydrate saturation and morphology on fluid-occupied pore shapes during hydrate formation. Main conclusions are drawn as follows.

Intrinsic porosity, host particle size, and sphericity not only have obvious effects on the intrinsic maximum equivalent, incircle, and hydraulic diameters of fluid-occupied pores within hydrate-free porous media but also lead to discrepancies in the maximum pore diameters even through hydrate saturation and morphology are seemingly identical.

Hydrate pore habits have relatively minor effects on the maximum equivalent diameter of fluid-occupied pores decreasing with increasing hydrate saturation. However, pore-filling hydrates reduce the maximum incircle and hydraulic diameters of fluid-occupied pores much more

significantly than grain-coating hydrates especially when hydrate saturation is higher. Values of normalized maximum equivalent diameter Λ_i^* generally fall in the region limited by upper $\sqrt{1 - S_h}$ and lower $1 - \sqrt{S_h}$ bounds. The upper bound can capture the essential physics of normalized maximum incircle and hydraulic diameter reductions due to the presence of grain-coating hydrates, and the lower bound is generally consistent with values of normalized maximum hydraulic diameter during pore-filling hydrate formation. In addition, values of normalized maximum incircle diameter Λ_i^* during the pore-filling hydrate formation approach $\Lambda_i^* = (1 - \sqrt{S_h})/2$ especially when hydrate saturation is larger. The published empirical model $\Lambda^* = 1 - (1 - m)\sqrt{S_h} - mS_h^n$ can be used to predict normalized maximum equivalent, incircle, and hydraulic diameters of fluid-occupied pores during hydrate formation.

Shapes of fluid-occupied pores change little due to the presence of grain-coating hydrates, and corresponding geometry factors for incircle and hydraulic diameters are generally unchanged during hydrate formation. On the contrary, pore-filling hydrates lead to significant variations in fluid-occupied pore shapes (i.e., more fibrous). Normalized geometry factor c_{if}^* for incircle diameter increases with increasing pore-filling hydrate saturation S_h as $c_{if}^* = 10^{3.7S_h}$, and normalized geometry factor c_{hf}^* for hydraulic diameter increases as $c_{hf}^* = 1 + 15S_h^2$. Theoretical models $c_{if}^* = 4(1 + \sqrt{S_h})/(1 - \sqrt{S_h})$ and $c_{hf}^* = (1 + \sqrt{S_h})/(1 - \sqrt{S_h})$ can capture the essential physics of geometry factor enhancements due to pore-filling hydrate formation.

In this study, how the maximum incircle pore diameter changes with increasing hydrate saturation has a potential to benefit two-dimensional pore network modeling of hydraulic properties, and conclusions about the maximum hydraulic diameter are able to facilitate capillary-bundle-based theoretical analyses.

Data Availability

All images of artificial porous media in this study can be downloaded from FigShare at https://figshare.com/articles/Artificial_Porous_Media/11988594.

Additional Points

Key Points. (i) Effects of host particle properties on the maximum equivalent, incircle, and hydraulic diameters of fluid-occupied pores are analyzed. (ii) Similarities and differences in different maximum pore diameters of fluid-occupied pores changing with hydrate saturation are clarified. (iii) Variations of fluid-occupied pore shapes due to the presence of grain-coating and pore-filling hydrates are quantitatively characterized.

Conflicts of Interest

The authors declare that there is no conflict of interest regarding the publication of this paper.

Acknowledgments

This research is funded by the National Natural Science Foundation of China (Nos. 41872136 and 41876051), the Fundamental Research Funds for the Central Universities (China University of Geosciences, Wuhan) (No. CUGG C04), the Taishan Scholar Special Experts Project (No. ts201712079), the National Key Research and Development Project (No. 2018YFE0126400), and the China Geological Survey (No. DD20190221), and their supports are gratefully acknowledged.

References

- [1] N. Vedachalam, S. Srinivasalu, G. Rajendran, G. A. Ramadass, and M. A. Atmanand, "Review of unconventional hydrocarbon resources in major energy consuming countries and efforts in realizing natural gas hydrates as a future source of energy," *Journal of Natural Gas Science and Engineering*, vol. 26, pp. 163–175, 2015.
- [2] R. Boswell and T. S. Collett, "Current perspectives on gas hydrate resources," *Energy & Environmental Science*, vol. 4, no. 4, pp. 1206–1215, 2011.
- [3] R. A. Kerr, "Gas hydrate resource: smaller but sooner," *Science*, vol. 303, no. 5660, pp. 946–947, 2004.
- [4] D. Cyranoski, "Japanese test coaxes fire from ice," *Nature: International Weekly Journal of Science*, vol. 496, no. 7446, p. 409, 2013.
- [5] M. Terzariol, G. Goldsztein, and J. C. Santamarina, "Maximum recoverable gas from hydrate bearing sediments by depressurization," *Energy*, vol. 141, pp. 1622–1628, 2017.
- [6] S. Uchida, J. S. Lin, E. M. Myshakin, Y. Seol, and R. Boswell, "Numerical simulations of sand migration during gas production in hydrate-bearing sands interbedded with thin mud layers at site NGHP-02-16," *Marine and Petroleum Geology*, vol. 108, pp. 639–647, 2019.
- [7] R. Boswell, E. Myshakin, G. Moridis et al., "India National Gas Hydrate Program Expedition 02 summary of scientific results: numerical simulation of reservoir response to depressurization," *Marine and Petroleum Geology*, vol. 108, pp. 154–166, 2019.
- [8] L. Liu, X. Lu, X. Zhang, C. Liu, and B. Du, "Numerical simulations for analyzing deformation characteristics of hydrate-bearing sediments during depressurization," *Advances in Geo-Energy Research*, vol. 1, no. 3, pp. 135–147, 2017.
- [9] Y. Li, F. Ning, N. Wu et al., "Protocol for sand control screen design of production wells for clayey silt hydrate reservoirs: a case study," *Energy Science and Engineering*, vol. 8, no. 5, pp. 1438–1449, 2020.
- [10] L. Liu, X. Lu, and X. Zhang, "A theoretical model for predicting the spatial distribution of gas hydrate dissociation under the combination of depressurization and heating without the discontinuous interface assumption," *Journal of Petroleum Science and Engineering*, vol. 133, pp. 589–601, 2015.
- [11] L. Huang, Z. Su, N. Wu, and J. Cheng, "Analysis on geologic conditions affecting the performance of gas production from hydrate deposits," *Marine and Petroleum Geology*, vol. 77, pp. 19–29, 2016.
- [12] T. Ajayi, B. J. Anderson, Y. Seol, R. Boswell, and E. M. Myshakin, "Key aspects of numerical analysis of gas hydrate reservoir performance: Alaska North Slope Prudhoe Bay Unit "L-Pad"

- hydrate accumulation,” *Journal of Natural Gas Science and Engineering*, vol. 51, pp. 37–43, 2018.
- [13] H. Singh, N. Mahabadi, E. M. Myshakin, and Y. Seol, “A mechanistic model for relative permeability of gas and water flow in hydrate-bearing porous media with capillarity,” *Water Resources Research*, vol. 55, no. 4, pp. 3414–3432, 2019.
- [14] S. Dai, J. Kim, Y. Xu et al., “Permeability anisotropy and relative permeability in sediments from the National Gas Hydrate Program Expedition 02, offshore India,” *Marine and Petroleum Geology*, vol. 108, pp. 705–713, 2019.
- [15] X. Y. Chen, R. Verma, D. N. Espinoza, and M. Prodanovic, “Pore-scale determination of gas relative permeability in hydrate-bearing sediments using X-ray computed microtomography and lattice Boltzmann method,” *Water Resources Research*, vol. 54, no. 1, pp. 600–608, 2018.
- [16] N. Mahabadi, S. Dai, Y. Seol, T. Sup Yun, and J. Jang, “The water retention curve and relative permeability for gas production from hydrate-bearing sediments: pore-network model simulation,” *Geochemistry, Geophysics, Geosystems*, vol. 17, no. 8, pp. 3099–3110, 2016.
- [17] S. Dai and Y. Seol, “Water permeability in hydrate-bearing sediments: a pore-scale study,” *Geophysical Research Letters*, vol. 41, no. 12, pp. 4176–4184, 2014.
- [18] S. Dai and J. C. Santamarina, “Water retention curve for hydrate-bearing sediments,” *Geophysical Research Letters*, vol. 40, pp. 1–5, 2013.
- [19] H. Minagawa, Y. Nishikawa, I. Ikeda et al., “Characterization of sand sediment by pore size distribution and permeability using proton nuclear magnetic resonance measurement,” *Journal of Geophysical Research*, vol. 113, no. B7, 2008.
- [20] J. Katagiri, Y. Konno, J. Yoneda, and N. Tenma, “Pore-scale modeling of flow in particle packs containing grain-coating and pore-filling hydrates: verification of a Kozeny-Carman-based permeability reduction model,” *Journal of Natural Gas Science and Engineering*, vol. 45, pp. 537–551, 2017.
- [21] D. Wang, Y. Li, C. Liu et al., “Study of hydrate occupancy, morphology and microstructure evolution with hydrate dissociation in sediment matrices using X-ray micro-CT,” *Marine and Petroleum Geology*, vol. 113, p. 104138, 2020.
- [22] C. Li, C. Liu, G. Hu et al., “Investigation on the multiparameter of hydrate-bearing sands using nano-focus X-ray computed tomography,” *Journal of Geophysical Research: Solid Earth*, vol. 124, no. 3, pp. 2286–2296, 2019.
- [23] Z. Zhang, C. Li, F. Ning et al., “Pore fractal characteristics of hydrate-bearing sands and implications to the saturated water permeability,” *Journal of Geophysical Research: Solid Earth*, vol. 125, no. 3, 2020.
- [24] J. Wang, J. Zhao, M. Yang, Y. Li, W. Liu, and Y. Song, “Permeability of laboratory-formed porous media containing methane hydrate: observations using X-ray computed tomography and simulations with pore network models,” *Fuel*, vol. 145, pp. 170–179, 2015.
- [25] S. Tian, W. Ren, G. Li, R. Yang, and T. Wang, “A theoretical analysis of pore size distribution effects on shale apparent permeability,” *Geofluids*, vol. 2017, Article ID 7492328, 9 pages, 2017.
- [26] N. Nishiyama and T. Yokoyama, “Permeability of porous media: role of the critical pore size,” *Journal of Geophysical Research: Solid Earth*, vol. 122, no. 9, pp. 6955–6971, 2017.
- [27] J. Cai, Z. Zhang, W. Wei, D. Guo, S. Li, and P. Zhao, “The critical factors for permeability-formation factor relation in reservoir rocks: pore-throat ratio, tortuosity and connectivity,” *Energy*, vol. 188, p. 116051, 2019.
- [28] B. Yu and P. Cheng, “A fractal permeability model for bi-dispersed porous media,” *International Journal of Heat and Mass Transfer*, vol. 45, no. 14, pp. 2983–2993, 2002.
- [29] L. Liu, S. Dai, F. Ning, J. Cai, C. Liu, and N. Wu, “Fractal characteristics of unsaturated sands – implications to relative permeability in hydrate-bearing sediments,” *Journal of Natural Gas Science and Engineering*, vol. 66, pp. 11–17, 2019.
- [30] J. Cai and B. Yu, “Prediction of maximum pore size of porous media based on fractal geometry,” *Fractals*, vol. 18, no. 4, pp. 417–423, 2011.
- [31] A. G. Kostornov, L. E. Lunin, V. P. Semenets, and L. I. Chernyshev, “Comparative study of permeable materials from metal powders and fibers,” *Soviet Powder Metallurgy and Metal Ceramics*, vol. 22, no. 3, pp. 199–201, 1983.
- [32] R. Pitchumani and B. Ramakrishnan, “A fractal geometry model for evaluating permeabilities of porous preforms used in liquid composite molding,” *International Journal of Heat and Mass Transfer*, vol. 42, no. 12, pp. 2219–2232, 1999.
- [33] J. Wu and B. Yu, “A fractal resistance model for flow through porous media,” *International Journal of Heat and Mass Transfer*, vol. 50, no. 19–20, pp. 3925–3932, 2007.
- [34] C. Liu, Q. Meng, X. He et al., “Characterization of natural gas hydrate recovered from Pearl River Mouth basin in South China Sea,” *Marine and Petroleum Geology*, vol. 61, Supplement C, pp. 14–21, 2015.
- [35] T. Ito, Y. Komatsu, T. Fujii et al., “Lithological features of hydrate-bearing sediments and their relationship with gas hydrate saturation in the eastern Nankai Trough, Japan,” *Marine and Petroleum Geology*, vol. 66, Part 2, pp. 368–378, 2015.
- [36] M. Oshima, K. Suzuki, J. Yoneda et al., “Lithological properties of natural gas hydrate-bearing sediments in pressure-cores recovered from the Krishna-Godavari Basin,” *Marine and Petroleum Geology*, vol. 108, pp. 439–470, 2019.
- [37] L. Liu, Z. Zhang, C. Li et al., “Hydrate growth in quartzitic sands and implication of pore fractal characteristics to hydraulic, mechanical, and electrical properties of hydrate-bearing sediments,” *Journal of Natural Gas Science and Engineering*, vol. 75, p. 103109, 2020.
- [38] J. Cai, E. Perfect, C.-L. Cheng, and X. Hu, “Generalized modeling of spontaneous imbibition based on Hagen–Poiseuille flow in tortuous capillaries with variably shaped apertures,” *Langmuir*, vol. 30, no. 18, pp. 5142–5151, 2014.
- [39] M. Tuller, D. Or, and L. M. Dudley, “Adsorption and capillary condensation in porous media: liquid retention and interfacial configurations in angular pores,” *Water Resources Research*, vol. 35, no. 7, pp. 1949–1964, 1999.
- [40] G. Mason and N. R. Morrow, “Capillary behavior of a perfectly wetting liquid in irregular triangular tubes,” *Journal of Colloid and Interface Science*, vol. 141, no. 1, pp. 262–274, 1991.
- [41] S. Jiang, Y. Kang, and Z. Sun, “A digital image method for analysis of soil pores,” in *IFIP International Federation for Information Processing*, pp. 1029–1038, Boston, Massachusetts, USA, 2009.
- [42] G. Breyiannis, S. Varoutis, and D. Valougeorgis, “Rarefied gas flow in concentric annular tube: estimation of the Poiseuille number and the exact hydraulic diameter,” *European Journal of Mechanics - B/Fluids*, vol. 27, no. 5, pp. 609–622, 2008.

- [43] D. Silin and T. Patzek, "Pore space morphology analysis using maximal inscribed spheres," *Physica A: Statistical Mechanics and its Applications*, vol. 371, no. 2, pp. 336–360, 2006.
- [44] A. Golparvar, Y. Zhou, K. Wu, J. Ma, and Z. Yu, "A comprehensive review of pore scale modeling methodologies for multiphase flow in porous media," *Advances in Geo-Energy Research*, vol. 2, no. 4, pp. 418–440, 2018.
- [45] B. Dietrich, W. Schabel, M. Kind, and H. Martin, "Pressure drop measurements of ceramic sponges—Determining the hydraulic diameter," *Chemical Engineering Science*, vol. 64, no. 16, pp. 3633–3640, 2009.
- [46] A. M. Lewis, "Measuring the hydraulic diameter of a pore or conduit," *American Journal of Botany*, vol. 79, no. 10, pp. 1158–1161, 1992.
- [47] A. Koponen, M. Kataja, and J. Timonen, "Tortuous flow in porous media," *Journal of Physical Review E*, vol. 54, no. 1, pp. 406–410, 1996.
- [48] L. Li and M. Iskander, "Evaluation of dynamic image analysis for characterizing granular soils," *Geotechnical Testing Journal*, vol. 43, no. 5, 2019.
- [49] J. Cai, W. Wei, X. Hu, and D. A. Wood, "Electrical conductivity models in saturated porous media: a review," *Earth-Science Reviews*, vol. 171, pp. 419–433, 2017.
- [50] B. Yu, "Analysis of flow in fractal porous media," *Applied Mechanics Reviews*, vol. 61, no. 5, p. 050801, 2008.
- [51] K. Falconer, *Fractal Geometry: Mathematical Foundations and Applications*, Wiley, Hoboken, New Jersey, U.S., 2005.
- [52] B. Yu and J. Li, "Some fractal characters of porous media," *Fractals*, vol. 9, no. 3, pp. 365–372, 2011.

Research Article

A Numerical Study on Gas Flow through Anisotropic Sierpinski Carpet with Slippage Effect

Shuxia Qiu,^{1,2} Lipei Zhang,² Zhenhua Tian,³ Zhouting Jiang,² Mo Yang ¹ and Peng Xu ^{2,4}

¹School of Energy and Power Engineering, University of Shanghai for Science and Technology, Shanghai 200093, China

²College of Science, China Jiliang University, Hangzhou 310018, China

³Institute of Geophysics and Geomatics, China University of Geosciences, Wuhan 430074, China

⁴State Key Laboratory Cultivation Base for Gas Geology and Gas Control, Henan Polytechnic University, Jiaozuo 454000, China

Correspondence should be addressed to Mo Yang; yangm@usst.edu.cn and Peng Xu; xupeng@cjlu.edu.cn

Received 13 February 2020; Revised 10 May 2020; Accepted 12 May 2020; Published 8 July 2020

Academic Editor: Wei Wei

Copyright © 2020 Shuxia Qiu et al. This is an open access article distributed under the Creative Commons Attribution License, which permits unrestricted use, distribution, and reproduction in any medium, provided the original work is properly cited.

A pore-scale model has been developed to study the gas flow through multiscale porous media based on a two-dimensional self-similar Sierpinski carpet. The permeability tensor with slippage effect is proposed, and the effects of complex configurations on gas permeability have been discussed. The present fractal model has been validated by comparison with theoretical models and available experimental data. The numerical results show that the flow field and permeability of the anisotropic Sierpinski model are different from that of the isotropic model, and the anisotropy of porous media can enhance gas permeability. The gas permeability of porous media increases with the increment of porosity, while it decreases with increased pore fractal dimension under fixed porosity. Furthermore, the gas slippage effect strengthens as the pore fractal dimension decreases. However, the relationship between the gas slippage effect and porosity is a nonmonotonic decreasing function because reduced pore size and enhanced flow resistance may be simultaneously involved with decreasing porosity. The proposed pore-scale fractal model can present insights on characterizing complex and multiscale structures of porous media and understanding gas flow mechanisms. The numerical results may provide useful guidelines for the applications of porous materials in oil and gas engineering, hydraulic engineering, chemical engineering, thermal power engineering, food engineering, etc.

1. Introduction

Fluid flow through natural and artificial porous media such as soils, rocks, minerals, sludge, ceramics, textile, food, paper, plants, tissues, organs, and fuel cell plays an important role in daily life and practical applications [1–3]. The permeability which represents the capability of a porous medium to permit the flow of fluids through its pore spaces is commonly used to characterize fluid flow through a porous medium. In order to determine the permeability, direct experimental measurement can be performed on a porous medium based on Darcy's law proposed in 1856 [4–7]. Although the measured permeability is accurate and reliable, it can only be applied to a particular kind of porous material. With the rapid development of computer technology, numerical simulation has become an effective method to estimate the permeability of porous media [8–13]. A few continuous models

including finite difference method (FDM), finite element method (FEM), finite volume method (FVM), and Monte Carlo method as well as lattice Boltzmann method (LBM) have been proposed to investigate fluid flow properties in porous media.

As one of the key macroscopic transport properties of a porous medium, the value of permeability depends on the microscopic structures of the medium. Therefore, pore-scale mathematical models on fluid flow through porous media are significant for predicting the permeability and understanding the physical mechanisms of fluid flow through porous media [14]. However, it is difficult to characterize the complex and irregular structures of porous media with traditional Euclidean geometry. Many porous materials are widely accepted to indicate fractal scaling laws, and fractal dimensions such as pore/mass fractal dimension, tortuosity and surface fractal dimensions, Hausdorff dimension, and

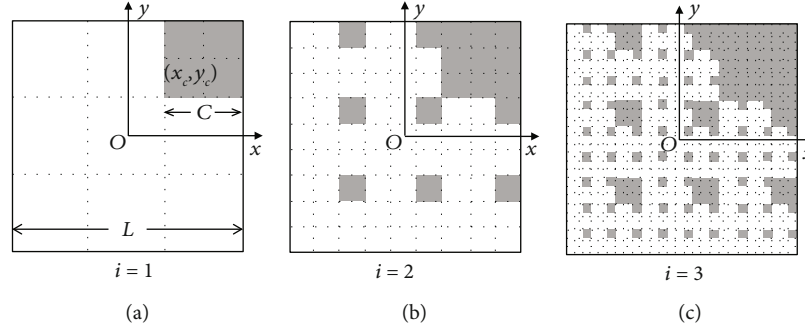


FIGURE 1: A schema for the construction process of the 2D Sierpinski carpet with $s = 3$, $n = 1$, $\varepsilon_x = 1$, and $\varepsilon_y = 1$: (a) $i = 1$, (b) $i = 2$, and (c) $i = 3$ (white and gray areas represent solid and pore phases, respectively).

TABLE 1: Parameters of the isotropic Sierpinski carpet models.

Group no.	s	n	D_f	ϕ				
				$i = 1$	$i = 2$	$i = 3$	$i = 4$	$i = 5$
S1	3	1	1.893	0.889	0.790	0.702	0.624	0.555
S2	4	4	1.792	0.750	0.563	0.422	0.316	0.237
S3	5	1	1.975	0.960	0.922	0.885	0.849	0.815
S4	5	9	1.723	0.640	0.410	0.262	0.168	0.107
S5	6	4	1.934	0.889	0.790	0.702	0.624	0.555
S6	6	16	1.672	0.556	0.309	0.171	0.095	0.053
S7	7	1	1.989	0.980	0.960	0.940	0.921	0.902
S8	7	9	1.896	0.816	0.666	0.544	0.444	0.363
S9	7	25	1.633	0.490	0.240	0.118	0.058	0.028
S10	8	4	1.969	0.938	0.879	0.824	0.772	0.724
S11	8	16	1.862	0.750	0.563	0.422	0.316	0.237
S12	8	36	1.602	0.438	0.191	0.084	0.037	0.016

spectral dimension have been proposed to characterize the fractal features governing the transport properties [15–21]. For example, Yu and Cheng [22] introduced pore and tortuosity fractal dimensions to characterize the pore structures and presented a fractal capillary bundle model for a single-phase flow through bidispersed porous media. Xu and Wei et al. [23, 24] presented analytical expressions for Kozeny-Carman constant by employing the pore fractal theory. While, Yu et al. and Xu et al. [25, 26] proposed analytical expressions for the relative permeability for the wetting and nonwetting phases with the assumption that pore size distribution follows statistically fractal scaling laws. Xu et al. [27] used fractal scaling laws to characterize the size and topology of the fracture system and presented a fractal network model for fluid flow through fractured porous media. Recently, Cai et al. [28] proposed a three-dimensional fractal model to characterize heterogeneous pore sizes in a shale stratum and presented an apparent permeability for shale. Except for fractal dimensions, Xia et al. [29] proposed two more fractal parameters (lacunarity and succolarity) to characterize the complex and irregular structures of porous media. Among various fractal models, the exactly self-similar Sierpinski carpet model with the flow path of simulating a wide range of pore sizes and configurations has long been used as a model substrate for solving transport problems through

TABLE 2: Parameters of the anisotropic Sierpinski carpet models.

Group no.	s	n	D_f	ε	
				ε_x	ε_y
A1	3	1	1.893	0	1
				1	1
A2	4	4	1.792	0	1
				1	0
A3	5	1	1.975	1	1
				1	2
				2	0
				2	1
				2	2
				0	1
A4	5	9	1.723	1	0
				1	1
A5	6	4	1.934	0	1
				0	2
				1	0
				1	1
				1	2
				2	0
A6	6	16	1.672	2	1
				2	2
				0	1
				1	0

natural porous media [30]. This fractal geometry is commonly adopted to model the complex pore space geometries of porous media, and different computational methods can be performed to develop pore-scale mathematical models for fluid flow through porous media [30–33]. However, most of fractal models are limited to isotropic porous media.

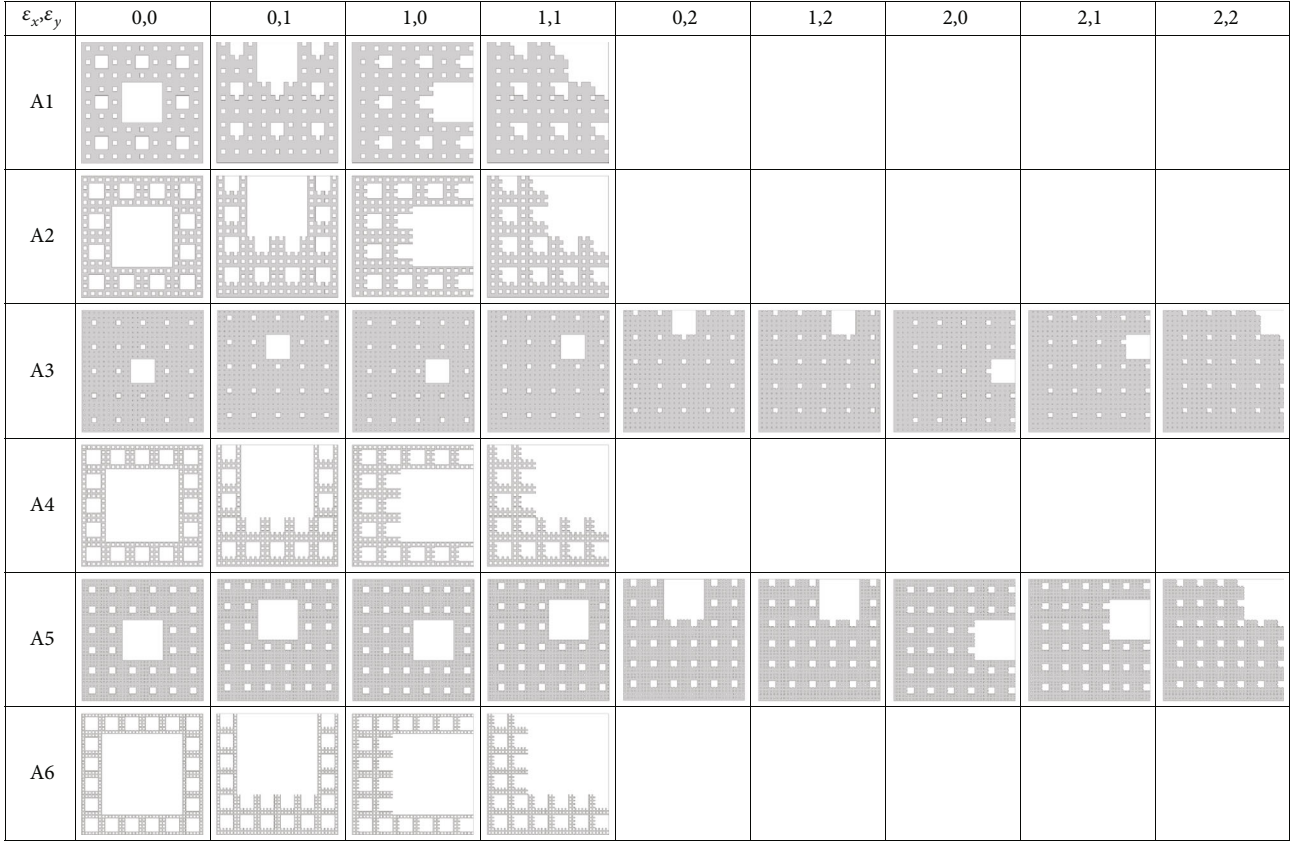


FIGURE 2: The 3rd order of the isotropic and anisotropic Sierpinski carpet models.

Because of the wide range of applications of anisotropic porous materials such as fibrous media, layered media, and rod bundles [34, 35], the discussions on fluid flow through anisotropic porous media are needed.

Recently, gas flow through microscale and nanoscale porous media has attracted increasing interests from science and engineering as it is of great significance for fuel cell, open-cell foams, membrane, microelectromechanical system, low-permeability reservoirs, energy storage devices, etc. [36–43]. When the gas molecule's mean free path is comparable to the pore size, the gas molecules and their collision with solid wall in the microscale and nanoscale pores takes an important effect on the gas flow [44, 45]. According to Klippenberg's effect, the rarefied gas effect should be taken into account for the fluid regime that the Knudsen number is greater than 10^{-3} . However, the influence mechanisms of slippage effect on the permeability of anisotropic porous media are not clear. Therefore, the present work is aimed at developing a pore-scale model for gas flow through multiscale anisotropic porous media with slippage effect based on the Sierpinski carpet model and exploring the relationship between the macroscopic gas permeability and microscopic structures of porous media.

2. Fractal Model

In order to characterize the multiscale structures, an exactly self-similar Sierpinski carpet model is used to generate the

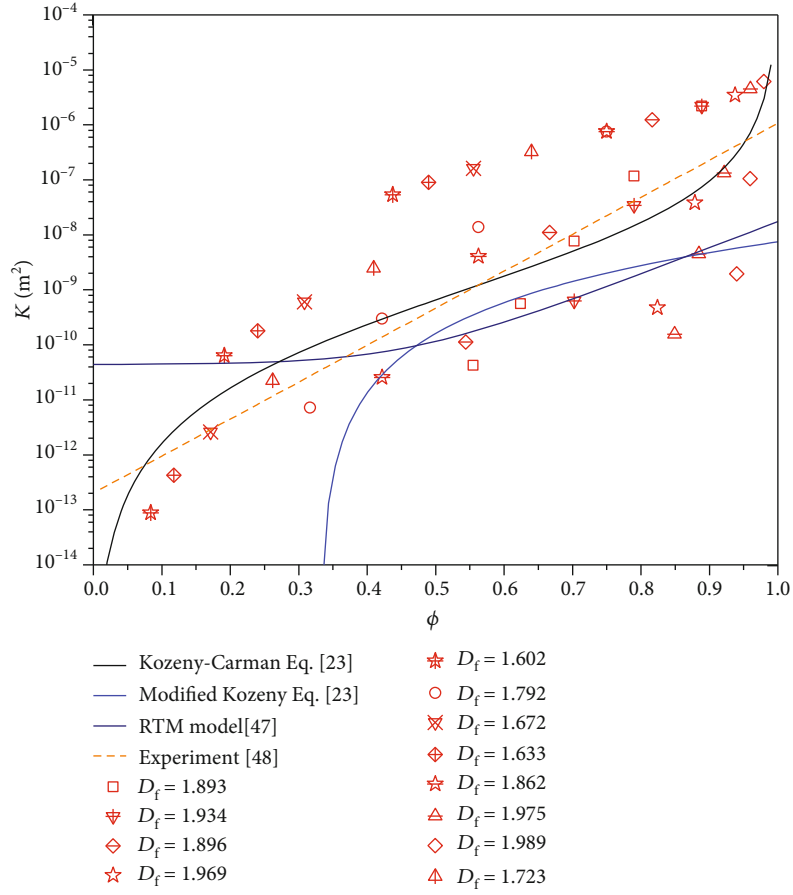
geometrical structure of the porous media. The 2D Sierpinski carpet model can be constructed by applying recursive algorithms on a void square with a size of L . Then, n square solid particles with size of C located at coordinate (x_c, y_c) are removed. The same procedure is recursively applied to the remaining squares in the next generation. Thus, the pore phase (gray area in Figure 1) in the present Sierpinski carpet model is exactly self-similar fractal, while the solid phase (white area in Figure 1) is nonfractal. That is, the statistical property of the pore size distribution of porous media can be characterized by the 2D Sierpinski carpet model. The pore fractal dimension can be calculated by [15, 46]:

$$D_f = \frac{\log(s^{D_E} - n)}{\log(s)}, \quad (1)$$

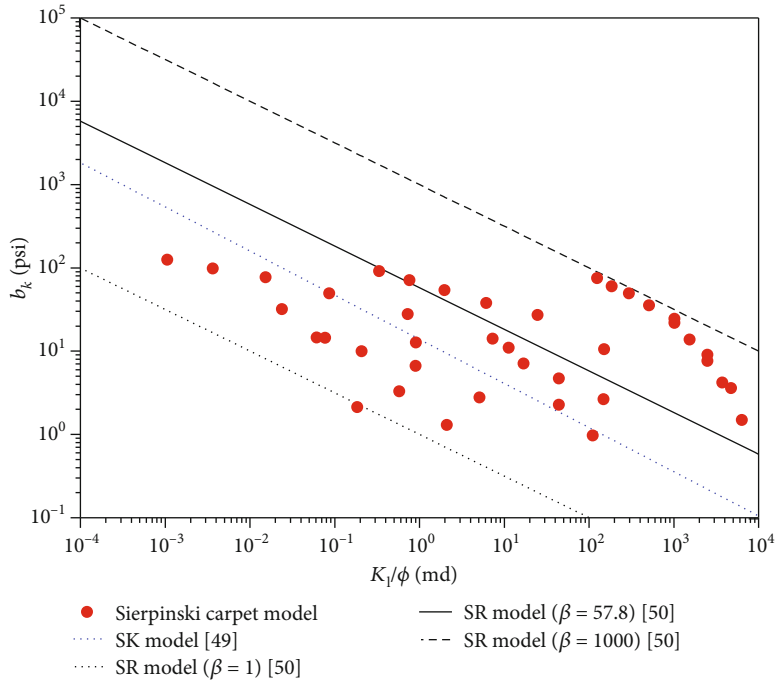
where the scaling factor is defined as $s \equiv L/C$, and the Euclidean dimension $D_E = 2$ in a two-dimensional space. The area porosity of the i^{th} generation of the Sierpinski carpet model can be determined by

$$\phi_i = \left(\frac{s^{D_E} - n}{s^{D_E}} \right)^i. \quad (2)$$

The relationship between porosity and pore fractal dimension can be gotten by combining Equations (1) and (2).



(a)



(b)

FIGURE 3: A comparison of present numerical results with theoretical models and experimental data: (a) permeability without slippage effect and (b) gas slippage factor vs. absolute permeability.

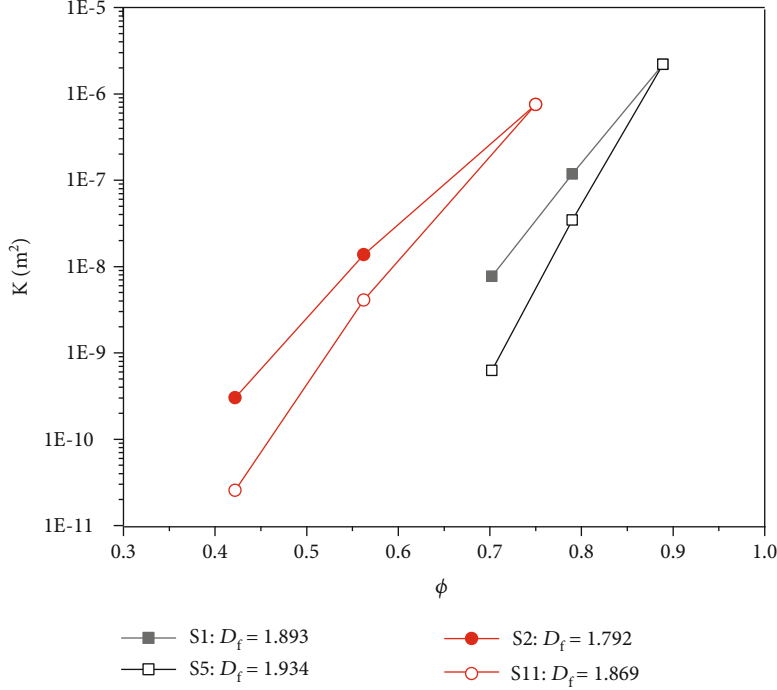


FIGURE 4: The effect of pore fractal dimension on the permeability of isotropic porous media.

$$\phi_i = (s^i)^{D_f - D_E} \tag{3}$$

In order to quantitatively characterize the anisotropic properties of porous media, two anisotropic factors are introduced.

$$\begin{aligned} \epsilon_x &= \frac{x_c}{C}, \\ \epsilon_y &= \frac{x_y}{C}. \end{aligned} \tag{4}$$

As shown in Figure 1, the anisotropic factors of $\epsilon_x = 0$ and $\epsilon_y = 0$ represent an isotropic Sierpinski carpet model, while the cases with $\epsilon_x \neq 0$ or $\epsilon_y \neq 0$ denote anisotropic Sierpinski carpet models. Table 1 lists the calculated pore fractal dimension and porosity of isotropic Sierpinski carpet models. The range of pore fractal dimension varies from 1.602 to 1.989, and the porosity value is in the range of 0.016 and 0.960. Due to computer capacity limitations, only five orders of the Sierpinski carpet model were simulated. The parameters of the anisotropic samples are summarized in Table 2. In order to compare the gas flow through anisotropic porous media with that of isotropic porous media, six groups of anisotropic Sierpinski carpet models (A1-A6) with the same pore fractal dimension and porosity as the isotropic Sierpinski carpet models (S1-S6) were used. Figure 2 shows an example of the 3rd order of the isotropic and anisotropic Sierpinski carpet models.

For the gas flow through porous media at very low Reynolds numbers, the inertial term in the Navier-Stokes equa-

tions can be neglected. Thus, the governing equations for a steady peristaltic flow of the incompressible Newtonian fluid through the Sierpinski carpet models are the continuity equation for the conservation of mass and Stokes equations for the conservation of momentum.

$$\rho \nabla \cdot \mathbf{u} = 0 \tag{5}$$

$$\nabla \cdot (P\mathbf{I} + \mathbf{H}) + \mathbf{F} = 0 \tag{6}$$

where ρ is the fluid density, \mathbf{u} is the velocity vector, P is the pressure, \mathbf{I} is the unit diagonal matrix, \mathbf{F} is the volume force vector, $\mathbf{H} = \mu(\nabla \mathbf{u} + (\nabla \mathbf{u})^T)$ is the viscous stress tensor, and μ is the dynamic viscosity. It was assumed that there are no viscous effects at the slip wall, and hence, the slippage boundary on the solid particles can be expressed by

$$\mathbf{u} \cdot \mathbf{n} = 0 \tag{7}$$

$$\mathbf{H} - (\mathbf{H} \cdot \mathbf{n})\mathbf{n} = 0 \tag{8}$$

where \mathbf{n} is the normal vector of the flow direction. While the fluid velocity relative to the wall velocity is zero for the no-slip boundary condition on a stationary wall, it can be expressed as $\mathbf{u} = 0$.

The creeping flow module in COMSOL Multiphysics was used to solve the gas flow through the 2D Sierpinski carpet models. Methane (CH_4) with density $\rho = 0.648 \text{ kg/m}^3$, viscosity $\mu = 1.1067 \times 10^{-5} \text{ Pa} \cdot \text{s}$, and mean molecular free path $\lambda = 6.22 \times 10^{-8} \text{ m}$ was adopted as working gas. The pressure inlet and outlet were settled on the left and right sides of the initial square of the Sierpinski carpet model,

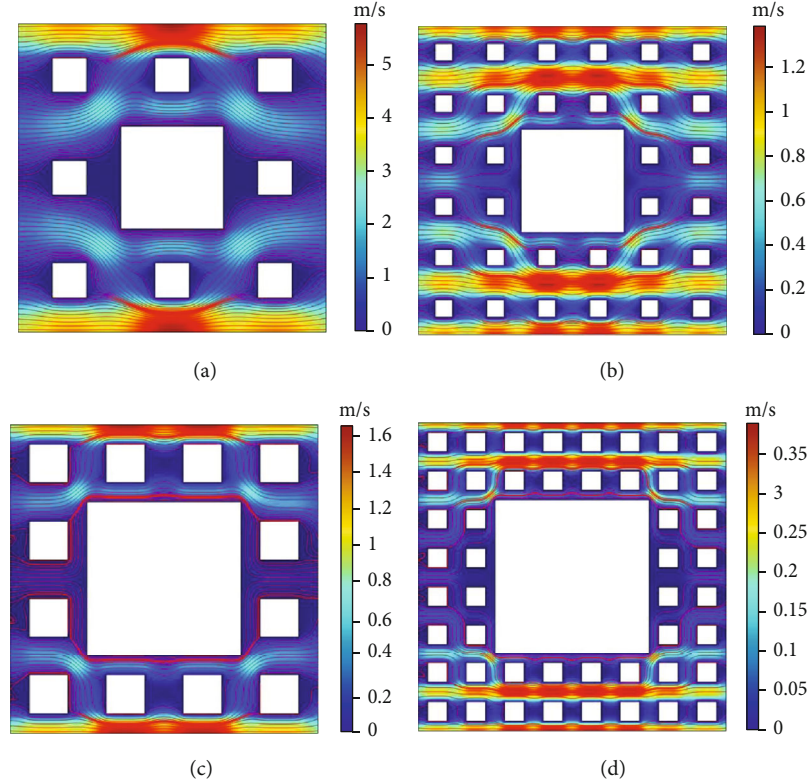


FIGURE 5: The velocity contour with streamlines for the 2nd order of the isotropic Sierpinski carpet models: (a) S1 ($D_f = 1.893$), (b) S5 ($D_f = 1.934$), (c) S2 ($D_f = 1.792$), and (d) S11 ($D_f = 1.869$).

respectively. The pressure difference along the flow direction from left to right was set to be 0.75 Pa. The upper and lower walls of the Sierpinski carpet are symmetrically bordered. The mesh was controlled by a physical mesh in which a free triangle mesh was used. The fluid flow through a porous medium without source terms can be described by Darcy's law.

$$\mathbf{u}_{\text{out}} = -\frac{\mathbf{K}}{\mu} \nabla P, \quad (9)$$

where \mathbf{K} is the permeability tensor and \mathbf{u}_{out} is the flow flux through the porous medium. In most cases, the porous medium is laterally isotropic but vertically anisotropic. If the principal permeability direction is assumed to be along the coordinate axes, the permeability tensor can be expressed as

$$\mathbf{K} = \begin{bmatrix} K_x & 0 \\ 0 & K_y \end{bmatrix}, \quad (10)$$

where K_x and K_y are the principal permeabilities along the x and y axes, respectively.

3. Results and Discussion

In order to validate the present mathematical model, the predicted permeability of the isotropic Sierpinski carpet models

was compared with that of the theoretical models and experimental data. As shown in Figure 3(a), the current fractal model without slippage effect presents acceptable agreement with Kozeny-Carman equation [23] and RTM model [47] as well as available experimental results [48]. It can be seen that the permeability of porous media without slippage effect increases with the increment of porosity. However, the permeability of porous media depends not only on the porosity but also on pore fractal dimension and pore size range [22]. Thus, it is difficult to accurately estimate the permeability of porous media with permeability-porosity relationships such as the Kozeny-Carman equation and its modifications.

Based on the linear correlation for gas permeability of the Klinkenberg equation, the gas slippage factor can be expressed by

$$b_k = \left(\frac{K_g}{K_l} - 1 \right) \bar{P}, \quad (11)$$

where K_g and K_l are, respectively, the gas permeability and equivalent liquid permeability (absolute permeability) and \bar{P} is the mean pressure. Sampath and Keighin [49] proposed Sampath-Keighin (SK) correlation for gas slippage factor based on ten tight sandstone samples as $b_k = 13.851 (K_l/\phi)^{-0.53}$. While Florence et al. [50] presented a general square-root (SR) model as $b_k = \beta (K_l/\phi)^{-0.5}$, where β is a fitting constant. They obtained an empirical correlation $\beta = 293.9M^{-0.586}$ with molecular weight (M) by fitting the

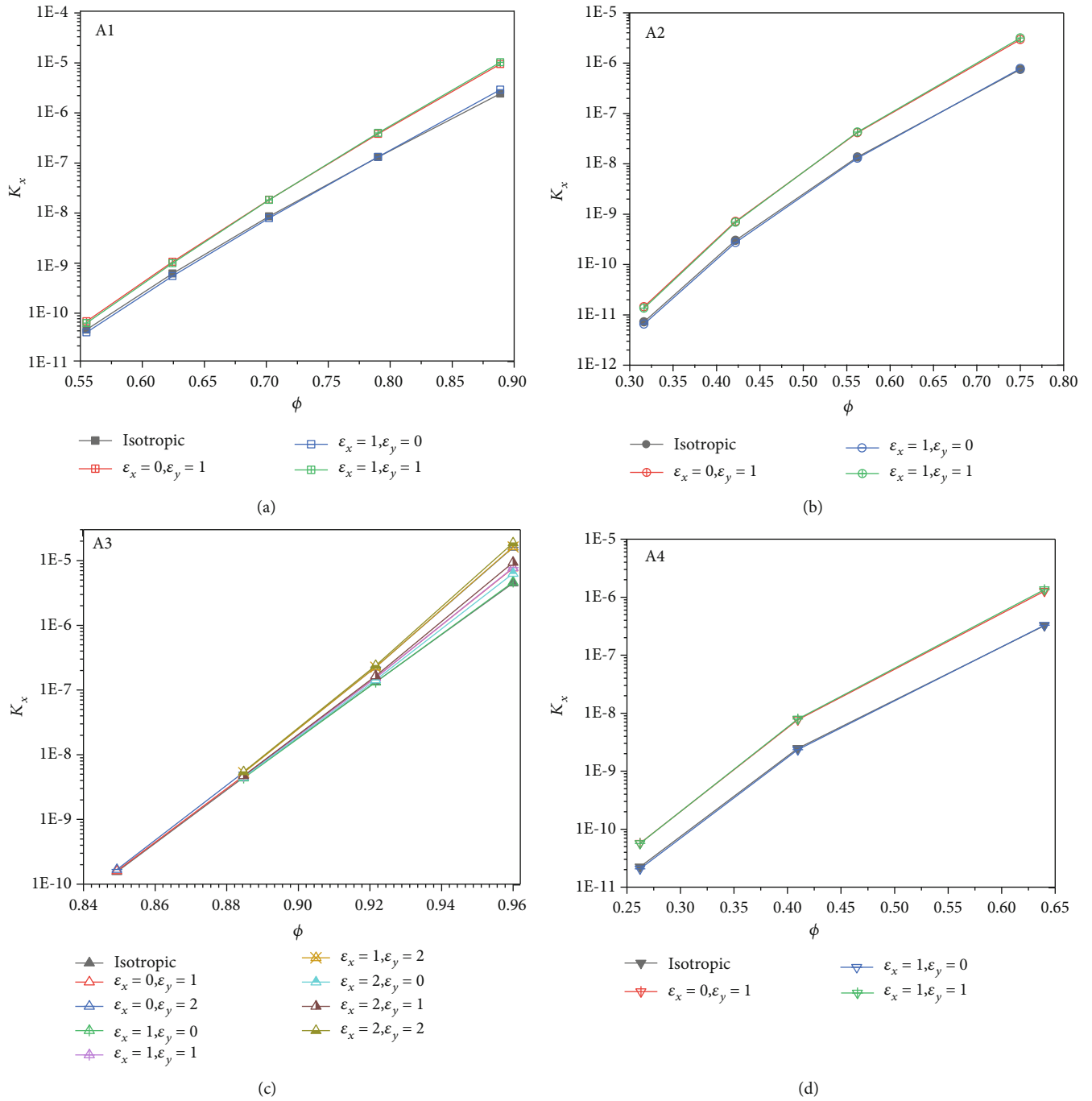


FIGURE 6: Continued.

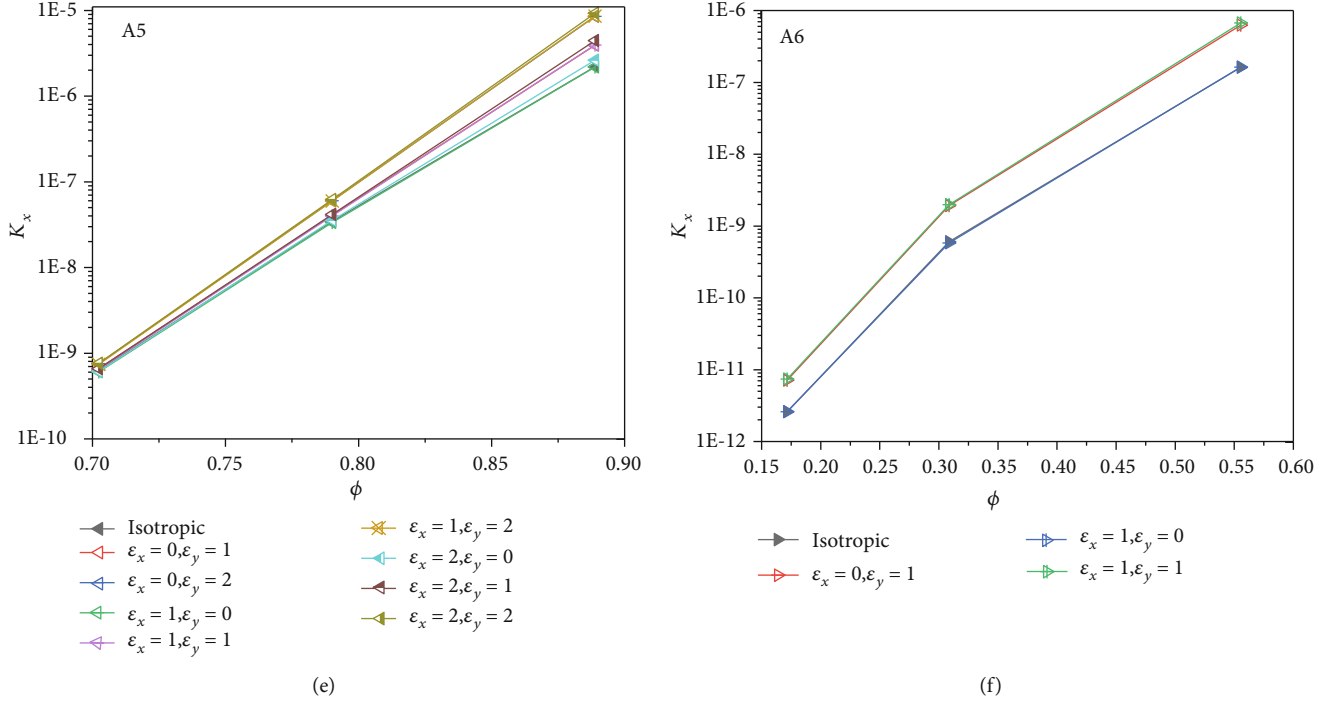


FIGURE 6: The permeability of anisotropic Sierpinski carpet models: (a) A1 ($D_f = 1.893$), (b) A2 ($D_f = 1.792$), (c) A3 ($D_f = 1.975$), (d) A4 ($D_f = 1.723$), (e) A5 ($D_f = 1.934$), and (f) A6 ($D_f = 1.672$).

experimental data for hydrogen, helium, air, nitrogen, and carbon dioxide. As can be seen in Figure 3(b), the calculated gas slippage factors by the present Sierpinski carpet model fall within the predicted range of the SK and SR models.

In order to explore the effect of fractal dimension on the permeability, a pore size range (ξ) defined as the ratio of minimum pore size to maximum pore size was introduced. The pore size range of the Sierpinski carpet model can be calculated by $\xi = n^{1/2}/s^i$. For example, the pore size range for S1, S2, S5, and S11 are, respectively $\xi_{S1} = 1/3^i$, $\xi_{S2} = 2/4^i$, $\xi_{S5} = 2/6^i$, and $\xi_{S11} = 4/8^i$. According to Equation (2), the porosity for samples S1 ($D_f = 1.893$) and S5 ($D_f = 1.934$) with same order are the same, $\phi_{S1} = \phi_{S5} = (8/9)^i$. While the porosity for samples S2 ($D_f = 1.792$) is same as that of S11 ($D_f = 1.869$) with same order, that is $\phi_{S2} = \phi_{S11} = (3/4)^i$. It can be found from Figure 4 that the permeability of the porous media with the same porosity decreases with increased pore fractal dimension. It can be explained as that the proportion of small pores increases as the pore fractal dimension increases under fixed porosity, which induces the increment of tortuosity (Figure 5).

Figure 6 shows the permeability of the anisotropic Sierpinski carpet models (A1-A6). It can be clearly seen from Figure 6 that the permeability of the anisotropic Sierpinski carpet models is different from that of isotropic cases. As shown in Figure 7, the influence of anisotropy induced by $\epsilon_x \neq 0$ on the gas flow along the x axis is not evident. Thus, it can be found in Figure 6 that the effect of anisotropy induced by $\epsilon_x \neq 0$ on the permeability K_x is marginal. While the anisotropy induced by $\epsilon_y \neq 0$ can significantly enhance the permeability K_x , which can be attributed to the large cap-

illaries formed in the case of $\epsilon_y \neq 0$ (Figures 7(c) and 7(d)). Similar results can be found for the relationship between anisotropy induced by $\epsilon_x \neq 0$ and the permeability K_y . Therefore, it can be concluded that the anisotropic factor is beneficial to the vertical fluid flow and can enhance the corresponding permeability.

In order to study the slippage effect in microscale porous media, the slippage boundary was performed on the surface of solid particles in the isotropic Sierpinski carpet models. A dimensionless parameter was defined to characterize the gas slippage effect:

$$\tau = \left| \frac{K_{\text{slip}} - K_{\text{no-slip}}}{K_{\text{no-slip}}} \right|, \quad (12)$$

where K_{slip} and $K_{\text{no-slip}}$ represent the permeability with and without slippage effect, respectively.

Because the pore fractal dimension decreases with the decrease of porosity, it can be found in Figure 8 that the slippage effect strengthens as the pore fractal dimension decreases. However, the slippage effect is not a monotonically decreasing function with porosity for certain groups of samples with the same pore fractal dimension ($D_f = 1.862$, $D_f = 1.896$, $D_f = 1.934$, $D_f = 1.969$, $D_f = 1.975$, and $D_f = 1.989$). The reduced pore size by decreasing porosity can enhance slippage effect. While the increased proportion of solid particles by decreasing porosity can increase flow resistance and then lower the slippage effect. Therefore, the slippage parameter τ may decrease when the porosity decrease for the samples with a certain pore fractal dimension because the increased flow resistance takes a dominate effect on gas

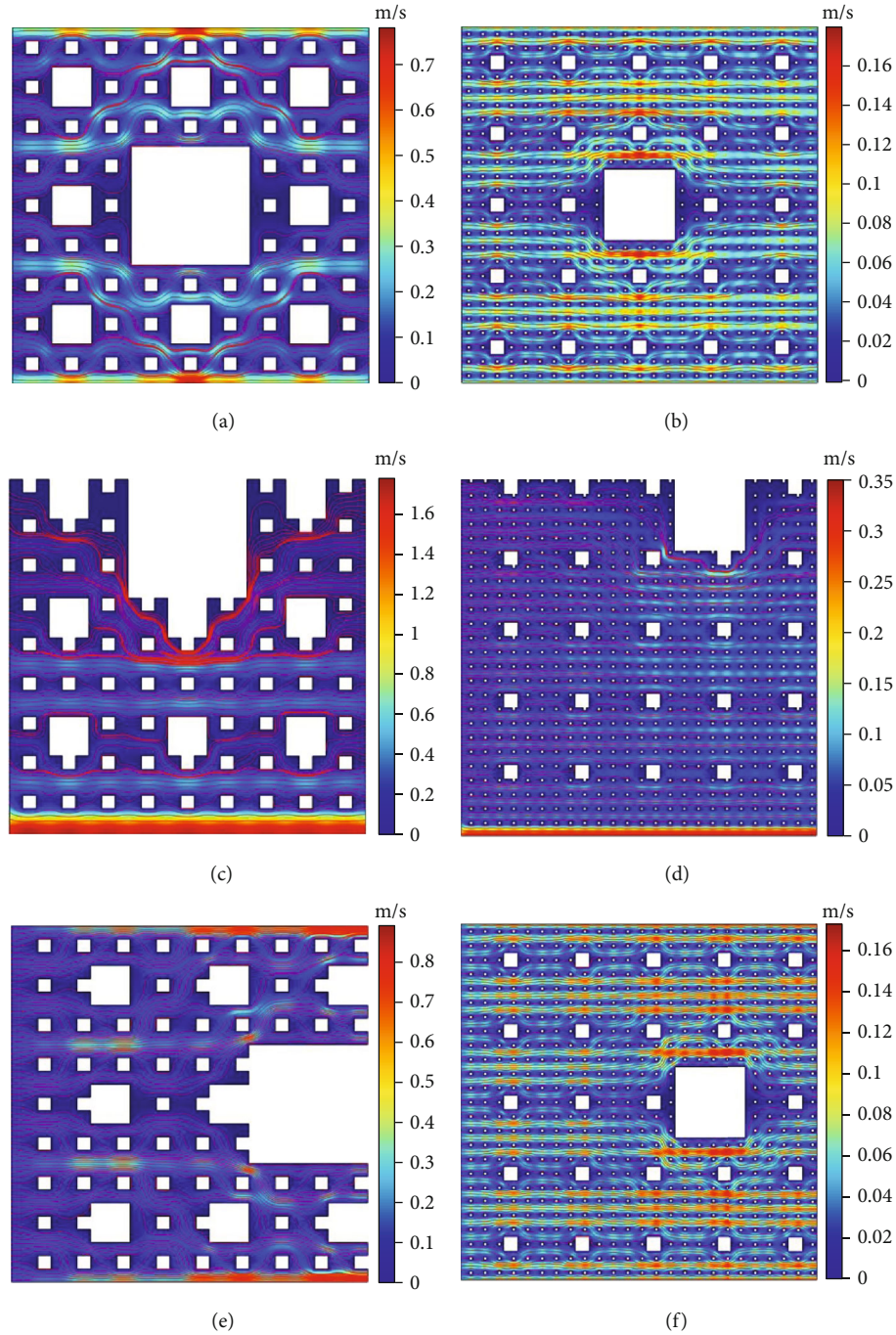


FIGURE 7: The velocity contour with streamlines for the 3rd order of anisotropic Sierpinski carpet models: (a) A1 (isotropic), (b) A3 (isotropic), (c) A1 ($\epsilon_x = 0, \epsilon_y = 1$), (d) A3 ($\epsilon_x = 1, \epsilon_y = 2$), (e) A1 ($\epsilon_x = 1, \epsilon_y = 0$), and (f) A3 ($\epsilon_x = 1, \epsilon_y = 0$).

slippage. It should be noted that only gas slippage effect in the micro- and nanoscale pores has been taken into account in the present work, other microscale effect such as transition flow and free molecular flow may be included when the Knudsen number is larger than 0.1.

4. Conclusions

In this work, a two-dimensional Sierpinski carpet model has been adopted to characterize the multiscale microstructures

of porous media. And a pore-scale mathematical model has been developed to study the gas flow through both the isotropic and anisotropic porous media. The influence of microstructures and anisotropy as well as slippage effect on the permeability has been discussed. It has been found that the permeability of porous media depends on the porosity and pore fractal dimension as well as pore size range. The value of permeability increases with increased porosity and decreases as pore fractal dimension increases under fixed porosity. The flow field and permeability of anisotropic

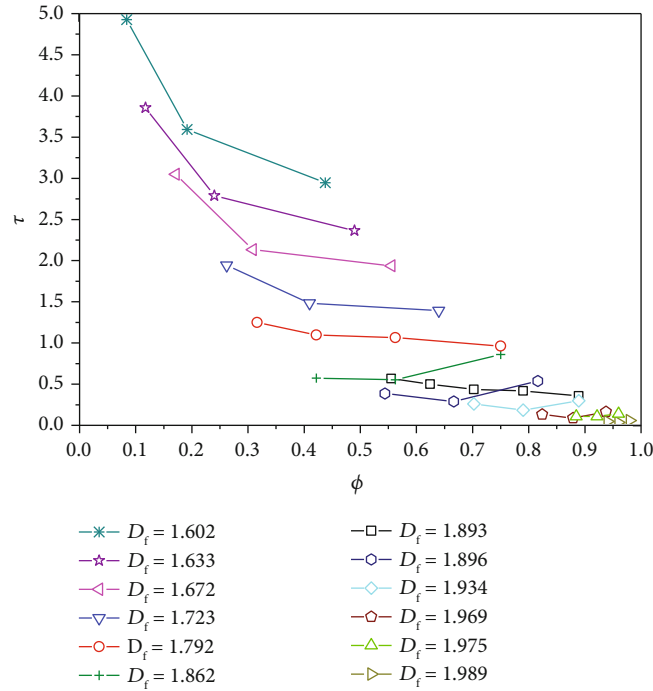


FIGURE 8: The effect of slippage effect on the permeability of the Sierpinski carpet models.

porous media are different from that of isotropic porous media. The anisotropic factor is beneficial to the vertical fluid flow and can enhance the corresponding permeability. For the microscale porous media, gas slippage phenomena show a significant effect on the effective permeability. The numerical results indicate that the slippage effect strengthens as the pore fractal dimension decreases. However, it may be reduced by increased porosity under certain pore fractal dimensions as two competitive factors (pore size and flow resistance) are involved. The proposed fractal model shows advantages in characterizing the complex and irregular microstructures of porous media and provides a conceptual tool to understand the flow mechanisms of gas flow through the porous media. It should be pointed out that some complications such as dead-end pores, contact and overlap of solid particles, pore/particle configurations, and morphology were neglected in the proposed fractal model. As an extension to this study, it would be helpful to investigate randomly a three-dimensional fractal model.

Data Availability

The numerical data used to support the findings of this study are available from the corresponding author upon request.

Conflicts of Interest

The authors declare that there is no conflict of interest regarding the publication of this paper.

Acknowledgments

This work was jointly supported by the Natural Science Foundation of China (grant numbers 51876196, 51736007, and 21873087), the Zhejiang Provincial Natural Science Foundation of China (grant number LR19E060001), and the State Key Laboratory Cultivation Base for Gas Geology and Gas Control of Henan Polytechnic University (grant number WS2018A02).

References

- [1] M. Sahimi, *Flow and Transport in Porous Media and Fractured Rock: From Classical Methods to Modern Approaches*, Wiley-VCH, Weinheim, 2011.
- [2] K. Vafai, *Handbook of Porous Media*, CRC Press, Boca Raton, FL, USA, 2019.
- [3] P. Xu, A. P. Sasmito, and A. S. Mujumdar, *Heat and Mass Transfer in Drying of Porous Media*, CRC Press, Boca Raton, FL, USA, 2019.
- [4] E. Charlaix, A. P. Kushnick, and J. P. Stokes, "Experimental study of dynamic permeability in porous media," *Physical Review Letters*, vol. 61, no. 14, pp. 1595–1598, 1988.
- [5] P. M. Adler and J. F. Thovert, "Real porous media: local geometry and macroscopic properties," *Applied Mechanics Reviews*, vol. 51, no. 9, pp. 537–585, 1998.
- [6] X. Cui, A. M. M. Bustin, and R. M. Bustin, "Measurements of gas permeability and diffusivity of tight reservoir rocks: different approaches and their applications," *Geofluids*, vol. 9, no. 3, pp. 208–223, 2009.
- [7] Z. Yang, Z. Ma, Y. Luo, Y. Zhang, H. Guo, and W. Lin, "A measured method for in situ viscosity of fluid in porous media by

- nuclear magnetic resonance,” *Geofluids*, vol. 2018, Article ID 9542152, 8 pages, 2018.
- [8] A. Koponen, M. Kataja, and J. Timonen, “Permeability and effective porosity of porous media,” *Physical Review E*, vol. 56, no. 3, pp. 3319–3325, 1997.
- [9] L. Hao and P. Cheng, “Lattice Boltzmann simulations of anisotropic permeabilities in carbon paper gas diffusion layers,” *Journal of Power Sources*, vol. 186, no. 1, pp. 104–114, 2009.
- [10] P. Xu, B. Yu, X. Qiao, S. Qiu, and Z. Jiang, “Radial permeability of fractured porous media by Monte Carlo simulations,” *International Journal of Heat and Mass Transfer*, vol. 57, no. 1, pp. 369–374, 2013.
- [11] R. Guibert, P. Horgue, G. Debenest, and M. Quintard, “A comparison of various methods for the numerical evaluation of porous media permeability tensors from pore-scale geometry,” *Mathematical Geosciences*, vol. 48, no. 3, pp. 329–347, 2016.
- [12] X. Yan, Z. Huang, J. Yao et al., “Numerical simulation of hydro-mechanical coupling in fractured vuggy porous media using the equivalent continuum model and embedded discrete fracture model,” *Advances in Water Resources*, vol. 126, pp. 137–154, 2019.
- [13] R. Liu, N. Huang, Y. Jiang, H. Jing, and L. Yu, “A numerical study of shear-induced evolutions of geometric and hydraulic properties of self-affine rough-walled rock fractures,” *International Journal of Rock Mechanics and Mining Sciences*, vol. 127, article 104211, 2020.
- [14] M. J. Blunt, *Multiphase Flow in Permeable Media: A Pore-Scale Perspective*, Cambridge University Press, Cambridge, 2017.
- [15] B. B. Mandelbrot, *The Fractal Geometry of Nature*, Freeman, New York, NY, USA, 1982.
- [16] A. J. Katz and A. H. Thompson, “Fractal sandstone pores: implications for conductivity and pore formation,” *Physical Review Letters*, vol. 54, no. 12, pp. 1325–1328, 1985.
- [17] E. Perfect and B. D. Kay, “Applications of fractals in soil and tillage research: a review,” *Soil & Tillage Research*, vol. 36, no. 1–2, pp. 1–20, 1995.
- [18] B. Yu, “Analysis of flow in fractal porous media,” *Applied Mechanics Reviews*, vol. 61, no. 5, article 050801, 2008.
- [19] B. Wang, Y. Jin, Q. Chen, J. Zheng, Y. Zhu, and X. Zhang, “Derivation of permeability-pore relationship for fractal porous reservoirs using series-parallel flow resistance model and lattice Boltzmann method,” *Fractals*, vol. 22, no. 3, article 1440005, 2014.
- [20] P. Xu, “A discussion on fractal models for transport physics of porous media,” *Fractals*, vol. 23, no. 3, article 1530001, 2015.
- [21] Y. Jin, X. Liu, H. Song, J. Zheng, and J. Pan, “General fractal topography: an open mathematical framework to characterize and model mono-scale-invariances,” *Nonlinear Dynamics*, vol. 96, no. 4, pp. 2413–2436, 2019.
- [22] B. Yu and P. Cheng, “A fractal permeability model for bi-dispersed porous media,” *International Journal of Heat and Mass Transfer*, vol. 45, no. 14, pp. 2983–2993, 2002.
- [23] P. Xu and B. Yu, “Developing a new form of permeability and Kozeny–Carman constant for homogeneous porous media by means of fractal geometry,” *Advances in Water Resources*, vol. 31, no. 1, pp. 74–81, 2008.
- [24] W. Wei, J. Cai, J. Xiao, Q. Meng, B. Xiao, and Q. Han, “Kozeny–Carman constant of porous media: insights from fractal-capillary imbibition theory,” *Fuel*, vol. 234, pp. 1373–1379, 2018.
- [25] B. Yu, J. Li, Z. Li, and M. Zou, “Permeabilities of unsaturated fractal porous media,” *International Journal of Multiphase Flow*, vol. 29, no. 10, pp. 1625–1642, 2003.
- [26] P. Xu, S. Qiu, B. Yu, and Z. Jiang, “Prediction of relative permeability in unsaturated porous media with a fractal approach,” *International Journal of Heat and Mass Transfer*, vol. 64, pp. 829–837, 2013.
- [27] P. Xu, C. Li, S. Qiu, and A. P. Sasmito, “A fractal network model for fractured porous media,” *Fractals*, vol. 24, no. 2, article 1650018, 2016.
- [28] J. Cai, D. Lin, H. Singh, W. Wei, and S. Zhou, “Shale gas transport model in 3D fractal porous media with variable pore sizes,” *Marine and Petroleum Geology*, vol. 98, pp. 437–447, 2018.
- [29] Y. Xia, J. Cai, E. Perfect, W. Wei, Q. Zhang, and Q. Meng, “Fractal dimension, lacunarity and succolarity analyses on CT images of reservoir rocks for permeability prediction,” *Journal of Hydrology*, vol. 579, article 124198, 2019.
- [30] S. W. Coleman and J. C. Vassilicos, “Transport properties of saturated and unsaturated porous fractal materials,” *Physical Review Letters*, vol. 100, no. 3, article 035504, 2008.
- [31] Y. Chen, C. Shen, P. Lu, and Y. Huang, “Role of pore structure on liquid flow behaviors in porous media characterized by fractal geometry,” *Chemical Engineering and Processing*, vol. 87, pp. 75–80, 2015.
- [32] A. E. Khabbazi, J. Hinebaugh, and A. Bazylak, “Analytical tortuosity–porosity correlations for Sierpinski carpet fractal geometries,” *Chaos, Solitons and Fractals*, vol. 78, pp. 124–133, 2015.
- [33] H. Rostamzadeh, M. R. Salimi, and M. Taeibi-Rahni, “Permeability correlation with porosity and Knudsen number for rarefied gas flow in Sierpinski carpets,” *Journal of Natural Gas Science and Engineering*, vol. 56, pp. 549–567, 2018.
- [34] Y. Kuwata and K. Suga, “Direct numerical simulation of turbulence over anisotropic porous media,” *Journal of Fluid Mechanics*, vol. 831, pp. 41–71, 2017.
- [35] J. Cao, H. Gao, L. Dou, M. Zhang, and T. Li, “Modeling flow in anisotropic porous medium with full permeability tensor,” *Journal of Physics: Conference Series*, vol. 1324, no. 1, article 012054, 2019.
- [36] F. Javadpour, D. Fisher, and M. Unsworth, “Nanoscale gas flow in shale gas sediments,” *Journal of Canadian Petroleum Technology*, vol. 46, no. 10, pp. 55–61, 2007.
- [37] L. M. Pant, S. K. Mitra, and M. Secanell, “Absolute permeability and Knudsen diffusivity measurements in PEMFC gas diffusion layers and micro porous layers,” *Journal of Power Sources*, vol. 206, pp. 153–160, 2012.
- [38] H. Wang, W. Xu, J. Shao, and F. Skoczylas, “The gas permeability properties of low-permeability rock in the process of triaxial compression test,” *Materials Letters*, vol. 116, pp. 386–388, 2014.
- [39] K. Wu, Z. Chen, and X. Li, “Real gas transport through nanopores of varying cross-section type and shape in shale gas reservoirs,” *Chemical Engineering Journal*, vol. 281, pp. 813–825, 2015.
- [40] C. Li, P. Xu, S. Qiu, and Y. Zhou, “The gas effective permeability of porous media with Klinkenberg effect,” *Journal of Natural Gas Science and Engineering*, vol. 34, pp. 534–540, 2016.
- [41] L. Wu, M. T. Ho, L. Germanou et al., “On the apparent permeability of porous media in rarefied gas flows,” *Journal of Fluid Mechanics*, vol. 822, pp. 398–417, 2017.

- [42] J. Wang, L. Yu, and Q. Yuan, "Experimental study on permeability in tight porous media considering gas adsorption and slippage effect," *Fuel*, vol. 253, pp. 561–570, 2019.
- [43] X. Li, Z. Gao, S. Fang, C. Ren, K. Yang, and F. Wang, "Fractal characterization of nanopore structure in shale, tight sandstone and mudstone from the Ordos basin of China using nitrogen adsorption," *Energies*, vol. 12, no. 4, p. 583, 2019.
- [44] Y. Ichikawa and A. P. S. Selvadurai, *Transport Phenomena in Porous Media: Aspects of Micro/Macro Behaviour*, Springer, Heidelberg, 2012.
- [45] K. S. Lee and T. H. Kim, *Integrative Understanding of Shale Gas Reservoirs*, Springer, Switzerland, 2016.
- [46] Y. Feng, B. Yu, M. Zou, and D. Zhang, "A generalized model for the effective thermal conductivity of porous media based on self-similarity," *Journal of Physics D: Applied Physics*, vol. 37, no. 21, pp. 3030–3040, 2004.
- [47] R. Gauvin, A. Kerachni, and B. Fisa, "Variation of mat surface density and its effect on permeability evaluation for RTM modelling," *Journal of Reinforced Plastics and Composites*, vol. 13, no. 4, pp. 371–383, 2016.
- [48] S. N. Ehrenberg and P. H. Nadeau, "Sandstone vs. carbonate petroleum reservoirs: a global perspective on porosity-depth and porosity-permeability relationships," *AAPG Bulletin*, vol. 89, no. 4, pp. 435–445, 2005.
- [49] K. Sampath and C. W. Keighin, "Factors affecting gas slippage in tight sandstones," *SPE/DOE Low Permeability Symposium*, *SPE*, vol. 9872, pp. 27–29, 1981.
- [50] F. A. Florence, J. Rushing, K. E. Newsham, and T. A. Blasingame, "Improved permeability prediction relations for low permeability sands," in *Rocky Mountain Oil & Gas Technology Symposium*, Denver, Colorado, U.S.A, April 2007.

Research Article

A Discrete Fracture Modeling Approach for Analysis of Coalbed Methane and Water Flow in a Fractured Coal Reservoir

Tianran Ma,^{1,2} Hao Xu,³ Chaobin Guo,⁴ Xuehai Fu¹ ,¹ Weiqun Liu,^{2,5} and Rui Yang^{2,5}

¹Key Laboratory of CBM Resources and Dynamic Accumulation Process, Ministry of Education, China University of Mining and Technology, Xuzhou, Jiangsu 221116, China

²School of Mechanics and Civil Engineering, China University of Mining and Technology, Xuzhou, Jiangsu 221116, China

³Lawrence Berkeley National Laboratory, Energy Geosciences Division, Berkeley, CA 94720, USA

⁴Chinese Academy of Geological Sciences, Beijing 100037, China

⁵State Key Laboratory Geomechanics and Deep Underground Engineering, China University of Mining and Technology, Xuzhou, Jiangsu 221116, China

Correspondence should be addressed to Xuehai Fu; fuxuehai@cumt.edu.cn

Received 16 March 2020; Revised 23 May 2020; Accepted 3 June 2020; Published 25 June 2020

Academic Editor: Wen-Dong Wang

Copyright © 2020 Tianran Ma et al. This is an open access article distributed under the Creative Commons Attribution License, which permits unrestricted use, distribution, and reproduction in any medium, provided the original work is properly cited.

As a complex two-phase flow in naturally fractured coal formations, the prediction and analysis of CBM production remain challenging. This study presents a discrete fracture approach to modeling coalbed methane (CBM) and water flow in fractured coal reservoirs, particularly the influence of fracture orientation, fracture density, gravity, and fracture skeleton on fluid transport. The discrete fracture model is first verified by two water-flooding cases with multi- and single-fracture configurations. The verified model is then used to simulate CBM production from a discrete fractured reservoir using four different fracture patterns. The results indicate that fluid behavior is significantly affected by orientation, density, and fracture connectivity. Finally, several cases are performed to investigate the influence of gravity and fracture skeleton. The simulation results show that gas migrates upwards to the top reservoir during fluid extraction owing to buoyancy and the connected fracture skeleton plays a dominant role in fluid transport and methane production efficiency. Overall, the developed discrete fracture model provides a powerful tool to study two-phase flow in fractured coal reservoirs.

1. Introduction

Coalbed methane (CBM) as a form of high-quality clean energy has attracted considerable interest for sustainable development in both industrial and academic realms [1, 2]. Although several countries (e.g., China, Australia, USA, and Canada) have achieved commercial CBM production from coal reservoirs, the prediction and analysis of CBM production remain challenging because of complex two-phase flow in naturally fractured coal formations [3–7].

Coal is typically composed of matrix and fractures [8, 9]. The matrix refers to the collection of pores of different scales including micropores, mesopores, and macropores [7, 8, 10, 11]. The fracture system comprises four types of fractures:

cleats, fracture swarms (or cracks/tertiary cleats), structure fractures (or faults), and hydraulic fractures [7]. Cleats refer to two sets of perpendicular fractures, called face and butt cleats. Fracture swarms and structure fractures refer to randomly distributed microfractures and large-scale fractures, respectively [7, 12–14]. Hydraulic fractures are artificial fractures induced by industrial injection activities called hydrofracturing [15–17]. The unique coal structure results in complex coupled fluid transport between matrix and fractures in a coal reservoir [18]. The coal matrix acts as a primary reservoir for CBM storage, although it has relatively low permeability and may even be impermeable. Large amounts of CBM are adsorbed on the inner surface of the coal matrix [19]. The fracture system provides a primary

pathway for the migration of CBM and water through underground coal reservoirs. Storage and transfer of fluid are the essential properties of fractured coal reservoirs and are described by adsorption/absorption and diffusion and seepage models, respectively.

The complexity of pores and fracture networks complicates in situ analysis of water and methane transport, which introduces errors into the evaluation of methane production performance. Hence, the analysis of flow in fractured porous media is of great importance in fluid flow and thus methane production [20, 21]. A series of conceptual and numerical models across multiple scales has been developed and proposed to clarify transport mechanisms [22–29]. In general, fluid in fractured porous media is approached with two conceptual models, which are continuum models and discrete fracture-matrix (DFM) models. In continuum models, fractures are represented implicitly in fractured porous media. The equivalent properties are calculated with crack tensor theory [30, 31], in which orientation, size, and aperture of fractures are considered. This type of upscaling technique is widely used for large-scale simulation, especially for the reservoirs with dense fracture networks. Generally, coal is treated as a structure with a single porosity and single permeability (SPSP), dual porosity and single permeability (DPSP), dual porosity and dual permeability (DPDP), or even triple porosity and dual permeability (TPDP) [29, 32–36], in which matrix and fractures overlap. The representative elementary volume (REV) inside the reservoir is assumed to simultaneously satisfy the flow mass balance equations of matrix and fractures. The aforementioned methods use a continuum model or equivalent porous media for modeling fractured rocks or coal rock. Several well-known reservoir simulators, including ECLIPSE [37], CMG [38], COMET2 [39], and TOUGH2 [40], utilize the continuum models. Considering the dominant role of fractures in fluid transport, an alternative conceptual discrete fracture model has been proposed where the matrix is assumed to be impermeable and fluid processes are controlled by the fracture network [41]. In the discrete fracture model, the fractures are described explicitly by lower-dimensional lines or interface, which has the advantage of mesh generation and thus reduces the computational time greatly. In light of the mass exchange between matrix and fracture, a single-phase discrete fracture-matrix model has been developed to investigate the influence of adsorbed and free gas and fracture networks on gas production [42]. In this model, flow behavior of fluid occurs in both fracture and surrounding matrix system.

In this paper, we first develop a mathematical model to simulate water and methane flow through fractured coal reservoirs. Two water-flooding cases containing multiple fractures and a single fracture are then simulated to verify the accuracy of the proposed model. We then test four cases with multifracture configurations to investigate the influence of fracture orientation and distribution pattern on fluid behavior and methane production performance. Finally, we carried out several simulation cases with discrete fracture networks to investigate the effects of gravity and connectivity on fluid transport.

2. Governing Equations

2.1. Water and CBM Flow in Porous Media. In the mathematical model presented here, the coal reservoir is assumed to be saturated with methane and water in gas and aqueous phases, respectively. Hence, the sum of the saturated gas (nonwetting) phase S_{mg} and wetting (water) phase S_{mw} is equal to 1. Moreover, the model assumes that methane adsorbed on the coal grain surface diffuses instantaneously into the pores. Thus, the methane mass in the matrix system consists of free and adsorbed phases. The general mass balance equations for immiscible-phase (water and gas) flow in the coal reservoir matrix are given by gas phase pressure p_{mg} and water saturation S_{mw} , where the velocity of each phase v_α is described by Darcy's law. The governing equations for water and methane are described as follows.

$$\phi_m \rho_{mw} S_{mw} C_{mw} \frac{\partial p_{mg}}{\partial t} + \left(\phi_m \rho_{mw} - \phi_m \rho_{mw} S_{mw} C_{mw} \frac{\partial p_{mc}}{\partial S_{mw}} \right) \frac{\partial S_{mw}}{\partial t} + \nabla \cdot \left(-\rho_{mw} \frac{K_m k_{mrw}}{\mu_{mw}} \left(\nabla p_{mg} - \frac{\partial p_{mc}}{\partial S_{mw}} \nabla S_{mw} + \rho_{mw} \mathbf{g} \right) \right) = 0, \quad (1)$$

$$\left(\phi_m \rho_{mg} S_{mg} C_{mg} + \rho_{mc} \frac{V_{mL} p_{mL}}{(p_{mg} + p_{mL})^2} \right) \frac{\partial p_{mg}}{\partial t} - \phi_m \rho_{mg} \frac{\partial S_{mw}}{\partial t} + \nabla \cdot \left(-\rho_{mg} \frac{K_m k_{mrg}}{\mu_{mg}} \left(\nabla p_{mg} + \rho_{mg} \mathbf{g} \right) \right) = 0, \quad (2)$$

where K_m is the absolute permeability of the matrix, k_{mrw} and k_{mrg} are the relative permeabilities of the water and gas phase, respectively, p_{mw} is the water pressure, $\rho_{m\alpha}$ is the density of each phase ($\alpha = w$ and g refer to water and methane, resp.), which is calculated by $1/C_m (d\rho_{m\alpha}/dp_{m\alpha})$ [14], $C_{m\alpha}$ is the fluid compressibility, V_{mL} is the Langmuir volume constant, p_{mL} is the Langmuir pressure, ρ_{mc} is the density of the coal matrix, and ϕ_m is the porosity of the matrix system. The capillary pressure p_{mc} is the pressure difference between these two immiscible fluids, given as

$$p_{mc} = p_{mg} - p_{mw}. \quad (3)$$

2.2. Water and CBM Flow in Fractures. In this study, we represent fractures in the coal reservoir as low-dimensional grid cells [26]. Fractures are described as two-dimensional interfaces and one-dimensional lines in a three-dimensional or two-dimensional domain, respectively. A two-dimensional domain contains discontinuous fractures, as shown in Figure 1. The total simulation space Ω is decomposed into

$$\Omega = \Omega_m + \Omega_f = \Omega_m + \sum_{i=0}^n d_{fi} \Omega_{fi}, \quad (4)$$

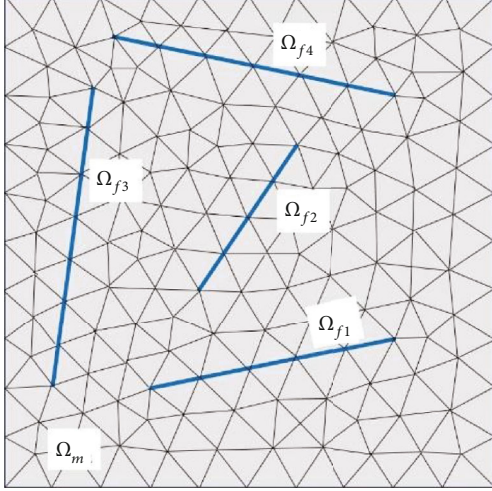


FIGURE 1: Schematic of the matrix Ω_m and fractures $\Omega_{f1} \sim \Omega_{f4}$ subdomains.

where Ω_m and Ω_f represent the matrix and fracture domains, respectively, d_{fi} is the fracture aperture of i^{th} fracture subdomain Ω_{fi} , and n is the total number of fractures.

We assume pressure continuity across the whole model space, which means the gas pressure, water pressure, and capillary pressure are the same for the matrix and fracture grids, which means that the jump of pressure and saturation on the interface of matrix and fracture are not considered in this work. The equations for methane and water flow through fractures are expressed as

$$d_f \phi_f \rho_{fw} S_{fw} C_{fw} \frac{\partial p_{fg}}{\partial t} + d_f \left(\phi_f \rho_{fw} - \phi_f \rho_{fw} S_{fw} C_{fw} \frac{\partial p_{fc}}{\partial S_{fw}} \right) \frac{\partial S_{fw}}{\partial t} + \nabla_\tau \cdot \left(-d_f \rho_{fw} \frac{K_f k_{frw}}{\mu_{fw}} \left(\nabla_\tau p_{fg} - \frac{\partial p_{fc}}{\partial S_{fw}} \nabla_\tau S_{fw} + \rho_{fw} \mathbf{g} \right) \right) = 0, \quad (5)$$

$$d_f \left(\phi_f \rho_{fg} S_{fg} C_{fg} + \rho_{fc} \frac{V_{fL} P_{fL}}{(p_{fg} + p_{fL})^2} \right) \frac{\partial p_{fg}}{\partial t} - d_f \phi_f \rho_{fg} \frac{\partial S_{fw}}{\partial t} + \nabla_\tau \cdot \left(-d_f \rho_{fg} \frac{K_f k_{frg}}{\mu_{fg}} \left(\nabla_\tau p_{fg} + \rho_{fg} \mathbf{g} \right) \right) = 0, \quad (6)$$

where d_f is the fracture aperture or thickness. The variables in equations (3)–(6) have the same physical characteristics and subscripted m and f represent these variables inside the matrix and fracture system, respectively. We demonstrate the detailed process of the weak form of equation (5). All items in equation (5) are first moved to the right-hand side, and both sides are multiplied by the test function for wetting

saturation \widetilde{S}_{fw} , integrating over the simulation domain Ω_f :

$$0 = - \int_{\Omega_f} \left[d_f \phi_f \rho_{fw} S_{fw} C_{fw} \frac{\partial p_{fg}}{\partial t} + d_f \left(\phi_f \rho_{fw} - \phi_f \rho_{fw} S_{fw} C_{fw} \frac{\partial p_{fc}}{\partial S_{fw}} \right) \frac{\partial S_{fw}}{\partial t} \right] \widetilde{S}_{fw} d\Omega_f - \int_{\Omega_f} \nabla_\tau \cdot \left(-d_f \rho_{fw} \frac{K_f k_{frw}}{\mu_{fw}} \left(\nabla_\tau p_{fg} - \frac{\partial p_{fc}}{\partial S_{fw}} \nabla_\tau S_{fw} + \rho_{fw} \mathbf{g} \right) \right) \widetilde{S}_{fw} d\Omega_f. \quad (7)$$

According to Green's first identity and divergence theorem, the third part of the right side in equation (7) is then expressed as

$$\int_{\Omega_f} \nabla \cdot \left(-d_f \rho_{fw} \frac{K_f k_{frw}}{\mu_{fw}} \left(\nabla_\tau p_{fg} - \frac{\partial p_{fc}}{\partial S_{fw}} \nabla_\tau S_{fw} + \rho_{fw} \mathbf{g} \right) \right) \widetilde{S}_{fw} d\Omega_f = \int_n \left[-d_f \rho_{fw} \frac{K_f k_{frw}}{\mu_{fw}} \left(\nabla_\tau p_{fg} - \frac{\partial p_{fc}}{\partial S_{fw}} \nabla_\tau S_{fw} + \rho_{fw} \mathbf{g} \right) \right] \cdot \mathbf{n} \widetilde{S}_{fw} dn - \int_{\Omega_f} \nabla_\tau \widetilde{S}_{fw} \cdot \left(-d_f \rho_{fw} \frac{K_f k_{frw}}{\mu_{fw}} \left(\nabla_\tau p_{fg} - \frac{\partial p_{fc}}{\partial S_{fw}} \nabla_\tau S_{fw} + \rho_{fw} \mathbf{g} \right) \right) d\Omega_f. \quad (8)$$

Finally, equation (8) is rearranged and the governing equation is obtained as

$$0 = - \left[d_f \phi_f \rho_{fw} S_{fw} C_{fw} \frac{\partial p_{fg}}{\partial t} + d_f \left(\phi_f \rho_{fw} - \phi_f \rho_{fw} S_{fw} C_{fw} \frac{\partial p_{fc}}{\partial S_{fw}} \right) \frac{\partial S_{fw}}{\partial t} \right] \widetilde{S}_{fw} d\Omega_f - \int_n \left[-d_f \rho_{fw} \frac{K_f k_{frw}}{\mu_{fw}} \left(\nabla_\tau p_{fg} - \frac{\partial p_{fc}}{\partial S_{fw}} \nabla_\tau S_{fw} + \rho_{fw} \mathbf{g} \right) \right] \cdot \mathbf{n} \widetilde{S}_{fw} dn + \int_{\Omega_f} \nabla_\tau \widetilde{S}_{fw} \cdot \left(-d_f \rho_{fw} \frac{K_f k_{frw}}{\mu_{fw}} \left(\nabla_\tau p_{fg} - \frac{\partial p_{fc}}{\partial S_{fw}} \nabla_\tau S_{fw} + \rho_{fw} \mathbf{g} \right) \right) d\Omega_f. \quad (9)$$

Similarly, we can obtain the weak expression for the water flow equation by multiplying equation (6) by the test function for water pressure \widetilde{p}_{fg} , integrating over the simulation domain Ω_f , and applying Green's first identity and divergence theorem as

$$0 = \int_{\Omega_f} -d_f \left(\phi_f \rho_{fg} S_{fg} C_{fg} + \rho_{fc} \frac{V_{fL} P_{fL}}{(p_{fg} + p_{fL})^2} \right) \frac{\partial p_{fg}}{\partial t} \widetilde{p}_{fg} + d_f \phi_f \rho_{fg} \frac{\partial S_{fw}}{\partial t} \widetilde{p}_{fg} d\Omega_f - \int_n \left[-d_f \rho_{fg} \frac{K_f k_{frg}}{\mu_{fg}} \left(\nabla_\tau p_{fg} + \rho_{fg} \mathbf{g} \right) \right] \cdot \mathbf{n} \widetilde{p}_{fg} dn + \int_{\Omega_f} \nabla_\tau \widetilde{p}_{fg} \cdot \left(-d_f \rho_{fg} \frac{K_f k_{frg}}{\mu_{fg}} \left(\nabla_\tau p_{fg} + \rho_{fg} \mathbf{g} \right) \right) d\Omega_f. \quad (10)$$

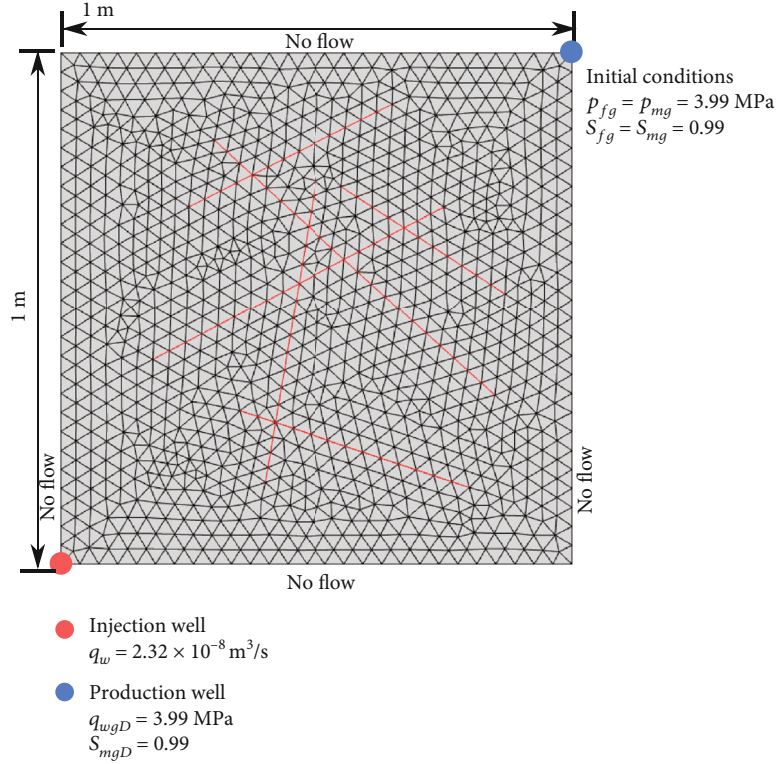


FIGURE 2: Scheme depicting geometry, mesh boundary, and initial conditions of the simulation model.

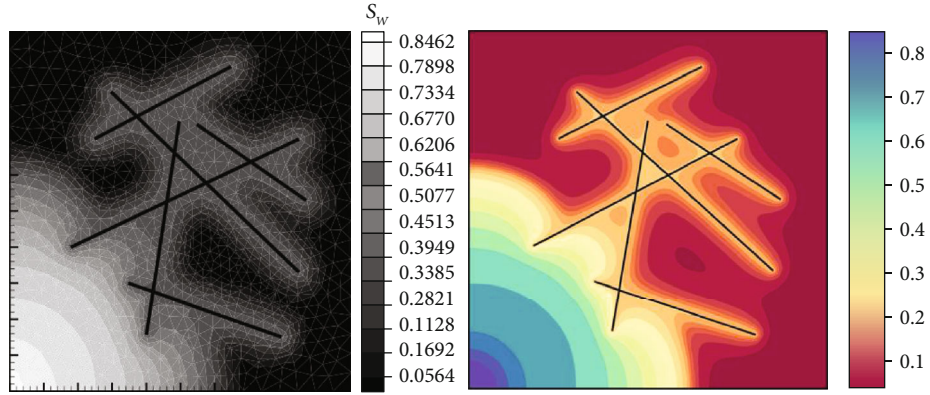


FIGURE 3: Distribution of water saturation after 25 days of water injection into a reservoir initially saturated with oil. Previous modeling results²² and our simulation results are displayed on (a) and (b), respectively.

Equations (9) and (10) are referred to as the weak forms of water and CBM mass balance equations.

To solve equations (1), (2), (9), and (10), the auxiliary equations of capillary pressure, $p_{\beta c}$, gas and water relative permeability of the nonwetting $k_{\beta rg}$ and wetting $k_{\beta rw}$ phases are adopted as follows⁵:

$$\begin{aligned} p_{\beta c} &= p_{\beta c} (S_{\beta e})^{-1/\lambda_{\beta}} \\ k_{\beta rg} &= (1 - S_{\beta e})^2 (1 - S_{\beta e}^2), \\ k_{\beta rw} &= \sqrt{S_{\beta e}} \left\{ 1 - (1 - S_{\beta e}^{-1/m_{\beta}})^{m_{\beta}} \right\}^2, \end{aligned} \quad (11)$$

where $\beta = f$ and m refer to variables inside the fracture and matrix systems, respectively, $p_{\beta c}$ is the entry pressure, and λ_{β} and m_{β} are coefficients determined by laboratory experiments. The effective saturation $S_{\beta e}$ is defined as

$$S_{\beta e} = \frac{S_{\beta w} - S_{\beta wr}}{1 - S_{\beta wr} - S_{\beta gr}}, \quad (12)$$

where $S_{\beta wr}$ and $S_{\beta gr}$ represent the residual saturations of the water and gas, respectively.

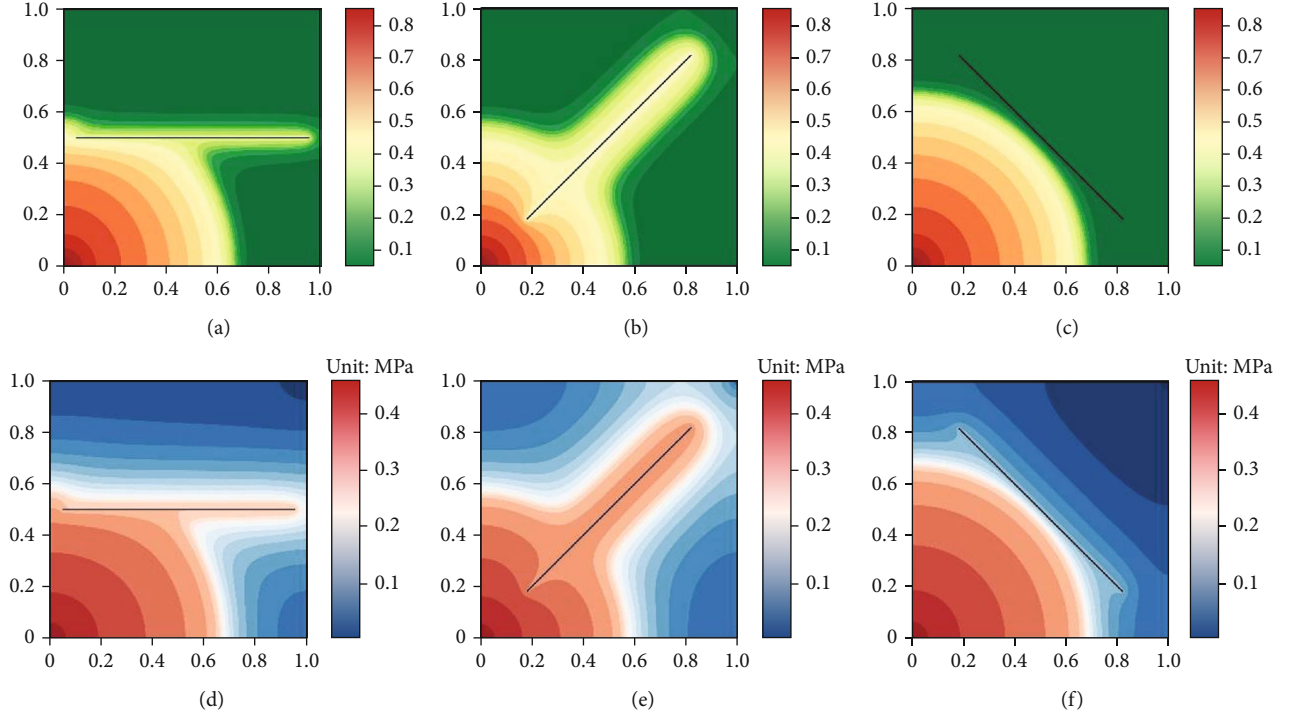


FIGURE 4: Spatial distribution of (a–c) saturation and (d–f) pressure after 50 days of water injection with different fracture orientations.

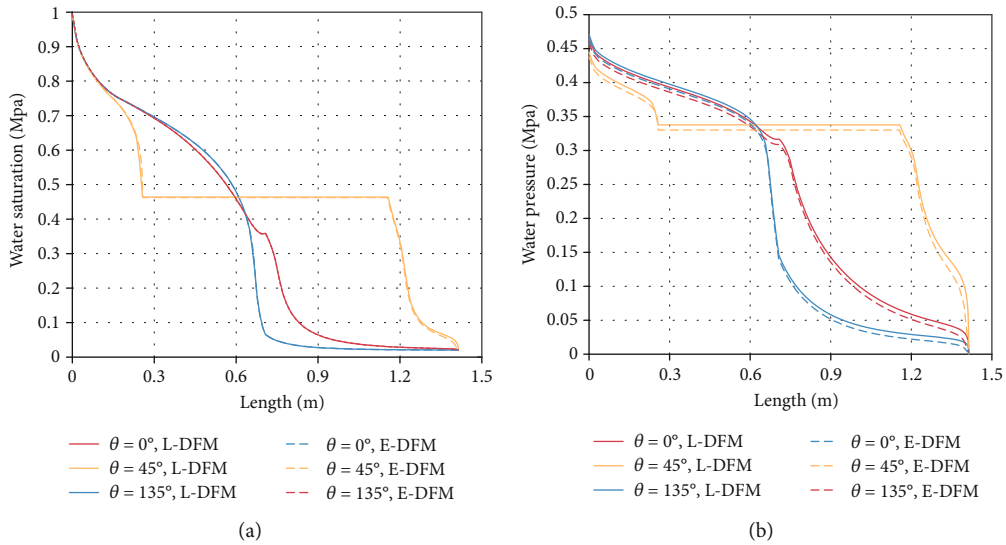


FIGURE 5: Comparisons of water saturation and pressure along the diagonal line from the injection well to the production well after 50 days of water injection with L-DFM and E-DFM.

The initial condition for the gas pressure and water saturation is

$$\begin{aligned} p_{\beta g}(t=0) &= p_{\beta g0}, \text{ in } \Omega, \\ S_{\beta w}(t=0) &= S_{\beta w0}, \text{ in } \Omega. \end{aligned} \quad (13)$$

As boundary conditions, the two-phase flow can have the following.

The Dirichlet boundary conditions for the gas pressure and water saturation are given as

$$\begin{aligned} p_{\beta g} \Big|_{\Gamma} &= P_{\beta gD}, \\ S_{\beta w} \Big|_{\Gamma} &= S_{\beta wD}. \end{aligned} \quad (14)$$

The flux conditions, called as natural boundary

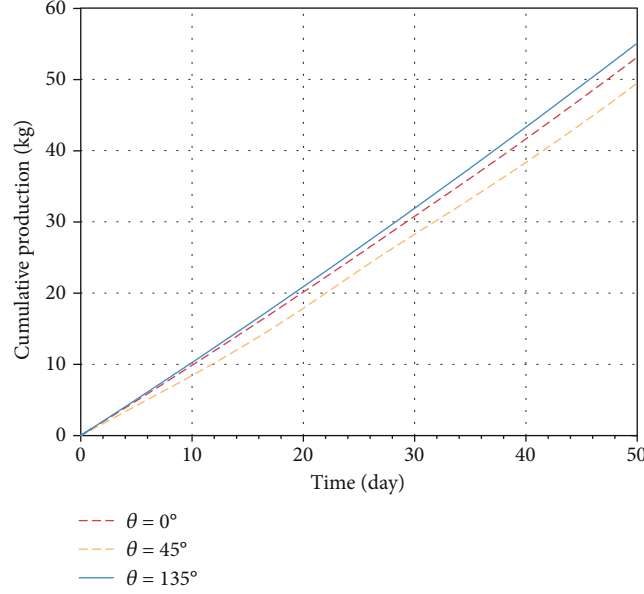


FIGURE 6: Cumulative production with different fracture orientations.

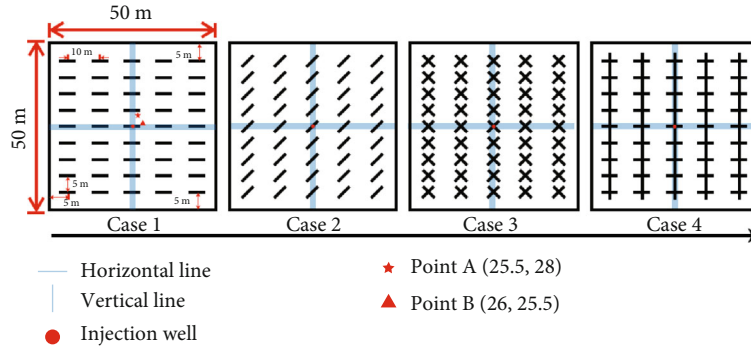


FIGURE 7: Model domain, fracture configuration, monitoring lines, and points for four cases. In cases 1 and 2, 45 fractures uniformly distributed through the entire coal reservoir are aligned at orientations of $\theta = 0^\circ$ and 45° , respectively, and cases 3 and 4 contain two sets of orthogonal fractures with angles $\theta = 45^\circ$ and -45° and $\theta = 0^\circ$ and 90° , respectively.

conditions, which are included in the weak form of two-phase equations

$$\begin{aligned} \rho_{\beta g} \mathbf{V}_g \cdot \mathbf{n} \Big|_{\Gamma} &= q_g, \\ \rho_{\beta w} \mathbf{V}_w \cdot \mathbf{n} \Big|_{\Gamma} &= q_w. \end{aligned} \quad (15)$$

3. Model Verification

We solve the above equations with the finite element software COMSOL. The equations of flow mass balance in the matrix are implemented with equations (1) and (2) using the partial differential equation (PDE) interface. The two immiscible phase flow in fractures with equations (9) and (10) are implemented with a weak contribution module. We then test two configurations of water flooding in an oil reservoir to investigate the accuracy of the model and numer-

ical solution proposed in the paper. Two cases with different fracture configurations are adopted as follows.

(1) *Multifracture Case.* Figure 2 depicts the model geometry and mesh scheme. In this case, water is injected into a fractured porous medium with six fractures for 25 days. Detailed information of these fractures is provided in the references [26].

(2) *Single-Fracture Case.* In the simulation region, a single fracture with an arbitrary angle is modeled. Simulations were performed with three fracture orientations $\theta = 0^\circ, 45^\circ$, and 135° to investigate the influence of fracture angle on flow behavior. The simulation time was 50 days.

The model regions in the two configurations are $1 \text{ m} \times 1 \text{ m}$. The domain is initially nearly saturated with oil. The porosity and permeability of matrix are 0.20 and $9.87 \times 10^{-16} \text{ m}^2$ (1 millidarcy), respectively. The fracture porosity

TABLE 1: Simulation parameters for water-flooding cases.

Parameters	Value	Unit
Simulation area	50×50	m^2
Permeability of fracture, K_f	1.00×10^{-10}	m^2
Porosity of fracture, ϕ_f	1.00	
Fracture aperture, d_f	1.00×10^{-4}	m
Permeability of matrix, K_m	1.00×10^{-16}	m^2
Porosity of matrix, ϕ_m	0.20	
Initial reservoir pressure, p_{fg} and p_{mg}	1000	Pa
Initial water saturation, S_{fg} and S_{mg}	0.70	
Entry capillary pressure, p_{fe} and p_{me}	0.10	MPa
Initial residual water saturation	0.00	
Initial residual nonwetting saturation	0.00	
Viscosity of water, μ_{fw} and μ_{mw}	10^{-3}	Pa·s
Viscosity of nonwetting phase, μ_{fg} and μ_{mg}	1.84×10^{-5}	Pa·s
Density of water, ρ_{fw} and ρ_{mw}	1000	kg/m^3
Density of nonwetting phase, ρ_{fg} and ρ_{mg}	0.864	kg/m^3

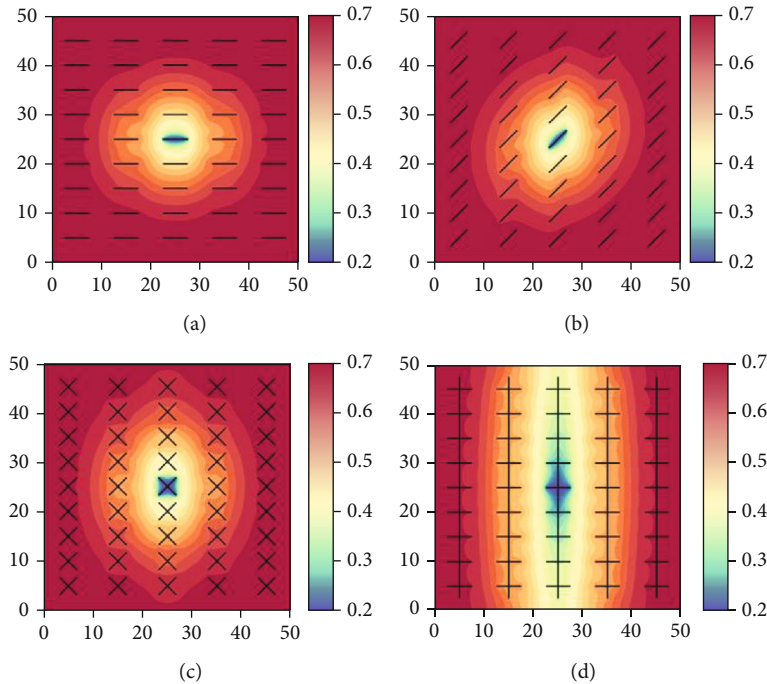


FIGURE 8: Spatial distribution of water saturation after 100 days of production for different fracture patterns.

is 1. All fractures in the domain are assumed to have the same aperture of 1.00×10^{-4} m. Based on the cubic law, the corresponding permeability of the fractures is $8.33 \times 10^{-10} \text{ m}^2$. The density and viscosity of the wetting phase are $1000 \text{ kg}/\text{m}^3$ and $1 \times 10^{-3} \text{ Pa} \cdot \text{s}$, respectively. The density and viscosity of the nonwetting phase are $600 \text{ kg}/\text{m}^3$ and $0.45 \times 10^{-3} \text{ Pa} \cdot \text{s}$. Fluid compressibility is neglected for both phases, which is justifiable because flow velocities are very small. The

injection and production wells are located in the lower left and upper right corners. Water is injected into the fractured porous media at a constant rate of $2.32 \times 10^{-8} \text{ m}^3/\text{s}$. The initial pressure and nonwetting phase saturation are set to 3.99 MPa and 0.99 , respectively.

Pointwise constraints are applied at the production well with constant pressure and saturation. All boundaries are impermeable. The capillary pressure p_c and relative

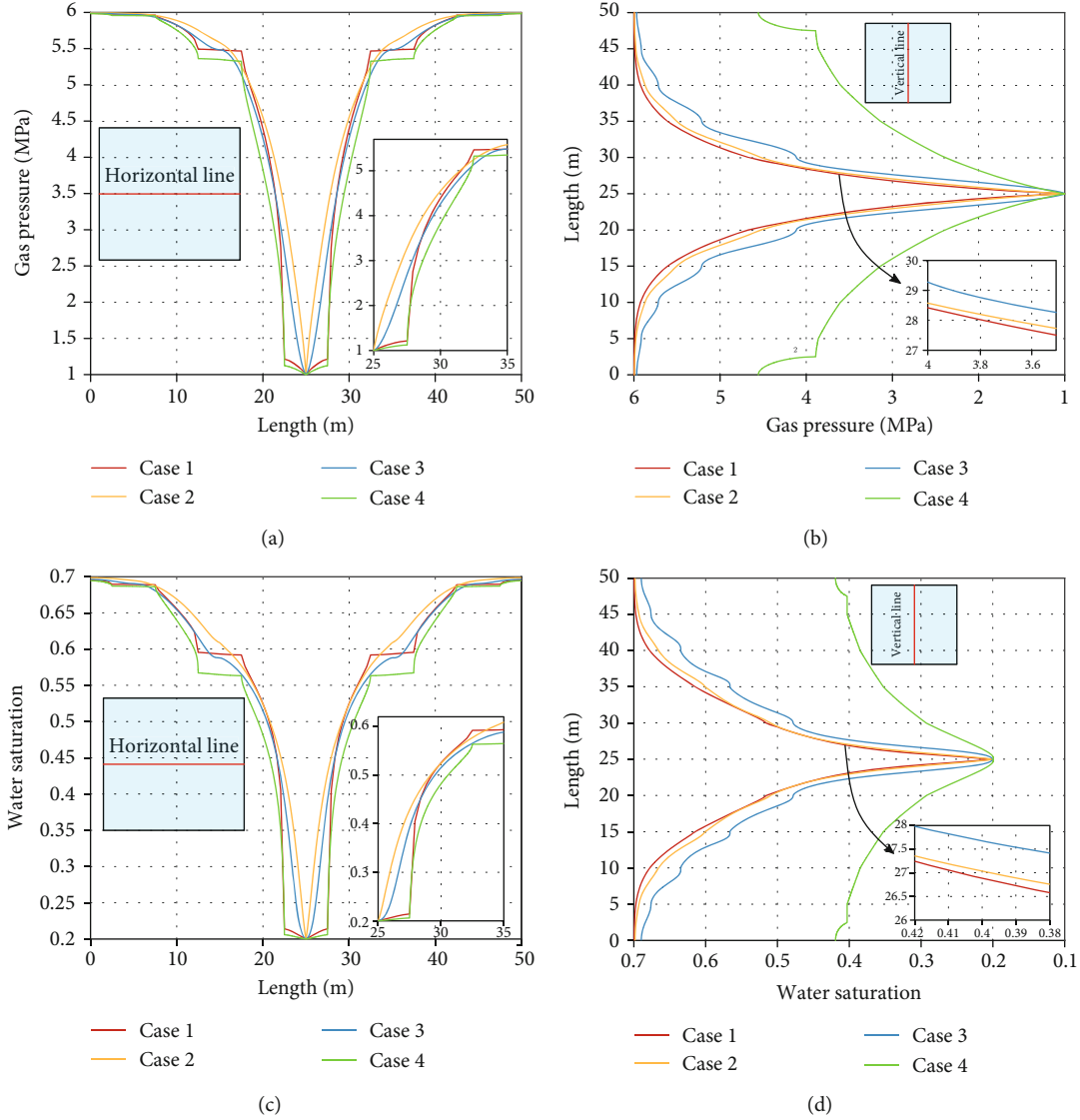


FIGURE 9: (a, b) Gas pressure and (c, d) water saturation along the horizontal and vertical lines, respectively, after 250 days of production in the four cases.

permeability of water k_{rw} and oil k_{rn} are described as a function of water saturation S_w , shown as [26, 43]

$$\begin{aligned} p_c &= -B \log(S_w), \\ k_{rw} &= S_w^2, \\ k_{rn} &= (1 - S_w)^2, \end{aligned} \quad (16)$$

where the parameter B in the matrix and fracture is equal to 1 atm.

The spatial distribution of water saturation after 25 days of water injection into a nearly saturated oil reservoir is shown in Figure 3. A good match is achieved between reference models and our simulation results, which demonstrates the accuracy of the proposed model.

Figure 4 shows the spatial distribution of water saturation and gas pressure after 50 days of water injection with differ-

ent fracture angles. The results obtained from the numerical simulations are in good agreement with reference studies^{22,41}. Comparisons of water saturation and pressure along the diagonal line from the injection well to the production well after 50 days of water injection with low-dimensional discrete fracture model (L-DFM) and equidimensional discrete fracture model (E-DFM) are shown in Figure 5. It can be seen that the result of L-DFM is in good agreement with the result of E-DFM, which indicates that the L-DFM proposed in the paper can accurately simulate the two-phase flow in fractured porous media. For the large absolute permeability of a fracture, the fluid preferentially propagates into the reservoir through the fracture and causes significant pressure changes. A steady-state flow along the fracture is observed in the case with fracture angle $\theta = 45^\circ$ (blue lines in Figure 5). The simulation results illustrate that the fluid flow behavior is largely controlled by the angles of the fractures.

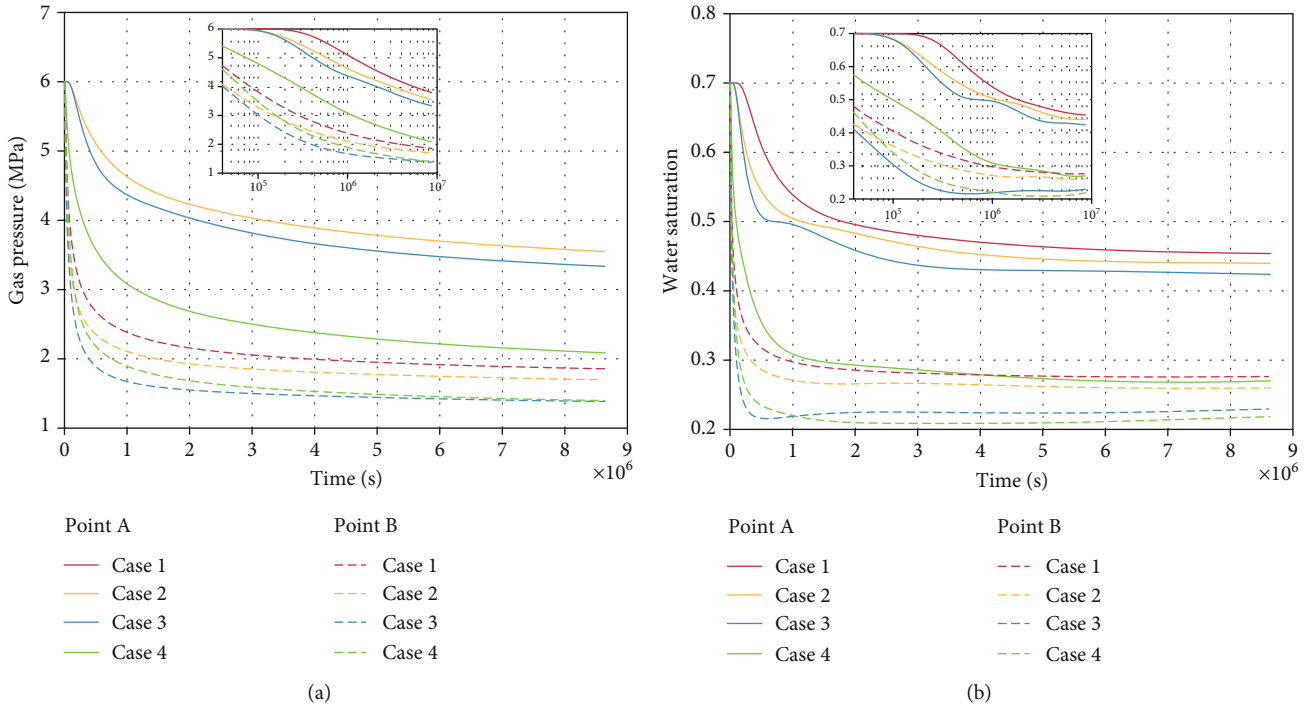


FIGURE 10: Temporal evolution of (a) gas pressure and (b) water saturation at points A and B for the four cases. Solid and dashed lines represent the results at points A and B, respectively.

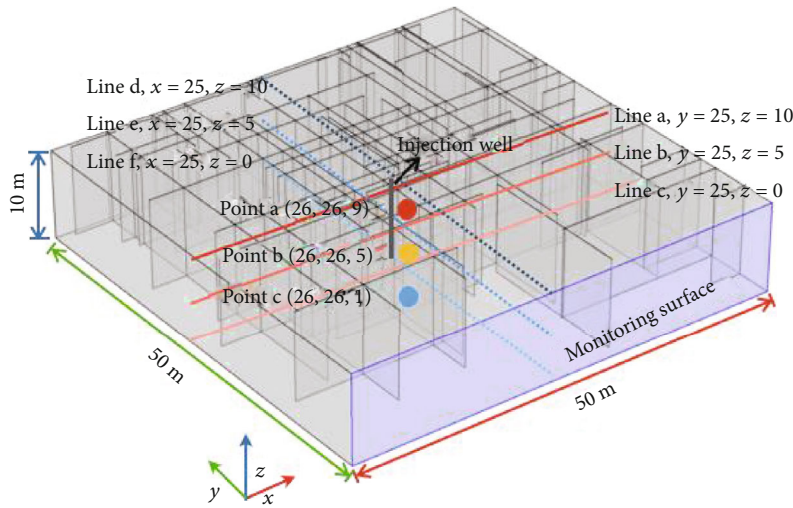


FIGURE 11: Scheme depicting model domain, fracture configuration, monitoring surface, lines, and points for the three-dimensional cases.

The curves for oil cumulative production with different fracture orientations are shown in Figure 6. The cumulative production is the lowest in the case with fracture angle $\theta = 45^\circ$, which can be explained by the fact that injected water prefers to migrate aligned with fracture orientation, and thus, less oil is pushed out of the reservoir by water injection.

4. Simulation Cases

4.1. *CBM Production from Discrete Fractured Reservoirs.* In this section, we introduce the four cases with different pat-

terns (Figure 7) that were tested to investigate the influence of fractures on flow fluid behavior and methane production. In the first two cases, 45 parallel fractures are uniformly distributed through the entire coal reservoir at orientations of $\theta = 0^\circ$ and 45° , respectively. In the third and fourth cases, there are two sets of orthogonal fractures with angles $\theta = 45^\circ$ and -45° and $\theta = 0^\circ$ and 90° , respectively. The simulation domain is 50×50 m, in which the aperture and length of all the fractures are assumed to be 10^{-4} m and 5 m. The production well is located at the center of the simulation model with a constant gas pressure of 1 MPa and water saturation of 0.2.

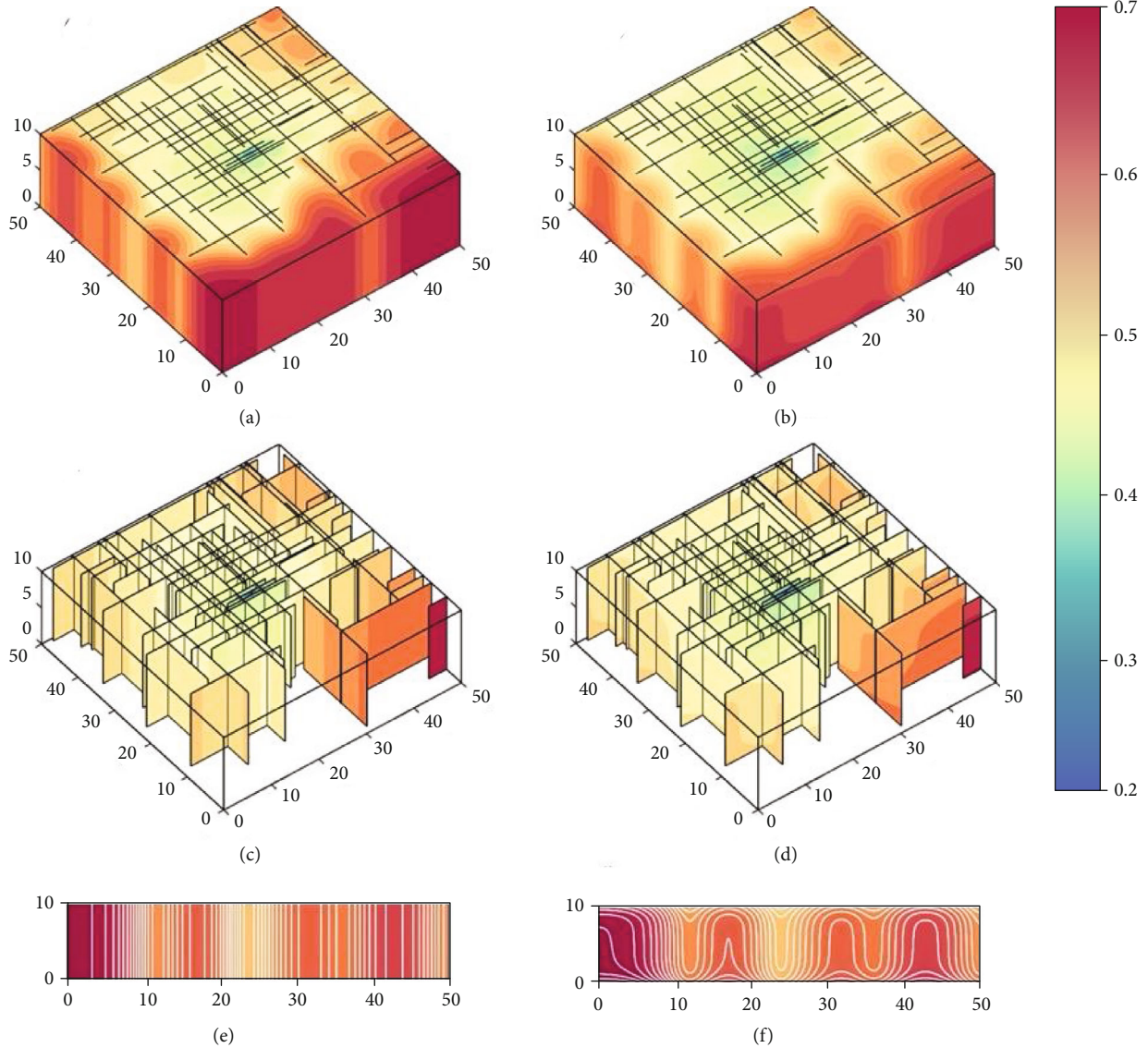


FIGURE 12: Water saturation after 50 days of production from the three-dimensional model with randomly distributed fractures. The results for case 2 with consideration of gravity are shown in (b), (d), and (f).

The initial gas pressure and water saturation are 6 MPa and 0.7, respectively. The total simulation time is 100 days. The surrounding boundaries are set to no flow. Other simulation parameters are listed in Table 1.

Figure 8 shows the spatial distributions of water saturation after 100 days of production for the four cases with different fracture configurations. The simulation results show that fracture geometry has a critical influence on flow path. Figure 9 shows the gas pressure and water saturation along the vertical and horizontal lines. During production, the water saturation and gas pressure decrease from the outer lateral boundaries to the production well. The speed of saturation and pressure front extraction from the coal seam differ for the four cases. In case 4, the pressure and saturation along the lines are lower than the initial conditions, which signify that drainage has approached the surrounding boundaries.

The temporal evolution of gas pressure and water saturation at points A and B is shown in Figure 10. A decrease in

pore pressure and saturation is observed in the early stage of all cases because of the pressure and saturation drawdown at the production well. The water saturation and gas pressure in cases 3 and 4 are lower than those in cases 1 and 2 likely owing to the increased density (or number) of fractures, which enhances the overall reservoir permeability and fluid velocity. In case 4, the fractures in the vertical direction coincidentally connect to form a long fracture with a length of 45 m. Fluid migration is the fastest in case 4, which demonstrates that fracture connectivity dominantly impacts fluid transport and production efficiency.

4.2. Sensitive Analysis

4.2.1. Effect of Gravity. In this section, we set up two simulation cases with three-dimensional models that consider two sets of orthogonal fractures with angles $\theta = 0^\circ$ and 90° . The model geometry is shown in Figure 11. The apertures of the

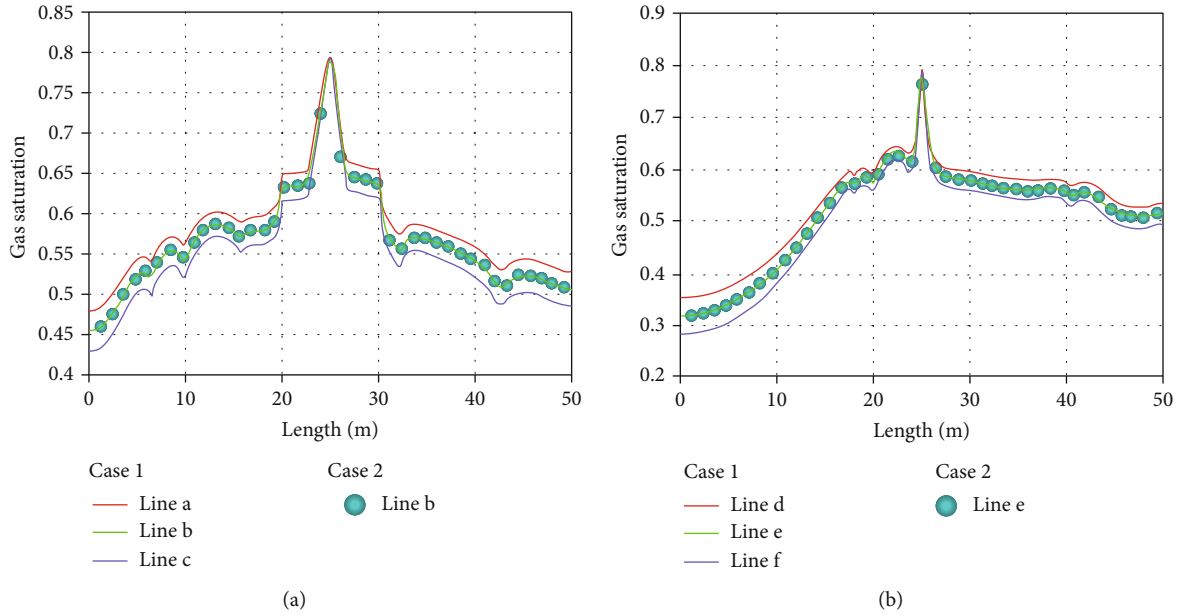


FIGURE 13: Gas saturation along the lines in the (a) x - and (b) y -directions after 50 days of production.

whole fractures is assumed to be 10^{-4} m. The length and position of the two sets of fractures are randomly distributed in the simulation domain. Two simulation cases are performed to investigate the effect of gravity on fluid migration. Gravity is neglected in case 1 and considered in case 2. In these simulations, the coal height is 10 m and the simulation time is 50 days. Other settings and parameters are the same as those in Section 4.1.

Figure 12 shows the spatial distribution of water saturation of the whole domain (Figures 12(a) and 12(b)), inner surfaces of fractures (Figures 12(c) and 12(d)), and surface monitoring after 50 days of production in the three-dimensional reservoir with randomly distributed fractures (Figure 12(d)). The water saturation in the reservoir decreases extensively during drainage gas production. Without considering gravity, the water saturation is uniformly distributed in the vertical direction, whereas a nonuniform saturation distribution is observed along the fractures and monitoring surface in case 2. Gas saturation after 50 days of production along lines in the x - and y -directions is shown in Figure 13. The gas saturation exhibits a “wave-type” reduction from the wellbore to the lateral boundaries. Gas saturation along lines d, e, and f in the y -direction is smoother than that along lines a, b, and c in the x -direction because of fewer fractures cross the y -direction lines. The gas saturation is the largest along the upper lines (a, d) and lowest along lower lines (c, f) as a result of the buoyancy effect.

Figure 14 shows the temporal evolution of gas saturation at point b in case 1 and points a, b, and c in case 2. The gas saturation increases rapidly in a relatively short time as a result of continuous dewatering. Gas continues to migrate upwards, which causes more gas to gather at the top reservoir surface during production (Figures 13 and 14).

4.2.2. Effect of Fracture Skeleton. This section carries our several cases to study the influence of fracture skeleton on the

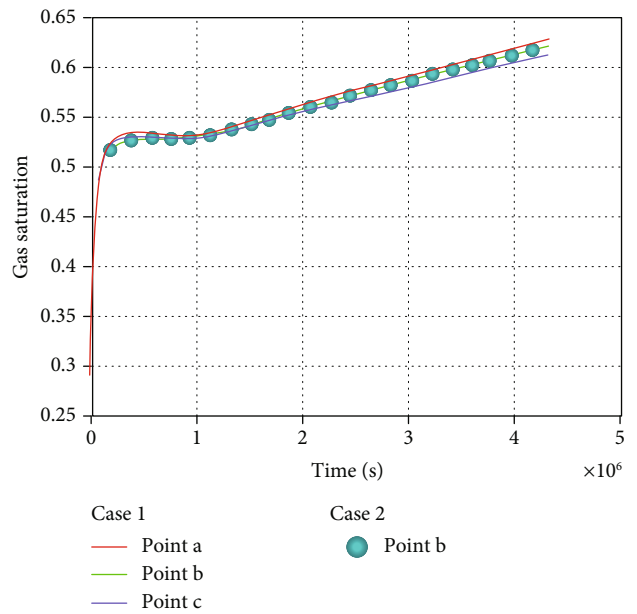


FIGURE 14: Temporal evolution of gas saturation at point b in case 1 and points a, b, and c in case 2.

migration path of fluid. The discrete fracture network is generated by the open source tool DFNE [44]. Two sets of fractures are oriented of 45 and 135 degrees in a 10 m \times 10 m coal reservoir. Each set of fractures has 40 individual fractures. The minimum and maximum lengths of fracture lines are 1 and 7 m, respectively. Then, disconnected and isolated fractures are removed to investigate the effect of fracture skeleton. The original fracture network (Case a) and a connected fracture skeleton after processing (Case b) are shown in Figure 15. The total simulation is 2.0×10^4 s and other parameters are listed in Table 1.

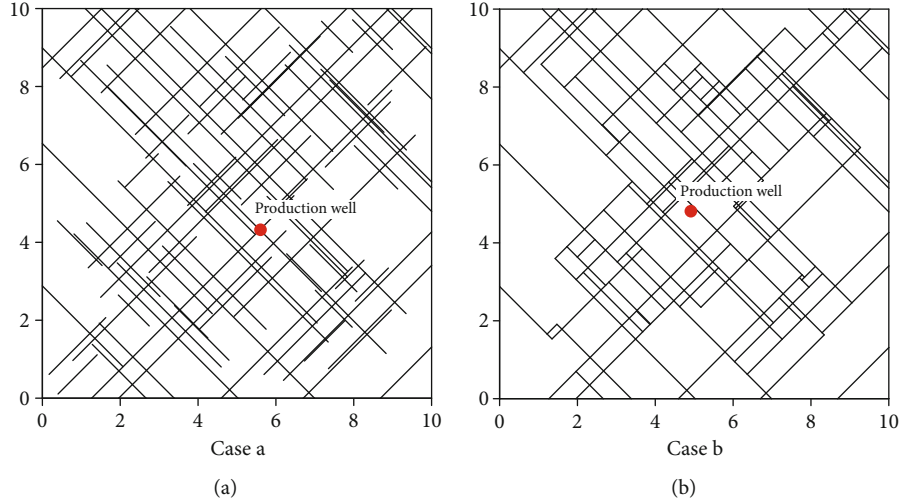


FIGURE 15: The original fracture network (Case a) and connected fracture skeleton (Case b).

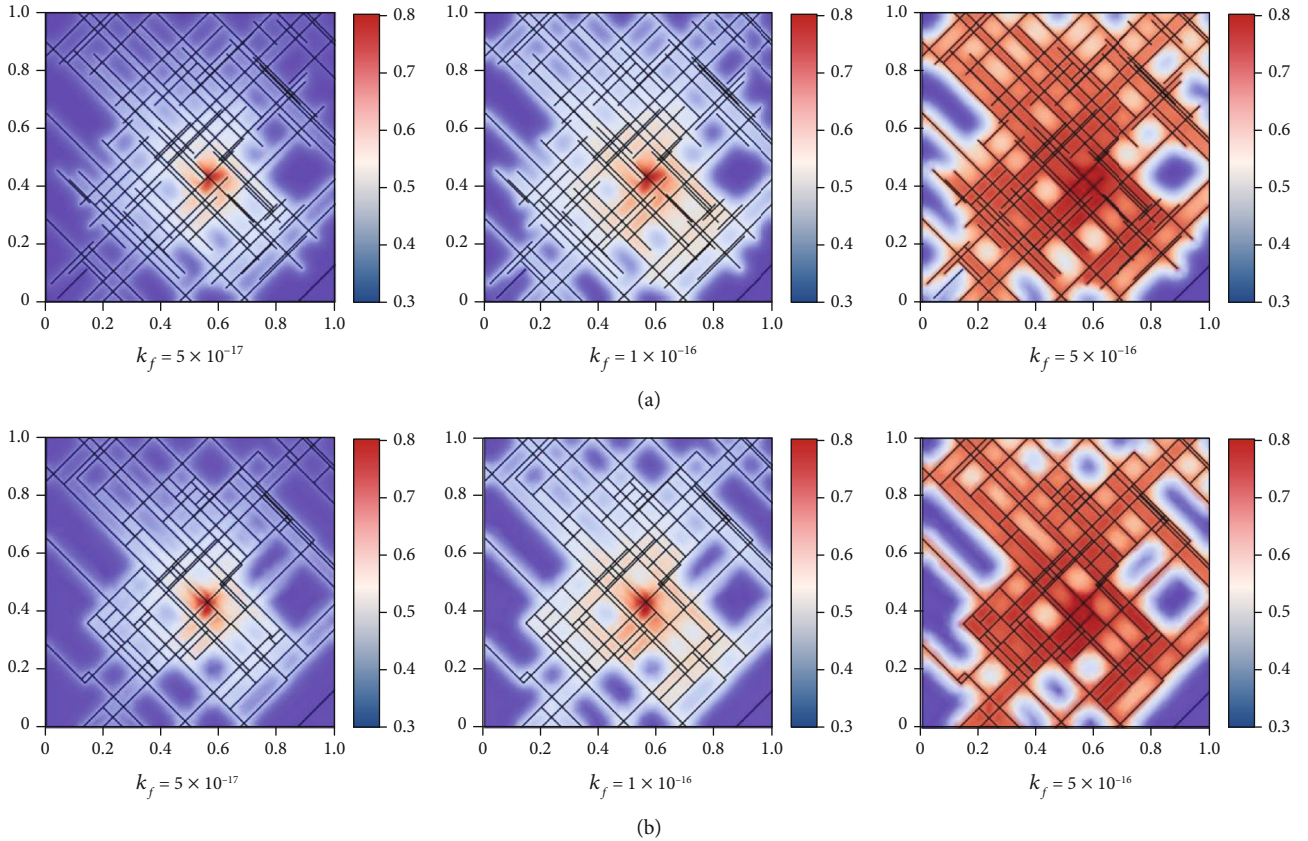


FIGURE 16: The spatial distribution of methane saturation after 2.0×10^5 s in Case a and Case b with different fracture permeabilities of $k_f = 5.0 \times 10^{-17}$, 1.0×10^{-16} , and 5.0×10^{-16} m².

The spatial distribution of methane saturation after 2.0×10^4 s with different fracture permeabilities of $k_f = 5.0 \times 10^{-17}$, 1.0×10^{-16} , and 5.0×10^{-16} m² in two different simulation domains is shown in Figure 16. Generally, the simulation results show that the distributions of gas saturation in two domains are similar. The distribution of saturation in Case

b is smoother than that in Case a. The fact can be explained by that a large saturation gradient appears at the end of the disconnected fracture due to large permeability between fracture and matrix.

Figure 17 shows the evolution of average gas-phase pressure ($\overline{p}_g = \int_l p_g dl/l$) along the vertical line $x = 4.5$ for two

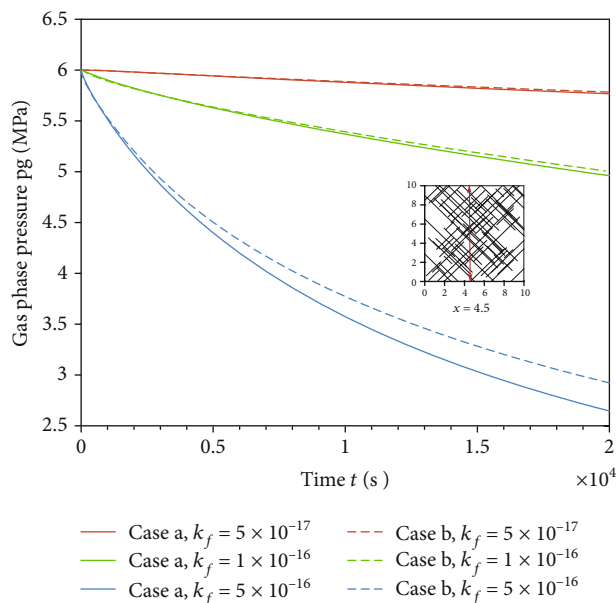


FIGURE 17: The temporal evolution of average gas pressure along the vertical line $x = 0.45$ with different fracture permeabilities of $k_f = 5.0 \times 10^{-17}$, 1.0×10^{-16} , and $5.0 \times 10^{-16} \text{ m}^2$.

different cases with different fracture permeabilities of 5.0×10^{-17} , 1.0×10^{-16} , and $5.0 \times 10^{-16} \text{ m}^2$. The pressure decreases as the methane is continuously produced out of the fractured coal reservoir. Pressure drops significantly in the case with larger fracture permeability. In Figure 17, solid lines are simulation results in Case a while the dashed lines are the results in Case b. It can be seen that a good agreement has been achieved between those two cases, which demonstrates that the skeleton of fracture networks has an influential contribution to methane production. A larger difference is observed for the two cases with a higher fracture permeability of $5.0 \times 10^{-16} \text{ m}^2$. Several reasons, involving boundary effect and fracture numbers according to the vertical line, lead to the phenomenon.

5. Conclusions

In this study, we developed and applied a discrete fracture model to simulate two-phase (coalbed methane and water) flow through fractured coal reservoirs. The proposed two-phase model in fractured porous media was verified by two oil-reservoir water-flooding cases with single and multiple fractures. The simulation results are in good agreement, which confirms the model feasibility and accuracy. We simulated CBM production from discrete fractured coal reservoirs with four types of fracture configurations. The simulation results clearly show that the patterns of fluid flow and production performance are significantly affected by fracture orientation, density, and connectivity. The fluid prefers to migrate aligned with the fracture orientation. Increasing fracture density enhances production efficiency. Moreover, fracture connectivity seems to contribute significantly to fluid transport and methane production efficiency. Later, two three-dimensional cases were studied to investi-

gate the influence of gravity. The results show that gas continues to migrate upwards to the top reservoir surface during fluid extraction as a result of the buoyancy of methane, which provides the possibility of methane leakage. Finally, we performed two cases of original discrete fracture network and a connected fracture network to study the effect of fracture skeleton. Simulation results demonstrate that the connected fracture skeleton is of great importance to fluid migration and methane production. Overall, the developed model provides a powerful approach to study coalbed methane and water flow in fractured coal reservoirs.

Data Availability

The data used to support the findings of this study are available from the first author upon request.

Conflicts of Interest

The authors declare that they have no conflicts of interest.

Acknowledgments

This study was supported by the Special Subject Grant of National Basic Research Program of China (973 program) (No. 2015CB251602), the National Science and Technology Major (2016ZX05043), the Jiangsu Natural Science Foundation (BK20180636), the Independent Innovation Project for Double First-Level Construction of CUMT (2018ZZCX04), the Advance Research Program (LTKY201803), and the China and Jiangsu Postdoctoral Science Foundation (2019M65201). We also thank Curtis Oldenburg (Lawrence Berkeley National Laboratory) for comments on an earlier draft.

References

- [1] T. A. Moore, "Coalbed methane: a review," *International Journal of Coal Geology*, vol. 101, pp. 36–81, 2012.
- [2] S. Tao, S. Chen, and Z. Pan, "Current status, challenges, and policy suggestions for coalbed methane industry development in China: a review," *Energy Science & Engineering*, vol. 7, pp. 1059–1074, 2019.
- [3] F. Bertrand, B. Cerfontaine, and F. Collin, "A fully coupled hydro-mechanical model for the modeling of coalbed methane recovery," *Journal of Natural Gas Science and Engineering*, vol. 46, pp. 307–325, 2017.
- [4] S. Chen, T. Yang, P. Ranjith, and C. Wei, "Mechanism of the two-phase flow model for water and gas based on adsorption and desorption in fractured coal and rock," *Rock Mechanics and Rock Engineering*, vol. 50, no. 3, pp. 571–586, 2017.
- [5] T. Ma, J. Rutqvist, C. M. Oldenburg, W. Liu, and J. Chen, "Fully coupled two-phase flow and poromechanics modeling of coalbed methane recovery: impact of geomechanics on production rate," *Journal of Natural Gas Science and Engineering*, vol. 45, pp. 474–486, 2017.
- [6] C. M. White, D. H. Smith, K. L. Jones et al., "Sequestration of carbon dioxide in coal with enhanced coalbed methane Recovery A Review†," *Energy & Fuels*, vol. 19, no. 3, pp. 659–724, 2005.
- [7] R. Yang, Z. Huang, G. Li et al., "A semianalytical method for modeling two-phase flow in coalbed methane reservoirs with

- complex fracture networks,” in *Proceedings of the 4th Unconventional Resources Technology Conference*, San Antonio, Texas, USA, August, 2016.
- [8] G. Wang, J. Shen, S. Liu, C. Jiang, and X. Qin, “Three-dimensional modeling and analysis of macro-pore structure of coal using combined X-ray CT imaging and fractal theory,” *International Journal of Rock Mechanics and Mining Sciences*, vol. 123, article 104082, 2019.
- [9] J. Warren and P. J. Root, “The behavior of naturally fractured reservoirs,” *Society of Petroleum Engineers Journal*, vol. 3, pp. 245–255, 2013.
- [10] X. Fu, Y. Qin, X. Xue, G. Li, and W. Wang, “Research on fractals of pore and fracture-structure of coal reservoirs,” *Journal of China University of Mining and Technology*, vol. 30, pp. 225–228, 2001.
- [11] S. Tao, Z. Pan, S. Chen, and S. Tang, “Coal seam porosity and fracture heterogeneity of marcolithotypes in the Fanzhuang Block, southern Qinshui Basin, China,” *Journal of Natural Gas Science and Engineering*, vol. 66, pp. 148–158, 2019.
- [12] Y. Jing, R. T. Armstrong, and P. Mostaghimi, “Rough-walled discrete fracture network modelling for coal characterisation,” *Fuel*, vol. 191, pp. 442–453, 2017.
- [13] C. Ö. Karacan and E. Okandan, “Fracture/cleat analysis of coals from Zonguldak Basin (northwestern Turkey) relative to the potential of coalbed methane production,” *International Journal of Coal Geology*, vol. 44, no. 2, pp. 109–125, 2000.
- [14] T. Ma, W. Liu, J. Rutqvist, H. Zhang, and X. Zhao, “Anisotropy permeability model for highly fractured coal seams associated with coupled THM analysis of CO₂-ECBM,” *Journal of China Coal Society*, vol. 42, pp. 407–416, 2017.
- [15] L. B. Colmenares and M. D. Zoback, “Hydraulic fracturing and wellbore completion of coalbed methane wells in the Powder River Basin, Wyoming: implications for water and gas production,” *AAPG Bulletin*, vol. 91, no. 1, pp. 51–67, 2007.
- [16] S. Holditch, J. Ely, M. Semmelbeck, R. Carter, J. Hinkel, and R. Jeffrey Jr., “Enhanced recovery of coalbed methane through hydraulic fracturing,” in *SPE Annual Technical Conference and Exhibition*, Houston, TX, USA, 1988.
- [17] J. Zhang and X. Bian, “Numerical simulation of hydraulic fracturing coalbed methane reservoir with independent fracture grid,” *Fuel*, vol. 143, pp. 543–546, 2015.
- [18] R. Yang, T. Ma, H. Xu, W. Liu, Y. Hu, and S. Sang, “A model of fully coupled two-phase flow and coal deformation under dynamic diffusion for coalbed methane extraction,” *Journal of Natural Gas Science and Engineering*, vol. 72, article 103010, 2019.
- [19] A. Al-Jubori, S. Johnston, C. Boyer et al., “Coalbed methane: clean energy for the world,” *Oilfield Review*, vol. 21, pp. 4–13, 2009.
- [20] W. Shen, Y. Xu, X. Li, W. Huang, and J. Gu, “Numerical simulation of gas and water flow mechanism in hydraulically fractured shale gas reservoirs,” *Journal of Natural Gas Science and Engineering*, vol. 35, pp. 726–735, 2016.
- [21] L. Xizhe, L. Detang, L. Ruilan et al., “Quantitative criteria for identifying main flow channels in complex porous media,” *Petroleum Exploration and Development*, vol. 46, pp. 998–1005, 2019.
- [22] B. Flemisch, I. Berre, W. Boon et al., “Benchmarks for single-phase flow in fractured porous media,” *Advances in Water Resources*, vol. 111, pp. 239–258, 2018.
- [23] B. Flemisch, A. Fumagalli, and A. Scotti, “A review of the XFEM-based approximation of flow in fractured porous media,” in *Advances in Discretization Methods*, SEMA SIMAI Springer Series, G. Ventura and E. Benvenuti, Eds., pp. 47–76, Springer, Cham, 2016.
- [24] D. Gläser, R. Helmig, B. Flemisch, and H. Class, “A discrete fracture model for two-phase flow in fractured porous media,” *Advances in Water Resources*, vol. 110, pp. 335–348, 2017.
- [25] C. Guo and Y. Cui, “Pore structure characteristics of debris flow source material in the Wenchuan earthquake area,” *Engineering Geology*, vol. 267, article 105499, 2020.
- [26] J. Monteagudo and A. Firoozabadi, “Control-volume method for numerical simulation of two-phase immiscible flow in two- and three-dimensional discrete-fractured media,” *Water resources research*, vol. 40, no. 7, 2004.
- [27] V. Reichenberger, H. Jakobs, P. Bastian, and R. Helmig, “A mixed-dimensional finite volume method for two-phase flow in fractured porous media,” *Advances in Water Resources*, vol. 29, no. 7, pp. 1020–1036, 2006.
- [28] M. Sahimi, *Flow and Transport in Porous Media and Fractured Rock: From Classical Methods to Modern Approaches*, John Wiley & Sons, 2011.
- [29] P. Thararoop, Z. T. Karpyn, and T. Ertekin, “Development of a multi-mechanistic, dual-porosity, dual-permeability, numerical flow model for coalbed methane reservoirs,” *Journal of Natural Gas Science and Engineering*, vol. 8, pp. 121–131, 2012.
- [30] Q. Gan and D. Elsworth, “Production optimization in fractured geothermal reservoirs by coupled discrete fracture network modeling,” *Geothermics*, vol. 62, pp. 131–142, 2016.
- [31] M. Oda, “An equivalent continuum model for coupled stress and fluid flow analysis in jointed rock masses,” *Water Resources Research*, vol. 22, no. 13, pp. 1845–1856, 1986.
- [32] A. Gilman and R. Beckie, “Flow of coal-bed methane to a gallery,” *Transport in Porous Media*, vol. 41, no. 1, pp. 1–16, 2000.
- [33] F. Gu and R. Chalaturnyk, “Sensitivity study of coalbed methane production with reservoir and geomechanic coupling simulation,” *Journal of Canadian Petroleum Technology*, vol. 44, no. 10, 2013.
- [34] M. Meng, S. Baldino, S. Miska, and N. Takach, “Wellbore stability in naturally fractured formations featuring dual-porosity/single-permeability and finite radial fluid discharge,” *Journal of Petroleum Science and Engineering*, vol. 174, pp. 790–803, 2019.
- [35] X. Wei, G. Wang, and P. Massarotto, “A review on recent advances in the numerical simulation for coalbed methane recovery process,” in *SPE Asia Pacific Oil and Gas Conference and Exhibition*, Jakarta, Indonesia, 2005.
- [36] Z. Wei and D. Zhang, “Coupled fluid-flow and geomechanics for triple-porosity/dual-permeability modeling of coalbed methane recovery,” *International Journal of Rock Mechanics and Mining Sciences*, vol. 47, no. 8, pp. 1242–1253, 2010.
- [37] F. Budinsky, D. Steinberg, R. Ellersick, T. J. Grose, and E. Merks, *Eclipse Modeling Framework: A Developer's Guide*, Addison-Wesley Professional, 2004.
- [38] T. Gentzis and D. Bolen, “The use of numerical simulation in predicting coalbed methane producibility from the Gates coals, Alberta inner foothills, Canada: comparison with Mannville coal CBM production in the Alberta syncline,” *International Journal of Coal Geology*, vol. 74, no. 3-4, pp. 215–236, 2008.
- [39] S. Reeves and L. Pekot, “Advanced reservoir modeling in desorption-controlled reservoirs,” in *SPE Rocky Mountain Petroleum Technology Conference*, Keystone, Colorado, 2001.

- [40] K. Pruess, C. M. Oldenburg, and G. Moridis, *TOUGH2 User's Guide Version 2*, Lawrence Berkeley National Lab.(LBNL), Berkeley, CA, USA, 1999.
- [41] J. D. Hyman, S. Karra, N. Makedonska, C. W. Gable, S. L. Painter, and H. S. Viswanathan, "dfnWorks: a discrete fracture network framework for modeling subsurface flow and transport," *Computers & Geosciences*, vol. 84, pp. 10–19, 2015.
- [42] H. Wang, "Discrete fracture networks modeling of shale gas production and revisit rate transient analysis in heterogeneous fractured reservoirs," *Journal of Petroleum Science and Engineering*, vol. 169, pp. 796–812, 2018.
- [43] A. Khoei, N. Hosseini, and T. Mohammadnejad, "Numerical modeling of two-phase fluid flow in deformable fractured porous media using the extended finite element method and an equivalent continuum model," *Advances in Water Resources*, vol. 94, pp. 510–528, 2016.
- [44] Y. F. Alghalandis, "ADFNE: open source software for discrete fracture network engineering, two and three dimensional applications," *Computers & Geosciences*, vol. 102, pp. 1–11, 2017.

Research Article

Effect of Perforation Interval Design on Gas Production from the Validated Hydrate-Bearing Deposits with Layered Heterogeneity by Depressurization

Yingli Xia, Tianfu Xu, Yilong Yuan, and Xin Xin 

Key Laboratory of Groundwater Resources and Environment, Ministry of Education, Jilin University, Changchun 130021, China

Correspondence should be addressed to Xin Xin; xxxx@jlu.edu.cn

Received 9 April 2020; Revised 22 May 2020; Accepted 3 June 2020; Published 20 June 2020

Academic Editor: Jianchao Cai

Copyright © 2020 Yingli Xia et al. This is an open access article distributed under the Creative Commons Attribution License, which permits unrestricted use, distribution, and reproduction in any medium, provided the original work is properly cited.

Natural gas hydrate is considered as one of the best potential alternative resource to address the world's energy demand. The available geological data at the Mallik site of Canada indicates the vertical heterogeneities of hydrate reservoir petrophysical properties. According to the logging data and sample analysis results at the Mallik 2L-38 well, a 2D model of geologically descriptive hydrate-bearing sediments was established to investigate the multiphase flow behaviors in hydrate reservoir induced by gas recovery and the effects of perforation interval on gas production performance. Firstly, the constructed model with vertical heterogeneous structures of permeability, porosity, and hydrate saturation was validated by matching the measured data in the Mallik 2007 test. The excessive residual methane in the hydrate reservoir observed in simulated results indicates insufficient gas production efficiency. For more effective methane recovery from a hydrate reservoir, the effect of perforation interval on long-term gas production performance was investigated based on the validated reservoir model. The simulation results suggest that both the location and length of the perforation interval have significant impact on hydrate dissociation behavior, while the gas production performance is mainly affected by the length of the perforation interval. To be specific, an excellent gas release performance is found in situations where the perforation interval is set at the interface between a hydrate reservoir and an underlying water-saturated zone. By increasing the perforation interval lengths of 5 m, 8 m, and 10 m, the gas release volumes from hydrate dissociation and gas production volumes from production wells are increased by 34%, 52%, and 57% and 37%, 58%, and 62%, respectively.

1. Introduction

Natural gas hydrate (NGH) is a crystalline solid, in which the gas molecules are restricted in a water molecular structure under befitting situations of low temperature and high pressure [1]. A large volume of NGHs with high density occur mainly in permafrost regions and deep marine sediments [2, 3]. As one of the best potential alternative resources to address the world's energy demand, NGH has attracted quite a lot of attention. Over the last few decades, a considerable amount of research has been focused on extracting gas from methane hydrate [4]. However, it has been proven that the economical energy recovery from a hydrate reservoir is extremely challenging [5, 6].

The natural gas exploitation from methane hydrate is a process of dissociating solid hydrate into a fluid phase (e.g., gas and water), involving a complicated multiphase flow, an endothermic reaction [7], and reservoir deformation [8]. At present, in situ dissociation of hydrate is considered as an efficient method for gas recovery from hydrate-bearing sediments (HBS). The popular techniques include depressurization [9, 10], thermal stimulation [11], inhibitor injection [12], gas replacement (such as CO₂ and N₂) [13], and their combinations [14]. The comprehensive consideration of economical factor, energy recovery efficiency, implementation feasibility, and environmental impact infers that depressurization is accepted as the best potential method for utilizing the gas hydrate resource. Consequently, depressurization-

induced gas production has been widely investigated recently [15–21]. The successful applications in field tests at the Mallik site [22], the eastern Nankai Trough [23, 24], and the South China Sea [25] indicated the feasibility and effectiveness of depressurization both in terrestrial permafrost and marine hydrate deposits. However, the gas production durations and rates of the above field tests are way below the commercial production level. So the production method and wellbore construction need to be further improved.

Numerical simulation is regarded as an economical and valid way to investigate the long-term production performance of a hydrate reservoir and to optimize the production scheme. Moridis et al. [26–28] investigated the gas production performance from Class 1, Class 2, and Class 3 hydrate deposits with varying porosities, anisotropies, and boundaries by depressurization. They determined that conventional technology could induce the dissociation of hydrates effectively, and they obtained continuously high gas production rates. In addition, they inferred that long-term production was needed to realize the full potential of any HBS. For different NGH sites, numerical simulation was used to evaluate the production potential of hydrate reservoirs and to conduct sensitivity analysis. Based on the geological data in the Eastern Nankai Trough, Konno et al. [29], Yuan et al. [30], and Sun et al. [31] investigated the long-term production performance through depressurization from the hydrate-bearing sediments. All of their results showed excessive simulated water production. For the typical terrestrial permafrost hydrate reservoir, Uddin et al. [32, 33] forecasted the long-term gas and water production potential based on the geological data and operational parameters of the Mallik 2008 test. Moreover, they assessed the effects and relative importance of reservoir heterogeneity, thermal conductivity, salinity, and permeability. The simulation results indicated that long-term gas production from the Mallik deposit appeared feasible. In addition, numerical simulation was also used to investigate the effects of different hydrate dissociation methods and stimulation approaches on gas production performance. Su et al. [34], Yang et al. [35], Jin et al. [36], and Wang et al. [37, 38] numerically evaluated the methane production performance from multiple hydrate deposits by thermal stimulation and depressurization. The results showed that gas recovery can be improved significantly by combining depressurization and thermal stimulation. Moreover, the combination of hydraulic fracturing and depressurization method was applied by Sun et al. [39, 40] and Feng et al. [17] to enhance gas production. They indicated that hydraulic fracturing could significantly enhance the production potential at the early depressurization-induced production stage, especially for silty hydrate reservoirs. Generally, the significant importance of reservoir geological parameters (e.g., permeability, porosity, and initial hydrate saturation) on gas production performance could be indicated from the above research results. In previous investigations, the sensitivity analyses of gas production performance were mainly focused on these intrinsic reservoir characteristics (e.g., permeability, porosity, and salinity) or production methods (e.g., depressurization and thermal stimulation). However, relatively few studies reflected the effects of the perforation

interval of a production well, which has been proven to have a significant effect on gas production performance from a hydrate reservoir induced by depressurization through a laboratory test.

The drilling results indicate that almost all of the actual hydrate deposits are distinctly complex and heterogeneous by analyzing the well-logging data. Obviously, the behaviors of gas hydrate dissociation, gas production, water production, and spatial distributions of pressure, temperature, and phase saturations are closely relevant to the geophysical properties of a hydrate reservoir. However, in most of the previous numerical simulation studies, the hydrate reservoir has been described as a homogeneous model with a single layer, leading to an inexact evaluation of gas production potential. Recently, Yuan et al. [41] suggested that the homogeneous hydrate reservoir model with uniform values of intrinsic permeability and hydrate saturation may underestimate the gas productivity when compared with a reservoir using layered heterogeneous descriptions. Earlier investigation of the Mount Elbert site also showed that the heterogeneity of hydrate deposits has a significant effect on gas production over time [42]. Therefore, the precise depiction of a hydrate reservoir is the foundation for ensuring the reliability of the established numerical model, which is critical to evaluating the gas production performance of a hydrate reservoir.

In this paper, based on the detailed borehole geophysical logging data at the Mallik site of the Mackenzie Delta, Northwest Territories of Canada, a more realistic reservoir model, which considers the layered heterogeneous structure of permeability, porosity, and hydrate saturation, was constructed to investigate the long-term hydrate production performance. The availability of the model was validated by matching the actual measured test data, including gas and water production rates. On this basis, the main goal of this work was to investigate the effects of the perforation interval of a production well on the hydrate production performance through the validated geologically descriptive hydrate-bearing sediments. In addition, the changes of multiphase flow behaviors and evolutions of reservoir pore pressure, temperature, and phase saturations were analyzed in detail. It is hoped that the results of this work may provide some valuable references for future commercial production and utilization of the hydrate reservoir with similar conditions.

2. Overview of Production Tests at the Mallik Site

2.1. Geological Background. The Mallik production-test site is located at the northern margin of the Mackenzie Delta, Northwest Territories [43]. The gas hydrate deposits are mainly concentrated in the Tertiary sediments of the Oligocene Kugmallit Sequence and the Oligocene to Miocene Mackenzie Bay Sequence, which is capped by over 600 m of permafrost [44]. The reservoir consists of more than 10 discrete hydrate layers, which can be roughly divided into three main hydrate zones. The high hydrate saturation that exceeds 80% in some cases and the terrestrial convenience for

engineering make the Mallik hydrate field one of the best potential resource-rich fields of gas hydrate in the world [45].

2.2. Well Distribution and Field Tests. At the Mallik site, two production wells (2L-38 and 5L-38) and three monitoring wells (L-38, 3L-38, and 4L-38) were drilled to investigate the distribution of the gas hydrate reservoir and collect permafrost methane hydrate core samples during the 30-year period from 1972 to 2002. The location of the Mallik site and the distribution of these drilling wells are depicted in Figure 1(a). In order to evaluate the gas production potential and investigate the environmental response, a total of four trial tests were implemented in the Mallik hydrate field from 2002 to 2008 [46, 47].

In 2002, the first 124-hour thermal stimulation trial test and the second depressurization-induced gas production test were carried out at the 5L-38 well, in which the production intervals were set at the layers from 907 m to 920 m (Zone C) and from 974 m to 1106.5 m (Zone B and Zone A) below the land surface (Figure 1(b)), respectively [48]. Based on the reentry and recompletion of the Mallik 2L-38 well, two trial tests were conducted with a 12 m perforation interval (1093 m~1105 m, Zone A) on April in 2007 and March in 2008, respectively. In the 2007 test, the total gas and water production volumes were about 830 ST m³ and 20 m³ during the 27-hour period. The gas production test lasted for about 144 hours in 2008, and the production rates of gas and water during the test were about 2000~3000 ST m³/d and 10~20 m³/d, respectively [49]. Considering that the reservoir structures of the 2008 test were damaged by sand production in the 2007 test and the damaged situation is hard to accurately depict, the measured data of the 2007 production test was selected for history matching in this study.

2.3. Reservoir Petrophysical Properties. As mentioned above, the 2007 test was conducted at the lower hydrate reservoir named "Zone A" (1060 m~1112 m). The petrophysical properties such as absolute permeability, porosity, and hydrate saturation were derived from the open logging data and core sample analysis results of the Mallik 2L-38 well [51, 52]. As depicted in Figure 2, the reservoir petrophysical properties of Zone A present obvious layered heterogeneity in the vicinity of the wellbore. The hydrate reservoir is composed of two main parts, upper thin alternations of sand and mud layers and a lower sand-dominant layer.

The absolute permeability (Figure 2(a)) was estimated from the ECS logging data by the K-lambda model and calibrated with the field core data. And the permeability value of the lower part is larger, which ranges from 100 mD to 1000 mD. The porosities (Figure 2(b)) mainly ranging from 0.30 to 0.60 were interpreted from well-log and core sample analysis data. The hydrate saturation (Figure 2(c)) is estimated from the resistivity log with Archie relationships [53]. The saturation in the lower reservoir of Zone A is relatively high, ranging from 0.6 to 0.85. Additionally, the hydrate reservoir is overlain by silt-dominant layers and underlain by a thick water-saturated sand layer.

3. Simulation Setup

3.1. Reservoir Conceptual Model

3.1.1. Construction of Reservoir Model. On the basis of the borehole log information and core data of the Mallik 2L-38 well, a RZ2D conceptual reservoir model using a cylindrical symmetry is established for later history-matching simulation as Figure 3 depicts. The top floor of this model is at a depth of 1040 m below the land surface. The total thickness of the entire model is 92 m, which is composed of three layers including the hydrate reservoir (52 m), an overlying silt-dominant zone (20 m), and an underlying sand-dominant zone (20 m). The model size in R-direction is 1000 m to avoid the boundary effect. According to the 2007 field operational data, the vertical production wellbore is set as a pseudoporous medium with a radius of 0.1 m. The production interval with a length of 12 m is located in the lower part (depth 53 m~65 m) of the hydrate reservoir, where the permeability and hydrate saturation conditions are excellent.

Considering that the hydrate dissociation impacts mainly occur in a limited area near the production well in the short-term, thus the discretization around the wellbore is an encryption for simulation precision, and the grid spacing along the radial direction has a geometric increase. The discretization in the vertical direction is determined by variations of petrophysical properties, and the thickness of each fine layer is 0.5 m. As a result, the model domain has been discretized into 130 × 184 (23920) unequally spaced grid blocks.

3.1.2. Initial and Boundary Conditions. According to the data measured by DTS at the Mallik 4L-38 well, the initial pressure and temperature at the bottom of the methane hydrate reservoir (depth = 1112.5 m) are approximately 11.3 MPa and 12.55°C [48], respectively, with the condition of 0.05 salinity. Based on that, the initial pressure in this sediment system is calculated according to the water depth under the assumption of following a hydrostatic pore pressure distribution. The initial temperature distribution is assigned to vary linearly as a function of depth with a geothermal gradient of 0.030°C/m [22, 49].

The radial extension distance of the established model is sufficient to avoid the boundary effects in a 27-hour production duration, so the outside of this domain can be regarded as the no-flow and no-heat exchange boundary. The top and bottom floors are set at constant pressure and temperature boundaries.

In addition, the depressurization method is utilized for methane extraction in the 2007 test. The depressurization process of simulation remains in accordance with that measured at a memory gauge in the 2007 test. The production duration is about 27 hours, and the detailed variation of the bottom-hole pressure is depicted as shown in Figure 4.

3.1.3. Model Parameters. Based on the reported logging data and core sample analyses of the Mallik 2L-38 well, the main modeling parameters and physical properties are depicted as shown in Table 1. Considering the geological features of the Mallik site, (a) the absolute permeability, (b) porosity,

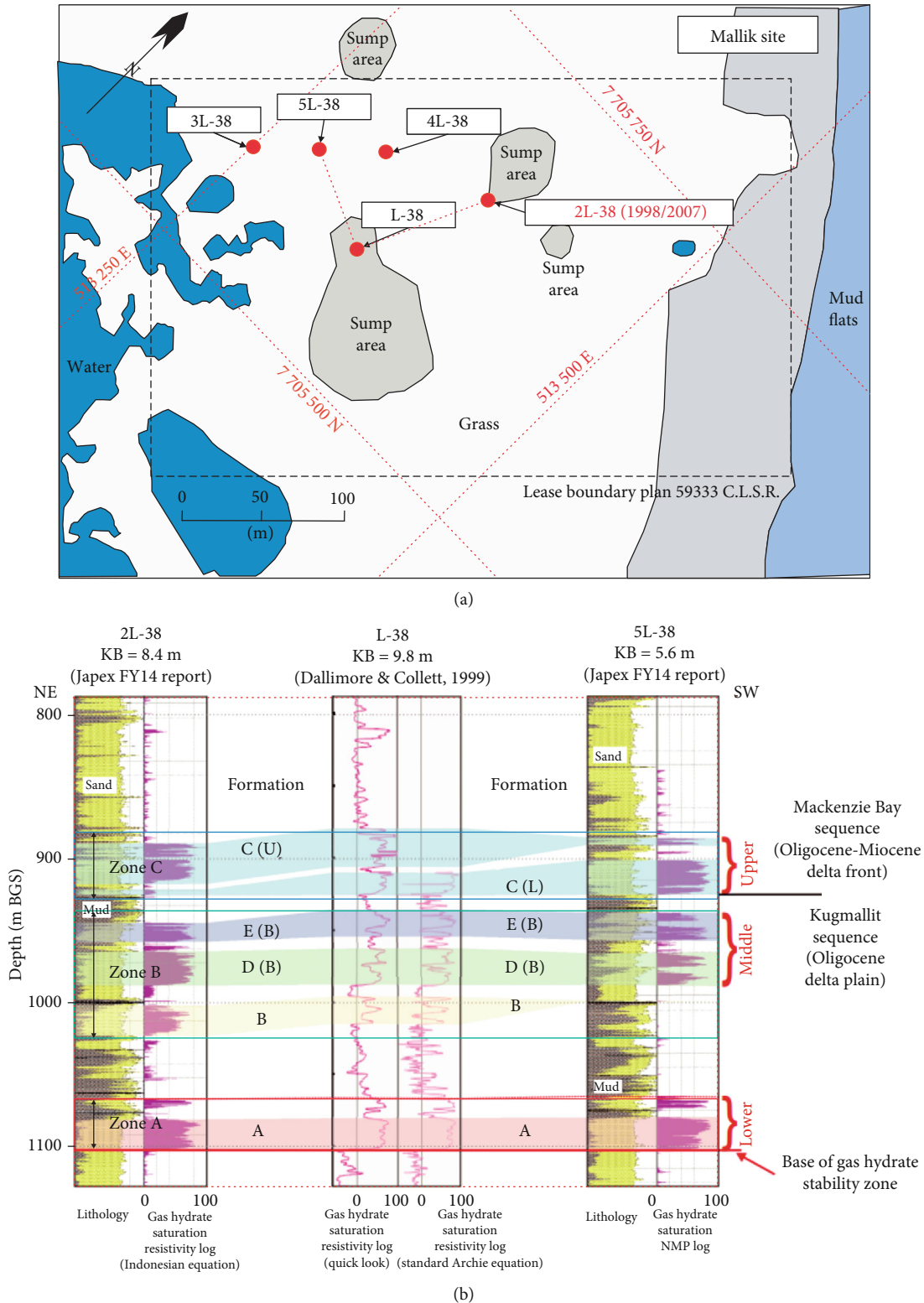


FIGURE 1: Location of the Mallik hydrate field and distribution of drilling wells (modified from Fujii et al., 2012) [50].

and (c) hydrate saturation show obvious layer heterogeneities as Figure 5 illustrates. The properties are determined from the actual well-logging data (Figure 2) and assumed to be uniformly distributed in each fine layer with a thickness of 0.5 m. The permeability, porosity, and hydrate saturation in

each layer are calculated by averaging the values in the fine layer of logging data. It is worth mentioning that the permeability profiles were slightly calibrated for the replication of a field test process, and the calibrated results are shown in Figure 5(a). In our model, hydrate is regarded as a pure

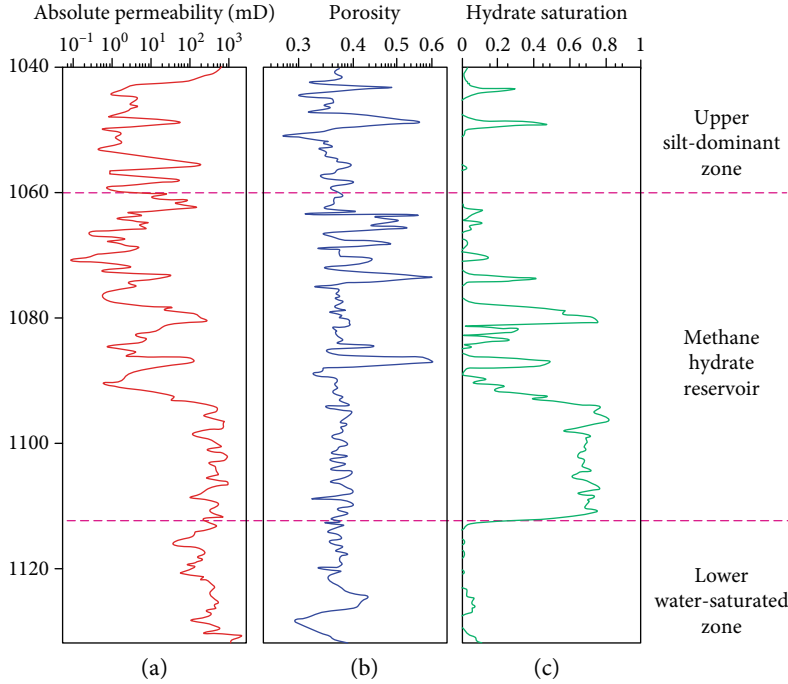


FIGURE 2: Depth profiles of (a) absolute permeability, (b) porosity, and (c) hydrate saturation based on the logging and core data [33].

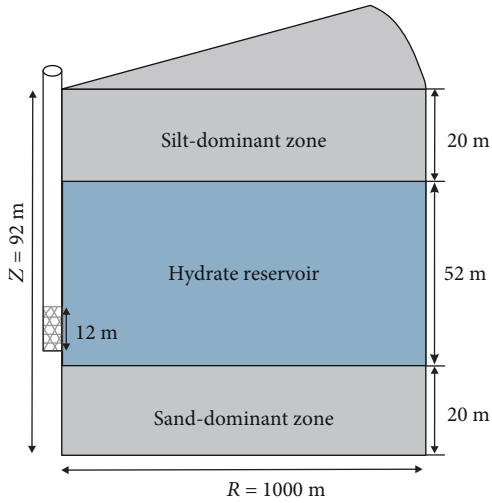


FIGURE 3: Schematic of geological model with production well.

methane hydrate, and the water salinity is set to 0.05 according to sample analysis.

In the multiphase flow system, each phase only takes up a part of the whole pore space, thus its effective permeability may be reduced due to the existence of other phases. In this study, the modified version of Stone's first three-phase relative permeability method was used:

$$k_{rA} = \max \left\{ 0, \min \left\{ \left[\frac{S_A - S_{irA}}{1 - S_{irA}} \right]^n, 1 \right\} \right\}, \quad (1)$$

$$k_{rG} = \max \left\{ 0, \min \left\{ \left[\frac{S_G - S_{irG}}{1 - S_{irG}} \right]^{n_G}, 1 \right\} \right\}, \quad (2)$$

$$k_{rH} = 0, \quad (3)$$

where k_{rA} , k_{rG} , and k_{rH} are the relative permeabilities of the aqueous, gas, and hydrate phases, respectively; S_A and S_G are the saturation of the aqueous and gas phases; S_{irA} and S_{irG} are the irreducible saturation of the aqueous and gas phases, respectively; and n , n_G are the relevant indices of the aqueous and gas phases.

In addition, surface tension influences between different phases can cause capillary pressures, which may be changed due to solid evolution (e.g., hydrate and ice). The capillary pressure functions used can be expressed as follows (van Genuchten's function):

$$P_{cap} = -P_0 \left[(S^*)^{-1/\lambda} - 1 \right]^{1-\lambda}, \quad (4)$$

$$S^* = \frac{(S_A - S_{irA})}{(S_{mA} - S_{irA})}, \quad (5)$$

where P_{cap} is capillary pressure, P_0 is entry capillary pressure, and λ is the porosity structure index.

The relevant parameters used in the functions mentioned above were mainly determined by core sample analysis data from multiple sites (e.g., the Mallik site, the North Slope of Alaska, and the Nankai Trough site) [24, 42, 54] and calibrated through trial-and-error tests in a history-matching process.

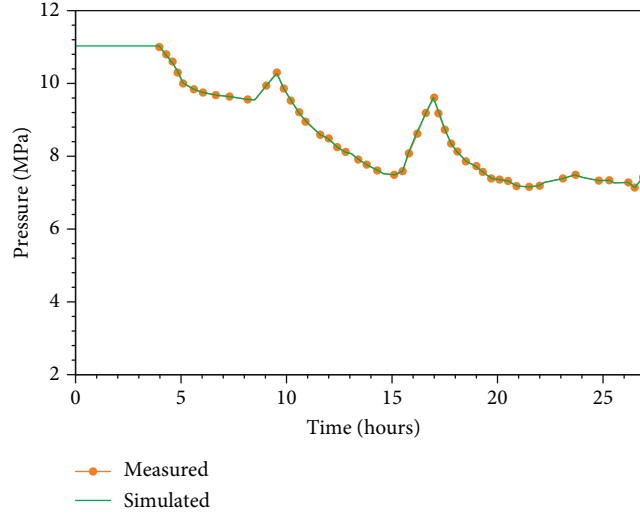


FIGURE 4: Depressurization process measured in the 2007 test and used in the simulation [48].

TABLE 1: Main parameters of hydrate deposits in the model [22, 33, 48, 54].

Parameter	Value
Thickness of model, H	92 m
Length of perforation interval	12 m
Borehole radius, r_w	0.1 m
Initial pressure at the bottom of reservoir, P_s	11.3 MPa
Initial temperature at the bottom of reservoir, T_s	12.55°C
Wet thermal conductivity, λ_w	3.1 W/m/K
Dry thermal conductivity, λ_D	1.0 W/m/K
Water salinity, X_i	5.00%
Gas composition	100% CH ₄
Absolute permeability of hydrate reservoir, k_{H}	Layered heterogeneous as shown in Figure 5(a)
Porosity, ϕ	Layered heterogeneous as shown in Figure 5(b)
Hydrate saturation	Layered heterogeneous as shown in Figure 5(c)
Pore compressibility, α_p	$1.0 \times 10^{-9} \text{ Pa}^{-1}$
Parameters in capillary pressure model	
S_{mxA}	1.0
λ	0.45 (sand), 0.15 (clay)
P_0	10^4 Pa (sand), 10^5 Pa (clay)
Parameters in relative permeability model	
n_A	3.5 (sand), 5.0 (clay)
n_G	2.5 (sand), 3.0 (clay)
S_{irA}	0.20 (sand), 0.40 (clay)
S_{irG}	0.02 (sand), 0.05 (clay)

3.2. *Simulation Code.* In order to model the complex multi-component, multiphase fluid and heat flow processes involved in gas production from hydrate deposits, several widespread simulators have been proposed to solve the governing equations of hydrate dissociation, such as MH-21 HYDRES, TOUGH+HYDRATE, HydrateResSim, STOMP-

HYD, and CMG STARS [42]. In this work, TOUGH+HYDRATE is employed to address the issues of hydrate dissociation behavior and gas production evaluation. TOUGH+HYDRATE is a member of the TOUGH+ family developed by the Lawrence Berkeley National Laboratory. The modeling scenes include the nonisothermal gas release and the

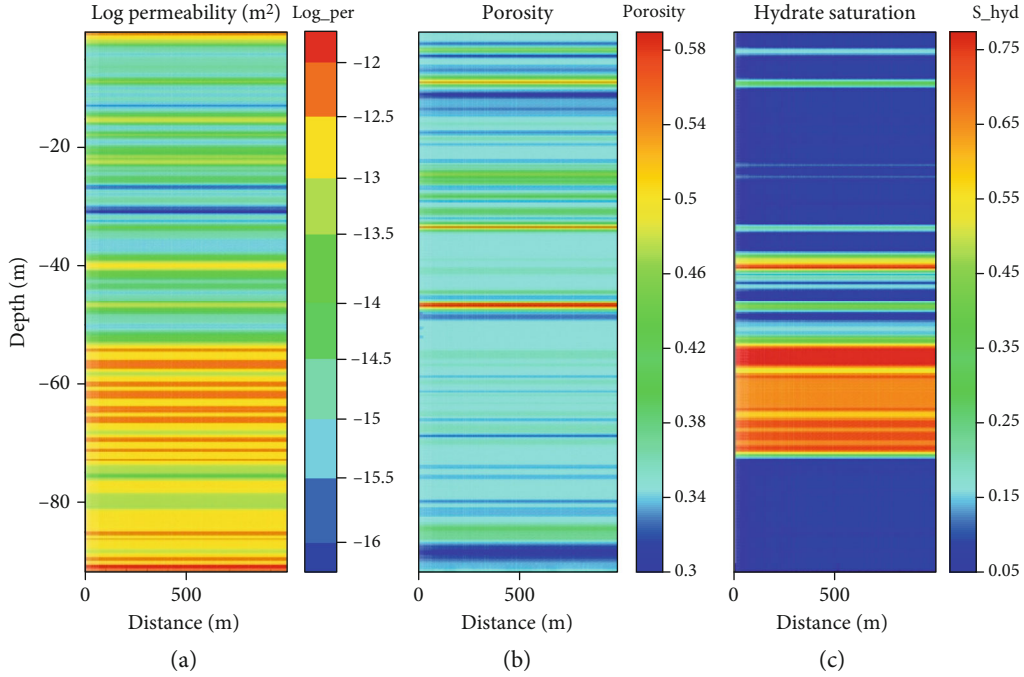


FIGURE 5: Cross-section depicting initial properties of hydrate-bearing sediment.

behavior of each possible phase under conditions of common natural hydrate sediments. In this code, four components (water, hydrate, CH_4 , and water-soluble inhibitor) partitioned among possible solid hydrate, aqueous, gaseous, and solid ice phases are considered, and two reaction models [55] (the equilibrium model and the kinetic model) are applied to describe hydrate dissociation and formation [20, 56]. The equilibrium model is utilized in this study because it has less computing requirements and it is favorable for long-term simulation.

4. Results and Discussion

4.1. History-Matching Results and Analysis. As introduced above, the reservoir conceptual model was constructed based primarily on the interpretation results of well log and core analysis acquired in the 2007 test. Under the circumstance that the depressurization processes of numerical simulation and field tests were consistent, mainly two classes of reservoir parameters were calibrated for the reproduction of the field test process by the trial method. Firstly, we obtained the approximate rates between the simulated and measured gas production by slightly adjusting the permeability values in the model, due to the crucial role of reservoir permeability for fluxion. It is worth noting that the reservoir permeability after adjustment remains in the data range of two logging results (i.e., one is interpreted from ECS logging data by the K -lambda model, and the other one is interpreted from CMR logging data and gamma ray by the JOE model). Moreover, the value of absolute permeability in a vertical direction was lowered by a factor of 1/5 compared to that in a radial direction. This was mainly due to the reasonable consideration of the existence of interbedded sand and mud layers

[7, 48]. Subsequently, the parameters involved in relative permeability and capillary pressure models were calibrated for sand and clay layers, in order to realize the replication of a measured gas and water production process in a field test. Consequently, the calibrated reservoir model has been validated with history-matching results.

4.1.1. Gas and Water Production Behaviors. The decrease of bottom-hole pressure (BHP) can be reflected in the reservoir pressure gradient, which induces the dissociation of hydrate and accompanying gas production. Figure 6(a) shows the dynamic evolutions of test-measured gas production in a wellbore (Q_{g1}), simulated gas production in a wellbore (Q_{g2}), and simulated gas released from hydrate dissociation (Q_d). The gas was not measured in the field test during the first 16 hours, because the new round of pumping started at the 16th hour as a fact, while the simulated gas production rate has a significant increase from about the 10th hour due to the distinct depressurization of the hydrate reservoir. Generally, the simulated gas production rate matches reasonably well with the measured data. Both the measured and simulated gas production rates in a wellbore remain in the range of 1000~2000 ST m³/d. Figure 6(b) depicts the comparison results of test-measured cumulative gas production volume in a wellbore (V_{g1}), simulated cumulative gas production volume in a wellbore (V_{g2}), and simulated cumulative gas released volume from hydrate dissociation (V_d). On the whole, V_{g2} is higher than V_{g1} in the process of gas production, because the gas has not been measured in the early stage of the field test. By eliminating the difference between simulated and measured cumulative gas production volumes in the first 16 hours, the evolution of calibrated simulated

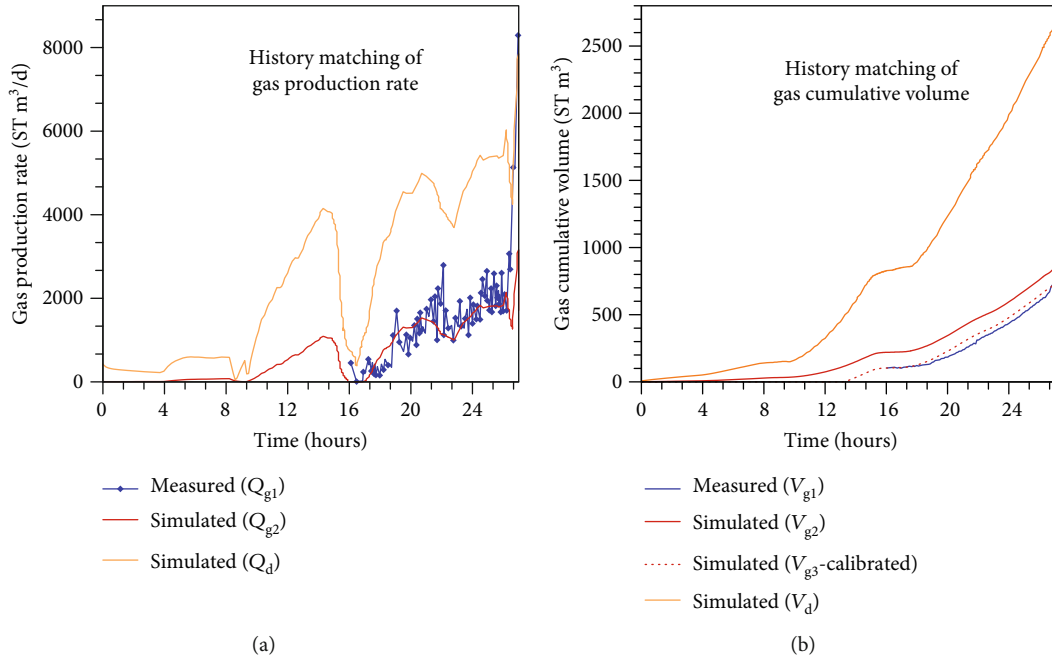


FIGURE 6: Comparison of (a) measured and simulated gas production rates and (b) measured and simulated gas cumulative volumes during the 27-hour depressurization test.

cumulative gas production volume (V_{g3}) is shown in Figure 6(b). And V_{g3} is closed to V_{g1} during the 27-hour depressurization test. Moreover, the final high production rate (approximately 8200 ST m³/d) in the field test contributed to the leap of cumulative volume at the end of the test. At the 27th hour of gas production, the predicted total cumulative volume is about 849 ST m³, which is roughly in accordance with measured data (830 ST m³) in the 2007 test. The modest gas production performance is mainly caused by the relatively thin perforation interval (only 12 m). In addition, the released gas rate Q_d (5000~6000 ST m³/d) and cumulative volume V_d (2703 ST m³) are obviously higher than the gas production rate Q_{g2} and cumulative production volume V_{g2} from a wellbore (Q_{g2}) that indicates the excessive residual methane in the hydrate reservoir. Consequently, considering the modest recovered gas volume in the test, the production strategies and well completion schemes need to be further optimized to promote methane extraction.

Figure 7 displays the matching result of measured and simulated water production (Figure 7(a) Q_{w1} and Q_{w2} ; Figure 7(b) V_{w1} and V_{w2}) in a wellbore during the 27-hour depressurization test. The evolution trend of the predicted water recovery rate is basically consistent with that of the depressurization procedure. The simulated water production rates have an obvious increase after the 4th hour due to a decrease of reservoir pressure, and the water production rate throughout the test period is about 20~30 m³/d. In the first half of water production, there are some slight differences between Q_{w1} and Q_{w2} . And the slight differences were enlarged when they were reflected in the cumulative volume. The simulated cumulative water production volume is higher than the measured cumulative water volume V_{w1} . At the 27th

hour of production, V_{w2} (38.4 m³) is about one times higher than V_{w2} (19 m³) at the end of test. And the calibrated water cumulative volume of simulation V_{w3} (obtained by eliminating the difference between simulated and measured cumulative water production volumes in the first 10 hours) is about 32.7 m³. The gaps between simulated and measured water production may be the results of reservoir disturbance during well recompletion, which was not considered in our model. In addition, compared with gas, the transmission nature of water is more closely related to the reservoir properties, so the spatial heterogeneity of each thin layer and pore compressibility caused by geomechanics may also affect the water production performance. Consequently, a difference between the measured and simulated cumulative water volumes is considered acceptable, as long as it is not too large. In general, the simulated water production rate matches well with the measured data in a wellbore at the Mallik site. Combined with the matching results of gas production, the calibrated reservoir model has been validated for subsequent investigation.

4.1.2. Reservoir Responses. The dynamic evolutions of reservoir parameters are the critical reference for the analysis of hydrate dissociation behavior. Additionally, the geomechanical expressions (e.g., sand production and seafloor subsidence) of hydrate deposits are closely related to the evolution characteristics of temperature, pressure, hydrate saturation, and gas saturation based on the relevant investigation results. So the evolutions of these reservoir parameters are analyzed in detail for giving the engineering reference.

Figure 8 depicts the dynamic evolution of pressure and temperature in a gas hydrate deposit. In the early stage of

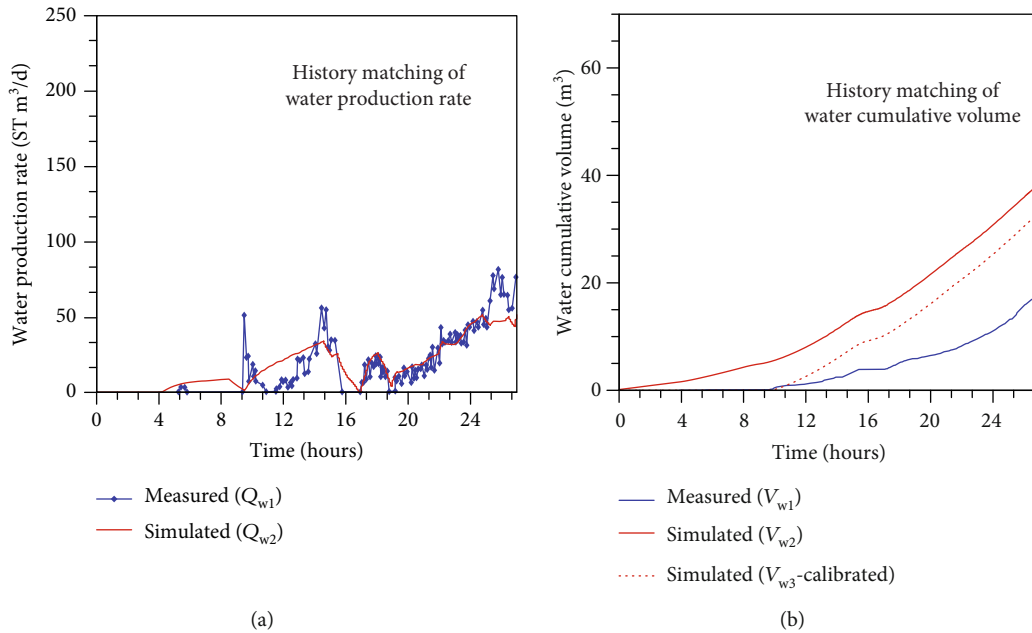


FIGURE 7: Comparison of (a) measured and simulated water production rates and (b) measured and simulated water cumulative volumes during the 27-hour depressurization test.

gas production, the relatively low pressure was concentrated in the vicinity of a wellbore due to the low effective permeability caused by high hydrate saturation. Because of the dissociation of gas hydrate, the pressure gradient extends more rapidly in the range of hydrate dissociation. However, on account of the transmitted nature of pressure, the region of depressurization was not confined by hydrate dissociation. During the 27-hour production test, the predicted front of lower pressure in the reservoir exceeded 20 m horizontal distance, while the radial region of declined temperature is less than 5 m. Due to the endothermic feature of hydrate dissociation, an apparent temperature decrease occurs near the wellbore with the lowest temperature of about 8.4°C. In addition, both the fronts of lower pressure and temperature extend more rapidly and present as heterogeneous in a horizontal direction, because the sand layers with high permeability are hydraulically restricted by alternative silt layers with poor hydrodynamic conditions.

The depressurization in the production interval drives the dissociation of hydrate and the release of methane gas around the wellbore, as Figure 9 shows. The anisotropy conditions of reservoir parameters induce more advantageous dissociation in the horizontal direction. As the hydrate dissociates, this status becomes more distinct due to the significant increase of effective permeability. In addition, the heterogeneous dissociation front occurs in the reservoir, mainly because of the vertical heterogeneous geophysical features. Compared with the spatial distribution of hydrate saturation in the early stage, the ultimate predicted front of the dissociation zone is at an approximately 5 m distance from the production well after the 27-hour production test. The spatial distribution of gas saturation in the hydrate reservoir is important for us to understand the gas release behavior. As

a sustainable depressurization, the occurrence region of free gas gradually enlarges and reaches a distance 5 m away from the wellbore with the maximum gas saturation of 0.065. Moreover, different with the homogeneous reservoir, the buoyancy effects in the upward gas diffusion are restricted by the clay layers with low permeability, while more free gas occurs in the lower part of the production well due to the concentration of high permeability and hydrate saturation. This phenomenon reminds us to pay attention to the influx of water from the underlying water-saturated sandy zone due to the dissociation of blocked hydrate in long-term gas production.

4.2. Effect of Perforation Interval on Gas Production Performance. The perforation interval is regarded as a critical factor for recovering methane from the hydrate reservoir. In view of the high hydrate saturation and prominent permeability conditions, the perforation interval with a length of 12 m was located at the zone from 1093 m to 1105 m (53 m ~65 m in model) in the Mallik 2007 trial test. The lower part of the hydrate reservoir with a thickness of 7.5 m was used to block the water influx from the underlying sand-dominant zone, due to its low effective permeability caused by high hydrate saturation. The availability of this design has been validated by test data and by the simulated results above. However, the long-term gas production performance is ambiguous, because the barrier may disappear with the hydrate dissociation and excessive water is likely to flow into the production well. In addition, as mentioned above, the gas from the hydrate dissociation in the reservoir could not be produced completely, but it mainly accumulates around and below the wellbore in the 2007 depressurization test. These suggest the importance of well configuration optimization in future gas production tests.

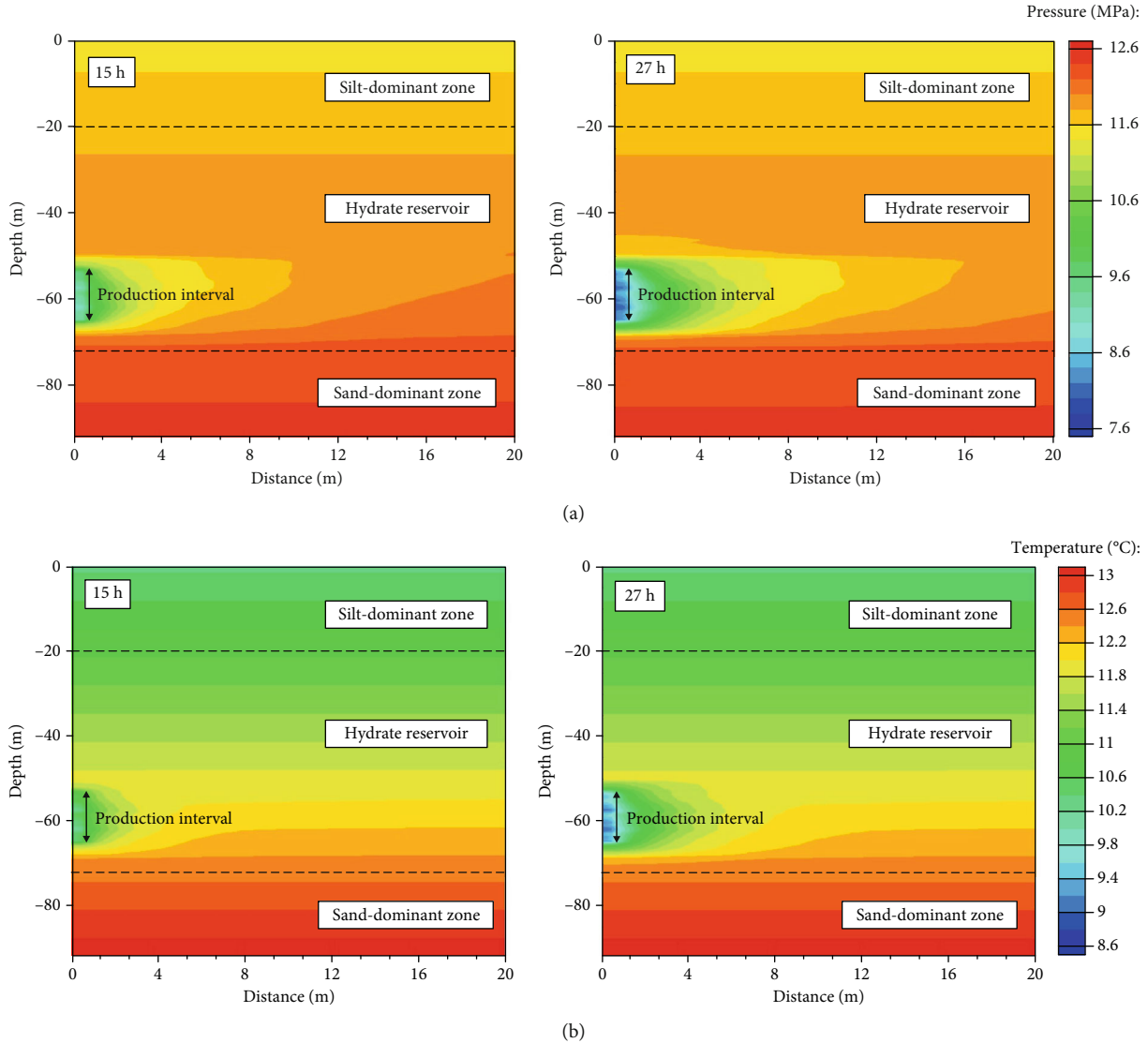


FIGURE 8: Dynamic evolutions of (a) pressure and (b) temperature in a hydrate reservoir at 15th and 27th hours.

4.2.1. Simulation Cases. In this study, we designed five cases with different locations and lengths of perforation intervals for investigating the effect of a perforation interval on long-term gas production performance and hydrate dissociation behaviors. As Table 2 shows, in Case 1 (base case), the perforation interval is located at the original site (i.e., $Z = 53 \text{ m} \sim 65 \text{ m}$) of the 2007 test with a length of 12 m. In Case 2, the perforation interval is lowered by 8 m (i.e., $Z = 61 \text{ m} \sim 73 \text{ m}$) and stretches into the underlying water-saturated zone. Therefore, Case 1 and Case 2 are designed to illustrate the effect of the location of the perforation interval on gas production performance. However, the other three cases are designed to discuss the influence of perforation length. The lengths of the perforation intervals in Case 3, Case 4, and Case 5 are 17 m, 20 m, and 22 m, respectively. As a consequence, the distance between the bottom of the perforation interval and the bottom of hydrate reservoir is 2.5 m, -0.5 m, and -2.5 m, respectively (“-” indicates that the bottom

of the perforation interval is lower than the bottom of the hydrate reservoir).

Another thing worth mentioning is the depressurization process in long-term gas production simulation. Based on the validated hydrate reservoir model, the long-term (more than 450 days) gas production performance of different cases are predicted. After the first 27-hour test, the BHP remains at 7 MPa until the 10th day. Considering the feasible depressurization scheme in the Mallik 2008 test, the BHP gradually reduces from 7 MPa to 4 MPa in the next 20 days. And then, the constant pressure of 4 MPa is used to recover gas from the hydrate reservoir throughout the simulation run. The anticipative simulated gas production durations in all cases are 2 years (730 days). However, in fact, the final simulated durations of these cases are different (450 days~650 days), due to some computational problems (nonconvergence, etc.). In addition, the radial distance of the simulation reservoir model is

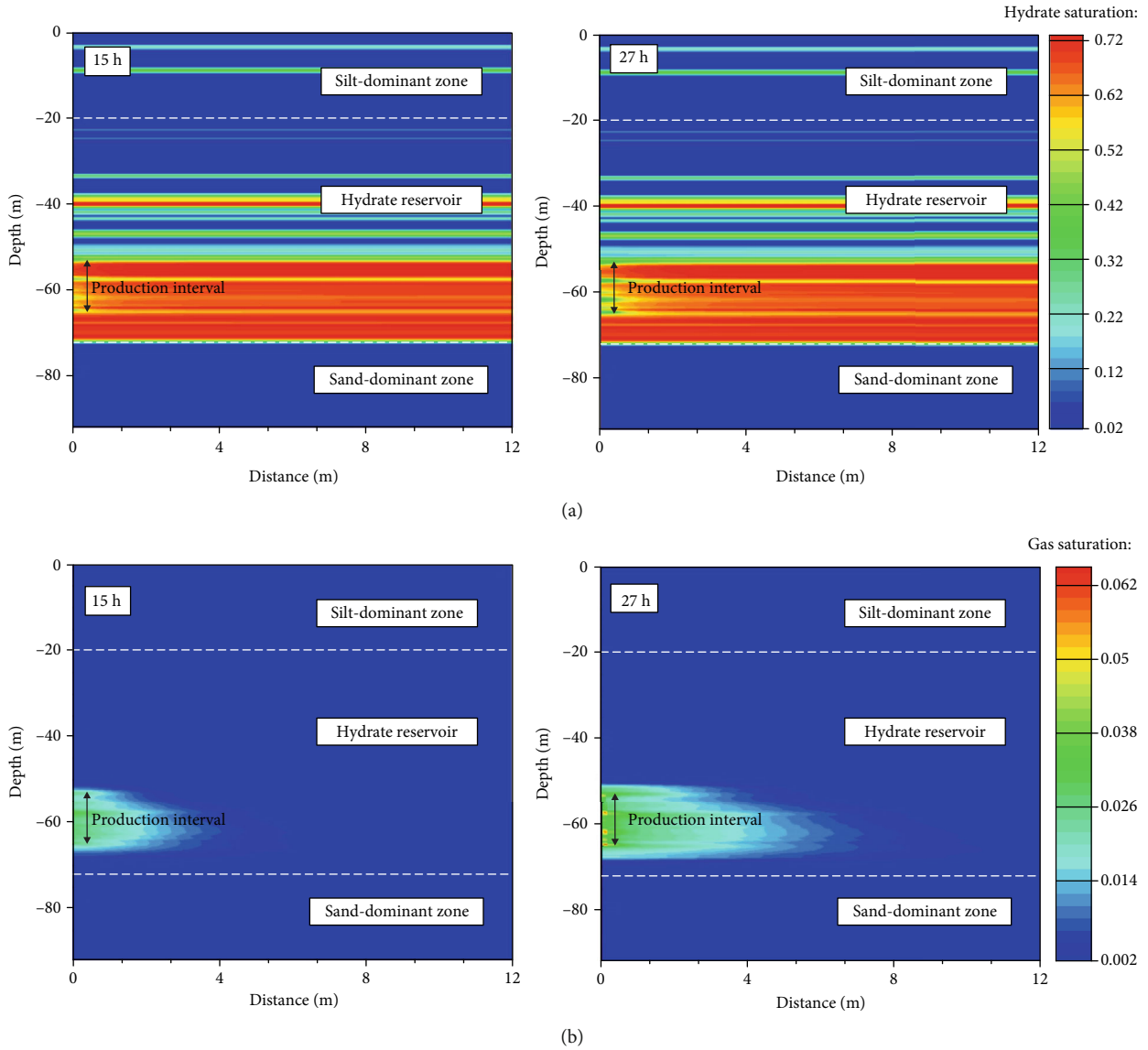


FIGURE 9: Dynamic evolutions of (a) hydrate saturation and (b) gas saturation in the hydrate reservoir at 15th and 27th hours.

TABLE 2: Different design simulation cases related to the location and length of a perforation interval.

Case number	Case 1	Case 2	Case 3	Case 4	Case 5
Location of production interval (m)	53~65	61~73	53~70	53~73	53~75
Length of production interval (m)	12	12	17	20	22
Variable factor	Base case	Location	Length	Length	Length

extended to 10 km away from the production well for the longer production period.

4.2.2. *Gas Release from Hydrate Dissociation.* The hydrate dissociation characteristic reflects the methane-storing capacity of the hydrate reservoir and the real effect of depressurization on the reservoir. Figure 10 indicates the evolutions of (a) simulation-predicted gas release rates (Q_R) and (b) cumulative gas release volumes (V_R) from hydrate dissociation

in different cases of perforation intervals. The Q_R of all cases increases rapidly in the early days, while after that, all the Q_R increases with a decreasing rate and gradually reaches the maximum rate using a constant BHP of 4 MPa. This is mainly because (1) the depressurization results in a significant increase of the hydraulic gradient between the production well and the reservoir initially, which gradually builds balance in the later depressurization stage; (2) there is a significant increase of the dissociation area; and (3) there is a

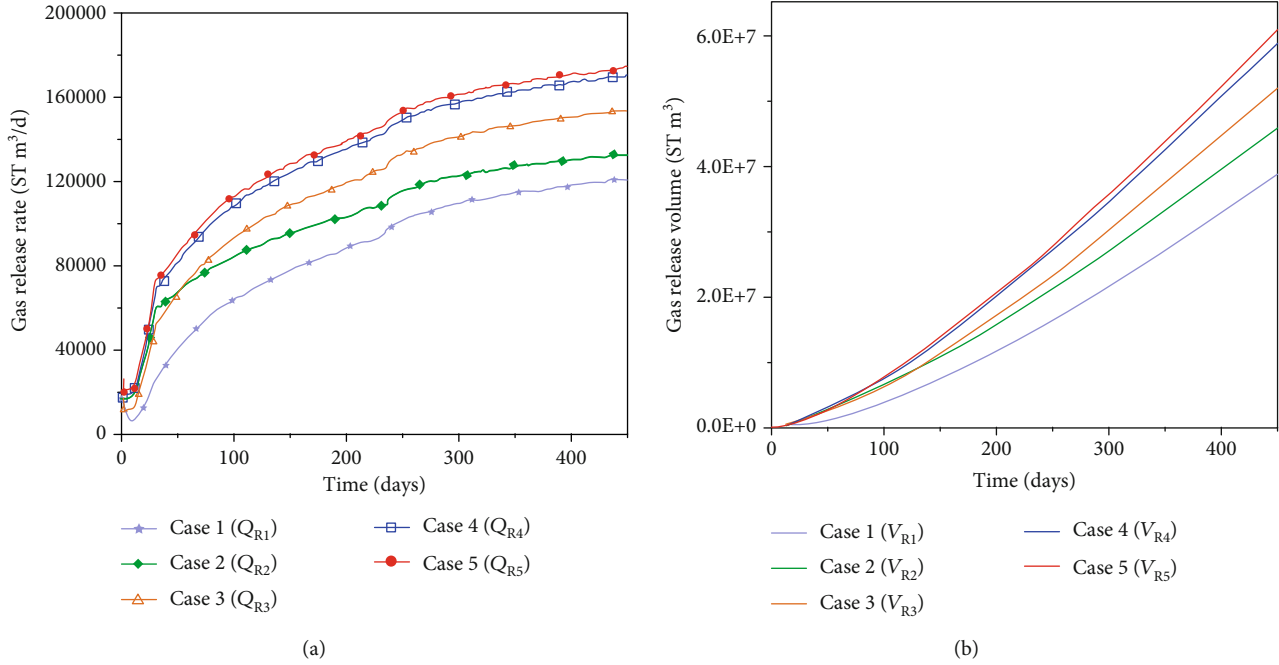


FIGURE 10: Simulated (a) gas release rates and (b) gas release volume from hydrate dissociations in hydrate reservoirs in different cases of perforation intervals for a 450-day period.

decrease of reservoir temperature due to the endothermic effect of hydrate dissociation, which inhibits the rapid dissociation of the hydrate in the reservoir.

For the 450-day depressurization test, the average gas release rates from hydrate dissociation in the five cases are about 8.60×10^4 , 1.02×10^5 , 1.16×10^5 , 1.31×10^5 , and 1.35×10^5 ST m³/d, and the cumulative gas release volumes are 3.87×10^7 , 4.60×10^7 , 5.20×10^7 , 5.90×10^7 , and 6.06×10^7 ST m³, respectively. Compared to Case 1, the V_R in Case 2, Case 3, Case 4, and Case 5 is increased by 19%, 34%, 52%, and 57%.

Obviously, the gas release rate in Case 1 is lower than that of the other cases. This can be explained from two aspects: (1) A lower part of the perforation interval in Case 2 extends to the lower water-saturated zone with high permeability, which significantly enhances the propagation of depressurization in the interface between the hydrate reservoir and the underlying water-saturated zone (i.e., a dominant dissociation interface in this study), and then enlarges the hydrate dissociation zone in a radial direction. The comparison of gas release rates in Case 2 and Case 3 also suggest the effect of a dominant dissociation interface, because the longer perforation interval (17 m in the hydrate reservoir) in Case 3 did not cause more hydrate dissociation than Case 2 (11.5 m in the reservoir and 0.5 m in the underlying aquifer) in the first 60 days. In addition, the higher temperature in the lower part of the reservoir promotes the hydrate dissociation significantly. (2) The longer the perforation length, the larger the contact area between the wellbore and the hydrate reservoir. As a consequence, the area of the hydrate dissociation zone increases obviously with the increase of the length of the perforation interval. It is worth noting that the effective length of the perforation inter-

val (i.e., the length in the hydrate reservoir) is the main factor affecting hydrate dissociation performance, which can be inferred by the comparison results of the gas release rates in Case 3, Case 4, and Case 5.

4.2.3. Gas and Water Production Behaviors. Figure 11 shows evolutions of predicted gas production rates from the wellbore (Q_G) under different locations of perforation intervals. In general, the gas production rates increase rapidly in the initial phase of gas production and then have a speedy decrease. This is mainly due to the struggle between the depressurization and temperature decline caused by the endothermic effect of hydrate dissociation. With the development of gas production, the Q_G tends to be stable gradually. The final (650 days) gas production rates from the wellbore in Case 1 and Case 2 are about 2.18×10^3 and 2.36×10^3 ST m³/d, respectively. Additionally, the 650-day simulated period can be divided into three stages: (1) at Stage 1 (day 0~day 257), the gas production rate of Case 1 is higher than that of Case 2; (2) at Stage 2 (day 258~day 430), the gas production rates of Case 1 and Case 2 are closed; and (3) at Stage 3 (day 431~day 650), the gas production performance of Case 2 gradually surpasses that of Case 1. This is mainly because of the following considerations: (1) In the early depressurization stage, excessive water inflow reduces the gas relative permeability and impedes the horizontal pressure gradient propagation, which restricts gas recovery from the hydrate reservoir in Case 2. However, the high hydrate saturation layer with a thickness of 7.5 m acts as a barrier to the water influx from the underlying aquifer in Case 1. (2) As the passage of time, the barrier sealing the water inflow disappears due to hydrate dissociation, which brings a

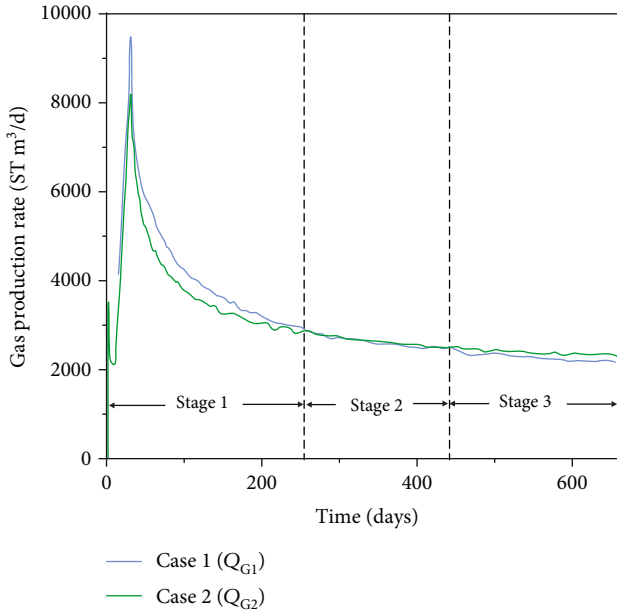


FIGURE 11: Evolutions of predicted gas production rates from a wellbore under different locations of perforation intervals in a 650-day period.

negative effect on the gas production rate in Case 1. Simultaneously, the advantageous hydrate dissociation amount in Case 2 (as Figure 10 depicts) leads to a larger gas production rate.

Figure 12 illustrates the evolutions of predicted gas production rates from a wellbore (Q_G) with different lengths of perforation intervals in a 450-day period. Obviously, the gas production rate increases with the increase of the length of the perforation interval because of the extension of the hydrate dissociation front. In addition, the increment of gas production rates between Case 4 and Case 3 is significantly higher than that between Case 5 and Case 4. This suggests that the overlong perforation interval in the aquifer will cause more water to flow into the reservoir, which will affect the gas production rate. The average (450 days) gas production rates of Case 1, Case 3, Case 4, and Case 5 are about 3.47×10^3 , 4.73×10^3 , 5.44×10^3 , and 5.62×10^3 ST m³/d, respectively.

Figure 13 depicts the predicted cumulative gas production volumes from a wellbore (V_G) in five cases in 365 days and 450 days. The comparison results indicated that V_G increases with the length of the perforation interval, while the moving down of the perforation interval decreases the gas production volume superficially. For the 450-day depressurization test, the length of the perforation interval increases from 12 m to 17 m, 20 m, and 22 m, leading to the V_G increases from 1.56×10^6 to 2.13×10^6 , 2.45×10^6 , and 2.53×10^6 ST m³, increased by 37%, 58%, and 62%, respectively. Hence, the gas production performance can be effectively improved by befittingly increasing the length of the perforation interval in the hydrate reservoir, while in Case 2, the V_G after the 450-day depressurization test is 1.47×10^6 ST m³, which is 0.945 times that in Case 1. The modeling results indicate that the insufficient gas production performance in Case

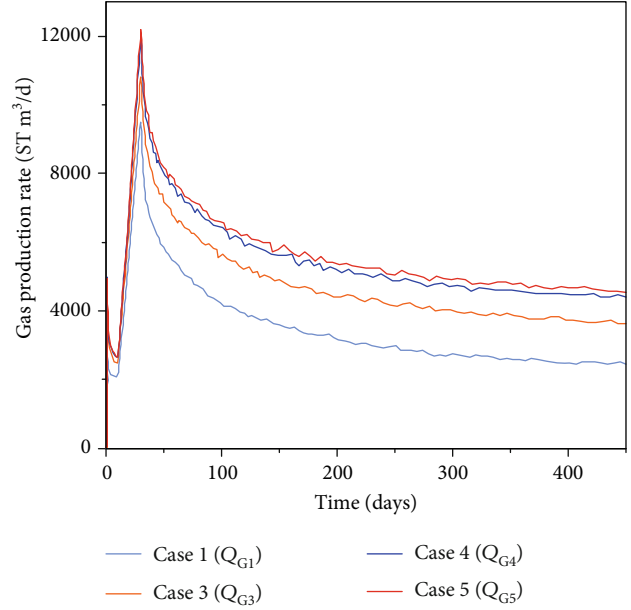


FIGURE 12: Evolutions of predicted gas production rates from a wellbore with different lengths of perforation intervals in a 450-day period.

2 is mainly caused by the restriction of the water influx at the earlier stage.

The ratio of gas production volume to gas release volume is an important reference for evaluating the gas recovery efficiency. Figure 14 depicts the predicted ratios (R_{GR}) of gas production volumes (V_G) to gas release volumes (V_R) in five cases on 365 days and 450 days. Obviously, from 365 days to 450 days, all of the R_{GR} decrease due to the increases of gas release rates and the decreases of gas production rates. Moreover, the R_{GR} in Case 2 is lower than those in others. The comparison results indicated that the R_{GR} slightly increases with the lengthening of the perforation interval. The R_{GR} on 450 days in five cases are 4.01%, 3.19%, 4.10%, 4.15%, and 4.16%, respectively.

Figure 15 depicts the predicted cumulative water production volumes from a wellbore (V_W) in five cases on 365 days and 450 days, respectively. The effect of the perforation interval on water production is similar to that on gas production, except that the value of V_{W2} is larger than V_{W1} . For the 450-day depressurization test, compared to the V_{W1} with a value of 4.81×10^5 m³, the V_W in Case 2, Case 3, Case 4, and Case 5 are 5.64×10^5 , 6.12×10^5 , 6.79×10^5 , and 6.93×10^5 m³, increased by 19.9%, 28.8%, 43.4%, and 46.7%, respectively. Obviously, the increased degree of V_W caused by the lengthening of the perforation interval is lower than that of V_G (i.e., 37%, 58%, and 62% as Figure 13 shows). This is also the evidence that the suitable lengthening of the perforation interval can significantly improve the gas production efficiency. Additionally, from 365 days to 450 days, the gas production volumes in five cases increase with the values of 1.09×10^5 , 1.17×10^5 , 1.33×10^5 , 1.45×10^5 , and 1.47×10^5 m³ (i.e., increased by 29.2%, 26.3%, 27.7%, 27.2%, and 27.0%), respectively.

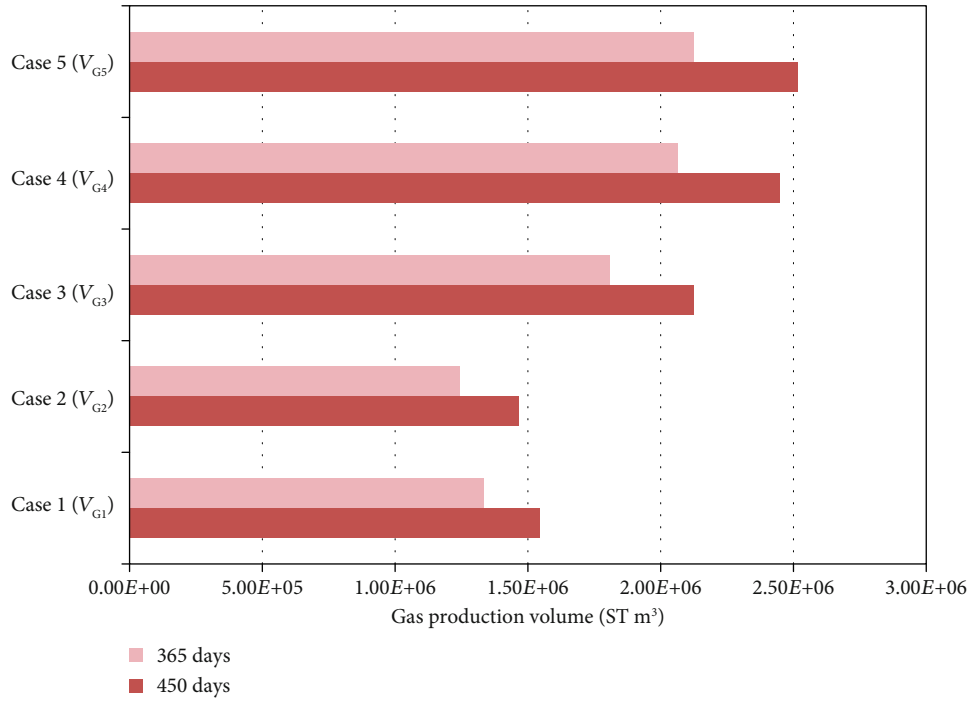


FIGURE 13: Predicted gas production volumes from a wellbore in different cases of perforation intervals on 365 days and 450 days.

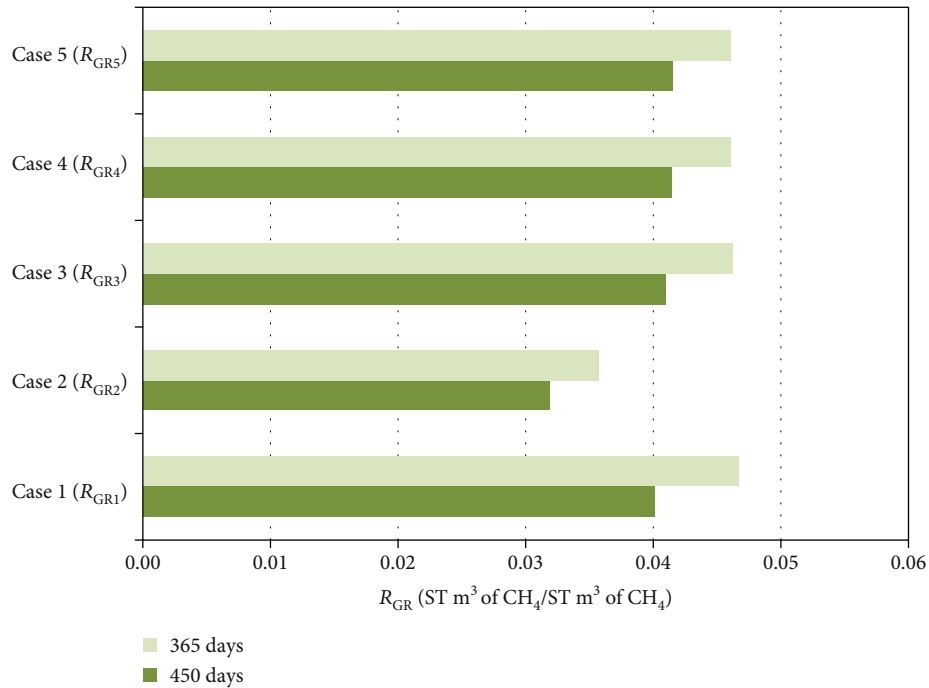


FIGURE 14: Predicted ratios of gas production volumes to gas release volumes in different cases of perforation intervals on 365 days and 450 days.

Figure 16 indicates the evolutions of predicted ratios of gas production volumes to water production volumes (R_{GW}) in different cases for a 450-day period. The significant advantage of Case 1 can be observed in the first 257-day period of gas production, due to the efficient water-sealing

barrier with high hydrate saturation. With the downward extension of the hydrate dissociation front, the R_{GW} in the cases with the longer perforation interval are gradually higher than that of Case 1. In addition, all of the R_{GW} decrease rapidly in the initial phase of gas production, with

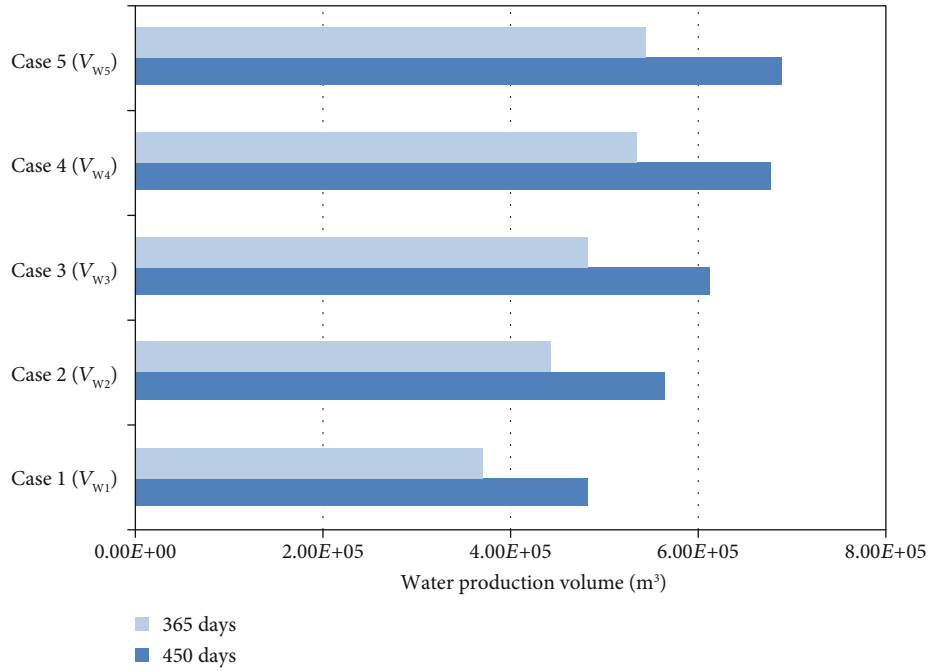


FIGURE 15: Predicted water production volumes from a wellbore in different cases of perforation intervals on 365 days and 450 days.

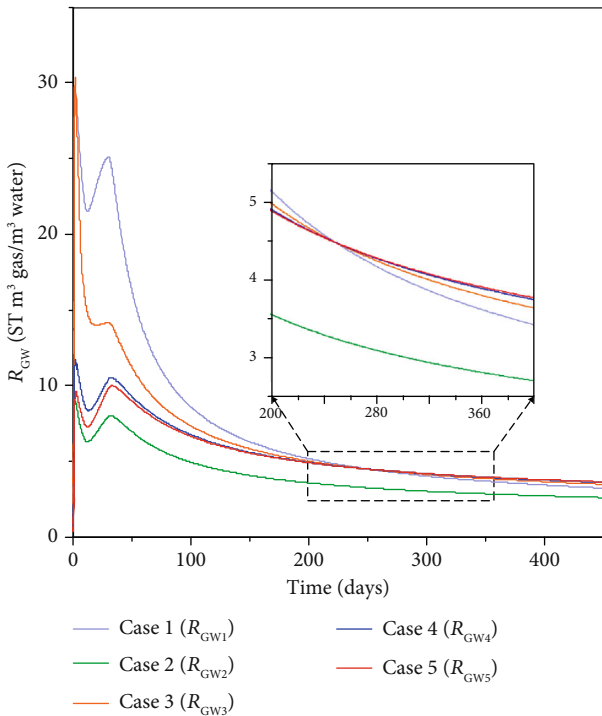


FIGURE 16: Predicted ratios of gas production volumes to water production volumes in different cases of perforation intervals for a 450-day period.

the similar causation to the gas production rate. For a 450-day production period, the average values of R_{GW} in five cases are 12.01, 5.13, 10.47, 6.81, and 6.21.

Based on the comprehensive comparison and analysis of Figures 10–16, the following results are suggested: (1) The

hydrate dissociation behavior can be improved by moving the perforation interval to the interface between the hydrate reservoir and the underlying water-saturated zone, while the gas and water production behaviors are mainly affected by the length of the perforation interval. (2) For short-time gas production, the perforation interval should be set in the high permeability zone of the reservoir with high hydrate saturation, under the presence of a bottom barrier for water influx. However, the advantages of high temperature and an extensive hydrate dissociation front in the dominant dissociation interface should be considered in a long-term gas production test. (3) In the later stage of production, the effect of perforation length on gas production rate is greater than that on water production, which indicates that the proper lengthening of an effective perforation interval can enhance methane gas recovery in both absolute and relative terms.

4.2.4. Reservoir Responses. Figure 17 depicts the dynamic evolutions of the spatial distribution of hydrate saturation in five cases on 30, 100, and 365 days, respectively. In the earlier stage of the depressurization test, the hydrate layer underneath the production interval acting as a barrier for blocking water enters into the production well before being completely dissociated in Case 1 and Case 3, inducing relatively higher values of R_{GW} in a short-time test. However, the area of the hydrate dissociation zone in Case 2 is larger than that in Case 1 with the same length of the perforation interval, because the excellent permeability conditions and rapid depressurization in the interface between the reservoir and the underlying aquifer have been utilized in Case 2. Moreover, the hydrate dissociations are more likely to occur in the lower part of the reservoir, due to the promotion of higher temperature caused by a geothermal gradient. The predicted fronts (only

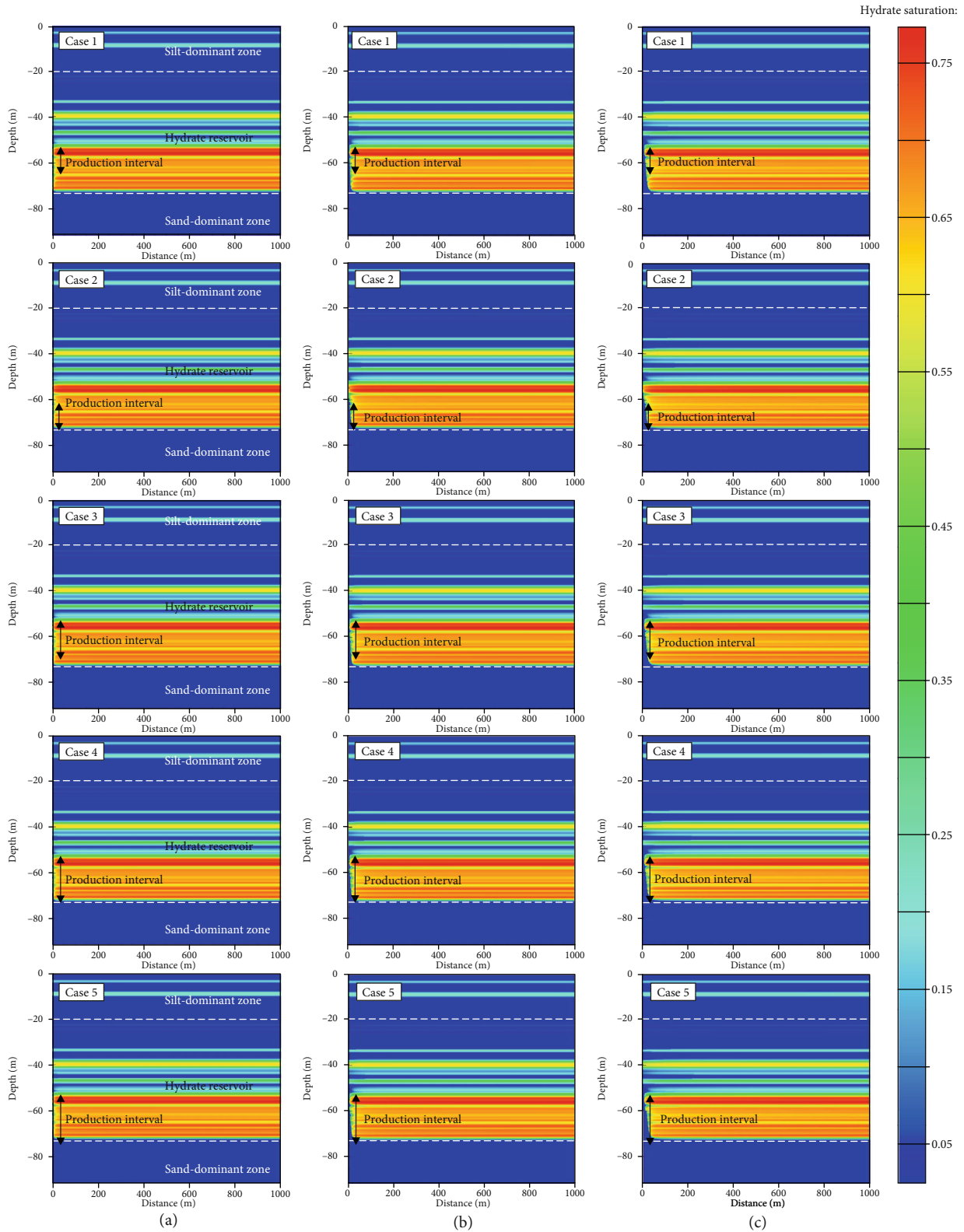


FIGURE 17: Dynamic evolutions of the spatial distribution of hydrate saturation in five cases on (a) 30 days, (b) 100 days, and (c) 365 days, respectively.

consider the fronts paralleling to the production interval) of the dissociation zone in five cases on 365 days are about 350 m, 690 m, 720 m, 950 m, and nearly 1000 m. The spatial

distribution of hydrate saturation confirms the significant impacts of location and length of the perforation interval on hydrate dissociation behavior again.

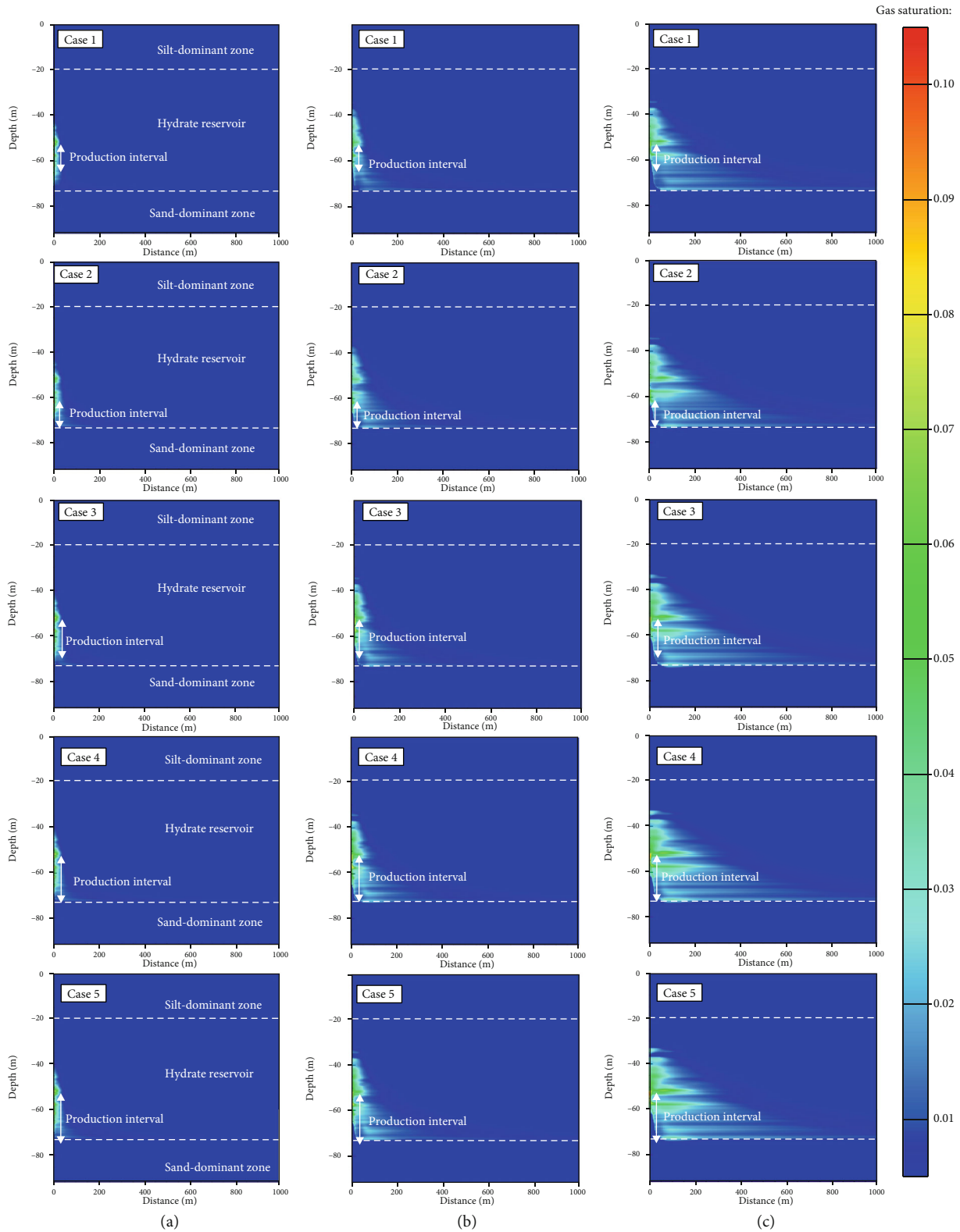


FIGURE 18: Dynamic evolutions of spatial distribution of gas saturation in five cases on (a) 30 days, (b) 100 days, and (c) 365 days, respectively.

Figure 18 depicts the dynamic evolutions of the spatial distribution of gas saturation in five cases on 30, 100, and 365 days, respectively. The occurrence region of free gas gradually expands as the constant depressurization. Obvi-

ously, at the earlier stage of the depressurization test, the free gas mainly concentrates around the production well in Case 1 and Case 3 before hydrates dissociate completely. However, a direct connection between the hydrate reservoir and the

underlying aquifer in Case 2, Case 4, and Case 5 leads to more gas accumulations in the lower part of the reservoir, because there occurs significant hydrate dissociation. Moreover, this situation also occurs in Case 1 and Case 3 after the blocking hydrates dissociate. All the fronts of gas occurrence regions reach the distance of more than 1000 m away from the wellbore in five cases, while the area of the free gas occurrence region is distinctly enlarged by increasing the length of the perforation interval. This also suggests the feasible method to enhance gas recovery by reasonably increasing the length of the perforation interval. In addition, the gas saturation in the upper layer of the production interval is higher than that of the lower zone due to the buoyancy effects.

5. Conclusions

According to the available geological data from the 2L-38 well at the Mallik site, a geologically descriptive hydrate-reservoir model is constructed and validated by the field-measured data in the 2007 test. The dynamic production behaviors during the depressurization test are analyzed in detail. In addition, the effects of the perforation interval (e.g., length and location) on hydrate dissociation and multi-phase flow behaviors have been investigated based on the validated hydrate reservoir model. Some conclusions can be drawn as follows:

- (1) The simulated gas and water production rates from the heterogeneous hydrate reservoir model based on the geological description can match the measured data in the field test considerably well
- (2) The hydrate dissociation front in the reservoir presents a hackly profile due to the alternations of sandy layers and silty layers. And the hydrate dissociation front in the interface between the hydrate reservoir and the underlying water-saturated zone shows preponderance
- (3) The hydrate dissociation behavior is strongly affected by the location and length of the perforation interval. More excellent gas release performance occurs in the situation where the perforation interval is set at the lower zone of the hydrate reservoir. In addition, increasing the length of the perforation interval promotes the hydrate dissociation to a large extent
- (4) The perforation interval is suggested to set at the zone with high hydrate saturation and high permeability before the complete dissociation of hydrates serving as the water blocking barrier. However, the gas production performance in the case where the perforation interval is located at the dominant dissociation interface is more excellent in the later stage of a long-term production test
- (5) The increase of the effective length of the perforation interval can strongly enhance the gas recovery (including the gas release rate and the production rate) from the hydrate reservoir based on both abso-

lute and relative criterions. As the length of the perforation interval increases, compared to the gas release volume, the gas production volume has a relatively higher degree of increase. It indicates the improvement of length increase on gas production efficiency.

Data Availability

The [.dat] data used to support the findings of this study are available from the corresponding author upon request.

Conflicts of Interest

The authors declare that there is no conflict of interest regarding the publication of this paper.

Acknowledgments

This work was supported by the National Program on Key Research and Development Project (No. 2017YFC0307304).

References

- [1] J. Hou, Y. Ji, K. Zhou, Y. Liu, and B. Wei, "Effect of hydrate on permeability in porous media: pore-scale micro-simulation," *International Journal of Heat and Mass Transfer*, vol. 126, pp. 416–424, 2018.
- [2] G. J. Moridis, T. S. Collett, S. R. Dallimore, T. Satoh, S. Hancock, and B. Weatherill, "Numerical studies of gas production from several CH₄ hydrate zones at the Mallik site, Mackenzie Delta, Canada," *Journal of Petroleum Science and Engineering*, vol. 43, no. 3–4, pp. 219–238, 2004.
- [3] K. P. Lijith, B. R. C. Malagar, and D. N. Singh, "A comprehensive review on the geomechanical properties of gas hydrate bearing sediments," *Marine and Petroleum Geology*, vol. 104, pp. 270–285, 2019.
- [4] X.-S. Li, C.-G. Xu, Y. Zhang, X.-K. Ruan, G. Li, and Y. Wang, "Investigation into gas production from natural gas hydrate: a review," *Applied Energy*, vol. 172, pp. 286–322, 2016.
- [5] G. J. Moridis, T. S. Collett, R. Boswell, S. Hancock, and C. Coh, *Gas Hydrates as a Potential Energy Source: State of Knowledge and Challenges*, Springer, New York, 2013.
- [6] J. A. Ripmeester and S. Alavi, "Some current challenges in clathrate hydrate science: nucleation, decomposition and the memory effect," *Current Opinion in Solid State & Materials Science*, vol. 20, no. 6, pp. 344–351, 2016.
- [7] Y. Feng, L. Chen, A. Suzuki et al., "Numerical analysis of gas production from reservoir-scale methane hydrate by depressurization with a horizontal well: the effect of permeability anisotropy," *Marine and Petroleum Geology*, vol. 102, pp. 817–828, 2019.
- [8] L. Liu, X. Lu, and X. Zhang, "A theoretical model for predicting the spatial distribution of gas hydrate dissociation under the combination of depressurization and heating without the discontinuous interface assumption," *Journal of Petroleum Science and Engineering*, vol. 133, pp. 589–601, 2015.
- [9] P. Bhade and J. Phirani, "Gas production from layered methane hydrate reservoirs," *Energy*, vol. 82, pp. 686–696, 2015.
- [10] M. Yu, W. Li, M. Yang, L. Jiang, and Y. Song, "Numerical studies of methane gas production from hydrate decomposition by

- depressurization in porous media,” *Energy Procedia*, vol. 105, pp. 250–255, 2017.
- [11] Z. R. Chong, G. A. Pujar, M. Yang, and P. Linga, “Methane hydrate formation in excess water simulating marine locations and the impact of thermal stimulation on energy recovery,” *Applied Energy*, vol. 177, pp. 409–421, 2016.
 - [12] N. Daraboina, S. Pachitsas, and N. Von Solms, “Experimental validation of kinetic inhibitor strength on natural gas hydrate nucleation,” *Fuel*, vol. 139, pp. 554–560, 2015.
 - [13] C.-G. Xu, J. Cai, Y.-S. Yu, K.-F. Yan, and X.-S. Li, “Effect of pressure on methane recovery from natural gas hydrates by methane-carbon dioxide replacement,” *Applied Energy*, vol. 217, pp. 527–536, 2018.
 - [14] Y. Liu, Y. Bai, Z. Xia, and J. Hou, “Parameter optimization of Depressurization-to-Hot-Water-Flooding in heterogeneous hydrate bearing layers based on the particle swarm optimization algorithm,” *Journal of Natural Gas Science and Engineering*, vol. 53, pp. 403–415, 2018.
 - [15] B. Li, X. S. Li, G. Li, J. C. Feng, and Y. Wang, “Depressurization induced gas production from hydrate deposits with low gas saturation in a pilot-scale hydrate simulator,” *Applied Energy*, vol. 129, pp. 274–286, 2014.
 - [16] Y. Konno, Y. Masuda, Y. Hariguchi, M. Kurihara, and H. Ouchi, “Key factors for depressurization-induced gas production from oceanic methane hydrates,” *Energy & Fuels*, vol. 24, no. 3, pp. 1736–1744, 2010.
 - [17] Y. Feng, L. Chen, A. Suzuki et al., “Enhancement of gas production from methane hydrate reservoirs by the combination of hydraulic fracturing and depressurization method,” *Energy Conversion & Management*, vol. 184, pp. 194–204, 2019.
 - [18] Y. Feng, L. Chen, A. Suzuki et al., “Numerical analysis of gas production from layered methane hydrate reservoirs by depressurization,” *Energy*, vol. 166, pp. 1106–1119, 2019.
 - [19] X. Sun, L. Wang, H. Luo, Y. Song, and Y. Li, “Numerical modeling for the mechanical behavior of marine gas hydrate-bearing sediments during hydrate production by depressurization,” *Journal of Petroleum Science & Engineering*, vol. 177, pp. 971–982, 2019.
 - [20] D. Han, Z. Wang, Y. Song, J. Zhao, and D. Wang, “Numerical analysis of depressurization production of natural gas hydrate from different lithology oceanic reservoirs with isotropic and anisotropic permeability,” *Journal of Natural Gas Science and Engineering*, vol. 46, pp. 575–591, 2017.
 - [21] M. Zhou, K. Soga, K. Yamamoto, and H. Huang, “Geomechanical responses during depressurization of hydrate-bearing sediment formation over a long methane gas production period,” *Geomechanics for Energy and the Environment*, vol. 23, article 100111, 2018.
 - [22] M. Kurihara, K. Funatsu, and H. Ouchi, “Analyses of production tests and MDT tests conducted in Mallik and Alaska methane hydrate reservoirs: what can we learn from these well tests?,” in *Proceedings from the 6th International Conference of Gas Hydrates*, Vancouver, British Columbia, CANADA, 2008.
 - [23] T. Yu, G. Guan, and A. Abudula, “Production performance and numerical investigation of the 2017 offshore methane hydrate production test in the Nankai Trough of Japan,” *Applied Energy*, vol. 251, article 113338, 2019.
 - [24] T. Fujii, K. Suzuki, T. Takayama et al., “Geological setting and characterization of a methane hydrate reservoir distributed at the first offshore production test site on the Daini-Atsumi Knoll in the eastern Nankai Trough, Japan,” *Marine and Petroleum Geology*, vol. 66, pp. 310–322, 2015.
 - [25] J. F. Li, J. L. Ye, X. W. Qin et al., “The first offshore natural gas hydrate production test in South China Sea,” *China Geology*, vol. 1, no. 1, pp. 5–16, 2018.
 - [26] G. J. Moridis, “Numerical studies of gas production from class 2 and class 3 hydrate accumulations at the Mallik site, Mackenzie Delta, Canada,” *SPE Reservoir Evaluation & Engineering*, vol. 7, no. 3, pp. 175–183, 2013.
 - [27] G. J. Moridis and M. T. Reagan, “Estimating the upper limit of gas production from class 2 hydrate accumulations in the permafrost: 2. Alternative well designs and sensitivity analysis,” *Journal of Petroleum Science & Engineering*, vol. 76, no. 3–4, pp. 124–137, 2011.
 - [28] G. J. Moridis, M. T. Reagan, K. L. Boyle, and K. Zhang, “Evaluation of the gas production potential of some particularly challenging types of oceanic hydrate deposits,” *Transport in Porous Media*, vol. 90, no. 1, pp. 269–299, 2011.
 - [29] Y. Konno, T. Fujii, A. Sato et al., “Key findings of the world’s first offshore methane hydrate production test off the coast of Japan: toward future commercial production,” *Energy & Fuels*, vol. 31, no. 3, pp. 2607–2616, 2017.
 - [30] Y. Yuan, T. Xu, X. Xin, and Y. Xia, “Multiphase flow behavior of layered methane hydrate reservoir induced by gas production,” *Geofluids*, vol. 2017, Article ID 7851031, 15 pages, 2017.
 - [31] J. Sun, F. Ning, L. Zhang et al., “Numerical simulation on gas production from hydrate reservoir at the 1st offshore test site in the eastern Nankai Trough,” *Journal of Natural Gas Science & Engineering*, vol. 30, pp. 64–76, 2016.
 - [32] M. Uddin, J. F. Wright, S. R. Dallimore, and D. Coombe, “Gas hydrate production from the Mallik reservoir: numerical history matching and long-term production forecasting,” in *Geological Survey of Canada*, pp. 261–289, Canada GSo, 2012.
 - [33] M. Uddin, F. Wright, S. Dallimore, and D. Coombe, “Gas hydrate dissociations in Mallik hydrate bearing zones A, B, and C by depressurization: effect of salinity and hydration number in hydrate dissociation,” *Journal of Natural Gas Science & Engineering*, vol. 21, pp. 40–63, 2014.
 - [34] Z. Su, Y. Cao, N. Wu, and Y. He, “Numerical analysis on gas production efficiency from hydrate deposits by thermal stimulation: application to the Shenhu Area, South China Sea,” *Energies*, vol. 4, no. 2, pp. 294–313, 2011.
 - [35] M. Yang, Z. Fu, Y. Zhao, L. Jiang, J. Zhao, and Y. Song, “Effect of depressurization pressure on methane recovery from hydrate-gas-water bearing sediments,” *Fuel*, vol. 166, pp. 419–426, 2016.
 - [36] G. Jin, T. Xu, X. Xin, M. Wei, and C. Liu, “Numerical evaluation of the methane production from unconfined gas hydrate-bearing sediment by thermal stimulation and depressurization in Shenhu area, South China Sea,” *Journal of Natural Gas Science & Engineering*, vol. 33, pp. 497–508, 2016.
 - [37] B. Wang, H. Dong, Y. Liu et al., “Evaluation of thermal stimulation on gas production from depressurized methane hydrate deposits,” *Applied Energy*, vol. 227, pp. 710–718, 2018.
 - [38] B. Wang, Z. Fan, J. Zhao, X. Lv, W. Pang, and Q. Li, “Influence of intrinsic permeability of reservoir rocks on gas recovery from hydrate deposits via a combined depressurization and thermal stimulation approach,” *Applied Energy*, vol. 229, pp. 858–871, 2018.
 - [39] J. Sun, F. Ning, H. Lei et al., “Wellbore stability analysis during drilling through marine gas hydrate-bearing sediments in

- Shenhu area: a case study,” *Journal of Petroleum Science and Engineering*, vol. 170, pp. 345–367, 2018.
- [40] J. Sun, F. Ning, T. Liu et al., “Gas production from a silty hydrate reservoir in the South China Sea using hydraulic fracturing: a numerical simulation,” *Energy Science & Engineering*, vol. 7, pp. 1106–1122, 2019.
- [41] Y. Yuan, T. Xu, Y. Xia, and X. Xin, “Evaluation of gas productivity from layered heterogeneity methane hydrate reservoirs by depressurisation,” in *Offshore Technology Conference Asia*, Kuala Lumpur, Malaysia, 2018.
- [42] E. M. Myshakin, B. J. Anderson, K. Rose, and R. Boswell, “Simulations of variable bottomhole pressure regimes to improve production from the double-unit Mount Elbert, Milne Point Unit, North Slope Alaska hydrate deposit,” *Energy & Fuels*, vol. 25, no. 3, pp. 1077–1091, 2011.
- [43] G. Bellefleur, M. Riedel, T. Brent, F. Wright, and S. R. Dallimore, “Implication of seismic attenuation for gas hydrate resource characterization, Mallik, Mackenzie Delta, Canada,” *Journal of Geophysical Research*, vol. 112, no. B10, 2007.
- [44] J. W. Huang, G. Bellefleur, and B. Milkereit, “Seismic modeling of multidimensional heterogeneity scales of Mallik gas hydrate reservoirs, Northwest Territories of Canada,” *Journal of Geophysical Research*, vol. 114, no. B7, 2009.
- [45] G. Guerin and D. Goldberg, “Sonic waveform attenuation in gas hydrate-bearing sediments from the Mallik 2L-38 research well, Mackenzie Delta, Canada,” *Journal of Geophysical Research*, vol. 107, no. B5, 2002.
- [46] T. Collett, J. J. Bahk, M. Frye et al., *Historical Methane Hydrate Project Review*, Consortium for Ocean Leadership, 2013.
- [47] G. Bellefleur, M. Riedel, and T. Brent, *Seismic Characterization and Continuity Analysis of Gas Hydrate Horizons near the Mallik Research Wells, Mackenzie Delta, Canada*, Agu Fall Meeting, 2005.
- [48] M. Kurihara, K. Funatsu, and H. Ouchi, “Analysis of the JOGMEC/NRCAN/AURORA Mallik gas hydrate production test through numerical simulation,” in *Proceedings of the 6th International Conference on Gas Hydrates, Vancouver, Canada*, Vancouver, British Columbia, Canada, July 2008.
- [49] M. Kurihara, “Analysis of 2007/2008 JOGMEC/NRCAN/AURORA Mallik gas hydrate production test through numerical simulation,” in *Proceedings of the 7th International Conference on Gas Hydrates, Edinburgh, Scotland, United Kingdom*, Edinburgh, Scotland, United Kingdom, 2011.
- [50] T. Fujii, S. Noguchi, D. R. Murray et al., “Overview of wireline-logging analysis in the Aurora/JOGMEC/NRCAN Mallik 2L-38 gas hydrate production research well,” in *Geological Survey of Canada*, pp. 125–140, Canada GSo, 2012.
- [51] J. Dvorkin and R. Uden, “Seismic wave attenuation in a methane hydrate reservoir,” *The Leading Edge*, vol. 23, no. 8, pp. 730–732, 2004.
- [52] W. J. Winters, S. R. Dallimore, T. S. Collett et al., “Relation between gas hydrate and physical properties at the Mallik 2L-38 research well in the Mackenzie Delta,” *Annals of the New York Academy of Sciences*, vol. 912, no. 1, pp. 94–100, 2000.
- [53] G. E. Archie, “The electrical resistivity log as an aid in determining some reservoir characteristics,” *Transactions of the AIME*, vol. 146, no. 1, pp. 54–62, 1942.
- [54] T. Fujii, S. Noguchi, D. R. Murray et al., *Overview of Wireline-Logging Analysis in the JOGMEC/NRCAN/Aurora Mallik 2L-38 Gas Hydrate Production-Test Well*, Scientific results from the JOGMEC/NRCAN/Aurora Mallik 2008, 2007.
- [55] M. B. Kowalsky and G. J. Moridis, “Comparison of kinetic and equilibrium reaction models in simulating gas hydrate behavior in porous media,” *Energy Conversion & Management*, vol. 48, no. 6, pp. 1850–1863, 2007.
- [56] G. J. Moridis, *User’s Manual for the Hydrate v1.5 Option of TOUGH+ v1.5: A Code for the Simulation of System Behavior in Hydrate-Bearing Geologic Media*, LBNL-6869E: Lawrence Berkeley National Laboratory, 2014.